Characterization of Minerals, Metals, and Materials 2015

Edited by

John S. Carpenter
Chenguang Bai
Juan Pablo Escobedo
Jiann-Yang Hwang
Shadia Ikhmayies
Bowen Li
Jian Li
Sergio Neves Monteiro
Zhiwei Peng
Mingming Zhang

TMS

WILEY

Characterization of Minerals, Metals, and Materials 2015

Cover Images: Scanning electron microscopy images of voids in DC04 steel prepared by ion slope cutting (Front) and of the fracture surface of a DC04 tensile test specimen (Back). For further information please refer to the article entitled 'Comparison of the Mechanisms of Void Formation by Plastic Deformation in Single and Dual Phase BCC Steels' by G. Gerstein, H.-B. Besserer, F. Nürnberger, and H. J. Maier of the Leibniz Universität Hannover.

Characterization of Minerals, Metals, and Materials 2015

Proceedings of a symposium sponsored by
the Materials Characterization Committee of
the Extraction and Processing Division of
The Minerals, Metals & Materials Society (TMS)
held during

TMS2015
144th Annual Meeting & Exhibition
March 15-19, 2015
Walt Disney World • Orlando, Florida, USA

Edited by
John S. Carpenter
Chenguang Bai
Juan Pablo Escobedo
Jiann-Yang Hwang
Shadia Ikhmayies
Bowen Li
Jian Li
Sergio Neves Monteiro
Zhiwei Peng
Mingming Zhang

WILEY | TMS

Published by John Wiley & Sons, Inc., Hoboken, New Jersey.
Published simultaneously in Canada.

Library of Congress Cataloging-in-Publication Data is available.

ISBN 978-1-119-08246-0

Printed in the United States of America.

10 9 8 7 6 5 4 3 2 1

WILEY | TMS

TABLE OF CONTENTS
Characterization of Minerals, Metals, and Materials 2015

Characterization of Ferrous Metals

Characterization of Welding and Solidification

Method Development in Characterization

Characterization of Material Processing and Corrosion

Characterization of Composites

Characterization of Non-Ferrous Metals

Characterization of Materials Extraction

Characterization of Soft Materials

Characterization of Minerals

Characterization of Clays and Ceramics

Characterization of Electronic, Magnetic, Environmental, and Advanced Materials

Poster Session

PREFACE

The relationships between processing, microstructure, and properties form the basis for the materials science field. Characterization is a critical step along the pathway of discovery in understanding these relationships. This collection of proceedings covers the use of characterization across the entire life cycle of materials, from extraction to processing to utilization to recycling. In addition, the breadth of this volume is meant to cover characterization across the spectrum of science and engineering consistent with technology or manufacturing readiness levels from one to nine. This will serve the dual purpose of furnishing a broad introduction of the field to novices while simultaneously serving to keep subject matter experts up-to-date.

The Materials Characterization Committee of TMS sponsors a symposium on Characterization of Minerals, Metals, and Materials as a major event during the annual TMS meeting. The 2015 symposium held in Orlando, Florida, USA received more than 250 submissions and is expected to have 109 oral presentations and 127 poster presentations. Of these presentations, more than 100 accompanying papers were accepted for publication in this book after a peer review process. The Characterization of Minerals, Metals, and Materials symposium at TMS is not only one of the largest and most broad symposia in terms of scientific coverage but in speaker participation as well. Twenty-three countries will be represented by the presenters with speakers from Africa, Asia, Europe, the Middle East, Australia, South America, Central America, and North America.

Manuscripts included within this volume will include characterization studies on materials such as ferrous metal, non-ferrous metal, clay, ceramic, composite, polymeric, electronic, magnetic, environmental and advanced materials. Also included are papers related to the characterization of welding, solidification, processing, corrosion, and extraction of materials. Various characterization technologies are developed and utilized throughout this volume to solve current problems in materials science. Although sections in this book are generally divided among material (e.g., minerals vs. soft materials) or processing step lines (e.g., welding vs. extraction), the editors entreat the readers to view the entire book as potentially being of use in providing applicable solutions across the entire spectrum of materials.

The editors of this book are very grateful to the authors of the included papers. Their willingness to share their scientific endeavors and knowledge are critical to the passing and advancing of knowledge in this field. In addition, they are grateful to the publisher, Wiley, for their help in producing an aesthetically pleasing volume. The editors would also like to express gratitude to TMS for providing the Materials Characterization Committee with the opportunity to publish a stand-alone volume

which illustrates the importance and interest level in materials characterization. Finally, they would like to thank all past members and chairs of the committee for their desire to serve the greater materials science community through the sacrifice of their time and talents.

John S. Carpenter
Chenguang Bai
Juan Pablo Escobedo
Jiann-Yang Hwang
Shadia Ikhmayies
Bowen Li
Jian Li
Sergio Neves Monteiro
Zhiwei Peng
Mingming Zhang

EDITORS

John S. Carpenter is a technical staff member in the Materials Science and Technology Division at the Los Alamos National Laboratory. Dr. Carpenter received his Ph.D. in Materials Science and Engineering from The Ohio State University in 2010 after performing his undergraduate studies at Virginia Tech.

His research interests include the characterization, processing, and mechanical testing of metallic nanocomposites fabricated via severe plastic deformation as well as additive manufacturing. Currently, his work focuses on understanding the relationship between plastic strain, texture, and the mechanical properties of bimetallic nanocomposites fabricated via accumulative roll bonding and joined using friction stir processing. This research involves the use of several characterization techniques including neutron scattering, x-ray synchrotron, PED, TEM, EBSD, and SEM. Mechanical testing for this work includes methods such as micropillar compression, microtension, and nanoindentation. He has 28 peer-reviewed journal publications, 1 book chapter, and 16 invited technical talks to his credit.

With regard to TMS service, Dr. Carpenter currently serves as both the chair for the Materials Characterization committee and as the vice chair for the Advanced Characterization, Testing and Simulation committee. He is also a participating member of the Mechanical Behavior of Materials and the Nanomechanical Behavior committees. He serves as a Key Reader for *Metallurgical and Materials Transactions A* and has co-edited special sections in *JOM* related to neutron characterization and coherent x-ray diffraction imaging methods for materials studies. He is the 2012 recipient of the Young Leaders Professional Development award for the Extraction & Processing Division of TMS. Dr. Carpenter was also awarded an honorable mention for the 2012 Los Alamos National Laboratory Postdoctoral Distinguished Performance Award.

Chenguang Bai is a Professor in the Department of Metallurgical Engineering, School of Materials Science and Engineering, at Chongqing University, China. He is also the Vice Chairman of University Council, Vice Chairman of Chongqing Society for Metals, Member of Advisory Committee of Experts, Department of Engineering and Materials Science, NSFC.

Dr. Bai received his B.S. degree from Chongqing University in 1982, M.S. in 1987 and Ph.D. in 2003. He also furthered his study in University of Toronto as a visiting scholar between October 1995 and January 1997. Dr. Bai has been actively involved in the teaching and scientific research works in ferrous metallurgy, especially in the field of comprehensive utilization of vanadium-titanium magnetite resources. He has more than 15 patents and has published nearly 180 research articles, about 40 of which were in the international metallurgical periodicals.

Juan Pablo Escobedo is currently a Lecturer in the School of Engineering and Information Technology at UNSW Australia at the Australian Defence Force Academy. He obtained his doctoral degree in Mechanical Engineering at Washington State University (WSU). Prior to taking up this academic appointment he held research positions at the Institute for Shock Physics (WSU) and Los Alamos National Laboratory. In 2014 he was a recipient of a Young Leader Professional Development Award by the TMS Structural Materials Division.

His main research interests center on the dynamic behavior of materials under extreme conditions, in particular high pressure and high strain rate. His focus has been on investigating the effects of microstructural features on the dynamic fracture behavior of metals and metallic alloys.

Jiann-Yang (Jim) Hwang is a Professor in the Department of Materials Science and Engineering at Michigan Technological University. He is also the Chief Energy and Environment Advisor of the Wuhan Iron and Steel Group Company. He has been the Editor-in-Chief of the *Journal of Minerals and Materials Characterization and Engineering* since 2002. Several universities have honored him as a guest professor, including the Central South University, University of Science and Technology Beijing, Chongqing University, and Kunming University of Science and Technology.

Dr. Hwang received his B.S. degree from National Cheng Kung University in 1974 and his M.S. in 1980 and Ph.D. in 1982, both from Purdue University. He joined Michigan Technological University in 1984 and has served as its Director of the Institute of Materials Processing from 1992 to 2011. He has been a TMS member since 1985. His research interests include the characterization and processing of materials and their applications. He has been actively involved in the areas of separation technologies, pyrometallurgy, microwaves, hydrogen storages, ceramics, recycling, water treatment, environmental protection, biomaterials, and energy and fuels. He has more than 20 patents, published more than 200 papers, and founded several companies. He has chaired the Materials Characterization committee and the Pyrometallurgy committee in TMS and has organized several symposia.

Shadia Ikhmayies received a B.Sc. from the physics department in the University of Jordan in 1983, a M.Sc. in molecular physics from the same university in 1987, and a Ph.D. in producing CdS/CdTe thin film solar cells from the same university in 2002. She worked in the Applied Science University in Jordan and now she works in Al Isra University in Jordan as an associate professor. Her research is focused on producing and characterizing semiconductor thin films, thin film bilayers, and thin film CdS/CdTe solar cells. Besides, she works in characterizing quartz in Jordan for the extraction of silicon for solar cells and characterizing different materials (NbN and doped Si) by computation. She has published 32 research papers in

international scientific journals, 3 chapters in books, and 49 research papers in conference proceedings.

Dr. Ikhmayies is a member of the Jordanian Renewable Energy Society (JRES), the Minerals, Metals & Materials Society (TMS), and the World Renewable Energy Network (WREN), where she became a member of the steering committee in 2014. She was an associate editor for the journal Physics Express (Simplex Academic Publishers). She is an associate editor for the journal *Peak Journal of Physical and Environmental Science Research* (PJPESR) (Peak Journals). She is a member of the editorial board of the *International Journal of Materials and Chemistry* (Scientific & Academic Publishing), the editor in chief of the book *Advances in the II-VI Compounds Suitable for Solar Cell Applications* (Research Signpost/ Transworld Research Network). She was the technical advisor/subject editor for *JOM* as a representative of the Materials Characterization Committee for the year 2014. Dr. Ikhmayies is a reviewer in 21 international journals and was an organizer and session chair for a number of international conferences.

Bowen Li is a Research Associate Professor in the Department of Materials Science and Engineering and Institute of Materials Processing at Michigan Technological University. His research interests include materials characterization, metals extraction, ceramic processing, antimicrobial additives, and applied mineralogy. He has over 80 publications and 12 patents. He received a Ph.D. in Mineralogy and Petrology from China University of Geosciences Beijing in 1998, and a Ph.D. in Materials Science and Engineering from Michigan Technological University in 2008. Dr. Li has been a TMS member since 2005, and has served as a member in Materials Characterization Committee, Powder Materials Committee, Biomaterials Committee, and EPD Award committee, and has been a *JOM* Subject Advisor.

Jian Li is a research scientist at CanmetMATERIALS in Natural Resources Canada. He has broad experience in materials processing and characterization including alloy deformation, recrystallization, micro-texture development, coating, and high temperature corrosion. Dr. Li also has extensive experience in developing advanced Focused Ion Beam (FIB) microscope techniques in materials science. He holds a patent, has authored three book chapters, and has published more than 100 technical papers in scientific journals and conference proceedings.

Sergio Neves Monteiro graduated as metallurgical engineer in 1966 from the Federal University of Rio de Janeiro (UFRJ). He received his M.Sc. in 1967 and Ph.D. in 1972 from the University of Florida, followed by a course 1975 in Energy at the Brazilian War College and Post-doctorate in 1976 at the University of Stuttgart. He joined the Metallurgy Department and in 1977 became a full professor of the post-graduation program in engineering (COPPE) of the UFRJ. He was elected head of department in 1978, coordinator of COPPE in 1982 and Under-Rector for Research in 1983. He was invited as Under-Secretary of Science for the State of Rio de Janeiro (1985) and Under-Secretary of College Education for the Federal Government (1989). He retired in 1993 from the UFRJ and joined the State University of North Rio de Janeiro (UENF), from where he retired in 2012. He is now Professor at the Military Institute of Engineering (IME), Rio de Janeiro.

Monteiro has published over 1,200 articles in journals and conference proceedings and has been honored with several awards including the ASM Fellowship. He is presently top researcher (1A) of the Brazilian Council for Scientific and Technological Development (CNPq) and Top Scientist of State of Rio de Janeiro (FAPERJ). In 2012, he was president of the Superior Council of the State of Rio de Janeiro Research Foundation, FAPERJ, and he is currently coordinator of the Engineering Area of this Foundation. He has been consultant for the main Brazilian R&D agencies and member of the editorial board of five international journals as well as associate editor of the *Journal of Materials Research and Technology*.

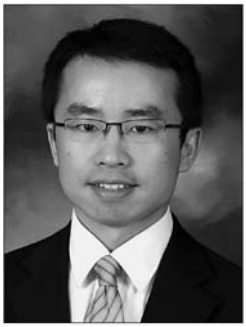

Zhiwei Peng is a Research Assistant Professor in the Department of Materials Science and Engineering at Michigan Technological University and a new faculty member at Central South University. He received his B.E. and M.S. degrees from Central South University in 2005 and 2008, respectively, and his Ph.D. degree in Materials Science and Engineering from Michigan Technological University in 2012. His research interests include heat transfer in microwave heating, dielectric characterization of materials, non-thermal microwave effects, extractive metallurgy, computational electromagnetics, and microwave absorbing materials.

He has published over 40 papers, including 23 peer-reviewed articles in multiple journals such as *International Materials Reviews*, *Metallurgical and Materials Transactions A*, *JOM*, *Journal of Power Sources*, *Energy & Fuels*, *IEEE Transactions on Magnetics*, *IEEE Transactions on Instrumentation and Measurement*, *Ceramics International*, *ISIJ International*, and *Applied Physics Express*. He has served as a reviewer for a number of journals and been on the editorial board of the *Journal of Minerals and Materials Characterization and Engineering* since 2012. He received a TMS Travel Grant Award for the 141st TMS Annual Meeting & Exhibition, the Doctoral Finishing Fellowship Dean's Award for Outstanding Scholarship of Michigan Technological University in 2012, and the Bhakta Rath Research Award of Michigan Technological University in 2013. He is a member of The Minerals, Metals & Materials Society (TMS), The Institute of Electrical and Electronics Engineers (IEEE), ASM International (ASM), and The Association for Iron and Steel Technology (AIST).

Dr. Peng is an active and passionate member of TMS. He has co-organized three TMS symposia (Characterization of Minerals, Metals and Materials in 2013, 2014, and 2015) and co-chaired eight TMS symposium sessions since 2012. He is a member of the Pyrometallurgy and Materials Characterization Committees, a *JOM* advisor for the Pyrometallurgy Committee, and a winner of the TMS EPD Young Leader Professional Development Award in 2014.

Mingming Zhang is currently a senior research engineer at ArcelorMittal Global R&D at East Chicago, Indiana. He is in charge of raw material characterization and process efficiency improvement in mineral processing and ironmaking areas. He also leads technical relationships and research consortia with university and independent laboratory members and manages a pilot pot-grate sintering test facility at ArcelorMittal Global R&D East Chicago. Dr. Zhang has over 15 years of research experience in the field of mineral processing, metallurgical and materials engineering. He obtained his Ph.D. degree in Metallurgical Engineering from The University of Alabama and his Master degree in mineral processing from General Research Institute for Non-ferrous Metals in China. Prior to joining ArcelorMittal, he worked with Nucor Steel Tuscaloosa, Alabama where he was metallurgical engineer leading the development of computer model for simulating slab solidification and secondary cooling process.

He has conducted a number of research projects sponsored by federal and private funding involving mineral beneficiation, thermodynamics and kinetics of metallurgical reactions, electrochemical processing of light metals, energy efficient and environmental cleaner technologies. He has published over 30 peer-reviewed research papers and he is the recipient of several U.S. and Chinese patents. Dr. Zhang also serves as editor and reviewer for a number of prestigious journals. These include *Metallurgical and Materials Transactions B*, *Journal of Phase Equilibria and Diffusion*, *Mineral Processing and Extractive Metallurgy*, and *Journal of Thermal Science and Engineering Applications*. Dr. Zhang has made more than 20 research presentations at national and international conferences including more than 10 keynote presentations. He has been invited to a number of international conference committee gatherings to serve as organizer and committee member. These conferences include 2011 International Manufacturing Science and Engineering Conference (MSEC), 2010 International Heat Transfer Conference (IHTC), and 2009 US-EU-China Thermophysics Conference - Renewable Energy (UECTC-RE).

SESSION CHAIRS

Characterization of Ferrous Metals
Tonya Stone
Jiann-Yang Hwang

Characterization of Welding and Solidification
Pasquale Russo Spena
Dhriti Bhattacharyya

Method Development in Characterization
John S. Carpenter
Jian Li

Characterization of Material Processing and Corrosion
Wenjing Li
Florian Nurnberger

Characterization of Composites
Frederico Margem
Jean Margem

Characterization of Non-Ferrous Metals
Juan Pablo Escobedo
Sreeramamurthy Ankem

Characterization of Materials Extraction
Sabriye Piskin
Simona Murph

Characterization of Soft Materials
Brian Patterson
Sergio Neves Monteiro

Characterization of Minerals
Bowen Li
Zhiwei Peng

Characterization of Clays and Ceramics
Robert Blair
Afonso Azevedo

Characterization of Electronic, Magnetic, Environmental, and Advanced Materials
Shadia Ikhmayies
Walman Castro

Characterization of Minerals, Metals, and Materials 2015

Characterization of Ferrous Metals

Session Chairs:
Tonya Stone
Jiann-Yang Hwang

Characterization of Minerals, Metals, and Materials 2015
Edited by: John S. Carpenter, Chenguang Bai, Juan Pablo Escobedo, Jiann-Yang Hwang, Shadia Ikhmayies, Bowen Li, Jian Li, Sergio Neves Monteiro, Zhiwei Peng, and Mingming Zhang
TMS (The Minerals, Metals & Materials Society), 2015

STUDY OF AGE HARDENING BEHAVIOR IN A 350 GRADE MARAGING STEEL

Leandro Gomes de Carvalho[1], Ronald Lesley Plaut[1], Marcelo de Aquino Martorano[1], Angelo Fernando Padilha[1]

[1]School of Engineering of the University of São Paulo; Avenida Professor Mello Moraes 2463; São Paulo, São Paulo, 05508-030, Brazil

Keywords: maraging steels, age hardening, precipitation, overaging.

Abstract

The age hardening behavior in the 480-600 °C temperature range was studied in maraging steel 350. The age hardening at 480, 520, and 560 °C was modeled by an equation derived from the Johnson-Mehl-Avrami-Kolmogorov (JMAK) model, while the overaging stage at 520, 560, and 600 °C was examined using a model based on the Orowan mechanism and on the Pardal model. The results show that the model based on JMAK for the early aging stages has good fitting with the experimental data in the 480-560 °C range. Furthermore, the precipitation seems to occur in two stages at 480 °C. In addition, the model based on the Orowan mechanism and on the Pardal model has good fitting at 520 and 560 °C, but the Pardal model fitting is better than that of Orowan at 600 °C. This behavior is due to the reversion of martensite, which becomes significant when the temperature increases.

Introduction

Maraging steels are low carbon martensitic steels that are hardened by precipitation of intermetallic phases when they are submitted to aging treatment [1,2]. Commercial maraging steels are usually iron-nickel-cobalt alloys with molybdenum, titanium and aluminum additions [1,2], commonly used in aerospace and nuclear technologies [2-4]. The lath martensite of maraging steels formed during quenching has a supersaturated matrix of alloying elements containing high density of crystalline defects, mainly dislocations [2].

Previous works showed that the precipitation in maraging steels is a complex phase transformation, involving the formation of several intermetallic phases during aging [5,6]. At temperatures below 450 °C, S, μ, and X phases are formed, while at temperatures above 450 °C, $Ni_3(Ti,Mo)$ and Fe_2Mo are formed [5,6]. At even larger temperatures, e.g., above 500 °C, both $Ni_3(Ti,Mo)$ dissolution and Fe_2Mo precipitation causes austenite nucleation owing to nickel enrichment of the matrix [7-9].

Age hardening of maraging steels has been studied by several authors [10-15]. These studies showed that maraging steels have a one-peak typical age hardening curve: a strengthening stage and a softening one [10-13]. Strengthening is attributed to the precipitation hardening caused by ordered phases, coherent with the matrix [4,9-12], while softening is due to a change in the precipitation hardening mechanism (Orowan mechanism) or to the martensite to austenite reversion [8,11,12]. In the present work, the models commonly applied to the age hardening of maraging steels are used to describe the experimental results obtained during the age hardening of a maraging steel 350 in the 480-600 °C range.

Materials and Methods

Samples were prepared by cutting disks of 10 mm thickness from 350 maraging steel bars of 140-mm diameter, supplied in the solution annealed condition. The chemical composition of the bars is given in Table 1.

Table 1: Chemical composition (% wt) of the 350 maraging steel bars.

Ni	Co	Mo	Ti	Al	S*	C*	O*	N*
18.16	11.92	4.81	1.22	0.074	30	30	8	2.0

*in ppm

This disk was cut into samples of approximately 5 mm x 10 mm x 10 mm for aging experiments. Each sample was aged at 480, 520, 560, and 600 ºC for different times from 0.1 to 18 hours in a muffle furnace. Furthermore, Vickers hardness measurements were carried out using a Zwick hardness tester with a 1 kgf load and dwell time of 20s. Fifteen measurements were made in each sample.

Results and Discussion

Figures 1 and 2 show the hardness of the sample as a function of time, illustrating the kinetics of aging at 480, 520, 560 and 600 °C. The time to the hardness peak depends on the aging temperature. Pardal et al. and Viswanathan et al. observed that this time depends on thermally activated processes in maraging steels and follows an Arrhenius model [11,14].

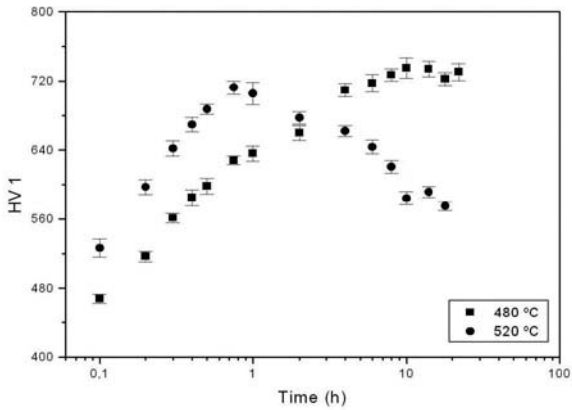

Figure 1: Kinetics of aging at 480 and 520 °C.

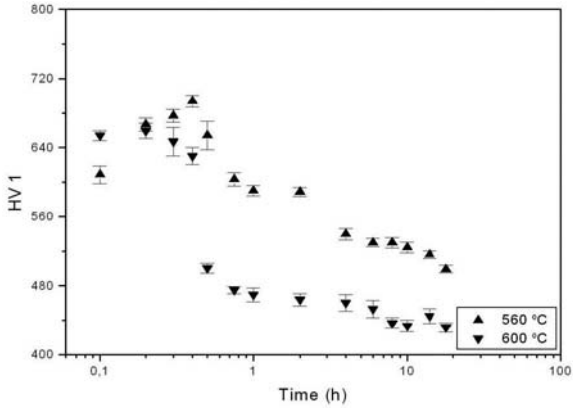

Figure 2: Kinetics of aging at 560 and 600 °C.

Wilson proposed a model for the early stage of aging based on the JMAK model and on the strengthening due to shearing of precipitates by dislocations [12,13], which is described by the following equation:

$$\Delta H = (kt)^n \quad (1)$$

where ΔH is the increment of hardness, and k and n are temperature-dependent constants. In 1962, Floreen and Decker also proposed a similar equation for the variation in hardness with aging time using an empirical aproach [15]. Constants k and n were calculated by fitting Eq. (1) to the experimental results given in Figures 1 and 2. Their values for different temperatures and time ranges are presented in Table 2. The resulting model curves are shown in Figure 3, compared with the experimental results.

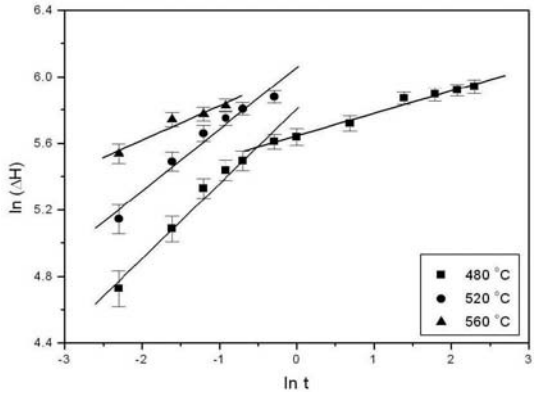

Figure 3: Hardening model curves based on the JMAK equation and experimental results (dots) for the samples aging at 480, 520, and 560 °C.

Table 2: Values of n and k constants of the hardening model based on the JMAK equation obtained in the present work (350 maraging steel) and those presented by Pardal et al. [11] and Sha [12] (300 maraging steel). The correlation coefficient of the fitting, R, is also given.

Reference	Temperature (°C)	Time range	n	K (h^{-1})	R
Pardal et al. [11]	440	0.25 h – 10 h	0.20 ± 0.02	1.3 x 10^{11}	0.97
Pardal et al. [11]	480	0.25 h – 2.0 h	0.20 ± 0.01	5.0 x 10^{11}	0.99
This work	480	0.1 h – 0.75 h	0.49 ± 0.03	1.5 x 10^{5}	0.99
This work	480	0.75 h – 10 h	0.14 ± 0.01	1.4 x 10^{18}	0.99
Pardal et al. [11]	510	0.25 h – 2.0 h	0.21 ± 0.02	3.9 x 10^{11}	0.99
Sha [12]	510	160 s – 25 min	0.29	3.1 x 10^{8}	0.95*
This work	520	0.1 h – 1 h	0.37 ± 0.03	1.2 x 10^{7}	0.98
Pardal et al.[11]	560	0.25 h – 0.75 h	0.16 ± 0.01	1.7 x 10^{15}	0.99
This work	560	0.1 h – 0.4 h	0.21 ± 0.03	5.6 x 10^{12}	0.99

*R^2

Visual examination of the fitting in Figure 3 and the correlation coefficient, R, in Table 2 show that the model based on JMAK for the early aging stages has good fitting with the experimental data between 480 and 560 °C. However, it was observed in Figure 3 that the precipitation behavior at 480°C should be divided into two stages, which is probably a result of the formation of several intermetallic phases at different times during the aging period [5].

The n values obtained in this work for the temperature of 480 °C were 0.49 ± 0.03 in the first stage and 0.14 ± 0.01 in the second stage. Pardal et al. suggested that this behavior can occur in a maraging steel 300 at 440 °C, where the parameter n for the first and the second stages were 0.29 ± 0.01 and 0.12 ± 0.01, respectively [11]. Table 2 also shows that the k and n values presented by Sha to describe the aging of the 300 maraging steel at 520 °C agree more closely than those suggested by Pardal et al. [11,12]. In addition, n > 0.25 was observed for aging times shorter

than approximately 1 h at 480 and 520 °C, while $n < 0.25$ was verified for aging times longer than 1 h at 480 °C, 520 °C or 560 °C.

Wilson also designed an equation for overaging based on the Orowan mechanism expressed by [12-14]:

$$\Delta H^{-3} = \Delta H_0^{-3} + M.(t-t_0) \quad (2)$$

where ΔH is the diference between the hardness of the overaged sample and the solution annealed one, M is the temperature-dependent rate constant, t_0 is the time at peak hardness, and ΔH_0 is the increment in hardness at the beginning of coarsening time t_0. Figure 4 shows the curves calculated with Eq. (2), compared with the experimental results of ΔH^{-3} as a function of aging time at 520, 560, and 600 °C. In Table 3, the fitting coefficients M and ΔH_0 obtained in the present work (350 maraging steel) are also compared with those presented by Pardal et al. for a 300 maraging steel.

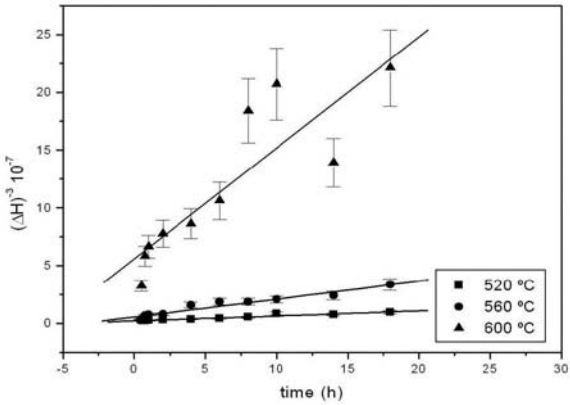

Figure 4: Curves calculated using an Orowan-mechanism based model compared with experimental results (dots) of ΔH^{-3} as a function of time for the softening during overaging at 520, 560, and 600 °C.

Table 3: Comparison of the ΔH_0, t_0, and M values of the softening model based on the Orowan mechanism obtained in the present work (350 maraging steel) and those presented by Pardal et al. (300 maraging steel) [11] at 520, 560 and 600 °C. The correlation coefficient, R, of the fitting process is also given.

Reference	Temperature (°C)	M	ΔH_0	t_0 (h)	R
This work	520	4.32×10^{-9}	344 ± 20	0.75	0.96
Pardal et al. [11]	560	4.57×10^{-9}	253	0.75	0.99
This work	560	1.55×10^{-8}	255 ± 16	0.4	0.97
Pardal et al. [11]	600	1.30×10^{-8}	184	0.2	0.91
This work	600	9.61×10^{-8}	120 ± 11	0.2	0.87

The model based on the Orowan mechanism agrees well with experimental results at 520 and 560 °. Furthermore, the fitting at 600 °C is worse, which might be a result of the reversion of martensite, which occurs more expressively when the aging temperature increases [9,11].
Pardal et al. also proposed the following empirical model to describe the change in hardness with aging time during overaging:

$$H = H_1.t^p \quad (3)$$

where H is the hardness value, t is the aging time, H_1 is the hardness value at t = 1 h and p is the time exponent. Figure 5 shows the fit of the Pardal model to the experimental results of the 350 maraging steel, while Table 4 gives a comparison between the fitting constants H_1 and p, indicating that Pardal model has good fitting at 520, 560, and 600 °C. The fitting is better than that for the model based on the Orowan mechanism at 600 °C.

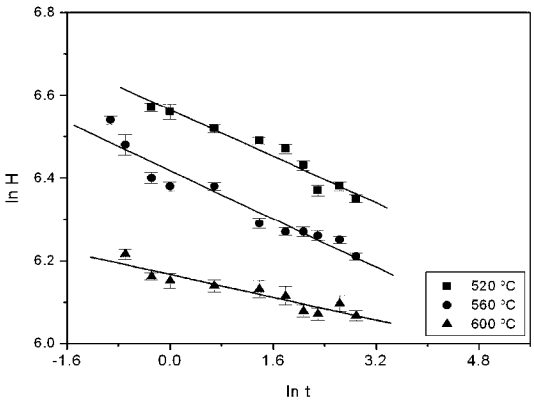

Figure 5: Pardal model for softening during overaging at 520, 560 and 600 °C.

Table 4: Comparison of the p and H_1 values of the Pardal model for different maraging steels at 520, 560, 600 and 650 °C.

Reference	Temperature (°C)	p	H_1	R
This work	520	-0.070	710 ± 9	0.97
Pardal et al.[11] (maraging 300)	560	-0.053	594.3	0.99
This work (maraging 350)	560	-0.073	613 ± 7	0.96
Pardal et al.[11] (maraging 300)	600	-0.054	523.3	0.99
This work (maraging 350)	600	-0.034	476 ± 4	0.94
Pardal et al. [11] (maraging 300)	650	-0.061	428.8	0.99

Conclusion

From the above observations and analysis, we concluded that:

1) The results indicated that hardness measurements can be very helpful to study age hardening behavior in maraging steels.

2) The results showed that the model based on JMAK for the early aging stages agrees well with experimental data in the range between 480 and 560 °C. At 480 °C, precipitation seems to occur in two stages.

3) The Pardal model and the model based on the Orowan mechanism show good fitting to experimental results during aging at 520 and 560 °C, but better agreement is observed with Pardal model at 600 °C. This behavior is probably due to the reversion of martensite, which is significant when the temperature increases.

Acknowledgements

The authors are grateful to the University of São Paulo for providing the experimental facilities, to CTMSP for the materials and to CNPq for the financial support.

References

[1] M. N. Rao, "Progress in understanding the metallurgy of 18% nickel maraging steels", *International Journal of Materials Research*, 97 (11) (2006), 1594-1607.
[2] M. Schmidt, K. Rohrbach. "Heat treatment of maraging steels". Metals Handbook, vol. 1 (Materials Park: ASM International, 1990), 219-228.
[3] G. S. Avadhani, "Optimization of process parameters for manufacturing of rocket casings: A study using processing maps", *Journal of Materials Engineering and Performance*, 12 (6) (2003), 609-622.
[4] L.G.de Carvalho, M. S. Andrade, R. L. Plaut, A. F. Padilha," A dilatometric study of the phase transformations in 300 and 350 maraging steels during continuous heating rates", *Materials Research*, 16 (4) (2013), 740-744.
[5] R. Tewari, S. Mazumder, I. S. Batra, G. K. Dey, S.Banerjee. "Precipitation in 18wt% Ni maraging steel of grade 350", *Acta Materalia*, 48 (2000), 1187-1200.
[6] W. Sha, A. Cerezo, G. D. Smith. "Phase chemistry and precipitation reactions in maraging steels: Part IV. Discussion and Conclusions", *Metallurgical Transactions A*, 24 (1993), 1251-1256.
[7] X. Li, Z. Yin, "Reverted austenite during aging in 18Ni (350) maraging steel", *Materials Letters*, 24 (4) (1995), 239-242.
[8] U. K. Viswanathan, G. K. Dey, V. Sethumandhavan, "Effects of austenite reversion during overageing on the mechanical properties of 18Ni (350) maraging steel", *Materials Science and Engineering A*, 398 (2005), 367-372.
[9] J. M. Pardal, S. S. M. Tavares, M. P. C. Fonseca, H. F. G. Abreu, J. J. M. Silva, " Study of the austenite quantification by X-ray diffraction in the 18Ni-Co-Mo-Ti maraging 300 steel", *Journal of Materials Science*, 41 (2006), 2301-2307.
[10] Z. Guo, W. Sha, "Quantification of precipitation hardening and evolution of precipitates", *Materials Transactions*, 43 (2002), 1273-1282.

[11] J. M. Pardal, S. S. M. Tavares, V. F Terra, M. R. da Silva, D. R. dos Santos, "Modelling of precipitation hardening during the aging and overaging of 18Ni-Co-Mo-Ti maraging 300 steel", *Journal of Alloys and Compounds*, 393 (2005), 109-113.
[12] W. Sha, "Quantification of age hardening in maraging steels and an Ni-base superalloy", *Scripta Materialia*, 42 (2000), 549-553.
[13] E. A. Wilson, "Quantification of age hardening in an Fe-12Ni-6Mn alloy", *Scripta Materialia*, 36 (1997), 1179-1185.
[14] U. K Viswanathan, G. K. Dey, M. K. Asundi, "Precipitation hardening in 350 grade maraging steel", *Metallurgical Transactions A*, 24 (1993), 2429-2442.
[15] S. Floreen, R. F. Decker, "Heat treatment of 18% Ni maraging steel", *Transaction of the American Society for Metals*, 55 (1962), 58-76.

Characterization of Minerals, Metals, and Materials 2015

Characterization of Welding and Solidification

Session Chairs:

Pasquale Russo Spena

Dhriti Bhattacharyya

Characterization of Minerals, Metals, and Materials 2015
Edited by: John S. Carpenter, Chenguang Bai, Juan Pablo Escobedo, Jiann-Yang Hwang, Shadia Ikhmayies, Bowen Li, Jian Li, Sergio Neves Monteiro, Zhiwei Peng, and Mingming Zhang
TMS (The Minerals, Metals & Materials Society), 2015

LASER WELDING BETWEEN TWIP STEELS AND AUTOMOTIVE HIGH-STRENGTH STEELS

Pasquale Russo Spena[1], Matteo Rossini[1], Luca Cortese[1], Paolo Matteis[2], Giorgio Scavino[2], Donato Firrao[2]

[1]Free University of Bozen-Bolzano, Faculty of Science and Technology;
Piazza Università 5; Bolzano, 39100, Italy
[2]Politecnico di Torino, Department of Applied Science and Technology;
Corso Duca degli Abruzzi 24; Torino, 10129, Italy

Keywords: high strength steels, laser welding, dissimilar steel joining, microstructure, mechanical properties, fracture

Abstract

Car-bodies are increasingly made with advanced high-strength steels in order to reduce weight and improve passenger safety. High-manganese austenitic steels have been recently proposed for such an application, due to their excellent combination of strength and toughness. However, a widespread usage of these steels in the automotive industry is conditional on the development of effective welding methods to join high-Mn steels with other steel grades employed for adjacent car-body parts. Therefore, dissimilar laser welding, without any filler metal, between a high-Mn austenitic sheet steel and some high strength steel grades, frequently employed in the fabrication of car body parts, are examined here. The weldments are characterized by means of metallography, tensile and microhardness tests. Fractographic examination was carried out on the fracture surfaces of the tensile samples.

Introduction

In recent years, automotive manufacturers are coping with environmental pollution and more restrictive environmental regulations. To tackle both these issues, car makers are increasingly employing advanced high strength steels (AHSS) and high strength steels (HSS) to reduce vehicles weight and, hence, fuel consumption. Currently, AHSS and HSS mainly comprise Dual Phase (DP), TRansformation Induced Plasticity (TRIP), and hot stamping boron steel grades. They are used for the fabrication of components obtained by sheet forming, such as B-pillar, reinforcement and bumper bars.
Research activity is mainly focused on the development of new AHSS with improved mechanical strength with the preservation, or improvement, of ductility [1-3]. The increase in strength enables car manufacturers to reduce the overall weight of vehicles, whereas improved ductility enhances crashworthiness capability. New high manganese AHSS (Mn usually ranges from 15 to 25 wt. %), known as TWIP, have been recently proposed for the fabrication of car body-in-white, due to their excellent combination of strength and ductility. These steels exhibit a remarkable combination of mechanical strength and ductility because of the formation of mechanical twins during plastic deformation. Mechanical twins are responsible for high strain hardening, thus preventing necking and maintaining a very high strain capacity. Tensile strengths higher than 1000 MPa and elongation at fractures larger than 50% are usually obtained [4-5].
A widespread usage of TWIP steels in automotive industry is conditional on proper welding operation to assemble car body components. The mechanical properties and ductility of dissimilar welded steel sheet depend considerably on the heating, melting, and solidification

stages during the welding process. Therefore, welding input parameters play a very significant role in integrity and quality of a weld joint [6-9]. Studies concerning arc welding of TWIP steel grades with other HSS and AHSS have shown that the significant thermal energy involved in the welding process badly influence the joint quality. Indeed, welding cracks, significant chemical segregations in the fusion zone, and poor mechanical properties are usually found in weld seams [7, 10-11]. The use of proper metal fillers (usually austenitic steel grades) are recommended to avoid the formation of extensive regions of hard and brittle martensite in the fusion zone, and to promote, instead, the formation of a ductile austenitic microstructure [7]. The use of laser welding, which notably reduces the thermal energy involved in the welding process, might reduce the occurrence of the abovementioned issues.
Therefore, in the framework of a large campaign on the introduction of advanced high strength steels in car body design and fabrication, it was decided to investigate the mechanical response of dissimilar butt joints between high carbon TWIP steels and commercial hot stamping boron (22MnB5) steels, DP and TRIP steels, obtained by Nd-YAG laser welding. Dissimilar butt joints between the DP steel and 22MnB5 or TRIP steels have also been examined for comparison. Optical microscopy and Vickers microhardness measurements have been also used to detect the metallurgical constituents of the microstructures encountered in the fusion zone, the heat affected zone (HAZ), and the base material. Thereafter, a series of tensile specimens, cut perpendicularly to the welding line, have been mechanically tested, their rupture surfaces being thereafter subjected to fractographic SEM examination.

Materials and experimental procedure

TWIP steel is a Fe-C-Mn alloy produced on industrial scale by continuous casting, hot and cold rolling, and continuous annealing. The employed sheets were 1.6 (±0.05) mm thick. Hot stamping 22MnB5 steel sheets were received in the as-fabricated condition, i.e. with a ferritic-pearlitic microstructure, as a 1.5 (±0.05) mm thick sheet; they were heat treated before welding in order to simulate industrial hot-stamping. To do this, the sheets were austenitized at 900 °C for 4 min and then press quenched to room temperature in a mold with flat faces. The DP and the TRIP steel consisted of commercial metal sheets with a thickness of 0.8 and 1.1 (±0.05) mm, respectively. The examined steels chemical composition is listed in Table 1.

Table I. Chemical composition (wt. %) of the examined steels. P+S<0.03% in all cases.

Steel	C	Si	Mn	Cr	Mo	Al	Ti	B
TWIP	0.66	0.20	23.4	0.13	0.12	0.038	-	0.0021
22MnB5	0.25	0.23	1.30	0.13	-	0.036	0.039	0.0047
DP	0.09	0.21	1.65	0.43	-	0.030	0.003	-
TRIP	0.23	1.50	1.90	0.03	0.01	0.052	0.007	0.0022

Dissimilar butt-joints of TWIP steels with the other steel grades, i.e. TWIP/DP, TWIP/22MnB, TWIP/TRIP combination, were produced by laser welding using an anthropomorphic industrial robot. TWIP/TWIP joints and dissimilar butt-joints DP/TRIP and DP/22MnB5 were produced by the same welding process for comparison. During welding the sheet edges were in direct contact and the sheet faces were aligned on the side opposite to the welding torch. A shielding gas (nitrogen), which flowed coaxially in the welding torch with a flow of 10 l/s, was used to protect the weld seams from environmental contaminants. During the welding tests, the laser power ranged from 1.25 to 1.5 kW (depending on the sheets thicknesses), the laser torch speed was 25 mm/s, and the focus of the laser beam was 1 mm above the surface of the sheets. No filler metal was used during the welding operations. Full weld penetration was achieved in all cases.

Optical microscopy was performed on metallographic cross-section of the welded joints, after nital etching. Microhardness line profiles were carried out on the same samples, with 100 g load, perpendicularly to the weld seam, in order to evaluate the mechanical inhomogeneity arising from the microstructures occurring after the welding process. Flat tensile specimens, cut in the direction perpendicular to the weld seams, were tested by a servohydraulic testing system under 0.2 mm/s actuator displacement control. Ultimate tensile strength was calculated by considering either the original cross section of the fracture region, or the average cross section of the two sides if the fracture occurred in the weld seam. Elongation to fracture was calculated by considering the actuator displacement and the estimated length of the deformed region (120 mm). The fracture surfaces were then examined by optical and scanning electron microscopy.

Results and discussion

Microstructure

The TWIP steel exhibits a fully austenitic microstructure with a homogeneous 5 μm grain size, (Figure 1). The 22MnB5 steel exhibits a homogenous martensitic microstructure, which is consistent with the prior laboratory heat treatment. The DP steel shows the typical ferrite-martensite microstructure; the martensite is homogeneously distributed in the ferrite matrix with about 15% volume fraction. The TRIP steel exhibits a ferrite-martensite-austenite microstructure.

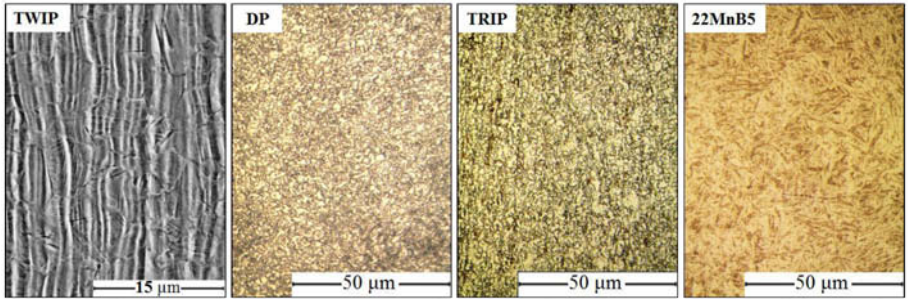

Figure 1. Microstructure of the TWIP, DP, and TRIP steels in the as-received conditions, and of the 22MnB5 steel after the laboratory heat treatment.

The microstructure of the TWIP/TWIP joint does not change after the welding process; it always consists of an austenitic phase both in the fusion zone and the HAZ. The microstructure exhibits a dendritic morphology in the fusion zone, and grain coarsening in the HAZ. No microstructural changes can be revealed beyond 0.1 mm from the border of the fusion zone.
The microstructure of the fusion zone of all dissimilar joints mainly consists of martensite, Figure 2.
Regardless of the type of dissimilar joint, the microstructure of the HAZ of the 22MnB5, DP, and TRIP steels are similar and are described hereafter. Close to the fusion zone, where the steel was fully austenitized during the welding process, the microstructure is completely martensitic, (Figure 3). Further away, the amount of martensite decreases and ferrite zones appear due to the lower cooling rates. Finally, in the HAZ region close to the base metal, which was not austenitized during the welding process, the original martensite underwent a subcritical tempering, and the original austenite in the TRIP steels transformed into martensite.

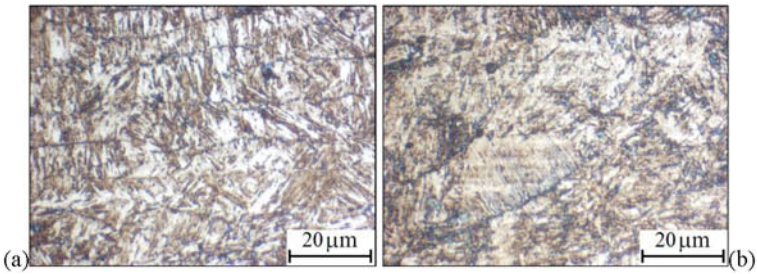

Figure 2. Microstructure of the fusion zone of the TWIP/DP (a) and DP/TRIP (b) joints.

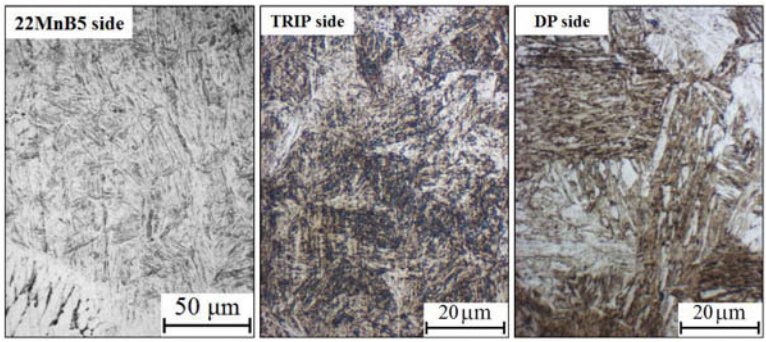

Figure 3. Microstructure of the HAZ of the 22MnB5, DP and TRIP steels, adjacent to the fusion zone of dissimilar TWIP welded joints.

Microhardness

The microhardness line profiles, through selected weld seams, are shown in Figure 4. The Vickers hardness of TWIP steel is about 250 HV30 due to the fully austenitic microstructure. The hardness of the 22MnB5 is 480 HV30, which is attributed to the preliminary press quenching that promotes the formation of a fully martensitic microstructure. DP and TRIP steels exhibit a hardness around 260 and 240 HV30, respectively. Regardless of the dissimilar welding counterpart, the HAZ of the TWIP steel exhibits a microhardness slightly lower than the base material (about 230 HV0.1), due to the softening and coarsening of the austenitic grains during the welding process. Regardless of the type of dissimilar joint, the fusion zone of the weldments exhibits a hardness always higher than 400 HV0.1, which is attributed to the fully martensite microstructure present in this region; in particular, the maximum hardness is found in the fusion zone of dissimilar joints between the TWIP steel and one low-alloy steel, probably due to the higher carbon content of the TWIP steel.. Overall, the DP side exhibits in the HAZ a maximum hardness of about 435 HV0.1 close to the fusion zone, which is attributed to a full austenitization of the steel followed by the martensitic transformation. Moving away from the fusion zone, the hardness gradually reduces up to that of the base material. A similar trend of the hardness profile is obtained in the TRIP side, due to the similar microstructure (except for the occurrence of small amount of austenite) and metallurgical phase transformation that occurred during the welding process.

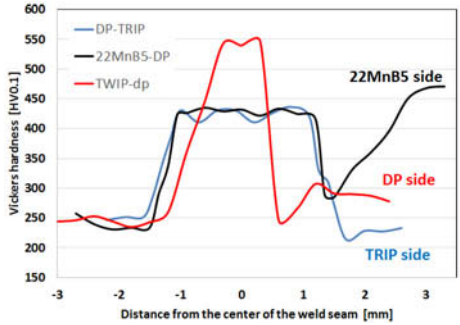

Figure 4. Vickers microhardness profile across the weldments.

The softening of the microstructure of the DP and TRIP steel in the HAZ close to the base material is attributed to the subcritical tempering of the original martensitic microstructure. At the 22MnB5 side in DP/22MnB5 joints, the HAZ consists of fully martensite close to the fusion zone, and of tempered martensite close to the base material. The extension of the tempered martensite region is more pronounced in the 22MnB5 steel in respect to the DP and TRIP steel, which is due to the larger amount of martensite in the initial microstructures.

Tensile tests

Results of the tensile tests carried out on the specimens before and after the laser welding are listed in Table II.

Table II. Tensile properties of the examined steels and welded joints, and fracture region of the welded joints. The UTS was calculated from the mean sheet thickness if the fracture was in the Fusion Zone (FZ), and from the thickness of the fracture region otherwise.

Steel	YS [MPa]	UTS [MPa]	e_f [%]	Fracture region
TWIP	460	1005	45	-
22MnB5	1050	1440	5	-
DP	470	690	19	-
TRIP	455	860	26	-
TWIP/TWIP	-	850	25	FZ
TWIP/22MnB5	-	620	3	FZ
TWIP/DP	-	410	0.5	FZ
TWIP/TRIP	-	500	1	FZ
DP/22MnB5	-	875	18	DP side
DP/TRIP	-	850	22	DP side

Unwelded TWIP steel exhibits a yield stress similar to the DP and TRIP steels, even though the tensile strength and the elongation to fracture are much larger. The 22MnB5 steel shows the highest yield stress and tensile strength, but the lowest elongation to fracture.
Regardless of the nature of the steels, the yield point of the welded samples was triggered by the sheet side that first reached yield strength, as the weld seams were more resistant.
The dissimilar butt joints of the TWIP steel failed along the weld seam exhibiting poor mechanical properties. Indeed, the latter joints experienced very low plastic deformations (less than 3%) and notably lower ultimate tensile strengths in respect to the parent steels. This clearly

indicates that the mechanical behavior of these welded joints is mainly affected by the microstructure of the fusion zone, which consists of martensite.
The butt joint TWIP/TWIP steel also failed in the fusion zone; however, the reduction in tensile strength is more limited (about 15%) in respect to the parent steel, whereas it is more pronounced for ductility (the elongation at fracture is down by about half).
The DP/22MnB5 and DP/TRIP welded joints failed at the DP side and exhibited similar tensile strengths and elongation at fractures. This is consistent with the fact that the tensile properties and plastic deformation of these welded joints are mainly triggered by yielding of the DP steel due to its lower tensile strength and sheet thickness in respect to the 22MnB5 and TRIP steel sheets.

Fractography

All the steels in the original condition mainly exhibit ductile fractures with the occurrence of dimples (Figure 5). In particular, the TWIP steel exhibits a bimodal distribution of the dimples, which can be attributed to the concomitance of several causes: i) mechanical twinning occurring during plastic deformation, as reported for other metal alloys [13]; ii) segregation lines of Mn and C elements; iii) orientation of the grains along the rolling direction.

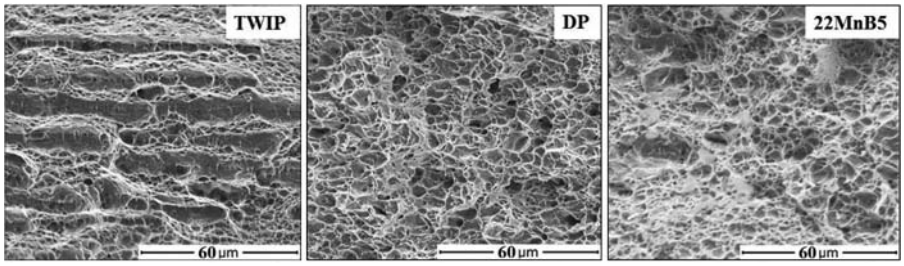

Figure 5. Fracture surfaces of the TWIP and DP steels in the as-received conditions, and of the 22MnB5 after the laboratory heat treatment.

The fracture of the TWIP/TWIP tensile specimens occurs in the fusion zone of the weld seam. The fracture surfaces are fully ductile, Figure 6(a), with the occurrence of dimples (Figure 6(b)). In this case, the morphology of the dimples is different in respect to those obtained in the TWIP steel in the as-fabricated condition; indeed, the bimodal distribution is absent and dimple depth is less pronounced than in the as-fabricated case, as in the case of constrained ductility.
The fracture of tensile specimens of the dissimilar joints of the TWIP steel always occurs in the fusion zone of the weldments. They exhibit a brittle appearance at microscopic scale, Figure 7, with the occurrence of intergranular decohesion among apparent grains boundaries (which may be prior austenite boundaries). This is consistent with the poor elongation at fractures of the corresponding tensile samples. Dimples are quite rare; they are a bit more numerous in the TWIP/22MnB5 joints (which also exhibit the higher elongation at fracture in respect to TWIP/DP and TWIP/TRIP joints). As stated by Mujica et al. [12], the high manganese content of TWIP steel is responsible for Mn chemical segregation during solidification of the weld seam. This may be the cause of the intergranular fractures encountered in the dissimilar welded joints of the TWIP steel.

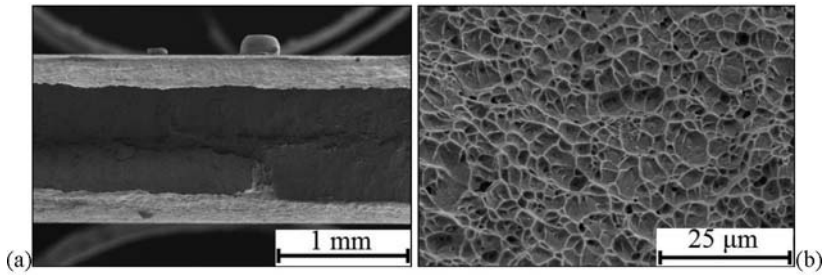

Figure 6. Fracture surfaces of the butt joint TWIP/TWIP in the weld seam: (a) macroscopic and (b) microscopic views.

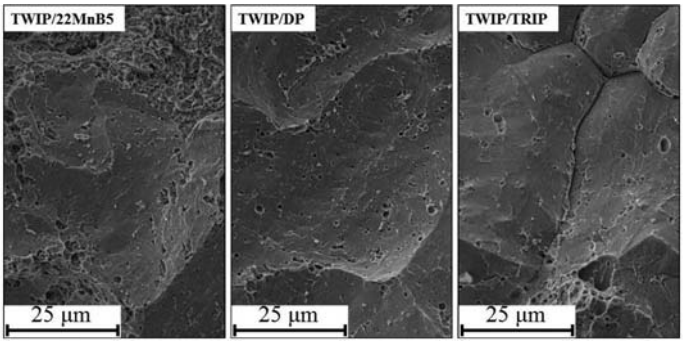

Figure 7. Fracture surfaces of the TWIP/22MnB, TWIP/DP, and TWIP/TRIP joints. Fractures in the fusion zone of the weldments.

Conclusions

Regardless of the type of joint, the HAZ of TWIP steel consists of slightly enlarged austenitic grains, of the order of 10 µm (the initial grain size was around 5 µm), whereas phase transformations occur in the HAZ of the 22MnB5, DP, TRIP steels. Fully martensitic microstructures occurs in the HAZ of the 22MnB5, DP, TRIP steels close to the fusion zone. A wider HAZ was identified in 22MnB5 steel in respect with the HAZ occurring in the welded joints of TWIP, DP, TRIP steels. Furthermore, the difference between the maximum and minimum hardness in 22MnB5 is higher than those in the TRIP and DP parts; however, the original hardness of the 22MnB5 steel is much higher than that of TRIP and DP steels. This is attributed to the lower carbon content of the latter steels, and to the tempering of the fully martensitic microstructure of the 22MnB steel during the welding operation; on the contrary, tempering affects only the limited amount of martensite which is present in the TRIP and DP steels, but not the ferrite. At all the welded joints of the TWIP steel, regardless of the other steel, the fracture surface of the welded tensile specimens occurs in the fusion zone of the weldments. The weldments of the TWIP/TWIP samples exhibit an austenitic microstructure with rather good mechanical properties, the fracture surface being ductile. The other weldment combinations (with the TWIP steel), instead, show low tensile strength and ductility, which is attributed to the formation of martensite in the fusion zone. In the dissimilar weldments of the DP steels with the other low-alloy steels, the fractures occur in the DP side due to its lower tensile strength and smaller resistance cross section in respect to the 22MnB5 and TRIP steels.

As reported in previous studies concerning dissimilar arc welding of TWIP steels, also the laser welding of TWIP steel with low carbon steels (alloyed and not) is not recommended without the use of the proper filler metal to avoid the formation of brittle martensite within the fusion zone. In particular, the ultimate tensile strength after laser welding of the TWIP/22MnB5 was about 20-30% lower than the one previously found after MAG welding [10].

Acknowledgments

The authors wish to thank the Free University of Bozen-Bolzano, for its financial contribution under grant number TN2001.

References

1. H. Hofmann, D. Mattissen, T.W. Schaumann, "Advanced Cold Rolled Steels for Automotive Applications," Steel Research International, 80(1) (2009), 22-28.
2. T. Senuma, "Physical Metallurgy of Modern High Strength Steel Sheets," ISIJ International, 41(6) (2001), 520-532.
3. E.K. Shakhpazov, A.I. Zaitsev, I.G. Rodionova, "Progress in the Technology for the Production of Automobile Sheet," Metallurgist, 51(5-6) (2007), 262-267.
4. O. Bouaziz, S. Allain, C.P. Scott, P. Cugy, D. Barbier, "High Manganese Austenitic Twinning Induced Plasticity Steels: a Review of the Microstructure Properties Relationships," Current Opinion in Solid State & Materials Science, 15(4) (2011), 141-168.
5. G. Scavino, F. D'Aiuto, P. Matteis, P. Russo Spena, D. Firrao, "Plastic Localization Phenomena in a Mn-Alloyed Austenitic Steel," Metallurgical and Materials Transactions A, 41(6) (2010), 1493-1501.
6. L .Mujica Roncery, S. Weber, W. Theisen, "Welding of Twinning-Induced Plasticity Steels," Scripta Materialia, 66(12) (2012), 997-1001.
7. O. Holovenko, M.G. Ienco, E. Pastore, M.R. Pinasco, P. Matteis, G. Scavino, D. Firrao, "Microstructural and Mechanical Characterization of Welded Joints on Innovative High-Strength Steels," Metallurgia Italiana, 105(3) (2013), 3-12.
8. K.Y. Benyounis, A.G. Olabi, M.S.J. Hashmi, "Effect of Laser Welding Parameters on the Heat Input and Weld-Bead Profile," Journal of Materials Processing Technology, 164-165 (2005), 978-985.
9. K. Manonmani, N. Nurugan, G. Buvanasekaran, "Effects of Process Parameters on the Bead Geometry of Laser Beam Butt Welded Stainless Steel Sheets," The International Journal of Advanced Manufacturing Technology, 32(11-12) (2007), 1125-1133.
10. P. Russo Spena, F. D'Aiuto, P. Matteis, G. Scavino, "Dissimilar Arc Welding of Advanced High-Strength Car-Body Steel Sheets," Journal of Materials Engineering and Performance, (2014), in press, doi:10.1007/s11665-014-1209-z.
11. P. Russo Spena, P. Matteis, G. Scavino, "Dissimilar Metal Active Gas Welding of TWIP and DP Steel Sheets," Steel Research International, (2014), in press, doi:10.1002/srin.201400154.
12. L. Mujica, S. Weber, H. Pinto, C. Thomy, F. Vollertsen, "Microstructure and Mechanical Properties of Laser-Welded Joints of TWIP and TRIP Steels," Materials Science and Engineering A, 527(7-8) (2010), 2071-2078.
13. R. Broadwell, C. Hickey, eds., Toughness and Fracture Behavior of Titanium (American Society for Testing and Materials, 1978), 169-172.

Characterization of Minerals, Metals, and Materials 2015
Edited by: John S. Carpenter, Chenguang Bai, Juan Pablo Escobedo, Jiann-Yang Hwang, Shadia Ikhmayies, Bowen Li, Jian Li, Sergio Neves Monteiro, Zhiwei Peng, and Mingming Zhang
TMS (The Minerals, Metals & Materials Society), 2015

UNDERCOOLING OF RAPIDLY SOLIDIFIED DROPLETS AND SPRAY FORMED STRIPS OF Al-Cu (Sc)

A. Bogno, P. Natzke, S. Yin, H. Henein

Department of Chemical and Materials Engineering, University of Alberta

Edmonton, Alberta, Canada

Keywords: Rapid solidification, Impulse Atomization, Spray deposition, Al-alloys, Microstructures

Abstract

Impulse Atomization (IA) (a single fluid atomization technique) was used to rapidly solidify Al-4.5wt%Cu and Al-4.5wt%Cu-0.4wt%Sc under argon atmosphere. In addition to the IA-generated droplets, the same technique was used to produce strips by Spray Deposition (SD) of the same alloys on a copper substrate with and without oil coating. The rapid solidification microstructures were analyzed using Scanning Electron Microscopy (SEM). From the SEM images, the amount of eutectic and the secondary dendrite arm spacing (SDAS) were measured. These SDAS results lead to the estimation of cooling rate. The eutectic fraction coupled with the metastable extension of the solidus and liquidus lines of Al-Cu (Sc) phase diagram lead to the estimation of primary and eutectic undercoolings. A comparison of the solidification path of the droplets and the strips was done as well as the analysis of the effects of scandium.

Introduction

Mechanical properties of industrial products are highly influenced by their solidification microstructures. Variation of solidification conditions, such as undercooling or cooling rate, gives the possibility to control size and morphology of the solidification microstructures which may substantially influence the physical and chemical properties of metallic alloys. High nucleation-undercooling results in rapid solidification and yields materials with improved mechanical properties [1]. Rapid solidification resulting in reduced microsegregation is quite often accompanied by the formation of a broad range of metastable microstructures and different phases.

To promote a high level of undercooling prior to solidification, it is necessary to minimize the nucleation potential of the melt. Knowing that nucleation could be triggered by impurities or the melt container walls, containerless solidification techniques have been developed [2]. These include Impulse Atomization (IA) and Spray Deposition (SD) which refer to the disintegration of a bulk liquid material into droplets in a spray chamber filled with gas [3]. This provides not only the containerless solidification advantages but also the isolation of potential nucleation sites into small fraction of droplets populations by disintegrating the bulk liquid into droplets. Thus, the probability to reach a high level of undercooling increases so that the atomized droplets solidify rapidly into powders or form a strip after landing on a substrate [3].

Aluminum alloys are widely used in automobile and aerospace industries due to their low thermal coefficient of expansion, high corrosion resistance and high strength to weight ratio. The addition of transition metals (TM), such as Cu or Sc, in Al-based alloys results in the formation of supersaturated solid solution during solidification. High cooling rate and high nucleation undercooling induced rapid solidification increases substantially the solubility of transition metals in solid aluminum. The development of metallurgical methods such as IA which involves high cooling rate and undercooling has led to a large number of investigations into Al-TM alloys. Al-Cu is one of the most widely used base alloys due to the relevant high age hardening effect of Cu. The addition of Scandium in Al-alloys not only promotes age hardening through the precipitation of finely dispersed Al_3Sc particles that can tightly pin up the grain boundaries and dislocations, but also yields good grain refining in binary aluminum alloys [4].

This paper reports on the study of rapidly solidified Al-4.5wt% Cu and Al-4.5wt% Cu-0.4wt% Sc droplets and spray formed strips generated by IA. The solidification paths of the two alloys are investigated under metastable solidification generated by IA and SD. Cooling rates have been estimated based on the measured Secondary Dendrite Arms Spacing (SDAS).The eutectic fractions have been measured and a microsegregation model has then been used to estimate the dendritic and eutectic nucleation undercoolings. For these investigations, different analytical tools have been used; these include Differential Scanning Calorimetry (DSC), X-Ray Diffraction (XRD), Scanning Electron Microscopy (SEM), Point-located Energy Dispersive X-ray spectroscopy (EDX) and Vickers microhardness tests.

Experimental

Impulse Atomization (IA) and Spray Deposition (SD)

Al-4.5wt% Cu and Al-4.5wt% Cu-0.4wt% Sc in the form of granules were prepared by Novelis from a 99.99 % pure Al element. Prior to atomization, the granules were melted at 850°C in a graphite crucible by induction heat in argon atmosphere. The melt was subsequently impulse atomized into droplets through a graphite plate with 37 nozzles of 250 μm hole size that was glued at the bottom of the crucible. The droplets rapidly solidified by losing heat to the stagnant argon atmosphere while falling through a 4 meters altitude chamber and were collected in a beaker filled with oil. The droplets were then washed, dried and sieved into different sizes ranging from 212 to 1000 μm.

During spray deposition, (SD) the atomized droplets were partially molten when they landed and formed a 50 mm wide and 5 mm thick, coherent and dense deposit on a 3 mm thick moving ($0.038 ms^{-1}$) copper substrate (heated up to 100 °C) at a distance of 40 cm from the nozzle plate. A schematic description of the SD experimental setup is given in Figure 1.

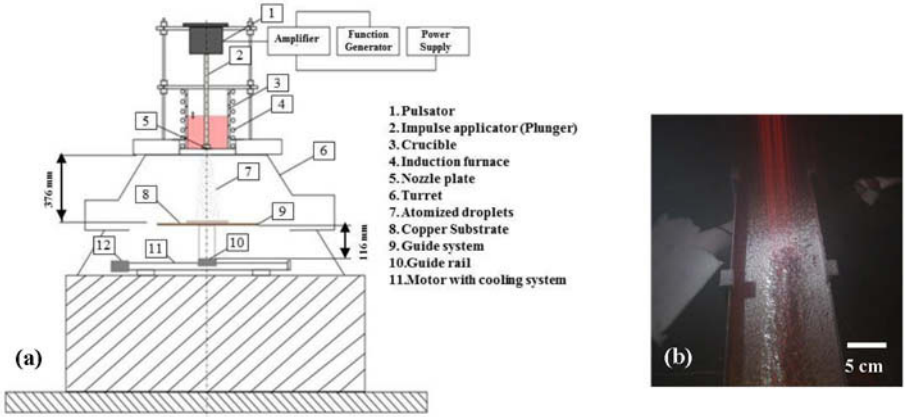

Figure 1(a) Schematic of the Spray Deposition (SD) setup (b) image of a SD of Al-4.5wt% Cu

Results

Measurement of cell spacing

Secondary dendrite arms spacing (SDAS) were approximated by the cell spacing (center-to-center distance between two cells) using lines intercepts method; measurements of cell spacing were performed on the micrographs obtained by SEM-BSE (Figure 2).

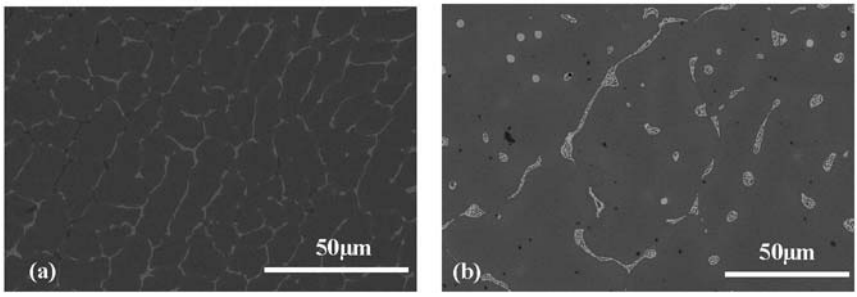

Figure 2. Typical microstructures obtained by SEM (BSE) images of samples rapidly solidified by Impulse atomization under argon (a) IA-0.4wt%Sc of average size 350µm (b) SD-0.4wt%Sc.

Variation of cell spacing with solidification parameters

Cell spacing variation over the range of particles size and cooling rates investigated for both Al-4.5wt% Cu (IA-0.0wt%Sc) and Al-4.5wtCu-0.4wt% Sc (IA-0.4wt%Sc) produced by impulse atomization are presented in Figure 3.

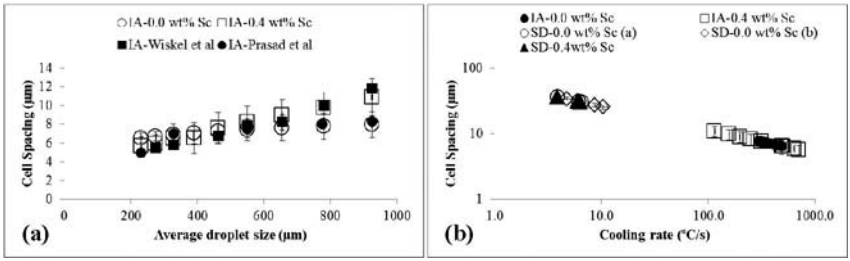

Figure 3 Variations of average cell spacing with average droplet size and cooling rate respectively (a) IA droplets under argon (b) IA droplets and SD on a copper substrate both under argon.

Cell spacing values for IA-0.0wt%Sc and IA-0.4wt%Sc are compared with published data for Al-4.5wt% Cu with Al purity of 99.9 % [5, 6]. Figure 3a shows that there is a good agreement with the above mentioned published results. The cell spacing decreases from 12μm to 6μm as the droplet size increases from 212 μm to 1000 μm. The average cell spacing is approximately the same for both IA-0.0wt%Sc and IA-0.4wt% Sc for the same droplet sizes. Hence, Sc has no significant refining effect on the rapidly solidified droplets within the investigated range of droplet sizes.

Cooling rates corresponding to each droplet and SD cross-section (cut-offs of each deposit at the center where the thickness is the most homogeneous) has been estimated using the empirical expression of the secondary dendrite arm spacing λ_2 (Eq.1) of Al - 4wt% Cu powder produced by close coupled gas atomization [7]:

$$\lambda_2 = B(\dot{T})^{-n} \quad (1)$$

Where $\dot{T}$ is the cooling rate, B=58.7, a parameter depending upon the Cu concentration of the alloy and the exponent n = 0.355 [8].

Figure 3b shows the variation of cell spacing for both IA droplets and SD. As expected, the average cell spacing decreases as the cooling rate increases. It is worth noting that average cell spacing for SD microstructures are much larger as compared to the IA droplets average cell

spacing. This is due to the fact that IA droplets fully solidify by losing heat to the stagnant argon atmosphere without any significant increase of temperature of the latter (40 °C). In contrast, during SD, the partially solidified droplets land on a copper substrate to which they lose heat. Indeed, prior to atomization, the substrate is heated up (100 °C) to minimize porosity at the interface between substrate and deposit. Also, subsequent mushy droplets will fall onto prior mushy droplets forming a deposit of up to 5mm in thickness. The solidification of such a thick deposit will clearly be slower than that for micron sized droplets solidifying in a gas. Therefore the resultant average cell spacing in the deposit is larger than IA droplets average cell spacing. Cooling rate variation across the SD sample cross-section from bottom (sample-substrate interface) to top (sample-atmosphere interface) is shown in Figure 4a. It is clear that the cooling rate at the bottom of the deposit (in contact with the Cu Substrate) is the highest due to the fact that copper substrate has a higher thermal conductivity, (400 w/ mK) as compared to argon (0.014 w/mK); hence the cooling rate at the top is lower; the middle part has the lowest cooling rate due to the fact that in the middle position, the heat is not directly transferred to the surrounding argon or the copper substrate, it has to transfer through top and bottom of the strip first; Therefore, the heat transfer rate from the middle of the deposit is the lowest and so is the cooling rate. For the same sample composition, the oil-coated substrate gives a higher cooling rate (IA-0.0wt%Sc (a)) as compared to the non-coated substrate (IA-0.0wt%Sc (b)) as oil provides a better contact between the deposit and the substrate. However, alloy composition has no visible effect on the cooling rate.

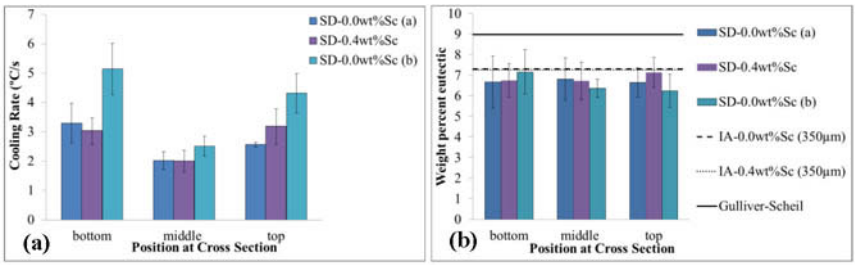

Figure 4. Cooling rate and weight percent eutectic at different positions of the SD cross sections compared with IA-droplets of equivalent size and the Gulliver-Scheil model prediction for the two investigated alloys.

Measurement of eutectic fractions and estimation of primary and eutectic undercoolings

Eutectic volume fractions (V^e) were estimated by stereology through measurement of area fraction of eutectic structure on the micrographs obtained by SEM-BSE on both IA-droplets and SD microstructures [6, 9]. Subsequently, V^e is converted into weight percent eutectic (W^e) following equation 2.

$$W^e = \frac{V^e \times \rho_e}{V^e \times \rho_e + V^\alpha \times \rho_\alpha} \quad (2)$$

The densities of the eutectic structure and the α-phase ρ_e and ρ_α were obtained from the elemental weight percent of the eutectic structure measured by Point-located Energy Dispersive X-ray spectroscopy (EDX). The densities of Al and Cu are ρ_{Al}=2700kg m^{-3} and ρ_{Cu}=8920kg m^{-3} [10] Figure 4b compares the eutectic fraction (wt %) at different positions of the deposit cross section. Despite the variation of cooling rate from top to bottom, the eutectic fraction is consistent throughout the cross-section area and equal to the eutectic fraction of a droplet of 350 µm in diameter which is the estimated value of the D50 of the spray through nozzles size of 250 µm [11]. This suggests that eutectic fraction is nucleation undercooling dependent rather than cooling rate dependent. And, as expected the eutectic fraction is lower than the well-known Gulliver-Scheil model prediction.

Subsequently, the eutectic fractions were used in the Al-Cu phase diagram with metastable extensions of solidus and liquidus lines (Figure 5) to determine the corresponding eutectic undercoolings. The eutectic undercoolings were then combined with an approximate coarsening model to determine the primary undercoolings. A detailed description of the steps is described in a previous work [12].

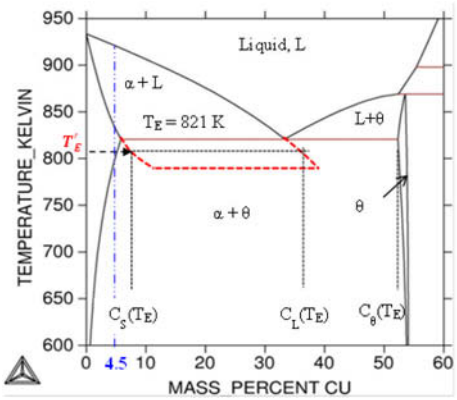

Figure 5. Aluminum rich hypoeutectic region of Al-Cu phase diagram calculated by Thermo-Calc. The dashed lines represent the extension of solidus and liquidus lines obtained by suspension of Al_2Cu.

Figure 6a shows the variation of eutectic undercooling from bottom to top of the deposits cross sections. The results are compared with a 350 µm droplet size of the same composition which corresponds to the D50 of the deposited spray. As can be seen, the eutectic undercooling does not vary much across the SD sample cross section from bottom to top. However, the results show higher eutectic undercooling in SD as compared to droplets, this suggest that when they landed on the copper substrate the partially solid spray (consisting of primary alpha-phase) has to cool few more degrees Celsius further before the remaining liquid reaches the eutectic composition, consequently the eutectic nucleation temperature gets lower as compared to an IA-droplet that solidified entirely in the argon atmosphere.

Figure 6b shows the primary undercooling variation from bottom to top across the deposit cross section. As can be seen, the primary undercooling remained quasi-constant all over the sample. The values are affected by neither the cooling rate (oil-coating) nor the Sc-addition. Also, the primary undercooling is found to be consistent with a 350 μm droplet size of the same composition corresponding to the D50 of the deposited spray, this is expected as the spray primary solidification occurs before they land, partially liquid, on the copper substrate.

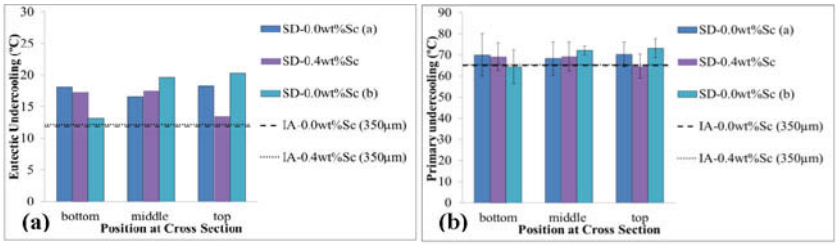

Figure 6. Eutectic and primary undercooling at different positions of the SD cross sections compared with IA-droplets of equivalent size for the two investigated alloys.

Conclusions

Impulse Atomization (IA) and Spray Deposition (SD) of Al-4.5wt Cu and Al-4.5wt% Cu-0.4wt% Sc were carried out under argon atmosphere. Copper substrates with and without oil coating were used for SD. Oil coated substrate is found to yield faster heat dissipation due to a better substrate-deposit contact. Average cell spacing is found to decrease with cooling rate. IA droplet microstructures are found to be finer than their corresponding deposits although Copper heat conductivity is much higher than Argon. This is explained by the fact that under argon atmosphere the micron size IA droplets fully solidify by losing heat to the gas without any significant increase of temperature of the latter; whereas, during SD, the partially solidified droplets land on a copper substrate to form a few millimeters thick deposits which clearly will not solidify fast enough to promote a finer microstructure as compared to the micron size IA droplets. However, the eutectic fractions are found to be the same, suggesting that eutectic fraction is nucleation undercooling dependent rather than cooling rate. The eutectic undercooling does not vary with cooling rate. A higher eutectic undercooling is achieved in SD as compared to IA, because when they land on the copper substrate the partially liquid spray has to be cooled further before it reaches the eutectic composition; and therefore, the eutectic nucleation temperature gets lower as compared to IA-droplets that solidify entirely in the argon atmosphere. The primary undercooling is found to be equal for both IA and SD samples regardless of the position on the SD and it is not affected by Sc-addition.

Acknowledgements

The authors are grateful to Novelis and Dr. Mark Gallerneault for providing raw materials and the Natural Sciences and Engineering Research Council of Canada (NSERC) for their financial support.

References

1. M. C. Fleming, *Solidification Processing* (McGraw-Hill, London, 1974).

2. Dieter M. Herlach and Douglas M. Matson ed., *Solidification of Containerless Undercooled Melts* (Wiley-VCH, Germany, 2012).

3. N. Ellendt et al, "Spray Deposition using Impulse Atomization Technique," *Materials Science and Engineering: A*, 383 (1) (2004), 107–113.

4. K.T. Conlon et al, "Processing and microstructural characterization of Al-Cu alloys produced from rapidly solidified powders," *Metallurgical and Materials Transactions A*, 31 (1) (2000), 249-260.

5. J. B. Wiskel, H. Henein, and E. Maire, "Solidification study of Aluminum alloys using Impulse Atomization: Part I: Heat transfer Analysis of an atomization droplet," *Canadian Metallurgical Quarterly*, 41 (1) (2002), 97-110.

6. A. Prasad et al, "A Solidification Model for Atomization," *ISIJ International*, 49 (2009), no. 7:992–999.

7. A. M. Mullis et al, "Estimation of Cooling Rates During Close-Coupled Gas Atomization using Secondary Dendrite Arm Spacing Measurement," *Metallurgical and materials Transactions B*, 44 (4) (2013), 992-999.

8. D. Eskin et al, "Experimental study of structure formation in binary Al–Cu alloys at different cooling rates," *Materials Science and Engineering: A*, 405 (1-2) (2005), 1–10.

9. A. Prasad, "Microsegregation studies of rapidly solidified binary Al-cu alloys" (Ph.D. thesis, University of Alberta, 2006), 80-98.

10. N. N. Greenwood and A. Earnshaw, *Chemie der Elemente* (Wiley-VCH, Germany 1988), 1509.

11. H.Henein, "Single fluid atomization through the application of impulses to a melt," *Materials Science and Engineering: A*, 326 (1) (2002), 92–100.

12. A. Bogno et al, "Quantification of Primary and Eutectic Undercoolings of Impulse Atomized Al-Cu Droplets" (Paper presented in the symposium: Light Metals for Transportation at MS&T 2013, Oct. 2013).

Characterization of Minerals, Metals, and Materials 2015
Edited by: John S. Carpenter, Chenguang Bai, Juan Pablo Escobedo, Jiann-Yang Hwang, Shadia Ikhmayies, Bowen Li, Jian Li, Sergio Neves Monteiro, Zhiwei Peng, and Mingming Zhang
TMS (The Minerals, Metals & Materials Society), 2015

SELECTIVE LASER MELTING: CHARACTERISTICS OF IN718 POWDER AND MICROSTRUCTURES OF FABRICATED IN718 SAMPLE

Xiao Sun, Shouping Liu, Jun Bao, Kai Kang,
College of Materials Science and Engineering, University of Chongqing, Chongqing, 400030, P.R.China

Keywords: IN718 alloy, Powder, Selective laser melting, Microstructure.

Abstract

Powder characteristics have a significant influence on selective laser melting (SLM) process. In this research, particle size, surface contour and the microstructure of IN718 powder used in SLM were tested, and the physical and chemical changes during heating process of the powder were investigated as well. The shape characteristic and fluid properties of IN718 powder were defined and measured. It is shows that most particles of IN718 powder exhibited nearly spherical shapes, and the particle size is about 22.95μm. On this basis, IN718 sample was fabricated by SLM process using the powder and the microstructure of the fabricated sample was investigated. The results indicated that the sample has a dense microstructure, no macro-defects but a few micropores and porosity. Compared with the powder, there was no new phase formed in the sample and melting point of the sample was little less than that of the powder.

Introduction

IN718 alloy has excellent high temperature mechanical properties and has been widely used in the aerospace industry. [1, 2] However, it is difficult to manufacture IN718 part by conventional machining methods at room temperature because of excessive tool wear and low material removal rates.[3, 4] In addition, the applied IN718 alloy parts are very complex in molding method and the traditional methods also waste materials. Thus new manufacturing processes such as selective laser melting (SLM) have come into the focus of the research.

Previous researches has concentrated on the influence of the SLM process parameters on the product properties such as the surface roughness and relative density, [5-7] or studied on the mechanical properties of fabricated parts. [8] Nevertheless, there is no completely research on the powder used in SLM.

Powder characteristics have special influence on SLM process such as particle size, surface contour, melting point, fluid properties etc. and these characteristics have important influence on the SLM process and fabricated part[9]. This article comprehensively investigated the IN718 powder used in SLM and the microstructure of IN718 sample fabricated by SLM.

Characteristics of IN718 powder used in SLM

Particle size

1. Measuring particle size by laser particle analyzer

Mastersizer 2000 Laser Particle Analyzer was used to measure the particle size of IN718 powder, and the reagent used to disperse the powder was alcohol. The result is shown in Table 1 and Figure 1.

As table 1 shows, volume average particle diameter of IN718 powder is 38.23μm, surface area average particle diameter is 29.201μm and specific surface area is 0.205 m^2/g. Figure 1 illustrated that: most particle size of the powder is range from 10μm to 50μm, particle size in this range is about 85% and particle size less than 10μm does not exist.

Table 1. Result of IN718 powder particle size by Laser particle size analyzer

volume average particle diameter D_1	surface area average particle diameter D_2	specific surface area SA
38.23μm	29.201μm	0.205m^2/g

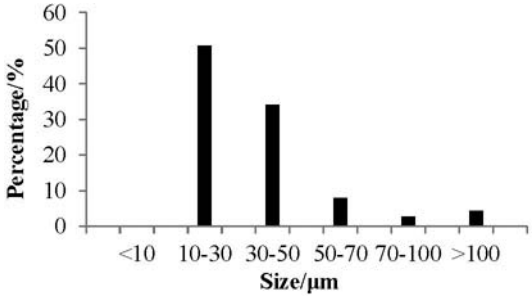

Figure 1. Size distribution of the IN718 powder

2. Measuring particle size by SEM

15 micrographs of IN718 powder were taken by SEM (as shown in Figure 2) and particle size of the powder in the micrographs was measured and averaged by Image-Pro-Plus (IPP) software, the result is shown in Table 2. The average particle size is 22.95μm, the maximum particle size is 112.27μm and the minimum particle size is 5.03μm, compared table 1 with table 2, the result of particle size obtained by the IPP software is less than the particle size tested by laser particle analyzer, this may indicate that using alcohol to disperse the powder leads to incorrect size measurements.

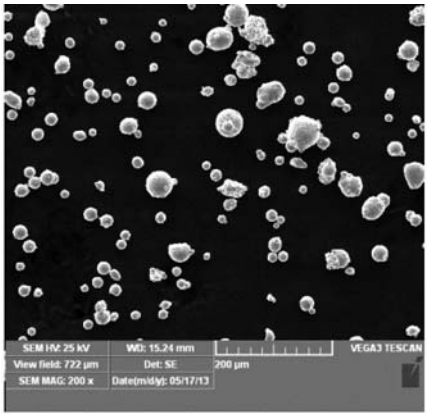

Figure 2. Representative SEM micrograph of IN718 powder

Table 2. the result of measuring the particle size by IPP software

Average particle size/μm	Maximum particle size/μm	Minimum particle size/μm
22.95	112.27	5.03

Particle shape and ellipsoid coefficient

Figure 3 shows the particle shape of IN718 powders. Most of the powder particle shape is an approximate sphere, but there are also some irregular particles in the powder, obviously, spherical particle is beneficial to spreading in SLM process. Figure 3 also illustrates that the surface of the particles is not smoothis not smooth, indicating that a rough surface is favorable for laser absorbing.

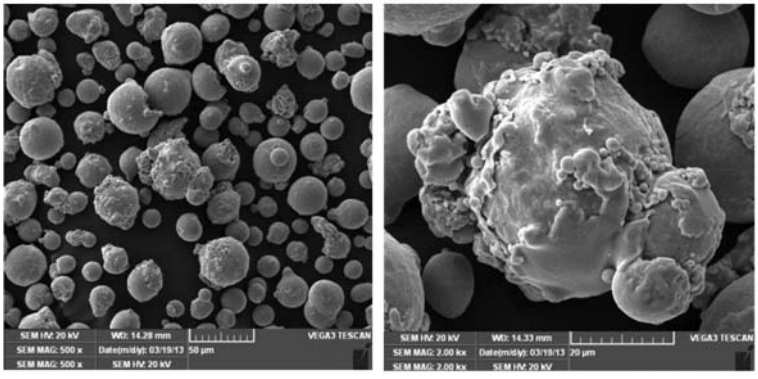

Figure 3. SEM images of IN718 powders

In order to represent the shape character of IN718 powder, the particle is regarded as an elliptical shape and the ratio of long axis to short axis (as seen in Figure 4) is measured. Fluid

properties are improved if the ratio of long axis to short axis, or ellipsoid coefficient, is close to one. For IN718 powder, the 15 micrographs were used to calculate the ellipsoid coefficient of the powder by IPP software again, and the average ellipsoid coefficient is 1.37.

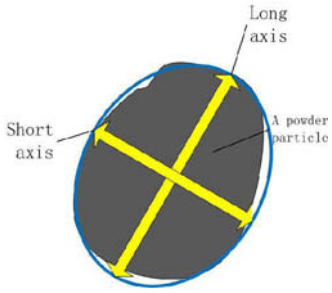

Figure 4. schematic diagram of coefficient of ellipsoid

Surface chemical composition of IN718 powder

Infrared spectrometer was used to detect if there is organic matter adhering to the surface of IN718 powder, the result is shown in Figure 5. The wave number between 3000cm-1 to 3500cm-1 illustrates the presence of moisture (-OH) that has been adsorbed on the powder surface when the powders were in contact with the environment during the sample preparation process for measurement. The IR spectrum of the phosphor indicates that there is no organic matter on the IN718 particle surface.

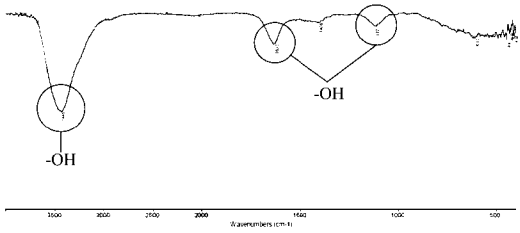

Figure 5. The infrared spectrum of IN718 powder

The microstructure of IN718 powder

The microstructure of IN718 powders is shown in Figure 6. Fine equiaxed grain is found, and the grain boundary is elongated. This result illustrates that the cooling rate in powder production is high.

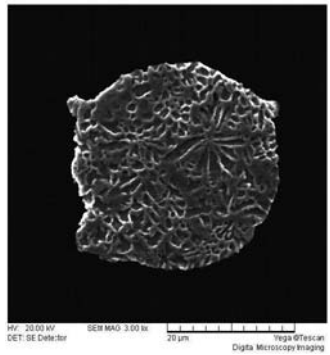

Figure 6. SEM image showing the particle internal microstructure of IN718 powder

Figure 7 shows XRD pattern of IN718 powder, the main phase of the powder is γ phase (Ni-Cr-Co-Mo) and the other phase is Fe_xNi_y.

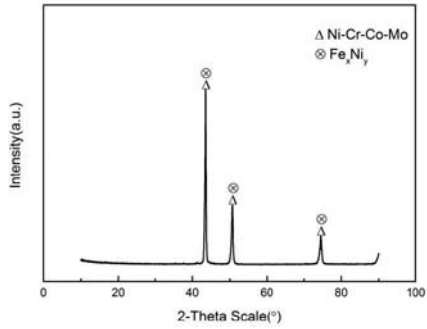

Figure 7. XRD pattern of the IN718 powder

Thermal analysis of IN718 powder

Some SLM manufacturing parameters are based on the physical and chemical changes of materials during heating process, so thermal analysis was used to research on the physical and chemical changes of IN718 powder in the SLM process. During the heating procedure, the powder was scanned from 25°C to 1500°C under argon atmosphere, with a heating rate of 20°C/min.

As the result shown in Figure 8, thermal transition observed at about 100°C has been ascribed to evaporation of water. Thermal transitions found between 500°C and 1100°C may be due to the phase transition. The transition at 1370°C is caused by powder melting. TG curves demonstrates that the powder has a little oxidation in the heating process at about 1100°C.

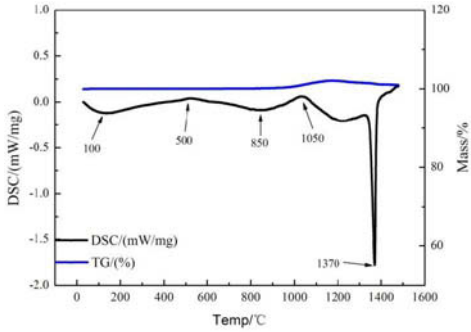

Figure 8. thermal analysis of the IN718 powder

Fluid properties of IN718 powder

Fluid properties of the powder include apparent density, tap density, and angle of repose. The apparent density means the density of natural powder; and the tap density means the density of compact powder; the angle of repose is defined to represent the fluid properties of the powder defining the angle of repose as: powder falls into the platform freely and forms a cone, the angle between the platform and slope of the cone is the angle of repose. Small angle of repose is good for the fluid properties of powder. Generally consider, when the angle of repose $\theta \leq 30°$, the fluid properties of powder is excellent, and when $30° \leq \theta \leq 40°$, the fluid properties of powder can meet fluidization, injection and spreading requirement of production process.

The BT-1000 machine was used to test the fluid properties of the IN718 powder, and the result is listed in Table 3. The angle of repose is 39° which means the IN718 powder can inject or spread during the SLM process.

Table 3. the result of the fluid properties

apparent density ρ_1 g/ml	tap density ρ_2 g/ml	Compressibility /%	angle of repose θ /°
4.03	5.00	19.30	39.00

SLM Experimental

SLM experimental equipment used to fabricate IN718 sample is CQU280, and the machine had a 200W Yb:YAG fiber laser. Before SLM process, the platform was preheated to 80°C and maintaining at that temperature in SLM process. The SLM experimental conditions used in this study were presented in Table 4.

Table 4. SLM experiment conditions used in IN718 sample fabrication

Manufacturing parameters	Value
Laser power P, W	195
Laser scanning speed v, mm/s	1200
Powder layer thickness d, μm	50
Protect atmosphere	Ar

Microstructure and Characteristics of fabricated sample

The fabricated IN718 sample was shown in Figure 9.

Figure 9. The fabricated IN718 sample by SLM

The microstructure of fabricated IN718 sample

Figure 10 gives the optical micrographs of the fabricated IN718 sample by SLM. A typical SLM microstructure is seen in Figure 10. It is found that the microstructure on vertical to building section (Figure 10a) and cross to building section (Figure 10b) is different, on vertical to building section the microstructure unit is an ellipse, and on cross to building section, microstructure unit looks like a squama. The ellipse and the squamous microstructure units are all formed by micro-molten-pool of IN718 particles during SLM process.

The microstructure of the fabricated samples is dense and has no macro-defects like inclusion and bubble. However, there are some micropores and porosity in both sections.

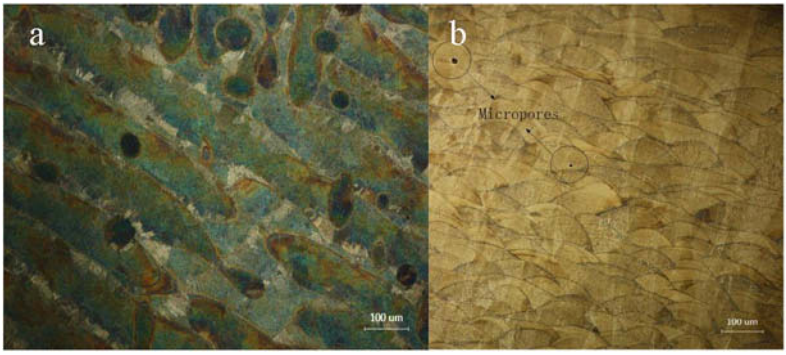

Figure 10. Optical micrographs of the fabricated IN718 sample

(a) vertical to buildingsection,(b) cross to building section

The XRD pattern of SLM fabricated IN718 sample is shown in Figure 11. Phase composition of the sample was almost the same as the powder, include γ phase (Ni-Cr-Co-Mo) and Fe-Ni. The reason may be that the solidification rate was very fast in both IN718 powder production and IN718 sample SLM fabrication process.

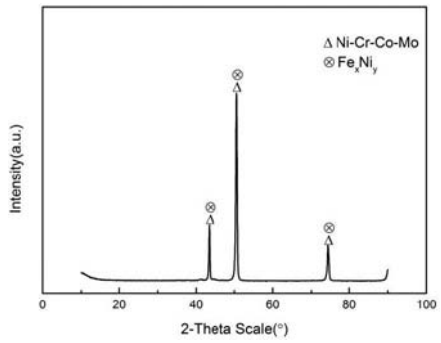

Figure 11. XRD pattern of fabricated sample

Thermal analysis of fabricated sample

Experimental conditions are the same as the conditions of IN718 powder. The result is shown in Figure 12.The thermal transition observed at about 150°C represents the evaporation of water absorbed on the sample surface. The thermal transitions found at about 1000°C may be ascribed to phase transition. The transition at 1335°C is caused by alloy melting. Comparing Figure 8 with Figure 12, the DSC curve of the fabricated sample is a little different from the powder's, several peaks caused by phase transition have disappeared in the sample DSC curve. TG curve has little changed during heating process.

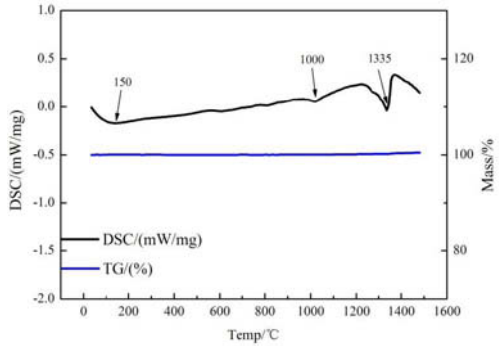

Figure 12. Thermal analysis of fabricated sample

Conclusions

This article intends to present the characteristics of IN718 powder used in SLM process and the microstructure of the IN718 sample fabricated by SLM. The result shows the powder used in SLM process has an approximate sphere shape and the ellipsoid coefficient is 1.37. The particle surface is not smooth but the shape characteristics are beneficial to spreading and absorbing laser power in the SLM process. The average particle size of the powder is about 22.95μm. The angle of repose of the powder is 39° which means the fluid properties of the powder can satisfy spread and injection requirement in SLM process. In the SLM experiment, samples have been successfully fabricated by the powder.

SLM fabricated sample using the IN718 powders has dense microstructure, but there are still a few micropores and porosity in the sample. A special microstructure is found in both cross to building section and vertical to building section, the microstructure unit is ellipse in vertical to building section and squamous microstructure in cross to building section. Melting point of the sample is about 1335°C and the main phase is γ phase (Ni-Cr-Co-Mo). Compare with the powder, melting point of the sample is a little lower and the phase composition is almost the same.

Acknowledgement

This work is supported by the Fundamental Research Funds for the Central Universities P.R.China through project No.CDJZR12110072

References

1 M. Anderson, R. Patwa, and Y.C. Shin. "Laser-assisted machining of Inconel 718 with an economic analysis." *International Journal of Machine Tools and Manufacture,* 46 (2006), 1879-1886.

2 Zemin Wang, Kai Guan, and Ming Gao, "The microstructure and mechanical properties of deposited-IN718 by selective laser melting." *Journal of Alloys Compounds,* 513 (2012), 518-523.

3 H. Attia et al., "Laser-assisted high-speed finish turning of superalloy Inconel 718 under dry conditions." *C.I.R.P. Annals, Manufacturing Technology,* 59 (2010), 83-89.

4 J.P. Costes et al., "Tool-life and wear mechanisms of CBN tools in machining of Inconel 718."*International Journal of Machine Tools and Manufacture,* 47 (2007), 1081-1088.

5 Yadroitsev I, Bertrand Ph, and Smurov I. "Parametric analysis of the selective laser melting process." *Applied Surface Science,* 253 (2007), 8064-8071.

6 Morgan R, Sutcliffe CJ, and O'Neill W. "Density analysis of direct metal laser re-melted 316L stainless steel cubic primitives." *Journal of Materials Science,* 39 (2004), 1195-1203.

7 Morgan R, Sutcliffe CJ, and O'Neill W. "Experimental investigation of nanosecond pulsed Nd:YAG laser re - melted pre - placed powder bed." *Rapid Prototyping Journal,*7 (2001), 159-170.

8 K.N. Amato, S.M. Gaytan, and L.E. Murr, "Microstructures and mechanical behavior of Inconel 718 fabricated by selective laser melting." *Acta Materialia,* 60 (2012), 2229-2239.

9 Lore Thijs et al., "A study of the microstructural evolution during selective laser melting of Ti - 6Al - 4V." *Acta Materialia, 59 (*2010), 3303-3312.

Characterization of Minerals, Metals, and Materials 2015

Method Development in Characterization

Session Chairs:

John S. Carpenter

Jian Li

Characterization of Minerals, Metals, and Materials 2015
Edited by: John S. Carpenter, Chenguang Bai, Juan Pablo Escobedo, Jiann-Yang Hwang, Shadia Ikhmayies, Bowen Li, Jian Li, Sergio Neves Monteiro, Zhiwei Peng, and Mingming Zhang
TMS (The Minerals, Metals & Materials Society), 2015

ADVANCED FIB APPLICATIONS IN MATERIALS RESEARCH AT CanmetMATERIALS

Jian Li, P. Liu, R. Zhang and J. Lo

CanmetMATERIALS, Natural Resources Canada, 183 Longwood Road South, Hamilton, Ontario, Canada L8P 0A5

Keywords: FIB, Microscopy, milling

Abstract

In the past decades, focused ion beam (FIB) has evolved into a powerful microscope that provides capabilities that no other microscopes can offer. The combination of high-resolution imaging and stress-free ion beam cross sectioning provides valuable microstructure information both at the specimen surface and beneath. FIB techniques are also the preferred method to prepare site-specific transmission electron microscope (TEM) specimens. CanmetMATERIALS owns a world-class microscopy facility, where advanced microscopy work provides strong supports to research programs that cover a wide range of subject areas. This paper is aimed to provide a few practical examples of FIB applications in microstructure characterizations that include cross-sectioning and imaging, serial sectioning, and advanced TEM specimen preparation in materials research at CanmetMATERIALS.

Introduction

FIB microscope has long surpassed the era when it was solely used by semiconductor industry [1]. With its applications extend into materials science and biology, the number of FIB systems has increased significantly [2-5].

A typical FIB microscope column contains a Ga ion source that produces a finely focused beam. The primary Ga ion beam is accelerated by typically 30 kV to provide both precision ion beam milling power and ion beam imaging capability. Secondary ions and secondary electrons are also collected by various types of detectors for high-resolution imaging purpose. Depending on the application, higher beam current (e.g. 60 nA) are used for rapid ion beam milling, while fine beam current (e.g. 1 pA) can be used for high-resolution ion beam imaging. High-resolution ion beam imaging can provide enhanced crystallographic contrast that outperforms the traditional BSE imaging in SEM. Site-specific micro-depositions (e.g., Pt, W, C, and SiO_2) and micro-etching (XeF_2 and Cl) can also be achieved by the interaction of the primary ion beam with the deposition (or etching) gas introduced into the system.

The development of second generation of FIB systems (Dual-Beam^{TM} or Cross-Beam^{TM}) has vastly replaced the original single beam FIB systems. Combining with high-resolution electron microscope columns, dual-beam FIBs have become powerful instruments that no other microscope can replace. The main capabilities of the modern FIB systems are listed below:

1) stress-free FIB cross-sectioning - subsurface information
2) high-resolution imaging – surface and FIB sections
3) chemical composition – energy dispersive X-ray spectroscopy (EDS)
4) Crystallographic orientation – Electron backscattered diffraction (EBSD)

5) Micro deposition and micro etching – circuit editing, protection to TEM foils
6) In situ lift out (micro manipulator) – TEM specimen preparation
7) TEM specimen preparation – site specific cross sectional and plan view TEM samples
8) Scanning transmission electron microscopy (STEM) – BF and DF imaging of TEM foils

High-quality FIB microscopy work has been a significant integral to deliver research projects at CanmetMATERIALS. This article is aimed to present a few examples of advanced FIB microscopy applications in materials research at CanmetMATERIALS.

Instrumentation

CanmetMATERIALS owns a set of state-of-the-art electron microscopes that includes a high-resolution SEM, a dual-beam FIB and a TEM. Aside from high-resolution imaging and rapid ion beam milling capabilities, the Helios NanoLab-650 dual beam FIB is equipped with EDS, EBSD, Omni Probe™ micro-manipulator, five gas injectors and a retractable STEM detector. Figure 1 shows a schematic diagram and the actual FIB microscope at CanmetMATERIALS.

Figure 1. Schematic diagram of dual beam FIB microscope and the Helios NanoLab FIB at CanmetMATERIALS

Practical Examples

High resolution imaging

High resolution imaging is always one of the prime tasks for any microscopy facility. Ability to achieve high-resolution imaging on bulk samples provides opportunities for rapid feedbacks to process parameter optimization and failure analyses.

TiO_2 is one of the most studied materials in recent years. Bulk TiO_2 is known to be a very useful, non-toxic, environmentally friendly, and corrosion-resistant material. It is frequently used in various types of paints, white pigments, and sun-blockers [6]. Nanocrystalline TiO_2 has been

used in solar cells and biomedical applications using its active photo catalytic property to decompose organic materials [7]. There have been interests to replace the TiO_2 from nano particular form to one-dimensional nanostructures due to both nanotubes and nano rods allowing for good control of the chemical or physical behavior [8, 9]. With the use of nanotubes, not only does the specific surface area increases significantly but also the electronic properties may change considerably. There have been indications of improved conversion efficiency by replacing TiO_2 nanoparticle with naontubes in dye-sensitized solar cells [6].

TiO_2 in nanotube form was produced at CanmetMATERIALS in experiment scale using electrochemical anodization process. A processing parameter – structure – properties relationship needs to be established. The size and structure of the nanotube is of critical importance as it not only determines the physical and chemical properties of the product, but also their electrical and biological properties. Whether the nanotubes are single-walled or double-walled is also of particular interest. Figure 2 shows examples of high-resolution secondary electron images of the TiO_2 nanotubes produced at CanmetMATERIALS. These nanotubes appear to be all single-walled and are about 100 nm in diameter with wall thickness of about 20 nm. Small agglomerates on the surface are a result of Pt plating using a Denton-IV vacuum sputter coater for conductivity purpose. High-resolution images of up to 2,000,000 X was obtained using the SEM column on the Helios NanoLab FIB. The ultimate achievable resolution measured from these images collected under 2 keV electron beam is 0.6 nm.

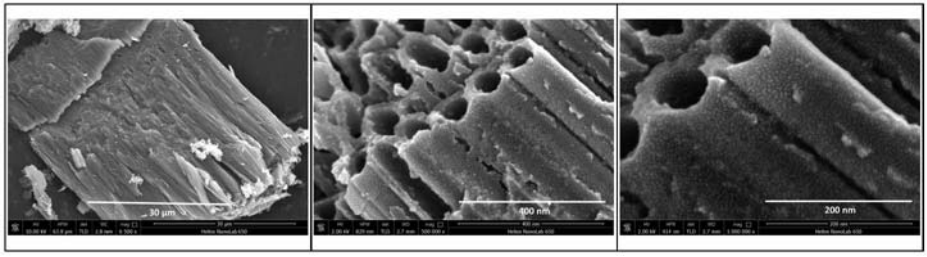

Figure 2. High-resolution images taken from the TiO_2 nanotubes produced at CanmetMATERIALS

Stress-free Cross-sectioning

One of the powerful functions that FIB microscopes provide is the ability to cross-section microscopic features. The ability to locate a feature of interest and prepare cross-section in-situ allows investigators to obtain microstructure, chemical composition and crystallographic orientation information in the third dimension – all in one microscope [10].

Oxide-dispersion strengthened (ODS) steels have been of great interest for high temperature application. For high temperature fuel cladding in supercritical water-cooled reactor (SCWR), ODS steel is a desirable material for its strength, creep resistance, enhanced corrosion and irradiation resistance at high temperature. However, production of ODS steel is still under heavy development. Typical process routine involves metal powder production by atomization, ball milling of steel powder with nanometer sized Y_2O_3 powder followed by extrusion. One of the challenge in ODS steel production is to incorporate Y_2O_3 into steel powder in the ball milling process. The microstructure and properties of the atomized powder is of critical importance.

Optimizing atomization process to obtain particles with preferred microstructure is a key factor to produce high quality ODS alloys.

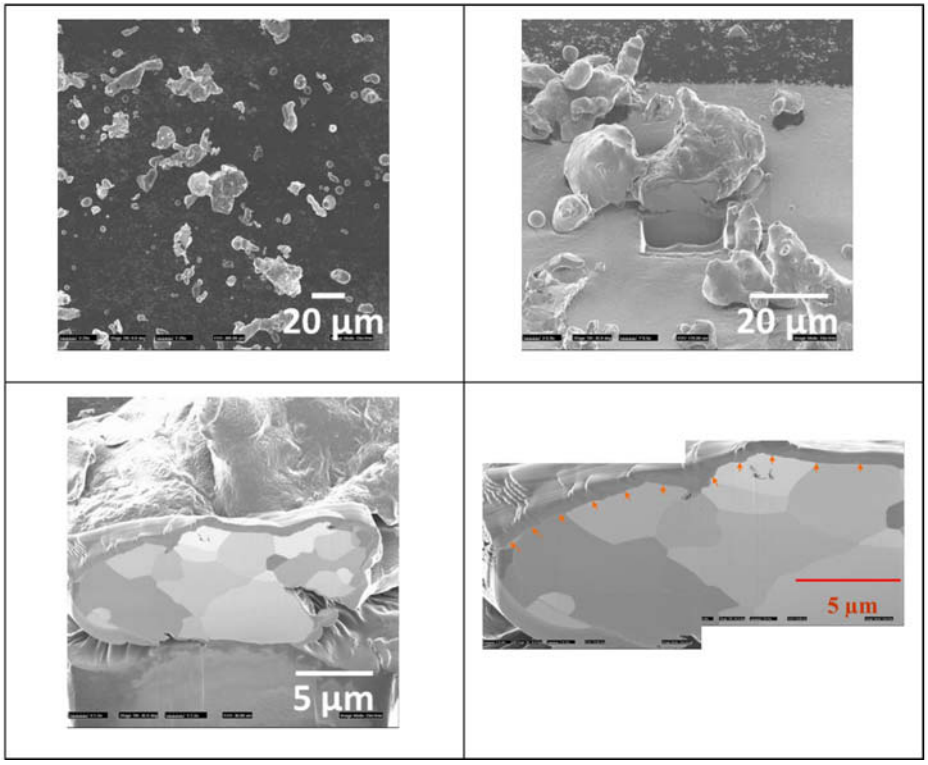

Figure 3. FIB cross section and high-resolution images of atomized stainless steel powder

Figure 3 shows a FIB cross section and secondary electron images of an atomized stainless steel metal particle. Under this processing condition, the small particle is found to have fully recrystallized ferrite grain structure. Ferrite phase is more malleable (as opposed to martensite) that allows more deformation during the ball milling process to incorporate (and potentially dissolve) Y_2O_3 nano particles more efficiently. Although it is still possible to use conventional metallography methods, FIB cross sectioning followed by in situ ion beam imaging is an effective technique to reveal the microstructure of these fine powders.

In some cases, multiple cross sections are desired to obtain microstructure information in three dimensions. In a study of high temperature corrosion resistance of stainless steels, small particles are found to form on the surface. Stainless steels passivate themselves by forming continuous Cr_2O_3 layer that reduces inward oxygen diffusion and outwards iron diffusion. The appearance of these microscopic particles can either be an early sign of passive film dissolution that could result in short-circuit oxygen inwards diffusion leading to accelerated corrosion, or simply be surface deposit during corrosion experiment. These particles are small, and conventional FIB section can be used to investigate particle-passive film-substrate relationship. However multiple

sections can provide a comprehensive view of the connection between these particles to stainless steels substrate. These particles are very small, and conventional metallurgical serial sectioning can only obtain images at approximately 50 µm per slice. At CanmetMATERIALS, we successfully performed automatic FIB serial sectioning on a selected particle formed on the corroded steel surface.

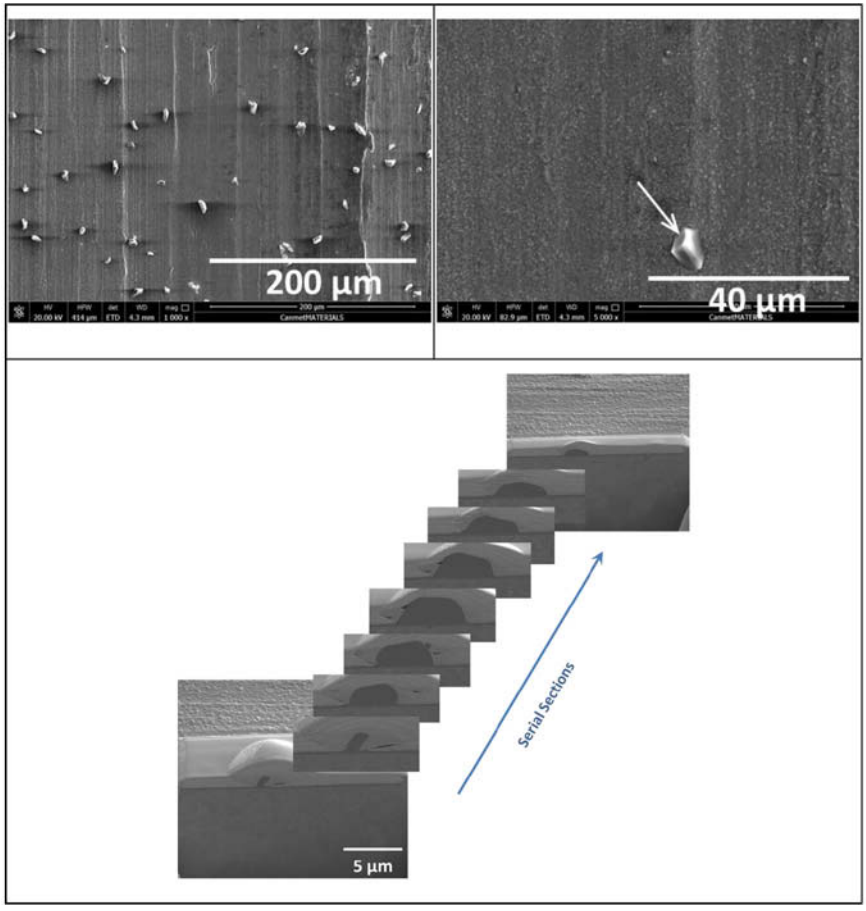

Figure 4. Selected images from FIB serial sectioning of an oxide particle found on stainless steel surface after high temperature corrosion test

The serial sectioning and imaging was set to run automatically with pre-set milling (slicing) intervals. In this particular case shown in Figure 4, the FIB milling of 300 nm per slice was achieved with a total of 80 slices. The entire particle was found to be above the passive Cr_2O_3 film, and not connected to the substrate at any point. With the serial sectioning in Figure 4, we were able to conclude with confidence that these particles are a result of surface deposition (precipitation) during cooling process in the high temperature corrosion experiment when

solubility of the dissolved ionic species in solution reduces. Corrosion resistance of the stainless steel was not compromised under this experimental condition.

Plan view TEM Specimen Preparation

FIB microscopes have become powerful tools in TEM specimen preparation [3, 11, 12], and these techniques have evolved rapidly. In many laboratories, making FIB lift out TEM specimens has become a daily routine. The lift out technique has shown significant advantages over the original H-bar technique that TEM specimens can be made directly from a bulk specimen without mechanical preparation [11]. The conventional lift-out technique since improved that much thicker specimens (typically 5 µm in thickness) are lifted out from the bulk and then transferred to TEM grids using a micromanipulator (in-situ or ex-situ) followed by final FIB thinning. However, in many cases, plan view TEM specimen is desired due to geometric configuration requirement. The plan view TEM specimen preparation is not a routine exercise [13, 14], and requires extensive FIB milling time and experienced operator especially when external micro-manipulator is used. Figure 5 shows a plan view TEM specimen was successfully prepared from a crack tip region at CanmetMATERIALS that allowed us to analyze the crack tip and surrounding region in great detail.

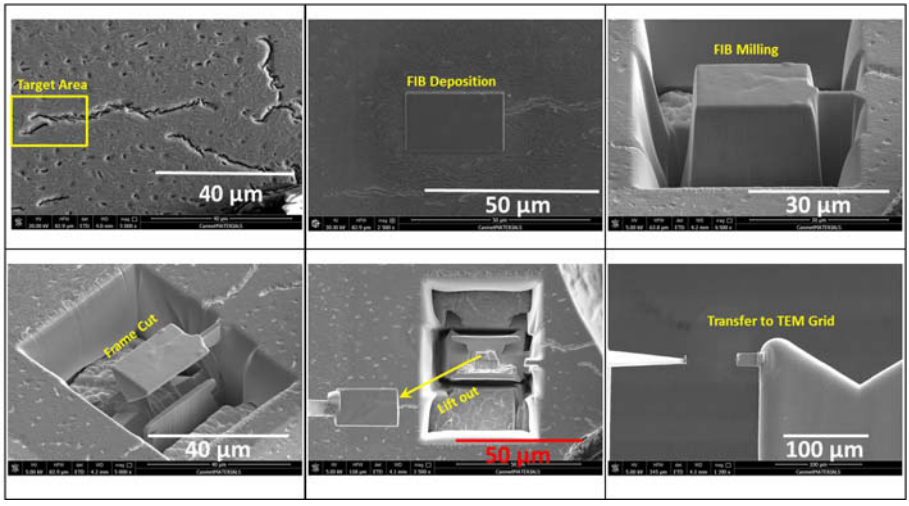

Figure 5. Plan view TEM specimen prepared from a crack tip region

The advantage of plan view TEM sample allows us to investigate specific microstructure features using all levels of microscopy techniques. In case of studying cracks (e.g. stress corrosion cracking, and delayed hydride cracking), conventional FIB lift out can't produce any TEM specimen with crack tip included in the foil. Understanding the crack tip morphology and the chemical composition near and ahead of active crack tip zone is of paramount importance in understanding crack propagation mechanism. Plan view lift out technique is the only reliable and practical method to produce high quality TEM specimen to study crack tip zone in microscopic scale [15].

Summary

In addition to make conventional TEM specimens as most of other FIBs do in other laboratories, FIB microscopes at CanmetMATERIALS has also been used as a powerful cross sectioning and imaging instrument. The FIB microscope has proven to be a backbone instrument that is essential in various fields of materials research at CanmetMATERIALS.

Acknowledgement

The authors would like to thank financial support from Her Majesty the Queen in Right of Canada, as represented by the Minister of Natural Resources.

References

[1] Melngailis, J. J. (1987). Focused ion beam technology and applications, Vac. Sci. Technol. B, 1987, vol. 5(2), pp. 469-495.

[2] Phaneuf, M. W.; Li, Jian and Malis, T. (1998). FIB techniques for analysis of metallurgical specimens, Microscopy and Microanalysis, 1998, vol. 4, pp. 492-493.

[3] Phaneuf, M. W. (1999). Imaging, spectroscopy and spectroscopic imaging with an energy-filtered field emission TEM, Micron, 1999, vol. 30, pp. 277-288.

[4] Li, Jian, McMahon, G.S. and Phaneuf, M.W. (2001). Proceedings of the Microscopically Society of Canada, 2001, vol. XXVIII, pp. 26-27.

[5] Li, Jian, Focused Ion Beam Microscope – More than a Precision Ion Milling Machine, Journal of Metal, 2006, vol.58 no.3, pp. 27-31.

[6] Roy, P., Berger, S. and Schmuki, P., Angew. Chem. Int. Ed. 2011, 50, 2904-2939.

[7] Gerischer, H., and Tributsch, H., Ber. Bunsen-Ges, 1968, 72, 437.

[8] Rao, C.N.R., Muller, A., Cheetham, A.K., The Chemistry of Nanomaterials: Synthesis, Properties and Applications, Wiley-VCH, Weinheim, Germany, 2006.

[9] Feldman, Y., Wasserman, E., Srolovitz, D.J. and Tenne, R., Science, 1995, 267, 222.

[10] Li, Jian, Advances in Materials Engineering Using State-of-the-art Microstructural Characterization Tools, in "New Material Science Research", Nova Science Publishers Inc., Invited. Ed. Lawrence V. Olivante, Nova Science Publisher, ISBN-13: 978-1-60021-654-1, 2008

[11] Giannuzzi, L.A. and Stevie, F.A. (1999). A review of focused ion beam milling techniques for TEM specimen preparation, Micron, 1999, vol. 30, pp. 197-204.

[12] Anderson, R. (2002). Comparison of FIB TEM Specimen Preparation Methods, Proceeding of Microscopy and Microanalysis, 2002, vol.8, pp. 44-45.

[13] Li, Jian Advanced Techniques in TEM Specimen Preparation, in: "The Transmission Electron Microscope", ISBN: 979-953-307-311-7, ed. Maaz Khan, 2011.

[14] Li, Jian, Malis, T., and Dionne, S., Recent Advances in FIB TEM Specimen Preparation Techniques, Journal of Materials Characterization, vol. 57, 64-70, 2006.

[15] Li, Jian, Elboujdaini, M., Gao, M., and Revie, R.W., Formation of Plastic Zone at the SCC Tip in a Pipeline Experienced Hydrostatic Testing, Materials Science and Engineering A, vol. 486, 496–502, 2008.

Characterization of Minerals, Metals, and Materials 2015
Edited by: John S. Carpenter, Chenguang Bai, Juan Pablo Escobedo, Jiann-Yang Hwang, Shadia Ikhmayies, Bowen Li, Jian Li, Sergio Neves Monteiro, Zhiwei Peng, and Mingming Zhang
TMS (The Minerals, Metals & Materials Society), 2015

Cyclic Hardness Test PHYBAL$_{CHT}$: A New Short-Time Procedure to Estimate Fatigue Properties of Metallic Materials

Hendrik Kramer, Marcus Klein, Dietmar Eifler

Institute of Materials Science and Engineering (WKK); University of Kaiserslautern;
P.O. Box 3049; 67653 Kaiserslautern, Germany

Keywords: Cyclic hardness test, fatigue properties, cyclic deformation behavior, short-time procedure, metallic materials, PHYBAL$_{CHT}$, cyclic hardening, TRIP-effect

Abstract

Conventional methods to characterize the fatigue behavior of metallic materials are very time and cost consuming. That is why the new short-time procedure PHYBAL$_{CHT}$ was developed at the Institute of Materials Science and Engineering at the University of Kaiserslautern. This innovative method requires only a planar material surface to perform cyclic force-controlled hardness indentation tests. To characterize the cyclic elastic-plastic behavior of the test material the change of the force-indentation-depth-hysteresis is plotted versus the number of indentation cycles. In accordance to the plastic strain amplitude the indentation-depth width of the hysteresis loop is measured at half minimum force and is called plastic indentation-depth amplitude. Its change as a function of the number of cycles of indentation can be described by power-laws. One of these power-laws contains the hardening-exponent$_{CHT}$ e_{II}, which correlates very well with the amount of cyclic hardening in conventional constant amplitude fatigue tests.
To identify heat-treatment-parameters and SAE 52100 TRIP-alloys with high hardening rates as well as their damage tolerance the PHYBAL$_{CHT}$- and PHYBAL$_{LIT}$-method were used. One modified SAE 52100 TRIP-alloy was investigated in detail. The fatigue behavior and the cyclic hardening of the selected SAE 52100 TRIP-alloy was investigated and compared with conventional SAE 52100. Conventional stress-controlled fatigue tests were performed on a servo-hydraulic test system with a frequency of 5 Hz and a load ratio of R = -1. Different rates of cyclic hardening were identified. The size of the nonmetallic inclusions leading to crack initiation and the number of cycles to failure were used to evaluate differences in the damage tolerance capability.

Introduction

One of the main reasons to initiate fatigue fracture in SAE 52100 steels are microstructural imperfections like nonmetallic inclusions [1]. Due to the wide spectrum of their size, microstructure and elastic properties, a high scattering in fatigue life is observed [2]. To reduce this, the TRIP-effect can be used to induce local hardening around imperfections with respect to an improved damage tolerance under cyclic loading. To identify SAE 52100 TRIP-alloys with a high hardening rate and a high damage tolerance the PHYBAL$_{CHT}$- and PHYBAL$_{LIT}$-method were used. PHYBAL$_{CHT}$ requires only a planar surface to perform cyclic force-controlled hardness indentation tests. To characterize the cyclic elastic-plastic material behavior the change of the force-indentation-depth-hysteresis was plotted versus the number of indentation cycles. Its change as a function of the number of indentation cycles can be described by power-laws. One of these power-laws contains the hardening-exponent$_{CHT}$ e_{II}, which correlates very well with the amount of cyclic hardening in conventional constant amplitude tests [3].

Material and heat treatment

Three alloy variants of SAE 52100 were considered. The first one was melted in industry in an electric arc furnace, forged to 100 x 100 mm², spheroidise annealed and is named in the following SAE 52100. The second alloy variant contains 1.9 % aluminum and the third alloy variant contains 1.0 % silicon in order to induce a TRIP-effect. The chemical compositions are given in Table I. SAE 52100 + 1.9 % Al and SAE 52100 + 1.0 % Si were produced as laboratory melts in a 2 kHz vacuum induction furnace and cast into 80 kg ingots with a cross-section of 140 x 140 mm². The as-cast materials were heated stepwise to 1250 °C, homogenized for two hours, open-die forged to 60 x 60 mm² and normalized. The steel was selected, melted and analyzed by the Department of Ferrous Metallurgy (IEHK) RWTH Aachen University. Fatigue specimens of steel SAE 52100 were austenized at 830 °C for 30 minutes, quenched in oil at 60 °C and finally annealed at 180 °C for 2 h. One batch, SAE 52100-I, was heat treated in a vacuum system with oil-quenching the second batch (SAE 52100-II) was heat treated in a bell furnace (atmospheric furnace flushed with N_2) with oil-quenching. The nominal heat-treatment parameters were identical. Dilatometer specimens of the steels SAE 52100 + 1.9 % Al and SAE 52100 + 1.0 % Si were austenized at 900 °C for 5 minutes, quenched by nitrogen to room temperature and austempered at 220 °C at different times of 3 h to 10 h. The fatigue specimens of steel SAE 52100 + 1.9 % Al were austenized at 900 °C for 35 minutes, quenched in a salt bath at 220 °C and austempered at 220 °C 5 h. The heat treatment processes were carried out at the Foundation Institute of Materials Science (IWT) in Bremen.

Table I. Chemical composition (wt.%) of the steels SAE 52100, SAE 52100 + 1.9 % Al, and SAE 52100 + 1.0 % Si

	C	Si	Mn	P	S	Cr	Mo	Ni	Al	Cu
SAE 52100 (I,II)	0.93	0.25	0.34	0.006	0.001	1.50	0.03	0.12	0.031	0.18
+ 1.9 % Al	0.92	0.25	0.37	0.004	0.002	1.52	0.04	0.13	**1.90**	0.19
+ 1.0 % Si	0.92	**1.00**	0.34	0.005	0.002	1.48	0.03	0.12	0.008	0.18

The PHYBAL$_{CHT}$-Method

The PHYBAL$_{CHT}$-method requires a planar material surface to perform ten cyclic force-controlled hardness indentation tests exactly at one identical position. For the investigations described in this paper a Vickers indenter, a sine load function and a compressive force of -1000 mN were used (Figure 1a)). According to the general procedure of Martens hardness tests, the indentation-depth h was measured. Thus, a force-indentation-depth-hysteresis can be plotted what is shown exemplarily in Figure 1b for the third cycle. In analogy to the plastic strain amplitude the indentation-depth width of the hysteresis loop was measured at mean load and named plastic indentation-depth amplitude $h_{a,p}$. To characterize the elastic-plastic material behavior, the change of the plastic indentation-depth amplitude was plotted versus the number of indentation cycles. To take into account scattering, the measurement was repeated at 20 different positions of the specimen. This results in an average-value-curve of the plastic indentation-depth amplitude which is characteristic for each material resulting of different heat treatment and alloy variants.

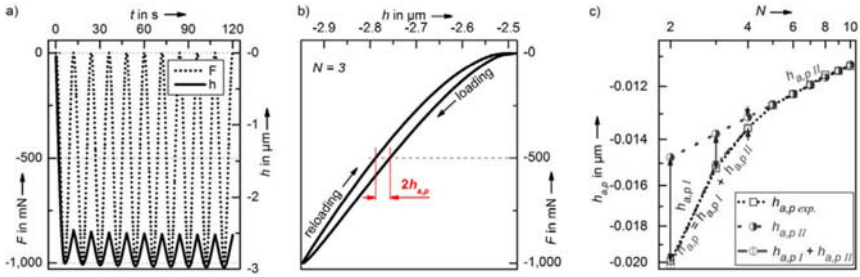

Figure 1. a) Test-procedure with the indentation depth h, b) Hysteresis exemplarily shown for the third cycle with the definition of the plastic indentation-depth amplitude $h_{a,p}$ and
c) Plastic indentation-depth amplitude $h_{a,p}$-N-curve described by two power-laws $h_{a,pI}$ and $h_{a,pII}$

Figure 1c) shows the plastic indentation-depth amplitude $h_{a,p}$ as a function of the number of indentation cycles N for a steel. The double-logarithmic plot reveals that after the fifth cycle the curve can be described by a single power-law which is specified as $h_{a,pII}$ in equation (1).

for $N > 4$: $$h_{a,p} = h_{a,pII} = a_{II} N^{e_{II}} \quad (1)$$

For the indentation cycles two to four the difference between the measured $h_{a,p}$-N-values and the $h_{a,pII}$-function can also be described by a power-law specified as $h_{a,pI}$. This means, the $h_{a,p}$-N-relationship can be described by the sum of the two power-laws $h_{a,pI}$ and $h_{a,pII}$ with equation (2).

for $2 \leq N \leq 4$: $$h_{a,p} = h_{a,pI} + h_{a,pII} = a_I N^{e_I} + a_{II} N^{e_{II}} \quad (2)$$

As the function $h_{a,pII}$ is a part of the mathematical description for all indentation cycles it is well suited to characterize the elastic-plastic behavior of metallic materials: The coefficient a_{II} describes the vertical position of the $h_{a,p}$-N-curves. This position is determined by the plasticity and the coefficient increases with increasing plasticity of the test material. Consequently, a_{II} is defined as plasticity$_{CHT}$. The exponent e_{II} describes the slope of the $h_{a,p}$-N-curves and thus the hardening rate of the different steel variants. Consequently, e_{II} was defined as hardening-exponent$_{CHT}$ e_{II}. e_{II} correlates very well with the amount of cyclic hardening in conventional constant amplitude tests. [3]

The PHYBAL$_{LIT}$-method

On the basis of one load increase test (LIT) and two constant amplitude tests (CAT) the physically based fatigue life calculation method PHYBAL$_{LIT}$ enables the calculation of the equations of Woehler curves in an excellent accordance to those determined conventionally with 20 or more specimens. The PHYBAL$_{LIT}$ procedure is described in detail for the steels SAE 1050 and SAE 4140 as well as the magnesium alloy MRI 230D in [4]. In the following, only the basic procedure is explained.

For the PHYBAL$_{LIT}$ tests described in this paper, axial stress-controlled fatigue tests were performed on a servo-hydraulic test system with a frequency of 5 Hz and a load ratio of R = -1. In the load increase tests a step length of $9 \cdot 10^3$ cycles and load steps of 20 MPa were applied. The change in specimen temperature ΔT was measured with one thermocouple fixed in the middle of the gauge length, T_1, and two thermocouples, T_2 and T_3, fixed at the elastically loaded shafts and calculated according to equation (3).

$$\Delta T = T_1 - \frac{T_2 + T_3}{2} \quad (3)$$

As shown by Starke et al., the change in temperature ΔT correlates with the plastic strain amplitude $\varepsilon_{a,p}$ and can be used to describe the cyclic deformation behavior as well as for the

calculation of fatigue life [4]. On the basis of $PHYBAL_{LIT}$ the pairs of values (σ_a, ΔT) measured in the load increase tests LIT and the two constant amplitude tests $CAT_{exp.}$ at 10^4 cycles (solid symbols ■● in Figure 2), a Morrow equation can be calculated. This Morrow equation is given by the $CAT_{calc.}$ open symbols (□, Figure 2) in analogy to cyclic-stress-strain-curves as cyclic-stress-temperature-curve. The ratio $Q(\sigma_a)$ of the values measured in the constant amplitude tests at 10^4 cycles and the corresponding load levels of the load increase test was determined by dividing $\Delta T(CAT_{exp.})$ and $\Delta T(LIT_{exp.})$. A linear relation between $Q(\sigma_a)$ and σ_a can be used [3]. The values (σ_a, ΔT) for constant amplitude loading $CAT_{calc.}$ are calculated by multiplying the ΔT-values of the load increase test LIT with the related ratio $Q(\sigma_a)$. Consequently the pairs of values (σ_a, ΔT) of the load increase test are used to calculate the Morrow equation, which is shown in Figure 2. With the exponent $n'_{\Delta T}$ of the generalized Morrow power-law the exponent $b_{\Delta T}$ of the generalized Basquin power-law can be calculated according to Figure 2. With the number of cycles to failure N_f of one constant amplitude test, a generalized Basquin equation can be calculated, describing the Woehler curve in excellent accordance to conventionally determined ones.

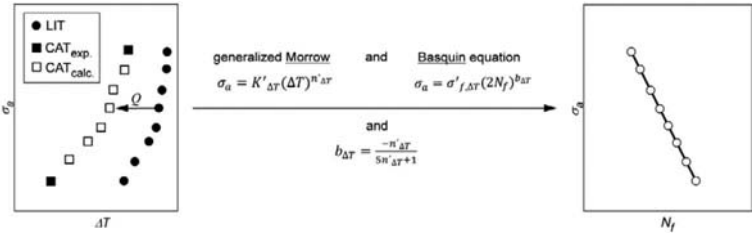

Figure 2. $PHYBAL_{LIT}$ based on the deformation-induced change in temperature ΔT, schematically.

Results and Discussion

$PHYBAL_{CHT}$ was used to identify an austempering time for SAE 52100 + 1.9 % Al to initiate an optimal TRIP-effect. Figure 3a) shows the influence of the austempering time at 220 °C on hardness, retained austenite (measured at IWT-Bremen), $hardening\text{-}exponent_{CHT}$ e_{II} and $plasticity_{CHT}$ a_{II}. The Martens hardness values were calculated from the first indentation cycle according to [5]. The content of retained austenite increases up to an austempering time of 5 h. Consequently, the hardness decreases. Due to the TRIP-effect $|e_{II}|$ and $|a_{II}|$ increase in direct correlation with the content of retained austenite. If the austempering time is longer than 5 h, the content of retained austenite decreases and the hardness increases (compare Figure 3a)). Furthermore the results indicate clearly, that the $hardening\text{-}exponent_{CHT}$ e_{II} is able to describe the linked reduction of hardening. Consequently, $PHYBAL_{CHT}$ is a suitable method to quantify the influence of retained austenite on hardening due to the TRIP-effect. The results show another remarkable benefit of $PHYBAL_{CHT}$, as it is able to detect the influence of heat-treatment parameters immediately on dilatometer specimens. Figure 3b) shows the $hardening\text{-}exponents_{CHT}$ e_{II} for SAE 52100 + 1.9 % Al and SAE 52100 + 1.0 % Si. Furthermore, Figure 3b) shows, that after the austempering time of 3 h different $hardening\text{-}exponents_{CHT}$ e_{II} for SAE 52100 + 1.9 % Al can be measured in comparison to SAE 52100 + 1.0 % Si although the content of retained austenite is similar. After an austempering time of 5 h the content of retained austenite decreases for SAE 52100 + 1.0 % Si to 17 % as well as the $hardening\text{-}exponent_{CHT}$ $|e_{II}|$ decreases.

However, $|e_{II}|$ is still higher for SAE 52100 + 1.0 % Si than for SAE 52100 + 1.9 % Al, although the content of retained austenite SAE 52100 + 1.0 % Si is only half of that of SAE 52100 + 1.9 % Al. This can be explained by the reduced mechanical stability of Si-caused block-type retained austenite in comparison to that of Al-caused film-type retained austenite also observed in [6]. PHYBAL$_{CHT}$ is capable to detect the differences in mechanical stability of retained austenite.

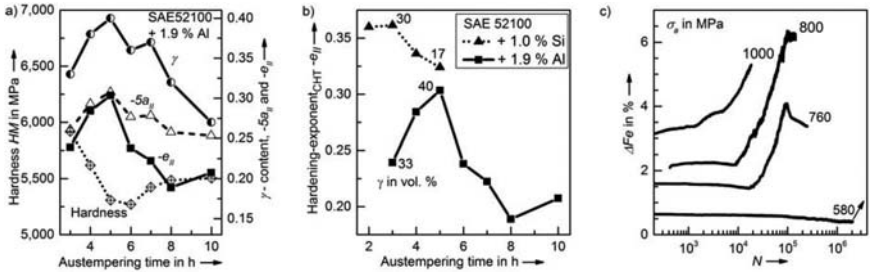

Figure 3. a) Influcence of austempering time on hardness, retained austenite γ (IWT-Bremen), hardening-exponent$_{CHT}$ e_{II}, and plasticity$_{CHT}$ a_{II} (note a_{II} is scaled 5 times)
b) Influcence of austempering time on hardening-exponent$_{CHT}$ e_{II} and comparison of selected contents of retained austenite (IWT-Bremen)
c) Change of the ferromagnetic content ΔFe versus N of SAE 52100 + 1.9 % Al

As a result of the PHYBAL$_{CHT}$ results shown in Figure 3 an austempering time of 5 h was used for the fatigue specimens of SAE 52100 + 1.9 % Al to induce a maximum cyclic hardening due to the TRIP-effect. Figure 3c) shows the phase transformation of SAE 52100 + 1.9 % Al as change of the ferromagnetic content ΔFe measured at the surface in the middle of the gauge length by a ferritescope versus N. Due to the Villari-effect, the start values of ΔFe increase with higher σ_a. The activation of the TRIP-effect for 760 MPa $\leq \sigma_a \leq$ 1,000 MPa is shifted to a lower number of cycles with increasing stress amplitudes. No TRIP-effect at the measured point on the surface is indicated at σ_a = 580 MPa. Figure 4a) shows cyclic deformation curves based on the change in temperature ΔT. The stress amplitudes between 760 MPa $\leq \sigma_a \leq$ 1,000 MPa show the same qualitative development: Until a thermal balance between the specimen's gauge length and the thermostatically controlled clamping is reached a maximum ΔT_{max} value is reached due to thermal conduction processes. Subsequently a continuous cyclic hardening can be observed by decreasing ΔT-values until a minimum value ΔT_{min} is reached right before failure. The difference $\Delta T_H = \Delta T_{max} - \Delta T_{min}$ can be calculated as exemplarily shown in Figure 4a) to quantify the amount of cyclic hardening. No significant cyclic hardening can be observed for the run-outs and, in addition, ΔFe (Figure 3c)) does not indicate any phase transformation. This is a very desirable behavior for a damage tolerant SAE 52100-TRIP-steel: It can be concluded that the TRIP-effect will not be activated in a component loaded in the range below the fatigue limit. This is very important because of the required high dimension stability for components e.g. bearings. However, when the local stress is higher around an imperfection, the TRIP-effect is induced only locally. In this case the TRIP-effect can reinforce the matrix locally and induce compressive residual stresses to prevent crack initiation or to stop cracks.
Cross-sections of the gauge length just beneath the fracture surface of the specimens loaded at σ_a = 1,000 MPa, 920, and 800 MPa were prepared and tested with PHYBAL$_{CHT}$. Figure 4b) shows the results in comparison to a cross-section in the origin state (σ_a = 0 MPa). The hardness

increases with increasing stress amplitudes σ_a, while the hardening-exponent$_{CHT}$ $|e_{II}|$ decreases. Consequently, the cyclic hardening ΔT_H shown in Figure 4a) reduces the hardening capability quantified by PHYBAL$_{CHT}$. The reduction of the hardening-exponent$_{CHT}$ -e_{II} due to fatigue is quantified by Δe_{II} (σ_a) = $|e_{II}$ (0 MPa)| - $|e_{II}$ (σ_a)|. Figure 4c) shows the correlation of cyclic hardening ΔT_H and the reduction of hardening-exponent$_{CHT}$ Δe_{II} after cyclic loading. PHYBAL$_{CHT}$ detects the reduction of the hardening capability very accurately.

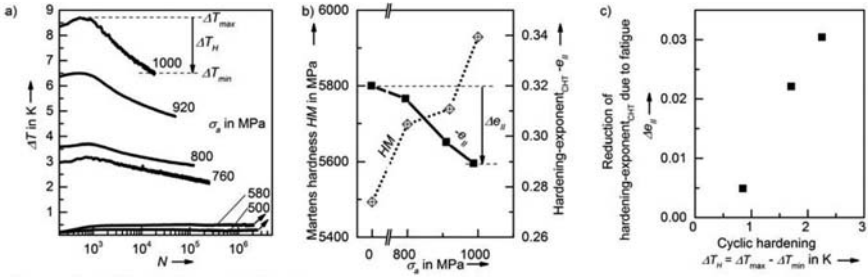

Figure 4. SAE 52100 + 1.9 % Al

a) Cyclic deformation curves based on the change in temperature ΔT versus N

b) Influence of the stress amplitudes σ_a on hardness and hardening-exponent$_{CHT}$ -e_{II} after cyclic loading

c) Correlation of cyclic hardening ΔT_H and the reduction of hardening-exponent$_{CHT}$ Δe_{II} after cyclic loading at different stress amplitudes σ_a

Figure 5a) shows several properties of the fatigue specimens in the origin state: The content of retained austenite of SAE 52100-I is significantly higher than that of SAE 52100-II. This indicates different temperatures in the effective heat-treatments compared to the nominal temperatures. The content of retained austenite of SAE 52100 + 1.9 % Al is significantly higher than that of both SAE 52100 batches. The hardening-exponent$_{CHT}$ -e_{II} specifies this difference as it increases in the same manner as the content of retained austenite. The hardness also indicates differences, although it cannot be attributed solely to the content of retained austenite, since SAE 52100-I has the highest hardness. Regarding hardness and the electrical resistance in the origin state R_0 it can be concluded, that there are more microstructural differences between SAE 52100-I and SAE 52100-II than only the content of retained austenite. These differences result in different Woehler curves shown in Figure 5b). The Woehler curves calculated by PHYBAL$_{LIT}$ reflect the differences in hardness. The failure was always caused due to nonmetallic inclusions. Figure 5b) reveals the chemical composition, the size as area$^{0.5}$ according to [2] and the position of the inclusion. The area$^{0.5}$-values vary for SAE 52100 + 1.9 % Al even a bit more than for the SAE 52100 batches: Largest inclusions are aluminum oxides of 25 µm in SAE 52100-II, 35.2 µm in SAE 52100-I and 45.5 µm in SAE 52100 + 1.9 % Al. The smallest inclusions are nitrides of 5.2 µm in SAE 52100-II, 5.2 µm in SAE 52100-I and 7.9 µm in SAE 52100 + 1.9 % Al. In contrast to this, the scatter of the experimental results is significantly lower for SAE 52100 + 1.9 % Al, than that of SAE 52100-I and SAE 52100-II. SAE 52100-II shows a scatter of about one decade N_f to the Woehler curve between the Al_2O_3 at σ_a = 1,000 MPa and the TiN at σ_a = 880 MPa. However, the scatter of SAE 52100 + 1.9 % Al is much lower, regarding the difference between N_f and the calculated Woehler curve of the AlN at σ_a = 920 MPa and the Al_2O_3 at σ_a = 760 MPa.

In other words: The size and the type of inclusion have a minor effect on fatigue life in SAE 52100 + 1.9 % Al, than for SAE 52100. This confirms the increased damage tolerance of the TRIP-alloyed SAE 52100 + 1.9 % Al. Furthermore, one specimen of SAE 52100 + 1.9 % Al reached the ultimate number of cycles of $12 \cdot 10^6$ at $\sigma_a = 500$ MPa, 580 MPa, and 600 MPa, marked as a), b), and c) in Figure 5b). It was cycled in part d) with $\sigma_a = 620$ MPa to reveal the largest inclusion inside the gauge length. Besides, a pre-damage caused in the parts a)-c) can be presumed, as it failed already at $1.7 \cdot 10^5$ cycles. However it is very remarkable, that the 58.3 µm large Al_2O_3- and SiO_2- inclusions did not lead to fracture in the parts b) and c), which shows a good accordance to the Woehler curve with a small scatter band. Furthermore, it is an impressive proof of the damage tolerance of the modified SAE 52100 + 1.9 % Al.

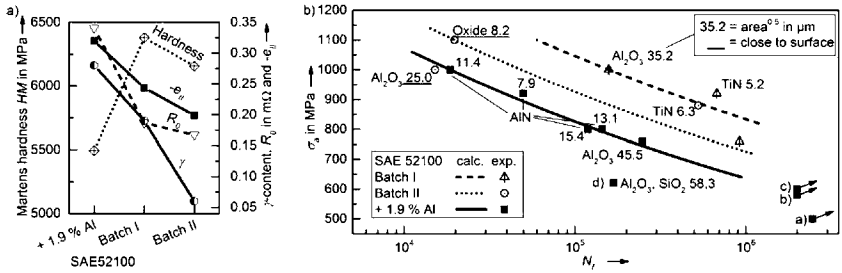

Figure 5. a) Comparison of SAE 52100 + 1.9 % Al versus SAE 52100-I and SAE 52100-II concerning hardness, hardening-exponent$_{CHT}$ -e_{II}, retained austenite γ (IWT-Bremen), and electrical resistance R_0 of the unloaded fatigue specimens
b) Woehler curves of SAE 52100 + 1.9 % Al, SAE 52100-I and SAE 52100-II with the size and composition of nonmetallic inclusions, which caused failure

Conclusions

To identify SAE 52100 TRIP-alloys with a high hardening rate and a high damage tolerance the methods PHYBAL$_{CHT}$ and PHYBAL$_{LIT}$ were used. Both methods are short-time procedures developed at the Institute of Materials Science and Engineering at the University of Kaiserslautern for the determination of fatigue data of metallic materials [3]. The cyclic hardness test PHYBAL$_{CHT}$ was used to evaluate the hardening rate due to variations in alloy composition and heat treatment. In this investigation the modified SAE 52100 + 1.9 % Al TRIP-alloy was selected for detailed investigations. The fatigue behavior and the cyclic hardening of SAE 52100 + 1.9 % Al was compared with conventional SAE 52100. Stress-controlled fatigue tests were performed on a servo-hydraulic test system with a frequency of 5 Hz and a load ratio of $R = -1$. The increase of the ferromagnetic content ΔFe in constant amplitude tests of SAE 52100 + 1.9 % Al indicates the TRIP-effect. The deformation-induced change in temperature was plotted versus the number of cycles to identify different rates of cyclic hardening. The amount of cyclic hardening could be correlated to the decrease of the hardening-exponent$_{CHT}$ e_{II} after loading. It could be shown that there is no TRIP-effect when the steel is loaded at stress amplitudes beneath the fatigue limit where elastic deformation dominates. This is very important because of the required high dimension stability for components e.g. bearings. However, when the local stress is higher around an imperfection, the TRIP-effect is activated locally. In this case the TRIP-effect strengthens the matrix locally and induces compressive residual stresses and prevents or stops fatigue cracks. The increased damage tolerance of the TRIP-alloyed

SAE 52100 + 1.9 % Al is confirmed with a minor effect of size and type of inclusions on the fatigue life time compared with standard SAE 52100.

Acknowledgements

The financial support of this work by the German Research Foundation (DFG) and the German Federation of Industrial Research Associations (AIF) is gratefully acknowledged. Special thanks to Prof. Dr. W. Bleck, M. Bambach and A. Stieben, Department of Ferrous Metallurgy (IEHK) RWTH Aachen University, and Prof. Dr. H.-W. Zoch, Prof. Dr. F. Hoffmann and Dr. H. Surm, Foundation Institute of Materials Science (IWT) Bremen, for their experimental support.

Refercences

1. Bathias, C., *Gigacycle fatigue of bearing steels.* Materials Science and Technologie, 2012. **26**(1).
2. Murakami, Y., *Metal Fatigue: Effects of Small Defects and Nonmetallic Inclusions*. 2002, Oxford: Elsevier.
3. Kramer, H., et al., *Cyclic hardness test PHYBAL$_{CHT}$ – Short-time procedure to evaluate fatigue properties of metallic materials.* International Journal of Fatigue, 2014.
4. Starke, P. and D. Eifler, *Fatigue assessment and fatigue life calculation of metals on the basis of mechanical hysteresis, temperature and resistance data.* MP Materials Testing, 2009. **51**(5): p. 261-268.
5. *DIN EN ISO 14577-1, Metallic materials – Instrumented indentation test for hardness and materials parameters – Part 1: Test method (ISO/DIS 14577-1:2012); German version prEN ISO 14577-1:2012*, 2012.
6. Seol, J.-B., et al., *Atomic scale effects of alloying, partitioning, solute drag and austempering on the mechanical properties of high-carbon bainitic–austenitic TRIP steels.* Acta Materialia, 2012. **60**: p. 6183–6199.

Characterization of Minerals, Metals, and Materials 2015
Edited by: John S. Carpenter, Chenguang Bai, Juan Pablo Escobedo, Jiann-Yang Hwang, Shadia Ikhmayies, Bowen Li, Jian Li, Sergio Neves Monteiro, Zhiwei Peng, and Mingming Zhang
TMS (The Minerals, Metals & Materials Society), 2015

INNOVATIVE PROCEDURE FOR THE CHARACTERISATION OF THERMO-MECHANICAL PROPERTIES OF CARBON BASE MATERIALS USING THE GLEEBLE® 3800 SYSTEM

Dany Racine[1], Dmitry Lukovnikov[1], Daniel Marceau[1], Denis Laroche[2]

[1] University Research Centre on Aluminium (CURAL) - Aluminium Research Centre (REGAL) - University of Québec at Chicoutimi; 555, Boul. de l'Université; Chicoutimi, Québec, G7H 2B1, Canada
[2] Rio Tinto Alcan (Arvida Research and Development Center); P.O. Box 1250; Jonquière, Québec, G7S 4K8, Canada

Keywords: carbon anode, thermo-mechanical properties, coefficient of thermal expansion, Gleeble®

Abstract

Carbon base materials play a critical role in the performance of Hall-Héroult cell. The determination of their thermo-physical properties is of primary importance for modeling and designing complete cell systems. However, overcoming the associated experimental hurdles is complex and often underestimated. Of them are the Poisson's ratio measurements and the continuous oxidation/burning of the materials at temperatures above ~200°C. The novel procedure developed in this research is based on the Gleeble® 3800 system. Its vacuum chamber allows test with a chosen atmosphere at temperature of more than 1000°C. Young's modulus, Poisson's ratio and the coefficient of thermal expansion values can all be adequately measured using a single test. Cylindrical carbon samples (∅: 50mm, L: 100mm) were tested in the modified system at temperatures ranging from room to 950°C without any trace of oxidation. The resulting values were also in good agreement with literature data for a specific graphite material.

Introduction

Carbon base materials are a critical part of the production of aluminum worldwide as they compose the heart of the Hall-Héroult electrolysis cell; the anode and cathode. Cell performances depend significantly on their thermo-mechanical behavior during operation. Varying the manufacturing recipe to reach the higher performance can affect the basic thermo-physical properties of the components such as Young's modulus (E), Poisson's ratio (v) and the coefficient of thermal expansion (CTE) [1]. Knowing precisely their resulting values at room and operating temperatures can be very useful. Small-scale testing combined with numerical simulation can select promising recipe and therefore limit costly physical implementation.

However, measuring those properties is accompanied by many experimental challenges because the samples are quasi-brittle carbon based agglomerate, akin to ceramic, which oxidize readily at temperatures above ~200°C. Their microstructure is also heterogeneous at the millimeter scale

with some cracks and pores [2, 3]. Also, the Poisson's ratio is already tricky to measure because of the very small associated displacement, even more so on brittle heterogeneous specimens which can be oxidized at high temperature.

The scope of this study is to validate the use of the Gleeble® for testing carbon base materials. The necessary modifications and the testing procedure are first explained. Then, the setup validation is done against a known material accompanied by repeatability test on carbon samples. Since Joule effect heating gives a parabolic temperature distribution with possibly a large thermal gradient at the edge, the temperature profile is measured to ensure it isn't too large. The temperature evolution of E and ν is measured at each targeted temperature on the same carbon sample, all within a two hours' time frame. After that, carbon samples are also compressed and broken to obtain complete strain-stress curves at specific temperatures. Finally, the CTE was extracted from the heating curve of a previous test.

The Gleeble® 3800 system

The Gleeble® 3800 system, partially shown on Figure 1, is a thermo-mechanical simulator that replicates processing conditions that occur during the manufacture/operation of a metallic material (welding, forging, cold rolling, etc). Its heating system is based on the Joule's effect which heat up the sample by passing a controlled amount of electric current through it.

Figure 1: Work area of the Gleeble®. On the right: vacuum chamber with compression setup.

The Gleeble® covers a wide variety of testing applications like hot/warm compression testing, thermal cycling/heat treatment, dilatometry/phase transformation and many others [4]. It offers a unique flexibility with configurable components that make it possible to overcome those difficulties. In this regard, it is possible to conduct a best suited compression test on brittle samples as it tends to close cracks and pores [5]. The exerted force is up to 200kN and is carried out in an inert gas filled vacuum chamber to avoid the oxidation problem. The setup can be modified to use a cylindrical carbon sample of 100mm length by 50mm diameter which is large enough to display a sufficiently homogenous behavior (diameter of >10x biggest particle size) and produce larger displacement [6]. The sample can be instrumented with two high temperature extensometers along with four thermocouples. As an added advantage, the Gleeble® has a very

low thermal inertia as only the sample is heated, giving fast turnaround time. All those features make the Gleeble® a prime candidate for high temperature testing of carbon base materials.

Some modifications on the existing design were made to satisfy experimental requirements. Figure 2 shows the resulting assembly that goes inside the vacuum chamber (see Figure 1).

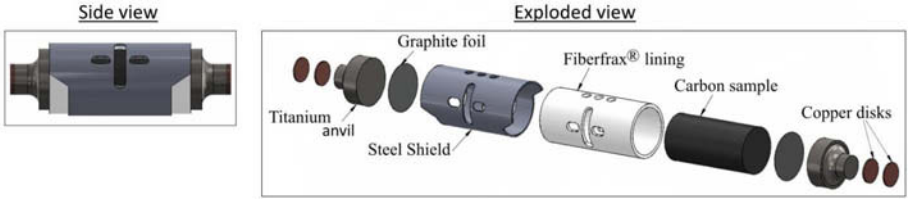

Figure 2: Components and assembly view.

First, the anvil assemblies were replaced by two customs made titanium 6Al-4V anvil of 50mm diameter able to resist temperature of up to 900°C.

Second, a shield with 56mm inner diameter was machined out of a steel tube to protect the surrounding equipment from the radiated heat and from red hot flying fragments resulting from eventual sample failure. The shield was slotted to accommodate both of the B-1 class axial (gage length 25mm, +12.5/-5mm) and B-2 class radial (gage length 50mm, ±6mm) extensometers as well as three thermocouples. It is lined with a disposable 3mm thick Fiberfrax® fired ceramic paper which serves as thermal and electrical insulator while also damping the specimen failure's shock to both extensometers without confining the sample.

Third, arm and grip modifications were made on the two extensometers to accommodate for the relatively big sample size, both shown on Figure 3. They were subsequently calibrated to ensure that the modifications would not affect their accuracy. Hanging extensometer supports were put on the base of each side, averaging displacement and keeping the extensometers on the sample center, thereby avoiding lateral movement that would pollute the instruments reading.

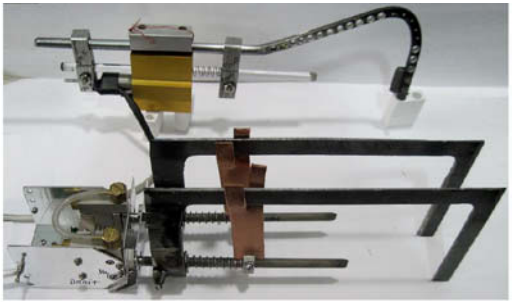

Figure 3: Axial (bottom) and radial (top) extensometer with arm/grip modifications.

Finally, since no spherical seats are present to compensate off-axis load caused by small machining deviation, mechanical compliance was use. Therefore, two replaceable pure copper disks are put at the bottom of each anvil and disposable graphite foils are put on both sides between anvil and sample. This also provides good electrical contact for the load assembly.

Experimental procedure

Preparation begins with the insertion of the Fiberfrax® paper on the inner shield wall and is fired 30min in an oven at 500°C. After cooling, a machined sample is inserted inside and some Fiberfrax® is cut away to give sample access to the extensometers and thermocouples through the shield's holes. The sample is drilled ~4mm deep through the middle shield hole to enable the measure and control of the specimen temperature. A thermocouple is then inserted with a bit of high temperature carbon glue to give better thermal contact and securing it into place.

The assembled shield is put inside the Gleeble® between the two anvils with a part resting on an insulating ceramic cord wrapped around both rims. The anvils are brought closer together and, before the full contact, two graphite foils 0.25mm thin by 50mm diameter are slid into place. The sample is centered after contact is made then a small preload is applied to stabilize the setup. The two extensometers are installed on the sample and suspended from their supports.

After the instruments are connected, a pretest is carried out at room temperature with a stress level at around half the yield point. This test is an adaptation of the procedure for compression test of concrete to stabilize setup and insure all instruments behave properly [6]. Once anomalies are corrected, the vacuum chamber is closed and filled with argon. Two kinds of tests were carried out: one using a single sample to repeatedly measure the elastic properties at 25, 400, 500, 600, 700, 800 and 950°C with pretest load condition and the other to conduct the measurement trough failure for a temperature of 25, 600, 700, 800, 950°C. For both tests, the sample is heated at a rate of 15°C/min to the target temperature. After one minute holding time, the sample is compressed at 1mm/min until half yield stress or failure. After the test, the sample is removed after cooling below burning temperature (~200°C). Subsequent inspections on the copper disks are made to verify their integrity and are replaced if noticeable damage is observed.

Results and discussion

Calibration tests

For the first calibration, the AA6061 aluminum alloy was chosen owing to its availability and well known properties. If tested successfully, its high stiffness compared to carbon (~10x) would ensure good measure of mechanical properties on carbon material. The testing conditions were kept as close as possible to the carbon experiment with a sample of 100mm length by 50mm diameter tested at a rate of 1mm/min up to 50MPa. However, the aluminum sample large diameter and low electrical resistivity doesn't allow any heating since it would quickly overheat the titanium anvil's base which has a smaller diameter and higher resistivity. Therefore, the tests were done only at room temperature. The obtained results are summarized in Table I.

Table I: Measured E and ν for AA6061 vs. literature (E = 69.7 GPa and ν = 0.33) [7].

Test number	E (GPa)	Error (%)	ν	Error (%)
1	65.3	-5.7	0.263	-20.2
2	69.1	-0.9	0.307	-7.0
3	68.5	-1.7	0.307	-7.1
4	75.1	7.7	0.309	-6.4
5	75.0	7.6	0.318	-3.7

The first test illustrates well why a pretest is needed after installation [6]. The anomalies of test one were corrected by reinstalling both extensometers followed by a second and third tests which were more stable. A reinstallation of the extensometers was done before test 4 and 5 with no anomalies detected in the curves. The measured and literature values are in good agreement with an average deviation of E and ν below 10%, which is more than needed for our purpose. To illustrate the measurement stability on an anodic carbon sample, a number of tests were made using the same sample with a reinstallation of instruments before each test. Figure 4 shows a representative stress-strain curve including radial and axial strain components for a room temperature test while Table II shows the compiled data.

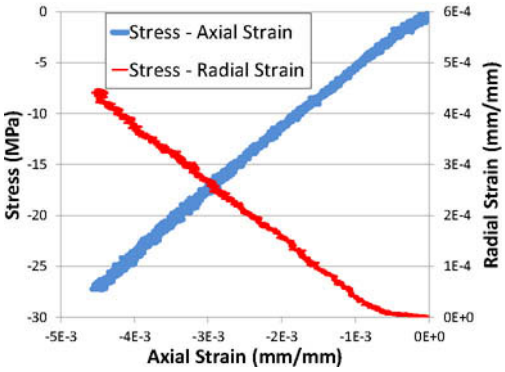

Figure 4: Room temperature stress-strain and radial – axial strain curve for an anode sample.

Table II: Elastic properties measure of an anode sample.

Test no.	E (GPa)	ν
1	6.30	0.110
2	6.67	0.121
3	6.04	0.111
4	6.76	0.119
5	6.46	0.117
6	6.12	0.115
7	6.14	0.108
8	5.96	0.113
Mean	*6.31*	*0.114*
St.d.	*0.30*	*0.004*

As expected, the results show a linear elastic behavior for both properties. Yet, it can be seen that the radial extensometer tends to stay put at low load. If this behavior persists at higher load, the test must be discarded because of the polluted instrument reading that affect the Poisson's ratio.

For the second calibration test, the thermal profile was measured in the middle hot zone of a carbon sample with three thermocouples placed at -15, 0, +15mm from the mid-length of the sample. The data was used to calculate the second order term, A, describing a parabolic temperature profile center on the sample mid length. It was then use to determine the total temperature gradient and the average temperature in between the axial extensometer legs which need to be as low and close as possible to the target temperature to assure that the studied sample behave like one at isotherm. The resulting values are listed in Table III.

Table III: Thermal gradient at different test temperatures.

Temperature (°C)	ΔT at +/-15mm (°C)	Temperature profile term A	ΔT for a 25mm gage length (°C)	Average temp. over 25mm (°C)
400	-5	-0.022	-3	399
500	-8	-0.034	-5	498
600	-10	-0.046	-7	598
700	-12	-0.054	-8	697
800	-13	-0.052	-8	797
950	-15	-0.068	-11	946

In the worst case at 950°C, the sample experiences a thermal gradient around -11°C with an average temperature of 946°C for a fourth of its total length which is excellent. This good performance is most probably due to the appropriate insulation provided by the steel shield and ceramic liner. Considering the material high thermo-physical stability and absence of transition temperature, testing in these conditions is fully satisfactory and should yield good results.

Single sample used at multiple temperatures

To determine evolution of a single sample's E and ν with respect to temperature, it is possible to perform one mechanical load-unload cycles for each targeted temperature on the same carbon sample. This method provides greater repeatability than use to obtain results shown in Table 2 since no instruments is manipulated after a measure and is best suited to determine the elastic properties at different temperatures. It is also very fast compared to conventional heating oven with all data available within 90 minutes after the beginning of the test. Three samples were tested with increasing temperature and the resulting value of E and ν are shown on Figure 5 and 6 respectively.

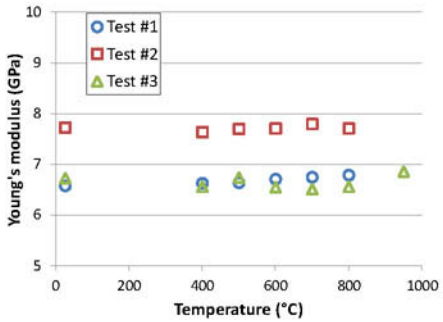

Figure 5: Young's modulus at various temperatures.

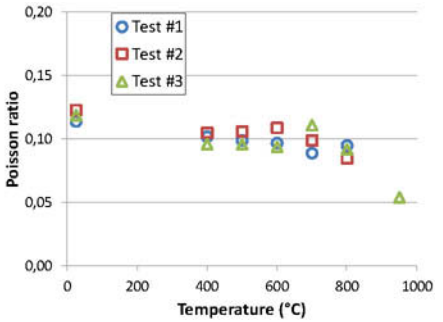

Figure 6: Poisson's ratio at various temperatures

The Young's modulus shows remarkable stability as temperature increase and the room temperature results also compare well with other published data on anodic carbon material [8, 9]. On the other hand, a small but significant downward trend is observed for the Poisson's ratio. Since samples are taken from the same anode, closer value of E would be expected considering the precision shown in Table 2. However, the anodic carbon orthotropic properties are well recognized and can largely cover this difference. Samples taken within a small region of an anode can display slight differences owing to density variation and anisotropy caused by the anode compaction process or simply because of their underlying heterogeneous nature [3].

Trough failure high temperature tests

To get an assessment of the behavior of carbon sample at different temperatures, 10 compression tests were carried-out until failure. Today, it is well known that the anodic carbon has a quasi-brittle behavior with softening before failure, which is of prime importance and must now be taken into account during the optimisation process of cell design. In this regard, Figure 7 shows a stress-strain curve, representative of the behavior until failure of anodic carbon sample, while Figure 8 present the evolution of the ultimate and failure stress at different temperatures.

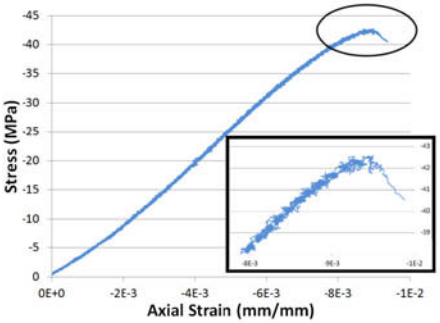

Figure 7: Representative stress-strain curve of an anodic carbon sample at 800°C.

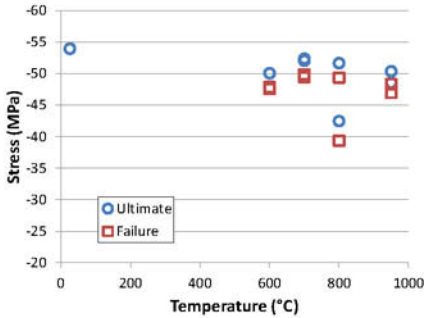

Figure 8: Ultimate and failure stress of anodic carbon samples at temperature.

The ensuing data dispersion is relatively low but only two tests were performed per temperature. It is an accepted fact that the ultimate and failure strength of materials having defects like anode are best described by a Weibull distribution [3, 5, 9]. Defining accurately such distribution to get valid trends require about 30 samples. Therefore, two tests can only give a rough estimate of the ultimate and failure stress, which are around 50 and 47 MPa respectively for all temperature.

Thermal dilatation tests

Last but not least, the CTE can also be extracted during the heating phase of a test. The dilatometry curve shown on Figure 9 was obtained using the axial extensometer data taken from failure tests at 950°C. It shows a linear expansion giving a CTE of about 5.19 $x10^{-6}$/K. This value is slightly above published data of around 4.5 $x10^{-6}$/K [9] for similar anodic carbon. A small deviation from that trend is detected at temperature below 200°C which can be explained by instability in the heating current at that stage. A higher preload could solve this issue.

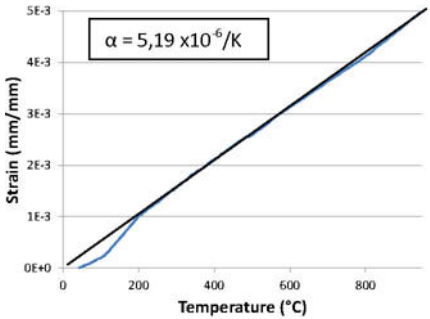

Figure 9: Dilatometry curve of an anode sample.

Conclusion

This paper presents a very interesting approach to obtain some of the thermo-mechanical properties of carbon base materials using the Gleeble® 3800 system. The proposed methodology

was firstly tested against an aluminum reference material at room temperature with good results and measurement of stability was also asserted. The mid-length hot zone of the samples had a thermal gradient of around -11°C with an average temperature within less than 5°C of any given testing temperature which assure a quasi isothermal behavior. Values of E, ν, CTE as well as the ultimate and failure stress of anodic carbon have all been successfully obtained from a series of experiment from room to 950°C without any detectable oxidation of the samples. In light of this, the Gleeble® 3800 system is, with minor modification, very well suited to investigate the high temperature properties of carbon base materials.

Acknowledgements

The authors acknowledge the financial support of the *Fonds québécois de la recherche sur la nature et les technologies* by the intermediary of the Aluminum Research Center – REGAL and Natural Sciences and Engineering Research Council of Canada (NSERC). Also, Rio Tinto Alcan (RTA) and particularly our industrial partners from Arvida Research and Development Center (ARDC) are greatly appreciated for providing financial support.

References

1. B. R. C. Perruchoud, "Effect of coke properties and its blending recipe on performances of carbon anode for aluminium electrolysis", *Journal of Central South University of Technology Eng.*, 13 (6) (2006), 647-652.

2. C. G. D'Amours et al., "Multi-axial mechanical behavior of the carbon cathode: understanding, modeling and identification", *TMS Light Metals*, 2003, 633-639.

3. O. E. Frosta, A. P. Ratvik, and H. A. Øye, "Properties and production condition affecting crack formation and propagation in carbon anodes", *TMS light metals*, 2012, 1293-1298.

4. Dynamic System Inc., http://www.gleeble.com/index.php/products/gleeble-3800.html.

5. Joshua Pelleg, *Solid Mechanics and Its Applications: Mechanical Properties of Ceramics* (Springer International Publishing Switzerland, 2014), 77 and 102-112.

6. ASTM C469-02, *Static Modulus of Elasticity and Poisson's ratio of Concrete in Compression* (West Conshohocken, PA: ASTM International, 2003).

7. ASM Handbook, vol. 2 (formerly 10th ed.), *Properties and Selection: Nonferrous Alloys and Special-Purpose Materials* (Metals Park, OH: American Society for Metals, 1993), 103.

8. J. Chmelar, "Size reduction and specification of granular petrol coke with respect to chemical and physical properties" (Ph.D. thesis, Norwegian university of science and technology, 1992).

9. D.H. Andersen, and Z.L. Zhang, "Fracture and physical properties of carbon anodes for the aluminum reduction cell", *Engineering Fracture Mechanics*, 78 (2011), 2998–3016.

Characterization of Minerals, Metals, and Materials 2015
Edited by: John S. Carpenter, Chenguang Bai, Juan Pablo Escobedo, Jiann-Yang Hwang, Shadia Ikhmayies, Bowen Li, Jian Li, Sergio Neves Monteiro, Zhiwei Peng, and Mingming Zhang
TMS (The Minerals, Metals & Materials Society), 2015

SOLID SOLUTION CHARACTERIZATION IN METAL BY ORIGINAL TOMOGRAPHIC SCANNING MICROWAVE MICROSCOPY TECHNIQUE

Eric Bourillot, Pauline Vitry, Virgil Optasanu, Cédric Plassard, Yvon Lacroute, Tony Montessin, Eric Lesniewska

ICB UMR CNRS-6303; 9 Avenue Alain Savary; Dijon; 21078; France

Keywords: Scanning Microwave Microscopy, Metal characterization, Oxygen diffusion, Buried defects

Abstract

A general challenge in metallic components is the need for materials research to improve the service lifetime of the structural tanks or tubes subjected to harsh environments or the storage medium for the products. One major problem is the formation of lightest chemical elements bubbles or different chemical association, which can have a significant impact on the mechanical properties and structural stability of materials. The high migration mobility of these light chemical elements in solids presents a challenge for experimental characterization. Here, we present work relating to an original non-destructive, with high spatial resolution, tomographic technique based on Scanning Microwave Microscopy (SMM), which is used to visualize in-depth chemical composition of solid solution of a light chemical element in a metal. The experiments showed the capacity of SMM to detect volume. Measurements realized at different frequencies give access to a tomographic study of the sample.

Introduction

The migration of light chemical elements in the metallic materials plays a key role in many phenomena like thermal oxidation. A wide range of technological applications is related to this topic: diffusion doping, fuel cells, surface treatment, and ultrapurification of gases, sintering or corrosion protection. The presence of some chemical diffusing species can strongly modify the mechanical properties of materials and can be a threat for the metal parts integrity. Measuring their spatial distribution is useful for understanding the mechanisms governing their diffusion, to identify the diffusion law by determining the parameters which govern it. The accurate measurement of light elements is not easy and often requires a heavy-duty experimental installation (nuclear microanalysis). Moreover, most of these techniques relies on surface measurements, induced by the interactions of an electron beam with the material and are thus

limited to few nanometers under the surface. So, the precise measurement of the concentration of light elements is impossible especially for very volatile species or when the surface contamination occurring during sample preparation cannot be avoided. The best examples are respectively the hydrogen in metals or the oxygen in reactive materials. Generally, the measurement corresponds to an average of the information obtained on a small volume (1μm^3 for EDS) including the contaminated surface, a fact that can present a substantial downside.

In this article we present an original tomography method based on the Scanning Microwave Microscopy (SMM). To illustrate this original approach, we will first study the case of a calibrated sample composed of buried material. Then, we will focus on the complex case of the solid solution of oxygen in zirconium.

Study of a calibrated sample

Scanning Microwave Microscopy

The Scanning Microwave Microscope (SMM) consists of an Atomic Force Microscope (AFM 5600LS, *Agilent Technology*) interfaced with a Vector Network Analyzer (VNA N5230A, *Agilent Technology*). A microwave signal is sent directly from the network analyzer and transmitted through a resonant circuit to a conductive AFM probe that is in contact with the sample being scanned. A half wavelength impedance transformer is placed directly across a 50 Ω load to form a matched resonance circuit. The cantilever and the probe play here the role of a local radiant antenna for emission and reception of the electromagnetic field. By analogy with optics, the probe also serves as a receiver to capture the reflected microwave signal from the contact point.

The reflected microwave signal is specific to the probe-sample interaction. A reflection coefficient (a complex number with magnitude and phase), which is the ratio between the incident and the reflected signals, gives an account of this interaction at the contact point. The magnitude and the phase of the ratio between the incident and the reflected signals are recorded simultaneously with the surface topography. The SMM typically operates at microwave frequencies of 300 MHz - 13 GHz.

The most important parameter lies in the choice of the conductive probe. The tips used are traditional AFM tips of silicon nitride Si_3N_4 (height: 3µm) of pyramidal form, associated with triangular levers (having a constant of stiffness ranging between 0.1 and 4 $N.m^{-1}$), covered with a conductive layer of Pt/Ir mixture (100 nm thick).

To characterize a sample in its thickness, it is necessary to use several frequencies. From the electromagnetic wave propagation properties in the metallic materials, it is possible to estimate the investigation depth by application of the "skin effect".

Indeed, this physical phenomenon shows that the electromagnetic wave of high frequency has a weaker power of penetration in a metal sample than that of low frequency:

$$\delta = \frac{1}{\sqrt{\pi \mu_0 \mu_r \sigma f}} \qquad (1)$$

with δ the skin thickness, μ_0 the magnetic permeability of vacuum ($4\pi.10^{-7}$), μ_r the permeability relating to the conductor, σ the electric conductivity (in $S.m^{-1}$), f the frequency (in Hz).

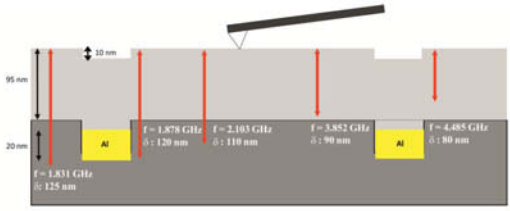

Figure 1. Penetration depth of electromagnetic wave in a copper cylinder according to the frequency.

Results

In order to evaluate the influence of microwave frequency on the investigation depth a calibrated sample was carried out by Electron Beam Lithography (EBL) by using a Scanning Electron Microscope (SEM) coupled to a device of lithography management RAITH.

The sample consists of L-shaped patterns of 30 nm depth were filled with aluminum (Al) film of 20 nm thickness. Then, a nickel (Ni) layer of 95 nm thickness was evaporated in order to cover these structures. Thus, we obtained buried structures of Al under a calibrated layer of Ni (figure 2(a)). AFM observations at this final step show the surface of patterns (with a height difference of 10 nm at the sample surface). On the topography (figure 2(b)), the outline of the patterns appears with a more important contrast.

Nevertheless, to show that the surface is only composed of nickel, an image of friction (scan at 90° compared to the classic direction) was carried out on this sample. Indeed, the phenomenon of friction allows the observation of differences of materials on a surface. On figure 2(c), it appears clearly that the substrate and the patterns are of the same composition since the color contrast is identical on the scale bar.

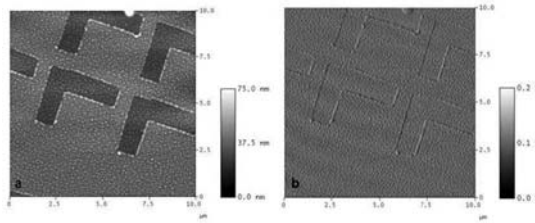

Figure 2. Calibrated sample: buried structures of aluminum under a calibrated nickel layer. (a)Schematic of the buried structures of Al (b) AFM image: topography. Scan size: 10 μm^2. Relative height: 75 nm. (c) AFM image: friction. Scan size: 10 μm^2. Friction scale: 0.2 V.

This sample requires the use of a large range of frequency in order to obtain a complete cartography on a representative thickness of the sample. For that, it is necessary to estimate the depths invested compared to the frequencies used. Knowing the magnetic permeability and the electric conductivity of nickel (material constituting the superior layer of the sample) and by applying the "skin effect" (see equation (1)), the values of depths corresponding to the various frequencies were calculated (figure 3).

The microwave images of phase obtained at various frequencies (f) are presented in Figure3. For f = 4.485 GHz (∂ =80 nm), the SMM image of phase doesn't show any difference in color contrast at this depth. We are in the presence of a single and homogeneous material (nickel). For f = 3.852 GHz (∂ =90 nm), the scanned plane is located just at the top of Al patterns, in the bottom of the layer of nickel. The SMM image of phase shows a light contrast of color between the Ni substrate and the proximity of the Al patterns, thus revealing different materials. Another significant observation relates to the outline of the patterns, which appears with a contrast of color much more distinguishable. This observation highlights a difference in materials nature since they are composed of residual PMMA resin whose physical properties are completely different from those of Ni and Al. For f =1.878 GHz (∂= 120 nm), the scanned plane is located inside the Al patterns. The SMM phase image clearly shows a difference in nature between the interior of the patterns (Al) and the Si substrate, being a semiconductor and having a weaker electric conductivity than that of metals. Its differences of properties are found on the SMM image on the level of the color contrast. For f =1.831 GHz corresponding to an investigation depth of 125 nm, the scanned plane is located just below Al patterns, in the Si substrate. On the SMM phase image, there is no difference in contrast between the interior of the patterns and the Si substrate. This means that the SMM image represents only the Si substrate. This sample made it possible to correlate the depth

invested at the frequency used. Thus, an in-depth cartography could be carried out on a representative thickness of the sample.

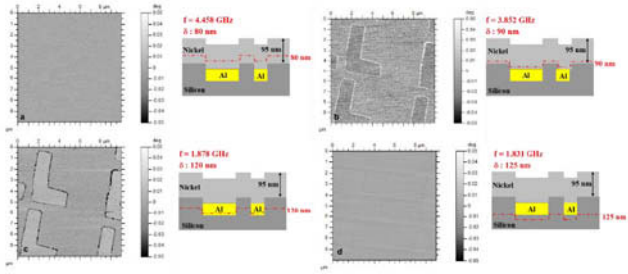

Figure 3. SMM images (phase) of buried Al under a calibrated Ni layer at different frequencies. Scan size: 10 μm^2. Phase scale: 0.1 deg.
(a) SMM image of phase at 4.485 GHz. (b) SMM image of phase at 3.852 GHz. (c) SMM image of phase at 2.103 GHz. (d) SMM image of phase at 1.878 GHz. (e) SMM image of phase at 1.831 GHz.

Characterization of oxygen diffusion in zirconium

Here, we are going to focus on the case of the diffusion of a light chemical element (oxygen) in a metal lattice (zirconium). We propose in this paragraph a novel method for in-depth investigation of material properties that is not influenced by the surface pollution.

Zirconium surface is very reactive under normal conditions and undergoes oxidation. This leads to the formation of a contamination layer, which may go up to several nanometers. A conventional technique to characterize the diffusion profile of an element inside a metal (with its percentage) by going under the polluted surface is Nuclear Reaction Analysis (NRA).

However the NRA technique presents limitation in the resolution. In fact the NRA results are obtained with a lateral resolution imposed by accelerator beam size (about 3 x 3 μm^2 and a depth of 3 µm) for a step scan size of 2 µm between each measure point. Also this measurement represents an average value. In this part, we are going to compare the results obtained by SMM and by NRA. By SMM, the lateral resolution is superior, since between two measure points, the step scan size is 100 nm for a 20 nm contact radius.

Experimental procedure

The oxidation of commercial pure zirconium plates (99.2% Zr from Goodfellow) is considered in this study. This choice of this material is driven by the significant solubility of oxygen in the zirconium, which is about 29 atomic percent. They were first annealed at 750 °C under a secondary vacuum for 2 hours and oxidized in air under atmospheric pressure at 650°C

for 72 hours. After oxidation, the samples were transversely polished, and analyzed by SMM. These results are next compared to those obtained by Nuclear Reaction Analysis (NRA).

The SMM images are acquired on a scan area of 80 µm X 80 µm with 515 pixel per ligne.

The frequencies of investigation used are chosen to scan a region under the polluted sub-surface between 3 and 7 µm. Thus we avoid the influence of the polluted surface. We focus in this study mainly on the oxygen-enriched metal zone.

The Nuclear Reaction Analysis was made at the Institut Rayonnement Matière de Saclay, France, and used a Van De Graaff linear accelerator (maximum 3.7 MeV).

Results

SMM measurements were performed for three different frequencies (2.21 GHz, 6.87 GHz and 11.83 GHz) that represent three investigation depths (6.8 µm, 3.9 µm and 3 µm) calculated from the relationship of skin effect given by Eq.1. A schematic representation of the sample studied is given in Fig.4a The topographical image of the sample shows well the transition zone between ZrO_2 and the other part of the sample without any distinction of the Zr-O and Zr presence. Moreover, one can observe on the cross-section related to this topographical image a more important roughness on the ZrO2 area (this additional roughness is due to polishing).

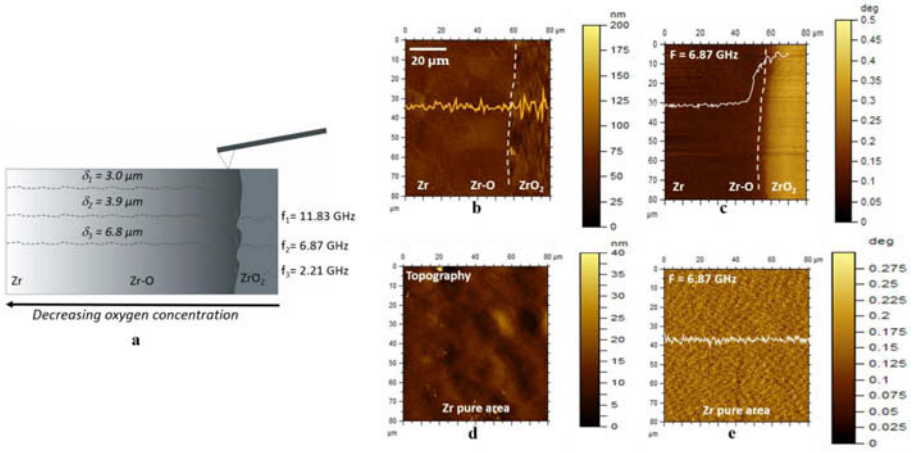

Figure 4. Schematic and AFM images (topography and phase) of the oxygen enriched Zr. (a) Schematic of the analyzed sample (b) AFM topography image of the analyzed area. Scan size: 80 µm^2. (c) SMM image of phase at 6.87 GHz. Scan size: 80 µm^2. (d) AFM topography image of pure Zr. Scan size: 80 µm^2. (e) SMM image of phase at 6.87 GHz of pure Zr area. Scan size: 80 µm^2.

The SMM phase images can be seen in Fig. b) c) d). The phase shift images (completely different from the topographical images) clearly show a change in the phase signal. This variation, for the material used here is introduced solely by a conductivity variation of the material since the relative permeability of Zr is equal to 1. Only the oxygen dissolution in the zirconium lattice produces variations of the conductivity.

Along the pure Zr area, one can notice that the phase shift signal remains flat and constant. So the phase variation observed previously can only come from the diffusion of oxygen inside the metal lattice of Zr.

In support to these results we compared them to the measurements obtained by NRA. The cross-sections of the phase SMM images realized at three different frequencies are superimposed on the NRA result (Fig.5).

One can see that the curves are in excellent agreement with the NRA profile, both in tendency and in the diffusion length (about 18 µm). Moreover, one can highlight a linear relationship between the phase shift measured by SMM and the percentage of oxygen diffused in Zr measured by NRA. This relationship can be expressed as following:

$$\varphi = K(c)\, c \quad (2)$$

With φ the phase shift, c the oxygen concentration and $K(c)$ the proportionality factor which can be function of the concentration.

Furthermore, by referring with a white dashed line the border between ZrO_2 and Zr-O, one can observe an evolution of the border's position depending on the frequency (and thus of the depth). (Fig.5).This highlights the inhomogeneous nature of the boundary in the volume can only be achieved only by this tomographic SMM measurement.

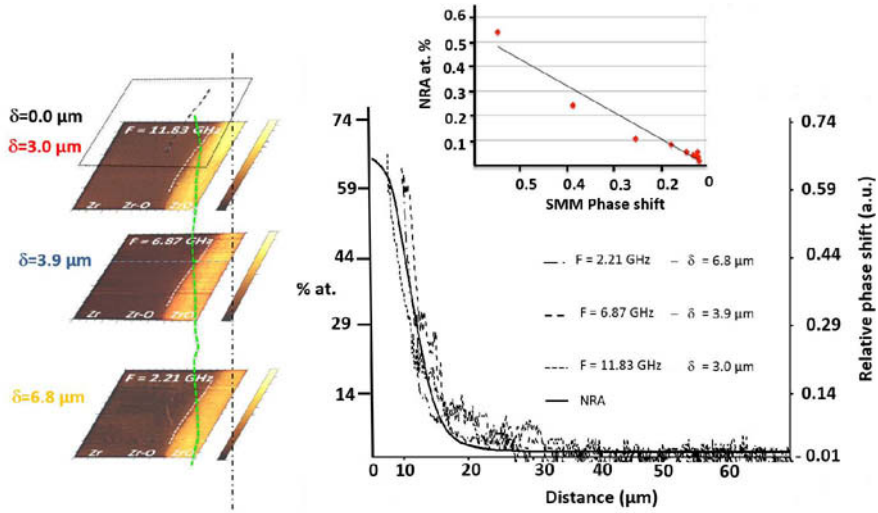

Figure 5. Superimposition of the cross-section obtained from SMM measurement at different frequencies – Comparison with NRA results.

Conclusion

As a conclusion, SMM technique allows the detection of sub-surface defects with high resolution. By varying the frequency one can have access to different depth in the sample volume and to know the depth position where the defect is buried. SMM also permits the characterization of a chemical specie gradient dissolved in a metal lattice (here presented with the diffusion of oxygen in zirconium). With this technique one can have access to volume information under the pollution layer without any sample preparation. The cartography of the oxygen distribution inside the zirconium has been realized at different depths. These results have been compared to those obtained by NRA and show an excellent concordance of the length of diffusion measured. Moreover, we notice a linear relationship between the phase shift measured by SMM and the oxygen concentration determined by NRA.

Acknowledgment

The authors thank the financial support of the Conseil Regional de Bourgogne, Institute Carnot ARTS, LabeX Action "Integrated Smart System", CNRS and European Regional Development Fund Feder. The authors thank Dr. Luc Lavisse (ICB UMR 6303 – Dijon FRANCE) for his help to access NRA technique.

Characterization of Minerals, Metals, and Materials 2015

Characterization of Material Processing and Corrosion

Session Chairs:
Wenjing Li
Florian Nurnberger

Characterization of Minerals, Metals, and Materials 2015
Edited by: John S. Carpenter, Chenguang Bai, Juan Pablo Escobedo, Jiann-Yang Hwang, Shadia Ikhmayies, Bowen Li, Jian Li, Sergio Neves Monteiro, Zhiwei Peng, and Mingming Zhang
TMS (The Minerals, Metals & Materials Society), 2015

COMPARSION OF THE MECHANISMS OF VOID FORMATION BY PLASTIC DEFORMATION IN SINGLE- AND DUAL-PHASE BCC-STEELS

Gregory Gerstein[1], Hans-Bernward Besserer[1], Florian Nürnberger[1], Hans Jürgen Maier[1]

[1]Leibniz Universität Hannover, Institute of Materials Science (Werkstoffkunde)
An der Universität 2, 30823 Garbsen, Germany

Keywords: Ductile damage, Ductile fracture, Damage mechanism, Voids, DC04, DP600

Abstract

The formation and development of voids in both the single-phase ferritic steel DC04 and the dual-phase ferritic-martensitic steel DP600 are discussed. Various mechanisms and kinetics of void formation are considered regarding the influence of dislocation glide, precipitates and other parameters. Different characteristic locations in the microstructure are investigated at which strain concentrations during plastic deformation can occur and cause the formation of voids and microcracks. For the specimen preparation ion slope cutting is applied. Voids and cracks revealing ductile damage are analyzed by Scanning Electron Microscopy (SEM). Stress concentrations in consequence of plastic deformation could be shown by extinction contours on images recorded by Transmission Electron Microscopy (TEM).

Introduction

The ductile damage of a material resulting from plastic deformation can be characterized by the initiation and development of microscopic voids [1, 2]. Gurson 1977 developed a model to characterize the plastic deformation behavior of porous metals [3]. In this model the volume fraction of pores is considered as an additional, internal variable. This model was extended by Tvergaard and Needleman to a theory for pore initiation and development [4, 5]. It is of major relevance to know the microstructural state as a function of the level of deformation, particularly for optimizing manufactured work pieces produced by forming processes. Moreover, the microstructural processes, which are responsible for the initiation, growth and coalescence of pores, must be analysed and quantifiable with respect to the level of deformation. This is necessary in order to be able to estimate, for example, the component's fatigue life. Various mechanisms are responsible for initiating pores, and these differ particularly for single and multi-phase materials.

Scientific work on single-phase materials

With the aid of electron microscopy, it was possible to verify that brittle inclusions in the matrix material fracture during forming operations and thus minute internal voids initiate in the region of the inclusions' fracture surfaces [6, 7]. Besides particle fracture, voids can also occur by means of decohesion between the particle and the matrix material. For single-phase steels having a ferritic microstructure, it has previously been shown that non-metallic [8] or carbide-like [9] inclusions are essentially responsible for initiating pores. It was also possible to show that the fracture of particulate inclusions is responsible for causing the occurrence of intercrystalline brittle fracture in high-strength aluminum alloys [10].

Scientific work on dual-phase materials

Two different types of pore initiation can be generally differentiated for dual-phase, ferritic-martensitic steels; such as the DP600. On the one hand, fracture of the martensitic needles occur which leads in turn to internal pore initiation in these hard phase fractions. This case is comparable to the fracture of inclusions in a single-phase material (see above).
On the other hand, decohesion at the phase boundaries can occur between the ferrite and martensite [11]. In a detailed study, it was also possible for Kadkhodapour to verify the latter case for the dual-phase steel DP600 [12, 13]: Pore formation at the grain boundaries between adjacent ferrite grains together with subsequent potential growth to a ferrite-martensite grain boundary, pore formation in direct proximity to martensite particles, pore formation due to decohesion at a ferrite-martensite phase boundary and, as Tasan also found, rare cases of pore formation due to broken martensite particles.

Mechanism of void initiation

The formation of pores at inclusions, grains and phase boundaries can be explained according to the theories of Griffith and Stroh [14, 15]. During the deformation of materials, stress concentrations occur at the tips of cracks or inclusions. These stress concentrations are responsible for the material's local decohesion and the formation of a cavity or a microcrack. According to Stroh, dislocations, which initially typically accumulate at inclusions, grain and phase boundaries, lead to a local stress concentration during plastic deformation.

Experiments and Analytical Methods

In the current work, the mechanisms of ductile damage and microstructural changes are investigated as a consequence of plastic deformation of the single-phase ferritic steel DC04 and the dual-phase ferritic-martensitic steel DP600. Local stress concentrations indicating a later pore formation are of interest during the investigations. The chemical compositions of both steels are given in Table 1. For the investigation, flat tensile specimens of both DC04 and DP600, which were deformed in a Zwick 100 universal testing machine with optical strain measurement according to the DIN EN ISO 6892-1 standard, were analyzed as well as samples from a workpiece of DC04 produced by a deep drawing process.

Table I. Constituent elements in weight percent [wt%] of the steel DC04 and DP600

Element/ Steel	C	Mn	Cu	Ni	Cr	Mo	Al	Ti	V	S	Si	Fe
DC04	0.015	0.192	0.06	0.047	0.02	0.003	0.037	0.026	0.024	0.005	0.003	bal.
DP600	0.10	1.4	-	≤ 1.0	≤ 1.0	≤ 1.0	0.02-0.06	-	-	0.008	0.15	bal.

Specimen preparation

To prepare the surfaces for the investigation, conventional methods such as grinding and polishing were not employed to reveal the internal material pores. During grinding, smearing effects occur which render cavity analyses impossible.

For this reason, specimens were initially polished and subsequently treated by ion slope cutting using an ion-polishing system made by the company *Gatan* type *Met Etch*. In this way, minute layers can be removed from the previously polished surface using ion bombardment without closing the pores by smearing. By selectively removing material, this procedure yields a relief on the specimen's surface which is typical for imaging using microscopy but which does not influence the analysis of pore volumes.

Microscopy

The microscopic examination was performed with an in-lens detector in a scanning electron microscope (SEM) - Zeiss Supra VP55. This type of detector retrieves a high density of information from secondary electrons emitted from the layer adjacent to the surface. By means of this, a high resolution is obtained in the scanning electron microscope for a relatively low voltage and thus a reduced penetration depth. In this way, pores can be imaged very well since their boundary generally appears brighter due to the edge effect. An undesirable effect is that contaminations are also more intensely imaged by the in-lens detector. This effect can impede the analysis and, as the case may be, make it necessary to specially clean the specimen.
The dislocation's microstructural development due to loading is investigated in this work with the help of TEM. For this purpose, TEM foils in the form of flat disks with a diameter of 3 mm and a thickness of approximately 500 µm were cut from the center of the deformed samples' deformation zone by wire eroding. These disks' thicknesses were mechanically reduced to 100 µm and electropolished on both sides. All TEM investigations were conducted using a JEOL JEM 2010 transmission electron microscope with a 200 kV electron gun.

Results and Discussion

In the following, the results of the SEM and TEM investigations of the DC04 and DP600 specimens are presented. Using the SEM images, pores are revealed and attributed to characteristic locations in the microstructure.
Fig. 1 shows the microstructures of the DC04 (Fig. 1a and b) and DP600 (Fig. 1c and d) in their deformed states. Fig. 2a depicts small round pores in the ferritic microstructure of the DC04. No clear precipitates or inclusions can be seen at which these pores could have initiated. For this reason, grain boundaries are assumed to be the initiators which are also seen in the ion-polished reliefs. Fig. 1b shows converging shear bands in DC04 which can also favor the initiation of pores. For the DP600, incipient microcracks are already visible in Fig. 1c which connect minute pores with each other. A manganese sulfide MnS precipitate in DP600 is depicted in Fig. 1d. Within this precipitate, cracks have initiated in which incipient voids have formed.

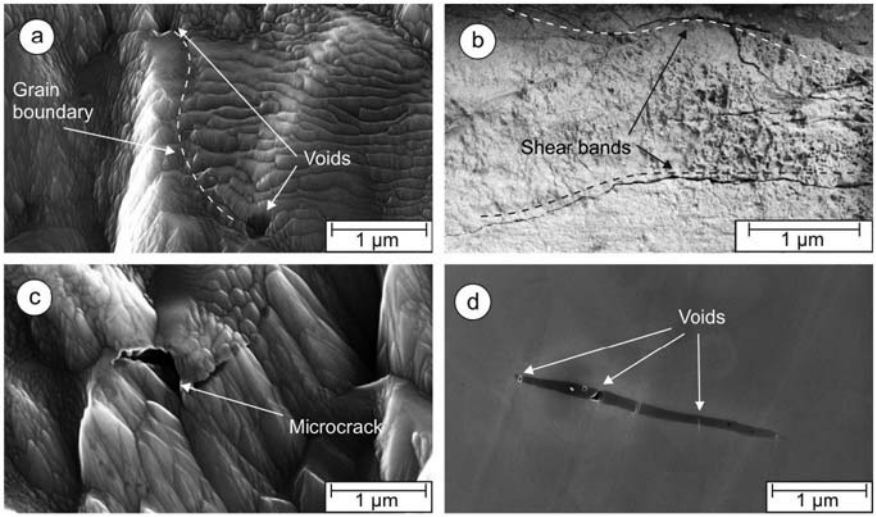

Figure 1. SEM images of defects in deformed steel DC04 and DP600
a) voids in steel DC04
b) void and microcrack formation in steel DC04 at the crossings of shear bands
c) void at microcrack in steel DP600,
d) void formation in steel DP600 around and within a fractured MnS precipitate

A fractographic analysis of the tensile specimens' surfaces of both steels provides additional information on the characteristic microstructural locations at which pores develop. A tensile specimen's fracture surface provides a possible insight into the material's state following loading to the maximum level of deformation. Fig. 2 shows a comparison of the fracture surfaces of DC04 and DP600.

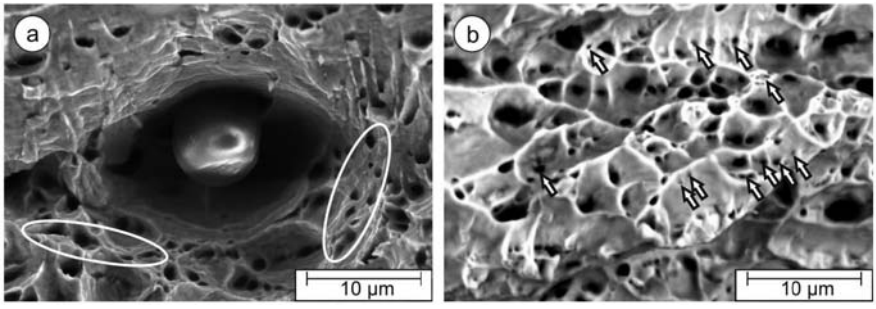

Figure 2. Fracture surfaces of tensile test specimens elongated until failure of
a) steel DC04, breaking elongation 44.7 %, accumulation of pores at the grain boundaries, and
b) steel DP600, breaking elongation 26.2 %, additional accumulation of smaller pores in the grain

The fracture surface of DC04 (Fig. 2a) depicts a crystalline inclusion whose size is approx. 2-3 µm. The matrix material yields a honeycomb structured fractograph in which pores are located particularly at the boundary surface to the precipitation. The fracture surface of DP600 shows more, finely distributed pores within the grains (Fig. 2b).

Rough calculation of the energy contribution by stress concentrators

In order to be able to represent the contribution from the lattice defects to changes in the pore volume, the energy can be estimated which is theoretically available in the microstructure for pore formation. The boundary surfaces considered here are the grain and phase boundaries as well as the interfaces between precipitates and the matrix. For this purpose, two limiting cases can be differentiated:
In the first case, the boundary surfaces are assumed to be stress-free and have no intrinsic energy. In this case, the boundary surface energy results from the dislocations piled-up at the boundary surface. By assuming that about every thousandth atom belongs to a boundary surface, results in a total microstructural boundary surface of approx. 10^5 cm/cm^{-2} (corresponding to one cm^3 of material volume). On assuming a surface energy density for the boundary surface of 10^{-4} J/cm^2, the total boundary surface energy amounts to 10 J/cm^3. This energy corresponds, to the total energy of the dislocations in the crystal, which can be estimated as having a dislocation density in the order of 10^{11} cm/cm^3 [16].
For the second limiting case, we assume that the grain boundaries represent the total energy or source of stress in the microstructure. The number of dislocations which form the boundary surface is considerably smaller than the total number of dislocations. It follows from this that the dislocations at the boundary surfaces only possess a smaller fraction of energy than those dislocations which lie in the grain's interior. Thus for this case, the dislocations which are free and randomly arranged in the crystal convey a considerably larger fraction of energy via lattice defects than those at the boundary surfaces. As a consequence of this, an elevated number of pores would accumulate in the grain's interior. Here, the fracture of brittle precipitates in the microstructure can not be taken into consideration. This theory forms the physical basis for modeling pore initiation during plastic deformation.
The investigations on single-phase DC04 and dual-phase DP600 have shown that voids occur both at boundary surfaces and in the grain's interior. Therefor none of these two assumptions can be clearly verified. In further investigations it has to be analyzed if accumulations of stress induced misorientations and structure compressions can be shown at different characteristic places in the microstructure around voids.

The occurrence of stress concentrations can be qualitatively verified by using extinction contours in TEM images, as depicted in Fig. 3. The Fig. 3a shows various extinction contours but one goes clearly along precipitations in the ferritic matrix. In Fig. 3b a martensite needle in the DP600 is shown, around whose tip dark lines stand out from the ferritic matrix. These lines become closer at the martensite needle's tip and thus provide verification of a zone in which the crystal lattice has been distorted due to elevated stresses.

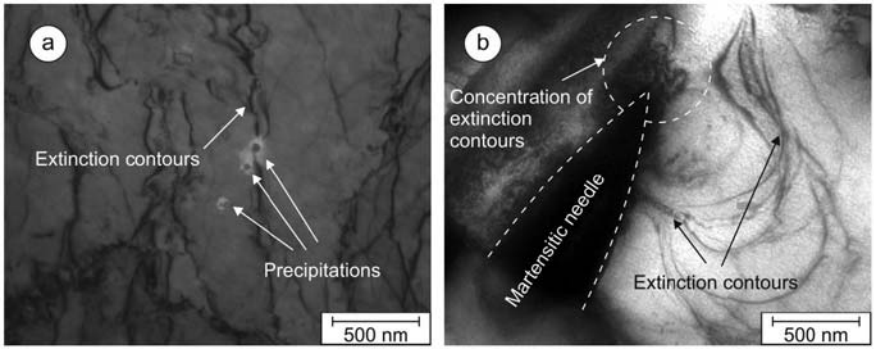

Figure 3. TEM images of steel
a) DC04 with extinction contours along precipitations and
b) DP600 with a concentration of extinction contours around tip of a martensitic needle

In the models of Griffith and Stroh, these mechanisms of damage development are described using the assumption that the local stress concentration is the cause of the initiation of pores and microcracks. Here, it should also be noted that not only tangential stresses develop at the tip of dislocation pile-up but also normal stresses occur in the region below and above the slip bands. In this way, a separating effect exists along the dislocation pile-ups.

Whilst the single-phase materials form these stress accumulations at grain boundaries and inclusions, these effects are comparatively smaller for dual-phase materials. The investigations of the DP600 demonstrated pore initiation especially at phase boundaries, and therefore at a transition from regions of differing hardness or toughness.

Conclusions

The initiation mechanisms differ for pores in single and in dual-phase steels. In both cases, pore formation occurs due to local stress concentrations. Whilst pore initiation cumulatively occurs at inclusions or grain boundaries in single-phase steels, phase boundaries are also responsible for both stress concentrations and pore initiation in multi-phase materials. Moreover, the fracture of brittle particle inclusions or zones of hard phases can be established for both groups of materials. However, the fraction of pores initiated by the fracture of particles is lower for multi-phase than for single-phase materials.

Acknowledgments

The authors would like to thank the German Research Foundation (DFG) for their financial support of the transregional collaborative research centre SFB/TR 73 in the subprojects C4 and C6.

References

1. T.L. Anderson, *Facture Mechanics. Fundamentals and Applications* (Boca Raton, FL: CRC Press, Taylor & Francis Group, 2005), 219.

2. K.E. Puttick, "Ductile Fracture in Metals", *Phil. Mag.*, 4 (44) (1959), 964-969.

3. A.L. Gurson, "Continuum Theory of Ductile Rupture by Void Nucleation and Growth: Path I-Yield Function and Flow Rules for Porous Ductile Media", *ASME Transaction, J. Eng. Mat. Tech.*, 99 (1977), 2-17.

4. A. Needleman, "A Numerical Study of Void Nucleation at Carbides", *Report of Brown University*, 1987.

5. V. Tvergaard, A. Needleman, "Analysis of the Cup-Cone Fracture in a Round Tensile Bar", *Acta Metall.*, 32 (1984), 157-169.

6. J. Plateau, G. Henry, C. Crussard, "Quelques Nouvelles Applications de la Microfractographie", *Rev. Met.*, 54 (3) (1957), 200-201.

7. S. B. Hosseini, C. Temmel, B. Karlsson, N.-G. Ingesten, "An In-Situ Scanning Electron Microscopy Study of the Bonding Between MnS Inclusions and the Matrix During Tensile Deformation of Hot-Rolled Steels", *Met. Mat. Trans. A*, 38 (5) (2007), 982-989.

8. W.A. Spitzig, R.E. Smelser, O. Richmond, "The Evolution of Damage and Fracture in Iron Compacts with Various Initial Porosities", *Acta Metall.*, 36 (1988), 1201-1211.

9. D. Kwon, "Interfacial Decohesion Around Spheroidal Carbide Particles", *Scripta Metall.*, 22 (1988), 1161-1164.

10. P.J.E. Forsyth, D.A. Ryder, "Fatigue Fracture: Some Results Derived from the Microscopic Examination of Crack Surfaces", *Aircraft Engineering and Aerospace Technology*, 32 (4) (1960), 96-99.

11. C.C. Tasan, J.P.M. Hoefnagels, C.H.L.J. ten Horn, M.G.D. Geers, "Experimental Analysis of Strain Path Dependent Ductile Damage Mechanics and Forming Limits", *Mech. Mater.*, 4 (2009), 1264-1276.

12. J. Kadkhodapour, A. Butz, S. Ziaei-Rad, S. Schmauder, "A Micro Mechanical Study on Failure Initiation of Dual Phase Steels Under Tension Using Single Crystal Plasticity Model", *International Journal of Plasticity*, 27 (2011), 1103–1125.

13. J. Kadkhodapour , A. Butz, S. Ziaei Rad, "Mechanisms of Void Formation During Tensile Testing in a Commercial, Dual-Phase Steel", *Acta Mater.*, 59 (2011), 2575–2588.

14. A.A. Griffith, "The Phenomena of Rupture and Flow in Solids", *Philos. Trans. R. Soc. Lond.*, A (221) (1921), 163-198.

15. A.N. Stroh, "A Theory of the Fracture of Metals", *Adv. Phys.*, 6 (1957), 418-465.

16. L. N. Larikov, *Healing of Defects in Metals* (Kiev, Naukova Dumka, 1980).

Characterization of Minerals, Metals, and Materials 2015
Edited by: John S. Carpenter, Chenguang Bai, Juan Pablo Escobedo, Jiann-Yang Hwang, Shadia Ikhmayies, Bowen Li, Jian Li, Sergio Neves Monteiro, Zhiwei Peng, and Mingming Zhang
TMS (The Minerals, Metals & Materials Society), 2015

CHARACTERIZATION OF SINTERING DUST, BLAST FURNACE DUST AND CARBON STEEL ELECTRIC ARC FURNACE DUST

Feng Chang[1], Shengli Wu[1], Fengjie Zhang[1], Hua Lu[1], Kaiping Du[1]

[1]School of Metallurgical and Ecological Engineering, University of Science and Technology Beijing; 30 Xueyuan Road, Haidian District, Beijing 100083, P. R. China

Keywords: Sintering dust; Blast furnace dust; Electric arc furnace dust; Characterization.

Abstract

In order to make a complete understanding of steel plant metallurgical dusts and to realize the goal of zero-waste, a study of their properties was undertaken. For these purposes, samples of two sintering dusts (SD), two blast furnace dusts (BFD), and one electric arc furnace dust (EAFD) taken from the regular production process were subjected to a series of tests. The tests were carried out by using granulometry analysis, chemical analysis, X-ray diffraction (XRD), scanning electron microscopy (SEM), energy dispersive spectroscopy via SEM (EDS), and Fourier transform infrared spectroscopy (FTIR). The dominant elements having an advantage of reuse are Fe, K, Cl, Zn, C. The dominant mineralogical phases identified in sintering dust are KCl, Fe_2O_3, $CaCO_3$, $CaMg(CO_3)_2$, NaCl, SiO_2. Mineralogical phases exist in blast furnace dust are Fe_2O_3, Fe_3O_4, with small amount of KCl and kaolinite coexist. While in electric arc furnace dust, Fe_3O_4, $ZnFe_2O_4$, $CaCO_3$, CaO, $Ca(OH)_2$ are detected.

Introduction

Since 2008, with procurement costs of raw materials and fuels continued to rise, steel plant production yearly overcapacity and the Chinese government's strict requirements in energy conservation and emission reduction, Chinese steel industry profit margins become smallest among the industry. Key steel enterprises profit margin was only 0.62% in 2013.

China's crude steel production in 2013 was 779 million metric tons, which accounted for about 73.6% of Asia steel production and 49.2% of the world steel production. So much steel production also brought a lot of metallurgical dust, such as, sintering dust, blast furnace dust, electric arc furnace dust and so on. Since 1980 the United States enacted laws placing the steel plant metallurgical dust under toxic waste, study of metallurgical dust abroad was earlier than China approximately 30 years. In order to save the cost, metallurgical dust has gradually become a major research focus in recent years.

Statistics shows that every one ton of sinter production will generate 20 to 40 kg of sintering dusts; every one ton of hot metal will produce 15 to 50 kg of blast furnace dusts; and every one ton of liquid steel will produce 10 to 20 kg of EAF dusts. [1] The output of metallurgical dust is huge as the steel production is enormous in China every year. Generally speaking, metallurgical dust has complex chemical component, very fine particles, and high content of valuable or harmful elements. How to handle the metallurgical dust and recover the valuable metals from them are very important at the present period not only for the resource and economy but also for the environment. To make full use of them, it is necessary to develop a new recycling process, which requires full understanding of basic mineralogy characteristics of these dusts.

This paper presents characterization results on dust samples collected from steelmaking process. These results can help future studies on their use as secondary materials in steelmaking process. The dusts contain two kinds of sintering dusts, two kinds of blast furnace dusts and one electric

arc furnace dust.

Experimental

To investigate the basic mineralogy characteristics of zinc-bearing dusts in steel industry, five kinds of dusts were sampled from three steel companies, including three from Bao Steel, one from Shougang Group and one from Guofeng Steel. They are sintering dust, blast furnace dust and carbon steel electric arc furnace dust from Bao Steel, blast furnace dust from Shougang Group and sintering dust from Guofeng Steel.
The samples were homogenized and successive quartering provided 1kg of each sample. All samples were dried for 8 h at 378 K and stored in a desiccator.
The dust granulometry distribution and the mean size of its particles were evaluated. A laser granulometer model SEISHIN LMS-30 from Japan was used, with anhydrous ethanol as dispersing medium. On one hand, the mineral elements of the dusts were detected using an X-ray fluorescence spectrometer (XRF-1800, Shimadzu, Japan). On the other hand, Total C in dust samples was determined by the Carbon and sulfur analyzer (EMIA-820V, Horiba, Japan). The blast furnace dusts sample was mixed with certain quantity of analytical grade silica reagents to meet detection limit of carbon content of the machine (max. 6%). The main compounds and present phases of the dusts were performed by X-ray diffraction analysis (D_{max}-RB 12kW, Rigaku, Japan). X-ray patterns of samples powdered to 300 meshes operating with Cu tube, continuous scanning, working at 40 kV and 150 mA, with scanning among 2θ (between 10° and 90°). Scanning electron microscopy (SEM) with X-ray energy dispersive spectrometry (EDS) was conducted to gain further knowledge of the dust particles structure, morphology and their chemical composition. FTIR spectra were collected on an Infrared spectroscopy (NEXUS 670-FTIR, Nicolet, America), on KBr pellets, between 4000 and 400 cm^{-1} with a 4 cm^{-1} resolution and 32 scans.

Results and discussion

Granulometry Analysis

Figure 1 presents the particle size distributions of the five dusts. Particle size and granulometry specific surface area characteristics are also listed in Table I. X10, X50, X90 refers to the corresponding size when cumulative particle size distribution reaches 10%, 50% and 90%, respectively.
Sintering dusts have an average particle size between 12.550 and 13.774 micron, and the particle size are all less than 200 mesh. The particle size distribution curve of blast furnace dusts are in most right position. Furthermore, blast furnace dust from Baosteel is significantly coarser than the one from Shougang, probably due to different operating processes or dust removal devices. The mean particle diameter of EAFD determined by laser granulometer is 1.469 micron, which is in agreement with previous works. [2-3] In contrast, EAFD has a relatively heterogeneous distribution of particle size, where 100% have size between 0.33 and 4.24 micron, with granularity specific surface area up to 6.141 m^2/cm^3.
Peng et al. pointed out that 50% volume of particles in sintering dusts is below 10 micron, and the other half is between 10 and 54.64 micron. [4] N. Menad and H. Tayibi pointed out that the dust particles generated from sinter plants are finer than blast furnace emissions. [5] It is important to note that the effective filtering of microscopical sized particles and aerosols is a major problem, for which no solution exists for a long time. Wang indicated that blast furnace gravity and baghouse dusts have an average particle diameter of 159.23 micron and 26.23 micron,

respectively. [6]
These lower granulometry of the dusts favours their use as secondary raw material in the production of some materials, because it has the advantage of elimination of the grinding stage. In terms of particle size, mechanical separation method is not suitable for processing EAFD.

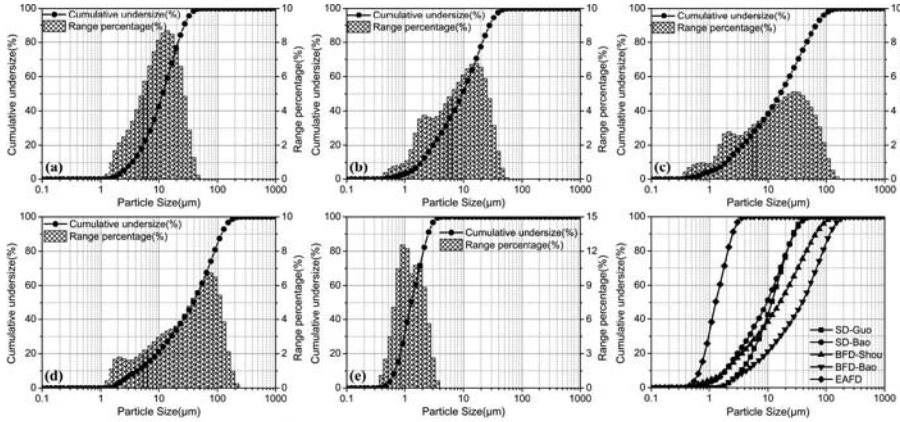

(a) SD-Guo; (b) SD-Bao; (c) BFD-Shou; (d)BFD-Bao; (e) EAFD.
Figure 1. Particle size distribution of dust samples

Table I. Particle size and specific surface area of dust samples

Samples	X10(μm)	X50(μm)	X90(μm)	Average particle size (μm)	Specific surface area (m^2/cm^3)
SD-Guo	3.494	11.632	27.042	13.774	0.912
SD-Bao	1.900	9.566	27.830	12.550	1.547
BFD-Shou	1.912	16.057	67.206	26.373	1.427
BFD-Bao	4.277	38.259	116.586	51.015	0.567
EAFD	0.686	1.277	2.480	1.469	6.141

Chemical Analysis

The chemical composition of dusts depends on the dust species, technological and operating conditions and the degree of return of the dust into the process. The results of the chemical analysis of the dust samples are shown in Table II. As can be seen, the dusts contain 30 different elements, and the common elements are Fe, O, Ca, Mg, Si, Al, K, Na, Zn, Pb, Cl, S and C. In general, the contents of potassium, sodium, lead, sulfur and chlorine in the particles from the sintering process are higher than particles from other processes. The main components of the EAF dust in the present study are 44.81% iron, 9.32% zinc and 9.24% calcium. Due to high water solubility, potassium and sodium elements in sintering dust are suitable for extracting by hydrometallurgical. While zinc in the electric arc furnace dust has an advantage to be recycled by pyrometallurgical owe to its lower volatilization temperature. Carbon in blast furnace dusts is about 20%, indicating that iron oxides can be directly reduced under high temperature. In addition, Chen et al. found that electric arc furnace dust had 7.02 ± 0.69 percent of chlorine element. [7]
Most elements in the dusts exist in the form of oxides. In fact, basicity is an important parameter

during iron oxide reduction, and it has an effect on metallic iron whisker formation and growth. [8] Ternary basicity represents the mass ration of (w (CaO) + w (MgO)) / w (SiO_2). It can be calculated that ternary basicity of the five dusts in Table II from left to right is 2.45, 3.05, 0.80, 0.42 and 4.98, respectively. Wang et al. concluded that the favorable ternary basicity is 0.9 in pellets containing dusts and carbon. [9]

Table II. The chemical composition of dust samples

Element	Wt. %				
	SD-Guo	SD-Bao	BFD-Shou	BFD-Bao	EAFD
Fe	29.89	28.47	37.27	44.28	44.81
O	25.34	24.66	29.59	26.93	28.95
Ca	7.82	6.50	2.07	2.09	9.24
Si	2.50	1.57	2.32	3.63	1.31
Al	1.33	0.92	1.34	2.10	0.14
Mg	1.30	0.70	0.66	0.27	0.62
Mn	0.24	0.13	-	0.08	2.23
K	8.50	9.52	0.73	0.06	0.79
Na	2.04	2.56	0.47	0.08	-
Zn	0.18	0.05	1.43	-	9.32
Pb	1.31	1.01	0.23	0.23	0.19
Cu	0.05	0.09	-	-	0.05
Ti	0.09	-	-	0.09	0.05
Cr	0.08	0.06	-	0.01	0.35
Ni	0.03	0.02	-	-	0.02
Rb	0.06	-	-	-	-
Ra	0.03	-	-	-	-
Se	-	0.03	-	-	-
Cs	-	0.02	-	-	-
Tl	-	0.02	-	-	-
Mo	-	-	-	-	0.02
Sn	-	-	-	-	0.02
V	-	-	-	-	0.01
S	1.09	2.45	0.68	0.38	0.35
P	0.05	0.04	0.03	0.13	0.13
Cl	13.44	15.43	2.02	0.05	0.74
F	-	0.39	-	-	-
Br	0.14	0.31	-	-	-
I	0.05	0.08	-	-	-
C	4.46	4.97	21.14	19.59	0.65

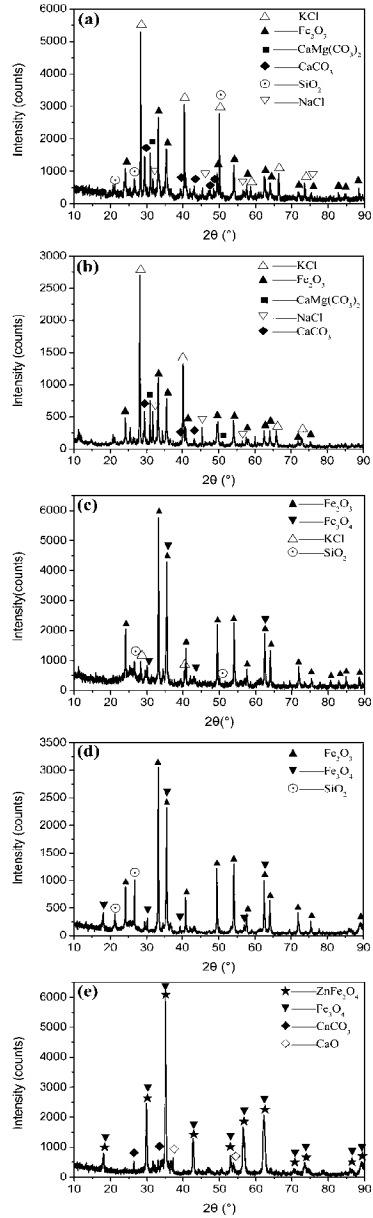

(a) SD-Guo; (b) SD-Bao; (c) BFD-Shou; (d) BFD-Bao; (e) EAFD.

Figure 2. X-ray diffraction (XRD) patterns of dust samples

X-Ray Diffraction Analysis

Figure 2 shows the X-ray diffraction pattern of the dust samples. As it can be seen, $ZnFe_2O_4$, Fe_3O_4, $CaCO_3$, CaO are present in the EAFD sample. The main phases in blast furnace dust are Fe_2O_3、Fe_3O_4、SiO_2, and a small amount of KCl is found to be existed in blast furnace dust from Shougang. Sintering dust shows clear diffraction peak of KCl and Fe_2O_3, and some information about NaCl、$CaCO_3$、$CaMg(CO_3)_2$ and SiO_2. Peng et al. indicated that, the possible mechanism of KCl formation is that the iron ore which contain potassium element become into potassium silicate after going through reduction、oxidation reaction, and then reacted with calcium chloride converting into KCl at last. [4] Chen et al. also found KCl, NaCl in EAFD. [7]

Scanning Electron Microscopy and Micro-Analysis

Scanning electron micro-structural examination of the five dusts microstructure was performed and the results are shown in Figure 3. The chemical composition at spots designated by numbers in part (a) to (e) was investigated using EDS. For a summary of EDS results refers to Table III.

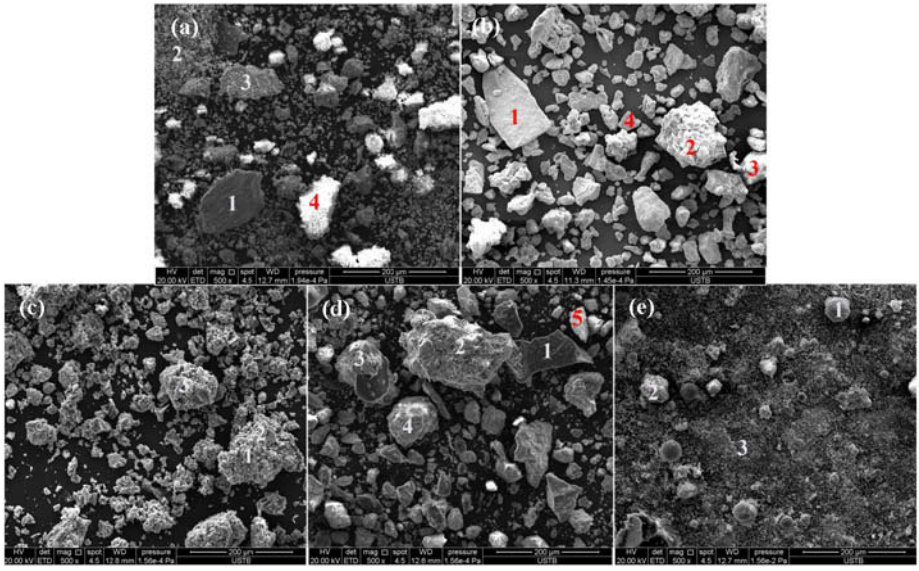

(a) SD-Guo; (b) SD-Bao; (c) BFD-Shou; (d)BFD-Bao; (e) EAFD.
Figure 3. Scanning electron microscopy and micro-analysis of dust samples

Based on these microphotographs and the results of X-ray energy dispersive spectrometry (EDS), it can be seen that the samples are not homogeneous. In Figure 3, the morphological aspect of the samples is first shown. Sintering dusts appear to relatively loosely agglomerated, and some of them are bright under SEM. Irregular shape is also reflected in blast furnace dusts, but their particle size are large than sintering dusts, which could be clarified by Figure 1. BF dust from Shougang has a maximum degree in reunited. Different from the others, most particles in EAFD

are spherical. It is in agreement with the main generation mechanism, i.e., ejection of the slag and metal particles by bubble-burst. [10-11] This morphology has also been observed in previous works. [2] [12-13] Submicron particles are uniformly distributed in the range of vision, with some of them covering the surface of the bigger balls.

For sintering dust, it can be concluded that the smooth, black particles are carbon. The gray black massive particles are iron oxides. KCl largely distributed in gray fine and bright particles, which contains calcium and iron oxides. Some lead compounds coexsit with KCl.

For blast furnace dust, the smooth, black particles are coke fines or pulverized coal. The ingredient in white aggregates is a large proportion of iron oxides and some gangue. Spots 1, 2, 3 in part (d) of Figure 3 indicate that some carbon particles emerge alone; some were partly wrapped by iron oxides. In addition, spots 1, 2 in part (c) of Figure 3 instruct that some carbon particles were almost entirely wrapped by iron oxides.

Table III. Summary of SEM image and spot analysis

SEM image	Spot	Major elements	Minor elements	Possible phases
SD-Guo	1	Fe, O	Ca, K, Cl	Fe_xO_y
	2	Pb, Cl, K, O	Fe, Ca	KCl, $PbCl_2$, Pb(OH)Cl, $Ca_xFe_yO_z$
	3	Fe, O	Ca, Cl, K, Si	$Ca_xFe_yO_z$, KCl
	4	Fe, O, Cl, K	Ca, S	$Ca_xFe_yO_z$, KCl
SD-Bao	1	Fe, O	Al, Ca, Si, Mg	Fe_xO_y
	2	Fe, O, Ca	S, Cl, Si, Al, K, Mg	$Ca_xFe_yO_z$
	3	K, Cl	-	KCl
	4	O, Ca, Fe	Mg, Al	CaO, Fe_xO_y, $Ca_xFe_yO_z$
BFD-Shou	1	C	O	C
	2	Fe, O	Ca, Mg, Si, Al, Zn, Cl	Fe_xO_y, ZnO, $Ca_x(Mg, Al)_ySiO_z$
BFD-Bao	1	C	O, Al	C
	2	Fe, O	Ca, Si	Fe_xO_y, $Ca_xFe_ySiO_z$
	3	Fe, O	Al, Ca, Si	Fe_xO_y, $Ca_xAl_ySiO_z$
	4	Fe, O	C	Fe_xO_y, C
	5	Fe, O	Ca	Fe_xO_y, $Ca_xFe_yO_z$
EAFD	1	Fe, O, Ca	Zn, Na	Fe_xO_y, $ZnFe_2O_4$, CaO
	2	Fe, O, Ca	Zn	Fe_xO_y, $ZnFe_2O_4$, CaO
	3	Fe, O, Zn	Ca	Fe_xO_y, $ZnFe_2O_4$, $Ca_xFe_yO_z$

For electric arc furnace dust, the smooth, spherical particles are mainly occupied by iron oxides. With the increase of attachments at the surface of the ball, Ca and Zn content rise. The EDS analysis of submicron particles shows that it contains $ZnFe_2O_4$、Fe_3O_4 and small amount of $CaFe_2O_4$.

FTIR Spectra Analysis

The infrared spectra of all dusts can be seen in Figure 4. All spectra present a broad band, around 3425 cm^{-1} due to the O–H stretch of hydrogen bonded water. O–H bend of hydrogen bonded water is also found near 1621 cm^{-1}. The sharp band located at 3642 cm^{-1} in part (e) confirmed that calcium hydroxide only exists in EAFD. Kaolinite may mixed in the sintering dust from Guofeng and blast furnace dust from Baosteel for small peaks around 3696 cm^{-1} and 914 cm^{-1}. Asymmetric stretching vibration and out of plane bending vibration feature from all samples reveal that carbonate presences in every dust. The bands in the region from 1110 to 1000 cm^{-1} and 799 cm^{-1} are assigned to Si–O stretch vibrations, while the peaks around 546 and 466 cm^{-1} belong to Si–O bend vibrations. The bands located at 571, 440 cm^{-1} in EAFD are arranged to

vibrations of spinels (AB_2O_4). In both spectra of sintering dusts, the bands around 3138 cm^{-1} and 2950 cm^{-1}, are assigned to C–H stretch of aliphatic carbon chain indicating the presence of organic matter. The peak at 1152 cm^{-1} in sintering dusts and blast furnace dust from Shougang may contribute to C–O stretch by dioxins.

F.M. Martins et al. determined the infrared spectra of weathered and recent electric arc furnace dust, but they did not find $Ca(OH)_2$ in EAFD. [14]

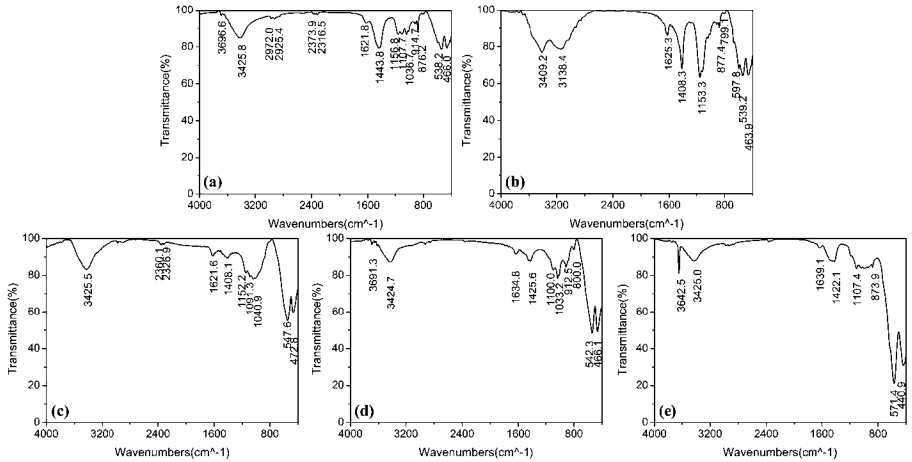

(a) SD-Guo; (b) SD-Bao; (c) BFD-Shou; (d)BFD-Bao; (e) EAFD.

Figure 4. FTIR spectra of samples prepared as KBr pellets

Conclusions

(1) The mean particle diameter of SD, BFD, EAFD are 12.550 ~ 13.774 μm, 26.373 ~ 51.015 μm, and 1.469 μm, respectively.

(2) Fe, K, Cl are present in SD with about 29%, 9% and 14%; Fe, C are present in BFD with about 40% and 20%, Fe, Zn, Ca are being in EAFD with 44.81%, 9.32% and 9.24%, respectively.

(3) XRD technique shows that: the dominant mineralogical phases in SD are KCl, Fe_2O_3, $CaCO_3$, $CaMg(CO_3)_2$, NaCl, SiO_2. Mineralogical phases in BFD contain Fe_2O_3, Fe_3O_4 and small amount of KCl. Fe_3O_4, $ZnFe_2O_4$, $CaCO_3$, CaO are detected in EAFD. C was not discovered.

(4) SEM and EDS analysis obtains that: potassium and zinc elements are abundant in dispersed fine particles in SD and EAFD, respectively. Some carbon particles emerge alone, some partly wrapped iron oxides, and other carbon particles almost entirely wrapped iron oxides.

(5) FTIR spectra analysis demonstrates that calcium hydroxide and spinel exist in EAFD, kaolinite present in the SD from Guofeng and BFD from Baosteel, organic matter containing dioxins and polycyclic aromatic hydrocarbons both emerge in SD. In addition, carbonate exists in every dust.

Acknowledgements

The financial support of the National Natural Science Foundation of China (U1260202) is gratefully acknowledged.

References

[1] C.H. Zhang et al., *Metallurgical resource comprehensive utilization* (Beijing: Metallurgical Industry Press, 2011), 17-125.

[2] J.G.M.S. Machado et al., "Chemical, Physical, Structural and Morphological Characterization of the Electric Arc Furnace Dust," *Journal of Hazardous Materials*, 136 (3) (2006), 953-960.

[3] X.F. She, "Fundamental Research of Technological Process about Treatment Zinc-Containing Metallurgical Dust by Direct Reduction on RHF". (Ph.D. thesis, University of Science and Technology Beijing, 2011), 26-28.

[4] C. Peng et al., "Discovery of Potassium Chloride in the Sintering Dust by Chemical and Physical Characterization," *ISIJ International*, 48 (10) (2008), 1398-1403.

[5] N. Menad et al., "Minimization Methods for Emissions Generated from Sinter Strands: A Review," *Journal of Cleaner Production*, 14 (8) (2006), 740-747.

[6] C.L. Wang, "Study on the Utilization of Zinc-Bearing Dust from Guofeng BF" (Master degree thesis, University of Science and Technology Beijing, 2009), 40-47.

[7] W.S. Chen et al., "Removal of Chloride from Electric Arc Furnace Dust," *Journal of Hazardous Materials*, 190 (1-3) (2011), 639-644.

[8] K.S. Abdel Halim, et al., "Metallic Iron Whisker Formation and Growth during Iron Oxide Reduction: Basicity Effect," *Ironmaking and Steelmaking*, 36 (8) (2009), 631-640.

[9] D.Y. Wang et al., "Direct Reduction Process of Pellet Containing Carbon with Addition of Zn-Pb-Bearing Iron and Steel Plant Dust," *Journal of University of Science and Technology Beijing*, 19 (2) (1997), 130-133.

[10] A.G. Guézennec et al., "Dust Formation by Bubble-Burst Phenomenon at the Surface of a Liquid Steel Bath," *ISIJ International*, 40 (8) (2004), 1328-1333.

[11] A.G. Guézennec et al., "Dust Formation in Electric Arc Furnace: Birth of the Particles," *Powder Technology*, 157 (1-3) (2005), 2-11.

[12] T. Sofilic et al., "Characterization of Steel Mill Electric-Arc Furnace Dust," *Journal of Hazardous Materials*, 109 (1-3) (2004), 59-70.

[13] M.C. Mantovani et al., "Electric Arc Furnace Dust-Coal Composite Pellet: Effects of Pellet Size, Dust Composition, and Additives on Swelling and Zinc Removal," *Ironmaking and Steelmaking*, 29 (4) (2002), 257-265.

[14] F.M. Martins et al., "Mineral Phases of Weathered and Recent Electric Arc Furnace Dust," *Journal of Hazardous Materials*, 154 (1-3) (2008), 417-425.

Characterization of Minerals, Metals, and Materials 2015
Edited by: John S. Carpenter, Chenguang Bai, Juan Pablo Escobedo, Jiann-Yang Hwang, Shadia Ikhmayies, Bowen Li, Jian Li, Sergio Neves Monteiro, Zhiwei Peng, and Mingming Zhang
TMS (The Minerals, Metals & Materials Society), 2015

INFLUENCE OF MINERALOGICAL CHARACTERISTICS OF IRON ORE ON FORMATION AND FLOW OF LIQUID PHASE

Bo Su[1], Sheng-li Wu[1], Guo-liang Zhang[1]

[1]School of Metallurgical and Ecological Engineering, University of Science and Technology Beijing; 30 Xueyuan Road, Haidian District; Beijing; 100083 P. R.; China

Keywords: Iron ore; Mineralogical characteristics; Assimilation characteristics; Fluidity of liquid phase.

Abstract

The mineralogical characteristics of iron ores can influence their high temperature sintering performance. In this study, eight iron ore samples from Brazil, Australia, and South Africa were characterized by their chemical composition, mineral types, particle morphology, and gangue dispersity. Meanwhile the influence rules between the mineralogical characteristics and the high temperature characteristics were evaluated and analyzed. The results showed that the effect of SiO_2 on assimilation characteristic of iron ores was relatively complex, Al_2O_3 and LOI of iron ores had negative correlation with assimilation temperature of iron ores, the dense slab-flaky mineral granule restrained to the assimilation characteristics of iron ores; liquid phase of iron ores with high SiO_2 content and low Al_2O_3 content had high fluidity, and the higher dispersity of gangue minerals in iron ores was good to the fluidity of liquid phase.

Introduction

Iron ore fines are important raw material for sintering. Its basic characteristics would influence the yield and quality of sintering product. Therefore, it's necessary to study fundamental features of iron ore to improve the quality of sinter. The basic characteristics of iron ore include the mineralogical characteristics of iron ore (e.g. the raw material condition, micro-characteristic) and the high temperature characteristics of iron ore (e.g. assimilation, liquid phase fluidity).
Research shows that the high temperature properties of iron ore fines, such as assimilation characteristics and liquid phase fluidity, played an important role in behaviors at high temperature during sintering and had important influence on quality of sinter [1, 2]. There is evidence of a relationship between the mineralogical characteristics of iron ore and its high temperature characteristics. And through these researches, can summarize some impact rules to guide the sintering manufacturing practice. However, few of researchers study the micro-characteristics of iron ore influences the high temperature properties.
Therefore, in this paper, based on mini-sintering test experiments, the high temperature characteristics of eight import iron ore fines which commonly used in China were measured. Then compared and analyzed the effect of mineralogical properties of iron ore fines, particularly the micro-characteristics, on the assimilation characteristics and liquid phase fluidity.

Experimental

Experimental Materials

The chemical compositions of the eight kinds of imported iron ore fines are shown in Table I. IOA~IOD are from Brazil, IOE~IOG are from Australia, IOH is from South African.

Table I. Chemical Compositions of Iron Ore Powders

Ore	TFe	FeO	SiO_2	CaO	Al_2O_3	MgO	LOI
IOA	63.42	0.59	5.64	0.01	1.34	0.06	1.81
IOB	63.10	0.73	5.56	0.06	0.97	0.27	1.86
IOC	64.14	0.58	5.19	0.02	0.86	0.07	1.68
IOD	64.81	0.17	2.77	0.02	1.24	0.06	2.12
IOE	58.60	0.20	4.44	0.04	1.63	0.07	10.07
IOF	61.44	0.29	3.68	0.03	2.26	0.08	5.45
IOG	60.77	0.32	4.19	0.02	2.28	0.06	6.07
IOH	64.44	0.32	5.21	0.11	1.33	0.03	0.55

* Mass Fraction

Experiment Method

In this experiment, XRD and SEM methods were employed to analyze mineral composition, micro-structure of iron ore. The mini-sintering test equipment (as shown in Figure 1) was used to research assimilation temperature and liquid phase fluidity of the iron ore, the concrete steps are as follows.

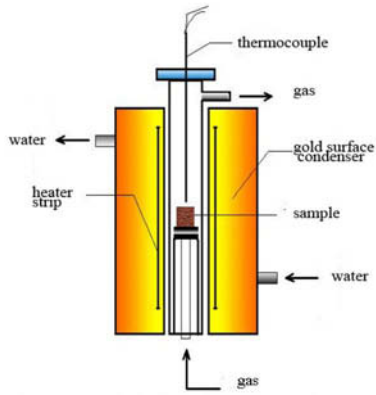

Figure 1. Mini-sintering test equipment

Assimilation Characteristics. The lowest assimilation temperature (LAT) in the interface of the iron ore fines and CaO reagents was measured to evaluate the assimilation capacity of different iron ore. The lower LAT indicated the stronger the assimilation characteristics it was. The CaO and ore fines were extruded to two cakes respectively, and the ore cake was positioned on the CaO cake. Then the sample was heated in air according to the sintering temperature variation curve. The start of melting was taken as the start of assimilation, and the lowest start reaction temperature of different iron ore were measured. The sketch map of the test for assimilation capacity is shown in Figure 2 [1~3].

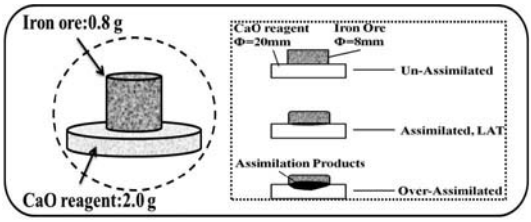

Figure 2. Schematic diagram of the assimilation capacity experiment

Fluidity of Liquid Phase. The index of fluidity of liquid phase (IFL) of the sample composed of different iron ore fines and CaO reagents was used to evaluate the liquid phase fluidity. The lower IFL, the poorer the liquid phase fluidity is. The ore and CaO were mixed according to binary basicity was 4.0, and then extruded into a cylindrical cake sample. The vertical projected area of the cake after the test was measured to calculate the index of fluidity of liquid phase (IFL). The sketch map of the experiment for the liquid phase fluidity is shown in Figure 3. The IFL is the data which the projected area of the sample after heated decrease the projected area of the sample before heated, divide the projected area of the sample being before heated [4].

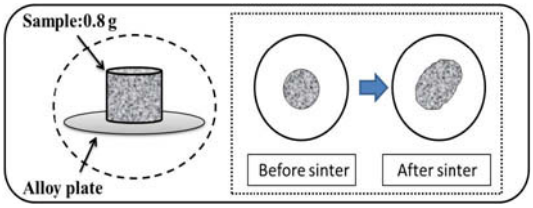

Figure 3. Schematic diagram of the fluidity experiment

Results and Discussion

The results of XRD (shown in Figure 4), assimilation and liquid phase fluidity of the 8 kinds of iron ore are shown in Table II.

Table II. Results of XRD,LAT and FI of Iron Ore Fines

Ore	Iron-containing minerals	Gangue minerals		LAT/℃	IFL/--(1280℃)
		Si	Al		
IOA	Hematite and few goethite	Quartz	Gibbsite	1263	1.949
IOB	Hematite and few goethite	Quartz	Gibbsite	1290	2.183
IOC	Hematite and few goethite	Quartz	Gibbsite	1285	1.917
IOD	Hematite and few goethite	Quartz	Gibbsite	1270	0.000
IOE	Goethite and few hematite	Quartz	kaolinite	1215	1.824
IOF	Hematite and goethite	Quartz	kaolinite	1235	1.123
IOG	Hematite and goethite	Quartz	Gibbsite	1225	1.656
IOH	Hematite	Quartz	kaolinite	1237	2.859

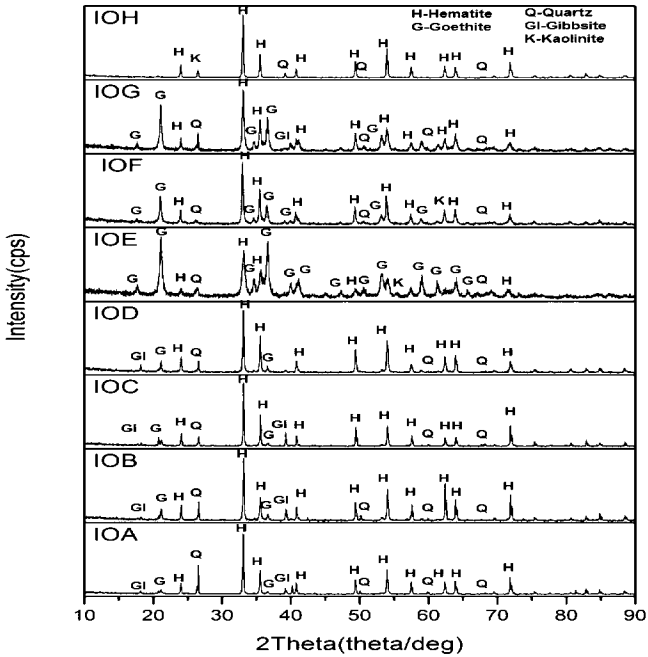

Figure 4. X-ray diffraction spectra of iron ores

Influence of Mineralogical Characteristics on Assimilation

Effect of Chemical Composition. The main chemical composition factors which influence the assimilation temperature were the content of SiO_2, Al_2O_3 and LOI (shown in Figure 5). According to the previous research [3], the more SiO_2, the higher assimilation temperature the ore was. However, this law was adapted when the SiO2 less than 4.5 mass%. With the resources of iron ore become inferior grade, gangue content ascend, for some iron ores, the content of SiO_2 has climbed around to 6 mass%. Figure 5-A is shown the relationship between SiO_2 contents of the iron ores and their LATs. It manifested that SiO_2 contents were not a simple linear relationship with LATs. In the condition of SiO_2 content under a value (e.g. $w(SiO_2)\approx 4.5\%$),the LATs become higher with more SiO_2 in ores; When exceed the value, the law was contrasted to the previous. This was thought that increased SiO_2 content has benefited to produce low melting point substances, such as the series of Fe_2O_3-CaO-SiO_2 eutectic melt, its melting point is 1192℃. But with the content of SiO_2 continued to increase and arrived at higher level, the SiO_2 was relative excess, and then produced higher melting point substances, such as the series of CaO-SiO_2. Moreover, SiO_2 elevated the melting point of the system, as SiO_2 was a high melting point substance.

The relationships between the content of Al_2O_3, LOI and the LATs are illustrated in Figure 5-B and 5-C, respectively. When Al_2O_3 content and LOI of iron ores increased, their LATs showed a descending trend.

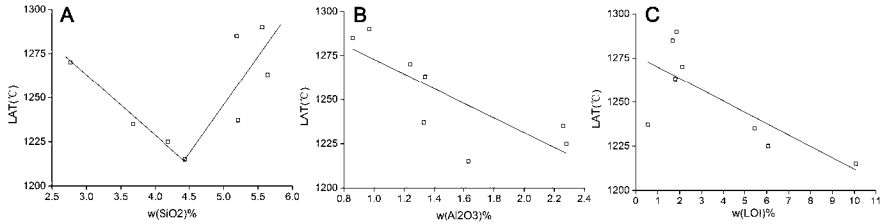

Figure 5. Influence of SiO_2, Al_2O_3 and LOI on LATs

The increased of Al_2O_3 promoted to produce low melting point substance, SFCA, moreover, the primary SFCA enhanced the contact between CaO cake and ore particles, improved the chemical kinetic parameters. Therefore, it reduced the LATs. The iron ores of high LOI commonly possessed loosen structure and higher porosity [5],such as limonite, after the crystal water and carbonate resolved. This improved dynamic condition of Ca^{2+} diffuseness through increased reaction contact area, thus promoted to produce low melting point materials, lessened the LATs.

Effect of Mineral Types. Iron-containing mineral types largely influenced its assimilation characteristics. Different types of minerals have obviously distinction in aspect of assimilation, as shown in Figure 6-A. Because of the limonite has loosen and porosity structure, the assimilation reaction dynamic condition was better than hematite. According to the compare in Figure 6-A, this order of assimilation capacity for the different iron mineral types is: Limonite> Half-Limonite> Hematite.

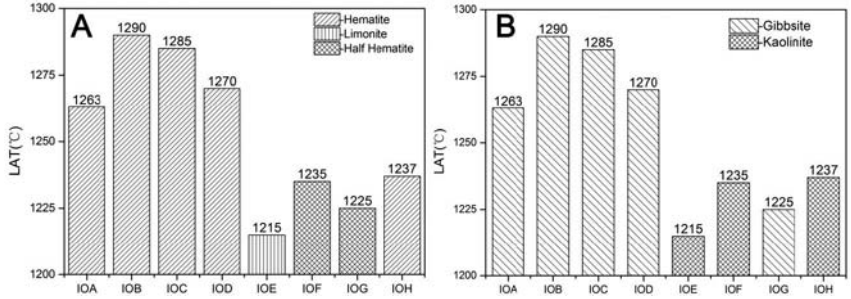

Figure 6. Comparison of the LATs of iron-containing and gangue minerals

Figure 6-B indicated gangue mineral types also have some influences on assimilation characteristics, though it's not notable as iron-minerals. In general, the assimilation temperature of iron ore fines which gangue minerals are quartz and gibbsite were higher than gangue minerals are quartz and kaolinite. The reactivity of kaolinite was higher than gibbsite [6], result into the LATs were lower. In addition, IOG was a special case which needed to be researched further.

Effect of Particle Morphology. Through microscopy observed the particle morphologies of iron ores, as shown in Figure 7 indicated that granules of IOB and IOC have dense slab-flaky structure. Compared IOB, IOC with IOA, have similar chemical composition and same mineral types, but LAT of IOA was obviously lower than IOB and IOC. It indicated the dense slab-flaky

granules have inhibition function to assimilation characteristics. Not only because the dense and glazed surfaces of particles dropped down kinetics condition of the reaction with CaO, but also they could cause more void in iron ore fines cake, influenced the contact of iron ore granules, the primary melted liquid couldn't father developed. Therefore, influence the assimilation temperatures of ores. The results shown the iron ore granules have bulk or pisolitic structure which have good uniformity would have better assimilation characteristics.

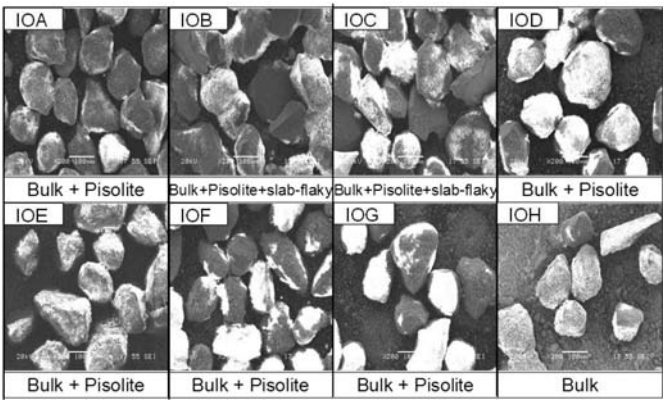

Fig 7. Images of particle morphologies of iron ore fines

Influence of Mineralogical Characteristics on Liquid Phase Fluidity

Effect of Chemical Composition. The influence tendencies of SiO_2, Al_2O_3 and LOI on liquid phase fluidity were respectively shown in Figures 8. According to Figure 8-A shown the IFLs ascend with the increase of SiO_2. Because a certain amount of SiO_2 were benefited to produce low temperature substances, such as a series of Fe_2O_3-CaO-SiO_2 mixture or SFCA, accelerated to liquid phase generate, enhanced the IFLs. For another, in the situation of fixed binary basicity, the additive amount of CaO was proportional to SiO_2 content. The increased content of CaO promoted to produce low melting point materials, thus it enhanced liquid phase fluidity [7, 8].

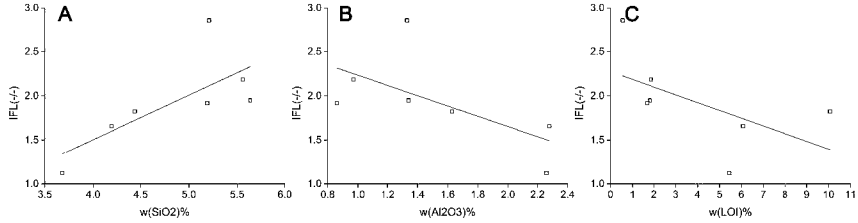

Figure 8. Relationship between SiO_2, Al_2O_3,LOI and the IFLs

With Al_2O_3 content increased, IFLs descended, as shown in Figure 8-B. The content of Al_2O_3 has dual function to liquid phase fluidity. On the one hand, Al_2O_3 is benefit to produce SFCA which is low melting point, enhanced the liquid phase fluidity capacity. On the other hands, Al_2O_3 is a high melting substance, with the content ascended, the melting point of liquid phase also arose, meanwhile, increased the viscosity of liquid phase.

In addition, the content of LOI also influenced the fluidity of iron ore. As the Figure 8-C indicated that the IFLs descend with the LOI content ascend. Because of the iron ore fines formed new gaps and holes after calcination process. Primary liquid generated and penetrated into cracks, decreased the volume of outflow liquid phase, descended the fluidity index [9].

Effect of Gangue Minerals. In this study, SiO_2 of iron ore fines main exist modes was quartz, and Al_2O_3 was gibbsite or kaolinite. The previous researches shown [2, 4], the gangues in the form of clay minerals have higher reactivity. It could enhance the liquid phase fluidity. Kaolinite belongs to clay minerals. It has higher reactivity and easier produced low melting point liquids than gibbsite. Compared with the 4 ores (IOA, IOB, IOC, IOH) which have similar content of SiO_2 (shown in Figure 9), the results correspond with this law.

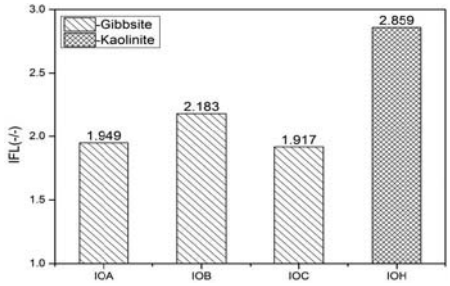

Figure 9. Comparison of the IFLs of gangue minerals

Effect of Gangue Dispersity. Adopted iron ore of IOA, IOB and IOC which own the similar chemical component and the same mineral types to compare to the influence of gangue dispersity on liquid phase fluidity. The research founded that the gangues of IOA and IOC were relatively concentrated and the sizes were bigger. The gangues of IOB were tiny and tight integrated with iron minerals, as shown in Figure 10. The quartz granules could obviously find in ore of IOA and IOC.

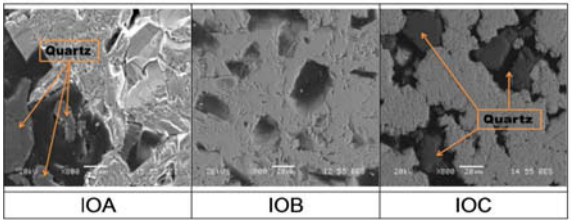

Figure 10. SEM images of IOA, IOB and IOC

According to the results of LATs and IFLs of the iron ores, IOB has the highest LAT of 1290 °C. This is an indication that the IOB needs a higher temperature to melt and produce liquid phase. Under the same heating mechanism, it should have produced less liquid phases. But the IFL of IOB is the highest in these ores. Even though the LATs of IOA and IOC were lower than IOB, and they would have produced more liquid phases than IOB, but the gangues of IOA and IOC were concentrated and the sizes were bigger. The gangue granules could not completely dissolved into liquid phase in the relatively short time. These gangue particles in the liquid phase would ascend the viscosity of liquid phase [10], hindered the flowing.

Conclusions

In summary, the main factors which influence of mineralogical characteristics of iron ore on assimilation characteristics and liquid phase fluidity were chemical composition, mineral types, particles morphology and gangue dispersity. $w(SiO_2)\%<4.5$, the assimilation characteristics of iron ores arose with the increased of SiO_2, but dropped down if the excessive content of SiO_2. Al_2O_3 and LOI were conducive to assimilation characteristics, but not propitious for fluidity of liquid phase. Gangues exited mainly in the form of kaolinite would better than gibbsite to liquid phase fluidity capacities. In the micro-characteristics of iron ores aspect, the dense slab-flaky granules of iron ores inhibited the assimilation capacities in dynamics conditions, and independently accumulated gangue particles which have digger sizes restrained the liquid phase fluidity.

References

[1] S. L. Wu, Y. Liu, J. X. Du, "Experiment Study of Assimilation Ability between Iron Ores and CaO," *Univ. Sci. Technol. Beijing*, 24 (3) (2002), 258-261.

[2] S. L. Wu, M. L. Bian, Q. F. Wang, "Fusion Characteristics of Iron Ore Fines and Its Evaluation Method," *Univ. Sci. Technol. Beijing*, 32 (12) (2010), 1526-1531.

[3] D. Debrincat, C.E. Loo and M.F. Hutchens, "Effect of Iron Ore Particle Assimilation on Sinter Structure," *ISIJ international*, 44 (8) (2004), 1308-1317.

[4] S. L. Wu, J. X. Du, H. B. Ma, "Fluidity of Liquid Phase in Iron Ores during Sintering ," *Univ. Sci. Technol.* Beijing, 27 (3) (2005), 291-293.

[5] T. Otomo, Y. Takasaki and T. Kawaguchi, "Properties of Core Ore in Quasi-Particle Required for Large Amounts Usage of Limonitic Ores in Iron Ore Sintering Process," *ISIJ international*, 45 (4) (2005), 532-537.

[6] E. Kasai, Y. Sakano, T. Kawaguchi and T. Nakamura, "Influence of Properties of Fluxing Materials on The Flow of Melt Formed in The Sintering Process," *ISIJ international*, 40 (9) (2000), 857-862.

[7] J. Okazaki, K. Higuchi, Y. Hosotan and K. Shinagawa, "Influence of Iron Ore Characteristics on Penetrating Behavior of Melt into Ore Layer," *ISIJ international*, 43 (9) (2003), 1384-1392.

[8] C. E. Loo, "A Perspective of Goethitic Ore Sintering Fundamentals," *ISIJ international,* 45 (4) (2005), 436-448.

[9] H. G. Li, J. L. Zhang and Y. D. Pei, et al., "Melting Characteristics of Iron Ore Fine during Sintering Process," *Journal of iron and steel research international*, 18 (5) (2011), 11-15.

[10] X. W. Lv, C. G. Bai and Q. Y. Deng, et al., "Behavior of Liquid Phase Formation during Iron Ores Sintering," *ISIJ international*, 51 (5) (2011), 722-727.

Characterization of Minerals, Metals, and Materials 2015
Edited by: John S. Carpenter, Chenguang Bai, Juan Pablo Escobedo, Jiann-Yang Hwang, Shadia Ikhmayies, Bowen Li, Jian Li, Sergio Neves Monteiro, Zhiwei Peng, and Mingming Zhang
TMS (The Minerals, Metals & Materials Society), 2015

EFFECT OF PRESSURE ON THE CORROSION OF MATERIALS IN HIGH TEMPERATURE WATER

W. Li[1]*, O. T. Woo[1], D. Guzonas[1], J. Li[2], X. Huang[3], R. Sanchez[3], and C.D. Bibby[2]

[1]Atomic Energy of Canada Limited, Chalk River Laboratories, Chalk River ON, Canada K0J 1J0
*Corresponding author, email address liw@aecl.ca
[2] CANMET – Materials Technology Laboratory, 183 Longwood Rd. S., Hamilton, ON, CANADA, L8P 0A1
[3] Mechanical and Aerospace Engineering, Carleton University, 1125 Colonel By Drive, Ottawa, ON, Canada, K1S 5B6

Keywords: Austenitic stainless steel 310, Super-Critical Water-cooled Reactor, Corrosion mechanism

Abstract

One of the major challenges for the Canadian Gen IV Super-Critical Water-cooled Reactor (SCWR) concept is the selection of fuel cladding materials. The Canadian SCWR concept will operate at a core outlet temperature of 625 °C and 25 MPa of pressure with peak cladding temperature reaching as high as 800 °C. Corrosion resistance is an important factor for material selection. Austenitic stainless steels that contain Cr contents greater than 18 wt.% are generally considered to provide adequate corrosion resistance. In this work, the pressure dependence of the corrosion of austenitic stainless steel 310 containing 24 wt% Cr is assessed at 625 °C for exposures of 1000 hours to evaluate the suitability of superheated steam as a surrogate for supercritical water at 25 MPa. Transmission Electron Microscopy (TEM) revealed that 310 exposed to different pressure conditions at 625 °C. (i.e., 0.1, 8 and 29 MPa) had generally the same type of the oxide structure, i.e., a Cr-rich oxide with the spinel structure on outer surface adjacent to the water phase. The material exposed at 8 and 29 MPa had a double layer oxide structure, with the outer oxide layer having a much larger grain size, while the samples exposed at 0.1 MPa showed only a single spinel-phase oxide layer. Cr-depleted recrystallized austenite grains were found underneath the spinel phase oxide. The adjacent large-grained austenite substrate had $M_{23}C_6$ carbides in the grain interior. The implications of these results are discussed.

Introduction

As a member of the Generation IV International Forum (GIF), Canada has chosen to focus on the development of the Super-Critical Water-cooled Reactor (SCWR) system, one of six systems that best fits Canada's expertise, technical capabilities and potential interests. The Generation IV Canadian SCWR concept is an extremely energy-efficient advanced reactor that is targeted to come on line in about 2030. Development of a new reactor design for deployment in this time-frame requires a significant research and development effort.

The current Canadian SCWR concept has a core outlet temperature of 650 °C at 25 MPa with a peak cladding temperature as high as 800 °C. High-temperature mechanical properties, corrosion resistance, stress-corrosion cracking (SCC) and radiation damage are some of the key factors in selecting materials for fuel cladding applications.

Allen et al. [1] summarized the SCW corrosion resistance of the major alloy groups. Most of the reported test data have been obtained at temperatures below 650 °C as this is close to the expected peak cladding temperature for most SCWR concepts other than the Canadian one. In general, the most corrosion-resistant alloys under SCWR conditions contain high concentrations of Cr (> 18 wt.%); these include austenitic steels such as 304, 310H, 800H, and the Ni-based Alloy 625. Cho and Kimura [2, 3] examined the weight gain for alloys containing a range of Cr content and found that increasing amounts of Cr led to decreasing weight gain. Ni alloys have excellent mechanical properties at high temperatures [4-6], but may be more susceptible to SCC in SCW. Helium production in alloys containing a large amount of Ni may also be an issue.

As the peak cladding temperature of the Canadian SCWR concept is 800 °C, corrosion data are required up to this temperature. While no autoclave exists that can operate above about 700 °C at supercritical pressures, Guzonas and Cook [7] have argued that at temperatures well above the critical temperature, 'superheated steam'[1] and SCW are essentially the same fluid, differing only in density. As part of a larger study to assess the use of superheated steam at 0.1 MPa as a surrogate for SCW at 25 MPa for scoping studies of corrosion at 800 °C, an austenitic stainless steel 310 containing 24 wt.% Cr was tested for its corrosion resistance at 625 °C for 1000 hours at 0.1 MPa (supercritical temperature and low pressure), 8 MPa (supercritical temperature and high but subcritical pressure) and 29 MPa. TEM analyses were performed to examine the changes in oxide microstructure as a function of water density at constant temperature.

Experimental

The austenitic stainless steel 310 samples were cut from bar stock and manually ground with 600 grit abrasive paper. They were properly cleaned, baked for 2 hours at 200 °C, and weighed and dimensioned before corrosion exposures. The chemical composition of the stainless steel is shown in Table 1.

Table 1 Nominal chemical composition of 310 austenitic stainless steel (wt.%)

C	Mn	S	P	Cr	Si	Ni	Fe
0.25	2.00	0.030	0.045	24.0 to 26.0	1.50	19.0 to 22.0	Balance

The specimens were exposed to water at 625 °C at 8 MPa and 29 MPa for 1000 hours in a static autoclave at Carlton University, Ottawa, Canada. The test samples were held in place by a sample tree during exposure. Exposure at 625 °C and 0.1 MPa was carried out by placing the samples in ceramic tubes through which steam passed in a furnace. The coupons were weighed after the corrosion test and the weight change of the specimens before and after exposures and the mass change per unit area were calculated. Electron-transparent cross-section TEM foils were prepared using a dual-beam Focused Ion Beam (FIB) using a conventional H-bar lift out technique [8, 9]. Microstructure characterization was performed using a FEI-CM 30 TEM operated at 300 keV. Energy dispersive X-ray (EDX) and electron diffraction analyses were performed to determine the phases present in the oxidized samples.

Results

Basic metallography and Scanning Electron Microscopy (SEM) work was reported elsewhere [10]. The weight change measurements showed very little weight gain after exposure at 0.1 and

[1] 'Superheated steam' is steam at temperatures above the saturation temperature.

29 MPa for 1000 hours, while exposure at 8 MPa resulted in more than a one order of magnitude greater weight gain, as shown in Figure 1 [10].

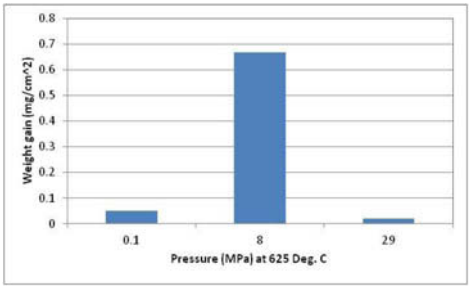

Figure 1 Weight change of austenitic stainless steel 310 exposed at different pressures at 625 °C for 1000 hours (0.1 MPa, 8 MPa and 29 MPa) [10].

Figure 2 shows the SEM images of the surface oxides on the samples reported in [10]. For the sample tested at 29 MPa, a uniform layer of oxide covered the whole sample surface, with a few larger octahedral particles randomly distributed over the uniform oxide layer (Figure 2 (a)). The surface of the sample exposed at 8 MPa was covered with a higher density of large octahedral particles with a uniform layer of small oxide particles underneath, Figure 2 (b). The morphology of the oxide on the sample exposed at 0.1 MPa was featureless, Figure 2 (c), in distinct contrast from those produced in other two conditions.

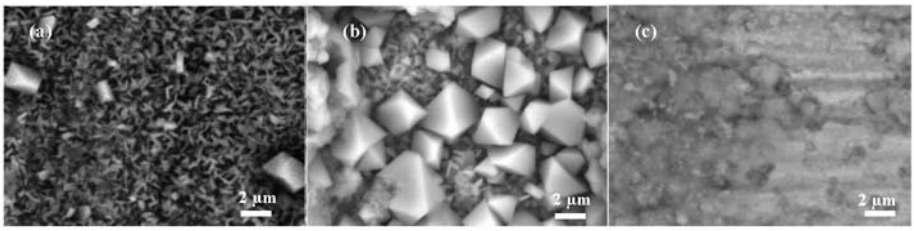

Figure 2 SEM micrographs showing the surface morphologies of the austenitic stainless steel 310 after exposures at 625 °C for 1000 hours at (a) 29 MPa; (b) 8 MPa and (c) 0.1 MPa [10].

Figure 3 (a) and (b) are the cross-section TEM images of the surface corrosion from the sample after 1000 hours at 625 °C at 29 MPa. The surface oxide is made up of two layers of Cr-rich spinel (~55 wt.% Cr) with a total thickness of about 1 µm. The chemical composition of these two spinel phases are almost identical, Table 2; but the outer layer has a larger grain size, about 0.3 to 0.4 µm in diameter, and these grains were distributed randomly. The inner layer spinel phase had much smaller grain size and was uniformly distributed. This observation is consistent with the SEM results shown in Figure 2 (a). Figure 3 (b) is a region of the oxide cross section that shows the two distinct layers of spinel-structure oxide (arrowed area in Figure 3 (a)). A layer of Cr-depleted recrystallized austenite grains (~10 wt.% Cr) was found between the γ-austenite substrate and the small-grained spinel phase.

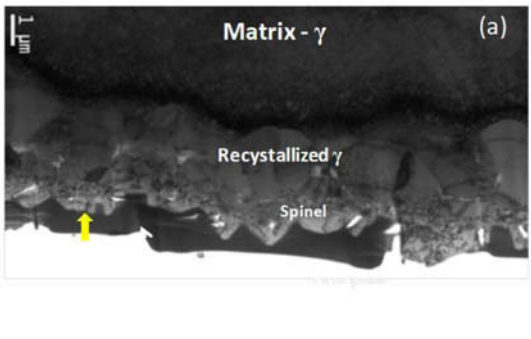

Figure 3 TEM images of the cross sections from the austenitic stainless steel 310 samples exposed for 1000 hours at 29 MPa, 625 °C.

Table 2 EDX analyses of the surface oxide and austenite matrix exposed at 29 MPa, 625 °C for 1000 hours

	Chemical composition (wt.%)					
	O	Si	Cr	Mn	Fe	Ni
Outer Layer Spinel Phase	33.11	-	56.17	6.09	3.73	0.90
Inner Layer Spinel Phase	33.10	-	53.37	5.19	6.29	1.57
Recrystallized γ	-	3.20	10.08	-	63.35	23.57
Matrix γ	-	1.19	25.67	1.70	52.48	18.96

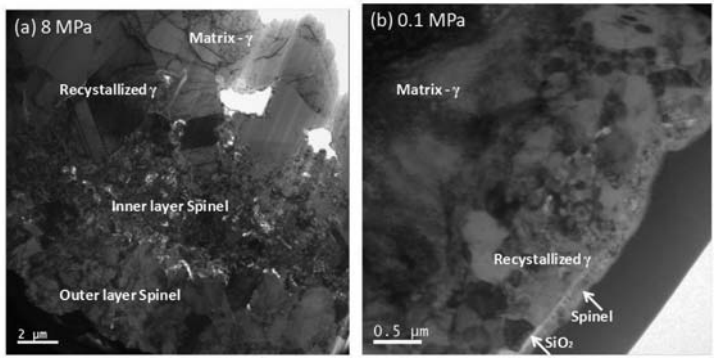

Figure 4 TEM images of the cross sections from the austenitic stainless steel 310 samples exposed at 625 °C for 1000 hours at (a) 8 MPa and (b) 0.1 MPa.

Table 3 EDX analyses of the surface oxide and austenite matrix exposed to subcritical water for 1000 hours at 8 MPa, 625 °C

	Chemical composition (wt. %)					
	O	Si	Cr	Mn	Fe	Ni
Outer Layer Spinel Phase	22.25	0.27	24.15	3.72	48.18	1.90
Inner Layer Spinel Phase	30.91	4.08	40.22	2.56	10.72	12.34
Recrystallized γ	-	0.88	9.86	2.68	61.33	27.04
Matrix γ	-	1.42	25.00	1.64	52.30	19.64

The surface oxide on the sample exposed at 8 MPa also had a double layer structure consisting of two spinel structure oxides, Figure 4 (a), but the total thickness of the oxide layers is much higher (~ 8 μm). Significantly, the outer layer spinel had a lower Cr content (~ 24 wt.%) than that of the second layer, which contained about 40 wt.%, Table 3.

Unlike the two samples exposed at 29 and 8 MPa, the surface oxide of the sample exposed at 0.1 MPa consisted of only one layer of Cr-rich spinel (~ 42 wt.%) with a thickness of ~ 0.2 μm. A continuous layer of silica was found just underneath the single spinel phase layer on the sample exposed at 0.1 MPa, as shown in the EDX element maps in Figure 5 (a). However, at 8 and 29 MPa the silica appears in the recrystallized small austenite grain layers and concentrated along the grain boundaries, e.g., Figure 5 (b) from the sample exposed at 8 MPa. The chemical composition for the sample exposed at 0.1 MPa is given in Table 4.

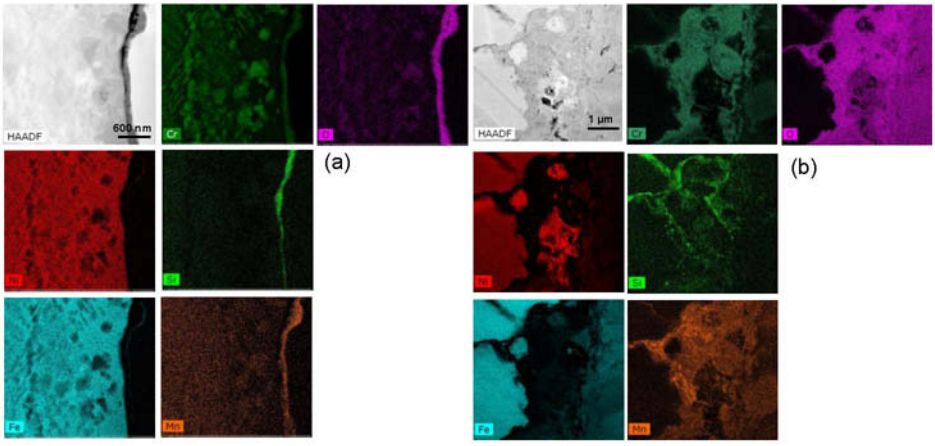

Figure 5 High angle annular dark field (HAADF) image and EDX maps of the austenitic stainless steel 310 sample after exposed at (a) 0.1 MPa and (b) 8 MPa.

Table 4 EDX analyses of the surface oxide and austenite matrix exposed at 0.1 MPa at 625 °C for 1000 hours

	Chemical composition (wt.%)					
	O	Si	Cr	Mn	Fe	Ni
Outer Layer Spinel Phase	33.26	1.71	42.52	8.57	14.19	6.37
SiO_2 Layer	50.37	49.30	0.33	-	-	-
Recrystallized γ	-	-	13.38	-	63.57	22.29
Matrix γ	-	1.43	25.89	1.75	52.00	18.93

In all three samples, $M_{23}C_6$ carbide precipitates were found in the interior of the substrate austenite. Figure 6 (a) gives a dark field image of grain matrix taken from the sample exposed at 8 MPa, showing precipitated carbide $M_{23}C_6$ in the grain interior at B= <-114>γ // <-114>$_{M_{23}C_6}$. The SAD pattern shown in Figure 6 (a) indicates that the $M_{23}C_6$ carbide and austenite substrate have the same orientation relationship, and the lattice parameters of the carbide are three times greater than those of the austenite matrix. In addition, some individual $M_{23}C_6$ carbide grains were found between the recrystallized small austenite grains. Figure 6 (b) shows an example of

$M_{23}C_6$ grains found in the middle of the recrystallized austenite layer from the sample exposed at 29 MPa after 1000 hours. The carbide $M_{23}C_6$ contains much more Cr (65 wt.%) compared to the adjacent recrystallized small grain austenite (10 wt.%) and substrate matrix (25 wt.%) as shown in Table 2. No intermetallic σ (sigma) phase was identified in any of the three samples. Table 5 summarizes the surface layers of the austenitic stainless steel 310 samples after exposure at 0.1, 8 and 29 MPa at 625 °C for 1000 hours.

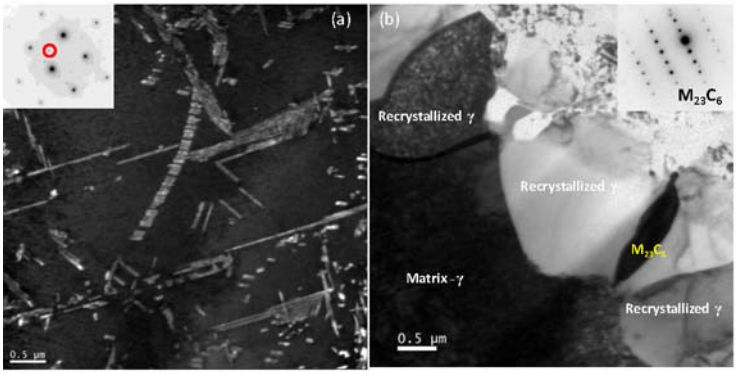

Figure 6 (a) Dark field TEM image with B=<-114>$_\gamma$ //<-114>$_{M23C6}$, showing precipitated $M_{23}C_6$ in the grain interior of austenite matrix of the sample exposed at 8 MPa, 625 °C for 1000 hours (Note that the circled spot in the SAD is the carbide reflection used for the dark field image.); (b) Cross-section TEM image of surface corrosion tested at 625 °C, 29 MPa after 1000 hours, showing the carbide formed in the middle of recrystallized austenite layer, B=<012> $_{M23C6}$.

Table 5 Summary of the structure layers of the austenite stainless steel 310 sample exposed to the different pressures at 625 °C for 1000 hours

Exposure pressure (MPa)	Surface oxide layer			Recrystallized grain layer		Matrix (substrate)
	Structure	Thickness (μm)		Structure	Thickness	
		Outer	Inner			
29	Spinel	0.5	0.4	γ w/t $M_{23}C_6$	2 μm	γ with $M_{23}C_6$
8	Spinel	4.2	3.3	γ w/t $M_{23}C_6$	8 μm	γ with $M_{23}C_6$
0.1	Spinel	0.2		γ w/t $M_{23}C_6$	1 μm	γ with $M_{23}C_6$

Discussion

Samples tested at all three pressures developed a Cr-rich spinel layer that provided the substrate material some protection from further oxidation, and there was a depletion of Cr in the recrystallized γ layer. Thus, Cr diffuses outwards during oxidation process, causing Cr depletion in subsurface layer. The sample tested at 8 MPa had the thickest surface oxide, while the sample tested at 0.1 MPa showed the thinnest oxide. The electron diffraction indicates that the spinel phase in all three conditions have essentially the same lattice parameters (diamond cubic, a=b=c=0.851 nm and α=β=γ=90°). The inner spinel phase layer formed at 8 and 29 MPa and the single spinel phase oxide formed at 0.1 MPa had roughly similar compositions (Tables 2, 3 and 4), containing 40-56 wt.% Cr and only 4-14 wt.% Fe. It is this inner oxide layer that provides the corrosion protection by acting as a barrier to diffusion of reactants and products to and from the water. In contrast, the outer oxide composition showed a much greater dependence on the

pressure, ranging from no outer oxide at 0.1 MPa to a very Fe-rich layer at 8 MPa. The similarity of the inner layer compositions and thickness at different pressures suggests that corrosion testing in superheated steam will give results in qualitative agreement with those expected at 25 MPa (SCWR operating pressure), and confirms that superheated steam at 0.1 MPa is a suitable surrogate for SCW corrosion testing.

Phase stability is an important aspect for fuel cladding material selections in the SCWR condition. Carbide and sigma phase can be formed in austenitic stainless steel when using at 400-900 °C for a long period of time [11]. In all the three samples, carbide precipitates were observed in the austenitic substrate, and some individual $M_{23}C_6$ carbide grains were also found between the recrystallized small austenite grains as shown in Figure 6. However, no intermetallic σ (sigma) phase was identified in any of the three samples. The precipitation of both the $M_{23}C_6$ carbide and σ phase are diffusion-controlled phase transformations, and the Cr atom had an important effect on the acceleration of the precipitation rate of the $M_{23}C_6$ carbide and σ phase [12, 13]. Weiss et al. [11] reported that the $M_{23}C_6$ carbides appeared in 316 austentic stainless steel (17 % Cr) after very short times at 400-900 °C while σ (sigma) phase was formed only after aging times longer than 1000 hours. At 650 °C, σ phase formation in an austenitic stainless steel that contains 25% Cr and 22% Ni (similar to 310) only starts after 100 hours, and the transformation could take 10,000 hours to complete [14]. In addition, the formation of the Cr-rich carbide may further prolong initiation of the Cr-rich σ phase formation in the current tested 310 samples. However, carbide precipitation may cause the embrittlement and loss of toughness.

It is known that Si improves the high temperature oxidation resistance of stainless steel in air by forming a continuous vitreous silica layer at the interface between the scale and metal; the silica layer can act as a diffusion barrier to provide better high temperature corrosion resistance [15, 16]. The continuous silica layer formed on the sample exposed at 0.1 MPa may have provided increased corrosion protection in these tests. It is not clear at this time why a continuous Si layer only formed on the sample exposed at the lowest pressure.

Conclusions

Three austenitic stainless steel 310 samples were exposed to 625 °C for 1000 hours to assess the effect of pressure on the corrosion resistance. The sample exposed at 8 MPa had the largest amount of surface oxide formation, while the sample exposed at 0.1 MPa had the thinnest oxide layer. The results shows that the all three samples have the similar construction of surface oxide, i.e., Cr-rich spinel phase on the outermost surface, Cr-depleted recrystallized γ in the intermediate layer and substrate austenite γ in the interior. The Cr-rich spinel phase provides a protection barrier for further oxidation.

Acknowledgements

The authors would like to thank financial support from NSERC/NRCan/AECL Generation IV Technologies Program; and the facility support from University of Ottawa. Thanks are also given to J. Smith for helpful discussions.

References

1. T.R. Allen, Y. Chen, X. Ren, K. Sridharan, L. Tan, G.S. Was, E. West, E and D.A. Guzonas, "*Material Performance in Supercritical Water*". In: Konings, R.J.M. (Ed.), Comprehensive Nuclear Materials, Elsevier, Amsterdam, 5 (2012), 279.
2. H.S. Cho, A. Kimura, S. Ukai and M. Fujiwara, "*Corrosion Properties of Oxide Dispersion Strengthened Steels in Super-critical Water Environment*", J. Nucl. Mater. 329-330 (2004) 387-391.
3. A. Kimura et al., "*Fuel Cladding Materials R&D for High Burn-up Operation of Advanced Water-cooling Nuclear Energy Systems*", Proc. ICAPP'05, Seoul, Korea, Paper 5338, May 15-19, 2005.
4. G.T. Hong, D.W. Ordway and V.A. Ziberstein, First Int. Workshop on Supercritical Water Oxidation, Jacksonville, Florida, Feb 6-9, 1995.
5. P. Kritzer, N. Boukis and E. Dinjus, "*The Corrosion of Alloy 625 (NiCr22Mo9Nb; 2.4856) in High-temperature, High Pressure Aqueous Solutions of Phosphoric Acid and Oxygen. Corrosion at Sub- and Supercritical Temperatures*", NACE, Houston, TX Corrosion 98, Paper No. 415, 1998.
6. S. Huang, K.W. Daehling, T.E. Carleson, M. Abdel-latif, P.Taylor, C.Wai, and A. Propp, "*Electrochemical Measurements of Corrosion of Iron Alloys in Supercritical Water*", Supercritical Fluid Science and Technology, K. P. Johnston and J. M. L. Penninger (eds.), ACS Symposium Series 406, ACS, Washington, , DC, (1989) 287-300.
7. D.A. Guzonas, W.G. Cook, "*Cycle Chemistry and its Effect on Materials in a Supercritical Water-cooled Reactor: A Synthesis of Current Understanding*", Corrosion Science 65 (2012) 48-66.
8. J. Li, "*Focused Ion Beam Microscope*", Journal of Metal, 58 (3), (2006) 27-31.
9. J. Li, T. Malis and S. Dionne, "*Recent Advances in FIB TEM Specimen Preparation Techniques*", Journal of Materials Characterization, 57 (2006) 64-70.
10. R.G. Sanchez, "Corrosion Performance of Candidate Materials for Canadian Gen IV Supercritical Water Cooled Reactor", Master Thesis, Carleton University, 2014.
11. B. Weiss and R.Stickler, "*Phase Instability During High Temperature Exposure of 316 Austenitic Stainless Steel*", Metallurgical Transactions, 3, April (1972), 851-865.
12. M. Farooqa, R. Sandström and M. Lundberg, "*Precipitation During Long Time Ageing in the Austenitic Stainless Steel 310*", Materials at High Temperatures, 29 (1), (2012), 8-16.
13. K. Shinohara, T. Seo, and K. Kumada, "*Recrystallization and Sigma Phase Formation as Concurrent and Interacting Phenomena in 25%Cr-20%Ni Steel*", Materials Transactions, 20 (12), (1979), 713-723.
14. E. Folkhard, Welding Metallurgy of Stainless Steels, 1st edition, (New York, NY: Springer, 1988), 130-135.
15. Shyh-An. Lin, Ju-Tung Lee and Wen-Ta Tsai, "*Microstructural Aspects and Oxidation Behavior of Laser Surface Cladded Silicon-containing Stainless Steels*", Scripta Materialia, 38 (1998), 559-563.
16. S.N. Basu, D. Nath and J. Tebbets., "*Microstructural Evolution of Multilayered Oxide Scales on Stainless Steel*", Materials Research Society Symposium Proceedings, 280 (1993) 541-544.

Characterization of Minerals, Metals, and Materials 2015
Edited by: John S. Carpenter, Chenguang Bai, Juan Pablo Escobedo, Jiann-Yang Hwang, Shadia Ikhmayies, Bowen Li, Jian Li, Sergio Neves Monteiro, Zhiwei Peng, and Mingming Zhang
TMS (The Minerals, Metals & Materials Society), 2015

THE EFFECT OF STRAIN REVERSAL DURING HIGH PRESSURE TORSION ON THE MICROSTRUCTURE EVOLUTION AND TEXTURE OF ALUMINUM ALLOYS

K. Chadha[1], P.P. Bhattacharjee[2], M. Jahazi[1]

1. Department of Mechanical Engineering, École De Technologie Superieur, Montreal Qc Canada

2. Dept. of Materials Science and Engineering, Indian Institute of Technology, Hyderabad, Yedumaillarum, Dist. Medak, Andhra Pradesh

Keywords: Aluminum Alloys, Strain Reversal, High Pressure Torsion, Microstructural evolution, Texture.

Abstract

The present work investigated the effect of strain reversal during high pressure torsion on the evolution of microstructure, texture and hardness properties of two different materials with different dynamic recovery behavior, namely, high purity (99%) Aluminum (2N-Al) and Aluminum-Magnesium (Al-2.5%Mg) alloy. In the two aluminum alloys subjected to different routes, the evolution of the ultrafine structure followed same trend. At lower strain level, sub grains with prominent LAGBs network were observed and at higher strains, ultrafine equiaxed grains separated by HAGBs were observed throughout the disk. The texture evolution in monotonically and strain reversal processed 2N-Al and Al-2.5%Mg showed presence of typical torsion texture components at different strain levels. The strength of the components was observed to follow different trends depending on the processing routes.

Introduction

Development of high strength structural materials through grain size reduction as conceived in the Hall-Petch relation ($\sigma_Y = \sigma_0 + kd^{-1/2}$) [1] has been a major driving force in the fabrication of Ultrafine Grained (UFG with grain size <1μm) and Nanostructured (NS with grain size <100 nm) materials with large fraction of high angle grain boundaries (HAGBs). Severe Plastic Deformation (SPD) is the most well-known approach for fabricating UFG and NS materials. SPD techniques such as Equi Channel Angular Processing (ECAP) [2], Accumulative Roll Bonding (ARB) [3] and High Pressure Torsion (HPT) [4] can now successfully produce wide variety of bulk Ultra Fined Grained and Nano structured materials.

Amongst various SPD processing techniques HPT has gained significant attention due to fact that large plastic strain value can be easily achieved in this process. The sample in the form of thin disc is placed between two anvils and a very high compressive load is applied with simultaneous torsion strain.

The equivalent strain value in HPT can be calculated by:

$$\varepsilon \approx \frac{1}{\sqrt{3}} \frac{r}{h} \varphi \qquad (1)$$

Where r = radius of the disc in mm, h = height of disc in mm, φ = angle of rotation in radians and ε = equivalent strain value. According to the equation the strain is directly

proportional to the radius of the disc which indicates that at the centre the strain is ideally zero whereas the strain is highest at the edges of the disc. Extensive research has been conducted on aluminum alloys to investigate the effect of HPT on the evolution of microstructure and mechanical properties [5, 6]. It is generally observed that HPT processing leads to development of ultrafine grains at high strain levels separated by high angle grain boundaries (HAGBs).

In contrast texture studies on HPT materials are rather limited and have been carried out by few researchers only [7, 8]. Torsion texture development in F.C.C. metals are expressed by{hkl}<uvw> notation, where {hkl} set of planes parallel to the shear plane and <uvw> is the shear direction Θ . Four types of ideal orientations are observed.

Table I: Ideal texture components for fcc metals

Component	{hkl}<uvw>
A	$\{1\bar{1}\bar{1}\} < 110 >$
A-	$\{\bar{1}11\} < \bar{1}\bar{1}0 >$
A*	$\{\bar{1}\bar{1}1\} < 112 >$
A*-	$\{11\bar{1}\} < 112 >$
B	$\{\bar{1}12\} < 110 >$
B-	$\{1\bar{1}\bar{2}\} < \bar{1}\bar{1}0 >$
C	$\{001\} < 110 >$

Torsion texture evolution in Al and Cu has been studied by Montheillet et al [8]. The report discussed development of torsion texture during conventional deformation. The study reveals that A component $\{1\bar{1}\bar{1}\} < 110 >$ dominates at lower strains whereas the C component {001}<110> dominates at higher strain values. The strain path change during HPT can be easily achieved by reversal strain deformation through the combination of clockwise (CW) and subsequent anticlockwise rotation (CW-CCW). The effect of strain reversal during HPT on the evolution of hardness and microstructure has been reported by few researchers [10, 11]. It has been reported by Orlov et al [11], that strain reversal retards the formation of HAGBs and thereby less grain refinement in case of 99.99% pure aluminum. Orlov et al. investigated on the development of texture during monotonic and strain reversal in high purity aluminum [9]. It is reported that there is development of A fibre in both deformation modes at lower strain levels whereas at higher strain levels, C component becomes the dominant in monotonic deformation and (001) [100] becomes dominant in strain reversal deformation.

It might thus be clearly pointed out that understanding the evolution of microstructure and texture of different aluminum alloys subjected to both monotonic and strain reversal deformation during HPT processing is insufficient and there are greater needs to address these issues which are the major focus of the present work.

Experimental

Commercially purity (99%) 2N-Al and Al-2.5%Mg alloy were used for the present study. 2N-Al was received in the form of fully annealed plates of approximately 2mm thickness. The as-received Al-2.5%Mg block (160mm(length) × 60mm (width) × 10mm (thickness)) was cold rolled to ~80% reduction in thickness and annealed in air

furnace at 673K for one hour. The above two materials were used as the starting materials for further procesasing. Disks with the diameter of 10mm were then cut from the sheet using EDM wire cut equipment. A total of 2 disks of each alloy were cut for further HPT processing. These disks having 2.5mm starting thickness were manually grinded to ~1.5mm thickness using SiC grit papers The disks were then designated according to the strain value or the number of rotations as per the given chart.

Table II: Designation of the samples according to the strain

Monotonic	Strain Reversal	Equivalent Strain
CW 30°	CW(15°)-CCW(15°)	1
CW120°	CW(60°)-CCW(60°)	4

CW- Clockwise Rotations, CW-CCW – Clockwise followed by counter clockwise

The disks were then deformed by HPT to the desired strain levels. The imposed load was fixed at 390KN (~5GPa) and a rotation speed of 1 rpm was used at quasi-constrained conditions [15]. The processing of the disks was done at POSTECH, South Korea in the group of Prof. H.S. Kim. To measure the hardness variation across the disk, Vickers microhardness test (Make: EMCO-TEST, Austria; Model: Dura Scan-70) was conducted on the disks. The disks were mounted using Hot Mounting Equipment (Make: Struess Citupress-10) and then manually grinded and polished in order to obtain a mirror finish. The microstructure and texture of the processed HPT disks were characterized by Electron Back Scattered Diffraction (EBSD) attached to a FEG-SEM (Make: Carl Zeiss; Model Supra 40) using Channel 5™ Software (Oxford Instruments, UK). The EBSD measurements were taken on the r-ɵ plane of disks at edge region. For EBSD investigations, the sample were polished mechanically using SiC paper of grit size 2000, followed by electropolishing using a mixture of perchloric acid and ethanol as electrolyte (1:9) at 20V and -30^{0}C (using Liquid N_2) for 20 sec. The microtexture analysis was done by assuming triclinic sample symmetry.

Results

Microstructure Evolution

Commercially Pure Aluminum (2N-Al)

The grain boundary (GB) maps of the samples deformed by different deformation modes are shown in Figure 1. Only the edge region has been considered here as maximum strain is accumulated at the edge of the specimen because of the torsional geometry. The high angle grain boundaries HAGBs having misorientation ($\theta_{mis} \geq 15^o$) are highlighted in black and low angle grain boundaries LAGBs with misorientation ($15^o \geq \theta_{mis} \geq 2^o$) are highlighted in red.

After ε=1 (CW 30°), Figure 1 (a), the microstructure consists of starting recrystallized grains but inside the starting recrystallized grains LAGBs network can be easily observed. Further deformation upto ε=4 (CW 120°), refines the microstructure so that equiaxed microstructure could be observed. Deformation at this level (at ε=4 (CW 120°) results in the evolution of an ultrafine microstructure at the edge regions characterized by rather equiaxed grains separated by HAGBs. The

average grain size continuously decreases at the edge as the number of rotations increases. The average grain size at the edge reduces from ~3.6μm after 30° clockwise rotation to 1.7μm after 120° rotation. The fraction of HAGBs, at the edge increases drastically to 80% after 120° clockwise rotations from 30% after 30° rotation. Figs. 1 ((c) & (d)) show the GB maps of strain reversal specimens at different strain levels. The microstructural evolution for edge regions appears very similar for both the deformation modes such that at lower strains the structure consists of huge fraction of LAGBs and with increasing strain gradually transformation into an ultrafine-grained structure could be observed. After 30° clockwise-counter clockwise (CW (15°)-CCW (15°)) rotation, the average grain size decreases from ~28 μm to ~4 μm in edge region. The average grain size reduces from ~4μm after 30° strain reversal ((CW(15°)-CCW(15°))) rotation to 1.5μm after 120° strain reversal rotations (CW(60°)-CCW(60°)). HAGBs fraction increases from 30% at edge region after 30° strain reversal (CW(15°)-CCW(15°)) to 64% after 120° strain reversal (CW(60°)-CCW (60°)).

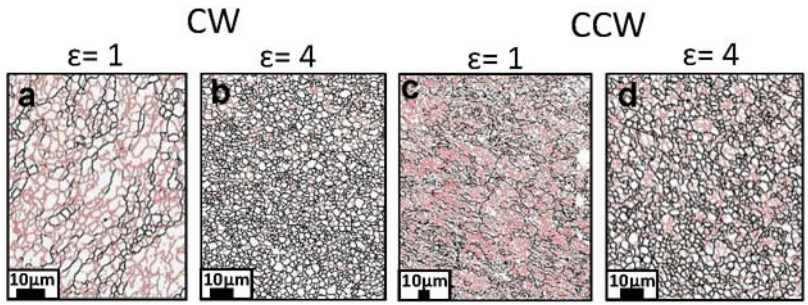

Figure 1. Grain boundary maps of 2N-Al clockwise rotations of monotonous deformed specimens (a & b) and strain reversal deformed specimens (c & d).

Aluminium Magnesium Alloy (Al-2.5%Mg)

The grain boundary (GB) maps of the samples deformed by different deformation modes are shown in Fig 2. After ε=1 (Fig 2 (a)), the microstructure consists of mostly sub grains with prominent LAGB network inside the grains. At ε=4 a much finer structure is observed at the edge region. The average grain size at the edge reduces from ~8μm after ε=1 to 760nm after ε=4. The fraction of HAGBs, at strain level after ε=1 increases from 14% respectively to 62% after ε=4. Figs. 2 ((c) & (d)) show the GB maps of strain reversal specimens at different strain levels. The microstructure evolution for edge region is similar for both deformation modes, such that at lower strains the structure consists of huge LAGBs and with increasing strain gradually transforms into an ultrafine grained structure. The average grain size decreases from 31 μm to 4 μm after ε=1. The average grain size edge region reduces continuously from 4μm, after ε =1 to 400nm at ε=4. HAGBs fraction increases from 21% in case at edge region after ε=1 to 82% after ε=4.

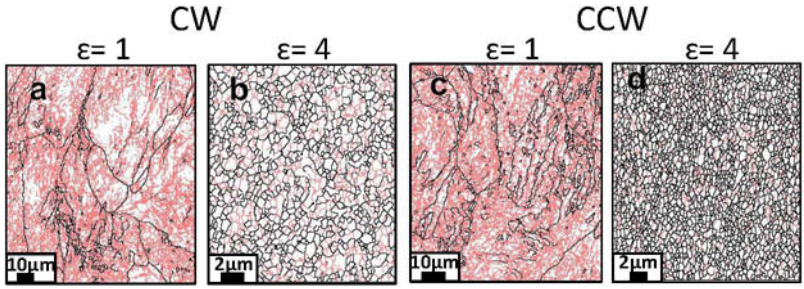

Figure 2. Grain boundary maps of Al-2.5%Mg clockwise rotations of monotonous deformed specimens (a & b) and strain reversal deformed specimens (c & d).

Microtexture Evolution

The (111) pole figure for the monotonically ((a)-(b)) and strain reversal deformed specimens ((c)-(d)) is shown in Figure 3 and Figure 5 for 2N-Al and Al-2.5%Mg respectively. Figure 4 and Figure 6 shows the orientation maps depicting the spatial distribution of different texture components for the monotonically ((a)-(b)) and strain reversal deformed specimens ((c)-(d)) of 2N-Al and Al-2.5%Mg alloys respectively. The ideal shear texture components are shown in (111) pole figure in Figure (k).

Commercially Pure Aluminium (2N-Al)

During monotonous deformation, at ε =1 (Figure 3 (a)) a strong presence of the (001)[100] fibre can be observed having a volume fraction of ~18% (Figure 3). Other components are present only in negligible proportion. At ε=4 (Figure 3(b)), the strong presence of the C component having a volume fraction of ~15% along with considerable presence of A/A^- fibre (~6%) can be observed (Figure 4).

During strain reversal deformation, at ε=1 (Figure 3 (c)), presence of the B/B^- fibre can be observed with the volume fraction of ~9% (Figure 4). A^*/A^{*-} fibre is also observed at this strain level with the volume fraction of ~8%. At ε= 4 (Figure 3(d)), presence of the A/A^- is noticed having the volume fraction of ~9% (Figure 4). Presence of the C component is increased to ~6%.

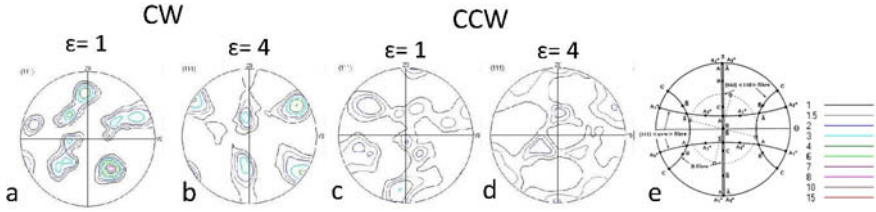

Figure 3. (111) pole figure of 2N-Al for monotonous rotation (a & b) and strain reversal (c & d) at r/r_0=1. The ideal texture components in (111) pole figure (e). [15]

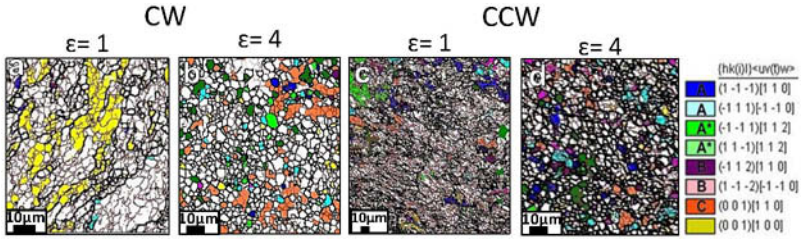

Figure 4. EBSD orientations for 2N-Al for monotonous rotation (a & b) and strain reversal rotations (c & d).

Aluminium Magnesium Alloy (Al-2.5%Mg)

During monotonic deformation, at ε =1 (Figure 5 (a), noticeable presence of the C component can be observed having a volume fraction of ~9% (Figure 6). Other components are present only in minor proportion and texture appears to be not very strong. The strength of the C component does not change much following straining to ε=4 (Figure 5 (b)) which is confirmed from the volume fraction of the C component (~8%).

The texture evolution in the strain reversal deformed specimens show characteristic differences with the monotonically deformed specimens. During strain reversal deformation after an imposed strain of ε=1 (Figure 5 (c)), the texture appears quite weak such that the volume fraction of the A*/A*$^{-}$ component is only 4%. Other components are present even in minor proportions while the volume fraction of the C component is ~2% (Figure 6). All the components are strengthened after an imposed strain of ε= 4 (Figure 5(d)). The A*/A*$^{-}$ component appears relatively stringer having a volume fraction of ~15% while the volume fraction of A/A^{-} is found to be ~9% (Figure 6). The fraction of the C component is almost negligible.

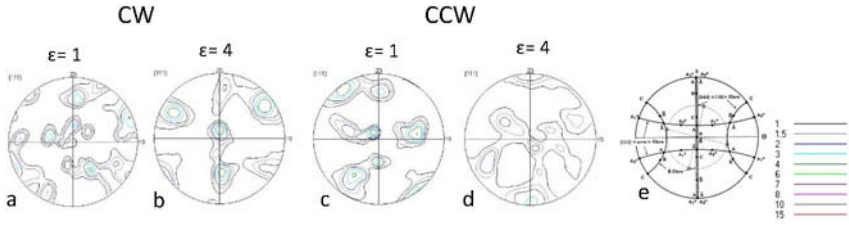

Figure 5. (111) pole figure of the edge regions for Al-2.5%Mg of monotonically (a & b) and strain reversal (c & d) specimens. The ideal texture components in (111) pole figure is shown in (e) [15].

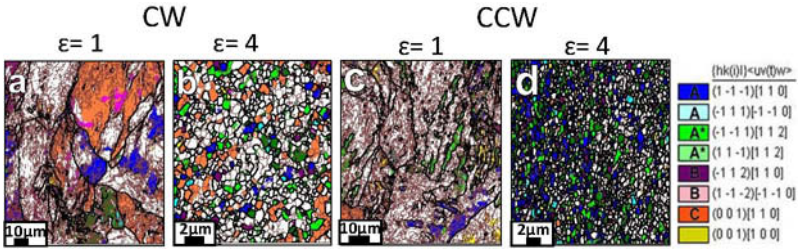

Figure 6. EBSD orientations for Al-2.5%Mg for monotonous rotation (a & b) and strain reversal rotations (c & d).

Conclusions

1. The microstructural evolution reveals that the grain refinement for the two deformation modes for the two alloys follows similar trend i.e. initial recrystallized microstructure with large grain size throughout the disk develop prominent LAGBs network inside the grains and ultimately at higher strain i.e. at ε=4 ultrafine equiaxed grains separated by HAGBs throughout the disk evolve. The final grain size of 2N-Al and Al-2.5%Mg deformed by both deformation modes at higher strain level is observed to be similar. However, lower grain size is observed in case of strain reversal in the two materials.
2. The fraction of HAGBs increases with the imposed strain for the Al-2.5%Mg alloy in both deformation modes. However the fraction of HAGBs for monotonically deformed is found to be higher than strain reversal deformed 2N-Al whereas the trend seems to be opposite in case of Al-2.5%Mg.
3. The evolution of A/A$^-$ and C components in 2N-Al deformed by the two deformation modes follows similar trend i.e. increasing with increase in strain. However, A*/A*- and B/B$^-$ component shows reverse trend. The (001)[100] component is observed at lower strains and a mixed texture is observed to be dominating whereas C component dominates at ε=4 during monotonic deformation. In strain reversal, a mixed texture but relatively stronger B/B$^-$ component is observed at lower strains whereas weak texture is observed at higher strain.
4. In Al-2.5%Mg, similar trend is observed for A/A$^-$, C and B/B$^-$ component for both the deformation modes. A strong C component is observed at lower strains and a strong A*/A*- along with C component is observed at higher strains for monotonically deformed specimens. During strain reversals, a weak texture is observed at the lower strains and with the increase in the imposed strain, the A*/A*- and A/A$^-$ components becomes stronger.

Acknowledgements

The authors gratefully acknowledge the financial support received from CSIR, India (Grant No. 22(0584)/12/EMR-II), Natural Science and Engineering Research Council (NSERC) and Mitacs. The authors would like to gratefully acknowledge Professor H.S. Kim, POSTECH, South Korea for his kind support for carrying out the HPT processing.

References

[1] T. Shanmugasundaram et al., "On the Hall-Petch relationship in a nanostructured al-Cu alloy," *Materials Science and Engineering A*, 527 (2010), 7821-7825.

[2] R.Z. Valiev, R.K. Islamgaliev, I.V. Alexandrov, "Bulk nanostructured materials from severe plastic deformation," *Progress in Materials Science*, **45(2) (2000),** 103-189.

[3] Y. Saito et al., "Novel ultra-high straining process for bulk materials—development of the accumulative roll-bonding (ARB) process," *Acta materialia*, **47(2) (1999),** 579-583.

[4] AP. Zhilyaev, T.G. Langdon, "Using high-pressure torsion for metal processing," *Fundamentals and applications Progress in Materials Science*, **53(6) (2008),** 893-979.

[5] M.Kawasaki et al., "The development of hardness homogeneity in pure aluminum and aluminum alloy disks processed by high-pressure torsion." *Materials Science and Engineering A*, **529 (2011),** 345-351.

[6] Cheng Xu, Zenji Horita, Terence G. Langdon, "The evolution of homogeneity in an aluminum alloy processed using high-pressure torsion," *Acta Materialia*, **56 (10) (2008),** 5168-5176.

[7] G.R. Canova, U.F. Kocks, J.J.Jonas, "Theory of torsion texture development," *Acta Metall.*, **32(2) (1984),** 211-226.

[8] F.Monthellet, M.Cohen, J.J.Jonas, "Axial stresses and texture development during the torsion testing of Al, Cu and α-Fe," *Acta metall.*, **32 (11) (1984),** 2077-2089.

[9] D. Orlov et al., "Texture evolution in pure aluminum subjected to monotonous and reversal straining in high-pressure torsion," *Scripta Materialia*, **60 (10) (2009),** 893-896.

[10] Jiuwen Zhang, Nong Gao, Marco J. Starink, "Microstructure development and hardening during high pressure torsion of commercially pure aluminium: Strain reversal experiments and a dislocation based mode," *Materials Science and Engineering A*, **528(6) (2011),** 2581-2591.

[11] D.Orlov et al., "Role of strain reversal in grain refinement by severe plastic deformation," *Materials Science and Engineering A*, **499 (2009),** 427-433.

[12] Hyoung Seop Kim, "Finite element analysis of high pressure torsion processing," *Journal of Materials Processing Technology*, **113 (1-3) (2001),** 617-621.

[13] L.S. Toth, J.J.Jonas, D. Daniel, J.A.Bailey, "Texture development and length changes in copper bars subjected to free end torsion," *Textures and Microstructures*, s**19 (1992),** 245-262.

Characterization of Minerals, Metals, and Materials 2015

Characterization of Composites

Session Chairs:
Frederico Margem
Jean Margem

Characterization of Minerals, Metals, and Materials 2015
Edited by: John S. Carpenter, Chenguang Bai, Juan Pablo Escobedo, Jiann-Yang Hwang, Shadia Ikhmayies, Bowen Li, Jian Li, Sergio Neves Monteiro, Zhiwei Peng, and Mingming Zhang
TMS (The Minerals, Metals & Materials Society), 2015

BENDING MECHANICAL BEHAVIOR OF POLYESTER MATRIX REINFORCED WITH FIQUE FIBER

Giulio Rodrigues Altoé, Pedro Amoy Netto[1], Mariana Barcelos[1], André Gomes[1], Frederico Muylaert Margem[1], Sergio Neves Monteiro[2].

[1] State University of the Northern Rio de Janeiro, UENF, Advanced Materials Laboratory, LAMAV; Av. Alberto Lamego, 2000, 28013-602, Campos dos Goytacazes, Brazil
[2] Instituto Militar de Engenharia , IME, Praça Gen. Tibúrcio, nº80 Urca, Rio de Janeiro - RJ, 22290-270
giulioaltoe@gmail.com

Keywords: fique fiber, polyester composite, flexural properties.

Abstract

Environmentally correct composites, made from natural fibers, are among the most investigated and applied today. In this paper, we investigate the mechanical behavior of polyester matrix composites reinforced with continuous fique fibers, through bending tensile tests. Specimens containing 0, 10, 20 and 30% in volume of fique fiber were aligned along the entire length of a mold to create plates of these composites, those plates were cut following the ASTM standard to obtained bending tests specimens. The test was conducted in a Instron Machine and the fractured specimens were analyzed by SEM, the results showed the increase in the materials tensile properties with the increase of fiber amount.

Keywords: Fique fiber, polyester composite, tensile test, SEM.

Introduction

Polymeric composites reinforced with natural lignocellulosic fibers, from different parts of plants, have been increasingly studied [1-3] and adopted by industry [4-6] by its technical and economical advantages.

The engineering application of natural fibers extracted from cellulose-containing vegetables, also recognized as lignocellulosic fibers, is presently considered an environmentally correct alternative to replace more expensive, non recyclable and energy-intensive synthetic fibers [7,8]. In Brazil, the variety of natural fibers is an additional motivation for the research of new composites with those fibers [9,10], treated as green composites.

In addition to environmental, economical and social benefits, some lignocellulosic fibers present specific properties that are comparable with synthetic ones used for polymer composite reinforcement. For instance, the specific strength (GPa.cm^3/g) of curauá (1.31), sisal (0.92) and ramie (0.93) fibers, for very thin diameters [11], are relatively closer to that of glass fiber E (1.33).

Therefore, it would be technically justified to replace glass fiber, which is more expensive, toxic and represents a problem to the environment [12], by a strong lignocellulosic fiber. However, some drawbacks such non-uniform dimensions and heterogeneous properties and incompatibility with a hydrophobic polymer matrix, reduce the potential of lignocellulosic

fiber to be used as composite reinforcement [13, 14]. In particular, a low interfacial strength causes a weak adhesion between the hydrophilic fiber and the polymer matrix.

Despite the drawbacks, natural fiber materials are being intensively studied as alternative to synthetics composite materials and the fique fibers can be used as reinforcement in polymer composites, however, little is known about the mechanical properties of fique fibers composites. Therefore, the aim of this work was to study the mechanical properties of the polyester matrix composites reinforced with continuous and aligned fique fibers by bend tests.

Experimental Procedure

The basic material used in this work was the fiber extracted from the leaf of fique plant (*Furcraea Andina),* Fig. 1(a), supplied by a producer in Colombia. No treatment was applied on fique fibers, Fig. 1(b).

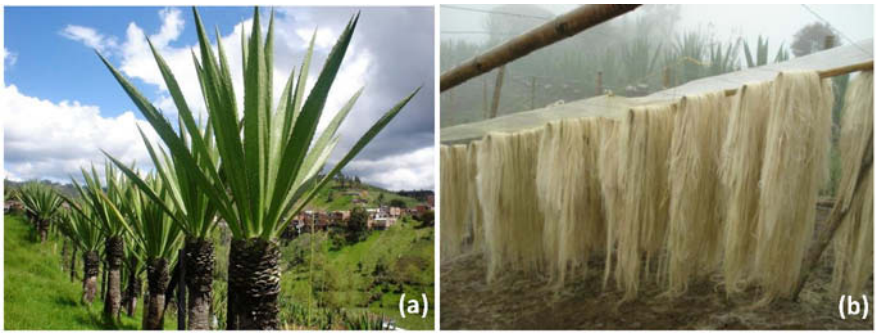

Figure 1. Fique plant (a) and its fibers (b).

The as received fibers of fique were cleaned and dried before use. The composites with 0, 10%, 20% and 30% in volume of aligned fique fibers were manufactured through accommodation of the fibers in a rectangular mold 152 x 122 x 10 mm and soaked with polyester resin to complete the cavity, the procedure origins plates with were cut following the ASTM standard and the samples were three points bend tested in a model 5582 Instron machine with 100 kN of capacity at a strain rate of 1.6×10^{-2} s^{-1} and a span-to-depth ratio of 9. The fracture surface was sputter coated with gold, then examined in a Shimadzu SEM operated at 15 kV. Secondary electron images were collected to reveal details on the fracture surface.

The flexural strength, σ_f, were calculated by the following equation:

$$\sigma_m = \frac{3F_m L}{2bd^2} \quad (1)$$

where F_m is the maximum resistance force, L the distance between supports, and the extension associated with maximum force, the width b and d the thickness of the specimen.

Results and Discussion

Figure 2 illustrates the typical appearance of load vs. elongation curves. The curves were recorded directly from the Instron machine, they revealed that fique fibers reinforced polyester composites present limited plastic deformation. After a straight line, a sudden

fracture occurs, indicating a brittle behavior for both pure polyester an fique fiber composites tensile specimens.

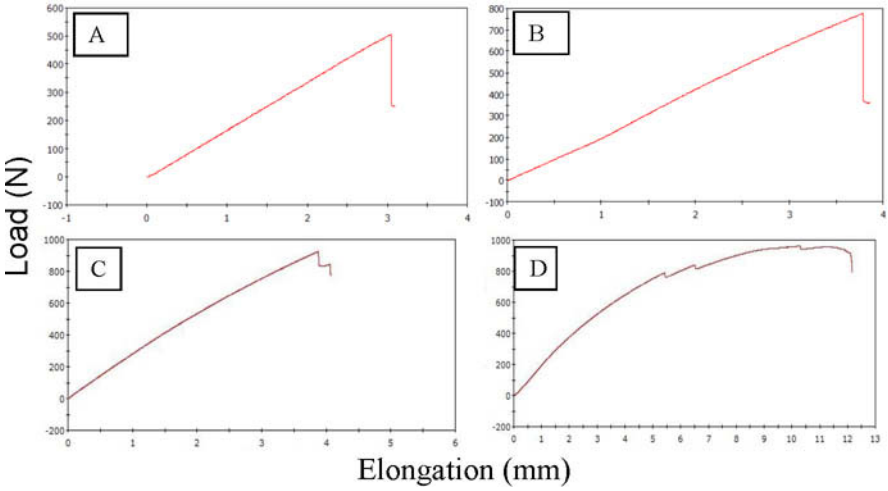

Figure 2. Load versus elongation curves for fique/polyester composites with different amount of fiber (a) 0%, (b) 10% (c) 20% & (d) 30%.

From the curves of Figure 2 was obtained the value of the maximum forces, F_m, and the corresponding strain and was calculated by the equation 1 shown, flexural strength. Table 1 shows the average flexural strength resulting composite polyester with different fractions of fique fiber.

Table 1. Flexural strength and rupture displacement for the fique fiber composites.

Amount of Fique Fiber (%)	*Flexural Rupture Stress (MPa)*
0	23.53 ± 6.9
10	42.79 ± 7.9
20	49.93 ± 4.0
30	61.39 ± 9.3

The graph for the flexural strength variation with the amount of fiber is shown in Figure 3. This graph implies that with the fiber volume increase the flexural stress increases too with a linear relation. So the results interpretation of the bending tests in Figure 3 indicate that the aligned fibers of fique constitute an effective reinforcement for over 10% composites with polyester matrix. That is, as the fiber matrix is incorporated an increase in resistance occurs, which may be attributed a higher adhesion of the fibers by the resin.

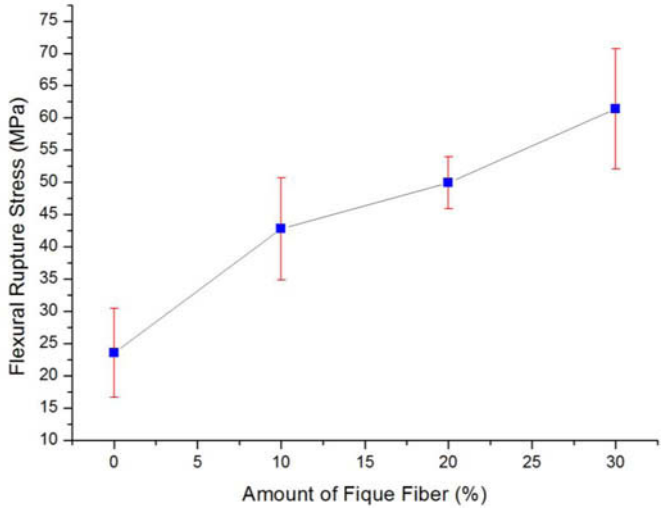

Figure 3. Variation of the flexural stress with the amount of fique fibers

Figure 4 shows micrographs of typical fracture obtained by SEM with different magnifications of a 30% fique fiber polyester composite fracture surface. In Fig. 4 (a), is visible some fibers loose of matrix, which suggests a low interfacial shear stress. Is possible to see too evidences in interface of nucleated cracks between fique fiber and polyester matrix. With higher magnification, Fig. 4 (b), is visible some fique fibers well fix to polyester matrix. Is notable the crack propagation is blocked by the fibers, opening a space between the fiber and the matrix. Even after of polyester matrix fracture the fibers continue resisting to tensile effort, because this behavior the composite find higher resistance values in correlation with pure matrix.

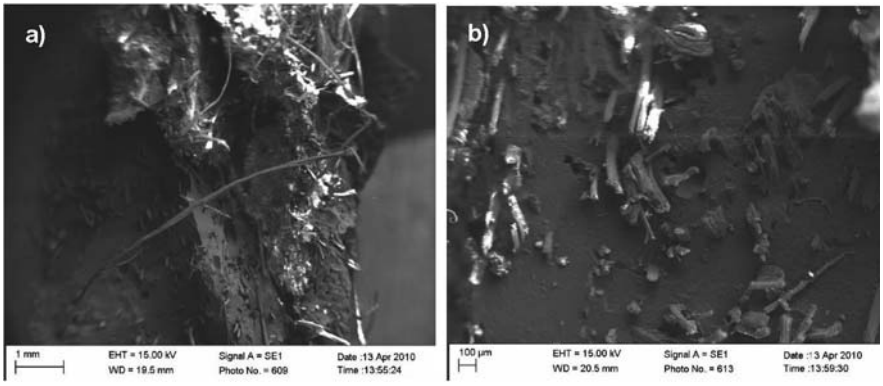

Figure 4 - SEM micrograph of composite obtained in 30% fique fiber reinforced polyester resin (a)30X and (b) 100X.

In this figure, it can be noted, with smaller magnification (Figure 4a), the broken polyester matrix with embedded fibers. With biggest increase (Figure 4b), it can be seen, pulling out evidences of fiber from the matrix. This seems to be a consequence of the weak adhesion

between the fiber and the matrix so when exposed to the flexural stress the fiber slide a little bit and bakes when its not possible to slide anymore.

Conclusions

- Polyester matrix composites incorporated with continuous and aligned fibers of fique fibers becomes more resistant to flexural for amount of fibers that exceeds 10% in volume.
- For 30% of fique fiber volume fraction, the flexural strength increases around 260% in comparison to pure polyester.
- SEM fractograph analysis revealed that the fique fiber are well adhered to polyester matrix and served as an barrier to crack propagation. This Justify the reinforcement effect

References

1. Bledzki, A .K and Gassan, J. Composites Reinforced With Cellulose-Based Fibers. *Prog. Polym. Sci*, 4 (1999) 221-274.
2. Nabi Saheb, D. and Jog, J.P. Natural fiber polymer composites: A review. *Advances in Polymer Technology*, v. 18, p. 351-363, 1999.
3. Eichhorn, S. J.; Baillie, C.A.; Zafeiropoulos, N.; Mwakambo, L.Y.; Ansell, M.P.; Dufresne, A. Review of current international research into cellulosic fibres and composites. *J. Mater. Science*, v. 36, p. 2107-2113, 2001.
4. Hill, S. Cars that grow on trees. *New Scientists*, v. 153(2067), p. 36-39, 1997.
5. Marsh, G. Next step for automotive materials. *Mater. Today*, v. 6(4), p.36-43, 2003.
6. Zah, R.; Hischier, R.; Leão, A.L.; Brown, I. Curaua fibers in automobile industry – A sustainability assessment. *J. Cleaner Production*, v. 15, p. 1032-1040, 2007.
7. Mohanty, A.K., Misra M. and Hinrichsen, G. Biofibers, biodegradable polymers and biocomposites: an overview, *Macromolecular Mat. And Engineering*, 276/277 (2000), 1-24.
8. Satyanarayana, K.G.; Wypych, F.; Guimarães, J.L.; Amico, C.S.; Sydenstricker, T.H.D.; Ramos, L.P. Studies on natural fibers of Brazil and green composites. *Met. Mater. Proc.*, v. 17(3-4), p. 183-194, 2005.
9. Satyanarayana, K.G.; Guimarães, J.L.; Wypych, F. Studies on lignocellulosic fibers of Brazil. Part I: Source, production, morphology, properties and applications. *Composites: Part A*, v. 38, p. 1694-1709, 2007.
10. Monteiro, S. N.; Satyanarayana, K. G.; Lopes, F. P. D.; High strength natural fibers for improved polymer matrix composites, *Materials Science Forum*, 638-642 (2010) 961-966.
11. Wambua, P.; Ivens I.; Verpoest, I. Natural fibers: can they replace glass and fibre reinforced plastics?, *Composites Science and Technology*, 63 (2003) 1259-1264.
12. Crocker, J. Natural materials innovative natural composites. *Materials Technology*, 2-3 (2008) 174-178.
13. Monteiro, S.N.; Lopes, F.P.D.; Ferreira, A.S.; Nascimento, D.C.O. Natural fiber polymer matrix composites: cheaper, tougher and environmentally friendly, *JOM,* 61 (2009) 17-22.
14. Mohanty, A.K., Khan, M.A., Hinrichsen, G. Influence of Chemical Surface Modification on the Properties of Biodegradable Fique Fabrics-Polyester Amide Composites. *Composites: Part A*, v. 31, (2000) 143-150.
15. Mohanty, S., Verma, S.K., Nayak, S.K. Dynamic Mechanical and Thermal Properties of MAPE Treated Fique/HDPE Composites. *Composites Science and Technology*, v. 66, (2006) 538-547.

Characterization of Minerals, Metals, and Materials 2015
Edited by: John S. Carpenter, Chenguang Bai, Juan Pablo Escobedo, Jiann-Yang Hwang, Shadia Ikhmayies, Bowen Li, Jian Li, Sergio Neves Monteiro, Zhiwei Peng, and Mingming Zhang
TMS (The Minerals, Metals & Materials Society), 2015

WEIBULL ANALYSIS OF THE BEHAVIOR ON TENSILE STRENGTH OF HEMP FIBERS FOR DIFFERENT INTERVALS OF FIBER DIAMETERS

Lázaro A. Rohen[1], Frederico M. Margem[1], Anna C. C. Neves[1], Maycon A. Gomes [1-4], Sérgio N. Monteiro[2] , Carlos Maurício. F.Vieira[1], Rafael G. de Castro[3], Gustavo X. Borges[5]

[1] State University of the Northern Rio de Janeiro, UENF, Advanced Materials Laboratory, LAMAV; Av. Alberto Lamego, 2000, 28013-602, Campos dos Goytacazes, Brazil;

[2] Instituto Militar de Engenharia , IME, Praça Gen. Tibúrcio, nº80 Urca, Rio de Janeiro - RJ, 22290-270

[3]ISECENSA – CENSA Instituto Superior de Instrução.

[4] Instituto Federal Fluminense, Rua Dr Siqueira, 273 - Pq Dom Bosco - Campos dos Goytacazes, RJ - 28030-130

[5] Faculdade Redentor Rodovia BR 356. n° 25 Itaperuna RJ - 28.300-000

Keywords: Weibull analysis, hemp fiber, tensile strength

Abstract

Economic and environmental benefits are motivating studies on natural fibers, especially lignocellulosic extracted from plants, have been studied to substitute synthetic fibers, such as glass fiber as reinforcement in polymer matrices. By contrast to synthetic fibers, natural fibers have the disadvantage of being heterogeneous in their dimensions specially the diameter. About the hemp fiber, little is known of their dimensional characteristics. The aim of the present work was to statistically characterize the distribution of the diameter of hemp fibers. Based on this characterization, diameter intervals were set and the dependence of the tensile strength of theses fibers with a corresponding diameter was analyzed by the Weibull method. The diameter was measured with precision using a profile projector. Tensile tests were conducted on each fiber obtain mechanical strength. The results interpreted by Weibull statistical showed a correlation between the resistances of the fiber to its diameter.

Introduction

In the past two decades, climate changes associates with the use of non renewable fossil fuels, mainly coal and petroleum derivatives, are motivating the substitution of natural materials for the energy-intensive synthetic ones. The so-called "green" materials are currently permeating in many industrial sectors and replacing traditional synthetic materials not only due to environmental but also to economical, societal and technical

reasons. Among these successful "green" materials stands the natural fiber obtained from cellulose–based plants, also known as lignocellulosic fibers. From house construction to automobiles, the lignocellulosic fibers are replacing glass fiber especially as reinforcement of polymer composites [1-4]. All synthetic composites reinforced with carbon and glass fibers are, however, associated with environmental drawbacks. Their production is energy-intensive and they cannot be easily recycled. Moreover, glass fiber is related to health problems like lung diseases. Less known natural fibers like ramie [5], curaua [6], buriti [7] and piassava [8] are currently being investigated for their potential as composite reinforcement. The growing interest for lignocellulosic fibers has been limited by the marked difference that exists regarding the mechanical strength. In fact, on average, the strongest lignocellulosic fibers have tensile mechanical strength below 1000 MPa [3], while the glass fiber reaches more than 3000 MPa [9]. This, together with the poor adhesion between any lignocellulosic fiber and most polymeric matrix [10], result in a much lower composite strength as compared to glass fiber composites, known as "fiberglass". Indeed, the best lignocellulosic fiber composites display strengths around 100 MPa [4] while fiberglass exceeds 1000 MPa [9]. The future competition against the glass fiber, as possible reinforcement of structural composites, depends on the improvement of both the polymer matrix adhesion and the mechanical strength of the lignocellulosic fibers. Hemp is certainly the lignocellulosic fiber with least knowledge as far as mechanical properties are concerned. Even review works on the application of natural fibers in composites [3,11] fail to report on hemp fibers. Since the heterogeneous characteristics of lignocellulosic fibers is a limitation for their use in composites, the present work carried out a statistical analysis on the mechanical properties of hemp fibers. This analysis was performed through precise geometrical measurements in association with tensile tests.

Experimental Procedure

The basic material used in this work was untreated hemp fiber. The fibers were supplied by the company *Desigan* natural fibers. Statistical analysis were performed on one hundred fibers randomly removed from the as-received the lot. These fibers were then measured in ten different points along the length, and were 90° rotated to be measured again, assuming a cylindrical structure for the fibers. The rotation guarantees the correct values of the mean diameter for each fiber. Figure 1 shows the histogram for the distribution of hemp fiber diameters by considering 6 diameter intervals. From this distribution, presented elsewhere an average diameter of 0.065mm was found for the as-received lot.

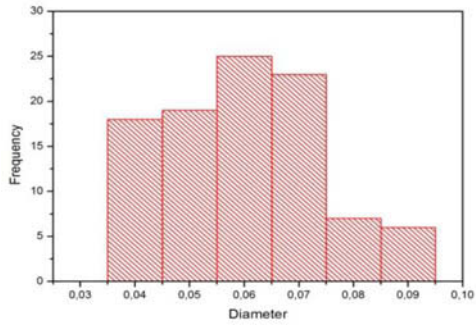

Figure 1. Histogram of the frequency of the hemp fiber for each diameter interval.

For each interval in Figure 2, a total of 20 fibers were selected and individually tensile tested at a temperature of 25 ± 2°C in a model 5582 universal Instron machine. The tests were conducted at a constant deformation velocity of 1 mm/s corresponding to a strain rate of 3 x 10-3 s-1. The values obtained for the ultimate tensile stress, i.e., the tensile strength, were statistically interpreted using the program Weibull Analysis.

For the objective of the present work, it was important to consider different intervals for the cross section different intervals for the cross section area to associate with corresponding intervals for the tensile strength.

Results and discussions

With the data provided on test machine Instron curves were constructed for each fiber tensile. Figure 2 shows examples of curves for each interval considered equivalent diameter. This figure also shows that the force versus elongation curves have the same general characteristics. After a continuous elastic regime, a point of maximum resistance, virtually without showing deflection of the elastic line that could characterize an initial plasticity occurs. However, since the maximum or soon after, the curve shows discontinuities that come with process of decline in resistance until full rupture. In fact, these discontinuities are associated with partial ruptures of the various fibrils that constitute the hemp fiber. At this point is important to mention that the thinner the equivalent diameter of the fiber, the smaller the number of fibrils. As a result, fibers with thinner diameters, as interval $0.035<d<0.045$ mm, shows less fluctuations to rupture compared to fibers of larger diameter, such as interval $0{,}085<d<0{,}095$ mm in Fig. 3. The analysis of the generated Weibull probability that typical graphs are shows in Fig. 3 for all ranges of equivalent diameter. Furthermore, this analysis also generated Weibull parameter values that are listed in Table 1 along with corresponding results from the statistical mean and standard deviation of the maximum stresses obtained for each range of equivalent diameter.

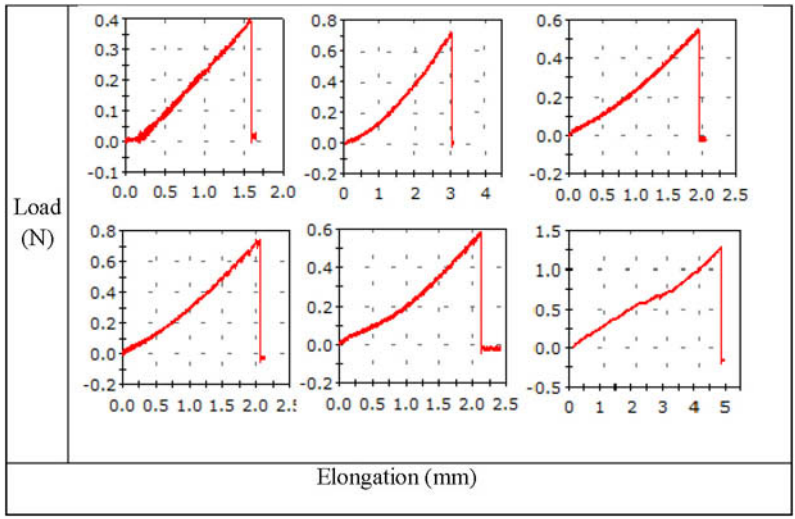

Figure 2: Representative load *vs.* elongation for the 6 intervals of diameters (mm) of hemp fibers.

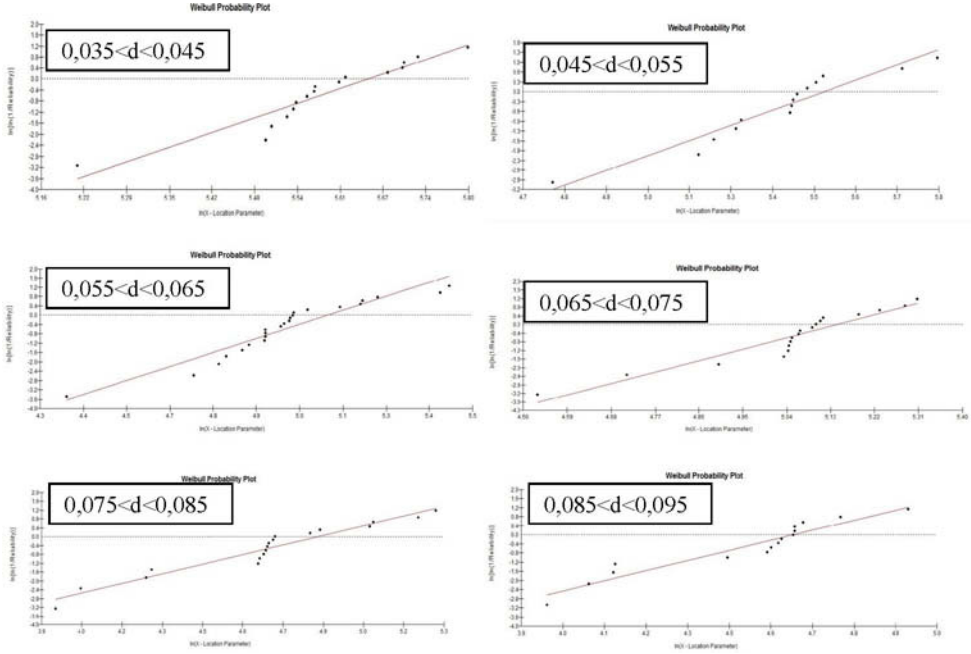

Figure 3. Weibull graphs for the tensile strenght of hemp fibers for different diameter intervals.

Table 1. Weibull parameter for the tensile strength of hemp fibers associated with different diameter intervals.

Diameter interval (mm)	Weibull Modulus, β	Characteristic Stress, θ (MPa)	Precison Adjustment, R^2	Average Stress (Mpa)	Statistical Deviation (MPa)
0,035<d<0,045	8,287	284,2	0,9014	268,1	38,49
0,045<d<0,055	4,523	243,3	0,9252	222,1	55,74
0,055<d<0,065	5,011	163,7	0,9034	150,3	34,36
0,065<d<0,075	5,919	171,2	0,9009	158,7	31,14
0,075<d<0,085	3,104	128,6	0,9375	115	40,54
0,085<d<0,095	4,03	101,4	0,9146	91,95	25,62

Based on all tensile results such as those exemplified in Figure 4, the tensile strength, i.e. the ultimate stress associated with the point of maximum load, was evaluated. These values of tensile strength were analyzed by the Weibull statistic method for each one of the 6 diameter intervals shown in the histogram of Figure 1. Actually, the Weibull Analysis computer program provides the following parameters: θ (characteristic strength), β (Weibull modulus), R^2 (precision adjustment) as well as a mean strength based on the Weibull distribution with related deviations. The values of theses parameters are listed in Table 1.

Figure 4 shows the variation of **θ**, the Weibull characteristic strength, with the mean hemp fiber diameter for each interval in the Fig. 1 histogram. In this figure there is a tendency of **θ** to increase the thinnest the fibers. Aparently, this tendency is associated with an inverse correlation of the fiber strength with its diameter.

In the present work, a hyperbolic equation can be used as an adjustment of **θ** to the values of **d** shown in Table 1. The best hyperbolic fit is associated with the following equation:

$$\theta = \frac{13.03}{d} - 34.2 \qquad (1)$$

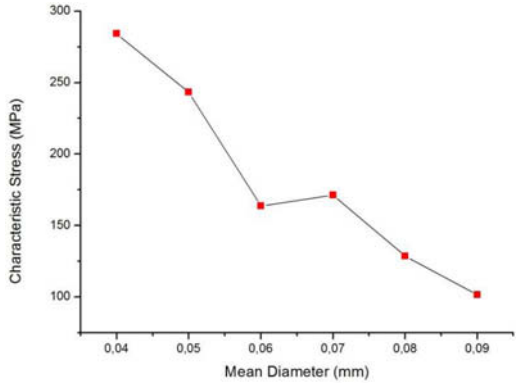

Figure 4. Variation of the characteristic strength with the mean diameter of hemp fibers.

To better assess the possibility of an inverse correction, we compared the characteristic voltage and medium voltage corresponding standard deviation for each diameter band as shown in Figure 5.

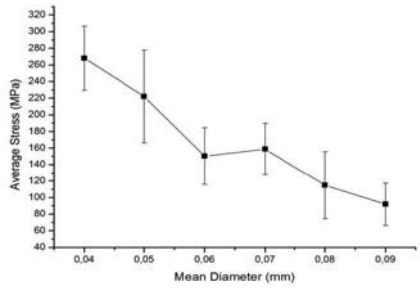

Figure 5. Variation of the average tensile strength with the mean diameter for hemp fibers.

Based on results of Figure 5 also obtained with reasonable accuracy a hyperbolic relation between the tensile strength, σm, and the mean diameter for the six intervals of Figure 1.

$$\sigma m = \frac{12.44}{d} - 40.11 \qquad (2)$$

As a final remark regarding the inverse strength/diameter correlation given by Equation (2), one could in practice obtain stronger fibers by selecting the thinner ones. This

would allow polymer composites to be fabricated with improved mechanical of properties by reinforcement with these thinner fibers.

Conclusions

Hemp fibers are relatively weak in tension and should not reinforce polymeric composites that usually have stronger matrices.

The non-uniform microstructure of the hemp fiber composed of filaments with empty spaces apparently contributes to weaken its mechanical performance in tensile tests.

The tensile strength of the hemp fibers increases with reduction in the equivalent diameter, which can also be attributed to the fiber's filamentary structure.

Acknowledgements

The authors thank the support to this investigation by the Brazilian agencies: CNPq, CAPES, FAPERJ and TECNORTE/FENORTE.

References

1- WANBUA, P., IVENS, I., VERPOEST, I., "Natural fibers: can they replace glass and fibre reinforced plastics?", *Composites Science and Technology*, v. 63 , pp. 1259-1264, 2003.

2- ZAH, R., HISCHIER, R., LEÃO, A.L., BROWN, I., "Curaua fibers in automobile industry – A sustainability assessment", *Journal Cleaner Production*, v. 15, pp. 1032-1040, 2007.

3- SATYANARAYANA, K.G., GUIMARÃES, J.L., WYPYCH, F., "Studies on lignocellulosic fibers of Brazil Part I: Source, production, morphology, properties and applications", *Composites: Part A*, v. 38, pp.1694-1709, 2007.

4- MONTEIRO, S.N., LOPES, F.P.D., FERREIRA, A.S., NASCIMENTO, D.C.O., "Natural fiber polymer matrix composites: cheaper, tougher and environmentally friendly", *JOM – The Member Journal of TMS*, v. 61, n. 1, pp. 17– 22, 2009

5- C. Z. Paiva Jr., L.H. Carvalho, V.M. Fonseca, S.N. Monteiro, J.R.M. d'Almeida, "Analysis of the tensile strength of polyester/hybrid ramie–cotton fabric composites", *Polymer Testing*, 23(2) (2004) 131-135.

6- S.N. Monteiro, R.C.M.P. Aquino, F.P.D. Lopes, E.A. Carvalho and J.R.M. d'Almeida, "Mechanical Behavior and Structural Characteristics of Polymeric Composites Reinforced with Continuous and Aligned Curaua Fibers" (in Portuguese), *Rev. Mater.*, 11(3) (2006) 197-203.

7- R.S. Santos, E.L.C. Silveira and C.M.L. Souza, "Study of the mechanical properties of thermoset polymeric matrix composites reinforced wit buriti fibers" (in Portuguese), *Proceedings of the 30th Annual Meeting of the Brazilian Chemistry Society*, (Aguas de Lindoia, Brazil, 2007) 1.

8- J.R.M. d'Almeida, R.C.M.P. Aquino and S. N. Monteiro, "Tensile Mechanical Properties, Morphological Aspects and Chemical Characterization of Piassava (Attalea funifera) Fibers". *Composites. Part A*, 37 (2006), 1473-1479.

9- CALLISTER JR., W.D., *Materials Science and Engineering – An Introduction*, 5 ed., New York, NY, John Wiley & Sons, 2000.

10- VASQUEZ, A., RICCIERI, J., CARVALHO, L., "Interfacial properties and initial step of water sorption in uniderectional unsaturated polyester/vegetable fibre composites", *Polymer Composites*, v. 20, pp. 29-27, 1999.

11- D. Nabi Sahed and J.P. Jog, "Natural fiber polymer composites: a review", *Advances in Polymer Technol.*, 18 (1999), 221-274

12- MONTEIRO, S.N., SATYANARAYANA, K.G., LOPES, F.P.D., "High strength natural fibers for improved polymer matrix composites", *Materials Science Forum*, v. 638-642, pp. 961-966, 2010.

Characterization of Minerals, Metals, and Materials 2015
Edited by: John S. Carpenter, Chenguang Bai, Juan Pablo Escobedo, Jiann-Yang Hwang, Shadia Ikhmayies, Bowen Li, Jian Li, Sergio Neves Monteiro, Zhiwei Peng, and Mingming Zhang
TMS (The Minerals, Metals & Materials Society), 2015

PREPARATION AND CHARACTERIZATION OF NATURAL RUBBER/ORGANOPHILIC CLAY NANOCOMPOSITES

GONZALES-FERNANDES, M. [1, 2, 3], ESPER, F. J. [3], SILVA-VALENZUELA, M. G. [4], MARTÍN-CORTÉS, G. R. [4], VALENZUELA-DIAZ, F. R. [1], WIEBECK, H. [1]

[1] PMT (Metallurgical and Materials Engineering Department of Polytechnic School); Av. Prof. Mello Moraes, 2463; São Paulo, SP, 05508-000, Brazil

[2] IFES (Federal Institute of Education, Science and Technology of São Paulo); Rua Pedro Vicente, 625; São Paulo, SP, 01109-010, Brazil

[3] FMU/FISP (United Metropolitan Colleges); Av. Brigadeiro Luís Antônio, 1089; São Paulo, SP, 01324-010, Brazil

[4] Centro Universitário Estácio Radial de São Paulo; Av. dos Remédios, 810; São Paulo, SP, 05107-001, Brazil

Keywords: elastomers, natural rubber, nanocomposites, organophilic clays.

Abstract

Natural rubber/organophilic clay nanocomposites were prepared and characterized. A brown bentonite from Paraiba's State, Brazil was modified with a sodium salt and treated with quaternary ammonium salt hexadecyltrimethyl ammonium chloride. The clay in its natural state, after cation exchange with sodium and after organophilization was characterized by XRD, IR, SEM, thermal analysis. Nanocomposite samples were prepared containing 10 resin percent of organophilic clay. The vulcanized samples were analyzed by XRD, SEM. The nanocomposites obtained showed improvement in their mechanical properties in comparison with samples without clay.

Introduction

The incorporation of fillers homogeneously dispersed in a matrix of elastomer brings a significant improvement in physical, chemical, mechanical and thermal properties, barrier / gas permeability and inhibiting flame propagation of elastomeric composite cross link. Montmorillonite is a clay mineral commonly used in polymer composites consisting of nanolayers silicate intercalated by galleries occupied by metal cations such as K^+, Na^+, Ca^{2+} and Mg^{2+}, which can be easily replaced by inorganic salts of ammonia, thereby producing the organophilic clay or organoclays, so that there is better compatibility with polymers. [1] The polymeric matrix used is natural rubber (NR), which has origin in the polyisoprene extracted from *Hevea brasiliensis* (*seringueira*). [2]

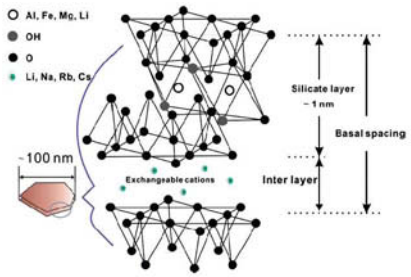

Figure 1: Schematic diagram of structural units in montmorillonite (MMT) crystal.

Materials and Methods

Elastomers

Raw gum elastomers, polyisoprene, NR, poly (cis-1, 4-isoprene) rubber, were obtained from *Industria de Artefatos de Borracha Esper Ltda.*

Natural clay

Light brown chocolate clay was provided by mine Lages, Boa Vista County, State of Paraiba, Brazil. Ca–bentonite is characterized by its low water absorption and poor swelling capability and by its inability to stay suspended in water, was supplied by *BENTONISA - Bentonita do Nordeste S.A.*

Accelerators and vulcanizing agents

The addition of activators, zinc oxide (ZnO) and stearin (stearic acid and glycerol (glyceryl tristearate)) ($C_{57}H_{110}O_6$) and accelerators, thiazoles, benzothiazyl disulfite (MBTS), curing speeds moderate, thiurams, tetramethylthiuram disulfide (TMTD), curing speeds fast and sulfur (S), cross-linking agent, all were standard commercial grade materials. [1]

Quaternary ammonium salt

Hexadecyl trimethyl ammonium chloride (HDTMA-Cl), commercial grade.

Organoclay preparation

The clay mineral that haves the calcium (Ca^{2+}) as the predominant cation in the interlayer spaces will not swell in water. To make the organophilic mineral clay two steps are needed; the first necessary step is to add sodium into the clay where the amount of sodium silicate (Na_2SiO_3) is calculated, and where the exchange of calcium for sodium is performed. In the second step the exchangeable cation Na^+ present in the galleries, are replaced by an organic cation of quaternary ammonium salts, cationic surfactants, which is the hexadecyl trimethylammonium chloride (HDTMA-Cl). [3]

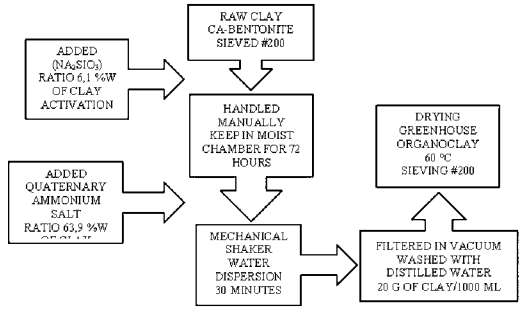

Figure 2. Block diagram organoclay production

NR nanocomposites preparation

The zinc oxide reacts with stearin forming the zinc stearate, which combined with other accelerators and the sulfur speeds up the vulcanization process.
Raw gum elastomer is placed into the gap between the two mill rolls, the mill nip at room temperature. It then bands, as a continuous sheet, onto one of the rolls. The speeds of the two rolls are often different, the back roll rotating faster than the front. The difference in speed between the two rolls is called the friction ratio and allows a shearing action (friction) at the nip to disperse the ingredients and to force the compound to stay on one roll, preferably the front one. A friction ratio of 1.25:l is common. The vulcanization ingredients were added, first stearin and after their incorporation into the gum mass, the zinc oxide except the sulfur were to the elastomer before the incorporation of the clay. Ten phr of organoclay were added to the rubber, to the nip in a specific way. The process produces friction which creates heat. The compounding formulations used for study are given in Table 1. After mixing, the compound was homogenized by passing several times through the tight nip of the mill and finally sheeted out. Optimum cure time was determined using an oscillating disc rheometer (TEAMETRO). The compounds were vulcanized at a temperature of 170±2 °C and at a pressure of 20 MPa in an electrically heated hydraulic press, to their respective cure times. [4]

Table I. Formulation of the rubber compounds

Ingredients	Mix 1	Mix 2
	Phr	
Natural rubber	100	100
Organoclay	10	-
ZnO	5	5
Stearin	1	1
MBTS	1	1
TMTD	0,5	0,5
Sulfur	1	1

parts per hundred parts of rubber (phr)

Measurement of Mechanical Properties

Tensile tests were performed on dumbbell shaped specimens, they were mechanically cut from the vulcanized sheets (vulcanized slabs). The measurements were carried out at a crosshead speed of 500 mm per min on a MAQTEST Model Universal Testing Machine according to ASTM standards, D 412.

Results and discussion

Scanning electron microscopy

The homogeneity of the particles dispersion was investigated by SEM, Figure 3. As seen in Figure 3a and 3b, organophilic clays with a more open structure, with greater separation of the sheets as compared with the raw clay. For the others 3c and 3d much finer particles appear, although a presence of larges pieces is also visible, hence it has to be concluded that besides good dispersion forming small particles close to nanosize, the mixing conditions do not allow for exfoliation of all filler particles. [5]

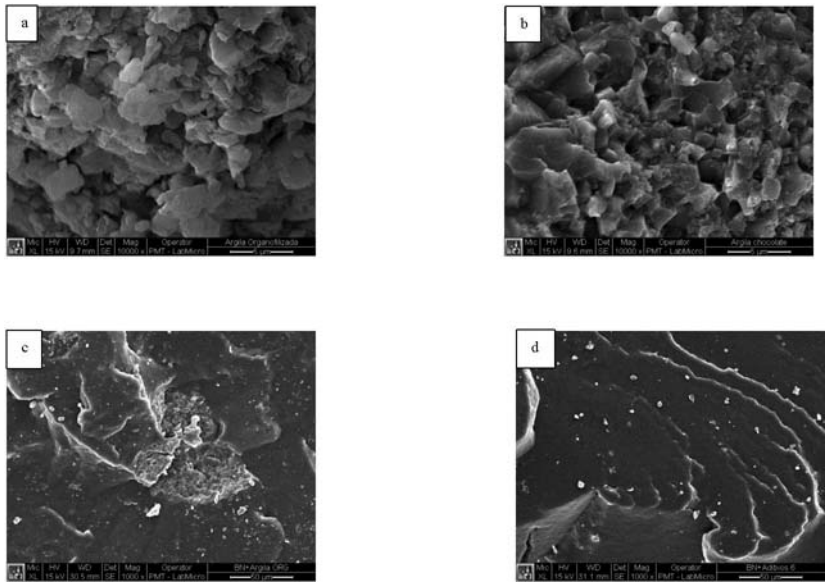

Figure 3: SEM micrographs organoclay (a), unmodified clay (b), natural rubber composites with 10 per of organoclay fillers (c), vulcanized rubber without fillers. (d)

Mechanical properties

The mechanical properties of the unfiled NR vulcanized and NR-organoclay vulcanized are given in Table 2. The tensile properties measured are the modulus at different strains (100, 200

and 300% elongation), the tensile strength and elongation at break. A marked increase in mechanical properties is observed for the NR-organoclay vulcanized than the unfiled NR vulcanized. The mechanical properties increase in NR-organoclay vulcanized, a 42% increase in tensile strength is obtained Figure 4.

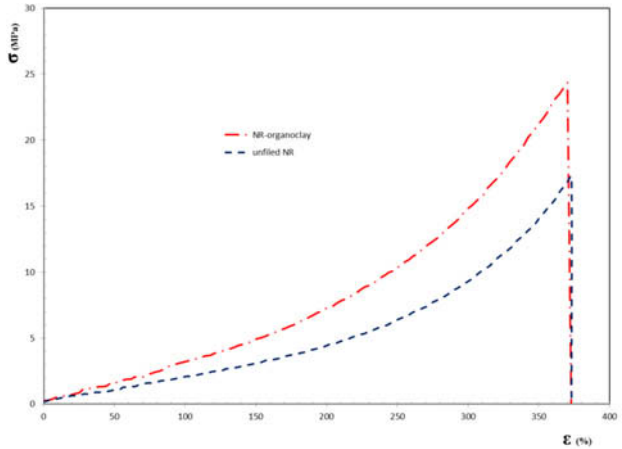

Figure 4: Examples of engineering stress–strain diagrams (σ–ε diagrams)

Table 2. Mechanical properties

Parameter	Unfiled NR	NR-organoclay
Maximum strength (MPa)	17,23	24,37
Elongation at break (%)	373,10	370,19
Modulus, 100% (MPa)	2,09	3,19
Modulus, 200% (MPa)	2,21	3,63
Modulus, 300% (MPa)	3,10	4,94

Thermal characterization

The thermal decomposition expressed in terms of weight loss as a function of temperature for unmodified clay, Na rich clay and organoclay is graphically shown in Figure. 5. The weight loss of the unmodified clay and Na rich clay is 13 and 9%, respectively, which corresponds to the surface and interlayer adsorbed water, as well as the water resulting from the structural OH groups of the clay. However, the decomposition of the organoclay starts to 120 °C since the absorbed water has disappeared due to the organophilic character of the modified clay and the total weight loss is about 27%

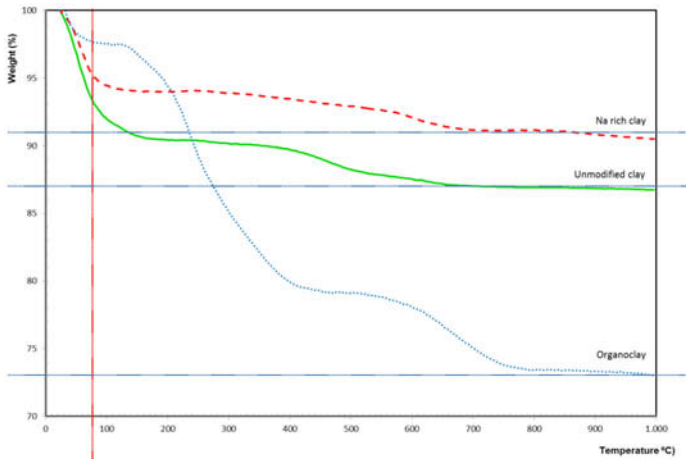

Figure 5: TGA curves for unmodified clay (solid line), Na-rich clay (dashed line) and organoclay (dotted line)

X-ray diffraction analysis

The interlayer spacing of the natural clay was 14.50 Å. With the addition of Na_2SiO_3 the interplanar space increase to 15.11 Å, and after the addition of the ammonium salt this space increase to 20.0 Å. That value indicates the effective intercalation of the ammonium salt between the clay mineral layers Figure 6.

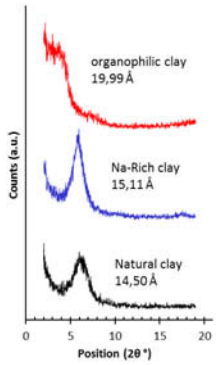

Figure 6: XRD patterns of natural clay, Na-rich clay and organophilic clay.

Infrared spectroscopy

The FTIR spectra Figure. 7 show information on chemical composition of the filler; presence of organic cations in clays is demonstrated in the C-H stretching and bending bands in the 2800-3000 and 1400-1500 cm^{-1} region, respectively, the infrared spectrum of the peak which correspond the interlayer water deformation is 1600-1700 cm^{-1} vibration. The band at the peak 1400-1500 cm^{-1} is assigned to the ammonium salt.

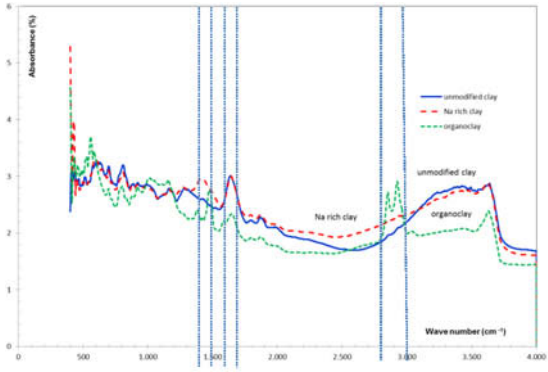

Figure 7. FTIR spectroscopy of unmodified clay, Na rich clay and organoclay.

Conclusions

Small amounts of organoclay resulted in significant positive changes in the mechanical properties of composites with vulcanized NR matrix. As the interlayer distances increases of fillers, polymers chains could penetrate more easily into the clay layers, which results in a formation of an intercalated structure. The nanocomposites obtained showed improvement in their mechanical properties in comparison with samples without clay.

References

[1] Kingery, W.D.; Bowen, Harvey Kent; Uhlmann, Donald Robert;, Introduction to ceramics, John Wiley & Sons, 1976.

[2] M. Galimberti., Ed., *Rubber-Clay Nanocomposites: Science, Technology, and Applications, First Edition.,* John Wiley & Sons, Inc., 2011.

[3] M. M. Rippel e F. d. C. Bragança, "Natural rubber and nanocomposites with clay," vol. 32, n. 3, pp. 818-826, 2009.

[4] A. R. M. F. R. V. D. L. B. de Paiva, "Organophilic clays: characteristics, preparation methods, intercalation compounds and characterization techniques," *Ceramica,* n. 54, pp. 213-226, 2008.

[5] A. Jacob, P. Kurian e A. S. Apren, "Cure Characteristics and Mechanical Properties of Natural Rubber-Layered Clay Nanocomposites," *International Journal of Polmeric Materials,* pp. 593-604, 2007.

Characterization of Minerals, Metals, and Materials 2015
Edited by: John S. Carpenter, Chenguang Bai, Juan Pablo Escobedo, Jiann-Yang Hwang, Shadia Ikhmayies, Bowen Li, Jian Li, Sergio Neves Monteiro, Zhiwei Peng, and Mingming Zhang
TMS (The Minerals, Metals & Materials Society), 2015

TENSILE PROPERTIES OF EPOXY COMPOSITES REINFORCED WITH CONTINUOUS PALF FIBERS

Gabriel O. Glória [1], Giulio R. Altoé[1], Ygor M. Moraes[1], Rômulo L. Loyola[1], Frederico M. Margem [1], Sergio N. Monteiro[2],

1 State University of the Northern Rio de Janeiro, UENF, LAMAV; Av. Alberto Lamego, 2000, 28013-602, Campos dos Goytacazes, Brazil.
2 Instituto Militar de Engenharia , IME, Praça Gen. Tibúrcio, nº80 Urca, Rio de Janeiro - RJ, 22290-270

Keywords: PALF fiber, Epoxy composite, Tensile properties.

Abstract

The tensile properties of DGEBA/TETA epoxy matrix composites reinforced with different amounts of PALF fibers were evaluated. Composites reinforced with up to 30% in volume of long, continuous and aligned PALF fibers were tested in an Instron machine at room temperature. The fracture was analyzed by SEM. This one revealed a weak fiber/matrix interface, which could be responsible for the performance of some properties. The results showed significant changes in the mechanical properties with the amount of PALF fibers.

Introduction

New materials are been developed to neutralize or at least minimize the environmental impacts caused from industrial activities. In this tendency, cellulose-based natural fibers, known as lignocellulosic fibers, become a promising solution. Some lignocellulosic fibers present specific properties that are comparable with synthetic ones used for polymer composite reinforcement. For instance, the specific strength (GPa.cm^3/g) of curauá (1.31), sisal (0.92) and ramie (0.93) fibers, for very thin diameters [1], are relatively closer to that of glass fiber E (1.33). The application of these natural fibers is also motivated by advantages like good toughness and less wear of equipment used in the processing of composites. Nowadays, they are being considered as a substitute for synthetic fibers, used by the industry on a large scale [2-6]. In addition, such composites are environmentally friendly because they are renewable, biodegradable and neutral with respect to CO_2 emissions, the main responsible for global warming and climate changes [4,6,7].

Lignocellulosic fibers also have some disadvantages in relation to synthetic fibers such as the difficulty of coupling with polymer matrices, due to the hydrophilic character of fiber and the hydrophobic nature of the matrix, as well as dimensional heterogeneity [5,6]. This is the nature of this material and constitutes an obstacle to the use of these fibers in certain projects, especially those that aim high performance. These advantages are the prime reasons for limited strength, as indicated by the rule of mixtures for composites [8].

Previous works [9,10] demonstrate that the incorporation of lignocellulosic fibers in polymeric matrices gives rise to composites with mechanical resistance directly proportional of the fiber content, where these fibers act as reinforcement for matrix due to their high mechanical properties.

Therefore, the objective of this study was to evaluate the tensile properties of epoxy matrix composites reinforced with continuous and aligned PALF fibers.

Experimental Procedure

100 PALF fibers shown in fig. 1 are randomly selected from the bundle, the equivalent diameter corresponding to the average between the larger and smaller (90° rotation) cross section dimensions at five locations for each fiber, was measured in a profile projector Nikon 6C.

Figure 2 presents histogram corresponding to the distribution of diameter of the as-received PALF fibers. The equivalent diameter of each fiber was actually the average value obtained by 10 different measurements performed in a profile projector at five distinct locations (two with 90° rotation at each location).

Figure 1. A small bundle of PALF fibers

The histogram in Fig. 2 reveals a relatively large variation in the diameter, which is a consequence of the non-uniform physical characteristics of a lignocellulosic fiber [2,3,11-13]. It should be noiced that the diameter range was 0.10-0.28 mm with an average of 0.20 mm.

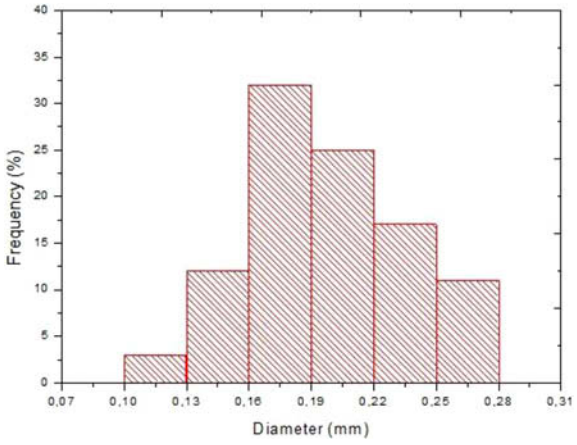

Figure 2. Histogram for the distribution of diameter of the as-received PALF fibers.

In order to produce composites with properties that are acceptable for industrial applications, the PALF fibers were selected randomly to serve as reinforcement to an epoxy matrix. These fibers, with diameter varying from 0.10 to 0.28 mm, were laid down inside silicone dog bone-shaped molds with distinct volume fractions up to 30 %. The fibers were continuously aligned along the 35 mm length of the mold, coinciding with the tensile axis. The still fluid epoxy resin mixed with TETA (trietylene tetramine) as hardener was poured onto the fibers. The already processed composites were allowed to undergo an initial cure at room temperature for 24 hours.

Each specimen was tested at 25 ± 2°C in a model 5582 Instron machine at a strain rate of 3 x 10-3 s-1. Samples cut from the fracture tip of representative specimens were coated with gold prior to microscopy work using a Shimadzu SSX-550 scanning electron microscope.

Results and Discussion

Typical load versus elongation curve obtained for each specimen with the respective volume fraction of PALF fibers are shown in Fig. 3. These curves were directly recorded from the Instron machine data acquisition system. The common aspect of all curves is that they present practically only elastic behavior up to fracture. The initial curvature is a consequence of specimen's adjustment to the tensile grips until the linear elastic begins. The abrupt end of this linear stage indicates that the PALF fiber reinforced epoxy composites behave as brittle materials.

Tab. 1 shows the values for the tensile strength, elastic modulus and total tensile strain for the different composites investigated. The total tensile strain initially increases but apparently decreases from 10% to 20% of PALF fibers, but regrows from 20% to 30% of PALF fibers.

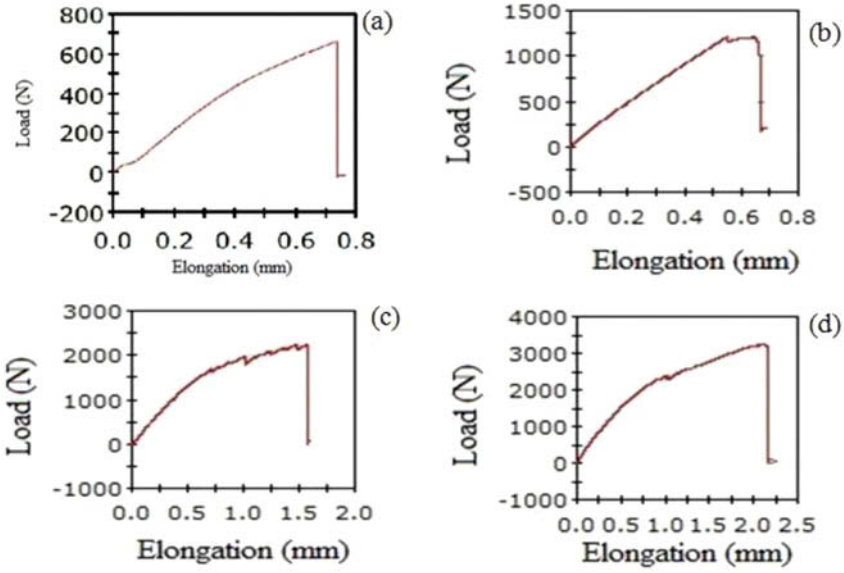

Figure 3. Typical load vs. elongation tensile curves: (a) 0%, (b) 10%, (c) 20% and (d) 30 of volume fraction of PALF reinforcing epoxy composites.

Table 1. Tensile properties for the PALF reinforced epoxy composites.

Volume fraction of PALF fiber (%)	*Tensile Strength (MPa)*	*Elastic Modulus (GPa)*	*Total Deformation (%)*
0	28.99 ± 6.58	0.83 ± 0.23	3.66
10	53.68 ± 10.88	1.31 ± 0.59	5.44
20	85.54 ± 10.62	1.71 ± 0.26	5.17
30	119.84 ± 10.59	1.83 ± 0.31	6.95

Based on the results in Table 1, Fig. 4 presents the curves of tensile strength (a) and elastic modulus (b) variation with the volume fraction of PALF fibers. In these curves, one may verify a significant increase in both the tensile strength and in the elastic modulus with the amount of PALF.

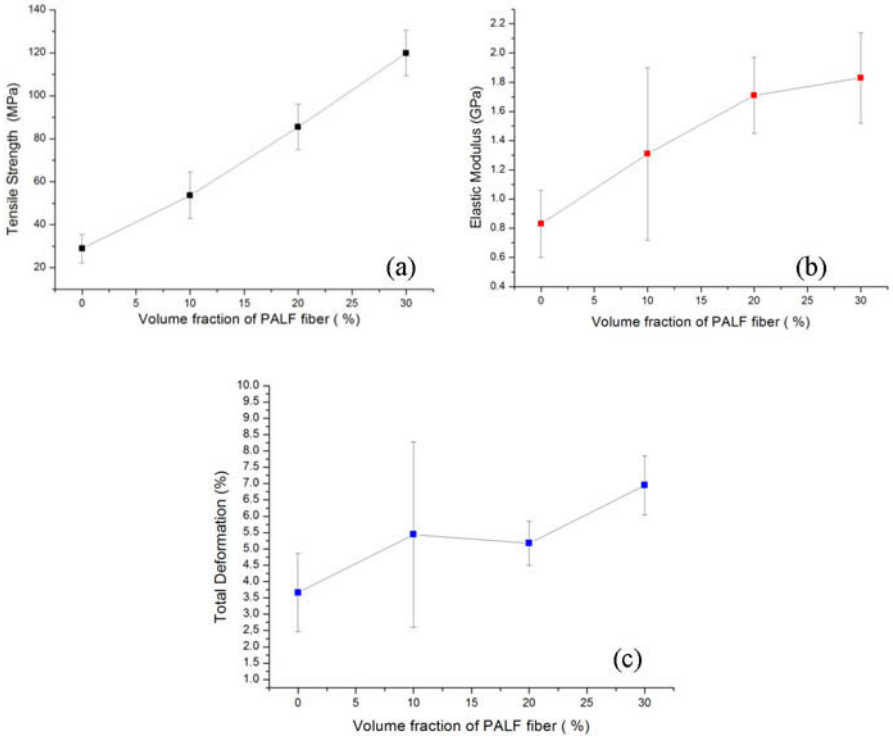

Figure 4. Variation of the tensile strength (a), elastic modulus (b) and the total deformation (c) with the volume fraction of PALF reinforcing epoxy composites.

As shown in Fig. 4(b), the incorporation of PALF fibers significantly increases the elastic modulus, but it appears to maintain constant with fiber incorporation above 20%, with a value around 1.8 GPa. It is also possible to verify that the incorporation of PALF fibers increase the maximum elongation of the composites when compared with neat epoxy. This can be associated with the flexible behavior of the fibers, which is able to elongate more than the neat epoxy matrix. Therefore,

their incorporation tends to increase the elongation capacity of the material, but do not show a big difference between the amount of fibers.
The fracture surface was examined in the SEM. Figure 5 shows typical SEM fractographs of a 30% volume fraction of PALF fiber reinforced epoxy composite. With lower magnification, Fig 5(a), the fracture surface display evidence of broken fibers sticking out of the epoxy matrix. Apparently, these fibers are well adhered to the matrix, which justifies the significant improvement on the composites strength and stiffness with increasing amount of fibers up to 30%, as shown in Fig. 4.

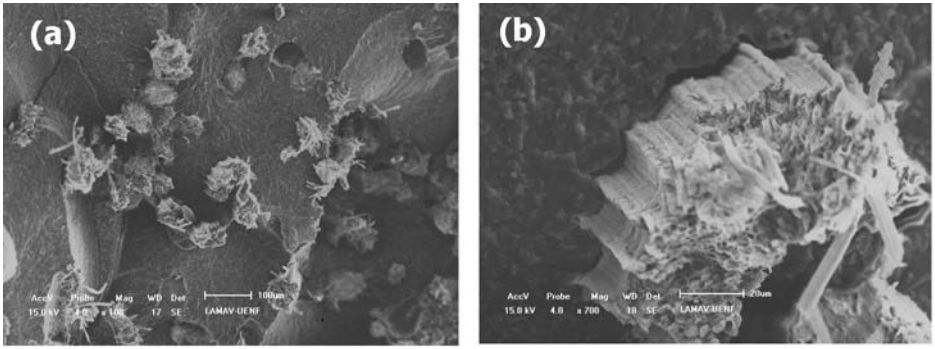

Figure 5. Microstructure of composite with 30% vol. of fibers: (a) 100X and (b) 700X.

However, a few holes in the surface of Fig 5(a) could also indicate a low fiber/matrix interfacial resistance, as indeed happens in lignocellulosic fibers reinforcing epoxy matrices [2,3,11-13]. In this respect, Fig 5(b) with higher magnification shows a crack alongside a PALF fiber beginning to detach it from the epoxy matrix. Therefore, although PALF fiber could improve the strength of epoxy composites, the weak adhesion between the fiber and the composite matrix is still an important limitation to further increase in the mechanical strength and stiffness. This weak adhesion is probably responsible for the fiber debonding from the matrix, which causes the longitudinal rupture and relatively lower stiffness at 30% of volume fraction (Fig. 5(b)).

Conclusions

- Selected PALF fibers significantly improve the strength of epoxy matrix composites. This improvement corresponds basically to a linear increase up to 30% in volume of fiber.
- The elastic modulus of the epoxy composites is also increased with the volume fraction of PALF fibers and the total deformation also is improved but only when compared with the pure epoxy, different amounts of fiber do not show significant variation.
- SEM analysis indicates that the PALF fibers act as effective reinforcement for the brittle epoxy matrix despite the weak fiber/matrix interface. In fact, the same fibers are well adhered to the epoxy matrix but evidence of fiber pullout from the matrix indicates a relatively low interfacial shear stress. This is an important limitation for further composite improvement.

References

1. WAMBUA, P.; IVENS, I.; VERPOEST, I. Natural fibers: can they replace glass and fiber reinforced plastics? Composites Science and Technology, 63 (2003) 1259-1264.
2. BLEDZKI, A.K.; GASSAN, J. Composites reinforced with cellulose-based fibres. Program Polymer Science, v. 24, p. 221-274, 1999.
3. NABI SAHED, D.; JOG J.P. Natural fiber polymer composites: a review, Advances in Polymer Technology, v.18, p. 221-274, 1999.
4. MOHANTY, A.K.; MISRA, M.; HINRICHSEN, G. Biofibres, biodegradable polymers and biocomposites: An overview. Macromolecular Matererials and Engineering, v. 276, p.1-24, 2000.
5. CROCKER, J. Natural materials innovative natural composites. Materials technology, v.2-3, n. 3, p. 174-178, 2008.
6. MONTEIRO S.N.; LOPES, F.P.D.; FERREIRA, A.S.; NASCIMENTO, D.C.O. Natural fiber polymer matrix composites: cheaper, tougher and environmentally friendly. JOM, v.61, n. 1, p. 17-22, 2009.
7. GORE, A. An Inconvenient Truth. The Planetary Emergency of Global Warming and What We Can Do About It. Emmaus, Pennsylvania, USA: Rodale Press, 2006.
8. CALLISTER Jr., W.D. Materials Science and Engineering – An Introduction, 5a Edição, Nova York : John Wiley & Sons, 2000.
9. ROHEN, L.A.; MARGEM, F.M.; MONTEIRO, S. N.; NEVES, A.C.C. Tensile strength of epoxy composites reinforced with thinner sisal fibers
10. SIMONASI, N.; MARGEM, F.M.; MONTEIRO, S. N.; LOIOLA, R.L. Tensile test of high strength thinner curaua fiber reinforced polyester matrix composites
11. S.J. Eichhorn, C.A. Baillie, N. Zafeiropoulos, L.Y. Mwakambo, M.P. Ansell, A. Dufresne, "Review of current international research into cellulosic fibres and composites", *J. Mater. Science*, 36 (2001) 2107-2113.
12. A.K. Mohanty, M. Misra and L.T. Drzal, "Sustainable biocomposites from renewable resources: opportunities and challenges in the green material world", *J. Polym. Environ.*, 10 (2002), 19-26.
13. K.G. Satyanarayana, J.L. Guimarães, F. Wypych, "Studies on lignocellulosic fibers of Brazil. Part I: Source, production, morphology, properties and applications". *Composites: Part A*, 38, (2007) 1694-1709.

Characterization of Minerals, Metals, and Materials 2015
Edited by: John S. Carpenter, Chenguang Bai, Juan Pablo Escobedo, Jiann-Yang Hwang, Shadia Ikhmayies, Bowen Li, Jian Li, Sergio Neves Monteiro, Zhiwei Peng, and Mingming Zhang
TMS (The Minerals, Metals & Materials Society), 2015

REPLACEMENT OF CARBON BLACK ON NATURAL RUBBER COMPOSITES AND NANOCOMPOSITES – PART 1

Guillermo R. Martín-Cortés[1]; Fabio J. Esper[2]; Antonio J. Santana de Araujo[2], Wildor T. Hennies[1], Maria G. Silva Valenzuela[1], Francisco R. Valenzuela-Díaz[2]

[1]Mining & Petroleum Eng. Dept. – Polytechnic School – University of São Paulo Av. Prof. Mello Moraes, 2373 Cid. Universitária 05508-900 São Paulo, SP, Brazil.
[2]Raw Materials & Non-metallic Solids Laboratory – Metallurgic & Materials Eng. Dept. – Polytechnic School - University of São Paulo. Av. Prof. Mello Moraes, 2463 Cid. Universitária 05508-900 São Paulo, SP, Brazil.

ABSTRACT
Seeking to replace carbon-black as filler of rubber in the production of vulcanized goods, researchers from University of São Paulo have studied different materials types as minerals, vegetal or wastes agricultural and industry. Results of rubber composites filled with MA1 a waste of mineral treatment provided by Esper Industries are presented. MA1 was characterized through X-ray diffraction; Thermal analysis; Scanning Electronic Microscopy; and others laboratory methods. The composite and shaped masses were evaluated by these methods plus their mechanical properties such as tensile strength, elongation at break and hardness. Exceptional results were obtained in the mechanical properties evaluated, better than those obtained with the traditional carbon-black. Seeing the kind of material used as filler, it can conclude that the environmental benefit is present, as well as economic development, giving credibility to the use of these alternative material in replacement carbon-black.

Keywords: Composites and nanocomposites, fillers for rubber vulcanized products, waste of mineral treatments.

Introduction

Rubber vulcanized products have among others substances carbon-black as main active filler. Carbon black is the traditional reinforcer filler, of rubber vulcanized products because its properties concerning: Nano metric grain size, color, good interaction with polymers, transfer properties such as tensile strength, hardness, abrasion resistance, compression strength in addition to not affecting the resilience. Carbon black show nanometric grain sized distribution and a depth black color, because these properties it is also used for computer printers inks production. The carbon black is substance derived from the oil gotten during the final phases of the mineral fuel treatment with consequent pollution of the environment. [1]
Using carbon-black rubbers are black or a very dark color. But they can have different appearance when filler of distinct composition of the carbon black is used. Substitution of carbon-black as a reinforced load in the rubber production, will have to contribute in such a way to diminish the dependence of these products as to diminish the pollution of the environment. [2]
This paper in its title presents the indication to be the Part 1 of an extensive research that used different formulations based on different materials coming from different sources. Among these sources there are discarded minerals from purification treatment of non-metallic minerals or substances discarded during industrial production processes between others. This paper the results of the use of MA1, another kind of nanoparticulate material formula

substituting carbon black in the production of some rubber products. [3]

Materials

- MA1 – Nanoparticulate material provided by Esper Rubber Industries Ltda. and used as is.

- Commonly additives for the process of vulcanization the nanocomposite material rubber + MA1 was treated applying the formularizations traditionally used by the company ESPER Ltd. There are: Native sulphur (S), Zinc Oxide; Stearic Acid and the Accelerators for rubber: TMTD; MBTS; MBT by its commercial names. [4]

- Natural Rubber. It was used natural rubber (known technically as polyisoprene) of the same type as traditionally used by Esper Rubber Industries Ltda. and provided by Hevea Tech. Ltda. It was obtained from the Hevea Brasiliensis tree. [5]

Methods

As on the production of vulcanized goods, carbon-black fill the rubber at least in 40 phr (parts of filler by hundred parts of rubber), then, MA1 was used

Before development of the nanocomposite there were characterized the MA1 and the rubber materials under the following test: DRX – X-Ray Diffraction Powder Test, SEM – Scanning Electronic Microscope.

Nanocomposite vulcanized plates had been fabricated according to process traditionally used by the ESPER Ltd. Company and on the basis of the established one in standard ASTM D 3182 adjusted to the carpet production for cars and synthetic floors between others rubber vulcanized goods. [5]

Results

XRD – X-Ray diffraction assays.

In order to show the whole characterization, below are presented the results by type of test performed. First, on Fig.1 the natural rubber XRD, after that the Carbon black XRD on fig. 2 and the MA1 XRD on fig. 3.

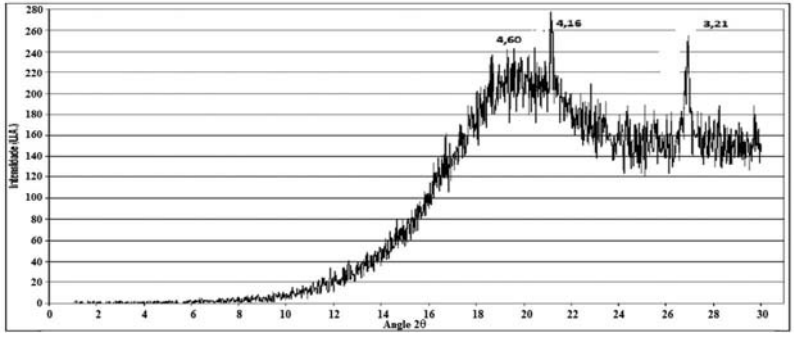

Figure 1 XRD of natural rubber. Peak values in Angstrom. [5]

On figure 1 it is observed a sharp peak at 4.60 Å characteristic of natural rubber and two sharp peaks at 4.2 Å and 3.2 Å that must match the additives contained in the plate. [5]. On

figure 2 is observed for the carbon black peaks at 3.5 Å and other at 2.1 Å that will be followed in the next assays. Peaks on 7,69 Å, 4,25 Å, 3,25 Å and 3,38 Å are observed at figure 3 from the XRD assay of the MA1 alternative additive.

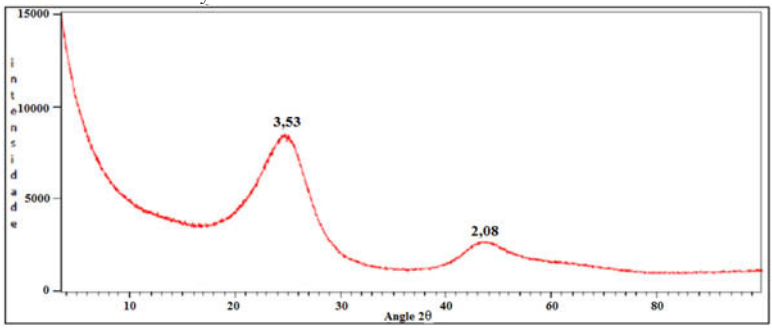

Figure 2 XRD of Carbon-black. Peak values in Angstrom. [5]

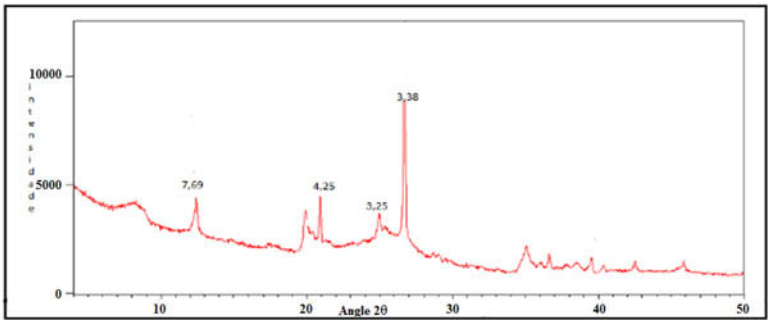

Figure 3 XRD of MA1 alternative filler. Peak values in Angstrom. [5]

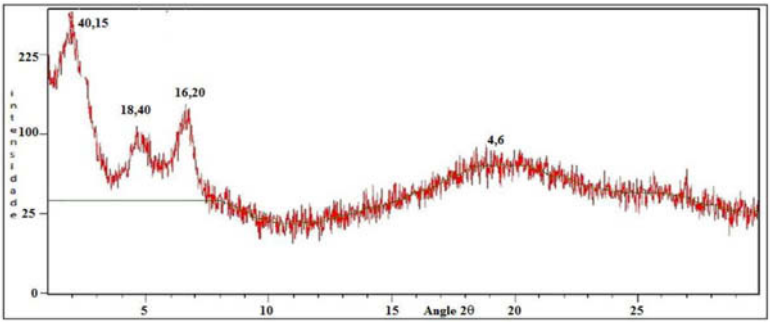

Figure 4 XRD of the vulcanized plate of rubber with 40 phr of carbon black. Peak values in Angstrom. [5]

The peaks at 3.5 Å and 2.1 Å of figure 2; are not observed in figure 4, the XRD of the plate, which highlights the homogenization of load on the plate mass. Appear three peaks at 40.1 Å, 18.4 Å and 16.2 Å (Figure 4). They should match the black smoke and indistinguishable in the figure for not being in the range of measurement equipment and the other by the same low

intensity compared with the intensity of the peaks of Fig. 4th.
Most peaks of MA1 (Fig. 5) were absorbed by the structure of the rubber showing good assimilation of alternative filler by the rubber.

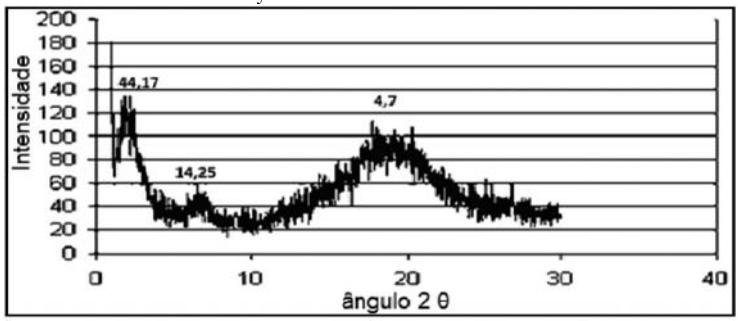

Figure 5 XRD of vulcanized nanocomposite plate of rubber containing 40 phr of MA1 alternative filler. Peak values in Angstrom. [5]

THERMAL ANALYSIS

On Fig. 6 is the thermal analysis curves of natural rubber plate. Observed an beginning of weight loss at 180 °C and the start of significantly higher weight loss at approximately 320 °C. The sample showed a total loss of 95.64% of its initial mass.
In FIG. 7 is visualized the thermal analysis curves of the plate prepared with 40 phr of carbon black. The observed beginning of weight loss at 180 °C and the start of significantly increased weight loss at about 280 ° C. The sample showed a total loss of mass of about 90%.

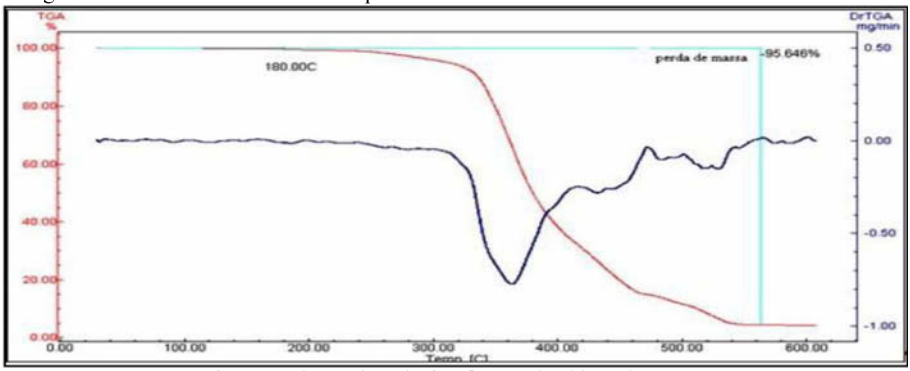

Figure 6 Thermal analysis of natural rubber plate. [5]

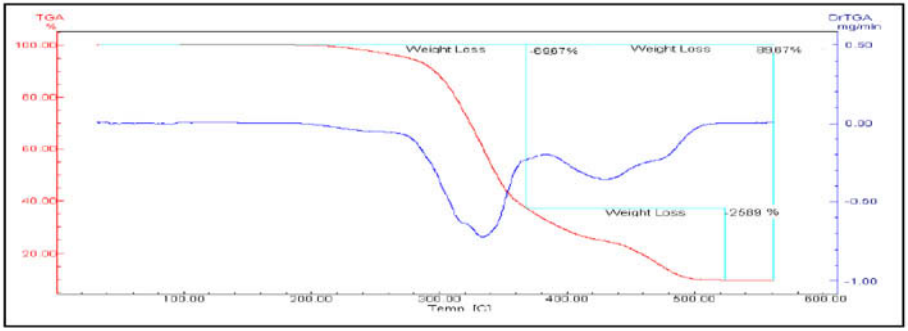

Figure 7 Thermal analysis of rubber + 40 phr of carbon-black plate.[5]

In Fig 8. Is the thermal analysis curves of the plates with 40 phr of MA1. Observed a beginning of weight loss at approximately 240 °C and the start of significantly higher weight loss at approximately 320 ° C. The sample showed a total loss of 80.0% of its initial mass.

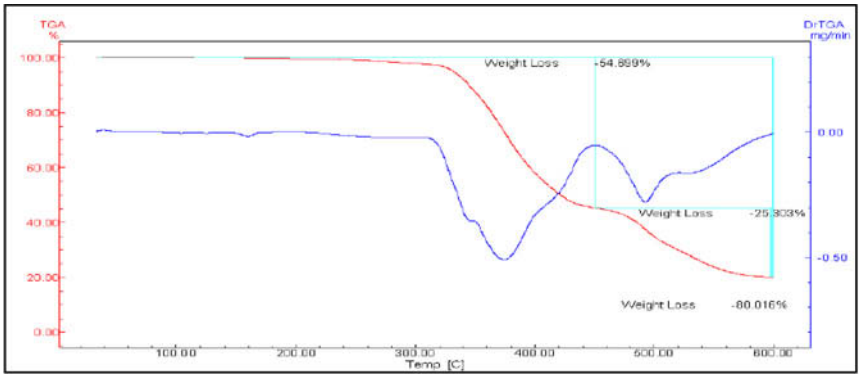

Figure 8. Thermal Analysis of rubber + MA1 plate. [5]

Table 1 Thermal analysis data [5]

MATERIAL	Weight loss start at ≈ ºC
Natural rubber	180
Carbon-black	180
MA1	240

MA1 shows start temperature of thermal degradation up to 17% of carbon black and natural rubber plates.

SPECTROSCOPY IN THE INFRARED REGION

Great similarity is showed at the infrared spectroscopy curves (Fig.9) of natural rubber plate without any filler (a); of the natural rubber + carbon-black plate (b), and with the MA1 alternative filler (c).

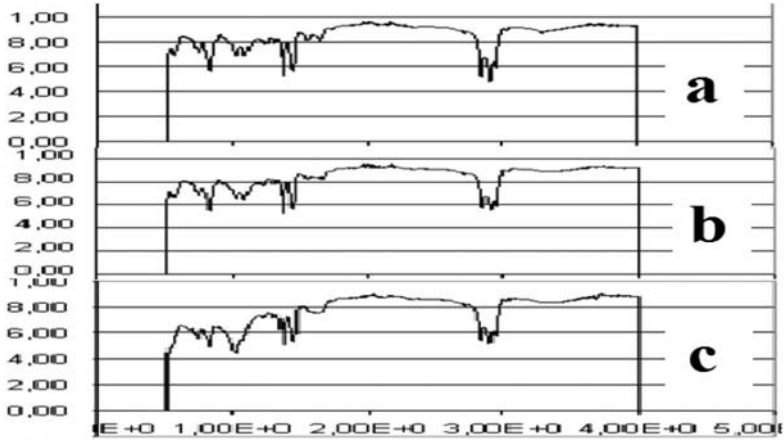

Figure 9. IR spectroscopy curves of pure natural rubber (a); natural rubber + carbon-black plate (b) and of natural rubber + MA1 plate (c). Transmittance axes (x 100%) and wavenumber (cm^{-1}) x 1000. [5]

As a summary of all graphs spectrometry in the infrared region can say that in general there is great similarity between the curves obtained for all samples, observing basically corresponding to natural rubber peaks. The same should apply the preponderance of the amount of natural rubber in the composite. The absorption bands of the links of carbon-black and MA1 and products are in very close links presented by natural rubber, making them imperceptible regions, only competing with them.

SCANNING ELECTRON MICROSCOPY

The micrograph of the plate of vulcanized natural rubber is shown in Figure 10. On figure 11 is showed the SEM micrograph of the rubber + carbon-black plate and finally on figure 12 is showed the SEM micrograph of the rubber + MA1 alternative filler.

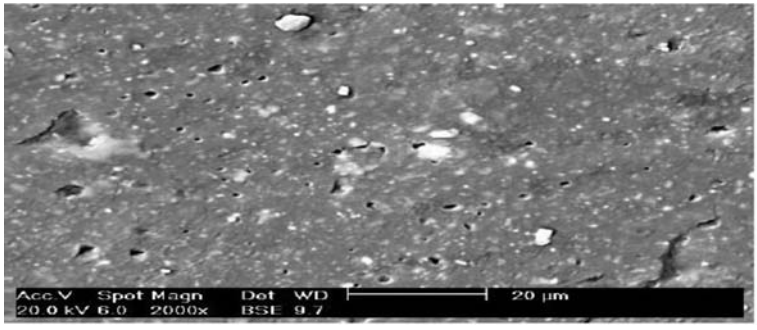

Figure 10 SEM micrograph of natural rubber. [5]

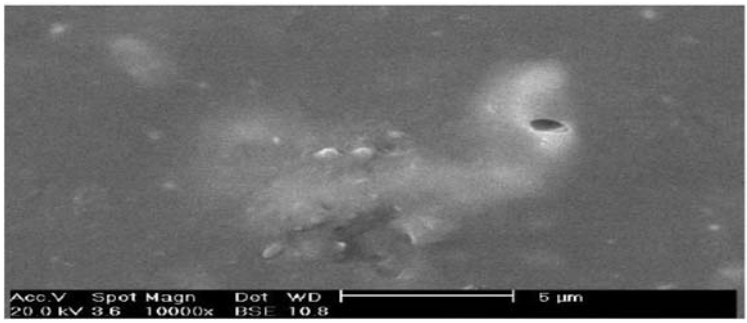

Figure 11 SEM micrograph of rubber + carbon-black plate. [5]

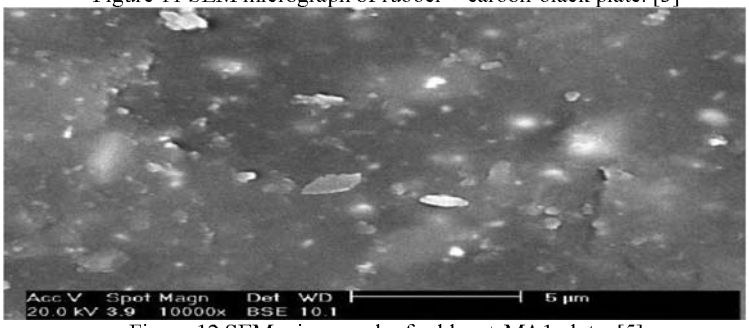

Figure 12 SEM micrograph of rubber + MA1 plate. [5]

RESULTS OF PHYSICAL ASSAYS

Table 2 below show the mechanical assays results seeking data on: rupture stress, elongation at break and hardness.

Table 2 Mechanical Assays Results. [5]

FORMULA	RUPTURE STRESS	ELONGATION AT BREAK	SHORE A HARDNESS
Natural rubber	4,2 MPa	675%	43
Natural rubber + carbon-black	11,2 MPa	315 (%)	52
Natural rubber + MA1 alternative filler	25,8 MPa	757%	58

CONCLUSIONS

- New nanocomposites and composite materials have been developed for the production of vulcanized plates showing the potential to replace the traditional carbon-black pollutioner filler by the MA1 non-conventional particulate fillers and to date no known economical use.
- Testing of thermal analyzes showed significant increases in temperatures beginning of thermal degradation of MA1 alternative filler with respect to charged plates with carbon-black meaning big gain over traditional materials.

- Tests of scanning electron microscopy were useful to verify the homogeneity of the charges in the polymer matrix.
- Plates were obtained with the alternative reinforcer MA1 with values of tensile strength significantly higher than those of corresponding plates loaded with carbon black, without prejudice to the values of elongation and hardness, presenting the best performances.
- This filler with costs, in principle, lower the carbon black is friendly to the environment and will minimize environmental impacts and liabilities.

The materials have a high potential for substitution, with advantages of carbon black composites and nanocomposites of natural rubber.

REFERENCES

1. Martín-Cortés, G. R., Esper, F. J., Dantas, L. S. G., Hennies, Wildor Theodoro, Valenzuela-Diaz, F. R. Discarded Ultrafine Particulate Carbonaceous Materials Used as Reinforcers of Rubber Vulcanized Products In: TMS 2012 - 141 ANNUAL MEETING & EXHIBITION, 2012, Orlando, USA. **TMS 2012 - 141 ANNUAL MEETING & EXHIBITION**. Warrendale, PA; USA: TMS - The Minerals, Metals & Materials Society, 2012.

2. Esper, F. J., Martín-Cortés, G. R., Dantas, L. S. G., Cutrim, A. A. S., Hennies, Wildor Theodoro, Valenzuela-Diaz, F. R. Properties of Additional Reinforcers Materials Used to Complement NAOB – A Rubber / Organoclay Nanocomposite Material In: TMS 2012 141 ANNUAL MEETING & EXHIBITION, 2012, Orlando, FL; USA. **TMS 2012 141 ANNUAL MEETING & EXHIBITION**. Warrendale, PA; USA: TMS - The Minerals, Metals & Materials Society, 2012.

3. Costa, M. V. V., Esper, F. J., Martín-Cortés, G. R., Valenzuela-Diaz, F. R., Hennies, W. T., Wiebeck, H. COMPÓSTOS DE BORRACHA PROVENIENTE DO DESCARTE DE LUVAS CIRÚRGICAS / CINZAS DE CASCA DE ARROZ In: 11 Congresso Brasileiro de Polímeros, 2011, Campos dõ Jordão. **11 Congresso Brasileiro de Polímeros** 2011.

4. Martín-Cortés, G. R., Wiebeck, H., Esper, F. J., Hennies, Wildor Theodoro, Valenzuela-Diaz, F. R. NANOCOMPOSITE RUBBER MATERIAL WITH INDUSTRIAL WASTE In: REWAS 2008—Global Symposium on Recycling, Waste Treatment and Clean Technology, 2008, Cancún. **REWAS 2008—Global Symposium on Recycling, Waste Treatment and Clean Technology**. Warrendale, PA: TMS - The Minerals, Metals & Materials Society, 2008. v.CD-ROM.

5. Esper, Fabio J. SUBSTITUIÇÃO DO NEGRO DE FUMO EM COMPÓSITOS E NANOCOMPÓSITOS DE BORRACHA NATURAL. Tese de Doutorado. Escola Politécnica da Universidade de São Paulo. 105p. 2010.

Characterization of Minerals, Metals, and Materials 2015
Edited by: John S. Carpenter, Chenguang Bai, Juan Pablo Escobedo, Jiann-Yang Hwang, Shadia Ikhmayies, Bowen Li, Jian Li, Sergio Neves Monteiro, Zhiwei Peng, and Mingming Zhang
TMS (The Minerals, Metals & Materials Society), 2015

FLEXURAL MECHANICAL CHARACTERIZATION OF EPOXY COMPOSITES REINFORCED WITH CONTINUOUS BANANA FIBERS

Foluke S. de Assis[1], Pedro A. Netto, Frederico M. Margem[1], Rômulo L. Loiola[1], Sergio N. Monteiro[2].

[1 1] State University of the Northern Rio de Janeiro, UENF, LAMAV; Av. Alberto Lamego, 2000, 28013-602, Campos dos Goytacazes, Brazil.
[2] Military Institute of Engineering, IME, Praça Gen. Tibúrcio, nº80 Urca, Rio de Janeiro - RJ, 22290-270

Abstract

Banana fibers are among the lignocellulosic with great potential for use in polymer composites, such as the variety from the *Musaceae* family, due to its low density and good mechanical properties. In this work, epoxy matrix composites incorporated with continuous and aligned banana fibers were tested for their flexural behavior. Specimens with up to 30% in volume of fibers were bend-tested until rupture. The results showed an increase in both the composite mechanical strength and the stiffness with incorporation of these fibers. A fractographic analysis by SEM examinations a moderate adhesion mechanism between the banana fiber and the epoxy matrix. This mechanism is apparently responsible for the improved performance of the composites.

Keywords: banana fiber, epoxy, flexural properties, fracture analyses.

Introduction

In recent years, the substitution of energy-intensive synthetic materials for natural ones is being considered in many industrial sectors including automobile, packing and textile [1]. A typical case is that of natural fibers, mainly those obtained from cellulose-based plants also known as lignocelluloses fibers. They have been investigated in the past two decades, aiming to replace synthetic fibers, particularly the glass fiber, commonly used as polymer composite reinforcement [2,3]. From the engineering point of view, lignocellulosic fibers present today important environmental, economical, societal and technological advantages already discussed [4,5,6]. The banana fiber, although strong and flexible [1] has not yet been applied in composites for automobile components. Actually, the fibers obtained from the pseudo-stem of the banana tree commonly is mainly used to fabricate ropes and baskets owing to its high strength .The mechanical properties of banana fiber composites are well known [9-10].Moreover, several lignocellulosic fibers are known since the beginning of our civilization and still cultivated or naturally extracted all over temperate and tropical regions of the world. According to Kalia et al [1], these fibers can be classified by their origin, as shown in Table 1.

Table 1: Classification of lignocelluloses fibers according to their origin [1].

ORIGIN	LIGNOCELLULOSIC FIBERS
leaf	abaca, cantala, curaua, date, palm, henequen, pineapple, sisal
seed	cotton
bast/stem	flax, hemp, jute, ramie
fruit	coir, kapok, palm oil
grass	alfalfa, sugarcane bagasse, bamboo
stalk	banana, straw

Experimental Procedure

The banana fibers investigated in this work were commercially supplied by a local producer. Figure 1 illustrates the typical banana plant, the died stem, some extracted plates and a bundle of fibers extracted from it.

Figure 1. Typical banana plant (a) the Pseudo stem with average diameter of 15-30 cm(b), the sun-dried for a week plates(c) and the group of fibers after the defibrillation(d).

Initially, one hundred fibers were randomly taken out from the bundle for a statistical evaluation of diameter as show in the histograms in figure 2. From the histogram an average diameter of 0.20 mm was obtained.

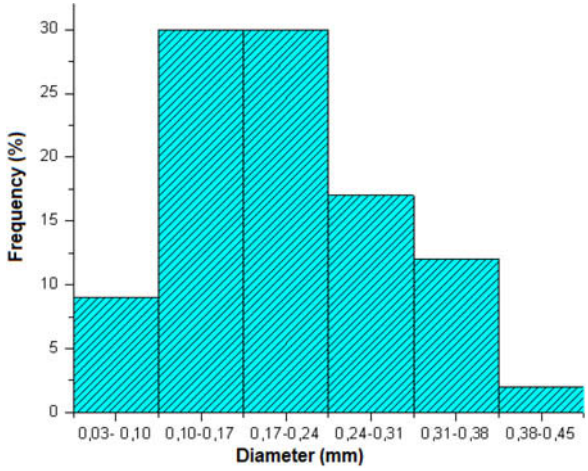

Figure 2. Statistical distribution of the banana fibers.

Composites with amounts of 0, 10, 20 and 30 % in volume of banana fibers were fabricated by mixing the proper percentage of fibers with a still fluid epoxy resin diglycidyl ether of bisphenol A (DGEBA) with triethylene tetramina (TETA) as hardener. Each specimen was set to cure at room temperature for 24 hours inside the mold before taking out for testing.

The mixture was set to cure at room temperature for 24 hours inside a 152 x 122 x 10mm rectangular mold under 0.53 MPa of pressure. The banana fibers were aligned along the 122mm width of the mold, which corresponds to the length of seven specimens cut from the composite plate, extracted from the mold after curing. These specimens, for each different amount of banana fibers were three points bend tested in a model 5582 Instron machine with 100 kN of capacity at a strain rate of 1.6×10^{-2} $s^{-1}$and a span-to-depth ratio of 9. Pure epoxy specimens and fractured composites were analyzed by scanning electron microscopy, SEM.

Results and Discussion

Typical flexural force *vs.* deflection curves directly obtained from the machine acquisition data program are shown in Figure 3. In this figure it should be noticed that not only the flexural curve for the pure epoxy (0% fiber) specimens but also for the banana fiber reinforced composite specimens display limited plastic deformation. Indeed, after the first linear elastic part of the curves in Figure 3, a sudden drop associated with the rupture occurs, which indicates a brittle behavior.

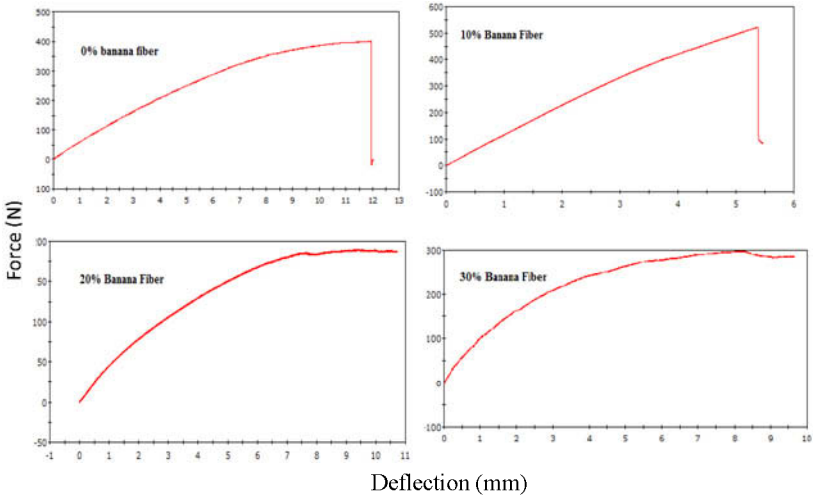

Figure 3. Typical force *vs.* deflection curves for flexural test of epoxy composites with 0,10, 20 and 30 % of volume fraction banana fibers.

From curves such as the ones shown in Figure 3, the flexural strength (maximum bend stress) was calculated. Table 2 presents these values for composites with different volume fraction of banana fibers.

Table 2: flexural results for the epoxy composites reinforced with banana fibers.

Volume Fraction of Fiber (%)	Flexural Strength (MPa)
0	56.2 ± 8.4
10	62.3 ± 7.6
20	67.5 ± 5.6
30	73.2 ± 7.2

From the results in Table 2, the variation curve flexural strength with the volume fraction of banana fibers are presented in Figure 4.

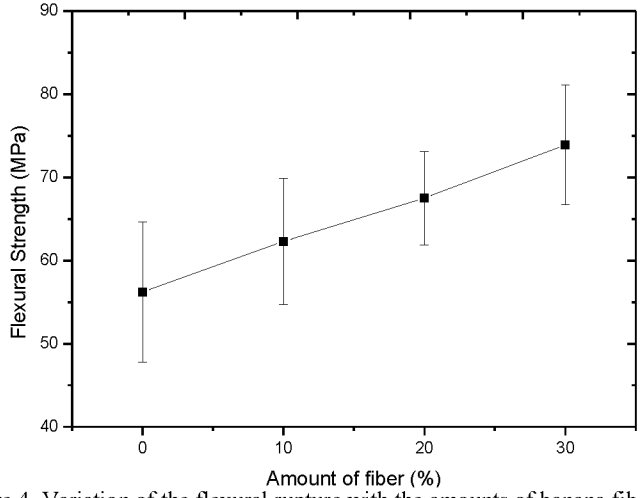

Figure 4. Variation of the flexural rupture with the amounts of banana fibers in the composites.

Figure 5 shows a SEM image of a typical rupture of 30% banana fiber composites. Low magnification image shown in Fig. 5(a) shows the transversally fractured epoxy with embedded fibers and voids corresponding to holes from where fibers have been pulled out [10].

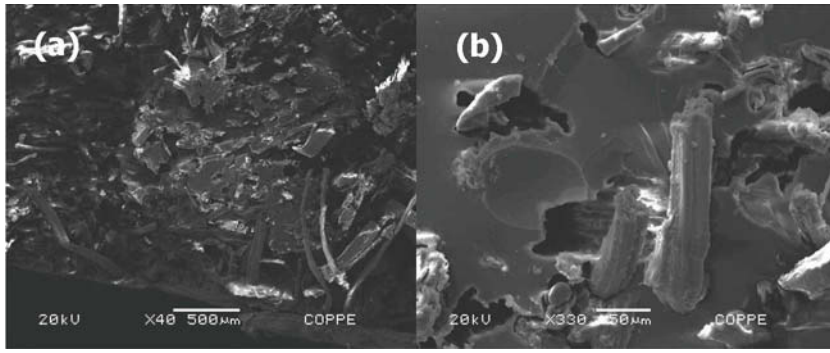

Figure 5. Fractograph of a 30% in volume of banana fiber composite; (a) general view and (b) detail of a fiber/matrix interface debonding.

With higher magnification, Fig. 5(b), it is revealed that the interface between the banana fiber and the epoxy matrix is not continuous. In fact, most of the interfaces present evidence of debonding in the form of a separation, Fig. 5(b), of the fiber surface from the epoxy matrix [10].

Finally, it is relevant to discuss the implication of this rupture mode to the mechanical response of the composites. The rupture that initiates inside the epoxy matrix and propagates transversally to the fibers alignment provides a longer path to the rupture what consume more energy to complete the material rupture that provides the increase in the flexural strength [11].

Conclusions

- Epoxy matrix composites reinforced with continuous and aligned banana fibers show an improvement in the strength as compared to the epoxy matrix.
- The flexural strength is increased for fiber incorporation above 10% of volume fraction owing to the effective participation of the fibers.
- The visual observation and SEM fractographs revealed that above 10%, transversal cracks are effectively arrested by the fibers. As a consequence, longitudinal propagation through the weak fiber/matrix interface causes delamination and results in an efficient contribution to the relatively stronger banana fiber to the final rupture of the composite, which then occurred at higher strength.

Acknowledgements

The authors thank the support to this investigation by the Brazilian agencies: CNPq, CAPES, FAPERJ and TECNORTE/FENORTE. It is also acknowledged the permission to the use of the SEM microscope by the PEMM from COPPE/UFRJ.

References

1- S. Kalia, B. S. Kaith, I. Kaur "Pretreatment of natural fibers and then application as reinforcing material in polymer composites – A review" *Polym. Eng. Sci.* 49(7) (2009) 1253-1272.

2- D. Nabi Sahed and J.P. Jog, "Natural fiber polymer composites: a review", *Advances in Polymer Technol.*, 18 (1999), 221-274.

3- A .K. Bledzki, and J. Gassan, "Composites Reinforced With Cellulose-Based Fibers". *Prog. Polym. Sci*, 4 (1999) 201-274.

4- A.K. Mohanty, M. Misra and G. Hinrichsen, " Biofibers, biodegradable polymers and biocomposites: an overview", *Macromolecular Mat. And Engineering*, 276/277 (2000), 1-24.

5- P. Wambua, I. Ivens and I.Verpoest, "Natural fibers: can they replace glass and fibre reinforced plastics?", *Composites Science and Technology*, 63 (2003) 1259-1264.

6- A. Netravali, S. Chabba, "Composites get greener", *Material Today* 6 (2003) 22-29.

7- K.G. Satyanarayana, J.L. Guimarães, F. Wypych, "Studies on lignocellulosic fibers of Brazil. Part I: Source, production, morphology, properties and applications". *Composites: Part A*, 38, (2007) 1694-1709.

8- S.N. Monteiro, F.P.D. Lopes, A.S. Ferreira and D.C.O. Nascimento, "Natural fiber polymer matrix composites: cheaper, tougher and environmentally friendly". *JOM*, 61(1) (2009) 17-22.

9- S. N. Monteiro, F. M. Margem, R. L. Loiola, F. S. Assis, M. P. Oliveira, Characterization of banana fibers functional groups by infrared spectroscopy, Materials Science Forum Vols. 775-776 (2014) pp 250-254 (2014) Trans Tech Publications, Switzerland doi:10.4028/www.scientific.net/MSF.775-776.250.

10- S. N. Monteiro, F. M. Margem, F. S. de Assis, R.L. Loiola, M. P, Oliveira, Izod impact tests in polyester matrix composites reinforced with banana fibers, Materials Science Forum Vols. 775-776 (2014) pp 261-265 (2014) Trans Tech Publications, Switzerland doi:10.4028/www.scientific.net/MSF.775-776.261.

11- W.D. Callister Jr., *Materials Science and Engineering – An Introduction*, 5 ed., (New York, NY: John Wiley & Sons, 2000).

Characterization of Minerals, Metals, and Materials 2015
Edited by: John S. Carpenter, Chenguang Bai, Juan Pablo Escobedo, Jiann-Yang Hwang, Shadia Ikhmayies, Bowen Li, Jian Li, Sergio Neves Monteiro, Zhiwei Peng, and Mingming Zhang
TMS (The Minerals, Metals & Materials Society), 2015

INFLUENCE OF THE NANOCLAY CLOISITE 20A INCORPORATION ON PROPERTIES OF ACRYLONITRILE BUTADIENE STYRENE (ABS)

Jorge N. Sales[1*], Andressa A. Silva[1*], Francisco R. Valenzuela-Diaz[2], Esperidiana A. B. Moura[1]

[1]Instituto de Pesquisas Energéticas e Nucleares – IPEN-CNEN/SP
Av. Prof. L. Prestes, 2242 São Paulo, SP, 05508-000, Brasil

[2]Universidade de São Paulo, Escola Politécnica,Dep. de Eng. Metalúrgica e de Materiais. Av. Prof. Mello de Moraes, 2463, São Paulo, SP, 05508-030 - Brasil

***jnsales@usp.br**

Keywords: ABS, Nanocomposite, Clay, Cloisite 20A

Abstract

This work aims to study the influence of the nanoclay Cloisite 20A incorporation on mechanical properties of ABS (acrylonitrile butadiene styrene). The incorporation of Cloisite 20A was made in two steps; firstly,a masterbatch was preparated and then, it was incorporated in ABS. The Cloisite 20A masterbatch using 40 % of nanoclay and 60 % of SAN (Styrene Acrylonitrile) was prepared in an adiabatic mill. After that, Cloisite 20A masterbarch at 1 and 5 % (wt) was added in ABS. The resulting nanocomposites were characterized by tensile tests and the correlation between properties was discussed.

Introduction

From the beginning of his existence man has been in contact with polymeric materials, in antiquity, with natural polymers, Romans and Egyptians used resin materials and lubricants for various applications, the exploration of the New World by the Spanish and Portuguese who had the first contact Havea with Brasislis base for exploration of the latex. From the macromolecule proposed by Hermann Staudinger in 1920 and the work of Wallace H Crothers, who in 1929 formalized the condensation reactions that gave rise to polyesters and polyamides, discoveries of new materials and new applications for polymers entered an accelerated pace growth [1].
The technological advances in various areas were accompanied by demand for materials with increasingly higher properties. In response to this demand, the composites [2] consist of two or more physically distinct materials or chemically, conveniently distributed and arranged in stages, with an interface separation characteristics and have emerged which can't be portrayed by any of the separate components.
Polymeric Nanocomposites are defined as a class of materials formed by hybrids of organic and inorganic materials, wherein the inorganic phase is dispersed in nanometer level in a polymer matrix. Polymeric Nanocomposites are defined as a class of polymeric materials modified with inorganic fillers which exhibit at least one of the dimensions in the nanometer, lower than 100 nm range. This group of materials is one of the latest advances in polymeric materials. These materials began to be studied in the 80s by the Research Laboratory of Toyota with the development of nanocomposites of polyamide and clay [3].

The Acrylonitrile-Butadiene-Styrene (ABS) was introduced in the North American market by the US Rubber Company, has since been continuously expanded to offer a good combination of tensile, impact, hardness and modulus of elasticity in a wide range of temperatures (-40 ° C to 150 ° C). Moreover, their pieces feature high gloss, dimensional stability and low density. These properties make it ideal for various applications such as electronic components, home appliances and automotive components [4].
The ABS resins are obtained by the copolymerization of acrylonitrile, butadiene and styrene by chemical or mechanical processes. The primary chemical process is initiated by the polymerization of butadiene, polybutadiene passing then added to the reactor are acrylonitrile and styrene. This process is also known as graft polymerization, as the resins thus conceived consist of a mixture of two phases by the addition of a rubber in a glass matrix. The main mechanical process for obtaining ABS bamburys is carried out in extruders or twin screw. The process basically consists in making the mixture of two monomers have polymerized SAN (styrene-acrylonitrile) with polybutadiene [5].
The ABS obtained by mechanical process causes a reduction in compatibility between the styrene-acrylonitrile butadiene phase and the matrix which tends to improve the impact resistance of the polymer.
The properties of ABS vary according to the proportion of monomers used, high concentrations of acrylonitrile contribute to an increase in heat and chemical resistance of the polymer, increasing the concentration of styrene contributes to gloss properties, stiffness and processability general conditions for so the concentration of butadiene results in a polymer having higher impact resistance and toughness at low temperatures [5].

The first uses of clays refer to the beginning of civilization at that time men used to help meet their needs for food, housing, clothing and aesthetics. The clays are part of almost all soil types and can also be found in the pure state in mineral deposits [6]. Clays are rocks consisting essentially of finely divided clay minerals, organic materials and other impurities naturally have lamellar or fibrous form due to the crystalline structure present in their argilomierais. [7].
The surface modification of clays is an area that has received much attention because it allows broaden the horizons of the application of clays, with its main focus directed to materials science, whose goal is to obtain organoclays for use in polymer nanocomposites. Organophilic clays are clays containing organic molecules interspersed between the structural layers. The intercalation of species causes expansion occurs between the planes of the clay, and changes its hydrophilic nature to hydrophobic or organophilic. [8].
The clays used in the preparation of organophilic clays are bentonites. The term bentonite, according to literature, it was first applied to a type of plastic clay and colloidal discovery of a rock Fort Benton, Wyoming, USA. Although originally the term was referring to bentonite clay rock discovery, currently designates clay composed primarily of montmorillonite clay mineral. This smectite clay mineral group is part of a family of clays having similar properties. The term bentonite is also used to designate a product with high content of smectite. [9].
Montmorillonite is the most abundant clay mineral of the smectite group, the general chemical formula is given by Mx (Al4-xMgx) Si8O20- (OH) 4. Has particle sizes which can vary from 2 mM to very small sizes, such as 0.1 m in diameter with an average size of 0.5 m and a plate or strip format. Belongs to the group of phyllosilicates 2: 1, whose plates are characterized by structures composed of two silica tetrahedral sheets with a central octahedral sheet of alumina, which are joined together by oxygen atoms that are common to both sheets. The leaves have continuity in the directions of the axes a and b and generally have orientation in the approximately parallel planes (001) of the crystals, which makes the laminated structure. The

plates of montmorillonite have irregular profiles, are very thin, has a tendency to aggregate in the drying process, and have a good capacity of delamination when placed in contact with water. The diameter is approximately 100 nm, the thickness may reach up to 1 nm and lateral dimensions can vary from 30 nm to several microns, resulting in a high aspect ratio and can reach approximately 1,000 stacking these plates is governed by weak and van der Waals forces, and between the plates polar forces respect, there are gaps called galleries or intermediate or interlamellar layers that reside exchangeable cations such as Na +, Ca2 +, Li +, fixed electrostatically and the function of compensating negative charges generated by isomorphic substitutions occurring in the lattice, such as Al3 + by Mg2 + or Fe2 + or Mg2 + for Li + [10].
The smectite group of clays, especially montmorillonite (bentonite composing) are widely used in the preparation of organoclays because of the small size of the crystals, the high exchange capacity for cations, and the ability to swell in water which causes the intercalation of organic compounds used in the synthesis is rapid and 100% complete [8].
The use of nanocomposites obtained by dispersing loads with nanometer dimensions at low concentrations has been shown to be an excellent alternative to traditional composites showed highly superior physical properties to these materials. The improvements depend on the properties of the nanocomposites of the interfacial interaction and uniform dispersion of the components, or between the matrix and nanocarga. [11]

Materials and Methods

Materials

- Styrene-acrylonitrile - Chi Mei Kibsan PN 117C
- Acrylonitrile-Butadiene-Styrene - Sansung SD-0150W
- Clay Cloisite 20A

Preparation of Nanocomposites

Two master will be prepared containing 40 wt% nano-clay (Cloisite 20 A) and 60 wt% SAN, using an adiabatic mill (Mixer "dryss").
Incorporation of the master ABS: master containing 1 to 5% of nanoclay are incorporated into ABS using a twin screw extruder.
The extruded material is pelletized and fed into the injection molding machine to obtain the test specimens.

Results obtained

The prepared nanocomposites were subjected to tensile tests according to ASTM D 638-01 [12]. The results obtained were as follows:

Table 1: Mechanical tests results

	Natural ABS	1% wt of nanoclay	5% wt of nanoclay
Tensile Strength (MPa)	1276	1298	1405
Tensile max force (MPa)	48,32	47,04	47,45
Tensile at Break (Mpa)	34,79	41,39	46,18
Elongation max force (%)	4,502	4,358	3,982
Elongation at Break (%)	12,68	6,073	4,195

Figure 1: Tensile at Break (MPa) X Prepared nanocomposites

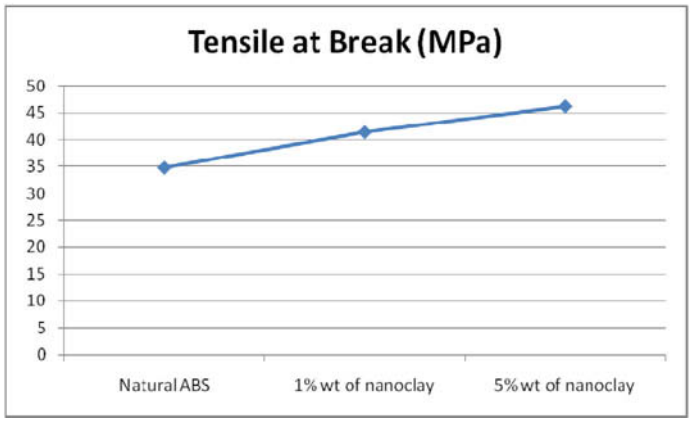

Figure 2: Elongation at break (%) X Prepared nanocomposites

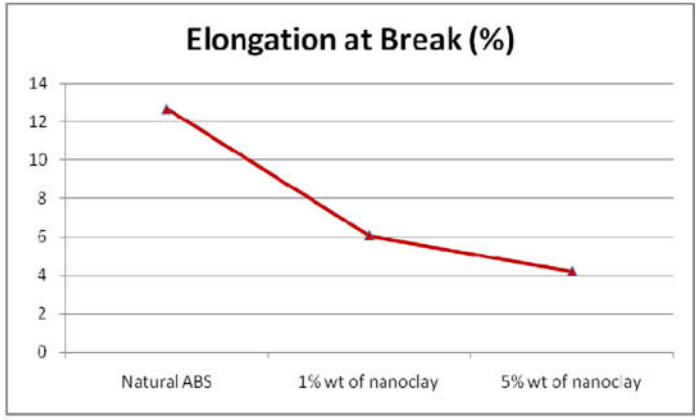

Conclusion

According to the obtained results it can be noticed that incorporation of nanoclay ABS polymeric matrix resulted in an increase of the maximum force required to break the specimens; The nanocomposite prepared with 1% nanoclay presented a increased by 18.97% in the values of Tensile at Break, since the nanocomposite prepared with 5% nanoclay presented a increased by 32.74% of the values for the same property. On the other hand there is a considerable decrease in elongation properties .

References and Notes

1.Sebastião V. Canevaloro. *Ciência dos Polimeros*: Um texto básico para tecnólogos e engenheiros. (São Paulo: Editora Artliber, 2006) 17-19.

2. Krishan K. Chawla., *Composite Materials Science and Engineering*. (1ªed, New York, Springer – Verlag, 1997) 35 - 48.

3.A.R Morales., and L.B Paiva, *Propriedades Mecânicas de Nanocompósitos de Polipropileno e Montmorilonita Organofílica.* Polímeros: Ciência e Tecnologia, vol. 16, n° 2, (2006) 136-140.

4. Paulo A. Santos.; Edson R. Simielli. *Plásticos de Engenharia*: Principais tipos e sua moldagem por injeção. (São Paulo: Editora Artliber, 2010) 15-28.

5. Helio Wiebechk, and Julio Harada. *Plásticos de Engenharia: Tecnologia e Aplicações*. (São Paulo: Editora Artliber, 2005) 112 - 132.

6.F.R.V. Diaz *"Preparação a nível de laboratório de algumas argilas esmectíticas organofílicas"*. (Ph.D. thesis, Departamento de Engenharia Química da Escola Politécnica da Universidade de São Paulo, 1994) 20 - 30

7. Percio S. Souza. *Ciência e tecnologia de argilas*. (São Paulo, Edgard Blucher, v.3, 2 Ed., 1992) 12-27

8. L. B. Paiva, and A. R. Morales, and F. R. V. Diaz *Argilas organofílicas: características, metodologias de preparação, compostos de intercalação e técnicas de caracterização*, Cerâmica (54), (2008) 213-226

9. A. B. Luz, F. A. F Lins.; *Rochas & Minerais Industriais*, CETEM/MCT, (2008) 239-255.

10. Silva, Isabelle A. et al. *Studies of new occurrences of bentonite clays in the State of Paraíba for use in water based drilling fluids. Rem: Rev. Esc. Minas* [online]. (2013), vol.66, n.4. 485-491.

11. Esperidiana.A. B. Moura et al. *Avaliação Da Incorporação Da Nanoargila Bentonita Chocolate Na Blenda De Copoliéster Aromático-Alifático/Amido De Milho*, CBPol (2013), 2013

12. American society for testing and materials. – ASTM. *Standard test method for tensile properties of plastics*, D 638-01. ASTM, 2001.

Characterization of Minerals, Metals, and Materials 2015

Characterization of Non-Ferrous Metals

Session Chairs:

Juan Pablo Escobedo

Sreeramamurthy Ankem

Characterization of Minerals, Metals, and Materials 2015
Edited by: John S. Carpenter, Chenguang Bai, Juan Pablo Escobedo, Jiann-Yang Hwang, Shadia Ikhmayies, Bowen Li, Jian Li, Sergio Neves Monteiro, Zhiwei Peng, and Mingming Zhang
TMS (The Minerals, Metals & Materials Society), 2015

CHARACTERIZATION OF CLOSED-CELL ALUMINIUM FOAMS SUBJECTED TO COMPRESSIVE LOADING

M.A. Islam[1], J.P. Escobedo[1], P.J. Hazell[1], G.J. Appleby-Thomas[2], and M.Z. Quadir[3]

[1]UNSW Australia at the Australian Defence Force Academy, Canberra, ACT 2610, Australia
[2]Centre for Defence Engineering, Cranfield University, Defence Academy of the United Kingdom, Shrivenham, SN6 8LA
[3]UNSW Australia, Sydney, NSW 2502, Australia

Keywords: Aluminium foams, microstructure, micro-CT, cell topology, compression deformation

Abstract

The mechanical response of closed-cell aluminium metallic foams subjected to low and high strain-rate loading has been investigated. A set of quasi-static and dynamic (shock) compressive tests have been conducted on closed-cell aluminium foams (CYMAT) with densities of 0.50 and 0.30 g/cc. Post-mortem characterization via optical microscopy and electron backscatter diffraction (EBSD) was performed on pristine and deformed specimens to elucidate the dominant deformation mechanisms in these materials. The combination of these techniques allowed for the assessment of critical deformation parameters such as changes in cell geometry and morphology, as well as microstructural evolution and deformation of the aluminium cellular network. These findings aim to aid in the design and development of optimized material structures for impact and blast protection.

Introduction

Closed-cell aluminium foams have gained high interest due to their novel physical, mechanical, thermal and acoustic properties such as light weight, high energy absorption capacity, stability in elevated temperature, high damping capacity and fully recyclable [1-13]. In specific, their high energy absorption capacity per unit mass makes them very attractive as light-weight materials in applications that involve blast and impact events [13-17].

A summary of the fundamentals of mechanical behaviour of metallic foams can be found in Ashby [18]. In general, studies on the high strain-rate behaviour have reported that the energy absorption relies heavily on the applied strain-rate [19-24]. For instance, Christ et al. [20] reported that closed-cell materials lose their ideal deformation behaviour under high strain-rate compressive loading due to an increase in material stiffness. Xiang et al. [21] observed that a decrease of relative density or an increase in impact velocity led to an increase in the shock velocity propagating through the foam. Tan's et al.[5] work, on similar CYMAT foams, showed that cell collapse changes with compaction rate. Their work also found that the dynamic response depends on the direction of loading relative to the foam geometry, i.e. along the through-thickness vs. in-plane directions.

Although the general view (stress-strain and energy absorption) of metallic foams is well established an understanding of the microscopic deformation mechanisms at different strain rates and their effects on the overall performance is still limited. To this end, the aim of this study was

to conduct a comprehensive characterization via optical microscopy and electron backscatter diffraction (EBSD) measurements to reveal the deformation mechanisms in these materials.

Initial Material Characterisation

Two kinds of closed-cell aluminium foams (CYMAT Aluminium Corporation, Canada) with nominal densities of 0.50g/cc and 0.30 g/cc were utilized in these experiments. For convenience, we designated the foams with density in the 0.48-0.51g/cc range as HD (high density) and foams with density in the 0.31-0.35 g/cc as LD (low density) foams. The measured physical properties of the given foams are shown in Table I.

Table I. Measured physical properties of supplied foams

Property	HD	LD
Density (g/cc)	0.48-0.51	0.31-0.35
Relative density (%)	17.00-18.80	11.40 – 12.90
Porosity (%)	81.20–83.00	87.10-88.60
Mean Cell-size (mm)	1.75	3.95
Std. dev. of cell-size (mm)	1.13	1.98
Wall thickness (mm)	0.10-0.23	0.10-0.21

The nominal dimensions of the compression samples were 40 mm×40 mm×23 mm. Electro discharge machining (EDM) was utilized to avoid distortion in the sample boundaries. Figure 1 shows optical images of the compression specimens. It is observed that the local density was fairly homogeneous along the X and Y directions, whereas a highly heterogeneous cell structure was displayed along the Z direction. Details on the morphological and topological cell features for these two kinds of foams obtained via X-ray computed tomography has been provided in our previous work [25].

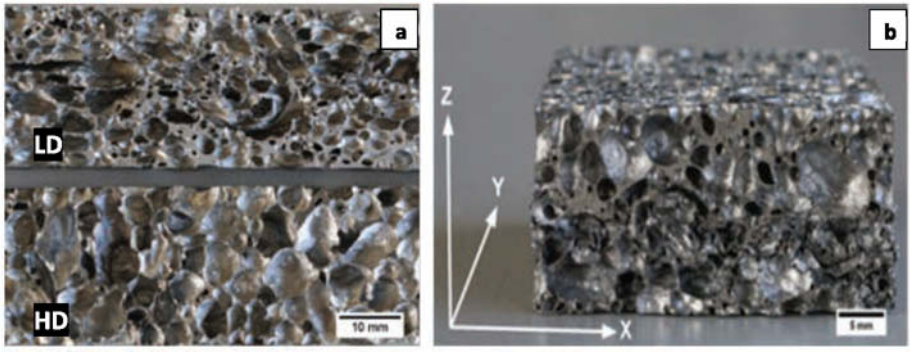

Figure 1. Supplied CYMAT foams: (a) plane perpendicular to axis of compression (HD: 0.49 g/cc and LD (0.31 g/cc). (b) Test sample of LD foam (density 0.29g/cc). Uniaxial compressive test was performed along Z-direction.

It was also observed that the cell shape does not follow a specific geometrical shape, but it can approximately be considered as elliptical. Average cell-size values for HD were measured to be around 1.75 mm to 2 mm, whereas for the LD the values were 3.75 mm to 4.00 mm. The range

of cell–wall thickness for the HD was 0.1 mm to 5.5 mm, whereas for the LD foam it was 0.25 mm to 9.5 mm.

Figure 2 shows a higher magnification optical micrograph of the cell wall of a HD specimen. It is readily observed that the cell-wall thickness varies within the network. Also, a large number of imperfections (inclusions/precipitates) and micro-pores are present, predominantly near the wall edges.

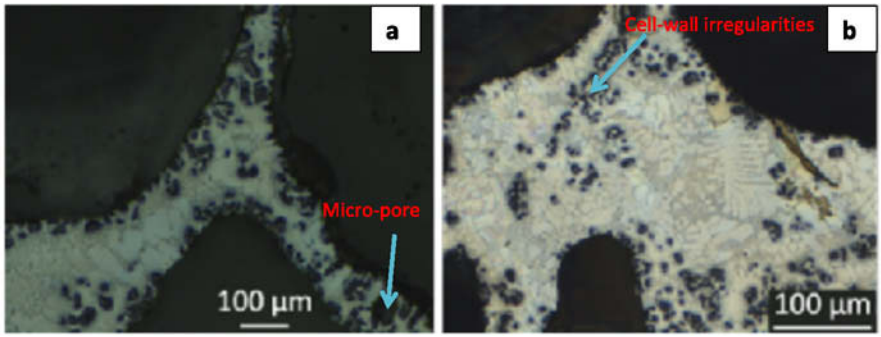

Figure 2. Microstructural image of cellular network and cell-wall of HD (0.49 g/cc): (a). Cell-wall joint (b) Cell-wall surface.

To further characterize the microstructure within cell walls, electron backscatter diffraction (EBSD) measurements were performed in several locations. A representative image is shown in Fig. 3. A polycrystalline grain structure is observed with each of the grains spanning several hundred micrometres. Furthermore, a dentritic sub-grain structure is also visible in figure 3.

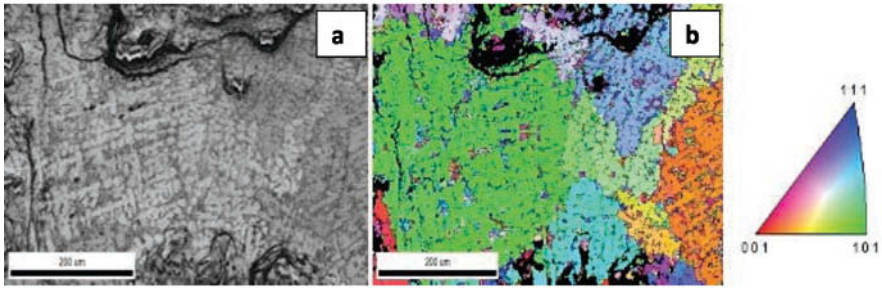

Figure 3. EBSD maps of area within the cell-wall (a) SEM image, (b) Orientation map. The colour in (b) correlates with the crystallographic orientation key (triangle).

To analyze the chemical composition of the precipitates observed in figure 2, energy dispersive spectroscopy (EDS) measurements were conducted at several locations, a representative area is shown in figure 4.

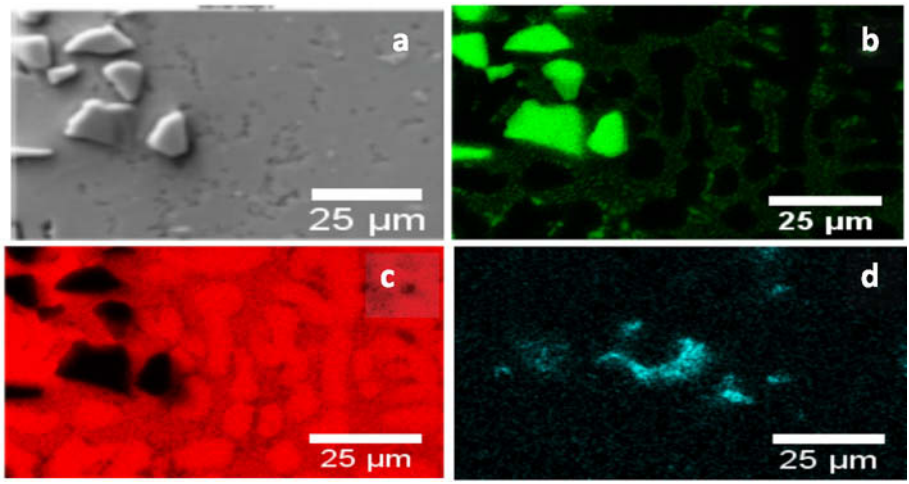

Figure 4. EDS image of an area within the cell-wall. (a) Two different intermetallic phases (b). Iron (Fe) (c). Silicon (Si) (d). Oxygen (O)

The elemental maps in Fig. 4 qualitatively show that the particles contain traces of Si, O, Fe. Quantitative assessments are currently underway to determine the exact chemical composition of the precipitates.

Results and Discussion

Quasi-static compression

The quasi-static compression stress-strain results are shown in figure 5. The deformation characteristics are observed to follow the typical stress-strain response of closed-cell aluminium foams reported in the literature. This response consists of three distinctive regions: an initial linear elastic region; an extended plateau state and final densification due to cell collapse. Furthermore, it is observed that the plateau stress for the higher density foam constantly rose although the stress remained constant for the lower density foam.

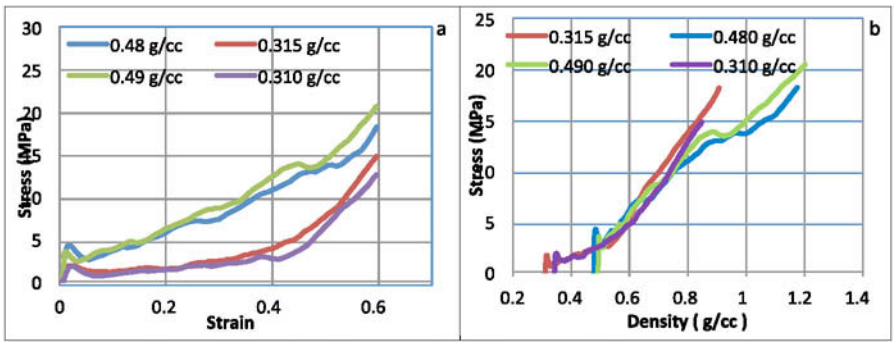

Figure 5. Quasi-static test results a) Stress-strain b) stress-density.

Snapshots of the quasistatic compression tests are shown in figure 6.

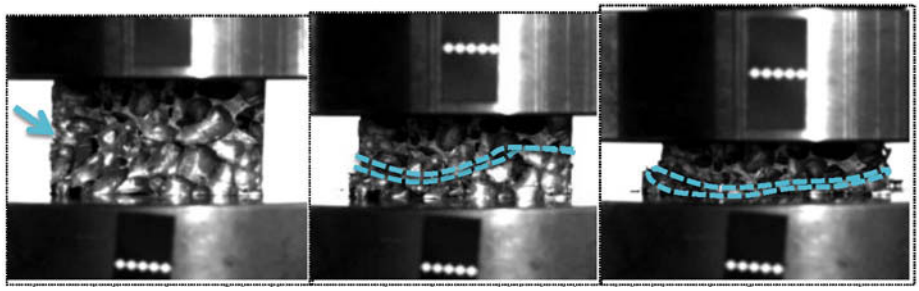

Figure 6. Snapshots of the live camera imaging at 0%, 25% and 45% strain of a LD specimen (from left to right)

During the compression tests, live video showed that the commencement of cell collapse started in the middle part of the foam structure almost in every specimen. The cell collapse stage is the longest stage during these tests, nearly from 2% to 60% of the total strain. In general, this stage is a continuous process of cell-wall buckling, yielding and fracturing. Furthermore, it was observed that plastic deformation preferentially started in the regions where the foam's density was relatively lower (big cell size and large void space).

Dynamic (Shock) Compression

Plate impact testing was carried out on a 5 meter single-stage gas gun using aluminium flyer plates of 10-mm thick. Three experiments were carried out with three thicknesses of 10mm, 12 mm, and 14 mm. The flyer plates were launched at~220 m/s or ~480 m/s. The passage of the shock wave in the materials was measured using a Heterodyne velocimeter (Het-v). A schematic of the experimental technique is shown in figure 7.

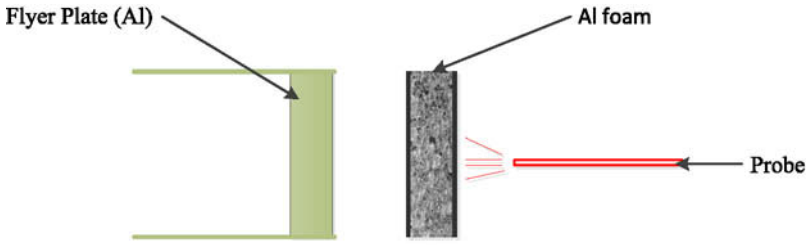

Figure 7. Schematics of plate impact test

The Het-v was used to track the velocity of the rear free surface of the sample. A disposable experimental probe was employed consisting of a collimating lens connected to a 5 m length of 9/125 μm single-mode fibre.

In these studies, the raw oscilloscope data from the interferometer were processed with MATLAB using a Gabor transform, to produce a time-frequency spectrogram. The spectrogram images were then processed using a standard image manipulation application (in this case Image

J) to manually select points on the plot and digitise those into (X, Y) pairs for subsequent data reduction using Microsoft Excel. Figure 8 shows the stress wave velocity verses time graph for the samples of size 10, 12 and 14mm. It is noticed that for the higher flyer plate's velocity case, the particle velocity at the rear of the target rises quicker than the lower-velocity- impact case. This data implies that the compaction wave evolves at a rate determined by the rate of loading (consistent with conservation of momentum). Similar results have been shown by Petel et al. [26]. The microstructural characterization shock loaded specimens is currently underway and will be reported in due time.

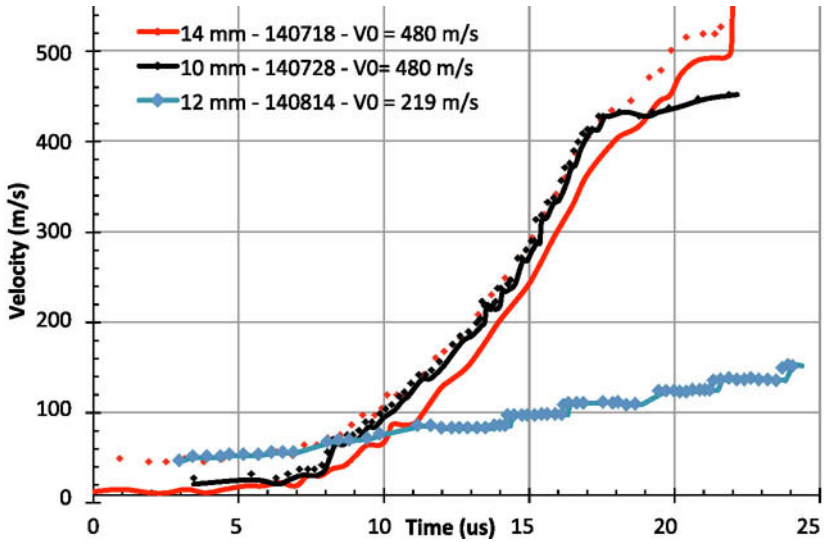

Figure 8. Velocity History diagram for the foam of density 0.5 g/cc.

Conclusions

Closed-cell aluminium foams with density 0.50 g/cc and 0.31g/cc were characterized at quasi-static and dynamic loading rates. The results of the study revealed that the foam structure had some elements such as O, Fe and Si. These elements likely contributed to the foams' brittle nature - particularly at high strain rates. Secondly, deformation initiated at the weakest point in the sample and propagated from this region until densification. Performance of closed-cell aluminium foams can be enhanced by minimizing structural defects and optimizing the structural parameters such as providing a regular cell distribution. Enhancing the smoothness of the cell wall is also likely to enhance performance.

Acknowledgements

The authors would like to acknowledge the contributions of David Sharp for his assistance in conducting the quasi-static tests and sample preparation. Stuart Gay is also thanked for assisting with the design and manufacturing of specimens used for testing. Finally, Adrian Mustey is also thanked for his help conducting some of the experiments.

References

1. Lorna J.Gibson, and Michhael F. Ashby, Cellular solids: structure and properties (Cambridge university press, 1999).
2. H.P. Degischer, B.E. Kriszt, "Handbook of Cellular Metals: Production, Processing Applications," Willy-VCH, 2002.
3. A. Jung, E. Lach, and S. Diebels, "New hybrid foam materials for impact protection". International Journal of Impact Engineering, 64(2014), 30-38.
4. R.P.Merrett, G.S. Langdon, and M.D. Theobald, "The blast and impact loading of aluminium foam," Materials and Design, 44(2013), 311-319.
5. P.J.Tan, S.R. Reid, J.J. Harrigan, Z. Zou,S. Li, "Dynamic compressive strength properties of aluminium foams. Part II - 'shock' theory and comparison with experimental data and numerical models," Journal of the Mechanics and Physics of Solids, 53(10) (2005), 2206-2230.
6. L. A. B. da-Chuda et al., "Plasticity and damage analysis of metal foams under dynamic loading," Materialwissenschaft und Werkstofftechnik 42(5) (2011), 356-364
7. M. Ashby and T. Lu, "Metal foams: A survey. Science in China Series B," Chemistry, 46(6) (2003), 521-532.
8. J.E. Field, S.M. Walley, W.G. Proud, H.T. Goldrein, and C.R. Siviour, "Review of experimental techniques for high rate deformation and shock studies," International Journal of Impact Engineering, 30(7) ((2004), 725-775
9. A.F. Bastawros, H.B. Smith and A.G. Evans, "Experimental analysis of deformation mechanics of closed-cell aluminium alloy foam," J. of Mechanics and Physics of Solids, vol. 48, 2000, pp.301-322.
10. Y. Mu, G.Yao,L. Liang , H. Lou and G. Zu , " Deformation of close-cell aluminium foam in compression" Scriptal Materilia, vol.63, 2010, pp. 629-632.
11. D. Ruan, G. Lu, F.L. Chen, E. Siores, " Compressive behavior of aluminium foams at low and medium strain rates" , J. Composite Structures, vol. 57, 2002, pp. 331-336.
12. Y. Sugamura , J. Meyer, M.Y. He, H. Bart-smith, J. Grenstedt and A.G. Evans, "On the mechanical performance of closed cell Al alloy foam." Acta Materilia , vol.45(12) , 1007, pp.5245-5259.
13. M. Vesenjak, M. Borovinšek, Z. Ren, S. Irie, and S. Itoh, "Behavior of Metallic Foam under Shock Wave Loading," Metals, 2(3) (2012), 258-264
14. P.J.Tan, S.R. Reid, J.J. Harrigan, Z.., Zou, and S. Li, "Dynamic compressive strength properties of aluminium foams. Part II - 'shock' theory and comparison with experimental data and numerical models," Journal of the Mechanics and Physics of Solids, 53(10) (2005), 2206-2230.
15. A.G. Hanssen, L. Enstock, and M. Langseth, "Close-range blast loading of aluminium foam panels," International Journal of Impact Engineering, 27(6) (2002), 593-618.

16. I. Elnasri, S. Pattofatto, H. Zhao, H. Tsitsiris, F. Hild, and Y. Girard, "Shock enhancement of cellular structures under impact loading: Part I Experiments,". Journal of the Mechanics and Physics of Solids, 55(12) (2007), 2652-2671
17. S.L. Lopatnikov, B.A. Gama, M.J. Haque, C. Krauthauser, and J.W. Gillespie Jr, "High-velocity plate impact of metal foams"' International Journal of Impact Engineering, 30(4) (2004), 421-445
18. M.F. Ashby, A.G. Evans, N.A. Fleck., L.J. Gibson, "Metal Foams: a design guide," Huchinson, J.W. & Wadley, H.N.G. Butterworth-Heinemann. Publications, 2000.
19. M. Vesenjak, M. Borovinšek, Z. Ren, S. Irie, and S. Itoh, "Behavior of Metallic Foam under Shock Wave Loading," Metals, 2(3) (2012), 258-264.
20. H.J.Christ , U. Krupp, A. Ohrndorf, P. Schmidt, "Mechanische untersuchungen eines geschlossenporigen aluminiumschaums" Proceedings of zur Werkstoffprüfung Bad Nauheim, Germany, 7-8 , (2000).
21. X.M. Xiang, Y.L. Li, T. Suo, and B. Hou, "Shock enhancement of aluminum foam under impact loading using FEM simulations," Advanced Materials Research, 160 (2011), 1077-1082.
22. A. Paul and U. Ramamurty , " Strain rate sensitivity of close cell aluminium foam," Materials science and Engineering , 281 (1-2) (2000),1-7.
23. Yi, F., Zhu, Z., Zu, F., Hu, S., & Yi, P. (2001). Strain rate effects on the compressive property and the energy-absorbing capacity of aluminum alloy foams. Materials Characterization, 47(5), 417-422
24. H.M. Hsiao, I.M. Daniel, R.D. Coreds "Strain rate effects on the transverse compressive and shear behavior of undirectional composites," J Compos Mater, 33 (1999), 1620–1642
25. M.A. Islam, P.J. Hazell, J.P. Escobedo and M. Saadatfar, "In-situ Quasistatic Compression and microstructural characterization of Aluminium Foams of Different Cell Topology," XII International Conference on Applied Mechanics and Mechanical Engineering (ICAMME 2014 :), 11-12 December, Melbourne, Australia
26. O.E. Petel, S. Ouellet, D.L. Frost and A.J. Higgins, "Shock Hugonoit measurements in Foam," Journal of Physics Series 500(2014), 112050.

Characterization of Minerals, Metals, and Materials 2015

Characterization of Materials Extraction

Session Chairs:
Sabriye Piskin
Simona Murph

Characterization of Minerals, Metals, and Materials 2015
Edited by: John S. Carpenter, Chenguang Bai, Juan Pablo Escobedo, Jiann-Yang Hwang, Shadia Ikhmayies, Bowen Li, Jian Li, Sergio Neves Monteiro, Zhiwei Peng, and Mingming Zhang
TMS (The Minerals, Metals & Materials Society), 2015

IMPROVEMENT ON PERFORMANCE OF Mg-C REFRACTORIES AS LINING OF VANADIUM-EXTRACTION CONVERTERS

Weijun Huang, Lei Xu, Shuai Zhang , Min Chen

School of Materials and Metallurgy, Northeastern University, Shenyang, 110004, China

Keywords: MgO-Fe Brick, Fe Powder, Vanadium-Extraction Converter, Sinterability, Oxidation Resistance, Slag Corrosion Resistance

Abstract

For the purpose of extending the service life of MgO-C bricks used as linings of vanadium-extraction converters, the effect of Fe addition on properties of MgO-C bricks was investigated. The results showed the addition of Fe could effectively improve the sinterability of the oxidized layer of the MgO-C refractory at 1400°C due to the effect of FeO (formed by oxidation of Fe) on formation of MgO-FeO_{ss} and modification of the microstructure, and excellent corrosion resistance against vanadium containing slag was also obtained due to the increase of compactness of the oxidized layer and concentration of FeO in the oxidized layer. Consequently, it is considered that MgO-C brick by introducing the new phase of Fe is a favorable substitute of MgO-C refractory to be used as linings of vanadium-extraction converters.

Introduction

Vanadium exists mainly in vanadium-titanium magnetite which is the mainly source of initial vanadium products. Converter vanadium recovery is a main method to produce vanadium, which obtains the slag containing V_2O_3 by oxidize the iron liquid from converter. Compared to traditional converters, the vanadium-extraction converters work in oxidizing atmosphere lower temperature (around 1400°C) and acid slag circumstance [1, 2]. Consequently, the service life of vanadium-extraction converter is only about 7000 heats while MgO-C bricks are used as working linings, and the application of slag splashing technology has shown little influence on extending of service life. So the requirement to extend the service life of vanadium-extraction converter has caused much attention [3-5]. For this purpose, the present work designed a novel refractory as linings refractories of vanadium-extraction converter, and the properties of this novel refractories were investigated by comparing to these of the traditional MgO-C bricks (without Fe).

Raw Materials and Procedures

Base on the practical production of MgO-C refractories, two batches of starting materials with 14% and 16% graphite with purity of more than 98.0% and the fused magnesia clinker with purity of more than 98.5% (for the linings used in the metal bath and the slag line) were well mixed respectively, with external addition of 8% to 12% Fe powder with purity of 99.5% and 4% phenol resin as binder for preparation of the novel refractories. The grain size composition of fused magnesia was the same as that of the practical production of MgO-C brick for converter linings, with maximum grain size of 3 mm. Then the mixed powders were shaped to the cylindrical samples sized *D*50 mm × ~60 mm under 500 MPa. The samples were dried at 200°C for 24h in air atmosphere for use. And then the bulk density and apparent porosity were measured in kerosene according to Archimedes' principle [6]. The oxidation resistance was evaluated by determining the thickness of oxidized layer of the bricks after heating at 1400°C for 3h in air atmosphere, and the cold compressive strength was determined by the average values of cold strength of 5 samples. For the evaluation of slag corrosion resistance against vanadium containing slag, the crucibles with inner diameter of 26 mm and depth of 40 mm were prepared by drilling the as-dried cylindrical bricks, and then the slag corrosion resistance was evaluated by measuring the depth of the vanadium containing slag penetrating into the crucibles and observation of the microstructure after soaking the crucibles at 1400°C for 4h. In addition, the phase compositions of the samples was examined by X-ray diffraction, and the microstructures and element distribution of the refractories were analyzed by scanning electron microscopy (SEM, 20 kV) attached with energy-dispersive X-ray (EDX).

Results and Discussion

Physical Properties

Figure 1 shows the bulk density and apparent porosity of the two batches of the dried and oxidative samples with different content of Fe; here C14 and C16 denote that the content of C are 14% and 16% in the refractories. Figure 1(a) shows the bulk density and apparent porosity of the dried samples (drying at 200°C for 24h in the air atmosphere). It is observed that the bulk density of MgO-C bricks with 14% and 16% graphite was 2.93 g/cm^3 and 2.89 g/cm^3 respectively while Fe content was 0%. After Fe was added, the bulk density of MgO-C bricks with 14% and 16% graphite was slightly increased, and it was 3.20 g/cm^3 and 3.15 g/cm^3 respectively while Fe content was 12%. Meanwhile, the apparent porosity of MgO-C brick was also slightly increased while Fe was introduced, and it increased from 3.60% to 5.20% with increasing the content of Fe from 0 to 12% for the sample with 14% graphite, while it increased from 5.05% to 6.25% for the sample with 16% graphite when the content of Fe increased from 0 to 12%. It is considered that the slight increase in bulk density of the bricks by introducing the new phase of Fe was due to its higher theoretic density compared with other phases in the bricks, and the slight increase in

apparent porosity is considered due to the variation of plasticity of the starting materials during shaping process with the content of graphite decrease caused by addition of Fe.

Figure 1(b) shows the bulk density and apparent porosity of samples after oxidation test (heating at 1400°C for 3h in air atmosphere). It is observed that the bulk density of MgO-C brick with 14% graphite and 0% Fe was decreased to 2.70 g/cm^3, with apparent porosity sharply increased to 20.99%. With increasing of graphite content to 16% and 0% Fe, the oxidation resistance was further decreased, and the apparent porosity further increased to 24.50%. By introducing Fe, the oxidation resistance of MgO-C bricks was improved for both batches of samples, and the apparent porosity was decreased to 16.50% and 17.00% respectively for the samples with 14% and 16% graphite while the content of Fe was 12%. This result indicates that the addition of Fe can effectively depress the degradation of compactness of MgO-C brick caused by oxidation of carbon in the refractories.

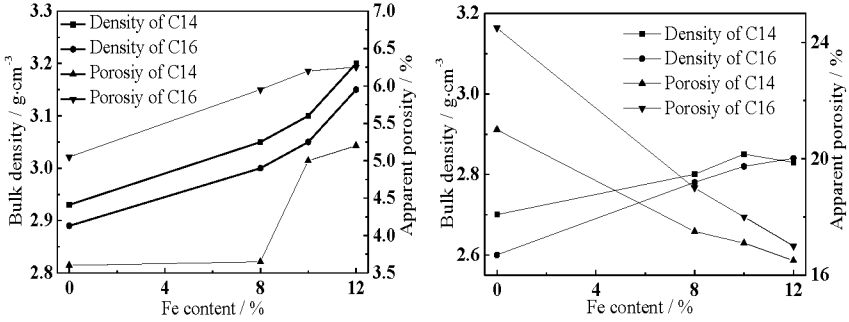

(a) Drying at 200°C for 24h (b) Heating at 1400°C for 3 h in air

Figure 1 The bulk density and apparent porosity of compactness of the bricks at different treatment conditions

Figure 2 shows the changes of cold compressive strength of the two batches of samples after drying and oxidation test. It is observed that the cold compressive strength was 27.5 MPa for the as-dried MgO-C brick with 14% graphite and 0% Fe, and it was abruptly decreased to 12.5 MPa after oxidation test. With increasing graphite content to 16% and 0% Fe, the strength was further decreased from 24.8 MPa to only 7.9 MPa. But the cold strength only slightly decreased from 26.5 MPa to 23.5 MPa for the sample with 14% graphite and 8% Fe, indicating that the addition of Fe showed excellent performance on maintaining compressive strength of MgO-C brick after the refractories were exposed to oxidizing atmosphere at higher temperatures. For the sample with 16% graphite, the effect of Fe addition showed a similar tendency on improvement of cold compressive strength of the oxidized samples.

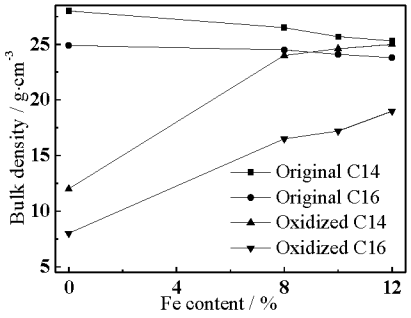

Figure 2 Cold compressive strength of the bricks after drying and heating at 1400°C for 3h in air.

Phase Composition and Microstructure

Figure 3 shows the XRD patterns of the refractories with 16% graphite after drying and heating at 1400°C for 3h in air. For the MgO-C brick without Fe, periclase and graphite were detected in the original brick layer, and only periclase was detected in the oxidized layer. But for MgO-C brick by addition 10% Fe powder, α-Fe was detected in the original brick layer besides periclase and graphite. This result indicates that Fe can coexist with graphite in MgO-C refractories at higher temperatures. It is also observed that magnesio-wustite (MgO-FeO_{ss}) and a small amount of magnesioferrite (MgO·Fe_2O_3) were detected in the oxidized layer. The reason is that graphite was firstly oxidized according to Reaction 1 when MgO-C refractories containing Fe were exposed to the oxidizing atmosphere. And after Reaction 1 finished, Reaction 2 happened and Fe transferred to FeO. Then the formed FeO further dissolved to periclase lattice in the refractories to form magnesio-wustite (MgO-FeO_{ss}) at higher temperatures according to Reaction 3. During temperature dropping process, FeO precipitated from wustite according the reverse direction of Reaction 3 and was further oxidized to Fe_2O_3 according to Reaction 4, and finally the formed Fe_2O_3 reacted with MgO to form magnesioferrite according Reaction 5 [7]. Therefore, it is considered that Fe would transfer to FeO at higher temperature and the formation of magnesioferrite is considered due to the precipitation and oxidation reactions during temperature dropping process.

$$2C + O_2(g) = 2CO \quad (1)$$

$$2Fe + O_2(g) = 2FeO \quad (2)$$

$$FeO + MgO \leftrightharpoons MgO\text{-}FeO_{ss} \quad (3)$$

$$2FeO + 0.5\,O_2(g) = Fe_2O_3 \quad (4)$$

$$Fe_2O_3 + MgO = MgO\cdot Fe_2O_3 \quad (5)$$

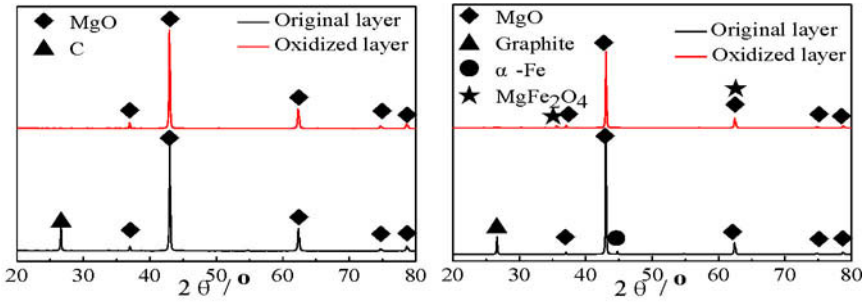

(a) *w*(Fe): 0% (b) *w*(Fe): 10%

Figure 3 XRD patterns of MgO-16%C bricks after drying and heating at 1400°C for 3h in air conditions.

Oxidation Resistance

Figure 4 shows the microstructure of bricks with 14% carbon after heating at 1400°C for 3h in air. For MgO-C brick without Fe addition, it is observed that the oxidized layer with maximum of 4~5 mm in thickness was formed (as shown in Figure 4a). By introducing 10% Fe, a thinner oxidized layer with maximum of 3~4 mm in thickness was formed (as shown in Figure 4b). For MgO-C bricks without Fe addition (as shown in Figure 4a), it is observed that there are many pores in the matrix of MgO-C refractories after carbon was oxidized, with periclase grains existed in isolation. This result indicates that the periclase grains were not well sintered under 1400°C after carbon in the refractory was oxidized, as the initial sintering temperature of MgO was much higher than 1400°C [8]. As a result, the bonding strength between the periclase grains in the oxidized layer was very poor, and the oxidized layer would easily drop off. For this reason, it is considered that the traditional MgO-C refractories that are usually used as linings of steel-making converter are not suitable used as linings of the vanadium-extraction converter.

After the MgO-C brick containing 10% Fe was heated at 1400°C for 3h in air and the oxidized layer was formed (as shown in Figure 4b), it is observed that the porous microstructure was also formed in the oxidized layer, but the oxidized layer looks compacter compared to that of MgO-C brick without Fe addition. Meanwhile, the grain size also looks larger than that in MgO-C brick without Fe addition, with most of these grains bonded together to form network microstructure. It is considered that the formation of network microstructure in the oxidized layer is favorable to improve the bonding strength of the periclase grains in the matrix and further to improve the erosion resistance of the oxidized layer. In addition, it is also observed that Fe disappeared in the oxidized layer, with bright grey phase formed around the surface layer of the large periclase grain, while the color of small periclase grain had completely transferred from grey to bright grey. EDX analysis showed that the bright grey zone was consisted of MgO-FeO_{ss} and magnesioferrite. Meanwhile the small periclase grains had completely transferred to MgO-FeO_{ss}, uniform color of bright grey was observed. But for the large periclase grains, solid solution

reaction was not finished, and MgO-FeO_{ss} only formed on the surface layer of periclase grains. It is considered that the formation of MgO-FeO_{ss} promoted the sintering of oxidized layer.

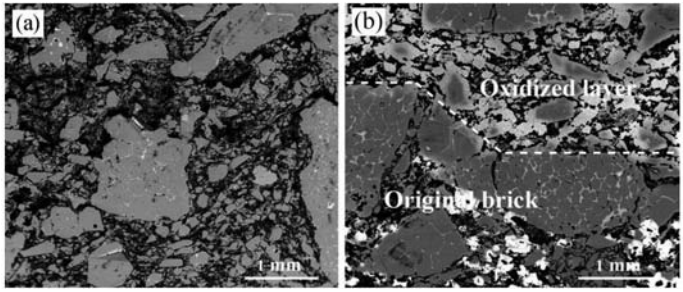

Figure 4 BSE images of the microstructures of the matrix of MgO-14%C bricks after heating at 1400℃ for 3h. (a) without Fe; (b) with 10% Fe.

Slag Corrosion Resistance

Figure 5 shows typical optical photograph of the longitudinal section of the crucible filled with vanadium containing slag after heating at 1400℃ for 4h in air. For the MgO-C crucible, it is observed that the slag deeply permeated into the crucible, with the most serious position almost permeated completely. For MgO-C crucible containing 10% Fe, the internal shape was well kept after slag corrosion test, with slag slightly permeated. This result further indicates that the slag corrosion resistance of MgO-C refractory containing Fe against vanadium containing slag was much better than that of the MgO-C refractory without Fe. The effect of Fe on the MgO-C refractories slag corrosion resistance is considered due to the increase of compactness and concentration of FeO in the oxidized layer by the formation of MgO-FeO_{ss} to retard the diffusion of FeO from slag to the oxidized layer.

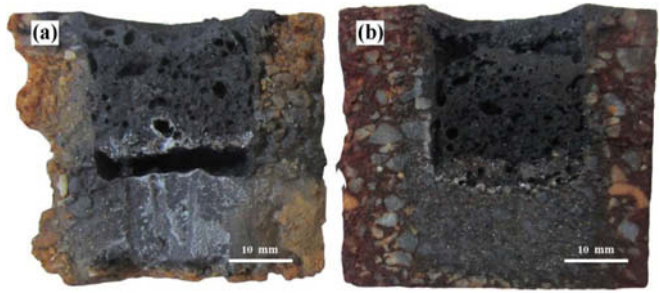

Figure 5 The longitudinal section photographs of MgO-16%C crucibles with vanadium slag after heating at 1400℃ for 4h. (a) without Fe; (b) with 10% Fe.

Conclusions

The properties of novel MgO-C refractory by addition of Fe as working linings of vanadium-extraction converters were investigated by comparison with the traditional MgO-C refractory. Based on the above results, the following conclusions have been drawn:

(1) The stable co-existing phases in MgO-C refractory by addition of Fe were periclase, graphite and Fe, and some of Fe and periclase transferred to MgO-FeO_{ss} after heating at 1400°C in air atmosphere, and a part of MgO-FeO_{ss} further transferred to magnesioferrite due to the further oxidation of FeO deposited from MgO-FeO_{ss} during temperature dropping process.

(2) The compactness of the oxidized layer of MgO-C brick by addition of Fe formed by heating at 1400°C was much higher than that of MgO-C brick without Fe addition due to the increase of sintering activity and volume expansion effect owing to the formation of MgO-FeO_{ss} to cause excellent compressive strength than that of traditional MgO-C bricks after heating at 1400°C in air condition.

(3) MgO-C refractory by addition of Fe showed excellent oxidation resistance against vanadium containing slag in vanadium-extraction converter compared to MgO-C refractory without Fe addition due to the increase of compactness of oxidized layer and concentration of FeO in the oxidized layer, and is considered to be a favorable substitute of the traditional MgO-C brick refractory to be used as linings of vanadium-extraction converter.

Acknowledgment

The authors gratefully acknowledge the National Natural Science Foundation of China (No. 51174049, 51374057) and the Fundamental Research Funds for the Central Universities of China (No.110402009) which has made this research possible.

References

1. L. Yu, Y.C. Dong, G.Z. Ye, et al., "Concentrating of Vanadium Oxide in Vanadium Rich Phase(s) by Addition of SiO_2 in Converter Slag," *Ironmaking & Steelmaking* 34(2)(2007), 131-137.

2. A.L. Li, X.T Liang, Y. Chen, et al., "Research on Extending the Lifetime of Combined Blowing Vanadium Recovering Converter," *Advanced Materials Research*, 581(2012), 895-898.

3. P. Chen, K. Xu, Y. Lan, et al., "Corrosion Mechanism of Lining of Vanadium-Extracting Converter and Improving Measures," *Naihuo Cailiao/Refractories*, 34(4)(2000), 220-221.

4. C.M. Wang, Q. Yang, Q. Gao, et al., "Corrosion of Mullite-SiC Materials by Vanadium Recovering Slag," *Naihuo Cailiao/Refractories*, 44(1)(2010), 17-19.

5. J.Q. Ao, N. Li, B.Q. Han, "Effect of Vanadium Contained Slag on Corrosion Resistance of MgO-C Bricks," *Naihuo Cailiao/Refractories*, 40(4)(2006), 287-290.

6. M. Chen, N. Wang, J.K. Yu, et al., "Effect of Porosity on Carbonation and Hydration

Resistance of CaO Materials," *Journal of the European Ceramic Society*, 27(4)(2007), 1953-1959.
7. B. Phillips, S. Sõmiya, A. Muan, "Melting Relations of Magnesium Oxide-Iron Oxide Mixtures in Air," *Journal of the American Ceramic Society*, 44(1)(1961),167-169.
8. N.S. Zhou, J.H. Liu, B.Y. Lin, "Refractory Raw Materials in China," *American Ceramic Society Bulletion*, 84(2)(2005), 20-24.

Characterization of Minerals, Metals, and Materials 2015
Edited by: John S. Carpenter, Chenguang Bai, Juan Pablo Escobedo, Jiann-Yang Hwang, Shadia Ikhmayies, Bowen Li, Jian Li, Sergio Neves Monteiro, Zhiwei Peng, and Mingming Zhang
TMS (The Minerals, Metals & Materials Society), 2015

ANALYSIS ON DEEP TREATMENT EFFECT OF COKING WASTEWATER USING 3D ELECTRODE COMBINED WITH FENTON REAGENT

Lei ZHANG[1], Lina WANG[1], Pu LIU[1], Benquan FU[1], Jiannyang Hwang[2], Shining Chen[3]
[1] R&D center of WISCO, Wuhan, 430080, China;
[2] Advanced Materials Research Center of WISCO (Beijing), Beijing, 102200, China
[3] Wuhan Institute of Shipbuilding Technology, Wuhan, 430050, China

Keywords: Coking wastewater; 3D electrode reactor; Fenton reagent; TOC removal rate; Advanced treatment

Abstract

A three-dimensional (3D) electrode reactor combined with Fenton reagent was used for advanced treatment of coking wastewater from secondary biological treatment. Effects of some key factors on total organic carbon (TOC) removal rate were investigated, and the results were compared with those of the common three-dimensional electrode reactor. Experimental results showed that TOC removal rate could reach 51.7%, when optimal operating conditions were as follows: initial pH value 3.5, H_2O_2 dosage 17.6mmol/L, reaction time 90min and $FeSO_4 \cdot 7H_2O$ dosage 3.5mmol/L. Analytical results from UV absorption spectra indicated that the organic substances in the coking wastewater were well degraded by this system, which provided good experimental basis for the practical application of this process in the treatment of coking wastewater. This can be meaningful for the treatment of other kinds of wastewater.

Introduction

Coking-plant wastewater containing phenol compounds, heterocyclic compounds, polycyclic aromatic hydrocarbons, ammonia, sulfide, cyanide, thiocyanate and other toxic and harmful substances, is a typical highly toxic organic wastewater [1-3]. The conventional treatment process of coking wastewater includes steam stripping of ammonia, followed by different forms of A/O biological nitrogen removal process. However, these processes are not sufficient to meet the strict requirements of the National Discharge Standard of China (COD <100 mg/L, GB16171-2012) [4,5]. Therefore, seeking high efficiency, low consumption, no secondary pollution and easily controllable coking wastewater advanced treatment technology is still necessary for researchers. 3D electrode electrochemical reactor has been widely used in organic

wastewater treatment, and has shown excellent effect[1,3-5]. The Fenton reaction is also considered suitable for the treatment of bio-refractory wastewaters due to its high efficiency, simplicity of operation and low cost[6]. The objective of this study is to investigate the feasibility of combination of Fenton reagent method and 3D electrode electrochemical oxidation processes applied in the advanced treatment of coking wastewater with TOC index as the main target parameter. It may reduce energy consumption and improve the efficiency of current.

Materials and Methods

Raw Wastewater and Materials

The raw wastewater used in the experiments was collected from the outlet of a WISCO coke plant with the treatment processes of steam stripping of ammonia and $O_1/A/O_2$ biological treatment and chemical coagulation precipitation, the main water quality indicators are shown in Table Ⅰ.

Table Ⅰ. Characteristics of raw wastewater

Parameter	pH	COD/ ($mg.L^{-1}$)	TOC ($mg.L^{-1}$)	BOD5/ ($mg.L^{-1}$)	NH_3-N/ ($mg.L^{-1}$)	Conductivity/ μS/cm
Raw	7.0±0.2	101±10	60±5	23±5	5.3±0.5	4500
Effluent standard	6.0～9.0	100	-	25	15.0	-

Note：Emission standard of pollutants for coking chemical plant(GB16171-2012)

All the chemicals of this study, including NaOH, HCl, 30%H_2O_2, $FeSO_4{\cdot}7H_2O_2$, $K_2Cr_2O_7$, $Mn(NO_3)_2$, $Zn(NO_3)_2$, etc, are in analytical reagents grade. They were produced by China Chemical Reagent Co., LTD.

Experimental Procedure

Batch experiments were conducted in a 3D fluidized bed electrode reactor (3.5 L) at room temperature. The schematic diagram of a home-made 3D fluidized bed electrode reactor and the prepared electrodes used were the same one reported previously [5]. The coking wastewater was treated in an electrolytic cell using two pieces of titanium based Ti/RuO_2-TiO_2-IrO_2 plane electrodes as anode, and two pieces of graphite plate as cathode. The effective surface area of the electrode and air aeration were 150 cm^2, 160L/h, respectively. A stabilized DC power supply was used as the source of electric current for the experiments. The current and voltage were 5 A and 6.4 V with digital displays. The anode and cathode were positioned vertically and parallel to

each other with an inter electrode gap of 1 cm. Since the electrochemical oxidation greatly affects the pH of effluent, the initial solution pH was controlled by adding HCl or NaOH solution. A given amount of H_2O_2 or Fe^{2+} were then mixed into the solution. The samples were taken at selected intervals and filtered through a 0.45μm filter film to remove suspended solid before analyses of the solution.

Analytical Methods

The water samples were analyzed by following the standard methods specified in the Monitoring and Analytical Methods of Water and Wastewater [7]. The total organic carbon (TOC) concentration was monitored using Multi N/C 2100 Analyzer (Analytik Jena AG Corporation, Germany). The pH was measured by using the glass electrodes; COD by the potassium dichromate method; NH_3-N by using Nessler's reagent spectrophotometry; UV absorption scan was conducted by UV–vis spectrophotometer (UV2450, SHIMADZU Corporation, Japan).

Results and Discussion

Effect of Initial pH on TOC Removal Rate

Figure 1 shows the evolution of TOC removal rate as a function of pH value when the 3D electrode reactor maintained a constant operating conditions. As shown in Figure 1, with the increasing of initial pH value of raw wastewater, the removal rate of TOC increases first and then decreases, the TOC removal rate reaches the peak when pH value is 3.5. Once the initial pH value is above 6, and the removal rate of TOC decreases. According to the mechanism of the Fenton reaction, hydroxyl radicals [·OH] can be generated by the Fe^{2+}catalytic decomposition of H_2O_2 and proceeds via a free radical chain process under acidic conditions [8]. The hydroxyl radicals [·OH] can oxidize any organic matter in the wastewater, and most organic pollutes can be degraded to small molecule organics or resulted in complete mineralization (CO_2 and H_2O). Fe^{2+} catalyst can be oxidized as Fe^{3+} as shown in reaction (1), then is regenerated by reaction (2). As can be seen from the reaction (1), when [OH^-] increases under alkaline conditions, hydroxyl radicals [·OH] tends to decrease. When initial pH is 3~5, [H^+] in solution can react [OH^-] produced in reaction (1), which is beneficial to the hydroxyl radicals[·OH] generation when neutralization reaction occurs. However, when pH increasing, hydroxyl radicals [·OH] generated in reaction (1) can be consumed, inhibiting the reaction (1) from moving to the right direction. Much flocs (complexes of Fe hydroxides and organic compounds) are formed in coagulation process when pH is above 8.0. The coagulation removes Fe^{2+} catalyst from the system, affecting

the [·OH] production and the catalytic decomposition of H_2O_2 generating O_2, thus the oxidation ability of Fenton reagent decreased [8,9].

$$Fe^{2+}+H_2O_2 \longrightarrow Fe^{3+}+OH^-+\cdot OH \quad (1)$$

$$Fe^{3+}+H_2O_2 \longrightarrow Fe^{2+}+HO_2\cdot+H^+ \quad (2)$$

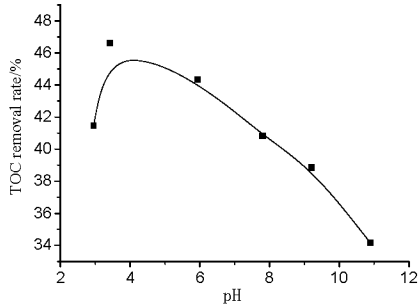

Figure 1. Effect of initial pH on TOC removal rate
(H_2O_2 dosage: 19.6mmol/L; Fe^{2+} dosage: 3.5mmol/L; time: 40min)

Effect of H_2O_2 Dosage on TOC Removal Rate

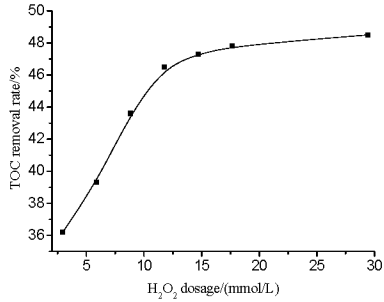

Figure 2. Effect of H_2O_2 dosage on TOC removal rate
(initial pH: 3.5: Fe^{2+} dosage: 3.5mmol/L;time:60min)

Figure 2 shows the effect of H_2O_2 dosage on TOC removal rate. With the increase of H_2O_2 dosage, TOC removal rate increases distinctly. When the H_2O_2 dosage is over 17.6mmol/L, TOC removal rate gradually levels off. The reason can be that at the lower H_2O_2 dosage range, the increase of dosage will increase hydroxyl radicals [·OH] concentration, which is conducive to the

rapid degradation of pollutants in wastewater. However, the higher H_2O_2 dosage (>17.6 mmol/L) does not enhance the TOC removal efficiency. It is because the H_2O_2 decomposition and more Fe^{2+} is rapidly oxidized to Fe^{3+}, which consumes more H_2O_2 dosage and inhibits the production of hydroxyl radicals [·OH], resulting in the slow increase of TOC removal rate[10]. Considering the economic aspect, the optimum of H_2O_2 dosage is 17.6mmol/L.

Effect of Fe^{2+} Dosage on TOC Removal Rate

Fe^{2+}, as the catalyst, plays a vital role in the Fenton system. Figure 3 shows the effects of Fe^{2+} dosage on TOC removal rate. The results indicate that TOC removal rate can obtain higher efficiency within a certain range. When the Fe^{2+} dosage increases to 5.5mmol/L and TOC removal rate will reach 48.9%. Continuing increase of Fe^{2+} concentration will result in the TOC removal rate decreasing. This behavior may be explained by the fact that lower Fe^{2+} dosage make less hydroxyl radicals [·OH], leading to seriously damage to Fenton system of chain reaction, thus affecting the oxidation ability of the reaction system. On the other hand, more Fe^{2+} dosage will generate more hydroxyl radicals [·OH] concentration. Higher dosages make much [·OH] free radicals reacting with themselves, instead of organic pollutes in wastewater. The occurrence of the complex self-reaction (side reaction) will result in [·OH] free radicals losing oxidation effect. In addition, adding more excessive Fe^{2+}, will increase cost and produce large amounts of chemical sludge to be treated. Therefore, the optimum of Fe^{2+} dosage is 3.5mmol/L.

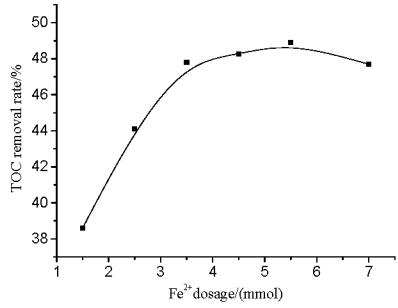

Figure 3. Effect of ferrous ion dosage on TOC removal rate
(initial pH:3.5, H_2O_2 dosage:17.6mmol/L, time: 60min)

Effect of Reaction Time on TOC Removal Rate

Reaction time is an important factor for considering the effect of operation cost. Longer reaction time means more energy consumption and higher cost. Figure 4 shows the effect of reaction time

on TOC removal rate. The experimental results show that, with the reaction time increasing, the removal rate of TOC will increase. TOC removal rate can increase quickly in 30min, and then increase slowly. This behaviors can be explained by that lots of [·OH] free radicals generated is first from the Fenton reaction system, and this combined process is very fast. Once Fe^{2+} concentration in the system decreases for the reaction consumption, [·OH] free radicals concentration also decreases, which inhibits the velocity of degradation process, then 3D electrode reactor is the dominant factor in producing [·OH] free radicals [11]. Figure 5 shows the UV scan results of coking wastewater treated by 3D electrode combined with Fenton reagent at different reaction time. It is found that with the reaction time increasing, the absorbance decreases, which indicates the organic pollutes in wastewater are degraded. Thereby, considering the economic cost, the optimal reaction time is 90min, and the TOC removal rate can reach 51.7%.

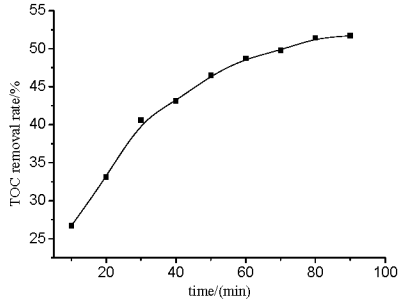

Figure 4. Effect of reaction time on TOC removal rate
(initial pH :3.5; H_2O_2 dosage:17.6mmol/L; Fe^{2+} dosage: 3.5mmol/L)

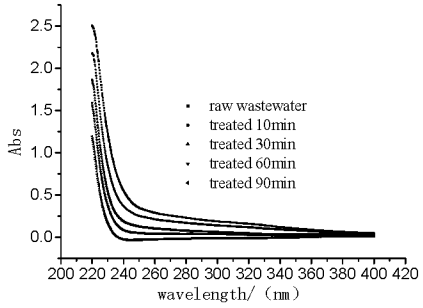

Figure 5. UV spectral change of coking wastewater with different reaction time

Comparison of Traditional 3D Electronic Oxidation and 3D Electronic Oxidation Combined with Fenton Oxidation

Under the same operating conditions, Figure 6 shows the results between 3D electrode combined with Fenton reagent and general 3D electrode reactor on the TOC removal rate of coking wastewater. As shown in Figure 6, 3D electrode combined with Fenton reagent shows superior degradation performances than the general 3D electrode reactor does after treatment at 30min and their TOC removal rate are 56.4% and 41.2%, respectively, which may be attributed to the synergistic effect of 3D electrode electro-oxidation and Fenton reagent oxidation at the former 30min. However, with the increase of reaction time, 3D electrode electro-oxidation dominates the whole reaction system gradually, and H_2O_2 in Fenton reagent is almost consumed completely after 70min of electrolysis time. The two methods of treatment effect will gradually approach together. The results of this study reveal that 3D electrode combined with Fenton reagent process will be available for overcoming higher energy consumption of general 3D electrode oxidation.

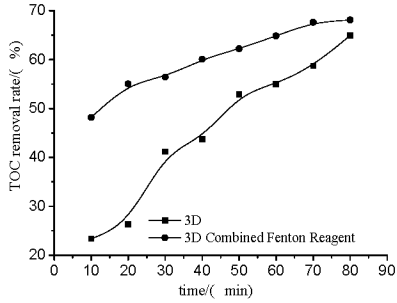

Figure 6. Comparison of treatment efficiency of 3D electrode reactor and 3D electrode combined Fenton reagent

Conclusions

The 3D electrode combined with Fenton reagent method is very promising for advanced treatment of coking wastewater. In the investigated conditions, complete mineralization of organic pollutants and removal of TOC is almost achieved. Compared to the single 3D electrode oxidation, the 3D electrode combined with Fenton reagent method can significantly speed up and improve the treatment efficiency of coking wastewater. The single factor test shows that the optimal parameters are pH 3.5, H_2O_2 dosage 17.6mmol/L, the reaction time 90min, $FeSO_4.7H_2O$ dosage 3.5mmol/L, respectively, and the TOC removal rate can reach 51.7%. This work provides

an efficient technique to avoid higher operation cost in general 3D electrode oxidation, which is also feasible for engineering application.

References

[1]Zhu X. et al., "Optimization of Fenton and electro-Fenton oxidation of biologically treated coking wastewater using response surface methodology," *Separation and Purification Technology*, 81(3)(2011),444-450.

[2]Kim Y.M. et al., "Inhibitory effects of toxic compounds on nitrification process for cokes wastewater treatment," *Journal of Hazardous Materials*, 152(3)(2008),915-921.

[3]Zhang M. et al., "Adsorption of organic pollutants from coking wastewater by activated coke," *Colloids and Surfaces A: Physicochemical and Engineering Aspects*, 362(1-3)(2010),140-146.

[4]Wang J. et al.,"Experimental research on advanced treatment process of coking-plant wastewater," *Chinese Journal of Environmental Engineering*, 3(10)(2009),1804-1807(in Chinese).

[5]Zhang L. et al.,"Advanced treatment of coking wastewater using three-dimensional fluid bed electrode reactor", *Ecology and environmental sciences*, 21(2)(2012) ,370-374(in Chinese).

[6]Jiang W. et al., "Combined fenton oxidation and biological activated carbon process for recycling of coking plant effluent",*Journal of Hazardous Materials*,189(1-2)(2011),308-314.

[7]State Bureau of Environmental Protection. The Editorial Pool of Analysis Method of Water and Wastewater. Analysis Method of Water and Wastewater. 4rd ed. Beijing: China Environmental Science Press, 2002.

[8]Li D.,"The progress of catalytic technologies in water purification:A review," *Journal of Environmental Sciences*, 21(6) (2009),713-719.

[9]XiaoY. et al., "Degradation of polyvinyl-alcohol wastewater by Fenton's reagent: Condition optimization and enhanced biodegradability," *Journal of Central South University of Technology*, 18(1)(2011),96-100.

[10]Xiao K. et al.,"Degradation of nitrobenzene wastewater by three-dimension electrode method coupling electro-Fenton,"*Journal of South China University of Technology (Natural Science Edition)* ,38(8)(2010),131-135.(in Chinese)

[11]Shi Y. et al., "Treatment of landfill leachate by three-dimensional-electrode electro-Fenton process, "*Journal of Tianjin University(Science and Technology)*, 42(3)(2009),248-252.(in Chinese)

Characterization of Minerals, Metals, and Materials 2015
Edited by: John S. Carpenter, Chenguang Bai, Juan Pablo Escobedo, Jiann-Yang Hwang, Shadia Ikhmayies, Bowen Li, Jian Li, Sergio Neves Monteiro, Zhiwei Peng, and Mingming Zhang
TMS (The Minerals, Metals & Materials Society), 2015

CHARACTERIZATION OF STEELMAKING DESULFURIZATION SLAG

Mallikharjuna R. Bogala[1], Mingming Zhang[2], Ramana G. Reddy[3*]

[a]*Graduate Student,* [b]*Senior Research Engineer,* [c]*ACIPCO Endowed Professor*
[1,3]*Department of Metallurgical and Materials Engineering, The University of Alabama, Tuscaloosa, AL 35487, USA*
[2]*ArcelorMittal Global R&D, 3001 E. Columbus Dr. East Chicago, IN 46312, USA*

Abstract

Steelmaking desulfurization slag samples were characterized using chemical, X-ray diffraction (XRD), scanning electron microscopy (SEM) and energy dispersive spectrometry (EDS) methods. The objective of this work is to investigate the occurrence of sulfur and phosphorus components in the slag samples and to identify their origin and associations with the iron phases. Thermodynamic calculations results confirm the presence of phosphorus and sulfur components in the slag sample at high temperatures (1400 to 1800°C). The main constituents of slag include Ca_3SiO_5 (28.1%), MgO (9.31%), $Ca_3(PO_4)_2$ (9.18%), CaS (8.39%) and CaO (5.68%). The major phosphorus and sulfur components of the slag are Ca_3PO_4 (99.2%) and CaS (79.3%) respectively. Characterization studies indicate the presence of microparticles of different sizes and shapes in the slag sample. Elemental analysis of these particles confirm the presence of major elements (O, Mg, Al, Si, S, Ca and Fe) in the slag sample.

Keywords: Steelmaking, desulfurization, slag, Gibbs energy, P and S components

Introduction

Steelmaking slag is one of the main by-products generated during the separation of molten steel from the impurities of steelmaking furnaces, either in basic oxygen furnace (BOF) of integrated steel plants or in electric arc furnace (EAF) mini-mills of the specialty steel plants [1, 2]. These steelmaking slags typically contain 20 – 25% iron and they are important iron unit supply for the upstream iron making. The iron in steelmaking slag has the advantage of either being partially converted to iron oxides, such as Magnetite (Fe_3O_4) or Wüstite (FeO), or being completely reduced to metallic Fe [3]. Commonly, the low iron content steelmaking slag is sold as aggregate, stockpiled, inventoried or in the worst case, it is landfilled at the costs of US $10–100 per ton. Various technologies have been developed to obtain higher recoveries of iron units in the steelmaking slag before its final application, both to improve the iron utilization efficiency and to reduce the slag volume.

According to the American Iron and Steel Institute (AISI) report on 'Steel Industry Technology Roadmap', every year only ~ 1.8 million tons of iron units is recycled from the total slag containing 3.9 million tons of iron units by US steel mills [4]. But, these are low estimates because only BOF and EAF slags were considered, while all other steel mill by-products such as

* Corresponding author. Tel.: +1 205 348 4246; fax: +1 205 348 2164.
E-mail address: rreddy@eng.ua.edu (R.G. Reddy).

hot metal pretreatment (desulfurization) slags and ladle slags were excluded from the production calculations of total slag. Table I summarizes the information from 'U.S. Geological Survey Minerals Yearbook' on iron and steel slag sold or used during the year 2002 by United States [5]. Therefore, there is a huge potential for the development of refining technology to improve iron recovery for each of the aforementioned steelmaking slags.

Table I. Iron and Steel slag sold or used in the United States in 2002 [5]

	Blast furnace slag[1]			Steel	Total iron
	Air-cooled	Granulated	Total[2]	furnace slag	and steel slag[2]
Quantity[3] (million metric tons)	7.4	3.7	11.0	7.9	19.0
Value[e,4] (million dollars)	55	210	265	29	294

[e]Estimated
[1]Excludes expanded slag to protect company proprietary data. The quantity is very small (less than 0.1 unit).
[2]Data may not add to totals shown because of independent rounding.
[3]Quantities are rounded to reflect inclusion of some estimated data and to reflect inherent accuracy limitations of reported data.
[4]Values are rounded because of the inclusion of a large estimated component.

For desulfurization slags, the main contaminant in slag is from sulfur and it is removed from the liquid ferro-alloys after deoxidation at high temperatures of 1550 - 1600°C [6]. The operation is performed by stirring the deoxidized liquid steel with a slag rich in lime. Usually, the slag is very alkaline in nature and it contain no easily reducible oxide that might increase the oxygen content of the metal. Any iron recovery technologies for the slags has to be effective in the separation of iron metal from sulfur and other undesired constituents.

Obtaining a comprehensive understanding on the composition and properties of the steelmaking desulfurization slags is very essential for assessment of the iron recovery technology. Therefore, the current study is mainly focused on the characterization of the chemical and microstructural properties and prediction of main phases of sulfur and phosphorus in the slag at high temperatures.

Materials and Methods

Steelmaking desulfurization slag sample needed for the current study was obtained from ArcelorMittal. About 5 to 10 g of the as-received greyish-black slag sample was placed in a mortar and sufficient amount of acetone solvent was added to it. The slag sample was grinded using a pestle, thoroughly mixed and then completely dried. The sample powder was characterized for (i) the phase and structure of slag components using X-ray diffraction (XRD), (ii) the surface morphology using high resolution scanning electron microscope (SEM) and (iii) the elemental composition using energy dispersive spectrometer (EDS) attached to the SEM instrument.

The initial weight% of slag components (from Table III) was entered as input and Gibbs energy minimization was performed to predict the major components associated with sulfur and phosphorus at high temperatures (1400 - 1800°C) and 1 atm pressure.

Results and Discussions

The initial composition of different components present in the as-obtained slag sample from ArcelorMittal is listed in the Table II. The significant components of the greyish-black slag sample are CaO, Fe (total), SiO_2, MgO, Al_2O_3 and MnO. Thermodynamic modelling studies were conducted to determine the main components associated with sulfur and phosphorus at high temperatures (1400 - 1800°C) and 1 atm pressure.

Table II. Weight% of different components in slag sample

Component	Al_2O_3	C	CaO	Cr_2O_3	Fe†	LOI*	MgO	MnO
Weight%	4.88	0.89	33.20	0.29	22.86	3.83	9.6	3.74
Component	Na_2O	P◊	S	SiO_2	Sr	TiO_2	ZrO_2	K_2O
Weight%	0.1	0.21	0.09	10.2	0.01	0.52	0.08	0.01

*†Fe = FeO, Fe_2O_3, Fe_3O_4, FeP, FeS and FeS_2; ◊P = CaP_2O_4 and CaP_2; *LOI = Loss-on-ignition*

Thermodynamic Modelling

Table III lists the initial wt.% of slag components that was given as input to the 'Equilibrium Compositions' module of HSC 7.1 software at room temperature. LOI from Table II was excluded for the calculations. $Ca(PO_3)_2$ and Ca_3P_2 phases were considered for CaP_2O_4 and CaP_2 phases (of Table II) respectively, since the later phases were not recognized by the HSC and the total wt% of P (0.21) is equally divided between the components. The total composition of Fe (22.86%) is evenly distributed among all the Fe components (FeO, Fe_2O_3, Fe_3O_4, FeP, FeS and FeS_2).

Table III. Input weight% of the slag components for thermodynamic calculations

Components	Al_2O_3	C	CaO	Cr_2O_3	FeO	Fe_2O_3	Fe_3O_4	FeS	FeS_2	FeP	MgO
Weight%	5.63	1.03	38.30	0.33	4.40	4.40	4.40	4.40	4.40	4.40	11.08
Components	MnO	Na_2O	$Ca(PO_3)_2$	Ca_3P_2	S	SiO_2	Sr	TiO_2	ZrO_2	K_2O	
Weight%	4.31	0.12	0.12	0.12	0.10	11.77	0.01	0.60	0.09	0.12	

Gibbs energy minimization was performed with 30 iterations on the initial input data of Table III at temperatures 1400 - 1800°C. A total of 580 compounds (solids, liquids and gases) were identified within the temperature range. Table IV shows the list of some components of slag in descending order of wt.% at temperatures 1400 - 1800°C. The major components include Ca_3SiO_5, MgO, $Ca_3(PO_4)_2$, CaS, CaO, Fe, Al_2O_3, $Ca_3Si_2O_7$, $CaSiO_3$ and $Mn(CO)_{10}$. Among all the determined phases, a total of 90 phosphorus components were predicted and Table V lists some of the P-components. The first 10 components of phosphorus based on wt.% are: $Ca_3(PO_4)_2$, $Ca_2P_2O_7$, P_4S_7(g), P_2O_3(l), $AlPO_4$, FeP, PO(g), $NaPO_3$, P and $NaPO_2$(g). The major P-component predicted at 1400 - 1800°C is Ca_3PO_4 (average wt% = 99.2).

Similarly, a total of 132 components containing sulfur were predicted and Table VI lists some of the S-components. The first 10 components of sulfur based on wt.% are: CaS, MnS, FeS(l), FeS, $Fe_{0.877}S$, P_4S_7(g), MgS, S(l), SrS and S. The major S-component predicted at 1400 - 1800°C is

CaS (average wt% = 79.3). Other significant components are MnS, FeS(l), FeS, and $Fe_{0.877}S$ with average wt% of 5.68, 5.03, 4.89 and 4.06 respectively. Therefore, phosphorus and sulfur components of calcium are predominant at high temperatures.

Characterization

The slag sample was mixed with acetone and grinded to uniform particle size using pestle and mortar. Small amounts of the sample were used to obtain the diffraction pattern using Phillips XRD instrument. Figure 1 shows the XRD spectrum of slag sample obtained at diffraction angles ($2\theta = 20^{o}$ - 120^{o}). A comparison of the diffracted peaks of Figure 1 with the standard ICDD diffraction data reveals the complex X-ray signal pattern of several slag components.

Table IV. Weight% of major slag components determined using thermodynamic calculations

	Temperature (^{o}C)				
Components	1400	1500	1600	1700	1800
Ca_3SiO_5	28.3	28.3	28.1	27.9	27.7
MgO	10.07	9.75	9.36	8.92	8.47
$Ca_3(PO_4)_2$	9.16	9.22	9.26	9.26	9.02
CaS	8.35	8.37	8.41	8.45	8.36
CaO	4.76	5.20	5.65	6.12	6.67
Fe	5.10	4.81	4.71	4.66	4.59
Al_2O_3	4.71	4.71	4.61	4.41	4.13
$Ca_3Si_2O_7$	4.35	3.66	3.02	2.41	1.86
$CaSiO_3$	3.63	3.83	3.97	4.02	3.98
$Mn_2(CO)_{10}$	3.71	3.73	3.76	3.78	3.80
$CaMgSiO_4$	2.21	2.08	1.93	1.75	1.55
MgO(l)	0.98	1.23	1.50	1.78	2.07
Al_2O_3(l)	0.41	0.66	0.97	1.36	1.79
$Fe_{0.947}O$	1.09	1.24	1.36	1.47	1.59
$FeAl_2O_4$	1.52	1.15	0.87	0.65	0.49
FeO(l)	1.29	1.38	1.43	1.48	1.53
FeO	1.29	1.38	1.43	1.48	1.53
CaO(l)	0.36	0.54	0.78	1.10	1.53
$Fe_{0.945}O$	1.11	1.12	1.10	1.08	1.07
$MnTiO_2$	1.11	1.11	1.12	1.12	1.09
MnO	0.93	0.87	0.76	0.65	0.55
MnS	0.71	0.66	0.60	0.55	0.48
FeS(l)	0.46	0.51	0.54	0.57	0.58
FeS	0.44	0.49	0.53	0.56	0.57
$MgSiO_3$(l)	0.15	0.24	0.34	0.45	0.57
$MgSiO_3$	0.25	0.29	0.34	0.45	0.57
MnO(l)	0.49	0.54	0.55	0.54	0.53

Table V. Weight% of major P- components determined using thermodynamic calculations

	Temperature (°C)				
P -component	1400	1500	1600	1700	1800
$Ca_3(PO_4)_2$	99.93	99.82	99.57	99.20	97.35
$Ca_2P_2O_7$	0.049	0.123	0.290	0.636	1.294
P_4S_7(g)	0.000	0.000	0.000	0.000	1.147
P_2O_3(l)	0.000	0.002	0.009	0.041	0.150
$AlPO_4$	0.004	0.008	0.015	0.026	0.042
FeP	0.001	0.002	0.006	0.015	0.031
PO(g)	0.000	0.000	0.000	0.002	0.012
$NaPO_3$	0.003	0.006	0.007	0.008	0.008
P	0.000	0.000	0.001	0.002	0.007
$NaPO_2$(g)	0.000	0.000	0.001	0.002	0.004
Fe_2P	0.000	0.001	0.001	0.002	0.004
$Mg_3(PO_4)_2$	0.000	0.000	0.000	0.001	0.002
PS(g)	0.000	0.000	0.000	0.000	0.002
NaOP(g)	0.000	0.000	0.000	0.001	0.001

Table VI. Weight% of major S-components determined using thermodynamic calculations

	Temperature (°C)				
S- Component	1400	1500	1600	1700	1800
CaS	79.73	79.34	79.33	79.37	78.77
MnS	6.808	6.216	5.673	5.145	4.546
FeS(l)	4.376	4.824	5.137	5.355	5.465
FeS	4.198	4.659	4.991	5.232	5.366
$Fe_{0.877}S$	4.392	4.260	4.071	3.879	3.679
P_4S_7(g)	0.000	0.000	0.000	0.000	1.001
MgS	0.240	0.322	0.416	0.513	0.603
S(l)	0.077	0.129	0.199	0.294	0.416
SrS	0.072	0.071	0.070	0.069	0.067
S	0.010	0.016	0.024	0.035	0.049
Na_2S	0.029	0.042	0.018	0.006	0.002
Na_2S(l)	0.021	0.031	0.013	0.005	0.002
S_2(g)	0.000	0.001	0.003	0.009	0.022
SO(g)	0.000	0.000	0.002	0.005	0.015
S(g)	0.000	0.000	0.001	0.003	0.009
NaS	0.005	0.006	0.005	0.003	0.002
SO_2(g)	0.000	0.000	0.001	0.002	0.007
PS(g)	0.000	0.000	0.000	0.000	0.002

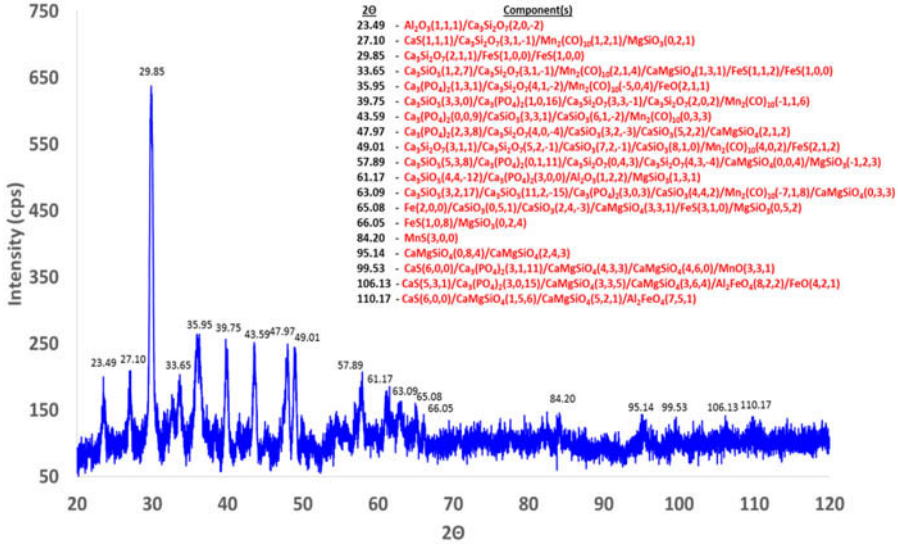

Figure 1. X-ray diffraction patterns of steelmaking slag sample

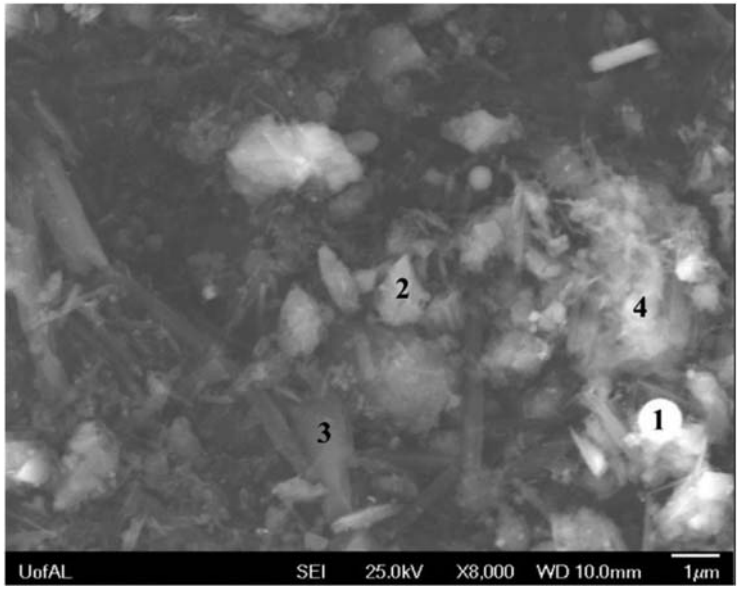

Figure 2. SEM image of different microparticles (1 - 4) in the slag sample

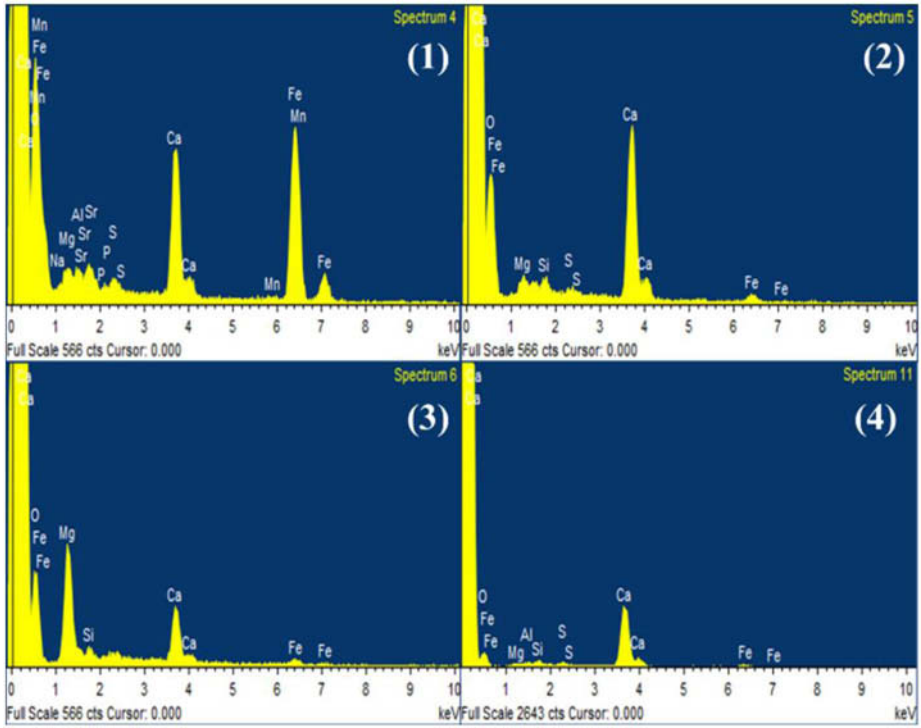

Figure 3. EDS spectra of different slag microparticles (1 - 4) shown in the SEM image (Figure 2). The huge signal at ~ 0 keV is due to the carbon tape

Peaks were assigned manually and presence of different slag components (Al_2O_3, $Ca_3Si_2O_7$, CaS, $Mn_2(CO)_{10}$, $MgSiO_3$, FeS, Ca_3SiO_5, $CaMgSiO_4$, $Ca_3(PO_4)_2$, Fe, MnS, FeO and Al_2FeO_4) were confirmed. Morphology and elemental analysis of the slag sample powder (on carbon tape) was determined using SEM and EDS methods. Figure 2 shows the SEM image of the slag sample powder showing different microstructures with variable size and shapes. The slag sample was then subjected to elemental analysis using the EDS detector attached to the SEM. The EDS of the selected microparticles (1- 4) of different shapes from the SEM image (Figure 2) is shown in the Figure 3. The presence of important elements like O, Mg, Al, Si, S, Ca and Fe in the slag sample was confirmed using the elemental composition data of EDS. The relative percent compositions of the elements varied for each of the different particles. Round white particles have high Fe content, rhombohedral/diamond particles have more Ca content, sponge particles have high Mg content and fibrous particle have more Al content. The elemental analysis matches well with the thermodynamic predictions for the majority of slag components. However, no presence of elemental phosphorus was identified in the slag sample using the EDS method.

Conclusions

Thermodynamic calculations were conducted on steelmaking slag sample to predict the major components of phosphorus and sulfur at high temperatures (1400-1800°C). The major components of slag within the temperature range include Ca_3SiO_5 (28.1%), MgO (9.31%) $Ca_3(PO_4)_2$ (9.18%), CaS (8.39%) and CaO (5.68%). The major components of phosphorus and sulfur determined at the high temperatures are Ca_3PO_4 (99.2 %) and CaS (79.3 %) respectively. Characterization studies of the slag sample was carried out using XRD, SEM and EDS techniques. The sample powder contain microparticles with different sizes and shapes. Elemental analysis confirm the presence of major elements (O, Mg, Al, Si, S, Ca and Fe) in the slag sample.

Acknowledgements

The authors are thankful to the financial support from the National Science Foundation (NSF) agency, Grant No. DMR-1310072 and American Cast Iron Pipe Company (ACIPCO) during the course of the project. The authors also acknowledge 'The University of Alabama' for providing the access to analytical and computational facilities in successful completion of the research work.

References

[1] Dippenaar, R., "Industrial uses of slag (the use and re-use of iron and steelmaking slags)," *Ironmaking & steelmaking*, *32*(1), 35-46, 2005.

[2] Manning, C. P., and Fruehan, R. J., "Emerging technologies for iron and steelmaking", *JOM*, *53*(10), 36-43, 2001.

[3] Chatterjee, A., "Hot metal production by smelting reduction of iron oxide", *PHI Learning Pvt. Ltd.*, 2010.

[4] AISI, 2001. American Iron and Steel Institute, "Steel Industry Technology Roadmap", *Strategic Planning for Research and Development Committee, Chicago*, 5–82, 2001.

[5] Van Oss, H. G., "Slag-iron and steel", *US geological survey minerals yearbook*, 70, 1-6. 2002

[6] Bhardwaj, B. P., "The Complete Book on Ferroalloys", *NIIR Project Consultancy Services*, 2014.

Characterization of Minerals, Metals, and Materials 2015
Edited by: John S. Carpenter, Chenguang Bai, Juan Pablo Escobedo, Jiann-Yang Hwang, Shadia Ikhmayies, Bowen Li, Jian Li, Sergio Neves Monteiro, Zhiwei Peng, and Mingming Zhang
TMS (The Minerals, Metals & Materials Society), 2015

DEVELOPMENT AND CHARACTERIZATION OF NANOMATERIALS FOR ZINC VAPOR CAPTURE

Paul S. Korinko[1] and Simona E. Hunyadi Murph[1]
[1]Savannah River National Laboratory, Aiken, SC 29808

Keywords: Zinc Vapor, Nanoparticles, Characterization, Getters

Abstract

To address a radiological contamination event, a materials and process project was initiated. During the course of this project, processes and materials were developed that successfully captured zinc vapors physically and chemically, respectively. However, the physical traps were placed in an undesirable area and it was determined that the chemically captured zinc reactions was reversible. Consequently, advanced nanomaterials are being developed to capture zinc vapors. The current state of the art of the science and engineering of these materials and their efficacy for zinc capture and retention is discussed in this paper.

Introduction

A radiological contamination [1] event several years ago, resulted in the planning and execution of a development program to capture and retain zinc vapors [2]. The initial approach resulted in physical [3] then chemical trapping methods for zinc capture [4]. During a simulated process evolution, it was observed that copper–tin alloy (bronze) zinc getters were prone to reversible reactions [5]. Dezincification is a known issue for brasses especially at high temperatures under vacuum conditions, but the temperature range of interest for this application is lower than what has typically been described [6, 7].

Due to the reversible zinc getter behavior for bronze, an investigation into using materials of higher temperature, and presumed higher thermal stability was conducted. Bulk cobalt, which is expected to react with zinc but not with hydrogen [8], was initially used but the zinc vapors physically deposited onto the substrate and no alloying occurred. Consequently, the concept of using nanomaterials of suitable composition, reactivity and process stability evolved. Nanomaterials exhibit unique properties due to their large surface area and quantum size effects [9, 10]. It was expected that they would be able to react at relatively low homologous temperatures, would coarsen due to the reactions, and would be more stable than the bronze materials that were initially tested. This paper presents preliminary results for gold, cobalt, and gold-cobalt alloys nanomaterials that were grown on stainless steel wool trap material.

Experimental

A total of seven different nanomaterials were grown on Type 316L stainless steel wool (SS-W), the material currently used for the process lid. The as-received stainless steel wool (control) was characterized using a Keyence VR 3000 profilometer and scanning electron microscopy (SEM).

All of the nanomaterials were grown onto substrates of SS-W that were nominally 50 mm diame-

ter x 10 mm diameter pads. The nanomaterials were grown from aqueous solutions using conditions that would produce the desired deposit size and shape. Gold and cobalt nanoparticles were prepared by a citrate reduction approach [9-11] in the presence of SS-W. With this synthesis, $1.25x10^{-4}M$ Au^{3+} was heated to boiling and 1 wt % sodium citrate solution was added. The boiling was continued until the solution turned ruby red, indicating the formation of gold nanoparticles. Gold cobalt alloys nanoparticles were prepared by a similar procedure by reducing a mixture of $1.25x10^{-4}M$ Au^{3+} and $1.25x10^{-4}M$ Co^{2+}. Core-shell Au-Co nanostructures were prepared in two steps (a) synthesis of Au (0) nanosphere core seeds and (b) Co shell by the procedure described above. The resulting nanoparticles were purified by three-five steps washing in deionized water.

The nanoparticle (NP) deposits were characterized using scanning electron microscopy (SEM), energy dispersive X-ray analysis (EDX) and EDX elemental mapping to elucidate their morphology, topography and composition. The NP optical properties were evaluated by UV-Vis spectroscopy. The adhesion of the NP deposit to the SS-W was tested using an ultrasonic cleaner and an aqueous solution using fixed time increments. The liquid was analyzed using inductively coupled plasma atomic emission spectroscopy (ICP-AES) to determine the amount of the deposit that was removed. ICP-AES experiments were also performed to quantify the amount of metals present on the support (Zn, Co, Au). This technique allowed quantification of chemical composition of our colloids and accurate Zn capturing/loading information.

Samples were exposed to zinc vapor from a high vacuum thermal deposition apparatus. The system is comprised of an all metal seals and Conflat™ flanges. The samples were supported on perforated metal with a stack of up to four samples being exposed during one exposure. A bronze pellet was included in the exposure as an experimental control and to verify that the deposition apparatus operated correctly. The zinc vaporization and filter temperature conditions, 350°C for both and an initial vacuum pressure of approximately 5 x 10^{-6} Torr, used were consistent with previous work [5].

Results

The SS-W was examined optically using the Keyence VR3000 with the results shown in Figure 1. Note the roughened surface condition of the wire filament. The nominal diameter of the wires is 50 µm. The surface roughness was also measured and it indicates a roughness of 5.44 Ra.

The nanoparticle's optical properties were evaluated by UV-Vis spectroscopy. In deionized water, the gold nanoparticles display the characteristic peak at around 525 nm that corresponds to the plasmon band (collective oscillation of electrons) for spherical gold nanoparticles while the cobalt nanospheres have

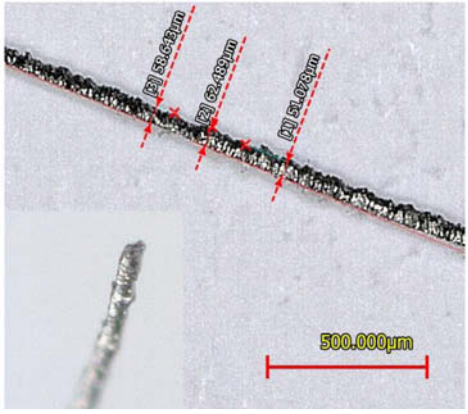

Figure 1. Appearance of a SS-W wire filament showing the surface condition and the shape.

a plasmon band around 384 nm [9-11]. The UV-Vis spectra of the bimetallic Au-Co nanostructures differ from the monometallic colloids. A continuous red shift of the Au nanospheres plasmon band, originally at approximatively 525 nm, confirms the formation of bimetallic Au-Co colloids with a plasmon band around 533 nm [10-12]. The nanoparticle composition and chemistry can be monitored using the solution color (inset photo) Figure 2.

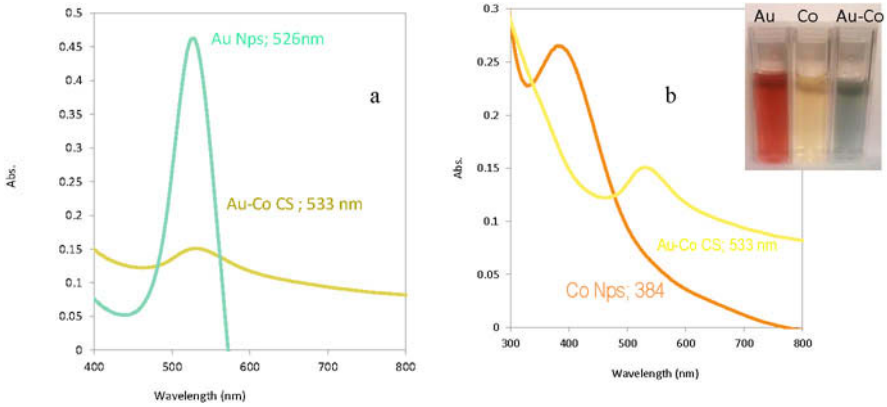

Figure 2. (a) Appearance of the solution and (b) the UV-Vis spectra for Au and Au-Co (c) the UV-Vis spectra for Co and Au-Co.

Nanoparticles of Au were grown onto SS-W using the described procedures. The Au NPS as-deposited condition of the wire is shown in Figure 3. Two different morphologies are formed on the SS-W surfaces, nanospheres and spherical nanoclusters. The nanospherical particles are nominally 26 nm in diameter (30%) while the spherical nanoclusters, formed by agglomeration of the 26 nm nanospheres, are approximatively 78 nm (70%) in diameter with a relative spacing of 100 nm. SEM images show that the nanoparticles are distributed over the entire wire surfaces. Despite the surface condition shown for the wires, the particles appear to be randomly deposited on the wire surface. This result is not surprising since the SS-W surface is non-uniform. The SS-W has a surface roughness of 5.44 RA. Figure 3 shows a multitude of valleys, steps and crevices that may be critical for random nanoparticle deposition.

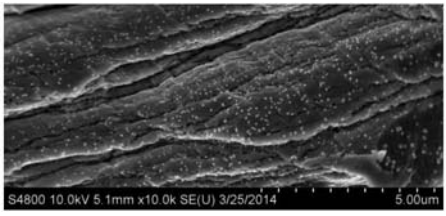

Figure 3. Gold nanoparticles deposited onto the 50 micron SS-W wires. Note the small size and random distribution.

Three Au-Co alloys and alloy-types with various quantities and morphologies of Au and Co were also deposited on SS-W. One of the Au-Co alloy samples is shown in Figure 4. In general, these nanomaterials also exhibit random particle deposition with a size range of 30 to 220 nm in diameter, for single and agglomerated particles, respectively. Selected sample particle size ranges are listed in Table I.

Single samples of Au, Co, and Au-Co alloy functionalized SS-W were exposed to zinc vapor using previously established conditions [5]. The typical thermal and pressure profiles observed are indicated in Figure 5. The filter reaches the target temperature before the zinc is heated so that the zinc vapor can be captured at the desired temperature. Previous work indicated that low temperatures result in physically trapped zinc with inadequate adhesion [5].

Visual examination of the bare and nanomaterial treated SS-W exposed to zinc did not reveal any change in color as is typically observed for the bronze pellets which are initially orange (bronze) colored and change to a golden tint (brass) after zinc alloying, as shown in Figure 6 for SS-W and bronze pellets, respectively. There may be a slight change in the sheen of the SS-W indicated by the photos, but this difference may simply be due to changes in lighting between the photos.

EDX microanalysis of Au, Co, and Au-Co nanomaterials before and after Zn exposure was performed to evaluate nanomaterial composition of mono and bimetallic colloids with representative data presented in Figure 7.

All of the zinc exposed samples were examined using SEM and EDX to characterize how effective the nano-materials were as zinc getters. SEM analysis was needed since mass changes were unmeasurable due to wire breakage, wire loss, and moisture evaporation during weighing. The control SS-W sample was examined after zinc exposure and no zinc was detected. The results are shown in Figure

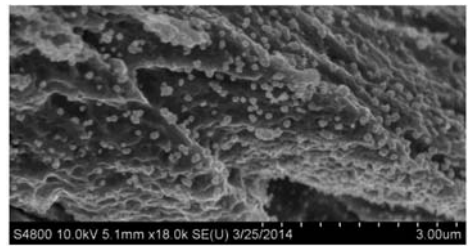

Fig.4. This is an image of the as deposited Au-Co (#1) on the stainless steel wire. The particles are generally randomly oriented a spherical shape. There are some agglomerated particles as well.

Table I. Particle size distribution of the gold-cobalt alloys and alloy-type nanostructures.

Au-Co Alloy (nm)	Au-Co CS (nm)	Au-Co-Co ACS (nm)
30	30	42
128	80	71
		101
		220

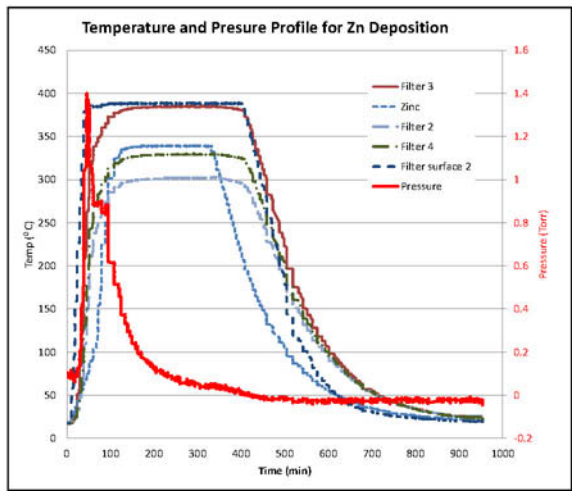

Figure 5. Typical zinc thermal and pressure response.

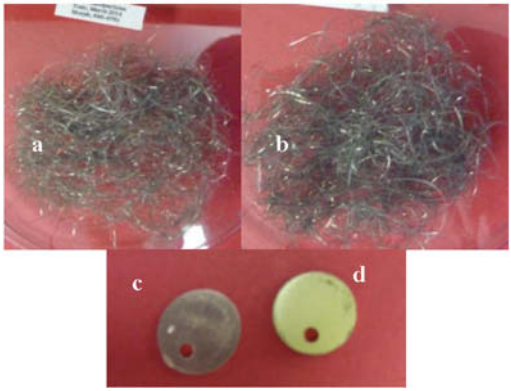

Figure 6. Appearance of SS-W before (a) and after (b) zinc exposure and typical bronze pellets before (c) and (d) after zinc exposure.

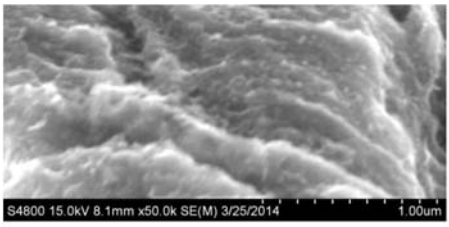

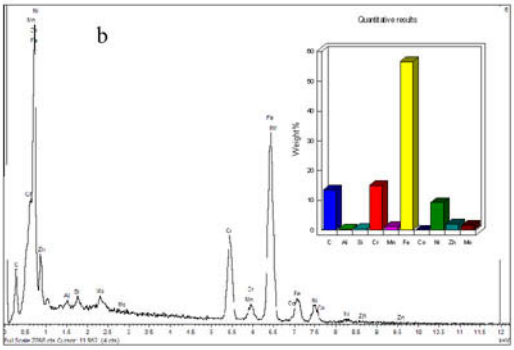

Figure 7 (a) Appearance of nano-cobalt (Co CT #4) deposited on SS-W after zinc exposure; (b) showing zinc was present on the sample, composition indicated in Table II.

8. Semi-quantitative analysis was conducted on the sample as well as X-ray dot mapping. The EDX mapping analysis demonstrates the accurate location of the elements of interest: Au, Co and Zn. The chemical analyses for the zinc exposed samples are listed in Table II.

Figures 7a, 9, and 10a show the surface appearance of Au, Co, and Au-Co alloy samples, respectively, after zinc exposure. The samples all exhibit coarsening of the nanodeposit getters. The relative size changes are shown in Figure 12. All of the samples that were treated with nanomaterials were effective at gettering the zinc vapor at a nominal temperature of 350°C. The Zn content ranged from ~2.5 to ~7 wt %. This range has little overall significance, since the areas examined include a substantial amount of non-treated SS-W as well as the beam interaction volume as indicated by the X-ray dot maps. These results clearly show that all the nanomaterials capture zinc while the control SS-W remains inert; a result that is consistent with the practical experience [1].

More rigorous metal quantification was conducted using ICP-AES. All nanoparticles deposited onto solid supports were sonicated at regular time intervals (10 min, 30 min and 60 min) in deionized water. The resulting aqueous colloids were dissolved in aqua regia and subjected to ICP-AES in order to quantify the amount of metals present. Representative data are presented in Figure 12.

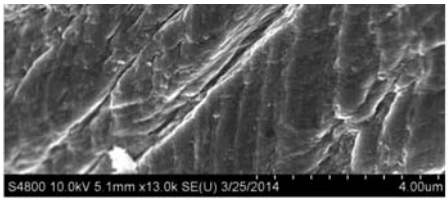

Figure 8. Appearance of baseline SS-W after zinc exposure. Zinc was not detected on the surfaces as indicated in Table 2.

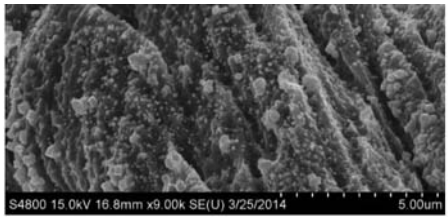

Figure 9. Appearance of nano-gold deposited on SS-W after zinc exposure. Zinc was present on the sample as indicated in Table 2.

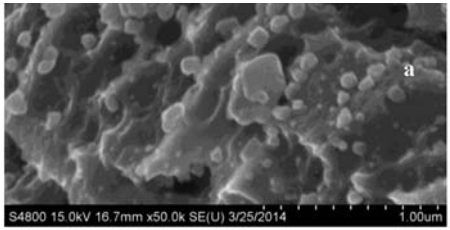

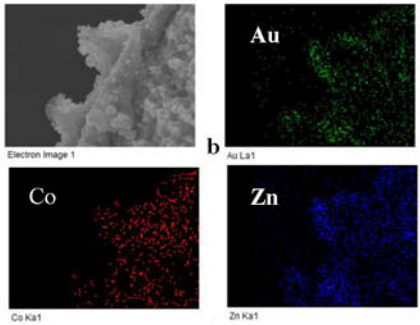

Figure 10. (a) Appearance of nano-gold-cobalt alloy deposited on SS-W after zinc exposure; and (b) X-ray dot map of the deposit, composition indicated in Table II.

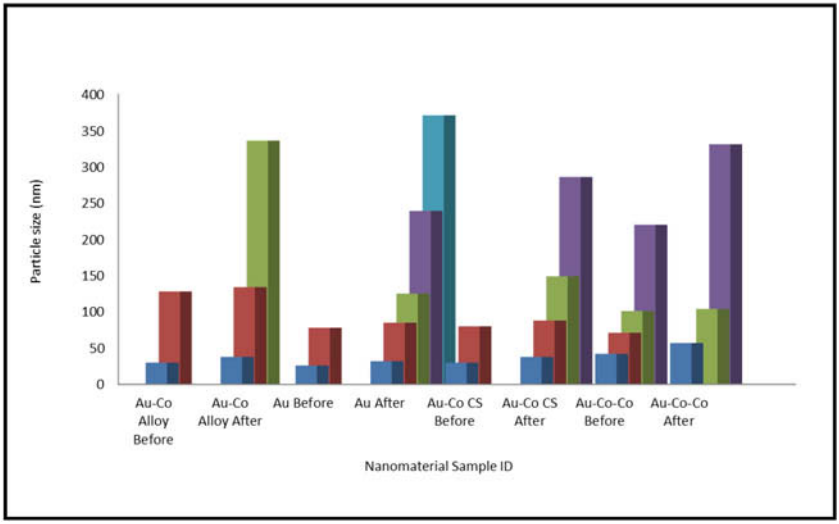

Figure 11. Zinc exposure increased the size of the particles observed

Table II. Composition of deposits based on semi-quantitative X-ray Energy Dispersion Analysis.

ID	#0	#1	#2	#3	#3	#4	#5	#5
Element	Wt %	Wt %	Wt %	Wt %	Wt %	Wt %	Wt %	Wt %
C K	10.98	11.16	24.62	5.53	56.03	4.55	14.75	53.57
O K	NM	2.85	4.01	0.89	5.01	NM	2.29	7.73
Al K	NM	0.36	NM	0.18	0.17	0.3	45.31	NM
Cr K	16.25	11.84	12.11	15.81	5.13	17.07	4.58	6.34
Mn K	NM	3.71	NM	1.05	NM	0.95	0.68	NM
Fe K	66.01	49.97	40.44	58.4	18.33	62.76	16.69	21.5
Co K	NM	NM	NM	0.04	0.07	0.33	0.08	0.01
Ni K	6.76	7.6	5.52	9.53	2.85	9.11	2.56	2.96
Zn L	NM	5.74	7.22	5.79	5.71	2.49	3.51	3.51
Au M	NM	6.77	6.08	2.78	6.71	NM	5.96	4.39
Mo L	NM	NM	NM	NM	NM	2.17	NM	NM
Si K	NM	NM	NM	NM	NM	0.27	NM	NM
Cu L	NM	NM	NM	NM	NM	NM	3.58	NM
Totals	100	100	100	100	100	100	100	100

#0 Control SSW; #1 Au-Co alloy; #2 Au; #3 Au-Co Coreshell; #4 Co CT; #5 Au-Co Co coreshell

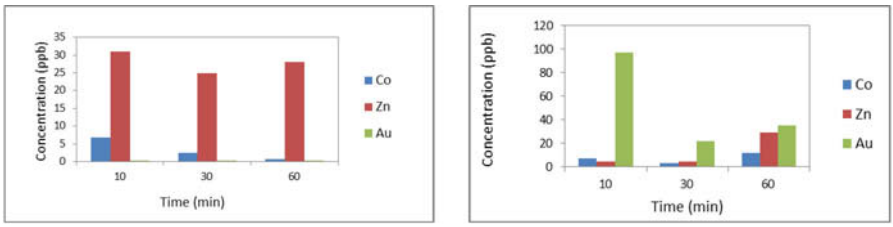

Figure 12. ICP-AES data on Au-Co colloids (a) before Zn exposure and (b) after Zn exposure.

Summary and Conclusions

Nanoparticles can be grown on stainless steel wool. The rough surface morphology and topography of the 50 nm SS-W lends itself to random particle growth with a narrow size distribution and some agglomeration.

Zinc is preferentially deposited onto SS-W that has been treated with nanoparticles. The zinc vapor does not deposit and grow on the control SS-W. Preliminary results indicate that Au nanoparticles are superior to Co and Au-Co alloys.

The composition of the nanoparticles after zinc exposure consists of 2.5-7% zinc, but the sample volume contains a significant amount of the SS-W substrate based on the high iron and chromium contents.

Acknowledgements

The authors would like to acknowledge Todd Woodsmall and Bob Snyder of the Savannah River Tritium Enterprise for providing funding for this work under contract DE-AC09-08SR22470. They would also like to recognize the contributions of summer interns Ansely Summer, Rebecca Lewis, and Jacqueline Polz.

References

1. Paul S. Korinko and Michael H. Tosten, "Analysis of Zinc 65 Contamination After Vacuum Thermal Process", *Journal of Failure Analysis and Prevention*, 13 (4), (2013), 389-395.
2. Paul S. Korinko, Andrew J. Duncan and Kevin J. Stoner, "Methods of Preventing the Spread of Zinc Contamination During Vacuum Processing", *Journal of Failure Analysis and Prevention,* 14 (1) (2014), 113-121.
3. Paul S. Korinko, "Zinc 65 Sequestration Path Forward" Correspondence/SRNL-L4410-2013-00004, Feb. 25, 2013.
4. M. Golyski and P. Korinko, "Effect of Thermal Processes on Copper-Tin Alloys for Zinc Gettering", SRNL Report/SRNL-STI-2013-00625, Oct. 8, 2013.
5. P. Korinko, "Effectiveness of Copper and Bronze for Zinc Capture", SRNL Report/SRNL-STI-2012-00616, Oct. 2012.
6. J.S. Broadley and E. Bevitt, "Evaporation of Zinc from Solid Solutions", United Kingdom Atomic Energy Authority, Risley, Warrington, Lancashire, March 1954.
7. I. Itoh and T. Hikage, "Dezincification Mechanism of Brass in Vacuum at High Temperature", *Trans Japan Institute of Metals*, 17 (1976) 165-169.
8. P.S. Korinko, "Zinc Mitigation Interim Report–Thermodynamic Study", SRNL Report/SRNL-STI-2010-00473, Dec 17, 2010.
9. S.E. Hunyadi Murph, et al., "Metallic and Hybrid Nanostructures: Fundamentals and Applications", in *Applications of Nanomaterials*, Vol.4: Nanomaterials and Nanostructures, Studium Press LLC, Houston TX, USA. 2012.
10. S.E. Hunyadi Murph, et al., "Tuning of Size and Shape of Au-Pt Nanocatalyst for Direct Methanol Fuel Cells" *J. Nanoparticle Research*, 13, (2011), 6347-6364.
11. S.E. Hunyadi and C.J. Murphy, "Synthesis and Characterization of Silver-Platinum Bimetallic Nanowires and Platinum Nanotubes", *Journal of Cluster Science*, 2009, 20, 319-330.
12. S.E. Hunyadi and C.J. Murphy, "Bimetallic Silver-Gold Nanowires: Fabrication and Use in Surface-Enhanced Raman Scattering" *J. Mater. Chem.*; Special Issue: Anisotropic Nanoparticles 16, (2006), 3929 - 3935.

Characterization of Minerals, Metals, and Materials 2015
Edited by: John S. Carpenter, Chenguang Bai, Juan Pablo Escobedo, Jiann-Yang Hwang, Shadia Ikhmayies, Bowen Li, Jian Li, Sergio Neves Monteiro, Zhiwei Peng, and Mingming Zhang
TMS (The Minerals, Metals & Materials Society), 2015

SEPARATION OF ROASTED COATING AND CORE IN DOUBLE-LAYERED PELLET ROASTING FOR PRETREATMENT OF SULFUR AND ARSENIC-BEARING GOLD CONCENTRATE

Tao Jiang, Xi-shan Li, Yong-bin Yang, Qian Li, Jie Ge

School of Minerals Processing and Bioengineering, Central South University, Changsha, Hunan, P R China, 410083

Keywords: Double-Layered Pellet Roasting, Sulfur & Arsenic-Bearing Gold, Refractory Gold Ore, Separation Method

Abstract

Compared with other pretreatments of sulfur & arsenic-bearing gold, double-layered pellet roasting has an advantage that sulfur dioxide and arsenic trioxide volatilizing from this refractory gold ores can be solidified into the coating without emission during the roasting. However, the separation of coating from roasted double-layered pellet should be focused on in the novel pretreatment. Based on the difference of physicochemical characteristics between roasted solidified coating and pellet core, several separation methods including grinding, drop impact and water quenching method had been systematically studied in this paper. The results showed that magnetic and gravity concentration could not obtain a satisfactory separation effect. The optimum separation rate of grinding was only 38.94% at grind time 12min, but it increased to 85.05% by drop impact under drop height 0.75m, drop times 20 and impact angle 45°, and that of water quenching taking advantage of slaking reaction of lime could approach 75.32%.

Introduction

Sulfur & arsenic-bearing gold ore is a typical refractory gold ore as regard to cyanide leaching. Those ores need pretreatment to remove sulfur and arsenic from pyrite, pyrrhotine, and arsenopyrit where gold occurs in the form of inclusion[1,2]. In contrast with other methods of pretreatment, double-layered pellet roasting has significant advantage in dealing with the type of refractory gold concentrate[3]. This method was developed from conventional roasting and bears high-efficiency and environment-friendly characteristics. However, so far there have been few researches referring to separation of roasted coating and core. Hence, the separation becomes the key procedure during the novel pretreatment.

In this study, several separation methods were detailedly studied, which were based on the difference of physicochemical characteristics between roasted solidified coating and core of pellet. Experiment on separation of roasted double-layered pellet would provide economic and effective way for industrial production.

Experiment

Materials

Sulfur and arsenic-bearing gold ore in which gold was enriched into concentrates after beneficiation comes from Gansu province in China. Main element composition and X-ray diffraction diagram are given in Table I and Figure 1.

Table I. Main element composition of sulfur & arsenic-bearing gold concentrate

Composition	Au*	S	As	TFe	FeO	SiO_2	Al_2O_3	CaO	MgO	Sb
Content/%	53.88	18.63	7.81	22.72	3.72	25.81	4.85	2.10	0.94	1.15

*represents the unit of Au composition is g/t.

It can be seen from Table I that the gold content in this ore accounts for 53.88 g/t, arsenic content 7.81% and sulfur content 18.63%. These show refractory characteristics of high arsenic and high sulfur. In order to clarify the phase of the main element, the chemical ingredient is analyzed by X-ray diffraction (XRD). The results are shown in Figure 1.

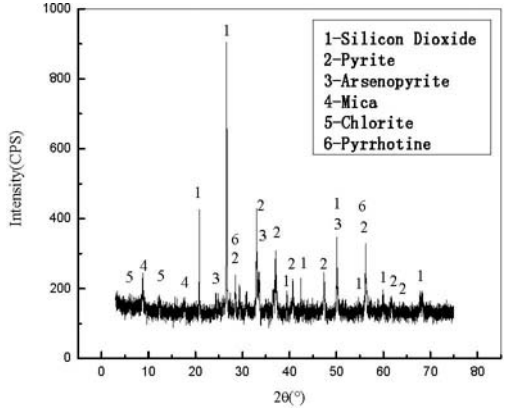

Figure 1. XRD diagram of raw gold concentrate

The XRD pattern analysis indicates that the main metallic mineral of raw gold ore are pyrite, arsenopyrite and pyrrhotine, and the main gangue minerals contained are silicon dioxide and mica.

Solidification agent used in experiment is hydrated lime with purity of analytical reagent(AR, ≥ 95%)[4-5]. However, lime cannot be used as solidification layer because of cracks in green ball resulting from lime slaking reaction. The usage of solidification agent is twice as much as pellet core of gold concentrate. After double-layered pellet roasting at 600℃ for 3h, the removal rate of arsenic and sulfur could reach 89.49% and 86.47% respectively.

Figure 2 and Figure 3 indicate chemical phase of roasted coating and core. The main chemical phase remaining in calcine existed only in the form of Fe_2O_3 and SiO_2. The arsenic and sulfur of coat layer mainly existed in the performance of $CaSO_3$, $CaSO_4$ and $Ca_3(AsO_4)_2$. Subsequently, when suitable separation method would be taken, the calcine could be easily applied to the process of cyanide treatment.

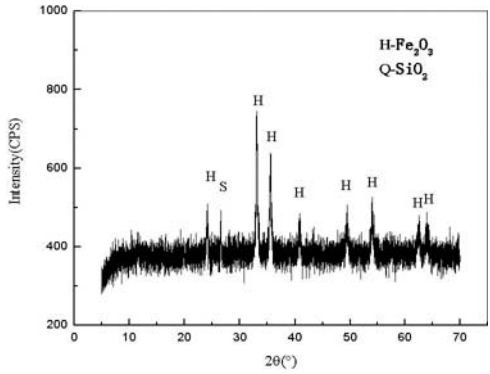

Figure 2. XRD diagram of calcine under double-layered pellet roasting

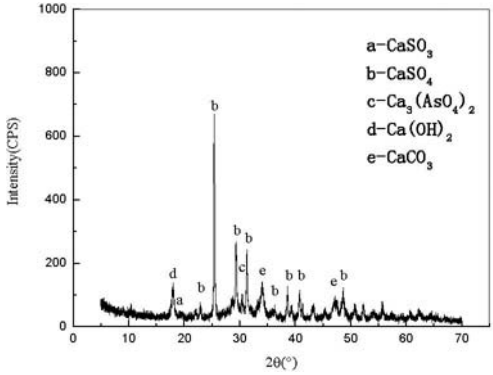

Figure 3. XRD diagram of coat layer under double-layered pellet roasting

Methods

Firstly, Sulfur & arsenic-bearing refractory gold concentrate was prepared to diameter of 8~10 mm balls by the pan pelletizer with 1.5% bentonite in 12 minutes. Then green balls were wrapped by hydrated lime in 12 minutes. After that the double-layered pellets were roasted in a horizontal furnace.

In this paper, several methods such as grinding, water quenching and drop impact for the separation of roasted double-layered pellet's coating and core were proposed. Shaking table(98 r/min , Φ160×60mm) was used for gravity concentration, davis tube supported the method of magnetic separation, and ball grinder was taken for grinding separation. In the method of drop impact, the roasted double-layered pellet was dropped from a certain height freely to the steel plate. The accumulated impact energy produced by freefall could be able to break the structure of the coating layer. Residual mass of roasted double-layered pellet after each freefall was recorded so that impact energy and the separation rate could be calculated. The impact energy was calculated as follow.

$$E = (\sum m_i) \cdot gh \tag{1}$$

E—accumulated impact energy
m_i—mass of residual pellet before i times to freefall
h—height of freefall

The main index for evaluating the separation efficiency of those most methods is separation rate as is shown below. Especially, termination of related experiments becomes whether the roasted core of pellet is broken.

$$\omega = (1 - \frac{m' - m_1}{m_0 - m_1}) \times 100\% \tag{2}$$

ω—separation rate
m'—mass of residual pellet after separation
m_1—mass of double-layered pellet's core after roasting
m_0—mass of double-layered pellet after roasting

Results and Discussion

Effect of magnetic and gravity concentration

Magnetic and gravity concentration of roasted double-layered pellet are based on the difference of magnetism and density between coating and core. In the experiment of magnetic/gravity separation, roasted double-layered pellets were grinded to -200 mesh.

Table II. Results of magnetic separation(magnetic field intensity:1000Gs)

Experimental subject	Proportion of magnetic substance /%
Roasted pellet core	13.95
Roasted double-layered pellet	7.45

From Table II, the effect of magnetic separation had poor performance. For roasted double-layered pellet, proportion of magnetic substance only reached 7.45%. The same situation also applied to study of gravity separation. Gold recovery in concentrate was 31%.

During 3h at roasting temperature of 600℃, pyrite, arsenopyrite and pyrrhotine are likely to be completely oxidized to weak magnetic substance such as α-Fe_2O_3. So magnetic separation doesn't meet demand of the novel pretreatment.

Adopting gravity separation method cannot achieve the desired effect, mainly because fine particles have huge specific surface energy. In addition, $CaSO_4$ as the by-product of solidification reaction and $Ca(OH)_2$ colloid in aqueous solution can be able to absorb other particles.

Effect of grinding separation

The grinding separation takes mostly advantage of tangential friction force which is produced between roasted pellets to separate the coating from double-layered pellet. There still exits radial force as a result of mutual collide and drop impact, but these are not the most important factor neither.

Effect of ball grinding on separation with no milling medium is indicated in Figure 4. According to the Figure, when grinding time increased(2~14 min), the separation rate were getting higher. Separation rate rose fast at the grinding time of 6~8min. Optimum separation effect was got under the time of 12min when ω arrived at 38.94%.

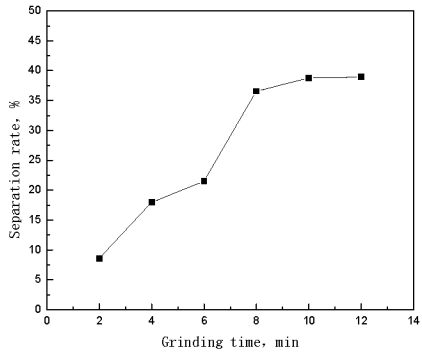

Figure 4. Effect of grinding separation in ball grinder with no milling medium

In order to raise the separation rate of coating and core, milling medium(steel balls which have the same diameter as double-layered pellets) was considered to strengthen the separation effect. Different ratios of medium number to double-layered pellet number were investigated. Experimental results are given in Figure 5.

As is shown in the figure above, when the ratio was raised from 0 to 2:1, the trend of separation effect towards worse. ω decreased to 30% around as the ratio rose. When the ratio came to 2:1, the roasted core was broken at grinding time of 10min.

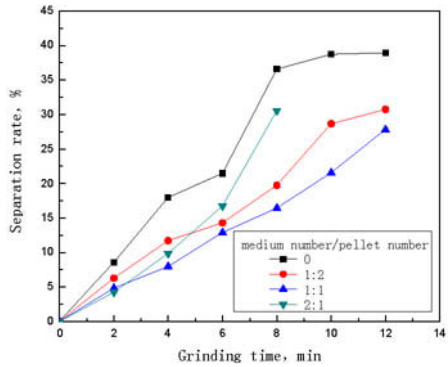

Figure 5. Effect of grinding separation in ball grinder with milling medium

Effect of drop impact

On the contrary, principle of drop impact mainly makes use of radial force other than tangential friction force. In small experiment, this method was simple and easy to carry out.

As can be seen from the Figure 6, with the same drop height, separation rate came up in pace with the increasement of drop times. Phenomenon that Roasted core cracked after the freefall occurred when the drop height was higher than 0.75m.

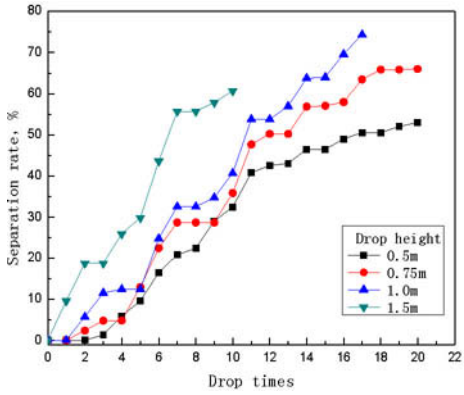

Figure 6. Effect of drop impact on separation under different drop height

The optimum separation rate 74.32% was obtained on the condition of drop height 0.75m,drop times 20. The impact energy E was about 0.55J.which represents the critical point for crack in drop impact.

In order to take advantage of tangential force, angle of steel plate was set freely to strengthen the separation effect. Effect of drop impact on separation under different impact angle is illustrated by Figure 7.

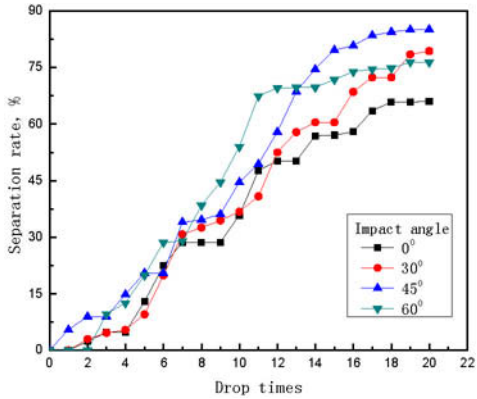

Figure 7. Effect of drop impact on separation under different impact angle

From experimental results of Figure 7, optimum separation rate increased to 85.05% by effect of drop impact under the drop height of 0.75m, drop times of 20, and impact angle 45°. When the impact angle reached 45°, the drop impact force was resolved into equal radial force and tangential force resulting in the best performance of drop impact on separation.

Effect of water quenching

Moreover, part of the hydrated lime in the outer coating which does not participate in the solidification reaction have digestion reaction in water. It informs that advantage of slaking reaction of lime could be conducive to the separation process of coating layer. Besides those characteristics, it deserves to be mentioned that effect of water quenching due to not thermo stress but chemical stress. So the water quenching method ask no limit for the temperature. Through related experiment of water quenching, separation of water quenching could approach 75.32% averagely.

Conclusion

Effect of magnetic and gravity separation had poor performance for weak magnetic product, huge specific surface energy, colloid character. The optimum separation rate of ball grinding appeared 38.94% at the grind time 12min with no milling medium. It increased to 85.05% by effect of drop impact under the drop height 0.75m, drop times 20 and impact angle 45°. However,

the separation rate of water quenching taking advantage of slaking reaction of lime could approach 75.32% averagely.

Acknowledgements

The financial supports from Natural Science Foundation of China, Grant No. 51074182 and from Postdoctoral Science Foundation of China, Grant No. 2014M550422 are gratefully acknowledged.

References

1. Li-yong Xi, Jin-hu Ma, Shou-pin Dai, "The preliminary analysis about the situation of China's gold mineral resources and geological exploration," *West-China Exploration Engineering*, 23(1)(2011), 129-131
2. H.G. Linge, N.J. Welham, "Gold recovery from a refractory arsenopyrite (FeAsS) concentrate by in-situ slurry oxidation," *Minerals Engineering*, 10(6)(1997), 557-566.
3. Chun-lin Jian, "Summarize of gold smelting technology," *Hydrometallurgy*, 27(1)(2008), 1-6.
4. Shu-yan Yin, Hong-ying Yang, "The oxidation pretreatment technology of refractory gold ores," *Precious Metals* , 29(1)(2008), 56-59
5. Mark G Aylmore, Frank J Lincoln, "Mechanochemical milling-induced reactions between gases and sulfide minerals: I. Reactions of SO2 with arsenopyrite, pyrrhotite and pyrite," *Journal of alloys and compounds*, 309(1)(2000), 61-74.

Characterization of Minerals, Metals, and Materials 2015
Edited by: John S. Carpenter, Chenguang Bai, Juan Pablo Escobedo, Jiann-Yang Hwang, Shadia Ikhmayies, Bowen Li, Jian Li, Sergio Neves Monteiro, Zhiwei Peng, and Mingming Zhang
TMS (The Minerals, Metals & Materials Society), 2015

PREDICTION FOR THE SURFACE TENSION OF FeO-TiO_2-Ti_2O_3-X(SiO_2, CaO, MgO) SLAG SYSTEMS

Yanhui Liu, Xuewei Lv, Chenguang Bai

School of Materials Science and Engineering, Chongqing University, Chongqing, 400044, China

Keywords: Surface tension, Molten slag, Ionic radii, Butler's equation

Abstract

A thermodynamic model for determining the surface tension of molten slag by considering the surface tension and molar volume of the pure oxide component, and their ionic radii was extended to the slag bearing high TiO_2 (varying from 80 to 67%) at 1973 K. The iso-surface tension curves for the FeO-TiO_2-Ti_2O_3 ternary system at 1973 K are almost parallel to the FeO-Ti_2O_3 line. TiO_2 plays a role of surface-active solute, and its surface-active effect is attenuating with increasing the TiO_2 content. The iso-surface tension curve shifts away from the TiO_2 corner, indicating that the surface tension of the ternary slag decreases along with the addition of SiO_2. The reasons include the addition of SiO_2 with lower surface tension and the decrease of the total ion moment at the surface. Both CaO and MgO can bring about that the iso-surface tension curve shifts towards the TiO_2 corner, indicating that the surface tension of the ternary slag increases along with the addition of CaO or MgO. CaO has a more pronounced effect on increasing the surface tension of the ternary slag than MgO at an equimolar amount addition. The increase of the surface tension results from both the compositional change and the variation of the slag structure.

Introduction

The surface tension of molten slag is a key parameter in industrial processes at high temperatures for controlling the various surface and interfacial phenomena [1-3] not only in ironmaking and steelmaking processes but also in electrosmelting processes. Phase separation [4-6], metal entrainment in slag and corrosion of refractory bricks by slag [1, 7-8] are apparent examples of phenomena influenced by surface tension effects. Particularly, during the process of electric arc smelting furnaces with Ilmenite, the mass percent of FeO content ranged from 3.3 to 15% while the corresponding TiO_2 content varied from 80 to 67%. Although a large number of experimental surface tension data has been reported for silicate melts [9-12], it is not possible to find appropriate data on the surface tension of molten slag bearing high TiO_2 because of the ultrahigh temperature encountered in performing experiments, resulting in a difficulty for a better understanding of the process of metal extraction from Ilmenite ores. Therefore, to fully understand the physical and chemical aspects of the slag bearing TiO_2, the contribution arising from surface properties cannot be overlooked. Besides, knowledge of the dependence of surface tension on liquid composition might provide useful insight into liquid structure.

Some models [13] have been developed for evaluating the surface tension of molten slag containing various components. Boni and Derge applied the additivity rule [14] to predict the surface tension of multi-component slag. Tanaka *et al.* [15, 16] applied thermodynamic databases to evaluate the surface tensions of liquid alloys, ionic melts and oxide melts by using a model based on Butler's equation [17]. Based on the coexistence theory of slag melt structure and Butler's equation, a calculation model was proposed for determining the surface tension of slag

melt by Cheng *et al* [18]. Although the calculated results were in good agreement with the experimental data, the applicability of this model to evaluate the surface tension of oxide melts was limited due to a lack of thermodynamic data for these particular multi-component systems. Recently, Tanaka *et al.* [19] have developed a new model for evaluating the surface tension of molten silicates, which takes into consideration the ionic radii of the components. This particular model can be readily applied to many kinds of molten ionic mixtures and molten slag, because the surface tension of silicate melts can be calculated using the information on the surface tensions and molar volumes of pure oxides, as well as the cationic and anionic radii of the component oxides in the system. This model has already been applied to the calculations of surface tension for several ternary silicate melts [20] comprising SiO_2, Al_2O_3, CaO, FeO, MgO or MnO. Nakamoto *et al* [21] applied this model was to evaluate the surface tension of silicate melts containing the following surface-active components, B_2O_3, CaF_2 or Na_2O. A further extension of the above modified model was attempted for determining the surface tensions of the more complex 6-component slag systems by Hanao *et al* [22].

In this study, another further extension of the above modified model was applied for determining the surface tensions of the molten slag bearing high TiO_2. The effects of MgO, SiO_2 and CaO on the surface tension of FeO-TiO_2-Ti_2O_3 slag system were analyzed based on the present model.

Evaluation model for the surface tension

A prediction model derived by Tanaka *et al* [19] for the evaluation of the surface tension of ionic mixtures was applied to the molten slag bearing high TiO_2 based on the Butler's equation. Here is an example for the surface tensions calculation of the FeO-TiO_2-Ti_2O_3-SiO_2 4-component molten slag shown in Equations (1)-(4):

$$\sigma=\sigma_{SiO_2}^{Pure}+\frac{RT}{A_{SiO_2}}\ln\frac{M_{SiO_2}^{Surf}}{M_{SiO_2}^{Bulk}} \tag{1}$$

$$\sigma=\sigma_{FeO}^{Pure}+\frac{RT}{A_{FeO}}\ln\frac{M_{FeO}^{Surf}}{M_{FeO}^{Bulk}} \tag{2}$$

$$\sigma=\sigma_{Ti_2O_3}^{Pure}+\frac{RT}{A_{Ti_2O_3}}\ln\frac{M_{Ti_2O_3}^{Surf}}{M_{Ti_2O_3}^{Bulk}} \tag{3}$$

$$\sigma=\sigma_{TiO_2}^{Pure}+\frac{RT}{A_{TiO_2}}\ln\frac{M_{TiO_2}^{Surf}}{M_{TiO_2}^{Bulk}} \tag{4}$$

Where

$$M_i^P=\left(\frac{R_A}{R_X}\cdot N_i^P\right)\Big/\left(\frac{R_{Si^{4+}}}{R_{SiO^{4-}}}\cdot N_{SiO_2}^P+\frac{R_{Fe^{2+}}}{R_{O^{2-}}}\cdot N_{FeO}^P+\frac{R_{Ti^{4+}}}{R_{O^{2-}}}\cdot N_{TiO_2}^P+\frac{R_{Ti^{3+}}}{R_{O^{2-}}}\cdot N_{Ti_2O_3}^P\right) \tag{5}$$

Subscript i refers to the following components: SiO_2, CaO, CaF_2, Al_2O_3, MgO, TiO_2. Subscripts A and X refer to the cations and anions of component i, respectively. Superscripts "Surf " and "Bulk" indicate the surface and bulk, respectively. R is the gas constant, T is the absolute temperature, σ_i^{Pure} is the surface tension of the pure molten component i, which is treated as a model parameter. $A_i = N_0^{1/3}\cdot V_i^{2/3}$ corresponds to the molar surface area in a monolayer of pure molten component i (N_0: Avogadro's number, V_i: molar volume of the pure molten component i).

N_i^P is the mole fraction of the component i in phase P (P=Surf or Bulk). R_A is the radii of the cation, and R_X is the radii of the anion.

For example:

$$R_A = R_{Si^{4+}}, R_{Ca^{2+}}, R_{Al^{3+}}, R_{Mg^{2+}}, R_{Ti^{4+}}, R_{Ti^{3+}}, R_{Fe^{2+}} \qquad R_X = R_{SiO_4^{4-}}, R_{O^{2-}}, R_{F^-} \tag{6}$$

where SiO_4^{4-} is considered to be the minimum anionic unit in SiO_2, and the value of $R_{Si^{4+}} / R_{SiO_4^{4-}}$ was experimentally determined to be 0.5 [20-23]. The above Equations (1)-(5) have been derived on the basis of Butler's equation by considering the following assumptions [1] and [2] [20-23]:

[1] It has been known that molten ionic mixtures readily undergo surface relaxation due to spontaneous changes in the ionic distance at the surface, which causes the energetic state of the surface to approach that of the bulk state. Thus, the contribution from excess Gibbs energy terms is neglected in Butler's equation.

[2] In ionic substances, it is well known that their ionic structures depend upon the ratio of the cation to anion radii. In order to evaluate the ionic structures and physical chemical properties of ionic materials, the cation to anion radii ratio should be considered.

Table I. Radii of the cationic and anionic ions

Ion	Radii (Å)
Si^{4+}	0.42
Ca^{2+}	0.99
Mg^{2+}	0.66
Ti^{3+}	0.67
Fe^{2+}	0.74
Ti^{4+}	0.61
O^{2-}	1.33

Table II. Temperature dependence for molar volume of the pure component

Oxide	Temperature(K) dependence of molar volume (m^3/mol)
SiO_2	$27.516\{1+10^{-4}(T-1773)\}\cdot10^{-6}$
CaO	$20.7\{1+10^{-4}(T-1773)\}\cdot10^{-6}$
FeO	$15.8\{1+10^{-4}(T-1773)\}\cdot10^{-6}$
MgO	$16.1\{1+10^{-4}(T-1773)\}\cdot10^{-6}$
Ti_2O_3	$\{77.237+0.0011T\}\cdot10^{-6}$
TiO_2	$22.2\{1-4.689*10^{-4}(T-1023)\}\cdot10^{-6}$

Table III. Temperature dependence of the surface tension of pure component

Oxide	Temperature(K) dependence of surface tension (mN/m)
SiO_2	243.2+0.031T
CaO	791-0.0935T
FeO	504+0.0984T
MgO	1770-0.636T
Ti_2O_3	742.5-0.0744T
TiO_2	1384.3-0.6254T

Data on the ionic radii and the molar volumes of the pure oxides except Ti_2O_3 used in previous study [20-23] were adopted in the present model. These values are listed in **Tables I** and **II**, respectively. The temperature dependences of the surface tension for pure SiO_2, CaO, TiO_2 and MgO were evaluated in previous work [20-23] and used in the current study. The equations for determining the temperature dependences of surface tension are listed in **Table III**. As for the

Ti_2O_3, the ionic radii recommended by the handbook [24] was adopted, and the molar volume and temperature dependence of surface tension reported by Ikeniya [25] were used.

Results and discussion

Iso-surface tension curves of FeO-TiO_2-Ti_2O_3 ternary slag system

The iso-surface tension curves for the FeO-TiO_2-Ti_2O_3 ternary system at 1973 K, such as 200, 250, 300, 350 and 400 mN/m, are plotted in **Figure 1**. Where, the dash dot represents the liquidus line obtained by the thermodynamics calculation software--FactSage 6.2. Easy to find that the surface tension for the slag decreases remarkably along with the increase of the TiO_2 content, proving that TiO_2 is a surface-active solute, which are consistent with previous experimental study [23]. With increasing the TiO_2 content, much more TiO_2 is needed for every 50 mN/m drop in the surface tension, indicating that the surface-active effect of TiO_2 is attenuating. The iso-surface tension curves of the ternary slag are almost parallel to the FeO-Ti_2O_3 line.

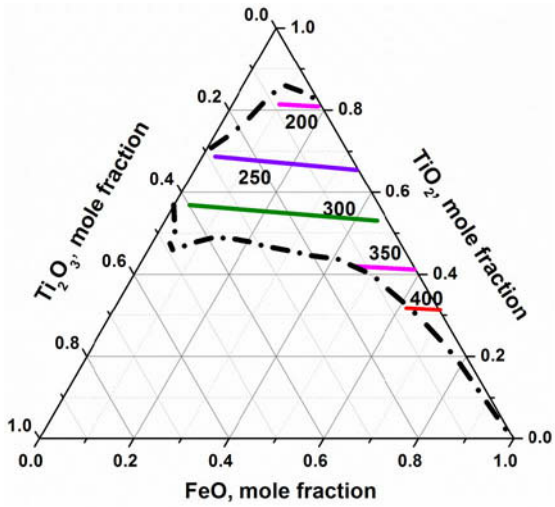

Figure 1. Iso-surface tension curves of FeO-TiO_2-Ti_2O_3 ternary system at 1973 K (Unit: mN/m)

Effect of CaO, MgO and SiO_2 on the surface tension of the ternary slag

Effect of SiO_2 on the iso-surface tension curve (300 mN/m) of the ternary slag is shown in **Figure 2**. The iso-surface tension curve shifts away from the TiO_2 corner, in other words, towards to the FeO-Ti_2O_3 line, indicating that the surface tension of the ternary slag decreases along with the addition of SiO_2. It is well known to us that the two principal parameters which influence the surface tension of liquid metals or alloys are the melt composition and temperature. As for the molten slag, the melt's structure may play an equally important role in the determination of the surface tension of the slag. Next the influence of melt composition and the melt's structure on the surface tension of the slag along with the compositional variation will be

discussed. For one hand, the addition of SiO_2 with lower surface tension as listed in **Table III** leads to the decrease of the surface tension of the slag.

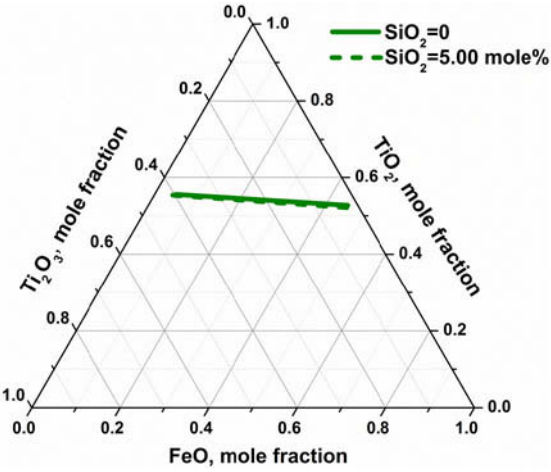

Figure 2. Effect of SiO_2 on the surface tension of slag (Unit: mN/m)

For another, it is generally recognized that there are three kinds of ions existing in the slag melts: cations (Ti^{4+}, Fe^{2+} and Ti^{3+} in this study), simple anions (O^{2-}) and complicated units (Q^1, Q^2, Q^3, Q^4 for Si). As a classic acid oxide, SiO_2 can promote the polymerization of the slag structure. In other words, the complicated units, such as Q^n(Si) (Here n=1, 2, 3, 4), will exist in the slag. Furthermore, the complicated units, Q^n, have a much smaller moment than that of the simple onion, O^{2-}, resulting in that Q^n will be excluded outside to the surface layer. As a consequence, the number of the complicated units in the surface phase will increase, while the number of free oxygen will reduce. As a result, the surface tension of the melt will drops down because of the decrease of the total ion moment at the surface. To sum up, the decrease of the surface tension of the melt results from both the compositional changes and the structural change along with the composition variation.

Effect of CaO on the iso-surface tension curve (300 mN/m) of the ternary slag is shown in **Figure 3**. The iso-surface tension curve shifts towards the TiO_2 corner, in other words, away from the FeO-Ti_2O_3 line, indicating that the surface tension of the ternary slag increases along with the addition of CaO. As for the reasons, one is that the addition of the CaO with higher surface tension as shown in **Table III** will lead to the increase of the surface tension of the slag, which is so-called the influence of melt's composition. As for the effect of melt's structural variation along with the compositional change, the hypothesis [26-27] proposed that molten high TiO_2 slags are constructed mainly from simple anions of the type [TiO_6] based on the fact that [TiO_6] octahedron is the basic structural unit in solid anosovite will be introduced. The addition of CaO can decrease the number of the [TiO_6] octahedron, resulting in the increase of the ionic total moment. As a consequence, the increase of the surface tension results from both the compositional change and the variation of the slag structure.

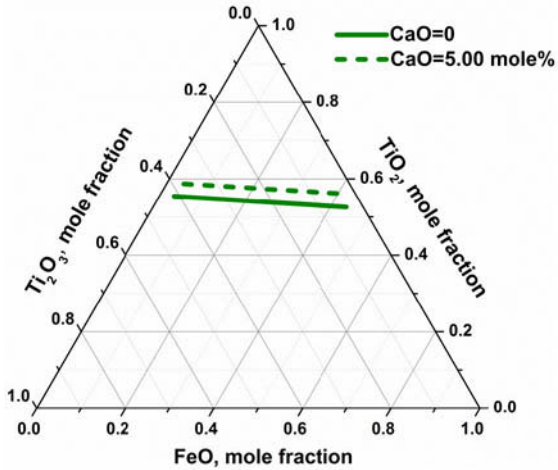

Figure 3. Influence of CaO on the surface tension of slag (Unit: mN/m)

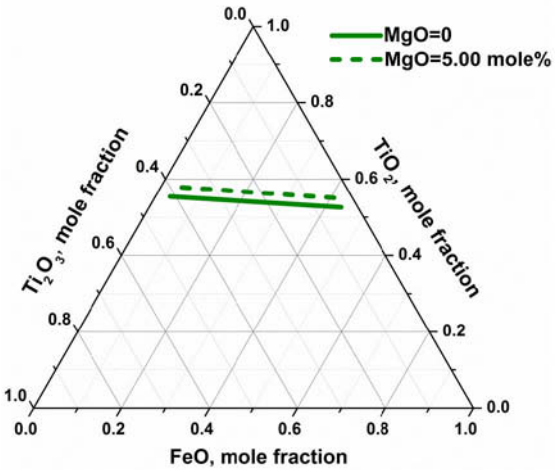

Figure 4. Variation of the surface tension of the slag along with MgO (Unit: mN/m)

As for MgO, its effect on the iso-surface tension curve (300 mN/m) of the ternary slag is shown in **Figure 4**. Similar to the role of CaO, with the increase of MgO, the surface tension of the ternary slag increases. However, it should be pointed out that CaO has a more pronounced effect on increasing the surface tension of the ternary slag than MgO at an equimolar amount addition. As for the reasons, the increase of the surface tension results from both the compositional change and the variation of the slag structure.

Conclusions

A thermodynamic model for determining the surface tension of molten slag by considering the surface tension and molar volume of the pure oxide component, and their ionic radii was extended to the high TiO_2 slags. The main conclusions are as following:

(1) The iso-surface tension curves for the FeO-TiO_2-Ti_2O_3 ternary system at 1973 K are calculated, and the iso-surface tension curves of the ternary slag are almost parallel to the FeO-Ti_2O_3 line. TiO_2 plays a role of surface-active solute, and its surface-active effect is attenuating with increasing the TiO_2 content.

(2) The iso-surface tension curve shifts away from the TiO_2 corner, indicating that the surface tension of the ternary slag decreases along with the addition of SiO_2. The reasons include the addition of SiO_2 with lower surface tension and the decrease of the total ion moment at the surface.

(3) Both CaO and MgO can bring about that the iso-surface tension curve shifts towards the TiO_2 corner, indicating that the surface tension of the ternary slag increases along with the addition of CaO or MgO. CaO has a more pronounced effect on increasing the surface tension of the ternary slag than MgO at an equimolar amount addition. The increase of the surface tension results from both the compositional change and the variation of the slag structure.

Acknowledgement

The authors are especially grateful to the National Natural Science Foundation of China (NSFC) (Grant No. 51374262).

References

1. K. Mukai, "Wetting and Marangoni Effect in Iron and Steelmaking Processes," *ISIJ International*, 32 (1) (1992), 19-25.
2. Y.A. Minaev, "Thermodynamics of Surface Phenomena in Liquid Metal at Phase Boundaries," *Metallurgist*, 50 (3-4) (2006), 168-175.
3. N. Siddiqi et al., "Slag-Graphite Wettability and Reaction Kinetics Part 1: Kinetics and Mechanism of Molten FeO Reduction Reaction," *Ironmaking & Steelmaking*, 27 (5) (2000), 367-372.
4. D. Durinck et al., "EAF Stainless Steel Refining-Part II: Microstructural Slag Evolution and Its Implications for Slag Foaming and Chromium Recovery," *Steel Research International*, 78 (2) (2007), 125-135.
5. R. Jiang, R. Fruehan, "Slag Foaming in Bath Smelting," *Metallurgical and Materials Transactions B*, 22 (4) (1991), 481-489.
6. Y. Zhang, R. Fruehan, "Effect of the Bubble Size and Chemical Reactions on Slag Foaming," *Metallurgical and Materials Transactions B*, 26 (4) (1995), 803-812.
7. Y. Ogawa et al., "Slag Foaming in Smelting Reduction and Its Control with Carbonaceous Materials," *ISIJ International*, 32 (1) (1992), 87-94.
8. S.Y. Kitamura, K. Okohira, "Influence of Slag Composition and Temperature on Slag Foaming," *ISIJ International*, 32 (6) (1992), 741-746.
9. R.D. Morales et al., "The Slag Foaming Practice in EAF and Its Influence on the Steelmaking Shop Productivity," *ISIJ international*, 35 (9) (1995), 1054-1062.
10. D. Walker, O. Mullins Jr., "Surface Tension of Natural Silicate Melts From 1,200-1,500 ℃ and Implications for Melt Structure," *Contributions to Mineralogy and Petrology*, 76 (4) (1981), 455-462.
11. D. Skupien, D. Gaskell, "The Surface Tensions and Foaming Behavior of Melts in The System CaO-FeO-SiO_2," *Metallurgical and Materials Transactions B*, 31 (5) (2000), 921-925.
12. W. Kingery, "Surface Tension of Some Liquid Oxides and Their Temperature Coefficients," *Journal of the American Ceramic Society*, 42 (1) (1959), 6-10.

13. K. Mills, "The Estimation of Slag Properties,"(Paper presented at the Proceedings of the International Conference of Southern African Pyrometallurgy, Cradle of Humankind, South Africa, F, 2011 [C]).
14. R. Boni, G. Derge, "Surface Tensions of Silicates," *Transactions of the American Institute of Mining and Metallurgical Engineers*, 206 (1) (1956), 53-59.
15. T. Tanaka et al., "Application of Thermodynamic Databases to the Evaluation of Surface Tensions of Molten Alloys, Salt Mixtures and Oxide Mixtures," *Zeitschrift für Metallkunde*, 87 (5) (1996), 380-389.
16. T. Tanaka, K. Hack, S. Hara, "Calculation of Surface Tension of Liquid Bi-Sn Alloy Using Thermochemical Application Library Chemapp," *Calphad*, 24 (4) (2000), 465-474.
17. G.G. Cheng, N.B. Liao, "Calculation Model for Surface Tension of Slag Melt," *Journal of Iron and Steel Research, International*, 6 (2) (1999), 17-20.
18. J. Butler, "The Thermodynamics of the Surfaces of Solutions," *Proceedings of the Royal Society of London Series A*, 135 (827) (1932), 348-375.
19. T. Tanaka, T. Kitamura, I.A. Back, "Evaluation of Surface Tension of Molten Ionic Mixtures," *ISIJ International*, 46 (3) (2006), 400-406.
20. M. Nakamoto et al., "Evaluation of the Surface Tension of Ternary Silicate Melts Containing Al_2O_3, CaO, FeO, MgO or MnO," *ISIJ International*, 47 (1) (2007), 38-43.
21. M. Nakamoto et al., "Surface Tension Evaluation of Molten Silicates Containing Surface-active Components (B_2O_3, CaF_2 or Na_2O)," *ISIJ International*, 47 (2) (2007), 211-216.
22. M. Hanao et al., "Evaluation of Surface Tension of Molten Slag in Multi-Component Systems," *ISIJ International*, 47 (7) (2007), 935-939.
23. Yanhui Liu et al., "Surface Tension of the Molten Blast Slag Bearing TiO_2: Measurement and Evaluation. *ISIJ International*, 54 (10) (2014), 2156-2163.
24. Beyer, H. William, ed., *CRC Handbook of Chemistry and Physics*. (Boca Raton, FL: CRC press, 1988), 69.
25. N. Ikemiya et al., "Surface Tensions and Densities of Molten Al_2O_3, Ti_2O_3, V_2O_5 and Nb_2O_5," *ISIJ International*, 33 (1) (1993), 156-165.
26. V.A. Reznichenko. "Review of Investigations on Metallurgy Chemistry and Electrochemistry of Titanium," *Russian Metallurgy-Metally-Ussr*, 43 (5) (1967), 6-&.
27. G. Handfield and G.G. Charette, "Viscosity and Structure of Industrial High TiO_2 Slags," *Canadian Metallurgical Quarterly*, 10 (3) (1971), 235-243.

Characterization of Minerals, Metals, and Materials 2015

Characterization of Soft Materials

Session Chairs:

Brian Patterson

Sergio Neves Monteiro

Characterization of Minerals, Metals, and Materials 2015
Edited by: John S. Carpenter, Chenguang Bai, Juan Pablo Escobedo, Jiann-Yang Hwang, Shadia Ikhmayies, Bowen Li, Jian Li, Sergio Neves Monteiro, Zhiwei Peng, and Mingming Zhang
TMS (The Minerals, Metals & Materials Society), 2015

Constitutive Modeling of a Glass Fiber-Reinforced PTFE Gasketed-Joint Under a Re-torque

James Williams and Ali P. Gordon

Department of Mechanical & Aerospace Engineering,
University of Central Florida, Orlando, FL 32816-2450

Keywords: Bolted-joint Relaxation, Gasket Creep, Viscoelastic Modeling.

Abstract

Joints gasketed with viscoelastic seals often receive an application of a secondary torque, i.e., re-torque, in order to ensure joint tightness and proper sealing. The motivation of this study is to characterize and analytically model the load and deflection re-torque response of a single 25% glass-fiber reinforced polytetrafluorethylene (PTFE) gasket-bolted joint with serrated flange detail. The Burger-type viscoelastic modeling constants of the material are obtained through isolating the gasket from the bolt by performing a gasket creep test via a MTS electromechanical test frame. The re-load creep response is also investigated by re-loading the gasket after a period of initial creep to observe the response. The modeling constants obtained from the creep tests are used with a Burger-type viscoelastic model to predict the re-torque response of a single bolt-gasket test fixture in order to validate the ability of the model to simulate the re-torque response under various loading conditions and flange detail.

Introduction

Bolted gasket joint systems are typically tightened and allowed to relax for a specific initial dwell period and then subsequently re-torqued to the desired torque levels. Re-torque is typically applied in order to re-tighten the joint, after the gasket has gone through some initial relaxation, to ensure optimal gasket sealing. The relationship between torque and the corresponding compressive load is given by:

$$F = \frac{T}{Kd} \tag{1}$$

where F is the compressive load and d is the nominal diameter of the bolt and K is the nut factor. The terms torque and load are used interchangeably for this study.

Joint designers are interested in conditions that (1) minimize the joint relaxation or (2) reduce required dwell time prior to re-tightening the joint. Hence prior efforts have been made to qualitatively describe gasket behavior combined within bolted joints. For example, Waterland and Frew investigated the compressive creep resistance of various PTFE types of gaskets within bolted joints with the goal of identifying materials not requiring re-torque. Furthermore, the minimum acceptable initial dwell periods of PTFE types were also studied [1]. In a technical report, Gordon et al. optimized the parameters of gasket thickness, lubrication, flange detail, load level and initial and final dwell period on the initial and re-torqued clamping load relaxation response of a 25% glass-filled PTFE gasket bolted flange system [2].

In addition to qualitatively describing gasket-joint behavior prior studies have analytically modeled the initial creep and relaxation of a bolted-gasket joint subject to an initial torque [3]. Alkalini et al. derived a closed form solution capable of predicting the creep and force relaxation of a single bolt, styrene butadiene rubber-gasket system, with un-serrated platens, subjected to an initial torque shown in Equation 2. Two key elements from Alkalini's research show that (1) bolted joint relaxation is a consequence of loss of elongation of the bolt resulting from the gasket creep and (2) the modeling constants for a styrene butadiene rubber gasket remain identical for each compressive load level and change only with the gasket thickness [3].

Re-tightening gasketed bolted joints remains the industry standard for insuring and maintaining tightness within these types of connections, therefore more research effort is needed to understand the re-torque response. Analytical modeling of the force relaxation of the re-torque response was attempted by Gordon et al. by considering the evolving gasket stiffness of 25% glass-filled PTFE gasket material at the end of the initial dwell period and substituting the corresponding value into Alkalini's equation [4]. The current study will extend these modeling efforts to model the re-torque response of 0.62 inch thick, 25% glass-filled PTFE gasket. It will also be determined if the experimental re-torque modeling constants will remain the identical at various load levels with the addition of serrated platens. It is suspected that the modeling constants will vary due to the addition of the serrations on the mating surface.

Experimental Approach

Creep Test

To obtain the modeling constants and to verify if any load or time dependence exists due to effects from the serrated mating surfaces, a series of constant force creep tests were performed. Gasket specimens were placed between platens (Fig.1) and compressed with a constant force by a MTS test frame and allowed to creep for twenty minutes. The dwell time of twenty minutes was selected in order to allow the material to enter into steady state creep. It was determined from previous studies that creep curves for PTFE gaskets enter steady state behavior in as short as eleven minutes [3]. Five individual creep experiments were performed at load levels of 200 lb., 800 lb., 1600 lb. and 2000 lb. All experiments measured gasket deflection, applied compressive load and time.

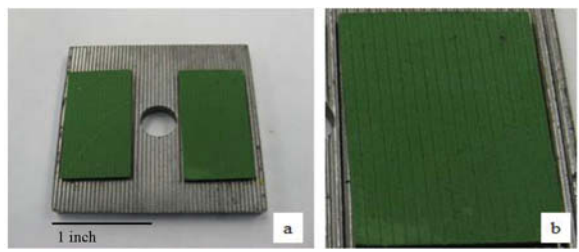

Figure 1. (a) Bottom platen with serrations loaded with PTFE specimens. (b) Serration indentations after loading.

Relaxometer

A Single bolt test fixture shown in Fig. 2 has been developed to test small gasket specimens. The test fixture, called the relaxometer, consists of a threaded bolt and nut in combination with gasket test specimens placed between serrated compression platens as depicted in Figure 2. The relaxometer is a departure from the ASTM test standards (F36 and F38) for testing of gasket materials [5,6]. The load relaxation response of the bolted set up is measured with the use of a

load cell. The strain response is acquired with a foil type strain gauge fixed to the bolt shank. (Fig.2).The load and strain data are acquired for final dwell period. The specimens consist of two small rectangular samples of 25% glass filled PTFE gasket cut from stock material to dimensions of 1.427 inches by 0.750 inches. The relaxometer is subjected to an initial torque with the use of a digital torque wrench and allowed to relax for a specific initial dwell period of 4 hours. After the initial dwell period the bolt is subsequently re-torqued and allowed to relax for a secondary dwell period of 4 hours. High and low (206 in/lb. and 246 in/lb.) torque levels were used for this study. Identical torque and re-torque levels were used for each test.

The torque was applied in a smooth motion with a digital torque wrench. The resulting compressive peak load values for an application of 206 in/lb. and 246 in/lb., i.e. low and high torque values were 2100 lb. and 3000 lb. respectively. The load and strain data were acquired with Futek software. Load and strain data were acquired for the re-torque response. The resulting high and low load experimental re-torque relaxation curves are shown in the experimental results section.

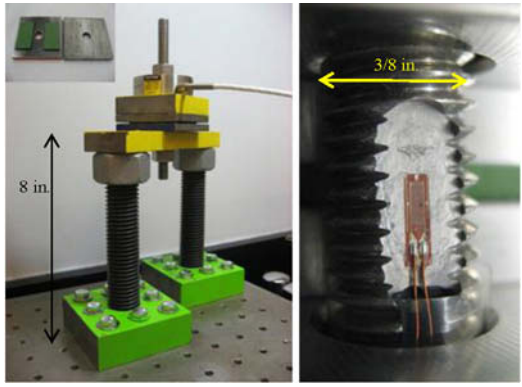

Figure 2. Experimental fixture (Left). Close-up view of stain gauge on bolt. (Right)

Modeling Re-torque

Observe that Alkalini's equation for predicting force relaxation response of a gasket joint after an initial tightening:

$$F(t) = \left[\delta_b(0) - \delta_g(0)\right]\left(\frac{K_b K_g(t)}{K_b - K_g(t)}\right) \tag{2}$$

where $F(t)$ is the compressive clamp load of the gasketed-joint as a function of time, $\delta_b(0)$ is the initial bolt elongation at time equals zero given by:

$$\delta_b(0) = \frac{F_0}{K_b} \tag{3}$$

where F_0 is the initial load at time equals zero and K_b is the bolt stiffness shown as Eq. 4, note that d is the nominal diameter of the bolt, E_b is the modulus of the bolt and L_{total} is the total grip length of the bolt. [7]

$$K_b = \frac{\pi d^2 E_b}{4L_{total}} \tag{4}$$

$\delta_g(0)$ refers to the initial gasket thickness at time equals zero and is presented as:

$$\delta_g(0) = \left[\frac{K_1 + K_2}{K_1 K_2} - \frac{1}{K_2}\right] F_0 \tag{5}$$

$K_g(t)$ is the gasket stiffness as a function of time given by Equation 6.

$$K_g(t) = \left[\frac{K_1 + K_2}{K_1 K_2} + \frac{1}{C_1} t - \frac{1}{K_2}\left(e^{\frac{-K_2}{C_2} t}\right)\right]^{-1} \tag{6}$$

K_1 and K_2 and C_1 and C_2 refer to the material constants and are analogous to springs and viscous elements. The gasket stiffness is obtained from the deflection equation $\delta_g(t)$ and is presented by the Burger-type viscoelastic models as:

$$\delta_g(t) = \left[\frac{K_1 + K_2}{K_1 K_2} + \frac{1}{C_1} t - \frac{1}{K_2}\left(e^{\frac{-K_2}{C_2} t}\right)\right] F_0 \tag{7}$$

The relationship between initial gasket deflection and force can be written as:

$$F(t) = K(t)\delta(0) \tag{8}$$

Experimental and Modeling Results

Creep Results

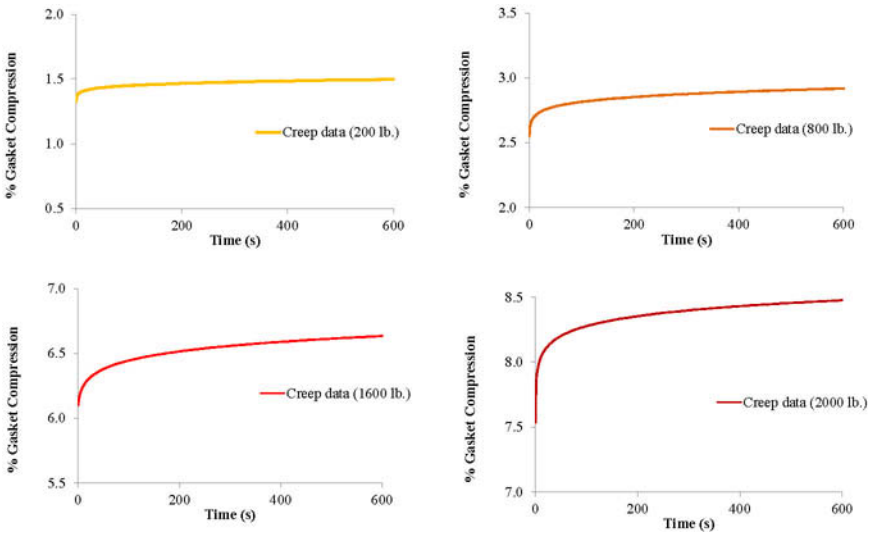

Figure 3. Experimental Creep Test Results.

Table 1: Viscoelastic Modeling Constants

Load Level	200 lb.	800 lb.	1600 lb	2000 lb.
K1 (lb/in)	5.11E+04	8.26E+04	4.92E+04	4.85E+04
K2 (lb/in)	1.37E+06	2.35E+06	1.01E+06	9.59E+05
C1 (lb-s/in)	9.80E+08	1.96E+09	1.93E+09	1.56E+09
C2 (lb-s/in)	4.47E+07	6.98E+07	9.85E+07	3.27E+07

The creep test results are shown in Figure 3. Observe that as the load increases the gasket compression and transient creep also increases. The experimentally determined modeling constants are shown in Table 1. The modeling constants K_1, K_2 and C_1 converge to similar values as load increases. A distinct trend for C_2 could not be established, however convergence is suspected at loads greater than 2000 lb. It is proposed that at sufficiently higher load levels the modeling constants become independent of load level. This proposal suggests that one set of global modeling constants can be used to predict the gasket deflection response at a various load levels above the convergence point, which in this case is 2000 lb.

The modeling constants obtained from the 2000 lb. creep test are used to predict the resulting gasket deflection from constant load creep tests at 1600 lb. and 2000 lb. Observe Fig 4 which depicts experimental (solid lines) and analytical creep results (dashed lines).

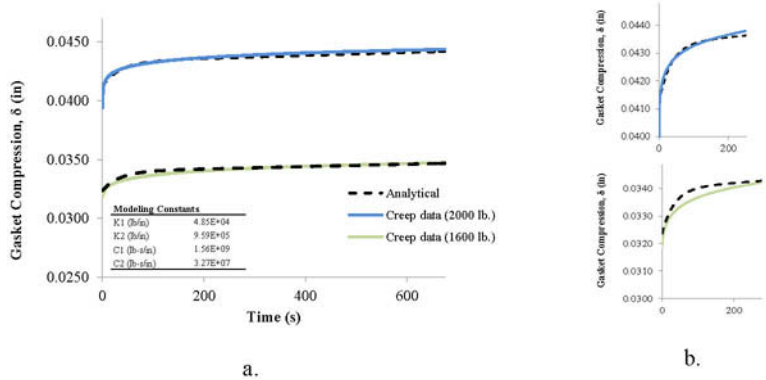

Figure 4. (a) Full-range experimental (solid lines) and analytical creep results (dashed lines) plotted with identical modeling constants at various load levels. (b) Analytical and experimental primary creep view 2000 lb. (top) and 1600 lb. (bottom).

The global modeling constants, at the proposed convergence-point (2000 lb.), when used with Eq. 7, show good agreement with both sets of experimental data. (Figure 4) The analytical model plotted with the global constants naturally produces the most accurate fit for the 2000 lb. test case, and approximates the 1600 lb. case.

Relaxometer Results

The relaxometer experimental and analytical results for both high and low torques are shown in Figure 4.

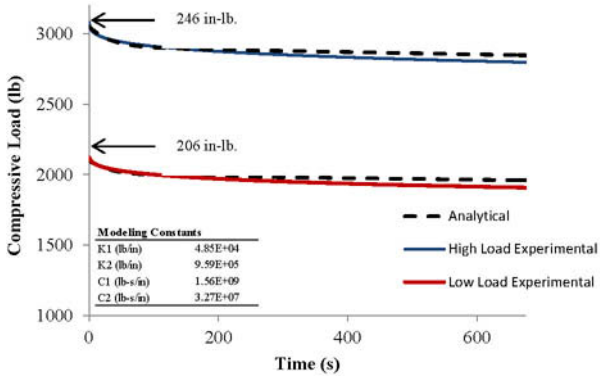

Figure 5. Experimental and analytical relaxometer results

Equation 8, which is the gasket stiffness, $K_g(t)$ as a function of time multiplied by the initial gasket deflection, $\delta_g(0)$ at time t=0, gives the force of the relaxometer as a function of time. Equation 8 is plotted with the global modeling constants and approximates both the low and high torque experimental relaxometer data well. This indicates that the experimentally determined global modeling constants that converge can be used to predict the re-torque response at various load cases above the convergence point.

Discussion

A key finding from the creep tests conducted is the modeling constants departure from load dependence at higher load levels. Contrast this finding with the study conducted by Alkalini where load independence was shown at all load levels tested. Alkalini's finding can be attributed to the type of gasket material used (styrene butadiene rubber) and the smooth gasket mating surface. Likewise for this investigation a 25 % glass-filled PTFE gasket with serrated gasket mating surface displays load independence at higher load levels. The relation given in Eq. 8 combined with load-independent modeling constants may be used to approximant the force relaxation of a single bolted gasketed joint subjected to a re-torque at similar or higher torque/load levels.

Conclusions

It was shown that the creep test modeling constants are load dependent for lower ranges, i.e. 200 lb. to 1600 lb. and begin to display independence at sufficiently higher load levels. It was found that the experimentally determined constants for the 2000 lb. creep test successfully predicted the similar the creep response at similar load levels and when combined with Eq. 8 could successfully predict the force relaxation of a single bolted-gasketed joint subjected to a re-torque. The experimental and analytical data showed good agreement.

Future Work

Future work for predicting the behavior of a bolted gasketed joint subjected to a torque or re-torque includes investigating and developing novel methods for determining the viscoelastic modeling constants from other methods besides the standard creep test. Future methods for obtaining the modeling constants might include using only the (1) initial creep tests, (2) a small fixture, such as a relaxometer, or from a (3) simple compression test. Other areas of research might include investigating deeper into the effects and mechanics of various types of gasket flange serrations. Thermal-mechanical behavior of PTFE gasket material used with bolted-joints is another possible exciting research area as these types of gaskets are often used in cryogenic applications and further understanding of the temperature dependence of the creep and relaxation behavior would be beneficial to designers. Overall, there is an abundance of active research possibilities for this and other viscoelastic gasket materials used within bolted joints.

References

[1] Waterland, A., F., and Frew, J. E. B. (2006)"Determination of Optimum Ambient Temperature Re-Torque Dwell Period for PTFE Based Gaskets" ASME Pressure Vessel and Piping Conference, Vancouver, British Columbia, CA, July 23rd-27th.

[2] Ali P. Gordon, Drilling B., et al. (2011) "Optimization of Re-Torque and Relaxation Parameters of the GUCP" ASME 2011 Pressure Vessels and Piping Conference, Baltimore, Maryland, USA, July 17–21, Volume 2: Computer Technology and Bolted Joints, Paper No. PVP2011-57682, pp. 57-65; 9 pages

[3] Alkelani, A. A. (2008) "A proposed Model for Creep Relaxation of Soft Gaskets in Bolted Joints at Room Temperature" *Journal of Pressure Vessel Technology*, 130: 011211-1-011211-6.

[4] Ali P. Gordon, Williams J., et al. (2011) "Analytical Modeling of the Mechanics of Re-Torque" ASME 2011 Pressure Vessels and Piping Conference, Baltimore, Maryland, USA, July 17–21, Volume 6: Materials and Fabrication, Parts A and B, Paper No. PVP2011-57718, pp. 1135-1143; 9 pages

[5] ASTM (2006) "Standard Test Methods for Creep Relaxation of a Gasket Material (F-38)" American Society for Testing and Materials, West Conshohocken, PA.

[6] ASTM (1999) "Standard Test Method for Compressibility and Recovery of Gasket Materials (F-36)" American Society for Testing and Materials, West Conshohocken, PA.

[7] Kobayshi, T., and Hamano K. (2004) "The Reduction of Bolt Load in Bolted Flange Joints due to Gasket Creep-Relaxation Characteristics" *ASME Conference on Pressure Vessels and Piping*, San Diego, CA, July 25th-29th

[8] Bouzid, A., Chaaban, A., and Bazergui, A. (1995), "The Effect of Gasket Creep Relaxation on the Leakage Tightness of Bolted Flanged Joints", *Journal of Pressure Vessel Technology*, 117(1): 71-78.

[9] Brinson, H., Brinson C., (2007) "Polymer Engineering Science and Viscoelasticity: An Introduction" (Springer Science & Business Media), 84

[10] Bickford, J. H., (1995) An Introduction to the Design and Behavior of Bolted Joints, Third Edition, Revised and Expanded, CRC Press, Boca Raton, FL.

Characterization of Minerals, Metals, and Materials 2015
Edited by: John S. Carpenter, Chenguang Bai, Juan Pablo Escobedo, Jiann-Yang Hwang, Shadia Ikhmayies, Bowen Li, Jian Li, Sergio Neves Monteiro, Zhiwei Peng, and Mingming Zhang
TMS (The Minerals, Metals & Materials Society), 2015

MICROWAVE ABSORPTION CHARACTERISTICS OF TIRE

Yuzhe Zhang[1], Jiann-Yang Hwang*[1,3], Zhiwei Peng[1,2], Matthew Andriese[1], Bowen Li[1,3], Xiaodi Huang[1,3], Xinli Wang[4]

[1]Department of Materials Science and Engineering, Michigan Technological University, Houghton, Michigan 49931, USA
[2]School of Minerals Processing and Bioengineering, Central South University, Changsha, Hunan 410083, China
[3]Advanced Materials R&D Center of WISCO, Beijing 102211, China
[4]School of Technology, Michigan Technological University, Houghton, Michigan 49931, USA

Keywords: Waste Tire, Rubber, Microwave, Characterization

Abstract

The recycling of waste tires has been a big environmental problem. About 280 million waste tires are produced annually in the United States and more than 2 billion tires are stockpiled, which cause fire hazards and health issues. Tire rubbers are insoluble elastic high polymer materials. They are not biodegradable and may take hundreds of years to decompose in the natural environment. Microwave irradiation can be a thermal processing method for the decomposition of tire rubbers. In this study, the microwave absorption properties of waste tire at various temperatures are characterized to determine the conditions favorable for the microwave heating of waste tires.

Introduction

The waste tire has been called "black pollution". With the development of automobile industry, the black pollution becomes worse. Processing of waste tires has been a big problem for more than 100 years since the auto transportation began to use rubber tires. According to statistics, more than 1.5 billion of waste tires are produced all over the world annually. Among them, the contribution from USA is more than 0.3 billion. For cities, states and industries, processing of discarded tires in the United States is a dilemma. Research shows that two to five billion waste tires are hold in landfills and stockpiles. The governmental agencies, municipalities, industrial corporations and community leaders have attempted to reduce the size of space for waste tire storage.

Waste tires have environmental and health problems. The scrap tires can take a lot of space. Most of the scrap tires are stored outside. With the sun and rain, the scrap tire

can promote breeding of mosquito which can carry acute infectious germs. What's worse, the scrap tire can easily cause fire.

In the landfill, the waste tires cannot be biodegraded. In addition, whole tires tend to work their way to the top of the fill and can cause damage to the landfill cap or seal. As a result, waste tires cannot be stored in landfills. Many tires are dumped illegally, due to the cost of placing them in sanctioned dumpsites.

Under this situation, almost all states of the United States have established laws and legislation for gathering the waste tires. Many attempts have been made to decrease the pollution of waste tires. Many of these states collect license fees or taxes from factories and companies for processing the waste tire [1].

Comprehensive utilization of waste tires are paid close attention by developed countries for reaching a target of resources recycling and environment protection. It is significant for waste rubber to be recycled. The reason is that the waste rubber causes serious environmental problems. Pets and mosquitoes are abundant around waste tire which is a good place for propagation. This condition can cause spreading of infections, for example, malaria, cephalitis and so on.

For countries, recycle of the waste tire can save the energy, because the raw material for the rubber industry depends largely on petroleum. This is particularly important for the countries which have little resources of natural rubber. These countries also use amount of waste tire rubber for producing raw materials. The waste rubber has the highest burning value of about 3.3×10^4 kJ/kg in the industrial division so that waste rubber is a kind of high-value bunkers the same as coal. Previous wok shows that the world would lost 3×10^{14} kJ heat without recycling rubber [2].

Methods for Waste Tire Recycling

Methods for waste tire recycling include landfill, stockpiles, road base, combustion and pyrolysis. The landfill method is a method which buries waste tires. It is the oldest method for treating waste materials. It can also be called as tip, dumping ground or rubbish dump. In history, landfill is the most normal way for the organization of waste charge all over the world. However, landfill is not suitable for waste tire treatment. Due to their large volumes and 75% void space, they consume space rapidly [3]. The waste tire may produce buoyant bubble on the surface since they are able to trap methane gases. The buoyant bubbles can damage the landfill liners which have been installed to promote prevent landfill wastes to pollute the surface and ground water. It just buries the waste tires without reuse so it is a waste of potentially valuable waste tires, although it is relatively easy to get and cheap for disposal purposes.

The stockpiles of waste tires can make serious safety and health risks. Waste tires are able to appear easily and seriously polluting the air and ground. The waste tire has another risk of health that it provides places for vermin and mosquitoes for breeding resulting in an increasing number of diseases. The stockpiles also can cause illegal dumping of waste tires. The illegal dumping of waste tires makes many states to pass waste tire regulation requiring suitable managing because it will pollute woods, deserts, ravines and empty lots. All of the organization members are able to dispose a limited number of waste tires free of charge and this can be funded by state waste tire programs. As a result of this illegal dumping [4], improper storage of waste tires may be increased. This activation is sometimes related to illegal activities and lack of environmental awareness.

Combustion of waste tires has been carried out, in many cases, as a coal replacement in industrial boilers or incinerators. Uncontrolled combustion at storage or stockpile sites have also been reported, which causes even worse problems. The combustion of waste tires emit dioxins (toxic hydrocarbon), zinc oxide poly-nuclear aromatic hydrocarbons i.e. potent carcinogens, leading to serious pollution of air. It is thus necessary to make use of this energy for electricity generation and to recover useful by-products such like char and steel, etc. taking use of new process, for example, by incineration and by pyrolysis which involves use of microwave heating or electric heating [5-10].

Pyrolysis has been widely used in chemical industry, such as producing activated carbon, methanol, charcoal and other chemicals from wood. It is used to make coke from coal and to convert biomass into biochar and syngas. The pyrolysis differs from other high-temperature processes, such as hydrolysis and combustion, because pyrolysis often includes reactions with no water and oxygen. Actually, it is impossible to get a totally anaerobic atmosphere.

Pyrolysis of waste tires can recover remaining solids after fluid reactions. For example, carbon black, steel and carbon, from volatile liquid and gaseous compounds that can be used as fuel [4]. The pyrolysis of waste tire has been widely used all over the world.

The pyrolysis way for waste tire recycling is a technology which heats particles or whole of waste tire in a reactor in anaerobic environment. Waste tires will be decomposed into small particles and become softened in the reactor. These particles will vaporize and emit from the reactor at the end of the process. The vapors are usually used as fuel that is burned directly for producing energy. Some particles which are not big enough for condensing remain as gas for burning as fuel. Some parts of waste tire which are about 40% by weight are removed as solids [4]. The pyrolysis of waste tire process can be very clean without waste or emissions.

In this study, the microwave heating characteristics of waste tire rubber is investigated. It is important to understand the fundamental microwave absorption properties before we can determine how microwave can be introduced to the high temperature process for the waste tire recycling.

Materials and Experiment

Materials

The waste tire sample was purchased from the Cooper Company, Michigan. It has the following description: 104T max load 900kg (2984 LBS), max press 300kg (44 P.S.I), tread 1 PLY NYLON + 2 PLY STEEL + 2 PLY POLYESTER, sidewall 2 PLY POLYESTER , made in USA. The samples were prepared by cutting off rubber rods from the center of the tire. These rods have a length of 12 mm.

A SEM examination has been conducted to look into the composition and structure of tire rubbers. The SEM study was carried with a Hitachi S-4700 field emission-scanning electron microscope (FE-SEM).

Table 1 shows the typical composition of a tire [2]. It contains natural rubber, synthetic rubber, carbon black, steel cord, weave cord, and others. Rubbers have a total weight of nearly half of the total weight. Carbon black and steel are major constituents of the tire, accounting for approximately 25% and 14% of the weight, respectively. From chemical composition analysis, C, H, O, N, S, Cl, Zn, and Fe were found to be the major elements. The contents of Fe and C amount to nearly 90% (13.5% and 73%). Sulfur and zinc are important elements in rubber, with the content ranging from 1 to 2%.

Table 1. Composition of tire (weight %) [2]

Material	Content (wt.%)	Element	Content (wt. %)
Natural rubber	23	C	73.0
Synthetic rubber	24	H	6.0
		O	4.0
Carbon black	25	N	1.4
		S	1.3
Steel cord	14	Cl	0.07
		Zn	1.5
Weave cord	4	Fe	13.5
Others	10		

Experiment

Microwave absorption (dielectric) properties of waste tire rubber was measured using a TM_{0n0} cavity system. Figure 1 shows the linear actuator with a sample lined in axis in the middle of the cavity and the quartz sample holder. There is a small hole in the quartz base which supports the sample in the holder so that gas can flow upwards using a (not shown) metered gas flow control system.

The measurement was performed in stagnant air using a short (~ 80 mm high) sample holder. The initial sample parameters were:

a) Diameter: 3.60 ±0.15 mm
b) Length: 13.59 ± 0.05 mm
c) Mass: 0.153 ± 0.002 gm
d) Room temperature density: 1.11 ±0.07 gm/cc.

The final sample parameters were:

a) Diameter: 3.4 ±0.15 mm
b) Length: 12.4 ±0.05 mm
c) Mass: 0.059 ±0.002 gm
d) Room temperature density: 0.52 ±0.05 gm/cc.

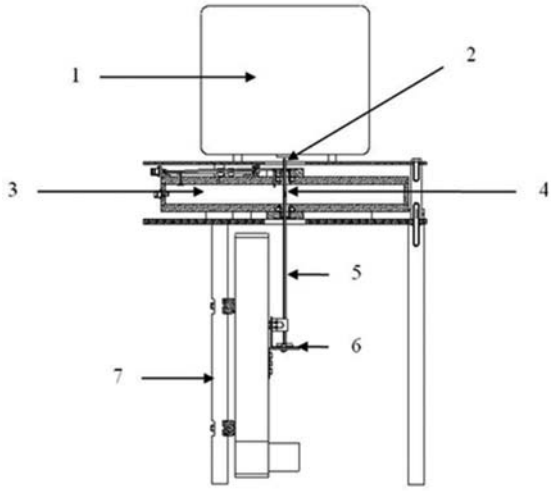

Figure 1. Schematic diagram of the TM_{0n0} cavity system (in cross-section). 1-High temperature resistance furnace, 2-Entry hole, 3-TM0n0 right cylindrical cavity, 4-Sample in quartz holder, 5-Quartz sample holder, 6-Sample stage on linear actuator, and 7-Support stand.

Results and Discussion

Characterization of Materials

Figure 2 shows a SEM micrograph of the waste tire rubber. The large gray grain to the left is designated as Area 1. The bright grain below the Area 1 is named Area 2. The groundmass with large amounts of small aggregates at the center right part of the photo is Area 3. The three areas were analyzed with EDAX for their compositions.

The results of analysis are shown in Table 2. It indicates that the area 1 may represent a filler particle in the rubber. The chemical composition of this grain is clearly a potassium aluminum silicate, which is most likely a feldspar mineral. In the tire description earlier from the manufacture, it didn't mention that silicate minerals are part of the tire. However, it is common to have mineral filler in the organics for cost reduction. It is believed that tire manufacturers also use mineral fillers as a cost reduction approach. So, this grain may represent a typical mineral filler grain. The area 2 is primarily iron, which is obviouly the steel reinforment in rubber. The composition of area 3 is primarily carbon, about 63% of the total weight. This area represents the groundmass of the material, and is thus the typical rubber dominant part of the material. The presence of sulfur (5.93%) for rubber vulcanization and zinc (12.11%, in form of zinc oxide actually) as the activator for rubber vulcanization reaction prove that this area is the rubber area.

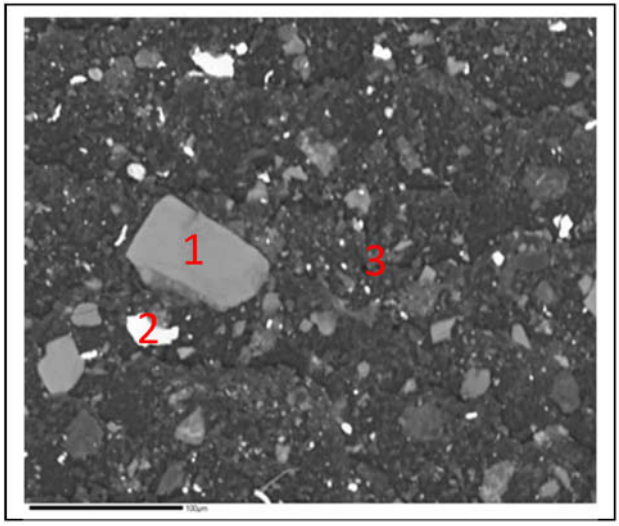

Figure 2. General morphology of tire rubber sample (scale bar 100 μm)

Table 2. Composition of the three areas in the waste tire (wt %).

Area	C	Mg	Al	Si	K	S	Cl	P	Ca	Fe	Zn	O
1	6.37	ND	23.52	34.25	16.75	ND	ND	ND	ND	ND	ND	15.34
2	0.66	ND	ND	1.32	ND	ND	ND	ND	ND	98.01	ND	ND
3	63.51	0.78	1.63	10.43	ND	5.93	1.29	0.91	0.63	2.77	12.11	ND

Microwave Absorption Properties

Figure 3 shows that variation of relative dielectric constant of tire rubber at 915MHz and 2466 MHz (for the common practice at 2.45GHz) in log value under stagnant air in the chamber. The results can be separated into different distinct stages. At 915 MHz, it keeps increasing in the range of room temperature to 650°C. For the second stage from 650 to 800°C, it decreases first and then keeps increasing. The relative dielectric constant of tire rubber at 2450 MHz behaves similarly to that at 915MHz. The relative dielectric constant of tire rubber at 915 MHz is higher than that at 2466 MHz.

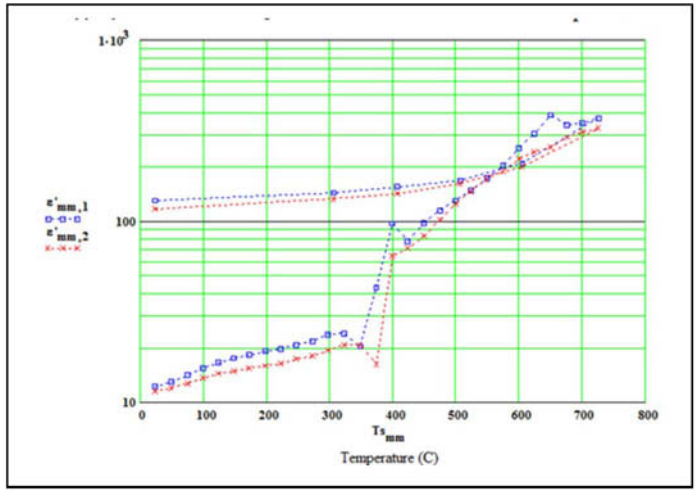

Figure 3. Temperature dependences of relative dielectric constant (in log scale) under stagnant air. The $\varepsilon'_{mm,1}$ denotes relative dielectric constant at 915MHz, while the $\varepsilon'_{mm,2}$ represents the relative dielectric constant at 2466 MHz.

As seen in Figure 3, although relative dielectric constant of tire rubber at 915MHz is higher than the relative dielectric constant of tire rubber at 2466MHz, the relative dielectric constant of the tire rubber is generally independent of microwave frequencies.

For most materials, the dielectric constants increase with temperature. In the tire rubber, the main component which absorbs microwaves is carbon black. Carbon black is an excellent microwave absorber because the material has strong polarity [11]. As the temperature is increased, the pyrolysis of tire rubber may produce more carbon black. This would result in the increase of carbon black content in the products. Consequently, the microwave absorption capability of the sample would increase with temperature.

Conclusions

The recycling of waste tires has been a big environmental problem. Pyrolysis is considered the most desired approach for the materials and energy recovery. Microwave absorption properties of tire rubbers at various temperatures are characterized in this study to determine the conditions favorable for the microwave heating of tire rubbers. It was found that the dielectric constant of waste tire increases with the rising temperature in the experimental range from room temperature to about 800 ^{o}C. Carbon black is an excellent microwave absorber. Since it is a major component in tire, it is believed that carbon black is responsible for the high microwave absorption capacity of the waste tire.

References

[1] D. F. Martinez , "Soaking in a Solvent to Reduce Tensile Strength, Applying Shear Force to Disintegrate Rubber from Reinforcement; Sorting," *United States Patent*, US5304576 A (1994),

[2] Y. Fang, M. Zhan, and Y.Wang, "The status of recycling of waste rubber," *Materials & Design*, 22 (2001) 123-127,

[3] H. Liu, J. Mead and R. Stacer, "Environmental Impacts of Recycling Rubber in Light Fill Applications: Summary & Evaluation Of Existing Literature University of Massachusetts,", *Chelsea Center For Recycling and Economic Development*, (1998).

[4] "Tire Recycling"http://en.wikipedia.org/wiki/Tire_recycling, April 8, (2014).

[5] W. Price = and E. D. Smith, ,"Waste Tire Recycling: Environmental Benefits and Commercial Challenges," *International Journal of Environmental Technology and Management* 63-64 (2006), 363-364.

[6] R. C. Walter, K. C. Bass, and W. E Roseveare, "Degradation of Rayon Tyres at Elevated Temperature," *Industrial Engineering Chemistry* .,48 (1978) 138–143,

[7] J. Shang, J. Mei, and J. Notestein, "Fluidized-Bed Combustion of Scrap Tyres, Technical Notes from Annual Report," *USA: Department of Energy*, (1981) No. DOE/METC-8614068,

[8] L. Berti, M. Marani, and R. Scialdoni, "Valutazione e Misuredelle Emissions di un, Impianto di Combustione di Pneumatici," *Risparmio Energetico*, 29 (1990), 23–32,

[9] K. Allott, "Crapped tires: Their Potential as a Source of Energy or Raw Materials," *Process Engineering and Environmental Protection*, (1991) 45–46.

[10] M. Coronidi and E. Ranaldi, "Prove di Combustionegranulato di Pneumatics

Nell'inceneritore a Lettofluido ABI-2000," *Relazione Finale*, 1 (1995) FISIA/AMB-TEIN-G-004 248,
[11] R. Rausa, P. Pollesel, "Pyrolysis of Automotive Shredded Residue: Influence of Temperature on the Distribution of Products," *Journal of Analytical and Applied Pyrolysis*, 40–41 (1997),369,

Characterization of Minerals, Metals, and Materials 2015
Edited by: John S. Carpenter, Chenguang Bai, Juan Pablo Escobedo, Jiann-Yang Hwang, Shadia Ikhmayies, Bowen Li, Jian Li, Sergio Neves Monteiro, Zhiwei Peng, and Mingming Zhang
TMS (The Minerals, Metals & Materials Society), 2015

OPTICAL EVALUATION FOR BIOMIMETIC MICROLENS ARRAY ON PDMS SHEET

Kenji Monden

Advanced Technologies Research Institute, Denki Kagaku Kogyo Kabushiki Kaisha;
3-5-1 Asahimachi; Machida-shi, Tokyo, 194-8560, Japan

Keywords: Microlens array, Nanoimprint, Optical property, PDMS

Abstract

A simple technique is presented to evaluate optical property of biomimetic microlens array (BMA) as an antireflective surface on a polydimethylsiloxane (PDMS) sheet. The integration of these structures is done by a thermoforming process. We have only UV-VIS spectrophotometer for optical evaluation apparatus. The transmittance of the sheet is measured with angled sample holder. The 50 deg. transmittance of 270nm pitch BMA on PDMS sheet increases from 87 to 92% after the moth-eye structure is introduced. The transmittance of 350nm pitch BMA on PDMS sheet increases from 87 to 96% after the moth-eye structure is introduced. The transmittance increases with increasing pitch of BMA. The results obtained using UV-VIS spectrophotometer with handmade sample holder.

Introduction

Nanoimprint is a method of fabricating micro- and nanometer scale patterns using fine molds [1]. Nanoimprint has demonstrated sub-micrometer feature size, pitch, vertical and smooth sidewalls, and nearly 90° corners. Further experimental study indicates that the ultimate resolution of nanoimprint could be sub-micrometer and the imprint process is repeatable. Nanoimprint has two basic steps. The first is the imprint step in which a mold with nanostructures on its surface is pressed into a thin resist cast on a substrate. This step duplicates the nanostructures on the mold in the film. In other words, the imprint step creates a thickness contrast pattern in the film. The second step is the removal of the mold. This step transfers the thickness contrast pattern into the independent film. During the imprint step, the film is heated to a temperature above its glass transition temperature. At that temperature, the film which is thermoplastic becomes a viscous liquid and can flow and, therefore, can be readily deformed into the shape of the mold. The resist's viscosity decreases as the temperature increases. In other hand thermosetting resins have not ever been used for imprint film. Silicone resin which is thermosetting resin has high quality for optical application. Silicone resin has been used an encapsulating resin of LED (light emitting diode) packages.
In this work, we applied imprint technique the biomimetic microlens array (BMA) [2, 3] as an antireflective surface on a polydimethylsiloxane (PDMS) sheet. Figure 1 shows schematic view of the nanoimprint process [4]. The biomimetic microlens array mold is immersed in PDMS mixture and cured. Finally the mold is removed. A simple technique is presented to evaluate optical property of silicone BMA.

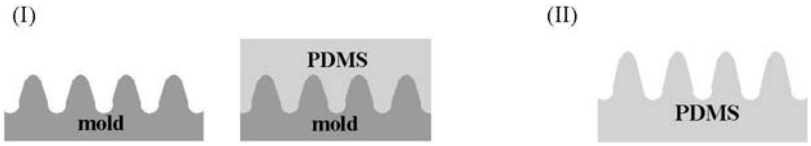

Figure 1. Schematic view of the nanoimprint process, (I) the biomimetic microlens array mold is immersed in PDMS mixture and cured, (II) the mold is removed.

Experimental

Specimen Preparation

The integration of BMA structures is done by a thermoforming process. The BMA mold is immersed in PDMS mixture. An imprinting temperature of 150 ℃ is chosen and the applied pressure is 1 MPa. Figure 2 shows our imprint equipment. In order to make the most accurate PDMS copies of the pattern, we have tested several PDMS solutions. 1:1 mixtures of PDMS base elastomer and curing agent solutions are prepared. A planetary centrifugal mixer is used for simultaneously dispersing the components uniformly and de-aerating the mixture.

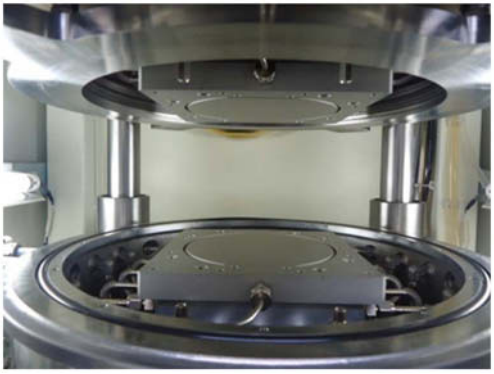

Figure 2. The photograph is the equipment to imprint.

Measurement of Optical Properties

We have only UV-VIS spectrophotometer, Shimadzu UV-1600, which is shown Figure 3 for optical evaluation apparatus. The transmittance of the sheet is measured with five angled sample holders. The angles of sample holders are 10, 20, 30, 40, 50 degree. The handmade sample holders are shown in Figure 4.

Figure 3. Optical evaluation apparatus is UV-VIS Spectrophotometer.

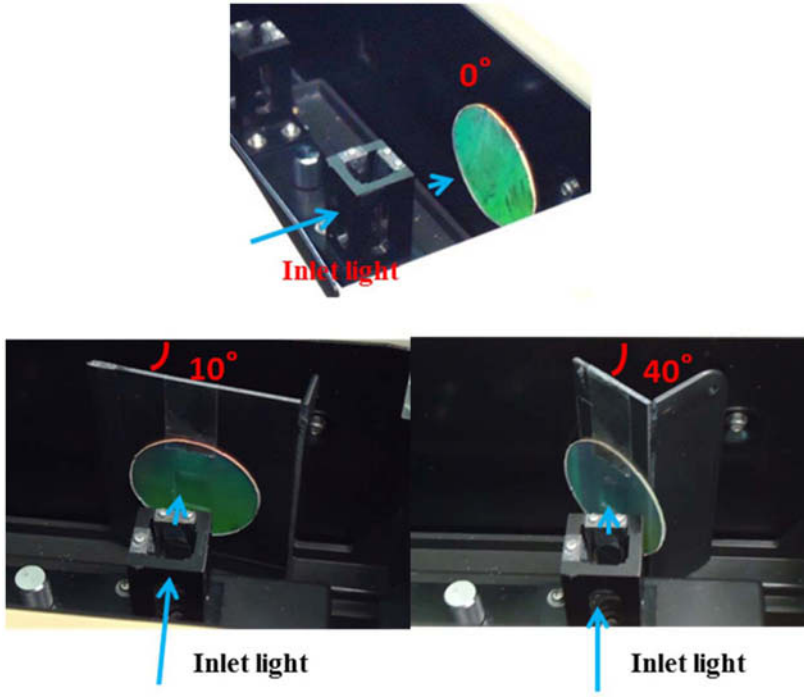

Figure 4. The photographs are handmade angled sample holders.

Results and Discussion

Shape of BMA

SPM (Scanning probe microscope) image of a BMA on PDMS sheet is shown in Figure 5. SEM (Scanning electron micrographs) image of the BMA on PDMS sheet are shown in Figure 6. Very good pattern definitions are obtained. The shape data of BMA on PDMS are shown in Table I.

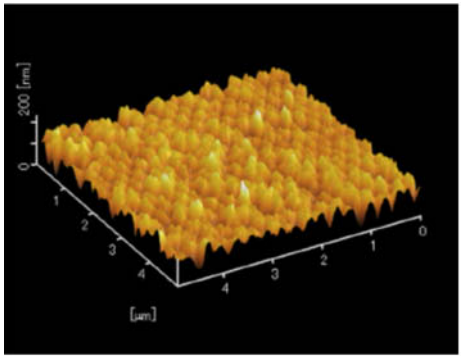

Figure 5. The SPM image is a biomimetic microlens array on PDMS sheet.

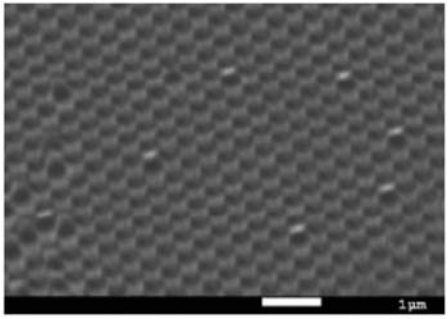

Figure 6. The SEM image is biomimetic microlens array on PDMS sheet.

Table I. Shape data of BMA on PDMS.

Sample name	Height [nm]	Pitch [nm]	Thickness [mm]
BMA1 on PDMS	200	270	1.21
BMA2 on PDMS	190	350	1.10

Optical Properties of BMA

The relationship angle of sample in UV-VIS spectrophotometer and transmittance of BMA on PDMS sheet at 540nm are shown in Figure 7. The 50 deg. transmittance of BMA1 on PDMS sheet (270nm pitch) increases from 87 to 92% after the moth-eye structure is introduced. The transmittance of BMA2 on PDMS sheet (350nm pitch) increases from 87 to 96% after the moth-eye structure is introduced. The transmittance increases with increasing pitch of BMA.

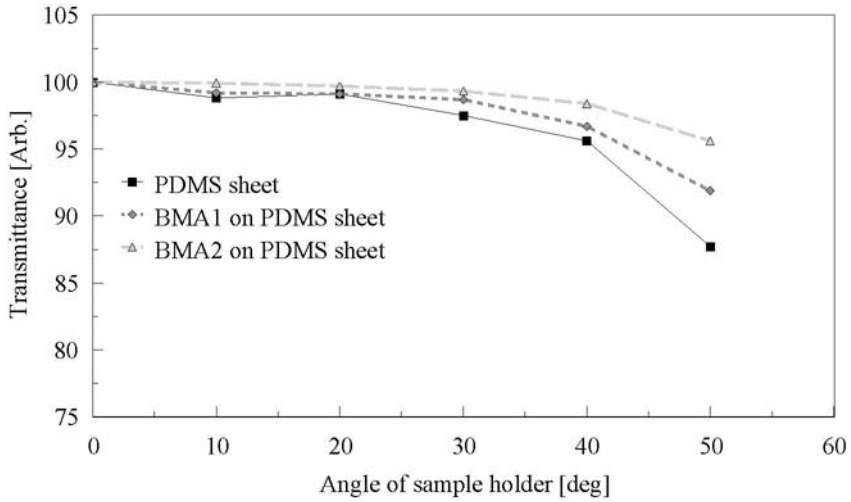

Figure 7. The graph shows the relationship angle of sample holder in UV-VIS spectrophotometer and transmittance of biomimetic microlens array on PDMS sheet at 540nm.

Assembly property measurement

For assembly property measurement we used blue LED apparatus. The blue LED apparatus is shown in Figure 8(I). The blue LED apparatus with PDMS sheet is shown in Figure 8(II). That with BMS2 on PSMS is shown in Figure 8(III). The diffusion degree of the blue light of Figure 8(II) is different from that of Figure 8(III).

(I)

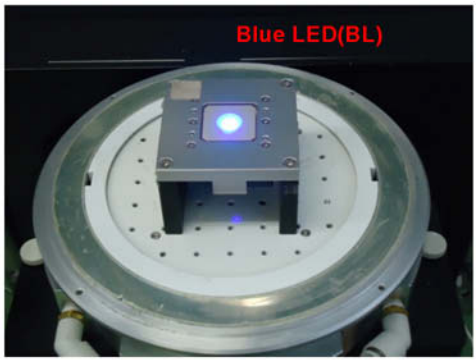

(II)

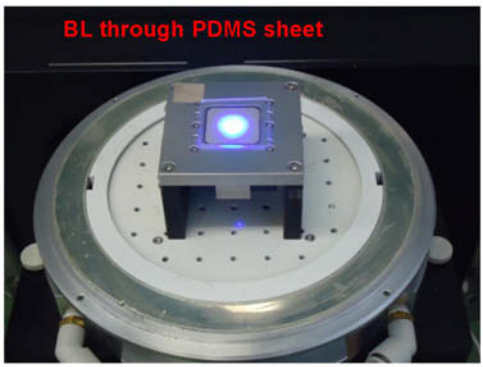

(III)

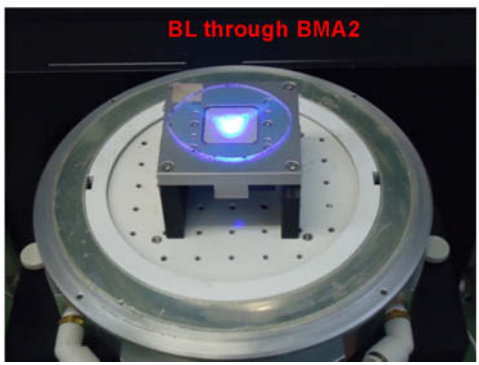

Figure 8. Assembly property measurement of (I) only blue LED, (II) blue LED through PDMS sheet, (III) blue LED through BMS2 on PDMS.

Conclusion

We applied imprint technique the biomimetic microlens array as an antireflective surface on a thermosetting resin, polydimethylsiloxane sheet. We have demonstrated a simple technique of optical evaluation for biomimetic microlens array on polydimethylsiloxane sheet. The results obtained using UV-VIS spectrophotometer with handmade sample holder and also assembly property measurement apparatus.

Acknowledgments

The help of Mr. M. Saito, DENKA Innovation Center, Denki Kagaku Kogyo K. K., is gratefully acknowledged.

References

1. S. Y. Chou, et al., *J. Vac. Sci. Technol.* B14 (1996), 4129-4133.
2. D.H. Ko, et al., *Soft Matter*, 7 (2011), 6404-6407.
3. V. Auzelyte, et al., *Microelectronic Engineering* 97 (2012), 269-271.
4. L. J. Guo, *Advanced Materials* 19 (2007), 495-513.
5. C.H. Chang, et al., *J. Vac. Sci. Technol.* B21 (2007), 2755-2759.

Characterization of Minerals, Metals, and Materials 2015
Edited by: John S. Carpenter, Chenguang Bai, Juan Pablo Escobedo, Jiann-Yang Hwang, Shadia Ikhmayies, Bowen Li, Jian Li, Sergio Neves Monteiro, Zhiwei Peng, and Mingming Zhang
TMS (The Minerals, Metals & Materials Society), 2015

Behavior of Linear Low Density Polyethylene Films under UV Ageing for Agricultural Application

Poveda, Patricia Negrini Siqueira[(1)*]; Viana, Hamilton Magalhães [(2)]; and Silva, Leonardo Gondim de Andrade [(1)]

[1] Instituto de Pesquisas Energéticas e Nucleares (IPEN / CNEN - SP)
Av. Professor Lineu Prestes 224205508-000 São Paulo, SP - Brazil
[2] Centro Universitário Fundação de Santo André (FSA – FAENG)
Av. Príncipe de Gales, 821 - Bairro Príncipe de Gales 09060-650 Santo André, SP - Brazil

*patricianegrini@usp.br

Keywords: polyethylene, nano, additive, ageing, UV.

Abstract. Polymers are susceptible to changes in their chemical structures that affect their mechanical properties under weather condition. Exposure of plastics to UV radiation causes a loss in their mechanical properties and/or change in appearance, including reduced ductility, color changes, yellowing and cracking. Today, there are several additive systems (light stabilizers) developed to work according to resin, final application, type of cultivation, and other characteristics. This study evaluates the different additive systems (Hindered Amine Light Stabilizer - HALS, nano calcium carbonate - NPCC, nZnO and nTiO2), applied 0.75% (in weight) in linear low density polyethylene (LLDPE). The samples were mixed by high rotation homogenizer and extrusion. Later, the samples were molded by injection and aged in QUV-B simulating 6 months of exposure to weather. Tests of FT-IR and tensile strength comparing to the non-aged samples were carried out in order to evaluate the performance of several additive systems.

INTRODUCTION

Aging is a term used for many branches of polymer science and engineering, when the properties of polymer change over a period of time. The changes can be observed on engineering properties as strength and toughness; physical characteristics as density; or chemical characteristics as aggressive chemical reactivity. The origins of these changes can be chemical or a result of interaction with the environment, such as when the oxidation leads to chain scission. Sometimes a series of aging-related phenomena occur simultaneously and or interactive form (1).

The main purpose served by examining data on weathering of materials is to predict any potential changes of physical properties and appearance of those materials. Natural sunlight is not standard; there are variations in clouds, smog, angle of the sun, rain, industrial environments, etc. Accelerated aging is used to guarantee the test is realized under standard methods (2).

Salem, Faouk and Kashif (3) studied films of low density polyethylene (LDPE) non-stabilized against formulations containing stabilizer type Hindered Amine Light Stabilizer (HALS) after exposure to ultraviolet radiation. The results showed the use of stabilizer HALS was effective to keeping mechanicals properties of LDPE films after UV exposition. It was also observed that the

rate of formation of carbonyl groups depends of time of UV exposure, as well as the polymer crystallinity is strongly influenced by UV radiation and presence of HALS (4).

Deschmane, Yun and Misra (5) investigated the effect of calcium carbonate in mechanical properties of high density polyethylene (HDPE) compounds. The characteristic of reinforcement was evidenced through the results of impact resistance where the fracture characteristics were attributed mainly to the nucleating effect promoted by the presence of calcium carbonate, decreasing the size of the espherulites (6).

Photodegradation of LDPE containing nano particles of zinc oxide (nZnO) was analyzed by Yang and other (7) by FT-IR to monitor the development of oxidation products of films. Although the absorption of wavelengths below 350nm by ZnO protect the polymer of photochemistry degradation, can induce heterogeneous photocatalytic oxidation of polymer. Apparently, the reduction of mechanical properties is more related to the carbonyl groups than the generation of CO_2 (8).

Yang and other (9) studied the effect of UV radiation in LDPE films containing different concentrations of nano particles of titanium dioxide ($nTiO_2$). When exposed on equipment for accelerated weathering test of type QUV, films resisted 400h, although TiO_2 presence had promoted the exposition time reduction 50% in mechanical resistance due carbonyl groups formation.

This study evaluates the additive systems (HALS, NPCC, nZnO and $nTiO_2$), applied 0.75% (in weight) in LLDPE. The samples were mixed by high rotation homogenizer and, further, extrusion. Later, the samples were molded by injection and aged in QUV-B simulating 6 months of exposure to weather. Tests of FT-IR, carbonyl index and tensile strength comparing to the non-aged samples were analyzed to evaluate the performance of additive systems in relation to the degradation behavior of linear low density polyethylene.

Materials and Methods

Material

Linear Low Density Polyethylene (LLDPE) butane-1 copolymer, narrow molar mass distribution, without slip additives, supplier Braskem, named ML 2400N, with melt index of 20.0 g/10min and density of 0.926 g/cm^3. This material was used as a vehicle for the production of masterbatches and obtaining specimens injected.
Tinuvin 783 is a mix 1:1 of Hindered Amine Light Stabilizer (HALS) with low molar mass (Chimassorb 944), and high molar mass (Tinuvin 622). This additive is produced by BASF and used as standard UV stabilizer, whose physical form is represented by slightly yellowish granules or tablets, with density 514 g/l and fusion of 55°C to 140°C.
The nano calcium carbonate was provided by Nano Materials Technology Pte Ltd., represented in Brazil by Lagos Química, called NPCC-201, with specific density of 2.5 g/cm^3, surface area of 40.0 m^2/g and average particle size of 40nm.
The nano titanium dioxide was supplied by Croda, named Atmer 7354, whose product is a concentrate of additive with 20% of active metal oxide content, compatible with polyolefin polymers.

The nano zinc oxide was provided by Croda, named Atmer 7355, whose product is a concentrate of additive with 30% of active metal oxide content, compatible with polyolefin polymers.

Preparation of samples

For the study of the nano composites, proposed formulations were presented below, whose compositions are expressed as percentage, in weight.

PE100 – 100% LLDPE
PECa75 – 0.75% NPCC additive in 99.25% LLDPE
PETi75 – 0.75% nTiO2 additive in 99.25% LLDPE
PEZn75 – 0.75% nZnO additive in 99.25% LLDPE
PEUV75 – 0.75% HALS additive in 99.25% LLDPE

The formulations that contained nano calcium carbonate and the ultraviolet stabilizer additive default, have been prepared initially by mixing in high rotation homogenizer for better dispersion of components, forming a concentrated (masterbatch). Then, pellets were formed by extrusion, and later, inject specimens. Samples of nano titanium dioxide and nano zinc oxide were provided as concentrated in polyethylene, therefore, were only applied to thermoplastic resin in appropriate proportion, and after, obtain injected specimens.
Components of formulations were weighed in balance Marte, model AS 5500, with capacity of 5000g. Formulations were prepared in high rotation homogenizer MH, model MH-600, capacity of 500g. The components of formulations were introduced at the same time in equipment and the mix occurred by shear, with velocity of 3600 rotations per minute (rpm). The molten material was ground into mill BGM, leading to reduced pieces and dosage of these in mono screw extruder.
Formulations were produced in mono screw extruder BGM, model EL-25, with screw diameter of 25mm and L/D = 30. The heat profile was 110/120/130°C for feed, compression and dosage zones, respectively, and 140°C on head. It was used screw rotation of 50rpm.
To prepare injected samples, an Arburg injector, model Allrounder 270S 400-100, was used with heat profile 120/130/150/155/160°C, funnel to nozzle.

Analytical methods

The accelerated aging was conducted in a test chamber UV condensation (QUV) to simulate the effects of degradation on the surface of specimens, usually generated by exposure to sunlight, rain and dew. The specimens were exposed to radiation generated by UV-B lamp-310, with 8h of UV cycle to 70°C and condensation cycle of 4h to 50°C, repeating for 172 hours, simulating natural exposure of 06 months.
The mechanical tests were carried out to evaluate the resistance of nano composites through properties at break, elongation at break and the secant module. The analyses were performed per ASTM D-638, in Zwick universal testing machine; model Z030, with speed of 50 mm/min and processing of data through Software Test Xpert Machine V.6.01.
Analyses of Fourrier Transform InfraRed (FT-IR) were carried out for verification of the oxidation of the polymer through the carbonyl index, according to ASTM D 5576, Perkin Elmer, spectrometer Spectrun One model, coupled with Universal ATR device ("Sampling Accessory"), in the range of 400 to 10000cm^{-1} with resolution 2cm^{-1}.

Results and Conclusion

The results of the measurements of mechanicals properties for the different compositions of samples studied are shown on Table 1. It is possible to observe the effects of photodegradation on sample PE100 when compared with PE100 STD. PE100 not contain additive, then UV radiation is very aggressive, caused the decline of the properties (decrease of 45.5% in tensile modulus and breaking of the sample while the PE100 STD did not break after stretching).
Considering PE100 the reference for sample post ageing, the nanoparticles presented increase in tensile modulus (71.85% to PECa75, 64.08% to PETi75 e 71.85% to PEZn75). These results showed that nanoparticles have given greater stiffness to the polymer. Due to this characteristic, it has greater tensile strength in breaking and lower elongation at break.
Despite the lower results in modulus of elasticity and strength resistance, it was verified that the sample PEUV75 had more deformation and not broke in the same test condition.
The composites with additive HALS (PEUV75 STD and PEUV75 QUV) were more tenacious, probably, this additive did not interfere on crystallinity of polymer or its influence was minimal.

Table 1. Results with polyolefin polymers after accelerated aging by QUV-B

Sample	Tensile Modulus E (MPa)	Breaking Strength (MPa)	Breaking Elongation (%)
PE 100 STD	188.80 ± 20.49	-	-
PE 100 QUV	103.00 ± 6.04	5.90 ± 1.47	173.47 ± 33.77
PE UV 75 STD	170.00 ± 23.10	-	-
PE CA75 STD	184.60 ± 29.23	-	-
PE ZN75 STD	153.60 ± 16.23	-	-
PE TI75 STD	150.80 ± 9.58	-	-
PE UV 75 QUV	175.60 ± 26.23	-	-
PE CA75 QUV	217.20 ± 29.24	10.51 ± 0.24	93.10 ± 31.48
PE ZN75 QUV	177.00 ± 5.66	8.41 ± 0.86	135.81 ± 22.95
PE TI75 QUV	169.00 ± 24.03	7.53 ± 1.28	128.68 ± 18.56

STD - reference sample, standard material, not aged.
QUV - sample post ageing by chamber QUV-B.
- no break.

The carbonyl index is calculated as the ratio of the intensity of the carbonyl band (1710-1730 cm^{-1}) in the FTIR spectrum and the intensity of the chosen reference band in the material examined (10, 11). In the case of Polyethylene, the band was chosen to group C-H stretching (1300-1400 cm^{-1}). Table 2 shows the values obtained and indicates that the carbonyl index suffers increase after aging for all samples, except for HALS. The most effective additive on reduction of carbonyl index is the HALS, followed by $nCaCO_3$. Samples with nZnO and $nTiO_2$ presented superior carbonyl index.

Table 2. Heights of the carbonyl stretching bands and C-H stretch.

Sample	Carbonyl index (CI) ($h_{C=O}$ / h_{C-H})	CI QUV / CI STD (%)
PE 100 QUV	0.10	1.83
PE 100 STD	0.05	
PE UV75 QUV	0.05	0.52
PE UV75 STD	0.03	
PE Ca75 QUV	0.02	5.75
PE Ca75 STD	0.12	
PE Zn75 QUV	0.03	6.55
PE Zn75 STD	0.20	
PE Ti75 QUV	0.03	10.17
PE Ti75 STD	0.30	

STD reference sample, not aged.
QUV sample post ageing by chamber QUV-B.

In general, all systems of light stabilizer additives had a positive effect on the LLDPE material, with different performances, according to the results presented.
The sample based HALS had a mechanical result (yield strength) close to the sample of LLDPE without additives (ageing), however, the sample not broke in tensile strength. The polymer with HALS additive (PEUV75) was more tenacious because, probably, this additive didn't interfere on crystallinity or its influence was minimal. It had presented the carbonyl index lowest among all the studied systems.
Nanoparticle-based samples, as well as increase the carbonyl index, showed an increase of mechanical properties. These results can be explained due to the physical characteristics of these materials, which can act as nucleating agent for the polyethylene, conferring mechanical reinforcement and turn the polymer more stiffness.
The balance between carbonyl and mechanical properties index showed $nCaCO_3$ the best formulation light stabilizer, among the analyzed nanoparticle systems (nZnO, $nTiO_2$ and $nCaCO_3$).
Thus, it was concluded that the best UV additives systems evaluated were based on HALS (PEUV75), keeping the tenacity of the polymer, and $nCaCO_3$ (PECa75), offering greater stiffness to polymer.

References and Notes

1. J. R. White, "Polymer ageing: Physics, chemistry or engineering? Time to reflect", *Chimie*, 9 (2006), 1396–1408.
2. L. K. Massey. *The effects of UV light and weather on plastics and elastomers*, (New York, NY: Wiliam Andrew Publishing, 2ed. 2007).
3. M. A. Salem; H. Faouk; I. Kashif, "Physicochemical Changes in UV- Exposed Low- Density Polyethylene Films", *Macromolecular Research*, 10(3) (2002), pp.168-173.
4. M. Osman; A. Atallah. "Effect of the particle size on the viscoelastic properties of filled polyethylene", *Polymer*, 47(7) (2006), pp.2357-2368.
5. C. Deshmane; Q. Yuan; R. Misra, "On the fracture characteristics of impact tested high density polyethylene-calcium carbonate nanocomposites", *Materials Science and Engineering: A*, 452 (2007), pp.592-601.
6. S. C. Li; Y. N. Li, "Mechanical and Antibacterial Properties of Modified Nano-ZnO/High-Density Polyethylene Composite Films with a Low Doped Content of Nano-ZnO", *Journal of Applied Polymer Science*, 116(5) (2010), pp.2965-2969.
7. R. Yang, P.A. Christensen, T.A. Egerton, J.R. White, "Degradation products formed during UV exposure of polyethylene-ZnO nano-composites", *Polymer Degradation and Stability*, 95(9) (2010), pp.1533-1541.
8. E. B. Zeynalov; N.S., Allen, "An influence of micron and nano-particle titanium dioxides on the efficiency of antioxidant Irganox 1010 in a model oxidative reaction", *Polymer Degradation and Stability*, 86(1) (2004), pp.115-120.
9. R. Yang, P.A. Christensen, T.A. Egerton, J.R. White, A. Maltby, "Spectroscopic Studies of Photodegradation of Polyethylene Films Containing TiO2 Nanoparticles", *Journal of Applied Polymer Science*, 119(3) (2011), pp.1330-1338.
10. G. Ahlblad, D. Forsström, B. Stenberga, B. Terselius, T. Reitbergerb, L. G. Svensson, "Oxidation profiles of polyamide-6,6 studied by imaging chemiluminescence and FT-IR", *Polymer Degradation and Stability*, 55(3) (1997), pp.287-293.
11. N. S. Allen, R. A. Ortiz, G.J. Anderson , "Comparison of the thermal and light stabilizing action of novel imine and piperazine based hindered piperidine stabilizers in polyolefin", *Polymer Degradation and Stability*, 46(1) (1994), pp.85-91.

Characterization of Minerals, Metals, and Materials 2015
Edited by: John S. Carpenter, Chenguang Bai, Juan Pablo Escobedo, Jiann-Yang Hwang, Shadia Ikhmayies, Bowen Li, Jian Li, Sergio Neves Monteiro, Zhiwei Peng, and Mingming Zhang
TMS (The Minerals, Metals & Materials Society), 2015

PHOTOACOUSTIC THERMAL CHARACTERIZATION OF MALVA FIBERS

Jean Igor Margem[3], Vinicius Alves Gomes[1], Roberto Faria Jr.[1], Frederico Muylaert Margem[1], Thallis Cordeiro[1], Marina Rangel Margem[1], Sergio Neves Monteiro[2]

[1] State University of the Northern Rio de Janeiro, UENF, Advanced Materials Laboratory, LAMAV; Av. Alberto Lamego, 2000, 28013-602, Campos dos Goytacazes, Brazil
[2] Instituto Militar de Engenharia , IME, Praça Gen. Tibúrcio, nº80 Urca, RJ, 22290-270
[3] Instituto de Ensino Superiores do Censa, ISECENSA, Rua Salvador Correa, 139, 28035-310, Campos dos Goytacazes, Rio de Janeiro , Brazil.
igormargem@gmail.com

Abstract

Natural fibers are attracting the interest of engineering sectors owing to specific advantages such as lightweight and lower cost as well as for their inherent condition of being renewable, biodegradable, recyclable and neutral with respect to CO_2 emission. In particular, the fiber extracted from the malva plant stem is nowadays recognized as one of the strongest lignocellulosic fibers. However, the thermal properties of the malva fibers have yet not been fully investigated. The present work had as its objective to investigate, by photoacoustic spectroscopy and photothermal techniques the thermal properties of diffusivity, specific heat capacity and conductivity of a pressed malva fibers sample. The results revealed that these fibers showed a superior thermal insulation capacity.

Keywords: Photoacoustic, Malva fibers, Thermal Properties.

Introduction

According to Kalia et al [1], cellulose-based fibers are gaining attention due to its "green" image, unlike the glass fiber widely used in modern technology, those lignocellulosic fibers are renewable and can be incinerated in the end of the useful life without the addition of air pollution, since the amount of CO_2 released during the combustion process is negligible compared to the amount absorbed by the plant throughout its life [2].

It should be notice that the use of lignocellulosic fibers in packaging, textile, construction and automobile industries is growing very fast. One of its applications is promising as reinforcement for polymeric composites. In fact, a considerable number of publications [3-8] has been devoted to lignocellulosic materials reinforcing polymer composites. In particular, the applications on automobile industry already in the market [9-12].

The lignocellulosic natural fiber extracted from the stem of malva plant, illustrated in Figure 1, can reach high values of tensile resistance [13], and the plantation, extraction and manufacture procedures do not cause problems to the environment.

Figure 1 - (A) Malva typical plant (B) Malva extracted fibers.

A preliminary thermal behavior investigation of the malva fiber by thermogravimetric analysis, TGA, and it's derivative DTG showed the material evolution conditions associated with water loss, for surface moisture, water release, cellulose and lignin decomposition and also calcium and silicon oxidation [14].

The photoacoustic spectroscopy and photothermal techniques characterizes thermal properties and acoustic insulation for the tested materials. These techniques are based on heat generation as a result of the absorption of radiation [15,16] and had already presented some interesting results in literature for polymeric materials [15]. The objective of this study was to perform photoacoustic and photothermal characterization of malva fiber.

Materials and Methods

The malva fibers used in this work were purchased from a local supplier in the Amazon region. After cleaned and dried at room temperature the fibers diameters were statistically analyzed following the procedure described elsewhere [13,18]. The diameter distribution goes from 20 to 110 μm with an average diameter of 65 micrometers.

This study samples was prepared using pure malva fibers carefully crushed under 25 tons of pressure to generate a thin disc with thickness less than 0.5 mm, the fibers were placed inside plastic film before the crushing process to prevent contaimination. The discs can be seen in Fig 2(b). Each sample was tested in a open photoacoustic cell as shown in Figure 2(a), to amplify the photothermal results materials were tested under continuous laser illumination. Both techniques were used to determine the thermal diffusivity αs, and specific heat capacity ρcp. From these parameters, the thermal conductivity, k, of malva fiber was evaluated by the following equation:

$$\mathbf{k = \alpha_s \rho c_p} \qquad (1)$$

The thermal diffusivity was measured by the photoacoustic technique which considers heat loss in a sample due to a process of thermal relaxation upon light absorption. The open photoacoustic cell (OPC) assemble the sample directly into a cylindrical microphone, as showed in Figure 2(a). The air chamber in front of the microphone works as a conventional gas chamber, normally applied in others photoacoustic techniques [16]. The results evaluation

is based on the fact that thermoelastic mechanism is dominant on the OPC method. The value of αs was then obtained by fitting the data of the experimental phase, ϕ, by the following equations:

$$\phi = \phi_o + \arctan\left(\frac{1}{x - 1}\right) \tag{2}$$

$$x = \ell_s \left(\frac{\pi f}{\alpha_s}\right)^{1/2} \tag{3}$$

Where ℓs is the sample thickness and f is photoacoustic signal frequency. It is assumed that the sample is optically opaque, and that the flow of heat into the surrounding air is negligible.

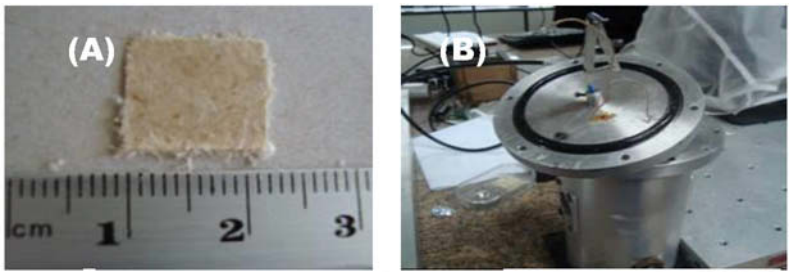

Figure 2. (A) Malva photoacoustic sample, (B) The open photoacoustic cell (OPC)

Results and Discussions

Figure 3 shows typical curves of the variation of the phase ϕ photoacoustic signal with a frequency f. It is worth mentioning that the signal phase is the phase difference between the generated signal and the detected signal. The frequency with varies in the graph is the modulation frequency of the laser.

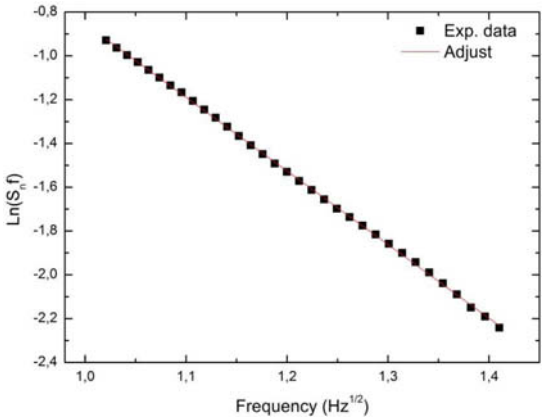

Figure 3. ϕ phase variation of the photoacoustic signal with frequency f to the malva fiber.

In Figure 3, the black dots represent the experimental data while the solid line corresponds to the best experimental points fit curve. Considering that the thickness of each sample is ℓs = 624 μm, the thermal diffusivity based on Eq (3) was determined as:

$$\alpha_s = (1{,}13 \pm 0{,}06)\ m^2.s^{-1} \quad (4)$$

Given malva sample evolution with time, when laser illumination is cleared, it was plotted the experimental curves as illustrated in Figure 4. In this figure, the points correspond to the data obtained experimentally. On the other hand, the solid line represents the mathematical best fit curve for the path of the experimental points. The continuous line was calculated considering the following equations:

$$\Delta T = \left(\frac{I_o \tau}{\ell_s \ \rho \ c_p}\right)\left(1 - e^{-t/\tau}\right) \quad (5)$$

$$\tau = \ell_s \ \rho \ c_p \ (2H) \quad (6)$$

$$H = 4\sigma \ T_o^3 \quad (7)$$

where Io is the intensity of the incident laser on the sample and τ is known as the time of rising temperatures ("temperature rise time"), which H is called the transfer coefficient of heat radiated and consist of the constant of Stefan-Boltzmann, σ, and the ambient temperature T_o. Using the value of τ as an adjustable parameter on the curve of Figure 4, the specific heat capacity can be obtained.

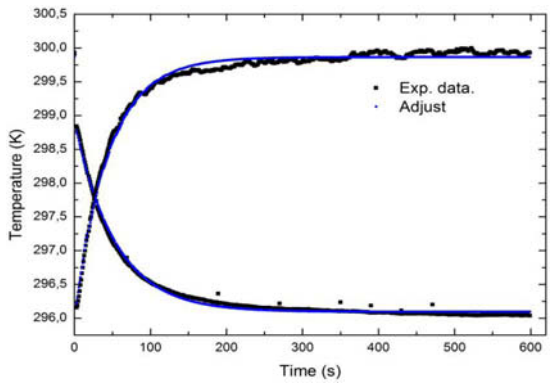

Figure 4. Back surface of the sample temperature evolution

Thus, considering Eq 5, 6 and 7, the value of the specific heat capacity of the malva fiber was obtained as:

$$\rho_c = (8{,}7 \pm 0{,}9)\ J.\ K^{-1}.m^{-3} \quad (8)$$

Was obtained the thermal conductivity of malva fiber using the values of thermal diffusivity, Eq (4) the specific heat capacity, Eq (8) together in Eq (1)

$$k = (0{,}09 \pm 0{,}01)\ W.m^{-1}.K \qquad (9)$$

The value is comparable to others obtained for polymeric materials [17]. The value of thermal conductivity in Eq (9) indicates that the jute fiber has good thermal insulator characteristics.

Conclusions

- Photothermal properties of malva fiber extracted from the stem of the plant were able to be characterized by open photoacoustic cell spectroscopy technique.
- The thermal diffusivity $\alpha s = (1.13 \pm 0.06)\ m^2.s^{-1}$ and thermal capacity $\rho c = (8{,}7 \pm 0{,}9)\ J.\ K^{-1}.m^{-3}$ were obtained with reasonable accuracy from mathematical adjustments of experimentals data.
- Finally, we calculated the thermal conductivity $k = (0{,}09 \pm 0{,}01)\ W.m^{-1}.K$, which indicates that the malva fiber is a good thermal insulator.

Acknowledgements

The authors thanks the financial and technical support of UENF, CAPES and FAPERJ.

References

1. S. Kalia, B. S. Kaith, I. Kaurs, Cellulose Fibers: Bio – and Nano – Polymer Composites (New York: Springer, 2011).
2. A. Gore, *An Inconvenient Truth. The Planetary Emergency of Global Warming and What We Can do About It* (Emmaus, Pennsylvania, USA: Rodale Press, 2006).
3. A .K. Bledzki, J. Gassan, "Composites Reinforced With Cellulose-Based Fibers". Prog. Polym. Sci, 4 (1999) 221-274.
4. D. Nabi Sahed J.P. Jog, "Natural fiber polymer composites: a review", *Advances in Polymer Technol.*, 18 (1999), 221-274.
5. A.K. Mohanty, M. Misra and L.T. Drzal, "Sustainable biocomposites from renewable resources: opportunities and challenges in the green material world", *J. Polym. Environ.*, 10 (2002), 19-26.
6. Crocker, J., "Natural materials innovative natural composites". *Materials Technology*, 2-3 (2008) 174-178.
7. S.N. Monteiro, F.P.D. Lopes, A.S. Ferreira, D.C.O. Nascimento, "Natural fiber polymer matrix composites: cheaper, tougher and environmentally friendly", *JOM*, 61 (2009) 17-22
8. R. Malkapuram, V. Kumar, Y. S. Nezi "Recent development in natural fiber rein forced polypropylene composites" J. Reinforced Plastics and composites; 28 (10)(2009) 1169-1189.
9. G. Marsh, "Next step for automotive materials". *Mater. Today*, 6(4) (2003) 36-43.
10. J. Hulbery, D. Houston, "Natural fiber reinforced polymer composites in automotive application", JOM, 58 (2006) 80-86.
11. R. Zah, R. Hischier, A.L. Leão and I. Brown, "Curaua fibers in automobile industry – A sustainability assessment". *J. Cleaner Production*, 15, (2007) 1032-1040.
12. S. N. Monteiro, K. G. Satyanarayana, F. P. D. Lopes "High strength natural fibers for improred polymer matrix composites" Mat. Sei. Forum 638-642 (2010) 961-966.
13. Simonassi, N. T.; Carreiro, R. S.; Loiola, R. L; Margem, F. M.; Monteiro, S. N.. Weibull Analysis of the density and Elastic Modulus of Curauá Fibers with Different Diameters. In: 67°

Congresso Internacional da Associação Brasileira de Metalurgia, Materiais e Mineração, 2012, Rio de Janeiro, RJ. Anais do 67 Congresso Internacional ABM, 2012. v. 1. p. 2342-2351.
14. S. N Monteiro, F. M. Margem, I. L. A. Silva, A. B. Bevitori, Thermal photoacoustic characterization of jute fibers, *Proceedings of the 204 TMS*, (San Diego, CA, USA, February 2014) 1653-1658.
15. ALMOND, D., PATEL P., "Photoacoustic and Photothermal Science and Techniques". Chapman and Hall: London, 1996.
16. VARGAS, H., MIRANDA L. C. M., Photoacoustic and related photothermal techniques. PHYS. REP. 161(2) (1988) 43-101.
17. CALLISTER, W. D., Ciência e Engenharia de Materiais: Uma Introdução. 5ed. LTC, São Paulo (2002).
18. Margem, J. I. ; Margem, F. M.; Monteiro, S. N.. Weibull Analysis of the density and Elastic Modulus of Malva Fibers with Different Diameters. In: 67º Congresso Internacional da Associação Brasileira de Metalurgia, Materiais e Mineração, 2012, Rio de Janeiro, RJ. Anais do 67 Congresso Internacional ABM, 2012. v. 1. p. 2341-2352.

Characterization of Minerals, Metals, and Materials 2015
Edited by: John S. Carpenter, Chenguang Bai, Juan Pablo Escobedo, Jiann-Yang Hwang, Shadia Ikhmayies, Bowen Li, Jian Li, Sergio Neves Monteiro, Zhiwei Peng, and Mingming Zhang
TMS (The Minerals, Metals & Materials Society), 2015

MECHANICAL, MORPHOLOGICAL AND THERMAL PROPERTIES OF AÇAÍ FIBERS REINFORCED BIODEGRADABLE POLYMER COMPOSITES

Célio H. Wataya[1], Roberta A. Lima[1], Rene R. Oliveira[1], Esperidiana A. B. Moura[1]

[1]Nuclear and Energy Research Institute, IPEN-CNEN/SP
Av. Prof. L. Prestes, 2242, 05508-000, São Paulo, Brazil

Keywords: Biodegradable composites, Açaí seed fibers, Mechanical tests, SEM, DRX.

Abstract

The purpose of this study was to investigate the mechanical, morphological and thermal properties of biodegradable composites based on aliphatic-aromatic copolyester/polylatic acid blends (PBAT/PLA blends) reinforced by açaí seed fibers, an abundant byproduct of the açaí fruit agro industry. The biodegradable polymeric composites were prepared by melting extrusion process using a twin-screw extruder machine. The fibers removed from the açaí seed were used as the reinforcement and PBAT/PLA blends as the matrix. The influence of the açaí seed fibers addition on properties of composites was investigated by tensile and impact tests, SEM, DSC, and XRD analysis. Correlation between properties was discussed. In addition, açaí seed fibers characterization by SEM, XRD and WDXRF have also been carried out. The addition of açaí seed fibers on biodegradable PBAT/PLA blends showed that it is possible to get interesting property gains in biodegradable polymer by using waste from renewable sources.

Introduction

Nowadays, the environment and sustainability issues have led to remarkable achievements in green technology in the field of materials science through the development of biocomposites. Biocomposites are obtained by the combination of biodegradable polymer as the matrix material and biodegradable fillers (e.g., lignocellulosic fillers). Since both components are biodegradable, the composite as the integral part is also expected to be biodegradable [1]. There is a growing trend to use vegetal fiber residues as fillers and reinforcement in biocomposites, due to their flexibility during processing, highly specific stiffness, large amount of these residues, low cost, and their biodegradability. As conventional plastics (polymer petroleum-derived) are resistant to biodegradation, the concept of using biobased plastics (biodegradable polymers or biopolymers) as reinforced matrices for biocomposites is gaining more and more approval day by day. A variety of natural and synthetic biodegradable polymers that can be used as biocomposite matrix are commercially avaiable. These biocomposite materials are designed to have a better environmental impact than conventional plastics [2, 3]. Furthermore, for short-term applications, biocomposites present strong advantages, and a large number of papers has been published on this topic [2-11]. Poly (lactic acid) (PLA), a linear aliphatic polymer, is known as a biodegradable thermoplastic polymer with widely potential applications [12, 13]. PLA has a number of interesting properties including biodegradability, biocompatibility, high strength, and high modulus [14]. Its high brittleness and low toughness limit its application [15]. To overcome these limitations, blending PLA with flexible polymers is a practical and economical way to obtain toughened PLA. If the flexible polymer is biodegradable resin, the blend obtained will be even more interesting, since its biodegradability will be maintained. Poly (butylene adipate-*co*-terepthalate) (PBAT), an aliphatic-aromatic copolyester, is considered a good candidate for the toughening of PLA due to its high toughness and biodegradability [16]. Blends of PLA and PBAT exhibited higher elongation at

break but lower tensile strength and modulus than the pure PLA due to the addition of a ductile phase. Therefore, the addition of filler to PLA/PBAT blends led to a modulus approaching that of the neat PLA. Moreover, biocomposites obtained from PLA/PBAT blends as the matrix material reinforced with vegetal fiber residues can lead to obtaining to material with better mechanical properties than blend ones, and it can also be expected that the material to be biodegradable [1-3]. Acaı´ (Euterpe oleracea Mart.) is a palm plant widely diffused and cultivated in Amazon regions especially in Pará, a state of Brazil, where the pulp of the fruit has a large consumption as beverages and in food preparations (about 180 tons/year). A wide variety of marketable products is produced from this palm, but the spherical fruits are its most important edible product. The juice prepared by macerating the pulp of the fruit is used to produce energetic snack beverages, ice cream, jam, and liqueur. The acaı´ industrial processing produces a large amount of waste, mainly seeds and fibers [11, 17]. It is estimated that only in the capital of Pará state, Belém, approximately from 100,000 to 120,000 tons of fruits are worked up commercially per year, yielding around 100,000 tons of residues [18, 19]. The growing amount of waste has resulted in a serious environmental and public health problem. The aim of this work was to prepare biocomposite material based on PBAT/PLA blends reinforced with by açaí seed fibers, residues from açaí fruit agro industry and to investigate the effects of the açaí seed fibers addition on the mechanical, morphological and thermal properties of biodegradable PBAT/PLA blends.

2 MATERIALS AND METHODS

2.1 Materials

The materials used in this work were biodegradable Aliphatic-aromatic copolyester (PBAT) with biodegradable Poly(lactic acid) (PLA), producing a blend with MFI = 8,59 g/ 10 min at 190°C / 2.16 Kg, and açaí seed fiber residues from açaí fruit agro industry

2.1.1 Açaí seed fibers residues preparation

Açaí seed fiber residues (fiber) were washed, and kept in distilled water for 24 h. The fiber were then dried at 80 ± 2 °C for 24 h in an air-circulating oven. The dry fiber were reduced to fine powder, with particle sizes equal to or smaller than 125 μm by using ball mills and then it were dried again at 80 ± 2 °C for 24 h to reduce its moisture content to less than 2 %.

2.1.2 Preparation of blend and composite

PLA and PBAT pellets were dried at 60 ± 2 °C for 4 h to reduce its moisture content to less than 2 %. The PBAT/PLA blend (50 %/ 50% based on wt%) and PBAT/PLA with 30 % (wt %) açaí seed fiber were prepared by melting extrusion process, using a co-rotating twin screw Haake Rheomex P332 operating in the L/D 3:1.33 rate. The temperature profile was 105/110/115/120/125/130 °C. Screw speed was 70 rpm. The extrudates coming out of the extruder were cooled down for a better dimensional stability, pelletized, dried at 80 ± 2 ° C for 24 h in a circulating air oven, and fed into injection molding machine to obtain specimens test samples.

2.2 Analyses: Blend and composite characterization:

2.2.1 Mechanical tests

Tensile tests (ASTM D 638), and Izod impact test (ASTM D 256-97) were performed in this work in order to evaluate the mechanical and thermo-mechanical behavior of the materials studied. Each value obtained represented the average of five samples.

2.2.2 Scanning electron microscopy (SEM)

Scanning electron microscopy (SEM) analyses were carried out using a LX 30 (Philips).The samples were cryo-fractured under liquid nitrogen, and then the fractured surface was coated with a fine layer of gold and observed by scanning electron microscopy.

2.2.3 Differential scanning calorimetry (DSC): analyses were carried out using a Mettler Toledo DSC 822e from 25 to 200°C at a heating rate of 10 °C/min under oxygen atmosphere. DSC analyses of the materials were performed on four samples.

2.2.4 X-Rays Diffraction (XRD)
XRD patterns of neat PLA/PBAT blend and it composite samples were obtained using a diffractometer Rigaku Denki Co. Ltd., Multiflex model, CuKα radiation (λ = 1.5406 Å) at 40 kV and 20 mA. With this procedure, the angles (2θ) of diffraction of all the samples were measured from 2° to 50°.

2.2.4 Açaí seed fiber residues Characterization :

Micrograhphy images were obtained by Scanning Electron Microscopy (SEM) and ash main components were determined by wavelength dispersive X-ray fluorescence (WDXRF) using a EDX-720 analyzer with vacuum atmosphere, Collimator in 3(mm) and no spin.

3. **RESULTS AND DISCUSSION**

3.1 Differential Scanning Calorimetry (DSC): Figure 1 shows the curve of DSC analysis of PBAT/PLA blend and acai seed fiber composite.

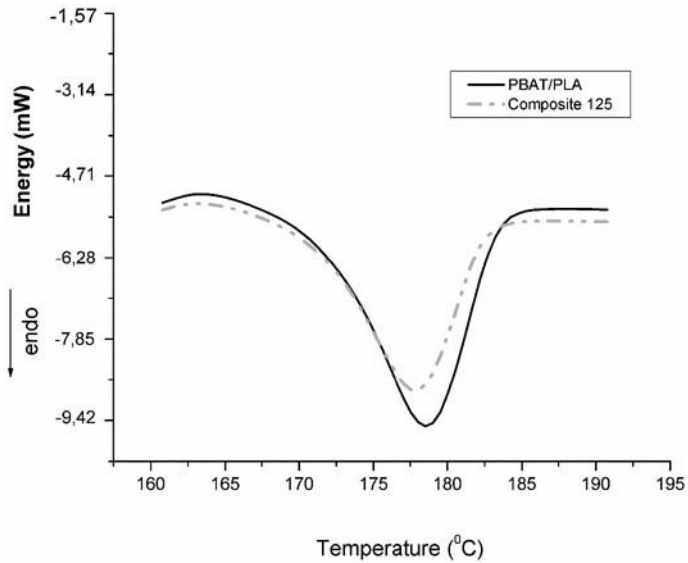

Figure 1. DSC analysis of PBAT/PLA blend and açai seed fiber composite.

From figure 3, it could be inferred that compared with the PBAT/PLA blend the endothermic melting enthalpy decreased due to blending with açai seed fiber. The addition of fiber (15% in wt) in PBAT/PLA blend leads to obtaining of new material with lower melting enthalpy than original blend. The decreases in the melting enthalpy can be attributed to the increase in amorphosity of material. The average values of melting enthalpy (ΔHm) and melting temperature (Tm) of the materials studied are given in Table 1. It indicated that blending PBAT with PLA, followed by biodegradable fiber addition caused structural changes in the polymeric chains of blend component. It means that blend processing and fiber addition had disarranged the polymeric molecules presents in order to obtain a composite material with low melting enthalpy and, consequently, low crystallinity percentage.

Table 1. DSC analysis results of materials studied

Materials	Melting Temperature (T_m, °C)	Melting Enthalpy (ΔH_m,Jg^{-1})
PBAT/PLA blend	178.53	137.10
PBAT/PLA/Açai seed fiber composite	178.03	134.58

As it can be seen, the melting temperature and enthalpy of blend and composite were lower than PBAT /PLA blend indicating little miscibility between the components of the blend and also suggesting a poor incorporation and dispersion of acai seed fiber in the final composite.

3.2 X-ray diffraction (XRD): the XRD results of açaí seed fiber residues are shown in Figure 2. Results show the presence of crystalline silica, identified by peaks at $2\theta = 13.8°$ and $2\theta = 21.6°$.

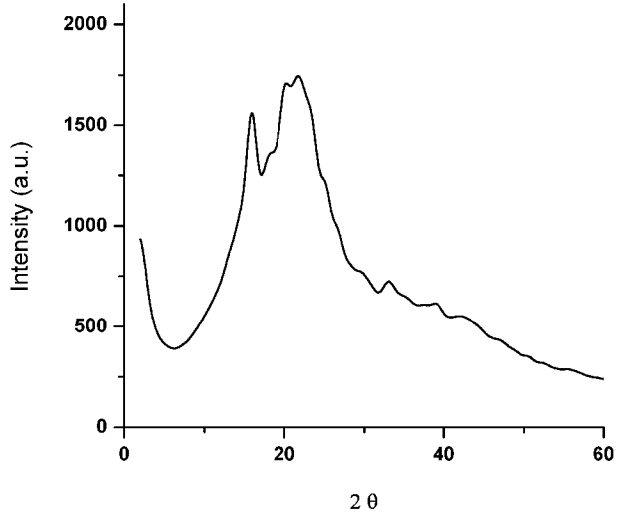

Figure 2. X-rays diffraction patterns of açaí seed fiber residues.

X-Rays Diffraction (XRD): the XRD patterns of PBAT/PLA blend and Açai seed fiber composite in the range of 2θ between 5° to 40° are showed in Figure 3.

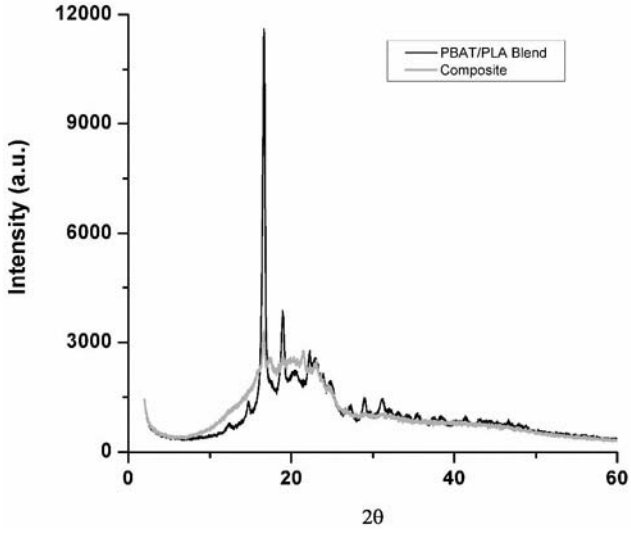

Figure 3. X-rays diffraction patterns of PBAT/PLA Blend and Açai seed fiber composite.

As It can be seen in Fig. 3, the XRD pattern for PBAT/PLA blend and Açai seed fiber composite show characteristic peaks in the range of 2θ = 17.05°; that is, the peak corresponding to the crystalline blend structure that has disappeared. This indicates that PBAT/PLA chains have diffused into the gallery of the fiber and that the fiber has been successfully intercalated in the PBAT/PLA matrix leading to the formation of hydrophilic structures.

3.3 Mechanical tests results

Figure 4 shows the diagram stress (MPa) X strain (mm/mm) for PBAT/PLA blend and PBAT/PLA/açai seed fiber composite. From the stress–strain it can be seen a reduction in tensile properties of PBAT/PLA blend due to acai seed fiber addition.

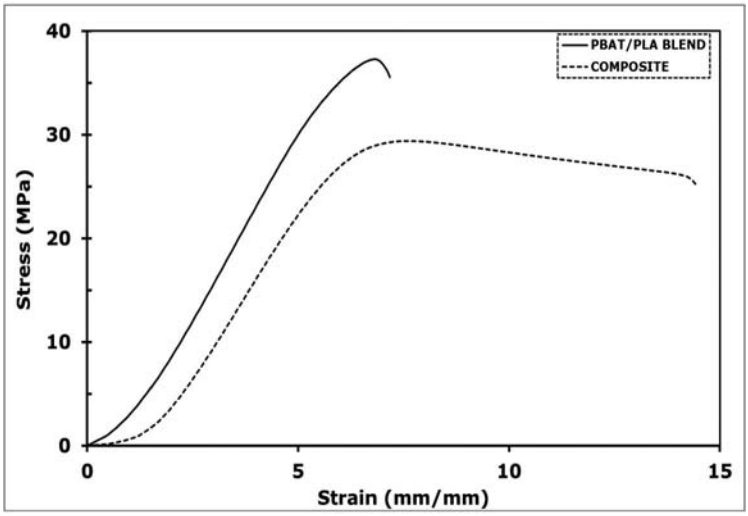

Figure 4. Diagram Stress (MPa) X Strain (mm/mm) for PBAT/PLA blend and açai seed fiber composite.

The Table 3 presents the results of mechanical tests of PBAT/PLA blend and PBAT/PLA/açai composite. The results presented show the average values calculated from data obtained in tests for five test specimens. This results showed that the addition of açai seed fiber in PBAT/PLA blend not improved the mechanical properties of it.

Table 3. Mechanical tests results of PBAT/PLA blend and it composite

Properties	PBAT/PLA Blend	Açai Seed Fiber Composite
Tensile strength at break (MPa)	26.5 ±1.26	20,95 ±0,13
Elongation at break (%)	12,8 ±0.39	15,02 ±0,95
Young's modulus (MPa)	385.4 ± 0.39	289.7 ± 0,4
Izod impact (J/m)	60.86 ±0.2	29.96 ±0.1

3.4 Scanning Electron Microscopy (SEM):

SEM micrographs of cryo-fractured surfaces of PBAT/PLA blend and PBAT/PLA/açai seed fiber composite are compared in Figure 5 (a). This micrographs of cryo-fractured surfaces blend and composite suggest a good interaction between blend and composite. It can not see any porus neither fractures. Composite , in Figures 5 (b) presents porus in many parts of samples probably this is the reason composite properties decreases.

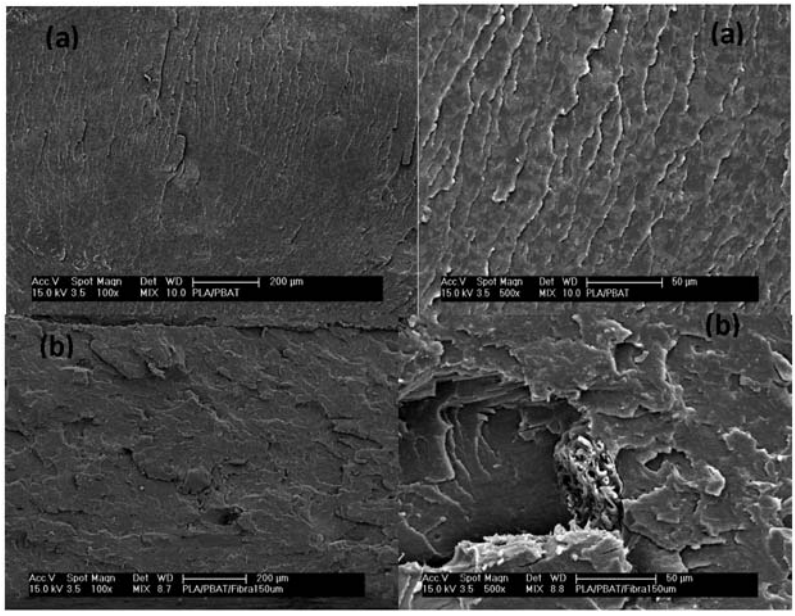

Figure 5. SEM micrographs of cryo-fractured surfaces of PBAT/PLA blend (a) and PBAT/PLA/açai seed fiber composite (b)

4. CONCLUSIONS

The purpose of this study was to process and evaluate the changes in the mechanical and morphological properties of the biodegradable composite due to the incorporation of acai seed fiber. 15% of the acai fiber were not enough to get good mechanical properties, but it were resulted in important fact because acai seed fiber is a biodegradable and can be used in an other composition with better properties.

ACKNOWLEDGEMENTS

The authors wish to thank BASF and FATEC ZL for the support for this work.

REFERENCES

1. Mohanty, A. K., Misra, M., & Hinrichsen, G. (2000). Biofibres, biodegradable polymer and composites: an overview. Macromolecular Materials and Engineering(276/277), 1–24.

2. Faruk, O, Andrzej, K, Bledzki, H-P, Fink, M S Biocomposites reinforced with natural fibers: 2000–2010. Progress in Polymer Science, 37(11)1552-1596 (2012).

3. Kalia, S, Dufresne, A, Cherian, B M, Kaith, B S, Avérous, L, Njuguna, J, Nassiopoulos, E Cellulose-Based Bio- and nanocomposites: a review. International Journal of Polymer Science (2011) Article ID 837875, 35 pages doi:10.1155/2011/837875.

4. Mohanty, A. K., Khan, M. A., & Hinrichsen, G. (2000a). Surface modification of jute and its influence on performance of biodegradable jute-fabric/Biopol composites. Composites Science and Technology, 60(7), 1115–1124.

5. Inamura, Patricia Y., Kraide, Felipe H., Drumond, Walker S., de Lima, Nelson B., Moura, Esperidiana A.B., del Mastro, Nelida L. Ionizing radiation influence on the morphological and thermal characteristics of a biocomposite prepared with gelatin and Brazil nut wastes as fiber source. Radiation Physics and Chemistry (1993). , v.84, p.66 - 69, 2013.

6. Oliveira, E. H., Silva, V. A., Oliveira, R.R., Soria, A, Abreu, A, Harada, J, Diaz, F. R. V., Moura, E.A.B. Investigation on mechanical and morphological behaviours of copolyester/starch blend reinforced with rice husk ash. In: Characterization of Minerals, Metals, and Materials 2014.1 ed.Hoboken: John Wiley & Sons, Inc., 2014, v.1, p. 491-498.

7. Huda MS, Drzal LT, Mohanty AK, Misra M. Effect of fiber surface treatments on the properties of laminated biocomposites from poly(lactic acid) (PLA) and kenaf fibers. Composites Science and Technology 2008;68:424–32.

8. Wu CS. Renewable resource-based composites of recycled natural fibers and maleated polylactide bioplastic: characterization and biodegradability. Polymer Degradation and Stability 2009;94:1076–84.

9. Okubo K, Fujii T, Thostenson ET. Multi-scale hybrid biocomposite: processing and mechanical characterization of bamboo fiber reinforced PLA with microfibrillated cellulose. Composites Part A: Applied Science and Manufacturing 2009;40:469–75.

10. Hodzic A, Coakley R, Curro R, Berndt CC, Shanks RA. Design and optimization of biopolyester bagasse fiber composites. Journal of Biobased Materials and Bioenergy 2007;1:46–55.

11. Liu D, Zhong T, Chang PR, Li K, Wu Q. Starch composites reinforced by bamboo cellulosic crystals. Bioresource Technology 2010;101:2529–36.

12. M. Baiardo, G. Frisoni, M. Scandola, M. Rimelen, D. Lips and K. Ruffieux. "Thermal and mechanical properties of plasticized poly (L-lactic acid)". J. Appl. Polym. Sci, Vol. 90, pp 1731-1738, 2003.

13. K. Arakawa, T. Madaa, S. Parka and M. Todoa. "Tensile fracture behavior of a biodegradable polymer, poly (lactic acid)". Polym. Test, Vol. 25, pp 628-634, 2006.

14. N. Ljungberg and B. Wesslen. "Tributyl citrate oligomers as plasticizers for poly (lactic acid): thermo-mechanical film properties and aging". Polymer, Vol. 44, pp 7679-7688, 2003.

15. J. Yeh, C. Huang, W. Chai and K. Chen. "Plasticized properties of poly (lactic acid) and triacetine blends". J. Appl. Polym. Sci, Vol. 112, pp 2757- 2763, 2009.

16. L. Jiang, M. P. Wolcott and J. Zhang. "Study of biodegradable poly (lactide)/poly (butylene adipate- co-terephthalate) blends". Biomacromolecules, Vol.7, pp 199-207,) 2005.

Characterization of Minerals, Metals, and Materials 2015
Edited by: John S. Carpenter, Chenguang Bai, Juan Pablo Escobedo, Jiann-Yang Hwang, Shadia Ikhmayies, Bowen Li, Jian Li, Sergio Neves Monteiro, Zhiwei Peng, and Mingming Zhang
TMS (The Minerals, Metals & Materials Society), 2015

INFLUENCE OF CLAY EXFOLIATION ON THE PROPERTIES OF EVOH/CLAY FLEXIBLE FILMS

Messias dos Santos Machado[2], Renato B. Godoy[1], Andressa Silva[1], Roberta Lima[1], Rene R. Oliveira [1], Francisco Valenzuela-Díaz[2], Esperidiana Moura[1]

[1]Nuclear and Energy Research Institute, IPEN-CNEN/SP, Av. Prof. L. Prestes, 2242, zip code 05508-000, Sao Paulo, Brazil
[2]Metallurgical and Materials Engineering Department, Polytechnic School, University of São Paulo, Av. Prof. Mello de Moraes, 2463, São Paulo, SP, 05508-030, Brazil

* Corresponding Autor: Tel. (+55) 11 31339337, e-mail: eabmoura@ipen.br

Keywords: EVOH, Clay, Flexible Films, DSC.

Abstract

This work aims to incorporate the Bof White Clay, from Boa Vista, Paraiba State, Brazil, as natural nanofiller in Ehylene vinyl alcohol copolymer (EVOH) and obtain flexible films. Nanocomposite was obtained using a twin-screw extruder, and film formed using a blow extruder machine. The flexible film nanocomposite was characterized, by tensile tests, XRD, DSC and their properties were evaluated. The results showed a good interaction between the clay and the EVOH resulting in an increase of properties of films nanocomposites as compared to films neat polymer.

1. Introduction

In nanotechnology, polymer matrix based nanocomposites have generated a significant attention in the recent literature. The achieved results were, at least initially, viewed as unexpected (''nano-effect'') offering improved properties over that expected from predictions. More recent results have, however, indicated that while the property profile is interesting, the clay-based nanocomposites often obey continuum mechanics predictions. There are situations where nanocomposites can exhibit properties not expected with larger scale particulate reinforcements [1]. However, a large increase in the amount of the clay addition can causes an inadequate dispersion with negative effects on the optical and mechanical properties [2].

Nanotechnology is the ability to work on a scale of about 1–100 nm in order to understand, create, characterize and use material structures, devices and systems with new properties derived from their nanostructures [3]. Because of their size, nanoparticles have proportionally larger surface area and consequently more surface atoms than their micro scale counterpart [4]. Polymer clay nanocomposites are, normally, obtained through the dispersion of clays chemically modified, within a polymer matrix either by in situ polymerization, melt intercalation or solution casting, where polymer chains diffuse into the space between the clay layers or galleries, followed by clay exfoliation [5,6].

The clays most commonly used to obtain nanocomposites are the ones from the smectite group, particularly the montmorillonite, smectite clay that consists of octahedral aluminate sheet sandwiched between two tetrahedral silicate layers [7]. Bentonites are defined as a sedimentary rock consisting of a large portion of expandable clay minerals with three-layer structures

(smectites) such as montmorillonites (80%), beidellite nontronite, etc. with minor amounts of non-clay minerals such as quartz, calcite, dolomite and feldspar [8]. Usually, in order to use the smectite clays in nanocomposites, the metallic cations are substituted by quaternary ammonium or other heteroatom organic salts. The method used to exchange the metallic cations by organics ones has a strong influence on the structure of the resultant Organoclay [5]. The great interest in organoclays and the large source of smectite clays in the Brazilian territory provides a great opportunity for developing organoclays in Brazil. However, in spite of the large number of works about polymer matrix/clay nanocomposites, only few works relate the use of organoclays of Brazilian origin [5, 9].

Ethylene Vinyl Alcohol Copolymers (EVOH) are semicrystalline materials regardless of vinyl alcohol (VOH) content. They are prepared commercially by transesterification (saponification) of Ethylene-vinyl acetate copolymers (EVA) [10]. It has one of the lowest oxygen permeability reported among polymers commonly used in packaging is the most important polymer with excellent barrier properties and have found extensive applications in food packaging [11, 12]. EVOH presents excellent chemical resistance, high transparency as well as excellent gas barrier properties to oxygen, organic solvents, and food aromas, show thermal stability and harmlessness toward health [13, 14]. Such properties are caused by strong hydrogen bond interactions, both inter and intra-molecular, which reduce the free volume of the polymer chains [15]. A major disadvantage of EVOH copolymers is that they lose oxygen barrier properties, stiffness or tensile strength due to water absorption in humid conditions, this happens due hygroscopicity of EVOH, as a consequence of the hydrophilic OH side groups and their interaction with the absorbed water molecules weakens the inter- and intra-molecular hydrogen bonds, increasing the free volume of the chains [10, 16- 18]. To overcome these problems and improve the physical properties of EVOH, some authors suggested a melt-blending process for preparation of nanocomposites. Polymers can be reinforced with inorganic fillers such as clay because they exhibit enhanced thermal stability, mechanical strength, chemical resistance, UV resistance [16, 19, 20]. The aim of this study is to analyze the structural modifications of the EVOH/ Clay nanocomposite extruded twin-screw and investigates their mechanical and morphological properties.

2. Materials and methods

2.1. Materials

The materials used in this study were Ethylene vinyl alcohol copolymer (EVOH) with 32 % mol/ ethylene content and 3% of natural Brazilian bentonite *Bofe* white clay from Boa Vista / PB, Brazil.

2.2. Preparation of Nanoclay

The *bofe* white clay extracted from nature presents calcic character (Ca^{2+}) then undergoes processes for its modification. The first step consists in dispersing the clay in deionized water under constant stirring for 30 min. The second phase is to turn it into sodium clay by adding sodium carbonate (Na_2CO_3) and keeping under constant stirring for 1h, so there is exchange of Ca^{2+} by Na^+ in the interlayer spaces of the clay. After this time, add quaternary ammonium salt and keep stirring for another 30 min. The organoclay is then filtered, washed with deionized water and dried at 60 °C for 48h, according to the methodology [21, 22]. After this time the clay is sieved and characterized by XRD to verify the interlayer distance obtained after the process, compared with the XRD clay before modification.

2.3. Preparation of nanocomposite

The pellets of EVOH were dried at 130 ± 5 ºC for 4h. The nanoclay (3%) was dried at 60 ºC for 12h. The nanocomposite was prepared by melting extrusion process, using a twin-screw extruder Haake Rheomex P332 operating in the L/D 3:1.33 rate. The temperature profile was 173/ 175/ 178/ 180/ 185/ 185 ºC. Screw speed was 50 rpm. The extrudates coming out of the extruder were cooled down for a better dimensional stability, pelletized by a pelletizer, dried again and fed into blow extrusion to obtain the film samples. The temperature profile of blow extrusion was 195/ 198/ 210/ 215/ 215/ 220 ºC and screw speed was 20 rpm.

2.4. Analyses

Mechanical tests: Tensile tests were determined using an INSTRON Testing Machine model 5564, according to ASTM D 882-91 in order to evaluate the mechanical behavior of the materials studied. Each value obtained represented the average of five samples.

X-rays diffraction (XRD): XRD is most commonly used to probe the nanocomposites structure and occasionally to study the kinetics of the polymer melt intercalation owing to its ease and availability. XRD, in this study was used to evaluate the modification of bentonite bof white clay and the intercalation in the EVOH matrix. XRD patterns were recorded on a Simens - D5000 diffractometer operated at 40 kV and 40 mA, with CuKα radiation (λ = 15.4 Å).

Differential scanning calorimetry (DSC): analyses were carried out using a Mettler Toledo DSC 822e from 25 to 250°C at a heating rate of 10 °C/min under nitrogen atmosphere (50 ml/min). DSC analyses of the materials were performed on four samples of the irradiated and non-irradiated materials.

3. Results and Discussion

3.1. Mechanical tests results

The mechanical tests of neat EVOH and EVOH/Clay nanocomposite flexible films were carried out in the longitudinal direction and the results are summarized in Table 1.These results shown the average values calculated from the data obtained in tests, with standard deviations less than 10 % for all tests.

Table 1. Mechanical Tests results

Test	EVOH	EVOH/*Bofe* White Clay	Variation (%)
Tensile strength at break (MPa)	6.43	16.65	160
Elongation at break (%)	47.18	16,2	- 66
Young´s Modulus (MPa)	367.38	314,82	- 14

Figure 1 shows the diagram stress against strain for neat EVOH and EVOH/Clay. From of this Figure it is possible observe that the addition of modified *Bofe* white clay makes the EVOH more ductile than neat EVOH, this is evident from the elongation at break has been reduced values of the nanocomposite. In addition, the important properties for films, tensile strength, has a significant increase. These changes should be associated with the good interfacial

adhesion between the matrix and *Bofe* white Clay. As it can be seen, the Yong´s Modulus has been reduced (of around 14 %).

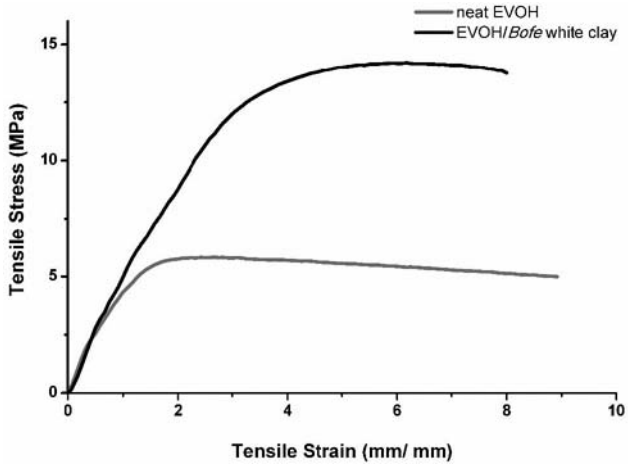

Figure 1. Diagram Stress (MPa) X Strain (mm/mm) for neat EVOH and EVOH/Clay nanocomposite

3.2. X-rays diffraction (XRD)

The XRD patterns of natural bentonite *Bofe* white clay and after be modified by quaternary ammonium salt in the range of 2θ between 2° to 10° are showed in Figure 2.

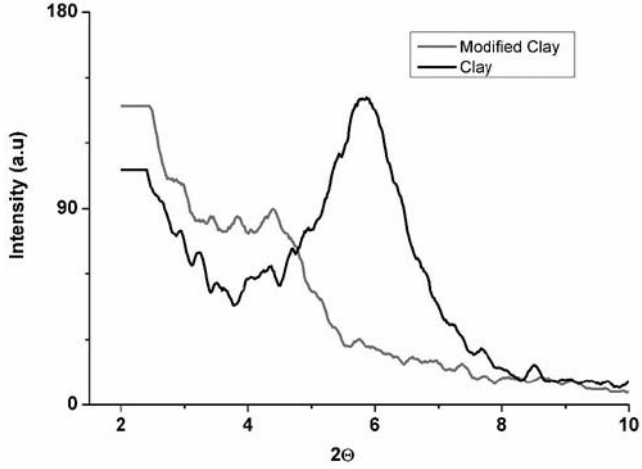

Figure 2. XRD patterns of natural *Bofe* white clay and after modification with quaternary ammonium salt.

The results shows that the natural *Bofe* white clay presented an interlayer distance (d001) of 1.55 nm in the range of 2θ = 6.0°, and after modification the interlayer distance increased to

(d001) of 2.17 nm in the range of 2θ = 4.11°. This increase confirms the major intercalation of the quaternary ammonium cation in the interlamellar spacing of the bentonite *Bofe* white clay took place. These results are also consistent with others clays results [23].

The XRD patterns of EVOH/*Bofe* white clay nanocomposite are showed in Figure 3. It can be seen that the XRD spectrum of EVOH/Bofe white clay nanocomposite not presented the characteristic organoclay peaks in the range of 2θ = 4.11° corresponding to the basal spacing of modified Bofe white clay. This indicates that EVOH chains have diffused into the gallery of the clay and that the clay has been successfully intercalated in the matrix.

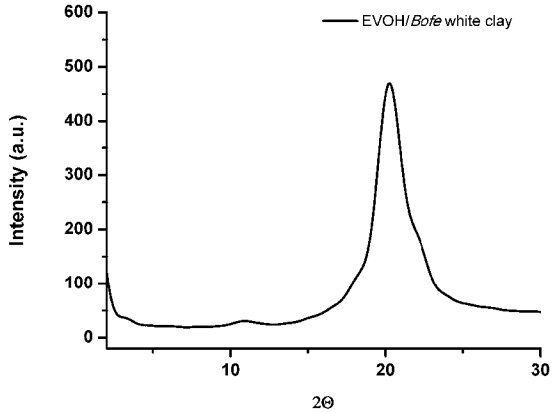

Figure 3. XRD patterns of EVOH/Bofe white clay nanocomposite

3.3. Differential Scanning Calorimetry (DSC)

The Table 2 shows the DSC analysis results for neat EVOH and EVOH/Bofe white clay nanocomposite. No significant differences in the melting temperature of the nanocomposite in comparison with neat material were observed. However, there were changes in melting enthalpy, which means more energy needed to start the fusion process in the composite. It means that the EVOH/CLAY nanocomposite formation contributed to a material with enhanced structural properties. The DSC curves of materials are presented in Figure 4.

Table 2. DSC analysis results of materials studied

Materials	Melting Temperature (T_m, °C)	Melting Enthalpy (ΔH_m,Jg^{-1})
Neat EVOH	180.62	214.53
EVOH_*Bofe* White Clay	181.86	258.24

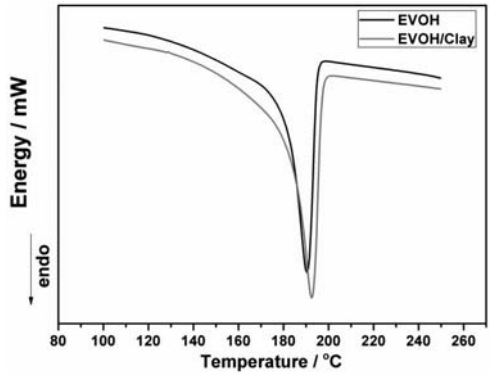

Figure 4. DSC analysis results of neat EVOH and EVOH/CLAY nanocomposite.

4. Conclusion

The search shows that the Brazilian Clay, *Bofe* White organofilic, promotes significant modifications in the EVOH main properties, typical and expected in a nanocomposite and the material synthesis technique was successful. Results showed that incorporation of 3 % (wt %) of *Bofe* white clay in the matrix of EVOH, resulted in a gain of mechanical properties of the film. The peaks of DSC analysis indicated that addition of *Bofe* white clay in the EVOH caused structural changes in the polymeric chains of EVOH component and leads to obtain a composite material with major melting enthalpy and, consequently, major crystallinity percentage. The superior mechanical properties of EVOH/Clay nanocomposite observed in this study can be attributed to the stiffness of Brazilian bentonite *Bofe* white clay, reinforcing effects, to the degree of the intercalation and good dispersion of the clay layers in the matrix. This result indicates that EVOH chains have diffused into the gallery of the clay and the clay has been successfully intercalated in the EVOH matrix leading to obtain flexible films with improved tensile strength and Young´s modulus properties when compared with the flexible film prepared from neat EVOH.

Acknowledgements

The authors wish to thank Intermarketing Brasil and Kuraray Group to provide the support for this work.

References

[1] Paul, D.R.; Robeson, L.M. Polymer nanotechnology: Nanocomposites. J. Polymer 2008; 49: 3187–3204

[2] Shikinaka, K.; Aizawa, K.; Fujii, N.; Osada, Y.; Tokita, M.; Watanabe, J.; Shigehara, K. Flexible, Transparent Nanocomposite Film with a Large Clay Component and Ordered Structure Obtained by a Simple Solution-Casting Method. J. Langmuir 2010; 26: 12493–12495.

[3] Roco, M. C. Nanotechnology: convergence with modern biology and medicine. Current Opinion in Biotechnology 2003; 14(3): 337–346.

[4] Henriette M.C. A. Review: Nanocomposites for food packaging applications. Food Research International 2009; 42: 1240–1253.
[5] Delbem, M.F.; Valera, T.S.; Valenzuela-Diaz, F.R.; Demarquette, N.R. MODIFICATION OF A BRAZILIAN SMECTITE CLAY WITH DIFFERENT QUATERNARY AMMONIUM SALTS. Quim. Nova 2010; 33 (2): 309- 315.
[6] Artzi,N; Tzur, A.; Narkis, M. The Effect of Extrusion Processing Conditions on EVOH/Clay Nanocomposites at Low Organo-Clay Contents. J. Polymer Composites 2005. Published online in Wiley InterScience (www.interscience.wiley.com).
[7] Modak, S. K.; Mandal, A.; Chakrabarty, D. Studies on Synthesis and Characterization of Poly(methyl methacrylate)-Bentonite Clay Composite by Emulsion Polymerization and Simultaneous In Situ Clay Incorporation. Polymer Composites 2013; 34: 32- 40.
[8] Sarkar, M.; Dana, K.; R Ghatak, S.; Banerjee, A. Polypropylene–clay composite prepared from Indian bentonite. Bull. Mater. Sci. 2008; 31: 23–28.
[9] Ribeiro, S. P. S.; Estevão, L. R. M.; Pereira, C.; Rodrigues, J.; Nascimento, R. S. V. Influence of clays on the flame retardancy and high temperature viscoelastic properties of polymeric intumescent formulations. J. Polymer Degradation and Stability 2009; 94 (3): 421- 431.
[10] Franco-Urquiza, E.; Santana, O. O.; Gámez-Pérez, J.; Martínez, A. B.; Maspoch, M. Ll. Influence of processing on the ethylene-vinyl alcohol (EVOH) properties: Application of the successive self-nucleation and annealing (SSA) technique.Express polymer Letters 2010; 4 (3): 153-160.
[11] Mokwena, K.K.; Tang, J. Ethylene Vinyl Alcohol: A Review of Barrier Properties for Packaging Shelf Stable Foods. Food Science and Nutrition 2012; 52: 640- 650.
[12] Ramakrishnan, S. Well-Defined Ethylene-Vinyl Alcohol Copolymers via Hydroboration: Control of Composition and Distribution of the Hydroxyl Groups on the Polymer Backbone. J. Macromolecules 1991; 24: 3753-3759.
[13] Lagaron, J. M.; Giménez, E.; Saura, J. J. Degradation of high barrier ethylene–vinyl alcohol copolymer under mild thermal-oxidative conditions studied by thermal analysis and infrared spectroscopy. J. Polymer International 2001; 50:635- 642.
[14] Lima, J. A.; Felisberti, M. I. "Poly(ethylene-co-vinyl alcohol) and poly(methyl methacrylate) blends: Phase behavior and morphology". J. European Polymer 2008; 44:1140-1148.
[15] Aucejo S.; Marco C.; Gavara R. Water effect on the morphology of EVOH copolymers. J. Applied Polymer Science 1999; 74: 1201–1206.
[16] Kim, D.; Kown, H.; Seo, J. EVOH Nanocomposite Films with Enhanced Barrier Properties under High Humidity Conditions. J. Polymer Composites 2013. DOI 10.1002/pc.22707.Published online in Wiley Online Library (wileyonlinelibrary.com). Acessed July 2014.
[17] Alvarez V. A., Ruseckaite V. A., Vázquez A.: Kinetic analysis of thermal degradation in poly(ethylene-vinyl alcohol) copolymers. Journal of Applied Polymer Science 2003; 90:3157–3163
[18] Cerrada M. L., Pérez E., Pereña J. M., Benavente R.: Wide-angle X-ray diffraction study of the phase behavior of vinyl alcohol and ethylene copolymers. Macromolecules 1998; 31: 2559–2564.
[19] Franco-Urquiza E.; Gamez-Perez J.; Sánchez-Soto M.; Santana O. O.; Maspoch M. L. The effect of organomodifier on structure and properties of poly(ethylenevynil alcohol)/organo-modified montmorillonite composites. J. Polymer International, in press 2010.
[20] Brito, G. F.; Oliveira, A. D.; Araújo, E. M.; Melo, T. J. A. Nanocompósitos de Polietileno/Argila Bentonita Nacional: Influência da Argila e do Agente Compatibilizante PE-g-MA nas Propriedades Mecânicas e de Inflamabilidade. J. Polímeros: Ciência e Tecnologia 2008; 18 (2): 170- 177.
[21] Silva, A. A.; Valenzuela-Diaz, F. R.; Martins, G. S. V.; Rodrigues, M. G. F. Preparação de argilas organofílicas usando diferentes concentrações de sal quaternário de amônio. J. Cerâmica 2007; 53: 417-422.
[22] Paiva, L. B.; Morales, A. R. Valenzuela-Díaz, F. R. Argilas organofílicas: características, metodologias de preparação, compostos de intercalação e técnicas de caracterização. J. Cerâmica 2008; 54: 213- 226.
[23] Paiva LB, Morales AR, Valenzuela-Díaz FR. Review article - Organoclays: Properties, preparation and applications. J. Applied Clay Science 2008; 42: 8–24.

Characterization of Minerals, Metals, and Materials 2015

Characterization of Minerals

Session Chairs:

Bowen Li

Zhiwei Peng

Characterization of Minerals, Metals, and Materials 2015
Edited by: John S. Carpenter, Chenguang Bai, Juan Pablo Escobedo, Jiann-Yang Hwang, Shadia Ikhmayies, Bowen Li, Jian Li, Sergio Neves Monteiro, Zhiwei Peng, and Mingming Zhang
TMS (The Minerals, Metals & Materials Society), 2015

CHEMICAL RESISTANCE OF ORNAMENTAL COMPOUND STONE PRODUCED WITH MARBLE WASTE AND UNSATURATED POLYESTER

Carlos E. Gomes Ribeiro [1,2], Rubén J. Sánchez Rodriguez [2], Carlos M. Fontes Vieira [2]

[1]Federal Institute of Espirito Santo, Campus Cachoeiro, Mechanical Engineering department; Km 05 Cachoeiro x Alegre Rd., Cachoeiro de Itapemirim, ES, 29300-000, Brazil;
[2]North Fluminense State University, Laboratory of Advanced Materials, Polymer and Composites Section; 2000 Alberto Lamego Av., Campos dos Goytacazes, RJ, 28013-602, Brazil.

Keywords: Compound Stone, Marble Waste, Polymer Composite

Abstract

Ornamental compound stone are produced by industry for decades, however, few published studies describe these materials. Brazil has many deposits of stone wastes and a big potential to produce these materials. This work aims to evaluate the chemical resistance of ornamental compound stones produced with marble waste and unsaturated polyester. An adaptation of Annex H of ABNT NBR 13818:97 standard, with reagents commonly used in household products, was used. The results were compared with those obtained for natural stone used in composite production.

Introduction

Brazil import in 2013 nearby 50,000 ton of Ornamental Compound Stone [1] and has many deposits of stone wastes, with demand and many deposits of mineral loads, Brazil presents a big potential to produce these materials. Ornamental compound stone (OCS) are produced by industry for decades, however, few published studies describes these materials, besides, these studies treat just of mechanical and physical properties of OCS [2,3,4,5,6,7]. Physical and mechanical properties are very important to specify OCS application, however, know the behavior of the material on the use conditions is critical to its correct specification.

In the present work, two compositions of ornamental compound stone (OCS) were produced and compared on their physical behavior and your chemical resistance. Chemical reagents commonly used in household products, were used. The results were compared with those obtained for natural stone used in composite production.

Materials and methods

Marble Residue

The residue of "Calcita" natural marble (NM), from Polita company, located in Cachoeiro de Itapemirim, ES, Brazil, was used in this study. Scraps of plates were collected in a discarding pile. After the material collection, the residue was crushed using a jaw crusher, such that particles could pass through a 2 mm sieve. Crushed residue was separated in three granulometric

ranges using dry sieving. The coarse particles are in range 0.710 - 2.000 mm, medium particles are in range 0.063 - 0.710 mm, and the fine particles are less than 0.063 mm.

Unsaturated Polyester

An orthophthalic unsaturated polyester (UPR) resin with a medium viscosity was used to formulate all composites. As initiator 1 wt% of a methyl ethyl ketone peroxide (MEKP) was used.

Fabrication of slabs from residue

For determine mechanical and physical properties, two material specimens were cast (Table I). The particles percentage range was chosen based in simplex mixture design for marble particles presented for Ribeiro and coworkers [2,8]

Table I. Test specimens

Specimen	Coarse (%[a])	Medium (%[a])	Fine (%[a])	UPR (%[b])
OCS 15	45	30	25	15
OCS 20	45	30	25	20

[a] Percentages by weight of mineral load (coarse + medium + fine)
[b] Percentages by weight of material (mineral load + unsaturated polyester)

Particles, that were previously crushed and classified, were dried, weighed and putted in a vacuum planetary mixer (100 mmHg). Dry particles are a necessary step because water may reduce the cure process efficiency related to adhesion between the composite components [9]. The unsaturated polyester was introduced into the mixer by vacuum suction. After marble waste and resin mixed, the mass was vacuum transferred to mold (100 x 100 mm), and the mold was vibrated to spread the mass. After vibration, the mold was uncoupled from mixer and hot vacuum pressed for 20 minutes at 90ºC and 1 MPa.

Density, water absorption and apparent porosity

Density water absorption and apparent porosity, from OCS15, OCS 20 and NM were determined. Twelve cubic specimens of each material were dried and immersed in water. Dried, suspended in water and saturated mass of specimens were determinate. The times of immersion and used equations are reported in ABNT NBR 15845:2010 [10].

Chemical resistance

An adaptation of Annex H of ABNT NBR 13818:1997 [11] standard, with reagents commonly used in household products, was used. OCS15, OCS 20 and NM were evaluated. Five specimens of each OCS and one specimen of NM were tested for each used reagent. Test specimens were cut with 70 × 25 × 10 mm. The used chemical reagents, concentrations and exposure times are presented in Table II.

After chemical exposition, the specimens were washed with hot water for 30 minutes. Were evaluated relative weight losses (WL), relative gloss losses (GL) and superficial alterations.

Table II. Chemical reagents, concentrations and exposure times

Chemical reagent	Concentration	Exposure time (h)
NH_4Cl	100 g/l	24
NaClO	20 mg/l	24
$C_6H_8O_7$	100 g/l	24
KOH	30 g/l	96
HCl	3% v/v	96

Results and discussion

Density, water absorption and apparent porosity

Values for confidence interval (95%) of density, water absorption and apparent porosity are presented in Table III for OCS's and NM.

Table III. Density, water absorption and apparent porosity for OCS and NM (CI = 95%)

Specimen	Density (g/cm^3)	Water Absorption (%)	Apparent Porosity (%)
NM	2,79 ± 0,03	0,11 ± 0,01	0,32 ± 0,03
OCS 15	2,35 ± 0,01	0,39 ± 0,10	0,93 ± 0,23
OCS 20	2,26 ± 0,00	0,17 ± 0,02	0,39 ± 0,05

Table III show that OCS 20 presents a lower density, and an apparent porosity near to NM. This is an advantage, representing less weight in buildings. On the other hand, OCS 15 presents a greater apparent porosity, circa of two times higher than presented by OCS 20, implying in a biggest superficial area susceptible to chemical attack.

Chemical resistance

Table IV presents relative weight and gloss losses for NM, OCS 15 and OCS 20. In general, acid chemical reagents (NH4Cl, C6H8O7 and HCl) promoted a higher degradation of evaluated materials, with greater losses of weight and gloss, when compared with alkaline chemical reagents (KOH and NaClO). Moreover, NM presents a higher degradation level, with greater weight loss when compared with OCS, pointing to NM as weaker portion of OCS.

Table IV. Relative weight and gloss losses for NM, OCS 15 and OCS 20

	NM		OCS 15		OCS 20	
	WL (%)	**GL (%)**	**WL (%)**	**GL (%)**	**WL (%)**	**GL (%)**
NH_4Cl	0.37	100	0.16	61	0.10	65
NaClO	0.22	18	0.08	13	0.04	17
$C_6H_8O_7$	3.59	96	1.21	81	1.06	85
KOH	0.74	25	0.48	19	0.13	28
HCl	1.56	74	1.55	72	1.22	64

Comparing OCS 15 and OCS 20, we observed that OCS 15 presents greater weight losses than presented by OCS 20, although, gloss losses were slightly greater in OCS 20. The greater weight loss in OCS 15 is associated, in part, with your greater porosity (Table III) that promotes a greater area to the chemical attack. Moreover, the greater weight losses presented by OCS 15 are associated mainly with your greater content of marble particles. The marble is a carbonate stone,

with alkaline behavior, highly susceptible to acids attacks, so a greater content of this constituent promotes greater weight losses in acids attacks.

Figure 1 presents attacked surfaces with acids reagents, and Figure 2 presents attacked surfaces with alkaline reagents, for OCS 15 and OCS 20, observed with SEM.

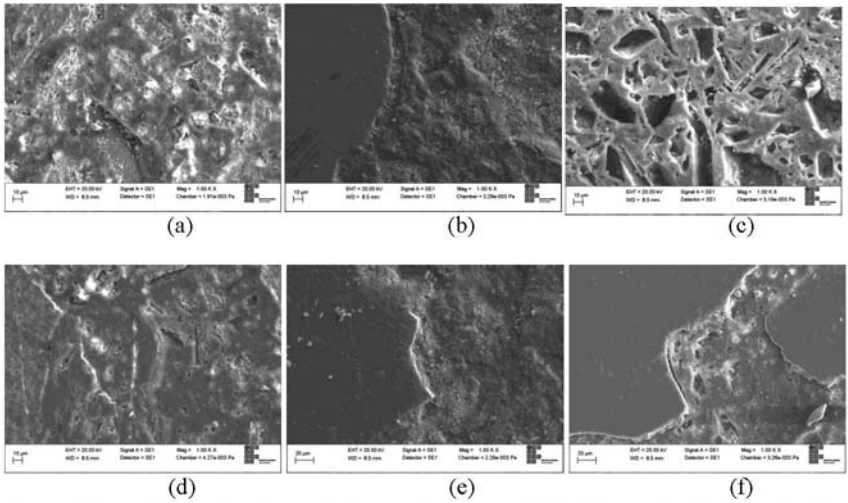

Figure 1. Attacked surface by acids chemical reagents (SEM - 1000 x). (a) OCS 15 – NH_4Cl (b) OCS 15 – $C_6H_8O_7$ (c) OCS 15 – HCl (d) OCS 20 – NH_4Cl (e) OCS 20 – $C_6H_8O_7$ (f) OCS 20 - HCl

Figure 1 presents how OCS 15 (a,b,c) is more attacked than OCS 20 (d,e,f), in all cases we see that specimens of OCS 15 presents most deep holes caused by chemical attacks when compared with specimens of OCS 20 submitted at same treatment.

For the specimens attacked with alkaline reagents, were observed a most superficial attack, but, until in this case, the marble particles were the most participative component in weight loss, what is represented by a greater weight loss in OCS 15 when compared with OCS 20, Figure 2 show that the regions around the particles are the most attacked regions. Moreover smaller gloss losses, shows us like most soft are the chemical attack caused by alkaline reagents in the OCSs.

We found publications with evaluations of chemical attacks in ornamental stones and one publication evaluating the chemical attacks in a polymer concrete, a composite with composition similar to OCS, but all cases are not comparables with this study.

Santos and Caranassios [12] studied alterations in a Tycoon Blue granite, with the same reagents used in this study and gloss losses evaluation, however, the granite presents chemical and mineralogical composition much different of marbles, granites are siliceous rocks, with acid behavior, while marbles, are calcareous rocks, with alkaline behavior, what in chemical attacks makes a great difference. In the same way, Silva, Godoy and Araújo [13] and Bolonini and Godoy [14] makes similar evaluations in your studies, but always with granitic stones. Gorninski and coworkers [15, 16] studied alterations in a polymer concrete produced with a polymeric resin

and stone particles, however, other chemical reagents were used, so the results are not comparables.

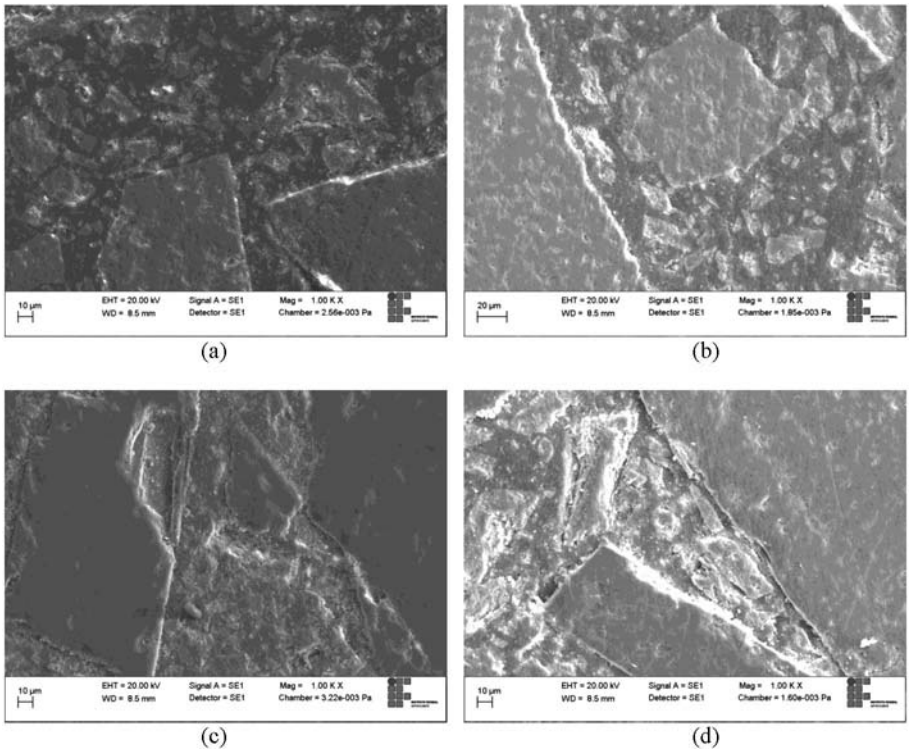

Figure 2. Attacked surface by alkaline chemical reagents (SEM - 1000 x). (a) OCS 15 – NaClO (b) OCS 20 – NaClO (c) OCS 15 – KOH (d) OCS 20 – KOH

Conclusion

The studied ornamental compound stones presents a chemical resistance greater than natural stone used in your production. Additionally, we observe that greater content of polymer promotes a higher chemical resistance to OCS, like illustrated by the lower weight losses in OCS 20 when compared with OCS 15.

In function of chemical nature of used stone particles, the acids reagents promoted a greater degradation of material structure, while alkaline reagents, promote a lower degradation, so the use of acids cleaners, in OCS's cleaning, is not recommended.

Thus, the use of ornamental compound stones, produced with marble particles, in kitchen countertops should be careful, and applications in toilets, bathrooms and wall coverings should be preferred.

Acknowledgements

The authors acknowledge the CNPq and CAPES for financial support.

References

[1] C. Chiodi Filho, "Balance of brazilian exports and imports of natural stone in the 1st half of 2014" (Report 09/2014, Brazilian Association of Ornamental Stones Industry – ABIROCHAS). (Portuguese)

[2] Carlos E. G. Ribeiro, Rubén J. S. Rodriguez, Carlos M. F. Vieira. "Production of Ornamental Compound Marble with Marble Waste and Unsaturated Polyester", *EPD Congress 2014*, ed. J. Yurko, L. Zhang, A. Allanore, C. Wang, J.S. Spangenberger, R.E. Kirchain, J.P. Downey and L.D. May (Hoboken, NJ, USA: John Wiley & Sons, 2014), 129-136.

[3] Carlos E. G. Ribeiro et al., "Fabrication of artificial stone from marble residue by resin transfer molding", *Materials Science Forum*, 775-776 (2014), 336-340.

[4] Carlos E. G. Ribeiro et al., "Production of synthetic ornamental marble as a marble waste added polyester composite", *Materials Science Forum*, 775-776 (2014), 341-345.

[5] M. Y. Lee et al., "Artificial stone slab production using waste glass, stone fragments and vacuum vibratory compaction", *Cement & Concrete Composites,* 30 (2008), 583–587.

[6] C. Borsellino, L. Calabrese and G. Di Bella, "Effects of powder concentration and type of resin on the performance of marble composite structures", *Construction & Building Materials,* 23 (2009), 1915-1921.

[7] L. dos Santos et al., "Temperature effects on mechanical behaviour of engineered stones" *Construction and Building Materials*, 25 (1) (2011), 171-174.

[8] Carlos E. G. Ribeiro, Rubén J. S. Rodriguez, Carlos M. F. Vieira. "Determination os apparent dry density for ternary mixture of crushed marble waste", *EPD Congress 2014*, ed. J. Yurko, L. Zhang, A. Allanore, C. Wang, J.S. Spangenberger, R.E. Kirchain, J.P. Downey and L.D. May (Hoboken, NJ, USA: John Wiley & Sons, 2014), 83-90.

[9] C. Ignacio, V. Ferraz, R. L. Oréfice, "Study of the behavior of polyester concretes containing ionomers as curing agents", *Journal of Applied Polymer Science*, 108 (2008), 2682–2690.

[10] Brazilian Association of Technical Standards, "Rocks coating: the test method", ABNT NBR 15845, Rio de Janeiro, 2010 (Portuguese).

[11] Brazilian Association of Technical Standards, "Ceramic plates coating: specification and test methods", ABNT NBR 13818, Rio de Janeiro, 1997 (Portuguese).

[12] E.S. Santos, A. Caranassios, "Technological characterization and changeability of a granite commercially called Blue Tycoon", *Institutional capacitation series,* ed. Z. C. Castilhos, S. C. A. França, A. C. L. Rizzo In. Castilhos, Z.C.; França, S.C.A.; Rizzo, A.C.L. (Rio de Janeiro, Brazil: CETEM, 2007). (Portuguese)

[13] J. A. Silva, A. M. Godoy, "Ornamental and coating Stones of southwest Mato Grosso state", *Geociências*, 28 (2)(2009), 129-142. (Portuguese)

[14] T. M. Bolonini, A. M. Godoy, "Technological caracterization of stones from Capão Bonito mass", *Geociências*, 31 (2)(2012), 229-246. (Portuguese)

[15] J. P. Gorninski, D. C. Dal Molin, C. S. Kazmierczak, "Strength degradation of polymer concrete in acidic environments", *Cement and Concrete Composites*, 29 (8) (2007), 637-645.

[16] J. P. Gorninski, D. C. Dal Molin, C. S. Kazmierczak, "Comparative assessment of isophtalic and orthophtalic polyester polymer concrete: Different costs, similar mechanical properties and durability", *Construction and Building Materials*, 21 (3) (2007), 546-555.

Characterization of Minerals, Metals, and Materials 2015
Edited by: John S. Carpenter, Chenguang Bai, Juan Pablo Escobedo, Jiann-Yang Hwang, Shadia Ikhmayies, Bowen Li, Jian Li, Sergio Neves Monteiro, Zhiwei Peng, and Mingming Zhang
TMS (The Minerals, Metals & Materials Society), 2015

CHARACTERIZATION OF FELDSPAR BY INSTRUMENTAL ANALYTICAL TECHNIQUES

Zainab Shehu Aliyu[1], Adele Dzikwi Garkida[1], Edwin Adoyi Ali[1] and Muhammad Dauda[2]

[1]Department of Industrial Design, Ahmadu Bello University, Zaria-Nigeria
[2]Department of Mechanical Engineering, Ahmadu Bello University, Zaria-Nigeria

Keywords: Feldspar, Characterization, Glassmaking

Abstract

Feldspar from Matari, Nigeria was analyzed using SEM, XRD and XRF techniques for micro-structural analysis, mineral phase analysis and chemical composition analysis respectively. Qualitative and quantitative XRD analyses revealed the presence of microcline 59.6%, albite 34.7% and quartz 5.71%. The XRF results showed that the feldspar contains 67.32% SiO_2, 17.54% Al_2O_3, 11.33% K_2O, 2.75% Na_2O, 0.12% CaO, 0.01% MgO, 0.02% MnO_2, 0.10% Fe_2O_3, 0.00% Ti_2O, etc and 0.14% LOI. SEM/EDX analysis shows the presence of microcline feldspar as the dominant phase, exhibiting lamellar twinning. The XRD has also revealed that potash has the highest peak, indicating its high concentration. The 0.10% Fe_2O_3 present is within the permissible level (0.1-0.3%) for glass making and also within the potash feldspar specifications (0.17%). The Matari feldspar is a microcline type, rich in potash, alumina and silica, enabling it meet the standard specifications for alumino-silicate glass.

Introduction

Feldspars are the most abundant groups of rock- forming minerals that make up 60 % of the earth's crust, and all the rock-forming feldspars are alumino-silicate minerals that contain varying proportions of potassium, sodium or calcium and they are the most abundant minerals of the igneous rock [1]. The common feldspars are potash feldspar namely orthoclase ($K_2O.Al_2O_3.6SiO_2$), meaning straight fracture, and a variety of crossed, hatched, twinned orthoclase known as microcline ($K_2O.Al_2O_3.6SiO_2$) also known as "small incline", soda feldspar is called albite ($Na_2O.Al_2O_3.6SiO_2$) and lime feldspar is anorthite ($CaO.Al_2O_3.2SiO_2$) or plagioclase known as "oblique fracture" [2].

These three feldspar groups are named on the basis of Na, K and Ca content in each case. Potash feldspar and soda feldspar occur as major constituents of such common igneous rocks as pegmatite, granite, syenite and feldspar porphyry among others [3]. These feldspars crystallize from magma as intrusive and extrusive igneous rocks as veins and are also present in many types of metamorphic and sedimentary rocks. Plagioclase feldspars lack potassium, they are light colour and are usually striated but potash feldspars are microcline and orthoclase. Although, orthoclase is more common of the potash feldspars, it exhibits striations occasionally on cleavage surfaces while microcline demonstrates lamellar twinning as its common feature. Between 400°C and less, microcline is the stable structure for potash feldspar ($K_2O.Al_2O_3.6SiO_2$), also between 500°C and 900°C, orthoclase is stable structure. The key difference between the structures is only the randomness of the aluminium and silicon atoms, because, in microcline, the ions are ordered and this produces the lower symmetry of triclinic. At high temperatures, the

positions of the aluminium and silicon become more disordered and produce the monoclinic symmetry of orthoclase [4].

Commercially, the most important members of the feldspar family are the potash feldspars (orthoclase and microcline) and soda feldspar (albite). 35 % of the World feldspar production is used in glass industry, 60% in ceramic industry and 5% in rubber, paint, plastic, welding electrode as filling material [5]. The total feldspar reserve of the World is 1.740×10^6 metric tons and the bulk of this reserve is found in Asia. Turkey has a reserve of 14% of the World feldspar reserves and it has the largest sodium feldspar reserves among other countries in the World [6]. In 2010, about 20 million tons of feldspars were produced mostly from three countries; Italy (4.7 Mt), Turkey (4.5 Mt) and China (2.0 Mt) [7].

In the glass industry, feldspar is used in varying proportions containing 10 to 15% of the batch and it is valued for two purposes, it acts as a fluxing material which prompts faster melting and fuel savings and the alumina content provides the resistance to thermal shock. It also improves mechanical properties, thermal durability and prevents devitrification [8]. However, in the manufacture of high- quality colourless glass, feldspar should have a maximum of 0.1% Fe_2O_3, although up to 0.03% is acceptable. The presence of iron oxide in the batch composition is very detrimental because its presence even in minute quantity tends to colour the glass.

Only alkali containing feldspars, potassium and sodium feldspars are used in the glass industry. Potash feldspar gives the product a higher viscosity, higher strength and greater transparency compared with sodium feldspar. The aim of the present work deals with the characterization of Matari feldspar deposit in order to determine its suitability for glass making. Matari is in Soba Local Government Area of Kaduna State, Nigeira and the feldspar deposit occurs in an undulating plain 40 kilometers East from Zaria City.

Materials and Methods

The feldspar utilized for this research was collected from Matari in Soba Local Government Area, some 40 kilometers east from Zaria in Kaduna State, Nigeria. The sample was randomly collected and about 10kg of the bulk sample was crushed to desired particle size distribution and then a small portion of the sample was taken from the milled material by coning and quartering technique for various analyses. The samples were subjected to various characterization techniques to determine their chemical composition, crystalline pattern and microstructural configuration, using Xray Flourescence (XRF), Xray Diffraction (XRD) and Scanning Electron Microscopy (SEM)/Energy Dispersive Xray spectroscopy (EDX), respectively. Loss on Ignition (LOI) was also determined by drying the sampe at 100°C and then roasting it at 1000°C .

The sample was analyzed for silica, lime, and oxides of sodium, potassium, magnesium, phosphorus, manganese, titanium, iron, copper, chromium, nickel, zirconium, vanadium among others. Identification of crystalline phases was carried out by XRD using a back loading technique. Scanning Electron Microscopy equipped with an energy dispersive spectrometer (FESEM/EDS) model number JEOL JSM 7500F was used to examine the microstructure.

Results and Discussion

Chemical Analysis

The chemical composition of the representative sample of the Matari feldspar deposit is composed of 11.33wt % K_2O (Table I) which falls within the range of 10-15wt % for potash feldspar needed in the glass industry as potash feldspar tends the melt to clear glass [9]. The potash content of Matari feldspar is higher than Richifa feldspar [10] and Turkish Manisa Demirci [11] as each contains 8.95% and 5.94% potash respectively.

Apart from the high percentage of potash, it was detected that the sample is composed of 0.1wt % of Fe_2O_3 content which is an unwanted impurity due to its colouring properties. However, in the manufacture of high-class, colourless glass, feldspars should have a maximum of 0.1% Fe_2O_3 although up to 0.3% is permissible [12]. For this reason, Matari feldspar deposit has met the common feldspar specifications and the requirement for the production of high quality colourless glass due to its low iron oxide content. In addition, Matari feldspar deposit has high potash content which allows it to be suitable for glass making because the high concentration of alkali (potash) in the feldspar makes it a very good fluxing agent for fast melting and energy saving.

Table I: Chemical Composition

OXIDE	Wt.%
SiO_2	67.32
TiO_2	0.00
Al_2O_3	17.54
Fe_2O_3	0.10
MnO	0.02
MgO	0.01
CaO	0.12
Na_2O	2.75
K_2O	11.33
P_2O_5	0.35
Cr_2O_3	0.01
NiO	0.01
V_2O_5	0.01
ZrO_2	0.01
CuO	0.01
LOI	0.14
TOTAL	99.69

Crystalline Pattern and Micro-structural Configuration

The qualitative and quantitative XRD analysis result in table 2 has revealed that microcline is the major mineral followed by albite and then quartz. The percentage of microcline in the feldspar is 59.6%, albite is 34.7% and quartz accounting for the remaining 5.71% (Table 2). Figure 1 indicates that potash has the highest peak showing the presence of potash in high concentration with a near zero percentage of iron oxide.

The SEM analysis given in figures 2 and 3 revealed the presence of microcline feldspar characterized by simple lamellar twinning and SEM/EDX analysis in figure 4 further reveals the major elemental composition of the Matari feldspar.

Table II: Quantitative XRD Analysis of the Matari Feldspar

	Wt%
Microline	59.6
Albite	34.7
Quartz	5.71

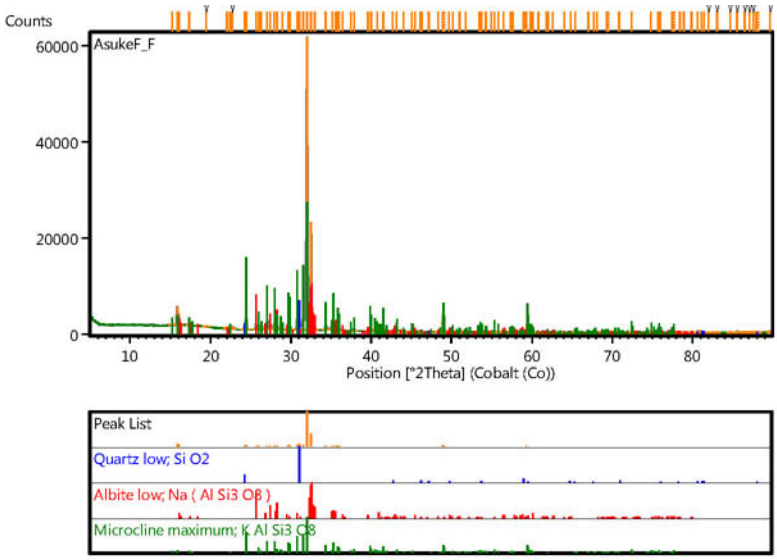

Figure 1: Qualitative XRD Analysis of the Matari Feldspar Sample

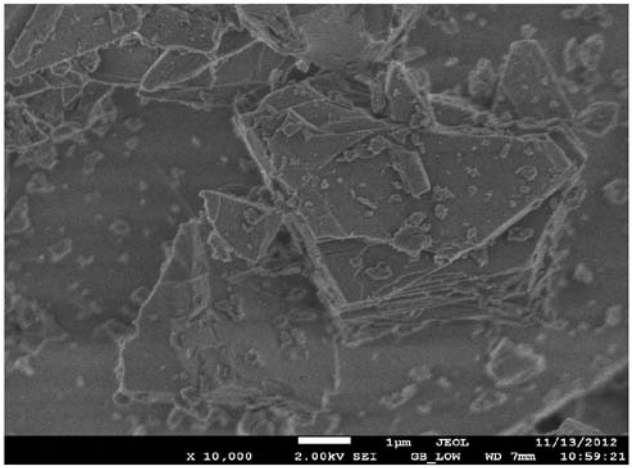

Figure 2: Matari microline feldspar at 10,000 magnifications showing lamellar pattern

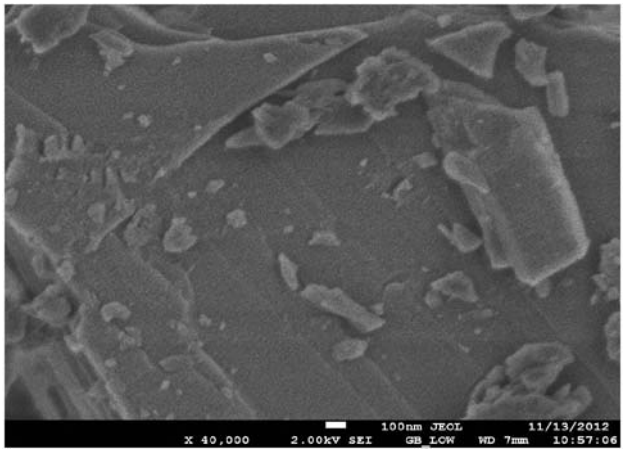

Figure 3:Matari microcline feldspar at 40,000 magnifications showing simple lamellar twinning.

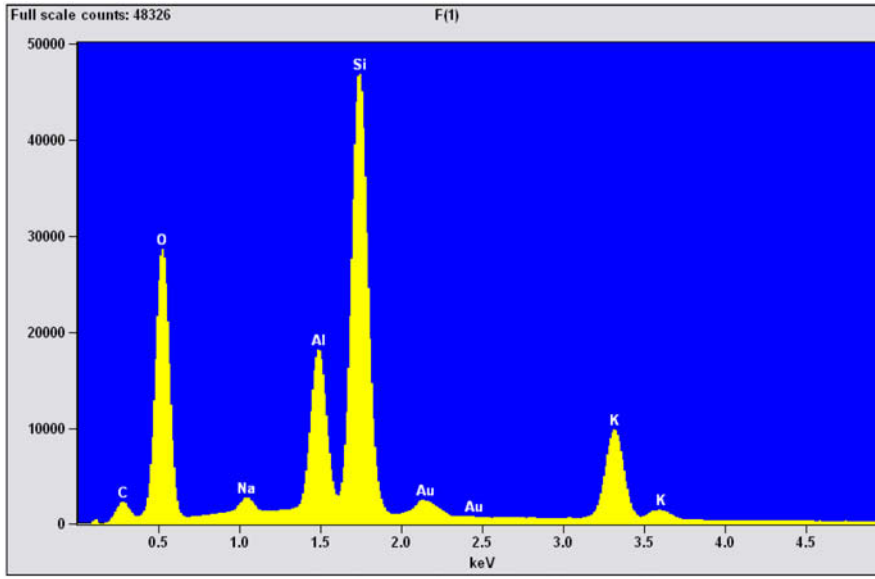

Figure 4: SEM/EDX Analysis of the Matari Feldspar

Conclusion

The result of the study has revealed that Matari feldspar is suitable for making a wide variety of commercial glass because the feldspar is rich in potash and potash is an excellent fluxing agent which reduces energy and of course the production cost. In addition, the feldspar has a near zero or low percentage of iron oxide 0.1% that promotes production of high class colourless glass. The feldspar deposit has high percentages of silica and alumina content 67.32% and 17.54% respectively. Therefore, Matari feldspar deposit is a good source of potash, alumina and silica for making alumino silicate glasses.

References

1. Michael, J.P., *Feldspar and Nepheline Syenite.*(US Geological Survey Mineral Year Book. 2002), 27.1-27.3

2. James, T. , Classification and Specification of Feldspar for Use in Various Industries. *Journal of the American Ceramic Society*, 2006, 367-370.

3. Immo, H.R., Flotation of Feldspar, Spodemene, Quartz and Mica from Pegmatites (Paper presented at the 13th Canadian Mineral Processors Annual Meeting 1981), 1-7.

4. Mineral Zones, http://www.mineralzone.com/minerals/feldspar.htm Retrieved l7/13/2013.

5. Hassan, H., Ilgin, K. and Mert, T., Beneficiation of Low-Grade Feldspar Ore using Cyclojet Flotation Cell, Conventional Cell and Magnetic Separator. *Journal of Physico chemical Problems of Mineral Processing* 48 (2) (2012), 381-392.

6. Kangal, O., Guney, A., Beneficiation of Low-Grade Feldspars using Free Jet Flotation. *Journal of Mineral Processing Extractive Metallurgy* 23 (2012), 3-4.

7. U.S. Geological Survey (USGS), Mineral Commodity Summaries. 2011

8. Michael, J.P., *Feldspar and Nepheline Syenite.*(US Geological Survey Mineral Year Book. 2002), 27.1-27.3

9. Gulsory, O.Y., Can, N.M. and Bayraktar, I., Production of Potassium Feldspar from a Low-Grade Pegmatite Ore in Turkey. *Journal of Mineral Processing and Extractive Metallurgy,* 144 (2) (2005), 80-86.

10. Ali, E.A., Abdulkarim, F. and Magaji, S. (2010). Chemical Analysis of Feldspar from Richifa-Soba and its Suitability as a Glass Making Raw Material. Ashakwu, *Journal of Ceramic,* 7 (2010), 1-8

11. Gulsory, O.Y., Can, N.M. and Bayraktar, I., Production of Potassium Feldspar from a Low-Grade Pegmatite Ore in Turkey. *Journal of Mineral Processing and Extractive Metallurgy,* 144 (2) (2005), 80-86.

12. Hassan, H., Ilgin, K. and Mert, T., Beneficiation of Low-Grade Feldspar Ore using Cyclojet Flotation Cell, Conventional Cell and Magnetic Separator. *Journal of Physico chemical Problems of Mineral Processing,* 48 (2) (2012), 381-392.

Characterization of Minerals, Metals, and Materials 2015
Edited by: John S. Carpenter, Chenguang Bai, Juan Pablo Escobedo, Jiann-Yang Hwang, Shadia Ikhmayies, Bowen Li, Jian Li, Sergio Neves Monteiro, Zhiwei Peng, and Mingming Zhang
TMS (The Minerals, Metals & Materials Society), 2015

MICROWAVE POWER ABSORPTION CHARACTERISTICS OF IRON OXIDES

Zhiwei Peng[1,2], Jiann-Yang Hwang[2,3], Matthew Andriese[2], Yuzhe Zhang[2], Guanghui Li[1], Tao Jiang[1]

[1]School of Minerals Processing and Bioengineering, Central South University, Changsha, Hunan 410202, China
[2]Department of Materials Science and Engineering, Michigan Technological University, Houghton, MI 49931, USA
[3]Advanced Materials R&D Center of WISCO, Beijing 102211, China

Keywords: Microwave Heating, Power Absorption, Iron Oxides, Dielectric Loss, Magnetic Loss

Abstract

The microwave power absorption characteristics of iron oxides, including Fe_2O_3, Fe_3O_4 and $Fe_{0.925}O$, have been studied by determining dielectric loss and magnetic loss distributions in 0.05-m-thick oxide slabs irradiated with 1.2-kW, 2.45-GHz microwaves. The results reveal that the dielectric loss is the main factor contributing to microwave absorption in Fe_2O_3 and $Fe_{0.925}O$, while the magnetic loss dominates the power absorption in Fe_3O_4 below its Curie point. Uneven power distributions are observed in the slabs and this phenomenon becomes even worse at high temperatures at which the permittivity increases significantly. Quantification of power absorption in the oxides is of great importance for efficient and uniform microwave heating.

Introduction

Microwave energy is widely employed in the synthesis and processing of numerous materials including iron oxides [1-3]. Many distinguishing advantages of microwave heating of materials, such as rapid and selective heating, high productivity and "green" processing with significant energy reduction, have been demonstrated. These interesting features are associated with microwave power absorption and heat transfer in the materials [4]. The power absorption is attributed to both dielectric loss and/or magnetic loss of the material, whereas the heat transfer relies on many factors, such as microwave frequency, power, and sample size. Although microwaves heat materials volumetrically which significantly improves the heat transfer to the interior of a sample, selecting an appropriate sample size is still important [5,6]. To obtain a suitable size, microwave power absorption characteristics, usually in terms of dielectric and magnetic losses distributions, must be determined. This is extremely important for large-scale microwave heating of materials which has a strict requirement for microwave power absorption and temperature uniformity. A proper sample size will not only eliminate the possibility of uneven heating but also prevent thermal runaway due to temperature sudden rise during the process. In this regard, a detailed study on the power absorption characteristics of the material is the starting point of optimizing the microwave heating process.

Iron oxides, including Fe_2O_3 and Fe_3O_4, are primary materials for ironmaking and steelmaking. Some oxides, such as Fe_xO, may also act as important intermediate phases during many relevant

metallurgical processes. As microwave-assisted ironmaking and steelmaking is receiving more and more attention, the microwave absorption properties (permittivity and permeability) of iron oxides have been extensively studied [7-9]. With these properties, one may predict the microwave heating efficiencies at different stages of iron oxide reduction. It provides an opportunity for precise control of the whole process. However, it should be pointed out that the use of microwave energy in ferrous metallurgy is far from satisfactory. This is to a large extent caused by lack of knowledge of microwave power absorption characteristics of iron oxides.

The purpose of this work is to study the characteristics of microwave power absorption in iron oxides during microwave heating. The sample size (slab thickness) dependence of power absorption in Fe_2O_3, Fe_3O_4 and $Fe_{0.925}O$ is investigated by determining dielectric loss and magnetic loss distributions in 0.05-m-thick oxide slabs irradiated with 1.2-kW, 2.45-GHz microwaves using the simplified loss equations. Through determination of the power distribution characteristics, optimal size of the oxides at various stages of microwave heating can be obtained, offering a useful guide for improving heating uniformity and energy efficiency.

Theory

Microwave power absorption in a material during microwave heating includes the contribution of dielectric loss and magnetic loss, which depends on the distribution of microwave electric and magnetic fields. Assuming that the microwaves are uniform plane waves incident from air to a material slab with a thickness of L propagating in the z direction (Figure 1), the contribution of dielectric loss Q_E to the power absorption per unit volume (W m^{-3}) can be determined by Poynting vector.

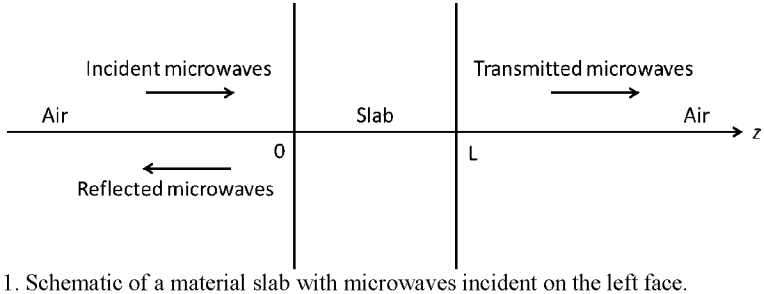

Figure 1. Schematic of a material slab with microwaves incident on the left face.

The equation for determining Q_E in microwave heating is given as [10]

$$Q_E(z) = \frac{1}{2}\omega\varepsilon_0\varepsilon_r''|E_0|^2|T|^2 \frac{e^{-2\alpha z} - 2|R|e^{-2\alpha L}\cos(2\beta L - 2\beta z - \delta) + |R|^2 e^{-2\alpha L}e^{-2\alpha(L-z)}}{1 - 2|R|^2 e^{-2\alpha L}\cos(2\beta L - 2\delta) + |R|^4 e^{-4\alpha L}} \quad (1)$$

where ω is the angular frequency, ε_0 is the permeability of free space (8.854×10^{-12} F m^{-1}), ε_r'' is the imaginary part of complex relative permittivity of the material (relative dielectric loss factor), E_0 is the incident microwave electric field strength, T and R are the transmission and reflection coefficients at the interface between free space and the medium, respectively, δ is the phase angle of reflection coefficient, and α and β are the field attenuation factor and phase constant

depending on the permittivity, permeability and microwave wavelength in free space, respectively. The contribution of magnetic loss Q_H to the power absorption in materials with non-zero magnetic susceptibility per unit volume (W m^{-3}) can also be determined by Poynting vector. It is given as [11]

$$Q_H(z) = \frac{1}{2}\omega\mu_0\mu_r'' \frac{|E_0|^2}{|\eta|^2}|T|^2 \frac{e^{-2\alpha z} + 2|R|e^{-2\alpha L}cos(2\beta L - 2\beta z - \delta) + |R|^2 e^{-2\alpha L}e^{-2\alpha(L-z)}}{1 - 2|R|^2 e^{-2\alpha L}cos(2\beta L - 2\delta) + |R|^4 e^{-4\alpha L}} \quad (2)$$

where μ_0 is the permeability of free space ($4\pi \times 10^{-7}$ H m^{-1}), μ_r'' is the imaginary part complex relative permeability of the material (relative magnetic loss factor), and η is the characteristic impendence of the material.

Results and Discussion

As indicated by eqs. (1) and (2), the dielectric and magnetic losses of Fe_2O_3, Fe_3O_4 and $Fe_{0.925}O$ depend on their permittivities and permeabilities. These properties were measured using the cavity perturbation technique [12-14] and used for calculation of loss distributions in the given oxide slabs in this study.

Dielectric and Magnetic Losses Distributions in Fe_2O_3

As mentioned above, both dielectric and magnetic losses contribute to microwave heating. Because Fe_2O_3 is one of main materials for ironmaking, the dielectric loss and magnetic loss distributions in a 0.05-m-thick ferric oxide slab at various temperatures (24, 296, 591, 982 °C) with 1.2-kW, 2.45-GHz microwaves was determined. The results are shown in Figures 2 and 3.

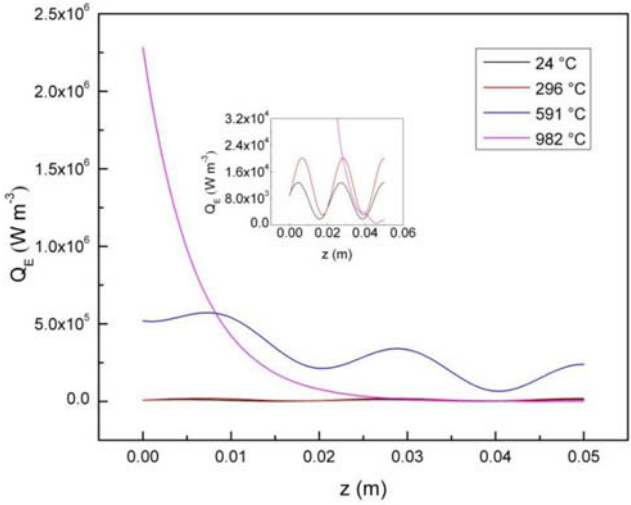

Figure 2. Dielectric loss distributions in the 0.05-m-thick Fe_2O_3 slabs irradiated with 1.2-kW, 2.45-GHz microwaves.

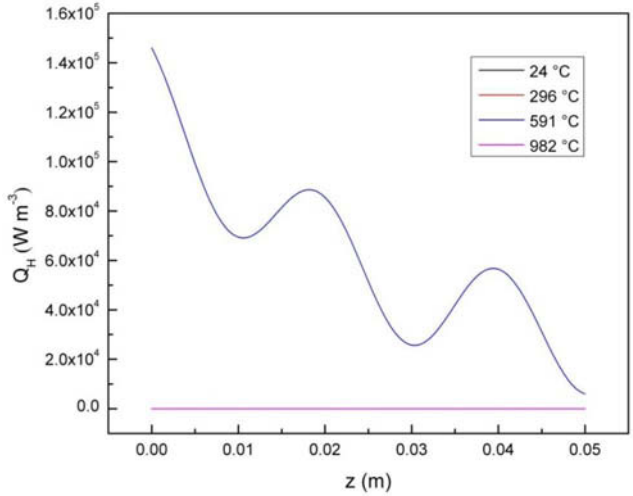

Figure 3. Magnetic loss distributions in the 0.05-m-thick Fe_2O_3 slabs irradiated with 1.2-kW, 2.45-GHz microwaves (some curves are overlapped).

A comparison between dielectric loss and magnetic loss distributions in Fe_2O_3 indicates that the dielectric loss of Fe_2O_3 is much larger than the magnetic loss of Fe_2O_3. This trend becomes more apparent as temperature increases. Therefore, it can be concluded that microwave heating of Fe_2O_3 is mainly attributed to the dielectric loss of Fe_2O_3. It is also noted that both losses dissipate rapidly with increasing slab size, especially in the range of z less than 0.01 m. The fluctuations in both losses distributions are attributed to the characteristics of sinusoidal waveforms.

Dielectric and Magnetic Losses Distributions in Fe_3O_4

Due to the strong magnetism of Fe_3O_4, it is expected that the magnetic loss of Fe_3O_4 plays an important role in microwave heating. For this reason, a comparison between dielectric loss and magnetic loss of Fe_3O_4 was performed. The results are shown in Figures 4 and 5. It is obvious that magnetic loss contributes more than dielectric loss to microwave heating of Fe_3O_4 at low temperatures (*e.g.*, 24 °C). However, as temperature goes up to the Curie point of Fe_3O_4, magnetic loss decreases considerably to nearly 0. Temperature increase in the sample is mainly ascribed to microwave dielectric loss beyond 600 °C. It can be seen that both losses dissipate significantly in the range of z smaller than 0.005 m. This observation agrees well with the fact that the Fe_3O_4 heats much faster than Fe_2O_3 under microwave irradiation.

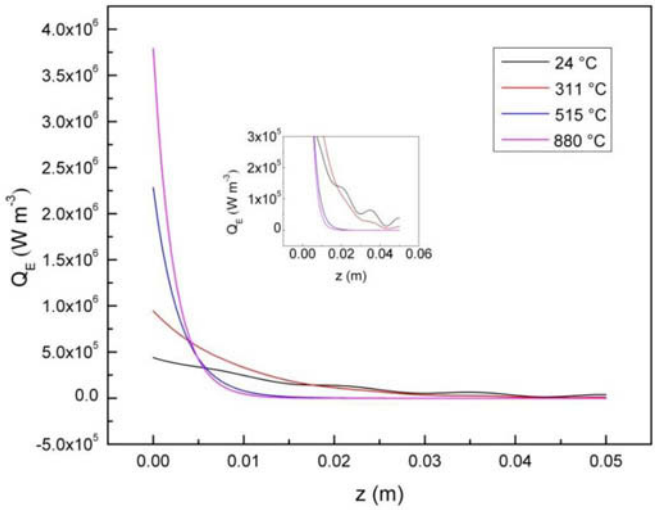

Figure 4. Dielectric loss distributions in the 0.05-m-thick Fe_3O_4 slabs irradiated with 1.2-kW, 2.45-GHz microwaves.

.

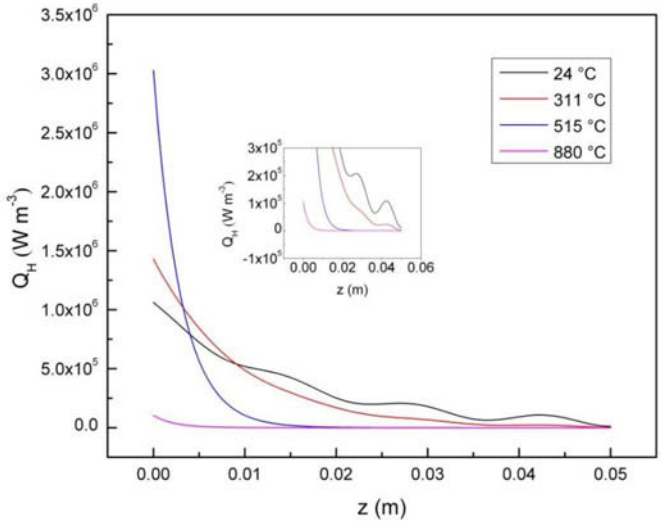

Figure 5. Magnetic loss distributions in the 0.05-m-thick Fe_3O_4 slabs irradiated with 1.2-kW, 2.45-GHz microwaves.

Dielectric Loss Distribution in $Fe_{0.925}O$

$Fe_{0.925}O$ is an important intermediate phase formed at approximately 600 °C during iron oxide reduction. Considering the non-magnetism of $Fe_{0.925}O$, only dielectric loss under the same conditions mentioned above is considered. The results are shown in Figure 6. Note that the temperatures selected for loss calculations are 24, 646, 842 and 1085 °C because $Fe_{0.925}O$ tends to decompose ($4Fe_{0.925}O \rightarrow 0.7Fe_3O_4 + Fe$) between 200 and 550 °C. It is found that dielectric loss of $Fe_{0.925}O$ remains relatively stable above 600 °C due to the slight changes in its dielectric properties. Unlike other oxides, the loss distributions in $Fe_{0.925}O$ present clear sinusoidal waveforms with increasing value of *z*.

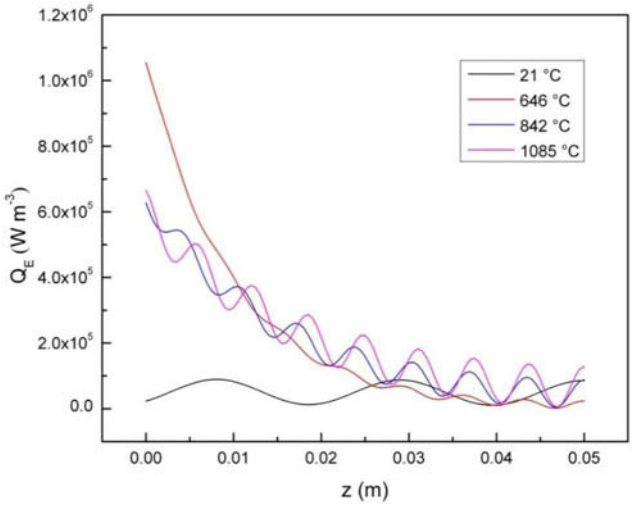

Figure 6. Dielectric loss distributions in the 0.05-m-thick $Fe_{0.925}O$ slabs irradiated with 1.2-kW, 2.45-GHz microwaves.

.

Conclusions

The microwave power absorption characteristics of Fe_2O_3, Fe_3O_4 and $Fe_{0.925}O$ have been investigated by determining dielectric loss and magnetic loss distributions in 0.05-m-thick oxide slabs irradiated with 1.2-kW, 2.45-GHz microwaves. It is demonstrated that the dielectric loss plays a major role in microwave absorption in Fe_2O_3 and $Fe_{0.925}O$, while the magnetic loss dominates the power absorption in Fe_3O_4 below its Curie point. Both losses dissipate rapidly in the range of *z* smaller than 0.01 and 0.05 m for Fe_2O_3 and Fe_3O_4, respectively. Compared with Fe_2O_3 and Fe_3O_4, the dielectric loss of $Fe_{0.925}O$ remains relatively stable above 600 °C. Uneven dielectric and magnetic losses distributions are observed in the slabs and this phenomenon becomes even worse at high temperatures at which the permittivity increases significantly. Quantification of power absorption in the oxides is of great importance for optimizing sample size, improving microwave heating efficiency and uniformity.

Acknowledgements

This work was supported by the Michigan Public Service Commission, U.P. Steel, the United States Department of Energy (Grant DE-FC36-01ID14209) and the Shenghua Lieying Program of Central South University (Grant 502035016).

References

1. D. E. Clark and W. H. Sutton, "Microwave Processing of Materials," *Annual Review of Materials Science*, 26 (1996), 299-331.
2. Z. Peng and J. Y. Hwang, "Microwave-Assisted Metallurgy," *International Materials Reviews*, DOI: http://dx.doi.org/10.1179/1743280414Y.0000000042
3. S. W. Kingman, "Recent Developments in Microwave Processing of Minerals," *International Materials Reviews*, 51 (2006), 1-12.
4. Z. Peng, J. Y. Hwang, and M. Andriese, "Absorber Impedance Matching in Microwave Heating," *Applied Physics Express*, 5 (2012), 077301-077301-3.
5. Z. Peng, J. Y. Hwang, M. Andriese, W. Bell, X. Huang, and X. Wang, "Numerical Simulation of Heat Transfer during Microwave Heating of Magnetite," *ISIJ International*, 51 (2011), 884-888.
6. Z. Peng, J. Y. Hwang, "Numerical Analysis of Heat Transfer Characteristics in Microwave Heating of Magnetic Dielectrics," *Metallurgical and Materials Transactions A*, 43A (2012), 1070-1078.
7. M. Hotta, M. Hayashi, A. Nishikata, and K. Nagata, "Complex permittivity and permeability of SiO_2 and Fe_3O_4 powders in microwave frequency range between 0.2 and 13.5 GHz," *ISIJ International*, 49 (2009), 1443-1448.
8. M. Hotta, M. Hayashi, and K. Nagata, "Complex permittivity and permeability of α-Fe_2O_3 and $Fe_{1-x}O$ powders in the microwave frequency range between 0.2 and 13.5 GHz," *ISIJ International*, 50 (2010), 1514-1516.
9. M. Hotta, M. Hayashi and K. Nagata: 'High temperature measurement of complex permittivity and permeability of Fe_3O_4 Powders in the frequency range of 0.2 to 13.5 GHz', *ISIJ International*, 51 (2011), 491-497.
10. Z. Peng, J. Y. Hwang, and M. Andriese, "Magnetic Loss in Microwave Heating," *Applied Physics Express*, 5(2012), 027304-027304-3.
11. Z. Peng, J. Y. Hwang, and M. Andriese, "Microwave Power Absorption Characteristics of Ferrites," *IEEE Transactions on Magnetics*, 49 (2013), 1163-1166.
12. Z. Peng, J. Y. Hwang, C. L. Park, B. G. Kim, M. Andriese, and X. Wang, "Microwave Permittivity, Permeability, and Absorption Capability of Ferric Oxide," *ISIJ International*, 52 (2012), 1535-1538.
13. Z. Peng, J. Y. Hwang, J. Mouris, R. Hutcheon, and X. Huang, "Microwave Penetration Depth in Materials with Non-Zero Magnetic Susceptibility," *ISIJ International*, 50 (2010), 1590-1596.
14. Z. Peng, J. Y. Hwang, J. Mouris, R. Hutcheon, and X. Sun, "Microwave Absorption Characteristics of Conventionally Heated Nonstoichiometric Ferrous Oxide," *Metallurgical and Materials Transactions A*, 42A (2011), 2259-2263.

Characterization of Minerals, Metals, and Materials 2015
Edited by: John S. Carpenter, Chenguang Bai, Juan Pablo Escobedo, Jiann-Yang Hwang, Shadia Ikhmayies, Bowen Li, Jian Li, Sergio Neves Monteiro, Zhiwei Peng, and Mingming Zhang
TMS (The Minerals, Metals & Materials Society), 2015

QUALITATIVE AND MINERALOGICAL CHARACTERIZATION OF LEAD DEPOSIT IN ISHIAGU, EBONYI STATE NIGERIA

[1]Onyedika G.O, [2]Onwukamike, K., [1]Onyenehide, C. and [1]Ogwuegbu M.O.C.

[1]Mineral Processing Unit, Department of Chemistry,Federal University of Technology, P.M.B. 1526, Owerri, Nigeria.
[2]Institute of Physics, University of Augsburg, Universitatsstrabe 2, 8b135, Augsburg, Germany.

Abstract

A detailed mineralogical and elemental characterization of a lead (Pb) ore deposit from Ishiagu, Ebonyi State, Nigeria was carried out with XRD, SEM-EDX, and ICP-OES based mappingtechniques. The results show that the most dominant and valuable metal is lead (Pb = 95.02%, mass fraction). The main mineral is galena. Ilmenite and sphalerite occur as minors, which account for 2.71% and 0.80% respectively. Elements like Al, Ca, Mg, Ti, Na, Mn, Si and Sn occurred in trace amounts and are disseminated in the entire ore body.The surface and interrelations of the crystals were examined with x-ray mapping and the result shows the pattern of dissemination of the minerals within the ore body.
(**Keywords:** Galena, Mineral, Lead, Characterization)

Introduction

Lead (Pb) is the principal metal extracted in the beneficiation of galena. Lead from galena is one of the earliest known metals in metallurgy. In Nigeria, lead occurs completely in the form of galena, most often in association with other minerals like sphalerite, argentite and heamatite [1]. Lead deposits in Nigeria are all similar in type and occur in rock of lower cretaceous age stretching over 580 kilometers in length in the NE-SW direction from Gwana in Bauchi State to Ishiagu in Ebonyi State. This galena ore serves as raw materials for local smelting industries and great potentials for foreign exchange [2]. Recently, ore characterization studies have provided improved and more reliable information on mineralogical composition and microstructure (textural) of materials. These studies have become important as they contribute to the determination of the ores downstream beneficiation operations. These have also been applied in investment education andsteel making, allowing improvements on both existing old and new processes. Various techniques have so far been used for ore characterization [3,4]. The mineralogy and chemistry of saprolitic nickel ores developed on ultramafic rock with different serpentinization degree from Soroako Sulawesi has been carried out using x-ray diffraction, thermal analybsis, FTIR and ICP-AES techniques [5]. We had earlier reported the characterization of Kurucassiterite ore using SEM-EDS, XRD and ICP [6]. It was observed that previous characterization of the cassiterite ore was based on one or two classical instruments,

which reported less accurate information about the actual composition of the ore. The combined information by the SEM-EDS, ICP-OES and the X- ray diffraction analyses revealed that the ore contained different minerals of cassiterite, coffinite, siderophyllite, ilmenite, quartz, rutile, manganocolumbite, zircon, tilleyite and monazite. The elemental analysis gave as per the follow: Sn (28.0%), Si (5.5%), Fe (5.16%), Ti (3.51%), Al (2.48%), Y (1.06%), and Nb (2.53%). The other trace elements found included Mn, K, Na, Mg, La, Ce, U and Ca. Further information on the benefits of ore characterization was given by Rao *et al* [7]. They carried out a detailed study of low grade iron ore of Bellary-Hospet sector using microscope, XRD, TG and EPMA techniques. Results obtained in these studies have exposed the indispensable role of geochemical and mineralogical characterization on the improvement of low-grade ores. Furthermore, iron pillar rust, sandstone deposits, industrial raw materials and certain atmospheric aerosols have also been characterized by XRD, Fourier transform infrared (FTIR), Mossbauer spectroscopy, ICPS and XRF [8, 9, 10, 11, 12]. Tin poly-metallic ore of Mengzi, in Yunnam Province of China has been quantitatively characterized through automated electron microscope-based mineral mapping. [13]. Today, there is no available information or comprehensive analysis of the Ishiagu lead deposit for interested public, investors and miners. This research work utilizes the combined information from the various analytical techniques - XRD, ICP-OES, SEM and EDS to fully characterize the poly-metallic lead deposit in Ishiagu, Ebonyi State of Nigeria.The objective of this work is to elucidate the chemical and mineralogical composition of the lead deposit, for the purposes of documentation and research information to miners, mineralogists, and metallurgist.

Experimental

The ore sample for this work was collected from the mining site located at Ishiagu in Ebonyi State of Nigeria. The sample was dried at 100 $^{\circ}$ C for 2 hours, and later crushed.Atypical piece was used for scanning electron microscope and energy dispersion spectroscopic studies for the mineral distribution [14]. This will allow forthe identificationof areas of special interest in the polished cross sections for more investigations.Part of the dried sample was ground to -200 mesh for x-ray diffraction and inductive coupled plasma – optical emission studies. Mineralogy was determined by collecting a series of x-ray maps showing the distribution of the elements.

Results and Discussion

Chemical Component of Ore

Table 1 shows the result of the elemental analysis of the sample by inductively coupled plasma – optical emission spectrophotometer. The result indicates Pb metal as the dominant and most valuable component while Al, Ca, Mg, Ti, Si, Na and Mn occurred in trace amounts. The result of the chemical phase analysis of the ore is shown in table 2. It shows galena as the major ore in which the lead metal occurred. The high distribution rate of ninety five (95.02) percent confirmed Pb dominance and accounts for the optimum theoretical recovery of lead.

Table 1: Elemental analysis of the ore sample by Inductively Coupled Plasma- optical emission spectrophotometer, (%).

Element	Si	Al	Ca	Mg	Fe	Ti	Na	Mn	Pb	Zn	Ce
% Composition	0.94	0.07	0.07	0.13	2.68	0.005	0.07	0.19	95.02	0.80	0.02

Table 2: Chemical phase analysis of the ore

Phase	Mass Fraction, %	Distribution Rate, %
Galena	0.94	95.02
Ilmenite	0.027	2.71
Sphalerite	0.008	0.8
Silicate	0.014	1.44

Mineral Composition of the Ore

Figure 1 shows the XRD pattern of the galena sample. From the peaks shown in the x-ray pattern, galena (G) was prominent as the major mineral, while sphalerite (S) had few and unpronounced peak areas. Mineral of quartz and ilmenite that contains the Si and Fe respectively was not detected by XRD. This is attributed to the insignificant amounts in which the occurred in the sample. The contents order for the minerals in the ore sample is galena » sphalerite › Ilmenite, quartz.

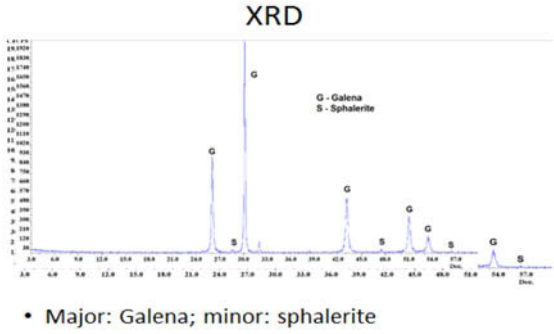

Figure 1: XRD analysis of the ore (G = Galena; S = Sphalerite)

Surface Characterization

Figure 2 are the pattern of the surfaces of the galena ore under scanning electron microscope (SEM). The surfaces are dull black and appeared amorphous with lots of white in reflected light. The surface image (A) shows much light reflected from the myriad indicating metallic tiny cleavage faces, whilesurface B shows the crystal nature of the galena ore with combination of cubic and octahedron structures. Figure 3 is the overall EDX on the crystal showing galena and quartz.

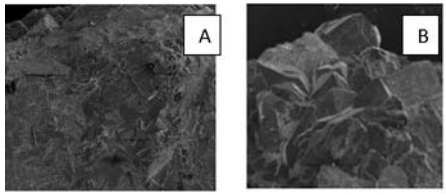

Figure 2: Overlook of the galena ore sample by SEM

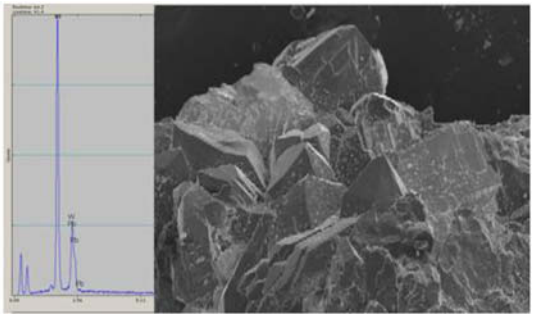

Figure 3: EDX analysis of Surface Crystal

Figure 4 is the x-ray surface mappings of the galena ore. The phase map shows the distribution of the various elements at the surface. The minerals are unevenly distributed. Lead (Pb) dissemination pattern filled along tungsten (W), quartz (Si), sphalerite (Zn), iron (Fe) and manganese (Mn). Figure 5 shows the result of the EDX on the included area. It indicated and reaffirms the presence of Si, Mn, Fe, W, Zn and Pb. This EDX compliments the XRD analysisas some of them were not detected by the XRD.

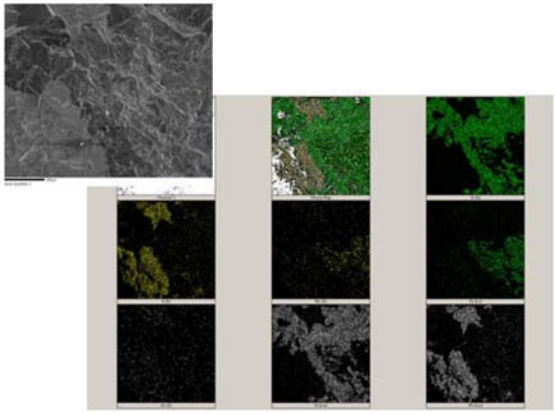

Figure 4: X-ray mapping of the galena ore sample (a) Phase map; (b) Si element mapping; (c) S element mapping; (d) Mn element mapping; (e) Fe element mapping; (f) Zn element mapping; (g) W element mapping; (h) Pb element mapping.

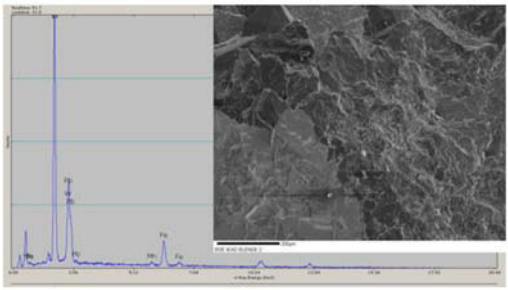

Figure 5: EDX analysis of the included area showing Si, Mn, W and Fe

Point Elemental Distributions

Figures 6a, 6b, 6c, 6d, are the EDX point analyses of the study area of the galena ore. Figure 6a shows Pb only, while at another point in figure 6b shows the presence of Fe, Mn, and Ca with Fe having distribution ratio of 84 %. The point at figure 6c shows Si, Mn, Zn, W, and Pb. The distribution ratio of Zn to the elements is 75 % while Pb (2.70 %); Si (16.46 %); Mn (3.22 %); and W (1.03 %). At this point, fewer Pb particles were observed. Figure 6d is the EDX analysis at another point within the study area showing the distribution ratios of Pb to be 91.66 % and sulfur (8.34 %). This result shows that the ore is PbS which is found in the form of galena.

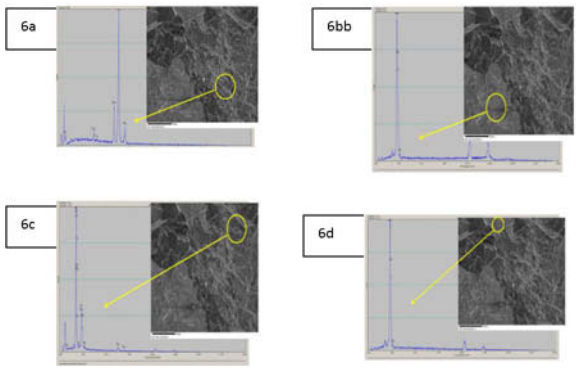

Figure 6: EDX point analyses of a study area with sub figures 6a, 6b, 6c, 6d.

Similarly, another study area within the galena ore body was considered which is shown in figure 7. The surface is clear and shows the interrelationships of the crystals. The area of right angle is associated with x-ray mapping shown in figure 8. Figure 8 clearly indicates the elements distribution of Pb, S, Zn and Si on the crystal. The distributions of Pb and S encompasses over 80 % of the entire surfaces.

Figure 7: EDX overall on a selected area.

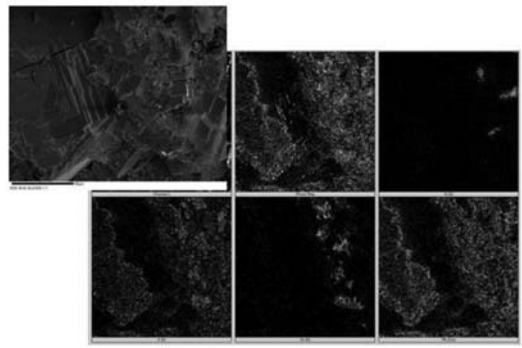

Figure 8: X-ray mapping of a selected study area within the ore body; (a) overall phase map; (b) Si mapping; (c) S mapping; (d) Zn mapping; (e) Pb mapping.

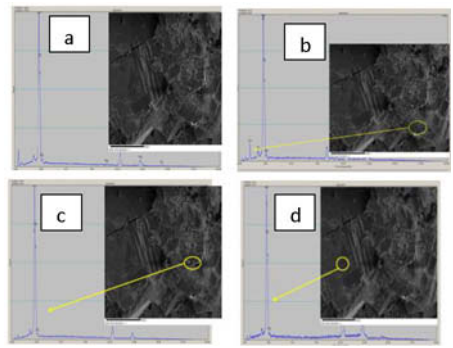

Fig 9: EDX analysis of points with sub figures (a,b, c and d)

Figure 9 shows the EDX analysis of the various points on the selected area. The associated peak areas indicates Pb element as the predominant element with other elements in trace amounts. This result agrees with other EDX analysis carried out on different points of the lump ore sample and affirms the fact that the ore sample under study is a galena ore.

Conclusion

The dominant mineral in the ore sample is galena, PbS. The minerals content order is galena » sphalerite › ilmenite ≥ quartz. The ore has a combination of both cubic and octahedron crystal structure. The most valuable metal element in the ore is Pb while Zn, Cu, Fe, W, Mn, and Si elements are found in trace amounts. The distribution ratio of Pb to other elements is 95.02 %.

References

1. Ofor, Ogbonnaya, *The Mineral Wealth of Nigeria* (1st Edition, Oliverson Publishers, Owerri,1997), 35-36.

2. A. Abubakar, "Raw Materials Development for Sustainable Economic Growth", *Proceeding of the 27th International Conference of Chemical Society of Nigeria*, 2004, 4-10.

3. M. Ogwuegbu, et al., "Differential Characterization of IkperejereIron Shale and Iron Sandstone" (Characterization of Minerals, Metals and Materials, San Diego, USA., Hwang et al (eds), John Wiley and Son, Inc., Hoboken, NJ) (2014), 401-411.

4. Q. Mohen, andA. El-Maghraby, "Characterization and Assessment of Saudi Clays Raw Materials at Different Areas", Arabian Journal of Chemistry, (3), 2010, 271-277.

5. A.I. Sufradin., et al.,"Study on Mineralogy and Chemistry of the Saprolitic Nickel Ores from Sokoako, Sulawesi, Indonesia: Implication from the Lateritic Ore Processing", J.SE Asian Applied Geology, 3(1), 2011, 23-33.

6. G. Onyedika et al., "Mineralogical Characterization of KuruCassiterite Ore by SEM-EDS, XRD and ICP Techniques", Journal of Minerals & Materials Characterization & Engineering, 10(9), 2011, 855-863.

7. D.S. Rao et al.,"Mineralogy and Geochemistry of a Low Grade Iron Ore sample from Bellary-Hospet sector, India and their Implication on Beneficiation", Journal of Minerals and Materials Characterization and Engineering, 8(2), 2009, 115-132.

8. R. Balasubramanian and A.V.R. Kumar, "Characterization of Delhi Iron Pillar Rust by XRD, Fourier Transform Infrared (FTIR) and Mossbauer Spectroscopy", Corrosion Science, 42, 2000, 2085-2101.

9. R. MacDonald, et al., "Using Elemental Geochemistry to Improve Reservoir Characterization: a case study from Unayzah interval of Saudi Arabia", SPWLA 51st Annual Logging Symposium, (2010), 19-23.

10. T. Pachauriet al., "SEM-EDX Characterization of Individual Coarse Particles in Agra", India, Aerosol and Air Quality Research, 13, 2013, 523-536.

11. D.M.A. Khan, "Raw Materials Characterization of Chromite", International Journal of Advanced Scientific and Technical Research, 5(2), 2012, 637.

12. P.C. Ryan andR.C. Reynolds, "The Chemical Composition of Serpentine/Chlorite in the Tuscaloosa formation, United States Gulf coast: EDX vs XRD determination, implications for mineralogical reactions and the origin of Anatase", Clays and Clay Minerals, 45(3), 1997, 339-352.

13. Y. Xu, et al.,"Mineralogical Characterization of Tin-PolymetallicOre occurred in Mengzi, Yunnam Province", China. Trans. Nonferrous Metal Society of China, 22, 2012. 725-730.

14. M. Pownceby, G. Sparrow, and M. Fisherwhite, "Mineralogical Characterization of Eucla Basin Ilmenite Concentrate- First Results from a new Global Resource", Mineral Engineering, 17(1), 2008. 39-51.

Characterization of Minerals, Metals, and Materials 2015
Edited by: John S. Carpenter, Chenguang Bai, Juan Pablo Escobedo, Jiann-Yang Hwang, Shadia Ikhmayies, Bowen Li, Jian Li, Sergio Neves Monteiro, Zhiwei Peng, and Mingming Zhang
TMS (The Minerals, Metals & Materials Society), 2015

SINTERING CHARACTERISTICS OF IRON ORES WITH ADDITION OF LATERITE NICKEL ORES

Xinyu Li[1], Jianliang Zhang[1], Chaoquan Yao[1], Yapeng Zhang[1], Zhiwen Shi[1], Fei Wang[1]

[1]School of Metallurgical and Ecological Engineering, University of Science and Technology Beijing, 30 Xueyuan Rd; Haidian District, Beijing, 100083, China

Keywords: Iron Ores; Laterite Nickel Ores; Sinter

Abstract

A great deal of iron ores which have special elements have been applied in the sintering process with the decreasing of high-grade quality iron ores resources. In this paper, the laterite nickel ores were added into three different kinds of iron ores respectively to make liquid phase formation research by software of Factsage and high temperature characteristic sintering experiments. The results showed that the adding proportion of laterite nickel ores should be less than 15% when the high temperature properties of the mixing ores were well. Increasing the mixing ration of laterite nickel ores in the sintering blending would play an important role in the reduction of the sintering cost.

Introduction

With the decreasing profit of the steel industry, the iron ores that have special elements have been used in the sintering ore blending process to decrease the cost of production in the iron and steel plant in China. The iron ores that have special elements have low TFe and high gauge content while the special elements are beneficial to the special steel-making with the advantages of low cost and so on. Hence, some researchers have studied the sintering process with adding the laterite nickel ores, sea sand ores, etc. in the sinter blending process to obtain the proper blending ratio of the iron ores that have special elements in order to decrease the cost and increase the production efficiency of iron-making system [1-3].

In present, the laterite nickel ores are used in the sintering blending production in some sinter plants of China. The nickel content varies in different laterite nickel ores. In some researches, when the adding ratio of high Fe low nickel of laterite nickel ores was less than 5% in the sinter blending, the various economic indicators and blast furnace production were well. The RDI could be improved and the cold strength and RI would be worse with the high proportion of laterite nickel ores. It is beneficial to lower the cost and improve the value of hot metal by increasing the adding ratio of laterite nickel ores in the sinter blending process [4-5].

In this article, the laterite nickel ore which is high nickel, low Fe and high water content (33.47%) was used to study the addition available of blending in the sintering process. The basic characteristic of the laterite nickel ore and three other typical iron ores were studied, and the high temperature characteristic experiments by adding the different proportion of laterite nickel ore to the other three iron ores were carried out as well. The proper laterite nickel ore blending ratio range can be obtained by analyzing the behavior of high nickel and low Fe of laterite nickel ore in the sintering process and the influence trend of the high temperature characteristic of iron ores.

Experimental

Materials

Hematite Ore A, limonite Ore B, magnetite Ore C and laterite nickel Ore D were used in the present experiment. Chemical compositions of each iron ore are listed in Table I. Ore A was a typical Brazilian hematite with TFe 63.26% and low silica and aluminum. Ore B was a typical Australian limonite characterized with high silica, burning loss and porous structure. Ore C was a kind of magnetite which was from Peru with TFe 69.43% and low gauge content. Ore D was a high nickel low TFe kind of laterite nickel with high silica and magnesium.

Table I Chemical compositions of iron ores (mass %)

Material	TFe	FeO	SiO_2	Al_2O_3	CaO	MgO	Ni	Ig	Type
Ore A	63.26	0.27	3.11	1.38	1.58	0.5	-	3.68	hematite
Ore B	57.23	0.40	5.59	1.36	0.22	0.21	-	9.46	limonite
Ore C	69.43	29.30	1.43	0.28	0.53	0.74	-	0.03	magnetite
Ore D	22.96	0.27	36.98	2.58	0.20	14.78	2.11	11.51	laterite nickel

Methods and facilities

The amount of liquid phase formation of the four iron ores was calculated by Factsage thermal software. The calculation temperature range was between 900~1300°C. The iron ores were crushed into the size less than 100 mesh, and then analyzed by X-ray diffraction analysis (XRD) to make a qualitative mineral composition analysis. The facility of X-ray diffraction was TTRIII multifunctional X-ray diffraction which used CuKα, scanning angle 10~90°, wavelength 0.15406nm. The high temperature characteristic experiments included the assimilation and fluidity. The iron ore which was less than 100 mesh was mixed firstly based on the different adding ratio of the Ore D into the other three iron ores. After that, the mixing iron ore was poured into the mold and agglomerated in a diameter of 8mm and 5mm high by a hydraulic jack to make the sinter sample. The pressure of the hydraulic jack was about 15MPa and the weight of each sample was 0.8g.The analytical CaO was compressed into a tablet with a diameter of 10mm and 2mm high as well under the iron ore sinter sample. In sequence, the material was sent to an infrared image furnace to simulate sintering thermal profile. Hence, the assimilation temperature of each iron ore was obtained by observing the iron ore reacts with the CaO tablet. The fluidity experiment was carried out with the mixing iron ore by adding analytical CaO and the same sinter sample making process as the assimilation experiment. The binary basicity and weight of each sample was 4.0 and 0.8g. Then the sample was set on the surface of the sheet which was made by alloy steel and heated to three different peak temperature in the infrared image furnace. The area of the melt formed on the sheet was measured with projection method. The fluidity index of the iron ore was calculated by the Eq. (1).

$$Fluidity = \frac{S_2 - S_1}{S_1} \tag{1}$$

Where, S_1 is the vertical projection area of original sinter sample, mm^2. S_2 is the vertical projection area of the sintered sample. The sintered sample was made into light sheet and analyzed by the reflective microscope to get the mineral structure of the sintered sample.

Results and Discussion

Liquid phase formation

Figure 1 shows the amount of liquid phase formation with the temperature range of 900~1300°C. It shows that the amount of liquid phase formation of Ore D was the highest with the number of 46.287% and the other three iron ores were almost 0 when the temperature was 900°C. With the temperature increased, the amount of liquid phase formation was with a linear increasing trend and the amount of it was 86.892%. The amount of liquid phase formation of Ore B increased sharply from the temperature of 1150°C and the amount of it was highest of the four iron ores with the number of 97.816% at the temperature of 1300°C which was related with the limonite Ore B itself. The crystal water of Ore B decomposed tremendously and formed larger pores with the temperature increasing which resulted in the rise of liquid formation. The liquid phase formation ability of Ore D was weak at the low temperature and it started to form liquid at 1150°C. Before the temperature of 1150°C, the liquid phase line of Ore A was same as Ore B while the liquid phase formation ability of Ore A was weaker with the temperature increased compared with Ore B which was consistent with the liquid formation characteristic of hematite and limonite ores.

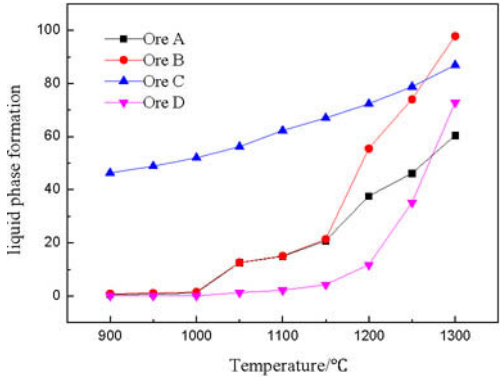

Figure 1. The relationship between the liquid formation and temperature of iron ores

XRD analysis

Figure 2 and 3 show the XRD results of the 4 iron ores. It can be seen that most of the characteristic peaks of Ore A, B and C is consistent with the chemical composition of each iron ore. As shown in Figure 3, there exists many different kinds of mineral types of Ore D which includes garnierite($(Ni, Mg)_3Si_2O_5(OH)_4$), clinochrysotile($Mg_3Si_2O_5(OH)_4$), antigorite($(Mg, Fe)_3Si_2O_5(OH)_4$), goethite, hematite, magnetite, quartz and the like.

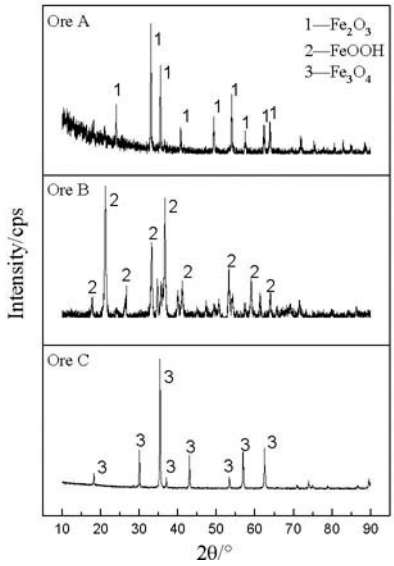

Figure 2. XRD results of the Ore A, B and C

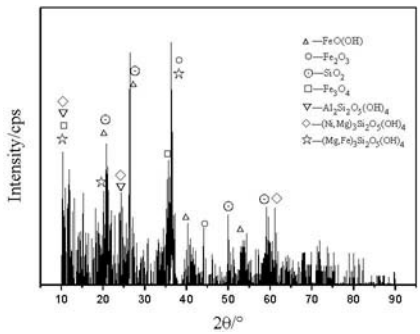

Figure 3. XRD result of Ore D

Assimilation

The assimilation of the iron ore is defined as the reaction ability of iron ore with CaO during the sintering process which represents the ease of generating liquid phase. The low assimilation temperature (LAT) usually represents the assimilation ability and the lower LAT is, the better assimilation of the iron ore. The three mixed iron ore LAT results are shown in Figure 4.

As shown in Figure 4, the LAT of Ore A, B and C is consistent with the study results before. The LAT of Ore B is the lowest due to the crystal water decomposes and increases the porosity of the limonite Ore B which promotes the reaction between the iron ore and CaO. In contrast, Ore C is a typical magnetite iron ore which is high TFe and relatively dense result in the worse reaction ability. In addition, the higher MgO content in Ore C inhibits the generation of calcium ferrite

which is bad to the assimilation and the LAT of the Ore C is the highest. The LAT of Ore A is moderate which is similar to the hematite type iron ore.

The LAT of the three mixed ore increases with the adding ratio of Ore D. The influence of Ore D on the mixed ore assimilation mainly reflected in its crystal water content and chemical composition. Ore D contains an amount of crystal water and high burning loss. When the temperature increases, the crystal water decomposes and the porosity increases which makes the assimilation easier to carry out. But there exists higher MgO content in the Ore D results in the generation of high-melting substances which influences the assimilation of iron ore. The MgO also promotes the decomposition of hematite to magnetite which inhibits the calcium ferrite formation. According to the assimilation results, the inhibitory effect of the high-melting material generated by the MgO is much greater than the promotion effect of the porosity generated by the decomposition of crystal water on the assimilation of the iron ore.

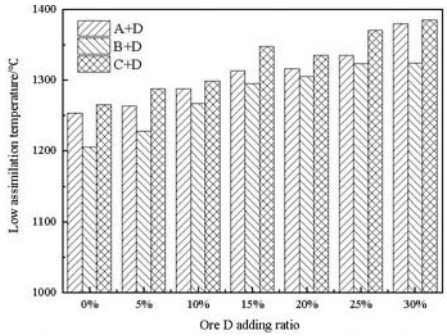

Figure 4. The assimilation temperature comparison of the three mixed iron ores

Fluidity

Figure 5 shows the three mixed ore fluidity index (FI) results. It can be seen that the FI of Ore A and D increases with the temperature increases when the adding ratio of Ore D less than 15% while the FI increases then drops with temperature increasing when the adding ratio more than 15%. The mixed ore FI is higher than that of Ore A when the Ore D blending ratio is 15% at 1280°C, R=4.0, thus the addition of Ore D inhibits the fluidity of Ore A. The FI of Ore B and D firstly increases and then decreases with temperature increasing when the blending Ore D 10% is the mostly obvious which is beneficial to improve the fluidity of Ore B. The FI of Ore C and D is gradually rising trend with increasing temperature. It is obvious to find that the adding ratio of Ore D more than 10%, the FI of mixed ore increases and the fluidity of Ore C improves as well. The fluidity ability plays a complementary effect when added the Ore D to Ore B or C, respectively. The Ore B liquid phase formation drops with the Ore D added because the large amount of MgO content in Ore D results in more high-melting material formation. The Ore B liquid phase formation increases with the Ore D added due to a great deal of SiO_2 in Ore D which makes more low-melting material formation in Ore C.

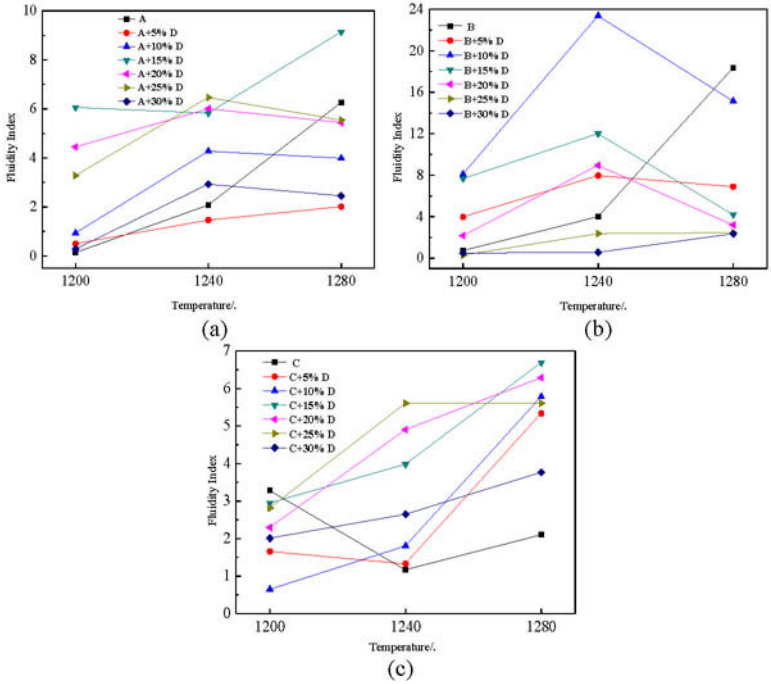

Figure 5. The fluidity index comparison of the three mixed iron ores

Calcium ferrite formation characteristic

The mineral phases were detected based on the assimilation and fluidity experiment results of some mixed ore sintered samples. The amount of silicon ferrite calcium and aluminum (SFCA) and mineral phase distribution are shown in Table 2 and Figure 6, respectively.

Figure 6(a) shows that a great deal of corroded calcium ferrite exists and some calcium ferrite, hematite and magnetite corroded together with little silicates existence. Figure 6(b) indicates that a little block calcium ferrite distributes with magnetite and the amount of silicates increase sharply.

As shown in Figure 6(c), the amount of calcium ferrite is small and most of it distributes with magnetite together while there exists a large amount of magnesium ferrite. Figure 6(d) shows that hematite and silicates distribute together densely and the amount of silicates increases heavily.

Figure 6(e) indicates that magnetite is the major mineral phase with magnesium ferrite and silicates distribute in it and there exists some pitting like calcium ferrite. As shown in Figure 6(f), the calcium ferrite bonding phase is little while the magnesium ferrite and silicates are the main bonding phase.

It can be included that there exists a large amount of corroded calcium ferrite when the adding ratio of Ore D is less than 5% which indicates that the Ore D almost has no impact on the sinter

mineral phase. There still exists some pitting like calcium ferrite which ensures the bonding phase of the sinter mineral phase when the adding ratio of Ore D is 15%. But there is also some existence of magnesium ferrite that is related to a certain MgO content of Ore D. Not only the amount of calcium ferrite decreases rapidly but the amount of silicates and magnesium ferrite increase sharply when the adding ratio of Ore D more than 20% which reduces the sinters strength significantly.

Table II The amount of SFCA in sintered specimens，%

Number	a	b	c	d	e	f
SFCA amount	22.3	13.3	12.8	5.7	11.5	3.5

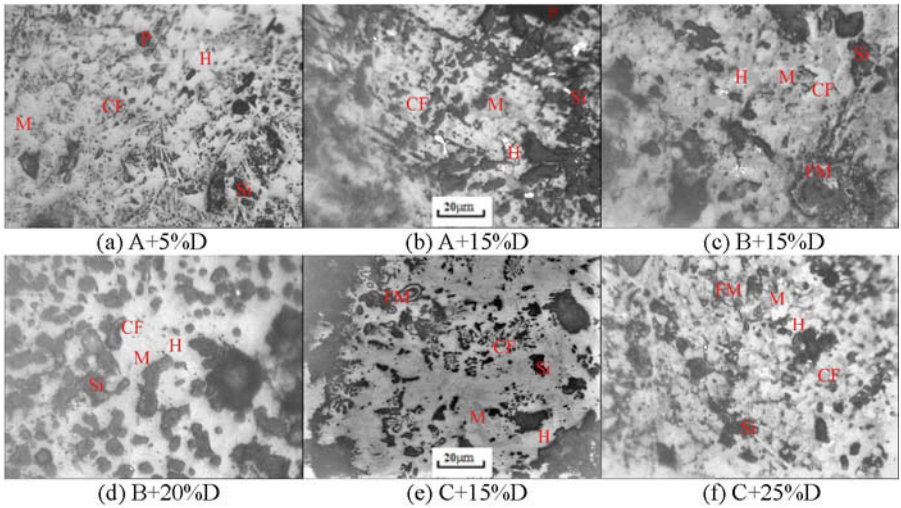

(a) A+5%D (b) A+15%D (c) B+15%D

(d) B+20%D (e) C+15%D (f) C+25%D

H-hematite，M-magnetite，CF-calcium ferrite，Si-silicates，FM-magnesium ferrite，P-pores

Figure 6. Calcium ferrite formation characteristics comparison of some sintered samples

Conclusions

(1)The basic characteristic of different kinds of iron ore varied widely based on the chemical composition, XRD and Factsage thermal calculation analysis. The liquid phase formation ability of Ore B was better and Ore A was worse. The liquid phase formation ability of Ore C and Ore D was moderate.

(2)The high temperature characteristic of different kinds of iron ore varied as well. The LAT was gradually rising of the mixed sintering ore with the Ore D adding ratio increasing. The liquid phase formation ability of Ore B and Ore C was improved by adding Ore D.

(3)When the ratio of the added Ore D was less than 15% in the mixture, it would have little effect on the high temperature characteristic of the blending iron ores, which contributed to lower the sinter blending cost.

References

[1]D. Liu, "Status Quo and Analysis of China's Iron Ore Import in Recent Years," *METAL MINE*, 1(2009), 12-15.

[2]L. B. Xu et al., "Study on Sintering Characteristics of New Zealand Sea Sand Iron Ore" (Paper presented at the 2014 iron-making production technology meeting, Zhengzhou, China, 12 May 2014), 371-377.

[3]T. Zhang et al., "Analysis of Application of High Proportion Laterite Nickel Ore in Sinter Production," *Sintering and Pelletizing*, 38(2013), 6-9.

[4]B. X. Su et al., "Sintering Characteristics of Iron Ores and Experiment Study on Optimizing Ore-Blending," *Iron and Steel*, 46(2011), 22-28.

[5]S. L. Wu et al., "Fluidity of liquid phase in iron ores during sintering," *Journal of University of Science and Technology Beijing*, 27(2005), 291-293.

[6]S. L. Wu et al., "Experimental Study of Assimilation Ability between Iron Ores and CaO," *Journal of University of Science and Technology Beijing*, 24(2002), 258-261.

[7]J. L. Zhang et al., "Dehydration mechanism and reduction process dynamics of laterite nickel ore," *The Chinese Journal of Nonferrous Metals*, 23(2013), 843-851.

Characterization of Minerals, Metals, and Materials 2015

Characterization of Clays and Ceramics

Session Chairs:

Robert Blair

Afonso Azevedo

Characterization of Minerals, Metals, and Materials 2015
Edited by: John S. Carpenter, Chenguang Bai, Juan Pablo Escobedo, Jiann-Yang Hwang, Shadia Ikhmayies, Bowen Li, Jian Li, Sergio Neves Monteiro, Zhiwei Peng, and Mingming Zhang
TMS (The Minerals, Metals & Materials Society), 2015

ALUMINA SUPERFINES BASED GEOPOLYMERES: DEVELOPMENTS AND CHARACTERIZATION

Nilton F. Nagem[1,2], Marcos Aurélio S. Costa[1], Valeria G. Silva[1], Andreia B. Henriques[2], Alexandra A. P. Mansur[2], Antonio E. C. Peres[2], Herman S. Mansur[2]

1- Rodovia BR 135 Km 18. Pedrinhas São Luís (MA), Brazil; ZIP 65095-050;
2- Av. Antonio Carlos – Campus UFMG- Pampulha – Belo Horizonte MG – Escola de Engenharia – Bloco 2 – Brazil; ZIP 31270-901

Keywords: Alumina superfines, Geopolymers, Charcterization, FTIR

Abstract

The superfine material generated in the Bayer process was used in one innovatively way as a precursor to geopolymerization techniques because of the presence of Gibbsite. Gibbsite can play a role in system adjustment because of the SiO_2/Al_2O_3 ratio. Furthermore in the geopolymeric system it was studied the influenceof the additives such as kaolin, metakaolin and sodium trisilicate in an alkaline media. Others conditions to form the geopolymer were also evaluated such as solid/liquid ratio, SiO_2/Al_2O_3 ratio and total alkaline. The raw materials and geopolymeric products were characterized by several techniques *e.g.* XRD, DSC, FTIR and SEM. Through the FTIR technique it was observed an increase in intensity and bandwidth in the region centered at 1010 cm^{-1}, which is related to the asymmetric vibration Si(Al)-O, this is an indicating of the possible geopolymer formation This broadening of the band promotes a relative disappearance (overlapping) peaks at 965 and 935 cm^{-1} associated with raw material (ESPDust).

Introduction

The Bayer process consists in concentration of the aluminum hydroxide existing in bauxite ore through solubilization and precipitation steps. During the calcination step occurs the transformation of aluminum $Al(OH)_3$ hydroxide on alumina Al_2O_3 [1]. During this stage occurs the breakage of the alumina crystals in small fraction, the superfines removal occurs by electrostatic precipitator. The removal of the superfine is necessary due to the potential harm in current efficiency and anodic effect in the Hall-Heroult process [2]. Thus, the alumina superfines (ESPdust) becomes a residue and it cannot be directly utilized in aluminum production neither be used directly in cover mix for the anodes setting in the pots. If this material is not sold in market, it is end up in a red mud disposal lake. Several studies tried to agglomerate the alumina superfines to be used in the anode cover mix composition with relatively success but with high capital costs. This paper presents the development of alumina fine base material as a geopolymer precursor for reuse in the mixing bath coverage.

The geopolymerization is an attractive solution since it has a generation of CO_2 equivalent lower than conventional agglomeration and briquetting techniques [3]. The first synthesized geopolymers used as precursor materials quartz, Kaolinite in an alkaline media at varying concentrations and synthesis temperature of 150°C. Thus, the geopolymers exhibit mineral base, aluminum-silicate (kaolin, metakaolin, fly ash, calcined soils), which under alkaline conditions promote reactions that allow the polymeric bonds of Si-O-Al-O chain. The geopolymers are similar to zeolites but have an amorphous microstructure [4]. The geopolymers chains are

formed by sharing of oxygen, similar organic polymer formed by the connections between the carbon atoms. The synthesis temperature may vary between 25 and 100°C, which will affect the reaction kinetics and the mechanical properties [3]. Sodium trisilicate, Kaolinite or metaKaolinite can were used as additional material.
The Kaolinite is a clay mineral has a white color and their lamellae are electrically neutral, its lamellae have a structure similar to Gibbsite octahedral and a tetrahedral structure formed by the structure of silica, in addition to having a low ion exchange capacity. If Kaolinite has substitution such as Si^{4+} by Al^{3+}, it may have surface charges [5, 6, 7]. It is know that the growth of its microcrystals have the form of plates with hexagonal profile. Due to their small interlamellar organic complexes (*e.g.* hydrazine derivatives, amines, urea, among others) can penetrate the expanding lamellae [6]. The process of dehydroxylation of Kaolinite is endothermic and occurs in the temperature range 550-900°C [8, 9], creating a new phase called metakaolin.

The study is innovative in the development of geopolymer based on ESPdust, furthermore evaluates the influence of additional material and processing parameters to meet the performance the required. The reactivity of the material with the electrolytic bath is the special characteristic needed [10], because it must be able to solubilize rather than be an inert material. The later is searched in most geopolymers [3].

Methodology

Materials and Methods

As base material, alumina superfine was used and it was divided in 4 subsamples of 250g. The surface area was performed by nitrogen adsorption technique using the BET method (Horiba, 6200 series) and the material density was obtained by gas picnometry (He).

Supplementary materials

Commercial Sodium Trisilicate - $Na_2Si_3O_7$ (Fluka 242.23 $gmol^{-1}$) was used as additive. Also Commercially Kaolinite was used, and in one previous study, has been extensively characterized (Rodrigues, 2009). The heat treatment for the transformation of Kaolinite to MetaKaolinite was performed at 750°C for 2 hours due to a more reactive structure [3].

Experiment Matrix for Geopolymers

All experiments were conducted in an aqueous medium in a closed system at 40°C. The following conditions were evaluated: the solid/liquid ratio (expressed in ratio H_2O/M_2O) where M is the sum of alkalis (Na_2O + K_2O), the variation of the ratio SiO_2/Al_2O_3. The sample identification starts with the letter "G" represents the nomenclature for geopolymer. Then, the group number are "2, 3 and 4", and after the base material name is in case "ESP" for ESPdust. Later, the activator is indicated with the word "Tri" for Trisilicate, "Caul" for Kaolinite and "MCa" for MetaKaolinite. The letters "A, B and C" indicate that there were changes in the ratio SiO_2/Al_2O_3 or H_2O/M_2O in the respective group (Table I).

Table I – Experiment Matrix

Group	ID	SiO_2/Al_2O_3	M_2O/SiO_2	M_2O/Al_2O_3	H_2O/M_2O	Temp. (°C)
1	G2ESPTrisA	2.6	1.1	2.8	34.5	40
	G2ESPTrisB	3.3	0.9	3.0	32.1	40
	G2ESPTrisC	3.9	0.8	3.2	29.9	40
2	G3ESPCaulA	1.2	1.9	2.2	32.0	40
	G3ESPCaulB	1.6	1.3	2.0	28.2	40
	G3ESPCaulC	1.8	1.1	2.0	25.9	40
3	G4ESPMCaA	1.2	1.9	2.2	32.0	40
	G4ESPMCaB	1.6	1.3	2.0	28.2	40
	G4ESPMCaC	1.8	1.1	2.0	25.9	40

Samples preparation

The procedure performed to prepare the samples was described below:
Initially the activating solution was prepared by solubilization of $200gL^{-1}$ of sodium hydroxide. This solution was stirred until its cool off. The dry mixed solids: Base materials and aluminosilicate fillers. The mixture was added to the activation solution and the system was stirred mechanically for 5 minutes. Poured in the mold and thickened through 5 beats. The curing of the material was performed in an oven for 24 hours. Subsequently, after demolding, the samples were dried for 24 hours at 40°C.

Analysis and Tests

The chemicals analyses for the raw materials were performed by ICP technique (Inductively Coupled Plasma Emission Spectrometer – ICP Optima 5300 DV - Perkin Elmer). For alumina phase determination was used X-ray Diffraction (XRD PANanalytical, CubiX3 model). Alumina size distribution was performed by Malvern particle analyzer MSS Mastersizer X.
The samples of geopolymers which had passed in mechanical test were subsequently coated with a thin film conductive carbon. Being examined and photographed in a scanning electron microscope (SEM) model INSPECT S50 - FEI Genesis - EDAX spectrometer and analyzed the X-ray dispersive energy (EDS).
All samples of raw material, additives and geopolymers formed were analyzed using infrared spectrometry were performed by the transmission diffuse reflectance spectroscopy technique (DRIFT) with KBr pellets 1:1000 with 64 scans and resolution of $2cm^{-1}$, Nicolet 6700 spectrometer, ThermoScientific.
Mechanical test was performed in the uniaxial compressive strength based on ASTM-C133-94 (Cold Crushing Strength) with a loading rate of 1-100ns. Cylindrical bodies in the dimensions of 25mm in diameter and 35mm in height were made. Results represent the average of two values obtained during the tests. Tests were performed one day after the drying due to the characteristic of the production process (manufacturer SOLOTEST series 6439).

Results and discussion

Alumina characterization

The chemical composition of the alumina superfines is presented in Table II.

Table II - Chemical composition and quantity of the alumina phase alpha-alumina.

ID	Sample (%)				Average	Stdv.
Al_2O_3	84.5	81.9	83.1	81.9	82.9	1.2
Na_2O	0.4	0.7	0.5	0.4	0.5	0.1
SiO_2	0.03	0.02	0.05	0.03	0.03	0.01
CaO	0.03	0.01	0.01	0.01	0.02	0.01
Fe_2O_3	0.02	0.01	0.01	0.01	0.01	0.01
M.O.I	10.7	13.2	12.6	13.3	12.5	1.2
L.O.I	4.3	4.1	3.7	4.4	4.1	0.3
α-Al2O3	10.8	7.6	15.6	15.8	12.5	4.0

Despite of the high concentration of alumina as Al_2O_3, only a part effectively contributes to the geopolymerization, since Gibbsite has a solubilization kinetics faster than Bohemite in the study conditions.

The particle size distribution of ESPdust is presented in terms of values of D10, D50, D90 as 8.0; 24.8 and 50.3μm and a deviation of 1.4; 3.7; 2.4μm respectively. The surface area was determined by nitrogen adsorption by the BET method and was $31{,}3 m^2 g^{-1} \pm 1.7$ m2 g^{-1}. The density of the material analyzed by gas picnometry (He) was $3{,}86 gcm^{-3} \pm 0{,}10 gcm^{-3}$.

The morphology of the alumina particles and the diffraction pattern are shown in Figure 1, the appearance of images of scanning electron microscopy are globular clusters.

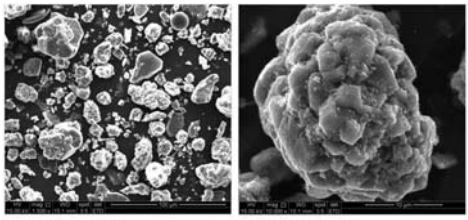

a) b)

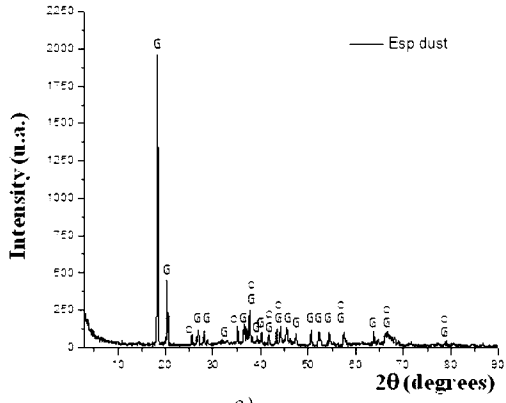

c)

Figure 1 - SEM of ESPDust a)1500x e b) 10000x and c) ESPDust diffractogram

In Figure 1(a) it is shown basically two types of particle, Gibbsite that had the aspect of agglomerated material and particles in the form of slabs or more defined, representing the α-Al_2O_3 (Dumortier, 2000). In Figure 1 (b) detail of Gibbsite particle is presented. The X-ray diffractogram is shown in Figure 1 (c), one may observe two crystalline phases Gibbsite (G) and α-Al2O3 (O).

Characterization of Additives for ESPDust System

Kaolinite chemical analysis is presented in Table III, indicating a SiO_2/Al_2O_3 ratio of 1.15.

Table III - Kaolinite chemical composition.

ID	Samples (%)		Average	Stdv.
SiO_2	44.9	46.6	45.8	1.2
Al_2O_3	38.3	39.6	39.9	0.9
TiO_2	1.3	1.5	1.4	0.2
Fe_2O_3	1.9	2.1	2.1	0.1
L.O.I	13.4	10.1	11.8	2.3

Alumina Geopolymerization

For reuse of alumina superfines in the aluminum production process as a bath composition of the coverage mix, a previous agglomeration is needed due to the high flow velocity caused by the size distribution lower than 20μm. However, the material shall have chemical reactivity with electrolytic bath (molten salts).

For the geopolymerization process it was used as a reference, only solution of sodium hydroxide and ESPdust as a sample. But unlike the red mud, the ESPdust do not have a pozzolanic

behavior. Thus, the samples did not form any kind of geopolymer also because the SiO_2/Al_2O_3 ratio of the cluster was initially 0.01, not suit for geopolymers.

The different kinds of additives (Trisilicate, Kaolinite and MetaKaolinite) were used as a comparative study. In the sodium trisilicate system, G2ESPtriC sample reached a value of 3,9MPa. In Figure 2, it can be observed the behavior of the three groups. Group 2 (G2ESPTri) while the molar ratio of SiO_2/Al_2O_3 is close to the ideal range for a geopolymer between 3.5 to 4.5, other relationships have changed, such as Na_2O/Al_2O_3 out of its respective track of geopolymerization due to the kind of additive. The Na_2O/Al_2O_3 ratio rises importance in this system, as the source of alumina becomes the dissolution of Gibbsite.

Another molar ratio that changes is the H_2O/Na_2O. NaOH is important for the dissolution of metastable aluminosilicate species, but does not guarantee the polycondensation [11]. This may have led to the formation of a structure rich in monomers which reduces the mechanical strength. As for Group 2, Kaolinite, and Group 3, metaKaolinite, there were increases in strength with increasing molar ratio SiO_2/Al_2O_3. However, for samples G3ESPCaulC and G4ESPMCaC, the parameters of curing and drying proved not to be adjusted since there was no integrity (NI). These, in turn, possessed the highest molar ratio Na_2O/Al_2O_3, on their group (1.8).

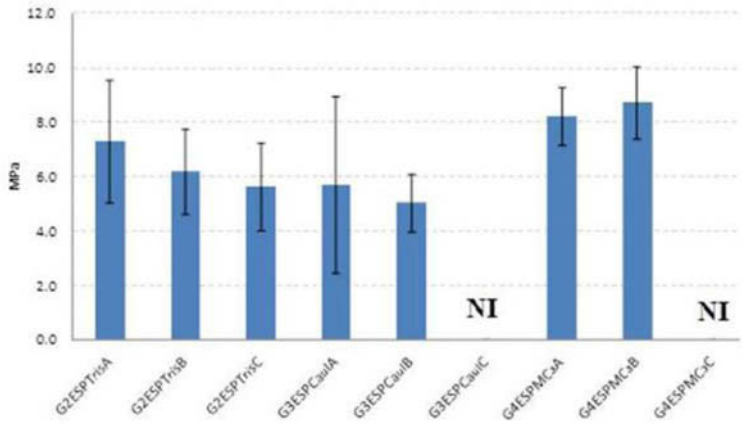

Figure 2 Variation ratio SiO_2/Al_2O_3 to different additives.

For the best performed geopolymers of each group a FTIR study was conducted and the spectrum was presented in Figure 3. The FTIR-based geopolymer matrix with Kaolinite additive G3ESPCaulB, shows a spectra in the region of 3500 cm^{-1} that represents Gibbsite and continues to be detected as well as Kaolinite. One the one hand it is observed the increase of the carbonate band in the region 1460 cm^{-1} [3]. In region 1200-500 cm^{-1} Kaolinite bands are attenuated but not disappear from the spectrum at 1090 and 980 cm^{-1}. This is an indication that there was no total solubilization of Kaolinite. However the peak of Si-O at 540 cm^{-1} is present.

As for metakaolin geopolymer G4ESPMCaB the basis of the spectrum in the region 3500 cm^{-1} shows whether the attenuated bands of Gibbsite and an increase in the vibration of the hydroxyl signal. In the spectrum is observed the formation of the sodium carbonate already described

above. The disappearance of the bands 1099 and 1019 cm^{-1} and appearance of a new band in 1009 is related to Si-O, indicating that the formation may have occurred in the geopolymer.

The FTIR of the geopolymer G2ESPTrisB shows the presence of Gibbsite, but there is an increase in intensity of links H_2O/hydroxyl in the region of 3500cm^{-1} due to the nature of the system. According to Davidovits (2008), the bands in the region of 1460cm^{-1} are related to the presence of sodium carbonate, arising from the migration of water during the drying and curing, which carries sodium hydroxide to the surface by reacting with atmospheric CO_2. One can observe the increase of intensity and bandwidth in the area centered at 1010 cm^{-1}, which is related to the asymmetrical vibration Si(Al)-O, indicating possible formation of the geopolymer. This broadening of the band promotes a relative disappearance (overlapping) peaks at 965 and 935 cm^{-1} associated with raw material (ESPDust).

Details can be seen in Figure 4 there a difference between treatments, but the geopolymers formed from metakaolin and sodium trisilicate show greater similarity. The geopolymer that used Kaolinite shows no indication of extensive geopolymerization because the additive can be observed even in the composition.

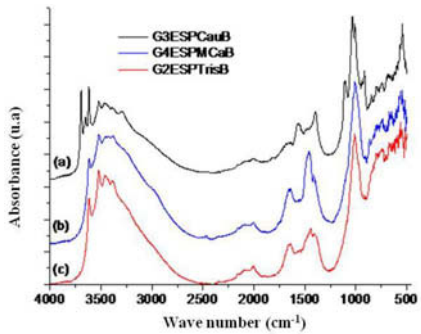

Figure 3- Comparison between geopolymers G3ESPCauB (a), G4ESPMCaB (b) and G2ESPTrisB (c).

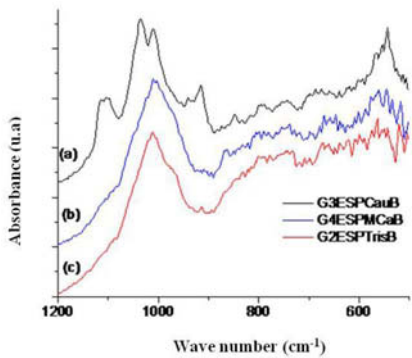

Figure 4- Details from comparison between geopolymers G3ESPCauB (a), G4ESPMCaB (b) and G2ESPTrisB (c).

The morphologies of the geopolymers are shown in Figures 5 the micrographs A and C, shows a more continuous fracture surface, while B shows depressions, or greater irregularity.

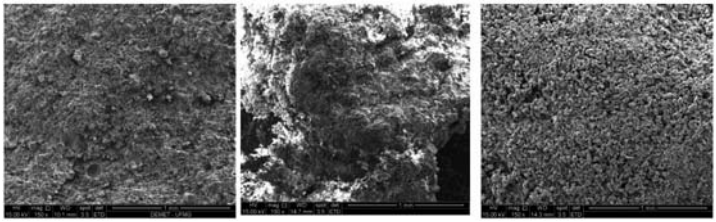

A) B) C)

Figure 5- Micrograph 150x a)G2ESPTrisB, b) G3ESPCauB, c) G4ESPMCaB.

These observations were agreement with the mechanical properties observed in Figure 2 and FTIR spectra's, the greater the extent of geopolymerization greater will be the mechanical resistance.

Conclusion

The study aimed not only develops and understand the geopolymeric systems derived from by-products of the aluminum industry, as well as presenting a potential industrial feasible solution for alumina superfines (ESPdust).

It was possible to geopolymerize ESPdust with supplementary materials, with potential application as part of the chemical composition of the bath cover. Since Gibbsite improve the SiO_2/Al_2O_3. The curing temperature of 40°C reveal to suit for geopolymerization system since mechanical resistance was higher than 2 MPa. Also for all evaluated the supplementary materials: Sodium Trisilicate, Kaolinite and MetaKaolinite.

The MetaKaolinite and Trisilicate developed a better geopolymeric structure for the conditions studied.

The geopolymer can be used in the composition of the bath cover electrolytic cells, the geopolymer will be crushed again to adjust the size and mixed with the other constituent materials.

Further studies are necessary to enhance geopolymer properties and understand the behavior of HF gas adsorption.

Acknowledgements

The authors thank FAPEMIG for partial funding of the project, as well as the Department of Metallurgical and Materials Engineering, Federal University of Minas Gerais (UFMG) and Alcoa / Alumar for help in developing the project.

References

[1]- Habashi, F. A textbook of hydrometallurgy, Editora Métallurgie Extractive Québec, Enr., Canada, 689p., 1993.

[2]-Tarcy, G., Torklep, P. Current efficiency in prebake and Soderberg cells, Light Metals, 2005.

[3]- Davidovits, J., Geopolymer Chemistry and Applications, Institut Geopolymere, Saint-Quentin, France, 584p., 2008.

[4]-Xu, H., Deventer, V. The geopolymerisation of alumino-silicate minerals. International Journal of Mineral Processing, v.59, p.247-266, 2000.
[5]-Grim, E. R., Applied Clay Mineralogy. 1 ed, New York: McGraw Book Company, 1962.
[6]-Weaver, C. E. Clays, Muds and Shales. 1 ed., Amsterdam: Elsevier, p.818, 1989.
[7]-Rahman, M. B. A.; et. al. Application of natural kaolin as support for
the immobilization of lipase from Candida rugosa as biocatalyst for effective esterification. Applied Clay Science, v. 29, p. 111-116, 2005.
[8]- Sand, L. B.; Comer, J. J. A study in morphology by electron diffraction. Clays and Clay Minerals, v. 3, p. 26-30, 1954.
[9]- Bergaya, F.; Theng, B. K. G.; Lagaly, G. Handbook of Clay Science. vol. 1, 1 ed., Amsterdam: Elsevier, p. 1752, 2006.
[10]-Grotheim, K., Kvande, H. Understanding the Hall-Héroult process for production of aluminium, Düsseldorf: Aluminium.Verlog, 164p., 1986.
[11]- Rees, C.A., Mechanisms and kinetics of gel formation in geopolymers, Thesis for Doctor of Philosophy Department of Chemical and Biomolecular Engineering The University of Melbourne, 198p., 2007.

Characterization of Minerals, Metals, and Materials 2015
Edited by: John S. Carpenter, Chenguang Bai, Juan Pablo Escobedo, Jiann-Yang Hwang, Shadia Ikhmayies, Bowen Li, Jian Li, Sergio Neves Monteiro, Zhiwei Peng, and Mingming Zhang
TMS (The Minerals, Metals & Materials Society), 2015

DENSIFICATION AND MECHANICAL PROPERTIES OF REACTION SINTERED Al_2O_3-MgO-CaO REFRACTORY

Lei Xu, Liang-yu Jin, Xue-liang Yin, Min Chen*

School of materials and metallurgy, Northeastern University, Shenyang 110819, China

Keywords: Al_2O_3-MgO-CaO, Refractory, Reaction process, Lightweight, Densification

Abstract

For the purpose to reduce the high cost and heat storage loss of Al_2O_3-MgO bricks used as ladle linings, Al_2O_3-MgO-CaO bricks with lower theoretical density were fabricated and the densification behavior as well as mechanical property of this refractory was investigated. With addition of CaO, the initial sintering temperature of Al_2O_3-MgO refractory was decreased from 1300 to 1100°C associated with the expansive formation of CA_2, and the compressive strength was also enhanced owing to the formation of bond linkage between CA_6 and spinel. At high temperature, brick with 4% CaO content showed poor sinterability with high porosity because of the formation of platelet structure of CA_6 grains, whereas brick with 8% CaO content was well sintered with higher relative density but lower bulk density than Al_2O_3-MgO brick, indicating that the densification as well as lightweight of Al_2O_3-MgO refractory was effectively promoted.

Introduction

The application of Al_2O_3-MgO bricks or castables has greatly increased the service life of steel ladles compared with other kinds of refractories, for the highly improved slag corrosion resistance and wearing resistance [1-3]. The reduction in slag penetration and Mn^{2+}, Fe^{2+} and Fe^{3+} cations absorbed by alumina rich spinel in the form of a solid solution were the key reasons for the improvement of the performance of the refractory [4, 5]. However, the application of this refractory has been hindered recently due to the following two aspects:

(1) Increase of the product cost of alumina containing refractories due to the short supply of alumina resource.

(2) Higher values of bulk density of Al_2O_3-MgO refractory due to the higher theoretical density of α-Al_2O_3 (3.99 g/cm^3), which requires higher energy consumption for the heat storage loss and does not fit the requirement of energy saving.

To solve these problems, lightweight Al_2O_3-MgO refractory has been fabricated by using porous aggregates [6-8], but little further works on the application of such lightweight refractory as working linings of ladles have been reported in the literatures mainly owing to the worry on the poor slag corrosion resistance.

Considering the abundant and inexpensive resource of limestone, Al_2O_3-MgO refractory would

become relatively low-cost and lightweight while using CaO (decomposed limestone with a theoretical density of 3.35 g/cm^3) as raw material to fabricate Al_2O_3-MgO-CaO refractory. Besides, materials designed in Al_2O_3-MgO-CaO system with a small amount of CaO present high refractoriness according to the phase relationships [9]. Therefore, Al_2O_3-MgO-CaO refractories with different CaO content were designed in the present work, and the densification behavior as well as mechanical property of these refractories has been investigated, for the purpose to fabricate dense and lightweight Al_2O_3-MgO-CaO refractory materials.

Experiment

The starting powders used in the present work were Al_2O_3 (analytical reagent with purity ≥99.5 mass% and d_{50} <10 μm), MgO (analytical reagent with purity ≥99.0 mass% and d_{50} <10 μm) and $CaCO_3$ (analytical reagent with purity ≥99.5 mass% and d_{50} <20 μm). Three batches of mixtures (with compositions shown in Table I) were prepared by ball-milling for 2 h in isopropanol respectively. After evaporation of the isopropanol by means of a rotating evaporator, the dry powder mixtures were shaped to pellet sizes of 40 mm × 40 mm × 10 mm under pressure of 40 MPa respectively. The chemical composition of A-batch was typical for Al_2O_3-MgO refractory, and the other two compositions were formulated on the basis of the information supplied by the ternary subsystem Al_2O_3-$MgAl_2O_4$-$CaAl_4O_7$, the initial liquid appearance of which starts at 1730°C [9]. The prepared pellets were dried at 120°C for 24 h, and then were fired in a high temperature electric furnace at the heating rate of 5 °C/min to the final temperature in the range of 1000-1600°C with soaking time of 2 h, and then cooled to room temperature in the furnace.

Table I. Mass composition of different batches, mass%

Batches	CaO ($CaCO_3$)	MgO	Al_2O_3	Total
A	0 (0)	10	90	100
B	4 (7.14)	10	86	100
C	8 (14.29)	10	82	100

The phase compositions were examined by X-ray powder diffraction (XRD, Cu Kα radiation, 40 kV and 40 mA) with a step of 0.02° (2θ). The compactness was characterized by bulk density and apparent porosity measured in kerosene using Archimedes principle, and the cold compressive strength was measured using computer-controlled hydraulic universal test (Model WEW-50). In addition, the microstructure was analyzed by scanning electron microscopy (SEM, SSX-550, Japan) attached with energy dispersive X-ray analyzer (EDX).

Results and discussion

Reaction process

The reaction processes of the different samples were studied by analyzing the evolution of the

phase compositions (shown in Fig. 1). The reaction of MA formation in A-batch (shown in Fig. 1a) was practically finished at around 1200°C, which was in agreement with reported [10]. For B-batch (shown in Fig. 1b), the complete formation temperature of MA was higher than 1200°C compared with A-batch. According to the study of Carter, higher MA formation rate is carried out at alumina interface by the diffusion of Mg^{2+} [11]. As a consequence of the reduction of alumina content by the reaction with CaO at lower temperatures, the diffusion distance of Mg^{2+} increased and hindered the formation of MA. In addition, the formation of CA_2 was finished completely at around 1100°C. At 1300°C, CA_6 was detected by reaction between CA_2 and excess alumina, which was finished completely at around 1500°C with extremely low intensity of CA_2 peak. The evolution of the reaction process of C-batch (shown in Fig. 1c) was almost as same as that of B-batch at temperatures in the range of 1000-1400°C. However, CA_2 still remained as a main constituent in this sample at temperatures higher than 1500°C, which was owing to the difference of locations in the ternary subsystem Al_2O_3-$MgAl_2O_4$-$CaAl_4O_7$ between these two samples.

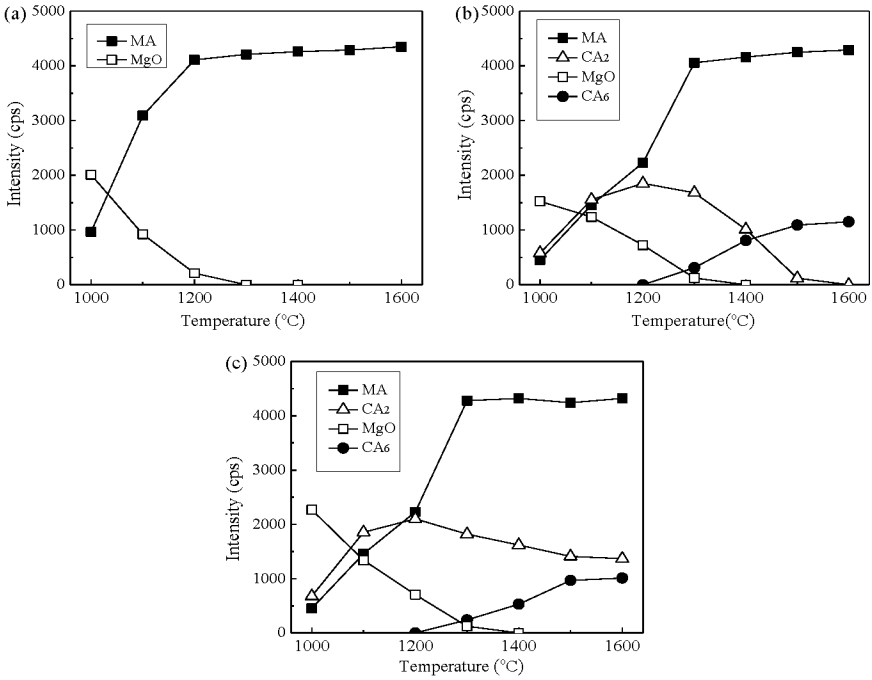

Fig. 1 Evolution of phase compositions with temperature of the different samples indicated from the following XRD peaks: MA (311); CA_2 (311); MgO (200); CA_6 (114): (a) without CaO, (b) 4% CaO, (c) 8% CaO.

Densification

Fig. 2 shows the variation of the densification process of the different samples with firing temperature and CaO content. In Fig. 2(a), the bulk density of the sample without CaO addition increased slightly at temperatures lower than 1300°C, with an appreciable increase in apparent porosity at the same time, which could be associated with the formation of new apparent pore channels by coalescing sealed pores formed in green pellets. Volume expansion of 3.7-8.4% caused by the formation of MA also occurred in the same temperature range, which was unfavorable for the densification process. Thus, densification process was not significant until higher than 1300°C, which is considered as the initial sintering temperature of Al_2O_3-MgO refractory under the present experimental condition.

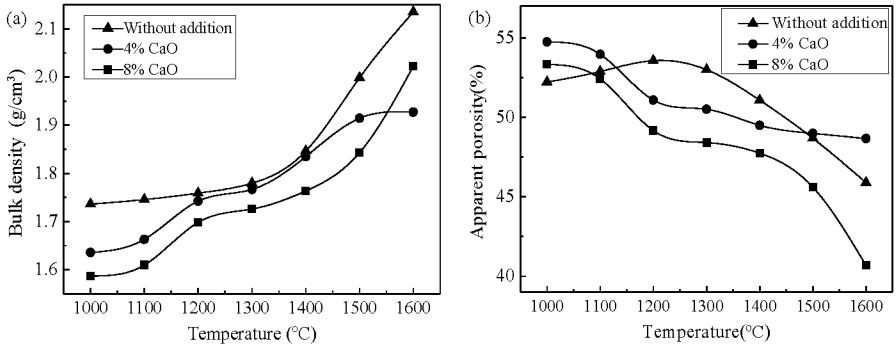

Fig. 2 Variation of the densification process of the different samples: (a) bulk density, (b) apparent porosity.

The bulk density of the samples with CaO addition was lower than A-batch at temperatures lower than 1200°C, which was mainly because of the abundant formation of CA_2 with low theoretical density (2.89 g/cm^3). Meanwhile, significant densification process of the CaO added samples was achieved from 1100°C to 1200°C, with a sharp decrease in apparent porosity. It was confirmed by the change of microstructure of C-batch in the same temperature range (shown in Fig. 3), which clearly showed a significant grain growth of CA_2 and a reinforcement of the grain–grain bonding. Thus, it could be considered that addition of CaO effectively decreased the initial sintering temperature of Al_2O_3-MgO refractory to 1100°C under the present experimental condition.

In Fig. 2(b), the densification of C-batch was rapidly promoted at temperatures higher than 1300°C. There was a decrease in bulk density from 2.15 to 2.01 g/cm^3 while 8% CaO was added at 1600°C because of the steady existence of CA_2. Furthermore, a decrease in apparent porosity from 45.3% to 40.6% was also observed, mainly owing to the resorption of porosity by the expansive formation of CA_2 in initial sintering stage [12] and promotion of grain growth associated with higher diffusion rates of ions at high temperatures, which suggested that the

lightweight and densification of Al_2O_3-MgO refractory were effectively promoted. However, brick with 4% CaO content showed poor sinterability with little decrease in porosity at the same temperature range. To explain this abnormal phenomenon, microstructures on both polished and fractured surfaces of this sample were analyzed (shown in Fig. 4). Typical platelet structure of CA_6 grains with an acicular shape was clearly identified on the polished surface, enclosing the MA grains, which hindered the grain growth of MA and the elimination of pores. Consequently, densification process slowed down rapidly and a porous structure formed. This enclosed structure was also observed in the fractured surface, showing a limited grain growth of MA.

Since both composition and particle size of the CaO added samples are similar to the typical matrices of the alumina-rich castables which are widely used as linings of ladles, the composition with 8% CaO content located in the ternary subsystem $MgAl_2O_4$-$CaAl_4O_7$-$CaAl_{12}O_{19}$ is more proper for the matrices considering its better compactness and less penetration of slags.

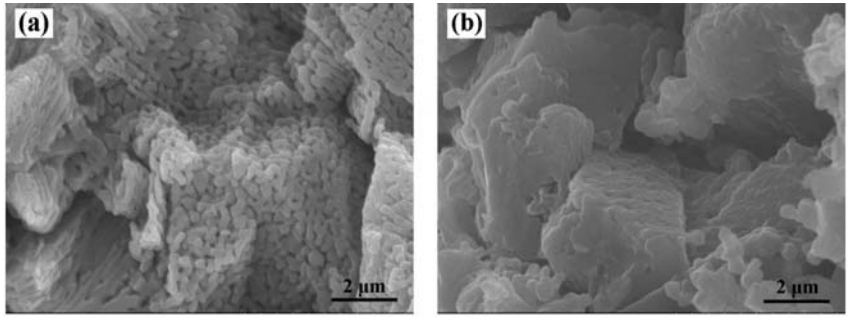

Fig. 3 SEM images of the fractured surfaces of Al_2O_3-MgO-CaO refractory with 8% CaO treated at (a) 1100°C and (b) 1200°C.

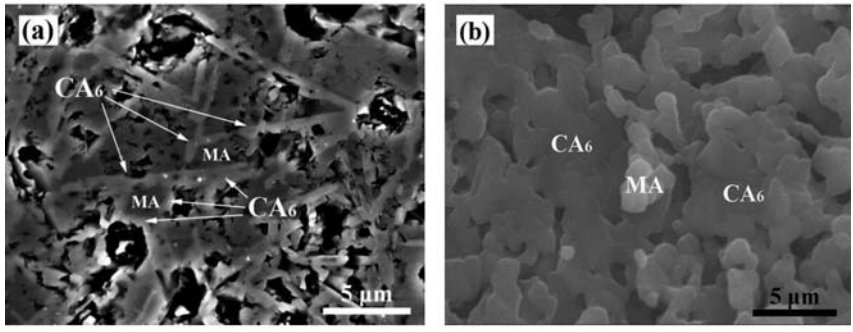

Fig. 4 SEM images of Al_2O_3-MgO-CaO refractory with 4% CaO treated at1600°C: (a) polished surface, (b) fractured surface.

Compressive strength

Fig. 5 shows the cold compressive strength (determined by the average values of the cold strength of 5 samples) of the different samples after fired at 1600°C. Though the compactness of the brick with 4% CaO content was poor, its strength was increased compared with the sample without addition. Such enhancement in strength was believed to be associated with the formation of linkage between CA_6 and spinel grains (shown in Fig. 4b) [13]. Brick with 8% CaO content presented the highest strength owing to the similar linkage structure as B-batch and the higher compactness compared with other samples.

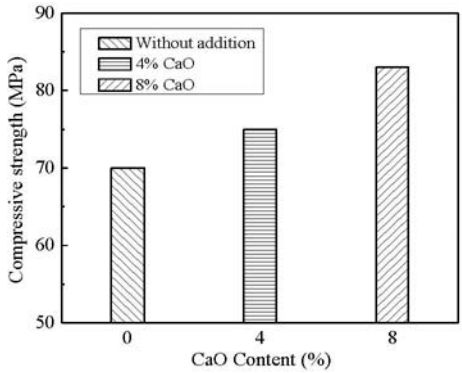

Fig. 5 Cold compressive strength of the different samples treated at1600°C.

Conclusions

Al_2O_3-MgO-CaO refractories with different CaO content were fabricated by firing mixtures of Al_2O_3, MgO and $CaCO_3$ powders, and the densification behavior as well as mechanical property of this system refractory was investigated. Based on the above results, the following conclusions have been drawn:

(1) The initial sintering temperature of Al_2O_3-MgO refractory was decreased from 1300°C to 1100°C by adding CaO associated with a reinforcement of the grain–grain bonding and significant grain growth of CA_2 from 1100 to 1200°C.

(2) Brick with 4% CaO showed poor sinterability with little decrease in porosity at high temperatures, but when 8% CaO was added, both the densification and lightweight were effectively promoted.

(3) The cold compressive strength was enhanced with addition of CaO due to the formation of linkage between CA_6 and spinel grains.

Acknowledgment

The authors gratefully acknowledge the National Natural Science Foundation of China (No. 51174049, 51174052, 51374057, 51374062) and the Fundamental Research Funds for the Central Universities of China (No.110402009), which has made this research possible.

References

1. I. Ganesh et al., "An efficient $MgAl_2O_4$ spinel additive for improved slag erosion and penetration resistance of high-Al_2O_3 and MgO–C refractories," *Ceram. Int.*, 28(2002), 245–253.
2. Y. Sato, H. Joguchi, and N. Hiroki, "Test results of alumina-spinel castables for steel ladle," *Taikabutsu Overseas*, 12(1992), 10–14.
3. K. Fujii, I. Furusato, and I. Takita, "Composition of spinel clinker for teeming ladle casting materials," *Taikabutsu Overseas*, 12(1992), 4–9.
4. Y. C. Ko, "Influence of the characteristics of spinels on the slag resistance of Al_2O_3–MgO and Al_2O_3–spinel castables," *J. Am. Ceram. Soc.*, 83(2000), 2333–2335.
5. L. A. Díaz et al., "Effect of spinel content on slag attack resistance of high alumina refractory castables," *J. Eur. Ceram. Soc.*, 27(2007), 4623–4631.
6. W. Yan, N. Li, and B. Q. Han, "High-strength, lightweight spinel refractories," *Am. Ceram. Soc. Bull.*, 84(2005), 1-3.
7. R. Salomão, M. O. Bôas, and V. C. Pandolfelli, "Porous alumina-spinel ceramics for high temperature applications," *Ceram. Int.*, 37(2011), 1393–1399.
8. S. Li, N. Li, and Y. Li, "Processing and microstructure characterization of porous corundum–spinel ceramics prepared by in-situ decomposition pore forming technique," *Ceram. Int.*, 34(2008), 1241-1246.
9. A. H. De Aza et al., "Ternary system Al_2O_3–MgO–CaO: Part II, Phases relationships in the subsystem Al_2O_3– $MgAl_2O_4$–$CaAl_4O_7$," *J. Am. Ceram. Soc.*, 83(2000), 919–927.
10. R. Sarkar, A. Ghosh, and S. K. Das, "Reaction sintered magnesia rich magnesium aluminate spinel: effect of alumina reactivity," *Ceram. Int.*, 29(2003), 407–411.
11. R. E. Carter, "Mechanism of solid-state reaction between magnesium oxide and aluminum oxide and between magnesium oxide and ferric oxide," *J. Am. Ceram. Soc.*, 44(1961), 116–120.
12. J. M. Auvray, C. Gault, and M. Huger, "Evolution of elastic properties and microstructural changes versus temperature in bonding phases of alumina and alumina–magnesia refractory castables," *J. Eur. Ceram. Soc.*, 27(2007), 3489–3496.
13. Y. C. Ko and C. F. Chan, "Effect of spinel content on hot strength of alumina-spinel castables in the temperature range 1000–1500°C," *J. Eur. Ceram. Soc.*, 19(1999), 2633–2639.

Characterization of Minerals, Metals, and Materials 2015
Edited by: John S. Carpenter, Chenguang Bai, Juan Pablo Escobedo, Jiann-Yang Hwang, Shadia Ikhmayies, Bowen Li, Jian Li, Sergio Neves Monteiro, Zhiwei Peng, and Mingming Zhang
TMS (The Minerals, Metals & Materials Society), 2015

INFLUENCE OF SINTERING TEMPERATURE ON MICROSTRUCTURE AND PROPERTIES OF MAGNESIA PARTIALLY STABILIZED ZIRCONIA CERAMICS

Lan Jiang[1], Shuqiang Guo[1], Yinhe Liu[1], Yuyang Bian[1], Song Chen [1], Xingxing Zhang[1], Gonghui Yang[1], Weizhong Ding[1]

[1]Shanghai Key Laboratory of Modern Metallurgy & Materials Processing, Shanghai University, Shanghai 200072, China

Keywords: MgO-PSZ, sintering temperature, densification, phase composition

Abstract

One of the most promising refractory materials for application is zirconia in melting superalloy. In this work, the properties and phase composition of magnesia partially stabilized zirconia ceramics (MgO-PSZ) under different sintering temperatures were systematically investigated. Commercial magnesia partially stabilized zirconia (MgO-PSZ) powders were selected as the starting materials. The magnesia partially stabilized zirconia phase composition was measured by X-ray diffraction (XRD), the density of sintered samples was tested by vacuum density instrument, the thermal expansion were obtained by thermal dilatometer from ambient temperature up to 1450°C, and the microstructures of MgO-PSZ were characterised by scanning electron microscope (SEM). The results indicated that the properties of thermal expansion, densification, microstructures and phase composition were significantly affected by sintering temperature. Densification was consistent with SEM micrographs of MgO-PSZ at different sintering temperatures.

Introduction

Zirconia ceramics have excellent potential to become important materials in certain parts of superalloy melting [1]. Generally, the resistance to corrosion by high temperature melts of a ceramic material was measured by a number of properties, including good thermo-dynamic stability, low solubility in liquid alloy and good thermal shock performance. Pure zirconia has three polymorphs, which are monoclinic (m), tetragonal (t) and cubic (c) [2-4]. The addition of small amounts of Y_2O_3, MgO or CaO stabilizers to ZrO_2 made the high-temperature phases retained at room temperature [5]. Magnesia partially stabilized zirconia (MgO-PSZ) is one of these ceramics which has a number of attractive properties. However, properties of MgO-PSZ are affected by phase composition. C.G. Aneziris et al. [6] reported that zirconia materials would present high porosity levels with high amounts of

monoclinic phase (above 50 vol %), caused the worse corrosion resistance and pour mechanical strengths. According to the ZrO_2-MgO phase diagram [7], phase composition is greatly influenced by sintering temperature. It is noteworthy to point out that in the results within existing published works by diverse researchers concerning to MgO-PSZ ceramics, the properties and phase composition of magnesia partially stabilized zirconia ceramics (MgO-PSZ) are strongly relied on the experimental conditions, particularly the sintering temperature.

In this work, commercial magnesia partially stabilized zirconia (MgO-PSZ) has been selected as the starting materials. The major objective of this paper is to investigate phase composition and properties including thermal expansion and densification of ZrO_2 with additions of 3.5 wt% MgO powders.

Experimental

Powders of commercial magnesia partially stabilized zirconia (3.5wt%MgO) were selected as the starting materials. In order to form suspensions, the 3.5 wt % MgO-PSZ powders were dispersed in deionized water with organic binder and ball-milled for 4 h. The solid discs (20 mm in diameter) and bars were attained by slip casting. The technique of slip casting was affected by particle size. The mean particle size of powders is 2.56μm measured by laser particle size analyzer (Malvern Mastersizer 2000). The distribution of particle size is shown in Fig. 1. For static sintering tests, green specimens were treated at different temperatures of 1600, 1620, 1650, 1670˚C with the soaking time of 4 h.

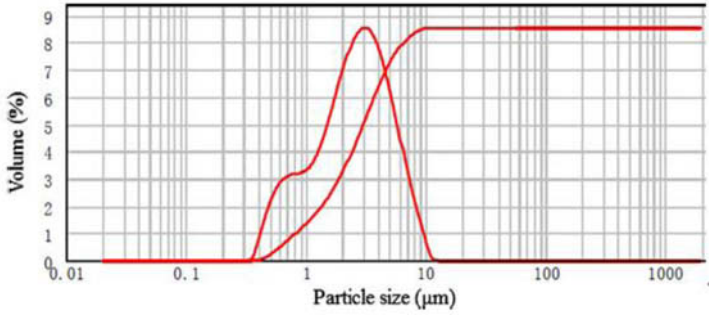

Fig1. Particle size distribution of 3.5wt%MgO–PSZ powders.

Phase identification was carried out by X-ray diffraction technique, equipped with Cu Kα monochromatic radiation. The data were collected over the 2θ range from 10° to 90°.The surface of samples as-sintered were observed by scanning electron microscope (SEM, Hitachi SU-1510) using an accelerating voltage of 15 kV after the gold coating to avoid charging during exposure to the electron beam. The density of sintered samples was tested by vacuum density instrument at room temperature. The

value of theoretical density of 3.5 wt % MgO-PSZ powders is 5.82g/cm^3. The thermal expansion were obtained by thermal dilatometer (Netzsch DIL 402C) from ambient temperature up to 1450°C.The dimension of the specimen is φ6×25 mm and the heating and cooling rate is 5°C min^{-1}.

Results and discussion

X-ray diffraction patterns of MgO-PSZ samples at different sintering temperatures are shown in Fig.2. From it shows that the m-phase is the main constituent in the unsintered sample. When sintering temperature reached 1600°C, the tetragonal and cubic phases appeared and the monoclinic reduced. It is clear that the $(101)_t$ plane belongs to the overlap diffraction of $(111)_c$ plane because they have nearly the same lattice parameters for the tetragonal and cubic phases [8].

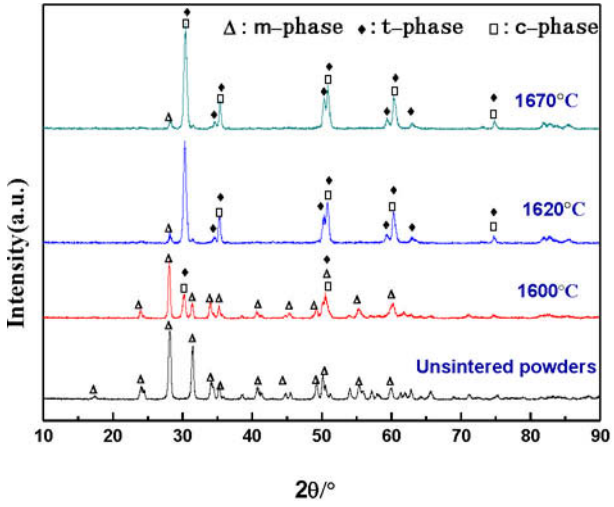

Fig2.X-ray diffraction patterns of MgO –PSZ powders sintered at different temperatures.

The relative content of monoclinic phase shown in Table I is calculated in the matrix method by using an expression [9] as

$$X_m = \frac{I_{m(11\bar{1})} + I_{m(111)}}{I_{t(101)+c(111)} + I_{m(11\bar{1})} + I_{m(111)}}$$

Where $I_{m(11\bar{1})}$, $I_{m(111)}$ and $I_{t(101)+c(111)}$ are the integrated intensities of the

corresponding peaks. With increasing sintering temperature, the amount of monoclinic phase reduced. Furthermore, the mainly phases in the as-sintered specimens are the tetragonal and cubic phases.

Table I. monoclinic phase relative content of MgO-PSZ powers sintered at different temperatures

sintering temperature(°C)	monoclinic phase relative content (%)
Unsintered powders	100
1600	56
1620	26
1650	18
1670	9

Fig.3 plots the relative density of sintered samples as a function of sintering temperature. It is indicated that relative density initially increased and then reduced with rising temperature, a maximum value is95.36% which can be obtained at 1670°C. A slightly decrease in the final density can be noticed when temperature is higher than 1670°C, which may be caused by abnormal grain growth.

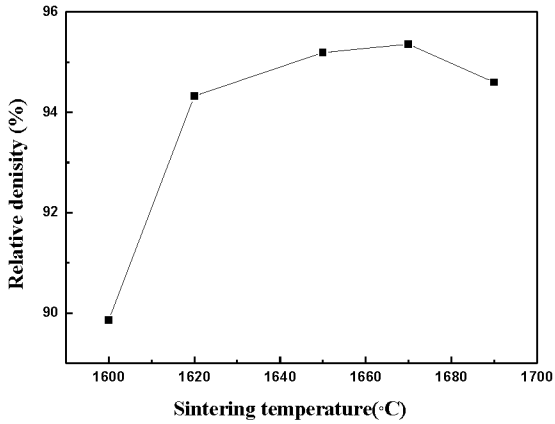

Fig3.Densification of MgO-PSZ powers sintered at different temperatures.

Actually, the fact that the densification of MgO-PSZ is affected by sintering temperature is proved by the SEM micrographs. Fig.4 shows SEM micrographs of MgO-PSZ powers sintered at different temperatures. As it can be seen the specimen still has an amount of pores at 1600°C (Fig4. 2a). The number of pores reduced as sintering temperature increased (Fig4. 2b). However, the microphotograph revealed

that when temperature reached 1690°C, the grains growth rapidly coarsening, some pores were wrapped by these grains, caused a reduction of densification(Fig4. 2d). Further, higher temperatures promote coarsening rather than further densification. Besides, a very homogeneous microstructure without agglomerates or exaggerated grain growth was obtained at 1670°C (Fig4. 2c).

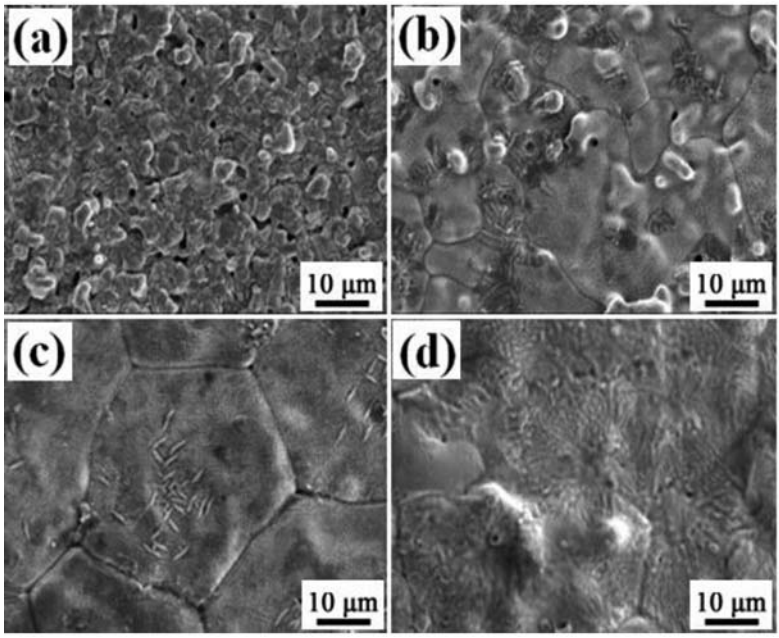

Fig4. SEM micrographs of MgO-PSZ powers sintered at different temperatures: (a) 1600°C, (b) 1650°C, (c) 1670°C, (d) 1690°C.

The thermomechanical behaviour of the microstructure at elevated temperatures depends on many factors, such as the matrix material, distributions of pores, phase transformations and heat treatments, but, the most important reason is the thermal hysteresis [6]. Materials cracking defects may be caused by thermal hysteresis, so it should be avoided. The more linear change of the thermal expansion has led to better thermal shock behavior of the samples. In Fig.5 the thermal expansions during heating up and cooling down are listed. Sample which sintered at 1600°C exhibits a remarkable thermal hysteresis. The thermal expansions present a linear change with increasing sintering temperatures. Moreover, the value of the thermal expansion of sample sintered at 1670°C is higher than that is sintered at 1650°C.

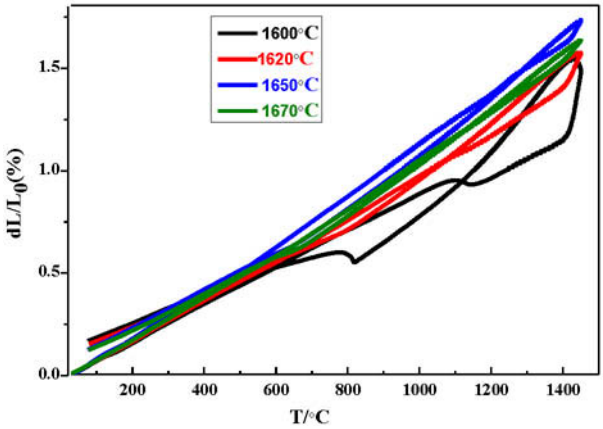

Fig5. Thermal expansion of MgO-PSZ sintered at different temperatures up to 1450°C.

Conclusion

By the research of influence of sintering temperature on microstructure and properties of magnesia partially stabilized zirconia (3.5wt%MgO-PSZ) ceramics, the following conclusions can be obtained:

(1)The properties of thermal expansion, densification, microstructures and phase composition were significantly influenced by sintering temperature.

(2) With increasing sintering temperature, the amount of monoclinic phase decreased, the properties of thermal expansion presented a linear change and the densification increased in the initial stage and then reduced.

(3) The densification of MgO-PSZ is affected by sintering temperature is proved by the SEM micrographs.

References

1. Alok Choudhury, "State of the Art of Superalloy Production for Aerospace and Other Application Using VIM/VAR or VIM/ESR," *ISIJ International*, 32 (1992) 563-574.
2. R.H. French, S.J. Glass, F.S. Ohuchi, Y.-N. Xu and W.Y. Ching, "Experimental and theoretical determination of the electronic structure and optical properties of three phases of ZrO_2," *Physical Review B (Condensed Matter)*, 49 (1994)

5133-5142.

3. R. H. J. Hannink, P. M. Kelly and B.C. Muddle, "Transformation toughening in zirconia-containing ceramics,"*Journal of the American Ceramic Society*, 83 (2004) 461-487.
4. B.Basu, J.Vleugels and O.Van Der Biest, "Transformation behaviour of tetragonal zirconia: role of dopant content and distribution," *Materials Science and Engineering: A*, 66 (2004) 338-347.
5. F.Abe, S.Muneki and K.Yagi, "Tetragonal to monoclinic transformation and microstructural evolution in ZrO_2–9.7 mol% MgO during cyclic heating and cooling,"*Journal of Materials Science*, 32 (1997) 513-522.
6. C.G. Aneziris *, E.M. Pfa. And H.R. Maier, "Fine grained Mg-PSZ ceramics with titania and alumina or spinel," *Journal of the European Ceramic Society*, 20 (2000) 1729-1737.
7. C.G. Aneziris *, E.M. Pfa. And H.R. Maier, "Corrosion mechanisms of low porosity ZrO2 based materials during near net shape steel casting," *Journal of the European Ceramic Society*, 20 (2000) 159-168.
8. C.J. Howard, R.J. Hill and B.E. Reichert, "Structures of ZrO_2 polymorphs at room temperature by high-resolution neutron powder diffraction," *Acta Crystallographica Section B*, 4 (1988) 116-120.
9. An Shengli, Wu Weijiang and Liu Qingguo, "The Phase ratio qualititative analysis for MgO paptially stabilized zirconia," *China's Refractories*, 4(1990) 48-51.

Characterization of Minerals, Metals, and Materials 2015
Edited by: John S. Carpenter, Chenguang Bai, Juan Pablo Escobedo, Jiann-Yang Hwang, Shadia Ikhmayies, Bowen Li, Jian Li, Sergio Neves Monteiro, Zhiwei Peng, and Mingming Zhang
TMS (The Minerals, Metals & Materials Society), 2015

EVALUATION OF STRUCTURAL CLAY BRICK MASONRY UNITS BY WEIBULL ANALYSIS AND BRAZILIAN CODE AND SPECIFICATIONS

Azeredo, N. G.[1]; Alexandre, J.[2]; Azevedo, A.R.G.[2]; Xavier, C.G.[2]; Monteiro, S.N. [3]; Zanelato, E. B.[2]; Oliveira, R. P.[2].
[1]UENF - State University of the Northern Rio de Janeiro, LECIV – Civil Engineering Laboratory; Av. Alberto Lamego, 2000, Campos dos Goytacazes, Rio de Janeiro, 28013-602, Brazil and IFF – Instituto Federal Fluminense, Rua Dr. Siqueira, 273 – Parque Dom Bosco – Campos dos Goytacazes , Rio de Janeiro, 28030-130, Brazil.
[2]UENF - State University of the Northern Rio de Janeiro, LECIV – Civil Engineering Laboratory; Av. Alberto Lamego, 2000, Campos dos Goytacazes, Rio de Janeiro, 28013-602, Brazil.
[3]IME – Military Institute of Engineering, Department of Materials Science, Praça General Tibúrcio, 80, Rio de Janeiro, Rio de Janeiro, 22290-270, Brazil.

Keywords: Weibull Frequence Distribution Model, characteristic compressive strength, heat treatment.

Abstract

This work dealt with the evaluation of engineering structural clay brick samples that were sintered at estimated temperatures of 700 and 800°C. They were collected in a red-brick plant in Campos dos Goytacazes, RJ, Brazil. From a lot, a sample already sintered in its kiln at 700°C were collected and also a sample from the same lot only dried by the air, which were then sintered at 800°C controlled temperature. The samples were subjected to Brazilian Standard tests (ABNT NBR 15270:2005) to determine their geometric, physical and mechanical properties. In order to be classified as structural clay brick it is required minimum 3.0 MPa for the characteristic compressive strength (f_{bk}) to be suitable for up to five floors structural building applications. We also used the Weibull Probability Plot and Weibull Maximum Likelihood Estimation to evaluate distribution parameters in order to compare the results of compressive strength obtained in the tests.

Introduction

One of the economic activities around Campos dos Goytacazes, Rio de Janeiro State, Brazil, is the production of red-ceramic artifacts. The municipality of Campos, for short, covering an area over four thousand km² with a population over 450 thousand inhabitants [11] has — according to information from Sindicato dos Ceramistas de Campos (Campos Red-ceramic Union) — 112 associated companies, whose productions go around artifacts such as solid clay bricks, usual sealing clay bricks, engineering structural clay bricks, red-ceramic tiles, red-ceramic blocks for precast slabs, among others.

The raw material—natural clay—which is abundant in the nature and besides that has a reduced cost , is used in red-ceramic products manufacturing process. However, it presents a wide variability in terms of chemical, physical and mineralogical composition. The red-ceramic products properties are extremely dependent on the ceramic masses composition and on the processing conditions employed in manufacturing them. In particular, the sintering temperature is a parameter which plays a great influence on the final mechanical properties. During the sintering process a set of very complex physical and chemical reactions takes place within the ceramic mass as the temperature is being raised. These reactions promote new ceramic phase's formations, which are decisive for final product physical-mechanical properties [16]. This work dealt with the evaluation of engineering structural clay brick

samples that were burnt at estimated temperatures of 700 and 800°C in order to compare specially the results of simple compressive strength obtained by the tests.

The Weibull Frequency Distribution Model (WFDM) is generally applied in several engineering problems such as the determination of the operational life and mechanical strength of industrial components. Its flexible formulation permits to emulate the majority of other frequency models. Indeed, the WFDM is often used to characterize brittle materials like ceramics, which may present defects that act as stress concentrators' elements [9]. Usually the defects show a random distribution, conducting the mechanical strength evaluated by testing to present dispersion. The mechanical strength mean value is not sufficient to represent experimentally the ceramic product mechanical strength, it is essential to take into account the dispersion results. The WFDM may provide quantitatively this mechanical strength values dispersion. For instance, the Weibull modulus (β) provides an indication of the product mechanical strength, once the higher β indicates lower mechanical strength dispersion and consequently more homogeneity of the ceramic product.

In 2003 a document was drawn up with the objective of establishing the criteria and requirements for constructing three to five floors residential buildings structure when it is composed mainly of structural masonry in projects financed by Caixa Econômica Federal (CEF) — the main Brazilian agent for the Federal Government public policies [13]. The Federal Government social program for housing (Minha Casa Minha Vida) promoted an increase in red-ceramic products; in particular the structural clay bricks used in structural masonry construction system. In order to be accepted as structural clay brick its f_{ck} must present at least 3.0 MPa referred to the clay brick's gross area.

The objective of the present work was to evaluate, by means of the WFDM and according to recommendations of the Brazilian technical norms ABNT NBR 15270:2005, structural clay bricks samples with nominal dimensions of 11.5 x 19.0 x 39.0 cm (width, height, length) for building applications. Clay ceramic bodies were fabricated with addition of waste from broken ceramic pieces generated in the industry. The samples were subjected to standard tests to evaluate geometrical characteristics as well as physical and mechanical properties [2, 3, 4, 5, 6, 7, 8].

The Brazilian standard recommends specific formulations to estimate the f_{bk} of structural clay bricks. So the results obtained from the Brazilian norm [8] and the corresponding parameters obtained from the Weibull Probability Plot and Weibull Maximum Likelihood Estimation was compared.

Weilbull Frequency Distribution Model

The Weibull probability density function is defined as [10]:

$$f(x) = \frac{\beta\,(x-\delta)^{\beta-1}}{\theta^{\beta}}\, e^{\left[-\left(\frac{x-\delta}{\theta}\right)^{\beta}\right]} \qquad 1$$

where:

β is the shape parameter also known as the Weibull Modulus;

θ is the scale parameter;

δ is the localization parameter.

In the present work, the location parameter was considered null, since $\delta \neq 0$ drastically alters the values of β and θ. In fact, the location parameter refers to an initial constant value, which is recommended to be $\delta=0$ for the present analysis.

The Weibull distribution average and variance are defined by expressions on [14]. The Reliability function describes the probability to survive with time, or the probability of rupture as function of stress. This Reliability function is defined by expression on [14]. The Hazard function is associated with the instantaneous rate of rupture and can be used to characterize fractured structures. This function is defined by expression on [14]. Several methods may be applied to

estimate the Weibull parameters: Probability Plot, Hazard Plot, Maximum Likelihood Estimation (MLE), Modified Moment Estimation (MME) and Bayesian Estimation. In the present work both the Probability Plot and the Maximum Likelihood Estimation (MLE) were used as estimator for the parameters composing the Weibull analysis.

The Rank Distribution is based on the determination of estimators $F(x_1)$, $F(x_2)$,..., $F(x_n)$ from an ordinate sequence of data: x_1, x_2, ..., x_n, corresponding to n samples with a cumulative distribution function F(x), with x as continuous. To estimate the value of $F(x_n)$ in the present work, the Mean Rank was adopted and defined by expression on [10].

The Central Limit Theorem predicts that the larger the investigated number of samples, the more normal will be the distribution. In the present work 13 samples were considered for each heat treatment. This is the minimum number recommended by the Brazilian Standard ABNT NBR 15270:2005 for simple compressive strength tests.

One of the methods used to determine the confidence interval of β is that of the Maximum Likelihood Estimation (MLE) which will be applied in the present work. The value of β is estimated by solving the equation on [17, 18]. Where K is the $[100(1 - \alpha/2)]^{th}$ normal percent for $100(1 - \alpha)$ as the percent limit. In the present investigation, for a limit of 95%, K is equal to the 97.5^{th} normal percent, which is equivalent to 1.96.

The Maximum Likelihood Estimation (MLE) estimates the value of θ by means of the expression on [17, 18]. The present work considers the Location Parameter with zero value; $\delta = 0$, according to Dodson recommendation [14]. In this respect will be applied an academic software to implement the Maximum Likelihood Estimation (MLE) as well as the Probability Plot.

Structural Clay Bricks Compressive Strength

The Brazilian standard instead of requiring the sample simple compressive strength mean value it requires the sample structural clay brick characteristic simple compressive strength, which is calculated by formulations found on page 7-8 [8]. The minimum value required, as mentioned before, is $f_{bk} = 3.0$ MPa referred to the gross area to be classified as structural clay brick suitable for structural building applications.

Materials and Methods

The raw material used in a red-ceramic industry passed through characterization tests and hollow structural clay bricks manufactured with it passed through technological tests [2, 3, 4, 5, 6, 7, 8]. The raw material used for manufacturing the structural clay bricks was taken directly from the mat that forwards to the extruder, where the bricks take the final shape. It is noteworthy that the manufacture of such structural clay bricks is given by extrusion using a mouthpiece with the required final shape.

The industrial clayey mass collected was air dried and divided following the Brazilian standards, then was crushed in a porcelain mortar and classified by sieving for the fraction <40 mesh (0.425 mm = 425 μm). The raw material physical characteristics were estimated by the particle size distribution determined through sieving and sedimentation combination process [4, 7]. The Atterberg limits — Liquid Limit (LL) and Plasticity Limit (PL) — were determined in advance in order to estimate the Plasticity Index (PI) [3, 5]. The Real Specific Gravity of the grains was estimated by using picnometers, following the Brazilian standard requirements [6]. The structural clay bricks were collected in a red-brick plant in Campos dos Goytacazes, RJ, Brazil (Figure 1).

Figure 1: Geometric shape of the hollow structural clay brick.

From a lot were collected a sample containing 20 clay bricks already burnt in its furnace at an estimated temperature of 700°C and also a sample containing 20 clay bricks from the same lot only dried by the air, which were then taken to the laboratory and burnt in a controlled muffle furnace at an estimated 800°C, although the minimum required are 13 structural clay bricks for compressive strength testing.

We also used the Weibull Probability Plot and Weibull Maximum Likelihood Estimation to estimate parameters distribution in order to compare the results of compressive strength obtained throughout the tests.

Results

The results for the characterization of the raw material used in manufacturing structural clay bricks and the technological tests results of the bricks sample are presented below and some comments are made.

Raw material tests results

The raw material sample collected was taken to the laboratory and submitted to drying process, lump breaking, four parts division and homogenization in order to be subjected to physical characterization. The particle size analysis was performed, which deals with the process to quantify the amount of soil fraction between predetermined diameters and express them as a relative percentage to the total sample. This test was done by wet sieving and sedimentation following the normative precepts [4, 7].

The results obtained for characterizing the particle size of the raw material constitutive of the structural clay bricks are presented as percentages of the fractions of sand, silt and clay. It is considered clay fraction of a natural raw material the fraction which the particle size dimension is below 0.002 mm [15]. Table I shows the estimated particle size of the natural raw material tested.

Table I - Particle size characteristics.

Grains Diameter (mm) - ABNT NBR 6502:1995 – Rocks and Soils [2]							
CLAY	SILT	SAND			SANDSTONE		
		Fine	Medium	Coarse	Fine	Medium	Coarse
< 0.002	0.002 to 0.06	0.06 to 0.2	0.2 to 0.6	0.6 to 2	2 to 6	6 to 20	20 to 60

Particle size characteristics							
SANDSTONE			SAND			SILT	CLAY
Coarse	Medium	Fine	Coarse	Medium	Fine		
-	-	-	1.10%	3.40%	8.10%	35.50%	51.80%

The raw material is classified as a bit sandy silty clay (51.8% clay fraction, 35.50% silt fraction, 8.10% fine sand fraction, 3.40% medium sand fraction and 1.10% fraction coarse sand) [4]. Observing the raw material particle size distribution studied in this work and considering several similar results obtained in the region of Campos for manufacturing red-ceramic artifacts (30% ≤ clay fraction ≤ 70%) we are able to estimate that the clay mass is suitable for the red-ceramic industries in general [1, 15, 16]. The determination of the grains real specific gravity, also called grains real density was made according to the Brazilian standard requirement [6]. The raw material classified by sieving for the fraction < 40 mesh (ABNT, 0.425 mm) was used in order to determinate the Atterberg Limits. Assays were done to determine the Liquid Limit and Plasticity Limit, thus producing the Plasticity Index [3, 5].

Table II shows the mean values of five determinations of Atterberg Limits and Real Grains Specific Gravity.

Table II - Atterberg Limits and Real Specific Gravity of the Grains

Atterberg Limits			Grains Specific Gravity (g/cm^3)
Liquid Limit	Plasticity Limit	Plasticity Index	
59.8%	32.9%	27.0%	2.69

The classification of the raw material by the Unified Soil Classification System (USCS) is that it is a little sandy, high plasticity silty clay (CH) once its Liquid Limit is over 50%. The raw material has Atterberg limits within the range of values of kaolinitic raw material used by the red-ceramic plants on the region of Campos. The Grains Real Specific Gravity of the raw material studied is within the range of values of the ones on the region under study. The values found for the physical characteristics reveal themselves similar to those found by other researchers, showing the typical dominant clays for the region, which are used as raw materials for manufacturing several red-ceramic artifacts [1, 12, 15, 16].

Results for the structural clay bricks samples tests

By definition, the structural clay bricks samples are taken randomly in a set from a batch to determine its geometric, physical, or mechanical properties. In this work 20 structural clay bricks were collected to be analyzed, however, the Brazilian standard recommends that the minimum number required is normally 13 for simple compression testing and six for water absorption 24h testing [8].

The dimensional test is an important step before the simple compression test, once there are codes and specification requirements for all dimensions of the structural clay bricks. They should have a prismatic shape and the gross areas must be measured (Width x Length), which correspond to the sections of the areas bounded by the edges of the structural clay bricks. Thus the hollows are not taken into account. Besides, both external and internal septa must be within normative requirements with minimum 8.0 mm and 7.0 mm averages respectively, with tolerance of ± 3 mm. It is noteworthy that the structural clay bricks are seated with hollows upright, as shown on Figure 1.

On Table III it can be observed the dimensions mean values, the gross areas, the Ultimate Loadbearing and the Ultimate Tensile Strength for the structural clay bricks burnt at 700 and 800ºC.

Table III – Dimensions (width, height, length), gross areas, Ultimate Loadbearing and Ultimate Tensile Strength.

Structural clay bricks 700ºC (13units)	Dimension (mm)			Gross Area (m^2)	Ultimate Loadbearing (kN)	Ultimate Tensile (MPa)
	Width	Heigth	Length			
Mean values	114.8	183.8	394.8	0.05	135.7	3.0
Standard deviation	1.48	1.48	1.48	0.000724	38.90	0.89
Coeff. Var. (CV)%	1.29	0.81	0.37	1.60	28.67	29.63
Structural clay bricks 800ºC (13units)	Dimension (mm)			Gross Area (m^2)	Ultimate Loadbearing (kN)	Ultimate Tensile (MPa)
	Width	Heigth	Length			
Mean values	117.2	183.8	397.9	0.05	183.42	4.0
Standard deviation	1.36	2.23	2.56	0.000782	32.35	0.69
Coeff. Var. (CV)%	1.16	1.21	0.64	1.68	17.64	17.65

To be considered as structural clay brick its characteristic compressive strength should be at least 3.0 MPa referred to the clay brick's gross area. The coefficient of variation (CV) in measuring width, length and height was at most 1.29% for the ones burnt at 700ºC and 1.16% for the ones burnt at 800ºC, which indicates a dimensional uniformity. Both external and internal septa came to be within normative requirements, which fits the tolerance related to the effective dimensions average mentioned before. Regarding compression test, the study estimates f_{bk} = 1.64 MPa for the clay bricks burnt at 700ºC on the red-brick plan kiln and f_{bk} = 3.03 MPa for the ones burnt at 800ºC at the muffle furnace. For compressive strength it is required CV ≤ 20% [13]. It is observed that only the clay bricks burnt at 800ºC fits the requirement.

Weibull Probability Plot and Weibull Maximum Likelihood Estimation of Weibull Parameters

The Weibull Probability Plot and Weibull Maximum Likelihood Estimation analysis were applied on the compressive strength results obtained on both sintering temperatures in order to estimate de Weibull Parameters, which are presented on Table IV and V for the samples sintered at 700 and 800ºC respectively.

Table IV: Weibull Probability Plot and Weibull Maximum Likelihood Estimation of Weibull Parameters. Localization parameter δ=0, confidence level 95% , sample sintered at 700ºC.

Structural clay brick sample sintered at 700ºC	Weibull Probability Plot	Weibull Maximum Likelihood Estimation	Lower 95% Confidence Limit	Upper 95% Confidence Limit
Weibull Modulus, shape parameter (β)	4.098	4.196	2.970	5.928
Characteristic simple compressive strength, scale parameter (θ)	3.2 MPa	-	2.83 MPa	3.56 MPa
Mean value	2.89 MPa	2.89 MPa	-	-
Standard Deviation (SD)	0.7932 MPa	0.7755 MPa	-	-
R^2 (R-Squared)	0.9019	-	-	-

Table V: Weibull Probability Plot and Weibull Maximum Likelihood Estimation of Weibull Parameters. Localization parameter δ=0, confidence level 95% , sample sintered at 800ºC.

Structural clay brick sample sintered at 800ºC	Weibull Probability Plot	Weibull Maximum Likelihood Estimation	Lower 95% Confidence Limit	Upper 95% Confidence Limit
Weibull Modulus, shape parameter (β)	6.233	6.377	4.508	9.021
Characteristic simple compressive strength, scale parameter (θ)	4.22 MPa	-	3.91 MPa	4.55 MPa
Mean value	3.93 MPa	3.93 MPa	-	-
Standard Deviation (SD)	0.7345 MPa	0.7194 MPa	-	-
R^2 (R-Squared)	0.9368	-	-	-

Conclusions

The results show that the raw material is a little sandy, high plasticity silty clay (CH) according to USCS. The raw material has Atterberg limits within the range of values of kaolinitic raw material used by the red-ceramic plants on the region of Campos dos Goytacazes, RJ, Brazil. The values found for the physical characteristics reveal themselves similar to those found by other researchers, showing the typical dominant clays for the region, which are used as raw materials for manufacturing several red-ceramic artifacts.

Regarding simple compression test, the study estimates a characteristic strength f_{bk} = 1.64 MPa for the sample of clay bricks sintered at estimated temperature of 700ºC on the red-ceramic industry plant. This value is below the minimum 3.0 MPa required, so the sample can't be classified as structural. The sample of clay bricks sintered at estimated 800ºC controlled temperature on muffle furnace presented f_{bk} = 3.03 MPa, which fits the Brazilian standard requirements.

Structural clay brick sample sintered at 700ºC presented a mean value of 2.89 MPa by Weibull Probability Plot and Weibull Maximum Likelihood Estimation. The Weibull Modulus by both Estimation was almost the same value, β = 4.1. The Weibull Probability Plot Estimation presented: R^2 = 0.9019; SD=0.7932 MPa; f_{bk} = 3.20 MPa. The Weibull Maximum Likelihood Estimation presented a Lower 95% Confidence Limit of 2.83 MPa and Upper 95% Confidence Limit of 3.56 MPa.

Structural clay brick sample sintered at 800ºC presented a mean value of 3.93 Mpa by Weibull Probability Plot and Weibull Maximum Likelihood Estimation. The Weibull Modulus by both Estimation was almost the same value, β = 6.2 . The Weibull Probability Plot Estimation presented: R^2 = 0.9368; SD=0,7345 MPa; f_{bk} = 4.22 MPa. The Weibull Maximum Likelihood Estimation presented a Lower 95% Confidence Limit of 3.91 MPa and Upper 95% Confidence Limit of 4.55 MPa.

Taking into account that the raw material is classified as suitable for manufacturing red-ceramic artifacts and commonly used by the region red-ceramic industries, the differences observed were due to heat treatment differential. The heat treatment at controlled temperature indicates that the structural clay bricks may achieve the standard level requirements. The characteristic compressive strength found by the Brazilian standard formulation and the Lower 95% Confidence Limit found by Weibull Maximum Likelihood Estimation keep a difference of approximately 29%, although both demonstrate the compliance of structural clay bricks sintered at 800ºC. On the other hand, the structural clay bricks sintered at 700ºC on the red-brick plant kiln presented f_{bk} value under the minimum required by the Brazilian standard using its formulation and the Weibull analysis. A difference of approximately 72% between the two approaches. The β for the structural clay bricks sintered at 800ºC higher than the β for the structural clay bricks sintered at 700ºC indicates lower dispersion values for mechanical strength and more homogeneity achieved by the 800ºC heat treatment. The study indicates that the heat treatment should be at least 800ºC, for manufacturing structural clay bricks suitable for building constructions applications up to five floors with better quality, which means $f_{bk} \geq 3.0$ MPa. Besides, for compressive strength it is required CV $\leq$ 20%, which only the structural clay bricks burnt at 800ºC show Brazilian Code and Specifications requirement.

References

[1] ALEXANDRE, J. Analysis of the raw materials and composition of a clay body used in red ceramics (in Portuguese). Thesis (Doctor), State University of the Northern Rio de Janeiro – UENF. Campos dos Goytacazes, RJ, Brazil. 174 pp. (2000).

[2] Brazilian Association for Technical Norms – ABNT. NBR 6502:1995. Rocks and Soils. (in Portuguese), Rio de Janeiro, RJ, Brazil. (1995).

[3] Brazilian Association for Technical Norms – ABNT. NBR 7180:1984. Soil –

determination of the plasticity limit in soils (in Portuguese). Rio de Janeiro, RJ, Brazil, corrected version, (1988).
[4] Brazilian Association for Technical Norms – ABNT. NBR 7181:1984. Soil – particle size analysis of soils, performed by sieving or by a combination of sieving and sedimentation (in Portuguese). Rio de Janeiro, RJ, Brazil, (1984).
[5] Brazilian Association for Technical Norms – ABNT. NBR 6459:1984. Soil – method for determining the liquidity limits soil (in Portuguese): NBR 6.459. Rio de Janeiro, R j, Brazil, (1984).
[6] Brazilian Association for Technical Norms – ABNT. NBR 6508:1984. Soil – method of determining the specific gravity of soil grains passing through the sieve of 4.8 mm (in Portuguese), Rio de Janeiro, RJ, Brazil, (1984).
[7] Brazilian Association for Technical Norms – ABNT. NBR 6457:1986. Preparation for compaction tests and characterization tests (in Portuguese): NBR 6457. Rio de Janeiro, R j, Brazil , (1986).
[8] Brazilian Association for Technical Norms – ABNT. NBR 15270:2005. Ceramic Components (in Portuguese). Rio de Janeiro, RJ, Brazil, (2005).
[9] ASKELAND, D.R; PHULÉ, P.P. The Science and Engineering of Materials, 5th ed., Thompson Engineering, (2005).
[10] KAPUR, K.C. ; LAMBERSON, L. R. Reliability in Engineering Design. John Wiley & Sons, (1977).
[11] Instituto Brasileiro de Geografia e Estatística (IBGE) – CENSO 2010 (in Portuguese). In: <http://www.ibge.gov.br/>. (2010).
[12] MILLER, C. P. Determination of mechanical parameters and numerical modeling in structural masonry ceramic blocks of Campos dos Goytacazes industry (in Portuguese). Thesis (Master), Civil Engineering. State University of the Northern Rio de Janeiro – UENF. Campos dos Goytacazes, Rio de Janeiro, RJ, Brazil. 161p. (2008).
[13] SABBATINI, F. H. Structural Masonry: materials, structure and implementation of technological control (in Portuguese). Caixa Econômica Federal (CEF).36 p. (2003).
[14] DODSON, B. The Weibull Analysis Handbook, 2nd ed., ASQ Quality Press, (2006).
[15] PEDROTI, L. G. Study conformities in relation to ABNT pressed and fired clay blocks (in Portuguese). Thesis (Master), Civil Engineering. 97 p. (2007).
[16] XAVIER, G. C. Strength, durability and changeability of red ceramic incorporated with granite waste (in Portuguese). Thesis (Master) Civil Engineering. State University of the Northern Rio de Janeiro – UENF. Campos dos Goytacazes, Rio de Janeiro, RJ, Brazil. 202 p. (2006).
[17] PRABHAKAR, D.N.; XIE, M.; JIAN, R.Weibull Models (Wiley Series in Probability and Statistics), Wiley Interscience, (2003).
[18] ABERNETHY, R. The New Weibull Handbook: 5th Edition, Reliability and Statistical Analysis for Predicting Life, Safety, Risk, Cost and Warrant Claims. Robert Abernethy Editor, (2006).

Characterization of Minerals, Metals, and Materials 2015
Edited by: John S. Carpenter, Chenguang Bai, Juan Pablo Escobedo, Jiann-Yang Hwang, Shadia Ikhmayies, Bowen Li, Jian Li, Sergio Neves Monteiro, Zhiwei Peng, and Mingming Zhang
TMS (The Minerals, Metals & Materials Society), 2015

BRAZILIAN BENTONITE SUBMITTED TO MILD ACID TREATMENT UNDER MODERATED CONDITIONS

C.G. Bastos Andrade[1*]; V.F. Justo[1]; D.M. Fermino[1]; M.G.S. Valenzuela[1]; C. Volzone[2]; F.R. Valenzuela-Diaz[1]

[1]Laboratory of Non Metalic Materials Pérsio de Souza Santos
Department of Metallurgical and Materials Engineering – Universidade de São Paulo
Zip Code 05508-900 – São Paulo - SP - Brazil
[2] CETMIC Centro de Tecnología de Recursos Minerales y Cerámica, Argentina

**gianesic@usp.br*

Keywords: clays, acid attack, nanocomposites, bentonite

ABSTRACT

The present paper presents the study of light green smectite clay, from Paraiba, Brazil, submitted to mild acid attack under moderated conditions. Usually, clays are subjected to treatment with strong inorganic acids at temperatures near the boiling point and at high acid concentrations and then, widely used as bleaching agents. The treatment occurred under bellow boiling temperature and at short times of reaction (90°C, reaction times of 1, 6, 12, 18 and 24 hours in close reactor, concentration of the aqueous solution of hydrochloric acid 1.5 M, clay/acid solution ratio of 1g/10mL). The purpose of these attacks is to reduce the concentration of impurities providing color, with minimal change in the clay minerals structure, aiming at use in products of high value such as cosmetics and polymer/clay nanocomposites. The raw clay and the attacked samples were characterized by X-ray diffraction (XRD), cation exchange capacity (CEC), stereomicroscopy, scanning electron microscopy (SEM) and energy dispersive X-ray detector (EDS).

1 INTRODUCTION

The industrial application of bentonites is vast, mostly used in oil industry as drilling fluids, in pharmaceutic and cosmetics as dissecant, in the food industry as oil bleaching, among others applications. For those aplications, bentonites needs to be clean of mineral impurities. Acid attack is a common method that provides a specific area increased by structure

disorganization, mesopores and mineral impurities cleaning. Other benefit of acid attack is improving of acid sites with more porosity, excellent properties when apply in catalysis [1-6]. Several groups have studied the clays preparation using acid attack with high concentration aiming to obtain bleaching, producing a clear color clay, or similar, mostly used in bleaching process or oil, grease and organic, minerals and animals fat. The industrial use for clays is also based on exchangeable cations and clay minerals properties [7-9].

Geologic origin of clays determinates a classification as bentonites, however, there is a common agreement that if the smectite clays presents the same properties of traditional bentonites and/or is commercialized to the same use, those clays can be classified as bentonites, which have a high grade of colloidal material, absolving capacity and activation capacity [10-13].

Among the bentonites for industrial use there are bentonites with highly water absorvation and non-water absorvation. The sodium interlayer is responsible for the capacity of bentonites absorvation instead those not, have calcium as a preponderate cation [14,15].

The polycathionic bentonite from Paraiba, Brazil is smectite clay with non-preponderate interlayer cation with light color providing by low iron concentration [16].

The light green smectite within methodologies for the production of bleaching clays may be a good alternative to material raw. The economic advantages over imported clays used in processes to obtain products with high value as cosmetics and nanocomposites.

2 MATERIALS AND METHODS

Start Materials

The light green smectite clay, in its natural form, was from Paraíba´s State, Brazil was submitted to mild acid attack using a concentration of the aqueous solution of hydrochloric acid 1.5 M, clay/acid solution ratio of 1g/10mL, at 90°C under bellow boiling temperature and at short times of reaction 1, 6, 12, 18 and 24 hours in close reactor.

The attacked clay was washed, by filtration, with distilled water until pH 7-8, and then subjected to drying at 60°C for 24 hours.

After drying, the clay was grounded using a manual mortar and vibratory ball mill until completely pass through #200 mesh sieve.

Materials Characterization

The raw clay and the attacked samples were characterized by X-ray diffraction (XRD), cation exchange capacity (CEC), stereomicroscopy, energy dispersive X-ray detector (EDS) and scanning electron microscopy (SEM).

The XRD were performed on diffractometer model X'Pert Pro MPD (Panalytical) with Cu anodes; scan from 5° to 90° 2Θ; 40kV and 35mA.

The scanning electron microscopy (SEM) and energy dispersive X-ray detector (EDS) was performed on scanning electron microscopy, Philips - EDAX INSPECT 50 with energy dispersive x-ray detector (EDS).

To observe the clay was used a stereomicroscopy Zeiss, model Stemi 2000C.

CEC was performed using the ammonium acetate method.

3 RESULTS AND DISCUSSION

Figure 1 shows the X-ray diffraction curves of light green smectite submitted only to H_2O for 24h at 90°C, we observe that the $d_{(001)}$ characteristic smectitic peak at 15,05Å with intensity of 120 counts. As impurity the sample presents quartz with a peak at 3,3Å and an intensity of 255 counts.

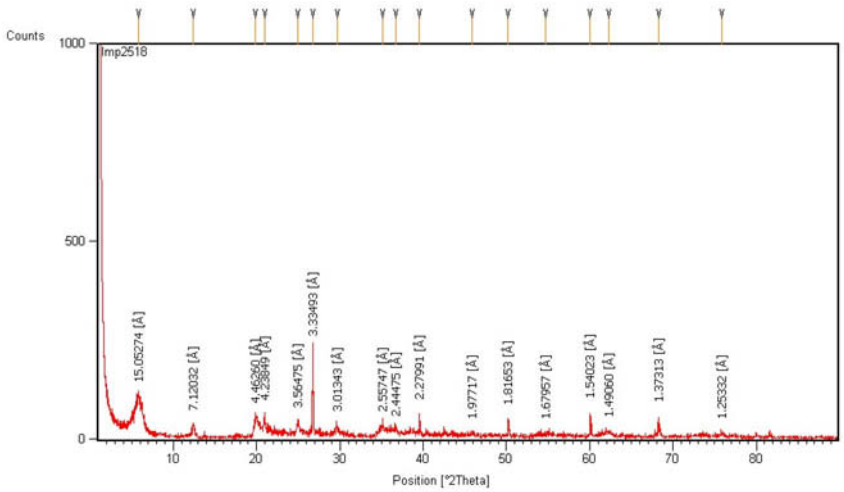

Figure 1. X-ray diffraction curve of Light green smectite, H_2O 24h at 90°C.

Figure 2 shows the XRD curve of Light green smectite submitted to mild acid attack during 24h at 90°C. The $d_{(001)}$ smectitic peak is present at 15,62Å with an intensity of 100 counts. The quartz, with peak at 3,33Å presents intensity of 340 counts.

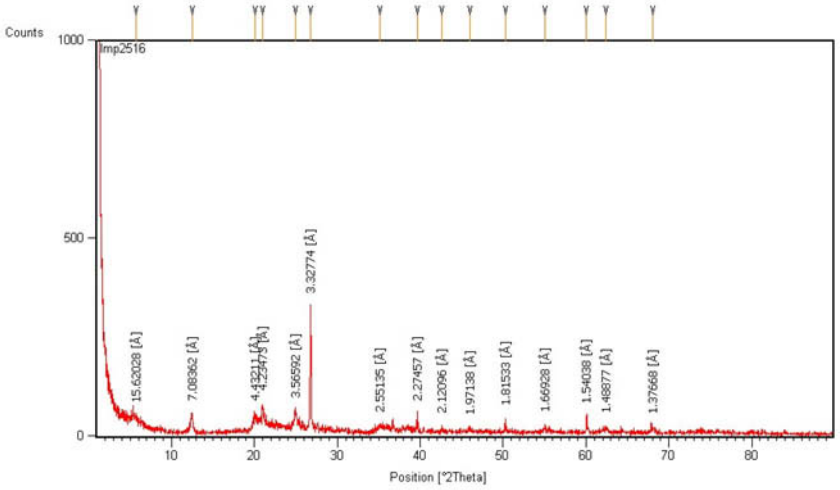

Figure 2 – X-ray diffraction curve of the Light green smectite, HCl 24h at 90°C.

Table I presents the interplanar distance of the $d_{(001)}$ smectite peaks for the samples attacked at different times and its intensities. The table shows also the intensities of the quartz peaks at 3,33Å.

Table 1. $d_{(001)}$ smectitic peaks, smectitic peaks intensities, and intensities of the quartz peaks for the samples of Light green bentonite attacked for different times.

Sample	Smectitic peak $d_{(001)}$ (Å)	Smectitic peak intensity (counts)	Quartz peak at 3,33 Å intensity (counts)
24h in water	15,05	150	255
1h attack	14,53	100	290
6h attack	15,14	90	590
12h attack	15,38	80	250
18h attack	15,31	70	300
24h attack	15,62	100	340

The intensity of the smectitic $d_{(001)}$ peak tend to diminish its intensity with the time of attack as the acid have more time to destroy the octahedral sheet of the clay mineral. The increase of the quartz peak with the time of acid attack is a possible indicative of the dissolution of part

of the clay minerals. It was verified that the clays submitted to mild acid attack during long times presented more bleaching than others.

The figures 3 and 4 presents the EDS results for samples treated with water for 24h and HCl for 24h at 90°C. Is possible to observe the peak reduction of metals, that indicates a good result of purification at sample treated with HCl for 24h.

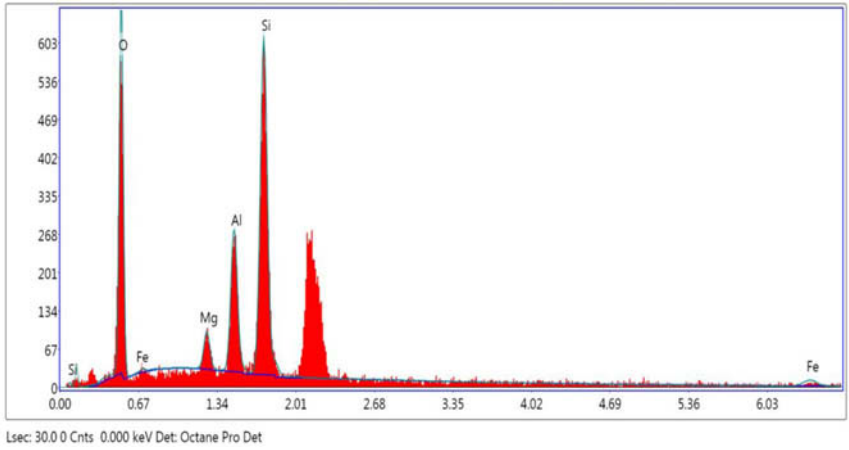

Figure 3 – EDS results of light green smectite treated with H_2O for 24h

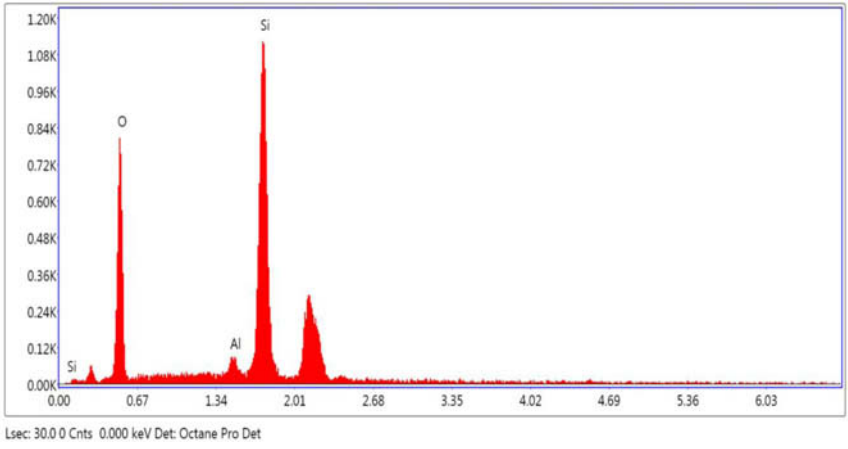

Figure 4 – EDS results of light green smectite treated with HCl for 24h

Table 2 presents the CEC values, that tends to diminish after treatment, with the time of attack with the 24 hours attacked sample having only 70% of the original value.

Table 2 - CEC results of light green smectite treated.

Sample	CEC (meq/100g)	% of the no attacked sample
24h in water	41,30	100
1h attack	38,29	92,72
6h attack	37,63	91,11
12h attack	33,27	80,55
18h attack	31,33	75,86
24h attack	28,99	70,20

At the stereomicroscopy image 1 is possible observe the impurity particles into the sample treated with water for 24h.

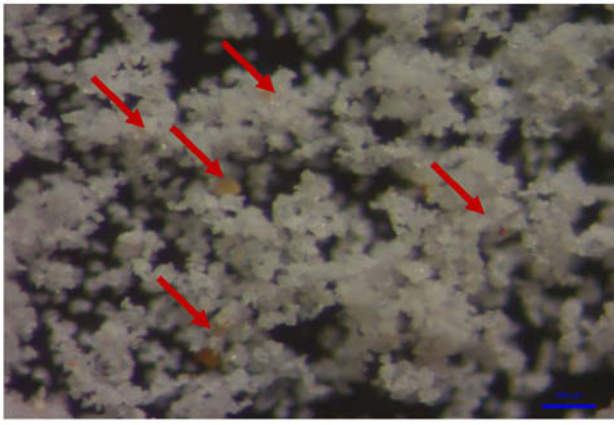

Image 1 - Micrographic of light green smectite treated with H_2O for 24h

At the stereomicroscopy image 2 the sample, treated with HCl for 6h, is clean of impurity particles.

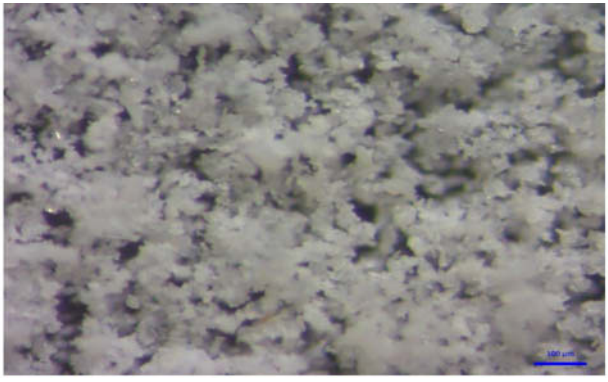

Image 2 - Micrographic of light green smectite treated with HCl for 6 h

The images of SEM micrographic are the sample treated with water and with HCl, both for 24h at 90°C.

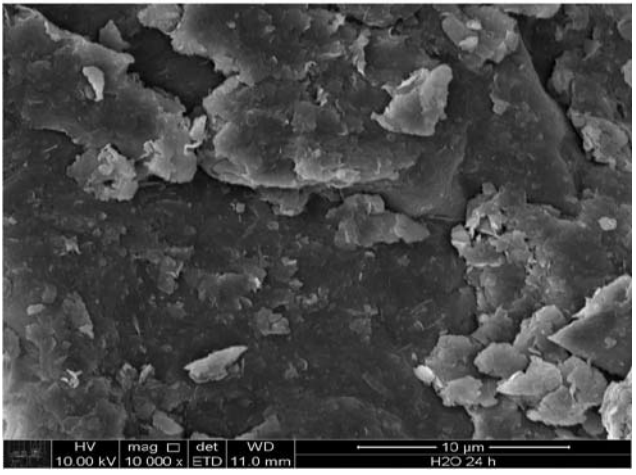

Image 3 – SEM micrographic of light green smectite treated with H_2O for 24h

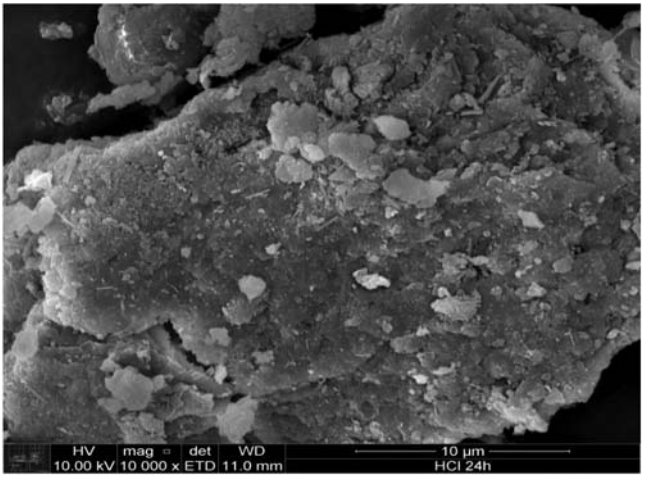

Image 4 – SEM micrographic of light green smectite treated with HCl for 24h

The lamellar structure of the samples is agglomerated in layers, mostly in same size. This is a possible indicator of the no complete destruction of crystal structures of smectite.

4 CONCLUSIONS

The light green smectite sample submitted to mild attack acid demonstrated a good response to the bleaching and purification at reaction time of 6 hours with a good preservation of crystalline structure and a significant bleaching and quartz purification.

The most evident modifications in decolorizing and CEC occurred in the first 12 hours of acid treatment.

In accordance with the methodology presented and from the results acquired, decrease the concentration of impurities that provides color, with no great change in the clay minerals structure, aiming at use in products of high value such as cosmetics and polymer/clay nanocomposites revealed an economical and environment efficient alternative.

5 REFERENCES

[1]Gomes,C.F.Argilas: o que são e para que servem, 1a Ed., Fundação Calouste Gulbenkian, Lisboa, Portugal Ed., Fundação Calouste Gulbenkian, Lisboa, Portugal, 1988.

[2]Murray, H.H, Appl. Clay Sci. 17, 2000.

[3]Ferreira, H.S,; Menezes, R.R; Ferreira, H. S. ; Martins, A. B. ; Neves, G. A. ; Ferreira, H. C.; Cerâmica 54 (2008) 77.

[4]Amorim, L. V. ; Farias, K. V. ; Viana, J. D. ; Barbosa, M. I. R. ; Pereira, E. ; França, K. B.; Lira, H. L. ; Ferreira, H. C. Cerâmica 51 (2005) 128.

[5]Pereira, K.R.O.; Hanna, R.A.; Ramos Vianna, M.M.G; Pinto, C.A.; Rodrigues, M.G; Valenzuela-Diaz, F.R. Brasilian organoclays as nanostructure sorbents of petroleum-derived hydrocarbons. Materials Research, v.8, n.1, p.77-80, 2005.

[6]Vaccari, A.; Applied Clay Science 14, 1999.

[7]Souza Santos, P. Ciência e Tecnologia de Argilas, 2a com a colaboração de Soza Santos H., V.3Ed., Edgar Blücher, S. Paulo, SP (1989)vol.1 e 1992 vol.2e3 1ed. Tecnologia das Argilas – vol.2 Edgar Blücher e EDUSP, São Paulo, SP, 1974.

[8]Valenzuela-Diaz, F.R.; Souza Santos, P. Studies on the acid ativation of Brasilian smetctitic clays. Química Nova, v.24, n.3, 2001.

[9]Grim, R.E. Bentonites – Elsevier, Amsterdam, 1978.

[10]Souza Santos, P. Ciência e Tecnologia de Argilas, vol. 1, 2a Ed., Edgar Blücher, S. Paulo, SP, 1992.

[11]Grim, R.E.; Clay Mineralogy, 2nd Ed., McGraw-Hill Book, New York, EUA, 1968.

[12]Valenzuela-Díaz, R.F.; Souza Santos, P.; Souza Santos,H.: A Importência das argilas industriais brasileiras. Química Industrial V.42 p.33-37, 1992.

[13]Abreu, S.F. Recursos minerais do Brasil, Ed. Edgard Blucher, 2ª. Ed., V.1, SãoPaulo, SP, 1973.

[14]Pereira, K.R.O. Ativação ácida e preparação de argilas organofílicas partindo-se de argila esmectítica proveniente do Estado da Paraíba. Dissertação (Mestrado), Orientadora: Meiry Gláucia Freire Rodrigues, Campina Grande – PB, 2003.

[15]Pereira, K.R.O.; Ramos Vianna, M.M.G; Rodrigues, M.G; Valenzuela-Diaz, F.R. Argila de alguns poluentes orgânicos em argilas organofílicas. Anais do XVI Congresso Brasileiro de Ciência e Engenharia dos Materiais, CD. Porto Alegre, RS 2004.

[16]Valenzuela-Diaz, F.R. Preparação a nível de laboratório de algumas argilas esmectíticas organofílicas. Tese (Doutorado). Departamento de Engenharia Química da Escola Politécnica da Universidade de São Paulo, SP, 1994.

Characterization of Minerals, Metals, and Materials 2015
Edited by: John S. Carpenter, Chenguang Bai, Juan Pablo Escobedo, Jiann-Yang Hwang, Shadia Ikhmayies, Bowen Li, Jian Li, Sergio Neves Monteiro, Zhiwei Peng, and Mingming Zhang
TMS (The Minerals, Metals & Materials Society), 2015

INCREASE OF FLEXURAL STRENGTH OF RED CERAMIC PIECES INCORPORATED WITH ORNAMENTAL ROCK WASTE: APPLICATION OF WEIBULL STATISTIC FOR DETERMINATION OF BEST FIRING TEMPERATURE

Piazzarollo, C.B[1,a], Xavier, G.C. [1], Alexandre, J. [1], Azevedo, A. R. G. [1], Monteiro, S. N. [2]

[1]State University of Norte Fluminense Darcy Ribeiro, Civil Engineering Laboratory – LECIV. Av. Alberto Lamego, 2000, Horto, CCT Campos dos Goytacazes/RJ – Brazil, ZIP: 28013-600.
[2] *Military Institute* of Engineering, IME, Materials Science Department. Praça General Tiburcio, Urca. Rio de Janeiro/RJ – Brazil, ZIP: 22290270.
[a]carlabp@gmail.com;

Keywords: red ceramic, ornamental rock waste, flexural strength.

Abstract

Ceramic materials exhibit dispersion results after being subjected to various levels of stress, from the point of view of mechanical strength. With the focus on sustainable development and to improve the strength of these material, was incorporated ornamental rock waste into clay in up to 10% in mass to conform some samples, that was fired to 750ºC, 850ºC and 950ºC and submitted to technological tests. This paper presents an analysis of the technological properties of the samples through the use of Weibull statistic to determine which the best firing temperature for these red ceramic materials. The Weibull Modulus indicates a greater homogeneity for samples with 10R at 950ºC.

Introduction

According to the International Council for Research and Innovation in Building and Construction (CIB), the durability is the capacity that a product, component or construction has to keep your performance up the minimum specified levels in order to meet the requirements in each specific situation [1].
About that, especially regarding the structural aspect, becomes important to analyze the durability of materials, since durability is closely related to the performance and safety of a construction.
Looking for the increase of durability of ceramics, [2] indicated the use of granite waste in red ceramics pieces for obtaining greater strength and less open porosity and [3] showed the possibility of using of this waste, showing an increase of durability over the service life of the material.

Thus, further searching improve the flexural strength (FS) and durability of red ceramic pieces, data of FS will be analyzed by Weibull Distribution in order to determinate the best firing temperature for this material.

The Weibull distribution describes the probability of the material fails when submitted to a given FS level [4, 5]. The equation [6] that describes the Weibull distribution is [Eq.1]:

$$f(\sigma) = \frac{m}{\sigma_r}\left(\frac{\sigma-\sigma_0}{\sigma_r}\right)^{m-1} exp\left\{-\left(\frac{\sigma-\sigma_0}{\sigma_r}\right)^{m}\right\} \quad \text{(Eq.1)}$$

Where σ_0 is the tension before the material begins to fail, σ_R is a referential tension value, where the probability of failure is 0.632.

Therefore, by the use of Weibull distribution, it can be analyze as the fractures behave in group of samples. Thus, it is possible to determine, by the Weibull modulus, where are the greater mechanical stability and the best firing temperature.

Materials and Methods

For this study, we used the following materials: clay from the municipal district of Campos-RJ and ornamental rock waste from Cachoeiro do Itapemirim, Espírito Santo state.

The Quantitative Chemical Analysis tests were carried out in the Materials Characterization Laboratory - LECIV/CCT/UENF. The samples were sieved on #325 mesh (0.045mm) and the drying process involved the temperature of 110ºC. Was used the energy dispersive X-ray equipment, model Shimadzu EDX-700.

The Differential Thermal Analysis were carried out in the Polymer Laboratory - LAMAV/CCT/UENF and was used 30 mg of each sample, in a nitrogen atmosphere, with a heating rate of 10 °C/min up to 1020ºC.

The samples were prepared with clay incorporated with three different waste contents (i.e. 0%, 5%, and 10%) and, to ensure the homogeneity of samples, the mass was reduced according to [7]. At first, the ornamental rock waste powder was sieved on #40 mesh (0.42mm) and the retained material was discarded. Next, the pass-through material was ground to pass through sieve #60 mesh (0.25mm).

After mixing the samples with 0%, 5% and 10% waste (identified as 0R, 5R and 10R, respectively), the ceramic pieces were molded in prismatic shapes of 11.70 cm x 2.70 cm x 1.70 cm. The number of pieces (5) and the measures was based on [8, 9] standards.

The drying process involved the temperature of 110ºC, and the firing process involved 750ºC, 850ºC and 950ºC in an electronic oven.

After firing, the ceramic pieces were submitted to a three loading point flexural strength test according to standard procedure [8] and also to the tests according to [9]. The obtained results represent the average of 5 determinations. The three loading point flexural strength test was carried out with a loading rate of 0.5 mm/min with a distance of 9.0 cm between supports on INSTRON 5582.

Results

Table 1 – Chemical Analysis

Raw Materials	SiO_2 (%)	Al_2O_3 (%)	Fe_2O_3 (%)	K_2O (%)	TiO_2 (%)	SO_3 (%)	CaO (%)	MnO (%)	V_2O_5 (%)	ZrO_2 (%)	CuO (%)	ZnO (%)	SrO (%)
Clay	48.83	35.46	8.87	3.17	1.62	1.13	0.54	0.14	0.10	0.03	0.03	0.03	0.01
Residue	50.09	17.60	12.47	3.70	1.83	1.56	12.39	0.19	0.55	0.03	-----	0.02	0.04

The Table 1 shows the composition of SiO_2+Al_2O_3 over 84% characterizes refractory clay. The clay color after fired is a consequence of 8.87% of Fe_2O_3. The K_2O and the CaO into clay in proportion of 3.17% and 0.54% respectively, are burning and melting agents and form eutectics, contributing to reduce the porosity of the material. The SO_3 present into clay has a deleterious effect due to the output of the gas of the pieces, breaking them.

For the ornamental rock waste, the silica content is about 50% and the Al_2O_3 is over than 17%, indicating chemical compositions of primary minerals (quartz, feldspar and minerals of the mica's group). The content of Fe_2O_3 (12.48%) contributes to the red color of the pieces after mixing with the clay. The K_2O (3.70%) present into ornamental rock waste are important at the firing process because reduce the porosity in the finished material.

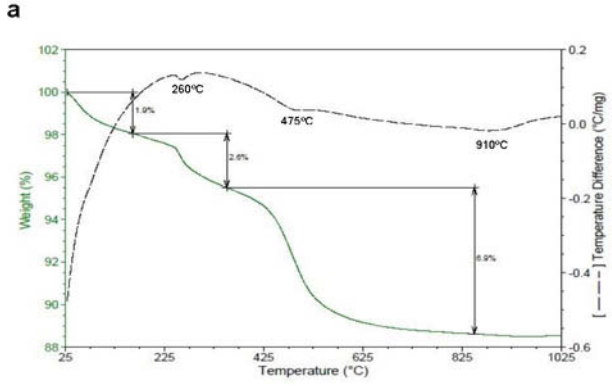

Figure 1 - DTA/DTG curves of clay.

By the DTA/DTG curves (Fig. 1) it is possible to note an endothermic event at 260ºC with a loss of 1.9% in mass, associated with a gibbsite hydroxyl loss. An event at 475ºC associated with a kaolinite hydroxyl loss, with a loss of 2.6% in mass and at the end, an endothermic band at 910 ºC associated with the transformation from metakaolinite to spinel, with a loss of 6.9% in mass. The total mass loss totalize 11.4%, typical behaves for clays from Campos – RJ [10].

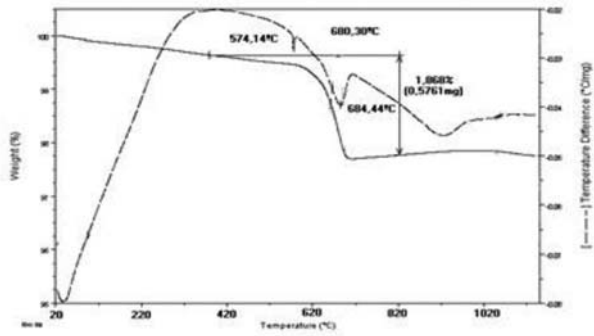

Figure 2 - DTA/DTG curves of ornamental rock waste.

For the ornamental rock waste, the DTA/DTG curves show an endothermic event with a little intensity at 574.14% due to the transformation from α-quartz to β- quartz, associated with a loss of 1.86% in mass, and a medium intensity endothermic event at 688.44ºC due to the mica hydroxyl loss.

The results of the technological tests are shown in the following figures.

For the water absorption (W.A.) and the flexural strength (FS), the found results are:

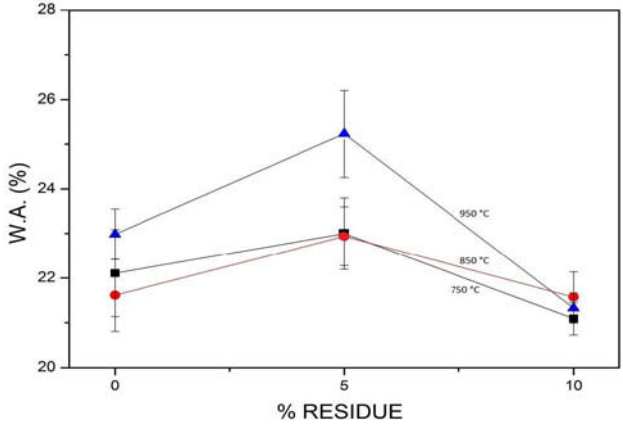

Figure 3 – Water Absorption of red ceramic pieces incorporated with ornamental rock waste fired at 750ºC, 850ºC and 950ºC.

The results presented in Figure 3, shows values between 21% and 25%, indicating an increase of AA in the samples with 5R, and an reduction of AA in the samples with 10R. The smaller percentage of AA was found at 750ºC in the samples incorporated with 10% of waste, this result can be associated with the presence of the fluxes oxides (Table

1). The incorporation of 10R reduces the AA, independent of the firing temperature, showing better results than 0R.

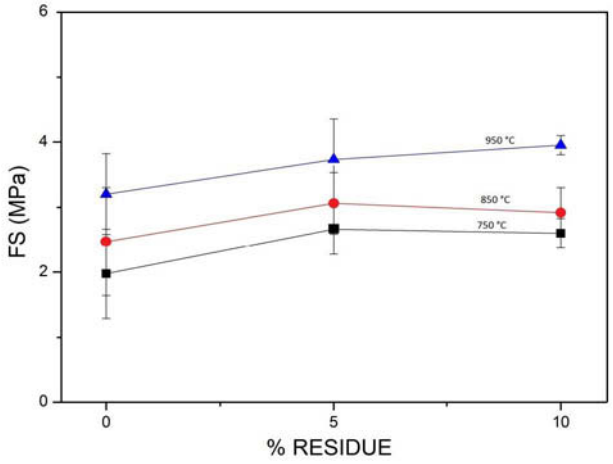

Figure 4 – Flexural Strength of red ceramic pieces incorporated with ornamental rock waste fired at 750ºC, 850ºC and 950ºC.

In the Figure 4 it is possible to note a resistance increase tendency for the ceramics, independent of the percentage of waste. The incorporation of 5R and 10R increases the FS, showing better results than 0R. This result can be associated with the presence of K_20 (Table 1).

The results showed strength gains for samples with 0% of waste for all temperatures, for samples with 5% of waste fired at 750ºC and 850ºC and for samples with 10% of waste fired at 950ºC.

It was used Weibull Statistics to evaluate changes associated with mechanical strength when the firing temperature and the percentage of waste was changed.

The Figure 5, 6 and 7 shows the Weibull Plot comparisons for the samples with 0R, 5R and 10R fired at different temperatures.

In the graph it's possible to determine, by the slope of the line, the Weibull modulus (m). The **m** value is a good standard for the analytical quality of ceramic materials [11], and his value represents a risk of rupture and characterizes the dispersion of the TRF data [6].

It's desired that the value of **m** is as large as possible. Higher the value of m, higher is the homogeneity of the batch. Thus, the determination of the Weibull modulus can shows what or which temperatures are the most appropriated for a smaller dispersion of defects.

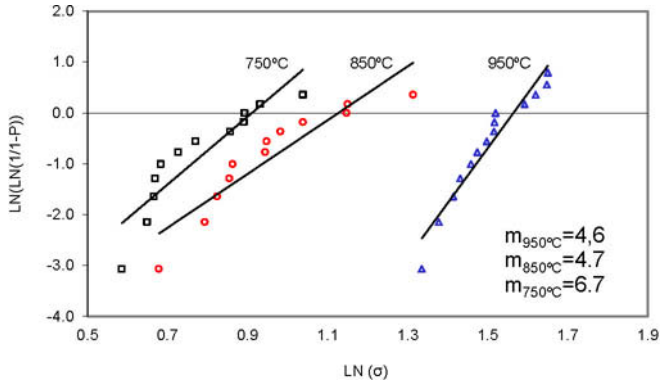

Figure 5 - Weibull distribution: samples with 0R fired at 750º, 850º and 950ºC.

According to the Fig. 4, the results at 750ºC presented the small medium values for all waste additions, however, by the Fig. 5, the batch presents a behave more homogeneous (m = 6,7), with a small probability of failure. It can indicate that at 750 ºC, the deformation of the material is smaller than to other temperatures.

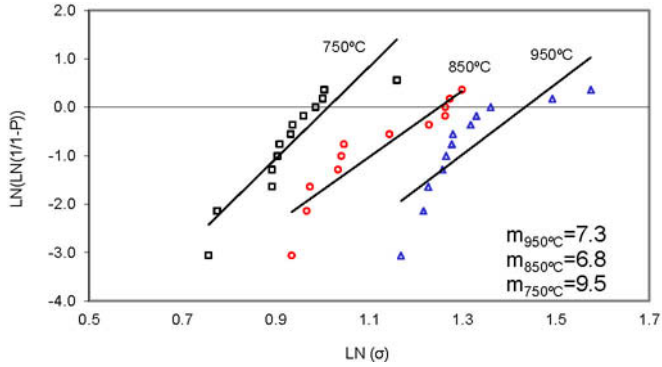

Figure 6 - Weibull distribution: samples with 5R fired at 750º, 850º and 950ºC.

By the Fig. 6, the biggest value of Weibull Modulus was 9.5 at 750ºC with 5R thus, this batch is the most homogeneous. The material showed a higher Weibull modulus, when compared with the Fig. 5, it ensuring the homogeneity and shows an influence of the ornamental rock waste, independent of the firing temperature.

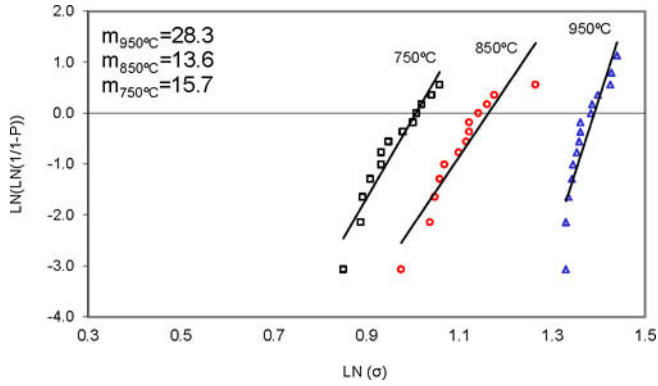

Figure 7 - Weibull distribution: samples with 10R fired at 750º, 850º and 950ºC.

The incorporation of 10R of ornamental rock waste into clay intensely influencied at Weibull modulus (m=28,3), at 950ºC. This batch was more homogeneous, i.e., with a less propability of failure. The samples presented a bimodal distribution, typical of the Weibull distribuction.

Conclusion

- The ornamental rock waste has K_2O> 3%, contributing to decreasing of the porosity, as happens for 10R samples at all temperatures;
- The K_2O melts at low temperatures forming glassy structure on cooling, decreasing the porosity;
- The clay has a refractory character due to the high content of SiO_2 + Al_2O_3 and her color is due to the presence of Fe_2O_3> 8%;
- The DTA/DTG of clay shows a typical kaolinitic clay behavior with a mass loss of 11.76%;
- The DTA/DTG of ornamental rock waste is steady up to 1020ºC, with an expansion from α-quartz to β-quartz at 574,14ºC, with a mass loss of 1.86%;
-The Water Absorption was lower at 10R, independet of the firing temperature;
- For the TRF, there wasn't statistical difference for the incorporation of ornamental rock waste at the same temperature. Only with the incorporation of 10R there were differences between the averages and their respective deviations. It can be seen in Fig.3 where low water absorption achieved value;
- Evaluating the Weibull distribution, the highest value of module (m = 28.3) was observed at 950 ° C with 10R, showing a greater homogeneity of the batch. However, it can be noted that the Weibull modulus for 0R and 5R, was more influenced at 750 °C. This may become another alternative in terms of lower energy consumption.

References

1. CIB W80/RILEM 71-PSL. Prediction of service life of building materials and components. Conseil International du Batiment Pour la Recherche L' Etude et la Documentation & Réunion Internationale des Laboratoires d'Essais et de Recherches sur les Matériaux et Les Construction. Rotterdam, 1983.
2. F. Saboya, G.C.Xavier, J. Alexandre, "The use of the powder marble by-product to enhance the properties of brick ceramic", Construction and Building Materials, Vol. 21 (2007), Pages 1950-1960.
3. C. B. Piazzarollo et al., "Statistical Analysis of Degradation Data of Red Ceramic Pieces Incorporated With Ornamental Rock Waste" (Paper presented at the 58th Brazilian Congress on Ceramics, Bento Gonçalves, Rio Grande do Sul - Brazil, 2014), 12.
4. D.C. Montgomery, G. C. Runger. Applied Statistics and Probability for Engineers. LTC Editora SP, 2, (2003) 463.
5. Brazilian Association of Technical Standards. Determination of Particle Size Analysis of Soils, Rio de Janeiro: ABNT 1984 (NBR 7181).
6. S. Somiya et al., *Handbook of Advanced Ceramics*. (New York, NY: Elsevier, 1990), 1046 -1058.
7. Brazilian Association of Technical Norms –ABNT NBR-6457, Soil samples – compaction tests and characterization tests (in Portuguese), Rio de Janeiro, Brazil, 1986.
8. American Society Technology Materials - ASTM C 674, Standard Test Method for Flexural Properties of Ceramic Whiteware Materials, 1977b.
9. American Society Technology Materials - ASTM C 373, Standard Test Method for Water Absorption, Bulk Density, Apparent Porosity and Apparent Specific Gravity of Fired Whiteware Products, 1977a.
10. S.N. Monteiro and C.M.F. Vieira, "Characterization of clays from Campos dos Goytacazes, north Rio de Janeiro State (Brazil)", Tile & Brick Int, v.18, n3.
11. L.M. Thurler, G. P. Souza, J.N.F. Holanda, "Avaliação do Módulo de Weibull para Argilas de Campos – RJ" (Paper presented at the 43rd Brazilian Congress on Ceramics, Florianópolis, Santa Catarina, 1999), 8.

Characterization of Minerals, Metals, and Materials 2015

Characterization of Electronic, Magnetic, Environmental, and Advanced Materials

Session Chairs:
Shadia Ikhmayies
Walman Castro

Characterization of Minerals, Metals, and Materials 2015
Edited by: John S. Carpenter, Chenguang Bai, Juan Pablo Escobedo, Jiann-Yang Hwang, Shadia Ikhmayies, Bowen Li, Jian Li, Sergio Neves Monteiro, Zhiwei Peng, and Mingming Zhang
TMS (The Minerals, Metals & Materials Society), 2015

SHAPE MEMORY CHARACTERISTICS OF RAPIDLY SOLIDIFIED Ti-37.8Cu-18.7Ni ALLOY RIBBONS

Alana Pereira Ramos[1] and Walman Benicio de Castro[2]

[1]PPGCEMat – UFCG – Aprigio Veloso, 882 – Bodocongó -58429-900 – Campina Grande/PB - Brazil
[2]UAEM - UFCG– Aprigio Veloso, 882 – Bodocongó -58429-900 – Campina Grande/PB - Brazil

Keywords: Shape memory alloys; Ti–Ni–Cu alloys; Melt spinning; Amorphous ribbon; martensitic transformation.

Abstract

Amorphization and martensitic transformation (*Ms*) characteristics of Ti–Ni-Cu alloy ribbons prepared by melt spinning were investigated by means of differential scanning calorimetry and X-ray diffraction. In these experiments particular attention has been paid to change the wheel linear velocity from 21 to 63 m/s. Then the cooling rates of ribbons were controlled. The effect of this cooling rate and alloy composition on martensitic transformation behavior is discussed.

Introduction

Ti–Ni–Cu alloys have been attracting attention by their high performance of shape memory effect and decrease of thermal and stress hysteresis in comparison with Ti–Ni binary alloys [1,2,3]. The martensitic transformation temperature (*Ms*) and the transformation hysteresis are very sensitive to a deviation of the stoichiometry or additional alloying elements [4]. Therefore, research on the transformation behavior of shape memory alloys as a function of composition variation has been extensively performed in recent years. However, rapidly solidified Ti–Ni alloy ribbons have been known to have the shape memory effect and superelasticity superior to the alloy ingots fabricated by conventional casting [5,6]. Generally there are four advantages of rapid solidification over the slower conventional solidification techniques. These are an ability to form metastable phases, increasing the solubility above the equilibrium solubility, decreasing the segregation of additions, and refining the microstructure. It is considered that all of these effects have been attempted to improve shape memory effects in the rapidly solidified ribbons. In the present study, shape memory behavior of Ti–Ni–Cu alloys ribbons fabricated at different cooling rates by the melt spinning was investigated and the influence of the rapidly solidified on shape memory behavior of $Ti_{43.5}Cu_{37.8}Ni_{18.7}$ (at.%) alloy was studied.

Experimental procedure

The experimental studies have been performed using a laboratory scale single roller melt spinning device operating in high vacuum atmosphere. Pre-synthesized $Ti_{43.5}Cu_{37.8}Ni_{18.7}$ (at.%) alloy were prepared by melting high purity nickel, copper and titanium in an arc melt system. Alloy ingots of 5 mm×5 mm×10 mm were cut and were placed into quartz crucibles of internal diameter 10 mm. The chamber of the melt spinning system had been evacuated to less than 1×10^{-4} Pa before re-melting. When the melt temperature reached the expected temperature, it was ejected through the nozzle with a circular shaped orifice on the outer surface of the rotating quenching wheel made of copper. The diameter of the orifice was 0.5 mm, the ejection pressure was 40 kPa and distance from the tip of the nozzle to the wheel surface was 300 μm throughout the study. The crystal structures of the ribbons were investigated by XRD diffraction using Cu Kα radiation. For the study of martensitic transformation behavior of the ribbons, the differential scanning calorimetry (DSC) measurements have been performed at heating and cooling rate of 10 K/min.

Results and discussion

The increase of the linear wheel velocity from 21 to 63 m/s results in a decrease of the ribbon thickness from 190 μm to 70 μm. As the increase of linear wheel velocity leads to a reduced ribbon thickness, the heat transfer coefficient at the quenching wheel–ribbon interface is enhanced and the cooling rate increases [7]. Therefore, this result clearly indicates that variations in the melt spinning wheel velocity allow the effective control of the cooling rates in melt spinning process.

In order to analyze the solidification structure of the ribbons, XRD experiments were carried and the results obtained from the free side and wheel side of the ribbons are shown in Figure 1, for a linear wheel velocity of 21 m/s. Diffraction peaks of the B2 parent phase and the B19 martensite were observed simultaneously. The diffraction peaks on wheel side are smaller than diffraction peaks on free side. This difference is attributed to the fact that the on wheel side cooling rate is higher than on free side cooling rate of the ribbons.

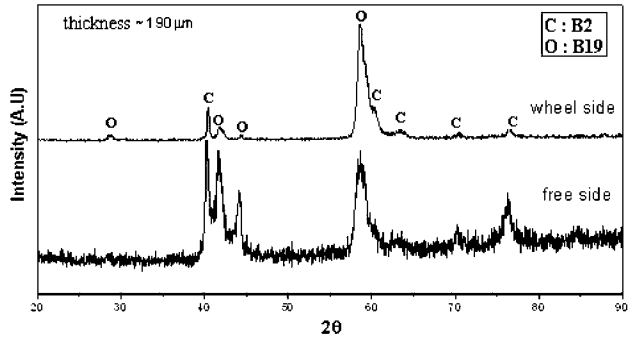

Figure 1. XRD patterns of the ribbon fabricated at 21 m/s wheel velocity from: (a) the free side and (b) wheel side.

For linear wheel velocity of 63 m/s, diffraction peaks show that a perfect amorphous ribbon can be produced from this alloy (Figure 2). When the ribbon is produced at a higher linear wheel velocity in melt spinning, the degree of undercooling becomes high because of its thinner thickness [8]. Eventually the amorphous ribbons without any crystal phases can be produced in $Ti_{43.5}Cu_{37.8}Ni_{18.7}$ alloy at the highest cooling rate.

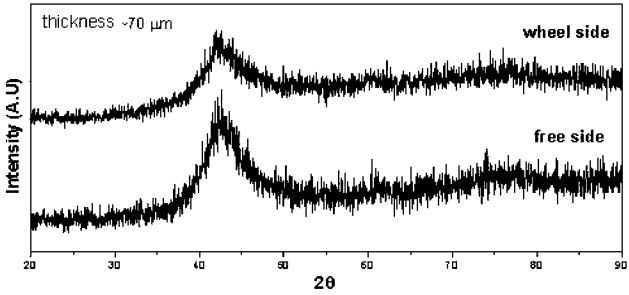

Figure 2. XRD patterns of the ribbon fabricated at 63 m/s wheel velocity from: (a) the free side and (b) wheel side.

Figure 3 shows DSC curves of the as-spun ribbons fabricated at the different linear wheel velocities. The ribbons fabricated at the linear wheel velocity of 21 m/s show one exothermic and endothermic peaks on cooling and heating of DSC curves as shown in Figure 3(a). This splitting of DSC peaks was also found in the Ti–Ni30–Cu20 alloy ribbons prepared by melt spinning, which was

attributed to the fact that one-stage transformation of the B2–B19 occurred in the alloy ribbons heavily strained by rapid solidification process [9]. The Ms (the B2–B19 transformation start temperature) was measured from Figure 3. The ribbons fabricated at the linear wheel velocity of 63 m/s show no DSC phase transformation peaks are visible on the curve of as-spun ribbon, indicating that as-spun ribbon is fully amorphous (Figure 3(b)). This result is in good agreement with the result of XRD experiment that the ribbon is amorphous as shown in Figure 2.

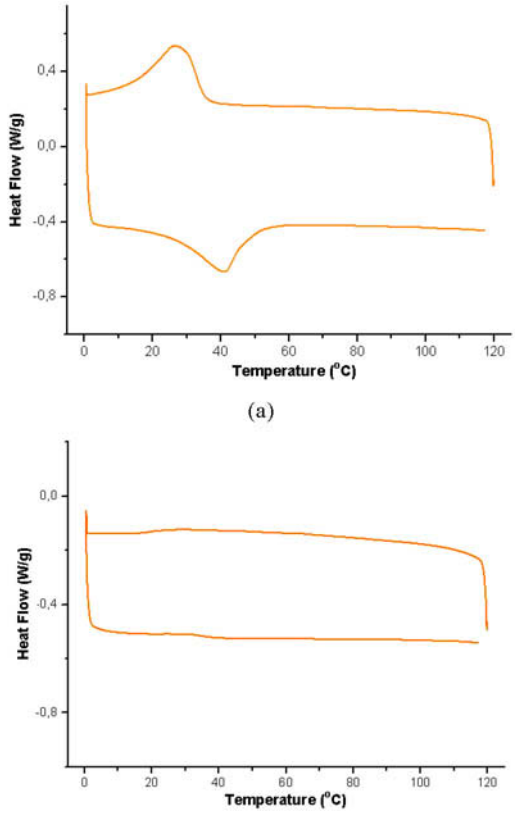

Figure 3. DSC curves of the ribbons fabricated at the wheel velocities of: (a) 21 m/s and (b) 63 m/s.

It has been reported that an amorphous ribbon can be fabricated in Ti–35 at.% Ni–25 at.%–Cu alloy by melt spinning and the crystallized ribbon exhibits a small transformation hysteresis and an excellent superelastic shape recovery [10]. The perfect amorphous ribbons can be also produced in $Ti_{43,5}Cu_{37,8}Ni_{18,7}$ (at.%) alloy by melt spinning and they are expected that excellent shape memory

characteristics can be achieved by controlling the microstructures of crystallized ribbons after proper heat treatment.

Conclusions

Structural analysis of melt-spun $Ti_{43.5}Cu_{37.8}Ni_{18.7}$ (at%) alloy ribbons showed that the proportion of amorphous solidification at the chilled side of the ribbon increased with wheel velocity. A perfect amorphous ribbon can be produced from this alloy by melt spinning when the ribbon is fabricated at a wheel velocity of 61 m/s. The splitting of DSC curves in the ribbon of part amorphous and part crystal is ascribed to the microstructual inhomogeneity introduced by rapid solidification. Based on these experimental results it is concluded that the martensitic transformation behavior could be controlled without chemical contributions by means of structural modifications achieved by the rapid solidification.

References

1. Y. Bellouard, *Materials Science and Engineering*, Volume (A 481–482), (2008), p. 582–589.
2. F. M. B. Fernandes, *Departamento de ciência dos Materiais / CENIMAT, Universidade de Lisboa, Lisboa,* (2006), p.1-32.
3. T. Saburi, IN: K. Otsuka, C. M. Wayman (Eds.), *Cambridge University Press, Cambridge, UK*, (1988), p. 49–73.
4. Duwez, P., Topics in Applied Physics, Volume (46), (1981), p. 19.
5. Y. Z. Chen et al., *Materials Characterization*, Volume (59), (2008), p. 412 – 416.
6. E. Karaköse and M. Keskin, *Materials characterization*, Volume (60), (2009), p. 1569–157.
7. N. K. Lin and S. K. Wu, *Journal of Alloys and Compounds*, Volume (424), (2006, p.171–175.
8. K. Mehrabi et al., *Journal of Alloys and Compounds*, Volume(526), (2012), p.45– 52.
9. S.-won Kang et al., *Scripta Materialia,* Volume (59), (2008), p. 186–1189.
10. A. V. Shelyakov et al., *Journal of Alloys and Compounds*, Volume (577), (2013), p. S251-S254.

Characterization of Minerals, Metals, and Materials 2015
Edited by: John S. Carpenter, Chenguang Bai, Juan Pablo Escobedo, Jiann-Yang Hwang, Shadia Ikhmayies, Bowen Li, Jian Li, Sergio Neves Monteiro, Zhiwei Peng, and Mingming Zhang
TMS (The Minerals, Metals & Materials Society), 2015

EFFECTS OF CASTING CONDITIONS ON THE STRUCTURE AND MAGNETIC PROPERTIES OF THE Co-19 at.%Al-6 at. %W ALLOY

N.V. Kazantseva, N.N. Stepanova, M.B. Rigmant, D.I. Davidov, D.A. Shishkin, E.P. Romanov

Institute of Metal Physics, Ural Division of RAS, Ekaterinburg, 620990, 18, S.Kovalevskaya Str. Russia

Keywords: Cobalt alloys, Phase transitions, Magnetic properties

Abstract

The Co-19 at.%Al-6 at.%W alloy was prepared by two methods of casting. We used arc melting under an argon atmosphere with casting into a copper water-cooled casting mold and induction melting furnace with casting into a ceramic Al_2O_3 mold. According to the X-ray and SEM analyses, phase compositions depend on the cooling rate of the ingot after melting. After arc melting, the cast alloy has a three-phase structure, consisting of γ cobalt (FCC), intermetallic phases CoAl (B2) type, and Co_3W (DO_{19}) type. After the induction melting, the alloy has a three-phase structure, consisting of γ cobalt (FCC), intermetallic phases CoAl (B2) type, and Co_7W_6 (μ) type. All phases in the investigated ternary alloy at the room temperature are ferromagnetic. Curie temperatures of all obtained phases were defined. It is shown that the magnetic properties of the studied alloy are typical for soft magnetic materials.

Introduction

Co-Al-W alloys are very interesting scientifically. Such alloys are considered as promising heat-resistant materials. Cobalt-based intermetallic alloys are comparable in strength to nickel superalloys [1-4], the latter being paramagnetic [4]. In contrast, cobalt-based heat-resistant alloys have properties of ferromagnetic materials. Cobalt has the highest Curie temperature (1121°C) among all known ferromagnets. This allows one to create cobalt-based materials with desired magnetic properties, such as the soft or permanent magnets [5]. Phase diagrams of the binary Co-W system have been studied in [6]. It is known that tungsten reduces the Curie temperature of the cobalt solid solution down to 865 °C at 6 at.% W. The Co-Al system has both paramagnetic (B2-CoAl) and ferromagnetic (cobalt solid solution) phases. Aluminum reduces the Curie temperature of the alloy down to 840 °C at 7 at.% Al [7]. The Co-Al-W system has both cobalt solid solution and different intermetallic compounds [1]. However, the isothermal sections of this phase diagram have been constructed only at high temperatures (≥ 900°C) [1-2, 8-12] and magnetic studies in this system are absent in the literature. The Co-Al-W alloys refer to the materials with large differences in their melting temperatures and in the specific weights of the alloying components. Therefore, the method of casting may have a significant impact on the structure and phase composition of the alloys, because of the nonuniform distribution of the chemical elements throughout the ingot. Usually, different mechanical processing (rolling, forging, hydrostatic extrusion) combined with the temperature aging can be used to improve the homogeneity of the samples.

In this report, we present a study of the structure and magnetic properties of the cobalt-based alloy (Co-19 at.%Al-6 at. %W) obtained by different methods of casting.

Experimental Procedure

The Co - 19 at.%Al - 6 at.%W alloy was prepared by two methods of casting: arc melting with casting into a cupper water cooling mold and melting in an induction furnace with casting into a ceramic (Al_2O_3) mold. The resulting cylindrical ingots with a diameter of 18 mm were tested in four conditions: (1) cast, (2) cast + annealing at 1200°C-10h followed by water quenching, (3) cast + forging at 1200 °C, (4) cast + forging + annealing at 1200 °C-10h followed by furnace cooling.

The structure and chemical composition of the alloys were studied using a scanning electron microscope (JSM 6490). Phase compositions of the alloys were investigated with the X-ray diffractometer DRON-3 with the Cu Kα, λ= 0.15418 nm radiation. Magnetic properties were studied using the magnetometer Lake Shore 7407. Measurements were done in an argon atmosphere, the magnetic fields were varied up to 17 kOe, the temperatures were changed from 20°C up to 1000°C, the frequency was 82 Hz, and the vibration amplitude was 1.5 mm. Relative errors of the measurements were below 1%.

Results and Discussion

The X-ray diffraction patterns of the samples show that the phase composition depends on the casting conditions and heat treatments (Figure 1).

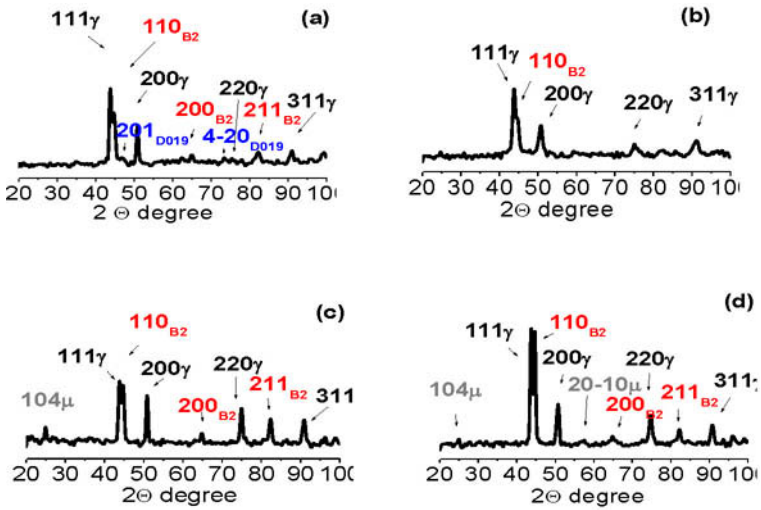

Figure 1. X-ray diffraction patterns: a- Sample 1; b- Sample 2; c- Sample 3; d- Sample 4.

Sample 1 has three phases: γ - phase cobalt-based solid solution (FCC), CoAl (B2), and Co_3W (DO_{19}) (see Figure 1a). After the heat treatment at 1200°C and water quenching (Sample 2), the diffraction lines of the DO_{19} phase disappeared (see Figure 1b). According to the equilibrium phase diagram, the alloy of this chemical composition at the temperature of 1200°C should correspond to the two-phase area γ+ β (B2) [8-10]. Samples 3 and 4 were melted in an induction furnace followed by the furnace cooling of the ingot. Although these samples also have a three-phase composition, we found the Co_7W_6 phase (μ-phase) instead of the $D0_{19}$ phase. This phase composition was retained after high temperature forging followed by a slow air cooling (Sample 3, see Figure 1c). After the heat treatment at 1200°C-10h followed by a slow furnace cooling, the sample had the same three-phase γ+ CoAl+ Co_7W_6 composition (Sample 4, see Figure 1d).

Microstructure of the studied samples is shown in Figure 2. The structure of Sample 1 consists of the alternating areas of the solid solution (γ-phase) and the Co(Al,W) (B2) phase. Thin plates of the Co_3(Al,W) (DO_{19}) phase were found inside the areas of the solid solution (see Figure 2 a). After the heat treatment at 1200°C-10h followed by water quenching, the $D0_{19}$-phase plates were dissolved (see Figure 2b). The microstructure of the forged sample (Sample 3) contains the small-sized μ-phase particles (Figure 2c), whose numbers increase after the heat treatment followed by a slow furnace cooling (Sample 4, see Figure 2d).

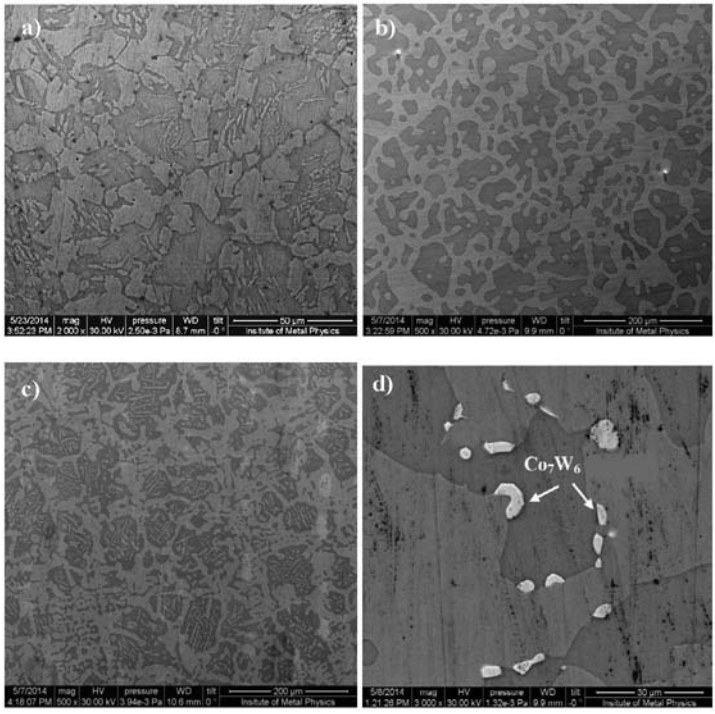

Figure 2. SEM results of the samples: a- Sample 1;
b- Sample 2; c- Sample 3; d- Sample 4.

Average chemical compositions of the samples obtained by statistical processing of 5 measurements are presented in Table I. As can be seen from the Table I, the average chemical compositions of the alloys obtained by the different methods of casting differ from each other. Cast sample (Sample 1) obtained by arc melting followed by fast quenching has considerable heterogeneity of the chemical composition. High-temperature homogenization of this alloy (Sample 2) equalizes the chemical composition of cobalt and aluminum throughout the ingot. We have used a precooked Co-Al alloy for melting of the samples by induction furnace and obtained more uniform chemical composition of the ingots.

Table I. Chemical composition of the samples, at.%, SEM (EDS)

Element	Initial composition of the alloy (batch)	Sample 1 (cast)	Sample 2 (cast + heat treatment)	Sample 3 (forged)	Sample 4 (forged + heat treatment)
CoK	75	77.05	73.15	72.41	72.95
AlK	19	18.46	22.45	21.52	21.29
WI	6	4.50	4.40	6.07	5.76

Chemical compositions of the different phase areas are presented in Tables II-III. The chemical composition of the Co(Al,W) (B2) phase is similar to the value obtained in [11] for the Co-18.5 at.%Al-6.3 at.%W alloy, where the B2 phase contained 26.9 at.%Al and 4.5 at.%W.

Table II. Chemical composition of Sample 2, at.%, SEM (EDS)

Element	γ-phase (FCC)	Co(Al,W) (B2)
CoK	74.89	72.51
AlK	20.63	23.02
WI	4.48	4.46

Table III. Chemical composition of Sample 3, at.%, SEM (EDS)

Element	γ-phase (FCC)	Co(Al,W) (B2)	Co_7W_6 (μ-phase)
CoK	79.31	67.25	48.96
AlK	13.63	27.58	3.78
WI	7.06	5.17	47.17

The appearance of the intermetallic Co_3W phase in the alloy obtained by arc melting (Sample 1) can be attributed to the cooling rate of the ingot. Fast quenching allows the sample to pass through the high temperature area of the equilibrium phase diagram and bypass the low temperature area. Our results show that the studied part of the phase diagram contain the high temperature area of the $D0_{19}$ phase and low temperature area of the μ-phase. This explains the discrepancy between the experimental results on the Co-Al-W phase diagram obtained by different authors. For example, a vertical slice of the equilibrium phase diagram in [12] contains the μ-phase area, but the same temperature part of the phase diagram in [1] contains the $D0_{19}$ phase.

Figures 3-4 present the dependence of the specific magnetization σ on the value of the magnetic field H when increasing magnetization up to 17 kOe. We find that all investigated samples have high specific saturation magnetization σ = 37-63 emu/g and their saturation induction B_S = 0.5 – 0.82 T. Figure 3 shows portions of the hysteresis loops near zero specific magnetization. The coercive force (at σ = 0) is minimal in Sample 1 (cast, arc melting) and increases under heat

treatment and forging. The results of the magnetic studies show that the hysteresis loop is narrow. This is typical for soft magnetic materials, which can be easily magnetized and remagnetized [5].

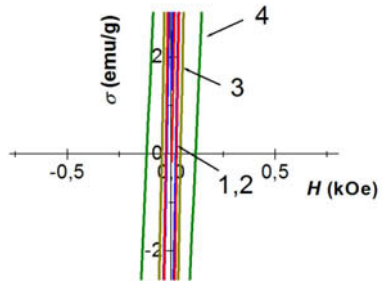

Figure 3. Results of the magnetic studies, zero crossing.

Effects of the casting conditions and thermo-mechanical treatments on the magnetic properties can also be seen in Figure 4. Saturation magnetization σ is reduced (by a factor of 1.5) in the samples containing μ-phase.

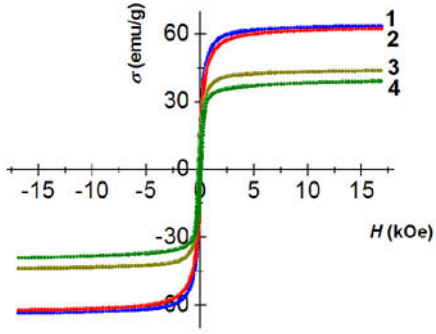

Figure 4. Hysteresis loops: 1- Sample 1; 2- Sample 2; 3- Sample 3; 4- Sample 4.

Curie temperatures of the different phases can be estimated from Figure 5. All investigated samples have a ferromagnetic state up to 800°C; sufficiently high values of magnetization σ (emu/g) ~10 are preserved up to 730°C. Three Curie temperatures may be seen in Figure 5a for Sample 1: ~800 K, 1000 K, and ~1100 K. Sample 3 also has three magnetic phases with the Curie temperatures of ~600 K, ~920 K, and ~1100 K. In Sample 4, (see Figure 5c), one can see only two Curie temperatures, ~600 K and ~1000 K; a broadening of the second peak should also be noted.

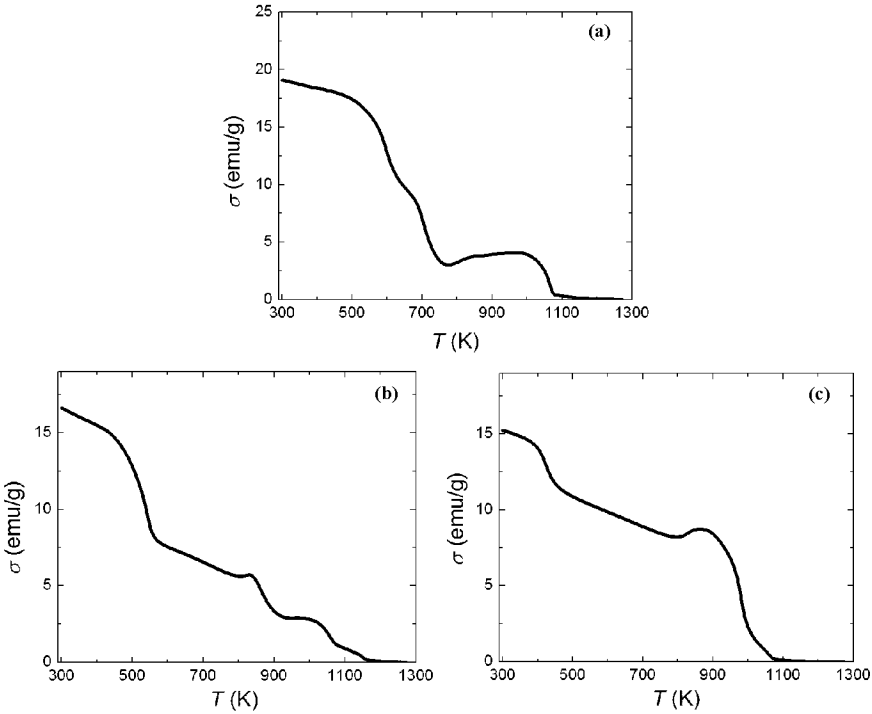

Figure 5. Results of the magnetic studies, H=100 Oe: a- Sample 1; b- Sample 3; c- Sample 4.

Taking into account the X-ray and SEM results, the elimination method allows us to suggest that the Curie temperatures of ~600 and ~800 K belong to μ-phase (Co_7W_6) and Co_3W-phase, correspondingly. According to the equilibrium phase diagram, most of the high-temperature phase is β (B2) in the alloy of this chemical composition; the two-phase γ+β (B2) area exists up to almost 1380°C [10]. Therefore, the definition of the Curie temperatures of these high-temperature phases requires further investigation.

Conclusions

1. Method of casting (especially the rate of cooling) followed by a thermo-mechanical treatment, significantly affect the chemical homogeneity, phase composition, and magnetic properties of the Co-19 at.%Al-6 at. %W alloy.
2. The intermetallic Co_7W_6 phase (μ-phase) reduces the value of the saturation magnetization and increases the coercive force; this phase decreases the service properties and is undesirable for the Co-Al-W alloys.
3. The best magnetic properties were found in the three-phase sample γ+β(B2)+Co_3W obtained by arc melting followed by a fast cooling. Annealing of this alloy at 1200°C-10h followed by quenching allows one to remove the Co_3W phase and to equalize the chemical composition of the alloy.

Acknowledgments

This study was supported financially by the Russian Fund for Basic Research No 14-08-00108.

References

1. J. Sato, et al., "Cobalt-base high-temperature alloys", *Science*, (2006), 312.90-91.
2. A. Suzuki, T.M. Pollock, "High-temperature strength and deformation of γ/γ′ two-phase Co-Al-W-base alloys", *Acta Materialia,* 56, (2008), 1288–1297.
3. N.V. Kazantseva, et al. "Phase transformations in nickel superalloy after shock-wave loading", *Physics of metal and metallography,* 99, (2005), 1-10.
4. N.N. Stepanova, et al., "Structure and magnetic properties of nickel heat-resistant alloy after high-temperature deformation", *Physics of metal and metallography,* 112, (2011), 328-336.
5. D.D. Mishin, *Magnetic materials*, (Moscow, M.: Vishaya skola, 1981), 335.
6. R. Rama, "The Co-W (Cobalt-Tungsten) system", *J. Alloy Phase Diagrams*, 2(1), (1986), 43-52.
7. N.P. Lyakishev, *Phase diagram of binary metal systems*, (Moscow, M: Mashinostroenie, 1996-2000), 32.
8. S. Kobayashi, "Determination of phase equilibria in the Co-rich Co–Al–W ternary system with a diffusion-couple technique", *Intermetallics*, 17, (2009), 1085-1089.
9. K. Ishida, et al., " Intermetallic Compounds in Co-Base Alloys - Phase Stability and Application to Superalloys", (Paper presented at Material Research Society Symposium, Boston, Massachusetts, November 3- December 4, 2009), 1128-U06-06.
10. G. Dmitrieva, V. Vasilenko, and I. Melnik, "Al–Co–W fusion diagram in the Co–CoAl–W part", *Chem. Met. Alloys,* (2008), 338-342.
11. G. Dmitrieva, T.S. Cherepova, and A.K. Shurin, "Phase equilibriums in the alloys of Co-CoAl-W system (P.1)", *Metallznavstvo ta obraoitka metali,* (2005), 3-6.
12. G. Dmitrieva, T.S. Cherepova, and A.K. Shurin, "Phase equilibriums in the alloys of Co-CoAl-W system (P.2)", *Metallznavstvo ta obraoitka metali,* (2006), 22-25.

Characterization of Minerals, Metals, and Materials 2015
Edited by: John S. Carpenter, Chenguang Bai, Juan Pablo Escobedo, Jiann-Yang Hwang, Shadia Ikhmayies, Bowen Li, Jian Li, Sergio Neves Monteiro, Zhiwei Peng, and Mingming Zhang
TMS (The Minerals, Metals & Materials Society), 2015

CHARACTERIZATION OF THE PHASE COMPOSITION OF NANOSIZED LITHIUM TITANATES SYNTHESIZED BY INDUCTIVE THERMAL PLASMA

François Quesnel[1], Gervais Soucy[1], Jocelyn Veilleux[1], Pierre Hovington[2], Wen Zhu[2], Karim Zaghib[2]

[1]Department of Chemical and Biotechnological Engineering, Université de Sherbrooke; 2500 Boulevard de l'Université; Sherbrooke, Qc, J1K 2R1, Canada,
[2]IREQ (Institut de recherche en électricité du Québec); 1800, boul. Lionel-Boulet; Varennes, Qc, J3X 1S1, Canada

Keywords: Lithium titanates, inductive thermal plasma, Rietveld refinement, $Li_4Ti_5O_{12}$, Li-ion batteries, X-Ray Diffraction (XRD), Differential Scanning Calorimetry (DSC)

Abstract

The properties of lithium titanates anodes in Li-ion batteries are highly dependent on their secondary constituents. While their main phase is usually constituted of $Li_4Ti_5O_{12}$, significant quantity of lithium titanates compounds of various stoichiometry are often present, due to either the processing, usage or aging of the material. These may go underreported, as many of these spectrums overlap or display low signal in X-ray diffraction (XRD). Samples of nanosized lithium titanates synthetized by inductive plasma were characterized by XRD and scanning electron microscopy (SEM), as they provide a regular yet typical crystallite size and shape including multiple phases. A Rietveld refinement was developed to extract the composition of these samples. Mass balance through further annealing and differential scanning calorimetry (DSC) enthalpy measurements from phase transformations were also used as identification and validation techniques.

Introduction

Lithium titanates have been studied as candidates for Li-ion anode material over the last two decades. $Li_4Ti_5O_{12}$ has demonstrated exceptional durability and safety features due to some of its rare characteristics such as the negligible strain during lithium insertion and its flat voltage profile [1]. Furthermore, the lack of a standard solid electrolyte interface (SEI) eases its use in nano sized format and power intensive applications. However, the full description of such material and their impurities can prove difficult.

The coexistence of multiple compounds in pseudo-binary mixtures restricts the characterization enabled by elemental analysis. The characterization of lithium titanates presents additional complexity, as many allotropes are present, the diffraction patterns of many major compounds overlap significantly and lithium presents both a weak response to X-rays and some volatility at annealing temperatures. The Rietveld method represents an interesting approach to solve these issues, should it be proven to be effective under these specific constraints.

The $Li_4Ti_5O_{12}$ spinel is typically produced by the annealing of TiO_2 (anatase) and Li_2CO_3 [2]. Depending on the temperature, the annealing duration, the stoichiometry and the quality of mixing in the reagents, some TiO_2 (anatase), TiO_2 (rutile), Li_2CO_3, $Li_2Ti_3O_7$, $Li_4Ti_5O_{12}$ and

Li_2TiO_3 may be present. Furthermore, aging reactions in-between the water or CO_2 present in air and the lithium rich surface of nanoparticles have been documented [3]. Even trace amount of these impurities can have significant impact on the functionalization of the material, as their electrical and ionic conductivities vary by many orders of magnitude [4]. Pure crystals of $Li_4Ti_5O_{12}$ spinel have been grown using flux [5] and pulsed laser deposition [6]. This determined that a plasma plume precursor can allow for a very high crystallinity while inductive plasma has also been demonstrated for the production of various lithium titanates nanoparticles in air plasma [7]. Hereby is presented the first report of nanoparticles of lithium titanates produced in an argon and helium plasma, which displays fairly regular shape and an intrinsic mixing. This type of plasma requires less energy than air plasma to achieve extremely high temperature, which could allow for better energy efficiency [8], while the variety and mixing achieved should help identify any blending and secondary effects. The product was characterized by SEM, DSC and XRD, to which Rietveld refinement was applied and validated through annealing. The effect of ball milling was also tested, as it constitutes a way to ensure proper mixing, yet it may distort the relative intensity of peaks, which represents one of the main ways to distinguish in-between $Li_4Ti_5O_{12}$ and β-Li_2TiO_3 in the diffraction pattern [9]. Hereby are also disclosed some of the first analysis towards the application of DSC as a high sensitivity tool in the identification of β-Li_2TiO_3 in $Li_4Ti_5O_{12}$ anodes.

Materials and methods

The exhaust from a 50 kW plasma torch (PS-50, TEKNA Plasma Systems) was injected in a water cooled reactor and filtering apparatus, as illustrated in Figure 1. These were operated under 40 kW, 66 kPa, with helium as the sheath gas and argon as the central and powder carrying gas. The solid reagents were TiO_2 (anatase) 99.9% and Li_2CO_3 99.9%, ball milled and sieved together and fed axially at 6 g/min.

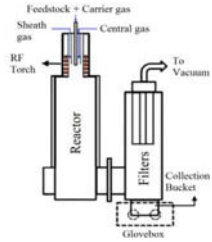

Figure 1. Experimental setup.

The material was kept under inert atmosphere to contain undesirable reactions. X-Ray diffraction was conducted using an X'pert Pro MRD device, under a Bragg-Brentano configuration with a CuK_α source. The Jade 10 software was employed for the Rietveld refinement. SEM imagery was completed with a metallized ethanol dispersion and a Hitachi S-4700 device, while the differential scanning calorimetry was completed under nitrogen atmosphere and a 10 °C/min heating ramp on a DSC 404 F3 Pegasus from Netzsch. The Table I identifies the plasma production runs.

Table I. Stoichiometry of the feedstock.

Identification of the test	Molar Ratio Li:Ti
A	0,8
B	1

The samples were ball milled for one and a half minute at a 30 Hz frequency in a Retsch MM300 device. Following a typical procedure, annealing was realized in air at 800°C.

Results

The produced material was sampled on the reactor walls (R) and in the filters (F) in tests A and B. The SEM imagery indicated a bimodal distribution, composed of nano sized, partly agglomerated and mostly spherical particles, ranging mostly from 20 nm to 100 nm. The presence of some residual partially vaporized spheres in the micrometers range was also noticed.

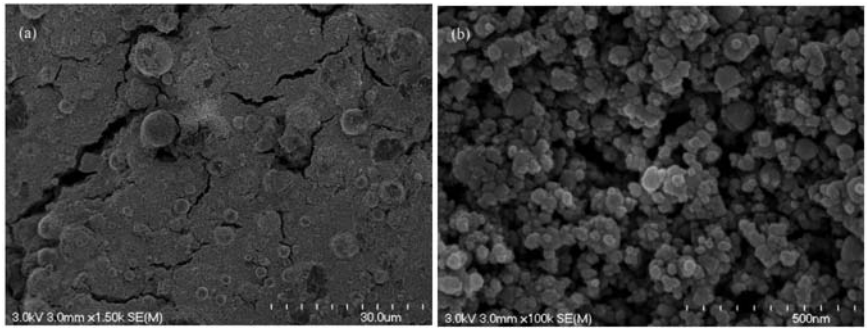

Figure 2. View at (a) 1500 X and (b) 100 000 X of Test A (R).

X-ray diffraction was then realized on four samples throughout four steps of processing: as produced, ball milled and annealed 2h and 8h. To minimize any sampling error, the same small specimen of material was followed throughout the processing for each sampled area. This small size also minimized the thermal inertia, but increased the relative volatility. Some partial results are shown in figure 3.

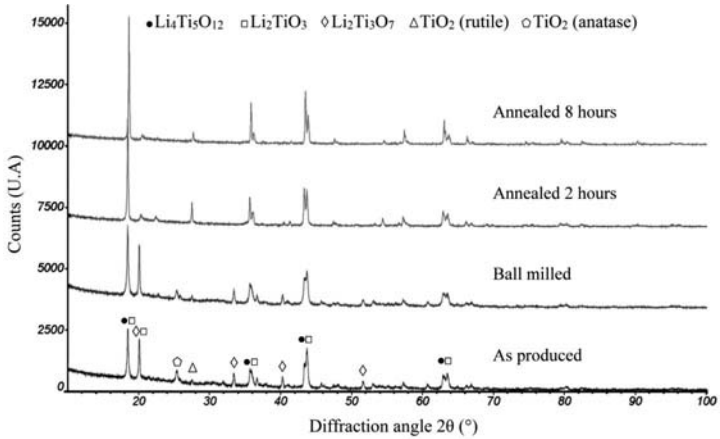

Figure 3. XRD patterns of the material from the test A (F); as produced, as milled and after annealing at 800°C.

These patterns were treated through the Rietveld refinement developed for that application. The main results are listed in table II & III and demonstrated how some reactions took place within the annealing process.

Table II. Quantification of test A through the Rietveld method.

	Test A (Reactor walls)				Test A (Filters)			
% Compound	Original	Milled	2h	8h	Original	Milled	2h	8h
$Li_4Ti_5O_{12}$	22,1	22,8	62,6	84,6	17,2	20,5	47,9	62,6
Li_2TiO_3	25,4	26,4	19,3	6,8	40,0	43,0	40,6	32,1
$Li_2Ti_3O_7$	36,6	38,3	0,6	0	25	24,8	0	0
TiO_2 (rutile)	3,4	3,8	17,5	8,6	1,9	2,3	11,5	5,3
Li_2CO_3	7,9	4,8	0	0	7,8	4,6	0	0
TiO_2 (anatase)	4,7	3,8	0	0	8,1	4,8	0	0
Residual (%)	12,94	11,72	13,13	13,66	12,36	10,81	13,68	13,70
E.s.d. (%)	6,01	4,11	6,06	6,00	6,07	4,05	5,60	5,96

Table III. Quantification of test B through the Rietveld method.

	Test B (Reactor walls)				Test B (Filters)			
% Compound	Original	Milled	2h	8h	Original	Milled	2h	8h
$Li_4Ti_5O_{12}$	27,7	29,1	46,0	56,5	28,6	29,8	44,1	53,8
Li_2TiO_3	42,6	41,0	39,3	32,8	48,3	50,2	49,1	42,8
$Li_2Ti_3O_7$	23,5	24,1	0	0	12,3	13	0	0
TiO_2 (rutile)	1,2	1,5	14,7	10,7	0,7	0,8	6,8	3,3
Li_2CO_3	5,1	4,4	0	0	6,9	4,6	0	0
TiO_2 (anatase)	0	0	0	0	3,1	1,6	0	0
Residual (%)	13,55	11,64	13,76	13,49	11,68	10,84	14,76	15,50
E.s.d. (%)	6,01	4,17	6,02	5,97	5,92	4,05	5,64	6,01

As illustrated in tables II& III, the ramsdellite was quickly consumed at 800°C, in a way that mainly appeared to correspond macroscopically to the following equations.

$$1\ Li_2Ti_3O_7 \rightarrow 2\ TiO_2\,(rutile) + 1\ Li_2TiO_3 \quad (1)$$

$$2\ Li_2Ti_3O_7 \rightarrow 1\ TiO_2\,(rutile) + 1\ Li_4Ti_5O_{12} \quad (2)$$

Similarly, the lithium carbonate reacted readily and the titanium oxide was subject to the phase transition from anatase to rutile [2].

$$2\ Li_2CO_3 + 5\ TiO_2 \rightarrow Li_4Ti_5O_{12} + 2\ CO_2 \quad (3)$$

$$Li_2CO_3 + TiO_2 \rightarrow Li_2TiO_3 + CO_2 \quad (4)$$

$$TiO_2\,(anatase) \rightarrow TiO_2\,(rutile) \quad (5)$$

The final reaction [2] appeared to be significantly slower under these conditions.

$$2\ Li_2TiO_3 + 3\ TiO_2\,(rutile) \rightarrow Li_4Ti_5O_{12} \quad (6)$$

These are supported by the evolution of the crystallite size, which also illustrated a lower crystallite size after milling for all phases. This quantification, based on Scherrer's equation, is illustrated in Figure 4. The error was estimated by the estimated standard deviation (e.s.d.), and it showcases that the effects are significant.

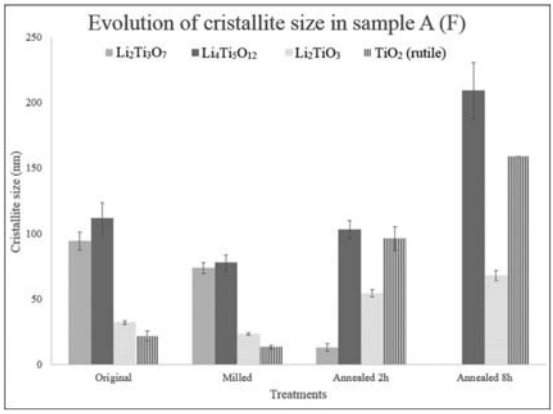

Figure 4. Crystallite size in sample from test A collected in the filters.

Mass balance was conducted on the treated sample to establish a true error evaluation to be compared with the e.s.d. evaluated by the software, as shown in table IV.

Table IV. Consecutive absolute errors in quantification.

Indicator	Milling	Annealed 2h	Annealed 8h
Averaged weight loss (%)	N/A	5.41	0.58
Consecutive averaged measured error (% Li_2O)	-0.35	0.84	-0.11
Consecutive sample standard deviation (% Li_2O)	0.48	1.84	0.44
Combined Software e.s.d. (% Li_2O)	0.31	0.28	0.30
P-value of the error estimates (*F*-test)	0.40	0.00034	0.43

The enthalpy of phase transition from β-Li_2TiO_3 to γ-Li_2TiO_3 was also evaluated through subtraction of a linear background, as it presented clear and relatively symmetrical peaks.

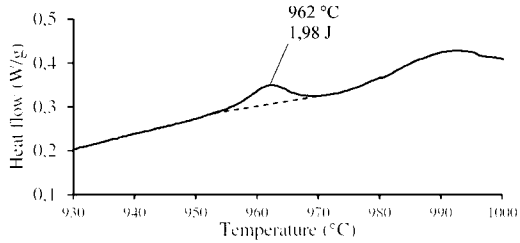

Figure 5. DSC measurement of phase transformation in the sample A (R).

This was computed with the enthalpy of phase transformation approximated from the equations proposed by Kleykamp [10]. These evaluations are summarised in table V.

Table V. Phase transition from β-Li_2TiO_3 to γ-Li_2TiO_3 by Differential Scanning Calorimetry.

Sample	Median temperature (°C)	Enthalpy (J·g-1)	Equivalence in β-Li_2TiO_3
Test A (R)	962	2,0	1,9 %
Test A (F)	963	22,6	21,8 %
Test B (R)	964	15,8	15,3 %
Test B (F)	966	14,2	13,7 %

Discussion

The analysis of plasma synthetized material presents a significant advantage in its spheroidal shape, which restrains the probability of preferential orientation and permits a regular packing. Notably, Li_2TiO_3 and rutile have been shown to display preferential orientation [4]. $Li_4Ti_5O_{12}$ has also been grown according to a few orientations [6]. Furthermore, the absence of amorphous humps is coherent with the high crystallinity expected from the plasma process. This improves the anticipated precision from the mass balance approach and facilitates the deconvolution by the Rietveld method, as the number of meaningful parameters is diminished. Yet, an extra level of care had to be taken in the selection of potentially interdependent variables, as they easily led to instability in the algorithm due to critical points representing false minimums. This composition appears particularly susceptible to errors resulting from averaged position values in-between Li_2TiO_3 and $Li_4Ti_5O_{12}$, correlation between displacement and asymmetry and induced enlargement of smaller peaks with significant redundancy. Despite that, the composition quantification of table IV depicts an underestimated error following the first annealing, which may be the consequence of unquantified lithium-rich phases, such as Li_2O.

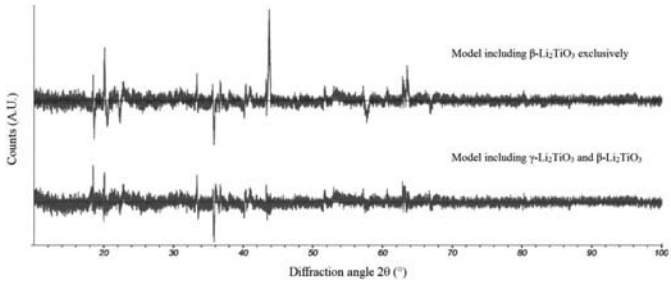

Figure 6. Residuals from the Rietveld refinements, from the sample A (F), as produced.

Some confusion remains in relation to the Li_2TiO_3 allotropes. While thermodynamics implies that γ-Li_2TiO_3, and possibly α-Li_2TiO_3, may have been present at the synthesis point, these would have been exposed to temperatures mostly ranging from 300°C to 900°C inside the reactor for the duration of the production run. This may have been sufficient to complete their transformation. As illustrated in Figure 6, limiting the Rietveld model to the presence of β-Li_2TiO_3 generated indications of high temperature γ-Li_2TiO_3 in the residual XRD pattern, but these were not conclusive. The γ-Li_2TiO_3 presents a pattern essentially covered by the β-Li_2TiO_3 phase, in which the minor diverging peaks present redundancy with other phases, and as such, the residual pattern can possibly be partly explained by preferred orientation and anisotropic broadening. Moreover, a two-phase model generates a diminution in residual, but is actually detrimental to the mass balance error measured. That statistical improvement is indeed partly related to an external phenomenon. It has been documented [11] that Li_2TiO_3 generated at high

temperature presents a large atypical asymmetric peak at 2θ angles between 20° and 25°. This pattern is visible in the samples collected. It is also worth noting that running the refinement with both β and γ phases returns a similar total amount of Li_2TiO_3, hence it cannot be discarded on the basis of the lithium mass balance. In the interest of a thorough investigation, the presence of the low temperature hexagonal $Li_2Ti_3O_7$ phase was scrutinized, nonetheless it was not identified.

The limited milling applied appears to have little effect over the measured composition from the X-ray diffraction, as it displays a level of variability in the Rietveld quantification within the range expected from the technique. That variability does present a pattern, as milling appears to lower the refined measurement over the quantity of the precursor materials Li_2CO_3 and anatase by an average of about 30%. Residual precursor materials are expected to be the result of partial vaporization and to be coarser than the bulk of the material. These should present a diameter under 80 μm as a result of sieving, but may be larger than 10 μm, as a result of the agglomeration of the soft lithium carbonate during grinding of the feedstock. This is not ideal as particles over 10 μm have been shown to induce micro absorption [9]. It would be reasonable to assume that the higher apparent density observed after the milling increases the relative visibility of the nano sized phase, as they varied in a similar proportion. This is supported by the data on the crystallite size, for it appears improbable that such short milling induced such important reduction in crystallite size.

Differential scanning calorimetry did confirm the presence of β-Li_2TiO_3, but the analysis engendered some significant margin of error. The phase transition can be partial and only occurs in presence of a TiO_2 rich phase, as the β-monoclinic phase possesses a low solid solubility and is otherwise stable until 1155°C. Some of the error margin may come from the deconvolution of the data, due to the slower kinetics of some reactions. These reactions also prove restricting, as some may consume or produce β-Li_2TiO_3, which explains part of the discrepancies observed in Table VI. However, it proves fortunate that the decompositions of $Li_4Ti_5O_{12}$ in $Li_2Ti_3O_7$ and γ-$Li_{i2}TiO_3$ is among these slower reactions [12], as some of these reactions share a similar temperature point with the monoclinic to cubic transition. Moreover, as the nanosized materials often present a high interstitial porosity, they may exhibit very low thermal conductivity, which can offset significantly the measured peaks.

Table VI. Comparative results in % β-Li_2TiO_3 between DSC and XRD.

Sample	DSC	Two phases Rietveld
Test A (R)	1,9	8,9
Test A (F)	21,8	16,0
Test B (R)	15,3	13,2
Test B (F)	13,7	21,0

Some marginal error was induced by the decomposition of Li_2CO_3 and, to a lesser extent, by the vaporization of lithium. Additionally, the incertitude on the referenced transition enthalpy is fairly important. Yet, it still appears that the DSC constitutes a very useful tool to detect the frequent impurities of β-Li_2TiO_3, as the method presents a high sensibility and this phase would usually be associated to $Li_4Ti_5O_{12}$ and TiO_2 (rutile), as a result from the kinetics of annealing.

Summary and conclusions

The Rietveld method can enable a proper quantification of lithium titanates, yet the usual approach for error estimation does sometimes underestimate the effective deviation. While

distinction between $Li_4Ti_5O_{12}$ and Li_2TiO_3 can be achieved to some level of accuracy, the distinction in-between allotropes of Li_2TiO_3 presents additional challenges in complex blends of lithium titanates. Limited ball milling of the plasma-produced sample was shown to have limited effect, relative to a higher apparent density and a proportionally reduced representation of the larger particles in the sample, while the volatility of Li_2O during annealing was shown to potentially have some significant effects.

DSC was demonstrated under a marked diversity of impurities as a powerful tool to identify the presence of β-Li_2TiO_3, as the distinctive peak from the phase transformation from β-Li_2TiO_3 to γ-Li_2TiO_3 is well marked, but further analysis would be required to improve its quantitative potential.

Acknowledgments

This research was enabled by the financial support of the Natural Sciences and Engineering Research Council of Canada (NSERC) and the Institut de Recherche en Électricité du Québec (IREQ). Special thanks are addressed to André Bilodeau for his contribution in the operation of the plasma reactor.

References

1. K. Zaghib, M. Dontigny, A. Guerfi et al., "Safe and fast-charging Li-ion battery with long shelf life for power applications," *J Power Sources*, 196 (8) (2011), 3949-3954.
2. Y. Shen, M. Søndergaard, M. Christensen, S. Birgisson, BB. Iversen, "Solid state formation mechanism of $Li_4Ti_5O_{12}$ from an anatase TiO_2 source," *Chem Mater.*, 26 (12) (2014), 3679-3686.
3. Y. Gao, Z. Wang, L. Chen, "Stability of spinel $Li_4Ti_5O_{12}$ in air," *J Power Sources,* 245 (0) (2014), 684-690.
4. Ģ. Vītiņš, G. Ķizāne, A. Lūsis, J. Tīliks, "Electrical conductivity studies in the system Li_2TiO_3-$Li_{1.33}Ti_{1.67}O_4$," *Journal of Solid State Electrochemistry*, 6 (5) (2002), 311-319.
5. K. Kataoka, Y. Takahashi, N. Kijima, J. Akimoto, K. Ohshima, "Single crystal growth and structure refinement of $Li_4Ti_5O_{12}$," *Journal of Physics and Chemistry of Solids*. 69 (5-6) (2008), 1454-1456.
6. M. Hirayama, K. Kim, T. Toujigamori, W. Cho, R. Kanno, "Epitaxial growth and electrochemical properties of $Li_4Ti_5O_{12}$ thin-film lithium battery anodes," *Dalton Transactions*, 40 (12) (2011), 2882-2887.
7. J. Grabis, A. Orlovs, D. Rasmane, "Nanosized lithium titanates produced by plasma technique," *Journal of Physics: Conference Series*, 93 (01) (2007), 012004.
8. MI. Boulos, "Thermal plasma processing," *IEEE Trans Plasma Sci.,* 19 (6) (1991) 1078-1089.
9. L. De Stefano, F. De Luca, G. Buccolieri, P. Plescia, "Milling effects upon quantitative determinations of chrysotile asbestos by the reference intensity ratio method," *Powder Diffraction,* 15 (01) (2000), 26-29.
10. H. Kleykamp "Phase equilibria in the Li–Ti–O system and physical properties of Li_2TiO_3," *Fusion Eng Des.* 61-62 (2002), 361-366.
11. U. Dash, S. Sahoo, P. Chaudhuri, S.K.S. Parashar, K. Parashar "Electrical properties of bulk and nano Li_2TiO_3 ceramics: A comparative study," *Journal of Advanced Ceramics,* 3 (2) (2014), 89-97.
12. A. Laumann, H. Boysen, M. Bremholm, K.T. Fehr, M. Hoelzel, M. Holzapfel, "Lithium migration at high temperatures in $Li_4Ti_5O_{12}$ studied by neutron diffraction," *Chemistry of Materials*, 23 (11) (2011), 2753–2759.

Characterization of Minerals, Metals, and Materials 2015
Edited by: John S. Carpenter, Chenguang Bai, Juan Pablo Escobedo, Jiann-Yang Hwang, Shadia Ikhmayies, Bowen Li, Jian Li, Sergio Neves Monteiro, Zhiwei Peng, and Mingming Zhang
TMS (The Minerals, Metals & Materials Society), 2015

IMPROVED HYDROGEN STORAGE PROPERTIES OF $Mg(BH_4)_2$-$Mg(AlH_4)_2$ COMBINED SYSTEMS

Haoyuan Xiao, Haiyan Leng, Zhigang Yu, Qian Li, Kuo-Chih Chou*
Shanghai Key Laboratory of Modern Metallurgy & Materials Processing, Shanghai University, Shanghai 200072, China,

Keywords: Hydrogen storage properties, Magnesium borohydride, Magnesium alanate

Abstract

Magnesium borohydride and Magnesium alanate were synthesized by mechanochemical metathesis reaction. The thermal decomposition behaviors of $Mg(BH_4)_2$-n$Mg(AlH_4)_2$(n=0.5,1) systems were investigated as potential hydrogen storage materials. The results showed that the systems started to desorb H_2 at 120 ℃ and desorbed 3.9 wt.% and 4.9 wt.% H_2 below 300 ℃ when n equals 0.5 and 1, respectively, while individual $Mg(BH_4)_2$ started to desorb H_2 at 250 ℃ and desorbed only 0.82 wt.% H_2. Because of the exist of the $Mg(AlH_4)_2$, the isothermal desorption kinetics of $Mg(BH_4)_2$ in the $Mg(BH_4)_2$-0.5$Mg(AlH_4)_2$ systems was 50% faster than that of pristine $Mg(BH_4)_2$. In addition, the re-hydrogenation rates also increased 49.4% and 37.9%.

Introduction

Hydrogen energy is known as the green energy carrier in the 21st century because of its abundant resources and high energy density. In order to promote the application of hydrogen energy, a safe, efficient and economic way for hydrogen storage is crucial. In recent years, metal borohydrides have attracted considerable interest as one of the best potential hydrogen storage materials due to their high gravimetric and volumetric hydrogen capacities[1-5]. Among the metal borohydrides, magnesium borohydride, for its relatively high gravimetric hydrogen capacity (14.9 wt.%), volumetric hydrogen densities (112 kg/m^3) and the relatively low decomposition temperature (285 ℃)[6], has been regarded as a promising candidate for practical hydrogen storage.

Over the past few years, many studies have been given to the combination of $Mg(BH_4)_2$ and some other light metal hydrides, in order to improve its hydrogen storage properties. Yang et al.[7] has reported that the sample of $Mg(BH_4)_2$-$LiAlH_4$ in the mole ratio of 1:2 started decomposing at ca. 120 ℃ and released 11.0 wt.% H_2 at 600 ℃, which was improved significantly compared with pure $Mg(BH_4)_2$. At the same time, the combined system in the mole ratio of 1:2 was able to desorb 6.0 wt.% H_2 below 300 ℃, while pure $Mg(BH_4)_2$ just began to decompose. However the improvement was ascribed to the metathesis reaction took place during the milling time (Eq.(1)), and the hydrogenation efficiency of the $Mg(BH_4)_2$-2$LiAlH_4$ system at an initial H_2 pressure of 100 bar and 300 ℃ reached 87%, mainly because of the re-generated $LiBH_4$ and MgH_2 by hydrogenation, but $Mg(BH_4)_2$ is also partially reversible.

$$Mg(BH_4)_2+2LiAlH_4 \rightarrow Mg(AlH_4)_2+2LiBH_4 \quad (1)$$

Among the group of alkali and alkali-earth metal alanates, $Mg(AlH_4)_2$ has very high theoretical hydrogen capacity (9.3 wt.%) and rather low decomposition temperature (< 150℃)[8].

$Mg(AlH_4)_2$ was first synthesized by direct wet chemical synthesis in 1950s by Wiberg and Bauer[9] and its thermal decomposition behavior was reported as follows (Eqs. (2) and (3)).

$$Mg(AlH_4)_2 \rightarrow MgH_2 + 2Al + 3H_2 \quad (2)$$

$$MgH_2 + 2Al \rightarrow \frac{1}{2}Al_3Mg_2 + \frac{1}{2}Al + H_2 \quad (3)$$

On the other hand, the presence of Al can destabilize the decomposition of $LiBH_4$ by means of the formation of AlB_2 phases in the dehydrogenation process[10]. Moreover, in situ formed Al or Al alloy was reported to be better in improving the hydrogen storage properties than the added Al particles[11]. At the same time, Jiang et al.[12] found that the different Al-sources from $LiAlH_4$ exhibit a similar improving effect on the dehydrogenation properties of $Mg(BH_4)_2$.

Herein, a binary system of $Mg(BH_4)_2$-$Mg(AlH_4)_2$ was designed and prepared by ball milling. The dehydrogenation properties of the composites were systematically investigated, and the reversible hydrogen storage property was also discussed in this article.

Experimental details

The source materials of $NaAlH_4$ (95%, J&K), $NaBH_4$ (98%, Alfa-Aesar) and $MgCl_2$ (99%, Alfa-Aesar) were obtained commercially. $Mg(BH_4)_2$ was synthesized by direct wet chemical synthesis from $NaBH_4$ and $MgCl_2$ based on reaction (4) and diethyl ether was used as a solvent[13].

$$2NaBH_4 + MgCl_2 \rightarrow Mg(BH_4)_2 + 2NaCl \quad (4)$$

$$MgCl_2 + 2NaAlH_4 \rightarrow Mg(AlH_4)_2 + 2NaCl \quad (5)$$

A mixture of $NaBH_4$ and $MgCl_2$ (in a molar ratio of 3:1) was ball-milled in diethyl ether at a rate of 400 rpm for 24 h in a planetary ball mill. A further desolvation under vacuum was conducted at 160 ℃ for 12 h followed by treatment at 220 ℃ for 3 h in order to remove the diethyl ether completely. $Mg(AlH_4)_2$ was synthesized with the mixture of $NaAlH_4$ and $MgCl_2$ in the molar ratio of 2:1 based on reaction (5) at a rate of 400 rpm for 4 h in a planetary ball mill. Although the reaction product contains a significant amount of inert salt as by-product, it does not contain any solvent adduct which can strongly influence on the thermal decomposition behavior of $Mg(AlH_4)_2$. The mixtures of $Mg(BH_4)_2$-$Mg(AlH_4)_2$ with a mole ratio of 1:0.5 and 1:1 were mechanically milled at 100 rpm for 1 h (FRITSCH-P4) under argon atmosphere with a ball-to-power ratio of 20:1. The stainless steel balls were 8 mm in diameter. All handling was performed in a glove box (MBRAUN) filled with high purity argon atmosphere where the water and oxygen concentrations were kept below 0.1 ppm.

The temperature-programmed desorption (TPD), kinetic properties, and reversibility were measured by a volumetric method using an automatic apparatus from SUZUKI HOKAN.CO., LTD. The sample was heated up to 500 ℃ at a heating rate of 5 ℃/min in a reactor initially under vacuum for the TPD measurements. In order to study the reversibility of the samples, the ball milled samples were dehydrogenated at 350 ℃ for 2 h, and then were hydrogenated at the same temperature with an initial hydrogen pressure of 4 MPa for 2 h.

Results and discussion

In the previous study[14], magnesium alanate was synthesized via a metathesis reaction of $NaAlH_4$ and $MgCl_2$ in a solvent such as diethyl ether or THF. However, it was not succeeded in preparing a pure product[15], and instead of using a solvent as ion carrier to promote chemical reaction, a high energy ball milling method was adopted without any solvent. NaCl was not removed because it doesn't have any effect on the mixtures.

XRD patterns and FTIR spectrum of the as-milled $Mg(BH_4)_2$-$nMg(AlH_4)_2$(n=0.5,1) systems are shown in Figures 1 and 2, respectively. It can be seen that only $Mg(AlH_4)_2$ and NaCl were detected by XRD, moreover, no pressure changed during the ball milling, indicating that no reaction occurred during ball milling. FTIR results of $Mg(BH_4)_2$-$nMg(AlH_4)_2$(n=0.5,1) showed the B-H stretching bands in the region between 2450 cm^{-1} and 2220 cm^{-1}, and the B-H bending bands at 1120 cm^{-1}, indicating that $Mg(BH_4)_2$ became amorphous phase during the ball milling. There also existed the Al-H stretching bands at 1837 cm^{-1} and the Al-H bending bands at 642 cm^{-1}[8,16]. The peaks at 1640 cm^{-1} could be attributed to the water molecules present in the atmosphere of the sample capsule during the FTIR measurement process. These results clearly show that no reaction occurred between $Mg(BH_4)_2$ and $Mg(AlH_4)_2$ during ball milling.

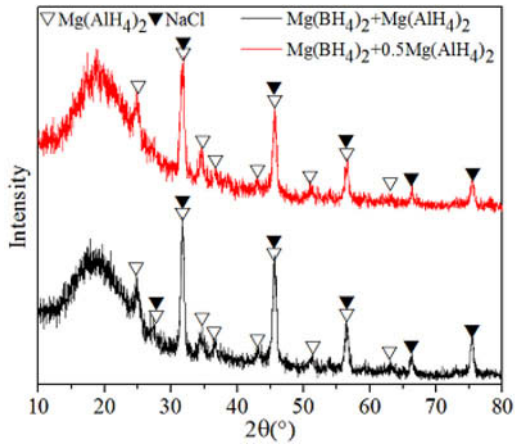

Figure 1. XRD patterns of the as-milled $Mg(BH_4)_2$-$nMg(AlH_4)_2$(n=0.5,1) systems.

TPD curves of the $Mg(BH_4)_2$-$nMg(AlH_4)_2$(n=0.5,1) combined systems are shown in Figure 3. For comparison, the synthesized $Mg(BH_4)_2$ and $Mg(AlH_4)_2$ are also shown. In order to eliminate the effect of NaCl by-product on the decrease of the dehydrogenation weight, we only take into account the mass of the materials which can desorb hydrogen. It can be seen all the combined systems show stepwise dehydrogenation behaviors. Individual $Mg(AlH_4)_2$ decomposes corresponding to the reactions (2) and (3)[17] and individual $Mg(BH_4)_2$ starts to desorb hydrogen at around 250 ℃, corresponding to the decomposition of $Mg(BH_4)_2$ to MgH_2 and B; and the MgH_2 decomposes at 390 ℃[4]. For $Mg(BH_4)_2$-$nMg(AlH_4)_2$(n=0.5,1) system, the first stage started at around 110 ℃, which is almost the same as $Mg(AlH_4)_2$. About 3.0 wt.% and 4.2 wt.% H_2 were desorbed for $Mg(BH_4)_2$-$nMg(AlH_4)_2$ systems at this stage for n=0.5 and 1, respectively.

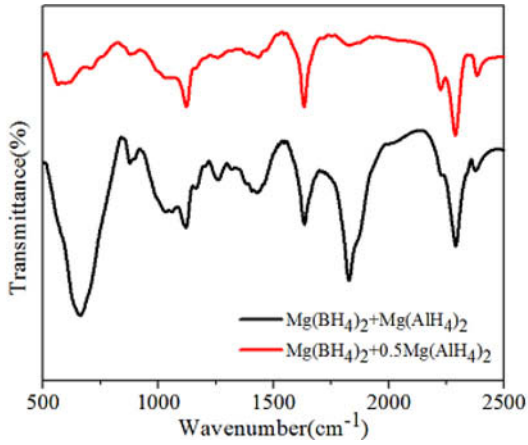

Figure 2. FTIR spectrum of the as-milled $Mg(BH_4)_2$-n$Mg(AlH_4)_2$(n=0.5,1) systems.

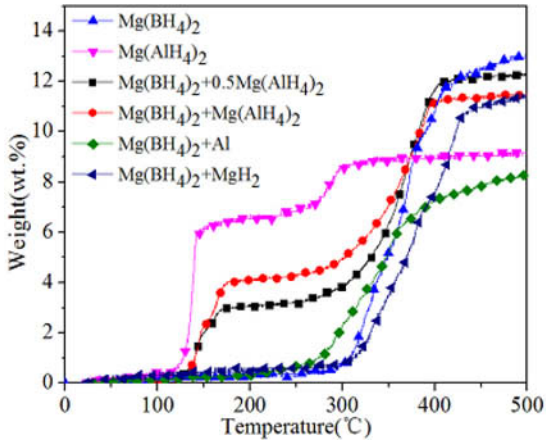

Figure 3. TPD curves of the $Mg(BH_4)_2$-n$Mg(AlH_4)_2$(n=0.5,1) combined systems.

The second dehydrogenation stage of $Mg(BH_4)_2$-0.5$Mg(AlH_4)_2$ started at ca. 250 ℃, and ended at ca. 410 ℃. The second dehydrogenation stage of $Mg(BH_4)_2$-$Mg(AlH_4)_2$ system also started at ca. 250 ℃, and ended at ca. 390 ℃, which was slightly lower than $Mg(BH_4)_2$-0.5$Mg(AlH_4)_2$ composite. When the temperature reached 500 ℃, the total desorbed H_2 was 12.3 wt.% and 11.4 wt.% for $Mg(BH_4)_2$-n$Mg(AlH_4)_2$ systems with n=0.5 and 1, respectively, a little lower than that of as-synthesized $Mg(BH_4)_2$. However, the composites can desorb about 3.9 wt.% and 4.9 wt.% H_2 when n=0.5 and 1 below 300 ℃, respectively, while the pristine $Mg(BH_4)_2$ can only desorb 0.82 wt.% H_2.

The desorption rate is an important property of hydrogen storage materials for the practical application. Figure 4 shows the isothermal dehydrogenation results for the $Mg(BH_4)_2$-n$Mg(AlH_4)_2$(n=0.5,1) composites compared with pure $Mg(BH_4)_2$ at 350 ℃ within 4000s. It can be seen that the $Mg(BH_4)_2$-n$Mg(AlH_4)_2$(n=0.5,1) systems release about 9.6 wt.% and 8.5 wt.%

H_2 with n=0.5 and 1, reached 76.6% and 73.5% of their theoretical hydrogen storage content, respectively, while the individual $Mg(BH_4)_2$ release 8.5 wt.%, only reached 57.2% of its theoretical hydrogen storage content.

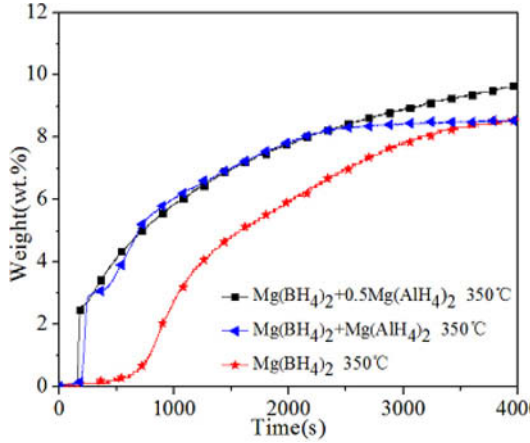

Figure 4. Isothermal desorption kinetics of the $Mg(BH_4)_2$-$nMg(AlH_4)_2$(n=0.5,1) composites.

In order to analyze the effect of $Mg(AlH_4)_2$ on the improvement of $Mg(BH_4)_2$, we eliminate the contribution of $Mg(AlH_4)_2$ on the total hydrogen desorption content. We regard the total isothermal dehydrogenation contents deduct the isothermal dehydrogenation content of the individual $Mg(AlH_4)_2$ as the isothermal desorption weight of $Mg(BH_4)_2$ in the $Mg(BH_4)_2$-$nMg(AlH_4)_2$(n=0.5,1) systems. As shown in Figure 5, it can be seen that at the initial time, $Mg(BH_4)_2$ in the $Mg(BH_4)_2$-$nMg(AlH_4)_2$(n=0.5,1) systems started dehydrogenation, about 500 seconds earlier than pure $Mg(BH_4)_2$. At the same time, in the $Mg(BH_4)_2$-$nMg(AlH_4)_2$(n=0.5,1) composites, $Mg(BH_4)_2$ can desorb 7.35 wt.% and 5.56 wt.% H_2 with n=0.5 and 1, respectively, indicating that 87.5% and 95.9% $Mg(BH_4)_2$ has been decomposed at this temperature within 4000s. For pure $Mg(BH_4)_2$, only 57.2% $Mg(BH_4)_2$ decomposed. The hydrogen dehydrogenation rates of $Mg(BH_4)_2$ calculated in the $Mg(BH_4)_2$-$nMg(AlH_4)_2$(n=0.5,1) systems are significantly improved by about 52.4% and 67.7% higher than that of individual $Mg(BH_4)_2$ for n=0.5 and 1, respectively.

The reversibility of the $Mg(BH_4)_2$-$nMg(AlH_4)_2$(n=0.5,1) systems were also investigated. The samples were re-dehydrogenated at 350 ℃ for 2 h under 4 MPa hydrogen. XRD patterns of the re-hydrogenated products (Figure 6) show that MgH_2 and Al are re-generated. The isothermal hydrogenation curves of the samples were shown in Figure 7. The results showed that the Mg-Al alloy indeed turned into MgH_2 and Al. At the same time, it can be seen that the hydrogen absorption process of the $Mg(BH_4)_2$-$nMg(AlH_4)_2$(n=0.5, 1) composites almost ended in 2635s and 3235s, respectively, while the time is 5211s for pristine $Mg(BH_4)_2$. The hydrogen absorption rates of the $Mg(BH_4)_2$-$nMg(AlH_4)_2$(n=0.5, 1) systems increased by about 49.4% and 37.9%, respectively.

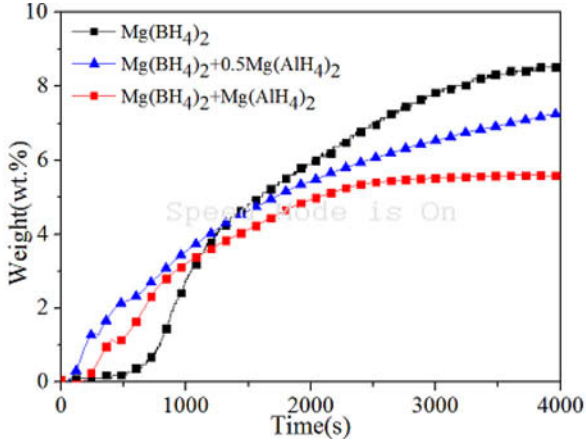

Figure 5. Isothermal desorption kinetics of $Mg(BH_4)_2$ in different composites.

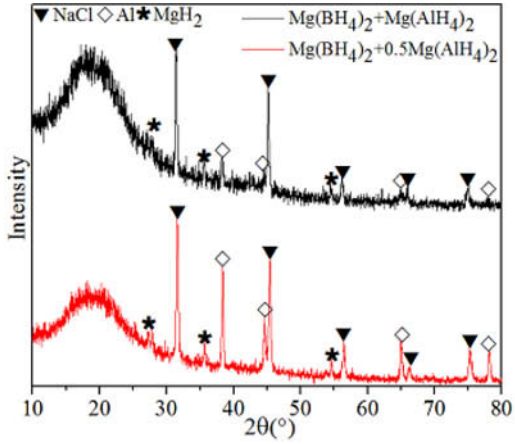

Figure 6. XRD patterns of the re-hydrogenated products.

In order to clarify the effect of MgH_2 and Al on the decomposing of $Mg(BH_4)_2$, we also prepared the samples of $Mg(BH_4)_2$-MgH_2, $Mg(BH_4)_2$-Al. As shown in Figure 3, the onset dehydrogenation temperature of $Mg(BH_4)_2$-Al is about 200 ℃, much lower than those of $Mg(BH_4)_2$-MgH_2 and $Mg(BH_4)_2$, which decompose at 290 ℃ and 250 ℃, respectively, indicating that the existence of MgH_2 is adverse to the decomposition of $Mg(BH_4)_2$. Furthermore, as can be seen from the slope of the TPD curves of the three samples, the slope of $Mg(BH_4)_2$-Al sample is the largest, which indicated that the desorption kinetic improvement of the samples contributes to the effect of Al but MgH_2. Similarly to the $LiBH_4$ systems destabilized by Al[10,18-19], the $Mg(BH_4)_2$-$nMg(AlH_4)_2$(n=0.5, 1) systems probably also formed AlB_2 which needs much less energy to break the Al-B bonding than that of the B-B bonding in the bulk B although AlB_2 was not observed during the reaction. However, the existence of MgH_2 may cause

the H-H exchange in the $Mg(BH_4)_2$-MgH_2 composites during the heating which would also suppress the desorption of hydrogen[20].

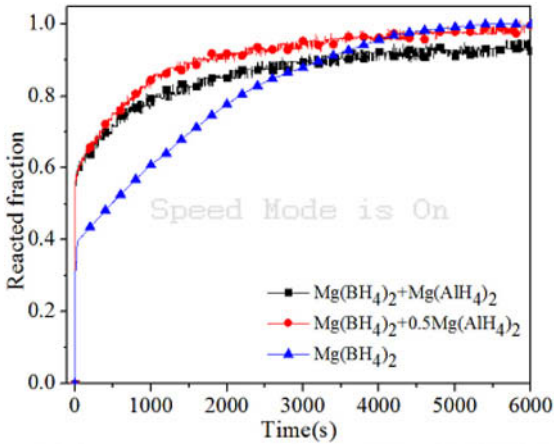

Figure 7. Isothermal hydrogenation curves of the $Mg(BH_4)_2$-$nMg(AlH_4)_2$(n=0.5,1) systems.

Conclusions

The borohydride-alanate combined systems, $Mg(BH_4)_2$-$nMg(AlH_4)_2$(n=0.5,1) were prepared by ball milling, and the hydrogen storage properties and mechanisms were investigated systematically. The ball milled $Mg(BH_4)_2$-$nMg(AlH_4)_2$(n=0.5,1) mixtures exhibited superior dehydrogenation properties compared with the pristine $Mg(BH_4)_2$. The onset dehydrogenation temperature of $Mg(BH_4)_2$-$nMg(AlH_4)_2$(n=0.5,1) systems is about 120 ℃, which is much lower than that of pristine $Mg(BH_4)_2$. About 3.9 and 4.9 wt.% H_2 can be desorbed from $Mg(BH_4)_2$-$nMg(AlH_4)_2$(n=0.5,1) composites below 300 ℃, respectively, while only 0.82 wt.% H_2 can be desorbed from individual $Mg(BH_4)_2$. The desorption kinetics of the $Mg(BH_4)_2$-$nMg(AlH_4)_2$(n=0.5,1) mixtures are improved by about 52.4% and 67.7%, respectively, compared with that of individual $Mg(BH_4)_2$. At the same time, the re-hydrogenation rates are also increased by 49.4% and 37.9%.

Acknowledgements

The authors thank Instrumental Analysis and Research Center of Shanghai University for their support of materials testing and research. This work was financially sponsored by the National Natural Science Foundation of China (51222402, 21071149), "Shu Guang" project supported by Shanghai Municipal Education Commission, Shanghai Education Development Foundation (13SG39) and the Science and Technology Committee of Shanghai (138014012).

References

1. Orimo S-I et al., "Complex hydrides for hydrogen storage," *Chemical Reviews*, 10(107)(2007), 4111-4132.
2. Li H-W et al., "Recent progress in metal borohydrides for hydrogen storage," *Energies*, 1(4)(2011), 185-214.

3. Züttel A et al., "Hydrogen storage properties of $LiBH_4$, " *Journal of Alloys and Compounds*, 356(2003), 515-520.
4. Chlopek K et al, "Synthesis and properties of magnesium tetrahydroborate, $Mg(BH_4)_2$," *Journal of Materials Chemistry*, 33(17)(2007), 3496-3503.
5. Kim J-H et al., "Thermal decomposition behavior of calcium borohydride $Ca(BH_4)_2$," *Journal of Alloys and Compounds*, 1(461)(2008), L20-L22.
6. Soloveichik G et al, "Magnesium borohydride as a hydrogen storage material: Properties and dehydrogenation pathway of unsolvated $Mg(BH_4)_2$," *International Journal of Hydrogen Energy*, 2(34)(2009), 916-928.
7. Yang Y J et al., "Multi-hydride systems with enhanced hydrogen storage properties derived from $Mg(BH_4)_2$ and $LiAlH_4$," *International Journal of Hydrogen Energy*, 14(37)(2012), 10733-10742.
8. Kim Y et al., "Mechanochemical synthesis and thermal decomposition of $Mg(AlH_4)_2$," *Journal of Alloys and Compounds*, 1(422)(2006), 283-287.
9. Barbaracs G et al., "The Preparation of the Hydrides of Zinc, Cadmium, Beryllium, Magnesium and Lithium by the Use of Lithium Aluminum Hydride," *Journal of the American Chemical Society*, 10(73)(1951), 4585.
10. Kang X D et al., "Reversible hydrogen storage in $LiBH_4$ destabilized by milling with Al," *Applied Physics A*, 4(89)(2007), 963-966.
11. Liu D et al., "Superior hydrogen storage properties of $LiBH_4$ catalyzed by $Mg(AlH_4)_2$," *Chemical Communications*, 20(47)(2011), 5741.
12. Jiang J et al., "Effect of Al on the hydrogen storage properties of $Mg(BH_4)_2$," *International Journal of Hydrogen Energy*, 25(38)(2013), 10919-10925.
13. Soloveichik G L et al., "Magnesium borohydride as a hydrogen storage material: Synthesis of unsolvated $Mg(BH_4)_2$," *International Journal of Hydrogen Energy*, 5(34)(2009), 2144-2152.
14. Fichtner M et al., "The Structure of Magnesium Alanate," *Inorganic Chemistry*, 22(42)(2003), 7060-7066.
15. Fichtner M and Fuhr O, "Synthesis and structures of magnesium alanate and two solvent adducts," *Journal of Alloys and Compounds*, 345(2002), 286.
16. Yuan F et al., "Structure and hydrogen storage properties of the first rare-earth metal borohydride ammoniate: $Y(BH_4)_3{\cdot}4NH_3$," *Journal of Materials Chemistry*, 3(22)(2012), 1061.
17. Fossdal A et al., "Determination of the crystal structure of $Mg(AlH_4)_2$ by combined X-ray and neutron diffraction," *Journal of Alloys and Compounds*, 2(387)(2005), 47-51.
18. Jin S-A et al., "Reversible hydrogen storage in $LiBH_4$–Al–LiH composite powder," *Scripta Materialia*, 11(58)(2008), 963-965.
19. Yang J, Sudik A and Wolverton C, "Destabilizing $LiBH_4$ with a Metal (M= Mg, Al, Ti, V, Cr, or Sc) or Metal Hydride (MH_2= MgH_2, TiH_2, or CaH_2)," *The Journal of Physical Chemistry C*, 51(111)(2007), 19134-19140.
20. Zeng L et al., "Superior Hydrogen Exchange Effect in the MgH_2– $LiBH_4$ System," *The Journal of Physical Chemistry C*, 30(114)(2010), 13132-13135.

Characterization of Minerals, Metals, and Materials 2015
Edited by: John S. Carpenter, Chenguang Bai, Juan Pablo Escobedo, Jiann-Yang Hwang, Shadia Ikhmayies, Bowen Li, Jian Li, Sergio Neves Monteiro, Zhiwei Peng, and Mingming Zhang
TMS (The Minerals, Metals & Materials Society), 2015

OPTICAL PARAMETERS OF $CdS_{1-y}Te_y$ THIN FILMS

Shadia J. Ikhmayies

Al Isra University, Faculty of Information Technology, Department of Basic Sciences-Physics, Amman 11622, Jordan.

Keywords: $CdS_{1-x}Te_x$ solid solution, thin films, solar cells, optical parameters

Abstract

CdS_xTe_{1-x} and $CdS_{1-y}Te_y$ solid solutions are usually formed in the interfacial region in the CdS/CdT thin film solar cells during the deposition of the CdTe layer and/or the processing steps of the device. It is well known that $CdCl_2$ heat treatment encourages the formation of the CdS_xTe_{1-x} alloy which improves the solar cell performance. In this work, indium doped $CdS_{1-y}Te_y$ thin films are produced by first producing CdS:In thin films by the spray pyrolysis (SP) technique on glass substrates, then annealing the films in nitrogen atmosphere in the presence of elemental tellurium. The films are characterized by scanning electron microscopy (SEM), energy dispersive X-ray spectroscopy (EDS), and transmittance measurements. The transmittance is used to deduce the optical parameters such as; the extinction coefficient, refractive index, besides to the real and imaginary parts of the dielectric constant. The dispersion parameters such as E_o (single-oscillator energy) and E_d (dispersive energy) of the deposited films are also estimated and discussed.

Introduction

Polycrystalline thin film CdS/CdTe solar cells are promising candidates for low cost and high efficiency photovoltaic applications. The fabrication process of these cells involves the deposition of a p-type CdTe absorber layer on top of an n-type CdS one which acts as a window. To improve the conductivity of the window layer it is recommended to dope it with certain dopants such as indium. During the fabrication of the CdTe layer and/or during the post deposition heat treatment of the device interdiffusion of CdS and CdTe at the CdS/CdTe junction takes place. The results of this process are the formation of a CdS_xTe_{1-x} layer, which is Te rich on the CdTe side and a $CdS_{1-y}Te_y$ layer, which is CdS rich on the CdS side. These interdiffusion processes have largely been realized to significantly improve the device performance, where they modify the spectral response of the solar cell. That is, a 10% lattice mismatch exists between CdS and CdTe, which should generates a large density of defects [1], and produces strain at the CdS/CdTe interface [2]. Intermixing at the CdS/CdTe interface is expected to reduce the effect of lattice mismatch, and then it relieves strain, reduces the number of interfacial states, and reduces the number of recombination centers [3], thus enhancing the solar cell performance. Hence a complete understanding of the compositional, structural, electrical, and optical properties of the intermixed layers CdS_xTe_{1-x} and $CdS_{1-y}Te_y$ that usually constitutes the interfacial region in the CdS/CdTe solar cell is essential.

Thin films of CdS_xTe_{1-x} and $CdS_{1-y}Te_y$ have been deposited by different methods, such as thermal evaporation [4,5], pulsed electrodeposition [6], brush plating [7] closed space sublimation [8], and spray pyrolysis technique (SP) [3,9]. In this work, $CdS_{1-y}Te_y$ thin films were prepared by first producing CdS:In thin films by the spray pyrolysis technique, then annealing

them in nitrogen atmosphere in the presence of tellurium vapor, because this method is easy, cheap, and it enables the production of large area films. The aims of this work are to produce $CdS_{1-y}Te_y$ thin films, deduce the optical parameters of the films such as the extinction coefficient, refractive index, and the real and imaginary parts of the dielectric constant, and to study the dependence of these parameters on composition of the films.

Experimental Procedure

Polycrystalline indium doped cadmium sulfide (CdS:In) thin films were first deposited onto glass substrates with the spray pyrolysis technique by using a precursor solution formed from stoichiometric ratios of thiourea ($(NH_2)_2$) and the hydrated cadmium chloride ($CdCl_2.H_2O$) dissolved in distilled water with indium chloride ($InCl_3$) as a doping compound. To produce $CdS_{1-y}Te_y$ films, the CdS:In thin films were annealed in nitrogen atmosphere in the presence of elemental tellurium. Different ratios of tellurium in the films were obtained by changing the period of annealing. A double beam Shimadzu UV 1601 (PC) spectrophotometer was used to measure the transmittance of the films with respect to a piece of glass similar to the substrates. The microstructure of the films was determined by scanning electron microscopy (SEM), and the composition was determined by energy dispersive X-ray spectroscopy (EDS). SEM observations and EDS analysis were taken by FEI scanning electron microscope (Inspect F 50) which is supported by energy dispersive X-ray spectroscopy. The thickness of the films was determined before annealing by using transmittance and Lambert law of absorption in a semiconductor.

Results and Discussion

A set of $CdS_{1-y}Te_y$ thin films of comparable thickness and different tellurium content were produced. The thickness and composition y of the films were inserted in table I, where y = [Te]/([S]+[Te]), where [Te] and [S] refer to the concentrations of Te and S in the films respectively obtained from the EDS reports. The films were doped with indium In, because the window layer is usually doped with a certain dopant such as indium to increase its conductivity, which means that the solid solution will be doped with the same dopant. The percentage ratios of the concentration of indium to that of cadmium ([In]/[Cd])% in the solution and in the films are listed in table I.

Table I The thickness t, composition y, and ratios of indium to cadmium concentrations in the precursor solution and in the films respectively.

t(nm)	$y \times 10^{-2}$	([In] /[Cd]) % in the solution	([In]/[Cd])% in the film
500	0	1.5	3.31±0.34
490	3.49±1.68	1.5	2.98±0.20
465	8.52±6.41	1.5	3.84±0.63
420	9.97±9.21	0.1	2.75±1.88
460	10.02±8.27	0.0055	3.08±1.24

Figure 1 displays the SEM micrographs of a CdS:In film and $CdS_{1-y}Te_y$ films of comparable thickness but different composition. The difference between the morphologies of the CdS:In film and the $CdS_{1-y}Te_y$ films is apparent, where the grains of the CdS:In film are large (100–200nm) and obvious, and the film appears to be compact and uniformly covered with material. On the other hand, the surfaces of the $CdS_{1-y}Te_y$ films appear to consist of smaller grains and aggregates of smaller grains, and they contain some pores.

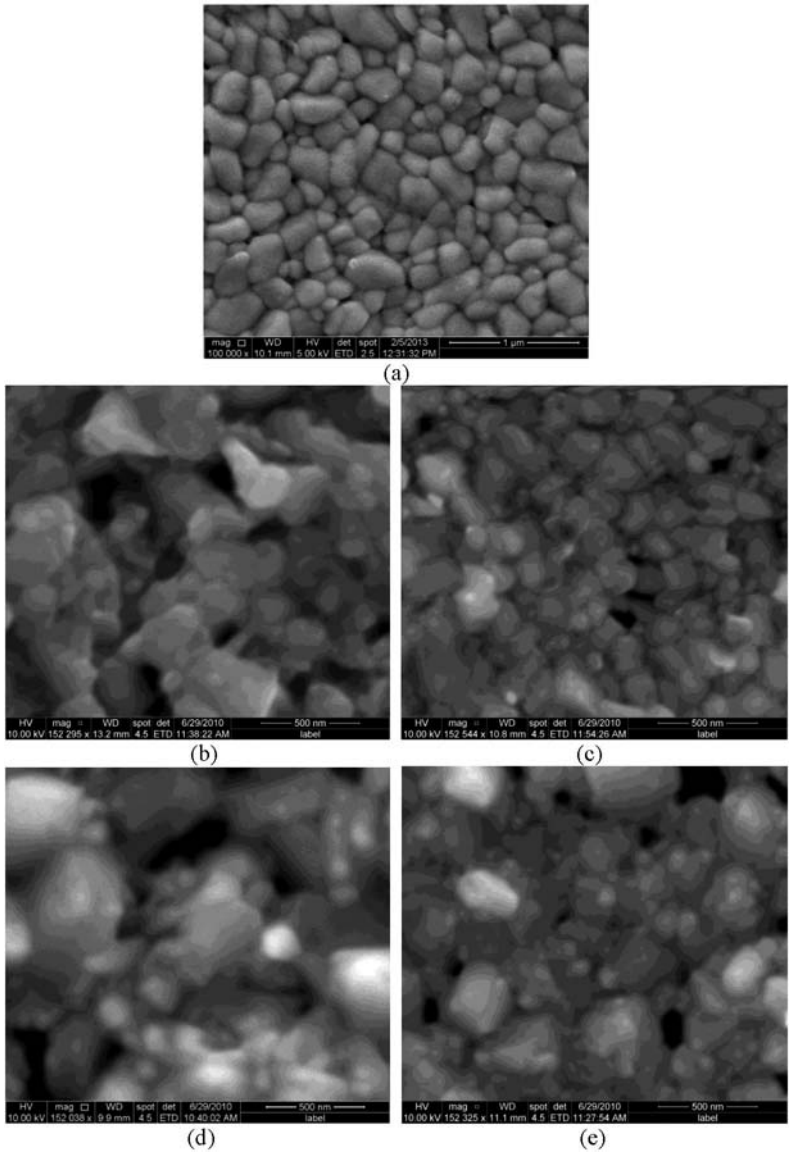

Figure 1. The SEM micrographs of $CdS_{1-y}Te_y$ thin films for y = 0.0 (CdS:In) (a), $y = 3.49\times10^{-2}$ (b), $y = 8.52\times10^{-2}$ (c). $y = 9.97\times10^{-2}$ (d), and $y = 10.02\times10^{-2}$ (e). Note: In (a) the scale is 1 μm, but from (b) to (e) it is 500 nm.

To explore the optical parameters of the films, the transmittance was recorded at room temperature in the wavelength range 290–1100 nm and displayed as a function of wavelength λ

in Figure 2. As the figure shows, the highest transmittance is that of the CdS:In film, and it decreases with y. In addition, it is obvious from the figure that the absorption edge shifts towards the side of longer wavelength, and its sharpness decreases with y. These observations can be interpreted by comparing the band gaps of CdS:In (2.5 eV) and CdTe (1.5 eV). So the increase of Te content of the films increases the absorption and decreases the transmission. As a result, the absorption edge shifts to the lower energy side, or in other words from the absorption edge of CdS:In to that of CdTe, but the relation is not linear [10].

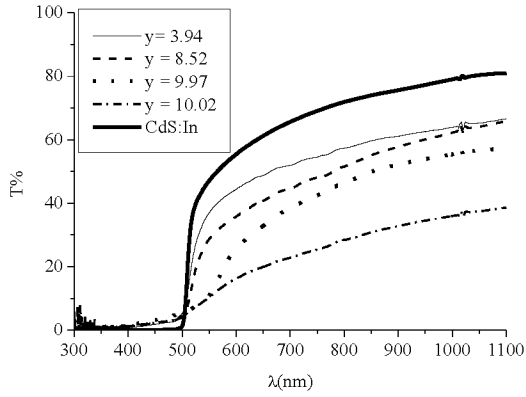

Figure 2. Transmittance of $CdS_{1-y}Te_y$ thin films of different composition y and comparable thickness besides that of a CdS:In film.

To find the refractive index and the extinction coefficient, the definition of the reflectance of a film for a light wave incident normally from air, with refractive index $n_0 = 1$, on a medium of complex refractive index n^* is used. Reflectance is given by the following relation [5]

$$R = \frac{(n^* - 1)^2}{(n^* + 1)^2} = \frac{(n-1)^2 + k^2}{(n+1)^2 + k^2} \tag{1}$$

The complex refractive index of the film is given by;

$$n^* = n + ik \tag{2}$$

where n is the refractive index and k the extinction coefficient of the film. Knowing the value of the absorption coefficient α which can be deduced from the transmittance, the extinction coefficient can be calculated using the relation

$$k = \frac{\lambda\alpha}{4\pi} \tag{3}$$

where λ is the wavelength in free space. Solving equation (1) for the refractive index n gives;

$$n = \frac{(1+R)+\left[(1+R)^2-(1-R)^2(1+k^2)\right]^{1/2}}{1-R} \tag{4}$$

The extinction coefficient k is calculated from Eq.3 and plotted against photon's energy hν and displayed in Figure 3. The extinction coefficient shows a non-zero value in the region before 2.5 eV. It is well known in the case of polycrystalline films, extra absorption of light occurs at the grain boundaries, which leads to non-zero value of k for photon energies smaller than the fundamental absorption edge [11]. In this region k is restricted in the range 0.042–0.174, where it increases with y. A sharp increase in k occurs at the absorption edges which vary according to x. As seen in Figure 2, the absorption edge shifts to the lower energy side with y, and the films with y = 9.97×10^{-2} and y = 10.02×10^{-2} show two absorption edges, which are not obvious in Figure 2. These are due to the presence of a mixed phase in the films (cubic and hexagonal), where the cubic phase has a slightly smaller optical bandgap [3,9]. After the sharp increase, k becomes constant equals to 0.291 for all $CdS_{1-y}Te_y$ films. For the CdS:In film, k slowly decreases with hν from 0.487 to 0.453 for the energy change from 2.5 to 3.0 eV.

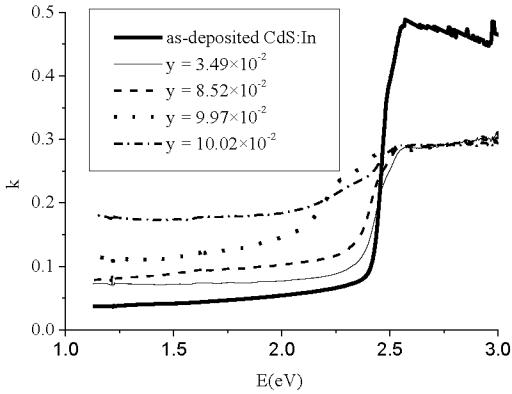

Figure 3. The extinction coefficient k of a CdS:In film and the $CdS_{1-y}Te_y$ thin films with comparable thickness and different composition y.

The refractive index n is calculated from Eq.4 and plotted against the photon's energy hν and displayed in Figure 4. It is observed that n increases slowly with hν until the absorption edge which depends on x, after which, it strongly increases with hν, and then reaches approximately a constant value –not shown in the figure. It is obvious that the sharpest absorption edge is that of the CdS:In thin film, then sharpness decreases with x. The shift of the absorption edge towards lower energy is also observed. As the figure shows, for energies before ≈ 2.25 eV, the refractive index increases slowly with x, and its value in this region at hν = 1.5 eV, which corresponds to the bandgap energy of CdTe lies in the range 2.10 for as-deposited CdS:In to 7.17 for x = 10.02×10^{-2}.

Below the absorption edge, refractive index dispersion can be analyzed by the single oscillator model. So the obtained data of refractive index n is also analyzed to yield the long wavelength refractive index (n_∞) together with the average oscillator wavelength (λ_0) for $CdS_{1-y}Te_y$ thin film using the following relation [12]

$$\frac{n_\infty^2 - 1}{n^2 - 1} = 1 - \left(\frac{\lambda_0}{\lambda}\right)^2 \tag{5}$$

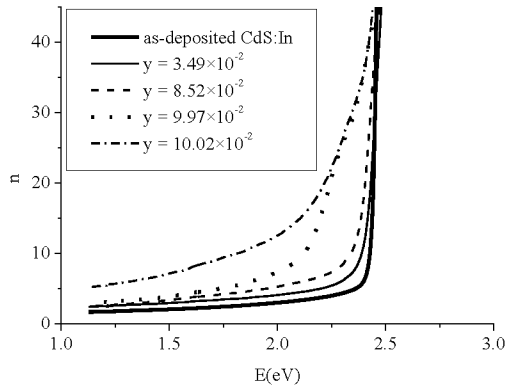

Figure 4. The refractive index of $CdS_{1-y}Te_y$ thin films of comparable thickness with different composition y.

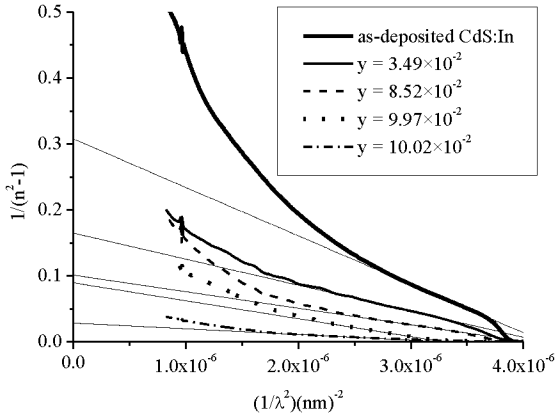

Figure 5. The plot of $\left(n^2 - 1\right)^{-1}$ against λ^{-2} for a CdS:In film and the $CdS_{1-y}Te_y$ thin films of different composition y.

The relation between $(n^2-1)^{-1}$ and λ^{-2} is shown in Figure 5, beside the linear fits in the linear parts of the curves, where λ_0, n_∞ and $n_\infty^2=\varepsilon_\infty$ are evaluated from the fit parameters and listed in table II. From these values, the average excitation energy for electronic transitions $E_0=hc/\lambda_0$, and the dispersion energy which is a measure of the strength of interband optical transitions $E_d=E_0(n_\infty^2-1)$ are also calculated and listed in table II. From table II it is observed that n_∞, ε_∞, E_d, M_{-1} and M_{-3} increase with the Te content of the films y,

Table II. The optical parameters of $CdS_{1-y}Te_y$ thin films with the thickness and composition of each film.

t(nm)	Composition y	n_∞	ε_∞	λ_0(nm)	E_0(eV)	E_d(eV)	M_{-1}	M_{-3}
500	0	1.628	2.649	591.7	2.096	3.457	1.649	0.376
490	3.49±1.68	2.208	4.873	591.9	2.095	8.115	3.873	0.882
465	8.52±6.41	2.177	4.740	666.3	1.861	6.960	3.740	1.080
420	9.97±9.21	2.548	6.495	648.9	1.911	10.500	5.495	1.505
460	10.02±8.27	4.321	18.671	667.3	1.858	32.838	17.671	5.117

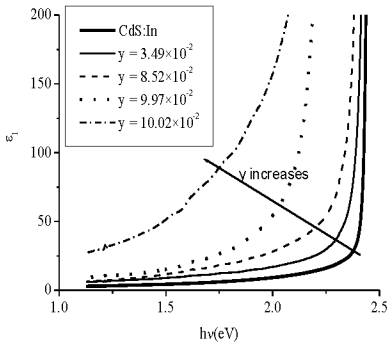

Figure 6.

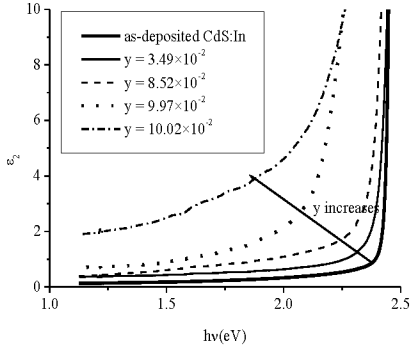

Figure 7.

Figure 6. The real part of the dielectric constant of $CdS_{1-y}Te_y$ thin films of comparable thickness but different composition.

Figure 7. The imaginary part of the dielectric constant of $CdS_{1-y}Te_y$ thin films of different composition but comparable thickness.

Figure 6 displays the real part of the dielectric constant ε_1 against the photon's energy hv for $CdS_{1-y}Te_y$ films with comparable thickness but different composition y. In the region before 1.5 eV, ε_1 increases with y, where it varies at hv = 1.15 eV from 2.99–28.21. It increases gradually with hv, and then sharply increases around the region of the absorption edge. The absorption edge moves towards lower energy with the increase in y. These observations are consistent with the behavior of the refractive index n and have the same explanations.

Figure 7 displays the imaginary part of the dielectric constant ε_2 against the photon's energy hv for the same set of films. In the low energy side at hv = 1.25 eV it increases with y and varies in the range 0.127– 1.913, and it increases slowly with hv. In the region of the absorption edge, ε_2 increases sharply with hv, where the rate of increase decreases with y. The presence of the two phases of the $CdS_{1-y}Te_y$ solid solution causes the decrease in the rate of increase of ε_2. In the high energy side after 2.5 eV, ε_2 becomes constant in consistence with the behavior of the extinction coefficient k. Both the real and imaginary parts of the dielectric constant show similar behaviors, but the imaginary part displays smaller values.

Conclusions

$CdS_{1-y}Te_y$ thin films were produced by first preparing CdS:In thin films by the spray pyrolysis technique on glass substrates, then annealing these films in the presence of Te vapor in nitrogen atmosphere at 400 °C. The composition of the films was revealed by the energy dispersive X-ray spectroscopy (EDS). Scanning electron microscope (SEM) micrographs showed that the films are polycrystalline. The transmittance of the films was used to get their optical parameters such as the absorption coefficient, extinction coefficient, refractive index, real and imaginary parts of the dielectric constant, and dispersion parameters. All of these parameters are found to increase with the composition y.

References

1. R. Dhere et al., "Formation and characterization of CdS_xTe_{1-x} alloys prepared from thin film couples of CdS and CdTe" (Paper presented at the 29th IEEE PV Specialists Conference, New Orleans, Louisiana, May 20-24, 2002).
2. Joel N. Duenow et al., "CdS_xTe_{1-x} alloying in CdS/CdTe solar cells" (Paper presented at the 2011 Materials Research Society Spring Meeting, San Francisco, California, April 25–29, 2011).
3. Shadia J. Ikhmayies and Riyad N Ahmad-Bitar, "$CdS_{1-y}Te_y$ thin films: Production and bandgap investigation", *Solar Energy*, 86 (9) (2012), 2613-2619.
4. G. Gordillo, F.Rojas, and C.Calderón, "Optical characterization of $Cd(S_x, Te_{1-x})$ thin films deposited by evaporation", *Superficies y Vasio*, 16 (3) (2003), 30–33.
5. Saeed Salem Babkair, Najat Mohammad Al-Twarqi, and Azhar Ahmad Ansari, "Optical characterization of CdTe films for solar cell applications", *Karachi University Journal of Science*, 39 (2011), 1-5.
6. K.R. Murali et al., "Pulse plated CdS_xTe_{1-x} films and their properties", *Solar Energy*, 83 (2009), 14–20.
7. R.Marymathelane, Ritajohn, K.R.Murali, "Optical properties of CdS_xTe_{1-X} nanocrystalline thin films", *The International Journal Of Engineering And Science (Ijes)*, 2(3) (2013), 14-18.
8. M. S. Kale, Y. R. Toda, D. S. Bhavsar, "Synthesis and characterization of nanocrystalline $(CdS)_{0.6}Te_{0.4}$ thin films deposited by closed space sublimation technique", *IOSR Journal of Applied Physics (IOSR-JAP)*, 6(2) (2014), 22-27.
9. Shadia J. Ikhmayies and Riyad N Ahmad-Bitar, "Photoluminescence and transmittance of $CdS_{1-x}Te_x$ thin films", *J. Luminouscence*. 132 (2012), 2826–2831.
10. R. Pal et al., "CdS_xTe_{1-x} films: Preparation and properties", *J. Phys. D: Appl.Phys.*, 26 (1993), 704-710.
11. P. P. Sahay, R. K. Nath, and S. Tewari, "Optical properties of thermally evaporated CdS thin films", *Cryst. Res. Technol.*, 42 (3) (2007), 275 – 280.
12. Ebru Şenadım Tüzemen et al., "Dependence of film thickness on the structural and optical properties of ZnO thin films", *Applied Surface Science* 255 (2009), 6195–6200.

Characterization of Minerals, Metals, and Materials 2015

Poster Session

Characterization of Minerals, Metals, and Materials 2015
Edited by: John S. Carpenter, Chenguang Bai, Juan Pablo Escobedo, Jiann-Yang Hwang, Shadia Ikhmayies, Bowen Li, Jian Li, Sergio Neves Monteiro, Zhiwei Peng, and Mingming Zhang
TMS (The Minerals, Metals & Materials Society), 2015

THE EFFECTS OF HIGH Al_2O_3 ON THE METALLURGICAL PROPERTIES OF SINTER

Wen-tao YU [1], Hai-bin ZUO [2], Jian-liang ZHANG [1], Tao Zhang [1]

[1]School of Metallurgical and Ecological Engineering, University of Science and Technology Beijing, Beijing 100083
[2]State Key Laboratory of New Advanced Metallurgy Technology, University of Science and Technology Beijing, Beijing 100083

Keywords: Sinter, Metallurgical performance, Al_2O_3

Abstract

Sintering-pot tests and metallurgical performances of sinter with 4 kind of different Al_2O_3 contents are experimented in this paper. Results show: when the Al_2O_3 contents increase from 2.0% to 3.5%, acicular calcium ferrites in mine phase will be gradually replaced by plate-like iron calcium. The increase of Al_2O_3 contents will lead to the addition of liquid viscosity and the reduction of permeability of sinter bed. Sintering time will be prolonged. The rate of yield is stable basically but production is low; besides, the increase of liquid viscosity will decrease of drum strength. The change of permeability of the material layer will make $RDI_{+3.15}$ decrease first and then increase when Al_2O_3 contents changed from 2.0% to 3.5%. RI of sinter shows a contrary trend because many open voids are formed by deterioration of liquidity first and then pores closed.

Introduction

As Chinese iron making production capacity increasing significantly, the world iron ore resources increasingly tense and market competition further intensify recently [1]. With technical innovation as a core, accelerating the technological transformation and reducing the cost have become the great important condition for the subsistence and development of enterprises [1]. As the Chinese steel mills depends more on seaborne material, use of imported high aluminum proportion must be increased in the blast furnace production. It can not only broaden the range of iron ore resources, but also reduce iron making raw material purchasing cost [2].

It is significant to improve the economic benefit of Chinese enterprises.However,the improvement of Al_2O_3 contents in the sinter will affect the various technical indicators of the sintering properties and metallurgical properties of sinter [2]. In order to ensure the normal operation of sintering and blast furnace production, we should improve the

metallurgical indexes of sinter of blast furnace through reasonable ore blending [3]. To solve this problem, in this paper, sintering-pot are carried out by using four different Al_2O_3 contents of iron ore and metallurgical performance test , and point the reason why the change of the metallurgical properties with mineral phase , analysis of the effect of Al_2O_3 on sintering process , which provided theoretical support for rational utilization of mineral resources with high Al_2O_3.

Experimental Materials and Conditions

7 kinds of iron ore powders and 3 kinds of fluxes have been used in this sintering-pot test, calculate the mixture ratio of iron ore powders and fluxes through the restrictive conditions including grade, alkalinity, Al_2O_3 contents and so on. The chemical composition and ratio are shown in Table I.

Table I. Chemical Composition of Original Fuel and Proportion Situation（%）

Raw Material	Chemical Composition					Proportion Situation			
	TFe	SiO_2	CaO	MgO	Al_2O_3	Plan 1	Plan 2	Plan 3	Plan4
Ore A	56.4	5.46	0.42	0.21	2.6	20	22	20	10
Ore B	61.5	3.87	0.23	0.16	2.13	35	27	17	9
Ore C	66.05	3.88	0.24	0.44	1.21	10	10	10	10
Ore D	48.0	18	0.8	0.61	3.3	4	5	7	11
Ore E	53.78	6.96	9.19	2.3	3.57	7	7	7	7
Ore F	60.39	2.42	3.11	4	0.83	4	4	4	4
Ore G	57.4	2.6	0.22	0.08	6.11	1	6	16	30
Flux A	0	3	81	0	0	7.5	7.5	7.5	7.5
Flux B	0	3	30	18	0	5	5	5	5
Flux C	0	8	1.31	42	0	2	2	2	2
Fuel	0	5.6	0.65	0.2	4.2	4.5	4.5	4.5	4.5

The sintering-pot test were carried out in 4 groups, and control basicity on 1.80 ± 0.05. The Al_2O_3 contents of sinter are controlled in 2.0%, 2.5%, 3.0% and 3.5% respectively. The composition of 4 kinds of schemes of sinter ore are shown in Table II.

Table II. Sinter Composition of 4 Kinds of Programs

Scheme	Sinter Composition（%）								R
	TFe	CaO	SiO_2	Al_2O_3	FeO	MgO	S	P	
plan1	54.89	10.10	5.59	1.96	6.90	2.63	0.033	0.076	1.81
plan2	54.85	10.36	5.71	2.42	6.30	2.56	0.034	0.076	1.81

plan3	54.74	10.32	5.67	2.87	7.00	2.65	0.034	0.077	1.82
plan4	54.66	10.64	5.88	3.26	7.70	2.47	0.035	0.080	1.81

In this experiment ,the diameter of the sintering-pot is ø300mm; The height of the material layer is 600mm; ignition pressure is 6kpa; ignition time is 3min; ignition temperature is1050℃ ±50℃; The sintering suction negative pressure is 12kPa.

Experimental Results and Analysis

Analysis Of Experiment Results——Mineral Phase

4 groups of sinter ore samples were carried out to make preparate and lap. Structure characteristics of high Al_2O_3 contents of sinter ore were observed by mineralographic microscope. The results are shown in figure 1.

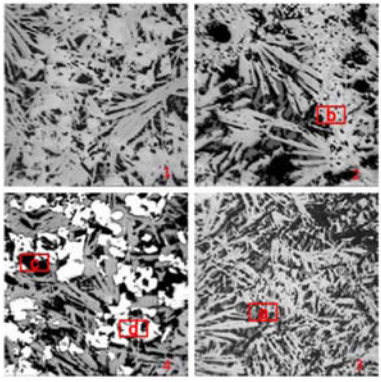

Plan1

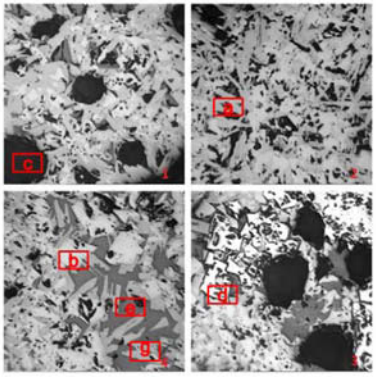

Plan 2

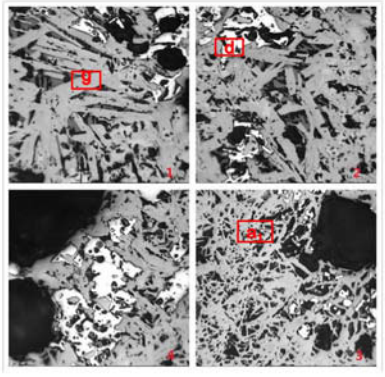

Plan 3

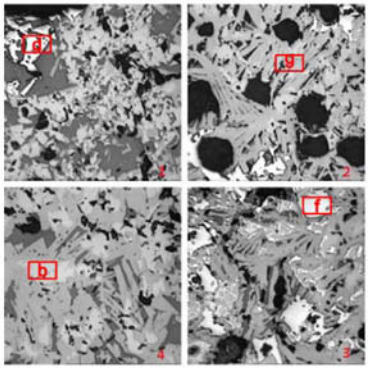

Plan 4

(*) a-acicular ferrite calcium a_1-not completely big acicular ferrite calcium b- magnetite ; c - pore; d-skeletal titan hematite ; e- fayalite ; f- hematite ;g-plate shaped calcium ferrite.

Figure 1. Ore Sinter Phase of 4 Different Al_2O_3 Contents

In plan 1, we can observe acicular calcium ferrites developed flourishing, the calcium ferrite had good strength and at same time plate shaped calcium ferrites were less. In plan 2, plate shaped calcium ferrites were obviously increased and acicular calcium ferrites appeared in some local areas. The amount of plate shaped calcium ferrites in plan 3 were more than plan2' s, beside some similar situations that acicular calcium ferrites appeared raised in the local areas . But the sizes of acicular calcium ferrites than in plan 2 were much smaller because of the growth not completely. The calcium ferrites in plan 4 were mainly composed of plate like, and the local areas of calcium ferrite -gathered into pieces. They were not in good shape.

As we can be seen from the ore phase, 4 kinds of ore phases formed by the sintering pot test were different. The main reason is that with the increasing of Al_2O_3 contents, heat that sintering process required also gradually increases. Carbon proportioned mixture in this experiment was certain, so heat supply was not sufficient which would cause the reaction of calcium ferrite (this reaction is endothermic reaction) not develop in the direction of balance .And improvement of Al_2O_3 contents would lead to the increase of liquid viscosity. It made the unreacted core of not mineralization increase, influenced the strength and weakened the reaction ability of the contact between liquid with the surrounding material. Ultimately improvement of Al_2O_3 contents would affect the formation of calcium ferrite [4].

The Analysis Of Sintering Pot Experiment——Sintering Indexes

Gradually increase of Al_2O_3 content in sinter would make sintering mixture form liquid phase and augment the liquid viscosity. The amounts of Al_2O_3 content in sinter also affected the permeability of sintering material layer, reduced the vertical sintering speed. The sintering time of 4 plans ascended with increase of Al_2O_3 content in sinter, while the vertical sintering speed descended.

Table III. Sinter and Technical Indicators Sintering-pot

Sintering indexes	Plan 1	Plan 2	Plan 3	Plan 4
Sintering speed (mm/min)	24.29	21.98	18.79	17.25
Rate of Yield (%)	94.32	93.76	93.83	93.22
Rate of Production (%)	78.9	77.8	75.2	74.2

In table III,with the increase of Al_2O_3 contents, sintering ore yield rate is reduced, but the underlying trend is basically stable. The main reason is that the amount of Ore G (limonite) mixed ascends gradually and the burning loss is relatively large [5]. The Production of sintering ore with the increase of Al_2O_3 contents is reduced.

In table IV,when the data were analyzed, there was a consistent trend between sinter ore production and the change of the sinter of particle sizes<16mm (＜5mm、5~10mm and 10~16mm) .In the other word, the Al_2O_3 contents in sinter is higher, the

sintering mixture viscosity is larger [6]. The decline of mineralization of the sintering process and the increase of unreacted core will lead to the increase small particle sizes of sinter.

Table IV. Distribution of Grain（%）

Grain distribution	Plan 1	Plan 2	Plan 3	Plan 4
>40mm	12.7	12.0	8.2	7.4
25~40mm	8.4	19.3	16.0	13.2
16~25mm	6.5	16.7	16.0	12.4
10~16mm	5.9	15.8	17.2	20.7
5~10mm	17.0	16.0	20.9	22.8
<5mm	19.5	20.2	21.7	23.5

The Effect Of Al_2O_3 Content On Drum Strength Of Sinter

In 4 plans, the variation of Al_2O_3 contents of sinter drum strength is shown in figure 2. It can be seen from Figure 2. With Al_2O_3 contents increasing in the experiments, the sinter drum strength showed a trend of gradual decline under the condition of 4 kinds of Al_2O_3 contents. When the Al_2O_3 contents were 2.0%, the sinter drum strength was highest.

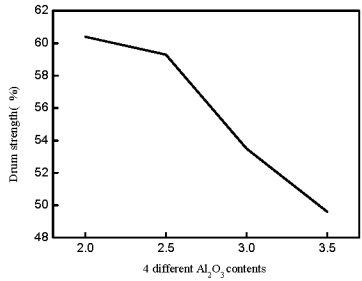

Figure 2. Drum Strength with 4 Al_2O_3 Contents

The increase of Al_2O_3 content makes the liquid viscosity increasing gradually, diminishs particle diffusion rate and reenforces the Oswald cure reaction of liquid phase cry-s tallization process [7]. Smaller crystal particles dissolve into the surrounding medium due to rate is larger, and the surface of the larger crystal particles precipitates again .It makes precipitated calcium ferrite develop into plate ,while iron oxide appears even larger crystal or grain development phenomenon.

The ore phase also confirmed that although the total amount of calcium ferrite increases, the plate structures are much more than other structures. In the high Al_2O_3 contents conditions, plate structures become the highest proportion of calcium ferrite structure instead of acicular calcium ferrite. However, the strength of the plate-like calcium ferrite and the ability to resist crack propagation are very poor. It is a big drawback for drum strength. On the other hand, Magnetite forms the crystal exhibition of stretching, compared with the close corrosion of structure of acicular calcium ferrite and small particles of magnetite under lowAl_2O_3 contents.

The strength of the plate-like calcium ferrite and the ability to resist crack propagation are also very poor. Because the two phase proportion of calcium ferrite and magnetite are larger[8]. In high Al_2O_3 levels, the main reason that decline of drum strength of sinter ore is the change of strength.

The Effect Of Al_2O_3 Content On Reducibility Of Sinter

In figure 3, 4 groups of reducibility indexes in the sintering pot experiments belonged to the good range, as in the 83%~87%. When Al_2O_3 contents of sinter ore was 2.5%, the reducibility of sinter ore is the highest. When the Al_2O_3 contents continued to increase to 3.5%, the reducibility indexes of sinter ore was gradually decreasing. But the decline trend was relatively slow.

At about 1200 ℃, When Al_2O_3 contents were up to 2.5%, liquid viscosity increased with Al_2O_3 content increasing, worsened liquid and a large of open gaps were formed. Consequently the reducibility of sinter was good when Al_2O_3 content was 2.5%. But with the Al_2O_3 contents continued to increase, liquid phase led by calcium ferrite system begins to form. Decomposition of the combined water produces large cracks quickly, and katogenic water immerges into limonite particles, assimilate these particles at a high speed and many large pores were formed [13]. Thus the liquid phase sintering material layers with the pores were closed and this phenomenon would exacerbate reducibility of sinter. The reducibility of sinter declined gradually due to accretion of Al_2O_3 contents in sinter.

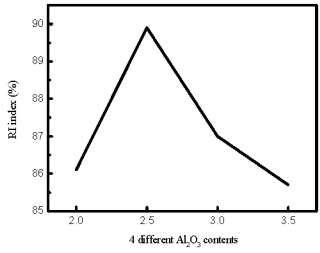

Figure 3. RI Index with 4 Al_2O_3 Contents

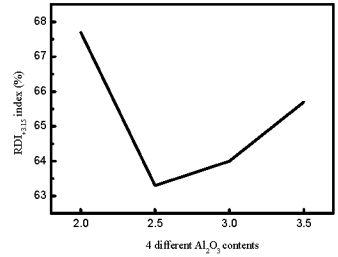

Figure 4. $RDI_{+3.15}$ Index with 4 Al_2O_3 Contents

The Effect Of Al_2O_3 Content On Low Temperature Reduction Degradation Of Sinter

The low temperature reduction degradation (RID) is one of the most important indexes in sintering. As shown in figure4, with the augment of Al_2O_3 contents, $RDI_{+3.15}$ shows descent at first and then ascent. The possible reason is that in the case of definite proportions of carbon, the liquid viscosity ascends with the ascent of Al_2O_3 contents and influences the permeability of layer [8]. When Al_2O_3 content is 2.5% or less, the liquid phase formed by sintered material layer in high temperature can meet the requirements of sinter permeability and the finally purpose is forming good pore structure. Skeletal hematite is usually found around the pores. So the increment of the amount of Al_2O_3 contents will lead to ascend the liquid viscosity and descend the pore structure in sinter. At last the formation of skeletal hematite was limited

and causes the RID $_{(+3.15)}$ index increase finally [8].

Conclusions

(1) In the case of definite proportions of carbon, as the content of Al_2O_3 increases from 2% to 3.5%, the endothermic quantity of mineralization process will increase. The acicular calcium ferrites are replaced by plate calcium ferrite in ore phase.
(2) When the content of Al_2O_3 content increases from 2% to 3.5%, the decrease of air permeability of sinter will lead to prolong sintering time .While the yield rate is stable. But the increase of Al_2O_3 content will lead to the augment of viscosity in sinter mixture, which influences the production rate of sinter.
(3) The content of Al_2O_3 increases from 2% to 3.5% will cause the decrease of drum strength of sinter ore. The main reason is that the addition of Al_2O_3 content gradually will make the viscosity of liquid phase increase, reduce the particle diffusion rate and add to the amount of plate calcium ferrite.
(4) The content of Al_2O_3 increases from 2% to 3.5% will lead to the addition of liquid viscosity gradually, which influences the permeability of material layer. The result is that RID indexes show a trend that decreases at first then increases.

References

1. Sinha, Moni, and R. V. Ramna, "Effect of variation of alumina on the microhardness of iron ore sinter phases," *ISIJ international* , 49(5) (2009), 719-721.
2. De. A, S. S. Gupta, and A. Chatterjee, "Effect of Alumina on Sinter Quality," *SEAISI Quarterly(Malaysia)*, 21(4) (1992), 35-46.
3. Das. A. K, Kumar. A, and De. A. K, "Characteristics and behaviour of high alumina iron ore sinter" (60 th Ironmaking Conference, 2001), 973-983.
4. Lu. L, R. J. Holmes, and J. R. Manuel, "Effects of alumina on sintering performance of hematite iron ores," *ISIJ international* , 47(3) (2007), 349-358.
5. Yamaoka. Y et al., "Effect of Gibbsite on Sintering Property and Sinter Quality," *Trans. Iron Steel Inst. Jap.* , 14(3) (1974), 185-194.
6. De. A et al., "Use of dunite in sintering of high alumina iron ores," *Iron & steelmaker* , 22(2) (1995), 49-56.
7. Paananen. Timo, Kyösti. Heinänen, and Jouko. Härkki, "Degradation of iron oxide caused by alumina during reduction from magnetite," *ISIJ international*, 43(5) (2003), 597-605.
8. Orrling. C, S. Sridhar, and A. W. Cramb, "In situ observation of the role of alumina particles on the crystallization behavior of slags," *ISIJ international* ,40(9) (2000), 877-885.

Characterization of Minerals, Metals, and Materials 2015
Edited by: John S. Carpenter, Chenguang Bai, Juan Pablo Escobedo, Jiann-Yang Hwang, Shadia Ikhmayies, Bowen Li, Jian Li, Sergio Neves Monteiro, Zhiwei Peng, and Mingming Zhang
TMS (The Minerals, Metals & Materials Society), 2015

CHARACTERIZATION OF FORMULATIONS WITH ORNAMENTAL ROCK WASTE AND CLAYS TO PRODUCE CERAMIC PAVER

Carlos Mauricio Fontes Vieira[1,a], Thiago Samarão Motta[1,b], Sergio Neves Monteiro[2,c]

[1] State University of the North Fluminense Darcy Ribeiro – UENF
Av. Alberto Lamego 2000, CEP 28013-602, Campos dos Goytacazes, RJ, Brazil

[2]Military Institute of Engineering, IME, Materials Science Department
Praça General Tibúrcio, 80, Praia Vermelha, Urca, CEP 22290-270, Rio de Janeiro, RJ, Brazil
[a]vieira@uenf.br; [b]thiagosdamotta@gmail.com; [c]sergio.neves@ig.com.br

Keywords: Characterization, Ceramic Paver, Clays, Incorporation, Ornamental rock waste.

Abstract

This work has as its objective to characterize ceramic bodies formulated with ornamental rock waste and two different clays to produce ceramic paver. Specimens were made by uniaxial press-molding at 20 MPa and then fired at 950 and 1050°C respectively. The determined technological properties were: plasticity, dry bulk density, linear shrinkage, water absorption and flexural rupture strength. The results showed that the type of the clay has strong influence on the properties of interest for heavy clay ceramics. The investigated waste must be incorporated in small amounts to avoid increasing in the porosity of the ceramics.

Introduction

Ornamental rock is a natural resource available in the municipal area of Santo Antônio de Pádua and located 150 km from the city of Campos dos Goytacazes, north of state of Rio de Janeiro, Brazil. Intense industrial activity related to ornamental stones, especially gneisses, is traditionally occurring in the region. After mining, the flagstone is submitted to sawing to obtain blocks and then, after a manual operation, the final products are small flagstones [1,2]. During the sawing operation, a sludge composed of water and fine particles of rock is generated. A monthly production of 1000 tons of ornamental rock waste is estimated to be produced at Santo Antônio de Pádua. The final disposal of this waste has brought serious environmental problems. Since most industries do not have an adequate sludge treatment, the waste is contaminating the soil and underground waters as well as obstructing rivers and lakes.

Ceramic bodies industrially fabricated in the municipal area of Campos dos Goytacazes, 280 km from the city of Rio de Janeiro, are elaborated using a mixture of local clays. These clays are predominantly kaolinitic mineral, associated with high plasticity. Due to the excessive plasticity of the ceramic bodies, it is common to have dimensional defects

in the final products after the drying and firing processes. Moreover, the kaolinitic structure and the presence of aluminum hydroxide confer a refractory behavior to the local clays during the firing stage. This impairs sintering during the firing operation. In the case of clay ceramics for civil construction, this results in greater porosity associated with elevated values of water absorption [3,4]. To avoid this problem, it is necessary to reformulate the clayey ceramic body composition. The addition of both non-plastic materials, to reduce plasticity, and fluxes to condition the refractoriness is a possible alternative, mainly to produce ceramic with higher aggregate values in comparison with bricks such as ceramic paver.

One technological method, which is already being tested to decrease porosity, is the incorporation of ornamental rock wastes, **ORW**, from the sawing process [5-7]. These rocks contain large amount of quartz, feldspars and mica. In the initial stages of the ceramic processing, these minerals act as non-plastic agents that permit the use of lower amounts of water in body forming, making an easier drying operation. During firing, the quartz generally behaves as an inert material decreasing the shrinkage, but it may also be partially dissolved in liquid phase. Both the feldspars and the mica favor the formation of liquid phases and contribute to lower the porosity of the final ceramic product.

Based on the need to correct the deficiencies of the clays from Campos dos Goytacazes, the present work had as its main objective to characterize clayey formulations with ornamental rock waste to produce ceramic paver. .

Experimental Procedure

The basic raw materials used in this investigation were two different clays denoted as Yellow (**YC**) and Red Clay (**RC**), respectively, as well as an ornamental rock waste, **ORW**, from the city of Santo Antônio de Pádua, State of Rio de Janeiro. The **YC** is from Campos dos Goytacazes, spite **RC** is from the city of Itaboraí. Itaboraí is another place inside the Rio the Janeiro State that produces heavy clay ceramics that is located in the half way between Campos dos Goytacazes and the major consumption market of ceramic from Campos, the city of Rio de Janeiro. Thus, the trucks that carry products to Rio de Janeiro can bring clay from Itaboraí at low cost. The Clays from Itaboraí presents some different characteristics in comparison to the clays from Campos, justifying their investigation in mixture with clay from Campos [8].
The chemical composition of the raw materials was obtained by fluorescence spectrometry (Philips, PW 2400) using a pressed powder pellets as sample. The particle-size distribution of the **ORW** was obtained by sieving and sedimentation techniques according to the Brazilian standard [9]. Upon receipt, the raw materials were dried at 110°C and manually disintegrated with a crusher. Five experimental ceramic bodies were formulated as shown in Table 1. Formulation **1** corresponds to the pure yellow clay. Formulation **2** was elaborated with a mixture of the clays in the same amount. The other formulations, **3**, **4** and **5** were elaborated with the use of the waste in partial replacement of the clays in amounts of up to 30 wt.%. Formulation with pure **RC** was not elaborated due to the elevated cost to produce red ceramics with 100% in mass of a clay from another place and distant 250 km from Campos dos Goytacazes.

In order to determine the technological properties of the ceramic bodies, 12.43 cm long rectangular specimens with 1.10 cm x 2.54 cm in cross section, were shaped by uniaxial

pressing at 20 MPa. Initially the specimens were dried at 110°C for 24 h. Finally, the specimens were fired at 950 and 1050°C in an electric laboratory kiln with a 180 min socket at maximum temperature, using a heating/cooling rate of 2°C/min. The measured technological properties were: dry bulk density, water absorption and mechanical strength, obtained by the flexural rupture stress, using the three-points method [10,11].

Table I. Investigated formulations (wt.%).

Formulations	YC	RC	ORW
1	100	-	-
2	50	50	-
3	45	45	10
4	40	40	20
5	35	35	30

Results and Discussion

Table I shows the chemical composition of the raw materials. The chemical composition of the clays is typical of a kaolinite-based material with low amounts of alkaline oxides and a high amount of Al_2O_3. The relatively high amount of Fe_2O_3 is response for a reddish color in the fired ceramic. The high percentage of LoI for the **YC** indicates a higher fraction of clay minerals. The chemical composition of the **ORW**, shows a relatively large amount of SiO_2 and alkaline and alkaline earth oxides, and a lower amount of Al_2O_3 and LoI, that confirms the flux potential of the investigated waste. Increasing the amount of **ORW** in the formulated bodies, it is expected an increase in the percentage of alkaline fluxes and SiO_2 as well as a decrease in the LoI and alumina content, as compared to the clays.

Table II. Chemical composition of the raw materials (wt.%).

	Yellow Clay	Red Clay	ORW
SiO_2	43.59	47.23	67.83
Al_2O_3	25.64	33.67	14.76
Fe_2O_3	10.38	6.63	4.18
TiO_2	1.55	0.81	0.71
K_2O	1.63	0.41	5.47
Na_2O	-	-	2.77
CaO	0.15	-	2.08
MgO	0.66	-	0.73
LoI	15.20	11.07	0.66

The Winkler diagram [12] shown in Fig. 1 is a ternary diagram with distinct granulometric ranges of particle sizes in its vertices. The range < 2μm, corresponding to the top corner in Fig. 1, is an important technological parameter, associated with the percentage of clay minerals, which is related to the plasticity of the clay-water system and directly influences the properties of the body such as the amount of forming water, drying shrinkage and mechanical strength. The numbered fields in the Winkler diagram

represent the suitability of the raw materials for making ceramic products normally used in civil construction. As shown in Fig. 1, the particle size distribution of the **YC** and **RC** clays are located in points inside the defined fields. The **YC** and **RC** are located in the upper limit of the field **3** and middle of field **4**, respectively. It is observed that the **YC** has a higher amount of clay minerals fraction, particles with size < 2μm, indicating an elevated plasticity. Ornamental Rock Waste **(ORW)**, a non-plastic material, which is predominantly constituted of particles with size between 2-20 μm and higher than 20μm. This result shows that the **ORW** can reduce the plasticity of the clays, that is specially recommended to the **YC** due to its elevated "clay fraction", i.e., < 2μm.

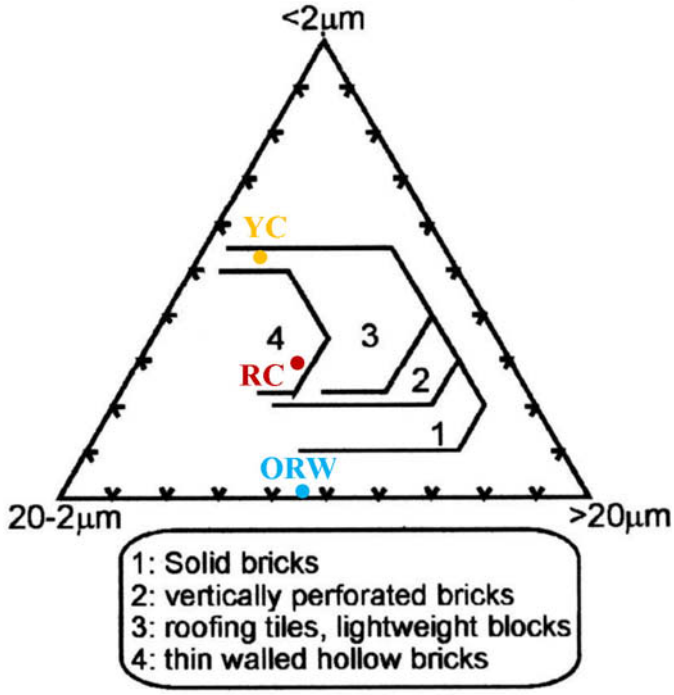

Figure 1. Winkler diagram.

Figure 2 shows the dry bulk density of the formulations. It is observed that the formulation **1**, **YC**, presents the lower packing after the forming and drying stage. This is due to the particle size with high amount of fines. The mixture of the both clays, formulation **2**, has intermediate value of dry bulk density. The **ORW** abruptly improved the packing of the clays, that is beneficial to the sintering process since it increases the contact area between the particles.

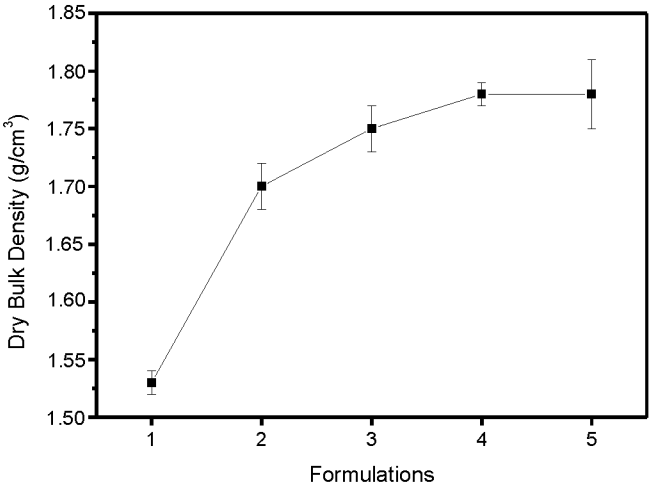

Figure 2. Dry bulk density of the formulations.

Figures 3 to 5 shows the water absorption, linear shrinkage and flexural rupture strength of the formulations, respectively. In these figures it is noted that the temperature exerts a strong influence on the evaluated properties, i.e., the water absorption decreases and the linear shrinkage and flexural rupture strength increase.

Figure 3 shows that the **formulation 1**, **YC**, presents the highest value for the water absorption at both investigated temperatures. It is observed that at 950 and 1050°C, the use of **RC** and **ORW** decreased the water absorption of the formulation **1**. However, only at 1050°C, all investigated formulations present water absorption compatible with ceramic paver type **MX**, indicated for exterior use and does not exposed at cool temperatures, lower than 14%. For interior use, there is no specification for water absorption [13].

Figure 4 shows that the **RC** and **ORW** decreased the linear shrinkage of the formulation **1**, **YC**, also at both investigated temperatures. This is due to the influence on the dry packing, as well as to the decrease on the weight loss during the firing stage, according to the LoI values, Table 2.

In Figure 5, it is observed that both **RC** and **ORW** abruptly decrease the mechanical strength of the formulation **1** at the investigated temperatures. This is due to the major presence of coarser quartz particles, as seen in Fig. 1.

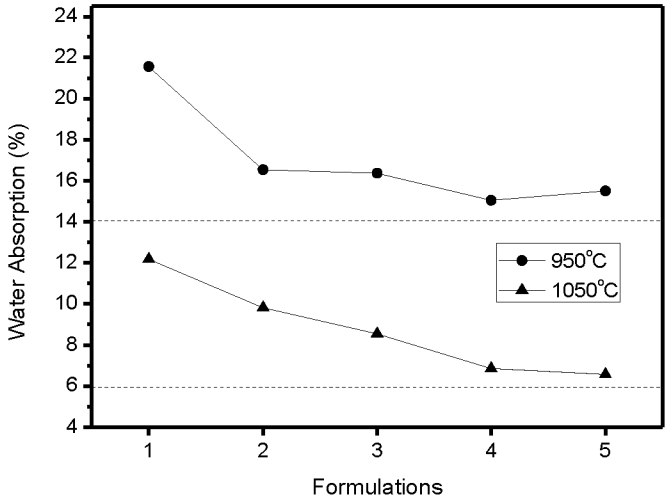

Figure 3. Water absorption of the formulations as a function the firing temperature.

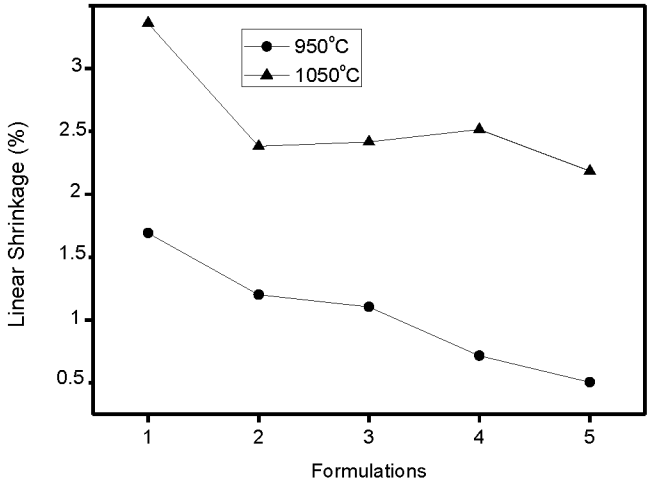

Figure 4. Linear shrinkage of the formulations as a function the firing temperature.

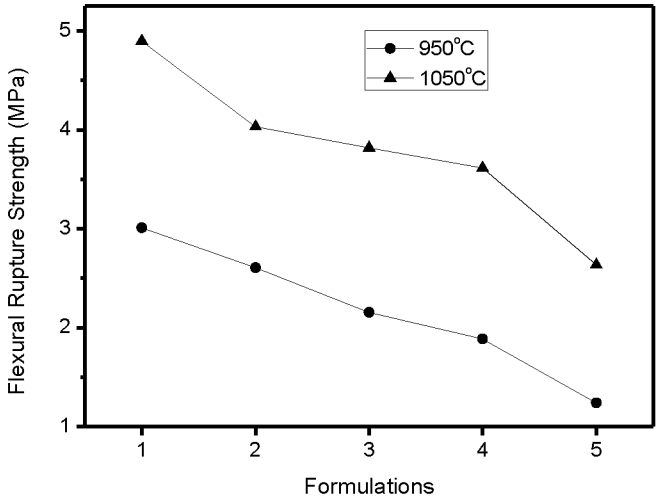

Figure 5. Flexural rupture strength of the formulations as a function the firing temperature.

Conclusions

⇒ The yellow clay from Campos dos Goytacazes has as main deficiencies to produce heavy clay ceramic products, a high loss on ignition and an elevated amount of fine particles. This last one also affects the packing during the forming stage. The red clay from Itaboraí, has a lower loss on ignition and a coarser particle size. The ornamental rock waste presents typical characteristics of flux material, such as elevated amount of alkaline and earth-alkaline oxides and fine particle size.

⇒ With respect to the evaluated fired technological properties, the yellow clay displays highest water absorption, linear shrinkage and mechanical strength at both investigated temperature, 950 and 1050°C. The use of red clay and ornamental rock waste abruptly changes the properties of the yellow clay. Both materials adjusted the particle size distribution of the yellow clay, indirectly decreasing its high plasticity, as well as decreased the water absorption and linear shrinkage. However, these materials also impaired the mechanical strength of the yellow clay, due to the coarser quartz particles.

⇒ The temperature exercises a strong influence on the evaluated properties, decreasing the water absorption and increasing the mechanical strength and linear shrinkage of all ceramics.

⇒ Finally, the results indicate that both red clay and ornamental rock waste have potential to use in mixture with the yellow clay to produce heavy clay ceramic of elevated aggregate value, such as ceramic paver. The main aspect that must be investigated to improve the mechanical strength of the formulations is the size of the quartz particles.

Acknowledgments

The authors would like to thank the financial support to this investigation provided by the following Brazilian agencies: CNPq (proc. n. 301778/2011) and FAPERJ (proc. n. E-26/103.211/2011).

References

[1] A.R. Campos, and A.O. Silva, "Instalação de Unidades de Tratamento de efluentes de Serrarias de Rochas Ornamentais, em Santo Antônio de Pádua – RJ," CETEM Report (1997).

[2] S.L.M. de Almeida, A.P. Chaves, and L.S. Leal Filho, "Primeras Jornadas Iberoamericanas sobre "Caracterización y Normalización de Materiales de Construcción," Programa CYTED, Madrid: Espanha (2001).

[3] C.M.F. Vieira, J.N.F. Holanda, and D.G. Pinatti, "Caracterização de massa cerâmica vermelha utilizada na fabricação de tijolos na região de Campos dos Goytacazes-RJ," *Cerâmica*, 46 (2000), 14-17.

[4] S.N. Monteiro, and C.M.F. Vieira, "Characterization of clays from Campos dos Goytacazes, north Rio de Janeiro State (Brazil)," *Tile & BricK Int.*, 18 (2002), 152-157.

[5] C.M.F. Vieira, T.M. Soares, R. Sánchez, and S.N. Monteiro, "Incorporation of granite waste in red ceramics," *Materials Science and Engineering A*, 373 (2004), 115-121.

[6] A.M. Segadães, M.A. Carvalho, and W. Acchar, "Using marble and granite rejects to enhance the processing of clay products," *Applied Clay Science*, 30 (2005), 42-52.

[7] W.Acchar, F.A. Vieira, and D. Hotza, "Effect of marble and granite sludge in clay materials," *Materials Science and Engineering A*, 419 (2006), 306-30.

[8] J.P.D Vitorino, C.M.F. Vieira, J. Duailibi Filho. Caracterização e avaliação das propriedades de queima de argilas utilizadas para faricação de telhas no município de Itaboraí-RJ In: Congresso Brasileiro de Cerâmica, 2010, foz do Iguaçu. Anais do 54º Congresso Brasileiro de Cerâmica. 2010. v.1. p.3–13.

[9] Associação Brasileira de Normas Técnicas – ABNT, "NBR 7181: Determinação da Análise Granulométrica de Solos," Rio de Janeiro (1984).

[10] American Society for Testing and Materials - ASTM, C 674-7: Flexural properties of ceramic whiteware materials, USA, 1977.

[11] American Society for Testing and Materials – ASTM, C 373-72: Water Absorption, Bulk Density, Apparent Porosity and Apparent Specific Gravity of Fired Whiteware Products, USA, 1972.

[12] Pracidelli, S., Melchiades, F., 1997. Importância da composição granulométrica de massas para cerâmica vermelha. Cerâmica Industrial 2 (1/2) 31-35.

[13] American Society for Testing and Materials - ASTM , C902, Standard Specification for Pedestrian and Light Traffic Paving Brick, USA, 2006.

Characterization of Minerals, Metals, and Materials 2015
Edited by: John S. Carpenter, Chenguang Bai, Juan Pablo Escobedo, Jiann-Yang Hwang, Shadia Ikhmayies, Bowen Li, Jian Li, Sergio Neves Monteiro, Zhiwei Peng, and Mingming Zhang
TMS (The Minerals, Metals & Materials Society), 2015

EVALUATION OF THERMOELECTRIC METHODS FOR THE DETECTION OF FRETTING DAMAGE IN 7075-T6 AND Ti-6Al-4V ALLOYS

Hector Carreon

[1]Instituto de Investigaciones Metalúrgicas;
Edif."U" C.U., 58000-888, Morelia, México

Keywords: Fretting Damage; Thermoelectric Measurements; Aerospace Materials

Abstract

During fretting, high points or asperities of the mating surfaces adhere to each other and small particles are pulled out, leaving minute, shallow pits and powdery debris. Sometimes these surface conditions are neglected, but they are important in some application such as the aerospace industry. In this research work, non-contacting and contacting thermoelectric power techniques are performed in fretted 7075-T6 and Ti-6Al-4V samples. It has been found that the contacting and non-contacting thermoelectric power measurements are associated directly with the subtle material variations such as work hardening and residual stresses due to plastic deformation produced in the fretting zone but surface topography. Therefore, both techniques could be used for a global characterization of the most relevant fretting induced effects. Potential of these techniques to monitor subsurface changes in other severe surface plastic deformation processes are clearly envisaged.

Introduction

Ti-6AL-4V and 7075-T6 alloys have an extensive application in aircraft structures since their combine high strength to weight ratio and corrosion resistance compare to other materials. However, fretting damage is a serious problem in the aerospace industries where structural assemblies are often subjected to intense vibration [1-3]. Fretting is caused by the oscillating movement with small amplitude that may occur between contacting surfaces subjected to vibration. It mainly results in two kinds of damage: wear, by which the debris is generated as a result of a loss of fit between contacting surfaces, and rapid crack nucleation and propagation as a result of failure of engineering parts. Some of the failures initiated by fretting have had serious consequence [4,5]. So nondestructive evaluation of the fretted zone where the cold work induces residual stresses at the surface of the component could be necessarily in order to improve the fretting wear-resistant performance of materials.Ti-6AL-4V and 7075-T6 alloys produce a change in the thermoelectric voltage from positive to negative when two pieces of the same material are rubbed against each other as shown in Fig. 1. Although this so-called tribo-electric method well illustrates the sensitivity of the thermoelectric method to detect fretting damage, this technique cannot be directly adapted to nondestructive inspection of critical engine components because of its poor reproducibility and the inevitable surface damage the inspection itself causes on the part to be inspected.
On the other hand, thermoelectric power (TEP) measurements have demonstrated their ability to nondestructively quantified grit blasting and laser shot-peening surface treatments and detected subsurface changes induced by both surface plastic deformation processes in metallic biomaterials such as Ti-6Al-4V and 316LVM alloys [6,7]. TEP measurements of surface treatment effects could be provided the option to quantitatively measured initial treatment effectiveness along with the effect of operationally induced changes over the life of the treated component. The goal of this research work is to use two non-destructive thermoelectric techniques (NDTT), the non-contacting and contacting thermoelectric power measurements to

detect and quantified the subsurface changes induced by fretting damage in aerospace materials such as Ti-6Al-4V and 7075-T6 alloys.

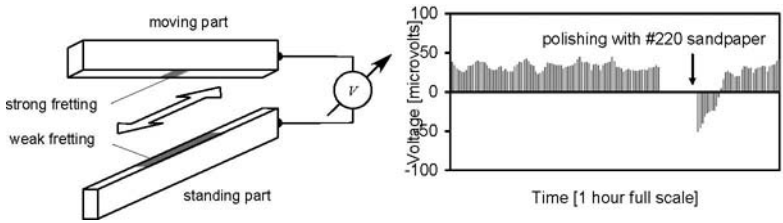

Figure 1. Tribo-electrically generated thermoelectric voltage when two pieces of the very same material are rubbed against each other.

Thermoelectric Power

Thermoelectricity is defined as the direct conversion of heat into electrical energy or vice verse, in conductor materials by means of different phenomena as the Seebeck effect, the Peltier effect and the Thomson effect. In order to understand this phenomenon, in particular the Seebeck effect, in a better way, it was considered a conductor material that is heat at one side and cooled at the other side. When a small temperature gradient ∇T is established across a conductor, the electrons in the hot side has higher energy than those of the cold side. Therefore the heat is carried from the hot region to the cold region by a net diffusion of electrons. In general, the diffusion rate is a function of electron energy and thus, a net electron current will result. The flow of electrons leaves behind exposed positive metal ions (charges) in the hot region while pile up electrons in the cold region. So the higher energy electrons at the hot region are able to lower their energies by diffusing to the cold region. This situation prevails until the electric field produced by the electron current opposes the further flow of electrons from the hot to cold region. Therefore the cold side becomes negatively charged, while the hot side positively charged and, as a result, a thermoelectric voltage is induced along the conductor. This potential difference ∇V across the conductor caused by a temperature gradient ∇T is called the Seebeck effect. The magnitude of this effect is given by the Seebeck coefficient that is define by the thermoelectric voltage developed per unit temperature difference in a conductor or $S = \Delta V/\Delta T$. By convention, the sign of the thermoelectric Seebeck coefficient is given by the potential of the cold region with respect to the hot region. Ordinary thermocouples based on the Seebeck effect can not operated in a non contacting way partly because they need strong conduction-type thermal coupling with the specimen to be tested and partly because they need direct electrical coupling with the measuring electronics. However, material imperfections naturally form such thermocouples in the specimen itself and, in the presence of an externally induced temperature gradient, these innate thermocouples produce thermoelectric currents around the imperfections, that can be detected by magnetic sensors from a significant lift-off distance between the tip of the sensor and the material surface imperfection.

Microstructural characterization and mechanical properties evolution are usually monitored by destructive testing, using tensile tests, metallographic techniques or hardness measurements. Thermoelectric power (TEP) measurements have recently gained a growing attention for the characterization of metallurgical properties in steels and other alloys. These measurements, based on Seebeck effect, are sensitive to changes in the electronic

structure of the material resulting from various metallurgical and mechanical processes [8-10]. The *contacting thermoelectric technique* analysis consists of measuring potential differences in the micro-volt range, generated by a small temperature difference along the sample. The Seebeck coefficient, S, is defined as the ratio between the voltage, ΔV, developed along the sample and the temperature difference, ΔT , given by $S = \Delta V/\Delta T$ as shown in Figure 2(a). Recently, this method was used in a non-contacting way by detecting the magnetic field produced by thermoelectric currents in metals called *non-contacting thermoelectric technique* [11-14]. Let us assume that we have a defect or imperfection in an otherwise homogeneous material and a temperature gradient is established throughout the specimen. Because of this temperature gradient, different points at the boundary between the defect or imperfection and the host material will be at different temperatures, therefore at different thermoelectric potentials. These minor thermoelectric potential differences will drive local thermoelectric currents around the affected area, which can be detected in a non contacting way by a high sensitive magnetometer as shown in Figure 2(b). This technique was originally suggested for the detection of metallic inclusions in the material, but was subsequently shown to be sensitive enough to sense subtle changes in the thermoelectric power of metals due to plastic deformation and the presence or residual stresses [15].

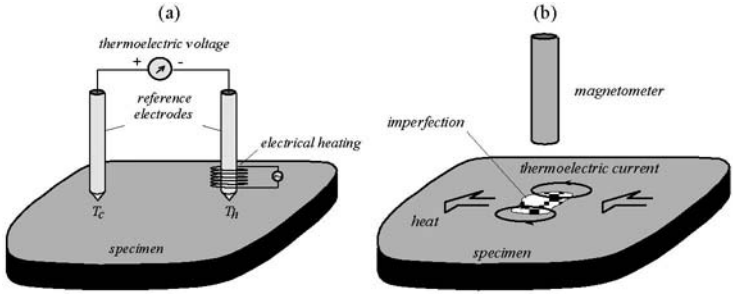

Figure 2. Schematic diagram of the TEP measurements by (a) contacting detection using the hot tip technique and (b) noncontacting detection by magnetic monitoring of thermoelectric currents.

Material and Thermoelectric Methods

In this section, the experimental setup will be described and the procedure used to detect and quantified subsurface changes on fretting damage Ti-6Al-4V and 7075-T6 samples. The fretting fatigue experiments were carried out using a special shape specimen with a round cross section and two flat sides. In this situation two zones of the contact were generated on the flat sides of the specimen. Figure 3 shows the fretting fatigue experimental test setup used in this study along with the servo hydraulic uniaxial testing machine. The capacity of the servo hydraulic testing machine is 600 kN under static conditions and 500 kN for fatigue loading. The maximum cyclic loading frequency of the machine is 50 Hz.

Figure 3. Servo hydraulic uniaxial testing machine used to induce fretting damage in Ti-6Al-4V and 7075-T6 samples

Two tests for each material (Ti-6AL-4V and 7075-T6) were carried out to see how the thermoelectric power measurements can change with the number of the cycles and to quantify the fretting fatigue damage. To achieve these objectives the first experiment on Ti-6AL-4V and 7075-T6 samples was interrupted after 100 cycles (low fretting) and the second interrupted after 500 cycles (high fretting) under different load conditions as shown in Table I.

Table I.- Load conditions for the fretting fatigue tests

Material	Axial load (kN)	Normal load (N)	Tangential load (N)
7075-T6	1.8	750	450
Ti-6Al-4V	3.4	800	1200

Firstly, we conducted thermoelectric measurements on three Ti-6Al-4V samples: low fretting damage sample, high fretting damage sample and unfretted sample. And secondly, we also conducted thermoelectric measurements on three 7075-T6 samples: low fretting damage sample, high fretting damage sample and unfretted sample respectively. The contacting TEP measurements were performed using a calibrated Alloy ThermoSorter. The operation of this instrument is based on the well known thermoelectric principle. The thermoelectric instrument induces the temperature difference in the sample by means of a dual-tipped reference probe. One tip is at room temperature and the other is heated to a specific temperature. In our case, a copper hot tip (standard probe) was used in order to measure the TEP of the fretted Ti–6Al–4V and 7075-T6 samples. The dual-tipped probe is placed on the sample, an electric circuit is completed and a signal is generated. This signal is then processed to obtain a peak reading, which is displayed on the microvolts digital display. The variation in this reading between unfretted and fretting zone on the sample is representative of the microstructural changes induced by the plastic deformation process.

On the other hand, in the non-contacting TEP measurements each sample is mounted into two pure copper supporters which are perforated by a series of holes and equipped with sealed heat exchangers to facilitate efficient heating and cooling and then mounted on a nonmagnetic translation table for scanning. In order to get a better heat transfer between the specimen and the copper heat exchangers, a layer of silicone heat sink compound was applied. One of the copper supporters is at 15ºC, while the other is at 25ºC. The temperature gradient is kept at ~ 1 ºC/mm in all non-contacting TEP measurements, which is more than sufficient to produce detectable magnetic signals on fretting damage Ti-6Al-4V and 7075-T6 samples. A pair of fluxgate sensors is

used in a gradiometric arrangement in order to detect the thermoelectric signals from the fretted damage zone. The inspection of the specimen is realized at the horizontal sensor polarization. The lift-off distance between the primary sensor and the fretted sample surface is ~ 1.5 mm.

Results and Discussion

It is widely accepted that fatigue loading coupled with contact pressure between two components causes premature crack nucleation and eventually accelerates crack growth causing components to fail unexpectedly, even at stress levels below their plain fatigue limit or at fewer life cycles than predicted by plain fatigue analysis [16,17]. The fretted surface was also examined by scanning electron microscopy (SEM). Figure 4a shows the high resolution images (with SEM) of the fretting fatigue surfaces for the specimen manufactured from 7075-T6 alloy, and figure 4b presents the high resolution images of the specimen from Ti-6Al-4V alloy. Since oxygen in titanium alloys is a promoter of α-phase, one might expect near surface transformation to a brittle layer by the combined effect of increased oxygen content and large plastic deformation. Figure 4b shows the "altered" surface layers induced by the high fretting Ti-6Al-4V sample. Transfer of material from one surface to the other was observed in fretting scars, especially for specimens subjected to the larger contact stresses. It has been shown that transfer during dry sliding of metals can produce a thin layer of "mechanically alloyed" material with extremely fine grain structure. This transfer material was found to shear off at the bond line and produce hard wear debris. The dry sliding wear effects could be part of the crack generation process as shown in Fig 4b.

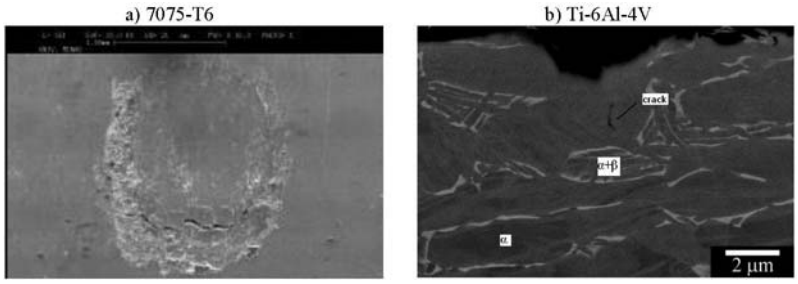

Figure 4. SEM micrographs of the high fretted aerospace alloys

In Figure 4a can be better seen the two zones of the contact region. In the centre of the contact it is localized a smooth zone, named stick zone and around this a rough zone, named slip zone. The presence of the stick and the slip zones in the contact region shows clearly the partial slip regime [18]. In figure 4a can be clearly seen a big crack that is located at the interface between the two zones present in the contact. Such location of the fretting fatigue crack has been described in several research papers [19,20].

All the Ti-6Al-4V and 7075-T6 samples were tested using the contacting and non-contacting thermoelectric techniques. In the case of TEP measurements with the contacting technique, Fig. 5, the relative TEP value of the 7075-T6 fretted samples decrease with regards to the unfretted sample (-0.217 µV/°C) at the low (-0.336 µV/°C) and high (-0.867 µV/°C) fretting conditions. In the case of the Ti-6Al-4V samples, the relative TEP also decreased gradually with regards to the unfretted sample (-4.95 µV/°C) at the low (-6.32 µV/°C) and high (-8.96 µV/°C) fretting conditions, which correlates well with the hardness gradients and grain size refinement reported for fretting aerospace alloys [21,22].

In the case of magnetic measurements with the non-contacting technique, Fig 6., the magnetic flux density increased slightly from ~0.088 nT (unfretted) to 2.36 nT (low fretting) and 4.06 nT (high fretting) in 7075-T6 fretted samples. In the case of the Ti-6Al-4V fretted samples, the magnetic flux density increased significantly from ~2.86 nT (unfretted) to 5.98 nT (low fretting) and 10.13 nT (high fretting) conditions.

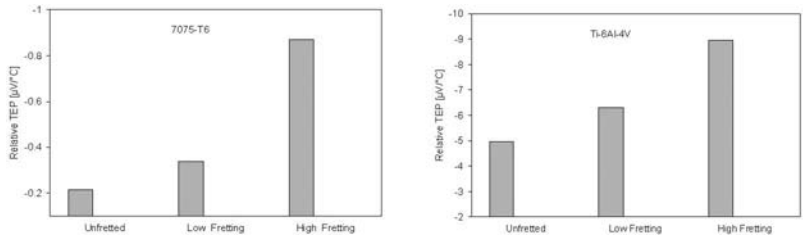

Figure 5. Relative TEP measurements of fretted 7075-T6 aluminum alloy and Ti-6Al-4V titanium alloy samples by contacting means.

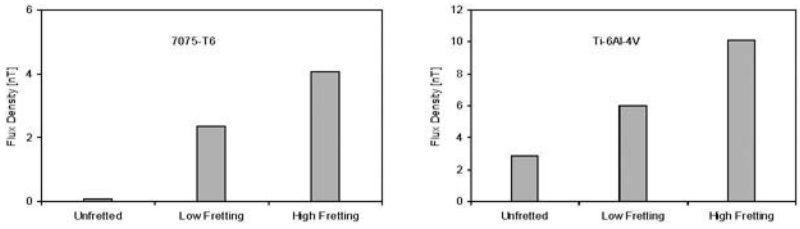

Figure 6. Relative TEP measurements of fretted 7075-T6 aluminum alloy and Ti-6Al-4V titanium alloy samples by non-contacting means.

Figures 7 and 8 shows the magnetic scans of the fretted Ti-6Al-4V and 7075-T6 samples taken at $\nabla T \approx 13.38$ °C/cm temperature gradient with a lift-off distance of 1.5 mm. The measured peak magnetic flux density **B** is also listed for comparison in both cases. As we expected, the main lobes (thermoelectric currents) get stronger and the magnitude of the magnetic flux increases as the cold work is more severe and the spatial distribution of the field become well defined. The magnetic image recorded from the unfretted Ti-6Al-4V titanium alloy samples exhibits a substantial background thermoelectric signature due to the crystallographic anisotropy as shown in Figure 7a. For example, in the two phases ($\alpha+\beta$) Ti-6Al-4V alloy the manufacturing process used to fabricate stock materials (bar, billet, plate ect.) tend to induce a preferred crystallographic orientation due to the restricted nature of mechanical slip (dislocations), leaving the material with a remarkable macroscopic anisotropy [23]. In this respect, the 7075-T6 aluminum alloy is a homogeneous or texture-free material that

results in a slight background thermoelectric signature as shown in Figure 8a. Correlation with the microstructural analysis and microhardness measurements indicated that such evolution of the magnetic flux density exclusively corresponds to the residual stresses [6]. Overall this study reveals that the non-contacting technique is more sensitive to the presence of residual stresses, whereas the contact technique is strongly influenced by the grain size refinements and work hardening [7].

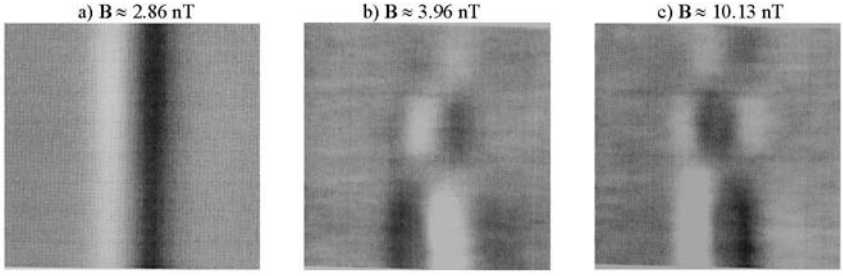

Figure 7. Magnetic signatures recorded on a) unfretted, b) low fretted and c) high fretted Ti-6Al-4V samples .

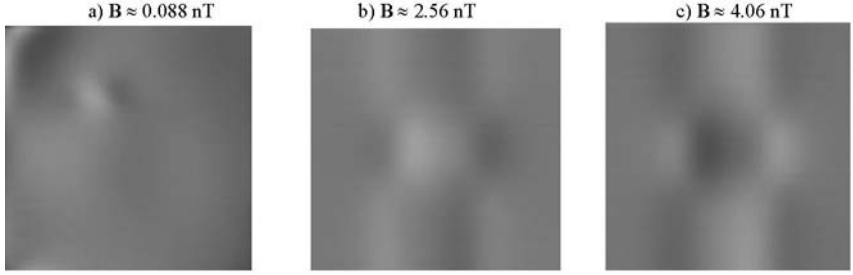

Figure 8. Magnetic signatures recorded on a) unfretted , b) low fretted and c) high fretted 7075-T6 samples .

Conclusions

In the current research, TEP measurements were applied as a non-destructive assessment technique to detect subtle material variations produced by fretting damage in aerospace materials. The TEP measurements were so sensitivity to the work hardening, grain refinement and residual stresses induced by plastic deformation in the fretting damage zone. The purpose of this research work is to suggest an alternative non-destructive method to detect and quantified subsurface changes in fretted 7075-T6 and Ti-6Al-4V samples by thermoelectric means.

The 7075-T6 alloy is more sensitive to fretting fatigue than the Ti-6Al-4V alloy, this being justified by its lower resistance to wear damage.

References

1. S.R Shinde., D.W Hoeppner, *Wear* 261, (2006) 426.
2. G.H Farrahi., M. Tirehdast, S. Parsa, M. Motakefpoor , *Eng. Fail. Analy.* 18 (2011) 474.
3. X. H. Cuiab, Y. S. Maob, M. X. Weib, S. Q. Wangab, *Tribol. Trans.* 55 (2012) 185.
4. A.L. Hutson, C. Neslen, T. Nicholas, *Wear* 36 (2003) 13.
5. B.P. Conner, A.L. Hutson, L. Chambon, *Wear* 255 (2003) 259.
6. H. Carreon, S. Barriuso, G. Barrera, J. L. González, F. G. Caballero, *Surf. & Coat. Tech.* 206 (2012) 2942.
7. H. Carreon, S. Barriuso, M. Lieblich, J. L. González, F. G. Caballero, *Mater. Sci. Eng. C* 33 (2013)1417.
8. F.G. Caballero, C. Capdevila, L. F. Alvarez, C. García de Andrés, *Scr. Mater.* 50 (2004) 1061.
9. J.P. Ferrer, T. Cock, C. Capdevila, F.G. Caballero, C. Garcia, *Acta Mater.* 55 (2007) 2075.
10. H. Carreon, A. Medina, *Nondestruct. Test. Eval.* 22 (2007) 299.
11. W. Morgner, *NDT&E Int.* 27 (1994) 263.
12. H. Carreon, J. L. González, *Rev. Mex. Fis.* 58 (2012) 372.
13. F. Yu, *NDT & E Int.* 43 (2010) 182.
14. H. Carreon, *Exp. Therm. & fluid Sci.* 44 (2013) 1673.
15. H. Carreon , P.B. Nagy, M. Blodgett, *Res. Nondestr. Eval.* 14 (2002) 59.
16. S. Fouvry, K. Kubiak, *Int. J. of Fatigue* 31 (2009) 250.
17. T.S. Slacka, B. D. Leonard, F. Sadeghia, *Tribol. Trans.* 56 (2013) 531.
18. A. Vadiraj, M. Kamaraj, U. K. Mudali, A.K. Nath, *Mat. Sci. & Tech.* 22 (2006) 1119.
19. A. Vadiraj, M. Kamaraj, *Trans. Indian Inst. Met.* 63 (2010) 217.
20. R. Sahooa, S. Mantrya, T.K. Sahooa, S. Mishraa B. Jhaa, *Tribol. Trans.* 56 (2013) 555.
21. B.P. Conner, A.L. Hutson, L. Chambon, *Wear* 255 (2003) 259..
22. A.L. Hutson, S. Sathish, T. Nicholas, *Tribo. Int.* 39 (2006) 1197.
23. H. Carreon, *J. Alloys Compd.* 427 (2007) 183.

Characterization of Minerals, Metals, and Materials 2015
Edited by: John S. Carpenter, Chenguang Bai, Juan Pablo Escobedo, Jiann-Yang Hwang, Shadia Ikhmayies, Bowen Li, Jian Li, Sergio Neves Monteiro, Zhiwei Peng, and Mingming Zhang
TMS (The Minerals, Metals & Materials Society), 2015

OPTIMIZATION RESEARCH OF PERITECTIC STEEL MOLD FLUX WITH Co_2O_3 DOPING

Chen Junfu[1,2,3], Xie Junlin[1], He Feng*[1], Jiann YangHwang[3], Wan Entong[2], Cao Tongyou[2], Peng Zhugang[2], Zhang Jianjun[2], Yang Chengwei[2], Fang De[1]
[1.] State Key Laboratory of Silicate Mateials for Architectures, Wuhan University of Technology, Wuhan 430070, China
[2.] Wuhan Iron and Steel Research Institute, Wuhan 430081, Hubei, China
[3.] Advanced Materials R&D center of WISCO, Beijing 102211,Beijing, China

Keywords: basicity, peritectic steel mold flux, Co_2O_3 doping, heat flux density

Abstract:

During the solidification process of peritectic steel (PS), the peritectic reaction often causes volume contraction which associated with surface longitudinal cracks, and using mould flux with low heat flux density help for alleviating surface longitudinal cracks. New peritectic steel mold flux with Co_2O_3 doping reduced the heat flux density, and the optimal content was found to be 2.0 wt %. Furthermore, basicity and Na_2O addition were designed, and the minimum heat flux density required basicity of 1.4 and 10.0 wt %. Na_2O content. As a result, the optimal peritectic composition was CaO(35.67wt%), SiO_2(25.48 wt %), Al_2O_3(3.7 wt %), MgO(2.53 wt %), Na_2O(10 wt %), CaF_2(14 wt %), Co_2O_3(2 wt %).

1. Introduction

Peritectic steels are those within a carbon content range between 0.08% and 0.17%, Peritectic steels are widely used in construction、shipbuilding、oil and gas transportation、machinery and other industries. peritectic reaction are well known to cause 4.7 % volume contraction of casting slab solidification, and result in an uneven solidifying shell that can act as an initiator for longitudinal cracking. As a result of the enormous output of peritectic steels, the optimization of peritectic steels quality has important economic value.

According to Kawamoto and Tang′ points [1-3], using a 'mild cooling' mould flux would contribute to alleviate the longitudinal cracking. Moreover, by adding transition metal oxides of Fe_2O_3 and MnO, heat transfer ability of mold flux can be decreased [4-6]. For further decreasing heat transfer ability, it needs to find new kind of transition metal oxide for peritectic steels mold flux. Cobalt oxide can be used as colorant in the glass industry, and it increases the heat resistance of glass by blackening the color. And it is well known that mold flux includes glassy layer and crystalline layer. If cobalt oxide is used in the peritectic steels mold flux, it maybe has the effect on changing transfer ability of peritectic steels mold flux.

2. Experimental

2.1Material and sample preparation

Wollastonite ore, bauxite, dolomite, fluorite and Na_2CO_3 were the experiment materials of the PS mold flux. They were supplied by the Wuhan Iron and Steel Group Corporation. Co_2O_3 and Na_2CO_3 of chemical grade were purchased from the Shanghai chemical industrial company, China. All the samples were prepared by mixing and calcinations method. Various amount of Co_2O_3 was added to wollastonite ore, bauxite, dolomite, fluorite, and Na_2CO_3 to prepare the PS mold flux, then the mixtures were ball milled at a speed of 150 rpm for 60 min to get the mixed batch (200 g).

2.2 Sample composition design

There were six kinds of mold flux for industry, and the optimal peritectic mold flux composition was CaO(35.67wt%), SiO_2(25.48 wt %), Al_2O_3(3.7 wt %), MgO(2.53 wt %), Na_2O(8 wt %), CaF_2(14 wt %). In order to develop a new kind of peritectic steel mold flux, this elements were chosen to use as the basis slag. By adding cobalt oxide into the basis slag, the heat transfer ability may be reduced.

Cobalt oxide content, basicity, sodium oxide content was the main impact factors for peritectic steels mold flux. According to this three influence, samples were designed as follows:

Table 1. The chemical compositions (wt %) of samples with different basicity, Co_2O_3 and Na_2O content

sample	R (CaO/SiO2)	CaO	SiO_2	Al_2O_3	Na_2O	CaF_2	Co_2O_3
0#(basis slag)	1.4	35.58	25.48	3.70	8.00	14.00	0
1#	1.4	35.58	25.48	3.70	8.00	14.00	1.00
2#	1.4	35.58	25.48	3.70	8.00	14.00	1.50
3#	1.4	35.58	25.48	3.70	8.00	14.00	2.00
4#	1.4	35.58	25.48	3.70	8.00	14.00	2.50
5#	1.0	25.48	25.48	3.70	8.00	14.00	2.00
6#	1.1	28.02	25.48	3.70	8.00	14.00	2.00
7#	1.2	30.58	25.48	3.70	8.00	14.00	2.00
8#	1.3	33.12	25.48	3.70	8.00	14.00	2.00
9#	1.4	35.67	25.48	3.70	8.00	14.00	2.00
10#	1.4	35.67	25.48	3.50	3.00	14.00	2.00
11#	1.4	35.67	25.48	3.50	4.00	14.00	2.00
12#	1.4	35.67	25.48	3.50	5.00	14.00	2.00
13#	1.4	35.67	25.48	3.50	6.00	14.00	2.00
14#	1.4	35.67	25.48	3.50	7.00	14.00	2.00
15#	1.4	35.67	25.48	3.50	8.00	14.00	2.00
16#	1.4	35.67	25.48	3.50	9.00	14.00	2.00
10#	1.4	35.67	25.48	3.50	10.00	14.00	2.00

3 Result and discussion

3.1 Heat flux density of mold slag with different cobalt oxide content

The samples were transferred into a HF–200 heat flux simulator (Fig.1), in which the samples was tested at 1400 °C. The testing result was shown as follows:

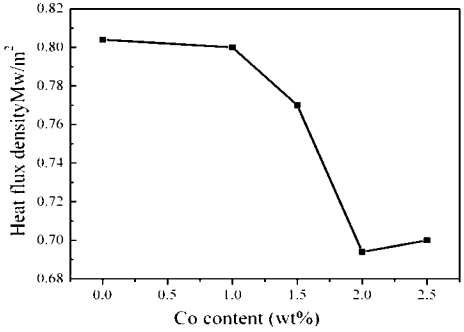

Figure1. Heat flux density of slag film with addition of Co_2O_3.

The heat flux density data of serials Co doped in 0# were the highest, and 3# (2 wt% Co_2O_3) was the lowest. When the cobalt oxide content in the basic slag increased from 1 to 2 wt %, the heat flux density decreased. Once the cobalt oxide content was increased from 2 wt % to 2.5 wt %, the heat flux density was increased. Whatever the cobalt oxide content was from 1% to 2.5 wt %, the heat flux density was much lower than the basis slag. Thus cobalt oxide plays a role of increasing the thermal resistance, and the cobalt oxide content in PS mold flux could change the heat flux density.

3.2 Basicity effect with different cobalt oxide content

The chemical compositions of mold fluxes with different basicity were listed in **table1**.The heat flux density testing result was shown as fig.2.

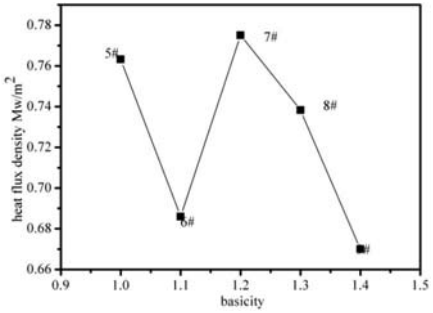

Figure2. Heat flux density of samples at different basicity.

Actually, basicity calculated as this formula: $R = \frac{\%wtCaO}{\%wt(SiO_2)}$

The heat flux density results demonstrated the samples followed the order: 7#>5#>8#>6#>9#. Corresponding, the basicity followed the order: 9#>8#>7#>6#>5#, and 9#(R=1.4) had the lowest heat flux density. Combined with heat flux density and basicity, the new peritectic steel mold flux could be prepared as basicity of 1.4. Xiao [7] pointed out CaO is an important component for crystallizing, with the increasing basicity, higher crystallization tendency can be detected. Consequently, the higher basicity brought better crystallinity ability, and the better crystallinity ability decreased the heat transfer ability of peritectic steels mold flux.

3.3 Heat flux density of cobalt oxide containing mold slag with different Na_2O content

with the addition of Na_2O, break temperature and melting temperature of mold flux decreased obviously[8]. Na_2O also could decrease the melting temperature of fluxes by the formation of compound with low melting temperature [9]. In order to study the effect of Na_2O on the heat flux density, the chemical compositions of mold fluxes with different Na_2O content were listed in **table 1**.

With the HF-200 heat flux simulator, the heat flux density result was shown as follows:

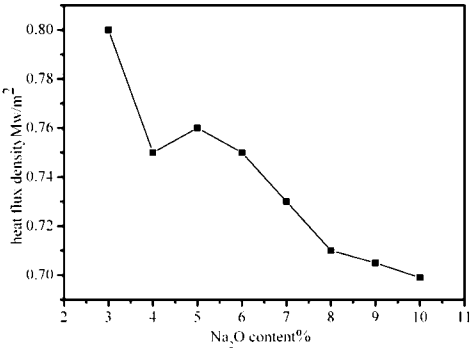

Figure3. Heat flux density of samples with different Na_2O addition.

The heat flux density data of serials Na_2O doped in samples were shown in Fig.3 If the Na_2O content in the basic slag increased from 3 to 5 wt %, the heat flux density decreased first and then increased. And when the Na_2O content increased from 5 to 10wt %, the heat flux density decreased. The heat flux density results demonstrated the samples followed the order: 10#>12#>11#>13#>14#>15#>16#>17#.

In summary, high Na_2O content did favor for decreasing heat flux density of mold flux, and 17# (10 wt % Na_2O) had the lowest heat flux density.

2.4 Chemical composition of optimization slag

Based on the above analysis, the optimization chemical composition of peritectic steel mold flux was shown in table 4.

Table4. The optimization chemical compositions (wt %) of peritecitc steel mold flux

sample	R	CaO%	SiO_2%	Al_2O_3%	MgO%	Na_2O%	CaF_2%	Co_2O_3%
18#	1.40	35.67	25.48	3.70	2.53	10	14.00	2.00

3. Conclusion

Co_2O_3 doped in Peritectic steel mold flux could decrease the heat flux density, meanwhile the PS mold flux with 2 wt % performed the optimal heat resistance properties.

In order to further optimize the Peritectic steel mold flux with Co_2O_3 doping, basicity and Na_2O flux were considered. The experiment results showed that high basicity and high Na_2O content helped with decreasing the heat flux density of mold flux.

To summarize, the optimal peritectic composition was CaO(35.67wt%), SiO_2(25.48 wt %), Al_2O_3(3.7 wt %), MgO(2.53 wt %), Na_2O(10 wt %), CaF_2(14 wt %), Co_2O_3(2 wt %). Comparing with others samples, this composition of peritectic mold flux had the lowest heat flux density.

References:

1. P. Tang，G. H. Wen, C. S. Xu, H. X. Hong, G. J. Hen, J. B. Wang, and W. F. Li, "Mold Powder Used for Slab Casting of Container Sheet Steel," *Journal Of Iron & Steel Research International*, 17(2) (2005), 16-18.

2. J. H. Chi and Y. N. Gan, *Mold Fluxes* (Shen Yang, SY: Northeastern University Press., 2000), 111.

3. M. Kawamoto, Y. Tsukaguchi, N. Nishida, T. Kanazawa and S. Hiraki, "Improvement of the Initial Stage of Solidification by Using Mild Cooling Mold Powder," *ISIJ International*, 37(2) (1997), 134-139

4. J. Diao, B. Xie, J. Xiao et al.,"Radiative Heat Transfer In Transition Metal Oxides Contained In Mold Fluxes," *ISIJ International*, 49(11) (2009), 1710-1714.

5. M. Susa, A. Kushimoto, H. Toyota et al., "Effects of Both Crystallization and Iron Oxides on the Radiative Heat Transfer in Mould Fluxes," *ISIJ International*, 49(11) (2009), 1722-1729.

6. W. L.Wang, K. Blazek, A. W. Cramb et al., "Study Of The Crystallization Behavior Of A New Mold Flux Used In The Casting Of Transformation-Induced-Plasticity Steels," *Metallurgical And Materials Transactions B*, 39(1) (2008), 66-74.

7. L. Xiao, S. P. HE, J. F. XU, X. L. HUO and Q. WANG, "Properties of High Basicity Mold Fluxes for Peritectic Steel Slab Casting ," *Journal Of Iron And Steel Research International*, 19(7) (2012), 39-45.

8. G. X. HU, "Influence of Na_2O Content on Crystallization Properties of Mold Fluxes," *Foundry Technology*, 33 (8) (2012), 964-966 (in Chinese).

9. S. P. HE, Q. WANG, D. Xie, C. S. Xu, and K. C. Mills, "Solidification and crystallization properties of Cao-SiO_2-Na_2O Based mold fluxes," *International Journal of Minerals, Metallurgy And Materials*, 16(3) (2009), 261-264.

Characterization of Minerals, Metals, and Materials 2015
Edited by: John S. Carpenter, Chenguang Bai, Juan Pablo Escobedo, Jiann-Yang Hwang, Shadia Ikhmayies, Bowen Li, Jian Li, Sergio Neves Monteiro, Zhiwei Peng, and Mingming Zhang
TMS (The Minerals, Metals & Materials Society), 2015

EFFECT OF POTENTIAL ON CHARACTERISTICS OF OXIDE PRODUCT LAYERS ON CHALCOPYRITE

Yu Juan[1], Yang Hong-ying[2]

[1]School of Metallurgical Engineering; Xi'an University of Architecture and Technology; Xi'an, 710055, China
[2]School of Materials and Metallurgy; Northeastern University; Shenyang, 110004, China

Keywords: Chalcopyrite; Potential Control Flotation; Electrochemical Impedance Spectroscopy; X-ray photoelectron spectroscopy.

Abstract

Electrochemical behavior of natural chalcopyrite in electrolyte solution at pH value of 6.97 was studied by cyclic voltammetry, X-ray photoelectron spectroscopy and electrochemical impedance spectroscopy. The results showed that the electrochemical processes occurred on electrode surface were controlled mainly by the growth of sulfur species at lower applied potentials (<0.35Vvs.SHE), and the oxidative dissolution of sulfur species and the hydroxylation of iron at higher applied potential (>0.45V). The EIS spectra of oxide product layers could be illustrated by the equivalent circuit of $Re(Q_{dl}R_{ct}(Q_fR_f))$, and the degree of hydrophilicity for chalcopyrite was higher when the value of charge transfer resistance Rct. was greater. The optimum potential range for the floatation of chalcopyrite in collectorless solution at pH value of 6.97 was between OCP (0.165V) and 0.35V.`

Introduction

Pulp potential control flotation technology has developed into an important direction in mineral processing field [1]. At different pulp potentials (Eh), the complex processes including redox reactions, chemical reactions, dissolution, adsorption and precipitation would occur, inducing a modification of mineral surface and forming oxide products with heterogeneous composition, and thus influences the hydrophobicity or hydrophilicity of mineral indirectly [2,3,12]. Most processes are related to electrochemical reactions, and therefore it is important to study the electrochemical oxidation mechanism for minerals.

As the most abundant copper bearing mineral, chalcopyrite is recovered from mineral ore by flotation. In electrochemically controlled condition, many research works in past few decades have been concentrated on the flotation behavior, identification of surface species, and determination of the degree of hydrophobicity for chalcopyrite [4-9]. Güler et al. (2004) proposed that natural chalcopyrite exhibited the property of hydrophobic at moderately oxidizing potentials (0-0.3Vvs.SHE) in neutral solution. Kocabag et al. (2007) confirmed that chalcopyrite could be floated in the potential range of 0 to +0.45V vs.SHE in neutral solution by the microflotation experiment. They explained their experiment results by reaction (1) proposed by Gardner and Woods, 1979, and considered that the hydrophobic CuS and S_0 species were responsible for the floatability of chalcopyrite in whole floatable potential range. The understanding of the chalcopyrite electrochemical oxidation mechanism is depended on

electrochemical techniques and surface analysis techniques. Cyclic voltammetry (CV) was extensively adopted to study the redox reactions for minerals surface in the flotation solutions [7,10,11]. As compared with CV analysis, electrochemical impedance spectroscopy (EIS) had more advantages on studying sulfide mineral surfaces. It could be employed to study reaction kinetics under redox conditions, which closely resemble flotation (Chander and Briceno, 1987). Velasquez et al. (2004) studied electrochemical oxidization mechanism of chalcopyrite by EIS in alkaline solution. However, there were few literatures studied the electrochemical oxidization processes in the neutral solution by EIS.

$$CuFeS_{2(s)} + 3H_2O \Leftrightarrow CuS_{(s)} + Fe(OH)_{3(s)} + S^0 + 3H^+ + 3e^- \quad (1)$$

Thus, the present work is to identify the composition of oxide product layers on the surface of chalcopyrite at different applied potentials by XPS, and to analyze the oxidization mechanism, reaction kinetics and relationship between the hydrophobicity of chalcopyrite surface and impedance characteristic of surface product layers in neutral solution by EIS.

The experimental strategy was divided into four parts. In the first part, the CV was performed to determine the applied potentials that are related to the contributions of main currents, and these contributions were associated to the different electrochemical processes that occurred on the surface of chalcopyrite electrode. In the second part, three applied potential values were selected at the contributions of main currents according to the CV results. Then the electrode was polarized to these applied potentials and kept for 600 s. The stable surface species could be formed during these treatments and the composition of these species were analyzed by XPS. In the third part, the EIS measurements were carried out at the selected applied potentials to study the electrochemical processes occurred at various applied potentials. In the final part, the electrode was polarized to these applied potentials and kept for 600 s, and then EIS measurements were carried out to study the impedance characteristic of oxide product layers that were formed during the treatment.

Experimental

Sample and solution

The natural chalcopyrite sample from Anhwei province, China, was prepared as working electrode. The sample was connected with copper wire, and then encapsulated in epoxy resin with $1\times1cm^2$ area exposed. The surface of working electrode was polished using 1200-grade silicon carbide papers before experiments.

The electrolyte solution with 0.1M KNO_3 was prepared in distilled water first, and then 0.025M Na_2HPO_4 and 0.025M KH_2PO_4 which could keep the pH value of the solution at 6.97 during experiments were added into the solution [7,12]. All chemical reagents are of analytical grade.

Electrochemical experiment

A conventional three-electrode cell system was used in electrochemical experiments. A piece of platinum and a satured calomel electrode (SCE) were employed as auxiliary electrode and reference electrode respectively. All the potentials mentioned in this paper have been converted

to the SHE values by adding 245mV to SCE values [14]. The electrochemical measurements were performed using a model 5210 lock in amplifier coupled with potentiostat model 273. The scan frequency range was 100 kHz to10 mHz, and the perturbation amplitude was 5 mV in AC impedance measurements. In CV test, the scan rate was 50mV/s, and the scanning regions were from -0.6 V to +0.9Vvs.SHE. The initial retard of 300 s for all the electrochemical tests was set to obtain a stable testing system. The data of impedance spectra was fitted using the Zimpwin3.20 software.

Results and discussions

Cyclic voltammetry

To determine the applied potentials that induced main current contributions (peaks) on the chalcopyrite surface in neutral solution, the cyclic voltammogram curve was measured and the results are shown in Fig.1. The scan potential is initiated at 0.042V and increases in positive direction. An anodic peak A1 (current contribution A1) appears in the potential range from 0.165V to 0.49V, and then peak A2 (current contribution A2) in the potential range from 0.49V to 0.7V can be observed. It suggests that, in these two potential ranges, different electrochemical reactions with certain degree of irreversibility occur on the chalcopyrite, and these reactions induce the modification of the chemical composition of chalcopyrite surface.

In negative sweep direction, the cathodic peaks C1, C2, and C3 may represent the unfully reversible reduction reactions related to the oxide products that formed in positive sweep direction.

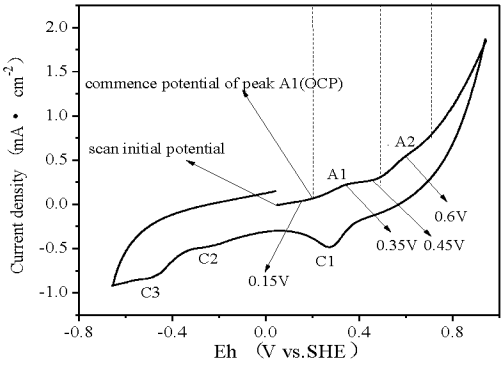

Fig 1. Cyclic voltammogram of natural chalcopyrite electrode in 0.1 mol/L KNO_3 solution at pH 6.97.

X-ray photoelectron spectroscopy

The chemical composition of oxide product layers formed on the chalcopyrite surface at different applied potentials has been analyzed by XPS in our previous work[13]. The selected potentials

included the open circuit potential (OCP) around 0.165V, and another two potentials at the contribution of main currents (A1, A2) in anodic sweep direction, 0.35V and 0.6V.

The XPS results indicate that plenty of S^{2-} ($CuFe_{1-x}S_2$,), S_2^{2-}(CuS_2), and polysulfide species are produced on the surface of chalcopyrite at the commence potential of electrochemical process A1 (OCP). At the applied potential of 0.35V, besides the species formed at OCP, a little of SO_4^{2-} species appears on the surface of chalcopyrite. Plenty of $Fe(OH)_3$ and SO_4^{2-} species covered the chalcopyrite surface when the potential is 0.6V, which is related to the electrochemical process A2.

Electrochemical Impedance Spectroscopy (EIS) results

The electrochemical oxidation processes of chalcopyrite electrode surface and relevant models. The EIS measurements at different applied potentials were conducted to investigate the electrochemical processes that occurred on electrode surface. The applied potentials are 0.15V, 0.35V, 0.45V and 0.6V, and they are related to contributions of peak A1 and A2 in Fig.1. The EIS results are shown in Fig.2. The Nyquist plot contains two capacitive loops The high frequency capacitive loop represents the properties of the electric double layer at the interface of electrode and solution [15], and the low frequency capacitive loop is induced by oxide product layers [16,17].

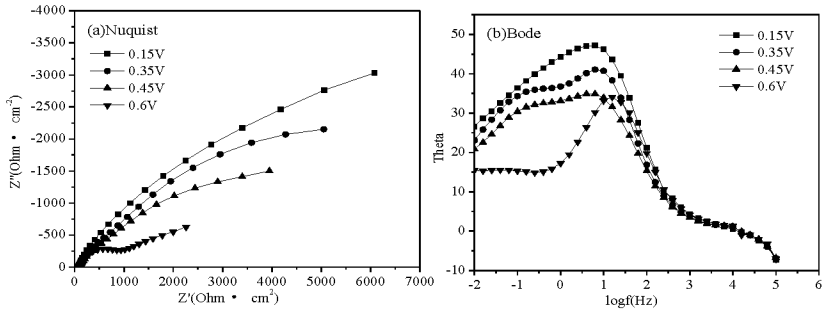

Fig 2. Nyquist and Bode plots for natural chalcopyrite electrode in 0.1 mol/L KNO_3 solution at pH 6.97 under different potential conditions (a)Nuquist; (b)Bode.

When the applied potential is 0.15V, slightly lower than OCP (0.165V), there is one time constant in bode diagram, which is induced by electric double layer of chalcopyrite electrode/solution interface. It suggests that no redox/electrochemical processes occur on the chalcopyrite surface. A new phase angle appears in low frequency region in bode diagram at the applied potential of 0.35V which is located at the current contribution labeled A1 in Fig.1, and it implied that the electrochemical reactions occur, $CuFe_{1-x}S_2$, CuS_2, S_n^{2-}, FeOOH, Fe_2O_3 species and a little of SO_4^{2-} species are formed on the electrode surface. This is in agreement with the CV results that the current contribution A1 is resulted from the redox reaction. These species enhances the hydrophobicity of the chalcopyrite electrode surface. Therefore, electrode surface is in the station of strong passivity by deficient-iron rich-sulfur layers at this potential. When the

applied potential reaches 0.45V, the characteristic of EIS plot is similar to that at 0.35V, but the dimension of high frequency capacitive loop slightly shrinks, which indicates that the anodic dissolution rate of electrode surface is accelerated. This potential is located in the potential range of the peak A1 between 0.165V and 0.49V. The iron and sulfur in deficient-iron rich-sulfur layers are further oxidized, and the amount of FeOOH, Fe_2O_3, and SO_4^{2-} species increase compared with that at OCP. Thus, at this potential, the hydrophobicity of electrode surface is slightly decreased. With the applied potential increases to 0.6V, the EIS spectra changes greatly, two capacitive loops are observed, but they are depressed greatly. It indicates that the anodic dissolution rate is further accerlated. This potential is located within the current contribution labeled A2 in Fig.1. A little CuO and plenty of $Fe(OH)_3$, SO_4^{2-} species are formed and are precipitated on the surface of chalcopyrite electrode. Therefore, the oxidative dissolution of rich-sulfur species and the hydroxylation of iron are the controlled step of electrode surface processes, which controlled the hydrophilicity of electrode surface.

Impedance characteristic of oxide product layers. In order to investigate the relation between the hydrophobicity of electrode surface and EIS of oxide product layers, the EIS measurements were done after the electrode was polarized to various applied potentials for 600s, and Fig.3 is the EIS spectra. All the EIS spectra are composed of one high-frequency capacitive loop and one low-frequency capacitive loop, and they represents the properties of electric double layer and products layer on electrode respectively. At OCP and 0.35V, the dimension high-frequency capacitive loop does not change much. With the increase of applied potential, the dimension high-frequency capacitive loops decreases.

Fig.4 is the equivalent circuit corresponded to the EIS spectra. R_e is the solution resistance; Q_{dl} （CPE_{dl}）is the double layer capacity and R_{ct} refers to the charge transfer resistance, R_{ct} in parallel with CPE_{dl} is used to describe the high frequency capacitance loop; R_f and Q_f corresponds to the resistance and capacitance of oxide product layers, R_f in parallel with C_f corresponds to the low frequency capacitance loop. The constant phase element (CPE) behaves as a capacitance, which varies with the frequency and is used to compensate for the non-homogeneity in the system including porosity, fractal geometry, the distribution of interfacial capacitances [18,19].

Fig.5 shows the fitting values of R_{ct} in equivalent circuit. At the applied potential of 0.35V, the charge transfer resistance R_{ct} is 4911Ω, slightly decreases compared with that at OCP. The values of R_{ct} decreases greatly when the applied potential is higher than 0.35V. It is obvious that R_{ct} values could be employed to illustrate the hydrophobicity or hydrophilicity of electrode. At OCP, the electrode surface of oxide product layers is composed mainly of $CuFe_{1-x}S_2$, CuS_2 and polysulfide species by iron atom migration. These species will improve the hydrophobicity of chalcopyrite. Thus, R_{ct} has largest value at this potential. When the applied potential increases to 0.35V, a little of sulfur species are oxidized to SO_4^{2-} species. The hydrophilicity of chalcopyrite is enhanced slightly, and thus R_{ct} slightly reduces to 4911Ω. With the increase of applied potential, plenty of $CuFeS_2$,CuS_2,S_n^{2-} are oxidized to SO_4^{2-} and plenty of $Fe(OH)_3$ that coveres the surface of electrode, and the electrode surface of hydrophilicity is greatly enhanced. Therefore, the charge transfer resistance R_{ct} shapely decreases. In a word, the EIS analysis proves that the chalcopyrite has a good hydrophobicity in the potential range from OCP to 0.35V, which is in agreement with the results proposed by Güler et al. (2004) and Kocabag et al. (2007).

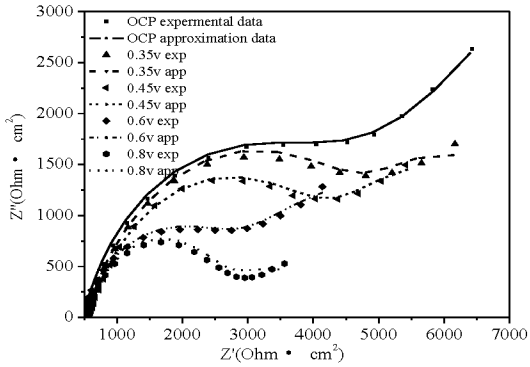

Fig 3. Nyquist plot for natural chalcopyrite electrode after electrochemical treatment under various indicated potentials for 600s in 0.1 mol/L KNO_3solution at pH 6.97.

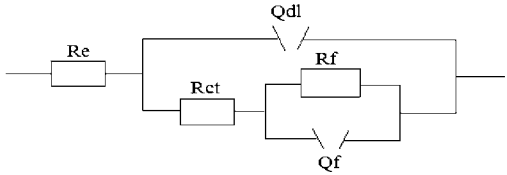

Fig 4. The equivalent circuit of chalcopyrite in 0.1M KNO_3 neutral solution.

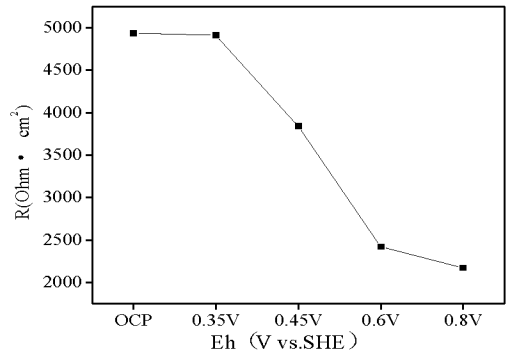

Fig 5. Values of R_{ct} in equivalent circuit at various applied potentials.

Conclusions

In electrochemical oxidization processes of chalcopyrite, there are two electrochemical processes in the scan potential range, A1 and A2, and they occur between (OCP) 0.165V and 0.49V, 0.49V and 0.7V, respectively. The electrochemical oxidization process A1 is mainly controlled by the growth of S^{2-} ($CuFe_{1-x}S_2$,), S_2^{2-}(CuS_2), and S_n^{2-}(polysulfide) species, and this process determines the hydrophobicity of chalcopyrite. The electrochemical oxidization process A2 is mainly controlled by the oxidative dissolution of sulfur species and the hydroxylation of iron, and this process influences the hydrophilicity of chalcopyrite. The EIS spectra of oxide product layers could be illustrated by the equivalent circuit of $R_e(Q_{dl}R_{ct}(Q_fR_f))$, and the degree of hydrophilicity for chalcopyrite is higher when the value of charge transfer resistance $R_{ct.}$ is at larger value.

References

1. G.Z. Qiu et al., "Corrosive Electrochemistry of Jamesonite," *Transactions of Nonferrous Metals Society of China*, 14 (2004), 1169-1173.
2. P. Velasquez et al., "Electrochemical Impedance Spectroscopy Analysis of Chalcopyrite $CuFeS_2$ Electrodes," *Colloids and Surfaces*, 140(1998), 177-182.
3. P. Velasquez et al., "A Chemical, Morphological, and Electrochemical (XPS,SEM/EDX,CV, and EIS) Analysis of Electrochemically Modified Electrode Surfaces of Natural Chalcopyrite ($CuFeS_2$) and Pyrite(FeS_2) in Alkaline Solutions," *Journal of Physical Chemistry B*, 109(2005), 4977-4988.
4. H. Guo and W.T. Yen, "Pulp Potential and Floatability of Chalcopyrite," *Minerals Engineering*, 16(2003), 247-256.
5. R. Woods, "Electrochemical Potential Controlling Flotation," *International Journal of Mineral Process*, 72(2003), 151-162.
6. D. Kocabag and T. Guler, "Two-Liquid Flotation of Sulphides: An Electrochemical Approach," *Minerals Engineering*, 20(2007), 1246-1254.
7. T. Guler et al., "Electrochemical Behaviour of Chalcopyrite in the Absence and Presence of Dithiophosphate," *International Journal of Mineral Process*, 75(2005), 217-228.
8. A. Uribe Salas et al., "Metallurgical Improvement of A Lead/Copper Flotation Stage by Pulp Potential Control," *International Journal of Mineral Process*, 59(2000), 69-83.
9. P. Velasquez et al., "Voltammetry and XPS Analysis of a Chalcopyrite $CuFeS_2$ Electrode," *Colloids and Surfaces A: Physicochemical and Engineering Aspects*, 140(1998), 369-375.
10. J.R. Gardner and R. Woods, "A study of the Surface Oxidation of Galena Using Cyclic Voltammetry," *Journal of Electroanalytical Chemistry*, 100(1979), 447-459.
11. I.C. Hamilton and R.Woods, "An Investigation of Surface Oxidation of Pyrite and Pyrrhotite by Linear Potential Sweep Voltammetry," *Journal of Electroanalytical Chemistry*, 118(1981),327-343.
12. T. Gulera and C. Hiyilmaz, "Hydrophobicity of Chalcopyrite with Dithiophosphate and Dithiophosphinate in Electrochemically Controlled Condition," *Colloids and Surfaces A: Physicochemical and Engineering*, 235(2004),11-15.
13. J. Yu et al., "Effect of ElectricPotential on Chemical Composition of Surface on Chalcopyrite in Collectorless Solution," *Journal of Northeastern Univer sity(Natu ral Science)*, 32 (5) (2011), 700-707.

14. S. Chander, "A Brief Review of Pulp Potentials in Sulfide Flotation," *International Journal of Mineral Process*, 72(2003), 141-150.
15. J.Q. Zhang and C.N. Cao, *Introduction of Electrochemical Impedance Spectroscopy* (Beijing, NY: Science Press, 2002), 113.
16. G. Baril and G. Celikten, "The corrosion of Pure Magnesium in Aerated and Deaerated Sodium Sulphate Solutions," *Corrosion Science*, 43(2001), 471-484.
17. M. Anik and G. Celikten, "Analysis of the Electrochemical Reaction Behavior of Alloy AZ91 by EIS Technique in H_3PO_4/KOH Buffered K_2SO_4 Solutions," *Corrosion Science*, 49(2007), 1878-1894.
18. Z. Kerner and T. Pajkossy, "Impedance of Rough Capacitive Electrodes: the Role of Surface disorder," *Journal of Electroanalytical Chemistry*, 448(1998), 139-142.
19. T. Pajkossy and L. Nyikos, "Diffusion to Fractal Surface- Ⅱ .Verification of theory," *Electrochimical Acta*, 34(1989),171-179.

Characterization of Minerals, Metals, and Materials 2015
Edited by: John S. Carpenter, Chenguang Bai, Juan Pablo Escobedo, Jiann-Yang Hwang, Shadia Ikhmayies, Bowen Li, Jian Li, Sergio Neves Monteiro, Zhiwei Peng, and Mingming Zhang
TMS (The Minerals, Metals & Materials Society), 2015

PULLOUT TESTS BEHAVIOR OF EPOXY MATRIX REINFORCED WITH MALVA FIBERS

Jean Igor Margem[(1)]; Sergio Neves Monteiro[(2)] ; Vinicius Alves Gomes[(3)]; Marina Rangel Margem[(3)]; Frederico Muylaert Margem[(3)]

(1) ISECENSA - Instituto de Ensino Superiores do Censa, Rua Salvador Correa,139, 28035-310, Campos dos Goytacazes, Rio de Janeiro , Brazil, (2) IME - Military Institute of Engineering, (3) UENF - State University of the Northern Rio de Janeiro, Advanced Materials Laboratory, LAMAV; Av. Alberto Lamego, 2000, 28013-602, Campos dos Goytacazes, Brazil.
igormargem@gmail.com

Abstract

The interface between the matrix and the reinforcing fiber plays an important role in the efficiency by which an applied load is transmitted through the composite structure. The shear stress at the fiber/matrix interface can be associated with this load transference and, consequently, affects the composite strength. In the present work, pullout tests were used to evaluate the interfacial shear stress of malva fiber in epoxy matrix composites. A small critical length was found for the malva fiber embedded in epoxy, which corresponds to a relatively weak fiber/matrix bond and lower interfacial strength.

Keywords: epoxy composite, pullout test, malva fiber, fracture analysis.

Introduction

Fiber reinforced composites are associated with a successful class of materials with modern applications in many industrial branches where optimum combination of properties is desirable [1-2]. Important examples are those of synthetic fibers like aramid and carbon reinforcing composites for which high mechanical strength, stiffness and toughness are required like in armor protection and airplane structure. Other uses such as light weight automobile interior components or chemical storing tanks that do not require high mechanical performance have been fabricated with glass fiber composites. In fact, glass fiber is today the most widely used reinforcement for polymeric composites mainly by its low cost as compared to other synthetic fibers [3].

Energy and environmental questions are presently favoring the replacement of glass fiber by natural fibers in its typical composite applications [4]. The advantage of natural fibers, especially those lignocellulosic extracted from plants, over the glass fiber are presently a great motivation for the increasing use of "green" composites in automobiles [5-6-7]. Glass fiber is more expensive, heavier and abrasive to processing equipment. Moreover, this synthetic fiber presents a health risk when inhaled and its fabrication is associated a high consumption of energy. None of these shortcomings applied to lignocellulosic fibers that, in addition, are renewable, biodegradable and neutral with respect to carbon dioxide emission, which is believe to be the root cause of the earth greenhouse effect and, by extension, the responsible for global warming.

One important disadvantage of natural fibers is their limited dimensions as compared with synthetic fibers that can be fabricated in a continuous way with required length and diameter. However, for composite reinforcement only a critical length is necessary for maximum reinforcement [8,9]. In other words, a long fiber for composite strengthening does not need to have a length 15 times greater than the critical length for effective reinforcement [9]. Therefore, the question for a lignocellulosic fiber is the value of its critical length, l_c, which also permits the evaluation of its interfacial strength, τ_i, with a specific polymer matrix. Kelly and Tyson [10] proposed a method to evaluate the value of τ_i based on the experimentally determined critical length by pullout tests.

$$\tau_i = \frac{r\ \sigma_f}{2\ l_c} \qquad (1)$$

Where **r** is the fiber radius and σ_f is the fiber tensile strength, and l_c is the critical length.

Equation (1) has been applied in different lignocellulosic fibers using polyester as matrix for the pullout tests [11-14]. In these works it was generally found that the interfacial strength was relatively low for natural fibers embedded in polyester capsules simulating the composite matrix. Epoxy is another thermoset polymer with extensive application as composite matrix. Therefore, the objective of the present work was to evaluate the interfacial shear stress of malva fiber reinforcing epoxy matrix composites by means of pullout tests.

Experimental Procedure

The fibers of malva (*Urena Lobbata, Linn*) were obtained from the Brazilian firm in the state of Pará, north of Brazil. Figure 1 illustrates a plant of malva that belongs to the family of the Malvaceae, and is native of the Amazon and Pará region. The malva fiber is known by its high strength, smoothness and low density [2].

Figure 1. A malva plantation (*Urena lobbata,linn*)

The fibers were used in the as-received condition, without any surface treatment, after a room temperature drying procedure. The length and the diameter of the fibers were statistically evaluated as shown in Fig. 2. In this figure, it can be seen that most of the malva fibers has an average length of 180 mm and a relatively small average diameter of 0.065 mm, explained by the large dispertion common in natural fibers.

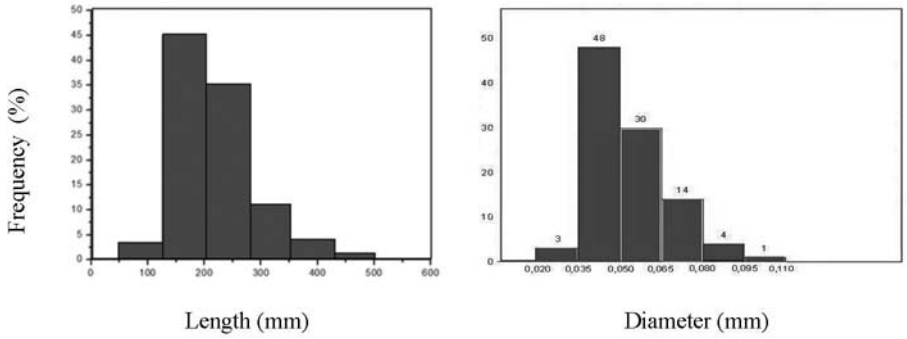

Figure 2. Statistical distribution of malva fiber dimensions.

The pullout test was performed according to the schematic drawing shown in Fig. 3. The embedded length **L** in Fig. 3 was varied from 3 to 50 mm in order to generate a pullout tensile stress versus **L** curve. The single malva fiber was mounted on cylindrical epoxy socket, Fig. 3, with 6 mm in diameter. The pullout test was conducted on a mechanically driven Instron machine with pneumatic action grips at a strain rate of 5×10^{-3} s^{-1}. A holding pressure of 0.15 MPa was experimentally determined to provide reliable test results. The polymeric resin used as the embedding material, simulating the composite matrix, was a commercially available stoichiometric epoxy type, phr13, diglycidyl ether of the bisphenol-A (DGEBA) resin mixed with a triethhylene tetramine (TETA) hardener. The fiber/epoxy socket was cured at room temperature for at least 24 hours. A minimum of 20 specimens were tested for each value of **L**. Scanning electron microscopy, SEM, observations of the curaua fibers were conducted in a model JSM6460 LV Jeol microscope, operating at 20kV.

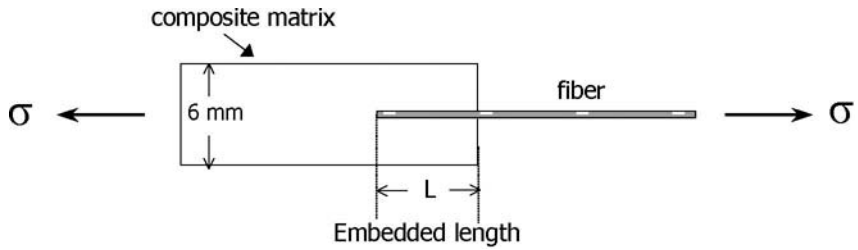

Figure 3. Schematic representation of the pullout test.

Results and Discussion

The results of more than 100 pullout test are summarized in Table 1 .

Table 1. Average Pullout Tensile Strength for each embedded malva fiber length.

L (mm)	Pullout Tensile Strength (MPa)
3	125.2 ± 81.3
5	134.0 ± 36.7
10	251.4 ± 101.5
15	374.0 ± 89.2
20	469.1 ± 75.5

In addition to pullout tests, conventional tensile tests were also performed in more than 20 single fibers. The results of these tensile tests correspond to those malva fibers within the statistical data presented in Fig. 2. The mean value obtained for the tensile strength of single fibers was:

$$\sigma_m = 309.2 \pm 279.1 \text{ MPa} \quad (2)$$

From the data in Table 1, the variation of the pullout strength with the embedded fiber length, **L**, was plotted in Fig. 4. In association with each point, the corresponding statistical limits of the standard deviation are also shown. The first thing to be noticed in the plot in Fig. 4 is the relatively large dispersion of values given by the statistical limits. This is a consequence of the intrinsic heterogeneous characteristics presented by natural fibers [16]. No matter how large could be the number of tested specimens for each **L**, a considerable dispersion would always be found. Therefore, it is not possible to interpret the pullout results of a natural fiber, Fig. 4, in the same manner as for synthetic fibers' results. In other words, no precise value of a critical length, l_c, can be determined from plots such as that for malva fibers.

Considering the mean values and their statistical limits in Fig. 4, it is proposed the following interpretation for the variation of the pullout strength with **L**. For values of **L** below 3 mm, the fiber normally slides out of the epoxy socket without rupture. This is a clear indication that the embedded length is shorter than that critically required to hold the fiber in contact with the polymeric matrix [9].

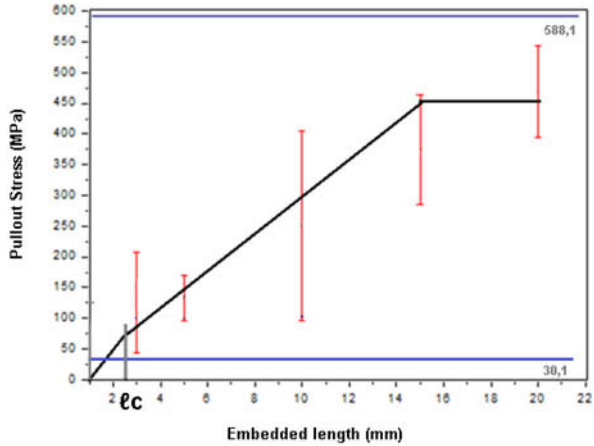

Figure 4. Variation of pullout strength as a function of the embedded fiber length.

The arbitrary consideration of the horizontal lines in Fig. 4 now allows the determination of the value of l_c. This corresponds to minimum embedded length investigated or the shorter embedded length in the matrix, causing slippage of the fiber and no rupture:

$$l_c = 2.6 \text{ mm} \tag{3}$$

The embedded length of the malva fibers was decreased until slippage from the matrix occuring without the rupture, leaving an empty cavity in the analysed matrix. More precise evaluation of the critical length could perhaps be done by considering the smaller embedded length. However, the relatively large dispersion in the statistical limits makes such a consideration in the case of malva fibers of no relevance. With the value of l_c from Eq. (3) one can calculate the shear strength at the malva fiber/epoxy interface using the Eq. (1). In this equation the value of **r** can be a source of error for natural fibers, since the cross section are not, usually, circular. Moreover, the resulting area of the fiber can vary in forms and dimensions over fairly large ranges [11]. For the calculation of the interface shear strength,τ_i, the mean radius **r** = 0.07 mm, obtained from Fig. 2, was considered. Thus, the calculated value and corresponding statistical limits for τ_i was obtained.

$$\tau_i = 3.1 \pm 1.17 \text{ MPa} \tag{4}$$

Comparing this value with others reported on the literature [11,17,19] it can be inferred that the malva fiber/epoxy interface is relatively strong. This corroborates the common trend found when lignocellulosic fibers [20,21] are used to reinforce polymeric matrix composites. For instance, the piassava fiber/polyester interface may reach τ_i = 2.8 MPa [11], while the sisal

fiber/polystyrene interface shear strength can be estimated as τ_i = 2.2 MPa [19]. By contrast, synthetic fibers/polymeric interfaces are comparatively stronger. For example, fiber glass/polypropylene has τ_i = 15.2 MPa and carbon fiber/polypropylene, τ_i = 18.2 MPa [18].

Figure 5 shows, by SEM, the aspect a malva fiber before and after testing. It is important, in this figure, to notice the heterogeneous characteristic of the fiber, which is composed of many naturally bound filaments.

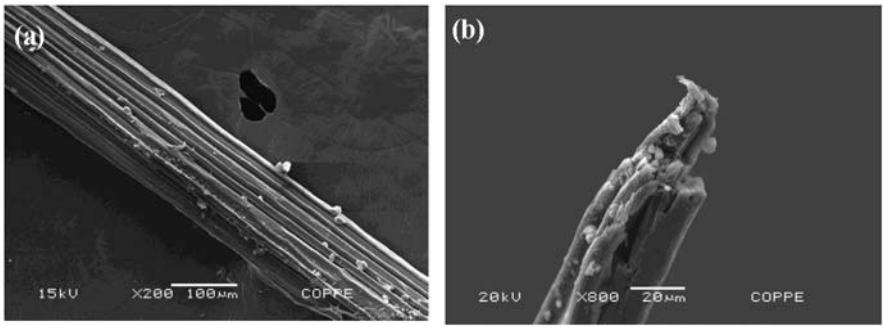

Figure 5. Typical aspects of malva fibers: (a) before testing and (b) after testing.

The experimental value determined in the present work for the critical length of the malva fiber/epoxy composites is of significant practical interest. Since the naturally extracted malva fibers have lengths that may reach l = 180mm, the critical length in Eq. (2) is much smaller than the commonly accepted [9] $l > 15\, l_c$ ratio that defines a continuous fiber. Therefore, the naturally extracted curaua fibers will normally act as continuous fibers for load bearing applications when used as reinforcement for polymeric composites.

Conclusions

- Malva fibers are among the strongest lignocellulosic fibers with tensile strengths that may reach values above 400 MPa.
- The critical fiber length evaluated by pullout testes was found to be l_c = 2.6 mm , which is comparable to others found for piassava, sisal and curaua.
- The calculated malva fiber/epoxy resin interface shear strength is relatively large, τ_i = 3.10 MPa, but of the same order expected for natural fibers.
- In terms of the commercially available lengths, the malva fibers correspond to continuous fibers for polymeric matrix composite reinforcement.

Acknowledgements

The authors thank the support to this investigation by the Brazilian agencies: CNPq, CAPES, FAPERJ. It is also acknowledged the use of the SEM microscope from COPPE/UFRJ.

References

1. B.D. Agarwal, L.J. Broutman, *Analysis and Performance of Fiber Composites* (New York: John Wiley & Sons, 1990).
2. K.H.G. Ashbee, *Fundamental Principles of Fiber Reinforced Composites*, (Lancaster: Technomic Pub. Co. Inc., 1993).
3. K.K. Chawla, *Composite Materials*, (New York: Springer–Verlag, 1993).
4. P. Wambua, I. Ivens, I.Verpoest, "Natural fibers: can they replace glass and fibre reinforced plastics?", *Composites Science and Technology*, 63 (2003) 1259-1264.
5. G. Marsh, "Next step for automotive materials". *Mater. Today*, 6(4) (2003) 36-43.
6. S. Hill, "Cars that grow on trees". *New Scientists*, 153(2067) (1997) 36-39.
7. R. Zah, R. Hischier, A.L. Leão, I. Brown, "Curaua fibers in automobile industry – A sustainability assessment". *J. Cleaner Production*, 15, (2007) 1032-1040.
8. A. Kelly, Strong Solids, Londres, University Press, 1966.
9. W.D. Callister Jr., *Materials Science and Engineering – An Introduction*, 3 ed., (New York, NY: John Wiley & Sons, 1994) 769.
10. A. Kelly, W.R. Tyson, *High Strength Materials* (New York: Wiley, 1965).
11. R.C.M.P. Aquino, S.N. Monteiro, J.R.M. d'Almeida, "Evaluation of the Critical Fiber Length of Piassava (*Attalea funifera*) Fibers using the Pullout Test", *Journal of Materials Science Letters*, 22 (2003) 1495-1497.
12. S.N. Monteiro, J.R.M. d'Almeida, J.F. de Deus, "Pullout tests to evaluate the critical length of natural fibers" (in Portuguese) *Proceedings of the 60thAnnual Meeting of ABM* (Belo Horizonte, Brazil, July 2005)1-10.
13. S.N. Monteiro, J.F. de Deus, J.R.M. d'Almeida, "Interfacial Strength of Curaua Fiber Reinforced Polyester Composites", *Proceedings of SAM-CONAMET* (Mar del Plata, Argentina, 2005) 1-6.
14. S.N. Monteiro, J.F. de Deus, R.C.M.P. Aquino, J.R.M. d'Almeida, "Pullout Tests of Coir Fiber to Evaluate the Interface Strength in Polyester Composites", Proceedings of the TMS Conference, (San Antonio, USA, March, 2006) 1-8.
15. T. G. Schuh and U. Gayer: *Lignocellulosic Plastic Composites* (Botucatu, SP, Brazil: UNESP, 1997)181-195.
16. A. N. Shah, S. C. Lakkad, "Mechanical properties of jute reinforced plastics", *Fiber Sci.& Technol.*, 15 (1981) 41-46.
17. F. Chen, F. R. Jones, "Injection-molding of glass-fiber-reinforced phenolic composites .1. Study of the critical fiber length and the interfacial shear-strength" *Plastics, Rubber & Comp. Process. & Applications*, 23(4) (1995) 241-248.
18. S.Y. Fu, B. Lauke, E. Mäder, X. Hu, C. Y.Yue, "Fracture resistance of short-glass-fiber-reinforced and short-carbon-fiber-reinforced polypropylene under Charpy impact load and its dependence on processing", *J. Mater. Process. Technol.*, 89-90, (1999) 501-507.
19. K.C.M. Nair, S.M. Diwan, S. Thomas, "Tensile properties of short sisal fiber reinforced polystyrene composites", *J. Appl. Polym. Sci.*, 60 (1996) 1483-1497.
20. A.K. Bledzki, J. Gassan, "Composites reinforced with cellulose-based fibres", *Prog. Polym. Sci*, 24 (1999) 201-274.
21. Margem, J. I. ; Margem, F. M.; Monteiro, S. N.. Weibull Analysis of the density and Elastic Modulus of Malva Fibers with Different Diameters. In: 67º Congresso Internacional da Associação Brasileira de Metalurgia, Materiais e Mineração, 2012, Rio de Janeiro, RJ. Anais do 67 Congresso Internacional ABM, 2012. v. 1. p. 2341-2352.

Characterization of Minerals, Metals, and Materials 2015
Edited by: John S. Carpenter, Chenguang Bai, Juan Pablo Escobedo, Jiann-Yang Hwang, Shadia Ikhmayies, Bowen Li, Jian Li, Sergio Neves Monteiro, Zhiwei Peng, and Mingming Zhang
TMS (The Minerals, Metals & Materials Society), 2015

TENSILE STRENGTH OF POLYESTER COMPOSITES REINFORCED WITH FIQUE FIBERS

Giulio Rodrigues Altoé, Pedro Amoy Netto[1], Maria Carolina Andrade Teles[1], Glenio Daniel[1], Frederico Muylaert Margem[1], Sergio Neves Monteiro[2].

1 State University of the Northern Rio de Janeiro, UENF, Advanced Materials Laboratory, LAMAV; Av. Alberto Lamego, 2000, 28013-602, Campos dos Goytacazes, Brazil
2 Instituto Militar de Engenharia , IME, Praça Gen. Tibúrcio, nº80 Urca, Rio de Janeiro - RJ, 22290-270
giulioaltoe@gmail.com

Keywords: Fique fiber, polyester composite, tensile test.

Abstract

The environmental concern is creating pressure for the substitution of high energy consumption materials for natural and sustainable ones. Compared to synthetic fibers, natural fibers have shown advantages in technical aspects such as flexibility and toughness. So there is a growing worldwide interest in the use of these fibers. Fique fiber extracted from fique plant, presents some significant characteristic, but until now only few studies on fique fiber were performed. This work aims to make the analysis of the tensile strength of polyester composites reinforced with fique fibers. The fibers were incorporated into the polyester matrix with volume fraction from 0 to 30%. After fracture the specimens were analyzed by a SEM (scanning electron microscope).

Introduction

The interest of this research is to develop composites with polyester resin matrix reinforced with continuous and aligned fique fibers, for applications in various industries, including construction and automotive industry. Conflicts related to the use of non-renewable forms of energy are increasing the interest to enter the market to replace natural materials, synthetic materials synthetics have a higher power consumption in its manufacture [1-4].

Therefore, applications of natural lignocellulosic fibers obtained from cellulose-based plants are receiving increased attention as an alternative to replace more environmentally correct non-recyclable materials, energy intensive and glass fiber composites in [5-6].

The use of composites reinforced with natural fibers is a reflection of the concerns with environmental issues such as pollution caused by waste that is not biodegradable or cannot be incinerated and climate change due to CO2 emissions associated with the processes of intensive energy and also motivates this work to develop self-sustaining, since natural fibers generate a source of income, especially in developing countries, where most originate, encouraging the cultivation of non-food agriculture [7-9]. Additionally, it is worth also remembering that these fibers come from renewable sources, in addition to being abundant, inexpensive and have a relevant set of mechanical properties [10].

Then, in order to have a composite rigid enough to compete with conventional products such as sheets of wood, only a limited percentage of fique fiber can be incorporated in the polymeric matrix [11-13]. This means that the final cost of the composite would more depending on its processing and polymer resin used as matrix. Therefore, the aim of this work was to study the mechanical properties of polyester matrix composites reinforced with continuous fibers and lined with fique.

Experimental Procedure

Composites were prepared with distinct volume fractions, up to 30%, of fique fibers incorporated into a commercial unsaturated polyester resin, already mixed with 0.5 wt% of methyl-ethyl-ketone. The as-received fique fibers were first cleaned in water and then dried at 60° C for 24 hours. Tensile specimens for each composite was fabricated by laying down the fique fibers in a flat and open dog-bone shaped silicone mold with 5.8 x 4.5 mm of reduced cross section and 35 mm of gage length of the specimen, which corresponds to the tensile axis. Still fluid polyester resin already mixed with the hardener was poured onto the fique fibers inside the mold and allowed to cure for 24 hours at room temperature.

A total of seven composite specimens were prepared for a given volume fraction of fique fiber. Each specimen was tensile tested in a model 5582 universal Instron machine at an acclimatized 25° C and a strain rate of 1.0 mm/s. The fracture surface of some representative specimens was attached to a metallic support by a conducting carbon tape and then coated with platinum to be analyzed by scanning electron microscopy, SEM, in a model SSX-550 Shimadzu microscope operating with secondary electron at an accelerating voltage of 15 kV.

Results and Discussion

Examples of tensile load vs. elongation curves for distinct volume fraction composite specimens are shown in Figure 1.

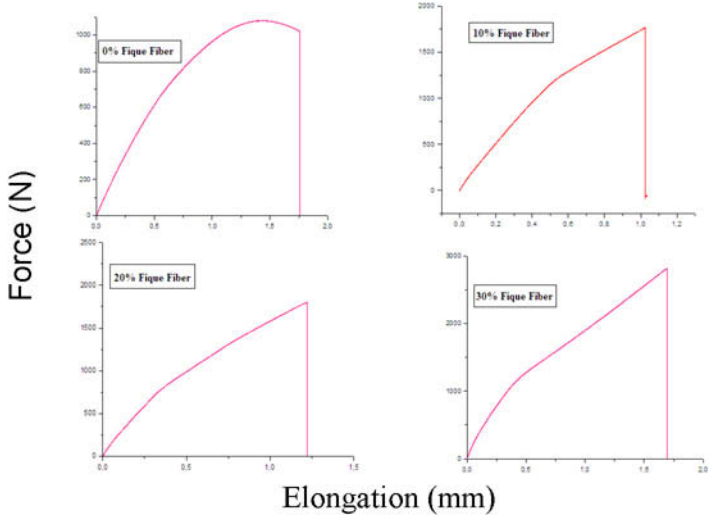

Figure 1. Tensile load vs. elongation curves for polyester composites of volume fraction of fique fibers

Figure 2 depicts the macro aspects of typical tensile ruptured specimens for each volume fraction of fique fiber incorporated into polyester composites.

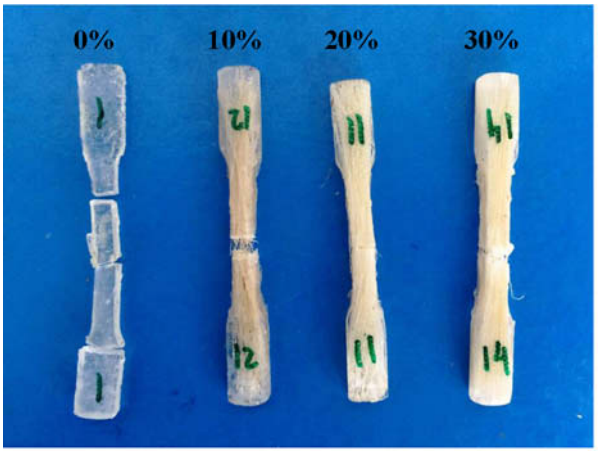

Figure 2. Typical tensile ruptured specimens of polyester composites with different volume fraction of continuous and aligned fique fiber

Based on the results of the tensile load vs. elongation curves, such as the ones shown in Fig 1, the tensile strength, elastic modulus and the total deformation were evaluated. Table 1 presents the average value of these tensile properties for the distinct volume fraction incorporated into polyester composite.

Table 1. Tensile properties of the polyester composites incorporated with continuous and aligned fique fibers

Volume Fraction of fique fiber (%)	Tensile Strength (MPa)	Elastic Modulus (GPa)	Total Deformation (%)
0	27.72 ± 7,22	0.31 ± 0.12	3.33 ± 2.80
10	32.98 ± 3.36	0.28 ± 0.23	7.30 ± 1.81
20	47.54 ± 6.42	0.68 ± 0.24	6.91 ± 1.31
30	61.65 ± 6.76	0.72 ± 0.11	8.88 ± 1.12

Figure 3 plots the variation of the tensile strength, elastic modulus and total deformation, presented in Table 1 for polyester composites, with the volume fraction of fique fibers.

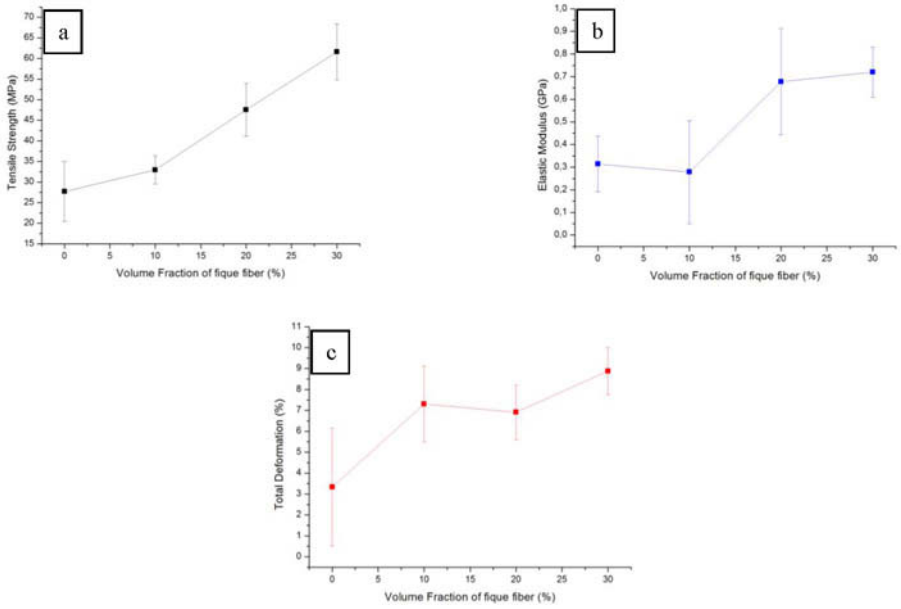

Figure 3. Variation of the tensile strength (a) and elastic modulus (b) and total deformation (c) with the volume fraction of fique fibers in polyester composites.

An important result to be mentioned in Fig. 3 is that, as the percentage of fique fiber increases, the tensile strength, elastic modulus and total deformation in a nearly linear relationship, although the elastic modulus practically do not vary between 0 and 10%.

Figure 4 shows with different magnifications the typical SEM fractographs of tensile ruptured specimens corresponding to polyester composite incorporated with a volume fraction of 30% of fique fibers.

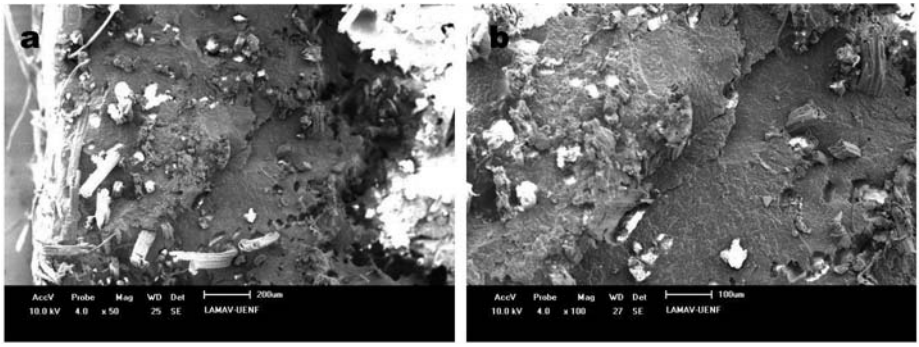

Figure 4. SEM fractographs of a polyester composite with 30% of volume fraction of fique fibers: (a) 50x and (b) 100x

The fracture analysis of representative tensile ruptured specimens was performed by microscopic (SEM) observations. Figure 4 shows typical SEM fractographs of a 30% volume fraction of fique fiber reinforced polyester composite. With lower magnification, Fig 4(a), the fracture surface display evidence of broken fibers sticking out of the polyester matrix. Apparently, these fibers are well adhered to the matrix, which justifies the significant improvement on the composites strength and stiffness with increasing amount of fibers up to 30%, as shown in Fig. 3.

Is notable the crack propagation is blocked by the fique fibers, opening a space between the fiber and the matrix, changing the crack propagation direction to transversal ones. Even after of polyester matrix fracture the fibers continue resisting to tensile effort, because this behavior the composite find higher resistance values in correlation with pure matrix and could explain the no homogeneous fracture on composites with higher fique fibers incorporation as seen in Fig 2.

Conclusions

- The incorporation of continuous and aligned fique fibers increases the tensile strength and stiffness of polyester matrix composites.
- The macro and microstructures indicates that the fique fiber acts as effective barrier to the propagation of the brittle break in the polyester matrix, being of great importance for the improvement of the mechanical properties of the composite.

References

1. S.N. Monteiro, F.P.D. Lopes, A.S. Ferreira, D.C.O. Nascimento, "Natural fiber polymer matrix composites: cheaper, tougher and environmentally friendly", *JOM*, 61 (2009) 17-22.
2. S.N. Monteiro, D.C.O. Nascimento, L.C. Motta, "Effect of jute waste fiber surface treatment on the reinforcement strength in epoxy composites", *Proceeding of the REWAS 2008 Conference*, (Cancun, Mexico, October, 2008) 1-6.
3. D.C.O. Nascimento; F.P.D. Lopes; S.N. Monteiro, "Tensile behavior of lignocellulosic fiber reinforced polymer composites: Part I jute /epoxy" *Rev. Mater*, 15(2) (2010) 199 -205.
4. A.K. Mohanty, M. Misra, L.T. Drzal, "Sustainable biocomposites from renewable resources: opportunities and challenges in the green material world", J. Polym. Environ., v.10, (2002) 19-26.
5. P, Wambua, I. Ivens, I. Verpoest, "Natural fibers: can they replace glass and fibre reinforced plastics?", Composites Science and Technology, v.63, (2003) 1259-1264.
6. A.N. Netravali, S. Chabba, "Composites get greener", Material Today, v.6, p. 22-29, 2003.
7. S.N. Monteiro, F.P.D. Lopes, A.S. Ferreira, Nascimento, D.C.O. "Natural fiber polymer matrix composites: cheaper, tougher and environmentally friendly", JOM, v.61, (2009) 17-22.
8. R.C.M.P. Aquino, J.R.M. D'Almeida, S.N. Monteiro, "Flexural Mechanical Porperties of Piassava Fibers (Attalea funifera)-Resin Matrix Composites", Journal of Materials Science Letters, v. 20, (2001) 1017-1019.
9. A.P. Kumar, R.P. Singh, B.D. Sarwade, "Degradability of Composites, Prepared from Ethylene-Propylene Copolymer and Jute Fiber under Accelerated Aging and Biotic Environments", Mat. Chemistry and Physics, v. 92, (2005) 458-469.
10. J. Crocker, "Natural materials innovative natural composites", Materials Technology, n.2-3, (2008)174-178.

11. S.N. Monteiro, F.P.D. Lopes, A.S. Ferreira, D.C.O. Nascimento, "Natural fiber polymer matrix composites: cheaper, tougher and environmentally friendly", JOM, 61(1), (2009) 17-22.
12. A.K. Mohanty, M.A. Khan, G. Hinrichsen, "Influence of Chemical Surface Modification on the Properties of Biodegradable Jute Fabrics-Polyester Amide Composites", Composites: Part A, v. 31, (2000) 143-150.
13. S. Mohanty, S.K. Verma, S.K. Nayak, "Dynamic Mechanical and Thermal Properties of MAPE Treated Jute/HDPE Composites", Composites Science and Technology, v. 66, (2006) 538-547.

Characterization of Minerals, Metals, and Materials 2015
Edited by: John S. Carpenter, Chenguang Bai, Juan Pablo Escobedo, Jiann-Yang Hwang, Shadia Ikhmayies, Bowen Li, Jian Li, Sergio Neves Monteiro, Zhiwei Peng, and Mingming Zhang
TMS (The Minerals, Metals & Materials Society), 2015

CHARACTERIZATION OF POLYESTER MATRIX REINFORCED WITH BANANA FIBERS THERMAL PROPERTIES BY PHOTOACOUSTIC TECHNIQUE

Foluke S. de Assis[1], Pedro A. Netto[1], Frederico M. Margem[1], Artur R. P. Junior Sergio N. Monteiro[2]

[1] State University of the Northern Rio de Janeiro, UENF, LAMAV; Av. Alberto Lamego, 2000, 28013-602, Campos dos Goytacazes, Brazil.
[2] Instituto Militar de Engenharia , IME, Praça Gen. Tibúrcio, nº80 Urca, Rio de Janeiro - RJ, 22290-270
sergio.neves@ig.com.br

Abstract

Synthetic fibers are being replaced gradually by natural materials such as lignocellulosic fibers. Compared to synthetic fibers, natural fibers have shown advantages in technical aspects such as environmental and economic. So there is a growing international interest in the use of those fibers. The banana fiber presents significant properties to be studied, but until now few thermal properties on banana fiber as reinforcement of polyester matrix were performed. The present work had as its objective to investigate, by photoacoustic spectroscopy and photothermal techniques the thermal properties of diffusivity, specific heat capacity and conductivity for polyester composites reinforced with banana fibers. In the polyester matrix will be added up to 30% in volume of continuous and aligned banana fibers. These values show that the incorporation of banana fibers in the polyester matrix changes its thermal properties.

Keywords: Polyester composites, natural fiber, thermal diffusivity.

Introduction

Due to growing concern about the ambient impacts from industrial activities, our society is ever more searching for environmentally friendly materials. In this regard, cellulose-based natural fibers, known as lignocellulosic fibers, become a promising solution. Nowadays, they are being considered as a substitute for synthetic fibers, such as glass fiber, used by the industry on a large scale [1-5].

The use of natural fibers to replace traditional materials, especially in aircraft and cars, is motivated by several advantages for the natural material, such as, good toughness and less abrasion on equipment used in processing composite [3, 5, 6], it should be noticed too the low cost and light weight. In addition, unlike the glass fibers [7] lignocellulosic fibers are relatively easy to use and the processing procedures produce less wear on

equipment. The environmental issue is another point in favor of natural fibers, which are renewable, recyclable, biodegradable and neutral with regard to CO_2 emissions [8-9].

According to Zah et al [10], the application of natural fiber composites is rapidly increasing in the automobile industry with annual growth at rates above 20%. Both interior and exterior components are already in market and studies point the main reason for that as the technical advantages such as the higher impact resistance. Lignocellulosic fibers such as coir, flax, jute, ramie, curaua and sisal are currently being used in automobile composite parts that require both strength and toughness [11]. The banana fiber, although strong and flexible [1] has not yet been applied in composites for automobile components. Actually, the fibers obtained from the pseudo-stem of the banana tree commonly is mainly used to fabricate ropes and baskets owing to its high strength .The mechanical properties of banana fiber composites are well known [12-13] however, some thermal properties have not yet been evaluated, so this work aims to evaluate the thermal diffusivity, specific thermal capacity and thermal conductivity of polyester composites reinforced with banana fibers for different fiber volume fractions by photoacoustic and photothermal technique.

Experimental Procedure

Fibers extracted from the stem of the banana plant of the scientific family *Musa balbisiana*) were supplied as a bundle by a group of artisans based in the North Fluminense State University (UENF).Fibers were cut from the pseudo-stem, cleaned with water and later dried for one hour at 60° C. No treatment was applied to the fibers.

Composite specimens were individually prepared with continuous and aligned banana fibers placed in a generic shape. The fibers in amounts of up to 30% of volume were aligned along the specimens tensile axis. Still fluid polyester resin was poured onto the banana fibers, and cured for 24 hours, after this, the samples were grounded to reach a specific thickness below 1,5mm for photoacoustic analysis, as seen in Fig 1(a). Each sample was tested in a photoacoustic open cell as shown in Figure 1(b) and then the photothermal method under continuous laser illumination was also used. Both techniques should determine the thermal diffusivity $\boldsymbol{\alpha_s}$, and specific thermal capacity $\boldsymbol{\rho c_p}$. From these parameters, the thermal conductivity of banana fiber polyester composites (k) was evaluated by equation:

$$k = \alpha_s \rho c_p \qquad [1]$$

The thermal diffusivity was measured by photoacoustic technique which considers heat loss in a sample due to a thermal relaxation process after light absorption. The open photoacoustic cell (OPC) obtains its results by placing the sample in front of the electrets microphone to measure its sound pulse, Figure 1(b). The air chamber in front of microphone works as a conventional gas chamber, usually applied in others photoacoustic techniques [14]. The results interpretation is based on the fact that in OPC method the Diffusion mechanism is dominant. The value of α_s was then obtained by fitting of experimental amplitude data by the equations:

$$\delta P = \frac{\gamma P_0 I_0 (\alpha_g \alpha_s)^{1/2}}{\pi l_g k_s T_0} e^{j(wt - \frac{\pi}{2} l_s \alpha_s)} \frac{e^{-b\sqrt{f}}}{w} \quad [2]$$

Where the α_g is the thermal diffusivity of the gas contained in the photoacoustic chamber, α_s is the thermal diffusivity of the sample, Io is the intensity of absorbed radiation, To is the temperature , the k_s is the thermal conductivity of the sample, the σ_s is the complex thermal diffusion coefficient calculated by the exponent of the exponential.

$$\phi = \phi_0 - b\sqrt{f} \quad [3]$$

Where ϕ is the signal phase after the analysis and ϕ_o is the initial phase before the test, ℓs is the sample thickness and f the photoacoustic signal frequency. It is assumed that the sample is optically opaque, and the heat flow in surrounding air is negligible. In this work the amplitude fit was used because this model produced a smaller error in comparison to a phase fit.

$$b = l_s \sqrt{\pi / \alpha_s} \quad [4]$$

Where l_s is the sample thickness and f the photoacoustic signal frequency. It is assumed that the sample is optically opaque, and the heat flow in surrounding air is negligible. In this work the amplitude fit was used because this model produced a smaller error in comparison to a phase fit.

The specific thermal capacity, ρc_p, and the transfer coefficient of radiated heat can be evaluated through the following equations:

$$\Delta T = \left(\frac{I_0 \tau}{\ell_s \rho C_p}\right) e^{-t/\tau} \quad [5]$$

Where Io is the laser incident intensity in the sample and τ , the temperature rise time, given by:

$$\tau = \frac{\ell_s \rho C_p}{(2H)} \quad [6]$$

Where the transfer coefficient of radiated heat, H, is given by:

$$H = 4\sigma T_o^3 \quad [7]$$

The analysis of thermal diffusivity (α_s) was done by the technique of open photoacoustic cell (OPC) [15-16]. The specimen was directly placed on an electret microphone. Then a modulated laser, with 110mW of power and 660nm of wavelength was focused on the sample. This creates a photoacoustical signal that was picked up by the microphone. The microphone air chamber below the sample works as a conventional gas chamber, usually applied in others photoacoustic techniques [15].

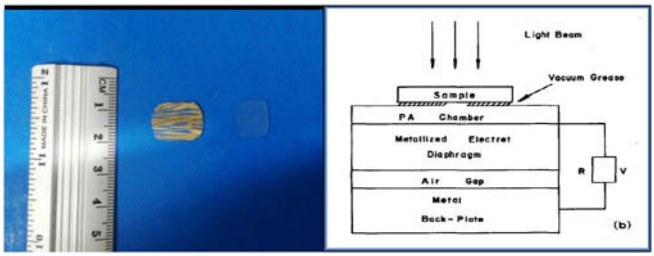

Figure 1. (a) Polyester photoacoustic samples and (b) schematic cross section of the Open photoacoustic cell setup.

Results and Discussion

The results analysis is based on the fact that in the OPC method the photoacoustical diffusion mechanism is dominant because the angular coefficient in the phase and amplitude adjustment are similar as shown in Fig. 2 following ROSENCWAIG & GERSHO (1976) [17].

In figure , the black dots present the experimental data while the continuous line corresponds to best mathematical fit curve to the trajectory of these experimental points when plotted depending on the natural logarithmic of amplitude and frequency product. Considering that the thickness sample is about 0.69mm, thermal diffusivity was obtained based on Eq. (2) and constructed the table below.

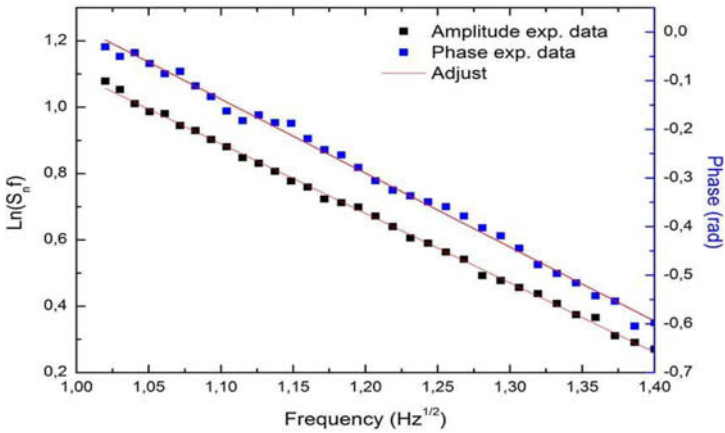

Figure 2. Linear fit for amplitude and phase in function to root square frequency.

Table 1 – Thermal diffusivity to pure polyester and its composites.

Fiber volume (%)	Thickness (mm)	α_s (10^{-7} m²/s)
0% banana	0.70	1.54 ± 0,03
10% banana	0.69	0.83 ± 0.05
20% banana	0.67	0.74 ± 0.02
30% banana	0.71	0.46 ± 0.02

The thermal conductivity was investigated by the technique of thermal capacity per unit volume. An Electro-Opties laser witch 25mW of power and 638nm of wavelength was focused on the sample. The radiation was absorbed by the sample until it becomes saturated. Thereafter, the radiation emission was stopped and the temperature vs. time was plotted as illustrated in Fig. 3. In this figure, solid points correspond to the experimentally obtained data and the continuous line represents the best mathematical curve, which fits the trajectory of the experimental dots. This continuous line was calculated considering the Eq. (5) to (7) [18-19].

That relates the Stefan-Boltzmann constant, σ, and the ambient temperature T_o. Using the τ value, Eq.7 as an adjustable parameter on the curve of Fig.3, the specific thermal capacity could be obtained.

Thus, considering Eq. (5), (6) and (7), the value of the specific thermal capacity of polyester composites with banana fiber was calculated. To complete this thermal characterization was obtained the thermal conductivity for banana fiber polyester composites and using the values of thermal diffusivity the specific thermal capacity was calculated by Eq. (5), (6) and (7) together in Eq. (1) as can be seen in Table 2.

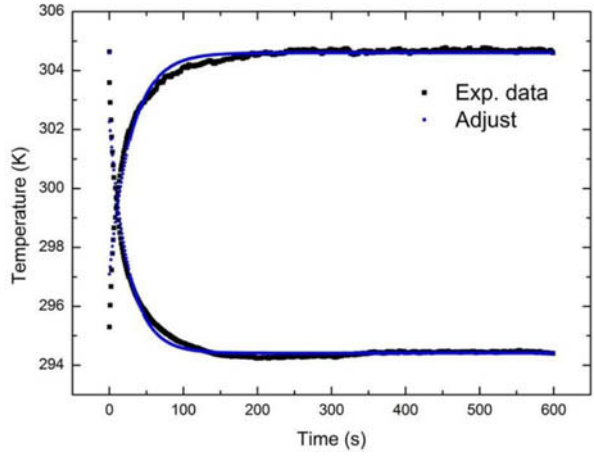

Figure 3. Temperature evolution with time on the back of the sample surface after switching off the illumination.

Table 2 – specific heat capacity and thermal conductivity to pure polyester and its composites

Fiber volume (%)	Thickness (mm)	ρ_c (10^5 J/K.m³)	K (W/m.K)
0% banana	0.71	6.4±0.3	0.093±0.019
10% banana	0.68	7.1±0.1	0.064±0.004
20% banana	0.66	7.3±0.2	0.057±0.002
30% banana	0.72	8.7±0.2	0.039±0.002

The mean values of the thermal properties, listed in Table 1 and Table 2 for polyester composites, are plotted in Figure 4 as a function of volume fraction of banana fibers:

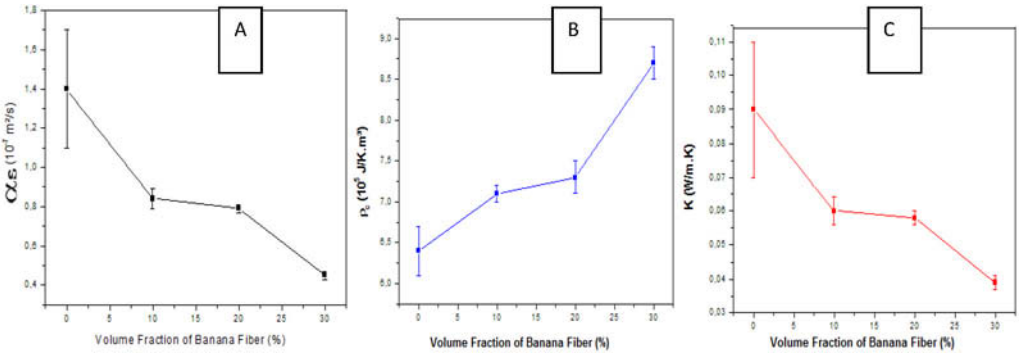

Figure 4 – Variation of thermal diffusivity (a), specific heat capacity (b) and thermal conductivity (c)

It is evident that the incorporation of banana fiber causes a slight decrease in the thermal diffusivity and thermal conductivity when the composite is compared to pure polyester this can be attributed to the high dispersion of the natural fibers, and the fabrication process can include in the material pores, gaps and bad fiber distribution, what can contribute to decline these properties. But it should be noticed that the incorporation of fibers increase the specific heat capacity of the material.

Conclusions

- The thermal diffusivity and the specific heat variation were obtained with reasonable accuracy from mathematical fit of experimental data. These values show that the incorporation of banana fibers in the polyester matrix changes its thermal properties.
- Finally, comparing the values of thermal conductivity (K) of pure polyester to the values of the composites, it may be concluded that the banana fibers act to reduce slightly the thermal conductivity of the material. It was also concluded that the composites of polyester and banana fibers are good insulating materials due to their low thermal conductivity values.

References

1. BLEDZKI, A.K.; GASSAN, J. Composites reinforced with cellulose-based fibres. Program Polymer Science, v. 24, p. 221-274, 1999.
2. NABI SAHED, D.; JOG J.P. Natural fiber polymer composites: a review, Advances in Polymer Technology, v.18, p. 221-274, 1999.
3. MOHANTY, A.K.; MISRA, M.; HINRICHSEN, G. Biofibres, biodegradable polymers and biocomposites: An overview. Macromolecular Matererials and Engineering, v. 276, p.1-24, 2000.
4. CROCKER, J. Natural materials innovative natural composites. Materials technology, v.2-3, n. 3, p. 174-178, 2008.
5. MONTEIRO S.N.; LOPES, F.P.D.; FERREIRA, A.S.; NASCIMENTO, D.C.O. Natural fiber polymer matrix composites: cheaper, tougher and environmentally friendly. JOM, v.61, n. 1, p. 17-22, 2009.
6. GORE, A. An Inconvenient Truth. The Planetary Emergency of Global Warming and What We Can Do About It. Emmaus, Pennsylvania, USA: Rodale Press, 2006
7. PEIJS, T. Natural Fibers Based Composites. Mater. Technol. v.15, p. 281-285, 2000.
8. WAMBUA P.; IVENS. I.; VERPOEST, I. Natural fibers: can they replace glass and fiber reinforced plastic?" Composites Science and Technology, v. 63, p. 1259-1264, 2003.
9. MOHANTY, A.K.; MISRA, M.; DRZAL, L.T. Sustainable biocomposites from renewable resources: Opportunities and challenges in the green materials world. J. Polym. Environ. v. 10, p. 19-26, 2002.
10. R. Zah, R. Hischier, A.L. Leão and I. Brown, "Sisal fibers in automobile industry – A sustainability assessment". J. Cleaner Production, 15, (2007) 1032-1040.
11. Joseph, A.; Sreekala, M. S.; Oomens, Z.; Koshy, P.; Tohomas, S. A. (2002) " A comparison of the mechanical properties of phenol formaldehyde composites reinforced with banana fiber and glass fibers". Composites Science and Technology, v. 62, p. 1857-68, 2002.
12. S. N. Monteiro, F. M. Margem, R. L. Loiola, F. S. Assis, M. P. Oliveira, Characterization of banana fibers functional groups by infrared spectroscopy, Materials Science Forum Vols. 775-776 (2014) pp 250-254 (2014) Trans Tech Publications, Switzerland doi:10.4028/www.scientific.net/MSF.775-776.250.
13. S. N. Monteiro, F. M. Margem, F. S. de Assis, R.L. Loiola, M. P, Oliveira, Izod impact tests in polyester matrix composites reinforced with banana fibers, Materials Science Forum Vols. 775-776 (2014) pp 261-265 (2014) Trans Tech Publications, Switzerland doi:10.4028/www.scientific.net/MSF.775-776.261.
14. ALMOND, D., PATEL P., "Photoacoustic and Photothermal Science and Techniques". Chapman and Hall: London, 1996.
15. VARGAS, H., MIRANDA L. C. M., Photoacoustic and related photothermal techniques. Phys. Rep. 161(2) (1988) 43-101.
16. A. Rosencwaig, A. Gersho, Theory of the photoacoustic effect with solids. Journal of Applied Physics, [s.l], v. 47, n. 1, p. 64–69, 1976.
17. Marquezini, M. V. et al. Open photoacoustic cell spectroscopy. Meas. Sci. Technol., v. 2, 1991.
18. I. Hatta, "Heat capacity measurements by means of thermal relaxation method in medium temperature range", Rev. Sci. Instrum., 50(3) (1979) p. 292-295.

19. L.H. Poley, A.P.L. Siqueira, M.G. da Silva, R. Prioli, A.M. Mansanaris, H. Vargas, "Photothermal methods and atomic force microscopy images applied to the study of poly (3-Hydroxybutyrate) and poly (3-Hydroxybutyrate-co-Hydroxyvalerate) dense membranes" J. Appl. Polym. Sci., 97 (2005) 1491-1497.
20. CALLISTER, W. D., Ciência e Engenharia de Materiais: Uma Introdução. 5ed. LTC, São Paulo (2002).

Characterization of Minerals, Metals, and Materials 2015
Edited by: John S. Carpenter, Chenguang Bai, Juan Pablo Escobedo, Jiann-Yang Hwang, Shadia Ikhmayies, Bowen Li, Jian Li, Sergio Neves Monteiro, Zhiwei Peng, and Mingming Zhang
TMS (The Minerals, Metals & Materials Society), 2015

HOT-PRESSING AND MECHANICAL PROPERTIES OF BN BASED COMPOSITES

Meng Liu [1,2,3]*, Yijie Song[2], Xiaohong Xu[3], Guotao Xu[1], Gaifeng Xue[1], Jixiong Liu[2]
[1] Research and Development Center of Wuhan Iron and Steel (group) Corporation, Wuhan 430080, China
[2] Advanced Materials R&D Center of Wuhan Iron and Steel (group) Corporation, Beijing 102211, China
[3] State Key Laboratory of Silicate Materials for Architectures, Wuhan University of Technology, Wuhan 430070, China

Keywords: Hot-pressing, h-BN, Mechanical properties, Thermal properties, Microstructure

Abstract

BN (Boron Nitride) based composites were prepared with hot-pressing by using h-BN as main material in ceramic preparation process. The relative density, bending strength, vickers' hardness, thermal shock resistance, thermal expansion coefficient, thermal conductivity, phase composition and microstructure were tested and analyzed by using modern testing technology. The results indicate that the best formula is B, the relative density is 97%, the bending strength is 260 MPa, the hardness is HV5 343kg/mm^2, the thermal expansion coefficient is 2.8×10^{-6}℃^{1}, the thermal conductivity is 22 W/(m.K) and have no crack after thermal shock for 20 times by water cool. XRD analysis indicates that the main phase compositions are h-BN, β-Si_3N_4 and sialon. SEM studies show that the grains wrapped up by solid solution.

Introduction

Twin roller continuous casting, a sort of near-net-shape technology, presents numerous advantages on economical production of thin strips, such as low energy consumption, low equipment and operating costs, and rapid solidification [1-4].The twin roll strip steel casting process, developed by the Usinor company under a project called Myosotis. In the process of twin roller continuous casting, the side dams in contact with the rollers act as un-replaceable roles on keeping molten metal from leakage in whole casting process [5-7]. For more than twenty years, continuous casting process has been actively developed and improved by several major steel companies. During casting process, molten metal is frequently dumped into pool region surrounded by rollers and dams, along with rolls rotate to drag metal strips. So side dams have to suffer extremely tough working conditions such as iterative thermal impact (especially more than 1000 °C for steel and iron), heavy abrasion against rolls and strips at high temperature, as well as erosion from different molten metals [8-11]. Therefore, for side dams it is necessary to have good combinations of properties including excellent mechanical properties and thermal

properties. So far, research on materials for side dams is seldom reported [5, 6]. And in the earlier working, other researchers have experimented tens of stuffs such as high temperature ceramics and refractory materials for side dams, unfortunately no solo commercial material was successfully found out. Therefore, it is imperative to develop an appropriate ceramic material to match the using condition in strip casting operations. Generally, each of the monolithic phase ceramic exhibits only a single physical and chemical property, which highly hinders its applications. Accordingly, to develop the multiphase ceramics has been attracting more and more attention because it can combine with the exceptional properties of each ceramic. In this work, a sort of new composite of BN based ceramics were successfully fabricated by hot pressing method. The properties, such as the mechanical properties and thermal properties as well as phase and microstructure were tested and discussed detailedly.

Experimental Methods

Materials preparation

Commercial available raw materials were used in this study. The h-BN (1μm, Zhongpu Co., Ltd., He Bei, China), α-Si_3N_4 (0.7 μm, Hefei Moke Co., Ltd., An Hui, China), AlN (0.5 μm, Hefei Moke Co., Ltd., An Hui, China), Al_2O_3 (2 μm, Luoda Co., Ltd., Shan Dong, China), β-SiC (4 μm, Zhongxintece Co., Ltd., Bao Tou, China), ZrO_2 (0.4 μm, Weina., Ltd., He Nan, China) partially stabilized by 3 % Y_2O_3, and Y_2O_3(3 μm, Shangyuan new material Co., Ltd., Jiang Xi, China) were used to prepare the BN based composites.BN-SiC-ZrO_2, BN-Si_3N_4 and BN-AlN system materials were designed and prepared by using Y_2O_3 and Al_2O_3 as additive material. Corresponding composites were marked as A (BN-SiC-ZrO_2), B (BN-Si_3N_4) and C (BN-AlN), respectively. These powder mixtures were ball-milled for 12 h in an aluminum bottle using aluminum balls as milling media and alcohol as carrier fluid. The mixed slurry was then dried in a rotary evaporator and sieved through an 80-mesh screen. The composites were fabricated by hot-pressing at 1780 °C for 90 min under a uniaxial load of 25 MPa in N_2 protection.

Characterization

Relative density of A, B and C composites were measured by the Archimedes method, while their theoretical densities were calculated using the mixture rule. Bending strength was tested in a three-point configuration (3 mm×4 mm×36 mm), with a span of 30 mm and a crosshead speed of 0.5 mm/min. Hardness was determined by a Vickers indentation tester(Model FV-700, Wuhan, China)using a diamond indenter with a load of 5 kg for 20 s. Thermal expansion coefficient was tested by the thermal expansion coefficient instrument (Model RPZ-03, Wuhan, China), the thermal conductivity was measured by the thermal conductivity tester (Model DRM-Ⅱ, Shenzhen, China). The phase constituents of sintered specimens were identified by X–ray diffraction (XRD) (Model D/MAX–ⅢI, RIGAKU., Japan) using Cu Kα radiation source. The observations of microstructures were performed by scanning electron microscope (SEM) (Model

JSM–5610LV, JEOL., Japan). The thermal shock resistance tests of the specimens were carried out by the silicon–carbide furnace (KSW, Yingshan Prime Partners Furnace Manufacturing Co.Ltd., China) under some thermal cycles from 1100 °C to room temperature using water cooling.

Results and discussion

Relative density and bending strength

The results of the relative density of specimen A, B and C are 92%, 97% and 93% respectively. Fig. 1 is the relationship of bending strength and hardness with different specimens. As can be seen from fig. 1, the bending strength of specimen A, B and C are 170 MPa, 260 MPa and 300 MPa. What's more, the hardness of specimen A, B and C are 67 kg/mm^2, 343 kg/mm^2 and 130 kg/mm^2 as well. The batch formula of A (BN-SiC-ZrO_2) has the lowest relative density, bending strength and hardness. The batch formula of C (BN-AlN) has the highest bending strength of 300 MPa, whereas, the hardness is lower than batch formula B (BN-Si_3N_4).The additive of Y_2O_3 and Al_2O_3 are beneficial to enhance density behavior of BN composite as sintering additive due to formation of liquid phase during the sintering process. Because of the thermal expansion mismatch between ZrO_2 and BN is bigger than it in BN and AlN, also binger in BN and Si_3N_4, which result the batch formula of A is difficult to densitification. So, the relative density, bending strength and hardness is the lower than B and C. In the sintering process of batch formula B and C, the formation of new phases filled in the pores between different grains in the sintering process, which can increase the force of grain boundary phases and make the increase of relative density and bending strength. All in all, compact from the result of relative density, bending strength and hardness, the specimen B can be choosed as the best batch formula.

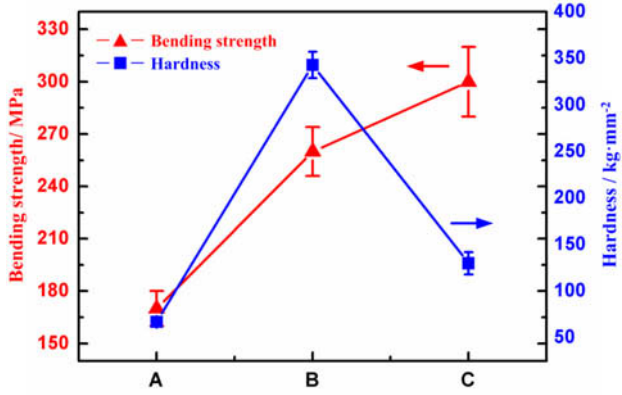

Fig. 1 Bending strength and hardness of BN based composite ceramics

Thermal properties

In the process of twin roller continuous casting process, it need the side dam material have good thermal shock resistance to resistant the shock of melt metal. The thermal shock resistance performance of ceramic materials are mainly depends on its thermal expansion properties, low expansion material has excellent performance in thermal shock resistance. Table I. shows the thermal expansion coefficient at room temperature, thermal conductivity at room temperature and thermal shock resistance. The thermal expansion coefficient of the prepared BN based composite specimen A, B and C are $3.8\times10^{-6}\,°C^{-1}$, $2.8\times10^{-6}\,°C^{-1}$ and $2.7\times10^{-6}\,°C^{-1}$.The thermal expansion coefficient of A is bigger than B and C mainly attribute to ZrO_2. The thermal conductivity of the prepared BN based composite specimen A, B and C are 38 W/(m·K), 22 W/(m·K) and 17 W/(m·K). The thermal conductivity of A is bigger than B and C mainly attribute to the addition of high conductivity of SiC. As seen from thermal shock times, the specimen A, B and C all have bear the thermal shock exceed 20 times, which show a good thermal shock resistance. In the thermal shock process, BN, Si_3N_4, AlN and SiC begin to be oxidized when exposed to air, the oxidation reaction should produce B_2O_3, SiO_2, and Al_2O_3.The amount of oxidation produced on the surface of the specimens are sufficient to form dense oxidation layer for healing microcrack and prevent the further oxidation of the specimen. Simultaneously, SiO_2 and B_2O_3 can react to form a stable borosilicate and silica glass, which can flow easily to cover and protect the surface of specimen. The borosilicate and silica glass phases have an influence on healing surface cracks. Also, in the sintering process, the formation of boundary phase in specimen B and C exhibit better performance than in specimen A. All in all, compact from the result of relative density, bending strength, hardness and thermal properties, the specimen B can be choosed as the best batch formula.

Table I. The Thermal Properties of BN Based Composite Ceramics

Specimen No.	Thermal expansion coefficient ($10^{-6}\,°C^{-1}$)	Thermal conductivity(W/(m·K))	Thermal shock(times)
A	3.8	38	>20
B	2.8	22	>20
C	2.7	17	>20

Phase composition and microstructure

Fig. 2 shows the XRD pattern of the optimized specimen B. As can be seen from the figure, the main phases of specimen B while sintered at 1780 °C are and h-BN, β-Si_3N_4, sialon (Si_5AlON_7). Fig. 3 reveals the typical SEM micrographs showing the fracture features of the specimen B sintered at 1780 °C. As seen from fig. 2 and fig. 3, h-BN and β-Si_3N_4 phases act as the basement; also, a large amount of solid solution exists in the micrographs as well. By contact the analysis of XRD patterns, it indicates that the solid solution is sialon. Phase composition, microstructural aspects and porosity level of the sintered specimen were the main factors influencing the

mechanical properties results. Nearly none porosity have found in fig. 3 and the sialon phase distribute evenly among the specimen who offer high relative density and good mechanical properties. To summarize the analysis of the relative density, mechanical properties, thermal properties, XRD patterns and microstructure, the synthesis of sialon phase among the specimen is useful for the improvement of the performance of relative density and bending strength while low thermal expansion coefficient severely helps to improve thermal shock resistance of the sintered specimen. So, it is acceptable that the multiphase BN based composite ceramic with a good thermal shock resistance, can be prepared completely by hot-pressing sintering technique, thus being suitable to use as the side dam materials in twin roller continuous casting.

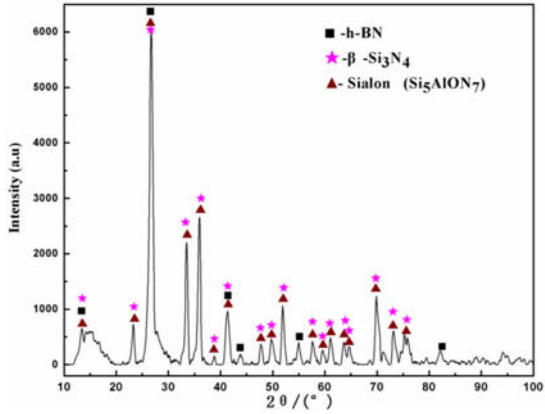

Fig. 2 XRD spectra obtained from the polished surface of the hot-pressed specimen B

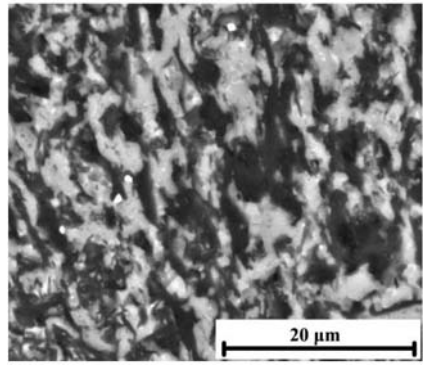

Fig. 3 SEM images of polished fractured surface of hot-pressed specimen B

Conclusions

Results from the present work show that the prepared BN based composite ceramic is suitable for use as side dam material in twin roller continuous casting. The optimum specimen is B which consists by using h-BN as the main material. The hot-pressing temperature of specimen B is 1780 °C with the relative density of 97%, the bending strength is 260 MPa,the hardness is HV5 343 kg/mm^2, the thermal expansion coefficient is 2.8×10^{-6} °C^{-1}, the thermal conductivity is 22 W/(m.K) and have no crack after thermal shock for 20 times by water cool. Analysis of XRD indicates that the main phases after hot-pressing are and h-BN, β-Si_3N_4, sialon (Si_5AlON_7). SEM observation shows that the specimen of B with a large amount of sialon solution which severely helps to improve relative density, mechanical properties and thermal shock resistance. The prepared multiphase BN based composite ceramic with a good thermal shock resistance can be prepared completely by the hot-pressing sintering technique, which is suitable for use as side dam material in twin roller continuous casting.

Acknowledgements

The financial support of Beijing Science and Technology Commission (No. Z131100002413002) is gratefully acknowledged. Also, the authors gratefully acknowledge the collaboration of several of their colleagues for materials synthesis and processing for their many useful discussions in this present work.

References

1. H. Toshio et al., "Twin roll casting of aluminum alloy strips," *Journal of Materials Processing Technology,* 153(2004), 42–47.
2. H. Toshio, "Semisolid strip casting using a twin roll caster equipped with a cooling slope," *Journal of Materials Processing Technology*, 131(2002),558–561.
3. R. Wechsler, "The status of twin roll casting technology," *Scandinavian Journal of Metallurgy*, 32(2003), 56–62.
4. H.L. Wang et al., "Study on side containment technology of twin-roll thin strip continuous casting," *Ironmaking & Steelmaking*, 23(2007), 54–58.
5. P. Fournier and F. Platon, "Laboratory wear studies of refractory side dams in the strip steel casting process," *Tribology Series*, 39(2001), 167–175.
6. P. Fournier and F. Platon, "Wear of refractory ceramics against nickel," *Wear*, 244(2000), 118–125.
7. Zehua Zhou et al., "Novel side dams including advanced laminated ceramic for twin roller continuous casting," *Ceramics International*, 38(2012), 1779-1783.
8. Z.H. Zhou et al., "A thermal shock resistance model for laminated ceramics and its validation," *Journal of European Ceramic Society*, 30(2010), 1543-1547.
9. R. Bermejo et al., "Optimal strength and toughness of Al_2O_3-ZrO_2 laminates designed with

external or internal compressive layers," *Journal of European Ceramic Society*, 28(2008), 1575-1583.
10. T. Lube et al., "Effective fracture toughness in Al_2O_3-Al_2O_3/ZrO_2 laminates," *Journal of European Ceramic Society*, 27(2007), 1449-1453.
11. S. Sarkar and B. Lee, "Evaluation and comparison of the microstructure and mechanical properties of fibrous Al_2O_3-(m-ZrO_2)/t-ZrO_2 composites after multiple extrusion steps," *Ceramic International*, 36(2010), 1971-1976.

Characterization of Minerals, Metals, and Materials 2015
Edited by: John S. Carpenter, Chenguang Bai, Juan Pablo Escobedo, Jiann-Yang Hwang, Shadia Ikhmayies, Bowen Li, Jian Li, Sergio Neves Monteiro, Zhiwei Peng, and Mingming Zhang
TMS (The Minerals, Metals & Materials Society), 2015

EXPERIMENTAL STUDY OF ADVANCED TREATMENT OF COKING WASTEWATER USING PFS COAGULATION-PHOTOCATALYTIC OXIDATION TECHNOLOGY

Lei ZHANG[1], Lina WANG[1], Pu LIU[1], Benquan FU[1], Jiannyang Hwang[2], Shining Chen[3]
[1] R&D center of WISCO, Wuhan, 430080, China;
[2] Advanced Materials Research Center of WISCO (Beijing), Beijing, 102200, China
[3] Wuhan Institute of Shipbuilding Technology, Wuhan, 430050, China

Keywords: Coking wastewater; PFS coagulation; Photocatalytic oxidation technology; TOC removal rate; Advanced treatment

Abstract

A PFS(polymeric ferric sulfate) coagulation-photocatalytic oxidation technology was used for advanced treatment of coking wastewater from secondary biological treatment. Effects of some key factors on TOC removal rate were investigated, and the results were compared with those of the common photocatalytic oxidation technology under the operating parameters of the photocatalytic oxidation defined. Single factor experimental results showed that TOC removal rate could reach 81%, when optimal operating conditions were as follows: TiO_2 loading: 4.0g/L, irradiation time: 4h, initial pH is 5.1and PFS dosage:700mg/L. PFS coagulation and photocatalytic oxidation have synergistic effect, which is meaningful for highly efficient treatment of coking wastewater.

Introduction

Coking phenol cyanogen wastewater is considered as the most toxic one to be treated before being discharged into the environment. It is mostly generated from coal gas purification and recovery of production process, and contains various toxic compounds such as ammonia, thiocyanate, phenols and cyanides in high concentration range [1-3]. Traditional treatment of highstrength cokes wastewater is based on A2/O, O/A/O, A/O2 and other biological nitrogen removal process, which has been widely used for the treatment of coking wastewater. However, these processes are not sufficient to meet the strict requirements of the National Discharge Standard of China (COD <100 mg/L, GB16171-2012). More strict legal limits and laws for the

coking wastewater released from coking industries will be implemented on January 1, 2015. Many researchers are attempting to use different kinds of methods for the treatment of coking wastewater. A number of review papers are available regarding the application of photocatalytic technology methods for environmentally friendly and low cost [4,5]. Used as semiconductors (such as,TiO_2), photocatalysts can oxidize contaminants via photochemical activity to non-toxic carbon dioxide and water under light with a superoxide radical ($O^{2-}\cdot$) and hydroxyl radical (·OH) during the oxidation reaction[6]. Coagulation is an important process in both solid–liquid separation and soluble containments removal from aqueous solution [7]. The polymeric ferric sulfate (PFS) has been widely used for its cheap, non-toxic and high efficient[8,9]. In this study, PFS coagulation-photocatalytic oxidation technology was used for advanced treatment of coking wastewater. The optimum parameters were evaluated in batch experiments for economic aspects.

Materials and methods

Raw wastewater and materials

The raw wastewater used in the experiments was collected from the outlet of a WISCO coke plant with the treatment processes of steam stripping of ammonia and $O_1/A/O_2$ biological treatment and chemical coagulation precipitation, the main water quality indicators are shown in Table 1.

Table 1 The water quality parameters(unit:mg/L,except pH)

Item	pH	TOC	COD_{Cr}	BOD_5	NH_3-N	TN
Raw	7.8	123.6	186	53	23	65
Effluent standard	6～9	-	80	20	10	20

Note：Emission standard of pollutants for coking chemical plant(GB16171-2012)

All the chemicals of this study, including NaOH, Ag_2SO_4, $HgSO_4$, $K_2Cr_2O_7$, TiO_2 powder (anatase), HCl (36%, 1.19g/cm^3), etc, are in analytical reagents grade. They were produced by Chemical Reagent Co., LTD. polymeric ferric sulfate solution (PFS, brown red liquid, iron content 11%, the basicity: 10%, pH (1% in solution) 2.3), was gained from the wastewater treatment facility and used in batch experiments.

Experimental procedure

Photocatalytic experiments were carried out using an experimental setup (see Figure 1), which consists of a 20W UV lamp(wavelength ~254nm), a 150L/h air blower and a pump. Batch

experiments were conducted in a photocatalytic oxidation reactor (1.0 L) at room temperature. About 0.5L of coking wastewater is placed in the reactor, followed by addition of a known amount of TiO_2 photocatalyst under continuous aerating. Turn on the light irradiation at room temperature for a period of time, and regular sampling. All the samples were taken at selected intervals and filtered through a 0.45μm filter film to remove suspended solid before analyses of the solution.

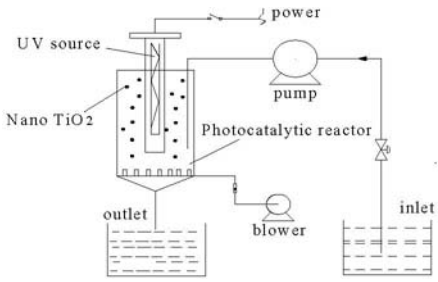

Fig. 1 Schematic diagram of TO_2 photo catalytic oxidation

Analytical methods

The water samples were analyzed by following the standard methods specified in the Monitoring and Analytical Methods of Water and Wastewater[10]. The total organic carbon (TOC) concentration was monitored using Multi N/C 2100 Analyzer (Analytik Jena AG Corporation, Germany). The pH was measured by using the glass electrodes; COD by the potassium dichromate method; NH_3-N by using Nessler's reagent spectrophotometry.

Results and discussion

Effect of TiO_2 dosage on the TOC removal rate

The TOC removal rate at different TiO_2 dosages is shown in Fig. 2. As can be seen from Fig.2, The removal efficiency increases with the TiO_2 dosage until an optimum level of 4g/L is reached. When the TiO_2 dosage exceeds this optimal level, the efficiency reduces with further increasing of TiO_2 dosages. Excessive TiO_2 dosages above the optimum level cause a shadow effect to interfere with the transmission of UV light so that the formation of electron–hole pairs cannot effectively occur[11, 12]. Thus, the TOC removal rate decreases. At the optimum dosage of 4g/L TiO_2, almost 45% of TOC removal rate is reached.

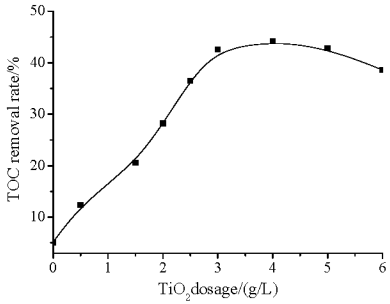

Fig. 2 Effect of TiO_2 dosage on the TOC removal rate
(pH: 7.8; air flow:150L/h; reaction time:2h)

Effect of reaction time on the TOC removal rate

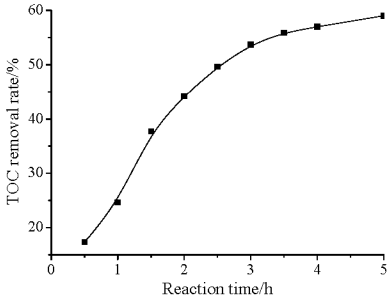

Fig. 3 Effect of reaction time on the TOC removal rate
(pH: 7.8; air flow:150L/h; TiO_2 dosage: 4g/L)

The TOC removal rate at different reaction time is shown in Fig. 3. The TOC removal rate increases with reaction time increasing. when the light reaction time is above 4h, TOC removal rate increases slowly, 59% of TOC removal rate is reached within 5h. According to the principle of TiO_2 photocatalytic oxidation, photocatalysis involves illumination with UV radiation of certain semiconductor catalysts, where electron-hole pairs are generated and eventually lead to surface redox reactions. Organic molecules, as pollutants, are degraded to smaller and less harmful species, eventually producing carbon dioxide and water. This can be explained that reaction time is an important factor affecting the adsorption and photocatalysis. The results indicate that the reaction rate plays a more important role than adsorption rate in the process. In other words, the photon-generated holes, electrons, hydroxyl radicals (·OH) can degrade organic

pollutant at short time. With illumination reaction time increasing, OH], TOC concentration decreases, and hence degrade velocity is limited by the diffusion of hydroxyl radicals (·OH).

Effect of pH on the TOC removal rate

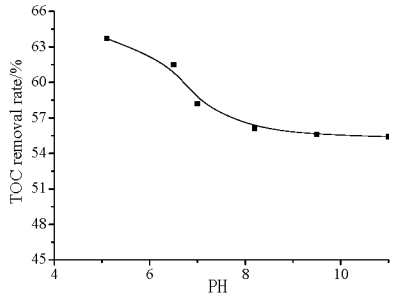

Fig. 4 Effect of pH on the TOC removal rate
(air flow:150L/h; reaction time:2h; TiO_2 dosage :4g/L)

Since TiO_2 surface is amphoteric, the surface interactions with substrates, particularly charged compounds, are sensitive to the solution pH[4]. Fig. 4 represents the TOC removal rate as a function of initial pH. As can be seen from Fig. 4, the TOC removal rate decreased with increasing pH value. The pH-effect is related to the point of zero charge of TiO_2 at pH 6.2[13]. In acidic media (pH<6.2), the surface of TiO_2 is positively charged, whereas it is negatively charged under alkaline conditions (pH>6.2)according to Eqs.(1) and (2) [14]. Because of a large amount of phenols and with hydroxyl organic compounds in coking wastewater is negative charge. The electrostatic attraction between the positive and negative charge at lower pH region (pH<6.2) fascinates the formation of hydroxyl radicals (·OH) on the surface of surface of the TiO_2. Considering the cost, he optimum initial pH is 5.1.

$$TiOH + H^+ \longleftrightarrow TiOH^+ \quad (1)$$

$$TiOH + OH^- \longleftrightarrow TiO^- + H_2O \quad (2)$$

Effect of PFS dosage on the TOC removal rate

The TOC removal rate at different PFS dosage is shown in Fig. 5. TOC removal rate increases with the increase of PFS dosage. The TOC removal rate can reaches 81%, 81.3% when the PFS dosage of is 700mg/L, 800mg/L, respectively. PFS floc is generated by the ferric sulfate

hydrolysis in water by polymerization, Intermediate gel precipitation in the process of transformation, which can absorb the colloid particles and suspended solids and coagulate each other [15]. Therefore, the addition of PFS, electric neutralization effect occurs in the coking wastewater colloid, which promotes coking wastewater colloid aggregation, destabilization of the precipitation process. At the same time, part of the small particles captured will form larger particles and then precipitate at last. In the experiment, considering the cost of processing and treatment effect, 700mg/L PFS dosage is favorable.

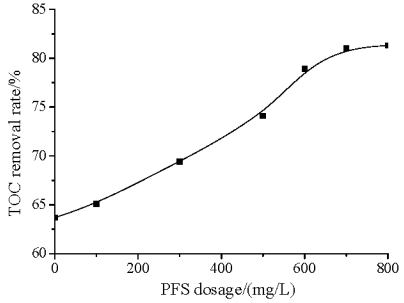

Fig.5 Effect of PFS dosage on the TOC removal rate
(pH: 5.1;air flow:150L/h; TiO_2 dosage :4g/L)

Comparison of photocatalytic oxidation coupling with PFS coagulation and photocatalytic oxidation

Fig.6 represents the comparison of photocatalytic oxidation coupling with PFS coagulation and photocatalytic oxidation at the different reaction time. As can be seen from Fig.6, photocatalytic oxidation coupling with PFS coagulation showed superior degradation performances than the single photocatalytic oxidation did after treatment at 30min, and their TOC removal rate were 41.8% and 19.3%, 41.2%, respectively, which might be attributed to the synergistic effect of photocatalytic oxidation and PFS coagulation. Therefore, these results indicated that photocatalytic oxidation coupling with PFS coagulation degradation of coking wastewater described in this study was more suitable in the practical engineering application, which is of great significance to improve the treatment efficiency.

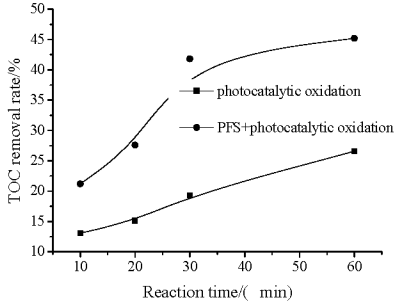

Fig. 6 Comparison of photocatalytic oxidation coupling with PFS coagulation and photocatalytic oxidation
(pH: 5.1;air flow:150L/h; TiO_2 dosage :4g/L;PFS dosage:700mg/L)

Conclusions

The experiments indicated that the photocatalytic oxidation coupling with PFS coagulation degradation of coking wastewater was very promising. The single factor test showed that the optimum values of reaction time, pH, catalyst dosage, and coagulation dosage were 4h, 5.1, 4g/Land 700mg/L, respectively, the TOC removal rate can reach 81%. Photocatalytic oxidation coupling with PFS coagulation can significantly improve the treatment efficiency of coking wastewater. The TOC removal rate is 2.2 times of the latter does under the comparable conditions. PFS coagulation-photocatalytic oxidation of coking wastewater has some advantages, such as easy operation, higher removal efficiency on TOC, COD, but total nitrogen (TN) removal is not obvious. Therefore, the advanced oxidation treatment coupling with biological treatment is necessary to meet all the indexes of the National Discharge Standard of China (COD <100 mg/L, GB16171-2012).

References

[1]WANG B. et al., "Electrochemical Oxidation of Refractory Organics in the Coking Wastewater and Chemical Oxygen Demand (COD) Removal under Extremely Mild Conditions",*Ind. Eng. Chem. Res.*,47(21)(2008) ,8478-8483.

[2]ZHANG L. et al., "Advanced treatment of coking wastewater using three-dimensional fluid bed electrode reactor," *Ecology and environmental sciences*, 21(2) (2012),370-374(in Chinese).

[3]TSUYOSHI O. et al., "Photoelectrochemical properties of TiO_2 photocatalyst and its applications for environmental purification," *J.Photochem.Photobiol. C: Photochem.*, 13 (4) (2012) ,247- 262.

[4]PARK H. et al., "Surface modification of TiO_2 photocatalyst for environmental applications," *J.Photochem.Photobiol. C: Photochem.*,15(2013),1-20.
[5]XIAO J. et al., "TiO_2 Photocatalytic Oxidation Treatment and Analysis of Organic Pollutant Components of Discharge Wastewater from Coking Wastewater Treatment Station," *Research of Environmental Sciences,* 22(9)(2009) ,1049-1055. (in Chinese)
[6]PARASKEVI P. et al., "Kinetics and mechanism of glycerol photo-oxidation and photo-reforming reactions in aqueous TiO_2 and Pt/TiO_2 suspensions," *Catalysis Today,* 209(2013),91-98.
[7]SONG Z. et al., "Properties and coagulation mechanisms of polyferric silicate sulfate with high concentration," *J. Environ. Sci.,* 20(2)(2008) ,129-134.
[8]LAI P. et al., "Study on treatment of coking wastewater by biofilm reactors combined with zero-valent iron process," *J. Hazard. Mater.,* 162(2-3) (2009),1423-1429.
[9]ABOOD R. A. et al., "Non-biodegradable landfill leachate treatment by combined process of agitation, coagulation, SBR and filtration," *Waste Management,* 34(2)(2014) ,439-447.
[10]State Bureau of Environmental Protection. The Editorial Pool of Analysis Method of Water and Wastewater. Analysis Method of Water and Wastewater. 4rd ed. Beijing: China Environmental Science Press, 2002.
[11]AGUSTINA T.E. et al., "Treatment of winery wastewater using a photocatalytic/photolytic reactor," *Chem. Eng. J.,* 135 (1-2) (2008),151-156.
[12]CHANG C. et al., "Decolorizing of lignin wastewater using the photochemical UV/TiO_2 process," *Chemosphere,*56(2004) ,1011-1017.
[13]CHOU J.C. et al., "Study on pH at the point of zero charge of TiO_2 pH ionsensitive field effect transistor made by the sputtering method," *Thin Solid Films,* 476 (1)(2005), 157-161.
[14]SHAHREZAEI F. et al., "Process modeling and kinetic evaluation of petroleum refinery wastewater treatment in a photocatalytic reactor using TiO_2 nanoparticles,"*Powder Technol.* ,2012,221:203-212.
[15]ZOUBOULIS A.I. et al., "Polyferric sulphate: Preparation, characterisation and application in coagulation experiments," *J. Hazard. Mater.,*155(3)(2008),459-468.

Characterization of Minerals, Metals, and Materials 2015
Edited by: John S. Carpenter, Chenguang Bai, Juan Pablo Escobedo, Jiann-Yang Hwang, Shadia Ikhmayies, Bowen Li, Jian Li, Sergio Neves Monteiro, Zhiwei Peng, and Mingming Zhang
TMS (The Minerals, Metals & Materials Society), 2015

PHASE TRANSFORMATION AND ELEMENT MIGRATION IN THE OXIDATION PROCESS OF NICKEL-COPPER SULFIDE ORE

Guangshi Li, Hongwei Cheng [†], Xingli Zou, Xionggang Lu [†], Changyuan Lu, Dan Wang, Zhongfu Zhou, Qian Xu

Shanghai Key Laboratory of Modern Metallurgy and Materials Processing, Shanghai University, Shanghai 200072, China

[†] Corresponding author. Ph.D., Prof.; Tel.: +86 21 56334042; Fax: +86 21 56335768; E-mail: hwcheng@shu.edu.cn (H.W. Cheng); luxg@shu.edu.cn (X.G. Lu).

Keywords: Ni-Cu sulfide ores; phase transformation; Rietveld; element migration; preoxidation

Abstract

The preoxidation of the ore has a profound significance to the concentration, separation and purification of nickel and copper from the lean complex ore. In this paper, the natural Ni-Cu sulfide mineral samples under the elevated temperature condition in air were investigated, as well as under isothermal condition at 600 °C in air. The mineralogical characterization was studied using XRF, ICP and the Rietveld method. The oxidation behavior and the element migration of the Ni-Cu sulfide ore were studied by XRD, SEM-EDS and TG. The XRD Rietveld method was successfully developed in the phase identification and quantification of this complex ore powder sample. The oxidative intermediates (Cu/Ni-ferrite) were detected by XRD, and the process of the element migration was obviously revealed by the line scans using SEM-EDS. It is the preoxidation of this mineral that provides guidance for the extraction of valuable metals from low-grade Ni-Cu sulfide ores in the future.

Introduction

The Ni-Cu sulfide deposit is one of the most important sources of nickel and copper in the world. And the Ni-Cu sulfide ore is mainly composed of pentlandite, chalcopyrite and pyrrhotite. Mineral processing of Ni-Cu sulfide ore strongly depends on the mineralogical composition, an important factor for efficient hydrometallurgical nickel and copper extraction. Recent efforts to develop the characterization of the Ni-Cu sulfide ores have been heavily addressed by several groups [1]. Oxidation reaction is the first step in smelting processes of the sulfide mineral. And an oxidation study on this sulfide ore is of crucial importance in the metallurgical process.

Dunn et al. investigated the oxidation of synthetic pentlandite samples using a thermogravimetric analyzer [2]. They presented a series of reactions based on the characterization of the products at different temperature using the X-ray diffraction (XRD). Researches have been further developed for the oxidation mechanism and the oxidation kinetics of pentlandite [3]. Prasad et al. summarized the previous studies about oxidative roasting of chalcopyrite and related constituents such as copper sulfide and iron sulfide [4]. The investigations of the mineralogy and flotation performance between pentlandite and pyrrhotite have revealed their interactions during the

metallurgical process [5-8]. But the phase transformation and element migration among pentlandite, chalcopyrite and pyrrhotite in the Ni-Cu sulfide mineral during the oxidation process are rarely investigated. The XRD is now routinely used in many laboratories to provide mineralogical information during processing of ores, as well as the scanning electron microscope interfaced with an energy dispersive X-ray spectrum (SEM-EDS) analyser [9, 10]. Additionally, the Rietveld method was used in the quantification of mineral phases [11-16].

The purpose of this paper is to investigate mineralogical characterization and the interactions among the three phases (pentlandite, chalcopyrite and pyrrhotite) of the Ni-Cu sulfide ore during the peroxidation process. These directly influence on the extraction of nickel and copper from the complex ores, and provide a theoretical basis for the separation and extraction of lean complex ore.

Materials and Methods

A. Sample Preparation

The Ni-Cu sulfide ores, originated from Xinjiang (China), were washed with deionized water, and then air-dried in the oven at 100 °C for 8 h. Several lump ores with metallic sheen were prepared (sorted manually and mounted in epoxy resin, thereafter polished and sputter-coated with gold) for the SEM test. The rest of the dried blocks were ground to powder samples (crushed in a wear resistant cast iron mortar, and then grinded to 300 mesh in an agate mortar).

The finely mineral powder samples were oxidized under non-isothermal condition (350, 400, 450, 500, 550 and 600 °C respectively), which was tested in a tube furnace (STF54453C Lindberg/Blue M, Asheville NC USA). The measurement was carried out with a heating rate of 10 °C min^{-1} in air flow (40 ml min^{-1}). The finely powder was also pressed into disks in a stainless steel module (8 mm i.d.) with the indication on the pressure gauge of 4.2 MPa using a hydraulic press. Then the samples were oxidized under 600 °C in air (40 ml min^{-1}) for 5, 10, 20, 30, 60 and 600 min, respectively. Subsequently, the six oxidized powder samples were prepared for the SEM characterization.

B. Characterization Methods

X-ray fluorescence (XRF)

Three samples (S1, S2, S3) were randomly selected from the finely mineral powder and analyzed in X-ray fluorescence spectrometer (XRF-1800, SHIMADZU LIMITED). The spectra were obtained with an Rh source (40kV, 95mA) using sequential scanning (8°/min) and semi-quantitative mode

Inductively coupled plasma atomic emission spectrometry (ICP-AES)

The inductively coupled plasma has been used to exact quantitative analysis elements in iron ores [17]. The ICP-AES was measured on a PERKINE 7300DV. This investigation was carried

out for the precise determination of several important elements (such as Fe, Ni, Cu, etc.) in three samples (S1, S2, S3).

Scanning electron microscopy with an energy-dispersive spectrometer (SEM-EDS)

The mineralogical characterization was performed by field emission scanning electron microscopy (FESEM; SU70, Hitachi, Japan). The elements distribution of the selected lumpish ore sample, as well as the sample which was oxidized for 1 h at 600 °C in air, was revealed by the EDS mapping features in SU70 within the TEAM™ EDS Analysis System, All the oxidized samples were measured using line scan capabilities, in order to determine the relative quantity of elemental sulfur and oxygen during the oxidation process.

X-ray powder diffraction (XRD)

The mineral phases of the ore sample was examined by the XRD with Cu radiation (40 kV, 40 mA) using a Bruker-AXS D8 ADVANCE diffractometer. The diffraction pattern of the selected lumpish ore sample was examined from 10 to 75° (2θ) with 0.02° per step and 2° per minute. And all the oxidized powder samples were also detected from 10 to 80° (2θ) in 0.02° steps with a scanning speed of 4° per minute. While the powder sample S1 was recorded from 10 to 80° (2θ), in 0.02° steps, by counting for 6 second per step.

Quantitative phase analysis using Rietveld method (QPA-RM)

Quantitative phase analysis of powder sample S1 was performed with the TOPAS 4.2 program (Bruker AXS). This software was based on the Rietveld full-pattern refining principle that first presented by Hill and Howard in 1987 [12]. The refinement strategy was based on the predecessors' achievements [18]. The evaluation of the refinement was indicated by the R values which are the criteria for judging the fit of the calculated pattern to the observed data. Crystal structure files of all phases were downloaded from the American Mineralogist Crystal Structure Database (http://www.minsocam.org/MSA/Crystal_Database.html) [19].

Thermogravimetric analysis (TGA)

The TGA was adopted to evaluate the thermal stability of the powder samples (S1, S2, S3) using a Thermogravimetric analyzer (NETZSCH STA 449 F3 Jupiter) under air atmosphere with a flow rate of 40 ml min^{-1}. About 100 mg of each sample was spread as thin layers in silica dishes, and heated to 1000 °C (10 °C min^{-1}), then incubated at 1000 °C for 1 h.

Results and Discussion

A. Characterization of raw ores

As demonstrated in Table 1, the comparison of the data shows a good agreement between the results using XRF analysis and that using ICP analysis, although there is some deviation in some certain elements (Na, Mg, Al, Si, Ca,) which are the major content of gangue minerals. The major metal element of the ore samples are iron, nickel and copper. As a result, this is a complex

ore with rich iron and lean Ni-Cu sulfide. The homogeneity of the powder mineral samples is confirmed at the same time.

Table1. Elemental analysis of three mineral samples (S1, S2, S3) using XRF and ICP

	S1 (wt%)		S2 (wt%)		S3 (wt%)	
	XRF	**ICP**	**XRF**	**ICP**	**XRF**	**ICP**
Fe	40.1241	43.31	38.4806	46.75	39.9853	42.34
S	26.6444	—	25.4869	—	26.4048	—
O	15.3163	—	15.9572	—	15.0945	—
Si	5.9607	3.15	6.5687	2.72	6.0919	2.82
Cu	3.5795	3.13	3.9035	3.08	3.4743	2.95
Ni	2.3516	2.33	2.5832	2.14	2.7001	2.22
Mg	2.2887	0.81	2.477	0.54	2.1582	0.64
Al	1.9387	0.93	1.8685	0.81	1.6953	0.81
Ca	0.9415	0.57	1.1763	0.43	1.0136	0.47
Na	0.5699	0.27	0.6548	0.28	0.5701	0.26
Co	0.1564	0.14	0.1685	0.091	0.1819	0.1

It is clearly revealed the elements distribution of the selected lumpish ore sample from the SEM-EDS image, as shown in Fig. 1. All the copper-sulfide and nickel-sulfide phases are evenly distributed and rimmed by the rich iron phase, and there is a little iron oxide scattered over surface of this ore sample. Further analysis of the XRD pattern presents that the selected lumpish ore sample is composed of Fe_7S_8, $CuFeS_2$, $(Ni,Fe)_9S_8$ and Fe_3O_4.

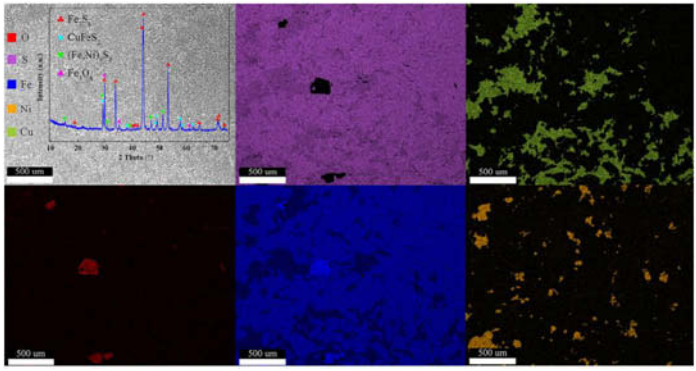

Fig. 1 X-ray map showing the element distribution of the selected lumpish mineral surface together with the XRD pattern overlayed the SEM micrograph

The mineralogy of the powder sample (S1) quantitatively determined in this paper by XRD data is shown in Fig. 2(a). In the picture: y_{obs} represents the observed pattern, y_{calc} states for the calculated profile, the y_{obs}-y_{calc} stands for the difference between observed and calculated curve, and all the Bragg peak position for each phase are presented in vertical lines. The quality of refinement, which is indicated by R_p, R_{wp}, R_{exp}, Gof, is revealed in the top right corner of the

figure. The result of the QPA-RM reveals that complex ore sample is composed of 50.27% Pyrrhotite 4C-Fe_7S_8, 10.56% Chalcopyrite-$CuFeS_2$, 7.20% Pentlandite-$(Fe,Ni)_9S_8$, 2.33% Magnetite-Fe_3O_4, 0.66% Pyrite-FeS_2 and 28.61% gangue mineral: 7.82% Anorthite-$CaAl_2Si_2O_8$, 6.11% Albite-$NaAlSi_3O_8$, 5.69% Clinochlore-$(Mg,Fe^{2+})Al(Si_3Al)O_{10}(OH)_8$, 2.56% Quartz-$SiO_2$, 4.74% Actinolite-$Ca_2(Mg_{4.5\text{-}2.5}Fe^{2+}{}_{0.5\text{-}2.5})Si_8O_{22}(OH)_2$, 1.69% Annite Mica-$KFe^{2+}{}_3AlSi_3O_{10}OH_2$. More specifically: goodness-of-fit (Gof= R_{wp}/ R_{exp})=3.01, R-expected (R_{exp})=2.33%, R-weighted pattern (R_{wp})=7.01%, R-pattern (R_p)=5.36%. The acquired quantification showed that the Pyrrhotite 4C (Fe_7S_8) appears in largest amounts as compared to the Chalcopyrite ($CuFeS_2$) and Pentlandite ($(Ni,Fe)_9S_8$) in this sulfide deposit.

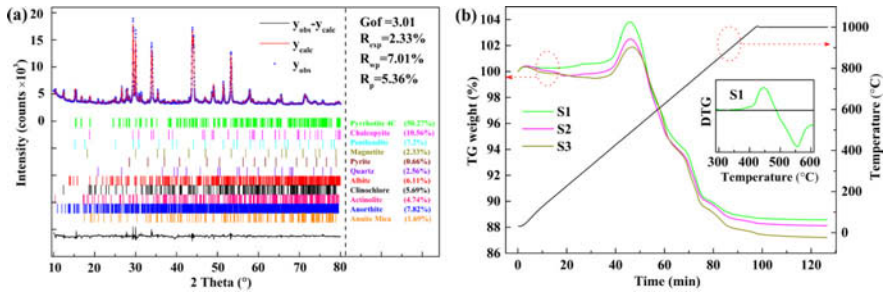

Fig. 2 - (a) The QPA-RM result of sample S1. **(b)** The TG analysis of three samples (S1, S2 and S3): heating rate was 10°C per min in air. The DTG (first derivative of TG curve) profile of sample S3 at the temperature range 300-600 °C is inset in this figure

B. Phase Transformation

As shown in Fig. 2(b), the initial slight linear weight decrease is attributed to the loss of adsorbed water. The weight gain between 400-490 °C is due to the formation of metal sulfates [2, 20]. And $FeSO_4$ and $CuSO_4$ were detected in the sample oxidized at 400 °C by XRD in Fig. 3(a). The DTG (first derivative of TG) of sample S1 with a temperature range 300-600 °C is also inset in Fig. 2(b). The rapid weight loss occurred by two steps (shown in DTG) at 490 °C and 550 °C, was assumed to be attributed to the release of SO_2 [5].

From Fig. 3(a), the main phases of this sample are Fe_7S_8, FeS_2, $(Fe,Ni)_9S_8$ and $CuFeS_2$ at the temperature of 350 °C. However, $FeSO_4$ and $CuSO_4$ were found at 400 °C, which verified the formation of sulfate with the weight gain in Fig 2(b). Nevertheless, the nickel phase wasn't detected in this sample, the reason may be that the $(Fe,Ni)_9S_8$ decomposed into many kinds of phases and it is difficult to demonstrate from the XRD pattern. The samples are mainly composed of Fe_2O_3 and ferrite ($M^*Fe_2O_4$, M^*=Fe, Ni, Cu) with the temperature range 450-600 °C.

The results mentioned above suggest that the oxidation process of the sulfide minerals is surprisingly complex. As illustrated in Fig 3(b), the mechanism of the phase transformation at 600 °C is very apparent. The $(Fe,Ni)_9S_8$ was firstly oxidized into $NiFe_2O_4$ after 5 min. The peaks of $NiFe_2O_4$ are weak on account of the small amount of nickel. With the extension of the oxidation time, the $CuFeS_2$ was transformed into $CuFe_2O_4$ gradually. Then the $CuFeS_2$ disappeared while the sample has been isothermal for 30 min. The large amount of Fe_7S_8 was

oxidized during the time range 10-60 min and the peaks of Fe_2O_3 increased rapidly from 10 to 20 min. However, the sample was basically unchanged as the isothermal time increased to 600 min. It indicates that the best oxidation time for $(Fe,Ni)_9S_8$ is 5 min, that for Fe_7S_8 and $CuFeS_2$ are 20 and 30 min respectively under this condition.

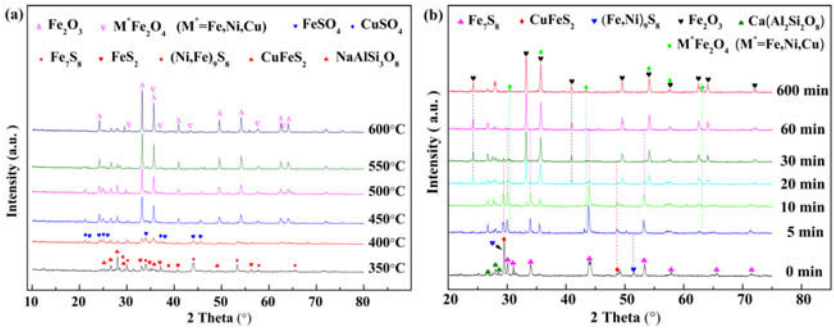

Fig. 3 – **(a)** XRD patterns of the ore powder samples oxidized under the non-isothermal condition: at 350, 400, 450, 500, 550 and 600 °C respectively in air; and **(b)** XRD patterns of the ore powder samples oxidized under the isothermal condition in air for different time: 0 min-(raw ore powder sample), 5, 10, 20, 30 n, 60 and 600 min respectively

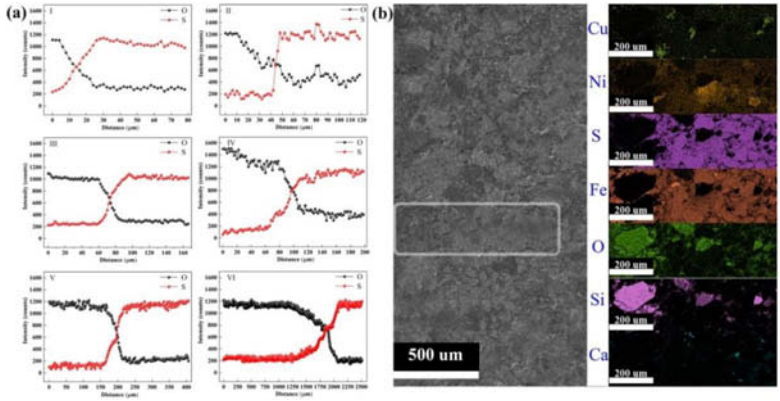

Fig. 4 – **(a)** SEM-EDS line scans of elements (O and S) on cross-section of samples oxidized for 5 (I), 10 (II), 20 (III), 30 (IV), 60 (V) and 600 min (VI) at 600 °C in air. **(b)** X-ray map of the elements (Cu, Ni, S, Fe, O, Si, Ca) over the cross-section of the sample oxidized for 60 min

C. Migration of Certain Elements

As presented in Fig. 4(a), the oxidation process of the sulfide ore samples is obviously observed. The line scans of the elements (O and S) from the edge to inside reveal that the amount of O decreased from the surface to the center, but the results of S were quite the contrary. The oxide layers become deepen as the thermostatic oxidized time increased. The elements distribution of

the sample oxidized at 600 °C for 1 h is presented in Fig 4(b). The O diffused into the center and reached with the sulfide to form sulfate and metal oxides. While the S in ore transformed into SO_2 and then diffused into air. The metal sulfides have transformed into metal oxides during the thermostatic oxidized process, while the gangue minerals have remained largely unchanged.

Conclusions

In this work, a variety of measurements were utilized to evaluate the mineralogical characterization of this Ni-Cu sulfide ore. The QPA-RM, a new method, is developed for the quantification of the mineralogical composition in this sulfide ore deposits using the TOAPS software. The natural lean complex ore is mainly composed of sulfide mineral (Pyrrhotite 4C (Fe_7S_8), Chalcopyrite ($CuFeS_2$) and Pentlandite ($(Fe,Ni)_9S_8$)), and other gangue minerals. Both the oxidation thermodynamics process and oxidation process under isothermal condition at 600 °C of this sulfide mineral were studied. The metal sulfates ($FeSO_4$, $NiSO_4$ and $CuSO_4$) were formed at 400 °C, then decomposed at 450 °C or higher temperature. The Cu/Ni-ferrites ($M^*Fe_2O_4$, M^*=Fe, Ni, Cu) generated at 450 °C and remained a fine stability even under 600 °C isothermal condition for 600 minutes in air. The main oxidized products are Fe_2O_3 and $M^*Fe_2O_4$ (M^*=Fe, Ni, Cu). In additionally, the elemental migration between O and S was obviously revealed: The oxygen diffused into the center and reached with the sulfide to form sulfate and metal oxides. While the sulfur in ore transformed into SO2 and then diffused out. These provided key information for the treatment and comprehensive utilization of this Ni-Cu sulfide deposit.

Acknowledgments

This work was supported financially by Grant 2014CB643403 from the National Key Program for Basic Research of 973 Program.

References

1. Pownceby, M., MacRae, C. and Wilson, N., "Mineral characterisation by EPMA mapping," *Minerals Engineering,* 2007. 20(5): p. 444-451.
2. Dunn, J. and Kelly, C., "A TG/MS and DTA study of the oxidation of pentlandite," *Journal of Thermal Analysis and Calorimetry,* 1980. 18(1): p. 147-154.
3. Zhu, H.H., et al., "Oxidation Behavior and Mechanism of Pentlandite at 973 K in Air," *Metallurgical and Materials Transactions B-Process*, 2012. 43(3): p. 494-502.
4. Prasad, S. and Pandey, B., "Alternative processes for treatment of chalcopyrite—a review," *Minerals Engineering,* 1998. 11(8): p. 763-781.
5. Becker, M., Villiers, J.D. and Bradshaw, D., "The flotation of magnetic and non-magnetic pyrrhotite from selected nickel ore deposits," *Minerals Engineering,* 2010. 23(11): p. 1045-1052.
6. Ekmekçi, Z., et al., "The relationship between the electrochemical, mineralogical and flotation characteristics of pyrrhotite samples from different Ni Ores," *Journal of Electroanalytical Chemistry,* 2010. 647(2): p. 133-143.
7. Ghorbani, Y., et al., "Use of X-ray computed tomography to investigate crack distribution and mineral dissemination in sphalerite ore particles," *Minerals Engineering,* 2011. 24(12): p. 1249-1257.

8. Becker, M., Wiese, J.and Ramonotsi, M., "Investigation into the mineralogy and flotation performance of oxidised PGM ore," *Minerals Engineering,* 2014. 65(0): p. 24-32.
9. Manias, C., Retallack, D. and Madsen, I., "Plant optimization and control using continuous on-line XRD for mineral phase analysis," *ZKG International,* 2001. 54(3): p. 138-145.
10. Siriwardane, R.V., et al., "Decomposition of the sulfates of copper, iron (II), iron (III), nickel, and zinc: XPS, SEM, DRIFTS, XRD, and TGA study," *Applied Surface Science,* 1999. 152(3): p. 219-236.
11. Rietveld, H., "Line profiles of neutron powder-diffraction peaks for structure refinement," *Acta Crystallographica,* 1967. 22(1): p. 151-152.
12. Hill, R. and Howard, C., "Quantitative phase analysis from neutron powder diffraction data using the Rietveld method," *Journal of Applied Crystallography,* 1987. 20(6): p. 467-474.
13. Bish, D. and Howard, S., "Quantitative phase analysis using the Rietveld method," *Journal of Applied Crystallography,* 1988. 21(2): p. 86-91.
14. Bish, D.L. and Post, J.E., "Quantitative mineralogical analysis using the Rietveld full-pattern fitting method," *The American Mineralogist,* 1993. 78(9-10): p. 932-940.
15. Young, R.A. and Nederland, S.E.C., "The Rietveld method," *Oxford University Press,* 1995.Vol. 1:p.1-309.
16. Rietveld, H.M., "The Rietveld Method," *Physica Scripta,* 2014. 89(9): p.1-9.
17. Date, A.R., et al., "Application of inductively coupled plasma mass spectrometry to the analysis of iron ores," *Journal of Analytical Atomic Spectrometry,* 1988. 3(5): p. 653-658.
18. McCusker, L., et al., "Rietveld refinement guidelines," *Journal of Applied Crystallography,* 1999. 32(1): p. 36-50.
19. Downs R.T and Hall W.M., "The American mineralogist crystal structure database," *The American Mineralogist,* 2003. 88(1): p.247-250.
20. Dunn, J. and Kelly, C., "A TG/DTA/MS study of the oxidation of nickel sulphide," *Journal of Thermal Analysis and Calorimetry,* 1977. 12(1): p. 43-52.

Characterization of Minerals, Metals, and Materials 2015
Edited by: John S. Carpenter, Chenguang Bai, Juan Pablo Escobedo, Jiann-Yang Hwang, Shadia Ikhmayies, Bowen Li, Jian Li, Sergio Neves Monteiro, Zhiwei Peng, and Mingming Zhang
TMS (The Minerals, Metals & Materials Society), 2015

SINTERING AND PERFORMANCE OF HIGH ALUMINA REFRACTORY WITH ZrO_2 ADDITION

Lei Xu[1], Min Chen[1]*

1. School of Materials and Metallurgy, Northeastern University, Shenyang 110819, China

Keywords: High alumina refractory, ZrO_2, Sintering, Densification, Thermal shock resistance

Abstract

Sintering behavior and performance of high alumina refractory based on the ternary subsystem $MgAl_2O_4$-$CaAl_4O_7$-$CaAl_{12}O_{19}$ were investigated using ZrO_2 as an additive up to 8 wt.% by solid state reaction sintering. It was found that the added ZrO_2 could dissolve in the CA_6 grains in the form of a solid solution, which enhanced the isotropic growth of CA_6 grains and then improved the sintering. As a result, the densification process was improved and areas with enrichment of ZrO_2 showed a more compact structure. With further increase of ZrO_2 addition, tetragonal ZrO_2 were found to locate in the grain boundaries for exceeding the solid solubility limit, which enhanced the thermal shock resistance, indicating that addition of ZrO_2 exhibited a positive effect on sintering behavior and performance of this refractory. In addition, it is considered that the optimal amount of ZrO_2 addition was about 4% considering the performance together with the cost.

Introduction

The high alumina refractory based on the ternary subsystem $MgAl_2O_4$-$CaAl_4O_7$-$CaAl_{12}O_{19}$ (MA-CA_2-CA_6) is widely used as steel ladle linings [1, 2]. The presence of magnesium spinel in the composition of this alumina-rich refractory has greatly improved slag corrosion resistance and reduced wear rates, providing a longer lifespan for steel ladles than other traditional refractory products [3]. However, it is reported in some literatures that the densification process of this refractory was not completed even at 1600°C, with apparent porosity higher than 20% [4, 5], which would result in poor resistance to penetration of the slag that had a good fluidity because of higher temperature smelting condition in steel ladles. The hexagonal morphology of CA_6 grains and their anisotropic growth into platelet shape were believed to result in an increase of porosity [6], but relevant literatures lack detailed studies on this subject, which is mainly focused on the phases and microstructure evolution [7, 8], thermodynamic behavior [9] and performance such as slag attack resistance and thermal shock resistance [4]. Therefore, considering the lack of studies on the improvement in densification of this refractory, high alumina refractories with different addition of ZrO_2 were prepared in the present work, and the effect of ZrO_2 addition on the densification of this refractory was investigated, for the purpose to

further promote the performance of high alumina refractory.

Experimental Procedures

The starting raw materials used in the present work were analytical reagents of Al_2O_3, MgO and $CaCO_3$ powders. Batch composition located in the ternary subsystem MA-CA_2-CA_6 was made from the raw materials with typical chemical composition as shown in the follows: 82% Al_2O_3, 10% MgO and 8% CaO (after converted). High purity ZrO_2 powder was added to the above compositions at 0, 2, 4, 6 and 8 wt.%. All the batches of mixtures were shaped to pellets after attrition milling for 2 h respectively. Then the prepared pellets were dried at 120°C for 24 h and then were fired in a high temperature electric furnace at the heating rate of 5 °C/min to 1600°C with soaking time of 2 h.

The sintered samples were characterized by compactness, thermal shock resistance, phase composition and microstructure. The compactness was characterized by bulk density and apparent porosity measured in kerosene using Archimedes principle, and the thermal shock resistance was evaluated by quenching the samples in air for 15 min after heating at 1100°C for 15 min, recycling till the sample ruptured. The phase compositions were examined by X-ray powder diffraction (XRD, Cu Kα radiation, 40 kV and 40 mA) with a step of 0.02° (2θ). In addition, the microstructures were analyzed by scanning electron microscopy (SEM, SSX-550, Japan) attached with energy dispersive X-ray analyzer (EDX).

Results and Discussion

Phase composition

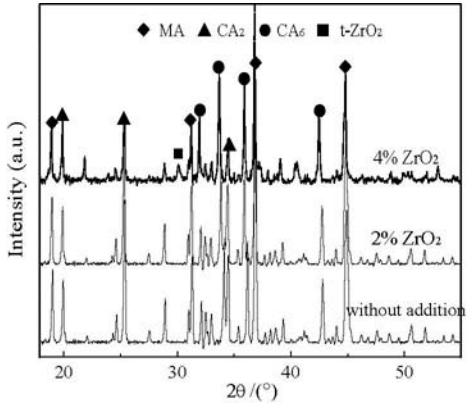

Fig. 1 XRD patterns of the fired samples with different ZrO_2 content

Fig. 1 shows the XRD patterns of the samples with different ZrO_2 content after heating at 1600°C for 2 h. For the sample without ZrO_2 addition, MA, CA_2, CA_6 were the main crystalline phases, which was in agreement with the result supplied by the mentioned ternary subsystem. For the ZrO_2 added samples, the compound $CaZrO_3$ formed between CaO and ZrO_2 was not detected, which was mainly owing to the lower temperature of the reaction between CaO and Al_2O_3 compared with that for $CaZrO_3$ formation. For the sample with 2% ZrO_2 addition, the peak of ZrO_2 was also not observed and the peak of CA_6 showed a shift to lower 2θ values, indicating that Zr^{4+} could be absorbed in the CA_6 grains. With further increase of ZrO_2 addition, tetragonal ZrO_2 were detected for exceeding the solid solubility limit.

Densification

Fig. 2 shows the effect of ZrO_2 addition on the densification process of the samples after heating at 1600°C for 2h. It was observed that the bulk density increased appreciably with ZrO_2 addition increasing from 2% to 4%, and then increased slightly with further increase of ZrO_2 content. Meanwhile, the evolution of the apparent porosity showed an opposite result accordingly.

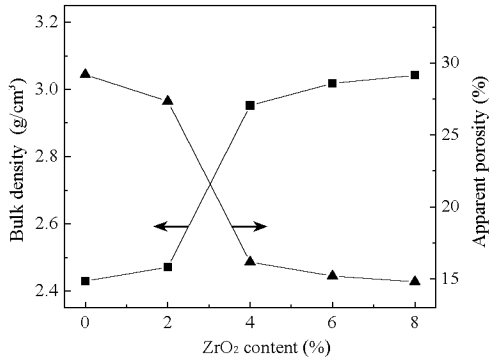

Fig. 2 Effect of ZrO_2 addition on the densification process of the high alumina refractory

To explain this evolution of densification process, microstructures using back-scattered electron (BSE) imaging on the polished surfaces of the different samples were analyzed (shown in Fig. 3). For the sample without addition, a porous structure was observed, which was associated with the formation of the platelet structure of CA_6 grains with high aspect ratio and an acicular shape (shown in Fig. 3a) as mentioned in the literature [6]. When 4% ZrO_2 was added (shown in fig. 3b), two types of areas of the polished surface were observed. One was the relatively porous area that was similar to the sample without addition. In this area, the platelet structure of CA_6 grains with anisotropic growth was observed and practically no Zr^{4+} was detected by EDX analysis in this area; the other was the dense area with no platelet structure observed. In this area, fine tetragonal ZrO_2 grains were located in the grain boundaries, and Zr^{4+} was also detected in the

rounded CA_6 grains in the form of a solid solution, indicating that the presence of ZrO_2 inhibited the anisotropic growth of CA_6 grains and enhanced the isotropic growth, which improved the diffusion of ions and grain growth. Consequently, the densification of this area was promoted.

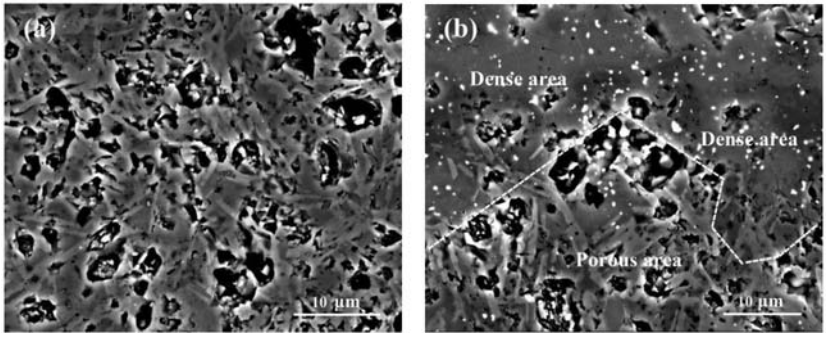

Fig. 3 BSE images of the microstructures on the polished surface of the different samples: (a) without addition, (b) 4% ZrO_2

Thermal shock resistance

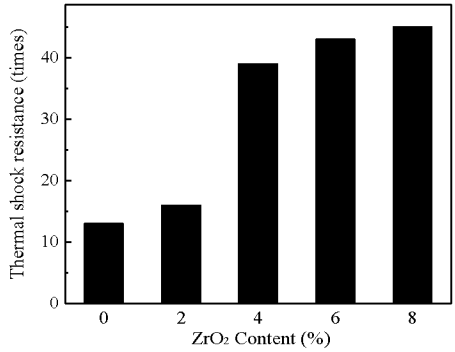

Fig. 4 Effect of ZrO_2 addition on the thermal shock resistance of the high alumina refractory

Fig 4 shows the effect of ZrO_2 addition on the thermal shock resistance of the fired samples. It was observed that the thermal shock resistance was greatly enhanced by addition of 4% ZrO_2. This would be due to the enhancement of grain–grain bonding by heterogeneous distribution of residual fine t-ZrO_2 crystals on the grain boundaries. It was also observed that the value trended to be a constant with further increase of ZrO_2. Therefore, it is considered that the optimal amount of ZrO_2 addition was about 4% considering the performance together with the cost.

Conclusions

High alumina refractories with different addition of ZrO_2 were prepared in the present work. The results showed that added ZrO_2 could dissolve in the CA_6 grains in the form of a solid solution, which enhanced the isotropic growth of CA_6 grains and then improved the diffusion of ions. As a result, the sintering behavior was improved and the dense area was expanded. Tetragonal ZrO_2 grains were found to locate in the grain boundaries when ZrO_2 addition exceeded the solid solubility limit, which enhanced the thermal shock resistance due to the enhancement of grain–grain bonding. In addition, it is considered that the optimal amount of ZrO_2 addition was about 4% considering the performance together with the cost.

Acknowledgment

The authors gratefully acknowledge the National Natural Science Foundation of China (No. 51174049, 51174052, 51374057, 51374062) and the Fundamental Research Funds for the Central Universities of China (No.110402009) which has made this research possible.

References

1. Y. Sato, H. Joguchi, and N. Hiroki, "Test results of alumina-spinel castables for steel ladle," Taikabutsu Overseas, 12(1992), 10–14.
2. K. Fujii, I. Furusato, and I. Takita, "Composition of spinel clinker for teeming ladle casting materials," Taikabutsu Overseas, 12(1992), 4–9.
3. Y.C. Ko, "Influence of the characteristics of spinels on the slag resistance of Al_2O_3–MgO and Al_2O_3–spinel castables," *J. Am. Ceram. Soc.*, 83(2000), 2333–2335.
4. L.A. Díaz et al., "Effect of spinel content on slag attack resistance of high alumina refractory castables," *J. Eur. Ceram. Soc.*, 27(2007), 4623–4631.
5. A. Ghosh et al., "The effect of ZnO addition on the densification and properties of magnesium aluminate spinel," *Ceram. Int.*, 26(2000), 605–608.
6. J.M. Auvray, C. Gault, and M. Huger, "Evolution of elastic properties and microstructural changes versus temperature in bonding phases of alumina and alumina–magnesia refractory castables," *J. Eur. Ceram. Soc.*, 27(2007), 3489–3496.
7. L.A. Díaz et al., "Alumina-rich refractory concretes with added spinel, periclase and dolomite: A comparative study of their microstructural evolution with temperature," *J. Eur. Ceram. Soc.*, 25(2005), 1499–1506.
8. E.Y. Sako et al., "In-depth microstructural evolution analyses of cement-bonded spinel refractory castables: novel insights regarding spinel and CA_6 formation," *J. Am. Ceram. Soc.*, 95(2012), 1732-1740.
9. F. Simonin et al., "Thermomechanical behavior of high-alumina refractory castables with synthetic spinel additions," *J. Am. Ceram. Soc.*, 83(2000), 2481-2490.

Characterization of Minerals, Metals, and Materials 2015
Edited by: John S. Carpenter, Chenguang Bai, Juan Pablo Escobedo, Jiann-Yang Hwang, Shadia Ikhmayies, Bowen Li, Jian Li, Sergio Neves Monteiro, Zhiwei Peng, and Mingming Zhang
TMS (The Minerals, Metals & Materials Society), 2015

IRON RECOVERY FROM COPPER SLAG THROUGH OXIDATION-REDUCTION MAGNETIC CONCENTRATION AT INTERMEDIATE TEMPERATURE

Zhiwen Wu[1], Chen Chen[1], Yahui Feng[1], Xin Hong*[1]

1.Shanghai Key Laboratory of Modern Metallurgy & Materials Processing, Shanghai University, 200072, China

*Corresponding Author: xingh@mail.shu.edu.cn

Keywords: copper slag; fayalite; oxidation; reduction

Abstract

Large amounts of copper slag containing about 40 wt% iron is generated during the process of producing copper. Recovery of iron from the copper slag is very essential not only for recycling the valuable metals and mineral resources but also for protecting the environment. The purpose of this study was to investigate the possibility of separating fayalite by oxidation-reduction process into Magnetite and silicate phases in intermediate temperature condition. Experimental results show that when the oxidation reaction at 1000℃ for 120min and the oxygen flow is 0.1L/min, most fayalite decompose to hematite, less part of magnetite and silica. And then, the mixture of carbon and oxidation product is pressed into blocks and reduced to magnetite and silica at 900℃ for 90min. A magnetic product containing about 57.9wt% iron was obtained from the magnetic separation under a magnetic field strength of 100 mT.

Introduction

With rapid development of China s metallurgical industry, about 10 million tons of copper slags were produced every year [1]. Most copper slag was piled up as waste, which will not only take up a lot of land, pollute the environment, but also be a waste of resources, and it became an obstacle to the sustainable development of copper smelting enterprises. Mineralogy analysis of slag shows that copper slag generally contain Fe, Mo, Cu, Zn, Co, and Ni and other metals and their oxides, iron content in about 40%, and most of Fe exists in form of fayalite (Fe_2SiO_4), mineral crystallization is not enough and most of it is amorphous, Cu and Fe particle size is very fine and well-distributed, and minerals wrap each other [1-6]. All these characters make slag structure hardness, isotropy, very compact and chemical property stable, therefore mineral separation cannot recovery Fe and other valuable elements except of raw materials of cement and concrete, and rust prevent grinding material [5-9].

Many studies have proved that the ideal method of recovering iron from copper slag is to transfer the Fe exists in fayalite (Fe_2SiO_4) into Fe exists in Fe_3O_4 or Fe at high temperature molten state, and then separate the Fe from slag by magnetic separation. But this method will consume a higher energy [10-11]. The purpose of this study was to investigate the possibility of separating fayalite by oxidation-reduction process into Magnetite and silicate phases in intermediate temperature condition, which will own a great significance for improving environment and relieving iron ore shortage condition. This study mainly includes raw material`s physical and chemical properties, the oxidation thermodynamics of fayalite, the reduction thermodynamics of hematite and phase transformation, magnetic separation of magnetic and non-magnetic products.

Experiment Material and equipment

Experiment Material

The copper slag is generated during the secondary recovery of copper by crushed, ground, flotation which is provided by a copper smelting company. The copper slag particle diameter and its polydispersity are determined with laser dynamic light-scattering method by BT-2001 Laser particle size analyzer shown in Fig 1. It is shown in Fig 1 that the size of copper slag is very small, and the median size of particle is less than 10μm. The chemical composition of slag is shown in Table I.

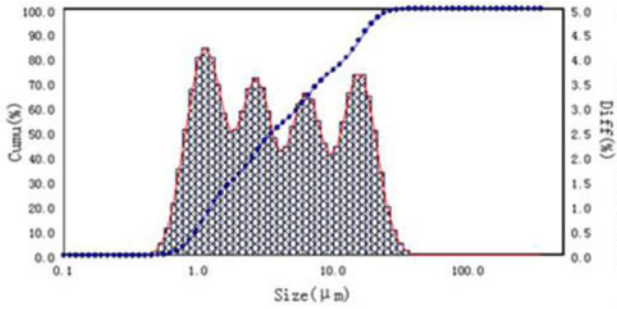

Particle Diameter (μm)	Content Percentage (%)
0.50	0.06
0.80	4.79
1.29	21.42
2.08	34.17
3.35	48.77
5.39	59.37
8.67	72.45
13.94	83.85
22.43	97.44
36.08	100.00

Fig 1 Particle size distribution of copper slag

Table I The chemical composition of slag (mass percent :%)

TFe	FeO	SiO2	Ca	Al	Zn	Cu	Mg	Pb	K	Others
38.52	45.67	38.57	1.27	1.55	2.67	0.48	0.91	0.47	0.54	7.87

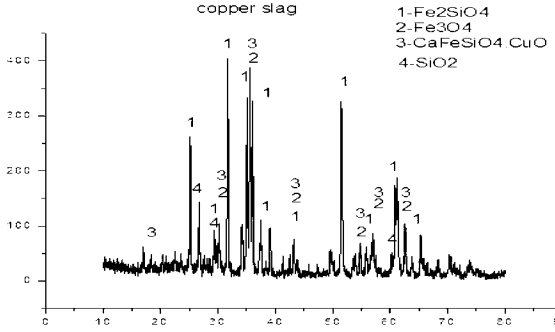

Fig 2 XRD pattern of copper slag

The instrument for identification of object phase is D/max2550 X-ray diffraction produced by RIGAKU . The slag XRD shows that the copper slag is amorphous mineral and the crystal mineral is fayalite (Fe_2SiO_4). In Fig.2, other mineral`s diffraction peak is not obvious and the corresponding spectral lines of other crystal mineral such as CuO, Fe_3O_4 etc. can be found.

Experiment equipment

The main laboratory equipment, including an electric resistance furnace, SRS3400 X-ray fluorescence spectrum analyzer, D/max2550 X-ray diffraction, JSM-6700 Scanning, BT-2001 Laser particle size analyzer, CXG-08SD magnetic separate tube, etc.

Oxidation-reduction experiment on copper slag

Experiment principle

The fayalite oxidation process by oxygen and Fe_2O_3 reduction process by carbon are analyzed. The oxidation thermodynamics of fayalite influenced by O_2 and the reduction thermodynamics of hematite influenced by carbon is calculated. The results are shown in equation (1), equation (2) and equation (3). The thermodynamics calculation indicates that the possibility of the fayalite oxidation process is very large.

$$2FeO{\cdot}SiO_2 + 0.5O_2 = Fe_2O_3 + SiO_2 \qquad \Delta rG_m^\theta = -250823 + 100.85T(J/mol) \quad (1)$$

$$2FeO{\cdot}SiO_2 = 2FeO + SiO_2 \qquad \Delta G_m^\ominus = -36200 + 21.09T(J/mol) \quad (2)$$

$$3Fe_2O_3 + C = 2Fe_3O_4 + CO \qquad \Delta rG_m^\theta = 120000 - 218.46T(J/mol) \quad (3)$$

Experimental scheme

Firstly, the copper slag is oxidized by O_2 in the tubular resistance furnace. Secondly, the oxidation products were grinded, then mixed with carbon and CaO, and pressed into blocks. Thirdly, the sample was charged into an electric resistance furnace and reduced for some time. At last, the sample was subjected to wet magnetic separation at a magnetic field of 100mT, then non-magnetic product was thrown into the tailings compartment and magnetic product was gripped, carried out of the influence of the field and deposited into the magnetic compartment. After magnetic separation, both magnetic and non-magnetic products were analyzed.

Results and Discussion

Copper slag oxidation process

The copper slag was calcined at 800℃, 850℃, 900℃, 950℃, 1000℃ respectively for 120min and the oxygen flow is 0.1L/min. The XRD pattern of the sample after calcined was analyzed shown in Fig 3. As calcination temperature increases, fayalite was oxidized into hematite and amorphous silica ($2FeO{\cdot}SiO_2 + 0.5O_2 \rightarrow Fe_2O_3 + SiO_2$), then the crystal morphology of magnetite was transform into hematite. The characteristic peaks of fayalite disappeared at 900 ℃, the characteristic peaks of magnetite increased with temperature rising then decreased while calcination temperature is higher than 900℃. The characteristic peaks of hematite increased as calcination temperature increased. The XRD pattern of the sample after calcined for 60min, 90min and 120min at 1000℃ and the oxygen flow is 0.1L/min was analyzed shown in Fig 4. It shows that the characteristic peaks of fayalite disappeared with time increased. The characteristic peaks of SiO_2 appeared at 21.7°, 27.5°, 36.6°, 41.7° and 50.2° when the calcination time reached to 120min.

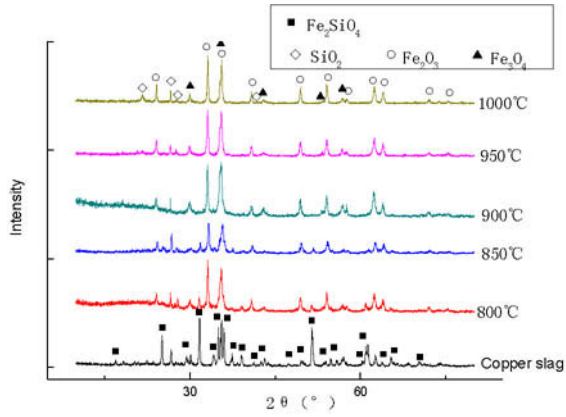

Fig 3 XRD patterns of natural and copper slag calcined under different temperature

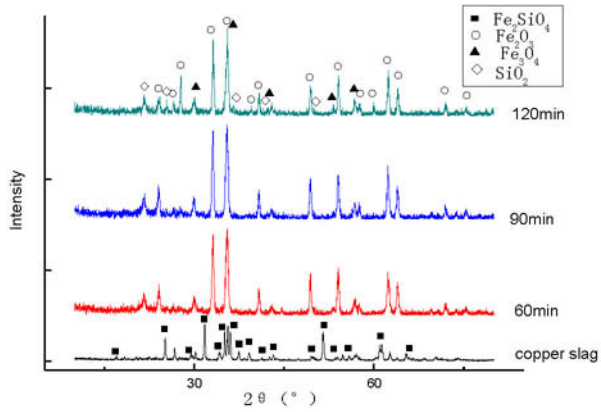

Fig 4 XRD patterns of copper slag calcined in different time

SEM / EDX analysis of the copper slag was uncalcined and calcined at 1000 ℃ for 120min shown in Fig 5. The SEM shows that the uncalcined copper slag was dense structure and smooth nonporous surface structure, and it`s surface color was dark gray. The EDX results of copper slag in point 1 and point 2 (shown in Fig 5) have shown in Table II. The test results by EDX analysis show that the ingredients of copper slag were almost fayalite. After the oxidation, the morphology of the calcined copper slag with bulky structure with holes was very different from the original copper slag, and the surface color changed to light gray. The test results by EDX analysis shows that was hematite. So, the experimental results of SEM/EDX analysis shows that the oxidation process can change the structural properties of copper slag, and it will promote Fe(II) transformed into Fe(III).

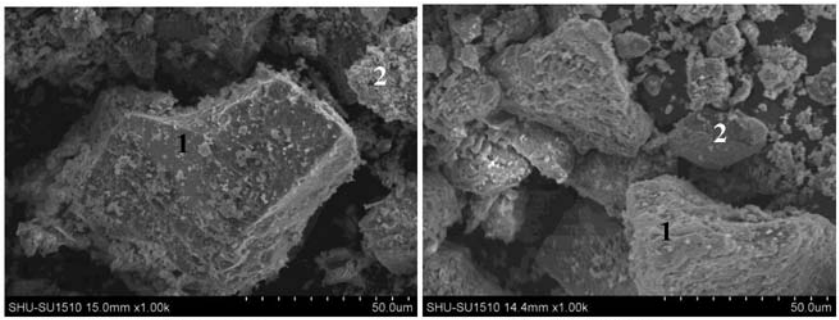

Copper slag 1000℃ 120min

Fig 5 SEM analyses of calcined copper slag

Table II The EDX results of copper slag (mass percent :%)

Samples	Point	Fe	O	Si	Zn	Ca	Al	K	Phase
Copper slag	1	41.96	34.02	17.05	2.12	1.27	1.55	0.54	Fayalite
	2	34.86	38.70	19.33	2.38	2.06	1.36	0.60	Silicate
1000℃ 120min	1	66.03	24.72	4.70	2.34	2.07	0.30	-	Hematit
	2	4.12	47.77	35.18	1.89	3.04	4.71	1.25	SiO_2

The calcined copper slag reduction process by carbon

Influence of reduction temperature. Experimental conditions: The reduction process is studied in which 6% carbon is added and the reduction time is 120 min. The influences of reduction temperature and XRD pattern of product after reduction on iron grade are shown in Fig 6 and Fig 7. It is shown in Fig 6 that the iron grade increases with temperature rising when reduction temperature below 900℃, that's because the reduction process is endothermic. Moreover the iron grade decreases while temperature is 950℃ for regenerating fayalite [12]. The characteristic peaks of hematite still exist when reduction temperature is 800℃ shown in Fig 7. The reduction temperature should be appropriate to ensure adequate reduction and will not generate fayalite.

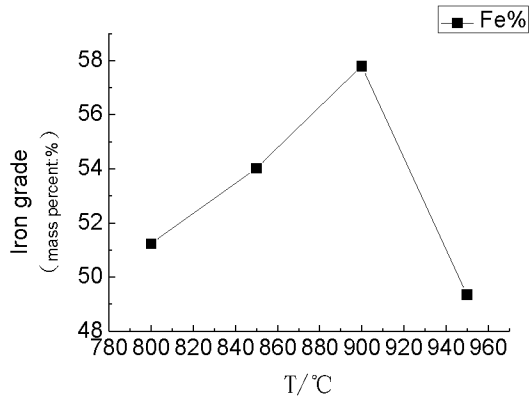

Fig 6 Effect of temperature on iron grade

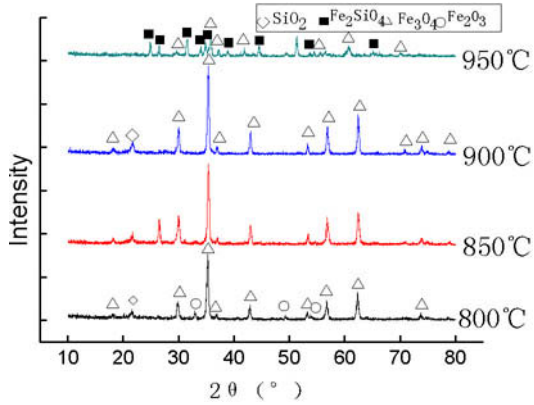

Fig 7 XRD pattern of product after reduction

Influence of carbon content. Experimental conditions: The reduction process is studied in which reduction temperature is 900℃ and the reduction time is 120 min. The influences of carbon content and XRD pattern of product after reduction on iron grade are shown in Fig 8 and Fig 9. It is shown in Fig 8 that the iron grade increases as the carbon content increases until to 6% because it needs enough carbon to ensure adequate reduction. And the characteristic peaks of hematite still exist when carbon content is 6% shown in Fig 9. Then the iron grade decreases because excessive carbon reduced Fe_3O_4 to FeO, and FeO was transform into Fe_2SiO_4 by SiO_2 [12], shown in Fig 9.

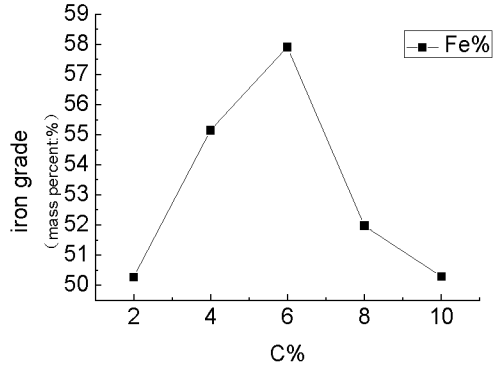

Fig 8 Effect of carbon content on iron grade

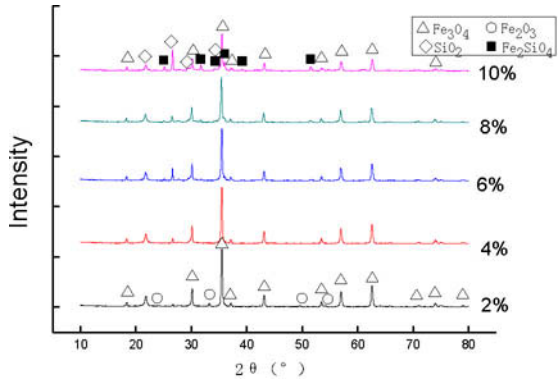

Fig 9 XRD pattern of product after reduction

Influence of reduction time. Experimental conditions: The reduction process is studied in which 6% carbon is added and the reduction temperature is 900℃. The influences of reduction time on iron grade are shown in Fig 10. It is shown in Fig 10 that the iron grade increases with time increased because the reduction process is more thoroughly as reduction time increased. Moreover the iron grade almost constant when reduction time is longer than 90min.

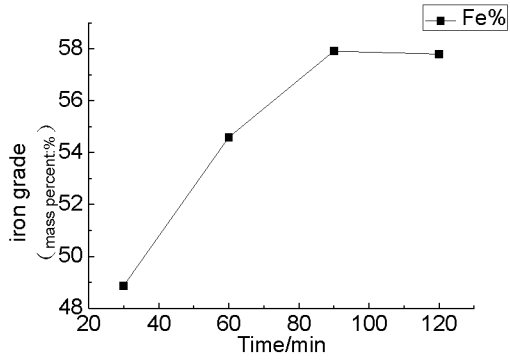

Fig 10 Effect of reduction time on iron grade

Conclusions

(1) Throughout the oxidation process as calcination temperature and time increased the characteristic peaks of hematite increased because fayalite is oxidized into hematite and amorphous silica, then the crystal morphology of magnetite is transform into hematite. The characteristic peaks of fayalite disappeared at 900 ℃, the characteristic peaks of magnetite increased with temperature rising then decreased while calcination temperature is higher than 900℃. The characteristic peaks of SiO_2 appeared at 21.7°, 27.5°, 36.6°, 41.7° and

50.2° when the calcination time reached to 120min. The oxidation process can change the structural properties of copper slag, and it will promote Fe (II) transformed into Fe (III).

(2) After the reduction process, hematite is transformed into magnetite and laboratory experiment offers a better condition that the iron grade of magnetic concentrate is increased to 57.91% from 38.52% when 6% carbon is added and reduction temperature and time are respectively 900℃ and 90min.

References

[1] Liao Zengli, Tang Pu, Zhang Bo, et al. Experimental study on oxidation modification of copper slag at middle-low temperature [J]. China Nonferrous Metallurgy, 2012(2): 74-78.

[2] Wang Heng. Recovery of copper and iron in the converter slag from a copper smelter [J]. Journal of Guangdong Non-ferrous Metals, 2003, 13(2): 83-88.

[3] Zhang Linnan. Study on Selective Precipitation Valuable Constituent in Copper Smelting Slags [D]. Shenyang: Northeastern University, 2005.

[4] Alter H. The composition and environmental hazard of copper slag in the context of the Basel convention [J]. Resources, Conservation and Recycling, 2005, 4, 3(4): 353-360.

[5] Najimi M, Pourkhorshidi A. Properties of concrete containing copper slag waste [J]. Magazine of Concrete Research, 2011, 63(8): 605-615.

[6] Lowinska K A, Piszora P, Darul J, et al. Characterization of chemical and physical parameters of post copper slag [J]. Central European Journal of Physics, 2011, 9 (2): 380-386.

[7] Tran L, Palacios J, Sanches M. Recovery of Molybdenum from copper slag [J]. Tetsu to Hagane-Journal of the Iron and Steel Institute of Japan, 2012, 98(2):48-54.

[8] Han Wei, Qin Qingwei. Recovery of copper and iron from copper slag [J]. Mining and Metallurgy, 2009, 18(2): 9-12.

[9] Gyurov S, Kostova Y, Klitcheva G, et al. Thermal decomposition of pyrometallurgical copper slag by oxidation in synthetic air [J]. Waste Management and Research, 2011, 29(2): 157-164.

[10] Wang Hongyu, Li Keqing, Ni Wen, et al. Experimental research of deep reduction and magnetic separation process of a high-iron copper slag [J]. Metal Mine, 2012(11): 141-144.

[11] Yang Huifen, Jing Lili, Dang Chunge. Iron recovery from copper slag with lignite-based direct reduction followed by magnetic separation [J]. Chinese Journal of Nonferrous Metals, 2011, 21(5): 1165-1170.

[12]Jia Yan, Ni Wen, et al. The growth characteristics of metallic iron grains in depth reduction of oolitic hematite [J]. Metal Mine, 2010, 412(10): 52-56.

Characterization of Minerals, Metals, and Materials 2015
Edited by: John S. Carpenter, Chenguang Bai, Juan Pablo Escobedo, Jiann-Yang Hwang, Shadia Ikhmayies, Bowen Li, Jian Li, Sergio Neves Monteiro, Zhiwei Peng, and Mingming Zhang
TMS (The Minerals, Metals & Materials Society), 2015

CHARACTERIZATION AND EVALUATION OF INCORPORATION THE CASTING SAND IN MORTAR

Zanelato, E.B. [1], Azevedo, A.R.G.[1], Alexandre, J.[1], Xavier, C.G.[1], Monteiro, S.N.[2], Mendonça, T.A.O.[1]

[1]UENF - State University of the Northern Rio de Janeiro, LECIV – Civil Engineering Laboratory; Av. Alberto Lamego, 2000, Campos dos Goytacazes, Rio De Janeiro, 28013-602, Brazil.

[2] IME - Military Institute of Engineering, Department of Materials Science, Praça General Tibúrcio, 80, Rio de Janeiro, Rio de Janeiro, 22290-270, Brazil.

Keywords: Mortar, Casting sand and civil construction.

Abstract

The process of casting metals and alloys occurs through the fusion of this metal and its subsequent casting into a mold with the dimensions and geometry close to the final piece. Most foundries use sand casting molds for making you. This work aims to characterize and evaluate the foundry sand to allow its use in segments of Civil Engineering, creating a viable destination for a residue is that discarded. The following characterization tests were performer: particle size, chemical analysis, X-ray Diffraction and Density Real grain. For the execution of the test specimens was used to 1:3 cement and sand, and the incorporation of 10% and 20% of the total mass replacing the sand, and the trace reference. The results show that best results in compression and bending tests were obtained by replacing 10 % of common sand for sand casting.

Introduction

The casting process of metal alloys occurs through the fusion of this metal and its subsequent leakage into a mold with the dimensions and geometry close to the final piece. After solidification, the metal is extracted from the mold, leaving only the desired part. In general, the casting sand is used for create these molds. These sands are composed of quartz, chromite and zircon, in addition to additives and binders.[1]

The sand is reused until no longer suited to the mold making process, being so discarded. This dispose generates a huge amount of waste in landfills, it is estimated that for every ton of molten metal has been around a ton of discarded sand.

To mitigate this problem, it is studied the development of a technique to reuse these sand, being civil construction a promising alternative for use as part of the raw material.

Some works have been developed to partially replace the aggregate for casting sand for making concrete[2] and pavement[3].

The objective of this work is to characterize and to replace partially in 10% and 20% of the aggregate for sand casting.

Materials and Methods

The residue used in this work was collected in one of the points of discard from the molding process.

After collecting the residue the particle size, Chemical Analysis, X-Ray Diffraction and Density Real grain were performed for material characterization.

The particle size test was done using the standard sieves and then the sedimentation test with the passing material sieve (sieve mesh 200, ABNT, 0.075mm)[4].

Chemical analysis was performed using the technique of X-ray spectroscopy by energy dispersive (EDX) using a Shimadzu EDX-700. The sample was ground using a ball mill at the Laboratory of Civil Engineering until the material was sieved (sieve mesh 325, ABNT, 0.045 mm), making it more uniform, which facilitates analysis.

The test of X-ray diffraction was performed by a X-ray Diffraction (XRD), using a Panalytical X'Pert powder diffractometer operating at 45kV, 40 mA with CuKα radiation.

The Density Real grain was performed using calibrated pyknometers in the Laboratory of Soil Mechanics.

Once characterized, the mortars were prepared for consistency test. The mortars were prepared according to NBR 13276 (ABNT, 2005) [5] using the 1: 3 ratio, making the replacement of fine aggregate for casting sand, in percentages of 10% and 20% beyond the reference composition without replacement.

The consistency test was performed according to NBR 13276 (ABNT, 2005)[5]. Several attempts with different additions of water masses were held until it was found the diameter required by standard, 260 ± 5 mm. The consistency test was conducted for the three different compositions, and discovered the water/cement ratio for each of them (Figure 1).

Figure 1. The consistency test - flow table.

The flexural strenght of a hardned mortar is determined by three point loading of a prism sample, subsequent to the rupture of this sample the compressive strenght is determined on each half of the prism. Prism mould compartments are required to be 160 mm x 40 mm x 40 mm (each mould assembly produces three prism samples), prior to use they are lubricated with a thin layer of mineral oil. After 7,14 and 28 days of curing the flexural strenght and the compression tests (Figure 2) in bending according to NBR 13279 (ABNT, 2005)[6].

Figure 2. Compression test.

Results

Figure 3 shows the particle size distribution curve of the casting sand. In this figure one sees that the so-called "clay fraction", corresponding to particle sizes (d) below 2 μm is 4.60%, while the "silt fraction" ($2 < d < 20\mu m$) is 87.30% and the "sand fraction" ($d > 20\mu m$) is 8.10%.

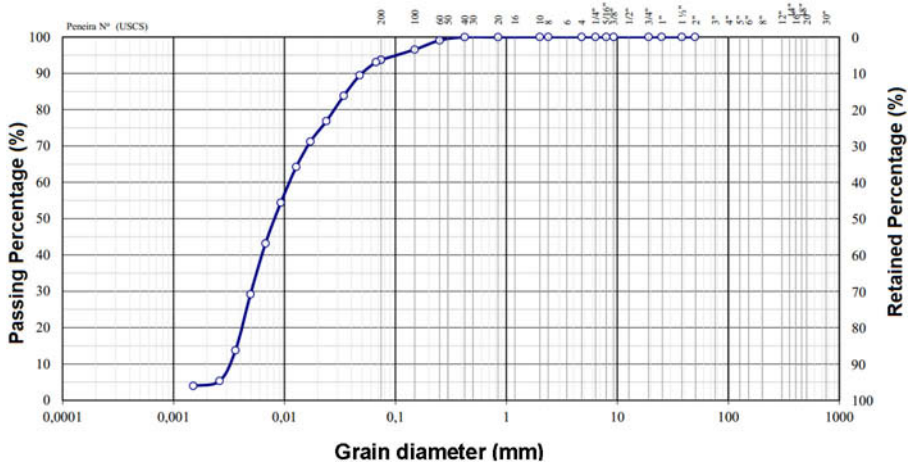

Figure 3. Particle size distribution of the raw material.

The chemical composition of the casting sand obtained by XRF, is presented in Table 1.

Table 1 – Chemical composition by XRF of the raw material given in terms of oxides (%).

Fe_2O_3	Al_2O_3	Cr_2O_3	SiO_2	SO_3	MnO	K_2O	TiO_2	ZrO_2	ZnO	V_2O_5	NiO
27.02	26.32	21.65	19.07	2.20	1.34	0.82	0.46	0.25	0.25	0.24	0.20

Figure 4 shows the characterization by X-ray Diffraction. In this figure the proportion of magnetite is consistent with the huge amount of (Fe_2O_3), as shown in Table 1.

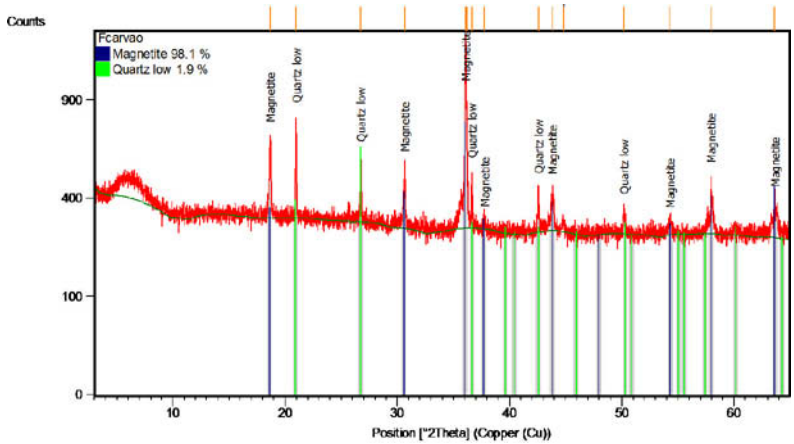

Figure 4. Results of characterization by X-ray Diffraction.

The real density of particles of casting sand is presented in Table 2.

Table 2. Real density of the casting sand.

Real Density of Particles (g/cm^3)
2.67

The three compositions tested and their consistencies are presented in the table 3.

Table 3 – The compositions and their consistencies.

Composition	Cement	Sand	Casting Sand	Water/cement	Consistence
Reference	1	3	0	0.69	263mm
10%	1	2.7	0.3	0.69	256mm
20%	1	2.4	0.6	0.78	256mm

The table 4 shows the medium values of the compression rupture strength of all the samples of each composition. It is important to mention that the minimum average strength for the samples is 1.5 MPa [7] (after 28 days). Based on this norm, all the types attend the above requirements.

Table 4. Compression rupture strength (MPa).

Rupture age (days)	Reference	10%	20%
7	2.46	3.53	3.55
14	3.80	4.09	3.97
28	4.30	4.59	4.32

The table 5 shows the medium values of the flexural strength of all the samples of each composition. It is important to mention that the minimum average strength for the samples is 1.0 MPa [7] (after 28 days). Based on this norm, all the types attend the above requirements.

Table 5. Flexural Strenght (MPa).

Rupture age (days)	Reference	10%	20%
7	0.84	1.05	0.82
14	1.10	1.27	1.11
28	1.30	1.51	1.29

Conclusion

- It can be concluded that all samples meet the requirements of the standard.
- The composition with 10% incorporation of casting sand showed the best performance. It can be concluded that the casting sand has potential for use in civil construction.

Acknowledgements

The authors thank the Brazilian agencies: CNPq, CAPES and FAPERJ for the support provided to this investigation.

References

1. MORO, N.; AURAS, A.P. Fabrication process – foundry. Santa Catarina: Centro Federal de Educação e Tecnológica de Santa Catarina, 2007.
2. KLINSKY, L. M. G. Proposed reuse of Foundry Sand in sub-bases and bases of flexible pavements through its incorporation in clay soils. 185 f. Thesis (Master in Civil Engeneering: Transportation) – Escola de Engenharia de São Carlos, São Carlos, 2008.
3. SIDDIQUE, R.; SINGH, G. Utilization of waste foundry sand (WFS) in concrete manufacturing. Resources, Conservation and Recycling, v. 55, p. 885-892, mai. 2011
4. Brazilian Association of Technical Norms –ABNT NBR NM 248, Aggregates - Sieve analysis of fine and coarse aggregates (in Portuguese), Rio de Janeiro, Brazil, 2003.
5. Brazilian Association for Technical Norms – ABNT NBR-13276, Mortars applied on walls and ceilings - Preparation of mortar for unit masonry and rendering with standard consistence index (in Portuguese), Rio de Janeiro, Brazil, 2005.
6. Brazilian Association of Technical Norms –ABNT NBR-13279, Mortars applied on walls and ceilings - Determination of the flexural and the compressive strength in the hardened stage (in Portuguese), Rio de Janeiro, Brazil, 2005.
7. Brazilian Association of Technical Norms –ABNT NBR-13281, Mortars applied on walls and ceilings - Requirements (in Portuguese), Rio de Janeiro, Brazil, 2005.

Characterization of Minerals, Metals, and Materials 2015
Edited by: John S. Carpenter, Chenguang Bai, Juan Pablo Escobedo, Jiann-Yang Hwang, Shadia Ikhmayies, Bowen Li, Jian Li, Sergio Neves Monteiro, Zhiwei Peng, and Mingming Zhang
TMS (The Minerals, Metals & Materials Society), 2015

CARBONIZATION OF COALS MIXED IRON ORE FINES AND GASIFICATION OF RESULTING IRON COKE WITH CO_2: TRANSFORMATION OF IRON MINERALS AND COKE PROPERTIES

Shengfu Zhang, Wei Liu, Shuxing Qiu, Mingrui Yang, Manjie Li, Haijun Peng
College of Materials Science and Engineering, Chongqing University, China

Keywords: Iron coke, Strength, ICRI, ICSR, Iron minerals, Crystal structure.

Abstract

It is important to produce and utilize highly reactive coke in order to reduce the energy consumption and CO_2 emissions through improving shaft efficiency in blast furnace. The present study aimed to investigate the transformation of iron minerals and properties of iron coke (the coke mixed iron ore fines). Along with the increase of iron ore fines, cold strength displayed a slight downtrend and the pore structure wasn't inferred to be a major factor affected the properties of iron coke. During carbonization, the majority of mixed iron oxides were reduced to metallic iron by CO and H_2 and the degree of metallization achieved to approximately 75%. Nevertheless, produced metallic iron was oxidized by pure CO_2 during gasification. Iron coke reactivity index (ICRI) was obviously enhanced and the iron coke strength after reaction (ICSR) drastically decreases, which were also significantly influenced by crystal structure of carbon.

Introduction

The blast furnace (BF) is an important and effective ironmaking technology. Currently, with the pressure of environmental protection and the soaring of coke price, improving the efficiency of BF reactions and reducing consumption of fuels have been brought into the concern of the ironmaker. Coke, one of the major raw materials, plays a significant role to ensure the BF working smoothly. Generally speaking, coke strength and carbon solution loss reaction are considered to influence importantly on the shaft efficiency. Naito *et al.* [1, 2] and Lyalyuk *et al.* [3] have concluded that the utilization of highly reactive coke could decrease the thermal reserve zone temperature, resulting from the stronger driving force of reduction reaction in BF.

Previous studies have indicated that the rank, maceral compositions and mineral matters of the parent coal affect the coke reactivity principally. Among of them, mineral matters have been considered as the most important factor [4, 5]. Particularly, the alkalis [6],alkaline-earth metals [7] and transition metals [8] present a strongly positive catalysis during the coke gasification with CO_2.

To be specific, alkali and alkaline-earth metals are undesirable as catalysts of metallurgical coke because of the scaffolding of BF brasque and the harder control of basicity of slag, respectively [9]. In recent years, scholars pay more attentions to iron coke and put forward some controversial viewpoints. M. Grigore considered that metallic iron (MFe), pyrrhotite ($Fe_{1-x}S$) and hematite (Fe_2O_3) could have a catalytic effect on the gasification, but it wasn't explicit about magnetite (Fe_3O_4) [4]. Some researchers revealed that the application of the iron coke containing 43% of TFe for BF resulted in an increase of shaft efficiency by 6.8% [10]. However, the catalytic mechanism of iron for coke reactivity remains poorly understood.

In present study, the properties of cokes such as the cold strength, pore structure and crystal structure were investigated. Furthermore, the transformation of the mixed iron minerals was analyzed after the carbonization and gasification.

Experimental

Preparation of coke sample

Two kinds of coals, coal NT (caking coal) and coal YH (moderately caking coal), and iron ore fines were selected for this study. **Table Ⅰ** and **Table Ⅱ** show the properties of coals and chemical component of iron ore fines, respectively. The coals were sieved by 0.5 and 3 mm apertures and the particle size of iron ore maintains less than 74 μm. Mixing conditions of raw materials for coke production are shown in **Table Ⅲ**. The blending ratio of coal NT and YH was fixed (NT/YH=7/3) while the iron ore fines were added by 0, 2.5, 5, 7.5, 10 and 15 wt-%. Preparation of samples was carried out by means of 'pre-addition of catalyst to coke' method. Mixed materials with a moisture content of 10% were charged into a coking reactor showed in **Figure 1(b)** (100 mm diameter and 500 mm high) at a bulk density of 900 kg m^{-3}. In order to ensure the homogenous density of briquette, the raw materials were packed into the retort in five increments of 440 g each and each of increments was tamped down to a predetermined height of 63.5 mm. Subsequently, the retort was placed into a 2 kg electrically heated test coke oven and then the oven kept a constant temperature for 6 h when the briquette was heated to 1050℃. The experimental apparatus are shown in **Figure 1(a)**.

Table Ⅰ Properties of coals used in the experiment

Coal	Proximate analysis/wt-%				Ultimate analysis/wt-%					$\overline{R_0}$ /%
	Mad	VM	Ash	FC	C	H	N	S	O	
NT	0.89	21.12	11.92	66.07	76.14	4.12	1.20	0.51	5.22	1.03
YH	2.38	26.26	10.08	61.28	73.22	4.41	1.72	1.96	6.23	0.95

*Mad: Air-dried Moisture, VM: Volatile Matter, FC: Fixed Carbon, $\overline{R_0}$: Mean Reflectance

Table Ⅱ Chemical component of iron ore fines used in the experiment/wt-%

TFe	FeO	SiO_2	Al_2O_3	CaO	MgO	P	S
65.27	23.53	5.92	0.70	0.27	0.39	0.01	0.26

Table Ⅲ Mixing conditions of raw materials for coke production/wt-%

Raw materials	No.1	No.2	No.3	No.4	No.5	No.6
Caking coal (NT)	70.00	68.25	66.50	64.75	63.00	59.50
Moderately caking coal (YH)	30.00	29.25	28.50	27.75	27.00	25.50
Iron ore fines	0	2.50	5.00	7.50	10.00	15.00

Evaluation test of cold strength and thermal properties of iron coke

After the carbonization processes from tests No.1 to No.6, the shatter index (SI^4_{25}) of

coke samples were tested by the method which described by Standardization Administration of China (SAC) GB/T15459-2006. The test method of mechanical strength was described by SAC GB/T2006-2008, the crushing strength (M_{25}) and the abrasion resistance (M_{10}) were measured after 100 revolutions in the I-type drum tester. In addition, the thermal properties of coke samples were evaluated by Nippon Steel Corporation (NSC) method and the coke gasifier is shown in **Figure 2**.

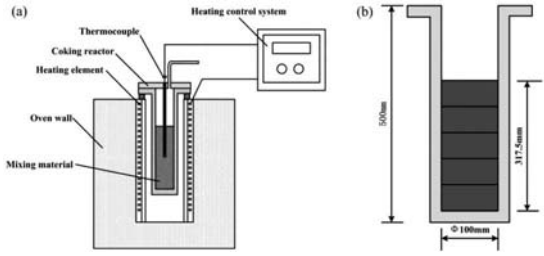

Figure 1 Carbonization apparatus in the test: (a) 2 kg electrically heated test coke oven; (b) coking reactor.

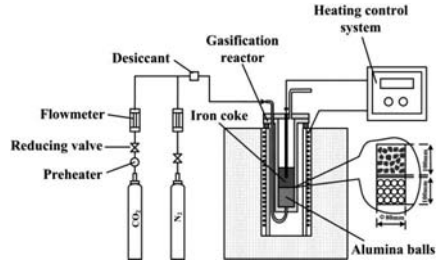

Figure 2 Experimental apparatus of gasification reaction

Evaluation test of pore structure of iron coke

The quality of coke was considered to be affected by pore structure. After carbonization, the measurements of surface area and pore volume were performed by adsorption of nitrogen gas at the temperature of 77 K and the parameters were calculated by the Brunauer–Emmett–Teller (BET) and Barrett-Joyner-Halenda (BJH) isotherm, respectively [11].

Test of phase and crystallite sizes for iron coke

In order to investigate the transformation of iron minerals of the coke during carbonization and gasification process, the phases were identified using X-ray diffraction (XRD) analysis. The XRD has a monochromator and a copper K_α X-ray source. The voltage and current in the X-ray emission tube on samples were set at 40 kV and 150 mA, respectively. In this study, iron coke samples were scanned with a scanning rate of 4° min^{-1} over the angular range of 10° to 90°, and the sampling interval was set in 0.02°/step [12]. Except the phase, the further details of crystallites

sizes were evaluated by analyzing the 002 and 100 carbon peaks of the XRD pattern following classical Bragg's law and Scherrer's equation,

$$L_c = k_1\lambda/(\beta_1 \cos\theta) \quad (1)$$

$$L_a = k_2\lambda/(\beta_2 \cos\theta) \quad (2)$$

Where λ is wavelength of X-ray and λ=0.15418 nm, θ represents the diffraction angular of carbon crystallite, β_1 and β_2 are the full width at half maximum (FWHM) of the diffraction peak (002 and 100), respectively. k_1=0.91 for L_c and k_2=1.84 for L_a [13].

Results and Discussion

The evaluation of cold strength of iron coke

The catalyst can reduce the caking property of coal in carbonization process [14]. Therefore, the cold strength of iron coke produced by coals and iron ore fines is analyzed, mainly about the shatter and mechanical strength. **Figure 3** describes the trend of SI^4_{25} for variational blending ratios and shows that the conventional coke presents a little higher SI^4_{25} than iron coke. Nonetheless, the SI^4_{25} can maintain upon 90% at least. The mechanical strength is represented by M_{25} and M_{10} which also are showed in the **Figure 3**. Below the blending ratio of 7.5 wt-%, the M_{25} of coke slightly declines and the M_{10} slightly increases. On the other hand, it shows much low cold strength with the ratio of 10 wt-% and 15 wt-%. To be compared with conventional coke, the descending ratios of M_{25} are 0.40%, 5.33%, 5.30%, 10.30% and 10.19%, respectively. Base on the tests, it declares that the cold strength presents a downtrend along with the increase of the blending ratios under same carbonization conditions. The reasons can be considered that the prevention of dilatation of coal particles is more serious with the increase of iron ore fines [10].

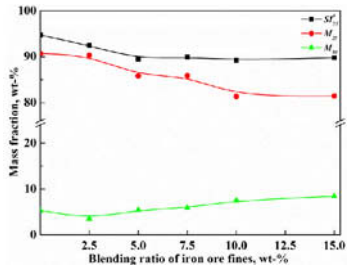

Figure 3 Cold strength of iron coke blending different ratios of iron ore fines

Some investigations of the iron coke after carbonization

Transformation of iron minerals of iron coke after carbonization

Since so many papers had manifested that some kinds of iron minerals revealed strongly catalytic impact on the gasification of coke [8, 15]. Therefore, it is necessary to investigate the transformation behavior during carbonization process and the XRD analysis was used. The **Figure 4(a)** describes major constituents of coke without iron ore fines, the sulfur presented in the coke can react with calcium oxide to form

calcium sulfide (CaS) when it was released during carbonization. **Figure 4(b), (c), (d), (e)** and **(f)** describe the transformation of iron minerals in coke bearing 2.5 wt-%, 5 wt-%, 7.5 wt-%, 10 wt-% and 15 wt-% iron ore fines, respectively. In the five figures, the Fe_xS which may be considered production of the reaction between iron oxides and hydrogen sulfide occurs. However, CaS doesn't appear any more. It can be inferred that the major sulfurs of coals have reaction with mixed iron oxides and there will be few sulfurs react with calcium oxide.

The carbon and coke oven gases (CO and H_2) contributed to the presence of metallic iron during carbonization and the degree of metallization could be calculated by the following equation: (measured mass of metallic iron)/ (calculated mass of iron oxides). In addition, the mass of metallic iron was assessed by means of chemical analysis and the mass of iron oxides was calculated via the TFe and mass ratio of FeO in the original iron ore fines. According to above, the degree of metallization was obtained and achieved to approximately 75%.

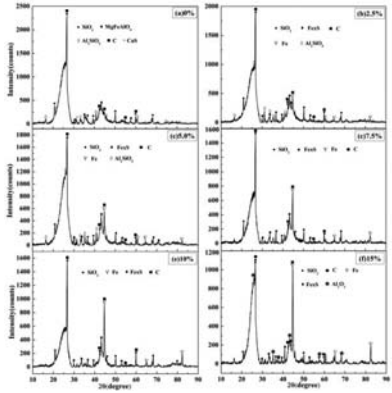

Figure 4 XRD patterns of coke bearing iron ore fines after carbonization

Crystal structure and pore structure analysis of iron coke after carbonization

Generally, coke is porous material which consists of pore and matrix. In present study, the pore structure of iron coke after carbonization is investigated, especially surface area and pore volume. The **Figure 5** indicates that both surface area and pore volume changed little when the blending ratio is less than 10 wt-%. Nevertheless, a high value appears under the ratio of 15 wt-%.

Although coke is an amorphous material, it contains a small quantity of crystal structure in the small scope, which is called crystallite. Crystal structure influences the coke strength and reactivity. Hence the crystallite sizes of coke bearing iron ore fines after carbonization are evaluated by means of XRD techniques and the results are described in the **Figure 6**. In order to represent crystal structure, the 002 and 100 peaks were mentioned. In this figure, 002 and 100 carbon peaks appear roughly at the 26° and 45°, respectively. Here, 002 carbon peak is lower and wider along with the increase of addition, which indicates that the degree of ordering of carbon structure of coke or graphitization (crystallite height, L_c) reduces [9]. Meanwhile, 100 carbon peak is higher and narrower (crystallite width, L_a). The L_c and L_a were calculated by the equation (1) and equation (2), where the FWHM of 002 and 100 carbon peaks measured from the XRD profile. It is considered that the crystal structure of cokes is

obviously affected by mixed iron ore fines.

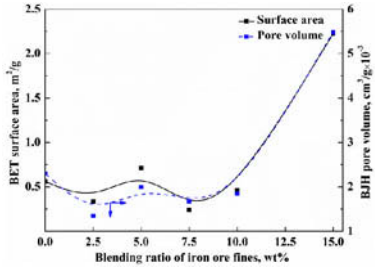

Figure 5 Changes in surface area and pore volume of coke products with blending ration of iron ore fines

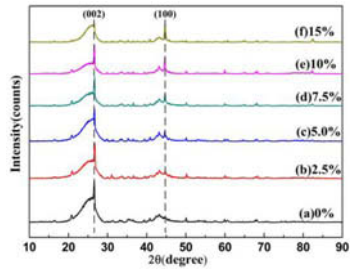

Figure 6 XRD patterns of crystal structure of iron coke after carbonization

Some investigations of the iron coke after gasification

The evaluation of the thermal properties of iron coke

Figure 7 shows the variation of both ICRI and ICSR. It can be obtained that the iron cokes indicate a higher ICRI than conventional coke, meanwhile, the increasing ratios are 0.7, 1.5, 1.9, 1.5 and 1.2 times, respectively. The ICRI achieves to the maximum at the blending ratio of 7.5 wt-% but above present an obviously reducing tendency. In addition, the active patches on the carbon surface where the carbon solution loss reaction occurs can increase owing to the variation of crystal structure. In consideration of the strongly negative influence of iron ores on the formation of plastic mass, the anisotropic microtexture would be restrained. Generally speaking, isotropic microtexture is believed to react more readily with CO_2 than the anisotropic microtexture [16]. Based on all factors introduced above, it can be inferred that the reactivity of coke is obviously enhanced when the iron ore fines are mixed in the raw coals.

A high degree of linear correlation between the two indices, CSR and CRI, is derived from the NSC method by various authors [17]. **Figure 7** illustrates that the ICSR has a significant downtrend while the additives increase. The ICSR is controlled by the expansion of coals and inner degradation. In addition, more carbon is consumed during gasification resulting from the high reactivity of iron coke, the carbon strength sharply declines. On the other hand, there is a positive correlation between ICSR and L_c shown in the **Figure 8**, which indicates that the ICSR increase obviously along with the increase of L_c values. It can be inferred that the increase of degree of

graphitization leads to the promotion of micro-strength of carbon.

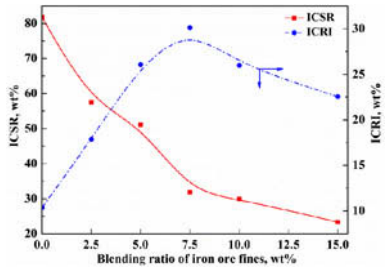

Figure 7 Changes in ICRI and ICSR values of coke products with blending ration of iron ore fines

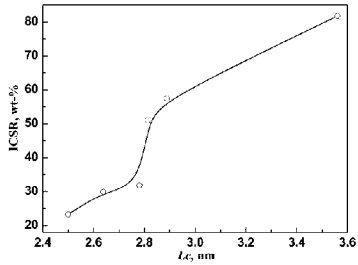

Figure 8 The relationship between ICSR and L_c

Transformation of iron minerals of iron coke after gasification

The test of gasification of coke with CO_2 was carried out and there were some changes of mineral matters in the process shown in **Figure 9**. Making a comparison, it seems to be considered that gasification reaction has no obvious influences on the mineral matters of conventional coke. To compare with other results shown in the **Figure 4**, the Fe_xS remains existent in the **Figure 9.**

In addition, the produced metallic iron during carbonization disappears as a result of the oxidization of Fe in the atmosphere of pure CO_2, which can be described by equation (3) and equation (4),

$$Fe + CO_2 = FeO + CO \quad (3)$$

$$3Fe + 4CO_2 = Fe_3O_4 + 4CO \quad (4)$$

$$2FeO + SiO_2 = Fe_2SiO_4 \quad (5)$$

The ΔG values of equation (3) and equation (4) were calculated and found to be negative, suggesting the reactions occurred in this atmosphere.According to equation (3) and (4), the FeO and Fe_3O_4 were produced by the oxidation of CO_2. Therefore, the weightlessness of cokes decreased after gasification and the values would be larger with the increase of addition. As a result, the non-monotone transition of ICRI appeared in the **Figure 7**.

In view of the situation, SiO_2 likely reacted with FeO and produced a low melting compound (fayalite), which could be described by equation (5). The production of fayalite was also determined the low ICSR, resulting in the formation of crack. To the

special, the whole iron oxides were combined to fayalite when the blending ratios were 2.5 and 5 wt-%. However, paying attention to the blending ratios of 7.5, 10 and 15 wt-%, the FeO was surplus for the formation of fayalite so that iron element could be seen as iron oxides. Except that, the iron minerals existed as spinel in all of samples.

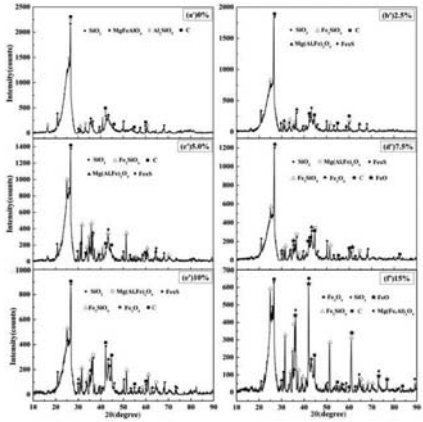

Figure 9 XRD patterns of coke bearing iron ore fines after gasification

Conclusions

In present study, the cold strength and thermal properties of iron coke were evaluated. The pore structure and the crystal structure were investigated by means of adsorption of gases and XRD analysis, respectively. Furthermore, the transformation of the mixed iron minerals was analyzed after the carbonization and gasification.

1 Along with the increase of iron ore fines, cold strength displayed a slight downtrend because of the prevention of dilatation of coal particles and the pore structure isn't inferred to be a major factor affected the properties of iron coke.

2 The majority of mixed iron oxides were reduced to metallic iron by CO and H_2 during carbonization and the degree of metallization achieved to approximately 75%. Nevertheless, produced metallic iron was oxidized by pure CO_2 during gasification. However, the reaction between produced ferrous oxide and ash of coke would lead to a serious degradation of iron coke.

3 ICRI was obviously enhanced by added iron ore fines and achieved to the maximum at the blending ratio of 7.5 wt-%. ICSR drastically decreases along with the increase of iron ore fines, which could be affected by excess gasification and serious degradation on account of reaction of minerals. Furthermore, the trend of ICRI and ICSR were also significantly influenced by the degree of graphitization which could be represented by the L_c. The lower values of L_c were, the higher the ICRI and the lower the ICSR.

Acknowledgements

This work was supported by the National Natural Science Foundation of China (Grant No. 51474042) and the Fundamental Research Funds for the Central Universities (Grant No. CDJZR13130034).

References

1. M. Naito et al., "Improvement of Blast Furnace Reaction Efficiency by the Temperature Control of Thermal Reserve Zone," *Shinnittetsu Giho*, 94 (2006), 103-108.

2. M. Naito et al., "Advanced Approach to Intelligent Ironmaking Processes. Improvement of Blast Furnace Reaction Efficiency by Use of High Reactivity Coke," *Tetsu to Hagane*, 87 (5) (2001), 357-364.

3. V. Lyalyuk, A. Tarakanov and D. Kassim, "Influence of the Reactivity of Coke on Blast-Furnace Performance," Coke and Chemistry, 54 (2) (2011), 47-52.

4. M. Grigore et al., "Influence of Mineral Matter on Coke Reactivity With Carbon Dioxide," *ISIJ International*, 46 (4) (2006), 503-512.

5. A. Babich, D. Senk and H. Gudenau, "Effect of Coke Reactivity and Nut Coke on Blast Furnace Operation," *Ironmaking & Steelmaking*, 36 (3) (2009), 222-229.

6. A.P. Dhupe, A. Gokarn and L. Doraiswamy, "Investigations into the Compensation Effect at Catalytic Gasification of Active Charcoal by Carbon Dioxide," *Fuel*, 70 (7) (1991), 839-844.

7. D. Cazorla-Amorós et al., "Carbon Gasification Catalyzed by Calcium: a High Vacuum Temperature Programmed Desorption Study," *Carbon*, 30 (7) (1992), 995-1000.

8. Y. Ohtsuka et al., "Chemical form of Iron Catalysts During the CO_2-Gasification of Carbon," *Fuel*, 65 (10) (1986), 1476-1478.

9. T. Hilding et al., "Degradation Behaviour of a High CSR Coke in an Experimental Blast Furnace: Effect of Carbon Structure and Alkali Reactions," *ISIJ International*, 45 (7) (2005), 1041-1050.

10. K. Higuchi et al., "Enhancement of Low-temperature Gasification and Reduction by Using Iron-coke in Laboratory Scale Tests," *ISIJ International*, 51 (8) (2011), 1308-1315.

11. T. Adschiri and T. Furusawa, "Relation Between CO_2-Reactivity of Coal Char and BET Surface Area," *Fuel*, 65 (7) (1986), 927-931.

12. S.F. Zhang et al., "High Temperature Pyrolysis Behaviour and Kinetics of Lump Coal in COREX Melter Gasifier," *Ironmaking & Steelmaking*, 41 (3) (2014), 219-228.

13. B.D. Cullity and S.R. Stock, *Elements of X-ray Diffraction.* Vol. 3. (Upper Saddle River, NJ: Prentice hall, 2001), 548-664.

14. S. Nomura et al., "Some Fundamental Aspects of Highly Reactive Iron Coke Production," *ISIJ International*, 47(6) (2007), 823-830.

15. A. Tomita, T. Takarada and Y. Tamai, "Gasification of Coal Impregnated with Catalyst During Pulverization: Effect of Catalyst Type and Reactant Gas on the Gasification of Shin-Yubari Coal," *Fuel*, 62 (1) (1983), 62-68.

16. S. Nomura et al., "Improvement in Blast Furnace Reaction Efficiency Through The Use of Highly Reactive Calcium Rich Coke," *ISIJ International*, 45 (3) (2005), 316-324.

17. M. Diez, R. Alvarez and C. Barriocanal, "Coal for Metallurgical Coke Production: Predictions Of Coke Quality and Future Requirements for Cokemaking," *International Journal of Coal Geology*, 50 (1) (2002), 389-412.

Characterization of Minerals, Metals, and Materials 2015
Edited by: John S. Carpenter, Chenguang Bai, Juan Pablo Escobedo, Jiann-Yang Hwang, Shadia Ikhmayies, Bowen Li, Jian Li, Sergio Neves Monteiro, Zhiwei Peng, and Mingming Zhang
TMS (The Minerals, Metals & Materials Society), 2015

EXPERIMENTAL INVESTIGATION ON HIGH TEMPERATURE ROASTING OF BASIC OXYGEN FURNACE SLAG

Ruirui Wei, Meilong Hu, Fangqing Yin, Yanhui Liu
College of Materials Science and Engineering, Chongqing University, China

Keywords: BOF slag, roasting, SFCA, sintering.

Abstract

In China, Basic Oxygen Furnace (BOF) slag is traditionally used as an aggregate for civil engineering, for road engineering and fertilizer. In order to make full use of BOF slag, the experiments of BOF slag with high temperature roasting has been carried out and the phase transformation is studied. The BOF slag from Chongqing Iron & Steel is roasted in the electric muffle furnace at three different temperature. The influences of the high temperature roasting on change the phase composition of BOF slag was characterized by XRD. The results revealed that SFCA was produced at the high temperature in air atmosphere and melting temperature of slag was lowered. Therefore, if the BOF slag which treated by roasting was utilized in the sintering process, it is advantageous to improve the sintering strength and the formation of the liquid phase and reduce fuel consumption in the sintering production process.

Introduction

Since the beginning of the industrial era, slags, which have been considered waste production, started appeared as a major by-product obtained during the extraction of metals from ores through metallurgical processes. According to the report of the World Steel Association, there are about 1580 million tons crude steel output around the world in 2013, and the crude steel output of China accounts for almost 49.2wt% of the global crude steel output. During the process of steel production in Basic Oxygen Furnace (BOF), for every ton of crude steel, about 100~150 kg of slag is generated in the form of waste[1]. Therefore, nearly 77.9~117 million tons BOF slag is being generated as a solid waste and this figure will increase in future years[2]. This is a huge figure so that researchers are looking for an efficient and environmental way to utilize BOF slag. At present, some of the slag is recycled to the blast furnace[3-5] while a significant portion is used in civil engineering application, such as cement and concrete[6-8], due to its superior skid and wear resistance[9]. However, the latter utilization of BOF slag has some restrictions in many regions owing to an undesirable expansion of the slag aggregate[10] leading to rapid deterioration of the roads. The volume expansion (up to 10%) is attributed to the short and long term hydration of the calcium and magnesium oxides content, especially free lime[10-14].

According to the composition of BOF slag, over half of it is made up of CaO and iron oxides, using this slag for land filling and road ballast does not justice to its potential value. Steel enterprises all the world face a same challenge in treating this under the prevailing environmental regulations. Therefore, researchers in different parts of world are looking for an efficient method to utilize BOF slag.

Normally, CaO occurs in BOF slag as $2CaO{\cdot}SiO_2$, $3CaO{\cdot}SiO_2$ and low melting point minerals [15-17]. Consequently, by the addition of certain percentage BOF slag is beneficial to form liquid phase, improve quality and strength of sinter ore and decease fuel consumption in

sintering process[18]. In addition, BOF slag can replace part of sintered flux to ensuring comprehensive utilization and recycling of resources.

In the present study, to form more SFCA in BOF slag, the experiments of BOF slag from Chongqing Iron & Steel with high temperature roasting has been carried out and the phase transformation is investigated as part of a large project on the recycling of BOF waste slag. Results obtained from the present study provide some fundamental information for the utilization of BOF slag in the sintering process.

Experimental

An industrial sample of BOF slag, come from Chongqing Iron & Steel is used for the experiments. The quantitative analysis and the chemical composition of the BOF slag, as measured by using X-ray fluorescence spectrometer (XRF-1800, SHIMADZU, Japan), were summarized in Table I[19]. The contents of TFe, Fe^{2+}, and Fe^{3+} in the BOF slag were also determined by chemical analysis. From Table 1,CaO、MgO and SiO_2 account for about two thirds of slag. And the phase identification of BOF slag was determined by X-ray diffraction as Fig.1. The main phase of slag were Ca_2SiO_4, $(Ca,Fe,Mg)_3SiO_5$, CaO, $Ca_2Fe_2O_5$ and Fe_3O_4.

Table I. Main composition of BOF slag, %

Composition	CaO	MgO	SiO_2	Al_2O_3	MnO	TFe	P	S
Content,wt%	40.21	8.19	14.69	2.40	2.54	18.44	0.75	0.13

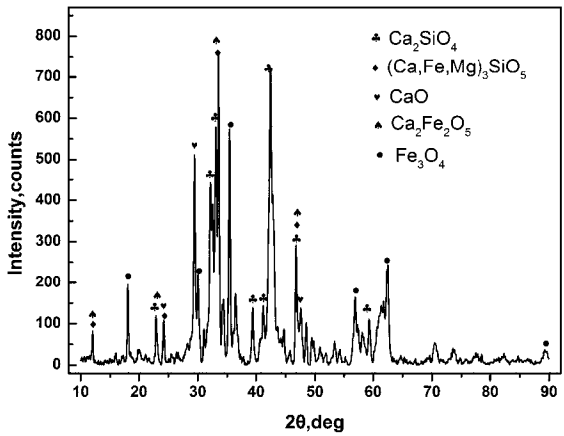

Fig.1. XRD pattern of the BOF slag.

The BOF slag was ground into 200 mesh with mill machine and place it into oven at 120°C for 2 hours. The thermal analysis (TA) measurements were carried out using a NETZSCH STA 449C TG-DSC instrument, at a heating rate of $10°C \cdot min^{-1}$, to heat to 1350°C in air atmosphere.

Subsequently, the BOF slag of 20g was placed in an alumina plate and roasted in an electric muffle furnace with automatic temperature control and the roasting process is prohibited in the temperature range of 800~1000°C, the process was as follows: 1) heating the slag to roasting temperature at 0.5h, 2) keeping the roasting temperature for 1h and stirring slag once, 3) Cooling with the furnace and taking it out when cooled to 150°C.

The adding weight during roasting experiments was calculated by measuring the change in weight of the samples before and after the roasting process, and phase identification of samples was determined by X-ray diffraction (D/MAX 3C, RIGAKU company, Japan).In the end, The hemisphere method was adopted to measure the melting temperature, including softening temperature, hemisphere temperature and flow temperature of slag unroasted and roasted at 1000 °C.

Results and discussion

Thermal analysis experiment

Some changes in weight, thermal activities were observed during TA experiments.Fig.2 represents a TG-DSC diagram obtained by heating BOF slag sample in air atmosphere.

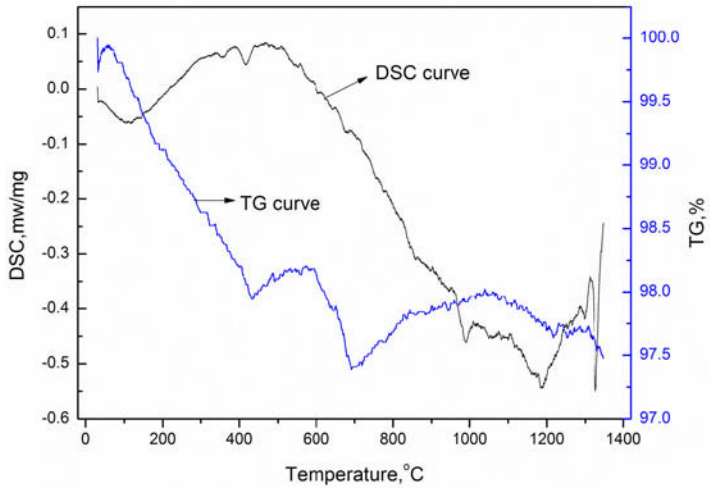

Fig.2. TG-DSC curve for BOF slag in air.

The TG curve in Fig. 2 shows two distinct stages of mass loss at 200~420°C and 580~690°C, accompanied by endothermic reaction on the DSC curve. A gradual mass gain between 690°C to 1060°C was also observed. The first stage is typical of dehydration of crystal water and the dehydroxylation of $Mg(OH)_2$.And the second stage is typical of the dehydroxylation of $Ca(OH)_2$ and the decomposition of $CaCO_3$, absorbing much heat, according to the following reactions:

$$Mg(OH)_2 - Mg + H_2O \quad (3.1)$$

$$Ca(OH)_2 - CaO + H_2O \quad (3.2)$$

$$CaCO_3 - CaO + CO_2 \quad (3.3)$$

The main gain between 690°C to 1060°C is due to the oxidation of iron and iron oxidation in the sample, which can be verified by the subsequent detection of X-ray diffraction. Two small endothermic peak can be observed in Fig.2 thanks to generation of new phase, such as $Ca_2(Fe,Al,Mg,Si)O_5$, $Ca_3(Al,Fe)(SiO_4)_3$, $(Ca,Fe)(Al,Fe)(SiO_4)_3$ and $Ca_5Si_2(Fe,Al)_{18}O_{36}$, which can be regarded as the different molecular formula of SFCA. In addition, from the tiny exothermic peak range from 840°C to 1310°C, it indicated that substitution reactions among cation in slag occurred, part of Fe^{3+} was replaced by Si^{4+},Mg^{2+} and Al^{3+} and crystal structure of compounds was changed[20].

Roasting experiments of BOF slag

The weight change of BOF slag roasting at 800~1000°C was showed in Fig.3. It was clear that weight gain rate decreased when roasting temperature was 800°C.This is because the thermal decomposition of calcium carbonate produces calcium oxide and carbon dioxide and dehydroxylation of calcium hydroxide and magnesium hydroxide. And then, weight gain rate increased due to the oxidization of iron and iron oxidation with a rise of temperature in air atmosphere. By and large, following the increase of roasting temperature, the mass gain rate increases, implying more iron and iron oxidation are oxidized, and maintain a growing tendency, but mass gain tends to unchanged after 1000°C. The reaction was shown as following equations 3.4~3.8:

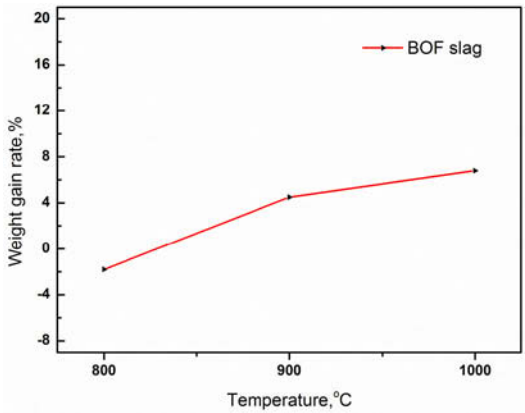

Fig.3. Weight change curve of roasting slag.

$$Mg(OH)_2 - Mg + H_2O \quad (3.4)$$

$$Ca(OH)_2 - CaO + H_2O \quad (3.5)$$

$$CaCO_3 - CaO + CO_2 \quad (3.6)$$

$$2Fe + 1/2O_2 - Fe_2O_3 \quad (3.7)$$

$$2Fe_3O_4 + 1/2O_2 - 3Fe_2O_3 \quad (3.8)$$

Fig.4 shows the XRD patterns of the three samples roasted in air under 800~1000°C. In this figure, it is obvious that the main phase of roasting slag range from 800°C to 1000°C are $Ca_2(Fe,Al,Mg,Si)O_5$, $Ca_3(Al,Fe)(SiO_4)_3$, $(Ca,Fe)(Al,Fe)(SiO_4)_3$, and $Ca_5Si_2(Fe,Al)_{18}O_{36}$, which is considered of different forms of SFCA. The substitution reactions were further verified by foregoing phase of roasting slag.The ion replacement mechanism of SFCA can be understood as the following reactions:

$$2(Fe^{3+}) - (Ca^{2+}, Fe^{3+}) + Si^{4+} \quad (3.9)$$

$$2(Fe^{3+}, Al^{3+}) - (Ca^{2+}, Fe^{2+}) + Si^{4+} \quad (3.10)$$

$$2(Fe^{3+}, Al^{3+}) - (Ca^{2+}, Fe^{2+}, Mg^{2+}) + Si^{4+} \quad (3.11)$$

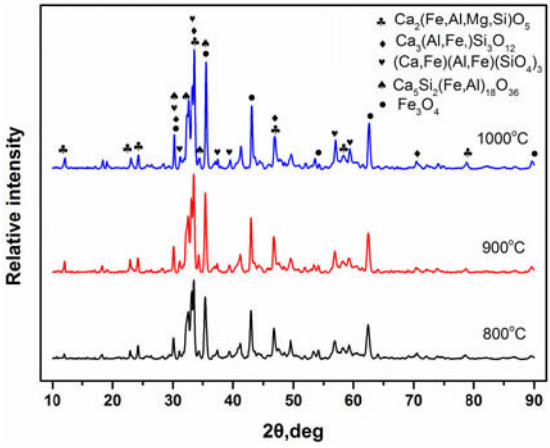

Fig.4. XRD patterns of the samples roasted in air.

The slag unroasted and roasted at 1000°C was used to measure the melting temperature with hemisphere method, and the result in Table II showed that lowering of melting point through roasting the slag in the air was preferably well. When roasting the slag 1h at 1000°C, the softening temperature of slag was decreased from 1350 °C to 1344 °C, hemisphere temperature from 1363°Cto 1358°C, and flow temperature from 1372 °C to 1356 °C. This should be attributed to the generation of SFCA after roasting. And it means that roasting the slag help

decrease the melting point of slag so that it can be reduce the consumption of power and energy and improve quality and strength of sinter ore if available in sintering process.

Table II. Melting temperature of BOF slag

BOF slag	Unroasted slag, °C	Roasted slag at 1000°C, °C
softening temperature	1350	1344
hemisphere temperature	1363	1358
flow temperature	1372	1356

Conclusions

The feasibility of BOF slag into a useful sintered flux by roasting at high temperature has been demonstrated.

(1) The BOF slag was roasted range from 800°C to 1000°C in air, mass gain increased with the increase of temperature due to more iron and iron oxidation were oxidized, and mass gain tended to unchanged after 1000°C. According to the XRD patterns of roasted slag, the phase of SFCA was observed. This means that roasting the BOF slag help the generation of SFCA.
(2) The experience of measuring the melting temperature of BOF slag unroasted and roasted at high temperature with hemisphere method has been carried out. The result shown that roasting the BOF slag at high temperature facilitated to lower the melting temperature.
(3) According to the present study, in the roasting slag at high temperature, the slag shows excellent phase composition and properties, observing the SFCA and lowering melting temperature of slag. The generation of SFCA is propitious to form more liquid phase easily, improve quality and strength of sinter ore in sintering process. And lowering the melting temperature of slag can decrease fuel consumption to save more energy during sintering process. Moreover, roasting slag can replace part of sintered flux to ensuring comprehensive utilization and recycling of resources.

Acknowledgements

This work was supported by "the Fundamental Research Funds for the Central Universities" (Grant No. CDJZR14135501) and "Specialized Research Fund for the Doctoral Program of Higher Education" (Grant No. 20130191110015).

References

1. Reddy, A.S., R.K. Pradhan, and S. Chandra, "Utilization of Basic Oxygen Furnace (BOF) slag in the production of a hydraulic cement binder," *International Journal of Mineral Processing,* 79 (2) (2006), 98-105.
2. Guangqiang Li, et al., "Recycle of Converter Slagby High Temperature Carbon Thernlal Reduetion," *Journal of Materials and Metallurgy,* (03) (2003), 167-172.
3. Das, B., et al., "An overview of utilization of slag and sludge from steel industries," *Resources, Conservation and Recycling,* 50 (1) (2007), 40-57.

4. Zhan Guo and Shangxing Guo. "Experimental Study on Hot Metal Dephosphorization by Converter Slag," *Proceedings of the 2011 Steelmaking Symposium of Five provinces in East China,* (2011). Anhui province,China.
5. Shangxing Guo and Zhan Guo, "Converter Slag Used for Dephosphorization of Hot Metal," *Journal of Iron and Steel Research,* (09) (2006), 13-16.
6. Motz, H. and J. Geiseler, "Products of steel slags an opportunity to save natural resources," *Waste Management,* 21 (3) (2001), 285-293.
7. Lundkvist, K., et al., "Analysis of Metallurgical Processes and Slag Utilisation in an Integrated Steel Plant Producing Advanced High Strength Steels," *4th International Conference on Process Development in Iron and Steelmaking,* 10 (2) (2012),415-424.
8. Yanling Yao and Jun Zhou, "Smelting slag, research and comprehensive utilization of ideas," *Manufacturing Automation,* (02) (2011), 111-113.
9. Xue, Y., et al., "Experimental investigation of basic oxygen furnace slag used as aggregate in asphalt mixture," *Journal of Hazardous Materials,* 138 (2) (2006), 261-268.
10. Liaosha Li, "Historical evolution and a vista of trend of converter slag recycling in future," *World Iron&Steel,* (04) (2011), 62-67.
11. Mikhail, S.A. and A.M. Turcotte, Thermal behaviour of basic oxygen furnace waste slag," *Thermochimica Acta*, 263 (1) (1995), 87-94.
12. Jianzhong Shen, "Review and Exploiture of Comprehensive Utilization and Treatment Process of Steel Slag," *China Metallurgy*, (05) (2008), 12-15.
13. Baicheng Liu, "Experimental Study of Preparation of Calcium Sulfate Whisker with BOF Slag," *Coal Ash*, (03) (2012), 30-31.
14. Weijun Tang, et al., "Distribution of free-calcium oxide in converter slags and its stablization," *Steelmaking*, (03) (2009), 34-36.
15. Yongquan Ling, "Development of disposal and application of iron and steel slag," *Iron and Steel,* (05) (1994), 71-74.
16. Hongjiang Xu, Guiqin Fu, and Miaoyong Zhong, "Experimental Study on Distensibility of BOF Slag," *China Metallurgy*, (06) (2006), 32-33.
17. Lijie Wu, "Selective Recovery of Valuable Metals From Rotary Furnace Slag," *Mining R&D*, (04) (2001), 29-31.
18. Zhulin Liu, "Experimental research on sintering of iron-containing converter waste," *Research on Iron&Steel*, (01) (2008), 50-54.
19. Dianying Zhang, Chao Li, and Jing Qian, "Determination of Eight Components in Slags by X-Ray Fluorescence Spectrometry," *Metallurgical Analysis*, (06) (2009), 41-46.
20. Jiaqing Yin, "Formation of Calcium Ferrites in Solid State and the Al2O3 Dissolution Kinetics into Its Melts, (2013), Chongqing University.

Characterization of Minerals, Metals, and Materials 2015
Edited by: John S. Carpenter, Chenguang Bai, Juan Pablo Escobedo, Jiann-Yang Hwang, Shadia Ikhmayies, Bowen Li, Jian Li, Sergio Neves Monteiro, Zhiwei Peng, and Mingming Zhang
TMS (The Minerals, Metals & Materials Society), 2015

EXPERIMENTAL STUDY ON SEMI-DRY FLUE GAS DESULFURIZATION ASH USED IN STEEL SLAG COMPOSITE MATERIAL

Lijun Lu, Honghui Fang
Research and Development Center of Wuhan Iron and Steel (group) Corporation, Metallurgical Road NO.28, Wuhan, 430080, China

Keywords: semi-dry desulfurization ash, steel slag composite material, setting time, strength of mortar.

Abstract

This article carried out the experimental study on using desulfurization ash in steel slag composite material. This was done by investigating the desulfurization ash content in formula one and formula two samples on the influence of setting time and strength of mortar. Through this study the following conclusions were reached for formula one: (1) a setting time of more than 10 hours is required, (2) a dosage of desulfurization ash of 1 ~ 2% is optimal, where flexural strength is reduced by 10% ~ 23% and compressive strength reduced by 5.7% ~ 16.4%. The conclusions of formula two were: (1) when the dosage of desulfurization ash is within 5%, the setting time is within 10 hours; (2) when the dosage of desulfurization ash is 1 ~ 2%, the flexural strength is increased by 5 ~ 7% and the compressive strength is reduced by 1 ~ 2%. The results show that the formula two is better.

Introduction

The sintering production in the traditional process generates a large volume of SO_2 gas, which causes significant long-term pollution. This has lead to an increase in environmental production requirements which has increased interest in sintering flue gas desulfurization in the iron and steel industry. Semi-dry desulfurization technology with the advantages of less investment, less land occupation, no corrosion and no wastewater etc are welcomed by the user[1]. However, with the promotion of semi- dry flue gas desulfurization project, the amount of the by-product of desulfurization ash generated increasingly large. In Wuhan Iron and steel for example, NO.3 sintering plant using NID semi dry technology, the annual production of desulfurization ash were 20,000~30,000 tons. NO.1 and 2 sintering machine still use semi-dry method, when all the project put into operation, the annual desulfurization ash content will be 100000 tons only produced by WISCO[2]. The understanding about desulfurization ash are still insufficient, therefore its resource utilization way is limited. A large number of stacked desulfurization ash can not handle, not only takes up the land but also caused serious pollution to the surrounding ecological environment. Steel slag composite material is composed of steel slag and compound slag powder, steel slag

**Corresponding author.* 54310572@qq.com, Tel: +86–18062693735.

refers BOF slag by the selection of iron, distributed through 4.75mm square hole sieve natural gradation tailings; composite slag powder comprises two water gypsum, slag, the right amount of Portland cement clinker, regulator, etc[3]. Desulfurization ash used on steel slag composite material, researching its influence on composite material properties, creating a new way for resource utilization of desulfurization ash.

Experimental Materials and Methods

Experimental Materials

The experiment uses cement as Huaxin card 42.5 ordinary portland cement, gypsum plaster of Hubei Yingcheng, desulfurization ash as a by-product of Wuhan Steel semi-dry desulfurization process, ore powder as Huaxin brand superfine powder, slag as BOF slag selected iron rear tail slag, the experiment sand as the standard sand of Xiamen ISO standard sand factory, the material chemical composition shows in table 1.

Table 1 Analysis of chemical composition of raw materials %

	SiO_2	Al_2O_3	CaO	MgO	S	Fe_2O_3	MnO	burning loss
Gypsum	1.08	0.72	41.21	1.85	17	0.054	/	5.29
PI cement	21.02	5.16	63.96	1.61	0.98	2.80	/	/
Ore powder	34.16	15.13	40.43	8.09	/	0.28	0.26	/
Slag[4]	10.54	1.99	39.79	9.77	0.068	10.59	1.42	3.86
Desulfurization ash	3.41	0.41	48.89	0.86	9.82	1.97	0.038	/

The experimental method

Cement, ore powder, gypsum and slag according to a certain ratio mixed of steel slag composite cementitious material, the desulfurization ash incorporated by volume 0%, 1%, 2% and 5% of steel slag composite material powder. Through the development of steel slag composite material performance experiment, investigating impacts of the desulfurization ash content change on index time and Mechanical intensity of steel slag composite material. The test results are analyzed and discussed, through optimizing formulation, so as to find reasonable method for desulfurization ash used of steel slag composite material.

Test method

Mortar strength testing method according to GB/T17671-1999 standards, setting time testing method according to GB/T1346-2001. Test equipment: YAW-300C electro-hydraulic cement compressive and flexural testing machine, cement setting time analyzer, mortar mixers, paste mixers, mortar shaker, cement constant temperature and humidity curing box, etc.

Experiments and Result Analysis

The effect of desulfurization ash dosage to the sample performance of slag composite material (formula one)

Formula one the proportion of powder and aggregate in Steel slag composite material is 1:3, the ratio of slag and sand in aggregate is 1:1, desulfurization ash instead of ore powder quantity is 0%, 1%, 2% and 5%, the material amount according to table 2. According to the corresponding national standard, preparation of mortar and testing setting time, mechanical strength index. The ratio of raw materials and the test results are shown in Table 2.

Table 2 The effect results of desulfurization ash dosage to the sample performance of slag composite material (formula one)

Name	Desulfurization ash%	Cement%	Powder%	Gypsum %	3days strength /MPa		28days strength /MPa		setting time/min	
					Flexural	Compressive	flexural	Compressive	Initial set	Final set
1#	0	24	70	6	9.03	37.48	14.46	55.28	294	770
2#	1	24	69	6	8.01	33.99	13.06	52.14	310	987
3#	2	24	68	6	6.98	31.82	12.27	51.90	312	1017
4#	5	24	65	6	5.48	25.35	10.85	49.42	315	1034

Influence of setting time

According to the results in Table 2, Respectively discuss the impact of desulfurization ash content to the sample setting time and mortar strength and other indicators.

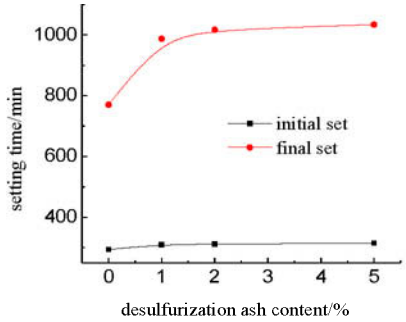

Figure 1 the influence of desulfurization ash content on steel slag composite material (formula one) setting time

It can be seen from Figure 1, with the dosage of desulfurization ash increased, in formula one, initial setting and final setting time of the sample have different levels of

growth, initial setting time were 290~320mins, the final setting time were 770~1040mins, desulphurization ash have a greater impact on the final setting time, but the change content has little effect on the setting time. Contains calcium sulfate and calcium sulfite in desulfurization ash, the function such as gypsum cases like, can be used as retarder, prolong the setting time of cement. Therefore, the incorporation of desulfurization ash makes the setting time of an sample extended to occur. In addition, in formula one, final setting time of each sample were more than 10hs, even desulfurization ash content of the sample is zero, the final setting time reaches to 770mins, description the formulation of gypsum dosage used excessive or a relatively small amount of cement, because gypsum is used to adjust the setting time of cement. So the next step requires the formulation of a proportion of each material to be adjusted to control the setting time within the standard range.

Influence of strength

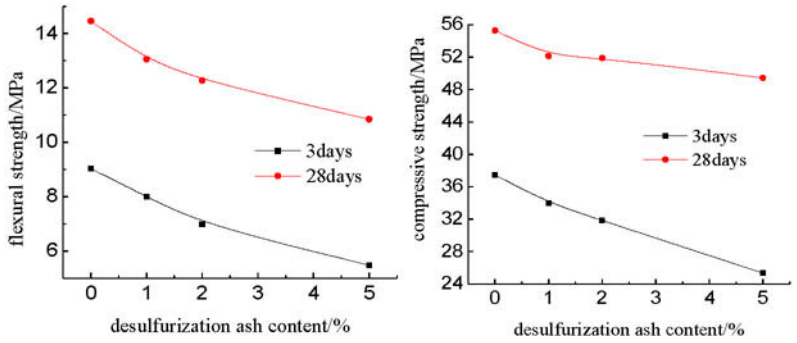

Fig.2 Effect of desulfurization ash content on flexural compressive strength of slag composite materials (formula one)

As can be seen from Figure 2, with the improvement of desulfurization ash content, formula one each sample 3 days, 28 days flexural and compressive strength were apparent decline. Retarding mechanism of Gypsum for Cement [5] are considered, C_3A contained in cement quickly dissolved in water, the rapid generation of calcium aluminate hydrate, so that the cement quickly condense, after adding gypsum, gypsum and C_3A and Ca $(OH)_2$ reacting and produced insoluble hydrated calcium aluminum sulfur in water that is ettringite, wrapped in C_3A particle surface layer is formed, preventing further C_3A hydration, so it play a decisive role in setting time will not C_3A, while slower reaction C_3S, its concentration increases, thereby delaying the setting time of cement. After desulfurization ash incorporation, in which calcium sulfate and calcium sulfite and cement C_3A same reaction, and with the content of desulfurization ash increasing, the scope of this reaction is further increased, so that the retarding time gradually extended, while the incorporation of desulfurization ash affects hydration reaction of C_3A in cement, and the greater desulfurization ash content, the less C_3A hydration reaction to lower cement strength.

The effect of desulfurization ash dosage to the sample performance of slag composite material (formula two)

As a result of desulfurization ash have a great influence on each performance index of mortar sample in formula one, adjusting distribution ratio of each group of formula one, forming formula two, it improves the cement content, while the same amount of gypsum, investigated the impact of desulfurization ash content on the performance of mortar sample in formula two. The ratio of raw materials and the test results are shown in Table 2.

Table 3 The effect results of desulfurization ash dosage to the mortar sample performance of slag composite material (formula two)

Order	Desulfurization ash%	Cement%	Powder%	Gypsum %	3days strength /MPa		28days strength /MPa		setting time/min	
					Flexural	Compressive	Flexural	Compressive	initial set	final set
5#	0	44	50	6	7.84	32.99	10.58	62.20	179	574
6#	1	44	49	6	7.90	33.10	11.40	60.99	183	580
7#	2	44	48	6	7.23	32.19	11.23	61.51	188	581
8#	5	44	45	6	6.88	29.17	10.90	60.92	179	574

Influence of setting time

For the results of Table 3, respectively discuss by mapping desulfurization ash content impact on setting time and mortar strength and other indicators.

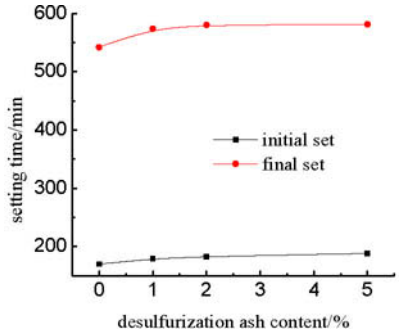

Figure 3 influence of desulfurization ash content on setting time

As can be seen from Figure 3, with the improvement of desulfurization ash content, the initial and final setting time appropriate to extend in formula two, the initial setting time were 170 ~ 190mins, final setting time were 570 ~ 590mins, this formula each sample were within the standard setting time range, the increase effect of desulfurization ash content on setting time is not obvious. Desulfurization ash content less, desulfurization ash contains calcium sulfate and calcium sulfite smaller, limited retarding effect on cement C_3A, so at a certain content desulfurization ash will not have to produce greater impact on setting time of cement.

Influence of strength

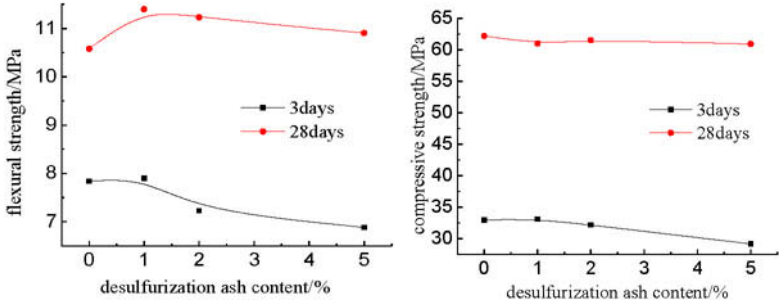

Fig.4 Effect of desulfurization ash content on flexural compressive strength of slag composite materials (formula two)

As can be seen from Figure 4, with the improvement of desulfurization ash content, the formula two each sample 3 days, 28 days flexural strength after the first increase and then decreased, while a slight decline in 3 days, 28 days compressive strength appears. Desulfurization ash have very fine particles, acts as a filler in cement hydration process, making cement hydration products more dense, so that the flexural strength of the sample is increased. However, desulfurization ash have a similar role as gypsum, can only play a part retarding effect, itself is not gelling, not like the cement hydration occurs the same, so after desulfurization ash incorporation, compressive strength decreased, and the greater the dosage, strength reduced more. The formulations suitable desulfurization ash content is 1 to 2%, the flexural strength of the sample increased by 5 to 7%, the compressive strength reduced by 1 to 2%.

Conclusion

In formula one, setting time of each sample were more than 10 hours, and the dosage of desulfurization ash is 1 to 2%, flexural strength decreased 10% to 22.7%, the compressive strength decreased 5.7% ~ 16.4%. In the optimized formula two, desulfurization ash content was less than 5%, the sample setting time were within 10 hours, the sample flexural strength increased by 5 to 7%, the compressive strength reduced by 1 ~ 2%.

References

1. Ying Tian, "Discussions on Desulphurization Process of Sintering Flue Gas", *Science & Technology of Baotou Steel(Group)Corporation*, 39 (3)(2013).
2. Lijun Lu,Jingfang Tang,Lei Zhang,etc, "Application of NID Technology in Desulphurization of Sintering Fume by WISCO", *Angang Technology*, 373(1)(2012), 47-49.
3. "GB/T 28294-2012Steel slag composite material[S]",*Chinese Standard Publishing House*,2012.
4. Honghui Fang,Shujing Zhu, "Experimental study on steel slag mud preparation of binding material", *Henan Building Materials*, (5)(2009), 54-56.
5. Suping Cui,Yanlin Zhang, "Influence of different gypsum on performance of Portland-sulphoalminate composite cement system", *Cement Engineering*, 2005,(1)38-40.

Characterization of Minerals, Metals, and Materials 2015
Edited by: John S. Carpenter, Chenguang Bai, Juan Pablo Escobedo, Jiann-Yang Hwang, Shadia Ikhmayies, Bowen Li, Jian Li, Sergio Neves Monteiro, Zhiwei Peng, and Mingming Zhang
TMS (The Minerals, Metals & Materials Society), 2015

EFFECT OF MANGANESE ON THE FORMATION MECHANISMS OF SILICO-FERRITE OF CALCIUM AND ALUMINUM (SFCA)

Leige Xia[1], Xinyu Li[1], Jianliang Zhang[1], Chaoquan Yao[1], Jian Guo[1], Chao Zhang[1]

[1]School of Metallurgical and Ecological Engineering, University of Science and Technology Beijing, 30 Xueyuan Rd; Haidian District, Beijing, 100083, China

Keywords: Effect mechanism, Manganese, SFCA, Sinter.

Abstract

In this research, analytical reagents were used for the sintering experiments. And the sinters were using X-ray diffraction, scanning electron microscope and mineralogical microscope analysis to study the effect mechanism of manganese on the silico-ferrite of calcium and aluminum (SFCA) bonding phase formation during the sintering process. The results indicated that the increasing content of manganese would greatly reduce the content of SFCA, and promote the formation of calcium aluminum silicate and the amount of pores and cracks. The existence of manganese inhibited the silicon form into the SFCA and a great deal of Fe_2O_3 was participated in the crystal transition to Fe_3O_4. When the ratio of the added manganese was less than 3% in the mixing, the calcium ferrite was in substantially interleaving corrosion with hematite and magnetite. Both the porosity and silicate glass phase content were low simultaneously, which contributed to the sintering production.

Introduction

Iron ore sinter constitutes a major proportion of blast furnace burden in Chinese iron and steel corporations. Hence, the quality of the sinters plays an important role in the blast furnace production. The main mineral composition of the sinters is iron oxides, ferrites (mostly SFCA), silicates and vitric phases, etc. and the mineralogy of the sinter significantly depends on its chemistry and process factors. The SFCA is believed to be the best bonding phase due to its relatively high reducibility and sufficient mechanical strength. The amount and the pattern of the SFCA directly influence the sinters quality, so the proper amount and appropriate pattern of the SFCA in the iron ore sinter have a significant impact on the increasing of the blast furnace productivity and efficiency [1].

The manganese is an important resource used in the metallurgy industry, and it is mainly used as the deoxidization and desulfurization in the iron-making and steel-making process and producing the manganese alloy as well. In the former researches, the manganese ores was focused on the production of manganese alloy, and there is little study about the existence of manganese in the iron ores on the mineral composition of the iron ore sinters [2-3]. Therefore, sintering experimental research is carried out whose analytical reagents are used by different ratio in the laboratory to analyze the existence of manganese on the effect of SFCA and other sinter mineral composition, getting the influence mechanism of different content of manganese on the morphology, quantity, structure of SFCA, magnetite and so on. And then the most appropriate ratio of iron ore containing manganese will be found. Thus the sintering burden cost will be greatly reduced and the economic benefits of iron and steel plant will be improved.

Experimental

Materials

The raw materials used in the experiment were all analytical reagents which contained Fe_2O_3, CaO, SiO_2, Al_2O_3, MgO and MnO_2. The purity of them was all 99.9999%. There was manganese -free sample during the ingredient processing. The binary basicity and the weight of the reference sample were 4.0(R_2=CaO/SiO_2) and 15g respectively. There were also six samples which contained MnO_2 in the ingredient processing, and the mass fraction of the nickel samples was 1%, 2%, 3%, 5%, 8% and 10%. The binary basicity of the six samples were all 4.0(R_2=CaO/SiO_2) and the weight were all 15g. The starting chemical compositions of the powder mixture were listed in Table I.

Table I Starting chemical compositions of the sinter samples (mass %)

Sample number	Fe_2O_3	CaO	SiO_2	Al_2O_3	MgO	MnO_2
1#	66	24	6	2	2	0
2#	65	24	6	2	2	1
3#	64	24	6	2	2	2
4#	63	24	6	2	2	3
5#	61	24	6	2	2	5
6#	58	24	6	2	2	8
7#	56	24	6	2	2	10

Methods and facilities

The six kinds of analytical reagents which were used in the ingredient processing were weighed by an analytical balance according to the mass fraction shown in Table I. Then the reagents were mixed and ground for half an hour in the carnelian mortar to make the reagents mix well. The mixed sample was poured into the mold and agglomerated in a diameter of 15mm and 20mm high by a hydraulic jack. The pressure of the hydraulic jack was about 30MPa and the weight of each sample was 15g.

The samples were placed in seven corundum crucibles (volume 15ml) and each crucible was marked. There was a piece of silicate aluminum refractory between the sample and the crucible which kept the sample from reacting with the crucible during the high temperature process. Then the seven corundum crucibles were placed in the muffle furnace and heated to 1280°C with a heating rate of 20°C /min, and the air was charged into the furnace and the oxygen partial pressure was kept at 5×10^2 Pa in the furnace. The samples were sintered at 1280°C for 10h. Then the sintered samples were quenched to room temperature with the N_2 atmosphere protection and subsequently ground into fine powders (<0.074mm). The procedure would be repeated two times for homogenization, and half of the each sample was ground into fine powders at the third time [4-6]. Then the fine powders would be analyzed by X-ray diffraction analysis (XRD) to make a qualitative mineral composition analysis. The facility of X-ray diffraction was TTRIII multifunctional X-ray diffraction which used CuKα, scanning angle 10~80°, wavelength 0.15406nm. The light sheet was made from the small remaining part of the sample, and it was analyzed by the reflective microscope. When the iron minerals region were detected, the light sheet was greased on the surface to get a better sintering mineral structure. The remaining part of the sample was made into polished section for scanning electron microscopy and spectroscopy detection. The FEI QUANTA250 environment scanning microscopy was used in this detecting.

Results and discussion

XRD analysis

Figure 1 shows the XRD result of the seven sintered samples. It can be seen that the existence of manganese has a little effect on the diffraction. The three sintered samples including 4#, 5# and 6# have some new characteristic peaks different from the others.

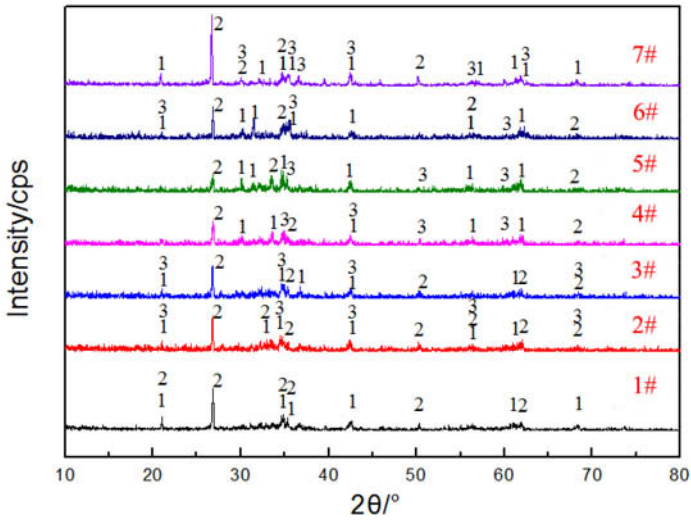

Figure 1. X-ray diffraction patterns of 7 sinter samples
1-SFCAM，2-Silicates，3-Manganese oxides(MnO_2 and Mn_3O_4).

As shown in Figure 1, the characteristic peaks of silicates is more obvious than that of the silico-ferrite of calcium aluminum and magnesium (SFCAM) in 1# sintered sample. The SFCAM characteristic peaks are easily to be recognized with the increasing of manganese while the intensity of the characteristic peaks are all weak. The position and intensity of manganese oxide characteristic peaks are fixed and constant in seven sintered samples.

Mineralogy analysis

Depending on the different gray colors which the different sintering mineral structures shown under the reflective microscope, their composition and structural characteristics would be distinguished.

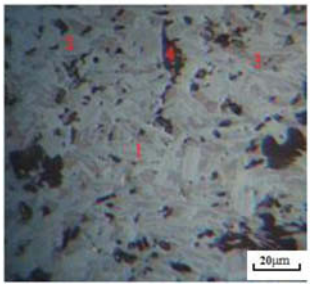

Figure 2. Phase morphology of 3# sample
1-SFCAM, 2-Hematite, 3-Magnetite, 4-Silicates and glassy.

As is shown in Figure 2, a great deal of corroded iron-rich SFCAM is distributed, and the offwhite and gray are the hematite concentration and the magnetite region respectively. The calcium aluminum silicates and glassy phase was irregular and distributed in the SFCAM.

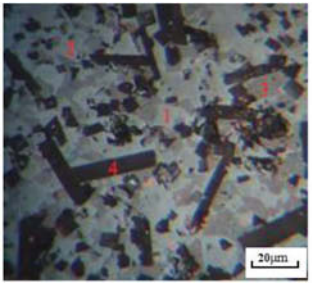

Figure 3. Phase morphology of 5# sample
1-SFCAM, 2-Hematite, 3-Magnetite, 4-Silicates and glassy.

As shown in Figure 3, the small block hematite and magnetite were distributed together and the amount of magnetite increased obviously. There is little SFCAM material and the lath calcium aluminum silicates with the small block shape was distributed together. There existed some glassy phase as well.

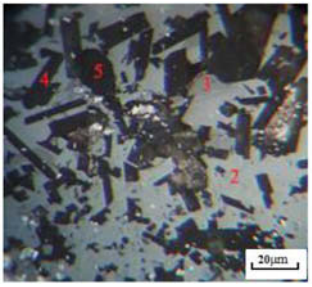

Figure 4. Phase morphology of 6# sample
1-SFCAM, 2-Hematite, 3-Magnetite, 4-Silicates and glassy, 5-Pore

It can be seen from the Figure 4 that most of the unreacted hematite accumulated and distributed together, and amount of lath calcium aluminum silicates increased as well as the pores.

Morphology analysis

The sintered samples were analyzed in terms of composition, structure, crystal shape and porosity by the scanning electron microscope.

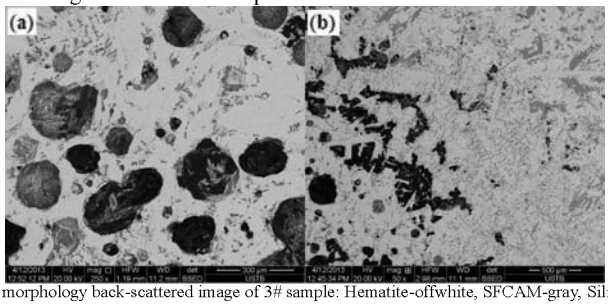

Figure 5. Surface morphology back-scattered image of 3# sample: Hematite-offwhite, SFCAM-gray, Silicates, Holes-black

As shown in Figure 5(a), the main morphology was the block hematite and the pitting like SFCAM was distributed together in some part of the image. The silicates distributed around the irregular pores. It can be seen from the Figure 5(b) that the needle fibrous calcium ferrites densely distributed and the irregular silicates was distributed together with the skeletal shape.

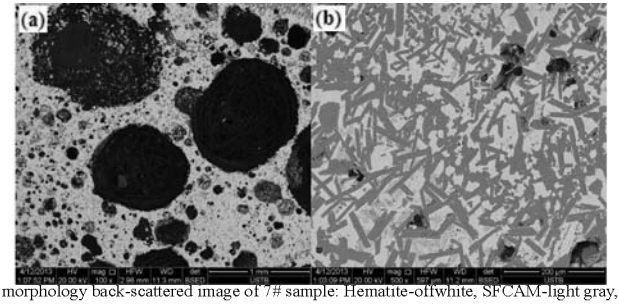

Figure 6. Surface morphology back-scattered image of 7# sample: Hematite-offwhite, SFCAM-light gray, Silicates-dark gray, Poles-black

As shown in Figure 6(a), the corroded SFCAM was densely distributed in some parts and the amount of that reduced greatly. There existed much larger pores and the ratio of the pores increased sharply. A great deal of lath silicates distributed in the Figure 6(b) with some portion of SFCAM and some irregular pores in it [7-9].

Table 2 shows the EDS analysis results of the SFCAM region composition of seven sinter samples. The chemical expression of SFCAM calculated by atom number is shown in Table 3.

Table II SFCAM region composition of seven sinter samples (At %)

Element	1#	2#	3#	4#	5#	6#	7#
Fe	35.56	36.79	35.31	37.01	34.06	32.89	35.53
Ca	8.80	8.41	9.51	7.55	7.87	7.92	8.84
Si	1.69	1.55	1.87	1.18	1.18	1.01	-
Al	6.87	6.34	7.37	6.86	6.62	6.42	2.21
Mg	2.97	2.41	2.14	3.88	2.48	2.10	2.84

Table III SFCAM or SFCA chemical expression of seven sinter samples

Sample number	Chemical expression of SFCAM or SFCA
1#	$5.2Fe_2O_3 \cdot 2.6CaO \cdot 0.5SiO_2 \cdot Al_2O_3 \cdot 0.9MgO$
2#	$5.8Fe_2O_3 \cdot 2.7CaO \cdot 0.5SiO_2 \cdot Al_2O_3 \cdot 0.8MgO$
3#	$4.8Fe_2O_3 \cdot 2.6CaO \cdot 0.5SiO_2 \cdot Al_2O_3 \cdot 0.6MgO$
4#	$5.4Fe_2O_3 \cdot 2.2CaO \cdot 0.3SiO_2 \cdot Al_2O_3 \cdot 1.1MgO$
5#	$5.2Fe_2O_3 \cdot 2.4CaO \cdot 0.4SiO_2 \cdot Al_2O_3 \cdot 0.8MgO$
6#	$5.1Fe_2O_3 \cdot 2.5CaO \cdot 0.3SiO_2 \cdot Al_2O_3 \cdot 0.7MgO$
7#	$16.1Fe_2O_3 \cdot 8CaO \cdot Al_2O_3 \cdot 2.6MgO$

Effect mechanism of manganese on the sintered samples

The effect mechanism of manganese on the sintered samples is analyzed according to the results of XRD, microscope and SEM.

(1) The Fe_3O_4 generation of the reference sample which is sintered without manganese has been detected by the XRD analysis. It shows that Fe_2O_3 transforms to Fe_3O_4 at the reaction temperature of 1280°C. There is a large amount of Fe_3O_4 formation due to the increasing of manganese and most of the manganese distributed in the SFCAM, which indicates that the manganese reduce the transformation temperature and increase the amount of the transformation.

(2) With the increasing manganese participates in the solid solution of SFCAM, the content of silicon and magnesium in the SFCAM decreases sharply, which makes the chemical expression of SFCAM mostly exists as the FCAM and FCA.

(3) The manganese inhibited the solid solution of silicon, and most of the silicon participates in the formation of the calcium aluminum silicates materials. With the increasing of manganese, both calcium aluminum silicates and vitric phase increase and distribute together. The calcium aluminum silicates exist as the columnar shape and the vitric phase exists with the penetrating cracks, which influences the cold strength of the sinters heavily.

Conclusions

(1) The amount of calcium ferrite decreased sharply with the increase of manganese; in contrast, the amount of calcium aluminum silicate and the pores as well as cracks increased which deteriorated the cold strength of the sinters.

(2) The manganese inhibited the solid solution of silicon, while promoted the transformation of Fe_2O_3 to Fe_3O_4. The existence of SFCA or SFCAM was the same in different sintered samples with the chemical expression of FCAM.

(3) When the ratio of the added manganese was less than 3% in the mixture, the calcium ferrite was in substantially interleaving corrosion with hematite and magnetite. Both the porosity and silicate glass phase content were low simultaneously, which contributed to the sintering production.

References

[1]J.W. JEON, S.M. JUNG and Y.SASAKI, "Formation of Calcium Ferrites under Controlled Oxygen Potentials at 1273K," *ISIJ International*, 50(8) (2010), 1064-1070.
[2]M.Z. Xu, "Situation and Trend of the Trade of Chinese Manganese Ore Supply and Demand," *International Economy Corporation*, 4(2011), 78-81.
[3]Z.C. Huang, B. Chai, P. Zhao and T. Jiang, "Reduction of high iron content manganese ore and its mechanism," *Journal of Central South University (Science and Technology)*, 45(1) (2014), 9-15.
[4]D. O., S. L. Wu, Y. M. Dai, J. Xu and H. Chen, "Sintering Properties and Optimal Blending Schemes of Iron Ores", *Journal Iron and Steel Research International*, 19(6) (2012), 1-5.
[5]S. L. Wu, J. X. Du, H. B. Ma, J. Q. Tian and H. F. Xu, "Fluidity of liquid phase in iron ores during sintering," *Journal of University of Science and Technology Beijing*, 27(3) (2005), 291-293.
[6]S. L. Wu, Y. D. Pei, H. Chen, P. Peng and F. Yang, "Evaluation on liquid phase fluidity of iron ore in sintering," *Journal of University of Science and Technology Beijing*, 30(10) (2008), 1095-1099.
[7]K. Sugiyama, A. Monkawa and T. Sugiyama, *ISIJ International*, 45(4) (2005), 560-568.
[8]L. S. Li, J. B. Liu, X. R. Wu, X. Ren, W. B. Bing and L. S. Wu, *ISIJ International*, 50(2) (2010), 327-329.
[9]N. A. S. Webster, M. I. Pownceby, I. C. Madsen and J. A. Kimpton, "Silico-ferrite of Calcium and Aluminum (SFCA) Iron Ore Sinter Bonding Phases: New Insights into Their Formation during Heating and Cooling," *Metallurgical and Materials Transactions B*, 43(2012), 1344-1357.

Characterization of Minerals, Metals, and Materials 2015
Edited by: John S. Carpenter, Chenguang Bai, Juan Pablo Escobedo, Jiann-Yang Hwang, Shadia Ikhmayies, Bowen Li, Jian Li, Sergio Neves Monteiro, Zhiwei Peng, and Mingming Zhang
TMS (The Minerals, Metals & Materials Society), 2015

IZOD IMPACT TEST IN EPOXI MATRIX COMPOSITES REINFORCED WITH HEMP FIBER

Lázaro A. Rohen[1], Frederico M. Margem[1], Anna C. C. Neves[1], Sérgio N. Monteiro[2], Maycon A. Gomes [1-4], Rafael G. de Castro[3], Carlos Maurício. F.V[1], Fernanda de Paula[5].

[1] State University of the Northern Rio de Janeiro, UENF, Advanced Materials Laboratory, LAMAV; Av. Alberto Lamego, 2000, 28013-602, Campos dos Goytacazes, Brazil;

[2] Instituto Militar de Engenharia , IME, Praça Gen. Tibúrcio, nº80 Urca, Rio de Janeiro - RJ, 22290-270

[3]ISECENSA – CENSA Instituto Superior de Instrução.

[4] Instituto Federal Fluminense, Rua Dr Siqueira, 273 - Pq Dom Bosco - Campos dos Goytacazes, RJ - CEP - 28030-130

[5] Faculdade Redentor Rodovia BR 356. n° 25 Itaperuna RJ - 28.300-000.

Keywords: Izod impact test, hemp fiber, composites

Abstract

Synthetic fiber has been gradually replaced by natural fiber, such as lignocellulosic fiber. In comparison with synthetic fiber, natural fiber has shown economic and environmental advantages. The natural fiber presents interfacial characteristics with polymeric matrices that favor a high impact energy absorption by the composite structure. However, until now little has been evaluated about the hemp fiber incorporated in polymeric matrices. This study has the purpose of evaluate the impact resistance of this kind of epoxy matrix composite reinforced with different percentages of hemp fibers. The impact resistance has substantially increased the relative amount of hemp fiber incorporated as reinforcement in the composite. This performance was associated with the difficulty of rupture imposed by the fibers resulting from the interaction of hemp fiber / epoxy matrix that helps absorb the impact energy.

Introduction

Natural fibers are steadily substituting synthetic fibers, particularly the common glass fiber, as the reinforced phase of polymeric composites in many engineering applications such as automobile interior components, cyclist helmets, housing panels and windmill fins[(1-4)]. The lignocellulosic fibers obtained from vegetables offer societal, economical, environmental and technical benefits[(5,6)] in comparison to the glass fiber as composite reinforcement. In particular, the impact resistance of a naturally flexible lignocellulosic fiber is a technical advantage over the brittle glass fiber in a situation of a crash event. This is the case of automobile parts such as the head-rest and the interior front panel that should not have a brittle rupture during an accident. In fact, the parts should be soft and able to absorb the impact energy without splitting in sharp pieces, to avoid injuring the passengers [(6)].
Lignocellulosic fibers such as coir, flax, jute, ramie, curaua and sisal are currently being used in automobile composite parts that require both strength and toughness [(4)]. The hemp fiber,

although strong and flexible [7] has not yet been applied in composites for automobile components. Actually, the fibers obtained from the petiole of the hemp palm tree commonly used to fabricate ropes and baskets owing to its high strength. This has motivated the study of the mechanical characteristic of the fibers.
In spite of existing works on the properties of hemp fiber composites[8-9], the impact resistance of continuous and aligned fiber reinforcing polymeric composites has yet to be evaluated. Therefore, the objective of the present work was to access the toughness through the energy absorbed by notched Izod impact specimens of epoxy composites reinforced with different amounts of continuous hemp fibers.

Materials and Methods

The material used in this work was untreated hemp fiber extracted from the stem hemp plant and epoxy resin. Statistical analysis were performed on one hundred fibers randomly removed from the as-received the lot. Figure 1 shows the histogram for the distribution of hemp fiber diameters by considering 6 diameter intervals. From this distribution, presented elsewhere an average diameter of 0.065mm was found for the as-received lot.

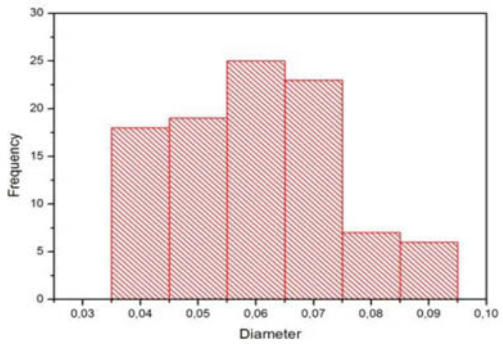

Figure 1. Distribution histogram for six diameter intervals.

Several other hemp fibers were cleaned in water and dried at 60°C in a stove to be used as composite reinforcement. Continuous and aligned fibers were laid down, in separate amounts of 10, 20, and 30 % vol, mixed with still fluid unsaturated epoxy resin, in a mold made of steel with 152 x 125 mm and 10 mm of thickness. Epoxy resin type commercial diglycidyl ether of bisphenol A (DGEBA) cured with triethylene tetramine (TETA) in stoichiometric proportion of 13 parts of hardener to 100 parts of still liquid resin was poured into the hemp fibers in the mold. A 24 hours cure at room temperature was allowed for these composite samples. After unmolded, the samples were cut following the ASTM D256 standard. Ten specimens for each percentage of hemp fiber composite were impact tested in a PANTEC pendulum, Fig. 2, set in the Izod configuration.

Figure 2: Pantec impact pendulum.

Results and Discussion

Figure 3 shows the macrostructural appearance of broken specimens with different amounts of hemp fibers, from 0 to 30% in volume. In this figure, it is important to note that only the pure epoxy specimen was completely separated in two parts. For the composite specimens, the impact failed to separate the sample in two parts. This indicates that the epoxy matrix without the addition of hemp fiber is brittle and the impact-generated crack propagates without being arrested until the specimen separates. However, for any proportion of hemp fiber the initial propagating crack is blocked and the rupture migrates to the fiber/matrix interface. The specimen then bends upon impact of the hammer, but does not separate due to the flexibility of the fibers that are not broken.

There are important factors related to the impact fracture characteristic of polymeric reinforced with long and aligned natural fibers. The relatively low interface strength between a hydrophilic natural fiber and a hydrophobic polymeric matrix contributes to an ineffective load transfer from the matrix to a longer fiber. This results not only in a relatively greater fracture surface but also a higher impact energy needed for the rupture. The impact energy obtained in the Izod impact tests of epoxy matrix composites reinforced with different volume fractions of fibers hemp are shown in Table 1.

Table 1 - Izod Impact energy for epoxy matrix composites reinforced with hemp fibers.

Fiber Content (%)	Impact Energy (J/m)
0	2.30± 0.55
10	1.97± 0.29
20	2.56± 0.37
30	4.00± 0.51

From the data in Table 1, the graph of the energy absorbed in the Izod impact vs. the corresponding volume fraction of hemp fibers in the epoxy matrix was plotted, as shown in

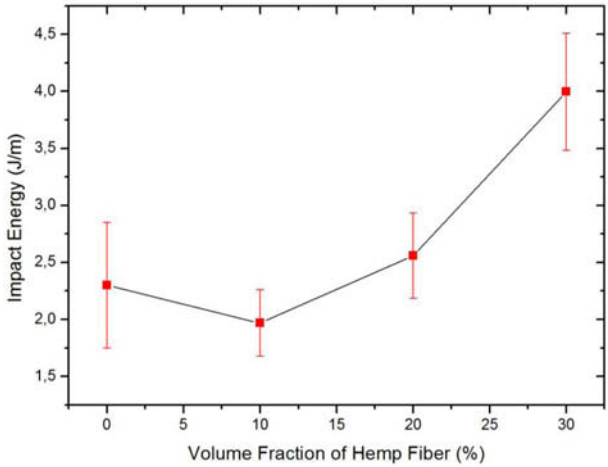

Figure 3: Variation of the Izod impact energy with the amount of fiber in the composites.

Other lignocellulosic fibers present the same behavior[4], which is due to the heterogeneous nature of these fibers, causing substantial dispersion in the composites properties. Even considering the error bars, it is possible to interpret the increase of impact energy, as following a linear relationship.

Indeed, for most lignocellulosic fibers, the increase in the Izod impact energy is directly related to the increase in the fiber volume fraction[9].

The fact that hemp fibers remain unbroken after the impact, as shown for the composites in Fig. 4, is an indication that cracks had propagated along the fiber/matrix interface causing the fiber separation from the epoxy but not the fiber rupture. This effect increases the cracks trajectory through the composite, creating a greater impact energy. Similar behavior was also observed in the pullout tests[10]. Thus, the composites absorb relatively larger amounts of energy, leading to an increase in the impact resistance.

Figure 4 shows the typical fracture surface of a 30% hemp fiber composite caused by an Izod impact test. With low magnification, Fig 4(a), the surface region where the fibers are bending, instead of breaking, can be observed. With higher magnification, Fig 4(b), one sees the interface fiber/matrix where a crack is propagating. The crack "river pattern" is observed at the left side of Fig. 4(b).

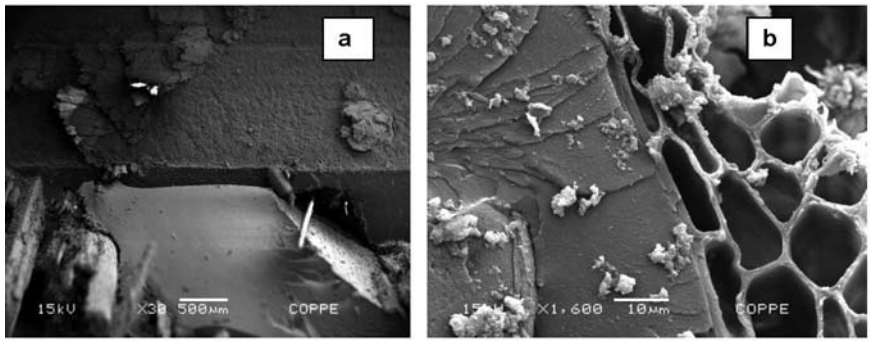

Figure 4: SEM micrograph of the fracture for a 30% hemp composite. (a) 30 x; (b) 1600 x.

Figure 4 (b) also shows a detail of the interface between the epoxy matrix and a hemp fiber, especially signs of adhesion between them. Some cracks may be observed, however, propagating through the fiber/matrix interface. This behavior confirms the mechanism of rupture between the hemp fiber and epoxy matrix associated with low interfacial resistance, resulting in greater impact energy.

Conclusions

Although we observed behavior small decrease in impact resistance of the reinforced composite fiber with 10% compared to the pure epoxy matrix with larger percentages of fibers increased the strength of the composite. The fibers may have acted as impurities, stress concentrators and caused a small fragilization in the matrix.

There is a significant increase in energy absorbed in Izod impact tests with the incorporation of hemp fibers in an epoxy matrix composite.

The weak interface between the hemp fibers and the epoxy matrix contributes greatly to increase the impact energy by changing the cracks trajectory in the composite.

Most of this increase in toughness is apparently due to the low hemp fiber/epoxy matrix interfacial shear stress. This results in a higher absorbed energy as a consequence of a longitudinal propagation of the cracks throughout the interface, which generates larger rupture areas, as compared to a transversal fracture.

Acknowledgements

The authors thank the support to this investigation by the Brazilian agencies: CNPq, CAPES, FAPERJ, TECNORT and FENORT.

References

1. Aquino, R. C. M. P.; Almeida, J. R. M; Monteiro, S.N. (2005). Análise do Compósito de Piaçava/Resina poliéster, como substituto da Madeira. In: 60º Congresso Anual da Associação Brasileira de Metalurgia e Materiais – ABM, 24-27 de julho de 2006, Belo Horizonte, MG, Brasil.

2. Hull, D.; Clyne, T. W. (1996) An Introduction to Composite Materials, 2a ed., Cambridge: Cambridge Univ. Press.

3. Monteiro, S.N, Costa, L.L., Santafé, H.P.G.,(2008) Tenacidade ao impacto Charpy de compósito epoxídico reforçado com fibras de coco, In: CBECIMAT – CONGRESSO BRASILEIRO DE ENGENHARIA E CIÊNCIA DOS MATERIAIS, outubro de 2008, Porto de Galinha – PE – Brasil.p. 1-12.

4. Bledzki, A.K.; Gassan, J. (1999) Composites reinforced with cellulose-based fibres. Prog. Polym. Sci, v. 24, p. 221-274.

5. Monteiro, S.N.; Lopes, F.P.D.; Ferreira, A.S.; Nascimento, D.C.O. (2009a) Natural fiber polymer matrix composites: cheaper, tougher and environmentally friendly. JOM, v. 61, n. 1, p. 17-22.

6. Leão, A. L.; F.X., Frollini, E. (1997) Lignocellulose-Plastics Composites, plastic composite. USP & UNESP.

7. Joseph, A.; Sreekala, M. S.; Oomens, Z.; Koshy, P.; Tohomas, S. A. (2002) " A comparison of the mechanical properties of phenol formaldehyde composites reinforced with banana fibre and glass fibres". Composites Science and Technology, v. 62, p. 1857-68, 2002

8. Monteiro, S.N., Lopes, F.P.D., (2007) Ensaios de impacto em compósito polimérico reforçado com fibras de curauá – In: 62° CONGRESSO ANUAL DO CONGRESSO ANUAL DA ASSOCIAÇÃO BRASILEIRA DE METALURGIA E MATERIAIS ,ABM, julho de 2007, Vitória, ES. p. 1-10

9. Yue, C.Y.; Looi, H.C; Quel, M.Y. (2005) Assessment of Fibre-Matrix Adhesion and Interfacial Properties Using the Pullout Test. Int. J. Adhesion and Adhesives, v. 15, p. 73-80, 1995.

10. Monteiro S.N; Margem F. M; Neto, J.B. Evaluation of the interfacial strength of ramie fibers in polyester matrix composites, TMS 2010 Annual Meeting & Exhibition, February 14-18, 2010 • Washington State Convention Center, Seattle, WA.

Characterization of Minerals, Metals, and Materials 2015
Edited by: John S. Carpenter, Chenguang Bai, Juan Pablo Escobedo, Jiann-Yang Hwang, Shadia Ikhmayies, Bowen Li, Jian Li, Sergio Neves Monteiro, Zhiwei Peng, and Mingming Zhang
TMS (The Minerals, Metals & Materials Society), 2015

ZINC RECOVERY FROM ZINC OXIDE FLUE DUST DURING THE NEUTRAL LEACHING PROCESS BY ULTRASOUND

Xuemei Zheng [1,2,3,4], Jing Li [*1,2,3,4], Aiyuan Ma [1,2,3,4], Jinhui Peng [1,2,3,4], Libo Zhang[1,2,3,4], Shaohua Yin[1,2,3,4]

[1] Yunnan Provincial Key Laboratory of Intensification Metallurgy, Kunming 650093, Yunnan, China.
[2] Key Laboratory of Unconventional Metallurgy, Ministry of Education, Kunming 650093, China;
[3] National Local Joint Laboratory of Engineering Application of Microwave Energy and Equipment Technology, Kunming 650093, China;
[4] Faculty of Metallurgical and Energy Engineering, Kunming University of Science and Technoloy, Kunming 650093, China.

Keywords: zinc; zinc oxide flue dust; neutral leaching; ultrasound

Abstract

Zinc recovery from zinc oxide flue dust (ZOFD) by ultrasound enhanced neutral leaching process was investigated. In this study, the effects of leaching temperature, liquid/solid ratio, leaching time and ultrasound power were studied, and the conventional leaching experiments were also performed. The experimental results showed that the leaching time was greatly shortened and the leaching rate of zinc was effectively improved by the assistance of ultrasound. The optimum conditions of ultrasound-assisted leaching were determined as leaching time 20 min, temperature 35℃, and the liquid/solid ratio of 5. Under these conditions, the leaching rate of zinc was close to 80% as the ultrasound power of 540W, which was increased by 7% or so, in comparison with that of conventional leaching process.

Introduction

As an important base metal, zinc has been widely used in many walks such as metallurgical, construction, marine, chemical and textile industries [1, 2]. It is primarily produced from sulphidic concentrates, while some from oxide-carbonate concentrates [1-3]. With the continuous exploitation of minerals, the secondary sources has been playing more and more important roles in recovering zinc as raw

Author: Xuemei Zheng, female, graduate student, Tel: +86-13629684143; E-mail: mylove.daisy@foxmail.com.

Foundation item: Project (51404115) supported by the National Natural Science Foundation of China; Project (2014CB643404) supported by the National Program on Key Basic Research Project of China; Project (2013HA002) supported by the Yunnan Provincial Science and Technology Innovation Talents Scheme-Technological Leading Talent.

Corresponding author: Jing Li; Tel: +86-13658872991; Fax: +86-5138997; E-mail: lijingkind@163.com.

materials, such as zinc ash, zinc dross, flue dust and leach residues, etc [1, 4-8].

Zinc oxide flue dust (ZOFD) is one of important secondary sources, which is mainly collected from zinc and lead smelting, copper smelting, galvanized steel scrap, steel dust, etc. Considering the hydrometallurgical processing for the dusts, several hydrometallurgical treatments for the recovery of zinc and other metals from these zinc-bearing wastes have been proposed [9-14]. In the process of leaching, sulphuric acid or spent electrolyte is usually used as lixiviant for the dissolution of zinc. Whereas, in order to extract zinc from the solution more profitably, other impurities such as iron, arsenic are not expected to be dissolved or most of them can be reprecipitated from solution using neutralizing hydrolysis method. Both of the demands can be met by the neutral leaching process. Thus, the neutral leaching process was usually taken as the first leaching process by most industries. In the existing studies conducted on the neutral leaching of ZOFD, some disadvantages such as long time or high temperature were presented, and the leaching result was not ideal. For example, the raw material related in this paper was subjected to conventional method in plant, and the leaching rate of zinc is only approximately 70%. Thus, it is necessary to develop some new technologies to augment the neutral leaching process.

Ultrasound has been applied into leaching yield due to the induced cavitation. This effect was performed as the creation, growth and subsequent destruction of cavitation bubbles. In this process, with the collapse of these bubbles, tremendous energy was produced for chemical and mechanical effects, results in a mass transfer increase and activation of the reaction surface, increasing the diffusion speed and accelerating the leaching. Hurşit et al. [15] reported ultrasound had a positive contribution on zinc leaching from smithsonite ore with gluconic acid being the leaching agent. Avvaru et al. [16] studied the mechanism of uranium leaching by nitric acid and sulfuric acid in the present and absence of ultrasound, the results indicated that ultrasound had a significant enhancement in the leaching rate of uranium. Swamy and Narayana [17] applied dual frequency ultrasound to intensify the leaching process of copper recovery from oxide ores, and the results showed a shorter process time and less reagent consumption as compared to conventional agitation method. Beşe Ayşe Vildan [18] reported ultrasound could increase the dissolution of Cu, Zn, Co and Fe in the slag by 8.87%, 3.04%, 5.35%,and 1.57%, respectively. An overall increased effectiveness of ultrasound-assisted leaching can be inferred in comparison with the conventional leaching process. It is the purpose of this study to develop the neutral leaching process by ultrasound.

Materials and Methods

Materials and Reagents

Both of the material, zinc oxide flue dust and the leaching agent, raffinate were obtained from the same zinc plant which is located in Yunnan, southwest China, the rest reagents used to adjust the pH value were of analytical reagent-grade.

The chemical compositions of the sample are shown in Table Ⅰ. The X-ray diffraction

(XRD) phase analysis results of the sample which determine the mineralogical composition is shown in Figure 1. XRD analysis shows that the ZnO and $ZnFe_2O_4$and SiO_2 are the major components in the sample.

Table Ⅰ. The main chemical compositions of the zinc oxide flue dust

Elements	Zn	Fe	Pb	SiO_2	In	Cr	Ca
Weight,%	34.79	12.29	10.06	5.02	0.045	0.013	1.272

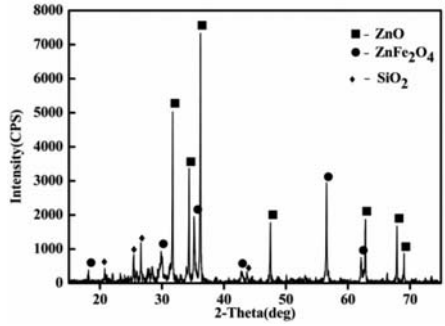

Figure 1. XRD patterns of zinc oxide flue dusts

Leaching Procedure

The main reaction can be described as follows,

$$ZnO+H_2SO_4=ZnSO_4+H_2O \quad (1)$$

The leaching experiments were carried out in a glass beaker of 1000 ml, immersed in a water thermostat to keep the temperature, the temperature could be controlled within ± 1℃. The ultrasonic transducer was inserted into the solution and connected to an ultrasonic generator which generates ultrasonic waves with a frequency of 20 kHz. The raffinate was used to prepare the desired leaching solutions in the glass beaker. The dependent variables were varied in the range: the leaching temperature (30℃-65℃), the liquid/solid ratio (3-6), the leaching time (20min-90min) and the ultrasound power (180W-1440W). In each of the experiments, the slurry was filtered immediately after the reaction time was reached, the residue was washed with appropriate deionized water and then dried for characterization. The zinc and iron contents of residue sample were estimated by chemical titration, and the experimental variations were less than ±2%. The scanning electron microscopy (SEM) was carried out to analyze the mineralogical morphology.

Results and Discussion

The ultrasound-assisted leaching experiments were first carried out, then the conventional leaching experiments were performed for comparison.

Effect of Temperature on Ultrasound-assisted Leaching

The experiments were carried out with the temperature of 30℃, 35℃, 40℃, 50℃,

60℃ and 65℃, the liquid/solid ratio of 5, the leaching time of 90 min and the ultrasound power of 540W. The results are shown in Figure 2. It can be seen that the leaching rate of zinc is nearly independent of the temperature when the temperature is from 35℃ to 65℃, while the leaching recovery of iron increases by 2%, as high iron content in solution is quite unfavorable to the subsequent iron removal process, it is better to keep a low leaching rate of iron. In addition, with the temperature increasing, the energy consumption and production cost increase. The leaching rate of zinc is 79.45% and iron of 5.18% with temperature of 35℃.

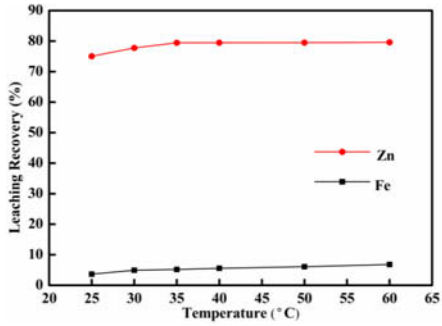

Figure 2. Effect of temperature on ultrasound-assisted leaching

Effect of Liquid/Solid Ratio on Ultrasound-assisted Leaching

The influence of liquid/solid ratio on zinc leaching rate was studied in the range of 3 to 7, the temperature of 35℃, the leaching time of 90 min and the ultrasound power of 540W. According to Figure 3. the leaching rate increases with increasing of liquid/solid ratio until 5, but only slightly increase with further increase in liquid/solid ratio, which is attributed to the fact that increasing liquid content will reduce the viscosity of slurry and then facilitate the diffusional mass transfer process, contributing to the improvement of leaching rate. The leaching rate of zinc is 79.46% and iron of 5.12% with liquid/solid ratio of 5.

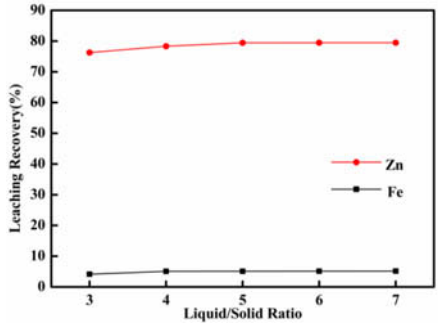

Figure 3. Effect of liquid/solid ratio on ultrasound-assisted leaching

Effect of Time on Ultrasound-assisted Leaching

The experiments were carried out with the time of 10 min, 20 min, 40 min, 60 min, 75 min and 90 min, the leaching temperature of 35℃, the liquid/solid ratio of 5 and the ultrasound power of 540W. The results are shown in Figure 4. It can be seen that the increasing reaction time is effective in increasing leaching rate until 60 min, which is attributed to the fact that diffluent zinc is constantly dissolving by acid with the increase of reaction. The leaching rate of zinc is 78.05% and iron of 4.47% with time of 20 min.

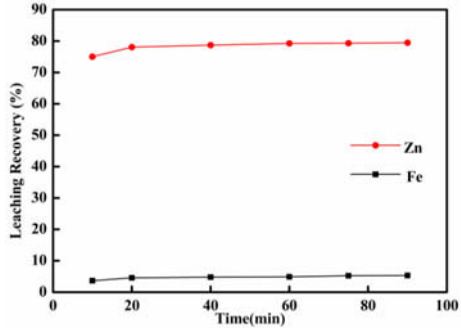

Figure 4. Effect of time on ultrasound-assisted leaching

Effect of Ultrasonic Power

The effect of ultrasonic power on leaching rate was investigated at the ultrasonic power of 180W, 360W, 540W, 720W, 1080W and 1440W, the temperature of 35℃, the liquid/solid ratio of 5, and the leaching time of 20 min. According to Figure 5, as the ultrasonic power increases, the leaching rate increases initially, after the ultrasonic power reaches 540W there is no significant changes of the leaching rate. The leaching rate of zinc is 78.11% and iron of 4.49% with ultrasonic power of 540W.

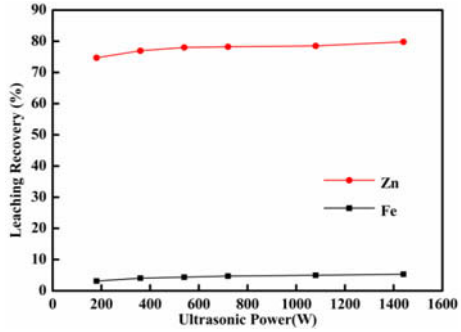

Figure 5. Effect of ultrasonic power on ultrasound-assisted leaching

Comparison of Ultrasound-assisted Leaching and Conventional Leaching

In order to study the different effects of ultrasound-assisted leaching and conventional leaching, the experiments were carried out in a 1000mL beaker. The conditions of ultrasound-assisted leaching were the same as those of the experiments of varied reaction time ultrasound-assisted leaching process. The results are shown in Figure 6. The results demonstrate that the ultrasound-assisted leaching has more obvious influence on the extraction of zinc than conventional leaching. Furthermore, Figure 6 shows that the maximum leaching rate of 79.46 of zinc with ultrasound, which is increased by 6.43%, in comparison with that without ultrasound when the temperature is 35℃ and the liquid/solid ratio is 5. These results indicate that the ultrasound can strengthen the zinc extraction from zinc oxide flue dust.

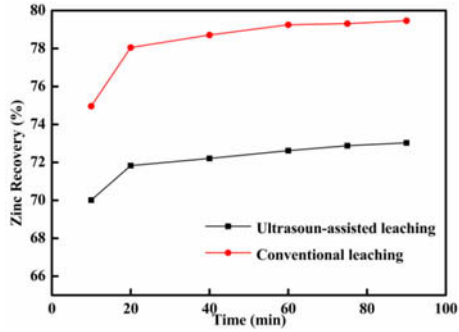

Figure 6. Effect of different leaching process on zinc recovery

Morphology of the Residues

Figure 7 and Figure 8 show the SEM images of zinc oxide flue dust and the leached residue sample, respectively. According to Figure 7, it can be observed that zinc oxide flue dust presents a rough surface, different shapes and sizes, and it is obvious that the particles agglomeration is common. In addition, insoluble substances are bonded on the surface of zinc particles, render the process diffusion controlled through insoluble substance layer.

As shown in Figure 8, The surface coatings of the residue sample become less after leaching by ultrasound, particles are more dispersive. The phenomenon can be explained by the act of a powerful impulse wave, which can peel off particle coatings from raw material into the liquid phase and then soluble ZnO can react with acid more easily and adequately. This implies that ultrasound are quite efficiently to strengthen the mass transfer process.

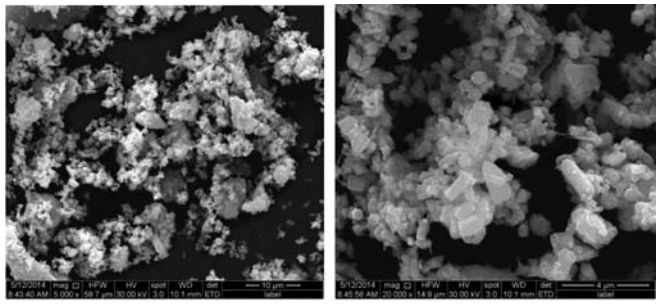

Figure 7. SEM micrograph of zinc flue oxide dust

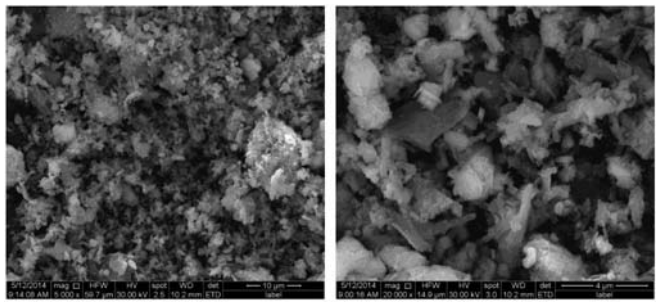

Figure 8. SEM micrograph of leached residue

Conclusions

1) Using ultrasound can effectively recover zinc from zinc oxide flue dust (ZOFD) during the neutral leaching process.

2) In comparison to conventional leaching, the leaching time can greatly shortened and the leaching rate of zinc can be effectively improved by the assistance of ultrasound.

3) The optimum conditions of ultrasound-assisted leaching are determined as leaching time 20 min, temperature 35℃, and the liquid/solid ratio of 5, the leaching rate of zinc is close to 80% as the ultrasound power of 540W, which is increased by 7% or so, in comparison with that of conventional leaching process.

Acknowledgements

The authors are grateful for financial supports by the National Natural Science Foundation of China (No.51404115), the National Program on Key Basic Research Project of China (2014CB643404), and the Yunnan Provincial Science and Technology Innovation Talents Scheme-Technological Leading Talent (2013HA002).

References

1. M.K. Jha, V.Kumar, and R.J. Singh, "Review of Hydrometallurgical Recovery of

Zinc from Industrial Wastes," *Resources, Conservation and Recycling*, 33 (2001), 1-22.
2. Y. Zhang et al., "The Electrowinning of Zinc from Sodium Hydroxide Solutions," *Hydrometallurgy*, 146 (2014), 59-63.
3. M.D. Turan, H. S. Altundoğan, and F. Tümen, "Recovery of Zinc and Lead from Zinc Plant Residue," *Hydrometallurgy*, 75(2004), 169-176.
4. B.A. Zeydabadi et al., "Zinc Recovery from Blast Furnace Flue Dust," *Hydrometallurgy*, 47 (1997), 113-125.
5. M.S. Lutandula, and G.N. Kashala, "Zinc Oxide Production through Reprocessing of the Electric Arc Furnace Flue Dusts," *Journal of Environmental Chemical Engineering*, 1 (2013), 600-603.
6. S.M. Abdel Basir, M.A. Rabah, "Hydrometallurgical Recovery of Metal Values from Brass Melting Slag," *Hydrometallurgy*, 53 (1999), 31-44.
7. H.P. Hu et al., "The Recovery of Zn and Pb and the Manufacture of Lightweight Bricks from Zinc Smelting Slag and Clay," *Journal of Hazardous Materials*, 271 (2014), 220-227.
8. M.A. Abdel-latif, "Fundamentals Of Zinc Recovery from Metallurgical Wastes in the Enviroplas Process," *Minerals Engineering*, 15 (2002), 945-952.
9. F.J. Alguacil, C. Caravaca, and A. Cobo, "Hydrometallurgical Treatments of Steelmaking Flue Dusts," *Revista De Metalurgia*, 30 (1994), 173-182.
10. Y.C. Zhao, and R. Stanforth, "Integrated Hydrometallurgical Process for Production of Zinc from Electric Arc Furnace Dust in Alkaline Medium," *Journal of Hazardous Materials*, 80 (2001), 223-240.
11. T. Havlik et al., "Atmospheric Leaching of EAF Dust with Diluted Sulphuric Acid," *Hydrometallurgy*, 77 (2005), 41-50.
12. N. Leclerc, E. Meux, and J.M. Lecuire, "Hydrometallurgical Recovery of Zinc and Lead from Electric Arc Furnace Dust Using Mononitrilotriacetate Anion and Hexahydrated Ferric Chloride," *Journal of Hazardous Materials*, 91 (2002), 257-270.
13. T. Hilber et al., "Solid/liquid Extraction of Zinc from EAF-dust," *Separation Science and Technology*, 36 (2001), 1323-1333.
14. I.M. Ahmed, A.A. Nayl, and J.A. Daoud, "Leaching and Recovery of Zinc and Copper from Brass Slag by Sulfuric Acid," *Journal of Saudi Chemical Society*, (2012).
15. M. Hurşit, O. Laçin, and H. Saraç, "Dissolution Kinetics of Smithsonite Ore as an Alternative Zinc Source with an Organic Leach Reagent," *Journal of the Taiwan Institute of Chemical Engineers*, 40 (2009), 6-12.
16. B. Avvaru et al., "Sono-chemical Leaching of Uranium," *Chemical Engineering and Processing*, 47 (2008), 2107-113.
17. K.M. Swamy, and K.L. Narayana, "Intensification of Leaching Process by Dualfrequency Ultrasound," *Ultrasonics Sonochemistry*, 8 (2001), 341-346.
18. B.A. Vildan, "Effect of Ultrasound on the Dissolution of Copper from Copper Converter Slag by Acid Leaching,"Ultrasonics Sonochemistry, 14 (2007), 790-796.

Characterization of Minerals, Metals, and Materials 2015
Edited by: John S. Carpenter, Chenguang Bai, Juan Pablo Escobedo, Jiann-Yang Hwang, Shadia Ikhmayies, Bowen Li, Jian Li, Sergio Neves Monteiro, Zhiwei Peng, and Mingming Zhang
TMS (The Minerals, Metals & Materials Society), 2015

MICROHARDNESS AND DEFORMATION STORAGE ENERGY DENSITY OF NiTi THIN FILMS

Yonghua Li[1]* Xiaodong Wang[2] Weitao Zheng[2,] Fanling Meng[2,]
[1]College of Sciences, Key Lab of In-fiber Integrated Optics, Ministry Education of China, Harbin Engineering University, Harbin 150001, China
[2]College of Materials Science and Engineering, Key Laboratory of Automobile Materials of MOE, Jilin University, Changchun 130012, China

Key words: Shape memory materials; Microhardness; X-ray diffraction profile analysis

Abstract

The NiTi thin films were deposited onto copper substrates by magnetron sputtering. Tensile tests were carried out on CSS-44100 electron universal test-machine. X-ray diffraction profile Fourier analysis method has been used to study the mechanical properties of deformation NiTi thin films. The surface micrographs of the NiTi thin film were obtained using scanning electron microscopy (SEM). It has been found that the dislocation density and the deformation storage energy density increased with elongation increased. Microhardness was calculated from the dislocation data. The results showed that the microhardness values were not in a good agreement between calculated values and measured values. The oxide layer on the surface of NiTi thin film affects the measured values of microhardness. The Vickers hardness measured values are larger than the calculated values. The experimental results showed that a series of parallel cracks grew in a concerted fashion across the thin film and the cracks were equally spaced.

Introduction

Ti-Ni thin films have attracted much attention as intelligent and functional materials for the fabrication of micro-electro-mechanical systems (MEMS) microactuators[1-3]. However, in order to achieve the effective development and a comprehensive understanding of shape memory thin films, the study of mechanical properties of sputter-deposited thin films is necessary. Tensile tests have been reported[4,5], but the deformations reported in these articles are only related to the study of stress-induced martensitic transformation. So far, the work of relating the dislocation density and the Vickers microhardness values to the strain in the film has not been reported. The microhardness values of coating materials can be obtained mainly from indentation, which is a well-known and reliable method. However, the measured value of hardness is influenced by the substrate materials and the surface oxidation. According to the definition of the material's hardness, it is plausible to relate the hardness of a material to the plastic flow stress. Therefore, the hardness can be deduced directly from the crystal defects. Wang et al. first adopted the X-ray diffraction profile analysis method to evaluate the hardness of coatings directly from the dislocation density and dislocation

*Corresponding author. Tel: +86 0431 85168444, E-mail address: mfl@jlu.edu..cn .

distribution[6]. In the present study, using the same methods we have investigated the change of the dislocation density and the Vickers microhardness values during tensiling

.

Experimental

The NiTi thin films were deposited onto Cu substrates by magnetron sputtering. The copper substrates were pre-punched into dog-bone specimens with 4.5mm×30mm(gauge portion) ×35μm(thickness). The sputtering conditions were as follows: argon pressure, 4×10^{-2} Pa; sputtering power, 640 W; deposition rate, 95 nm/min; substrate-to-target distance, 65 mm. The substrate temperature was about 673K. The NiTi films thickness was about 20μm. The films composition determined by energy dispersive X-ray spectroscopy is about Ti-51.45at.%Ni. The as-deposited films were first solution treated at 1073K for 1h, and then aged at 773K for 30min in a vacuum furnace. Tensile tests were carried out on CSS-44100 electron universal testing machine at ambient temperature. The strain rate was 1.1×10^{-4} s^{-1}. The stress-strain curve of the free-standing film was obtained from the experimental curve of copper substrate together with the thin film adhesive to the substrate compared with the curve of copper substrate without film. X-ray diffraction was carried out using a Rigaku 12 kW rotating and a graphite monochromator. The strong diffraction line profiles from NiTi B2(110) and (220) were recorded respectively and are shown in Fig.1 by step scanning with 2θ, steps of 0.02°. The average crack spacing of the NiTi thin film was measured using scanning electron microscopy (SEM). The Vickers microhardness values were determined by Everone MH-6 microhardness tests.

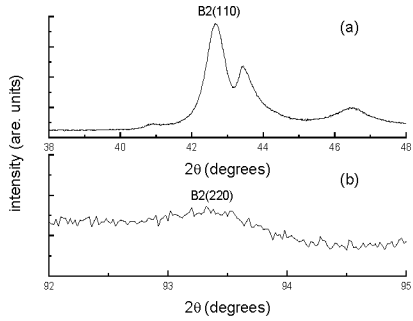

Fig.1. The X-ray diffraction line profile of NiTi thin film (a) (110) and (b)（220）planes.

*Corresponding author. Tel: +86 0431 85168444, E-mail address: mfl@jlu.edu..cn .

Results and discussion

We let $h(x)$ be the measured profile of (hkl) diffraction of the sample, and $g(x)$ the measured profile from a standard annealed sample as the instrument broadening profile. The physical broadening profile $f(x)$ can be obtained by Fourier deconvolution method given by Stokes[7]

$$h(x) = \int_{-\infty}^{\infty} f(x)g(x-y)dy. \qquad (1)$$

Each profile was divided into 60 parts for calculating the Fourier transform coefficients. In the physical broadening profile

$$f(x) = \sum_n (A_n \frac{\cos 2\pi nx}{60} + B_n \frac{\sin 2\pi nx}{60}). \qquad (2)$$

B_n, being much smaller than A_n, may be neglected, while A_n is normalized to $A_0 = 1$. It should be pointed out that $A_n = A(L)$, were $L = lt$, $t = 0,1,2,3...$, l is the reflection order. According to the Warren–Averbach method[8], assuming

$$A_l(L) = A_l^s(L) \cdot A^p(L). \qquad (3)$$

Where $A_l(L)$ is the Fourier coefficient of the diffraction profile; $A_l^s(L)$ and $A^p(L)$, the strain broadening and the size broadening coefficient respectively and l the reflection order, $A^p(L)$ being independent of l. There is only one strong diffraction profile which can be precisely measured. Based on the theory[9,10]

$$A(L) = A_l(L)/A_l(L), \qquad (4)$$

$$A^p(L) = \alpha - \frac{L}{D},$$

$$A_l^s(L) = \exp[-\pi\beta_c L - \pi\beta_g^2 L^2],$$

where α is the hook coefficient, D is the coherent domain size, β_c and β_g are the integral width of Cauchy and Gaussian functions, respectively. From a series of $A^p(L)$ values for a single profile, one can obtain α, D, β_c and β_g using the least-squares fitting procedure. Finally, the apparent dislocation density ρ^* and the apparent dislocation distribution parameter M^* can be deduced. According to the model of dislocation configuration, $k = \beta_c/(\sqrt{\pi}\beta_g)$ being the relative value of dislocations arranged in dipoles (ρ_d) and in pile-ups (ρ_p). All

*Corresponding author. Tel: +86 0431 85168444, E-mail address: mfl@jlu.edu..cn .

dislocations can be divided into two parts specified by ρ_d and ρ_p, the dislocation densities in dipoles and pile-ups respectively. Therefore

$$\beta_c \propto \sqrt{\rho_d}\ , \beta_g \propto \sqrt{\rho_p}\ . \tag{5}$$

In order to find the average dislocation density ρ and the average dislocation distribution parameter M in terms of the measured β_c and β_g, one must establish the dependence of the root mean square strain $\left\langle \varepsilon^2 \right\rangle^{1/2}$ on ρ and M. Wang *et al.*[9] ingeniously utilized first a set of experimental curves to determine the characteristic values ρ^* and M^* on the basis of Wilkens' study for single crystals[11]. The average ρ and M are obtained used a formula. The formula depends on the diffraction vector $g(hkl)$ and Poisson's ratio υ for a particular structure.

Wang et al. introduced a conception called the average elastic stored energy per unit volume, $\left\langle \frac{E}{V} \right\rangle$ (J/m^3). $\left\langle \frac{E}{V} \right\rangle$ can be regarded as the internal average microstress and may be calculated by a formula[12]:

$$\langle \frac{E}{V} \rangle = A\, G\, b^2 \rho \ln \frac{2M}{b\sqrt{\rho}}, \tag{6}$$

where b is the Burger's vector. G is the shear modulus, $A = 1/4\pi$ for screw dislocation, $A = 1/[4\pi(1-\upsilon)]$ for edge dislocation and υ is Poisson's ratio.

The characterization of material properties is carried out when the materials have different intrinsic microscopic objects, such as electron structure, atom distribution, point defect constituents, dislocation configuration etc., by macro-, micro- and mesoscopic approaches[13]. The mechanical properties of metals and alloys should be determined primarily by dislocation structure among these objects. The Vickers hardness values are

$$H_V(MPa) = \frac{10^{n+1} Gb[M(\rho)^{1/2} + (bd)^{-1/2} + 0.08^{1/2}/D]}{3.27 \times 8\pi(1-\upsilon)}. \tag{7}$$

Where d is the grain size, D is the subgrain size, and n(n<1) is the index of work hardening. For NiTi alloy, n=0.2, $\upsilon = 0.28$, $G = 2.7 \times 10^4 MPa$, b = 0.2596 nm[14]. The grain size was estimated to be 1.5μm from the microstructures of the thin film after heat treatment[15].

*Corresponding author. Tel: +86 0431 85168444, E-mail address: mfl@jlu.edu..cn .

$\left\langle \frac{E}{V} \right\rangle$ and H_V can be determined from Eq. 6 and7, respectively. The dislocation parameters and the calculated valves $\left\langle \frac{E}{V} \right\rangle$ and H_V are listed in Table 1.

Table 1 Dislocation structure parameters and the calculated valves of NiTi thin films

Strain (%)	D (nm)	ρ^* (10^{11}cm^{-2})	M^*	ρ (10^{11}cm^{-2})	M	$\left\langle \frac{E}{V} \right\rangle$ ($10^6 J \cdot m^{-3}$)	Calculated values H_V (MPa)	Measured values H_V (MPa)
0	41.0	1.424	1.052	3.875	1.030	3.780	229	1250
4.80	39.9	3.073	1.358	8.363	1.330	7.941	337	1353
6.78	31.1	3.757	1.977	10.369	1.937	10.405	483	1640
8.21	24.9	5.920	3.381	16.339	3.313	17.413	912	2302

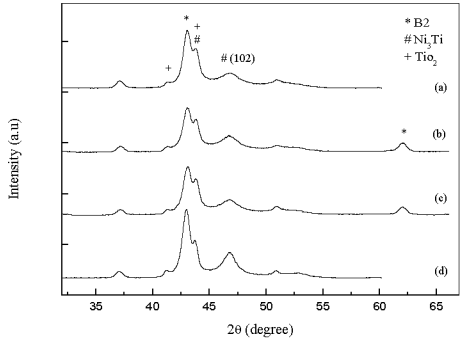

Fig.2. The XRD profiles of NiTi thin film after thermal treatment during tension: (a) $\varepsilon = 0$, (b) $\varepsilon = 4.8\%$, (c) $\varepsilon = 6.8\%$, (d) $\varepsilon = 8.2\%$

*Corresponding author. Tel: +86 0431 85168444, E-mail address: mfl@jlu.edu..cn .

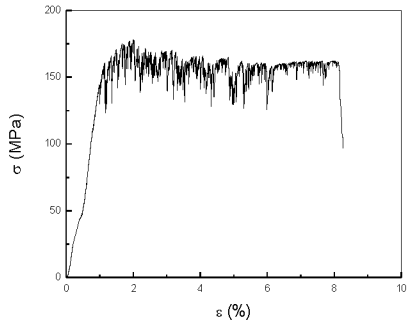

Fig.3. The stress-strain curve of NiTi thin film.

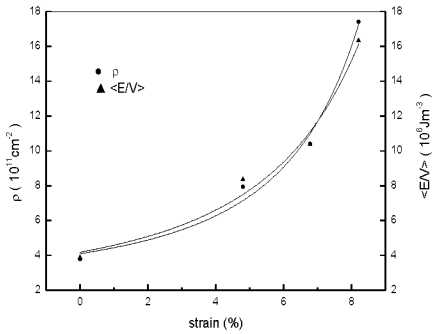

Fig.4. The average dislocation density and the average elastic stored energy density versus strain curves of NiTi thin film.

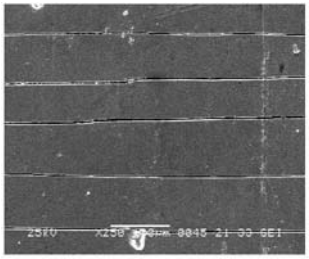

Fig.5. The SEM micrographs of NiTi thin film

*Corresponding author. Tel: +86 0431 85168444, E-mail address: mfl@jlu.edu..cn .

Figure 2 shows the XRD results of a Ti-51.45at.%Ni thin film subjected to solution treatment at 1073K for 1h followed by age treatment at 773K for 30min under different strain. The patterns are obtained after tension of NiTi thin film in B2-phase. There are TiO_2 and Ni_3Ti precipitation. During tension the (102) peak intensity of Ni_3Ti phase increases with elongation increased. Figure 3 shows the stress-strain curve of NiTi thin film. The stress-strain curve can be divided into two stages. The first linear stage corresponds to the elastic deformation of the parent phase[16]. In the following stage, serrations are observed. The serrations are considered to be the stress relaxation due to the cracks propagation and precipitation. The curves of the average dislocation density and the average elastic stored energy density values vs. strain are shown in Fig. 4. From Fig. 4, the average dislocation density and the average elastic stored energy density values gradually increase as strain increases in the strain range of 0 to 6.78% and rapidly increase in the strain range of 6.78% to 8.21%. Figure 5 shows the SEM micrographs of NiTi thin film. In Fig. 5, a series of cracks grow parallel to one another, and the direction of crack extension is perpendicular to the one of tension and the cracks are about equally spaced.

During tension the average dislocation density of NiTi thin film increased with elongation increase. Frank and Read discussed a possible explanation of this in terms of the reflection and multiplication of dislocation[17]. The hardness of materials is its resistance to local plastic deformation. The average elastic stored energy density $\left\langle \frac{E}{V} \right\rangle$ is increase with elongation increase, and the Vickers hardness calculated values is also increase. From table 1 we obtain that the Vickers hardness measured values are larger than the calculated values. This difference is caused by the oxide layer on the surface of NiTi thin film. After heat treatment in a vacuum furnace the samples are covered by an oxide layer with thickness of a few nanometers[18]. The intrinsic hardness of the film can be gained by X-ray diffraction line profile analysis from information of dislocation.

Conclusions

The mechanical properties of sputtering-deposited Ti-51.45at.% Ni thin film are investigated. The experimental results show that a series of parallel cracks grew in a concerted fashion across the thin film and the cracks are about equally spaced. The average dislocation density and the average elastic stored energy density values gradually increase as strain increases in the strain range of 0 to 6.78% and rapidly increase in the strain range of 6.78% to 8.21%. The Vickers hardness calculated values are also increase. The Vickers hardness measured values are larger than the calculated values. The oxide layer on the surface of NiTi thin film affects the measured values of microhardness.

*Corresponding author. Tel: +86 0431 85168444, E-mail address: mfl@jlu.edu..cn .

Acknowledgement

The works were supported by the 111 project (Grant No. B13015), to the Harbin Engineering University and the National Major Scientific Instrument and Equipment Development Project, China(Grant No. 2012YQ24026407-2).

References

[1]. Y. Q. Fu, H. Du, W. Huang et al., *Sens. Actuators A-Phys.* 112 (2004), 395-408.
[2]. Y. Q. Fu, W. Huang, H. Du et al., *Surf. Coat. Technol.* 145 (2001), 107-112.
[3]. B. Winzek, S. Schmitz, H. Rumpf et al., *Mater Sci Eng. A* 378 (2004) 40-46.
[4]. S. G. Malhotra, Z. U. Rek, S. M. Yalisove et al., *Thin Solid Films* 301 (1997), 45-54.
[5]. B. Gabry, C. Lexcellent, V. H. No et al., *Thin Solid Films* 372 (2000), 118-133.
[6]. N. Zhang and Y. Wang, *Thin Solid Films* 214 (1992), 4-5.
[7]. A. R. Stokes, *Proc Phys Soc* Lodon 61 (1948), 382.
[8]. B.E. Warren, *Progress in Metal Physics*. London. Pergamon, 8 (1959), 147.
[9]. Y. Wang, S. Lee, Y. Lee, *J. Appl. Cryst.* 15 (1982), 35-38.
[10]. W. Yuming, Z. Ziqung, *Appl. Phys. A* 35 (1984), 109-114.
[11]. M. Wilkens, *Phys. Status Solidi A* 2 (1970), 359.
[12]. F. Teng and Y. Wang, *J. Mater. Sci.* 21 (1986), 3223-3226.
[13]. E. Kotomin, M. Zaiser, W. Soppe, *Phil. Mag.* 70 (1994), 317.
[14]. F. Shan，Y. Huo，F. Teng et al., *Rare Metal Mat. Eng.* 27 (1998), 199-201.
[15]. F. Meng, Y. Li, Y. Wang et al., *J. Mater. Sci.* 40 (2005), 537-538.
[16]. A. Ishida, M. Sato, T. Kimura et al., *Phil. Mag. A* 80 (2000), 967-980.
[17]. F. C. Fank and W. T. Read, *Phys. Rev.* 79 (1950), 722.
[18]. Y. H. Li, L. M. Li, F. L. Meng et al., *Journal of Electron Spectroscopy and Related Phenomena,* 151 (2006), 144-148.

*Corresponding author. Tel: +86 0431 85168444, E-mail address: mfl@jlu.edu..cn .

Characterization of Minerals, Metals, and Materials 2015
Edited by: John S. Carpenter, Chenguang Bai, Juan Pablo Escobedo, Jiann-Yang Hwang, Shadia Ikhmayies, Bowen Li, Jian Li, Sergio Neves Monteiro, Zhiwei Peng, and Mingming Zhang
TMS (The Minerals, Metals & Materials Society), 2015

MORPHOLOGY AND DISTRIBUTION OF Nb-RICH PHASE AND GRAPHITE IN Nb MICROALLOYED DUCTILE IRON

Haicheng Li[1], Chao Yang[1], Zhang Wei[2], Xiangru Chen[1], Qijie Zhai*
1. Shanghai Key Laboratory of Modern Metallurgy & Materials Processing Shanghai University, Shanghai 200072, China, Email: qjzhai@shu.edu.cn
2. CITIC Metal Co., Ltd, Room 1903, Capital Mansion 6 Xinyuan Nanlu, Chaoyang District, Beijing 100004, China.

Keywords: Microalloyed, Ductile iron, Nb-rich phase, Graphite

Abstract

The Nb-rich phase generated by the addition of trace amounts of Nb(<0.1wt%) \ and the effects of different content of Nb on the morphology and distribution of graphite in ductile iron were studied in this paper. The results showed that when the content of niobium less than 0.1wt%, the two-dimensional morphology of Nb-rich phase existed in microalloyed ductile iron were mainly regular pattern such as square, triangle, polygon etc. Besides, Nb-rich phase in large size distributed in the matrix with a certain distance from graphite. With the increasing amount of niobium, the dispersion degree of graphite diameter, average diameter and roundness increased slightly, and the number of graphite decreased slightly.

Introduction

As a kind of strong carbide forming elements, Nb was also one of the most effective microalloyed element, which have been used widely presently. It could improve the properties of steel effectively by adding a small amount of Nb. Nb microalloyed technology has been drew attention in the field of casting materials gradually, and it has developed very quickly in recent years. Studies about the influence of Nb on the microstructure and mechanical properties of cast iron were approaching perfection day by day. The influences of microstructure and properties of materials by the addition of Nb have been extensively researched by Qijie Zhai, Tommy Nylén, Hongbo Zhu, and Yongsheng Yan, who have found that Nb could improve the properties of cast iron effectively[2~4]. In the ductile iron, the morphology and distribution of Nb-rich phase and graphite have great influence on its properties, but even until now only a few related references could be found. Thus, it was really meaningful to carry on such studies which the content of Nb in ductile iron was less than 0.1wt%.

Experimental

In this experiment, pig iron, scrap steel, ferrosilicon, ferromanganese, pure nickel, copper and niobium iron were used as the raw materials to melting in induction furnace of medium frequency. In the pouring process, the FeSiMg7RE5 was used as nodularizer, and 75SiFeAl was used as inoculant. The liquid iron was pouring at 1400±20℃. Besides, the spectrometer was used to measure the chemical composition of samples, as shown in table 1.

Table 1 chemical composition

Sample	C	Si	S	Mn	Cu	Ni	P	Cr	Nb
1#	3.9	1.9	0.017	0.34	0.46	0.61	0.06	0.024	0
2#	3.9	1.9	0.016	0.38	0.47	0.64	0.07	0.023	0.038
3#	4.0	1.9	0.016	0.36	0.46	0.61	0.07	0.029	0.074
4#	4.0	1.8	0.017	0.37	0.46	0.60	0.07	0.025	0.094

Results and discussion

The morphology and distribution of Nb-rich phase in ductile iron

Samples of different content of niobium was observed under the SU-1510 scanning electron microscopy (SEM) to analyzed the morphology and distribution of Nb-rich phase in the matrix after the grind and polish process, as shown in Fig.1. the morphology of Nb-rich phase existed in microalloyed ductile iron were mainly regular pattern such as square, triangle, polygon etc, which were similar to the morphology of Nb-rich phase with high content of Nb in gray cast iron[5]. It was worth to refer that there was almost a black region existed in the middle position of every Nb-rich phase. Energy spectrum analysis showed that Ti, N, O existed in this region, which verified the conclusion[6] that TiN could be the core of Nb-rich phase. Besides, with the increase of Nb content in ductile iron, the particle size in the matrix came up to 3μm, and the number of large size Nb-rich phase also increased. With the addition of Nb content increased to 0.04wt%, a few rich niobium phase appeared in the matrix, and its distribution was scattered. Because the hardness of Nb-rich phase is very high, its dispersed distribution in the matrix could strengthen the matrix effectively and improve the properties of ductile iron, especially the wear-resisting property[7]~[8]. When Nb content was 0.07wt%, the number of large Nb-rich phase increased largely, and individual Nb-rich phase even exhibited the clusters shape . When Nb content was 0.09wt%, large Nb-rich phase increased slightly, the number and overall distribution of Nb-rich phase were less differ from that with 0.07wt%Nb content.

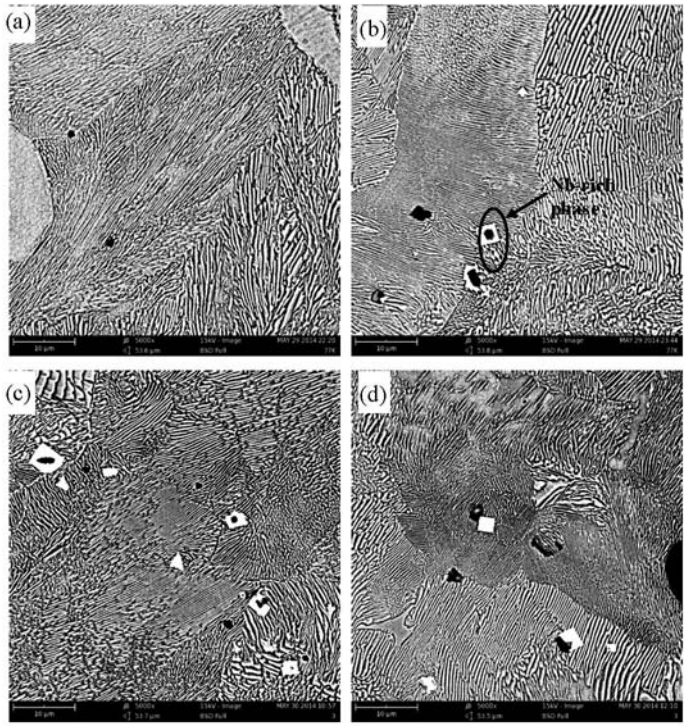

Fig.1 Distribution and morphology of Nb-rich phase: (a) 0%Nb, (b) 0.038%Nb, (c) 0.074%Nb, (d) 0.094%Nb

Effect of Nb on the morphology of graphite nodule in ductile iron

The properties of ductile iron depended largely on the uniformity, roundness and nodularity of graphite nodule in the matrix. To improved the properties of ductile iron, better nodularity, uniformity and roundness of graphite were needed. Metallographic samples with 25mm diameter were got to observed the morphology and distribution of graphite under 100 times of metallographic microscope after grind and polish process. The graphite morphology and distribution of ductile iron were shown in Fig.2.

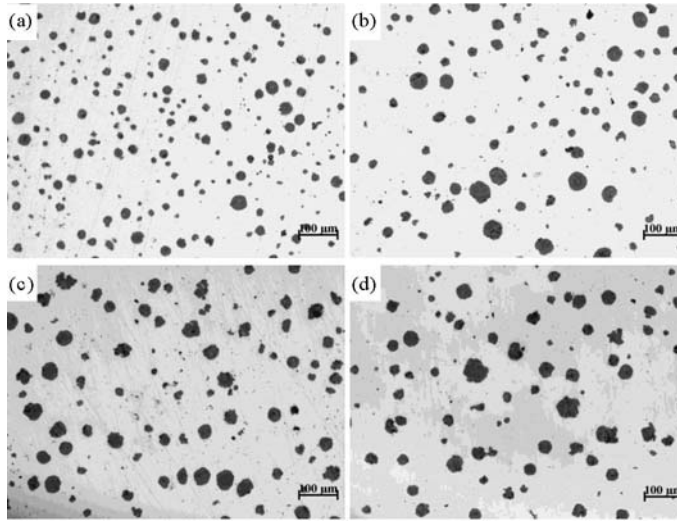

Fig.2 Distribution and morphology of graphite: (a) 0%Nb, (b) 0.038%Nb, (c) 0.074%Nb, (d) 0.094%Nb

The Image-Pro Plus graphic analysis software (Version 6.0) was adapted to measured the average diameter of graphite, as shown in Fig.3. With the increase of Nb content, the average diameter of graphite nodule increased firstly and then decreased, but the value of it changed range was not more than 5μm, which is not very large relatively. The average diameter of graphite were all in the range of 13~25μm, therefore, the effect of trace Nb on graphite diameter of ductile iron was slight which could almost be ignored.

According to the Chinese standard GB9941-1988, the nodularity and roundness of graphite nodule were calculated out, as shown in Fig.4. With the increase of Nb content, the nodularity of graphite in each kinds of samples were 89.8%, 88.9%, 87.3%, 88.4%, respectively, its nodularity grade belonged to level 3. And the roundness of graphite also increased slightly, which were 1.10, 1.17, 1.22, 1.17, respectively. Evidently, both the nodularity and roundness of graphite changed slightly.

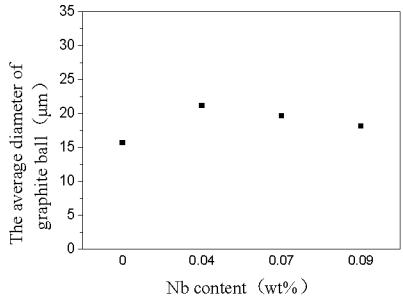

Fig.3 The relationship of the average diameter of graphite and Nb content

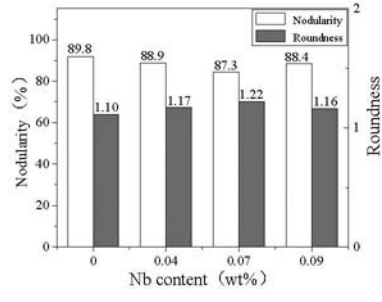

Fig.4 The relationship of nodularity and roundness of graphite and Nb content

Effect of Nb on the discreteness of graphite diameter

Five pictures about morphology and distribution of graphite in the matrix of each sample were taken into analyzed by Image-Pro Plus graphic analysis software (Version 6.0). Measured the number of graphite and diameter of graphite in each picture, and then got its average value, at finals, the diagram about the discreteness of graphite diameter could be got, as shown in Fig.5. The diameter of graphite nodule mainly concentrated in the range of 10~20μm for the 0wt% Nb sample. When the Nb content increased to 0.04wt%, each range of graphite diameter approached more evenly which range in 0~50μm, namely the discreteness of graphite diameter got larger. Whereas, when the Nb content added to 0.07wt% and 0.09wt%, the discreteness of graphite diameter got smaller relatively. Besides, with the increase of Nb content, the number of graphite nodule got bigger.

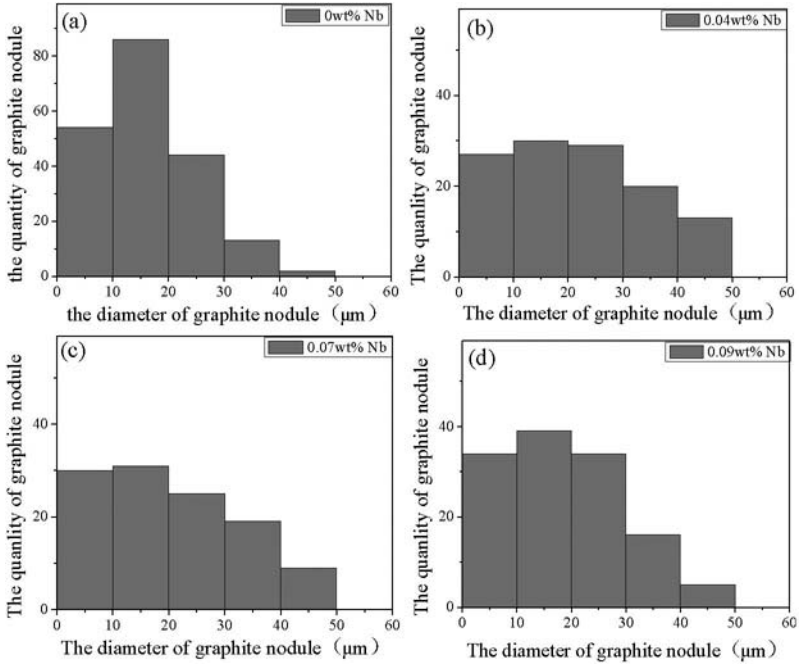

Fig.5 The relationship of discreteness of graphite diameter and Nb content

Variance was adapted to measure the deviation extent between the diameter of graphite nodule and its average. The Image-Pro Plus (Version 6.0) graphical analysis software and EXCEL software were used to calculate the variance of graphite diameter, as shown in Fig.5. The variance value changed between 80~160μm when the Nb content changed from 0wt% to 0.04wt%, 0.07wt% and 0.09wt%, respectively. Obviously, the variance value of graphite diameter increased firstly and then

decreased, and its change tendency was consistent with the discreteness of graphite diameter.

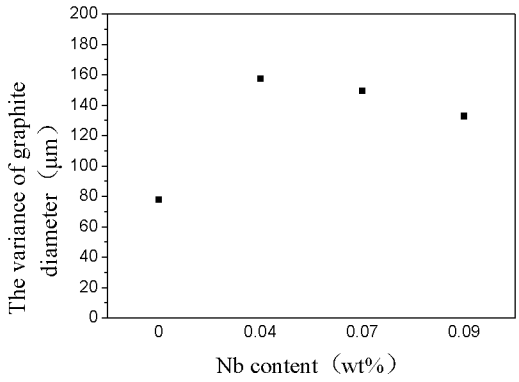

Fig.6 The relationship between variance and Nb content of graphite diameter

Conclusion

1. The two-dimensional morphology of Nb-rich phase existed in microalloyed ductile iron were mainly regular pattern, such as square, triangle, polygon etc.. With the increase of Nb content, the Nb-rich phase existed in the matrix increased. There were some individual Nb-rich phase gathering in the matrix when the Nb content reached 0.07 wt%.
2. With the increase of Nb content, the diameter of graphite nodule increased slightly. The value of the diameter increased less than 5μm, and the change of nodularity was about 2.5%. The change of roundness was about 0.1. Therefore, trace amount of Nb had little influence on the graphite diameter, nodularity and roundness of ductile iron.
3. According to the discreteness of graphite diameter and the calculation of variance, it could be found that the discreteness of graphite diameter increased with the increase of Nb content, which was consistent with the results of variance calculation. Meanwhile, the number of graphite nodule decreased.

Acknowledgement

The authors gratefully acknowledge the financial support from CITIC-CBMM niobium steel research and development fund (2013-D069).

References

[1] Junyan Fu. “The development and technological progress for Nb microalloying and steel containing Nb”. *steel*, 2005, 40(8): 1-5.
[2] QJ Zhai. “Application of Nb in Production of Cast Iron and Approaches the

Application Foreground". *Foundry*, 1998, 10: 41-46.
[3] Yongsheng Yan, Hongbo Zhu, Xiaoliang Sun, Qin Hua, Qijie Zhai. "Research about the mechanism of Nb to strengthen cast iron". *Modern Cast Iron*, 2011, (02): 24-27.
[4] Tommy Nylén. "Niobium in Cast Iron". *International Symposium on Niobium* 2001.
[5] Hongbo Zhu, Xiaoliang Sun, Rongsheng Yan, Qin Hua, Qijie Zhai. "The existence form of Nb in gray cast iron". *Modern Cast Iron*, 2011, (02): 33-36.
[6] Wenbin Zhou, Hongbo Zhu, Dengke Zheng. "Effect of Niobium on Solidification Structure of Gray Cast Iron". *Seattle, Washington: TMS (The Minerals, Metals & Materials Society)*, 2010.
[8] Xioaliang Sun, Hongbo Zhu, Yongsheng Yan, Qin Hua, Qijie Zhai. "The influence of Nb on wear resistance of high CE gray cast iron". *Modern Cast Iron*, 2011, (02): 52-56.
[9] T. Heller, I. Heckelmann, T. Gerber and T. W. Schaumann, "Potential of niobium in steels for the automotive industry". *Recent Advances of Niobium Containing Materials in Europe*, 2005, p. 21.
[10] GB9941-1988.*The examination of metallographic*.

Characterization of Minerals, Metals, and Materials 2015
Edited by: John S. Carpenter, Chenguang Bai, Juan Pablo Escobedo, Jiann-Yang Hwang, Shadia Ikhmayies, Bowen Li, Jian Li, Sergio Neves Monteiro, Zhiwei Peng, and Mingming Zhang
TMS (The Minerals, Metals & Materials Society), 2015

CAUSE ANALYSIS ON BUILDUP FORMATION OF CARBON SLEEVE IN CONTINUOUS ANNEALING FURNACE FOR NON-ORIENTED SILICON STEEL PRODUCED BY CSP PROCESS

Mingsheng He[1], Shoujun Peng[2], Gaifeng Xue[1], Yexian Ouyang[2], Jing Zhang[2], Huasheng Chen[1], Bin Liu[2]

[1]R&D Center of WISCO, Wuhan 430080, China;
[2]Silicon Steel Division of WISCO, Wuhan 430080, China

Keywords: CSP, non-oriented silicon steel, continuous annealing, carbon sleeve, buildup causes

Abstract

Based on the investigation and study of the topography, microstructure and composition of the buildups which form in the surface of carbon sleeve in continuous annealing furnace for low- and medium-grade non-oriented silicon steel produced by CSP process, combined with production process of silicon steel, the mechanism and major causes for forming buildups of carbon sleeve are discussed from the factors such as CSP process, the quality of carbon sleeve and so forth. Meanwhile, some countermeasures to reduce the formation of the buildups are put forward.

Introduction

Characterized by short process, low energy consumption and high efficiency, CSP (Compact Strip Production) process has developed rapidly in recent 20 years in China. At present, 14 short process production lines have been built and under construction domestically, covering from super-low carbon steel, low carbon steel to medium carbon steel, low alloy steel and so on [1]. The non-oriented silicon steel produced by CSP process can reach a higher finishing temperature under the condition of low heating. Due to the special cast structure of steel products, uniform temperature of the rolled pieces and full recrystallization of hot rolled plates, the magnetic induction obviously increases. Compared with the traditional hot rolling production process, in terms of temperature control, CSP process is more suitable for the production of non-oriented silicon steel and is an important innovation of silicon steel production process [2-5]. Silicon steel manufacturers using CSP process at home and abroad include the Nucor Crawfordsville in USA, the AST in Italy, TKS in Germany, the Hylsa in Mexico, ACB in Spain, Wuhan Iron and Steel (Group) Company(WISCO), Benxi Iron & Steel Group and so on in China. Many companies have realized the mass production of low- and medium-grade non-oriented silicon steel [6-8].
After CSP continuous casting and rolling, low- and medium-grade non-oriented silicon steel need go through cold tandem rolling and continuous annealing process. Silicon steel strip by cold rolling is decarburized, re-crystallized and annealed in continuous roller-hearth annealing furnace. The carbon sleeve is mainly used to support and convey steel strip in continuous annealing furnace [9-10]. During the decarburizing and annealing of low- and medium-grade non-oriented silicon steel in traditional production process, the service life of carbon sleeves is much longer, and embedded buildups seldom appear in the surface of carbon sleeves, while in CSP process, a lot of carbon sleeves frequently produce buildups only in 10-15 days of operation. Once embedded buildups come into being, they will easily indent, bruise and scratch the surface of steel strip, which seriously affects the quality of steel strip surface and even causes degraded

or waste products. The service life of carbon sleeve is shortened due to the shutdown caused by frequently grinding or changing rollers in production, which not only severely influences the production efficiency, but also causes huge economic losses to the company [9]. There are few literatures and researches on buildup formation of carbon sleeve in continuous annealing furnace for non-oriented silicon steel produced by CSP process. In this research, based on the analysis of embedded buildups forming in the surface of carbon sleeve during the decarburizing and annealing in CSP process, major causes for forming buildups of carbon sleeve in continuous annealing furnace for low- and medium-grade non-oriented silicon steel are discussed.

Buildup Topography and Composition Analysis

Topography of Buildups

Fig. 1 shows the embedded buildups forming in the surface of carbon sleeve during the decarburizing and annealing for low- and medium-grade non-oriented silicon steel produced by CSP process. Fig. 1(a) and 1(b) are in cylinder shape, and the axial direction of buildups parallels that of carbon sleeve. Most buildups produced during production are in cylinder shape, 1-5mm in length, 0.5-2mm in diameter, but a small number of buildups are in short column shape (Fig. 1 (c)), even in irregular shape (Fig. 1(d)). The buildups in cylinder shape are not like those produced in the surface of carbon sleeve by other processes in relatively regular cylinder shape, which may be greatly related to the short time of buildup formation.

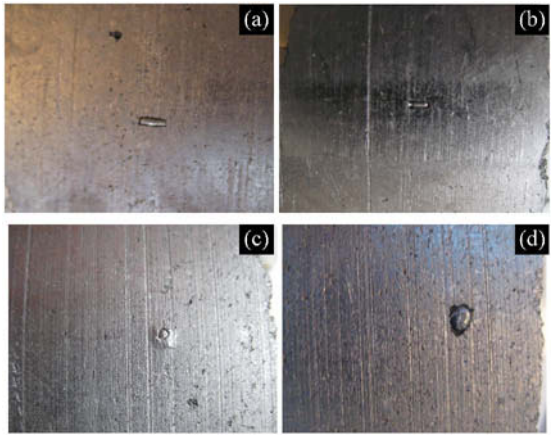

Fig. 1 Embedded buildups in the surface of carbon sleeve

Buildup Composition Analysis

In order to figure out the inner structure and compositions of the embedded buildups, the buildups are sectioned along radial, and then inlaid, ground, and polished. The as-prepared samples were observed and analyzed by a scanning electron microscope (SEM) (Quanta 400, FEI Co., Netherland) equipped with energy-dispersive X-ray spectroscopy (EDS).
The buildups forming in CSP process are in different shapes and sizes, but the buildup in slender cylindrical shape in Fig. 1(a) are relatively representative. Therefore, this buildup is selected as the key research object. Fig. 2(a) is the cross-section SEM micrographs of the buildup, its

diameter is about 0.8 mm, and there is a hole with the diameter of 0.5mm in the center. Figures 2 (b-f) are cross-section SEM micrographs of the different region partially enlarged. The structures are not as compact as those of other embedded buildups by other processes. Although there are some light and dark color annular belts, the regularity of light and dark belts is not obvious, which is not that kind of alternately dark and bright concentric circles of light and dark belts [9]. Fig. 3(b-f) are the corresponding EDS spectrums of Fig. 2(b-f) respectively. Table 1 is the result of EDS composition analysis in the different positions. The results show that the dark color belts of buildups are oxides of Al, Si, Cr, Mn, Fe. Cr may mainly come from chromium anhydride penetrated in carbon sleeves. The mass percent averages of Al, Si, Cr, Mn, Fe at the positions of three dark color belts 1, 2, 3 are respectively 2.84%, 18.31%, 4.18%, 7.37%, and 34.13%, among which Mn content at the position of 1 is as high as 11.95%. Si contents at the positions of 2 and 3 are as high as 19.04% and 22.78% respectively. Dark belts at the positions of 2 and 3 contain small amount of Mg and Ca. Al, Si, Cr, Mn, Fe contents of dark belts shown in Fig. 2(e) are 1.67%, 13.86%, 7.37% and 53.98%, which are much higher than those at other positions, and no Mg and Ca. Light belt positions shown in Fig. 2(f) only contain Fe and Si, with the content of 98.62% and 1.38%. According to the composition analysis results, Mn content of embedded buildups in CSP process is higher, which varies greatly from the buildups forming in the production of other products. Therefore, buildups are basically oxidation-reduction reaction products, and only Fe is reduced. Si, Mn, Al and Cr still exist in reduced iron substrates in the form of oxides, which result from different thermodynamics and kinetics conditions of oxidation-reduction physical and chemical reaction of various elements.

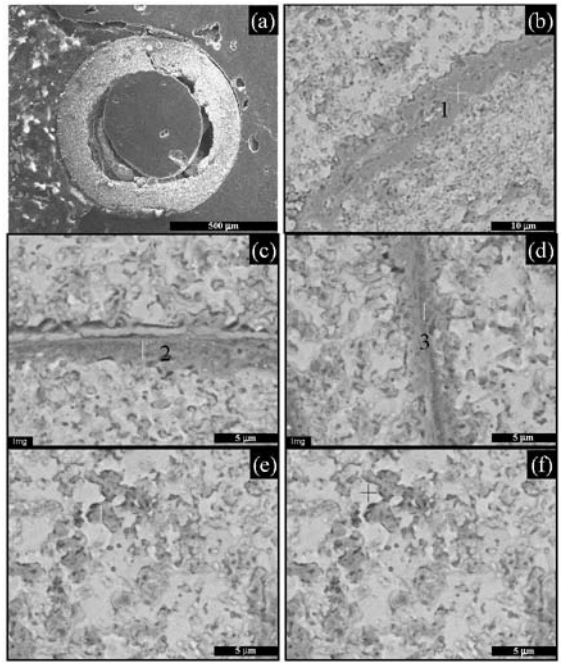

Fig. 2 Cross-section SEM micrographs of the buildup:(a) general view; (b-f) partially enlarged.

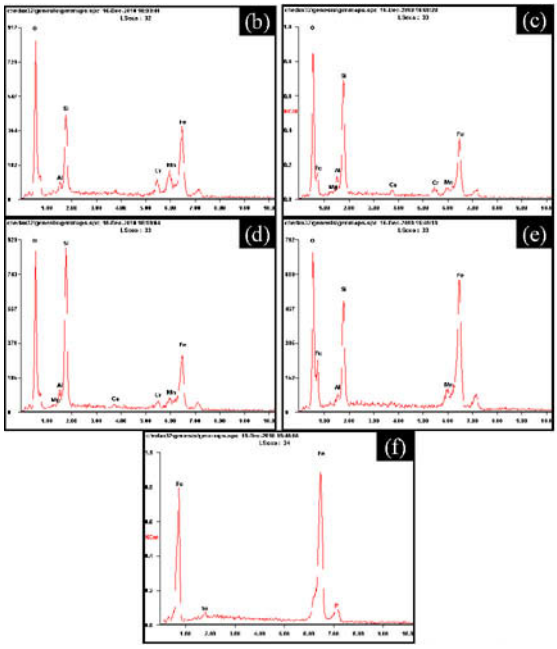

Fig. 3 EDS spectrums at different positions of the buildup.

Table 1 EDS composition analysis of buildup (%)

Analysis section	O	Mg	Al	Si	Ca	Cr	Mn	Fe
Dark color belt 1	29.42	—	2.09	13.10	—	6.25	11.95	37.18
Dark color belt 2	33.41	0.89	3.47	19.04	1.11	3.08	4.88	34.11
Dark color belt 3	33.20	0.82	2.97	22.78	0.65	3.21	5.27	31.09
Dark position	23.12	—	1.67	13.86	—	—	7.37	53.98
Light position	—	—	—	1.38	—	—	—	98.62

Causes for Buildup Formation of Carbon Sleeve

According to the results of the analysis above, it can be seen that the embedded buildups experience the "nucleation-growing up" process, and the main components are iron, a small amount of iron oxide, and oxides of Al, Si, Cr, Mn, Mg, Ca and so on. Obviously, the two necessary conditions for buildup formation are: (1) there exist pores in the surface of carbon sleeve; (2) rich material sources such as iron scale, iron rust, greasy dirt, dust, etc [9]. In combination with the study on the topography, composition and formation mechanism of buildups as well as the actual CSP technology and process of low- and medium-grade non-oriented silicon steel, it is proposed that formation of embedded buildups in short time is mainly related to CSP technology and the quality of carbon sleeve.

CSP Process

The elements of Si, Al, Mn, etc. in non-oriented silicon steel must be controlled within a certain range while C, S, N and O are harmful elements. The requirements of these elements are different according to different grades, different production process and conditions. Si is the most important alloy element for silicon steel because it can be dissolved in ferrite to form the substitution solid solution, improve matrix resistivity, decrease iron loss. Al can be dissolved in the ferrite to improve the matrix resistance, coarse crystal grains, and reduce the iron loss, meanwhile, also can be deoxidized nitrogen fixation, but likely to cause surface internal oxidation of the steel sheet product. Mn can increase the resistivity of steel, lower iron loss, form stable MnS with inevitable impurity S, eliminate the hazards of S on magnetic, can also prevent the hot brittlement, which is also dissolved in the ferrite to form substitution solid solution, and has lower iron loss function. Si, Al, Mn, Fe and other elements in silicon steel easily can be oxidized to form SiO_2, Al_2O_3, MnO, FeO, Fe_3O_4, Fe_2O_3 and other oxides, and may occur in the solid phase reaction between these oxides at lower temperatures, even the formation of eutectic liquid phase occurs at low temperature, such as the following reaction between Al_2O_3 and MnO is likely to occur at lower temperatures:

$$Al_2O_3 + MnO = MnAl_2O_4 \quad (1)$$

Especially, Mn content is relatively high in the production of non-oriented silicon steel by CSP process, which is also consistent with the component analysis results of buildup. Meanwhile, the descaling is not sufficiently in CSP process likely to produce more iron scale and inclusions in the steel surface, and many other problems will cause the steel plate surface to generate a large number of iron oxide, for example pickling is not sufficient, cold rolling heating temperature is too high, holding time is too long and so on. Therefore, during the production of non-oriented silicon steel by CSP process, multiple links may provide a rich source of iron scale, inclusions, dust and other substances for buildups formation.

Quality of Carbon Sleeve

Graphite is chemically inert in non-oxygen media. At normal temperature and pressure, graphite does not make any chemical reactions except the long-term immersion in nitric acid, hydrofluoric acid or in fluorine, bromine and other strong oxidizing atmosphere leads to form intercalation compounds slowly. Graphite is not subject to any acid, alkali and salt corrosion and does not react with any organic compound [9-10]. However, due to complex procedures and processes of producing carbon sleeves together with porous material itself, it is inevitable to form larger holes in the surface during production and processing. Carbon sleeves under different molding processes are shown in Fig. 4. Fig. 4 (a) shows carbon sleeve by extrusion forming (EF), and Fig. 4 (b) carbon sleeve by cool isostatic compression (CIP). As can be seen from the Fig. 4, the carbon sleeve in Fig. 4 (a) has high porosity, large stomatal aperture, and many long and narrow holes while the carbon sleeve in Fig. 4 (b) has higher density, even though there are many pores, its aperture is very small. In the actual production process, the performances of oxidation resistance, buildup formation resistance, and wear resistance of carbon sleeve by CIP are better than that by extrusion forming [10].

Generally speaking, graphitization degree of carbon sleeve is over 70%. Although the surface of carbon sleeve is smooth after soaking of various chemical substances and processing, graphite begin to react with water vapor over 700℃, with CO and CO_2 over 900℃. The carbon in silicon steel has great influence on the magnetic. Carbon not only strongly inhibits grain growth, but

also expands γ phase zone. Hence, the excessive amount of carbon makes the shift quantity of two phases α and γ increase in normalizing treatment, and refines crystal structure, causing the increase in iron loss.

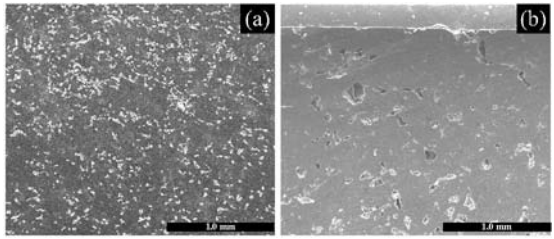

Fig. 4 Carbon sleeves by different forming processes: (a) EF; (b) CIP.

One of the important purposes of the annealing to the finished product of silicon steel is decarburization, therefore, holes inevitably appear due to oxidation during the use of carbon sleeves in continuous annealing furnace for silicon steel. As a result, these holes provide the necessary conditions for stubborn embedded buildups to form. When there are larger holes together with rich iron scale, iron rust, greasy dirt, dust, and other material sources, the stubborn embedded buildups could form in a relatively short time.

Other Factors

Many factors influence buildup formation of carbon sleeves, such as furnace atmosphere, dew point, uncleanness of alkali wash, outer-sync of the actual speed of carbon sleeves and the running line speed of steel strip, uncleanness of inside furnace, etc. These factors cause certain effect on buildup formation of the carbon sleeves of in continuous annealing furnace for low- and medium-grade non-oriented silicon steel produced by CSP process, but frequent buildup formation in a short time shows that these factors are not basic causes, and the main reason is that these buildups are caused by CSP process and defects of carbon sleeve by itself.

Measures to Control and Reduce Buildups

Compared with traditional technological process for steel sheet, silicon steel production by CSP process has its unique advantages. According to some defects of CSP process and the present annealing technology, equipment and conditions, it is impossible to completely eliminate buildups, but it is possible to take some process control in technology or preventive measures to reduce buildup formation. In order to control and reduce buildup formation, extend the service life of carbon sleeve, the following methods and measures are put forward:

(1) Improve descaling equipment and process, strengthen the pickling, and reduce iron scale and the source of inclusions;

(2) Under the condition of guaranteeing rolling temperature, strictly control the heating temperature and soaking time, and avoid producing a large amount of iron scale due to the local overheating of steel plate surface.

(3) Improve the surface quality of carbon sleeve and enhance its performances of oxidation resistance, wear resistance, buildup formation resistance;

(4) Strictly monitor atmosphere and dew point in annealing furnace;

(5) Strengthen the cleanness of steel strip and alkaline wash;

(6) Clean dust regularly in continuous annealing furnace;
(7) Regularly monitor and correct the motor of carbon sleeves and adjust the inconsistent roller speed of carbon sleeves in time.

References

1. W. Tan, B. Han. "Analysis of Surface Scar in CSP Products," *Continuous Casting*, 2010, (6): 35-38.
2. X.Y. Wang, X.H. Liu. "Current State and Advantages on Developing Electrical Steels in CSP Process," *China Metallurgy*, 2005, 15(12): 39-43.
3. L.F. Fan, E.B. Yue, L. Xiang. "Structure and Inclusion of High Grade Non-oriented Electrical Steel Produced in CSP Process", *Journal of Iron and Steel Research*, 2008, 20(1): 32-36.
4. C.Y. Li, T. Zhu, Z.D. Liu, et al. "Texture of Hot-rolled Non-oriented Electrical Steel by CSP Process," *Iron and Steel*, 2007, 42(7): 56-58, 71.
5. T. Zhu, E.B. Yue, L. Xiang, et al. "Experimental Study on Normalizing of High Grade Non-Oriented Electrical Steel Produced by CSP Process," *Journal of Iron and Steel Research*, 2010, 22(1): 32-36.
6. T. Zhu, Y.J. Wang, X. Zhai, et al. "Development of full-processed non-oriented electrical steel in a CSP line," *Journal of University of Science and Technology Beijing*, 2009, 31(7): 862-866.
7. Y. Sun, J. Li, Y. Zhao, et al. "Effect of Slab Reheating Temperature on Magnetic Properties of Non-oriented Electrical Steel Prepared by CSP Simulated," *Metallic Functional Materials*, 2008, 15(1): 5-7.
8. Y. Sun, J. Li, Y. Zhao, et al. "Effect of normalizing and annealing on magnetic properties of non-oriented electrical steel produced by simulated CSP process," *Special Steel*, 2008, 29(2): 10-12.
9. M.S. He, S.J. Peng, G.F. Xue, et al. "Cause analysis about buildup formation of carbon sleeve in continuous annealing furnace for silicon steel," *Advanced Materials Research*, 2011, 317-319: 1954-1959.
10. M.S. He, S.J. Peng, G.F Xue, et al. "Cause analysis about breakage of carbon sleeve in continuous annealing furnace for silicon steel," *Iron and Steel Research*, 2012, 40 (supplement): 24-27.

Characterization of Minerals, Metals, and Materials 2015
Edited by: John S. Carpenter, Chenguang Bai, Juan Pablo Escobedo, Jiann-Yang Hwang, Shadia Ikhmayies, Bowen Li, Jian Li, Sergio Neves Monteiro, Zhiwei Peng, and Mingming Zhang
TMS (The Minerals, Metals & Materials Society), 2015

ANALYSIS OF THE FEASIBILITY OF USING SOIL FROM THE MUNICIPALITY OF GOYTACAZES/RJ FOR PRODUCTION OF SOIL-CEMENT BRICK

Alexandre, J.[1], Azevedo, A.R.G.[1], Theophilo, M.M.D.[1], Xavier, C.G.[1], Paes, A.L.C.[1], Monteiro, S.N.[2], Margem, F.M.[3], Azeredo, N.G.[1]

[1]UENF - State University of the Northern Rio de Janeiro, LECIV – Civil Engineering Laboratory; Av. Alberto Lamego, 2000, Campos dos Goytacazes, Rio De Janeiro, 28013-602, Brazil.

[2] IME - Military Institute of Engineering, Department of Materials Science, Praça General Tibúrcio, 80, Rio de Janeiro, Rio de Janeiro, 22290-270, Brazil.

[3] UENF - State University of the Northern Rio de Janeiro, LAMAV - Advanced Materials Laboratory; Av. Alberto Lamego, 2000, Campos dos Goytacazes, Rio De Janeiro, 28013-602, Brazil.

Keywords: Soil-cement, brick and civil construction.

Abstract

The use of bricks of soil-cement is proving to be an important constructive methodology due to low environmental impact in the production process of these blocks comparing with conventional bricks are burnt, besides being easy to produce. However during the process of production of bricks, which are compressed, knowledge of the properties of the soil used is critical to the quality and durability of the blocks. The objective of this work is to evaluate the feasibility of using soil from the municipality of Goytacazes for the production of soil-cement bricks. Assays were performed the compaction, liquid limit, plastic limit, particle size analysis, EDX and X-Ray diffraction for later pressed blocks and analyze their compressive strength and water absorption.

Introduction

The issue of sustainability has been widely discussed around the world, by government or private entities. The carbon rate has been increased year after year, changing the environmental, causing more damages each day. A main barrier to be overcome by the society is to find out solutions in different kinds of sectors which aim at sustainability case.

Nowadays, one of the most harmful productive sectors is civil construction, being responsible for most part of gas emissions and generated waste, contributing in this context, the production of inputs and constructive step.

Besides, Brazil suffer with a huge housing deficit, according to Lima Neto *et al.* [1], in 2012 represented approximately 5,24 millions of houses, to amount to 8,53% of Brazilian families. However, this deficit has been falling with government policies as the project *Minha Casa, Minha Vida,* that has the main goal build houses for people who have more financial vulnerability.

In this context comes a solution that is building using soil cement brick, that is not innovate but it is not commonly used. This method of construction can ally practicality, economy and sustainability and also reduce the problem of housing deficit in Brazil (Figure 1).

Figure 1. Soil cementer construction

According to Portland Cement Brazilian Association soils having more percentage of sandy are stabilized with less quantity of cement, being necessary clay in its composition, aiming to give the mixture cohesion enough for the immediate withdrawal of forms, when moistened and compacted [2].

One of vantages of using soil cement is the possibility of utilization the local soil, having more proportion in the mixture, allowing less possible quantity of cement. In this way, the low environmental effect can be justified because this brick is not fired (fitting block) and the proportion of cement, a material extremely pollution in its production process, is low.

The goal of this project is the soil characterization from the municipality of Campos dos Goytacazes, located in Rio de Janeiro, for production of soil cement bricks, with 5%, 10% e 15% of cement addition and do test as mechanical resistance to compression and water absorption, which are important for this kind of material, being its values compared with the limits stipulated by Brazilian standard.

Materials and Methods

First of all, the soil was collected from a deposit located in Campos dos Goytacazes city and transported to Civil Engineering Laboratory (LECIV) of State University of the Northern Rio de Janeiro. Once at LECIV, it was correctly identified and separated in two parts, one to begin the physical and chemical characterization and the other part to bricks production.

To physical analyses the soil was processed according to NBR 6457 [3], which describes preparation procedures to compaction and characterization test (particle size analyses, determination of Atterberg limits and determination the real density of particles).

The particle size distribution curve, assay which determines the soil particle size and relative proportions, was performed by sieving and sedimentation according to NBR 7181 [4]. Later, the Atterberg limits were determinate (liquid limit, plastic limit and plasticity index), to, together with compaction test to identify the workability to find out the best ratio of water which must to be added to the mixture, according to NBR 6459 [5] (liquid limit) and NBR 7180 [6] (plastic limit). According Portland Cement Brazilian Association (ABCP), the liquid limit should be inferior than 45% and of plasticity index inferior than 18%.

After drying at 110ºC for 24 hours, samples of the clay body were homogenized by quartering and the density of the particles was measured according to the norm [7]. The particle size distribution was then determined by the sieving and gravimetric method according to the norm [4]. The chemical composition was obtained by X-ray dispersive energy in a model EDX 700 Shimadzu spectrometer. The mineral phases were determined by X-ray diffraction (XRD) in a model DRX 7000 Shimadzu diffractometer operating with CuKα radiation at 40 kV and 110 mA, with 2θ angle, varying from 5 to 80ºC in steps of 2º/min.

Using the second part of soil prepared initially, the mixture of soil cement was held, on a mechanic mixer, brand CSM, and the water was added to ensure ideal humidity of blocks, and this addition should be done with a manually spray to avoid the advent of lumps until the correct homogenization of mixture. After the mixture preparation, the bricks were molded using manual press Vimaq model V2, where the pressure of molding was kept constant between the blocks. With this method, a sample was prepared containing 21, and with this quantity was possible to have reliability at the mechanical assays (Figure 2).

Figure 2. Manual press Vimaq model V2 used to molding bricks.

Once the blocks were made, the rebounds withdrawal was carried out from the fitting surface, keeping uniform the distribution of load at rupture time and subsequent capping with cement paste, forming a prism with two blocks that was ruptured in press, Solotest brand, which velocity of rupture was 50kgf/s[8], and based on Brazilian standard the resistance of soil cement bricks should be superior than 2MPa.

At the same time, was realized the water absorption assay [8], putting the blocks immersed in water at ambient temperature (23ºC), weighing it before and after immersion. According Brazilian standard, the soil cements blocks should present maximum average water absorption of 20%, and no singular result should be over than 22% at 28 days old.

Results

Figure 3 shows the particle size distribution curve of the raw material, which may consist of a mixture of clays from different quarrying as well as sand to reduce the plasticity of the clay

body. In this figure one sees that the so-called "clay fraction", corresponding to particle sizes (d) below 2 μm is 43.00%, while the "silt fraction" (2 < d < 20μm) is 13.20% and the "sand fraction" (d > 20μm) is 37.60%. After drying, a comparison between the weights in 20 samples revealed a humidity content around 34% in the as-collected raw material.

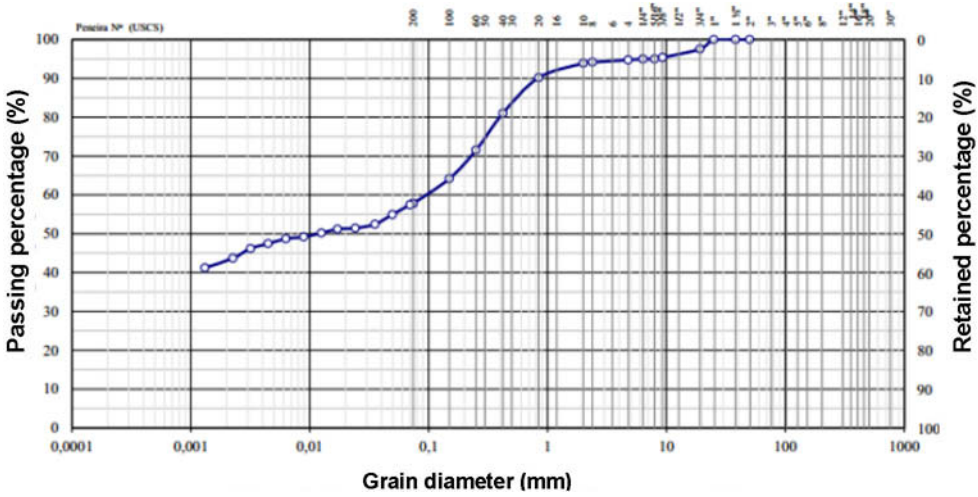

Figure 3. Particle size distribution of the raw material.

The chemical composition of the raw material obtained by XRF, is presented in Table 1 In this table the relative proportion between the silica (SiO_2) and the alumina (Al_2O_3) is consistent with the predominance of clay minerals. However, one should remember that SiO_2 may also exist as free quartz in the sand particle, while aluminum may also be in the form of another mineral such as gibbsite.

Table 1 – Chemical composition by XRF of the raw material given in terms of oxides (%).

SiO_2	Al_2O_3	Fe_2O_3	K_2O	SO_3	TiO_2	CaO	MnO	V_2O_5	ZrO_2	CuO	SrO
45.36	38.90	9.10	2.03	2.20	1.40	0.70	0.05	0.20	0.01	-	0.007

The mineralogical analysis of the precursor clay body by XRD of a dried, ground and 200 mesh sieved sample is shown in figure 4. In this figure, the most prominent and frequent peaks are those of quartz (Q), kaolinite (Ka) and goethite (Go).

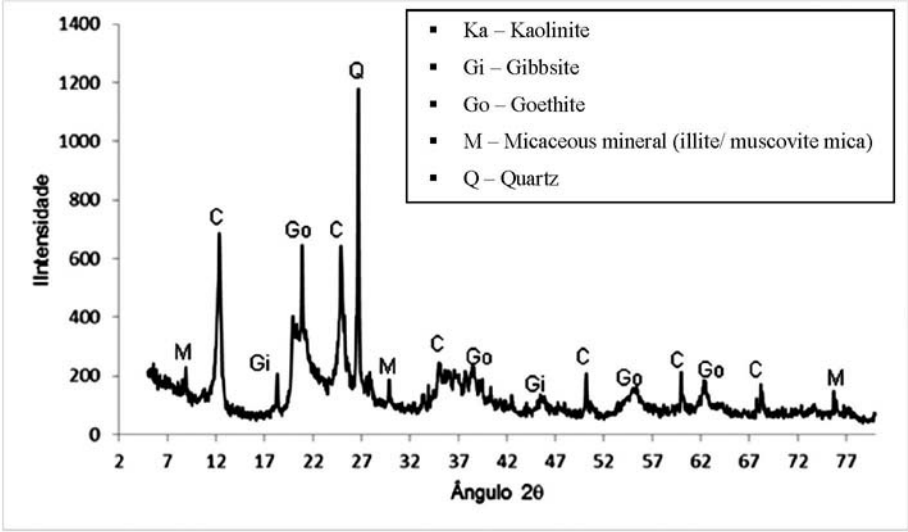

Figure 4. X-ray diffraction.

The Atterberg limits and the real density of particles of the precursor clay body are presented in Table 2.

Table 1. Atterberg limits and real density of the clay body.

Flow Limit	Plasticy Limit	Plasticity Index	Real Density of Particles (g/cm^3)
33.6%	20.5%	13.1%	2.67

The table 3 shows the medium values of the compression rupture strength of all the bricks of each type of soil-cement formulation. It is important to mention that the minimum average strength for soil-cement bricks is 2.0 MPa and no individual value should be inferior to 1.7 MPa [9] (after 28 days). Based on this norm, types 0% and 10% not attend the above requirements. In fact, only type 15%, with an average 2.33 ± 0.72 MPa and all values above 1.7 MPa, is within the specification for soil-cement brick [9].

Table 3. Compression rupture strength (MPa).

Rupture age	5%	10%	15%
7	0.20 ± 0.69	0.56 ± 0.35	1.10 ± 0.45
14	0.30 ± 0.60	0.86 ± 0.33	1.45 ± 0.52
28	0.42 ± 0.62	1.13 ± 0.36	2.33 ± 0.72

The average results of water absorption at soil cement block were not done on block of 5% and 10%, because the results of compression were not satisfactory.

Table 4. Average water absorption (MPa).

	5%	10%	15%
Water absorption	23.00	25.02	16.06

Conclusion

According this paper, can be concluded that exists different types of soil in north of the state of Rio de Janeiro, Brazil (region analysis). This soil objective in this study is appropriate to produce soil cement bricks, according the Brazilians Standards parameter and had revealed important characteristics, based on indicated proportions (due to the fact that distribution of particle size and physical index).

The resistance and water absorption is very important parameter about use in materials of the construction because evaluation resistance and durability of blocks. In this work are analyzed 5, 10 and 15% of cement addition, conclusion with 15% were within the parameters established by Brazilians standards (compression rupture strength and water absorption).

Must aware to the variability of soils in this region and the water percentage should be added in each case.

Acknowledgements

The authors thank the Brazilian agencies: CNPq, CAPES and FAPERJ for the support provided to this investigation.

References

1. F.J. Casanova, Soil as a construction material (in Portuguese), Revista Habitare, 4 (2004) 23-30.
2. Brazilian Association of Portland Cement – ABCP. Fabrication of soil-cement bricks using manual press equipment (in Portuguese). Pub. ABCP, São Paulo, Brazil, 1985
3. Brazilian Association of Technical Norms –ABNT NBR-6457, Soil samples – compaction tests and characterization tests (in Portuguese), Rio de Janeiro, Brazil, 1986.
4. Brazilian Association of Technical Norms –ABNT NBR-7181, Soil - Granulometric Analysis (in Portuguese), Rio de Janeiro, Brazil, 1988.
5. Brazilian Association for Technical Norms - ABNT NBR-6459, Determination of the fluidity limit (in Portuguese), Rio de Janeiro, Brazil, 1984.
6. Brazilian Association of Technical Norms –ABNT NBR-7180, Soil – Determination of the Plasticity Limit (in Portuguese), Rio de Janeiro, Brazil, 1988.
7. Brazilian Association of Technical Norms –ABNT NBR-6508, Soil – Determination of the Specific Mass of Particles (in Portuguese), Rio de Janeiro, Brazil, 1984.
8. Brazilian Association of Technical Norms –ABNT NBR-8492, Soil-cement brick - Dimensional analysis, compressive strength determination and water absorption - Test method (in Portuguese), Rio de Janeiro, Brazil, 2012.
9. Brazilian Association for Technical Norms - ABNT NBR-8491, Solid soil-cement brick – Specification (in Portuguese), Rio de Janeiro, Brazil, 1984.

Characterization of Minerals, Metals, and Materials 2015
Edited by: John S. Carpenter, Chenguang Bai, Juan Pablo Escobedo, Jiann-Yang Hwang, Shadia Ikhmayies, Bowen Li, Jian Li, Sergio Neves Monteiro, Zhiwei Peng, and Mingming Zhang
TMS (The Minerals, Metals & Materials Society), 2015

EFFECTS OF NIOBIUM MICROALLOYING ON THE PEARLITE OF DUCTILE IRON

Chao Yang[1], Wei Zhang[2], Haicheng Li[1], Xiangru Chen[1], Qijie Zhai[1]

1. Shanghai Key Laboratory of Modern Metallurgy & Materials Processing Shanghai University, Shanghai 200072, China
2. CITIC Metal Co., Ltd, Room 1903, Capital Mansion 6 Xinyuan Nanlu, Chaoyang District, Beijing 100004, China.

Keywords：Niobium, Ductile Iron, Pearlite, Pearlite Lamellar Spacing

Abstract

In this paper, ductile iron material with different content of niobium was prepared by a scientific melting method. Image Analysis Software was used to studied the effect of niobium microalloying on both pearlite content and pearlite lamellar spacing in ductile iron quantitatively. The results showed that the addition of a small amount of niobium could increase the pearlite content and decrease pearlite lamellar spacing of ductile iron effectively.

Introduction

Niobium has been widely used as an alloy element in the steel and iron for a long time. As the strong carbide forming element, niobium carbide it formed in matrix play a significant role in dispersion strengthening effect. Therefore, it improved the strength, ductility and toughness properties of iron[1~3].As a high melting point alloy element, the addition of a small amount of niobium in steel could improve the hardenability of steel effectively for the reason that niobium delayed the transformation time from austenite structure to pearlite structure[4].

In recent years, the application of niobium added in the steel act as the microalloying element also developed very quickly. This mainly contributed to the reason that compared with other alloying elements, the addition of only 0.001%~0.1% in steels could significantly improve its mechanical properties[5]. Hardy Mohrbacher[6] has researched very deeply about niobium microalloying in high strength automotive steel. Besides, Qijie Zhai, Wenbin Zhou et al [7~9] have deeply researched the existed form of niobium in cast iron and its fundamental role. But until now, researches about the effects of niobium on the changes of pearlite content and pearlite lamellar spacing in ductile iron were still relatively lacking and not comprehensive enough. So in this research, this was the main work.

Experimental Procedure

The raw materials, including casting pig iron, 75SiFe, 80MnFe, pure copper, pure nickel and niobium iron were added into induction furnace to get the ductile iron with designed chemical composition of 3.9%C, 1.9%Si, 0.3%Mn, 0.4%Cu, 0.6%Ni and 0~0.1%Nb. The main chemical component of nodularizer in this experiment was FeSiMg7RE5, with dosage of 1.2%. And the main component of inoculant was 75SiFeAl, with dosage of 0.8%. Both of them were added by pour-over treatment process. At finals, the chemical composition of four samples was showed in table Ⅰ.

Table Ⅰ Chemical composition of the samples（wt%）

sample	C	Si	P	Mn	Cu	Ni	S	Nb
1#	3.9	1.9	0.06	0.34	0.46	0.61	0.017	0
2#	3.9	1.9	0.07	0.38	0.47	0.64	0.016	0.038
3#	4.0	1.9	0.07	0.36	0.46	0.61	0.016	0.074
4#	4.0	1.8	0.07	0.37	0.46	0.60	0.017	0.094

Result and Discussion

Effect of Niobium on the pearlite content of ductile iron

The composition of phase content in the matrix (the relative distribution of graphite, pearlite and ferrite content) determined the tensile strength and hardness et al mechanical properties of ductile iron. Generally, pearlite microstructure acted as the main force-resistance phase in ductile iron matrix. Therefore, the higher pearlite content in matrix, the larger tensile strength material was. In this experiment, 4% nital was used to corrode the metallographic specimens. Finally, the typical pictures of ductile iron matrix were showed in Figure 1. Evidently, with the increase of niobium content in ductile iron, the content of ferrite (white bull eye like shape) gradually reduced, and that was to say, pearlite content increased gradually.

According to the national standard GB9941-2009 of China [10], pearlite content in ductile iron was analyzed quantitatively by Image-Pro Plus software. After statistic treatment, pearlite content values with different content of niobium were shown in Figure 2. For the 0% Nb containing sample, its pearlite content was 76.5%, which belonged to 75 pearlite level. When added 0.038%, 0.074% and 0.094% Nb in ductile iron, the pearlite content it contained were 85.4%, 89.7% and 91.6% respectively. As for the first two samples, they belonged to 85 pearlite level, and the last sample belonged to 95 pearlite level. It was obvious that the addition of niobium promoted the increase of pearlite content in ductile iron. This was because the existed NbC phase restrained the diffusion of carbon atoms in the liquid metal during solidification process, therefore decreased the graphite nodule content and naturally increased the

pearlite content of ductile iron.

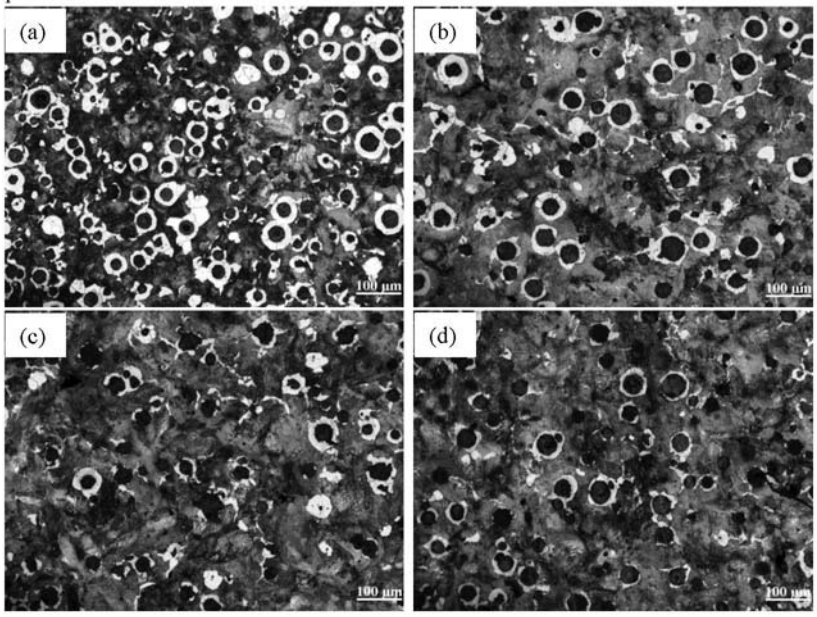

Figure 1 Cast microstructure of ductile iron: (a) 0%Nb, (b) 0.038%Nb, (c) 0.074%Nb, (d) 0.094%Nb

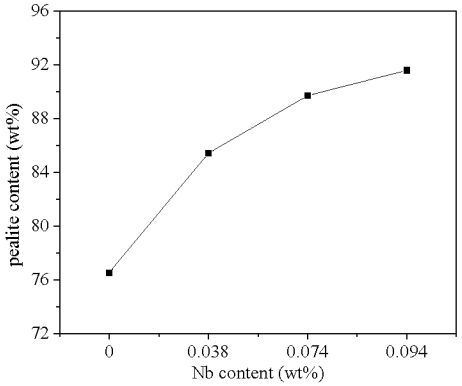

Figure 2 The relationship of niobium content and pearlite content

The effect of niobium on pearlite lamellar spacing

As for the ductile iron with lamellar pearlite microstructure in matrix, the lamellar spacing of pearlite determined the mechanical properties of the pearlite, and then

affected the mechanical property of ductile iron. Generally, the smaller pearlite lamellar spacing was, the better both hardness and tensile strength of material were. That was because when pearlite affected by external force, plastic deformation almost occurred in ferrite, and cementite layer it contained prevented the slip of dislocation. For the dislocation in materials, the maximum slip distance in pearlite was the lamellar spacing. Hence, smaller lamellar spacing in pearlite resulted in larger phase interface between ferrite and cementite in per unit volume. Of course, bigger plastic deformation resistance contributed to higher hardness and strength. After the samples et alhed by 4% nital, Carl Zeiss Scanning Electron Microscope was used to observed the pearlite lamellar spacing with different niobium content under the amplification of 5000 times which were shown in Figure 3.

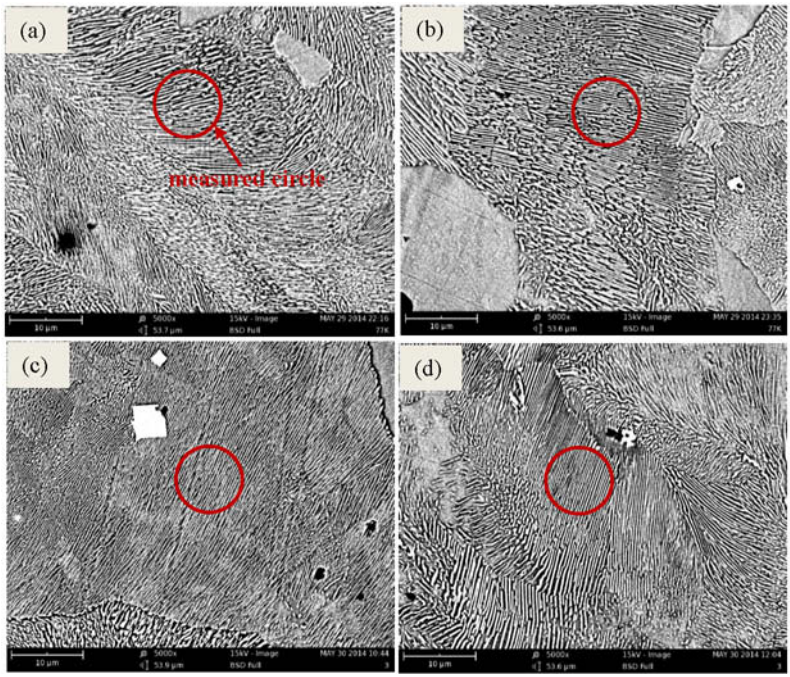

Figure 3 Pearlite microstructure: (a) 0%Nb, (b) 0.038%Nb, (c) 0.074%Nb, (d) 0.094%Nb

The method provided by literature [12] was adopted to quantitatively measure the pearlite lamellar spacing. Detail process described as follows: covered the pearlite with a constant diameter circle (25 mm) in the high amplification times pictures, as shown in Figure 3, then counted out the number of intersections between circumference and cementite layer.

$$S = \frac{\pi D}{nM} \qquad (1)$$

S: random pearlite lamellar spacing
D: constant diameter (25mm)
n: the number of intersections between circumference and cementite layer
M: amplified times

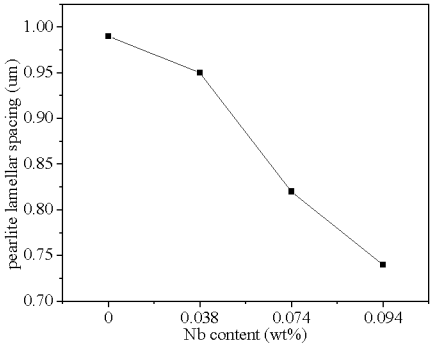

Figure 4 The relationship of niobium content and pearlite lamellar spacing

The mean pearlite lamellar spacing value could be calculated by formula (1), as shown in Figure 4. For the 0% Nb containing sample, the pearlite lamellar spacing was 0.99μm. When added 0.038%, 0.074% and 0.094% Nb in ductile iron, the pearlite lamellar spacing were 0.95μm, 0.82μm and 0.75μm respectively. Evidently, the addition of niobium decreased the pearlite lamellar spacing. The very reason was niobium, as a strong carbide forming element, took a strong drag function for carbon atom during the solidification process. Hence, it decreased the diffuse distance of carbon atom during solidification, and at finals got the pearlite matrix with smaller pearlite lamellar spacing. As discussed above, smaller pearlite lamellar spacing lead to better hardness tensile strength et al. mechanical properties of material. Therefore, considered only in this aspect, the addition of niobium could also improve those mechanical properties of ductile iron.

Conclusion

(1) With the increase of niobium content, pearlite content in ductile iron matrix increased gradually. Compared with 76.5% pearlite content of 0% Nb containing ductile iron, the pearlite content increased to 91.6% with 0.094% Nb in ductile iron.
(2) With the increase of niobium content, pearlite lamellar spacing decreased largely. Compared with 0.99μm pearlite lamellar spacing of 0%Nb containing ductile iron, pearlite lamellar spacing decreased to 0.75μm with 0.094% Nb in ductile iron.

Acknowledgement

The authors heartily acknowledge the financial support from CITIC-CBMM niobium steel research and development fund (2013-D069).

References

[1] Hardy Mohrbacher. "Introduction to Application and Effect of Niobium in Cast Iron". *Modern Cast Iron*, 2011, 02: 28-33.

[2] Tommy Nylén. "Niobium in Cast Iron". *International Symposium on Niobium* 2001.

[3] Shadrov N.S. Korshunov L.G. Cheremnikh V.P. "Influence of Molybdenum, Vanadium, and Niobium on the Abrasion Resistance of High-chromium Cast Iron". *Metal Science and Heat Treatment*, 1983, 4(25): 284-287.

[4] Lingfu Ding et al. "Research of As-cast Low Alloy Mo-Nb Bainite Steel".*Materials of Mechanical Engineering*, 1993, 17 (6): 6.

[5] Qingwei Guo. "Application of Niobium in Steel and Iron Industry". *Rare Metals Letters*, 2005, 24(3): 31-34.

[6] Hardy Mohrbacher. "Niobium Alloyed High Strength Steel for Automotive Applications". *International Society for Scientometrics and Informetrics*, 2006, 3(1):13-19.

[7] Qijie Zhai, Libo Zhang, Li Fu. "Application of Nb in Production of Cast Iron and Its Potential Application". *Foundry*, 1998, 10: 41-46.

[8] Qijie Zhai. "Effect of Niobium in Cast Iron and Its Application". *Modern Cast Iron*, 2001, 3:8-12.

[9] Wenbin Zhou. "The Fundamental Research about Actions of Niobium in Cast Iron and Its Application for Production of Brake Disc". *Shanghai University*, 2010, 02, 01.

[10] GB9941-2009. *Ductile Iron Metallographic Examination*.

[11] G. F. Vander Voort, A. Roosz. " Measurement of the Interlamellar Spacing of Pearlite". *Metallography*, 1984(17):1-17.

Characterization of Minerals, Metals, and Materials 2015
Edited by: John S. Carpenter, Chenguang Bai, Juan Pablo Escobedo, Jiann-Yang Hwang, Shadia Ikhmayies, Bowen Li, Jian Li, Sergio Neves Monteiro, Zhiwei Peng, and Mingming Zhang
TMS (The Minerals, Metals & Materials Society), 2015

EVALUATION OF PALF FIBERS ELASTICITY MODULUS WITH DIFFERENT DIAMETERS BY WEIBULL ANALYSIS

Gabriel O. Glória (1), Giulio R. Altoé(1), Ygor M. Moraes(1), Pedro A. Netto(1), Frederico M. Margem (1), Sergio N. Monteiro(2),

1 State University of the Northern Rio de Janeiro, UENF, LAMAV; Av. Alberto Lamego, 2000, 28013-602, Campos dos Goytacazes, Brazil.

2 Instituto Militar de Engenharia , IME, Praça Gen. Tibúrcio, nº80 Urca, Rio de Janeiro - RJ, 22290-270

gabrieloliveiragloria@hotmail.com

Abstract

Since environmental issues are becoming more and more important Worldwide. Nowadays, Natural fibers are been used to substitute the synthetic ones. Although PALF fiber is an important natural fiber and its mechanical Properties surpass in various aspects some other lignocelluloses fibers, such few studies have been conducted with the fiber obtained from leaf of PALF plant. In order to better evaluate the mechanical properties and possible applications, this paper aims to improve the elastic modulus of the PALF fiber by Weibull statistics, by evaluating their mechanicals properties and possible applications. The fibers were divided in diameter intervals and the tensile strength and elasticity modulus were measured in each range. The fractured surface was examined using scanning electron microscopy. The results, interpreted by the Weibull statistical method, showed a correlation between the fiber elastic modulus and its diameter.
Keywords: PALF fiber, tensile test, Analysis of Weibull modulus of elasticity

Introduction

According to Kalia, Kaith e Kaurs [1], cellulose-based fibers are being used due to its "green" image. Instead of glass fibers, widely used in modern technology, the lignocellulosic fibers are renewable and can be incinerated at the end of material useful life without the addition of air pollution, since the amount of CO_2 liberated during the incineration is negligible compared to the amount absorbed by the plant throughout its life.

Even if the industrial processing of an equivalent release of CO_2 is added, the lignocellulosic fiber can be considered neutral with respect to the emission of gases responsible for global warming [2].

The use of lignocellulosic fiber as packaging, textile, construction and automobilist is growing. One of its most promising applications is as reinforcement for polymer composites. In fact, a considerable number of publications [3-8] have been devoted to lignocellulosic fiber as reinforcement in polymer composites. In particular, in industrial applications are already on the market, mostly in automotive industry [9-12].

Despite environmental benefits and economic advantages, technical and social aspects of lignocellulosic fibers, as the deficiencies, dimensional heterogeneity and low interfacial adhesion with polymers typically used as composite matrix [3-7]. Another feature that can significantly affect the properties of lignocellulosic fiber is an appreciable dimensions transverse effect or cross-sectional area [3].

Experimental Procedure

The PALF fibers, Fig. 1 are extracted manually from randomly selected 100 fibers, the equivalent diameter corresponding to the average between the larger and smaller (90° rotation) cross section dimensions at five locations for each fiber, was measured in a profile projector Nikon 6C.

Figure 1. A small bundle of PALF fibers

The histogram in Fig. 2 shows the frequency of diameter distribution of PALF fibers used in the present work. The fiber diameter varies from 0.10 to 0.28 mm. For each interval of equivalent diameter in Fig. 2, 20 fibers were selected and all fibers were individually tensile tested at a temperature of 25 ± 2°C in a model 5582 universal Instron machine. Especial tensile grips were used to avoid both slippage and damage of the fiber. The values obtained for the elastic modulus were interpreted by means of the Weibull statistics using the computer program Weibull Analysis.

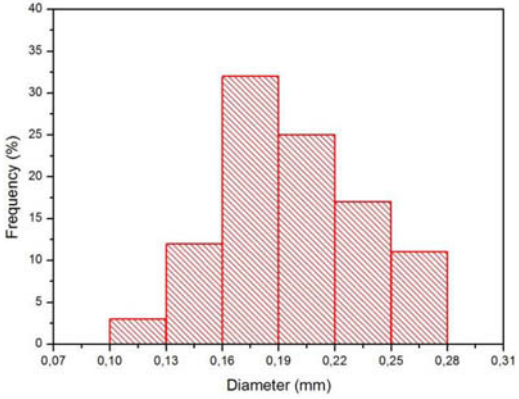

Figure 2. Distribution frequency of palf fibers equivalent diameter.

Results and discussion

Based on the maximum load, the tensile strength (σ_m) was determined for each fiber. With this last one and the deformation values, E_m was determined then statistically analyzed by means of the Weibull method for the 20 fibers associated with each of the seven diameter intervals shown in the histogram of Fig. 2. The *Weibull Analysis* program provided the probability plots of reliability vs. location parameter shown in Fig. 3 for all diameter intervals. Here it should be noted that all plots in Fig. 3 are unimodal, i.e. with just one single straight line fitting the points at each interval. This indicates similar mechanical behavior of fibers within the same diameter interval.

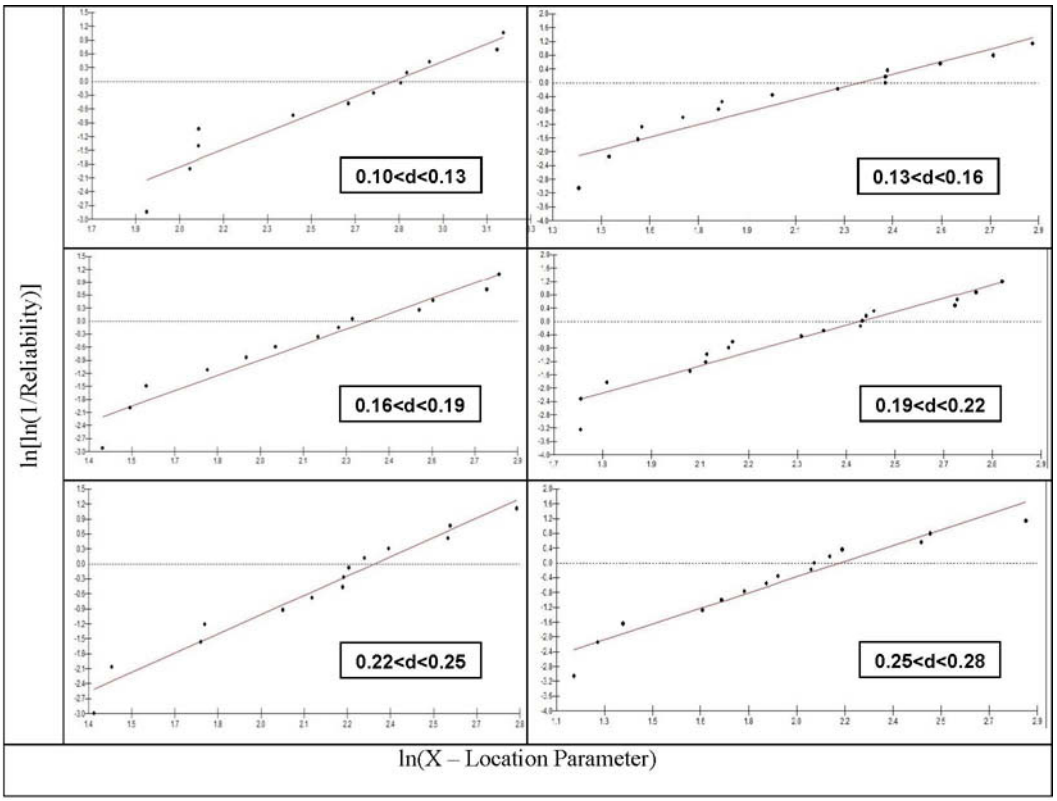

Figure 3. Weibull graphs for the different intervals in the histogram of Fig. 2.

In addition, the program also provided the corresponding characteristic elasticity modulus (θ), the Weibull modulus (β) and the precision adjustment (R^2) parameters. The values of these parameters as well as the average elasticity modulus (E_m) and associated statistical deviations, based on the Weibull distribution, are presented in Tab.1.

Table 1. Weibull parameters for the elasticity modulus palf fibers associated with different diameters.

Diameter interval (mm)	Weibull Modulus, β	Characteristic Elasticity Modulus, θ (GPa)	Precision Adjustment R^2	Average Elasticity Modulus (GPa)	Statistical Deviation (GPa)
0.10<d<0.13	2.394	16.41	0.9191	14.55	6.47
0.13<d<0.16	2.766	10.26	0.9635	9.13	3.57
0.16<d<0.19	3.382	11.64	0.9344	10.45	3.41
0.19<d<0.22	2.289	10.6	0.9430	9.39	4.35
0.22<d<0.25	2.286	10.09	0.9063	8.94	4.14
0.25<d<0.28	2.348	8.641	0.9368	7.66	3.47

The variation of the characteristic elasticity modulus with the average fiber diameter for each one of its intervals is presented in Fig. 5. In this figure there is a tendency for the θ parameter to vary inversely with the average palf fiber diameter. This means that the thinner the fiber the higher tends to be the characteristic elasticity modulus. Furthermore, the corresponding values of β and R^2, shown in Tab.1 statistically support the inverse correlation between **θ** and the average diameter **d** (mm). By means of a mathematic correlation, a hyperbolic type of equation was proposed to fit the data in Fig. 4.

$$\Theta\,(\text{Gpa}) = (1.27/\mathbf{d}) + 4.00 \qquad \text{(A)}$$

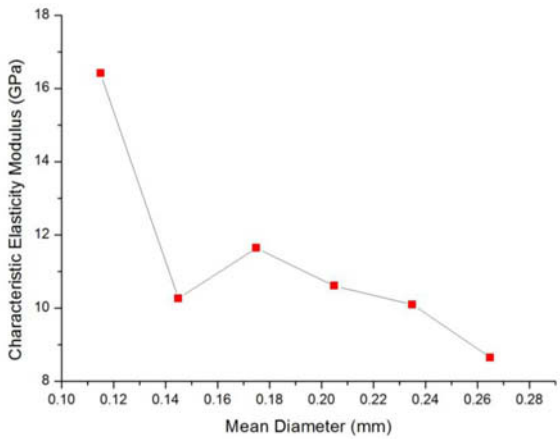

Figure 4. Variation of the characteristic elasticity modulus with the mean diameter for each interval in Fig.2.

In order to analyze the physical meaning of Eq. (A), the average elasticity modulus E_m evaluated in this work for the palf fibers was plotted as a function of the diameter in Fig. 5. In this figure an apparent hyperbolic inverse correlation also exists between E_m and **d** within the error bars (statistical

deviations) and investigated limits. an unequivocal hyperbolic inverse correlation also exists between E_m and **d**.

$$E_m\,(Gpa) = (1.13/\mathbf{d}) + 3.55 \qquad (B)$$

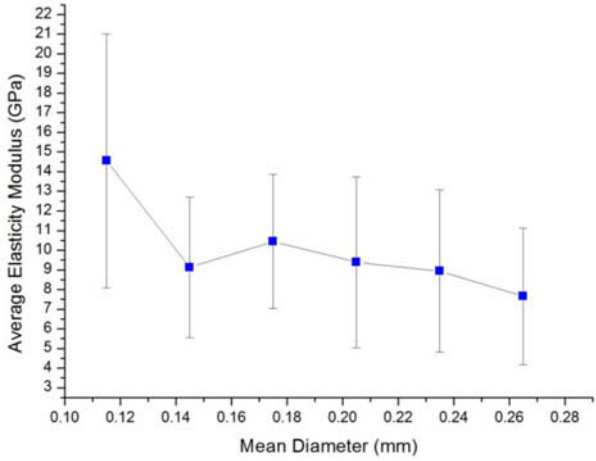

Figure 5. Variation of the mean elasticity modulus with the diameter for each interval in Fig.2.

Based on Eq. (A) and (B) it is suggested that, as in others lignocellulosic fibers [10, 11], a hyperbolic type of mathematical equation is the best statistical correlation between the elasticity modulus and the diameter of PALF.

Fig. 6 shows SEM fractographs of PALF with different diameters. It can be seen in this figure that the thinner fiber with d = 0.13 mm. Fig 6 (a). displays less natural malformation and few internal gaps. By contrast, the thicker fiber with d= 0.25 mm. Fig 6 (b). shows a heterogeneous surface comprising relatively more holes and gaps.

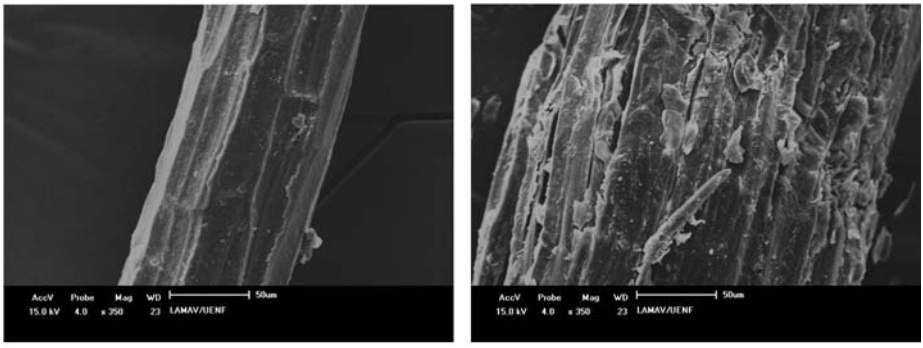

Figure 6. SEM fractograph of PALF fibers fibers: (a) thinner. d= 0.13mm and (b) thicker. d=

The microfibrillar nature of the PALF fiber could also be responsible for the results in Fig. 7. As illustrated in Fig. 7(a), the thinner fiber displays a more uniform structure with more uniform and compact microfibrils displacement. By contrast, the thicker fiber has more defects and

microstructural porosity associated with heterogeneous composition of microfibrils, Fig. 7(b). In other words, the thinner fibers tend to be more uniform with more close packed microfibrils. This contributes to less empty spaces and, consequently, higher elastic modulus results.

Conclusions

- A Weibull statistical application to analysis of elasticity modulus revealed an inverse hyperbolic correlation with the equivalent diameter of palf fibers
- The experimental results obtained for both the elastic modulus characteristic as for the average maximum modulus. showed a hyperbolic equation with similar coefficients.
- Statistically. the larger distribution of fibrils mechanical resistances of the thicker fiber allows a weaker fibril to rupture shortly than any of the fewer fibrils of the thinner fiber.

References

1. A. Gore. *An Inconvenient Truth. The Planetary Emergency of Global Warming and What We Can do About It* (Emmaus. Pennsylvania. USA: Rodale Press. 2006).
2. MONTEIRO S.N.; LOPES. F.P.D.; FERREIRA. A.S.; NASCIMENTO. D.C.O. Natural fiber polymer matrix composites: cheaper. tougher and environmentally friendly. JOM. v. 61. n. 1. p. 17-22. 2009.
3. S. Kalia. B. S. Kaith. I. Kaurs. Cellulose Fibers: Bio – and Nano – Polymer Composites (New York: Springer. 2011).
4. S.N. Monteiro. F.P.D. Lopes. A.S. Ferreira. D.C.O. Nascimento. "Natural fiber polymer matrix composites: cheaper. tougher and environmentally friendly". *JOM*. 61 (2009) 17-22
5. A .K. Bledzki. and J. Gassan. "Composites Reinforced With Cellulose-Based Fibers". Prog. *Polym. Sci*. 4 (1999) 221-274
6. D. Nabi Sahed and J.P. Jog. "Natural fiber polymer composites: a review". *Advances in Polymer Technol.*. 18 (1999). 221-274
7. A.K. Mohanty. M. Misra and G. Hinrichsen. "Biofibers. biodegradable polymers and biocomposites: an overview". *Macromolecular Mat. And Engineering*. 276/277 (2000). 1-24
8. S.J. Eichhorn. C.A. Baillie. N. Zafeiropoulos. L.Y. Mwakambo. M.P. Ansell. A. Dufresne. "Review of current international research into cellulosic fibres and composites". *J. Mater. Science*. 36 (2001) 2107-2113
9. A.K. Mohanty. M. Misra and L.T. Drzal. "Sustainable biocomposites from renewable resources: opportunities and challenges in the green material world". *J. Polym. Environ.*. 10 (2002). 19-26
10. S. N. Monteiro. K. G. Satyanarayana. F. P. D. Lopes "High strength natural fibers for improred polymer matrix composites" Mat. Sei. Forum 638-642 (2010) 961-966.
11. D.C.O. Nascimento. L.C. Motta. S.N. Monteiro. "Weibull analysis of tensile tested piassava fibers with different diameters". *Proceedings of the Characterization of Minerals. Metals & Materials – TMS Conference 2010* (Seattle. WA. USA. February 2010) 1-8.

Characterization of Minerals, Metals, and Materials 2015
Edited by: John S. Carpenter, Chenguang Bai, Juan Pablo Escobedo, Jiann-Yang Hwang, Shadia Ikhmayies, Bowen Li, Jian Li, Sergio Neves Monteiro, Zhiwei Peng, and Mingming Zhang
TMS (The Minerals, Metals & Materials Society), 2015

RESEARCH ON REASONABLE PARTICLE SIZE OF COAL BLENDS FOR BLAST FURNACE INJECTION: SEMI COKE AND BITUMINOUS COAL

Haiyang Wang[1], Runsheng Xu[1], Tengfei Song[1], Pengcheng Zhang[1]

[1]School of Metallurgical and Ecological Engineering, University of Science and Technology Beijing, 30 Xueyuan Rd; Haidian District, Beijing, 100083, China

Keywords: Semi Coke, Particle Size, Combustion, Activation Energy

Abstract

Semi coke, a byproduct in the chemical industry, is a new fuel for blast furnace injection in China. In this study, semi coke and bitumite were milled into different size, ranged from 0.147mm to under 0.074mm. The content of volatile matter and ash, which affect the combustibility of semi coke, were measured using muffle furnace. The mixture, in which the proportion of coal in different sizes changed, was blend by semi coke and bitumite with different size. Activation energy calculation and the comprehensive combustion characteristic index of all kinds of blends was also discussed. The result obtained by Thermogravimetry –Derivative Thermogravimetry curves indicates that the smaller the size of mixture is, the lower for the characteristic temperature, and the better for its combustibility, Semi coke can be a substitute for anthracite in blast furnace injection.

Introduction

Particle size, which influences specific surface area and pore structure seriously, is one of the most fundamental physical parameters. In addition, process of mass transfer, heat transfer and chemical reaction during combustion are influenced by particle size as well. Therefore, the effect of particle size on combustion is obvious. As a kind of fuel for blast furnace injection, semi coke is promising, therefore, study of effect of particle size on combustion of mixture of semi coke and bituminous coal is extremely meaningful.

There are many studies about effects of particle size on coal combustion at home and abroad. Liu Hui et al analyzed and discussed the effect of particle size on combustion of lignite by thermogravimetric experiments; [1] Ping Chuanjuan et al studied the effect of particle size on coal combustion and pyrolysis by combustion and pyrolysis experiments of multi- granularity coal; [2] Jiang Xiumin et al studied the fractal dimension of multi-granularity coal, and they concluded that the finer the coal is, the

greater of fractal dimension. Then the combustibility of coal gets improved; [3] Xue Xinghua et al researched the effect of enrichment of microlithotype, which is the result of size changes, on coal combustion from the view of coal petrology; [4] Xu Yuangang et al studied the effect of surface structure on coal combustion using saturated nitrogen absorption method at low temperature to find the mechanism of particle size; [5] Mustafa Versan Kök et al studied the influence of particle size on pyrolysis, and they find that the content of fix carbon and reduced, and ash content increased as the particle size decreased, as a result, chracteristic temperature for pyrolysis increased; [6] in addition, they researched the effect of particle size on combustion; [7] Yoshihiko Ninomiya et al studied the effect of particle size on the kind of release during combustion, they concluded that particle size influenced granular matter seriously; [8] Jonathan P.Mathews et al proved that the content of volatile matter changed as particle size of coal changed by experiments. [9]

Experimental

Materials

The samples used in this study were semi coke and bituminous coal obtained from Xinjiang Province in China. All samples were ground for two minutes in a ball mill and screened to ensure 100% passing sieving size. The bituminous coal and semi coke samples were sieved at two particle size range, one is less than 0.074 mm and the other one is between 0.148 and 0.074 mm. The proximate analyses of both samples are shown in Table I. Different samples with same size were mixed in proportion, and mixture, particle size of which are less than 0.074 mm and between 0.148 mm and 0.074 mm respectively, were obtained. And then, the mixture with different size were mixed again to obtain mixture samples, in which the proportion of samples less than 0.074 mm changed. The six experimental samples are in the Table II.

Table I. proximate analysis of the samples

coal	Particle size/(mm)	V_{ad} /%	A_{ad} /%	M_{ad} /%	FC/%
Bituminous coal	0.148~0.074	28.59	4.71	8.35	58.35
	<0.074	28.68	3.39	9.06	58.87
Semi coke	0.148~0.074	5.88	13.20	2.39	78.53
	<0.074	8.34	17.73	2.16	71.77

Table II. Experimental samples

Number	0.148mm~0.074mm	<0.074mm
1	100%	0%
2	90%	10%
3	80%	20%
4	70%	30%
5	60%	40%
6	0%	100%

Methods and facilities

Combustion experiments for all experimental programs were conducted using WCT-2C type microcomputer differential thermal balance. 10mg samples were tiled uniformly in a $\alpha - Al_2O_3$ crucible, the diameter of which is 5mm and the height is 1.5mm. The samples were heated from 25℃ to 900℃ with heating rate at 15℃/min, and the gas flow is 100ml/min. TG and DTG curves and obtained as a result.

Combustion characteristic temperature

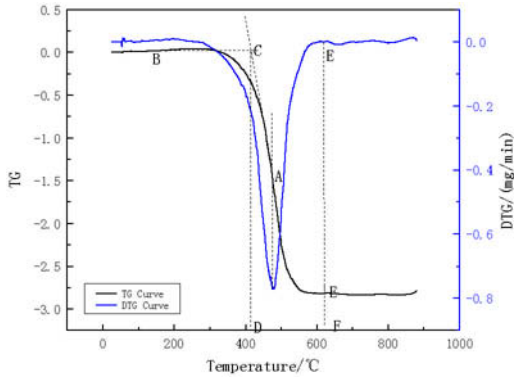

Figure 1 combustion characteristic temperature curves

Figure 1 shows the combustion characteristic temperature determined by TG-DTG method. [10] Point A is obtained in TG curve corresponding the same temperature with the peak of DTG curve, and a tangent line of TG curve corresponding point A is got, a horizontal line outlet from point B, which is in the TG curve in initial phase of the experiment, and the point C, the point of intersection of the horizontal line and tangent line, is obtained. The ignition temperature is defined as the temperature corresponding to the point C. point F, the start point of the initial part of TG and DTG curve, corresponding to the burnout temperature.

Kinetic analysis of the experimental results

Activation energy is one of the most important parameters, and it is usually used to describe complexity of the combustion process of coal. We assume that

non-isothermal process can be seen as isothermal process in infinitesimal time interval, then the gas-solid reaction kinetic equation can be described as :

$$\frac{d\alpha}{dT} = \frac{A}{\beta} \cdot \exp(-E_a/RT) \cdot (1-\alpha)^n \tag{1}$$

The conversion rate of weight α can be calculated as

$$\alpha = \frac{m_0 - m_t}{m_0 - m_i} \tag{2}$$

In equation (1) and (2), A is the frequency factor; β is the heating rate; E_a is the activation energy; R is the gas constant;m_0、m_t、m_i is the sample weight at the beginning, at t time during reaction and at the end of reaction.

To make calculation easy, Cumming define the combustion reaction of cola as first order reaction. Approximate solution is got by integration of equation (1): [11]

$$\ln\left(\frac{-\ln(1-\alpha)}{T^2}\right) = -\frac{E_a}{RT} + \ln\frac{AR}{\beta E} \tag{3}$$

Plotting using $\ln\left(\frac{-\ln(1-\alpha)}{T^2}\right)$against 1/T, a straight line is got. Activation energy can be calculated from the slope of the straight line.

Results and discussion

Combustion characteristic curve

Figure 2 is the TG and DTG curves of the mixed coal in all the experimental programs.

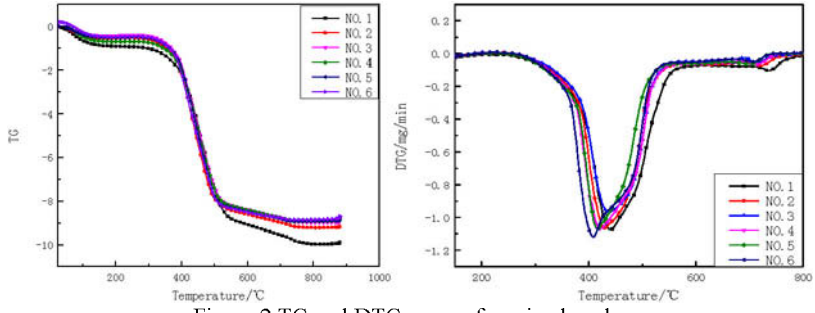

Figure 2 TG and DTG curves for mixed coal

TG curves indicates that, the TG curves of mixed coal in all experimental programs are very similar. it is the dehydration process when heated from room temperature to

about 150℃, and the volatile matter separates out and combusts during 300~500℃, at the same temperature range, part of fixed carbon reacted fiercely, and the residual coke combusts during 500~800℃, but this process is in some degree slow.

The DTG curves indicates that the maximum combustion rate of all the mixed coals occurs range from 400℃ to 500℃. As the proportion of coal, of which the particle size less than 0.074mm, increases, the DTG curves move to bottom left, the low temperature range, which indicates that as the particle size of mixed coal decreases, the combustion characteristics improves.

The calculation and analysis of combustion characteristic parameters

According to Figure 1 and TG-DTG method, the combustion characteristic parameters of the mixed coals, including ignition temperature(T_I/ ℃), burnout temperature(T_F/℃), maximum weight loss rate(dG/dτ)vmax(mg/min) and average weight loss rate(dG/dτ)vmean/(mg/min). in the experimental programs can be calculated. In addition, S_N is defined as comprehensive combustion characteristic index, [12] which is used to evaluate the combustion performance of mixed coals, and the larger the S_N is, the better the combustion performance.

S_N is calculated using the following equation:

$$S_N = \frac{\left(\frac{dG}{d\tau}\right)_{max} \cdot \left(\frac{dG}{d\tau}\right)_{mean}}{T_I^2 T_F}, \tag{4}$$

The (dG/dτ)max in equation (4) stands for maximum weight loss rate(mg/min), and (dG/dτ)mean stands for average weight loss rate. T_F stands for burnout temperature and T_I is the ignition temperature.

The calculation results for combustion characteristic parameters and comprehensive combustion characteristics index of all experimental samples are in Table III.

Table III. combustion characteristic parameters of all the mixed coals

Number	T_I(℃)	(dG/dτ)vmax(mg/min)	(dG/dτ)vmean/(mg/min)	T_F(℃	S_N[$\times 10^{-9}$ mg^2/(min^2·℃^{3})]
1	391.2	1.07	0.4016	766.5	3.66
2	385.9	1.07	0.3909	756.7	3.71
3	382.9	0.96	0.4287	757.5	3.75
4	382.6	1.06	0.4319	755.2	4.14
5	380.4	1.07	0.4209	735.5	4.23
6	377.5	1.12	0.4474	720.3	4.88

Table III indicates that the ignition and burnout temperature decrease as the proportion of the mixed coals with particle size less than 0.074 mm increases. The

former decreases slightly, however, the burnout temperature decreases sharply, when the proportion of coal the particle size less than 0.074mm is higher than 90%. It indicates that reducing particle size of mixed coal is in favor of decreasing the burnout temperature.

As the proportion of mixed coals, of which the particle size is less than 0.074mm, increases, the comprehensive combustion characteristic index increases, especially when the proportion is higher than 80%, S_N increases obviously. It indicates that increases the proportion of coal whose particle size is less than 0.074mm in the mixed coals mixed by bituminous coal and semi coke can improve the combustion characteristics.

Kinetic analysis

According to the ignition temperature and burnout temperature of the mixed coal mixed by bituminous coal and semi coke, calculation temperature range is determined at 350℃~800℃, and the conversation rate corresponding to 400℃,500℃,600℃ and 700℃ is calculated. A straight line plotted about $\ln\left(\frac{-\ln(1-\alpha)}{T^2}\right)$ against 1/T is obtained, and activation energy of all the mixed coal mixed by bituminous coal and semi coke is calculated according to the slope of the straight line. The results are in Table IV.

Table IV. Kinetic parameters of mixed bituminous coal and semi coke at different ratios

Number	Temperature range/℃	Activation energy E/（kJ.mol-1）	Correlation index R^2
1	350~800	36.99	0.99007
2		36.35	0.99302
3		34.83	0.99354
4		32.59	0.98949
5		31.88	0.99587
6		30.38	0.99108

Table IV indicates that the assumption that the combustion process of mixed coal is a first order reaction is appropriate. As the proportion of mixed coals, of which the particle size is less than 0.074mm, increases, the activation energy of the combustion reaction of the mixed coal mixed by bituminous coal and semi coke decreases. It agree with the former results that reducing the particle size of the mixed coal can improve the combustion characteristics of the coal mixed by bituminous coal and semi coke. The semi coke can be a substitute for anthracite.

Conclusions

(1)Reducing the particle size of coals mixed by bituminous coal and semi coke can decreases the ignition temperature and burnout temperature, and particle size influences burnout temperature mostly;

(2)The comprehensive combustion characteristic index increases as the particle size of the mixed coal decreases;
(3)The activation energy decreases as the particle size of the mixed coal decreases, reducing the particle size of mixed coal can improve the combustion characteristics of coal mixed by bituminous coal and semi coke;
(4)Semi coke can be used in blast furnace injection.

References

[1] LIU HUI, WU SHAO-HUA, ZHAO GUANG-BO, et al. Influence of coal particle size on the combustion characteristics of yuanbaoshan lignite[J]. Journal of Harbin Institute of Technology, 2008, 40(03): 419-422.
[2] PING CHUAN-JUAN, ZHONG YING-JIE, XU ZHANG. Influence of coal particle size on pyrolysis and combustion characteristics of coal samples from Shenhua Group[J]. China Coal, 2012, 38(01): 81-84.
[3]JIANG XIU-MIN, YANG HAI-PING, LI YAN, et al. Fractal analysis for coal particle size[J]. Journal of China Coal Society, 2003,28(04): 414-418.
[4] XUE XING-HUA, WANG YUN-QUAN, XIAO CHEN-SHENG, et al. Influence of the characteristics of coal particle size on coal combustion in power plant[J]. Coal Conversion, 2006,29(03): 58-61.
[5] CU YUAN-GANG, ZHANG CHENG, XIA JI, et al. Study of surface structure and combustion characteristics for coal with different particle size[J]. Journal of Engineering for Thermal Energy and Power, 2010, 25(01): 47-50.
[6] VERSAN K.K, et al. Effect of particle size on coal pyrolysis. Journal of Analytical and Applied Pyrolysis, 1998, 45(2): 103 - 110.
[7] K.K, M.V., et al. Effect of particle size on the thermal and combustion properties of coal. Thermochimica Acta, 1997, 302(1): 125 - 130.
[8] NINOMIYA, Y., et al. Influence of coal particle size on particulate matter emission and its chemical species produced during coal combustion. Fuel Processing Technology, 2004, 85(8-10): 1065-1088.
[9] MATHEWS, J.P., P.G., et al. Particle size dependence of coal volatile matter: is there a non-maceral-related effect? Fuel, 1997, 76(4): 359 - 362.
[10] HE XIN-JIE, ZHANG JIAN-LIANG, et al. Kinetic analysis and effect of catalysts on combustion characteristics of pulverized coal[J]. Iron and Steel, 2012，47(07)：74-79.
[11] Cumming J W .Reactivity assessment of coals via a weighted meanactivation energy [J]. Fuel, 1984,63 (10) :1436-1440.
[12] JIANG XIU-MIN, LI JU-BIN et al. study on combustion characteristics of micro-pulverized coal [J].Proceeding of the CSEE,2000,20(06):71-78.

Characterization of Minerals, Metals, and Materials 2015
Edited by: John S. Carpenter, Chenguang Bai, Juan Pablo Escobedo, Jiann-Yang Hwang, Shadia Ikhmayies, Bowen Li, Jian Li, Sergio Neves Monteiro, Zhiwei Peng, and Mingming Zhang
TMS (The Minerals, Metals & Materials Society), 2015

RECOVERY OF COPPER FROM SLOW COOLED AUSMELT FURNACE SLAG BY FLOATATION

Ping Xue[1,2], Guangqiang Li[1], Qingwei Qin[1]

[1]Key Laboratory for Ferrous Metallurgy & Resources Utilization, Ministry of Education, Wuhan University of Science & Technology; Jianshe Road; Wuhan, Hubei, 430081, China
[2]Jianghan University; Sanjiaohu Road; Wuhan, Hubei, 430056, China

Keywords: Ausmelt furnace, Slow cooled slag, Flotation, Copper.

Abstract

Ausmelt furnace slag contains about 0.9% Cu (mass %). With increasing the amount of Ausmelt furnace slag, the recovery of copper from it will produce an enormous economic yield. The recovery of copper by floatation from slow cooled Ausmelt furnace slag was studied in this paper. The phases and composition of the slow cooled slag were analyzed. The factors which affected the copper recovery efficiency such as grinding fineness, pH value of flotation medium, different collectors and floating process were investigated. It was shown that the size distribution of the primary grinding and secondary grinding of middling were 75% for particles less than 0.074mm and 82% for particles less than 0.043mm respectively. The closed-circuit experimental results with butyl xanthate as collector in laboratory showed that the copper grade reached 16.11% and the recovery rate of copper reached 69.90% and the copper grade of tailings was only 0.2%.

Introduction

Copper slag, as an important secondary metal resource, contains plenty of renewable resource. It is the byproducts of high temperature copper smelting process which contains mainly iron silicate, magnetite, a small quantity of Cu, Pb, Zn and the compounds of SiO_2, Al_2O_3, CaO, MgO and very tiny amount of precious metals. The property of copper slag is extremely complex, which is affected by the properties of copper concentrates, smelting conditions and cooling procedures of molten slag. Copper exists in forms of copper sulfide, metal copper and small amount of copper oxide in slag. Most of precious metals in slag coexist with copper, so the process which recovers copper can also recovers previous metals. At present, researchers have used a variety of methods to recover useful metals from the copper slag. The methods include pyrometallurgy (reverberatory furnace and electric furnace), mineral processing (flotation separation and magnetic separation), leaching (direct leaching, indirect leaching and bacteria leaching) and carbothermic reduction at high temperature [1-4]. The purpose is the recovery of Fe and Cu from copper slag. Moreover, copper slag has good mechanical-physical properties and it can be used as copper slag cement, abrasive tools and road material.
Ausmelt electric furnace slag has increased to about 900,000 tons each year in a domestic smelting plant in China and it contains about 0.7~0.9% Cu. With gradually increasing of market demand, the copper price remains at a high level. In this paper, the floatation experiments of Ausmelt slow cooled slag in a smelting plant were carried out to explore available process and

effective flotation conditions. The copper smelting plants would increase their profits if the copper grade of slag could be decreased from 0.7-0.9% to below 0.25% [5, 6].

Experimental

Experimental Material

The slag was chosen from a copper smelting plant in Huangshi city in China. It was firstly crushed by roll crushers and then sieved through 2mm as experiment samples. The slag was dark brown in appearance and most of copper minerals existed in the forms of copper sulfide and matte. Other minerals in slag such as fayalite, magnetite, glass phase, only contained tiny copper. The composition of copper slag is shown in Table I. The copper distribution in main copper-bearing phases in copper slag is listed in Table II.

Table I The chemical composition of copper slag（mass %）

Cu	Fe	Zn	Ni	S	CaO	MgO	SiO_2	Al_2O_3	Au(g/t)
0.76	42.14	1.86	0.045	1.62	4.47	3.74	31.98	4.52	0.07

Table II Copper concentration (mass %) and distribution (%) in main copper-bearing phases

Phase	Copper sulfide		Metal copper		Copper oxides		Cuprous oxides		Fayalite magnetite	
	conc.	dis.	conc.	dis.	conc.	dis.	conc.	dis.	conc.	dis.
	0.46	68.80	0.08	10.31	0.09	4.84	0.01	0.32	0.12	15.73

Note: conc. = concentration; dis. =distribution

Experimental Instruments

A XFD model hanging cell flotation machine and a XMQ-240×90 cone ball grinder made by Wuhan Exploring Machinery Factory were used for grinding and flotation of copper slag. The 200 mesh screener produced by Shangyu Jinding Standard Screener Factory was used for sieving of the grind slag powders. A GGX-9 model Atomic Absorption Spectroscopy (AAS) made by Beijing Haiguang Equipment Company was used for determination of copper concentration in slag before and after flotation.

Analysis Methods

The analysis method of copper recovery rate and grade of copper concentrates after flotation are as follow: 0.1000g drying foam concentrate was placed in a PTFE beaker adding 15mL HCl (1+1), 5mL HF and 5mL HNO_3 to dissolve. The samples were cooled when perchloric acid smoked after adding 10mL $HClO_4$. The sample was heated until the solution got clear with adding 15mL HCl(1+1). The solution was then cooled and filtered; the filtrate was kept in a 250mL volumetric bottle. Finally, the filtrate was analyzed by AAS.

Results and discussion

The experiment of copper flotation was performed in mechanical stirring flotation machine with 3L volume. The slag was weight at 1000g each time and the water for the experiment was running water. The main processing agents were Na_2S, buffering agents, collector agents such as Z-200#, butyl dithiophosphate, butyl xanthate and mixed xanthate. The flotation product was weighted after drying and then the recovery rate ε was calculated according to equation (1). The process flow of floating copper from slag is shown in Figure 1.

$$\Sigma=\frac{Cu_1}{Cu_2}\times 100\% \qquad (1)$$

Where Cu_1 is the mass of Cu in the flotation product (g).

Cu_2 is the total mass of Cu in the 1000g Ausmelt furnace slag (g).

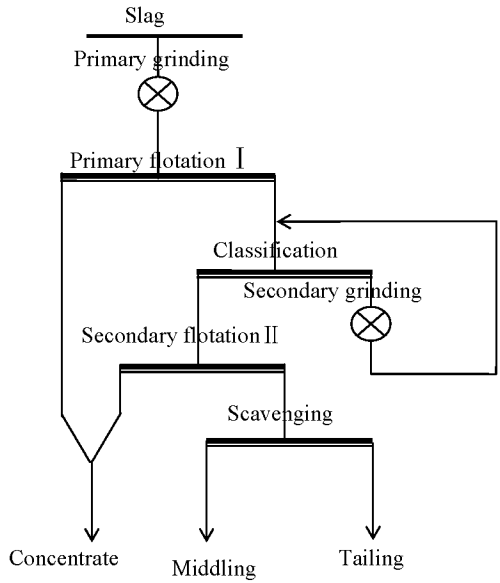

Figure 1. Flow chart of floating copper from slag

Effect of Grinding Fineness on Floating Copper

Based on the former researches [7], the slow cooled Ausmelt furnace slag was used to study the influence of the fineness of the primary grinding for slag and secondary grinding for middling on the copper concentrates grade and recovery rate. The influence curves of the primary and secondary grinding fineness on the copper concentrates grade and recovery rate were shown as Figures 2 and 3.

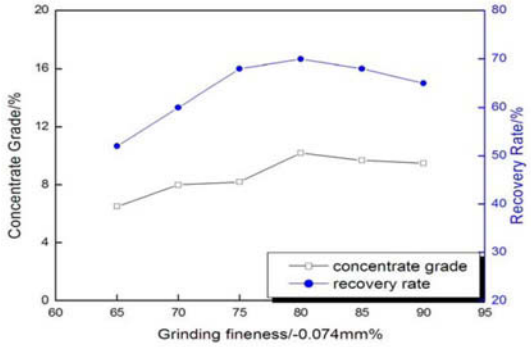

Figure 2. Primary grinding fineness

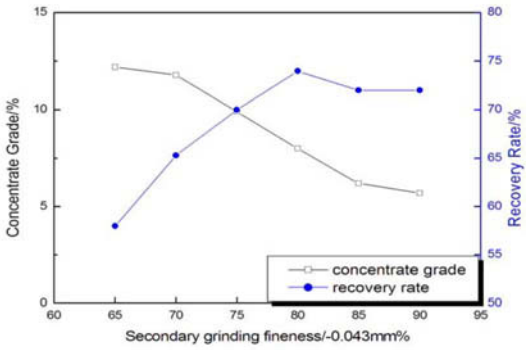

Figure 3. Secondary grinding fineness

As can be seen from Figures 2 and 3, the fineness of the primary grinding of slag and secondary grinding of middling has a great effect on the copper concentrates grade and recovery rate. With the increase of grinding fineness, both of the recovery rates firstly rose and then slightly decreased. As for the concentrate grade, they were totally different. The concentrate grade of primary grinding slag increased but the grade of secondary grinding slag of middling decreased sharply. This was due to the facts:1.the useful mineral was easily over grinded and resulted in the loss of tiny size metals;2.the floating gangue mineral would float on the surface and resulted in the degrade of concentrate grade. The suitable fineness of the primary grinding for slag and secondary regrinding for middling were –0.074mm 75% and –0.043mm 82% respectively according to the results.

Effect of pH Values on Floating Copper

The reacting agents were Na_2S, ethyl xanthate and buffering agents. The experiments were performed in different pH values. The pH values of slurry can be adjusted by adding buffering agents such as HCl, CH_2COOH and CH_2COONa. It can be seen from Figure 4 that copper recovery rate increased regularly and copper grade decreased with increasing pH value. Copper recovery rate started to decrease when pH was higher than 12, this was due to adding Na_2S. The surface electronegativity of the slurry will increase and appear CuS sediment. The sediment CuS will generate sol with the excessive amount of S^{2-} and increase the hydrophilic. The recovery rate and copper grade will decrease.

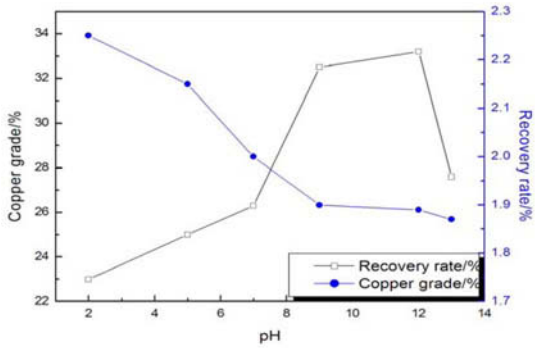

Figure 4. Effect of pH values on flotation with collector

Effect of Different Collectors on Floating Copper

To improve the technical index of flotation, the effect of different collectors on the primary copper flotation index of Austmelt slow cooled slag was investigated. The experiment procedure was one primary flotation; the grinding fineness was –0.074mm75%; the amount of collector was 90g/t; the amount of pine oil was 75g/t; the flotation time was 13min. Results in Table III showed that conventional collectors such as Z–200#, butyl dithiophosphate and butyl xanthate can effectively recover copper minerals. Butyl xanthate was an effective collector to float copper from slag considering recovery rate, concentrate grade and production cost.

Table III Effect of different collectors on concentrate grade and recovery rate（%）

No	Collector	Product	Yields	Copper grade	Recovery rate of copper
1	Z-200#	Concentrate	2.96	14.51	58.81
		Tailing	97.04	0.31	41.19
		Slag	100.00	0.73	100.00
2	butyl dithiophosphate	Concentrate	3.13	14.66	62.85
		Tailing	96.87	0.28	37.15
		Slag	100.00	0.73	100.00

3	butyl xanthate	Concentrate	3.31	15.05	67.33
		Tailing	96.69	0.25	32.67
		Slag	100.00	0.74	100.00
4	Mixed xanthate	Concentrate	3.41	14.87	69.54
		Tailing	96.59	0.23	30.46
		Slag	100.00	0.73	100.00

Closed-circuit test

Flotation flow has a great influence on the flotation index of slow cooled slag of Ausmelt furnace. The slag also abided by the dressing rule "early recovery early discard, early recovery more recovery". The closed-circuit experiments simulating continuous production were done based on the open-circuit experiments, the flow is shown in Figure 5. The experimental conditions are: the primary grinding fineness is –0.074mm75% and the secondary grinding fineness is –0.043mm 85%; the amount of activator Na_2S, collector butyl xanthate and the foamer 2# oil is 95g/t, 90g/t and 85g/t respectively, the results are shown in Table IV.

Table IV Closed-circuit flotation test for the Ausmelt furnace slow cooled slag（%）

Product	Yield	Grade	Distribution rate
		Cu	Cu
Concentrate Ⅰ	2.13	16.77	48.29
Concentrate Ⅱ	1.08	14.80	21.61
Total copper concentrate	3.21	16.11	69.90
Tailing	96.79	0.23	30.10
Slag	100.00	0.74	100.00

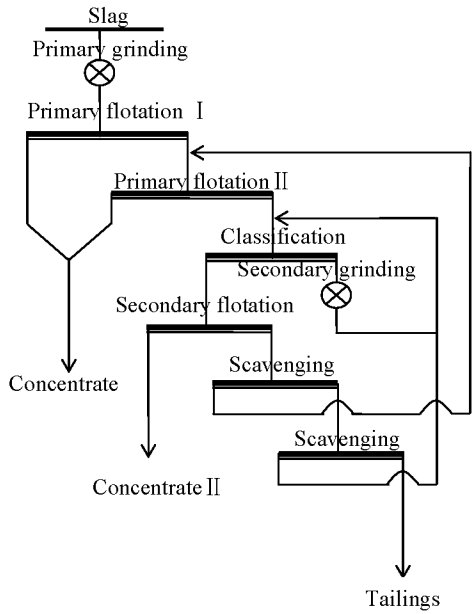

Figure 5. Flow chart of floating copper from slag with closed-circuit

Conclusions

（1）Flotation of slow cooled Ausmelt furnace slag was carried out to recover copper-bearing components. Based on the experimental results, the best flotation conditions were determined as follows: a) primary grinding: 75% passing 0.074mm;Secondary grinding: 82% passing 0.043mm 82%; b) pH of flotation media: 9; c) Collector: butyl xanthate.

（2）A closed-circuit test for slow cooled slag simulating continuous production was performed; the copper concentrate grade reached about 16～18% and copper recovery rate was about 65～70%.

Acknowledgement

This research was financially supported by Hubei Provincial Department of Education (XD2014094); Project of Jianghan University (No.SY012 [2013]).

References

1. H.Q. Chen, P.X. Li, and S.G. Liu, "Study on the strengthening depletion of copper from copper smelter slag by pyro-process," *Hunan Nonferrous Metals,* 22 (3)(2006), 16-18.

2. H. Wang, "Recovery of copper and iron in the converter slag from a copper smelter," *Journal of Guangdong Non-ferrous Metals*, 13(2) (2003), 83-88.

3. B. Gorai, "Characteristics and utilization of copper slag-a review," *Resources, Conservation and Recycling*, 39 (2003), 299-313.

4. G. Li, P. Zhang, and L. Zhang, "Enrichment and growth of magnetite from copper slag as a new iron ore resource," (Paper presented at the Proceedings of the International Workshop on Modern Science and Technology, Wuhan, Hubei,18 May 2006).

5. Y.Y. Liu, Z.L. Huang, and Q.W. Qin, "Study on recovering copper and zinc from slag by process of acid leaching and solvent extraction," *Mining and Metallurgical Engineering*, 32 (2) (2012), 76–79.

6. W. Han, Q.W. Qin, "Experimental study on copper recovery from Ausmelt slag," *Copper Engineering,* (3) (2012), 8–10.

7. Y.Y. Liu, "Recovery copper from Osborne Matt furnace slag," (Master Thesis, Wuhan University of Science and Technology, 2012).

Characterization of Minerals, Metals, and Materials 2015
Edited by: John S. Carpenter, Chenguang Bai, Juan Pablo Escobedo, Jiann-Yang Hwang, Shadia Ikhmayies, Bowen Li, Jian Li, Sergio Neves Monteiro, Zhiwei Peng, and Mingming Zhang
TMS (The Minerals, Metals & Materials Society), 2015

CHARACTERIZATION OF MECHANICAL PROPERTIES OF PP/HMSPP BLENDS WITH NATURAL AND SYNTHETIC POLYMERS SUBJECTED TO GAMMA-IRRADIATION

Cardoso, E.C.L; Scagliusi, S.R.; Lugão, A.B..

Instituto de Pesquisas Energéticas e Nucleares- IPEN/CNEN-SP – Av. Lineu Prestes 2242 - CEP05508-900 - Cidade Universitária, São Paulo/SP- Brasil.

Keywords: Gamma-irradiation, HMSPP, PLA, PHB, Sugarcane bagasse

Abstract

Hydrocarbon polymers, as PP, made from cheap petrochemical feedstock are important in many branches of industry. However, they have an undesirable influence on the environment and cause problems due to waste deposition and utilization. Polymeric materials composites account for an estimated from 20 to 30% of total volume of solid waste disposed. Thus, there is a tendency to substitute such polymers by those ones that undergo biodegradable processes. Polypropylene (PP) is a commodity, with high melting point, high chemical resistance, low density, with a balance between physical and mechanical properties and easy processing at low cost. Nevertheless, PP shows limitations for some special applications in automotive industry and civil construction. In order to minimize this deficiency, related to rheological behavior of polymer melt, especially referring to viscosity in processing temperature, a 50% mixture with HMSPP (High melt Strength Polypropylene) was used. PP/HMSPP was blended with 10, 15, 30 and 50% of natural (sugarcane bagasse) and synthetic polymers (PHB and PLA) aiming to partially biodegradable materials. The admixtures were subjected to gamma-irradiation at 50, 100, 150 and 200 kGy and then further assessed by mechanical tests in order to evaluate their degradability.

Introduction

Polymers are vastly employed for numerous purposes in different industrial segments [1,2,3], generating enormous quantities of discarding in the environment. Amongst the various components of waste in landfills, polymeric materials composites account for an estimated from 20 to 30% of total volume of solid waste disposed [4, 5]. Polypropylene (PP) undergoes crosslinking and extensive main chain scissions when submitted to ionizing irradiation [6]; and both chemical phenomena are known to induce changes in the polymer properties which may enable its use in various applications at distinct process conditions [7].

PP is one of the most widely used linear hydrocarbon polymers; its versatility arises from the fact that it is made from cheap petrochemical feed stocks through efficient catalytic polymerization process and easy processing to various products. Thus, enormous production and utilization of polymers, in general, lead to their accumulation in the environment, since they are not easily degraded by microorganisms, presenting a serious source of pollution affecting both flora and fauna. These polymers are very bio-resistant due to the involvement of only carbon atoms in main chain with no hydrolysable functional group. Non-degradable plastics accumulate in the environment at a rate of 25 million tons per year [8, 9, 10]. Several possibilities have been considered to minimize the environmental impact caused by the use of

conventional polymers. Polymeric materials can undergo physical, chemical, and biological degradation or combination of all these due to the presence of moisture, air, temperature, light (photo-degradation), high energy radiation (UV, gamma radiation) or microorganisms (bacteria or fungi) [11]. There are three main classes of biodegradable polymers: synthetic polymers, naturally occurring processable bacterial polymers and blends of polymers in which one or more components are readily consumed by microorganisms [12].

In recent years, as a result of growing environmental awareness, natural polymers (starch, cellulose, chitin, sugarcane bagasse, sisal, etc...) have been increasingly used as reinforcing fillers in thermoplastic composite materials. Sugarcane bagasse was used as reinforcing filler in this study, mainly because its availability in Brazil. As the world´s largest producer of sugarcane, Brazil produces 101 million tons of agro-industrial residue of sugarcane from 340 million tons of sugarcane every year [13].

PP/HMSPP biodegradation rate can be enhanced with biodegradable natural (sugarcane bagasse) and synthetic (PHB and PLA) and should present effective mechanical properties, when non-irradiated. Nevertheless, application of high energy (gamma-rays) will induce samples degradation, affecting mechanical behavior and so contributing for biodegradation.

This study aims to mechanicals assessments involving PP/HMSPP and blends with PHB, PLA and sugarcane bagasse.

Experimental

Materials

Polypropylene (PP): PP-440K, Quattor, 3.5 g/10 minutes M.F.I.

High Melt Strength Polypropylene (HMSPP): PP samples previously kept in nylon bags, 48h under acethylene, irradiated in a Co^{60} source at room temperature and 12.5 kGy dose at 10 $kGyh^{-1}$ radiation rate. After irradiation, samples air-forced oven annealed, 1 hour at 100°C, to eliminate remaining radicals to accomplish termination reactions [11].

Sugarcane bagasse: From Caçapava, São Paulo, running water washed, room temperature dried, environment protected for two months, air-forced oven at 60°C for 24h. Treated material grinded and kept for 4h at 60°C, sieve segregated in 355 μm meshes pan [15, 16].

Polylactic acid (PLA): Ingeo TM Biopolymer 3251D, designed for injection molding applications, from NatureWorks®

Polyhydroxybutyrate (PHB): PHB Biocycle®, from PHB Industrial S/A.

Preparation of mixtures

A 50% PP/HMSPP mixture was prepared using a twin-screw extruder (HAAKE Rheomex 332p, 3.1 L/D, 19/33 compression ratio), operated at 170°C and 60 rpm. Pelletized extrudates were used as basis for: Bagasse in PP/HMSPP, PHB in PP/HMSPP and PLA in PP/HMSPP at 10%, 15%, 30% and 30% level. All samples were further irradiated in a Co^{60} source at room temperature, 10 $kGyh^{-1}$ radiation rate, at: 50, 100, 150 and 200 kGy.

Characterization:

Mechanical tests: Samples were analyzed in a texturometer (TA-Hdi Stable Micro Systems Texture Analyser texturometer, 5 kg load cell, 0.5 m/s deformation rate, 2 mm/seg speed). Analyses were performed in accordance with ASTM D 638-08 [14], at room temperature.

Results and discussion

Mechanical assessments accomplished for PP/HMSPP polymeric basis and blends with natural (sugarcane bagasse) and synthetic (PHB and PLA) polymers are shown in Figures 1 through 6:

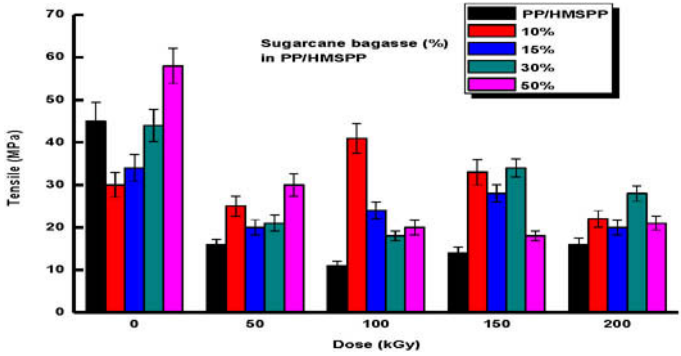

Figure 1: Tensile in sugarcane bagasse 10, 15, 30 and 50% in PP/HMSPP blends irradiated at 0, 50, 100, 150 and 200 kGy.

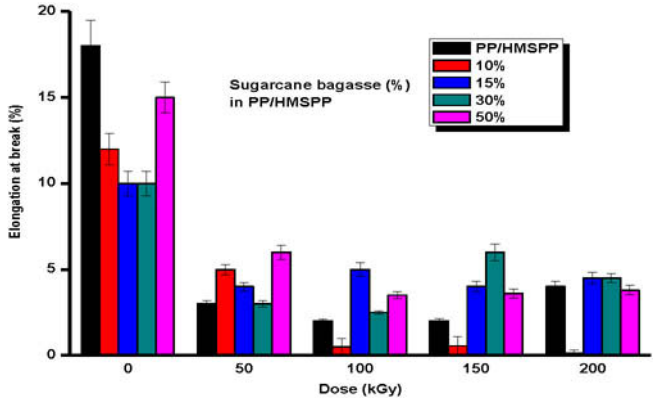

Figure 2: Elongation at break in sugarcane bagasse 10, 15, 30 and 50% in PP/HMSPP blends irradiated at 0, 50, 100, 150 and 200 kGy.

Figures 1 and 2 indicate that at 0 (zero) kGy there is an abrupt raise in tensile for 50% sugarcane bagasse in PP/HMSPP, in relation to PP/HMSPP; besides showing a higher elongation at break, when compared to other blends, its value was slightly lower than that one obtained for PP/HMSPP. Within a 50 to 200 kGy range pure PP/HMSPP and blends experienced lower values for tensile and elongation at break, without a precise pattern.

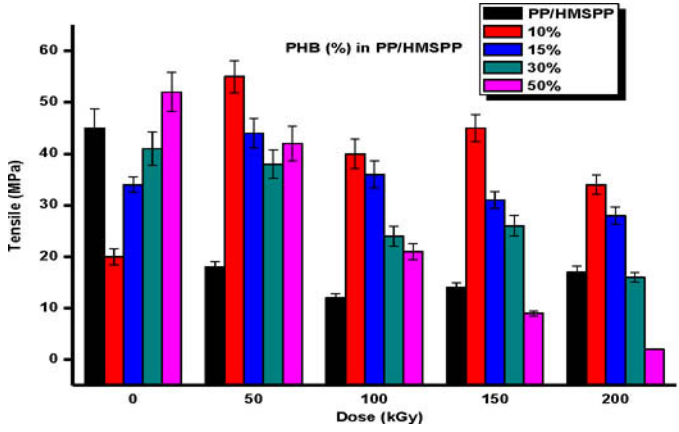

Figure 3. Tensile in PHB 10, 15, 30 and 50% in PP/HMSPP blends irradiated at 0, 50, 100, 150 and 200 kGy.

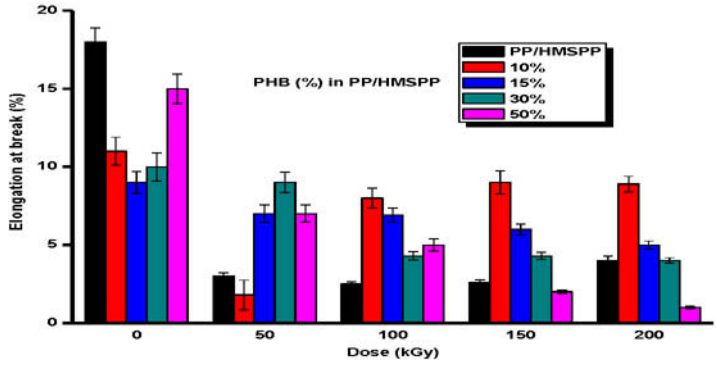

Figure 4: Elongation at break in PHB 10, 15, 30 and 50% in PP/HMSPP blends irradiated at 0, 50, 100, 150 and 200 kGy.

Figure 3 shows that at zero kGy, PP/HMSPP polymeric matrix showed higher tensile results , followed by 50% PHB in PP/HMSPP blend, keeping the same behavior for elongation at break in Figure 4. Within a 50 to 200 kGy range: 10% PHB in PP/HMSPP showed highest tensile values, followed by 15% PHB in PP/HMSPP blend; excepting at 50 kGy, the same behavior was presented by these blends in relation to elongation at break.

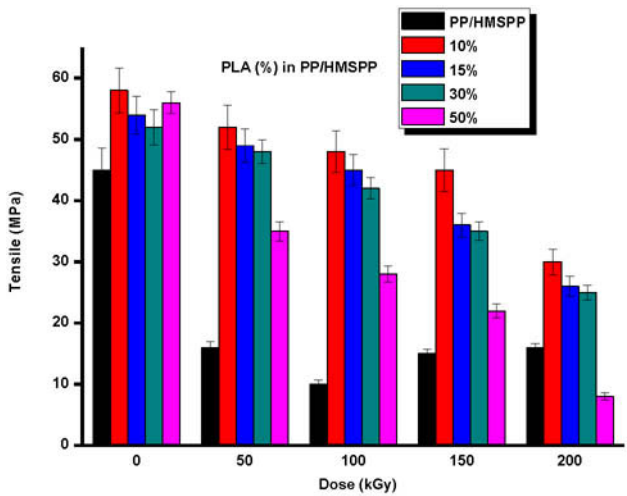

Figure 5. Tensile in PLA 10, 15, 30 and 50% in PP/HMSPP blends irradiated at 0, 50, 100, 150 and 200 kGy.

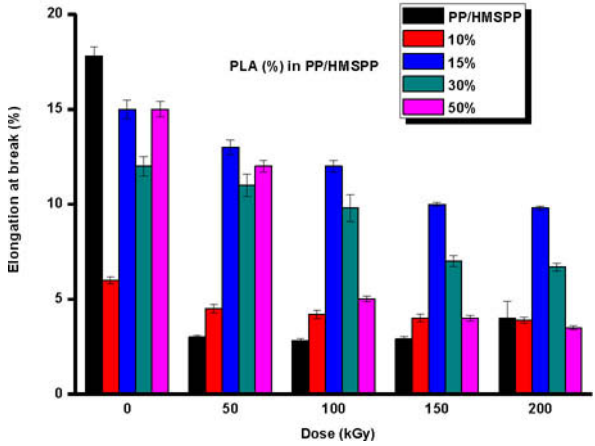

Figure 6: Elongation at break in PLA 10, 15, 30 and 50% in PP/HMSPP blends irradiated at 0, 50, 100, 150 and 200 kGy.

Figure 5 shows that except 50% PLA in PP/HMSPP blend at 200 kGy, all other blends showed proportional and higher tensile values when compared to pure PP/HMSPP, at 50, 100 and 150 kGy. At zero kGy PP/HMSPP showed the highest value for elongation at break; higher values were presented by 15 and 30% PLA in PP/HMSPP blends within 50 to 200 kGy range.

Conclusions

Sugarcane bagasse, PHB and PLA acted as reinforcing filler of PP/HMSPP polymeric matrix, based in tensile and elongation at break assessments, especially at zero kGy..

Sugarcane bagasse in PP/HMSPP blends irradiated at 50, 100, 150 and 200 kGy showed for mechanical essays higher values when compared to pure PP/HMSPP irradiated within this doses range; the only exception was registered for 50% sugarcane bagasse in PP/HMSPP, at 200 kGy.

PHB 10% in PP/HMSPP showed higher tensile in function of imparted doses; nevertheless, it experimented an abrupt reduction in elongation at break within this doses range.

PLA in PP/HMSPP blends showed a proportional loss in mechanical properties, in function of 50, 100, 150 and 200 kGy, especially PLA 50% in PP/HMSPP blend.

Acknowledgements

The authors acknowledge CBE, Braskem, PHB Industral S.A, Natureworks®,and IPEN, fundamental for work development.

References

1. Propylene Polymers, *Encyclopedia of Polymer Science and Engineering*, 13, (1990), pp. 464-529.

2. State of Order of Polymers, Chapter 1, *Plastics, Properties and Testing* (Ullmann´s Encyclopedia of Industrial Chemistry, A21, 1990).

3. Moore, E. P., *Polypropylene Handbook* (Hanser Gardner, New York, 1996).

4. Neeraj Mishra et al, *Route to Generate Fuel Oil via Catalytic Pyrolysis of Waste Polypropylene Bags: Towards Waste Management of >20 µm Plastic Bags* (Journal of Fuels, 2014).

5. S.M.M.Franchetti et al. *Uma solução para diminuir a quantidade dos resíduos plásticos* (Quimica Nova, 29, N. 4, 2006), 811-816.

6. A. G. Chmielewski, M. Haji-Saeid and S. Ahmed. Section B: *Beam Interactions with Materials and Atoms*, (Nuclear Instruments and Methods in Physics Research, 44, 2005), 236.

7. C.Longo et al. *Degradation Study of Polypropylene (PP) and Biooriented Polypropylene (BOPP) in the Environment* (Materials Research, 14(4), 2011), 442-448.

8. J.Arutchelvi et al.; *Biodegradation of Polyethylene and Polypropylene (* Indian Journal of Biotechnology, 7, 2008), 9-22.

9. Chandra,R; Rustgi.; *Polym. Degrad. Stab., 56*, 1997.

10. Y. Tokiwa et al.; *Biodegradability of Plastics (*Int. J. Mol. Sci, 10, 2009), 3722-3742.

11. A. AdurafimihanAbiona and A. Gabriel Osinkolu; *Gamma-irradiation induced property modification of polypropylene (*International Journal of Physical Sciences, 5(7),2010), pp. 960-967.

12. Satyanarayana K.G., Ramos LP and Wypych F. *Development of new materials based on agro and industrial wastes towards eco-friendly society.* (In: Ghosh T.N., Chakrabarti T, Tripathi G, editors. Biotechnology in energy management .New Delhi: APH Publishing Corporation: 2005). P.583-624.

13. Satyanarayana K.G., Ramos LP and Wypych F. *Comparative study of Brazilian natural fibres and their composite with other* (In: Thomas S., Potham L. A., editors.

Natural fiber reinforced polymer composites. Philadelphia: Maney Publishers, 2005). P.583-624.

14. ASTM D-638-08. Standard Test Method for Tensile Properties of Plastics, (2008).

15. E.Chiellini et al. *Thermomechanical Behavior of Poly(vinylalcohol) and Sugarcane Bagasse Composites* (Journal of Applied Polymer Science, 2004), 92, 426-432.

16. Ricardo José Brugnago et al. *The effect of steam explosion on the production of sugarcane bagasse/polyester composites*. (Composites, 2011, Part A-42) 364-370.

Characterization of Minerals, Metals, and Materials 2015
Edited by: John S. Carpenter, Chenguang Bai, Juan Pablo Escobedo, Jiann-Yang Hwang, Shadia Ikhmayies, Bowen Li, Jian Li, Sergio Neves Monteiro, Zhiwei Peng, and Mingming Zhang
TMS (The Minerals, Metals & Materials Society), 2015

EFFECT OF MERCERIZATION AND ELECTRON-BEAM IRRADIATION ON MECHANICAL PROPERTIES OF HIGH DENSITY POLYETHYLENE (HDPE) / BRAZIL NUT POD FIBER (BNPF) BIO-COMPOSITES

Rejane D. Campos[1]*, Maria Sotenko[2], Mahesh Hosur[3], Shaik Jeelani[3], Francisco R. V. Díaz[4], Esperidiana A. B. Moura[1], Kerry Kirwan[2], Emilia S. M. Seo[1]

[1]Nuclear and Energy Research Institute, IPEN-CNEN/SP, Av. Prof. Lineu Prestes 2242, São Paulo, SP, 05508-000, Brazil

[2]WMG, University of Warwick, Coventry, CV4 7AL, United Kingdom

[3]Material Science and Engineering Tuskegee University, Tuskegee, AL, 36088, USA

[4]Metallurgical and Materials Engineering Department, Polytechnic School, University of São Paulo, Av. Prof. Mello de Moraes, 2463, São Paulo, SP, 05508-030, Brazil

Keywords: bio-composite; mechanical properties; Brazil nut pod fiber; mercerization; electron-beam radiation

Abstract

The use of natural fibers with polymeric resins has spread rapidly. In order to improve the mechanical properties of material, in this work, two variables were used: mercerization and electron beam irradiation. This paper describes the preparation and characterization of bio-composites that were prepared in two different routes using green high density polyethylene (HDPE) and Brazil nut pod fiber (BNPF): the first was to irradiate the composite with 150 kGy and the second was to irradiate the matrix with 15 kGy followed by composite preparation. In both cases mercerized and non-mercerized fibers were used. The irradiation process was carried out using a 1.5 MeV electron beam accelerator, at room temperature and in the presence of air. The material was characterized to evaluate the effect of treatment on mechanical properties of material.

Introduction

Composites are materials which combine the best mechanical and physicochemical properties of two or more materials. This is the reason for composites to appear as an extremely favorable alternative to the several industries. The increased use of polymeric materials by industries is a result of the high degree of robustness and many advantages over conventional materials; such as greater design flexibility and economy in production [1]. In the last decade there has been a rapid development in the area of natural fiber-reinforced composites, thanks to cellulose fibers' low cost, low density, non-abrasiveness, non-toxicity and easiness to be modified by chemical agents, as well as the fact of being generated from abundant and renewable sources [2]. Improvements in processing technology, the development of suitable chemical coupling agents and economic factors spurred the use of wood as reinforcement in thermoplastic matrices [3]. In this paper we investigate the effect of two techniques – fibers mercerization and irradiation – on the mechanical properties of the manufactured composites. The process using ionizing radiation acts through scission of weak intramolecular bonds followed by the appearance of free radicals that, through different reaction paths, results in rearrangements and/or formation of new bonds. The result of these reactions is oxidation, grafting, degradation (scission of main chains) or cross-linking. The transformation depends on the radiation environment, dose rate and total adsorbed dose. Polymers that are cross-linked acquire better resistance to impact and stress cracking while, in many cases, improving

their chemical resistance [4,5,6,7]. In general on irradiation process is applied a dose rate between 15 - 50 kGy for grafting and for crosslinking between 50 -150 kGy [7].The mercerization process consists of a treatment of the fiber using sodium hydroxide solution to remove undesirable substances such as lignins, wax and oils from the surface of the fibers and exposes more of the fiber surface, improving the interaction between the polymeric matrix and fiber [8].

Materials and Methods

Materials

The following materials were used in this work: Green High Density Polyethylene (HDPE SGF 4950) from Braskem S/A, specific density of 0.956 g/cm, MFI (Melt flow index) of 0.34 g/10 min to 190°C/2.16 Kg and Brazil nut pod, residue disposed off by processing industries of Brazil Nut.

Fiber Preparation

The Brazil nut pod residue was ball milled, classified granulometrically with the aid of sieves ≤ 125 μm, the fibers particles were dried in a greenhouse (Quimis, model Q-317B) at a temperature of 80 ± 2 ºC for 12 h. For mercerization, the fibers were treated with a NaOH aqueous solution (20 % w/v) for one hour, then neutralized, washed with deionized water and then dried at 60 ± 2 ºC for 48 h.

Electron Beam Radiation

Samples of composites were irradiated at 150 kGy and samples of neat HDPE were irradiated at 15 kGy, for post injection. In both situations an electron beam accelerator (Dynamitron II, Radiation Dynamics Inc., 1.249 MeV energy, 5.05 mA current and 37.5 kW power), was used at room temperature in air and at a dose rate of 22.41 kGy/s. Ionizing radiation doses were measured using cellulose triacetate film dosimeters ''CTA-FTR-125'' from Fuji Photo Film Co. Ltd.

Composite Preparation

The polymeric matrix was compounded with 20 % (80:20 wt%) of Brazil nut pod particles mercerized and non mercerized, using a twin-screw extrusion process, with a processing temperatures of 125 ºC to 140 ºC. A twin screw extruder double thread model "AX 16LD40" of AX Plasticos Máquinas Técnicas Ltda. was used. After extrusion the composites were injected in an injection molding machine (thermoplastic DEMAG ergo tech pro 35-115) with the processing temperature range of 150 ºC to 180 ºC. Samples were prepared as described in Table I.

Table I. Samples prepared

Sample #	MATRIX (wt%)			FIBER (wt%)	
	Neat	Pre-Irradiated 15 kGy	Irradiated 150 kGy	Mercerized	Non Mercerized
HDPE	100	-	-	-	-
HDPE_PrI 15	-	100	-	-	-
HDPE_PoI 150	-	-	100	-	-
COMP_NMF_NI	80	-	-	-	20
COMP_NMF_PrI 15	-	80	-	-	20
COMP_NMF_PoI 150	-	-	80	-	20
COMP_MF_NI	80	-	-	20	-
COMP_MF_PrI 15	-	80	-	20	-
COMP_MF_PoI 150	-	-	80	20	-

Characterization

In order to understand the effect of mercerization and electron beam radiation on material, fiber morphology and mechanical properties were evaluated using a SEM, tensile, flexural and impact test machines.

The tensile test was performed in a room with temperature and humidity controlled, using an universal test machine (Instron 30 kN Test Machine) according to the procedure described in ASTM standard (D638), speed of testing was 2 mm/min. The flexural test was carried out in a room with temperature and humidity controlled, using an universal test machine (Instron 5800 100 kN Test Machine) according to the procedure A described on ASTM standard (D790), the depth and width of specimens were respectively 6 x 13 mm and span-to-depth ratio of 16:1, speed of testing was 2 mm/min and the results on table III represent the average of three samples. The impact test was performing using Ray Ran test equipment on unnotched specimens and impact blow in flatwise direction, according to the procedure described on Charpy Impact Strength ISO standard (179), the depth and width of specimens were respectively 12 x 6 mm.

Results and Discussion

Mechanical Analysis

The mechanical properties of a material provides information related to failure (brittle or ductile) and consequently determines the most suitable application of material. It is related to the behavior of material under stress [6].

Tensile Test

The Figure 1 represents the diagram stress versus strain of the materials prepared. The reduction in elongation was expected for composites, because the addition of the fibers changes the viscoelastic behavior of the matrix making it less ductile.

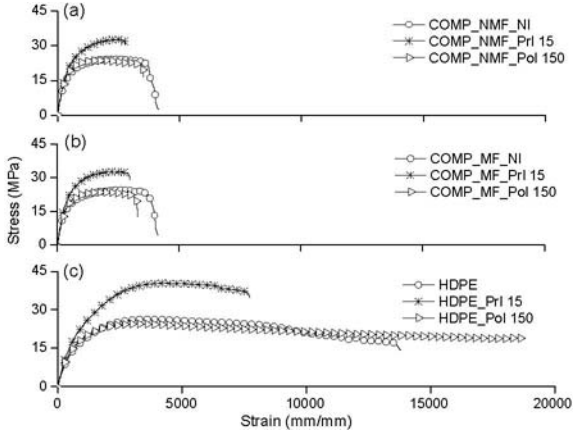

Figure 1. Diagram Stress (MPa) x Strain (mm/mm): (a) composite non-mercerized, (b) composite mercerized and (c) neat HDPE

The inclusion of BNPF as a reinforcement to HDPE matrix resulted in the improvement of tensile modulus properties and reduction in elongation at break. Comparing the composites, where the only treatment was the mercerization, an unexpected behavior was observed. The composite prepared using non mercerized fibers suggests a better performance in modulus (approximately by 7 %). Considering the irradiation process, the composite prepared with the irradiated matrix presented a significant advantage on modulus and tensile stress at tensile strength when compared with the irradiated composite. The material showed which showed

an improvement in modulus of approximately 135 %, when compared with the neat material, was the composite prepared using pre-irradiated matrix and mercerized fiber. The results suggest that the grafting effect was potentiated in approximately 8 % on modulus when using the mercerized BNPF.

The tensile modulus also presented improvements for non irradiated samples, the tensile stress at tensile strength presented a reduction indicating that the interfacial bonding between the filler and the polymeric matrix did not provide good stress propagation. The composite prepared with non mercerized fiber achieve better results for modulus when compared with the composite prepared with the mercerized fiber.

On pre-irradiated samples, the use of the irradiated matrix to prepare the composite indicated a good wetting of fiber. The result of tensile stress at tensile strength indicates that the interfacial bonding between the filler and the matrix polymer resulted in good stress propagation. It also means that eventual problems on mix due to the preparation process, observed on non irradiated samples, are minimized. The result for composites prepared using the pre-irradiated matrix and mercerized fiber, indicated better use of benefits provided by the both treatments. The result of the irradiated composites indicates that the benefits of mercerization were not important for flexural properties, because there is no significant difference between the composite prepared with mercerized fiber and non mercerized fiber (Table II). Here, we can see that the fibers mercerization does not have a significant effect on the final properties of the composites.

The results in Table II represent the average of four samples.

Table II. Tensile test results

	Tensile Modulus MPa	Tensile strength at break MPa	Elongation at Break %
COMP_MF_PoI 150 Composite mercerized fiber Post Irradiated	1,579.45 (± 13.77)	23.51 (± 0.27)	9.62 (± 0.00)
COMP_NMF_PoI 150 Composite non mercerized fiber Post Irradiated	1,575.69 (± 8.65)	23.69 (± 0.34)	9.71 (± 0.01)
COMP_MF_PrI 15 Composite mercerized fiber Pre Irradiated	1,607.59 (± 16.57)	32.52 (± 0.63)	8.14 (± 0.01)
COMP_NMF_PrI 15 Composite non mercerized fiber Pre Irradiated	1,484.27 (± 14.05)	32.71 (± 0.26)	8.07 (± 0.00)
COMP_MF_NI Composite mercerized fiber Non Irradiated	1,198.07 (± 15.17)	24.36 (± 0.40)	11.43 (± 0.01)
COMP_NMF_NI Composite non mercerized fiber Non Irradiated	1,287.83 (± 20.03)	24.16 (± 0.23)	16.06 (± 0.03)
HDPE_PoI 150 Post Irradiated	803.51 (± 8.65)	24.42 (± 0.87)	50.99 (± 0.08)
HDPE_PrI 15 Pre Irradiated	815.82 (± 12.12)	20.21 (± 0.04)	40.39 (± 0.65)
Neat HDPE Non Irradiated	683.02 (± 25.63)	26.26 (± 0.54)	39.30 (± 0.06)

Flexural Test

The flexural test results are presented in Table III. Composites prepared with mercerized fiber showed better results, this can be attributed to the more availability of cellulose and their ability to withstand bending force.

For all samples, it is possible to observe a reduction in flexure extension when comparing the neat matrix with their composite however, opposite behavior is seen with flexure load and modulus. The best modulus result, *ca*120 %, when compared to the neat material, was achieved on composite irradiated using mercerized fiber.
For the composites prepared with non mercerized fiber, no substantial difference between the pre-irradiated and post-irradiated material was observed, however, the irradiation process plays as an important role in improving the property when compared to the non-treated matrix. The mercerization improved the flexural modulus by approximately 14 % on post irradiated material. The results in Table III represent the average of four samples.

Table III. Flexural test results

	Flexural Modulus MPa	Flexure Load at Yield N	Flexure Extension at Yield mm
COMP_MF_PoI 150 Composite mercerized fiber Post Irradiated	1,484.76 (± 17.83)	97.68 (± 0.09)	14.94 (± 0.18)
COMP_NMF_PoI 150 Composite non mercerized fiber Post Irradiated	1,295.21 (± 24.05)	98.71 (± 1.19)	14.66 (± 1.03)
COMP_MF_PrI 15 Composite mercerized fiber Pre Irradiated	1,278.88 (± 48.13)	85.87 (± 1.24)	15.62 (± 0.27)
COMP_NMF_PrI 15 Composite non mercerized fiber Pre Irradiated	1,217.97 (± 17.49)	77.16 (± 0.99)	15.57 (± 0.38)
COMP_MF_NI Composite mercerized fiber Non Irradiated	1,143.88 (± 5.46)	77.29 (± 0.98)	15.45 (± 0.75)
COMP_NMF_NI Composite non mercerized fiber Non Irradiated	1,104.70 (± 13.93)	79.59 (± 2.79)	15.16 (± 0.24)
HDPE_PoI 150 Post Irradiated	819.19 (± 28.86)	83.20 (± 1.88)	18.21 (± 0.48)
HDPE_PrI 15 Pre Irradiated	873.96 (± 18.62)	69.72 (± 0.32)	19.24 (± 0.10)
Neat HDPE Non Irradiated	666.35 (± 22.98)	63.39 (± 1.60)	17.60 (± 2.25)

The inclusion of fiber in non-irradiated samples improved the flexural modulus by more than 60 %. An improvement on flexure load at yield also was evidenced. The use of irradiated matrix to prepare the composite acts as an important tool to improve the flexural properties of material. The result for composites prepared using pre-irradiated matrix, indicates the chemical treatment of fiber is not a major factor in flexural improvement. The results suggest that the crosslinking process was promoted by the irradiation process on composite and resulted in improvement on flexural modulus of material, mainly when it is used mercerized fiber is used.

Pendulum Impact Test

All composites showed a reduction in impact strength and complete rupture, it means that the material becomes more brittle with the inclusion of natural fiber.
The result suggests a poor adhesion between fiber and matrix and that the fiber deformation leading to micro-cracking and fracture, fiber splitting and pullout, these affirmations will be supported by SEM analyses. The decrease on impact resistance of composites can be

attributed to fragile surface adhesiveness between fillers and matrix and to cavities formed within the sample. The low capacity to absorb impact energy occurs because every fiber is a site of stress concentration, which can act as micro-crack initiator [9]. The results represent the average of three samples and are described on Table IV.

Table IV. Impact test results

	Impact Strength KJ/m^2
COMP_MF_PoI 150 Composite mercerized fiber Post Irradiated	25.50 (± 4.16)
COMP_NMF_PoI 150 Composite non mercerized fiber Post Irradiated	31.17 (± 3.74)
COMP_MF_PrI 15 Composite mercerized fiber Pre Irradiated	18.25 (± 3.27)
COMP_NMF_PrI 15 Composite non mercerized fiber Pre Irradiated	17.34 (± 2.47)
COMP_MF_NI Composite mercerized fiber Non Irradiated	26.49 (± 3.74)
COMP_NMF_NI Composite non mercerized fiber Non Irradiated	27.04 (± 2.53)
HDPE_PoI 150 Post Irradiated	46.38 (± 0.79)
HDPE_PrI 15 Pre Irradiated	60.05 (± 2.83)
Neat HDPE Non Irradiated	44.47 (± 2.15)

SEM – Scanning Electron Microscopy

The fracture surfaces examination of the composites provided information about how the processing and treatment - mercerization and irradiation - affected the morphology of the composite, and explaining the mechanical results. The morphological aspect of composites and fibers was studied using Scanning Electron Microscope (Carl Zeiss Gemini SEM). For composite evaluation the impact fractured surfaces were used. All samples were gold sputtered. The scanning electron microscopy (Figure 2) allowed the morphological characterization of the fibers before and after mercerization. The mercerization process worked as expected, removing the wax and oils from the surface, increasing the surface area facilitating the interaction between fiber and the polymeric matrix. The roughness promoted by the treatment improved the mechanical interlocking between fiber and matrix, suggesting an improvement of mechanical properties.

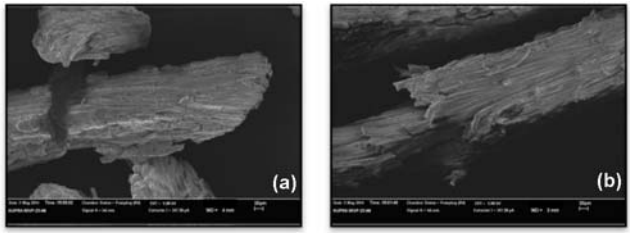

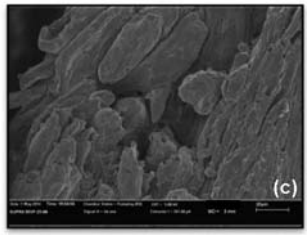

Figure 2. SEM of BNPF non-mercerized 166x (a), mercerized 166x (b), mercerized 630x (c)

Results presented on SEM micrograph corroborate the mechanical findings. The alteration on matrix appearance, due to the irradiation treatment, is evident.
On non irradiate samples, Figure 3 (a) and (b), and post irradiated samples, Figure 3 (c) and (d) the stretching of matrix is observerd indicating a plastic deformation. On pre irradiated samples, Figure 3 (e) and (f), the brittle fracture is characterized by the crystalline appearance explaining the low energy absorbed on impact test.

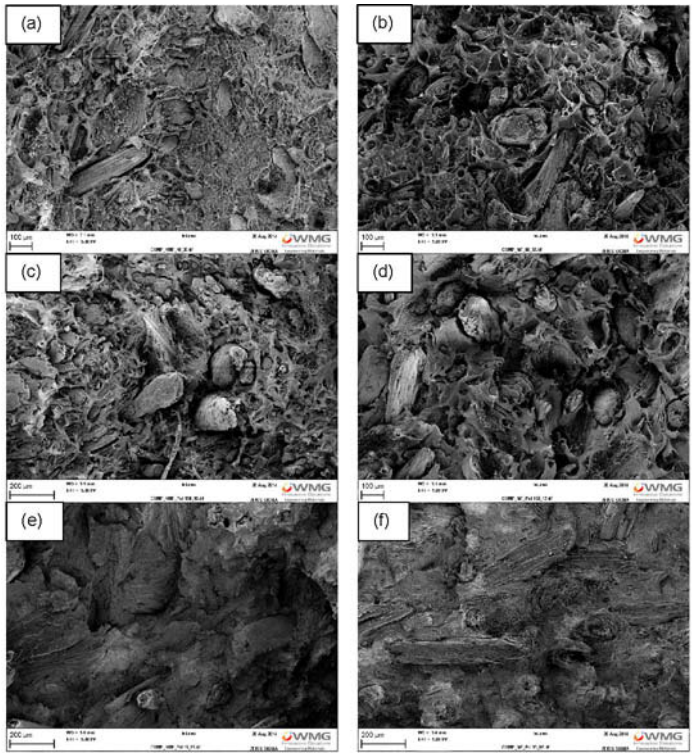

Figure 3. SEM 200x of: non irradiated composites - non mercerized fiber (a) and mercerized fiber (b); post irradiated composites - non mercerized fiber (c) and mercerized fiber (d); pre irradiated composites - non mercerized fiber (e) and mercerized fiber (f)

Conclusions

The effect of mercerization of Brazil nut pod fiber with 20 % w/v NaOH aqueous solution was found to be insignificant in improving the performance of the composite prepared with this fiber and high density polyethylene, however when combined with irradiation process, its action is drastically enhanced. Irradiation of matrix with 15 kGy followed by composite preparation showed better mechanical properties indicating that the interaction between the matrix and filler is enhanced.

Acknowledgments

The authors are grateful to CAPES Foundation, Ministry of Education of Brazil for the financial support, Braskem, CNEN-IPEN/SP, the members of CCN Lab, CCTM Lab and Warwick Manufacture Group of the University of Warwick.

References

[1] SANTOS, A.M., Estudo de Compósitos Híbridos Polipropileno / Fibras de Vidro e Coco para Aplicações em Engenharia. 2006. Dissertação (Mestrado em Engenharia Mecânica) – Universidade Federal do Paraná, Paraná, 2006.

[2] JOSEPH, K., MEDEIROS, E.S., CARVALHO, L.H., Compósitos de Matriz Poliéster Reforçados por Fibras Curtas de Sisal, **Polímeros: Ciência e Tecnologia – Out/Dez**, 1999, v9 n4, 136-141p.

[3] KIM J.K., PAL K., **Recent Advances in the Processing of Wood-Plastic Composites**. 1ª ed., Berlin; Springer, 2011.

[4] CLOUGH R.L., High-energy radiation and polymers: A review of commercial processes and emerging applications, **Nuclear Instruments and Methods in Physics Research B**, 2001, 8-33p.

[5] Controlling of Degradation Effects in Radiation Processing of Polymers – IAEA International Atomic Energy Agency – May, 2009 – **IAEA-TECDOC-1617** – Vienna Austria.

[6] BHATTACHARYA, A., RAWLING, J. W., RAY, P., **Polymer grafting and crosslinking**, 1ª ed., New Jersey; John Wiley & Sons, Inc. Hoboken, 2009.

[7] ZAHARESCU T., **Processamento de polímeros por altas energias**. (Programa de Tecnologia Nuclear). São Paulo: IPEN, Lecture on second quarter of 2013.

[8] BORYSIAK S., DOCZEKALSKA B., X-ray Diffraction Study of Pine Wood Treat with NaOH. **Fibers & Textiles in Eastern Europe**, 2005, n 5, v 13, 87-89p.

[9] KIM J.K., PAL K., **Recent Advances in the Processing of Wood-Plastic Composites**. 1a ed., Berlin; Springer, 2011.

Characterization of Minerals, Metals, and Materials 2015
Edited by: John S. Carpenter, Chenguang Bai, Juan Pablo Escobedo, Jiann-Yang Hwang, Shadia Ikhmayies, Bowen Li, Jian Li, Sergio Neves Monteiro, Zhiwei Peng, and Mingming Zhang
TMS (The Minerals, Metals & Materials Society), 2015

ANALYSIS OF POROSITY AND FLEXURAL STRENGTH CHANGES OF RED CERAMIC PIECES INCORPORATED WITH ORNAMENTAL ROCK WASTE

Piazzarollo, C.B[1,a], Xavier, G.C.[1], Alexandre, J.[1], Azevedo, A. R. G.[1], Monteiro, S. N.[2] and Pedroti, L.G.[3]

[1]State University of Norte Fluminense Darcy Ribeiro, Civil Engineering Laboratory – LECIV. Av. Alberto Lamego, 2000, Horto, CCT Campos dos Goytacazes/RJ – Brazil, ZIP: 28013-600.
[2] *Military Institute* of Engineering, IME, Materials Science Department. Praça General Tiburcio, Urca. Rio de Janeiro/RJ – Brazil, ZIP: 22290270.
[3] Federal University of Viçosa, UFV. Avenida Peter Henry Rolfs, s/n - Campus Universitário, Viçosa - MG, ZIP: 36570-000.
[a]carlabp@gmail.com;

Keywords: red ceramic, ornamental rock waste, porosity, flexural strength.

Abstract

Red Ceramic materials are widely used in Civil Construction in Tropical Countries. However, these materials have high porosity and low mechanical strength. Thus, in order to improve these properties, recycle mineral wastes was incorporated into clay from Campos - RJ, ornamental rock waste, from the gneisses cutting of Cachoeiro - ES, 150 km from Campos. After the addition of up 10% of waste in clay mass, ceramic pieces were produced and subjected to the tests of porosity (P) and flexural strength (FS). The test material contains 53.3% clay and 67% waste slit. The X-ray diffraction identified the presence of kaolinite, quartz and feldspar for the clay and, for the waste, quartz and orthoclase. The results of FS and P showed that the residue influenced, positively, the ceramic piece, with strength gains especially from 920° up to 960°C.

Introduction

Today, with the focus on sustainable development, there is a worldwide trend in encouraging the recycling. In the area of construction, the incorporation of solid waste into clay for the manufacturing of red ceramic pieces has been proposed by several national and international studies [1].

Campos dos Goytacazes, a Brazilian municipality, has a large reserve of clays and is a center of red ceramics, accounting for about 40% of the Rio de Janeiro state production [2] and therefore, emerges as object of study. Looking for the best quality products in the mildest temperatures, [3] indicated the use of granite waste in red ceramics for obtaining greater strength and less open porosity in firing temperatures of up to 950°C.

Thus, after subjecting red ceramic samples to flexural strength (FS) and porosity (P) tests, this paper presents different statistical analysis of data in order to evaluate the changes with the incorporation of ornamental rock waste into clay and indicate the best percentage of waste and firing temperature for ceramic pieces.

Materials and Methods

For this study, we used the following materials: clay from the municipal district of Campos-RJ and ornamental rock waste from Cachoeiro do Itapemirim, Espírito Santo state.

The Quantitative Chemical Analysis tests were carried out in the Materials Characterization Laboratory - LECIV/CCT/UENF. The samples were sieved on #325 mesh (0.045mm) and the drying process involved the temperature of 110ºC. The samples of clay and ornamental rock waste were sieved on #40 mesh (0.42mm) and dried at 110ºC and were subjected to X- ray tests. Was used the energy dispersive X-ray equipment, model Shimadzu EDX-700.

The particle size distribution curve, assay which determines the soil particle size and relative proportions, was performed by sieving and sedimentation according to NBR 7181 [4].

The samples were prepared with clay incorporated with three different waste contents (i.e. 0%, 5%, and 10%) and, to ensure the homogeneity of samples, the mass was reduced according to [5]. At first, the ornamental rock waste powder was sieved on #40 mesh (0.42mm) and the retained material was discarded. Next, the pass-through material was ground to pass through sieve #60 mesh (0.25mm).

After mixing the samples with 0%, 5% and 10% waste (identified as 0R, 5R and 10R, respectively), the ceramic pieces were molded in prismatic shapes of 11.70 cm x 2.70 cm x 1.70 cm. The number of pieces (5) and the measures was carried based on the standards [6,7].

The drying process involved the temperature of 110ºC, and the firing process involved 750ºC, 850ºC and 950ºC in an electronic oven.

After firing, the ceramic pieces were subjected to a three loading point flexural strength test according to standard procedure [6] and also to the tests according to [7]. The obtained results represent the average of 5 determinations. The three loading point flexural strength test was carried out with a loading rate of 0.5 mm/min with a distance of 9.0 cm between supports on INSTRON 5582.

Results

Table 1 – Chemical Analysis

Raw Materials	SiO_2 (%)	Al_2O_3 (%)	Fe_2O_3 (%)	K_2O (%)	TiO_2 (%)	SO_3 (%)	CaO (%)	MnO (%)	V_2O_5 (%)	ZrO_2 (%)	CuO (%)	ZnO (%)	SrO (%)
Clay	48.83	35.46	8.87	3.17	1.62	1.13	0.54	0.14	0.10	0.03	0.03	0.03	0.01
Waste	50.09	17.60	12.47	3.70	1.83	1.56	12.39	0.19	0.55	0.03	-----	0.02	0.04

The Table 1 shows the composition of SiO_2+Al_2O_3 over 84% characterizes refractory clay. The clay color after fired is a consequence of 8.87% of Fe_2O_3. The K_2O and the CaO into clay in proportion of 3.17% and 0.54% respectively, are burning and melting agents and form eutectics, contributing to reduce the porosity of the material. The SO_3 present into clay has a deleterious effect due to the output of the gas of the pieces, breaking them.

For the ornamental rock waste, the silica content is about 50% and the Al_2O_3 is over than 17%, indicating chemical compositions of primary minerals (quartz, feldspar

and minerals of the mica's group). The content of Fe_2O_3 (12.48%) contributes to the red color of the pieces after mixing with the clay. The K_2O (3.70%) present into residue is important in the firing because reduces the porosity in the finished material.

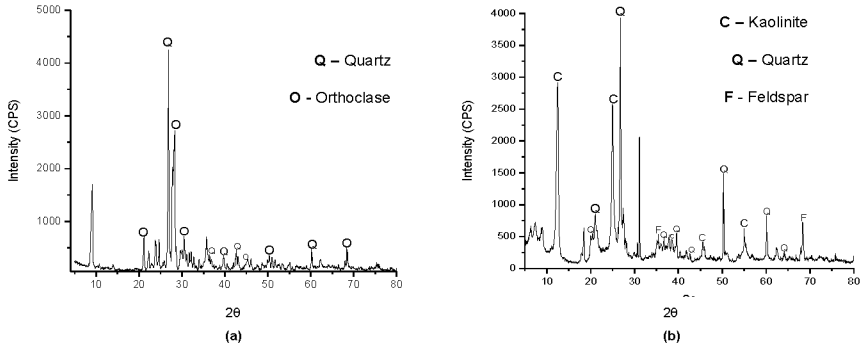

Figure 1 - X-ray diffraction spectra of ornamental rock waste (a) and clay (b).

The x-ray spectroscopy of ornamental waste, Fig. 1 (a), shows the presence of orthoclase ($KAlSi_3O_8$) and quartz (SiO_2). For clay, the Fig. 1 (b) shows the presence of kaolinite (Al_2O_3. $2SiO_2$. $2H_2O$), quartz (SiO_2) and feldspar.

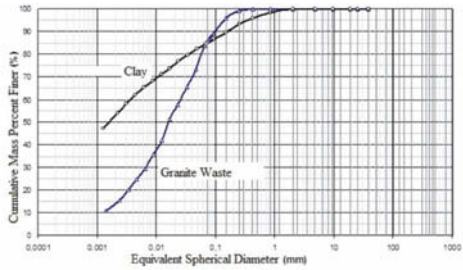

Figure 2 - Particle-size distribution of the raw materials.

The Fig. 2 shows the particle-size distribution of clay is composed by 52% clay, 32% of silt, 8% fine sand fraction, 6% medium sand fraction, and 2% for coarse sand fraction. For the granite waste the particle-size distribution shows 13% clay, 68% of silt, 16% fine sand fraction and 3% coarse sand fraction.

Porosity and flexural strength are shown in Figures 3 and 4.

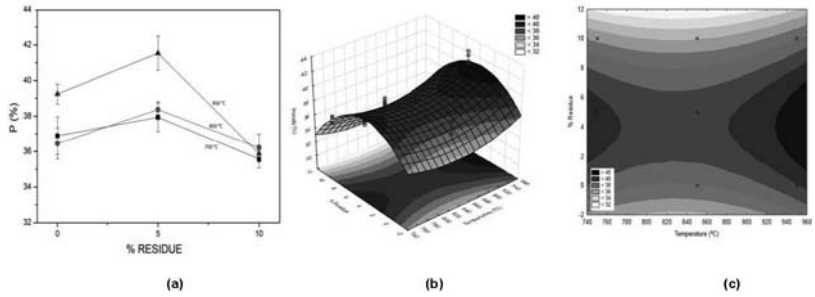

Figure 3 – Porosity (a), surface plot (b) and contour plot of red ceramic pieces incorporated with ornamental rock waste.

The Fig. 3 (a) indicates a decrease tendency of the Porosity of the red ceramic pieces with the incorporation of 10R, independent of the firing temperature. By the Fig. 3 (b) and (c), the surface and contour plot, it is possible indicate the incorporation from 9% up to 12% of ornamental rock waste into clay with firing temperature from 740ºC up to 960ºC.

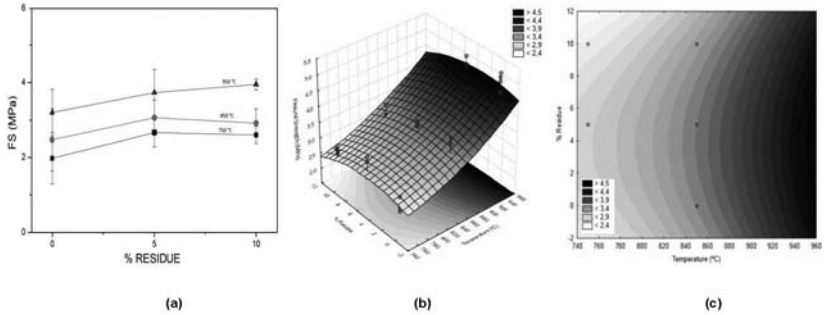

Figure 4 - Flexural Strength (a), surface plot (b) and contour plot (c) of red ceramic pieces incorporated with ornamental rock waste.

Regarding the Fig. 4 (a) it is possible to note an increase tendency of the FS of the red ceramic materials, independent of the incorporated waste percentage. The addition of 5R and 10R increases the FS, showing better results than 0R, due to the presence of alkaline mineral K_20 (Table 1) from Feldspar (Fig. 1b), and the amount of silt fraction, providing greater packing between particles.

By the Fig. 4 (b) and (c) it is possible indicate the incorporation from 8% up to 12% of ornamental rock waste into clay with firing temperature from 920ºC up to 960ºC.

Associating the best results of Porosity and Flexural Strength of the incorporation of ornamental rock waste, presented above, it is possible to note that the incorporation from 10R of waste is the most appropriated.

Thus, aims to ensure this observation, was applied the Weibull Statistics to evaluate changes associated with mechanical strength of 10R samples when the firing temperature was changed.

The Fig. 5 shows the Weibull Plot for the samples with 10R fired at different temperatures.

By the slope of the line, it's possible to determine, the Weibull modulus (m). The **m** value is a good standard for the analytical quality of ceramic materials [8], and his value represents a risk of rupture/failure and characterizes the dispersion of the FS data [9].

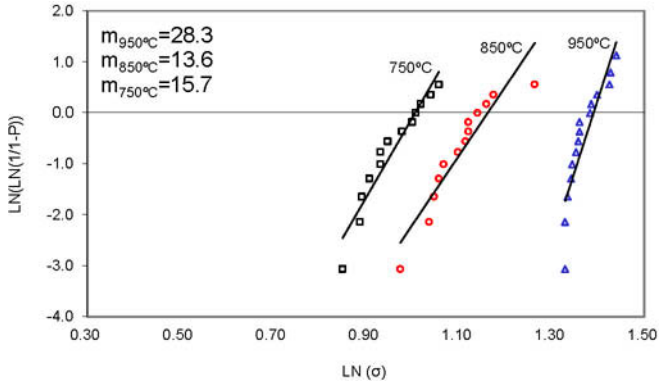

Figure 5 – Weibull distribution: samples with 10R fired at 750°, 850° and 950°C.

The incorporation of 10R of ornamental rock waste into clay intensely influencied at Weibull modulus (m=28.3) at 950°C. This modulus ensure that the batch was more homogeneous, i.e., has a less propability of failure. The samples presented a bimodal distribution, typical of the Weibull analisys.

Conclusion

- The clay has a refractory character due to the high content of SiO_2 + Al_2O_3 and her color is due to the presence of Fe_2O_3> 8%;
- The K_2O melts at low temperatures forming glassy structure on cooling, decreasing the porosity;
- The ornamental rock waste has K_2O> 3%, contributing to decreasing of the porosity, as happens for 10R samples at all temperatures;
- The x-ray spectroscopy shows the ornamental rock waste, composed of primary minerals (quartz and orthoclase), comes from basic rocks;
- The addition of 10R into clay improves a porosity decrease of the samples, especially for the firing temperature of 950°C;
- For the Flexural Strength, the incorporation of ornamental rock waste into clay resulted in strength gains;
- Analyzing the Weibull distribution, the biggest value of Weibull modulus (m = 28.3) is at 950°C with 10R, showing the greater homogeneity of this batch;
- By the surface and contour plot of the Porosity (P), it is possible indicate the incorporation from 9% up to 12% of ornamental rock waste into clay with firing temperature from 740°C up to 960°C;

-By the surface and contour plot of the Flexural Strength (FS), is possible indicate the incorporation from 8% up to 12% of ornamental rock waste into clay with firing temperature from 920ºC up to 960ºC.

- Lastly, associating the surface plots it is possible to conclude that to obtain higher strength and lower porosity, it is indicated the use from 9% up to 12% of waste into clay and the firing temperature from 920ºC up to 960ºC. Results ensured by the Weibull modulus.

References

1. S.P. Raut, R.V. Ralegaonkar and S.A. Mandavgane, "Development of sustainable construction material using industrial and agricultural solid waste: a review of waste-create bricks", Construction and Building Materials. Vol. 25, Issue 10, Pages 4037-4042, 2011.
2. C.M.F Vieira, J.N.F Holanda, and D.G. Pinatti, "Caracterização de massa cerâmica vermelha utilizada na fabricação de tijolos na região de Campos dos Goytacazes-RJ", Cerâmica, Vol. 46, São Paulo, 2000.
3. F. Saboya, G.C.Xavier, J. Alexandre, "The use of the powder marble by-product to enhance the properties of brick ceramic", Construction and Building Materials, Vol. 21 (2007), Pages 1950-1960.
4. Brazilian Association of Technical Norms –ABNT NBR-7181, Soil - Granulometric Analysis (in Portuguese), Rio de Janeiro, Brazil, 1988.
5. Brazilian Association of Technical Norms –ABNT NBR-6457, Soil samples – compaction tests and characterization tests (in Portuguese), Rio de Janeiro, Brazil, 1986.
6. American Society Technology Materials - ASTM C 674, Standard Test Method for Flexural Properties of Ceramic Whiteware Materials, 1977b.
7. American Society Technology Materials - ASTM C 373, Standard Test Method for Water Absorption, Bulk Density, Apparent Porosity and Apparent Specific Gravity of Fired Whiteware Products, 1977a.
8. L.M. Thurler, G. P. Souza, J.N.F. Holanda, "Avaliação do Módulo de Weibull para Argilas de Campos – RJ" (Paper presented at the 43rd Brazilian Congress on Ceramics, Florianópolis, Santa Catarina, 1999), 8.
9. S. Somiya et al., Handbook of Advanced Ceramics. (New York, NY: Elsevier, 1990), 1046 -1058.

Characterization of Minerals, Metals, and Materials 2015
Edited by: John S. Carpenter, Chenguang Bai, Juan Pablo Escobedo, Jiann-Yang Hwang, Shadia Ikhmayies, Bowen Li, Jian Li, Sergio Neves Monteiro, Zhiwei Peng, and Mingming Zhang
TMS (The Minerals, Metals & Materials Society), 2015

EFFECTS OF ACCELERATED THERMAL AGING ON POLYPROPYLENE MODIFIED BY IRRADIATION PROCESS

Washington Luiz Oliani[1], Danilo Marin Fermino[2], Luis Filipe Carvalho Pedroso de Lima[1], Ademar Benevolo Lugao[1], Duclerc Fernandes Parra[1]

[1] Nuclear and Energy Research Institute, IPEN-CNEN/SP, Av. Prof. Lineu Prestes, 2242 – Cidade Universitária - CEP 05508-000 São Paulo – SP - Brazil
washoliani@usp.br ; dfparra@ipen.br

[2] Department of Metallurgical and Materials Engineering - EPUSP (Escola Politécnica, Universidade de São Paulo), Av. Prof. Mello Moraes, 2463, Cidade Universitária, CEP 05508-030, São Paulo, SP, Brazil

Keywords: polypropylene, degradation, gamma rays, crosslinking, branching, thermal aging.

Abstract

The modified polypropylene was obtained from isotactic polypropylene (iPP) in spheres by irradiation with gamma rays in the presence of acetylene. A new morphology with distinct rheology is obtained by this process in which occurs: degradation, branching and/or crosslinking. The objective of this study was to investigate the effects of thermal aging on the crystallinity and morphology of the modified polypropylene, *High Melt Strength Polypropylene* (HMS-PP). The thermal stability was evaluated after aging of samples using a stove at temperature of 90 °C, in presence of air at different periods of time. Aging effects were characterized by: Thermogravimetry analysis (TG), Differential scanning calorimetry (DSC), Infrared spectroscopy (FTIR) and Scanning electron microscopy (SEM). In thermooxidative conditions, the formation of oxidation products essentially involves a hydrogen abstraction by the peroxyl radical, leading to hydroperoxides as primary products and chemical degradation in the immediate crack tips. The effect of thermal degradation (chain scission and oxygen diffusion) on iPP was a more intense crack formation. Surface cracks increased with the aging time. In comparison of iPP, the modified PP samples had a morphological barrier inhibiting the penetration of oxygen into the sample and in consequence limit the propagation of degradation.

Introduction

Isotactic polypropylene (iPP) is used extensively as a matrix material in thermoplastic composites due to its excellent mechanical properties and relatively low cost, in which the effects of aging have significant interest, particularly due to prolonged exposure at service temperatures. A common approach for characterizing aging response in a more practical time frame is to conduct accelerated aging tests at temperatures above the expected service limits [1].

The radiation induces changes in the degree of crystallinity of iPP, result from the combination of two opposing effects, crystallinity increase caused by chain scission and a decrease induced by crosslinking on the lamellae surfaces. The decrease in the degree of crystallinity additionally results from the radiation-induced defects within the crystals, as well as from those at the lateral grain boundaries [2]. Gamma irradiation modified the chemical structure of polypropylene by enhancing the content of carbonyl and hydroxyl suggesting the occurrence of oxidative degradation [3].

In thermal aging of semicrystalline polymers, the mobility of molecular segments is increased by thermal activation even with no changes in the molecular size. The subsequent annealing leads to secondary crystallization, which is facilitated by oxidative chain scission. It occurs at different rates depending on the depth below the surface and is influenced by oxygen diffusion and consumption in the polymer. Contraction of the surface layers is a consequence of

chemicrystallization and results in accelerated aging plastic materials heated in oven. To increase the effect of accelerated aging even further to obtain lifetime estimative of the thermooxidative stability has been suggested at temperatures above the melting point of the polymer [4].
The free-radical degradation of PP consists of initiation, propagation, chain branching and termination leading to non-radical products. Initiation results from thermal dissociation of chemical bonds, whereas the key reaction in the propagation is the reaction of the polymer alkyl radicals with oxygen to form polymer peroxy radicals in a very fast reaction. The next propagation step is the abstraction of a hydrogen atom by the polymer peroxy radical to yield hydroperoxide polymer (POOH) and new alkyl radical. The chain branching of POOH results in the formation of very reactive polymer alkoxy radicals and hydroxyl radicals. The polymer oxy radicals can react further to form in-chain ketones or can be involved in termination reactions. The termination of PP radicals occurs by various bimolecular recombinations [5, 6].
The state of the art relating to research aging of polypropylene films is possible in the temperature range between 60 and 150°C [7]. Monitoring of the intensity of the C=O absorption in the IR-spectrum provides information regarding the progress of ageing [4].
Branching increases the susceptibility of a polymer chain to thermal oxidation because of the reactivity of the tertiary carbon at the branch point [8].
The rate of degradation during processing as well as during service life depends on the chemical structure, presence of structural defects, impurities such as polymerization catalyst residues, the environment to which the polymer is exposed and the use of stabilizers. In the presence of oxygen, oxidation reactions mainly determine the degradation rate of the polymer. In the case of polyolefins even at processing temperature oxygen plays an important role [9, 10].
In many types of degradation the interference of oxidative attack, which has an accelerating role, happens auto-oxidation. However, in oxidative degradation, the most commonly known phenomena are photooxidation and thermal oxidation (T< 300°C) and the effects are color changes, hardening, and surface cracking or flaking [11].
If an elevated temperature is applied to a polymer in the presence of an aggressive chemical agent (often oxygen) then this may give rise to chemical reactions that may occur only very slowly, or not at all, at ambient temperature. During both thermal oxidation and photo-oxidation, chain scission occurs with releasing of molecular chain segments from entanglements, facilitating conformational rearrangements [12]. Therefore occurs pronounced reduction in the molar mass and melt viscosity of the polymer [1]. This allows the chain segments to take up lower energy states, characteristic of the equilibrium state for the material, so accelerating physical ageing. The material is changed irreversibly by the scission events; the physical aging occurs alongside the changes and it is not always obvious which has the controlling influence over the material properties [12].
To study degradation, two temperatures were used in oven: 1) at 110°C under air atmospheric pressure, 2) 80 °C under pure oxygen at 5 MPa pressure. Very different kinetic behaviors were observed since induction times differ at about one order of magnitude. In both cases, M_w decreases abruptly after the end of the induction period showing that oxidation induces predominant chain scission which in turn, induces chemicrystallization and embrittlement [13].
Our Institute developed the production of branched PP, based on the grafting of long chain branches on PP backbone using acetylene as a crosslink promoter under gamma radiation process. The objective of this study was to investigate the effects of thermal aging on the crystallinity and morphology of the radiation modified polypropylene.

Materials and Methods

The investigation was conducted with the following samples of polypropylene. (See Table I).

Table I - MFI of samples of polypropylene spheres no additives

Samples / spheres	Melt Flow Index / MFI = dg min^{-1}
1 - iPP	2.9
2 - PP 12.5 kGy	28.0
3 - PP 20 kGy	39.0

The HMS-PP samples were obtained from iPP spheres (MFI = 2.9 dg min^{-1} from Braskem, Brazil) without any antioxidant. The iPP pellets were conditioned into nylon bags in which were fluxed with nitrogen in order to reduce as much as possible the internal oxygen concentration. The bags were submitted to the irradiation process in a ^{60}Co γ-source, at a dose rate of 5 kGy h^{-1} monitored with Harwell Red Perspex 4034, with dose levels ranging from 12.5 up to 20 kGy in presence of acetylene [14-16]. After irradiation, the samples were heat treated at 90 °C for 1 hour with the aim of promoting recombination and termination reactions and also eliminate residual radicals [17-19].
The dumbbell samples were prepared by mold pressure at temperature of 190°C in type IV according to ASTM D 638-03 [20]. Experimental aging tests of the iPP and HMS-PP samples in air circulation stove are showed in Figure 1.

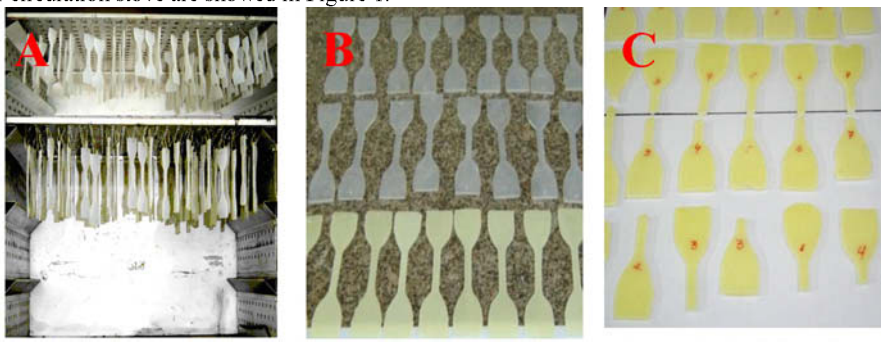

Figure 1. Experiment arrangement of the iPP and HMS-PP samples inside air circulation stove at the temperature of 90°C (A), Surface morphology of the samples iPP before (up) and after (down) aging in stove (B), Yellowing of HMS-PP 12.5 kGy and HMS-PP 20 kGy samples (C).

The iPP and HMS-PPs samples were set inside stove at temperature of 90 °C, in presence of air. Thermal stability was evaluated at different periods of time (6, 12 and 20 days), according to ASTM D 3045-2003 [16, 21].

Thermogravimetric Analysis
Thermogravimetry curves were obtained with an SDTA 851 thermobalance (Mettler-Toledo), using samples of about 10 mg in alumina pans, under nitrogen atmosphere of 50 mL min^{-1}, in range from 25 up to 600 ºC, at a heating rate of 10 °C min^{-1}, according to ASTM D 6370-2003 [22].

Differential Scanning Calorimetry
Thermal properties of specimens were analyzed using a differential scanning calorimeter (DSC) 822e, Mettler-Toledo. The thermal behavior of the films was obtained by: (1) heating from 25 to 280 ºC at a heating rate of 10 ºC min^{-1} under nitrogen atmosphere, (2) holding for 5 min at 280 ºC, and (3) then cooling to 25 ºC and reheating to 280 at 10 ºC min^{-1}, according to ASTM D 3418-08 [23]. The crystallinity was calculated according to the equation:

$$X_C(\%) = \frac{\Delta H_f \times 100}{\Delta H_0}$$

Where ΔH_f is melting enthalpy of the sample, ΔH_0 is melting enthalpy of the 100% crystalline PP which is assumed to be 209 kJ kg $^{-1}$ [24, 25].

Fourier Transform Infrared Spectroscopy

The FTIR was carried out with a Thermo Nicolet 6700 FTIR spectrometer with a Smart Orbit accessory, in the wavelength range 4000 to 400 cm^{-1}. In order to ensure satisfactory contact between the ATR diamond crystal and the sample, three or more FTIR spectra were recorded at various locations on the sample.

Scanning Electron Microscopy

Specimens were coated with gold in a sputter coater prior to examination to avoid charging. A Philips XL30 SEM was used for collect secondary electron images from the samples.

Results and Discussion

Thermogravimetry

The TG results indicated decomposition of the samples, Figure 2.

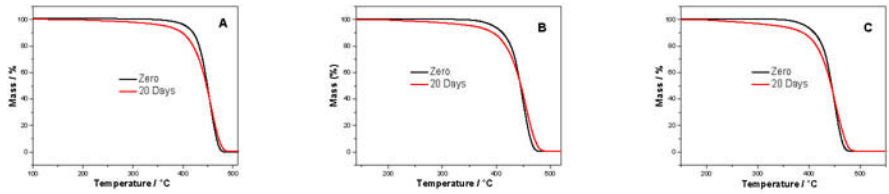

Figure 2. TG curves of samples: iPP (A), HMS-PP 12.5 kGy (B) and HMS-PP 20 kGy (C), under thermal aging in stove for 20 days.

As observed in the curves, Figure 2A, significant variation of onset temperature of the decomposition step (*Tonset*) displaced from 439 to 419 °C in samples. In the Figure 2B, *Tonset* decomposition of the samples displaced from 430 to 424 °C after aging. In Figure 2C, the temperature after 20 days was 418 °C while not aged was 432 °C. The higher difference between samples onset temperatures was evident in iPP, because the effect of scission chain was more accentuated in the non-irradiated polyolefins. Segments of the degraded polymer displaced the *Tonset* to lower values.

Differential Scanning Calorimetry

Duplication or multiplication of melting peaks observed can be attributed to structural reasons and processes. For this reason, beside the main melting peak of folded-chain crystallites, a higher temperature peak or shoulder appears on the melting curve [26].

The DSC technique was applied to evaluate the temperatures of second melting (T_{m2}), Figure 3A, and the degree of crystallinity (X_C), Figure 3B. In this controlled situation defected crystals had time to segregate.

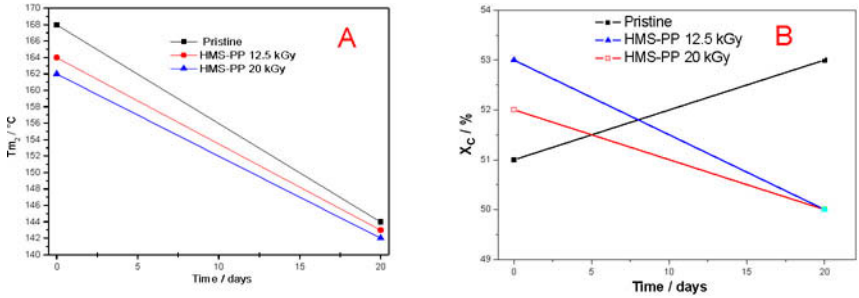

Figure 3. (A) Melting temperatures of samples: iPP; HMS-PP 12.5 kGy and HMS-PP 20 kGy; and (B) Polypropylene crystallinity calculated after 20 days aging.

Double melting peaks were observed in DSC and were shown to be due to re-organization during heating, but in some cases the segregation of highly molecules is the major reason for peak doubling [27]. Although the crystallinity has near values, the melting temperatures reveal that iPP is more degraded than irradiated samples.

In the iPP sample was observed melting temperature displacement ΔTm_2 = 24 °C, ΔTm_2 = 21 °C while for HMS-PP 12.5 kGy and ΔTm_2 = 20 °C for HMS-PP 20 kGy, indicating morphology modifications of the samples crystalline phase. Melting temperature decrease demonstrates that chain scission is the main mechanism of the degradation. This can be attributed to modification in the crystal structure of iPP which resulted in the mobility of the iPP molecules that increases with the dose radiation. The calculated decrease of crystalline content phase in HMS-PP 12.5 kGy and HMS-PP 20 kGy were plotted in Figure 3B, owing to chain scission mechanisms on aging. Contraction of the surface layers, resulting in surface cracks, is a consequence of chemicrystallization.

Infrared Spectroscopy

FTIR spectra of the samples thermal aging in stove, Figure 4.

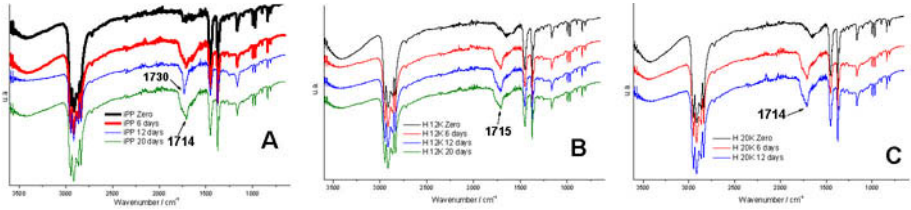

Figure 4. Infrared spectra by ATR technique of the: iPP (A), HMS-PP 12.5 kGy (B) and HMS-PP 20 kGy (C), under thermal aging in stove for 20 days.

The iPP, HMS-PP 12.5 kGy and HMS-PP 20 kGy, aged in stove for 12 days show typical absorption bands of carbonyl stretching in the region 1714-1730 cm^{-1}, Figure 4, shows a substantial content of oxidation products. During thermooxidative ageing in a circulation air oven, the polymer undergoes thermooxidative degradation. Carboxylic and carbonyl groups are present in the end products of the oxidation.

Scanning Electron Microscopy

Figure 5 shows SEM secondary electron images collected from the fracture surfaces.

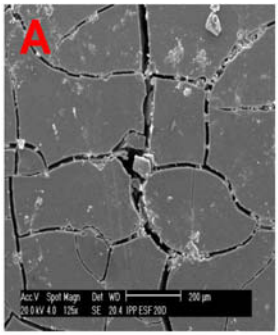

Longitudinal SEM photo of iPP.

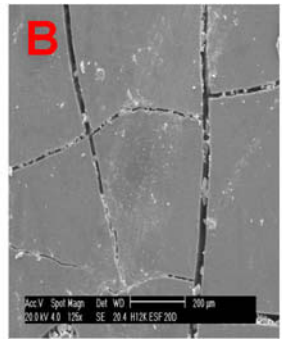

Longitudinal SEM photo of HMS-PP 12.5 kGy.

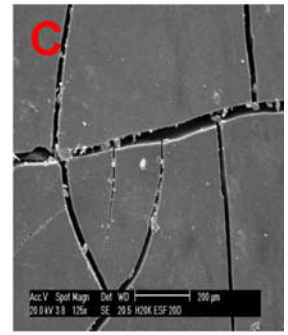

Longitudinal SEM photo of HMS-PP 20 kGy.

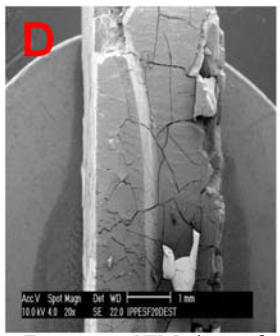

Transverse SEM photo of iPP.

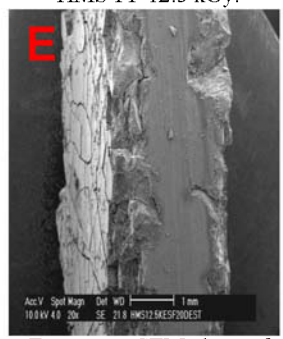

Transverse SEM photo of HMS-PP 12.5 kGy.

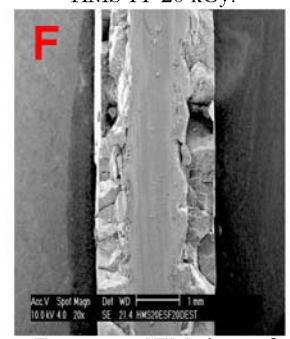

Transverse SEM photo of HMS-PP 20 kGy.

Figure 5. Development of cracks in longitudinal plane, 200 μm (A-C), and surface plus transversal cross section (at 30° - 45° of the samples corner), 1 mm (D-F), aged samples by 20 days.

These exposed surfaces show cracks propagation that increases with the aging time in stove with penetration. The diffusion of oxygen is considered significantly in accelerated test, especially in rapidly oxidizing polymers. Essentially all polyolefins, and particularly polyethylene and polypropylene, oxidize exclusively in the amorphous phase because the crystalline phase is impermeable to oxygen [28].

The SEM analysis, Figure 5, shows interesting aspects of the fractured surface of the materials, as a result of the process of chain scission. The cracks are more pronounced in iPP then HMS-PP 12.5 kGy and HMS-PP 20 kGy. Crack propagation is limited in the irradiated modified samples. The morphology of these samples with long-chain-branches was created and improves barrier property for O_2 [29]. A possible explanation to this fact is the crosslinking formation in irradiated samples with formation of barrier to oxygen diffusion. Intense changes in material properties were showed after thermal aging as well as color yellowness, crack formation, weight loss, surface roughness and changes in morphology.

Conclusions

The effects of thermal aging on iPP and HMS-PPs were mainly the intense crack formation. The chain scission and oxygen diffusion were more evident in the iPP. Surface cracks showed

propagation that increases with the aging time. The results indicate evidence that the sample of iPP suffered greater thermooxidative degradation and consequent chain scission than HMS-PP 12.5 kGy and HMS-PP 20 kGy. Crack propagation is limited in the irradiated modified samples as effect of crosslink promoted by irradiation.

Acknowledgments

The authors acknowledge CAPES for grants and the Centre of Materials Science and Technology – CCTM/IPEN for microscopy analysis (SEM), Eleosmar Gasparin for DSC analysis, CBE for irradiating the samples and FAPESP for Project n º 2012-00236-1.

References

[1] A. Law, L. Simon, P. L. Sullivan, "Effects of thermal aging on isotactic polypropylene crystallinity," *Polymer Engineering & Science*, 48(2008), 627-633.

[2] E. Suljovrujic, "The influence of molecular orientation on the crosslinking/oxidative behaviour of iPP exposed to gamma radiation," *European Polymer Journal*, 45(2009), 2068-2078.

[3] B. Keene, M. Bourham, V. Viswanath, H. Avci, R. Kotek, "Characterization of degradation of polypropylene nonwovens irradiated by γ-ray," *Journal of Applied Polymer Science*, 131, 4(2014), 39917 (1-10).

[4] Hans Zweifel, *Stabilization of Polymeric Materials* (Berlin, Springer-Verlag, 1998), 1-156.

[5] K. Pielichowski and J. Njuguna, eds., *Thermal Degradation of Polymeric Materials* (United Kingdom, UK, rapra technology, 2005), 47.

[6] S. Al-Malaika, "Oxidative degradation and stabilization of polymers," *International Materials Reviews*, 48 (2003), 165-185.

[7] F. Gugumus, "Effect of temperature on the lifetime of stabilized and unstabilized PP films," *Polymer Degradation and Stability*, 63(1999), 41-52.

[8] M. Philip, J. Attwood, "Evaluation of Weathering in mixed Polyethylene and Polypropylene Products," (United Kingdom, The Waste & Resources Action Programmer, 2004), 1-104. http://cms.esi.info/Media/documents/11653_1361534798115.pdf

[9] P. Gijsman, "Review on the thermo-oxidative degradation of polymers during processing and in service," *e-Polymers*, 065(2008), 1-34.

[10] M. C. Celina, "Review of polymer oxidation and its relationship with materials performance and lifetime prediction," *Polymer Degradation and Stability*, 98(2013), 2419-2429.

[11] C. Vasile and R. B. Seymour, eds., *Handbook of Polyolefins: Synthesis and Properties*, (New York, NY, Marcel Dekker, 1993), 1091.

[12] J. R. White, "Polymer ageing: physics, chemistry or engineering? Time to reflect," *Comptes Rendus Chimie*, 9(2006), 1396-1408.

[13] B. Fayolle, E. Richaud, J. Verdu, F. Farcas, "Review: degradation-induced embrittlement in semi-crystalline polymers having their amorphous phase in rubbery state," *Journal of Materials Science*, 43(2008), 1026-1032.

[14] A. B. Lugao, *U. S. Patent 0171712.,* 2004. Process for preparing high melt strength polypropylene and crosslinked prepared therewith.

[15] A. Yoshiga, D. F. Parra, H. Otaguro, L. F. C. P. Lima, A. B. Lugao, "Controlled degradation and crosslinking of polypropylene induced by gamma radiation and acetylene," *Polymer Bulletin*, 63(2009), 397-409.

[16] W. L. Oliani, "Study of HMS-PP (high melt strength polypropylene) behaviour under conditions of environmental and accelerated degradation" (Mater`s Dissertation, IPEN-USP, 2008), 1-151. http://www.teses.usp.br/teses/disponiveis/85/85134/tde-25082009-155558/pt-br.php

[17] W. L. Oliani, L. F. C. P. Lima, D. F. Parra, D. B. Dias, A. B. Lugao, "Study of the morphology, thermal and mechanical properties of irradiated isotactic polypropylene films," *Radiation Physics and Chemistry*, 79(2010a), 325-328.

[18] W. L. Oliani, D. F. Parra, L. F. C. P. Lima, A. B. Lugao, "Morphological characterization of branched PP under stretching," *Polymer Bulletin*, 68(2012), 2121-2130.

[19] W. L. Oliani, D. F. Parra, A. B. Lugao, "UV stability of HMS-PP (high melt strength polypropylene) obtained by radiation process," *Radiation Physics and Chemistry*, 79(2010b), 383-387.

[20] ASTM D 638-2003 – Standard Test Method for Tensile Properties of Plastics.

[21] ASTM D 3045-92-2003 - Standard Practice for Heat Aging of Plastics without Load.

[22] ASTM D 6370-99-2009 – Standard Test Method for Rubber – Compositional Analysis by Thermogravimetry (TGA).

[23] ASTM D 3418-2003 – Standard Test Method for Transition Temperatures of Polymers by Differential Scanning Calorimetry (DSC).

[24] J. Brandrup, E. H. Immergut and E. A. Grulke, eds., *Polymer Handbook* (New York, NY, Wiley Interscience, 1999), vol.1, 445-450.

[25] James E. Mark, *Physical properties of polymers handbook* (New York, NY, Springer, 2007), 639.

[26] J. Karger-Kocsis, "Polypropylene: Structure, blends and composites," *Crystallization, Melting and Supermolecular Structure of Isotactic Polypropylene* (Chapman & Hall, London, 1995), 56-113.

[27] M. S. Rabello, J. R. White, "Crystallization and melting behaviour of photodegraded polypropylene – II. Re-crystallization of degraded molecules," *Polymer*, 38, 26(1997), 6389-6399.

[28] J. Pospisil, Z. Horak, J. Pilar, N. C. Billingham, H. Zweifel, S. Nespurek, "Influence of testing conditions on the performance and durability of polymer stabilizers in thermal oxidation," *Polymer Degradation and Stability*, 82(2003), 145-162.

[29] H. Otaguro, L. F. C. P. Lima, D. F. Parra, A .B. Lugao, M. A. Chinelatto, S. V. Canevarolo, "High-energy radiation forming chain scission and branching in polypropylene," *Radiation Physics and Chemistry*, 79(2010), 318-324.

Characterization of Minerals, Metals, and Materials 2015
Edited by: John S. Carpenter, Chenguang Bai, Juan Pablo Escobedo, Jiann-Yang Hwang, Shadia Ikhmayies, Bowen Li, Jian Li, Sergio Neves Monteiro, Zhiwei Peng, and Mingming Zhang
TMS (The Minerals, Metals & Materials Society), 2015

MECHANICAL PROPERTIES OF POLYPROPYLENE NANOCOMPOSITES WITH ORGANOCLAY AND DISCARDED BOND PAPER

Danilo Marin Fermino[1*], Washington Luiz Oliani[2], Christiano Gianesi Bastos Andrade[1], Ademar Benevolo Lugão[2], Duclerc Fernandes Parra[2], Francisco R. Valenzuela Diaz[1]

[1] Department of Metallurgical and Materials Engineering - EPUSP (Escola Politécnica, Universidade de São Paulo), Av. Prof. Mello Moraes, 2463, Cidade Universitária, CEP 05508-030, São Paulo, SP, Brazil;

[2] IPEN/CNEN (Nuclear and Energy Research Institute) Av. Prof. Lineu Prestes 2242, Cidade Universitária, Postal Code 05508-000, São Paulo, SP, Brazil.

Keywords: Polypropylene nanocomposites, Organophilic clay, Bentonite, Cellulose

Abstract

This work concerns the study of the effect of discarded bond paper on the mechanical behavior of polypropylene/organophilic clay nanocomposites. A brown polycationic bentonite from the state of Paraíba, Brazil, was treated with sodium carbonate to transform it into a bentonite that swells in water and then treated with hexadecyltrimethylammonium ammonium chloride to transform it into a bentonite that swells in organic liquids. Polypropylene with 3 % polypropylene graft compatibilizer (PP-g-AM) was mixed with 1 % and 2 % by weight of discarded bond paper and with 1% and 2% by weight of organophilic clay using a twin-screw extruder. The specimens were prepared by the injection process. The clay as received and after organophilization was characterized by XRD, SEM, and capacity of swelling in water and in organic solvents. The nanocomposite specimens were characterized by XRD and thermal analysis. The mechanical behavior of the injected specimens was evaluated by strength, flexural and impact tests. The nanocomposites showed improved mechanical properties compared with the polymer without filler.

Introduction

In recent times, biofibers have found increasing applications as reinforcements in polymer composites due to of their key advantages of being renewable and having low densities, high specific strengths and abundant availability. Though, surface modification of biofibers by chemical/physical methods may help overcome some of the issues to achieve better composite properties. Lately, polymer composites containing natural fillers have received substantial attention in both the scientific literature and industry [1]. The vegetal fibers also decrease the thermoplastic environmental impact while improving its tensile and flexural mechanical properties. The lignocellulosic vegetal fibers can be obtained from different sources, depending on climate, localization and availability. On the other hand, working with vegetal fibers is challenging due to the dependence of the mechanical and chemical properties on different variables: such as species, climate, soil feedstocks, crop, and fiber extraction methods. These

conditions change for different cultivation sites, causing poor reproducibility of fiber properties and of the resulting composites [2]. Cellulose fibres are typically recognized for their applicability in ecofriendly composite materials, though unlocking their filler potential remains a challenge for load-bearing engineering applications [3, 4].

Polypropylene is one of the most important polymers due to its low density, low production cost, design flexibility, and recyclability, making it a popular preference as a matrix material in composites. It is hydrophobic, leading to compatibility issues when fillers with polar surfaces, such as cellulose, are utilized. The lack of compatibility causes heterogeneous dispersion of the cellulose fibers in the matrix and poor interfacial adhesion between fillers and matrix. To solve this problem, maleic anhydride grafted PP-g-MA has frequently been used as a compatibilizer for polypropylene/plant microfiber composites [5].

An important class of nanofillers includes nanoclays that belong to the smectite group, such as montmorillonite. The montmorillonite belongs to the family of 2:1 layered silicates, and its structure has layers that are in the order of 1 nm thick [6]. Montmorillonite has been used to prepare organoclays, because it has excellent properties, which include a high cation exchange capacity, swelling behavior, adsorption and a large surface area [7]. The intercalation of the melt polymer is the most attractive method because of its easy processability, no solvent requirement and cost effectiveness [8, 9]. Processing parameters such as temperature, residence time and shear stress have important effects on the structure of the resulting nanocomposites, which, in turn, influence the properties of the processed material. The nanocomposite properties strongly depend on the dispersion state of the clay; thus, an evaluation of clay dispersion is important [8, 10-11].

It is very important to understand how processing conditions have a big effect on the structure of nanocomposites during melt mixing in order to establish processing strategies which could lead to highly exfoliated polypropylene based nanocomposites. Few of the literatures in nanocomposites discussed the influence of processing conditions on the resulting nanocomposites' structure. An important aspect of the melt processing approach is to fulfill a dispersive mixing, to break the organoclay agglomerates down to individual layers [12-18].

To obtain polymer/clay nanocomposites, the clay layers are naturally in aggregates of several microns, require to be separated and dispersed into the polymer matrix. The more separated and dispersed the clay layers are, the higher the surface area for polymer/filler interactions, better are the properties [19].The objective of this work is to obtain a polypropylene nanocomposite with using Brazilian clay and used bond paper for increasing mechanical and thermal properties of this nanocomposite.

Materials and Methods

Isotactic polypropylene (iPP) with a melt flow index of 2.2 dg min^{-1} (230 ºC/2.16 Kg), was purchased from Braskem S.A., Brazil. An organophilic bentonite prepared with a commercial sodium bentonite (Chocolate Clay) from the state of Paraiba, Brazil, was used in this work. Four kilograms of discarded bond paper were collected and fragmented and placed in a plastic container with 40 liters of water. After 24 hours, this material was stirred with a mixer for

30 minutes at maximum speed of 2.800 rpm. After stirring the pulp was placed in a fabric bag and placed in a centrifuge to 2.300 rpm to facilitate drying. After centrifugation the paper pulp was passed on a 50 mesh sieve to reduce the size of the paper and then dried at 60 ºC for 72 hours. The organophilic clay and the paper with Irganox B215 FF (a blend of 0.2% of antioxidant and 0.4%, a thermal stabilizer) were manually mixed with coupling agent maleic anhydride (PP-g-MA), in a 2 wt% concentration to improve the clay adhesion to the polymer matrix.

A Thermo Haake twin screw extruder was used with a temperature range of 165 to 195 ºC and a 140 rpm rotation. A Battenfeld TM 750/210 injection was used to manufacture the specimens for tensile strength. The temperature injection was 190ºC, and the mold temperature was 60ºC. For X-ray diffraction (XRD) was used the Diffractometer Phillips X'Pert MPD, using Cu Kα radiation. The mechanical tests were performed with an Instron Universal Testing Machine according to the ASTM D638 type 1 test standard for tensile strength.

Thermal properties of specimens were analyzed using a differential scanning calorimeter DSC 822^e, Mettler Toledo. The thermal behavior of films was obtained by: (1) heating from -50 to 280 ºC at a heating rate of 10 ºC min^{-1} under nitrogen atmosphere; (2) holding for 5 min at 280 ºC, and (3) then cooling to -50 ºC and reheating to 280 °C at 10 ºC min^{-1}. Melting enthalpy value for 100% crystalline PP is 209 kJ kg^{-1}. The nanocomposites identification is presented in Table I.

Table I – Identification specimens

Specimen	Identification
PP	Polypropylene, pristine
PP AM	Polypropylene with PP-g-MA
PPA 1%	Polypropylene with 1 % in weight of organophilic clay
PPA 2 %	Polypropylene with 2 % in weight of organophilic clay
PPC 1%	Polypropylene with 1 % in weight of cellulose
PPC 2%	Polypropylene with 2 % in weight of cellulose
PPAC 1%	Polypropylene with 1 % in weight of organophilic clay and 1 % in weight of cellulose
PPAC 2%	Polypropylene with 2 % in weight of organophilic clay and 2 % in weight of cellulose

Results and Discussion

The Figures 1 and 2 show the values of tensile strength (MPa) and elongation at break (%) that were obtained from tension tests for the nanocomposite with organophilic ''chocolate'' clay and cellulose. By the results, the nanocomposite PPA 1 % had an increase of 7 % in the values of tensile strength compared to PP pristine. This result demonstrated enhancement with the addition of nanoclay. The remaining samples showed values close to tensile strength.
In the elongation at break, the PP AM sample obtained highest elongation (922 %) compared to PP pristine, due to maleic anhydride addition to give a plasticizing effect with increase elongation.

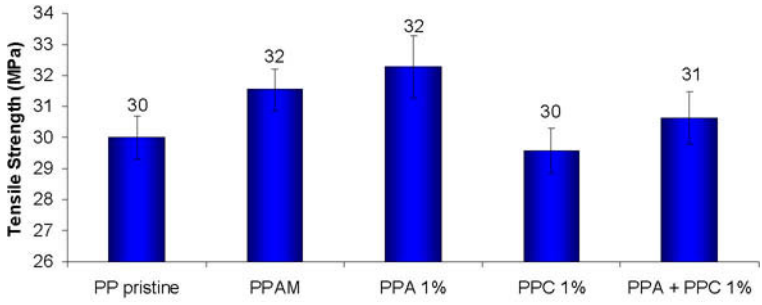

Figure 1. Tensile Strength (MPa)

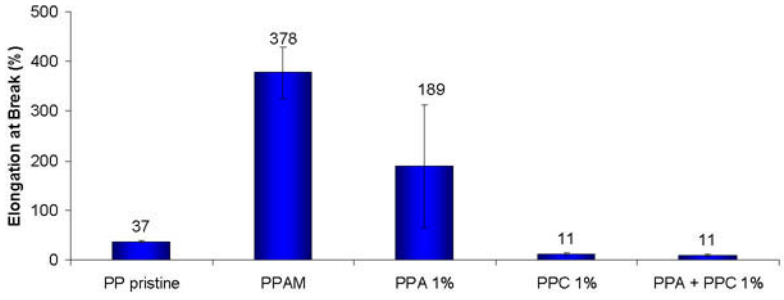

Figure 2. Strength – elongation at break (%).

The samples PPC 1 % and PPAC 1 % decreased in 236 % compared to PP pristine. This reduction was related with anchoring between clay and cellulose with polypropylene matrix. The better anchoring between clay and cellulose, the smaller will be the elongation, because it restricts the movement of the polymer chains. The elongation of nanocomposite PPA 1 % increased 411 % compared to PP pristine. It was attributed to clay structure delamination and anisotropy. The addition of the compatibilizing agent is accompanied by a decreased molar mass in the polymer and their effect on adhesion of structure to the clay.

The flexural strength values for the nanocomposite PP with clay and cellulose at three points for Young's modulus 0–1 % (MPa) are in Figure 3.
For sample PPC 2 % there was a decrease of 3 % in the modulus compared with PP pristine. The other samples compared with PP pristine decreased less than 3 %. Probably this reduction is due to difference polarity between clay and the cellulose and the polimeric matrix. The IZOD impact values for the nanocomposite PP with clay and cellulose are in Figure 4.

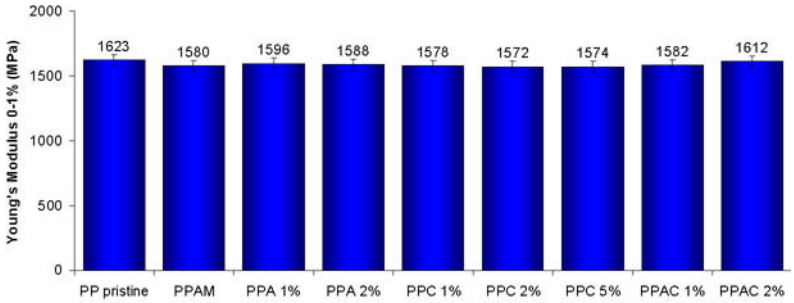

Figure 3. Flexural strength – Young's modulus

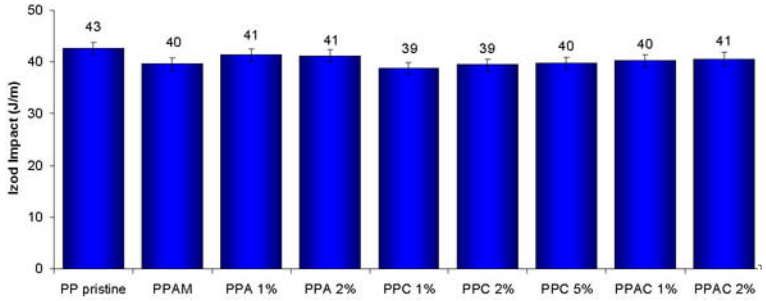

Figure 4. Test of IZOD impact in nanocomposites

All the samples presented a little reduction in the energy impact absorption compared with PP pristine. The samples PPC 1 and 2 % showed the higher decreased, 10 %. Possibly, this little quantity and the poor dispersion of cellulose in the polypropylene matrix generated internal tensions reducing the material ability to absorb impact energy.

In Table II are presented the temperatures value of crystallization peaks and in Table III are presented the temperatures melt peaks for the nanocomposites with bentonite clay and cellulose.

Table II - Temperatures of crystallization peaks (ºC) for the nanocomposites

PP pristine	PPAM	PPA 1 %	PPA 2 %	PPC 1 %	PPC 2 %	PPAC 1 %	PPAC 2 %
128	127	129	131	132	131	132	131

Table III - Temperatures of melt peaks (ºC) for the nanocomposites

PP pristine	PPAM	PPA 1 %	PPA 2 %	PPC 1 %	PPC 2 %	PPAC 1 %	PPAC 2 %
176	175	174	176	175	175	177	175

Table II shows the small changes in the crystallization temperature of PP pristine in relation to the nanocomposites with ''chocolate'' clay and cellulose; the difference of temperature in 3 °C in the nanocomposites is not significant. Table III shows small changes in the melting temperatures of the nanocomposites of "chocolate" clay and cellulose. There was a temperature change of 2 °C in the nanocomposites in relation PP Pristine.

In the Table IV are presented the crystallinity values for the nanocomposites from DSC curves.

Table IV - Crystallinity values (%) for the nanocomposites from DSC curves.

PP pristine	PPAM	PPA 1 %	PPA 2 %	PPC 1 %	PPC 2 %	PPAC 1 %	PPAC 2 %
47	47	47	48	49	50	46	46

The additions of nanoparticles in semi-crystalline polymers, in general, not affect significantly the crystallinity of the nanocomposite materials. It has been proposed, however, that these particles produce a large number of nucleating sites and in turn reduce the size of resulting spherulites. [21]. Figure 5 shows the X-ray diffraction patterns of the nanocomposites with "chocolate clay". Table V presents the basal spacing values that were obtained for the "chocolate" clay and the nanocomposites.

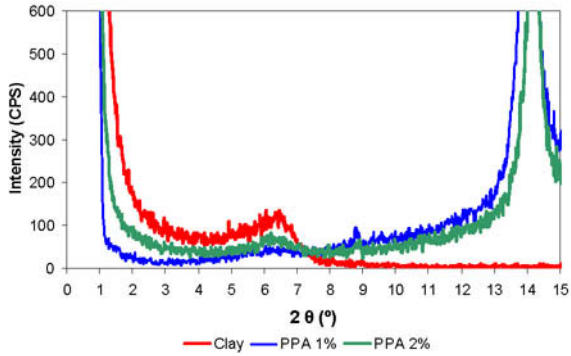

Figure 5. X-ray diffraction patterns of nanocomposite with ''chocolate'' clay.

Table V - Values of basal spacing obtained from the curves in the Figure 5

Specimens	d_{001} (Å)
"Chocolate" clay	13.5
PP pristine	6.2
PP AM	6.3
PPA 1%	14.6
PPA 2%	14.1

X-ray diffraction was used to evaluate the cation exchange efficiency. The diffractograms showed considerable increases in the interplanar distances, indicating an intercalation of PP between the 2:1 layers of the clay mineral. There were decreases in the intensity of the clay peaks in the nanocomposites compared to pristine clay (Figure 5). This peak intensity reduction suggests that a certain amount of disorganization of lamellae is present, indicating that a partially exfoliated/partially intercalated clay mineral structure was obtained.

Conclusions

There was formation of nanocomposites of intercalated and partially exfoliated clay as demonstrated in the test X-ray diffraction. In the tensile strength, the sample with "chocolate" clay presented an increase of 7 % and the cellulose samples not showed any loss of tensile strength in relation of pristine PP. The nanocomposite with "chocolate" clay presented over 400 % elongation compared to PP pristine. Samples with cellulose presented 236 % reduction of elongation in relation to the pristine PP. In the IZOD impact test there was 5 % reduction in the value of resistance in samples with clay and 10 % reduction in samples with cellulose. There were no significant changes in the thermal analysis by DSC for the hybrid nanocomposites of clay and cellulose.

Acknowledgments

The authors acknowledge CNPQ and CAPES for financial support and the Reimax Polymers Company.

References

[1] J. Chen and N. Yan, "Composites Mechanical properties and dimensional stability of organo-nanoclay modified biofiber polymer composites", *Composites Part B,* 47 (2013), 248–254.
[2] R. Gadioli, J. A. Morais, W. R. Waldman and M. A. De Paoli, "The role of lignin in polypropylene composites with semi bleached cellulose fibers: Mechanical properties and its activity as antioxidant", *Polymer Degradation and Stability*, 108 (2014), 23-34.
[3] T. Huber, J. Müssig, O. Curnow, S. Pang, S. Bickerton and M. P. Staiger, "A critical review of all-cellulose composites", *Journal of Materials Science*, 47 (3) (2012), 1171–1186.
[4] I. Sakurada, Y. Nukushina, and T. Ito, "Experimental determination of the elastic modulus of crystalline regions in oriented polymers", *Journal of Polymer Science*, 57 (165) (1962), 651-660.
[5] S. Iwamoto, S. H. Lee and T. Endo, "Mechanical properties of polypropylene composites reinforced by surface-coated microfibrillated cellulose", *Composites: Part A*, 59 (2014), 26-29.
[6] A. Ladhari, H. B. Daly, H. Belhadjsalah, K. C. Cole and J. Denault, "Investigation of water absorption in clay-reinforced polypropylene nanocomposites", *Polymer Degradation and Stability*, 95 (4) (2010), 429-439.
[7] L.B. Paiva, A.R. Morales and F.R.V. Diaz. "Organoclays: properties, preparation and applications", *Applied Clay Science*, 42 (2008), 8–24.
[8] D. M. Fermino, D. F Parra, W. L. Oliani, A. B. Lugao and F. R. V. Díaz, "HMSPP nanocomposite and Brazilian bentonite properties after gamma radiation exposure". *Radiation Physical and Chemistry*, 84 (2013), 176 - 184.
[9] S. Pavlidou and C.D. Papaspyrides, "A review on polymer–layered silicate nanocomposites", *Progress in Polymer Science*, 33 (2008) 1119–1198.

[10] S. S. Ray and M. Okamoto, "Polymer/layered silicate nanocomposites: a review from preparation to processing", *Progress in Polymer Science*, 28 (2003), 1539-1641.
[11] S. Xie, E. Harkin-Jones, Y. Shen, P. Hornsby, M. McAfee, T. McNally, R. Patel, H. Benkreira and P. Coates, "Quantitative characterization of clay dispersion in polypropylene-clay nanocomposites by combined transmission electron microscopy and optical microscopy", *Materials Letters*, 64 (2) (2010), 185–188.
[12] W. Lertwimolnun and B. Vergnes, "Influence of compatibilizer and processing conditions on the dispersion of nanoclay in a polypropylene matrix", *Polymer*, 46 (10) (2005), 3462–3471.
[13] J. Cho, and D. Paul, "Nylon 6 nanocomposites by melt compounding", *Polymer*, 42 (3) (2001), 1083-1094.
[14] H. R. Dennis, D. L. Hunter, D. Chang, S. Kim, J. L. White, J. W. Cho, D. R. Paul, "Effect of melt processing conditions on the extent of exfoliation in organoclay-based nanocomposites", *Polymer*, 42 (23) (2001), 9513-9522.
[15] R. K. Shah and D. R. Paul, "Nylon 6 nanocomposites prepared by a melt mixing masterbatch process", *Polymer*, 45 (9) (2004), 2991–3000.
[16] L. Zhu and M. Xanthos, "Effects of process conditions and mixing protocols on structure of extruded polypropylene nanocomposites" *Journal Applied Polymer Science*, 93 (4) (2004), 1891–1899.
[17] M. Treece, W. Zhang, R. D. Moffitt, and J. P. Oberhauser, "Twin-screw extrusion of polypropylene-clay nanocomposites: Influence of masterbatch processing, screw rotation mode, and sequence", *Polymer Engineering & Science*, 47(6) (2007), 898–911.
[18] T. D. Fornes P. J. Yoon, H. Keskkula, and D. R. Paul, "Nylon 6 nanocomposites: the effect of matrix molecular weight", *Polymer*, 42 (25) (2001), 9929-9940.
[19] D. D. J. Rousseaux, M. Sclavons, P. Godard and J. Marchand-Brynaert, "Carboxylate clays: A model study for polypropylene/clay nanocomposites", *Polymer Degradation and Stability*, 95 (7) (2010), 1194-1204.
[20] A. Yoshiga, H. Otaguro, D. F. Parra, L. F. C. P. Lima, A. B. Lugao, "Controlled degradation and crosslinking of polypropylene induced by gamma radiation and acetylene", *Polymer Bulletin*, 63 (2009), 397–409.
[21] C. M. Chan, J. Wu, J. X. Li, Y. K. Cheung, "Polypropylene/calcium carbonate nanocomposites", *Polymer*, 43 (10) (2002), 2981-2992.

Characterization of Minerals, Metals, and Materials 2015
Edited by: John S. Carpenter, Chenguang Bai, Juan Pablo Escobedo, Jiann-Yang Hwang, Shadia Ikhmayies, Bowen Li, Jian Li, Sergio Neves Monteiro, Zhiwei Peng, and Mingming Zhang
TMS (The Minerals, Metals & Materials Society), 2015

RECOVERY OF MERCURY AND LEAD FROM WASTEWATER BY SULFIDE PRECIPITATION-FLOTATION

Qian Li, Ting Liu, Peng Deng

School of Minerals Processing and Bioengineering, Central South University, China, Hunan, 410083.

Keywords：Heavy metal ions, Sulfide precipitation-flotation, Wastewaters, Recycle.

Abstract

The wastewater containing Hg^{2+} and Pb^{2+} does great harm to the environment and human bodies. Traditional wastewater treatment cannot fundamentally put a stop to heavy metals pollution for producing secondary pollution. In this paper, Hg^{2+} and Pb^{2+} in wastewater were removed and recovered by sulfide precipitation-flotation. Sodium sulfide was used as precipitant and butyl ammonium aerofloat was used as collector. Results indicated that Hg^{2+} and Pb^{2+} could be reduce to less than 0.03mg/L and 0.16mg/L respectively by both coprecipitation-floatation and fractional precipitation-floatation. In these two methods, fractional precipitation flotation could not only remove Hg^{2+} and Pb^{2+} from wastewater, but also could recover mercury and lead effectively. The infrared spectrograms showed that the adsorption between butyl ammonium aerofloat and mercury precipitate or lead precipitate is chemisorption.

Introduction

The industries such as mine, metallurgy, machine manufacturing, chemical industry, electronics and instrument, etc., produce large quantities of heavy metal wastewater every year, part of which is poured into waters without treatment or standard treatment, which results in the pollution of the aquatic environment. Heavy metal wastewater is characterized by a low pH value and containing heavy metal ions such as lead, mercury, chromium, cadmium, zinc, nickel, copper, cobalt, manganese, titanium, vanadium and bismuth. It have the following features：(1) they cannot be degraded by microorganisms; (2) they can be bioaccumulative in the body, which can endanger creatures, and endanger human body through food chains; (3)after entering the body heavy metal ions can be accumulated in certain organs of the body, which causes chronic poisoning. Therefore, heavy metal wastewater is a kind of industrial wastewater which seriously pollutes the environment and endangers human being and removing heavy metals in wastewater effectively have become an urgent task [1, 2].

Recently, numerous approaches such as precipitation, flotation, adsorption, membrane filtration, electrodialysis and photocatalysis have been studied to decrease the amount of wastewater produced and to improve the quality of the treated effluent [3]. But some of these treatments are costly, inefficient or easy to produce secondary pollution.

Precipitation including hydroxide precipitation and sulfide precipitation has been the most common approach to treat wastewater containing heavy metal ions. Hydroxide precipitation is a method that removing the heavy metal ions by adding alkali to generate hydroxide precipitates [4, 5]. It has the advantages of mature technology, less investment and easy to operate. But it is easy to produce large amounts of sludge which may cause secondary pollution. Some hydroxides will

be redissolved at higher pH value, so hydroxide precipitation is not a effective method to treat wastewater containing multi heavy metal ions. Besides, it is difficult to obtain satisfactory results for some toxic ions whose emission requirements are strict like Hg^{2+}, Cr^{2+} and Pb^{2+} by hydroxide precipitation. Sulfide precipitation is a method that removing the heavy metal ions by adding vulcanizing agent to generate sulfide precipitates [6, 7]. Solubility product of sulfide precipitate is small than solubility product of hydroxide precipitate, so the results are less influenced by pH value. Residual concentration of heavy metal ions after treatment are very low, and the sludge containing only a little water will not cause secondary pollution. But the sulfide particles are easy to form colloid suspending in the solution and difficult to be precipitated.

After precipitation treatment, recovery the heavy metals is in favor of recycling resource and avoiding secondary pollution. Flotation is a simple and effective method for recovering heavy metals from wastewater. It includes ion flotation, colloidal flotation and precipitation flotation for treating large volumes of wastewater. Ion flotation can be easily influenced by other ions in wastewater and need much more collector [8]. Colloid flotation involves the removal of metal ions by adsorption onto a carrier such as $Fe(OH)_3$ and $Al(OH)_3$. Precipitation flotation has several advantages that consuming a small amount of collector, could float the precipitation and has a high removal rate and the precipitate could be recycled as flotation concentrate [9].

Currently, the study on fractional recovery of multi heavy metals from wastewater is very destitute. In this paper, the study object is wastewater containing Hg^{2+} and Pb^{2+} and coprecipitation-floatation characteristics and fractional precipitation-flotation characteristics of Pb^{2+} or Hg^{2+} are studied. Treatment of wastewater containing multi heavy metal ions by fractional precipitation-flotation can not only remove heavy metal ions from wastewaters efficiently, but also can recycle heavy metals effectively.

Materials and methods

Reagents and solutions

Unless otherwise stated, all reagents used were of analytical-reagent grades. butyl ammonium aerofloat and terpenic oil are industrial reagents. All aqueous solutions were prepared in ultrapure water. Mercuric chloride ($HgCl_2$) was used as the source of Hg^{2+}. A stock mercury solution was prepared and the working solutions were made by diluting the former with ultrapure water. A lead nitrate ($Pb(NO_3)_2$) stock solution was prepared. The working solutions were made by diluting with ultrapure water. Sodium sulfide ($Na_2S \cdot 9H_2O$) is used as precipitant, butyl ammonium aerofloat is used as collector, terpenic oil is used as frother. The pH values were adjusted with nitric acid (HNO_3) or sodium hydroxide (NaOH), from 1 to 12 measured by a pH-meter.

Coprecipitation-floatation

Wastewater containing different concentrations of Pb^{2+} and Hg^{2+} with pH of 4 is carried out at sulfide/mercury molar ratio of 1.1, sulfide/lead molar ratio of 1.5, and reaction time is 12 minutes. Then the wastewater is directly poured into the flotation machine, adding 10 mg/L butyl ammonium aerofloat and 18 mg/L terpenic oil with the flotation time of 5 minutes to recover scum.

Fractional precipitation-flotation

Wastewater containing different concentrations of Pb^{2+} and Hg^{2+} with pH of 1 is carried out at sulfide/mercury molar ratio of 1.1, and reaction time is 12 minutes. Then the wastewater is directly poured into the flotation machine, adding 10 mg/L butyl ammonium aerofloat and 18 mg/L terpenic oil with the flotation time of 5 minutes to recover scum. Adjusting the pH value to 4, the wastewater was carried out with the sulfide/lead molar ratio of 1.5 and reaction time is 12 minutes. Then the wastewater was poured into the flotation machine, adding 10 mg/L butyl ammonium aerofloat and 9 mg/L terpenic oil, and flotation time is 3 minutes.

Results and discussion

Coprecipitation

The coprecipitation test results are shown in Table Ⅰ.

Table Ⅰ. The results of coprecipitation

Initial concentration (mg/L)		Residual concentration (mg/L)	
Hg^{2+}	Pb^{2+}	Hg^{2+}	Pb^{2+}
10	10	0.01	0.30
25	25	0.01	0.26
50	50	0.02	0.24
75	75	0.01	0.26
100	100	0.02	0.37

Table Ⅰ shows that, Hg^{2+} and Pb^{2+} can be co-precipitated effectively by sulfide precipitation, and there are no special requirement for the ion concentration. Sulfide precipitation has good adaptability for different concentration of Hg^{2+} and Pb^{2+}.

Floatation of coprecipitate

The results of the coprecipitation-floatation are shown in Table Ⅱ.

Table Ⅱ. The results of coprecipitation flotation

Initial concentration (mg/L)		Residual concentration (mg/L)	
Hg^{2+}	Pb^{2+}	Hg^{2+}	Pb^{2+}
10	10	0.01	0.05
	50	0.01	0.12
	100	0.01	0.12
50	10	0.02	0.09
	50	0.02	0.16
	100	0.01	0.14
100	10	0.01	0.04
	50	0.01	0.08
	100	0.03	0.13

Table Ⅱ shows that, for the wastewater containing different concentrations of Hg^{2+} and Pb^{2+}, the

residual Hg^{2+} concentration is less than 0.03mg / L and the residual Pb^{2+} concentration is less than 0.16mg / L after sulfide precipitation flotation

Fractional precipitation

In order to recover the heavy metals with floatation effectively, heavy metal ions should be separated out from the liquid and generating solid crystals. The solubility products of mercury sulfide (black) and lead sulfide are 1.6×10^{-52} and 8.0×10^{-28} respectively. Therefore, the sequence of sulfide precipitation is Hg^{2+}> Pb^{2+}. The precipitation effect of heavy metal ions depend on the pH value and the dosage of sodium sulfide, so Hg^{2+} and Pb^{2+} could be precipitated gradually by controlling the pH value and the dosage of sodium sulfide. The fractional precipitation test results are shown in Table III.

Table III. The results of fractional precipitation

Initial concentration（mg/L）		Precipitation period	Residual concentration（mg/L）	
Hg^{2+}	Pb^{2+}		Hg^{2+}	Pb^{2+}
10	10	First	0.01	9.85
		Second	0.01	0.15
	50	First	0.02	49.25
		Second	0.01	0.23
	100	First	0.03	98.15
		Second	0.02	0.25
50	10	First	0.01	9.86
		Second	0.01	0.10
	50	First	0.02	49.36
		Second	0.01	0.15
	100	First	0.02	99.25
		Second	0.01	0.12
100	10	First	0.01	9.85
		Second	0.01	0.08
	50	First	0.02	49.45
		Second	0.01	0.21
	100	First	0.03	99.35
		Second	0.01	0.25

Table III shows that, Hg^{2+} could be precipitated effectively at sulfide/mercury molar ratio of 1.1 and the residual concentration of sulfide ion is very low. Pb^{2+} can't generate either lead sulfide or lead hydroxide at the pH of 1, so there are little difference between the initial Pb^{2+} concentration and the Pb^{2+} concentration after first precipitation. Pb^{2+} concentration is very low after second floatation, while the pH value of wastewater is among 6 to 9. The small quantity of residual sulfide ion and collector can be removed with molysite.

Floatation of fractional precipitate

Under acidic conditions, butyl ammonium aerofloat has the best collection quality for mercury precipitate, the small reagent consumption, the low residual reagent concentration after floatation, and the little influence for the non-precipitated Pb^{2+} in the wastewater, so butyl ammonium aerofloat was chosen as the collector of fractional precipitation-flotation. The test results of

fractional precipitation-flotation are shown in Table Ⅳ.

As can be seen from Table Ⅳ, the residual Hg^{2+} concentration is less than 0.03mg/L after first floatation, there was little difference between the initial Pb^{2+} concentration and the Pb^{2+} concentration after first floatation. The XRD test result of first floatation scum was shown in Figure 1, the result shows that the first floatation scum which contained mercuric sulfide, trimercury disulfide dichloride, mercury disulfide dichloride and a small quantity of lead sulfide can be recovered as mercury product. The residual Pb^{2+} concentration was less than 0.14mg/L after second floatation, and the second floatation scum which didn't contain mercury can be recovered as lead product.

Table Ⅳ. The results of fractional precipitation-flotation

Initial concentration（mg/L）		Floatation period	Residual concentration（mg/L）	
Hg^{2+}	Pb^{2+}		Hg^{2+}	Pb^{2+}
10	10	First	0.02	9.05
		Second	0.01	0.04
	50	First	0.01	47.95
		Second	0.01	0.12
	100	First	0.03	94.15
		Second	0.02	0.16
50	10	First	0.01	9.46
		Second	0.01	0.10
	50	First	0.02	47.36
		Second	0.01	0.05
	100	First	0.02	94.25
		Second	0.01	0.14
100	10	First	0.01	9.00
		Second	0.01	0.08
	50	First	0.03	47.48
		Second	0.01	0.13
	100	First	0.02	95.35
		Second	0.01	0.10

Action mechanism between collector and precipitate

The infrared spectrograms of butyl ammonium aerofloat reacting with mercury precipitate and lead precipitate are shown in Figure 2 and Figure 3 respectively. The stretching vibration absorption peak and bending vibration absorption peak of N-H are 3109.6cm^{-1} and 1404.8cm^{-1} respectively. The asymmetric stretching vibration absorption peak and symmetric stretching vibration absorption peak of CH_2 are 2962.5cm^{-1} and 2877.7cm^{-1} respectively. The symmetric stretching vibration absorption peak of P-O-C is 969.4cm^{-1}. The stretching vibration absorption peaks of P=S are 684.5cm^{-1} and 556.9cm^{-1}. The infrared characteristic absorption peaks of butyl ammonium aerofloat reacting with lead precipitate are1616 cm^{-1}, 1465.5 cm^{-1}, 1385.5 cm^{-1}, 1268.9 cm^{-1} and 733.6 cm^{-1}. According to the study of Mingfei He [10], it can be known that the adsorption between butyl ammonium aerofloat and lead precipitate is chemisorption. A new characteristic absorption peak appears in the infrared spectrogram of butyl ammonium aerofloat reacting with mercury precipitate, the adsorption between butyl ammonium aerofloat and mercury precipitate is chemisorption. The characteristic of chemisorpption is that the absorption

is irreversible and the combination between collector and sulfide precipitate is very substantial, so desorption is difficult to occur in the flotation process.

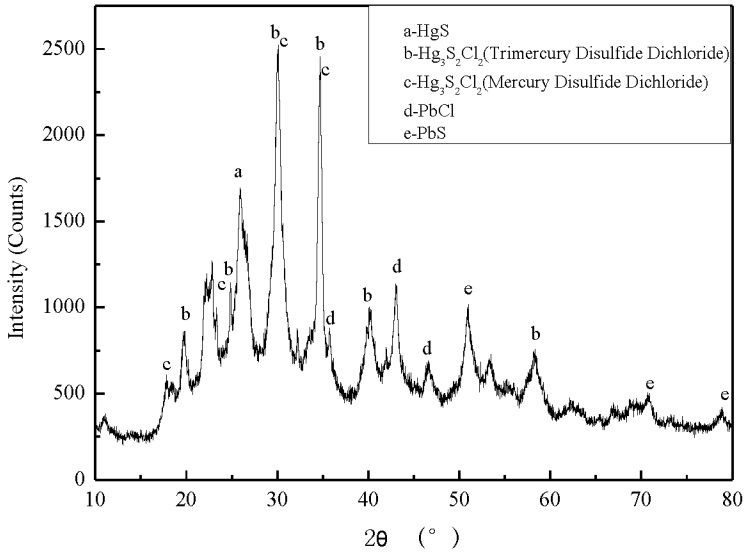

Figure 1. XRD pattern of scum produced by the first flotation

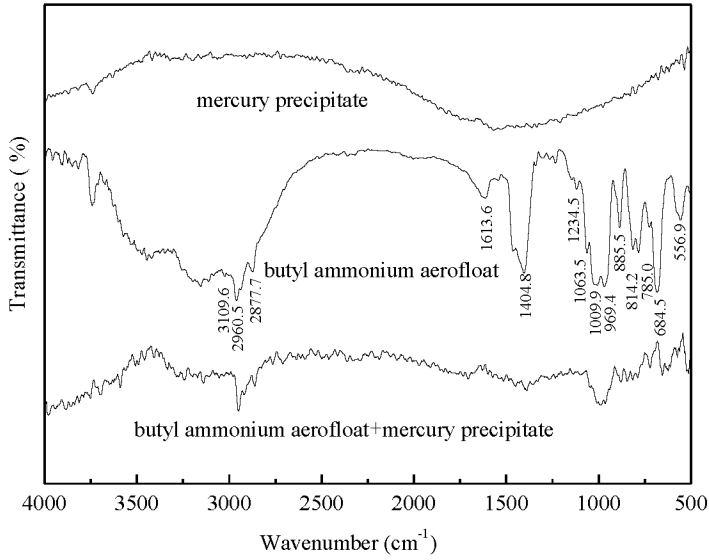

Figure 2. Infrared spectrogram of mercury precipitate and butyl ammonium aerofloat

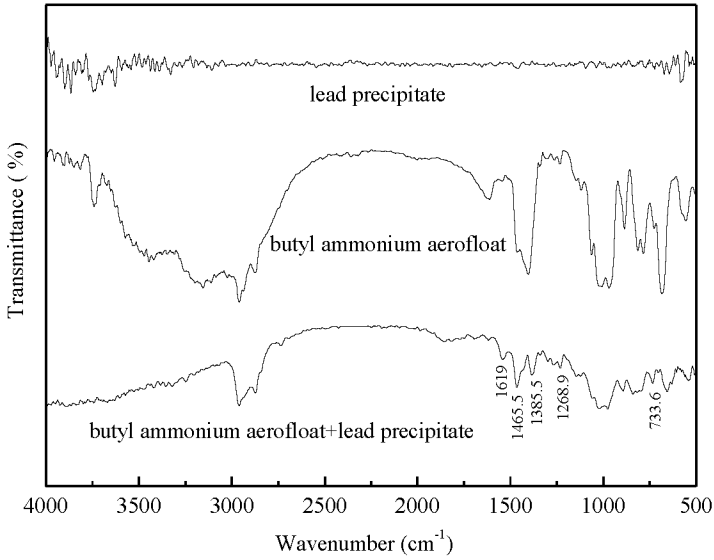

Figure 3. Infrared spectrogram of lead precipitate and butyl ammonium aerofloat

Conclusions

(1) For wastewater containing different concentrations of Hg^{2+} and Pb^{2+}, the residual concentrations of Hg^{2+} and Pb^{2+} can be reduced to less than 0.03mg/L and 0.16mg/L respectively by both coprecipitation-floatation and fractional precipitation-floatation, among which, fractional precipitation-flotation can separate and recover mercury and lead effectively. High ion concentration wastewater has higher recovery effect and recycling value.

(2) The adsorption between butyl ammonium aerofloat and mercury precipitate or lead precipitate is chemisorption, and the chemisorption is very substantial.

Acknowledgement

The authors want to express their thanks to National Science Fund for Distinguished Young Scholars (No.50725416) for financial support of this investigation.

References

1. S Santos et al., "Treatment of acid mining waters," *Minerals Engineering*, 17 (2004), 225-232.
2. Ying Xu and Fang Zhang., "Experimental research on heavy metal wastewater treatment with dipropyl dithiophosphate," *Hazard. Mater.*, 2006, no. 3:1636–1642.
3. M.A. Barakat, "New trends in removing heavy metals from industrial wastewater," *Arab. J. Chem.*, 2011, no. 4:361–377.
4. Yajie Zheng, Yinglin Peng, and Changhong Li. "Separation and recovery of Zn, Fe and Mn in

acid mine drainage," *Journal of Central South University (Science and Technology)*, 2011, no. 5:1215-1219.
5. Liyuan Chai, Xiangyu You, and Yude Shu, "Decoppering of copper-complexing wastewater fromprinted circuit boards," *Journal of Central South University (Science and Technology)*, 2010, no. 1:27-33.
6. Jianshe Liu, Haibo Xia, and Zhaohui Wang. "Treatment of Wastewater from powder blue productionwith sulphur precipitation coagulation," *Journal of Central South University (Science and Technology)*, 2004, no. 6:941-944.
7. Xuwen He, Jianlong Hu, and Jingwen Li, "Treatment of wastewater containing lead by sodium sulfide precipitation," *Chinese Journal of Environmental Engineering*, 2013, no. 4:1394-1398.
8. M.H. Salmani et al., "Removal of cadmium (II) from simulated wastewater by ion flotation technique," *Iranian J Environ Health Sci Eng*, 10(2013), 16.
9. R.W. Smith, "Liquid and solid wastes from mineral processing plants," *Mineral Processing and Extractive Metallurgy Review*, 16(1996), 1–22.
10. Mingfei He, "Study on key technology of floatation about refractory lead-zinc ore containing stannum in Southeast Yunnan," Doctor, *Central South University*, 2012.

Characterization of Minerals, Metals, and Materials 2015
Edited by: John S. Carpenter, Chenguang Bai, Juan Pablo Escobedo, Jiann-Yang Hwang, Shadia Ikhmayies, Bowen Li, Jian Li, Sergio Neves Monteiro, Zhiwei Peng, and Mingming Zhang
TMS (The Minerals, Metals & Materials Society), 2015

CLINKER PRODUCTION FROM WASTE: FROM CELLULOSE INDUSTRY AND PROCESSING MARBLE AND GRANITE INDUSTRY

Pedroti, G.L.[1],Vieira, C.M.F.[2], Alexandre, J. [3], Monteiro, S.N.[4], Justino, L[1], Xavier, C.G.[3]

[1] UFV – Federal University of Viçosa, DEC – Civil Engineering Departament; Av. PH Rolfs, Viçosa, Minas Gerais, 36570-900, Brazil.

[2] UENF - State University of the Northern Rio de Janeiro, LAMAV - Advanced Materials Laboratory; Av. Alberto Lamego, 2000, Campos dos Goytacazes, Rio De Janeiro, 28013-602, Brazil.

[3] UENF - State University of the Northern Rio de Janeiro, LECIV – Civil Engineering Laboratory; Av. Alberto Lamego, 2000, Campos dos Goytacazes, Rio De Janeiro, 28013-602, Brazil.

[4] IME - Military Institute of Engineering, Department of Materials Science, Praça General Tibúrcio, 80, Rio de Janeiro, Rio de Janeiro, 22290-270, Brazil.

Keywords: cement, clinker, waste.

Abstract

With the development of industrial processes and the consequent emergence of numerous products that quickly become necessities, industrial activity has acquired an essential character today. Although its importance is unquestionable, industrial activity is responsible for generating quite a large number of residues, with different shapes and characteristics. It has been observed, in particular the grits (Kraft process in the cellulose industry) and the residue from the processing of granite. And, given the importance of Portland cement as a building material, its vast employment and waste properties that resemble components of the clinker, it was decided to produce cementitious compounds from these industrial wastes. The residues were subjected to mineralogical, chemical, physical and morphological. And, the mixing ratio between the residues in the 70% and 30% grits residue granite was sintered at 1250 ° C furnaces to burn threshold of 6 hours forming new compounds observing tri-calcium aluminate and di-calcium silicate that are compounds found in portland cement.

Introduction

The incorporation of waste from various industrial activities in cementitious products is an alternative technology to reduce both cost and environmental impact caused by the indiscriminate release of these wastes.

Binder is a binder material, usually powdery, which promotes unity between the grains of inert material (aggregate). Are used in obtaining the folders, mortars and concretes. And a hydraulic binder widely used is Portland cement.

Portland cement is composed of silicates and aluminates which when mixed with water, is hydrated, resulting in the hardening of the mass, which may then provide high

mechanical strength. This binder depends for its manufacture of minerals: limestone, clay and gypsum (plaster). In the manufacturing step, the raw material (clay and limestone), finely ground and intimately mixed, are heated to melting principle (about 1400 ° C) in long rotary kilns which may be up to 90 m long and 3.5 m in diameter. The partially melted material leaving these furnaces is called "clinker." The "clinker" is cooled and mixed with a small amount (2% to 3%) of crude or ground gypsum. This mixture is then reduced to a very fine powder in large ball mills: the Portland cement trade.

Then it follows that the Portland cement is basically formed by limestone and clay, and previous studies it was observed that the Grits and industrial waste residue of Granite Court has properties similar to those of cement compounds.

The grits is generated during the chemical recovery cycle of pulp by the kraft process. This residue consists essentially of calcium carbonate. According CENIBRA (2013), the production of 1.0 ton of pulp produced 223 kg of solid waste, taking the study of application of the residue of cellulose production as an alternative material to become more relevant in the civil construction.

The residue consists of granite rock powder plus water and comes from using diamond wire looms. It is a silica-alumina material. The processing of dimension stone is divided into two stages: extraction of the blocks in the mines and processing in sawmills. In the step of processing the blocks, there is the generation of a large volume of waste. About 20 to 25% of the transformed block is split in powder sheets through the system looms. This amount can reach 25-30% of the block volume (REIS & TRISTAN) [1]. High value that justifies the search for better waste disposal.

Alternative materials have ecological benefits and will consequently enable buildings at lower cost. However the feasibility of recycling waste depends on a few factors such as: i) proximity to the processing facility; ii) cost of transportation of waste; iii) volume of waste available for reprocessing; iv) cost of storage of waste on site generation or away from the source.

Materials and Methods

For waste characterization used in this research, first samples of the generating industries were collected and then taken to the Laboratory of Building Materials of the Federal University of Viçosa. The residue was ground and passed through a sieve # 200, then mixed in the ratio 70% and 30% of grits residue granite. This ratio was established so that the mixture was in the range of production of cement industry, which will then be evaluated by EDX testing. The composition of a typical Portland cement clinker contains 67% CaO, 22% SiO_2, 5% Al_2O_3, 3% Fe_2O_3 and 3% of other components spread over four distinct stages, referred to as alite, belite, aluminate and phase ferrite. The alite is 50 to 70% of clinker, and is comprised of tricalcium silicate (Ca_3SiO_5) also referred to as C_3S modified in composition and crystal structure by the incorporation of ions, especially Mg^{2+}, Al^{3+} and Fe^{3+}, among others. The belite which constitutes 15 to 30% of clinker consists of dicalcium silicate (Ca_2SiO_4) also called C_2S modified by the incorporation of ions, especially Mg^{2+}, Al^{3+}, Na^{+}, Ti^{4+}, Ba^{2+}, Fe^{3+}. The aluminate phase is 5 to 10% of clinker and is formed by tricalcium aluminate ($Ca_3Al_2O_6$), known as C_3A, modified in composition and sometimes in structure by the incorporation of ions mainly of Si^{4+}, Fe^{3+}, Na^{+} and K^{+}. Already the ferrite phase which is 5 to 15% of clinker, is formed of iron tetracalcium aluminate (Ca_2AlFeO_5), known as C_4AF, modified in the composition ratio Al/Fe and incorporation of ions (Taylor, 1990) [2].

After mixing the materials were sintered at a temperature of 1250ºC in an oven and slowly cooled. This indicates a first problem for successful research, the cement industry as well as sintering at a temperature higher than 1450ºC, and then rapidly cools the clinker, which second (Martins, 2003) [3], if it occurs, can changing the crystal structure, damaging the crystal form of alite and belite, which significantly alters the mechanical strength. Figure 1-a and 1-b sets the rounded shape of the first due to rapid cooling, the second with slow cooling, the formation of crystals of belite.

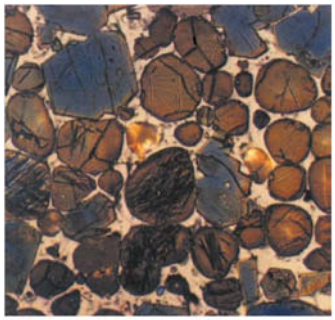

Figure 1-a

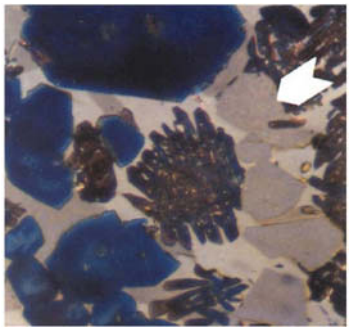

Figure 1-b

Figure 1. Photomicrograph of clinker - belite crystals (MARTINS, 2003)[3]

Tests for specific gravity (NM 23, 2000) [4] were performed, specific area (NBR 7224, 1984) [4], evaluation of the method pozzolanicity Luxan and the NBR 5752 [4], expandability Le Chatelier (NBR 3435, 1991) [4], XRF waste and the mixture before and after sintering, in addition to the testing of compressive strength of sintered and ground material passed through the sieve # 200. Figure 2-a shows the burning furnace and Figure 2-b, the sintered mixture.

Figure 2-a

Figure 2-b

Figure 2. Mixture before and after firing

Results

The density and specific area of the sintered and ground material was 3,09g/cm³ and 333.0 kg/m². The assay method of the pozzolanic Luxan is shown in Table 1 below.

Table 1 – Test Luxan

	Cement Portland	*Clinker (1250ºC)*	*Industrial Clinker*
Initial read (mS/cm)	12.17	11.27	11.47
End read (mS/cm)	13.34	11.06	11.87
Δ (mS/cm)	-1.17	0.21	-0.40

As was expected, the material showed no pozzolanic characteristic by Luxan method. The assay was also performed by pozzolanic NBR 5752 [4] method is shown in Figure 3 below.

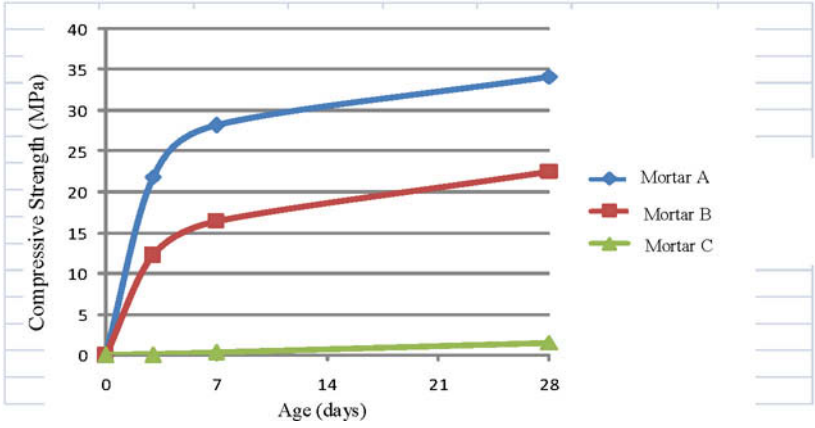

Figure 3. Evolution of compressive strength (Mortar A - commercial cement mortar B - 35% replacement of cement clinker by the 1250ºC, Mortar C - 100% of the clinker 1250ºC)

The strength of the sintered material 1250ºC (Mortar C) is much lower compared with the mortars A and B, which can be explained by the material being sintered suboptimal 1450ºC temperature and slow cooling, but showed an increase in resistance and caking properties

The chemical composition of the raw material obtained by XRF, is presented in Table 2.

Table 2 – Chemical composition by XRF of the raw material given in terms of oxides (%).

Composition	*CaO*	*SiO_2*	*Al_2O_3*	*Fe_2O_3*	*SO_3*
100% WGRA	3.78	68.83	15.82	2.05	1.84
100% WGRI	94.40	2.14	0.00	0.36	0.29
70% WGRA+30%WGRI	66.21	22.88	5.51	1.16	1.47
MIXTURE 1250ºC	60.90	26.50	7.67	1.38	0.96
CEMENT COMPOSITION (Petrucci, 2005)	60 a 67	17 a 25	3 a 8	0.5 a 6	< 3

WGRA – wast granit; WGRI – wast grits;

The sintered mixture 1250ºC showed values very close to the band indicated by PETRUCCI [5], the amount of SiO_2 getting very close to the ideal. The test expandability Le Chatelier, which have characteristic evaluate the scalability of the cementitious material with respect to both the instability of the curing mass into the cold water as curing in hot water is shown in the table below and according NBR 3435[4], the value should be less than 5 mm.

Table 3 – Expandability

Material	*Needle 01*	*Needle 02*	*Needle 03*	*Needle 04*	*Needle 05*	*Needle 06*
Expandability hot	0.0	0.0	0.5			
Expandability cold				0.0	0.0	0.0

The test can be observed that the material sintered at 1250ºC were lower than the values established in NBR 3435 [4].

Conclusion

• Material presented caking characteristics;
• The firing temperature is a determining factor in the quality, because the formation of crystalline compounds depends on the efficient sintering of the mixture;
• Cooling is also a factor, because the shape and performance of mainly crystals of Alita and Belita may be harmed;
• You can develop binders for different application from the mixture of industrial waste with similar chemical characteristics to the raw materials of cement industry;
• The pozzolanic material does not present characteristic thus increasing the pulp strength is related to the formation of calcium silicates and calcium aluminates and not the activity of silica present in the mixture;

Acknowledgements

The authors thank the Brazilian agencies: CNPq, CAPES and FAPEMIG for the support provided to this investigation.

References

1. REIS, Alessandra Savazzini dos; TRISTÃO, Fernando Avancini. Análise de argamassas com resíduo de corte de rochas ornamentais..
2. TAYLOR, H. F. W. Cement Chemestry. London: Academic, 1990.
3. MARTINS, J. M. Curso de microscopia do clínquer Portland. São Paulo, dez. 2003.
4. Brazilian Association of Technical Norms, Rio de Janeiro, Brazil.
5. PETRUCCI, Eládio G. R..Concreto de Cimento Portland. 14.ed. São Paulo: Globo, 2005.

Characterization of Minerals, Metals, and Materials 2015
Edited by: John S. Carpenter, Chenguang Bai, Juan Pablo Escobedo, Jiann-Yang Hwang, Shadia Ikhmayies, Bowen Li, Jian Li, Sergio Neves Monteiro, Zhiwei Peng, and Mingming Zhang
TMS (The Minerals, Metals & Materials Society), 2015

STUDY OF WETTABILITY OF CLAYEY CERAMIC AND FLUORESCENT LAMP GLASS WASTE POWDERS

Alline Sardinha Cordeiro Morais[1], Sergio Neves Monteiro[2], Sebastião Ribeiro[3], Leonardo Carneiro Sardinha[1], Carlos Maurício Fontes Vieira[4]

[1]Fluminense Federal Institute - IFF
Rua Dr. Siqueira, 273, 28030-130, Campos dos Goytacazes, RJ, Brazil
[2]Military Institute of Engineering - IME, Materials Science Department
Praça General Tibúrcio, 80, Praia Vermelha, Urca, 22290-270, Rio de Janeiro, RJ, Brazil
[3]University of São Paulo – USP, School of Engineering of Lorena
Pólo Urbo Industrial, Gleba AI6, CP 116, 12608-970, Lorena, SP, Brazil
[4]State University of the North Fluminense Darcy Ribeiro - UENF
Av. Alberto Lamego, 2000, 28013-602, Campos dos Goytacazes, RJ, Brazil

Keywords: Characterization, wettability, fluorescent lamp glass, waste

Abstract

The glass tube of spent fluorescent lamps is contaminated with mercury, which might be a serious hazard in the case of conventional recycling by melting with other glasses. A possible solution could be its incorporation into a clay body to fabricate common fired ceramics such as bricks and tiles. The objective of this work is to characterize a type of fluorescent lamp glass waste to be incorporated into a clayey ceramic. The characterization was performed in terms of wettability tests to evaluate the interaction between the surface of the clayey ceramic and glass waste as a function of the firing temperature. The results showed that the contact angle decreased with increasing temperature, reaching a value of 79°, at a temperature of 1100°C, but not sufficient to completely wet the ceramic. However, compatible chemical composition and reduction of porosity by the flow of soft glass waste between the clay particles favor the consolidation of the ceramics structure above 900°C.

Introduction

Fluorescent lamps use mercury (Hg) as a vital component for the emission of light. This toxic metal is associated with contamination of soils and waters as well as absorption by animals and plants causing serious diseases. As part of the food chain, these Hg-containing animals and plants could be responsible for human health problems. The environmental contamination by Hg from spent fluorescent lamps is a worldwide situation, which is aggravated in Brazil due to the accelerated substitution of incandescent lamps [1]. Indeed, the Brazilian government is promoting a saving in energy program, "Plano Nacional de Eficiência Energética" (National Plan for Energy Efficiency) [2] to replace all incandescent lamps by florescent ones. This program determines that, by July 2016, incandesce lamps shall no longer be produced or commercialized in Brazil. On the other hand, the production of lower energy consuming fluorescent lamps is now being encouraged in the country [3].

Despite the advantages of energy saving, the glass tubes of spent fluorescent lamps will pose an increasing environmental contamination and health problems in Brazil, owing to the Hg release to the ambient. A solution, which is already being conducted, is the Hg decontamination of the spent fluorescent lamps glass tubes [1]. However, the glass waste resulting from his decontamination process still contains traces of Hg and, therefore, should not be directly discarded or recycled in conventional smelting with other glasses. A more secure solution is the incorporation of limited amounts of fluorescent lamp glass waste (FLGW) into clayey ceramics for building construction [1]. The clayey ceramic production is currently one of the industrial sectors that have traditionally been used for incorporation of several types of wastes [4]. This has the advantage of not only mitigate the environmental impact but also recycle the waste to improve the clayey ceramic properties. In particular, glass wastes are being investigated as possible incorporation to clayey ceramics [4-10]. One aspect that has not yet been fully studied in the incorporation of glass wastes is its surface interaction with the clayey ceramic. This study is based on wettability tests that are essential to determine the efficiency of bonding formation between a solid substrate, the ceramic, and a fluid, the molten glass waste. The wettability test measures the contact angle (θ) between the tangent line separating the fluid/solid interface [11] from a drop, spontaneously spread onto the substrate, as schematically shown in Fig. 1.

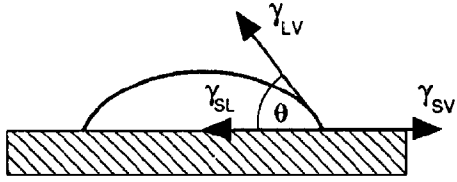

Figure 1. Schematic of a fluid drop spontaneously spread onto a solid substrate. Interface energies: solid/liquid = γ_{SL}; liquid/vapor = γ_{LV}; solid/vapor = γ_{SV}. [11]

The results of wettability tests, Fig. 1, allow the comprehension of the surface interaction mechanism and contribute to select the adequate formulation of phases as well as the convenient firing temperature. In the present work, the change with temperature of the wettability behavior of a FLGW with respect to a clayey ceramic was investigated.

Materials and Methods

The basic materials used in the present work were a fluorescent lamp glass waste (FLGW) and a clayey ceramic. The FLGW was supplied by Brazilian decontamination firm "Brazil – Comércio e Serviços", which uses a "Bulb Eater" equipment, Fig. 2(a), of the Air Cycle Corporation. The decontaminated FLGW was crushed, Fig. 2(b), and still contains a small amount of Hg that is not considered harmful. According to the supplier, the FLGW is a type of soda-lime glass and classified by Brazilian norm [12] as Class II-A; non-dangerous but not inert. In a previous work [1], it was found by optical dilatometry that the same FLGW exhibits a range of working temperature in its pasty condition from 868 to 1049°C and complete melting at 1117°C.

The clayey ceramic used as substrate, Fig. 1, was a typical mixture of kaolinitic clays kindly provided by the "Rodolfo Gama Azevedo – Sardinha" ceramic industry located at the municipal area of Campos dos Goytacazes, state of Rio de Janeiro, Brazil.

To perform the wettability tests, in which the contact angle θ in Fig. 1 is established by the balance between the surface tensions, both the clayey ceramic substrate and the FLGW had to be especially prepared. Press-molded 25 x 25 x 10 mm ceramic plates were first dried in a stove at 110°C for 24 h and then sintered in an electrical laboratory furnace at 1100°C for 120 min.

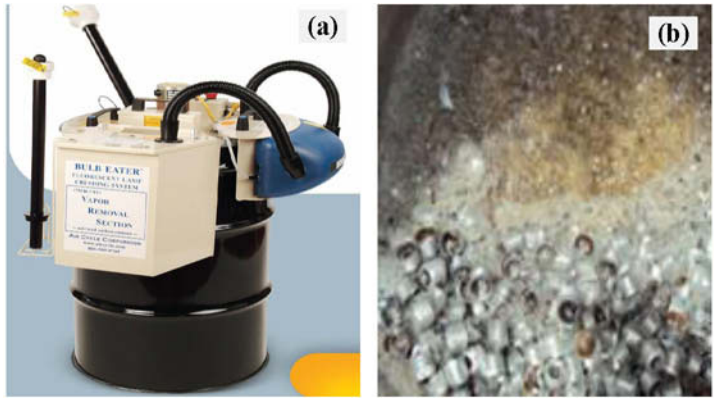

Figure 2. Hg decontamination of glass tubes of fluorescent lamps: (a) "Bulb eater" equipment, and (b) glass fragments produced in the crushing system of the equipment.

The as-received crushed FLGW, Fig. 2(b), was first sieved to 100 mesh (0.149 mm) and then mixed with about 10% of liquid styrene for a pasty consistency to facilitate handling. The mixture was press-molded at 50 MPa in a model MA 098/C Marconi hydraulic press to produce cylindrical samples with 4.0 mm in diameter and 4.5 mm in height.

Wettability tests were conducted with the cylindrical samples (FLGW powder mixed with styrene) placed onto she sintered clayey substrate, Fig. 3, and introduced inside an alumina tubular Lindberg/Blue electrical furnace. Separated samples were heated under air at different temperatures of 850, 900, 950, 1000, 1050 and 1100°C with a heating rate of 10°C/min and dwell time of 10 min. The image of the geometrical transformation of each heated sample was registered in a model Meteor 2 Matrox capture plate operating with a digital JVC-color video camera coupled with a 4/50 objective lens and controlled by a Leica image software. At the end of each experiment, the sample was rapidly cooled to preserve the geometrical change and a picture of the sample was taken with a digital Sony camera. The contact angle was measured in the picture using the Image J computer program.

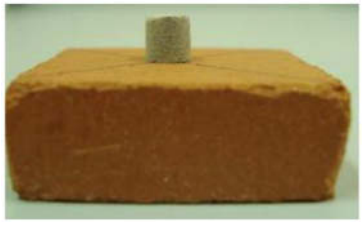

Figure 3. Wettability test sample of a cylindrical glass waste (FLGW) placed onto a clayey ceramic substrate.

The FLGW particles and the sintered clayey ceramic substrate were analyzed by scanning electron microscopy (SEM), after gold sputtering, in a model JSM 6460 Jeol microscope operating with 20 kV.

Results and Discussion

Figure 4 shows SEM images of FLGW particles (a) and the surface of a 1100°C sintered clayey substrate (b). In Fig 4(a) it is observed a broad range of particle sizes from about 1 to 100 μm. Most of the small particles are forming agglomerations, probably due to electrostatic forces. This condition did not apparently affect the high temperature softening to form the molten drop of glass for the wettability tests.

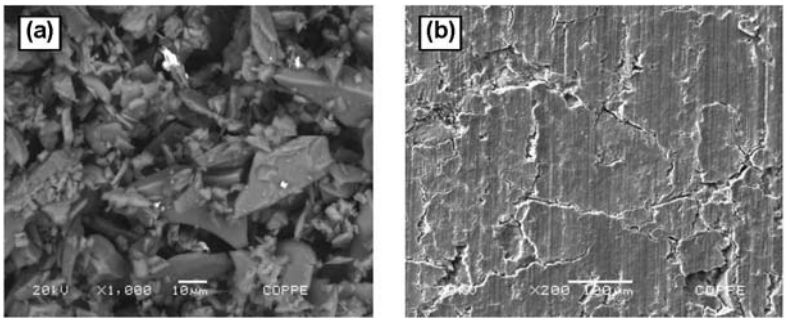

Figure 4. SEM images of (a) fluorescent lamp glass waste particles and (b) surface of the 1100°C sintered clayey substrate.

The relatively flat surface of the clayey ceramic substrate sintered at 1100°C, Fig. 4 (b) reveals a smooth appearance with cracked contours of possible regions associated with crystalline domains. This flat and smooth surface is convenient for the spread of the molten glass, which allows the contact angle in Fig. 1 to be measured.

Figure 5 shows a sequence of images illustrating the FLGW cylindrical sample, Fig. 3, behavior with increasing sintering temperature. In Fig. 5(a), at 850°C, the bulging of the cylindrical lateral surface indicates that the FLGW is beginning to soften, as expected for a soda-lime type of glass [1]. At 900°C, Fig. 5(b), an almost spherical shape of the sample, associated with a $\theta = 180°$, indicates that the glass waste is still unable to wet the substrate. This is interpreted as a non-adhesion condition between the two materials [14].

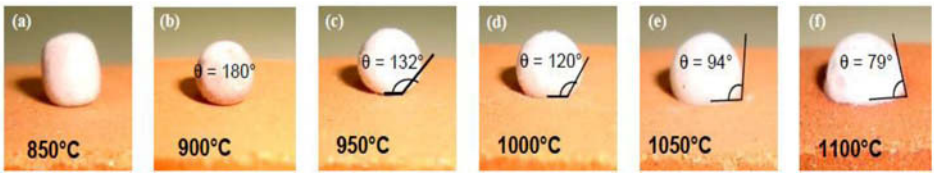

Figure 5. Fluorescent lamp glass waste behavior during wettability tests onto a clayey ceramic substrate at different temperatures.

At 1050°C, Fig. 5(e), the sample assumes an almost semi-spherical shape with $\theta = 64°$, which is related to the melting point [15]. Actually, this temperature is lower than the melting point of a soda-lime glass. However, as a waste, the FLGW is certainly contaminated with impurities that contribute to lower the melting point. At the limit temperature investigated of 1100°C, Fig. 5(f), the contact angle of $\theta = 79°$, is an indication that the FLGW has not yet presented a good wettability with the clayey ceramic. Indeed, a perfect wetting would occur for a contact angle close to zero, i.e., $\theta \approx 0°$. Therefore one may infer that the FLGW at 1100°C has not decreased its viscosity to permit and efficient infiltration inside the open pores of the clayey ceramic structure. In spite of the low wettability, the FLGW may still contribute to consolidate the clayey structure at temperatures above 900°C. The soft glass waste, even with low viscosity, might be squeezed in between the hard particles of the clayey ceramic during industrial firing operation. This process partially contributes to close the clayey particles open interspaces. Moreover, a typical soda-lime glass composition (74% SiO_2; 16% NaO; 5% CaO; 4% MgO; and 1% Al_2O_3) [16] is compatible with the clayey ceramic composition [5]. This also helps to form effective bonding between the soft/molten FLGW and the clay particles during high temperature sintering.

As a final remark, it should be emphasized that the wettability behavior shown in Fig. 5 indicates that, above 900°C, a sensible adherence begins to take place between the FLGW vitreous phase and the clayey ceramic substrate. Although the area of contact was slightly greater than $\boldsymbol{\pi r^2}$ (r = sphere radius) for a contact angle of 79° at 1100°C, the wettability might be enough to promote penetration of the vitreous phase between the clay particles. This results in porosity reduction at temperatures lower than those required for the contribution of solid state diffusion in the neat clayey ceramic. As a consequence, densification should primarily occur due to the flow of the FLGW soft/molten vitreous phase into the open spaces between clay particles. One might then expect that above 900°C the addition of the FLGW should improve the technical properties, mainly water absorption and mechanical strength, of clayey ceramics.

Conclusions

- Wettability tests of fluorescent lamp glass waste, as a fluid phase, onto a clayey ceramic substrate revealed a melting point at 1050°C and a contact angle of 79° at 1100°C.
- Despite the relatively higher contact angle, which is associated with a lower degree of wettability, the glass waste could effectively contribute to the consolidation of the clayey ceramic structure above 900°C, in which $\theta < 180°$.
- The compatible composition of the soda-lime type glass waste and the clay particles contributes to an efficient atomic bonding as the fluid vitreous phase penetrates between the clay particles and promotes densification of the ceramic structure.

Acknowledgments

The authors would like to thank the financial support to this investigation provided by the following Brazilian agencies: CNPq (proc. 306027/2008-9), FAPERJ (proc. E-26/103.023/2008) and CAPES. It is also acknowledged the permission of using the SEM microscope by the PEMM/COPPE/UFRJ.

References

[1] A.S.C. Morais, T.C.C. Caldas, S.N. Monteiro, C.M.F. Vieira. "Characterization of fluorescent lamp glass waste powder". *Mater. Sci. Forum*, 727-728 (2012) 1579-1584.

[2] PNEf - Plano Nacional de Eficiência Energética (in Portuguese) Premisses and Basic Directives, Brazil 2011. Available at

http://www.mme.gov.br/mme/galerias/arquivos/PlanoNacEfiEnergetica.pdf.

[3] MME - Ministério de Minas e Energia (Ministry of Mining and Energy) Interministry Decree 1.008, de 31 de dezembro de 2010 – Program of Compact Fluorescent Lamps (in Portuguese). Brazilian Federal Official Daily Newspaper 4, January 6, 2011, ISSN 1677-7042.

[4] S.N. Monteiro, C.M.F. Vieira, "On the production of fired clay bricks from waste materials: A critical update", *Constr. Build Mater.* 68 (2014) 599-610.

[5] T.C.C. Caldas, A.S.C. Morais, S.N. Monteiro, C.M.F. Vieira. "Characterization and thermal behavior of red ceramic incorporated with flat glass waste". *Mater. Sci. Forum*, 727-728 (2012) 994-1004.

[6] E. Furlani, G. Tonello, S. Maschio, E. Aneggi, D. Minichelli, S. Brucknera, E. Lucchini. "Sintering and characterisation of ceramics containing paper sludge, glass cullet and different types of clayey materials". *Ceramics International*, 37 (2011), 1293–1299.

[7] V. Loryuenyong, T. Panyachai, K. Kaewsimork, C. Siritai. "Effects of recycled glass substitution on the physical and mechanical properties of clay bricks". *Waste Management*, 29 (2009), 2717–2721.

[8] M. Dondi, G. Guarini, M. Raimondo, C. Zanelli. "Recycling PC and TV waste glass in clay bricks and roof tiles". *Waste Management*, 29 (2009), 1945–1951.

[9] Y. Pontikes, L. Espósito, A. Tucci, G.N. Angelopoulos. "Thermal behavior of clays for traditional ceramics with soda-lime-silica waste glass mixture". *Journal of the European Ceramic Society*, 27 (2007), 1657-1663.

[10] K.O. Godinho, J.N.F. Holanda, A.G.P. Silva. "Production and evaluation of technological properties of ceramic specimens based on the mix clay-recycled glass" (in Portuguese). *Cerâmica*, 51 (2005), 320.

[11] S. Ribeiro, S.P. Taguchi, F.V. Motta, R.M. Balestra. "The wettability of SiC ceramics by molten E_2O_3(ss)/AlN (E_2O_3(ss)=solid solution of rare earth oxides". *Ceramics international*, 33 (2007), 527-530.

[12] Brazilian Association of Technical Norms – ABNT NBR-10.004, Solid waste - Classification (in Portuguese), Rio de Janeiro, Brazil, 2004.

[13] F.V. Motta, R.M. Balestra, S. Ribeiro, S.P. Taguchi. "Wetting behaviour of SiC ceramics. Part I E_2O_3/Al_2O_3 additive system", *Mater. Lett.*, 58 (2004), 2805-2809.

[14] V. Vantomme, P. Deprez, A. Cornet. "Study glass-ceramic materials interfaces". *Materials Letters*, 36 (1998), 315-319.

[15] DIN 51730 – DEUTSCHES INSTITUT FÜR NOMUNG: Testing of solid fuels – Determination of fusibility of fuel ash. Berlin, 2007.

[16] WD. Callister Jr., Materials Science and Engineering: An Introduction, 8th ed, New York, John Wiley & Sons Ltd, 2011.

Characterization of Minerals, Metals, and Materials 2015
Edited by: John S. Carpenter, Chenguang Bai, Juan Pablo Escobedo, Jiann-Yang Hwang, Shadia Ikhmayies, Bowen Li, Jian Li, Sergio Neves Monteiro, Zhiwei Peng, and Mingming Zhang
TMS (The Minerals, Metals & Materials Society), 2015

BIODEGRADABLE STARCH/COPOLYESTERS FILM REINFORCED WITH SILICA NANOPARTICLES: PREPARATION AND CHARACTERIZATION

Roberta A. Lima[1], Rene R. Oliveira [1], Célio H. Wataya[1], Esperidiana A. B. Moura[1]

[1]Nuclear and Energy Research Institute, IPEN-CNEN/SP
2242 Prof. L. Prestes Av., São Paulo, SP, 05508-000, Brazil

Keywords: Nanocomposite, biodegradable polymers, SiO_2, mechanical properties, differential scanning calorimetry (DSC)

Abstract

Biodegradable starch/copolyesters/silica nanocomposite films were prepared by melt extrusion, using a twin screw extruder machine and blown extrusion process. The influence of the silica nanoparticle addition on mechanical and thermal properties of nanocomposite films was investigated by tensile tests; X-rays diffraction (XRD), differential scanning calorimetry (DSC) and Scanning electron microscopy (SEM) analysis and the correlation between properties was discussed. The results showed that incorporation of 2 % (wt %) of SiO_2 nanoparticle in the blend matrix of PBAT/Starch, resulted in a gain of mechanical properties of blend.

1. Introduction

Due to environment and sustainability issues, this century has witnessed remarkable achievements in green technology in the field of materials science through the development of biocomposites. The development of high-performance materials made from natural resources is increasing worldwide. With the developments of biodegradable materials, other researchers are trying to use directly the biomass constituents to manufacture polymeric materials [1, 2]. Increasing population, scarcity of raw materials coupled with global warming issues has governments and corporations looking for opportunities such as recycling and biodegradability to expand material performance [3]. Since plastic packaging materials are often contaminated by food materials and biological substances, recycling of these materials is often impractical and most of the time not economical [4]. Biopolymers should be used in those applications where biodegradability and/or the derivation of natural resources gives added value, particularly, where valuable petroleum-based plastics are used for applications with a short life time [5].

In recent years, the synthesis of potentially biodegradable polymers is of considerable significance and has receiving much attention. However, the mechanical properties of biodegradable polymers are very poor for many applications. Biocomposites obtained by the combination of biodegradable polymer as the matrix material and biodegradable fillers (rice husks, bagasse ashes) as the integral part is also expected to be biodegradable, since both components are biodegradable and can contribute to reduce the use of non-biodegradable plastic materials and improving management of solid waste disposal. Moreover, recent developments are raising the prospects that naturally derived resources, the biobased materials, will be a major contributor to the production of industrial products [6-8].

Among commercial biodegradable plastics, poly (butylene adipate-*co*-terepthalate) (PBAT), an aliphatic-aromatic copolyester is one of the most promising biodegradable materials because they are readily susceptible to biological attack [9]. PBAT has gained research and industry attention due to good processability in extrusion lines LDPE; besides PBAT begins to degrade after only few days in soil and enzymatic environments in contrast to petroleum derived polymers, such as polypropylene, polyethylene, that takes hundreds or even thousands of years to degrade [9,10].

Starch, is widely available raw material, a low cost renewable agro-resource composed of amylose and amylopectin polysaccharides and one of the most studied and promising agro-resources for the production of biodegradable polymers as matrices for biocomposite applications. However, starch itself is very brittle, hydrophilic and its mechanical properties are very poor for many applications [10-12]. The blending of starch with conventional polymers is a promising approach to improve its drawbacks. Recently, many efforts have been made to blend starch with biodegradable synthetic polymers [10-12]. Polymer blending is a well-used technique whenever modification of properties is required, because it uses conventional technology at low cost. The usual objective for preparing a novel blend of two or more polymers is not to change the properties of the components drastically, but to capitalize on the maximum possible performance of the blend [13]. The combination of PBAT with starch in a blend (PBAT/Starch), aims to bring the best characteristics for a biodegradable material, therefore aliphatic polyesters are the most promising biodegradable materials because they are readily susceptible to biological attack [14, 15].

The addition of nanofillers into a biodegradable polymer matrix leads to the creation of a novel class of materials, called nano-biocomposites, which combine nano-materials with an environmental approach. Lately, researchers have reported the improvements of biopolymer properties by incorporation of nano particles, such as clay, silica, layered silicate nanoparticles, calcium carbonate, zinc oxide and titanium dioxide. In general, these researchers have reported that the incorporation of nanoparticles improve mechanical properties, as well as barrier and antimicrobial properties of biopolymers [16, 17]. The aim of this work is to produce and evaluate the properties of biodegradable flexible film consisting of biodegradable copolyester, modified Starch and silica nanoparticle.

2. Material and Methods

2.1. Materials

The materials used in this work were biodegradable Aliphatic-aromatic copolyester (PBAT) with modified starch and silica nanoparticle.

2.1.2 Preparation of blend and composite

Modified starch and PBAT pellets and the silica nanoparticles were dried at 60 ± 2 ºC for 4 h to reduce its moisture content to less than 2 %. The Starch/PBAT blend (40 %/ 60% based on wt %) and Starch/PBAT with 2 % (wt %) of silica nanoparticle were prepared by melting extrusion process, using a co-rotating twin screw Haake Rheomex P332 extruder. The extrudates coming out of the extruder were cooled down for a better dimensional stability, pelletized by a pelletizer, dried again at 60 ± 2 ºC for 4 h and fed into an extrusion blow molding (laboratory line), and films samples were obtained.

3. Characterization

3.1. Mechanical tests

Tensile tests were determined using an INSTRON Testing Machine model 5564, according to ASTM D 882-91 in order to evaluate the mechanical behavior of the materials studied. Each value obtained represented the average of five samples.

3.2. X-rays diffraction (XRD) tests

X-rays diffraction (XRD) was recorded on a Simens - D5000 diffractometer operated at 40 kV and 40 mA, with CuKα radiation (λ= 15.4 Å).

3.3. Differential scanning calorimetry (DSC)

DSC analyses were carried out using a Mettler Toledo DSC 822e from 25 to 200°C at a heating rate of 10 °C/min under oxygen atmosphere. DSC analyses of the materials were performed on four samples of the irradiated and non-irradiated materials.

3.4. Scanning Electron Microscopy (SEM)

Scanning electron microscopy (SEM) analyses were carried out using a LX 30 (Philips).The samples were cryo-fractured under liquid nitrogen, and then the fractured surface was coated with a fine layer of gold and observed by scanning electron microscopy.

4. Results and Discussion

4.1. Mechanical tests results

Tensile test results – Table I summarizes the mechanical tests results for the flexible film from PBAT/Starch Blend and PBAT/Starch/SiO_2 nanocomposite. These results shown the average values calculated from the data obtained in tests, with standard deviations less than 10 % for all tests.

Table I. Mechanical tests results for the flexible film from PBAT/Starch blend and PBAT/Starch/SiO_2 nanocomposite

Test	PBAT/Starch Blend	PBAT/Starch/SiO_2
Tensile strength at break (MPa)	27.6	36.8
Elongation at break (%)	390	650
Young´s Modulus (MPa)	18.7	20.8

Figure 1 shows the diagram stress (MPa) against strain (mm/mm) for the PBAT/Starch blend and PBAT/PLA/SiO_2 nanocomposite. These results shown the average values calculated from the data obtained in tests, with standard deviations less than 10 % for all tests.

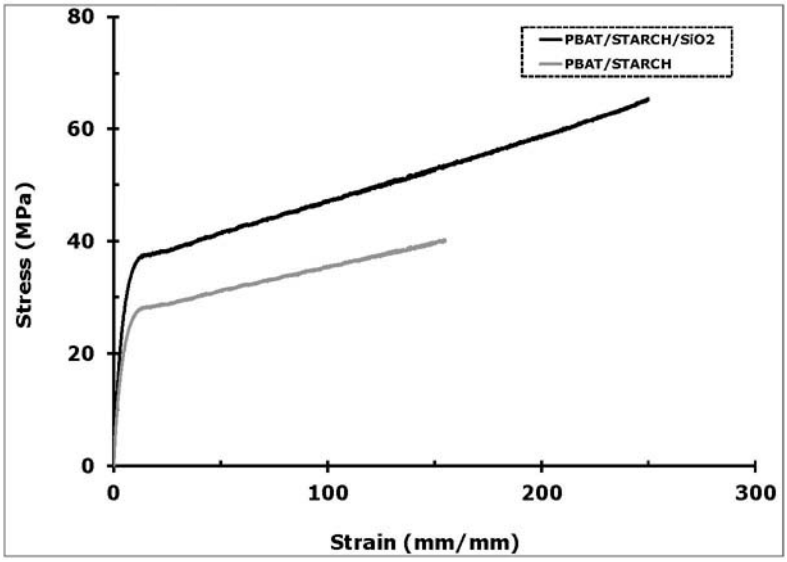

Figure 1. Diagram Stress (MPa) against Strain (mm/mm) the PBAT/Starch blend and PBAT/PLA/SiO_2 nanocomposite

As can be seen in this Figure the addiction of SiO_2 nanoparticle in PBAT/Starch blend improved the tensile strength, Young modulus and elongation at break.

4.2. X-rays diffraction (XRD) analysis results

The XRD patterns of PBAT/Starch blend and PBAT/Starch/SiO_2 nanocomposite are shown in Figure 2. It can be seen, the XRD spectrum of PBAT/Starch blend showed a prominent 2θ peak at around 6.70, which has drastically reduced of intensity due to SiO_2 nanoparticle addition.

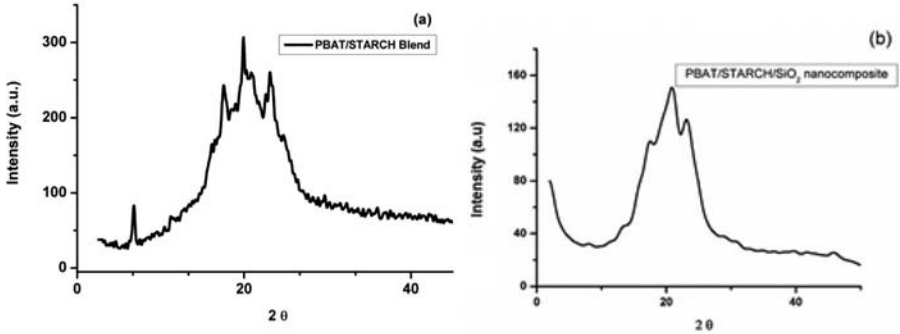

Figure 2. XRD diffraction patterns for the PBAT/Starch blend (a) and PBAT/Starch/SiO_2 nanocomposite (b)

4.3. Differential Scanning Calorimetry (DSC) analysis results

The average values of melting enthalpy (ΔHm) and melting temperature (Tm) of the materials studied are given in Table II. As it can be seen, the melting temperature and enthalpy of PBAT/Starch/SiO_2 nanocomposite were higher than PBAT/Starch blend indicating good miscibility between the components of the blend.

Table II. DSC analysis results of materials studied

Materials	Melting Temperature (T_m, °C)	Melting Enthalpy (ΔH_m, Jg^{-1})
PBAT/Starch blend	129.1	130.5
PBAT/Starch/SiO_2 nanocomposite	134.7	145.2

4.4. Scanning Electron Microscopy (SEM) analysis results:

SEM micrographs of cryo-fractured surfaces of PBAT/Starch blend and PBAT/Starch/SiO_2 nanocomposite are showed in Figure 3.

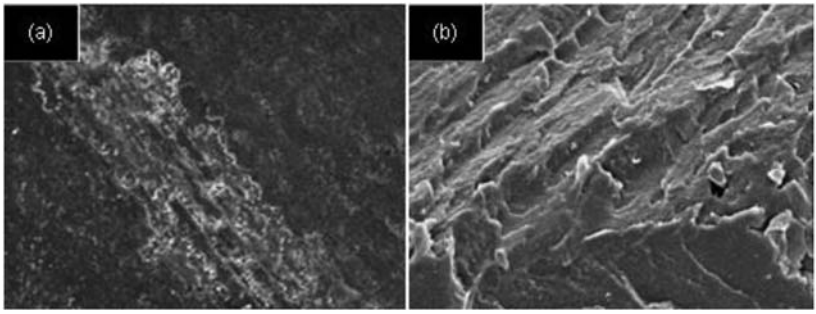

Figure 3. SEM micrographs of cryo-fractured surfaces of PBAT/Starch blend (a) and for the PBAT/Starch/SiO_2 nanocomposite (b)

As it can be seen, both blend Fig. (3a) and nanocomposite Fig. (3b) showed a slightly rough cryo-fractured surface. However, from Figure (3b), it can be see that there isn't agglomerates in the surface of the blend due to SiO_2 nanoparticle addition.

5. Conclusions

The aim of this study was to process and investigate the changes in the mechanical and morphological properties of the biodegradable PBAT/Starch blend due to the incorporation of SiO_2 nanoparticle. Results showed that incorporation of 2 % (wt %) of SiO_2 nanoparticle in the blend matrix of PBAT/Starch, resulted in a gain of mechanical properties of blend. The DSC analysis results indicated that blending PBAT with Starch, followed by of SiO_2 nanoparticle addition

caused structural changes in the polymeric chains of blend component, increased the original melting enthalpy and temperature of blend, and consequently, increased the crystallinity percentage.

Acknowledgements

The authors wish to thank BASF and FATEC ZL for the support for this work.

References

1. O Faruk, AK Bledzki, HP Fink, S Mohini. Biocomposites reinforced with natural fibers: 2000–2010. Progress in Polymer Science. 2012; Vol. 37: 1552– 1596.

2. G Bureau, et al. Les biopolymères comme matériaux d'emballage : le principe et les possibilités. Ind. Alim. Agr. 1996, avril, 235-237.

3. HA Alidedeoglu, G Kannan. Evaluation of biodegradable copolyester resins with increase green content. Antec. 2011.

4. MJ Kirvan, JW Strawbridge. Plastics in food packaging. Food Packaging Technology. 2003. 174-240.

5. M Avella, et al. Volpe MG. Biodegradable starch/clay nanocomposite films for food packaging applications. Food Chemistry. 2005; Vol. 93: 467 – 474.

6. AK Mohanty; M Misra; LT Drzal. Sustainable Bio-Composites from Renewable Resources: Opportunities and Challenges in the Green Materials World. Journal of Polymers and the Environment, v.10, n.1/2, p. 19-26, 2002.

7. MJ Ghazali; et al. "Characterisation of Natural Fibres (Sugarcane Bagasse) in Cement Composites", Proceedings of the World Congress on Engineering 2008, v. II WCE, July 2 - 4, 2008, London, U.K. (2008).

8. AP Kumar, RP Singh, 2008. Biocomposites of cellulose reinforced starch: improvement of properties by photo-induced crosslinking. Bioresource Technology 99 (2008) 8803–8809.

9. SJ Huang. Encycl Polym Sci Eng 2: Biodegradable polymers. New York: Wiley-Interscience; 1985.

10. M Yamamoto, et al. Biodegradable aliphatic-aromatic polyesters: "Ecoflex®". BASF.

11. L Chen, et al. (2006). Poly (Llactide)/starch blends compatibilized with poly(L-lactide)-g-starch copolymer. Carbohydrate Polymers, 65, 75–80.

12. JL Guimarães, et al. Studies of the processing and characterization of corn starch and its composites with banana and sugarcane fibers from Brazil. Carbohydrate Polymers 80 (2010) 130–138.

13. J Araújo, PBAT-PLA Blends Buried In Simulated Soil: Characterization by Differential Scanning Calorimetry, Raman Spectroscopy and Wide Angle X-Ray Diffraction. Journal of Chemical, Biological and Physical Sciences. 2013; Vol. 3: 2858 – 2866.

14. SJ Huang. Biodegradable Polymers. Encyclopedia Polymer Science and Engineering. 1985; Vol. 2.

15. Y Long, K Dean, L Li. Polymer blends and composites from renewable resources. Progress in Polymer Science. 2006; Vol. 31: 576 – 602.

16. A Sionkowska, et al. Molecular interactions in collagen and chitosan blends. Biomaterials 2004;25:795–801.

17. C Chawengkijwanich, Y Hayata. Development of TiO2 powder-coated food packaging film and its ability to inactivate Escherichia coli in vitro and in actual tests. International Journal of Food Microbiology, 2008. 123, 288-292.

Characterization of Minerals, Metals, and Materials 2015
Edited by: John S. Carpenter, Chenguang Bai, Juan Pablo Escobedo, Jiann-Yang Hwang, Shadia Ikhmayies, Bowen Li, Jian Li, Sergio Neves Monteiro, Zhiwei Peng, and Mingming Zhang
TMS (The Minerals, Metals & Materials Society), 2015

CYANIDATION STUDY OF SLAG RICH IN SILVER

Miguel Pérez-Labra[1]*, J. Antonio Romero-Serrano[2], E.O. Ávila-Davila[3], M. Reyes-Pérez[1], F. R. Barrientos-Hernández[1], I.A. Lira -Hernández[3]

1) Academic Area of Earth Sciences and Materials. Autonomous University of Hidalgo State. Road Pachuca-Tulancingo Km 4.5 Mineral de la Reforma Zip Code 42184, Hidalgo México. Tel.: (01771) 7172000 ext 6713
2) Metallurgy and Materials Department, ESIQIE-IPN. UPALM, Zacatenco, Zip Code 07738, México D.F.
3) Mechanical Engineering Department, Technological Institute of Pachuca, Road México-Pachuca km. 87.5 Pachuca de Soto Zip Code 42080, Hidalgo, México.

Abstract

Slag from smelting reduction processes were characterized by chemical analysis, XRD, SEM-EDS and XRF. The results revealed Ag concentrations of 362 g/t of slag, the slag mineralogical characterization by XRD and SEM-EDS showed mineralogical species oxidized complex containing Pb, Zn, Ca, Si, Fe, As, S in its structure, silver was found in globules associated lead in the slag and the furutobeite specie. The leaching study was conducted to evaluate process variables such as NaCN concentration: from $7.8x10^{-3}$M - $1.26x10^{-1}$M, temperature: 25-50°C, particle size: +140 mesh to -400 mesh, stirring speed of 750 rpm - 900 rpm. All studies were performed with a NaOH concentration of 0.2 M. The optimal values of silver recovery encountered in conditions of $7.8x10^{-3}$M NaCN, agitation rate of 750 rpm, temperature of 35°C and with a treatment time of 240 min. We also observed that a particle size -400 mesh will have optimum recoveries compared to +140 mesh, +200, +270 and +325.

Keywords: Slag, Silver Cyanidation

1 Introduction

In Mexico, through history, pyrometallurgical smelting reduction processes for primary lead production have generated large amounts of waste slag which belong to the multicomponent system PbO-ZnO-CaO-SiO2- "Fe_2O_3" [1] and also contain associated silver in its structure, which is originally incorporated in the original concentrates sulphide ores of galena (PbS). It has been found [2] the amount of Ag contained in the slag can equal or exceed the grades reported for some silver ores, for which recovery is potentially attractive. Leaching is the essential step in the process of silver recovery. The most common agents used for leaching gold and silver dissolution include cyanide, halides, thiourea, and thiosulfate [3-6]. The proposed method for the recovery of silver contained in slag is the cyanidation process [7,8] (MacArthur-Forrest process), which is an old and effective metallurgical process for dissolving silver low-grade ores, making metal ions in water-soluble complexes aurocyenide. The mechanism of dissolution of silver with cyanide is of considerable importance because the reactions which take place in it, it is essentially an electrochemical process similar to a process of corrosion of metals, in which the oxygen dissolved in solution is reduced to hydrogen peroxide and hydroxyl ions, with the overall reaction: [9]

$$2Ag + 4CN^- + O_2 + 2H_2O \rightarrow 2Ag(CN)_2^- + 2OH^- + H_2O_2 \quad (1)$$

The cyanidation method has been widely in argentiferous or auriferous minerals to dissolve silver and gold [10]. However there is little information regarding the processing of slag for silver recovery by this method, perhaps due to the presence of metals "cyanicide" behavior such as Fe, Cu, Zn, As and Sb. Which, depending on the mineral species that form, can form insoluble sulphide films. For this reason, this research takes scientific interest (provision of information regarding the process of cyanidation tailings) and economic (silver recovery). To address the problem, we must then demonstrate a methodology for the systematic analysis of cyanide process slag and thus provide information indicating the most suitable conditions of composition, pH, particle size, stirring speed and temperature at which maximum recoveries of silver in solution is achieved. Chemical analysis of slag concern in this project have determined approximate concentrations of 362 g of silver per ton of slag.

2. Experimental Work

Samples of slag collected were prepared mechanically sieved to different mesh (100, 140, 200, 270 325, 400 and -400) and characterized by diffraction of X-rays XRD (Bruker AXS D8 Advance), scanning electron microscopy SEM-EDS with analyzer EDS (JEOL 6300) and X-ray fluorescence XRF (Bruker D8 Focus). The chemical analysis of the elements present method was performed by inductively coupled plasma (ICP).The experimental study of the variables silver cyanidation was performed in a glass reactor with a capacity of 1 L using a hot plate (Barnstead / Thermolyne Super-nova) equipped with magnetic stirring and temperature control. The pH of the solution was kept constant by the controlled addition of NaOH 0.2 M. OH^- concentration was calculated based on the constant ionic product of water [11] and the pH of the alkaline solution according to the temperatures used. Three types of cyanidation tests were performed:

- At 25°C and 4 concentrations of NaCN ($7.8x10^{-3}$M, $1.5773x10^{-2}$M, $0.6309x10^{-1}$M, $1.26x10^{-1}$M), pH = 11 and 750 rpm.
- With a solution $7.8x10^{-3}$M NaCN, pH =11, 750 rpm and five temperatures: 25, 30, 35, 40 y 50°C.
- With a solution $7.8x10^{-3}$M NaCN, pH =11, 750 rpm and four particles sizes (75, 53, 45 y 38μm).

The reactor containing the NaCN concentration required for a volume of 0.5 L of solution was added NaOH 0.2M solution until the desired pH value, which is kept constant throughout the process, 10 grams of sized slag powder 38 μm were added. The cyanidation reaction progress was studied at different reaction times by obtaining successive samples of 10 mL and filtered with Whatman No. 42 filter paper. The process was monitored by measuring the concentration of silver in solution by the method of inductively coupled plasma (ICP).

3. Results and Discussion

Characterization of the slag

Figure 1 shows the XRD pattern of the slags studied, which confirms that the mineral species present correspond to: franklinite ($ZnFe_2O_4$) JCPD 221012, tennantite ($Cu, Fe)_{12}As_4S_{13}$ JCPD 110102, Hardystonita (Ca_2ZnSiO_7) JCPD 350745, Furutobeite ($Cu, Ag)_6PbSO_4$) 350534 JCPD and iron oxide Fe_2O_3 JCPD 391346. It can be noted that the Ag compound is formed furutobeite with Pb and S, which is consistent with the results of scanning electron microscopy, discussed later. The general morphology of the material after mechanical processing performed showed particles with angled surfaces (**Figure 2**), product type fracture of a brittle material, such as the slag studied, whose matrix consists vitreous species, similar to those previously reported by V. Ettler et al [12]. Other species such as lead and calcium silicates were not identified with much certainty, so that it is believed that some amorphous phases could be crystallized in the slag system studied. For this reason they were not placed in the spectrum shown.

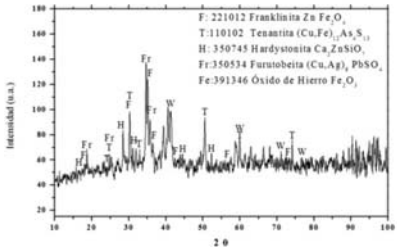

Figure 1 Diffraction pattern of slag

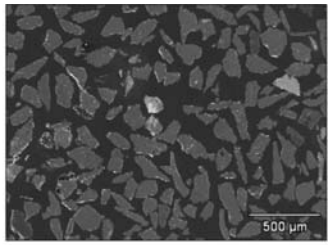

Figure 2 SEM micrograph of the morphology of slag particles

The chemical analysis of silver in the slag for each of the meshes (100, 140, 200, 270 325, 400 and -400) conducted by atomic absorption technique shown in **Table I**. It can be seen that the greater amount of silver is in the mesh - 400 (38µm particle size) with 304 gr Ag/ton slag, which is why it was decided to leaching studies with this particle size. The elemental analysis by XRF technique is shown in **Table II**, it can be seen that the Fe content is in the range of 38.2 to 45.6%. The elements theoretically [13] interfere with cyanidation process as "cyanicides" (substances that consume cyanide and form compounds that hinder the dissolution of silver) with the exception of Fe are found in low concentrations, these are: Cu: 0.24-0.38%, Zn: 0.33 0.49%, As: from 0.19-0.22% and Sb: from 0.23-0.28%.

Table I. Chemical analysis of Ag by AA for each mesh

Mesh	gr Ag/ton slag
100	163
140	147
200	180
270	174
325	220
400	235
-400	304

Table II. XRF analysis of the elements present in the slag

Element	Contained in each mesh (%)				
	100	140	200	325	400
O	28.76	27.18	24.7	28.58	25.97
Al	0.94	1.12	1.05	1.19	1.07
Si	15.2	14.2	13.4	14.9	12.7
P	0.21	0.19	0.18	0.19	0.17
S	1.57	1.47	1.35	1.33	1.52
K	0.97	0.9	0.79	0.91	0.7
Ca	7.76	7.12	6.27	7.32	5.62
Ti	0.12	0.12	0.11	0.12	0.1
V	0.02	0.02	0.02	0.02	0.02
Cr	0.01	0.01	0.02	0.01	0.02
Mn	0.02	0.06	0.09	0.05	0.11
Fe	38.2	41.2	45.9	39.2	45.6
Ni	0.01	0.01	0.02	0.01	0.03
Cu	0.24	0.3	0.31	0.35	0.38
Zn	0.49	0.43	0.38	0.38	0.33
As	0.19	0.19	0.19	0.21	0.22
Se	0.04	0.05	0.04	0.04	0.05
Sr	0.05	0.05	0.04	0.04	0.04
Mo	0.01	0.02	0.02	0.01	0.02
Sn	0.26	0.34	0.25	0.22	0.3
Sb	0.28	0.27	0.26	0.24	0.23
Ba	-	0.09	0.1	-	0.11

Figure 3 Shows SEM micrograph and elemental distribution mapping of Ag, W, Fe, S, Si, Ca, Pb, As, and Zn obtained by EDS-MEB for the slag 106 μm particle size mesh 140. It can be seen that the slag shows in the structure globules of metallic lead, which possibly trapped during melting lead sinter. It is also noted that the concentration of silver is in the majority in the lead globules, which is desirable, since in the smelting reduction process is

intended that this is adjacent to the lead [14]. The Fe meanwhile, is forming the matrix of the slag in an oxidized species with calcium and silicon. In electron image shown in the **Figure 3** have been identified mineral species present in the slag, based on the results obtained by XRD, XRF and elemental mapping own distribution according to the elements in themselves. The species identified correspond to: F: franklinita, T: tennantite, F: furutobeite and Fe: As Iron oxide. It is important to note that silver, targeted as the objective of the present study, this was found in the furutobeita species, which is a lead-silver sulfate and may contain copper. Also, silver is found in greater amounts in the lead globules as seen in the images of elemental distribution mapping.

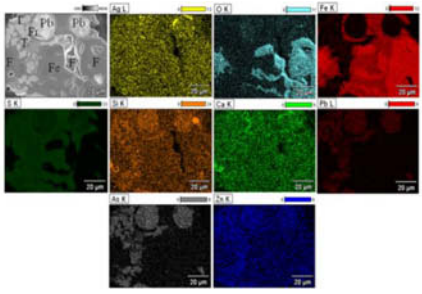

Figure 3 SEM-EDS mapping of elemental distribution for the slag mesh 140 (38µm)

Leaching slag

NaCN concentration effect

Figure 4 shows the percentage of Ag extracted from slag at different reaction times leaching with 4 different NaCN concentrations, It is noted that a recovery of 74.21% of Ag is obtained when a concentration $7.88x10^{-3}$ M NaCN is used. There is a decrease in the amount of Ag leached with increasing cyanide concentration, the concentration of cyanide solution required should be dependent on the characteristics of the material to leaching. Thus, it is expected that the rate of dissolution of metal increases linearly with increasing cyanide concentration reached a peak, after which increasing the amount of cyanide does not increase the amount of dissolved silver, rather, it creates a "retarding" effects, as observed on the graph. This is due to the increased concentration of NaCN increasing pH of the solution above 11.5 as this is hydrolyzed and form cyanates, which are insoluble. The pH used in the tests shown was kept constant at 11.0. This behavior is explained by the following reaction:

$$2Ag + 2HCN + O_2 \rightarrow 2AgCN + H_2O_2 \quad (2)$$

Temperature Effect

Figure 5 shows the effect of temperature on leaching reaction of silver into the slag to five different temperatures (25, 30, 35, 40 and 50 ° C) of $7.88x10^{-3}$M NaCN concentration, particle size 38µm, pH 11.0 and 750 rpm, NaCN concentration was chosen based on the

best results obtained from the above effect. It can be seen that the increase in temperature causes an increase in the amount of silver leached, obtaining a maximum recovery of 89.47% at 50°C. Increased temperature decreases the amount of oxygen dissolved in the leaching solution, this because the solubility of gases decreases with temperature, even with this knowledge, the silver solution increased knowing that oxygen is essential for the dissolution reaction (1), this can be explained because the capacity of an electrode to absorb H_2 at their surface which is less in a hot solution in a cold; so that, the maximum electromotive force of opposition due to the polarization is less, depending on how hot is the solution until dissolution the F.E.M. exceeds the polarization and dissolution of silver can continue without oxygen. So, the polarization can be prevented by the oxygen, which oxidizes the hydrogen on the surface of the silver and the disolution is allowed at lower temperatures. Or it can also be prevented by the heat which displaces the hydrogen of the silver surface and allows the dissolved silver without using oxygen. In the latter case, the dissolution of silver must be accompanied by hydrogen evolution. For the present study we considered 35°C (78.47% Ag) like optimum working temperature, despite higher recoveries obtained at 50°C, This is because it would be economically unfeasible heating a solution at this temperature.

Stirring speed effect

Figure 6 shows the effect of stirring speed. Two speeds were evaluated, both generated with magnetic stirring. Velocities were 750 and 900 rpm, using NaCN concentration of $7.88x10^{-3}$ M, 38μm particle size and pH 11.0. From the results obtained, can be seen that both agitations similar Ag dissolutions are obtained; 78.47% for 750 rpm and 81% to 900 rpm. The effect of the silver solution with the agitation speed is not very marked. Because during the experiment it was observed that the difference in turbulence generated with both velocities was not significant. However, it can be seen from the graph that there is little difference in the values of K_{exp} speed for each of the experiences. The highest slope value corresponds to the test performed at 900 rpm with 0.19148 min^{-1}, and that obtained for the 750 rpm speed was 0.16732 min^{-1}. This difference in the values of the slope indicates that, effectively there is an increase in the dissolution rate of silver to the system with more agitation. The slopes were calculated from the observed progressive conversion for both tests, and the value of the coefficients of linear correlation was 0.98732.

Particle size effect

Figure 7 shows the effect of particle size on the dissolution rate of silver contained in slag. 4 particle sizes were evaluated; (75, 53, 45 and 38μm), all tests were performed based on the best results obtained in the above effects; 750 rpm, 750 rpm, using a concentration $7.88x10^{-3}$ M NaCN, pH 11.0. It can be seen from the graph that the effect of the particle size has significant effect on the dissolution of Ag. As the size increases, The dissolution of Ag by cyanidation decreases to 25.4% for the particle size of 75μm, and conversely, this is increased to 78.47% for the particle size of 38μm. The first requirement to be fulfilled for the treatment of a mineral by leaching method is, The reduction of particle size, so that the leaching solution can penetrate and dissolve the values from the waste. This is explained

based on the available surface area for the dissolution reaction occurs. The smaller the particle, there is more surface area available for the reagent to react with all the mineral mass. And, the larger the particle the reverse direction, there will be less area available.

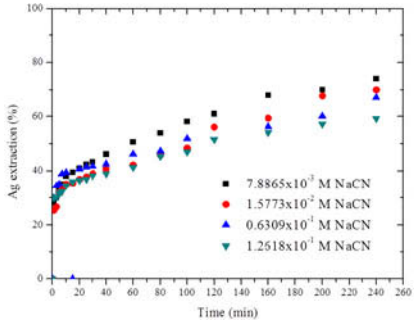

Figure 4 Effect of concentration of NaCN in the leaching of Ag progress in the slag at 25 ° C, pH: 11.0, 38µm particle size (400 mesh) and 750 rpm

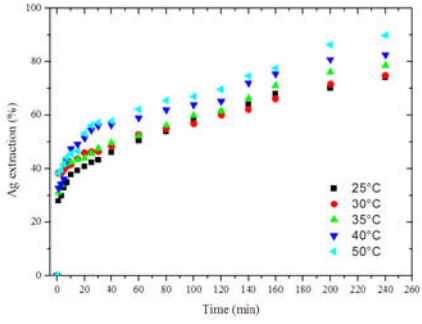

Figure 5 Effect of temperature on leaching progress of Ag in the slag: NaCN: 7.8865x10^{-3} M; pH: 11.0, particle size 38µm and 750 rpm

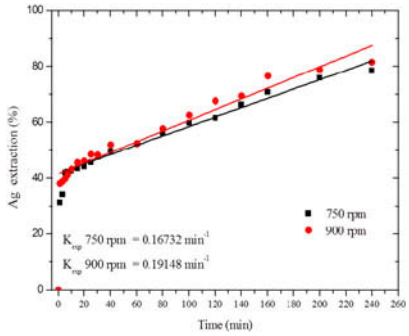

Figure 6 Effect of agitation rate on the progress of the leaching of Ag in the slag: NaCN: 7.8865x10^{-3} M; pH: 11.0, particle size 38µm temperature of 35°C

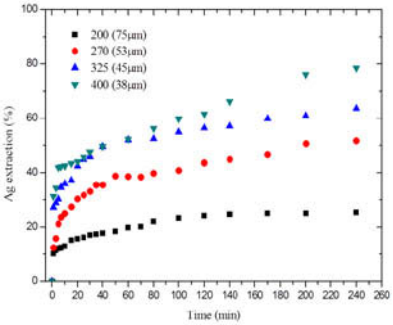

Figure 7 Effect of particle size on the progress of the leaching of Ag in the slag: NaCN: 7.8865x10^{-3} M; pH: 11.0, temperature of 35 ° C, 750 rpm

4. Conclusions

We have studied the leaching of silver contained in slag from smelting reduction processes and concludes:

- The species were identified by XRD in the slag were franklinta ($ZnFe_2O_4$) tennantite $(Cu, Fe)_{12}As_4S_{13}$, hardystonita (Ca_2ZnSiO_7) furutobeite $(Cu, Ag)_6$ $PbSO_4$) and iron oxide Fe_2O_3 JCPD 391346. Some corroborated by SEM-EDS.
- Ag was found associated in lead globules in the slag and the species furutobeite.

- Chemical analysis showed the silver content of 304 gr Ag / ton slag in 38μm particle size.
- It is possible to recover silver contained in slag smelting reduction processes using cyanidation technology. The optimal values of silver recovery were found in conditions $7.8x10^{-3}$ M NaCN, stirring speed of 750 rpm, temperature of 35°C, with a treatment time 240 min, pH 11.0.
- With the optimal conditions found recovery of 78.47% Ag is obtained.

5. Acknowledgements

The authors wish to thank PROMEP-UAEH for the financial support, the Academic Area of Earth Sciences and Materials (AACTyM) and the Department of Engineering Metallurgy ESIQIE-IPN.

6. References

[1] Jak, e. and Hayes, P.C., Phase Chemistry of Lead Smelting Slags. In: Proceedings of the Lead-Zinc 2010 Conference, Vancouver, Canada (ed: A. Siegmund, L. Centomo, C. Geenen, N. Piret, G. Richards and R. Stephens) pp. 1161-1176 (TMS).
[2] López Rodríguez Josué Jaime "Estudio de la separación de oro y plata de escorias" Tesis de maestría. México D.F. Diciembre 2012.
[3] Andrews, D., Raychaudhuri, A., Frias, C. Environmentally sound technologies for recycling secondary lead. J. Power Sources 2000, 88, 124–129.
[4] Chmielewski, A.G., Urbanski, T.S., Migdal, W., Separation technologies for metals recovery from industrial wastes. Hydrometallurgy. 1997, 45 (3), 333–344.
[5] Quinet, P., Proost, J., Van, A.L., Recovery of precious metals from electronic scrap by hydrometallurgical processing routes. Min. Metall. Process. 2005, 22 (1), 17–22.
[6] Sheng, P.P., Etsell, T.H., Recovery of gold from computer circuit board scrap using aqua regia. Waste Manage. Res. 2007, 25 (4), 380–383.
[7] Habashi, Fathi Avances recientes en la metalurgia del oro
[8] Logsdon, M.J., Hagelstein, K., Mudder, T.I., 1999. The Management of Cyanide in Gold Extraction. ICME Publications, Canada, Ottawa.
[9] Logsdon, M.J., Hagelstein, K., Mudder, T.I., The Management of Cyanide in Gold Extraction. ICME Publications, Canada, Ottawa. 1999.
[10] Deschenes G., Hodouind D., Lorenzel L. (eds.) Treatment of Gold Ores. Ed. Canadian Institute of Mining, Metallurgy and Peltroleum, 2005.
[11] Handbook of Chemistry and Physics, Cr. Press, 12 Edition, (1991-1992), pp 8-42
[12] V. Ettler, O. Legendre, F. Bodénan, J.C. Touray, Primary phases and natural weathering of old lead–zinc pyrometallurgical slag from Pribram, Czech Republic, Can. Mineral. 2001, 39, 873–888.
[13] Luis Rey Islas Arenas, Determinación de los parámetros hidrometalúrgicos para una plante de beneficio por cianuración dinámica. Tesis de licenciatura, UAEH, agosto 1993.
[14] Schlesinger, M.E. and Lynch, D.C., PbO Solubility in Lead-Blast Furnace Slags. Metall. Trans. B, 17B, (1986), pp. 817-827.

Characterization of Minerals, Metals, and Materials 2015
Edited by: John S. Carpenter, Chenguang Bai, Juan Pablo Escobedo, Jiann-Yang Hwang, Shadia Ikhmayies, Bowen Li, Jian Li, Sergio Neves Monteiro, Zhiwei Peng, and Mingming Zhang
TMS (The Minerals, Metals & Materials Society), 2015

Thermophysical Properties of Modified Ti-bearing Blast Furnace Slags

Yongqi Sun[1], Zuotai Zhang[1]
Department of Energy and Resources Engineering, College of Engineering, Peking University, Beijing 100871, P.R. China

Keywords: Ti-bearing blast furnace slag; crystallization behavior; viscosity; P_2O_5; B_2O_3

Abstract

Our study investigated the influence of P_2O_5 and B_2O_3 on the viscosity and crystallization behavior of Ti-bearing blast furnace (Ti-BF) slags for the purpose of Ti extraction. The investigation of the crystallization behaviors were carried out using a single hot thermocouple technique (SHTT) and the viscosity was obtained by rotating cylinder method. For the viscosity, the results showed that P_2O_5 substantially increased the slag viscosity. P_2O_5 is a network-forming oxide, which increased the degree of polymerization of slags and accordingly increased the slag viscosity. However, both of slag viscosity and apparent activation energy for viscous flow remarkably decreased with B_2O_3 addition. As a typical network forming oxide, B_2O_3 was introduced into the network and existed dominantly as 2-D structure, BO_3 triangular, which caused a simpler structure and a decreasing slag viscosity. As for the crystallization behaviors of Ti-BF slags, both P_2O_5 and B_2O_3 enhanced the crystallization trend of rod-shape rutile and suppressed the crystallization trend of dendrite $CaTiO_3$. Therefore the added P_2O_5 and B_2O_3 caused the primary phase change from $CaTiO_3$ to rutile. Additionally, it was found that the rod-shape rutile showed a 1-D growth, whereas the dendrite $CaTiO_3$ showed a 3-D growth style.

Introduction

China has abundant titanium resource, of which 91% is located in Sichuan province [1], in the form of vanadium titanium-magnetite ores. The valuable elements, such as iron and vanadium, are utilized through blast furnace process; and as typical solid residuals, the titanium-bearing blast furnace (Ti-BF) slags are generated. These slags generally contain 20~25 wt. % TiO_2 [2] and account for the most important secondary resources for titanium extraction. However, these slags are not effectively disposed and to reasonably utilize these slags, many routes have been exploited and investigated. Nowadays, more than 70 million tons of Ti-BF slags have been accumulated with an annual production rate of 3 million tons [3].

Amongst these utilization routes, selective crystallization and phase separation (SCPS) method shows some specific advantages including energy saving and high separation ratio. The most important step of SCPS method is to reasonably select a Ti-enriched phase and create a most appropriate condition for the crystal to growth. The initial basicity (CaO/SiO_2) is 1.2 and the primary crystalline phase in the slags is $CaTiO_3$, the crystallization behaviors of which have been extensively studied [4-5]. We can choose some additives, such as CaO, SiO_2, P_2O_5 and B_2O_3, to modify the slag compositions, which can change the crystalline phase in the slags, such as perovskite, rutile, or anosovite. Rutile has a good separation trend due to the rod shape structure and high density [6]. Our previous study [7] proved that SiO_2 can be used to modify the slags and make the primary crystalline phase change from perovskite to rutile and remarkably enhance the precipitation of rutile. In addition with SiO_2, two other kinds of additives, P_2O_5 and B_2O_3, were explored in this study.

P_2O_5 and B_2O_3 are two kinds of typical acid oxide, which may greatly substitute SiO_2 and improve the growth of rutile. In addition, the precipitation of crystal is determined by many factors, among which viscosity has a decisive effect because of its influence on mass transfer. As potential additives, the influence of P_2O_5 and B_2O_3 on the viscosity of slags should be clarified, and therefore the present study was motivated. In this study, a series of Ti-BF slags containing different levels of P_2O_5 and B_2O_3 with different basicity were designed. The viscosity of these samples was measured using a Brookfield digital viscometer and the crystallization behaviors of these slags were analyzed using Single Hot Thermocouple Technique (SHTT) [8], in order to identify the influence of these additives.

Experimental

Sample preparation

In this study, a series of samples with the basicity of 0.5 and 0.7, the TiO_2 content of 25% and the B_2O_3/P_2O_5 addition of 0~5%. Analytically regent (AR) oxides were used to prepare the samples. These oxides were fully mixed and pre-melted in a molybdenum (Mo) crucible (Φ40 mm × 45 mm × H40 mm) under an argon atmosphere at 1550 °C for 1 h to homogenize the chemical compositions. Then the liquid slags were rapidly poured into the cold water to obtain glassy phases. Subsequently, the glassy slags were dried at 120 °C for 12 h, crushed and ground into 300 meshes for compositional analysis and crystallization experiments. The results of X-ray diffraction (XRD) tests ensured the glassy phases of slags.

Viscosity measurements

We used a Brookfield digital viscometer (RTW-10) to measure the slag viscosity, as depicted in **Figure 1**, and the viscosity measurement followed several steps. First, the Mo crucible filled with samples was placed into the heat area of the furnace and the Ar gas with a flow rate of 0.3 NL/min was inlet into to prevent the oxidation of Mo components. Second, the furnace was heated to 1550 °C at a rate of 5 °C/min and held for 2h to homogenize the temperature and chemical compositions of the slags. Third, the furnace was cooled to a set temperature at a rate of 5 °C/min and held for 30 min to stabilize the slag temperature. The rotary Mo spindle was then immersed into the slag melts and rotated for viscosity measurement, during which 3 rotation rates (150, 175 and 200 r/min) were used and the average value was taken as the viscosity at the corresponding temperature.

Crystallization experiments

The crystallization behaviors of the slags were measured through a series of isothermal experiments using a Single Hot Thermocouple Technique (SHTT). During the isothermal experiments, around 10 mg sample was heated to 1500 °C, fully melted and held for 120 s to homogenize the chemical composition. The liquid slags were rapidly quenched to a set temperature at 50 °C/s and held at this point for crystalline evolution. It takes some time for the crystal to occur in the melts, defined as incubation time. The relationship between incubation time and holding temperature is generally presented in the Time Temperature Transformation (TTT) curves, which was obtained in this study.

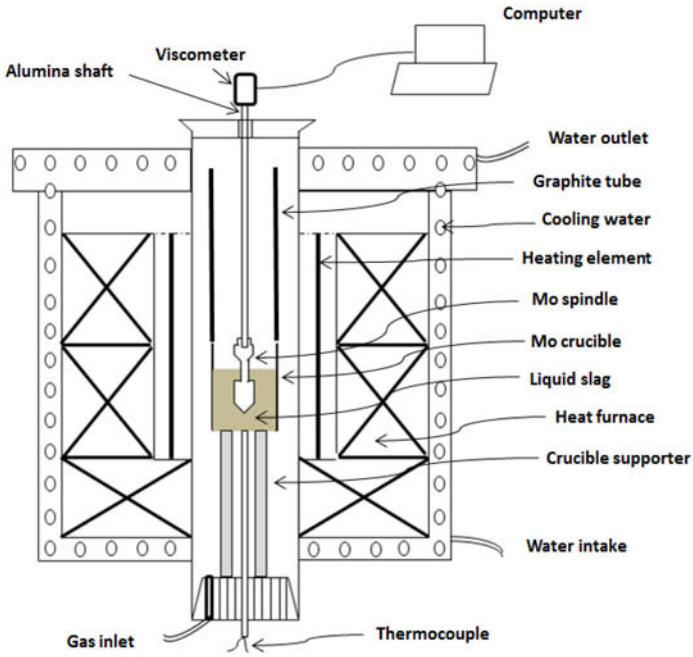

Figure 1. Schematic diagram of Brookfield digital viscometer

Results and discussion

Effect of P_2O_5 on viscosity of slags

Figure 2 shows the viscosity variation for various samples at different temperatures. There were two characteristics could be clearly observed from **Figure 2**. First, the viscosity remarkably increased with decreasing temperature. Conventionally, the viscosity of the slag melts was mainly determined by the interaction between the flow units when it was higher than break temperature. The linkage between flow units became weaker in virtue of the increasing distance caused by volume expansion with increasing temperature, resulting in the viscosity decrease. Second, the viscosity for each slag sample increased with increasing P_2O_5 content, which was in consistent with some previous studies. The variation trend of the viscosity caused by the added P_2O_5 could be easily explained. As an acid oxide, P_2O_5 mainly existed as PO_4 tetrahedral in the slag structures [9], which can substantially increase the degree of polymerization (DOP) of the slag networks. Thus, the viscosity was increased by the added P_2O_5; however, from point of view of crystalline growth, the increasing viscosity is detrimental to crystal growth, which may make up one of disadvantages of P_2O_5 as additive.

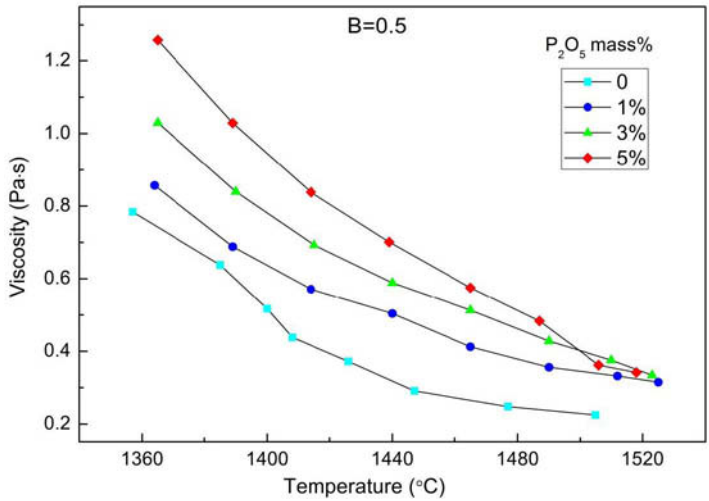

Figure 2. Viscosity of slags with varying P_2O_5 contents

Effect of B_2O_3 on viscosity of slags

Figure 3 shows the effect of B_2O_3 on the viscosity at different temperatures. There were two characteristics could be clearly observed from **Figure 3**. First, the viscosity remarkably increased with decreasing temperature, which was in agreement with the phenomenon of P_2O_5 series. Second, contrary to P_2O_5, the viscosity for each slag sample decreased with increasing B_2O_3 content, which was in consistent with some previous studies. As an acid oxide, the added B_2O_3 theoretically could increase the DOP of the slags and therefore increase the viscosity of the slags. However, according to the previous studies, the break temperature of slag was changed by the addition of B_2O_3. The melting point of B_2O_3 is 450 ^{o}C, and the addition of B_2O_3 could combine with many kinds of oxides to form eutectics with low melting points [10-11], which substantially lower the break temperature of slags. With the decrease of break temperature, the superheat degree was increased at a certain temperature higher than the break temperature, and ultimately the viscosity was decreased. Generally, acidic oxides acted as network formers and increased the viscosity of slags. However, this effect in the present system was smaller compared with the effect of low melting point, which caused decreasing viscosity with B_2O_3 addition. Actually, as a typical network forming oxide, B_2O_3 was introduced into the network and existed dominantly as 2-D structure, BO_3 triangular [12], which caused a simpler structure and a decreasing slag viscosity.

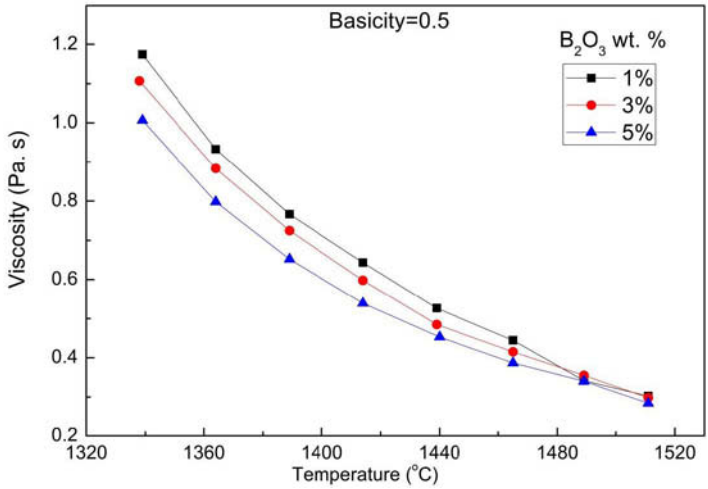

Figure 3. Viscosity of slags with varying B_2O_3 contents

Effect of P_2O_5 and B_2O_3 on crystallization behavior of slags

SHTT combined an advantage of observation of crystalline evolution and temperature control, as depicted in **Figure 4**. For the slag series with the basicity of 0.5, the primary crystalline phase was rod-shape rutile, while for the slag series with the basicity of 0.7, the primary crystalline phase was dendrite shape perovskite. However, with the addition of P_2O_5 and B_2O_3, the primary crystalline phase changed from perovskite to rutile with the additive content of 7 wt. %. Actually, both P_2O_5 and B_2O_3 are acid oxides, which could modify the basicity of the slags similar to SiO_2. As the P_2O_5 and B_2O_3 were added into the slags, more BO_3 triangular and PO_4 tetrahedral were generated, which would link with the Ca ions and restrict the linkage between Ca ions and Ti-related structures. Thus, the precipitation of perovskite was suppressed and the formation of rutile was enhanced. When the temperature further decreased, the pure primary crystalline phase changed into a situation of multiple phase coexisting and the present study mainly focused on the crystallization behavior at high temperatures.

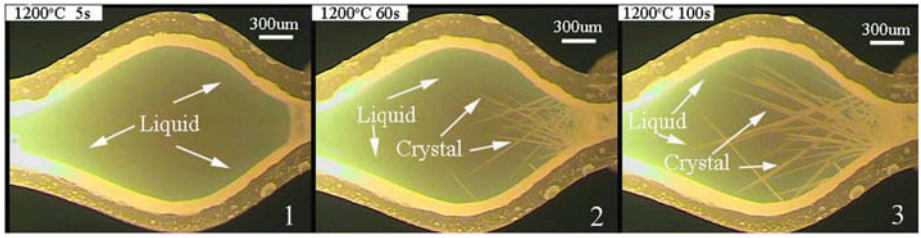

Figure 4. Schematic diagrams of rutile growth

Incubation time is an important parameter to characterize the crystallization property, and a longer incubation time indicated a weaker crystallization trend. For the slag series with the basicity of 0.5, the incubation time became shorter with the increase of P_2O_5 or B_2O_3 content,

which indicated that the crystallization in these slags was improved and the additives were beneficial for the rod-shape rutile. For the slag series with the basicity of 0.7, the situation became different. As the primary crystalline phase was perovskite, the incubation time became longer with the addition of P_2O_5 or B_2O_3. This suggested that the formation of perovskite was restricted, which was in agreement with the results of slags series with the basicity of 0.5 in an opposite direction. In addition, the kinetics of the primary crystalline phase growth was studied. First, the length of rod shape rutile presented a well linear relationship with holding time, which suggested that the rate-controlling step of rutile growth was interfacial reaction [13-14] and a 1-D growth model was reasonably to describe the growth of rutile. Second, according to the SEM detection and the calculation of the kinetic constants showed that the dendrite perovskite showed a 3-D growth style.

Conclusions

This study provided some fundamental study on the influence of P_2O_5 and B_2O_3 on the viscosity and crystallization behaviors of Ti-bearing blast furnace slags for the purpose of titanium extraction. The viscosity of the slags was increased by the added P_2O_5, whereas B_2O_3 showed an opposite effect. Both the added P_2O_5 and B_2O_3 enhanced the crystallization of rod-shape rutile while suppressed the crystallization of dendrite perovskite. Furthermore, the kinetics analysis indicated that the rod-shape rutile showed a 1-D growth, whereas the dendrite $CaTiO_3$ showed a 3-D growth style.

References

1. L.P. Wang, et al., "distribution and production status of titanium resources in China," *Chinese Journal of Rare Metals*, 28 (2004), 265-267.
2. L. Wen, and J.Z. Zhang, "Properties on titanium-bearing blast furnace slags" *Journal of Iron and Steel Research International*, 23 (2011), 1-3.
3. L. Zhang, et al., "Dynamic oxidation of the Ti-bearing blast furnace slag," *ISIJ International*, 46 (2006), 458-465.
4. L. Zhang, et al., "Effect of perovskite phase precipitation on viscosity of Ti-bearing blast furnace slag under the dynamic oxidation condition," *Journal of non-crystalline solids*, 352 (2006), 123-129.
5. L. Zhang, et al., "Precipitation selectivity of perovskite phase from Ti-bearing blast furnace slag under dynamic oxidation conditions," *Journal of non-crystalline solids*, 353 (2007), 2214-2220.
6. J. Li, Z.T. Zhang, and X.D. Wang, "Crystallization behavior of rutile in the synthesized Ti-bearing blast furnace slag using single hot thermocouple technique,", *ISIJ International*, 51 (2011), 1396–402.
7. J. Li, Z.T. Zhang, and X.D. Wang, "Precipitation behaviour of Ti enriched phase in Ti bearing slag," Ironmaking Steelmaking, 39 (2012), 414–418.
8. K. Yajima, H. Matsuura, and F. Tsukihashi, "Effect of simultaneous addition of Al_2O_3 and MgO on the liquidus of the $CaO\text{-}SiO_2\text{-}FeO_x$ system with various oxygen partial pressures at 1573 K," *ISIJ International*, 50(2010), 191-194.
9. B.O. Mysen, "Phosphorus speciation changes across the glass transition in highly polymerized alkali silicate glasses and melts", *American Mineralogist*, 81 (1996), 1531-1534.
10. S. Sridhar, et al., "Break temperatures of mould fluxes and their relevance to continuous casting," *Ironmaking & steelmaking*, 27(2000), 238-242.

11. A.B. Fox, et al., "Development of fluoride-free fluxes for billet casting," *ISIJ International*, 45 (2005), 1051-1058.
12. R. Ciceo-Lucacel, and I. Ardelean, "FT-IR and Raman study of silver lead borate-based glasses," *Journal of non-crystalline solids*, 353 (2007), 2020-2024.
13. K.A. Jackson: Liquid Metals and Solidification; ASM: Cleveland, Ohio, (1958), 174.
14. J. Huberty, and H. Xu, "Kinetics study on phase transformation from titania polymorph brookite to rutile," *Journal of Solid State Chemistry*, 181 (2008), 508-514.

Characterization of Minerals, Metals, and Materials 2015
Edited by: John S. Carpenter, Chenguang Bai, Juan Pablo Escobedo, Jiann-Yang Hwang, Shadia Ikhmayies, Bowen Li, Jian Li, Sergio Neves Monteiro, Zhiwei Peng, and Mingming Zhang
TMS (The Minerals, Metals & Materials Society), 2015

$PHYBAL_{SIT}$ - Fatigue Assessment and Life Time Calculation of the Ductile Cast Iron EN-GJS-600 at Ambient and Elevated Temperatures

Benjamin Jost[1], Marcus Klein[1], Dietmar Eifler[1]

[1]Institute of Materials Science and Engineering (WKK); University of Kaiserslautern; P.O. Box 3049; 67653 Kaiserslautern, Germany

Keywords: $PHYBAL_{SIT}$, ductile cast iron, EN-GJS-600, dynamic strain ageing, fatigue properties, life time calculation, cyclic deformation behavior

Abstract

This paper focuses on the ductile cast iron EN-GJS-600 which is often used for components of combustion engines. Under service conditions, those components are mechanically loaded at different temperatures. Therefore, this investigation targets at the fatigue behavior of EN-GJS-600 at ambient and elevated temperatures. Light and scanning electron microscopic investigations were done to characterize the sphericity of the graphite as well as the ferrite, pearlite and graphite fraction. At elevated temperatures, the consideration of dynamic strain ageing effects is of major importance. In total strain increase, temperature increase and constant total strain amplitude tests, the plastic strain amplitude, the stress amplitude, the change in temperature and the change in electrical resistance were measured. The measured values depend on plastic deformation processes in the bulk of the specimens and at the interfaces between matrix and graphite. The fatigue behavior of EN-GJS-600 is dominated by cyclic hardening processes. The physically based fatigue life calculation "$PHYBAL_{SIT}$" (SIT = strain increase test) was developed for total strain controlled fatigue tests. Only one temperature increase test is necessary to determine the temperature interval of pronounced dynamic strain ageing effects.

Introduction

Beneficial mechanical and physical properties connected with low production costs lead to numerous applications of ductile cast iron in the automotive and commercial vehicle technology, especially for components of combustion engines [1]. The goal to reduce fuel consumption and vehicle weight is realized by decreasing the number of cylinders and the engine stroke volume while increasing the specific power output [2, 3]. Application examples for the ductile cast iron EN-GJS-600 are camshafts, bearing covers, crankcases, pistons and especially crankshafts where the increased specific power output leads to maximum component stresses in a wide temperature range up to temperatures of 270 °C [4, 5]. To establish a weight-optimized dimensioning of such components, the influence of dynamic strain ageing effects on the fatigue behavior has to be considered.
This investigation focuses on the ductile cast iron EN-GJS-600. Light (LM) and scanning electron microscopic (SEM) investigations were performed to characterize the microstructure. To describe the fatigue behavior detailed, mechanical stress-strain (σ-ε) hysteresis, change in temperature (ΔT) and change in electrical resistance (ΔR) measurements were applied. The plastic strain amplitude $\varepsilon_{a,p}$, the change in temperature ΔT and the change in electrical resistance ΔR depend on plastic deformation processes and can be used as input data for the physically based fatigue life calculation "PHYBAL"[6, 7]. To characterize the temperature influence on the

fatigue behavior in total strain controlled fatigue, as a first step, one temperature increase test is necessary to determine the temperature interval between the first and the most pronounced dynamic strain ageing. This effective tool allows to identify the temperatures of minimum and maximum fatigue life due to dynamic strain ageing effects with only one fatigue test. As a second step, the physically based fatigue life calculation method "$PHYBAL_{LIT}$" (LIT = load increase test) was modified to "$PHYBAL_{SIT}$" (SIT = strain increase test) for total strain controlled fatigue testing. On the basis of only one total strain increase and two constant total strain amplitude tests the Woehler (ε-N) curve can be calculated. Thus, the combination of "$PHYBAL_{SIT}$" with a temperature increase test leads to significant scientific and economic advantages.

Material

The investigated cast iron EN-GJS-600 was provided by the Daimler AG in round bars with a diameter of 36 mm and a length of 300 mm. Figure 1 shows a provided bar and two fatigue specimens.

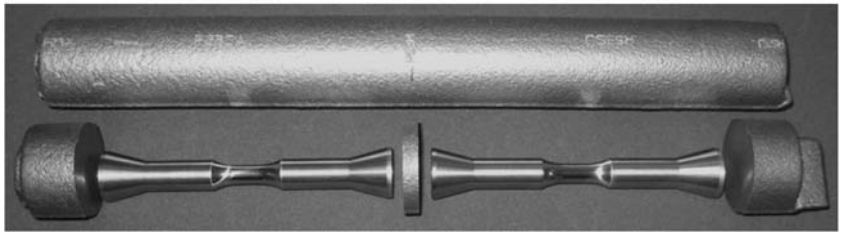

Figure 1. EN-GJS-600 bar provided by Daimler AG and machined fatigue specimens

Light (LM) and scanning electron micrographs (SEM) of the investigated EN-GJS-600 are shown in Figure 2. The microstructure is predominantly pearlitic, the ferrite is developed circular around the graphite spheroids.

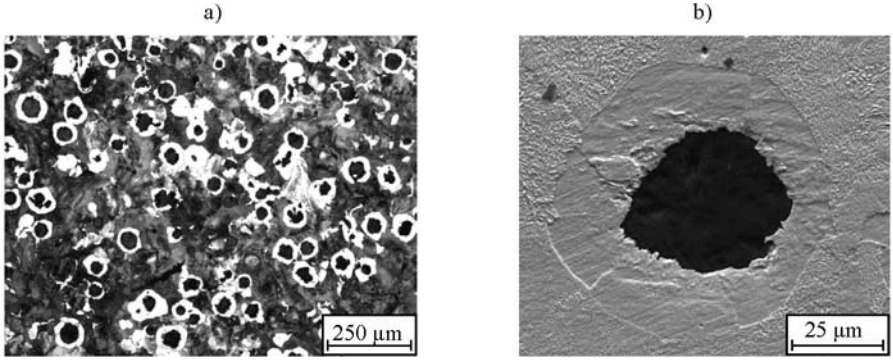

Figure 2. LM (a) and SEM (b) micrographs of the ductile cast iron EN-GJS-600

The Brinell hardness, the graphite and the ferrite fraction of the investigated materials are shown in Table I.

Table I. Microstructural parameters of the investigated cast iron EN-GJS-600

Brinell hardness [HBW 2,5/187,5]	234 ± 5
graphite fraction [area-%]	6.67 ± 0.89
ferrite fraction [area-%]	15.58 ± 1.34

Experimental setup

Total strain controlled constant amplitude (CAT), total strain increase (SIT) and temperature increase tests (TIT) were performed with a frequency of 5 Hz and a triangular strain time function at ambient and elevated temperatures with a strain ratio of $R_\varepsilon = -1$. The SITs were done with a step length of 9×10^3 cycles and total strain steps of 0.01 %. The TITs were performed at a constant total strain amplitude of 0.2 % while the temperature was increased stepwise from ambient temperature up to 425 °C, following a temperature increase of 25 °C every 2.5×10^3 cycles. Simultaneously the plastic strain amplitude $\varepsilon_{a,p}$ was measured. For electrical resistance measurements, a highly constant direct current was applied to the specimens. The change in electrical resistance ΔR was measured with two wires spot welded to the transition of the gauge length and the shafts. At ambient temperatures, the change in temperature ΔT was measured with one thermocouple applied in the middle of the gauge length (T_1) and two thermocouples at the elastic loaded shafts ($T_2 + T_3$). At elevated temperatures, thermocouple T_1 was used for furnace control, T_2 and T_3 allow to monitor the temperature gradient within the gauge length. Figure 3 shows the experimental setup for ambient (a) and elevated (b) temperatures.

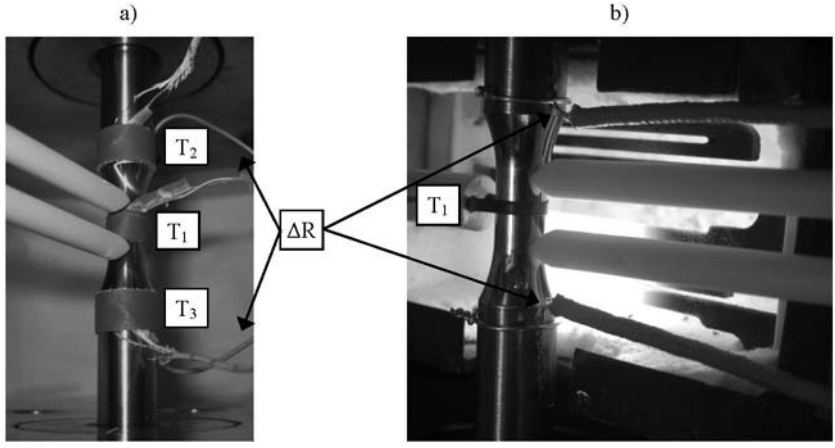

Figure 3. Experimental setup for ambient (a) and elevated (b) temperatures

The PHYBAL$_{LIT}$ – method

The physically based fatigue life calculation method "PHYBAL$_{LIT}$" allows the calculation of Woehler (S-N) curves on the basis of only one load increase test (LIT) and two constant amplitude tests (CAT). The PHYBAL$_{LIT}$ procedure is described in detail for several metallic materials in [6-10]. In the following, only the basic procedure is explained.

Fatigue data determined in one load increase test (LIT) are used as input for the fatigue life calculation. The measured values (M), e.g. the plastic strain amplitude $\varepsilon_{a,p}$, the change in temperature ΔT, the change in electrical resistance ΔR or other physically based fatigue parameters are plotted according to Morrow. With the fatigue data of two constant amplitude tests (CAT$_{exp.}$), the Morrow diagram is converted into single-step-loading (CAT$_{calc.}$ in Figure 4). CAT$_{calc.}$ allows to determine the generalized Morrow equation (equation (1)) as cyclic stress measured-data curves (CSM) in analogy to cyclic stress strain curves (CSS). According to Basquin, in analogy to the cyclic stress measured-data curves (CSM), a Woehler (S-N) curve can also be described by a powerfunction, as shown in the generalized Basquin powerfunction in equation (2). The Basquin exponent, describing the gradient of the Woehler (S-N) curve, correlates to the Morrow exponent by equation (3) [10]. Figure 4 explains PHYBAL$_{LIT}$ schematically.

$$\sigma_a = K'_M (M)^{n'_M} \qquad (1)$$

$$\sigma_a = \sigma'_{B,M} (2N_f)^{b_M} \qquad (2)$$

$$b_M = \frac{-n'_M}{5n'_M + 1} \qquad (3)$$

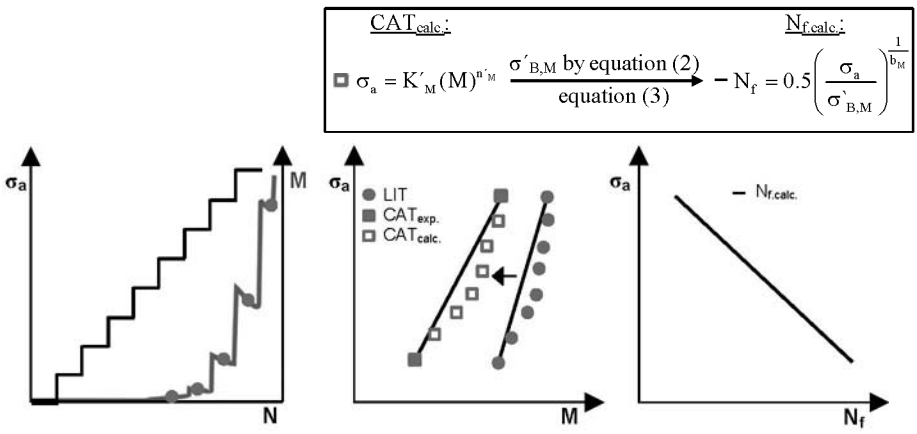

Figure 4. Schematical explanation of PHYBAL$_{LIT}$

Solving equation (2) for "N_f" leads to a load-dependent calculation rule (equation (4)):

$$N_f = 0.5 \left(\frac{\sigma_a}{\sigma'_{B,M}} \right)^{\frac{1}{b_M}} \qquad (4)$$

$\sigma'_{B,M}$ can be determined by performing one constant amplitude (CAT) fatigue test until failure and substituting "b_M" (equation (3)), "N_f" and "σ_a" to equation (2).

Results and discussion

To characterize the fatigue behavior of the ductile cast iron EN-GJS-600 from ambient up to elevated temperatures, several total strain controlled constant amplitude tests were performed. Those tests aimed to characterize the influence of dynamic strain ageing on fatigue life and the cyclic deformation behavior. All tests were carried out at a total strain amplitude of $\varepsilon_{a,t} = 0.2\ \%$.

A temperature increase up to 175 °C leads to the minimal fatigue life (relative fatigue life minimum) and an increase of the plastic strain amplitude $\varepsilon_{a,p}$ within the first cycles, figure 5a. Raising the temperature up to 300 °C the cyclic hardening is more pronounced due to dynamic strain ageing effects reaching the maximum cyclic hardening and the maximum number of cycles to failure (relative fatigue life maximum) at 300 °C. Highest values within the first cycles of the plastic strain amplitude $\varepsilon_{a,p}$ are shown in the range of 300 °C. A further temperature increase up to 400 °C results in reduced cyclic hardening. The initial plastic strain amplitude values are significant reduced and the fatigue life steadily decreases.
To determine the temperature interval between the first and the most pronounced dynamic strain ageing a temperature increase test (TIT) was performed. It shows, that the temperature of the relative fatigue life minimum (maximum) due to dynamic strain ageing is characterized by the lowest (highest) cyclic hardening in the respective temperature step (Figure 5b). This analogy to the constant amplitude tests verifies that a temperature increase test is well suited to figure out the temperatures of the relevant turning points (relative fatigue life minimum / maximum) in fatigue life behavior of the ductile cast iron EN-GJS-600. Therefore, temperature increase tests are an efficient investigation how dynamic strain ageing affects the fatigue behavior at elevated temperatures

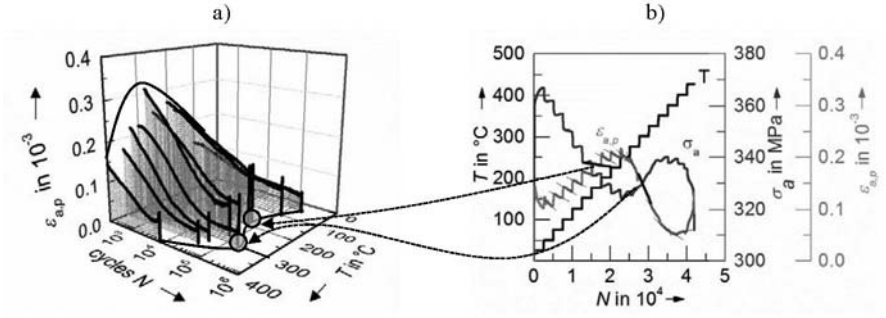

Figure 5. Cyclic deformation behavior and the relative fatigue life minimum / maximum up to 400°C (a) and the possibility to determine the relative fatigue life minimum / maximum with only one temperature increase test (b).

To characterize the fatigue life behavior in the temperature range up to 400°C, it is appropriate to calculate the respective Woehler (ε-N) curves at the relevant temperatures (ambient temperature, temperature of relative fatigue life minimum / maximum and a temperature above dynamic strain ageing). Therefore, $\text{PHYBAL}_{\text{SIT}}$ was developed.

$\text{PHYBAL}_{\text{SIT}}$ (fatigue life calculation for total strain controlled fatigue tests) offers a physically based fatigue life calculation method for total strain controlled fatigue tests. In analogy to $\text{PHYBAL}_{\text{LIT}}$, an efficient test procedure is developed to calculate the Woehler (ε-N) curve for the

ductile cast iron EN-GJS-600. The calculated Woehler (ε-N) curves were verified by total strain controlled constant amplitude tests.

Only one total strain increase test allows to evaluate the fatigue limit ε_w and the total strain amplitudes for the two constant amplitude tests. At the same time, the average measured values M ($\varepsilon_{a,p}$, ΔT and ΔR) of each strain step are the input parameters for the fatigue life calculation. Therefore, reflecting the work of Morrow, cyclic total-strain measured-values curves (CS_tM) are created by the pairs of values of the total strain increase test. Figure 6a shows the total strain increase test and the measured values (σ_a, $\varepsilon_{a,p}$, ΔT and ΔR). Regarding the change in the slope of σ_a-N, $\varepsilon_{a,p}$-N and ΔT-N curves at $\varepsilon_{a,t}$ = 0.14 %, the fatigue limit ε_w can be estimated for a total strain amplitude $\varepsilon_{a,t}$ = 0.14 % . The change in the slope of the ΔR-N curve can be observed slightly before reaching the estimated fatigue limit of $\varepsilon_{a,t}$ = 0.14 %. Constant amplitude tests confirmed a fatigue limit of $\varepsilon_{a,t}$ = 0.15 % in good accordance to the estimated fatigue limit. In the following, $PHYBAL_{SIT}$, using the plastic strain amplitude $\varepsilon_{a,p}$ as input fatigue parameter M is shown for total strain controlled tests at ambient temperature. According to Morrow, Figure 6b displays the cyclic total-strain plastic-strain curve (CS_tS_p) for $\varepsilon_{a,p}$.

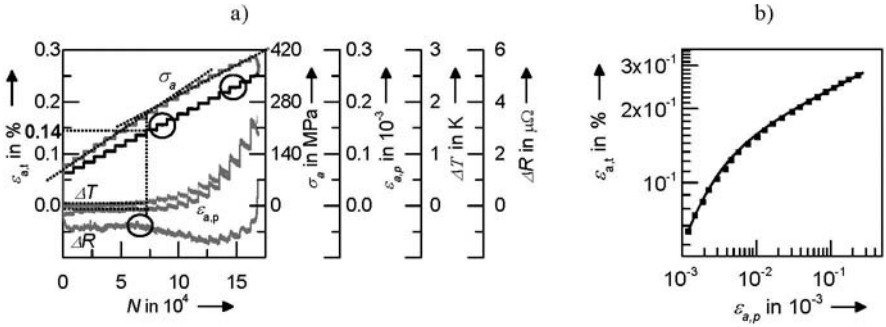

Figure 6. Strain increase test (SIT) of EN-GJS-600 (a) and the cyclic total-strain plastic-strain curve (CS_tS_p), value pairs are extracted out of SIT (b)

The total strain amplitudes for the constant amplitude tests are 0.16 % (lower CAT, slightly above ε_w) and 0.22 % (upper CAT, slightly below the damage causing total strain amplitude).To convert the cyclic total-strain plastic-strain curve (CS_tS_p) of the strain increase test into single steptests, two total strain amplitude tests were performed. This is essential, because the correlation between the Morrow and Basquin exponent (equation (3)) is only reliable for single step loading. Figure 7a shows the constant amplitude test with a total strain amplitude of 0.22 %. The value of the input parameter $\varepsilon_{a,p}$ is taken at 10^4 cycles. The converted cyclic total-strain plastic-strain curve (CS_tS_p) for single step loading is shown in Figure 7b. Modifying the generalized Morrow equation (equation (1)) for total strain controlled fatigue tests leads to equation (5) which describes a cyclic total-strain measured-value curve in general (CS_tM):

$$\varepsilon_{a,t} = K'_M(M)^{n'_M} \tag{5}$$

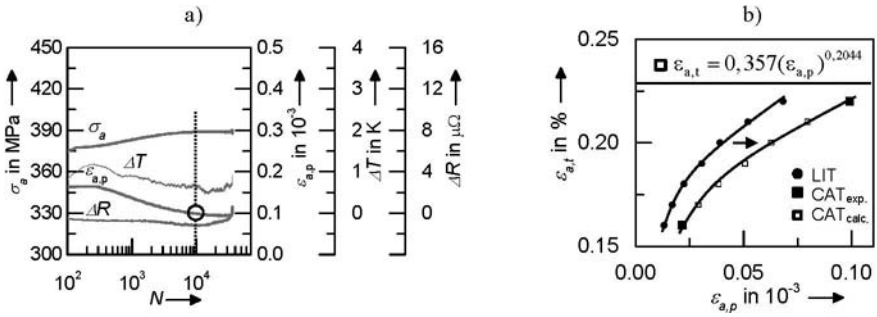

Figure 7. Constant amplitude test (CAT) of EN-GJS-600 (a) and the converted cyclic total-strain plastic-strain curve (CS_tS_p) for single step loading (b)

Modifying the generalized Basquin equation (equation (2)) for total strain controlled fatigue tests leads to equation (6) which describes a Woehler (ε-N) curve:

$$\varepsilon_{a,t} = \varepsilon'_{B,M}(2N_f)^{b_M} \quad (6) \longrightarrow b_M \text{ by equation (3):} \longrightarrow b_M = \frac{-0.2044}{5 \cdot 0.2044 + 1} = -0.101$$

Solving equation (6) for "N_f" leads to a load-dependent calculation rule for a Woehler (ε-N) curve (equation (7)):

$$N_f = 0.5\left(\frac{\varepsilon_{a,t}}{\varepsilon'_{B,M}}\right)^{\frac{1}{b_M}} \quad (7) \quad \underline{\text{CAT:}} \quad \frac{N_f = 36459 + b_M}{\varepsilon_{a,t} = 0.22\ \%} \longrightarrow \varepsilon'_{B,M} \text{ by equation (6)} \longrightarrow N_f = 0.5\left(\frac{\varepsilon_{a,t}}{0.682}\right)^{-9.892}$$

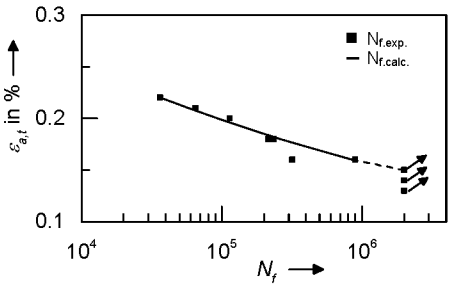

Figure 8. Calculated Woehler (ε-N) curve in excellent accordance to N_f evaluated experimentally

Conclusions

To establish a physically based fatigue life calculation, on the basis of the $PHYBAL_{LIT}$-method, $PHYBAL_{SIT}$ was developed for total strain controlled fatigue tests. One total strain increase test allows to identify the fatigue limit depending on the measured values σ_a, $\varepsilon_{a,p}$, ΔT and ΔR in good accordance to the conventionally determined fatigue limit. Using the generalized Morrow and

Basquin equations, modified for total strain controlled fatigue tests, allows the calculation of a Woehler (ε-N) curve. To characterize the fatigue behavior at elevated temperatures, the consideration of dynamic strain ageing effects has to be taken into account. Total strain controlled constant amplitude tests showed, that the cyclic hardening and the fatigue life are reduced by rising the temperature up to 175 °C. A further increase up to 300 °C causes more pronounced cyclic hardening and an increase in fatigue life due to dynamic strain ageing. Temperatures above 300 °C lead to a significant reduction of cyclic hardening and consequently fatigue life. Only one temperature increase test is necessary to determine the temperature range of dynamic strain ageing effects. The comparison with constant amplitude tests shows that a temperature increase test is well suited to identify the temperatures of the relevant turning points in the fatigue life behavior of the ductile cast iron EN-GJS-600. Thus, the combination of $PHYBAL_{SIT}$ and a temperature increase test provides an effective tool to calculate the fatigue life behavior in the temperature range from AT to 400°C and therefore leads to significant scientific and economic advantages.

Acknowledgements

The financial support of this work by the German Research Foundation (DFG) is gratefully acknowledged. Special thanks to the Daimler AG for providing the test material.

References

1. R. O´Rourke, *Cast iron: The engineered metal.* Advanced Materials & Prosesses, 2001. 159: p. 65-68.
2. C. Carey, et al., *Extreme engine downsizing*, in *Innovations in Fuel Economy and Sustainable Road Transport*, I.o.M. Engineers, Editor. 2011, Woodhead Publishing. p. 135-147.
3. R. Nozawa, Y. Morita, and M. Shimizu, *Effects of engine downsizing on friction losses and fuel economy.* Tribology International, 1994. 27(1): p. 31-37.
4. R. Basshuysen, F. Schäfer, *Handbuch Verbrennungsmotor.* Vol. 5. 2010: Vieweg + Teubner.
5. W. Weißbach, *Werkstoffkunde*. Vol. 18. 2012, Wiesbaden: Vieweg + Teubner / Springer.
6. D. Eifler, P. Starke, F. Walther, *PHYBAL—A new method for lifetime prediction based on strain, temperature and electrical measurements.* International Journal of Fatigue, 2005. 28.
7. P. Starke, D. Eifler, *Fatigue assessment and fatigue life calculation of metals on the basis of mechanical hysteresis, temperature and resistance data.* Material Testing, 2009. 51: p. 261-268.
8. B. Ebel-Wolf, F. Walther, and D. Eifler, *Influence of elevated temperatures on the cyclic deformation behaviour of the magnesium die-cast alloys AZ91D and MRI 230D.* Materials Science and Engineering: A, 2008. 486(1–2): p. 634-640.
9. H. Germann, et al., *Fatigue behaviour and lifetime calculation of the cast irons EN-GJL-250, EN-GJS-600 and EN-GJV-400.* Procedia Engineering, 2010. 2(1): p. 1087-1094.
10. P. Starke, *Lebensdauerberechnung bei ein- und mehrstufig beanspruchten Proben aus vergütetem 42CrMo4*. 2007, Lehrstuhl für Werkstoffkunde, TU Kaiserslautern.

Characterization of Minerals, Metals, and Materials 2015
Edited by: John S. Carpenter, Chenguang Bai, Juan Pablo Escobedo, Jiann-Yang Hwang, Shadia Ikhmayies, Bowen Li, Jian Li, Sergio Neves Monteiro, Zhiwei Peng, and Mingming Zhang
TMS (The Minerals, Metals & Materials Society), 2015

GOLD LEACHING CHARACTERISTICS AND INTENSIFICATION OF A HIGH S AND AS-BEARING GOLD CONCENTRATE

Yong-bin Yang[1], Xiao-liang Liu[1], Tao Jiang[1], Qian Li[1], Bin Xu[1], Yan Zhang[1]

[1]School of Minerals Processing & Bioengineering, Central South University, Changsha, Hunan, P R China, 410083, sklxl1987@163.com

Keywords: Gold, Cyanidation, Calcine, Pickling, Reduction roasting

Abstract

Some high sulfur and arsenic-bearing gold concentrate has a gold leaching rate less than 80% by oxidation roasting-pickling-cyanidation process. The characteristics and intensification of gold leaching were studied systemically. By combining chemical composition and phase analysis, the low gold leaching rate was found to lie in the capsulation of gold by iron-containing phases including iron oxides, arsenopyrite and pyrite. 96.66% of gold in the industrial leaching residue was capsulated and 95.88% of the capsulated turned out to be in the iron-containing phases. The results of laboratory pickling-cyanidation experiments on the calcine and industrial leaching residue presented further demonstration for the fact that gold capsulated in the iron-containing phases was hard to be leached. However, the gold cyanide leaching rate of calcine could be raised over 95% by a reduction roasting-pickling pretreatment which played such a significant role in exposing the capsulated gold that gold leaching was intensified remarkably.

Introduction

At present, cyanidation has been still in a dominant position among the main methods of gold leaching in gold industry, owing to its irreplaceable advantages compared with many other methods [1]. With the rapid development of gold industry, tractable gold ores are drying up gradually, while those of refractory are increasingly becoming the main processing objects. Currently, refractory gold ores from which one third of total world gold production comes, account for 60% of total world gold reserves [2]. China is rich in refractory gold ores among which as many as one third are sulfur and arsenic-bearing gold ores [3]. As for this kind of ores whose direct gold leaching is so poor that they have to be pretreated, there have been mainly three pretreatment processes including wet chemical, oxidation roasting and bacterial oxidation methods being widely applied till now [4, 5]. There was a low grade gossan type gold ore pretreated by "coal based direct reduction roasting-magnetic separation-cyanide leaching" process to achieve the separation of iron and gold, and its gold leaching recovery could increase by 36.47% compared with direct cyanide leaching [6, 7].

Some high sulfur and arsenic-bearing gold concentrate is pretreated by two-stage oxidation roasting process

which leads to a secondary capsulation of gold inevitably, resulting in an undesirable blocking to gold leaching by cyanide solution. The calcine obtained has a cyanide gold leaching rate as low as 80%. In the paper, characteristics and intensification of the gold cyanide leaching from the gold concentrate were studied systemically, which may provide a new idea for gold leaching from refractory gold ores.

Experimental

Materials

The high sulfur and arsenic-bearing gold concentrate came from a gold smeltery and its calcine as well as industrial leached residue was directly used in the whole study.

Table I. Multi-element Chemical Composition/%

Ore sample type	Au*	Ag*	Fe	S	As	Sb	Cu	SiO_2	CaO	MgO	Al_2O_3
Gold concentrate	45.77	20.66	24.07	23.89	8.73	0.44	0.091	27.24	1.27	0.59	5.14
Calcine	84.27	13.55	31.25	1.03	0.55	0.25	0.10	37.96	1.55	0.72	5.97
Leached residue	19.54	14.67	32.07	0.66	0.54	0.36	0.092	35.32	1.56	0.50	6.50

*The content unit of element is g/t.

The results of Table I show that the gold concentrate belongs to a typical high sulfur and arsenic-bearing ore. When pretreated by means of two-stage oxidation roasting and by dilute sulfuric acid leaching, the industrial cyanide leaching of calcine can just reach a gold leaching rate as low as 80%.

Methods

Phase analysis, pickling and cyanide leaching as well as reduction roasting experiments were conducted for the study. The leaching characteristics in terms of gold occurrence in industrial production samples were demonstrated by the analyses of XRD, chemical phase and elemental Au phase. Intensification of gold leaching had been realized effectively in laboratory by oxidation roasting-reduction roasting-pickling-cyanide leaching process for the high sulfur and arsenic-bearing gold concentrate. In addition, the oxidation roasting of gold concentrate to get rid of arsenic and sulfur was achieved by two-stage oxidation roasting process in a gold smeltery, and the calcine obtained was directly used as the processing object in the following study. With adequate coal as reductant, the reduction roasting of calcine was carried out for 0.5h~1.5h in an upright roaster whose furnace chamber temperature was stable at a value of 800℃~1200℃. The pickling experiments were conducted under the conditions of liquid-solid ratio 4:1, agitation speed 400rpm, leaching time 4h~6h and solution pH < 1.5 controlled by 10% sulfuric acid. The gold cyanide leaching was performed in a pulp with liquid-solid ratio 2.5:1, pH 11, ω(NaCN) 0.2%, agitation speed 600rpm, leaching time 48h, and $\omega(H_2O_2)$ 0.27% when necessary.

Results and discussion

Leaching characteristics in terms of gold occurrence in industrial production samples

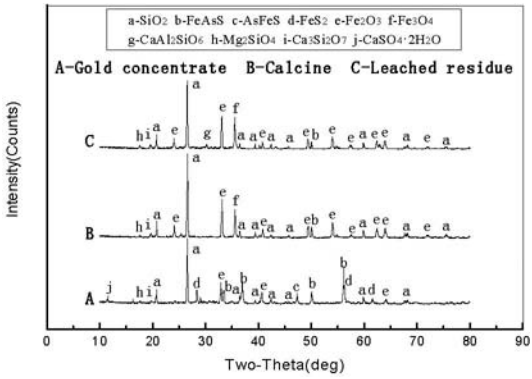

Figure1. XRD analysis of industrial production samples

Table II. Chemical Phase Analysis of Ore Samples/%

Ore sample type	Arsenopyrite	Pyrite	Iron oxides	Silicate	Other phases	Total
Glod concentrate	12.77	37.31	3.36	27.24	19.32	100.00
Calcine	0.02	0.05	50.50	37.96	11.47	100.00
Leached residue	0.26	0.04	52.37	35.32	12.01	100.00

Table III. Phase Analysis of Au in Ore Samples

Ore sample type \ Phase type		Single and associated gold	Arsenopyrite	Pyrite	Iron oxide	Silicate	Total
Glod concentrate	Content/(g/t)	1.21	33.46	2.90	7.79	0.41	45.77
	Distribution ratio/%	2.64	73.10	6.34	17.02	0.90	100.00
Calcine	Content/(g/t)	74.01	2.43	1.04	6.16	0.63	84.27
	Distribution ratio/%	87.83	2.88	1.23	7.31	0.75	100.00
Leached residue	Content/(g/t)	0.65	4.79	2.04	11.28	0.78	19.54
	Distribution ratio/%	3.33	24.51	10.44	57.73	3.99	100.00

The analysis of XRD and chemical phase (see Fig.1 and Table II) indicate that in the gold concentrate are pyrite, silicate and arsenopyrite in the majority, while in the calcine and leached residue are mainly iron oxides and silicate, with only small amounts of residual arsenopyrite and pyrite. Most of the pyrite and arsenopyrite convert into iron oxides during oxidation roasting, and here pyrite, arsenopyrite and iron oxides are all called iron-containing phase.

It is shown from the phase analysis of Au in industrial production samples (see Table III) that 79.44% of gold in the gold concentrate is capsulated in arsenopyrite and pyrite and 17.02% in iron oxides. According to the phase evolution and distribution change of gold after two-stage oxidation roasting pretreatment, it can be known that 96.06%, 80.52% of gold locked by arsenopyrite and pyrite gets exposed respectively, but there is still 12.17% being capsulated, of which as high as 93.84% is enclosed in the iron-containing phases, and the same to the leached residue, 95.88% of the capsulated still exists in the iron-containing phases.

The reasons why so much gold in leached residue that it could not be leached successfully are as follows:

(1) As high as 57.73% (see Table III) of the residual gold is capsulated in the iron oxides accounting for 52.37% (see Table II) of the leached residue, which illustrates that second gold capsulation by iron oxides happens inevitably during oxidation roasting process of the gold concentrate [8]. It is universally acknowledged that calcine sintering can be caused easily due to the overheating phenomenon, worse still, the structure destruction of iron oxides will lead to secondary capsulation of gold, which makes it hard to achieve an effective gold exposure even grounded finely.

(2) With 34.95% (see Table III) of the residual gold enclosed in arsenopyrite and pyrite which only account for about 0.30% (see Table II) of the leached residue, it demonstrates obviously that the small amounts of arsenopyrite and pyrite left after oxidation roasting are still the important phases concentrating gold as before. Under room temperature and atmospheric pressure, it is difficult for arsenopyrite to be dissolved in alkaline cyanide solution. However, the gold in arsenopyrite, especially those superfine gold particles, cannot be exposed even through ultra fine grinding [9]. Additionally, extra oxidant and leaching reagent will be consumed seriously by pyrite in gold leaching process, making finding an ideal gold leaching difficult.

(3) It is commonly known that most of the residual arsenic in calcine is arsenate (see Table III), probably the arsenopyrite left after the first stage of oxidation roasting at low temperatures generates ferric arsenate during the second stage at high temperatures. However, the ferric arsenate is apt to cover the gold surface, forming a passivation film and producing secondary capsulation of gold, which impedes gold cyanide leaching noticeably [8, 9].

Pickling-cyanide leaching results of industrial production samples

Experiment on extracting iron from pyrite cinder with the direct hydrochloric acid solution had been studied before [10], and pickling was applied before gold cyanide leaching in the study.

The results (see Table IV) indicate that the gold concentrate has an extremely poor gold cyanide leaching. When hydrogen peroxide is not utilized, the gold leaching rate of calcine is only 76.96% and that of leached residue is just as low as 12.73%. When hydrogen peroxide is added to perform assisted cyanide leaching [11-13], the gold leaching rate of calcine can only increase to 84.47% and that of leached residue is still as low as 16.70%. Neither the gold leaching rate of the calcine nor that of the leached residue is limited and difficult to increase further. Moreover, it has been known from Table 5 that the distribution ratio of single

and associated gold in calcine and that of capsulated gold in leached residue is 87.83% and 96.66%, respectively. All of the above provides further evidence that, without any other additional pretreatments, the gold capsulated in iron-containing phases, especially in the iron oxides, is so difficult to be exposed only by pickling that the gold leaching rate can hardly be further raised.

Table IV. Pickling-cyanide Leaching Results of Calcine and Leached Residue

Ore sample type	$\omega(H_2O_2)$/%	Gold content before leaching/(g/t)	Gold content after leaching/(g/t)	Gold leaching rate/%
Gold concentrate	0	45.77	41.66	12.68
Calcine	0	84.27	19.71	76.96
Calcine	0.27	84.27	13.29	84.47
Leached residue	0	19.54	17.27	12.73
Leached residue	0.27	19.54	16.81	16.70

Reduction roasting-cyanide leaching results of industrial leached residue

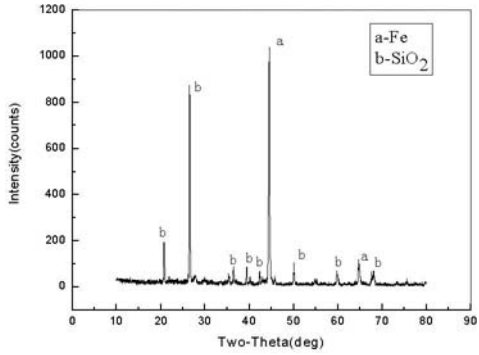

Figure2. XRD analysis of reduction roasting production at 1050℃

Table V. Reduction Roasting-cyanide Leaching Results of Industrial Leached Residue

Reduction roasting temperature/℃	Reduction roasting time/h	Gold content before cyanide leaching/(g/t)	Gold content after cyanide leaching/(g/t)	Gold leaching rate/%
800	1	22.37	21.18	6.14
900	1	23.41	20.64	12.78
1050	1	23.30	19.43	18.36

It has been known that most of the residual gold in industrial leached residue is enclosed in the iron-containing phases which are mainly composed of iron oxides (see Table II). Therefore, reduction roasting process can be utilized to achieve the structure destruction of iron oxides by

converting Fe_2O_3 or Fe_3O_4 into Fe phase during which the capsulated gold is hoped to get exposed. The XRD analysis of reduction roasting production at 1050℃ (see Figure 2) provides evidence that the structure of iron oxides has been destroyed successfully as expected, but the following cyanide leaching results (see Table V) show that the exposure of capsulated gold seems so terrible that the gold leaching rates are as low as 18.36%. It is probably that the gold is still capsulated in the new Fe phase, and the lixiviant and oxygen have been consumed by Fe. Therefore, the exposure of gold cannot be realized effectively by reduction roasting only.

Reduction roasting-pickling-cyanide leaching results of calcine

Corrosion process was once investigated in separating Ga and Ge from ferrous powder from zinc leach powder [14] and the enrichment of TiO_2 grade had been achieved by dilute hydrochloric acid leaching due to dissolving the impurities (Fe, Mg, Ca, etc) into solution [15]. In the same way, coming after the reduction roasting, pickling was also applied before gold cyanide leaching in laboratory.

Table VI. Reduction Roasting-pickling-cyanide Leaching Results of Calcine

Reduction roasting temperature/℃	Reduction roasting time/h	Gold content before cyanide leaching/(g/t)	Gold content after cyanide leaching/(g/t)	Gold leaching rate/%
800	1	165.44	30.17	82.04
900	1	162.64	23.97	85.37
1000	1	161.22	14.99	90.80
1050	1	166.19	14.58	91.27
1150	0.5	167.74	12.92	92.36
1150	1	189.86	7.98	95.84
1150	1.5	171.07	7.07	95.90
1200	1	169.76	10.14	94.09

Compared with gold enriching from 45.77g/t to 84.27g/t (see Table III) during oxidation roasting pretreatment, the results of experiments (see Table VI) show that gold in calcine achieves a further enrichment to different extents from 84.27g/t to 160g/t~190g/t after reduction roasting-pickling. Followed by gold cyanide leaching, the residual gold content in the final leached residue can be lowered to 7.07g/t~7.98g/t compared with 19.71g/t and the gold leaching rate comes up to 95.84%~95.90% which is far more than 76.96% (see Table IV). Currently, the gold leaching gets intensified significantly by the pretreatments of "reduction roasting-pickling" based on oxidation roasting.

As has been known from the above study, the structure of iron oxides cannot be destroyed effectively just relying on the picking process. However, after reduction roasting, iron oxides convert into Fe phase which can be dissolved into solution more easily by pickling. During the separation of Fe and Au, the full exposure of gold comes true and then the gold cyanide leaching is intensified remarkably. It is more beneficial for pickling effects on gold exposure when at higher reduction roasting temperatures not more than 1200℃ and roasting time is prolonged appropriately. When temperature is 1150℃ and time is 1h and 1.5h, the gold cyanide leaching rate can reach 95.84% and 95.90%,

respectively. Based on the oxidation roasting, it is the pretreatments of "reduction roasting-pickling" that realize the full exposure of gold capsulated in iron oxides and the remarkable intensification of gold cyanide leaching.

Conclusions

(1) The high sulfur and arsenic-bearing gold concentrate is extremely difficult to be directly leached by cyanidation. Inevitable capsulation of gold for the gold concentrate during two-stage oxidation roasting process happens due to gold capsulation by iron-containing phases including pyrite, arsenopyrite and iron oxides. Currently, gold capsulated in iron-containing phases leads to gold leaching rate being hard to be further raised.

(2) By oxidation roasting-reduction roasting-pickling-cyanide leaching process, gold leaching rate of the gold concentrate gets raised obviously. Using adequate coal as reductant and under full pickling, it is more beneficial for gold exposure by prolonging reduction time appropriately at a higher temperature not more than 1200℃. When temperature is 1150℃ and time is 1.5h, a gold cyanide leaching rate of 95.90% is obtained.

(3) Coming after oxidation roasting, Fe_2O_3 and Fe_3O_4 phases in calcine convert into Fe phase in the reduction roasting process. Then the pickling process achieves full exposure of gold by easily dissolving the new Fe phase into solution. Only by reduction roasting and pickling together can the intensification of gold cyanide leaching come true successfully.

Acknowledgements

The financial supports from National Natural Science Foundation of China, Grant No. 51074182 and from Postdoctoral Science Foundation of China, Grant No. 2014M550422 are gratefully acknowledged.

References

[1] Yun-fan Wang et al., "The development of optimization technique in gold ore cyanidation-leaching," Mining and Metallurgical Engineering, 20 (1) (2011), 59~63.

[2] Hai-dong Wang et al., "Experimental study of gold extraction process for a refractory gold ore," Nonferrous Metals (Mineral Processing Section), 2 (2011), 22~26.

[3] Jun Zhu, Su-ning Liu, "Status and research of leaching technology of gold ore that is difficult to be treated," Minerals Engineering, 8 (1) (2010), 35~37.

[4] Jun-zhuang Liu, Wan-fu Huang, "Progress of gold leaching process from the high arsenic gold ore," Modern Mining, 10 (2010), 26~29.

[5] Chun-rong Hu, Feng Yang, Hui-chun Yang, "Current status and developing tendency of gold extraction," Gold, 7 (27) (2006), 29~36.

[6] Xian-gong Mei et al., "The behavior of iron oxide in the direct reduction of gossan type-gold composite ores with coal base," Journal of Central South University, 08 (6) (1997), 533~535.

[7] Xian-gong Mei et al., "Extraction of gold in gossan type gold ores through direct reduction with coal," Conservation and Utilization of Mineral Resources, 06 (12) (1997), 27~30.
[8] Guang Xue et al., "Hydrometallurgy and analysis testing process of gold and silver" (Press of Science and Technology, Beijing, 2009)
[9] Jun-fang Nan et al., "Oxidation roasting pretreatment and metallurgy technology of gold concentrate" (Process of Metallurgical Industry, Beijing, 2009)
[10] Yan-ling Hao et al., "Experiment on extracting iron from pyrite cinder with the direct hydrochloric acid solution technique," Acta Petrologica et Mineralogica, 23 (3) (2004), 280~281.
[11] Yong-bin Yang, "Investigation on electrochemical kinetics and application for co-intensification of gold leaching" (Ph.D.thesis, Central South University, 2008)
[12] Guzman L et al., "Gold cyanidation using hydrogen peroxide," Hydrometallurgy, 52 (1999), 21~35.
[13] Yang Liu et al., "Research progresses on assistant leaching agent in cyanide leaching of gold ore," Mining and Metallurgy, 20 (2) (2011), 58~62.
[14] Guang-hui Li et al., "Fundamentals and applications of separating Ga and Ge from ferrous powder from zinc leach residue by corrosion process," The Chinese Journal of Nonferrous Metals, 14 (11) (2004), 1941~1945.
[15] Yu-feng Guo et al., "Enrichment of moderate and low grade titania feedstock by activated roasting-acidic leaching," The Chinese Journal of Nonferrous Metals, 15 (09) (2005), 1447~1451.

Characterization of Minerals, Metals, and Materials 2015
Edited by: John S. Carpenter, Chenguang Bai, Juan Pablo Escobedo, Jiann-Yang Hwang, Shadia Ikhmayies, Bowen Li, Jian Li, Sergio Neves Monteiro, Zhiwei Peng, and Mingming Zhang
TMS (The Minerals, Metals & Materials Society), 2015

ELECTROCHEMICAL PROPERTIES OF Al-Cu ALLOYS IN NaCl SOLUTIONS

Alejandra Silvina Roman[1], Claudia Marcela Méndez[1], Carlos Enrique Schvezov[1,2], Alicia Esther Ares[1,2]

[1] Materials Institute of Misiones, IMAM (CONICET-UNaM), University of Misiones; 1552 Azara Street, Posadas, Misiones, 3300 Argentina.
[2] Member of CIC of the National Research Council (CONICET) of Argentina.

Keywords: Al-Cu alloys, structural parameters, corrosion resistance.

Abstract

In this paper the structure of aluminum based alloys and their corrosion behavior by using different electrochemical techniques as characterization methods are considered. Currently, it becomes imperative to know the role of the Al_2Cu against the susceptibility to corrosion of these alloys. The present work aims to studying the electrochemical behavior of aluminum base alloys with the following compositions: Al-1wt.%Cu, Al-4.5wt.%Cu and Al-15wt.%Cu (with different grain structures), in 1M NaCl solutions, at room temperature. Cyclic potentiodynamic polarization tests were performed and were found that the alloys with more than 1wt.%Cu in the matrix have an unstable behavior and without tendency to reach passivity. The equivalent circuits derived from electrochemical impedance spectroscopy technique (EIS) generally showed two capacitive contributions. The susceptibility to corrosion becomes a complex function, not only of copper concentration and structure, but also with interdendritic spacings and distribution of phases in the alloys.

Introduction

Aluminum has important technological material properties, among which worth mentioning its low specific weight, good corrosion resistance in atmospheric media, and good electrical and thermal conductivity [1-4]. However, the use of pure aluminum is limited due to its low mechanical strength [2, 4]. This has led to the development of alloys to produce materials with improved properties.

It is known that copper is used as an alloying element in the aluminum since it increases hardness and tensile strength, fatigue and creep [5]. However, this procedure may produce a reduction in corrosion resistance [1-7]. The Al-Cu alloys are widely used in the automotive industry as a component of transport due to fuel savings associated with weight reduction benefits similar security. The first, and most widely used aluminum alloys are those containing from 4% to 10% in weight of Cu [1,3].

Osorio et al. analyzed the corrosion resistance of the alloys Al-wt.5%Cu and Al-8wt.%Cu directionally solidified with CET. They found that both morphologies (columnar and equiaxed) have similar experimental results in tests of EIS and polarization curves [7,10]. Recently, it has been found that there are complex interrelationships between the copper content in the alloy, and the secondary dendritic spacing structures [1-3, 6].

Numerous studies [1-3, 5-7, 11-15] mentioned that the presence of intermetallic compounds influences the corrosion susceptibility of the Al-Cu alloys. This is because the presence of precipitated alloying elements associated with the active regions located over the material surface [12]. Intermetallic behavior primarily depends on the potential difference between the particles and the matrix in a solution.

In previous work [2, 6, 15] have been studied Al-Cu alloys with hypoeutectic compositions assessing structural characteristics and corrosion resistance in 0.5 M NaCl solution. Evidence for the involvement of the intermetallic in the corrosion process thereof was found. The cathode character of the Al_2Cu particles in the interdendritic areas localized the attack and promoted dissolution of the Al rich metal matrix. This led to the conclusion that the corrosion susceptibility of the different assessed structures is influenced by the microstructure of the alloy. Several authors have pointed out that aluminium alloy surfaces will formulate a protective layer of corrosion aluminium oxide if left unprotected by anodizing and/or correct painting procedures. [4, 6, 11-16]. In the presence of aggressive ions, localized breakdown of the passive film may occur, causing the dissolution of metal [4, 11-16]. Vera et al. [4] report that the decreased concentration of the Cl^- ion resulting in more anodic potentials.

Therefore, in this paper the behavior against corrosion of Al-Cu hypoeutectic alloys will be assessed, depending on the composition and structure of them, in 1M NaCl solution. The results will be compared with those obtained previously in 0.5M NaCl solution.

Experimental Procedure

We worked with samples of hypoeutectic aluminum base alloys, with the following compositions: Al-1wt.%Cu, Al-4.5wt.%Cu and Al-15wt.%Cu. The samples were obtained by directional solidification upward in a cylindrical resistance furnace, in vertical disposition. They were grounded using SiC papers from # 100 to # 1200 grain, then were washed with demineralized water and dried by natural flow of air. In order to evaluate the performance of the same function of the structures formed during solidification, the macrostructure revealed was performed and identified by visual observation, the zones of columnar grains (C Zone) and equiaxed grains (E Zone) separated by a transition zone (CET zone) between both, in each of the samples. Etching was performed with two different solutions: for samples containing less than 10wt.%Cu a solution containing 15 ml HF, 4.5 ml HNO_3, 9 ml HCl and 271.5 ml H_2O was used; and for the case of the Al-15wt.%Cu sample a solution containing 320 ml HCl, 160 ml HNO_3 and 20 ml HF was used. Then, the samples were cut longitudinally to give a working electrode for each region of each alloy prepared.

Measures of Electrochemical Impedance Spectroscopy (EIS) were also conducted. An initial period of stabilization of system during 600 seconds was used to determine the open circuit potential and worked with an amplitude of 10 mV potential around this. To adjust the results the nonlinear method of least squares designed by Bouckamp was used [17].

Electrochemical tests were performed using a potentiostat/galvanostat Gamry Reference 600, and using as medium 1M NaCl solutions at room temperature, deaerated by nitrogen bubbling for 20 minutes.

Results and Discussion

Potentiodynamic curves corresponding to the Al-1wt%Cu tested in 1M NaCl solution are shown in Figure 1 (a). The potential range in which the current increases steadily decreases from the base of the cylinder (that is, from the columnar to zone to the equiaxed zone in the sample), showing that the C zone shows the corrosion potential E_c nobler (-829 mV), virtually no passivation is presented, but a direct dissolution of the material.

This potential coincides with pitting potential, Ep, corresponding to the CET and E zones. In contrast, the results found in a less concentrated solution of NaCl to the same alloy [6], showed that the three zones analyzed behaved very similarly to one another, remaining passive in 100mV range.

The cyclic potentiodynamic polarization curves for the Al-4.5%Cu alloy are shown in Figure 1 (b). No passivation is found, but dissolution of the material directly after reached the corrosion potential. Zone C presents the nobler Ep equal to -656 mV and has the lowest value at the transition zone equal to -691 mV. Similar behavior was found for the curves tested in 0.5 M NaCl solution [6]. In Figure 1 (c) potentiodynamic curves obtained for the Al-15wt.%Cu alloy are shown. In the case of the C zone is observed that the pitting of the material does not start immediately after reaching the corrosion potential, equal to -726 mV, since there is a potential range in which the current remains roughly constant. In contrast, E and CET zones have noblest Ec, dissolve rapidly after reaching their respective corrosion potentials.

Table 1 shows the corrosion potentials for the three alloys 1M NaCl solution, also presenting the potential measured in 0.5M NaCl solution [6]. In assessing the relationship between the content of copper in the alloys and corrosion potential, Ec, we found that the lowest values were for the alloy with lower copper content, i.e, Al-1wt.%Cu. However, the alloy showed in general a range of potential above of Ec, where the material is not pitted. In contrast, in the alloys of high copper, pitting starts immediately after reaching the corrosion potential of the material. Considering the behavior of Al-1wt.%Cu in two solutions, slightly more noble potential to work in the less dilute solution are evident, but the differences between them are very small.

Evaluating the results of potentiodynamic 1M NaCl solution, depending on the different zones was found that the greatest Ec for columnar region showed the alloy with 4.5wt.%Cu. For CET and E zones shows that the corrosion potential in both solutions increases with increasing copper content in the alloy.

No significant differences between the corrosion potentials of the alloys in the two solutions were found. However there may be a higher susceptibility of the material to be corroded in the more concentrated solution, since there is a tendency to dissolve the samples in the 1M NaCl solution is observed, decreasing or simply disappearing ranges of passivation observed in potentiodynamic curves obtained above in 0.5 M NaCl solution [6].

Microscopic observation of the samples tested in 1M NaCl solution shown in Figure 2 denotes that the most affected zones by localized corrosion match dendritic areas. The same trend was noted in previous work working in 0.5M NaCl solution [6,15]. This may indicate that the presence of Al_2Cu intermetallic in interdendritic zones would favor the dissolution of the metal matrix. The above is consistent with what the literature reported for the same system [1-3, 5, 6, 9].

Electrochemical Impedance Spectroscopy (EIS) is used to explain the behavior of the electrolyte/solution interfaces, and generally the data are adjusted to an equivalent circuit models for interpretation.

Impedance responses obtained for the three alloys in 1M NaCl solution were simulated using the equivalent circuits shown in Figure 3. The test results of EIS in 1M NaCl solution are shown in the diagrams of Figure 4. In the Bode plots three different regions can be observed: the low frequency zone, until values of 10^{-1} Hz represents the polarization resistance of the alloys studied. For Al-1wt.%Cu (Figure 4 (a)) can be seen that its increases from the base of the cylinder in the direction of heat extraction (that is, from the area of columnar grains to the area of equiaxed grains).

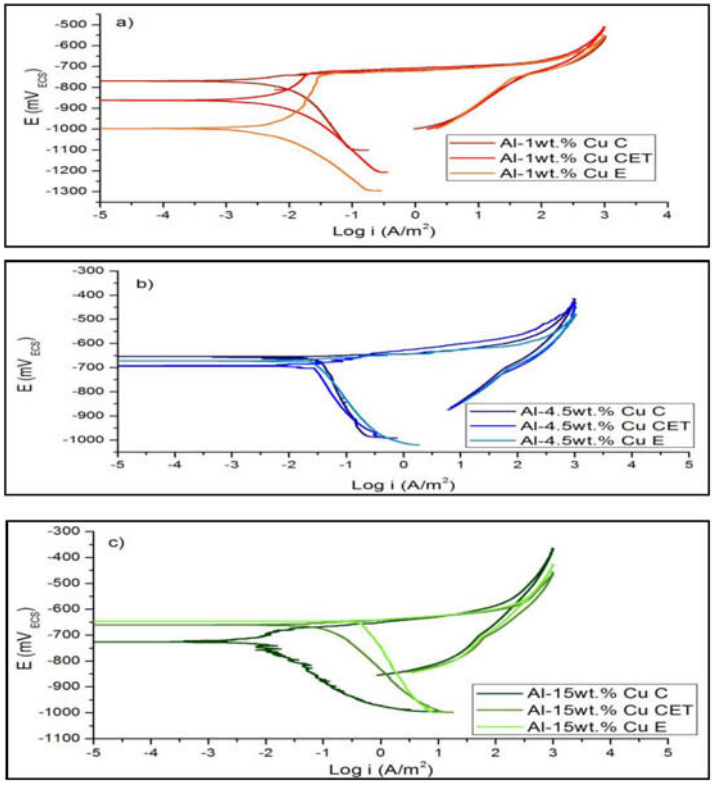

Figure 1. Cyclic potentiodynamic polarization curves in 1M NaCl solution.

Table 1. Corrosion potentials (in mV) of samples in NaCl solutions.

	Al-1wt.% Cu		Al-4.5wt.% Cu		Al-15wt.% Cu	
	1M	0.5M	1M	0.5M	1M	0.5M
C	-829	-820	-657	-645	-726	-756
CET	-862	-833	-691	-744	-760	-639
E	-998	-854	-673	-707	-646	-793

Instead, for Al-4.5wt.%Cu (Figure 4 (b)), the resistance decreases from C zone to the E zone. In the case of Al-15wt.%Cu, (Figure 4 (c)) the C zone has the highest resistance value. In the Bode diagrams which describing angles of phase, for intermediate values of frequency, i.e. 10^0 and 10^4, two capacitive contributions can be observed for all samples tested, except for the equiaxed zone of Al-1wt.%Cu, which evidence a single capacitive contribution (Figure 4 (a)). For values of frequencies higher than 10^4 impedance modules of alloys studied alloys tend to behave similarly in all cases, representing the resistance of the electrolyte.

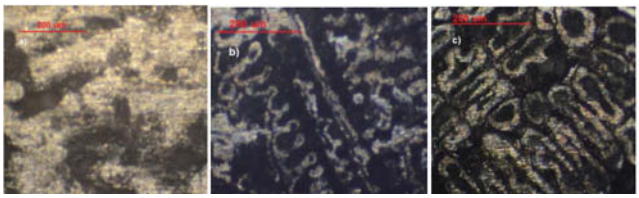

Figure 2. Micrographs of columnar zones: a) Al-1wt.%Cu; Al-4.5wt.%Cu; Al-15wt.%Cu.

In Table 2 the model for each of the three zones is indicated each of the alloys. Such circuits have been proposed by other authors for pure aluminum and aluminium-base alloys in different solutions [5, 12, 18]. The physical meaning of the elements of the proposed equivalent circuits has been reported in the literature [5,12, 18,19]. R_Ω corresponds to the resistance of the electrolyte, R_1 and R_2 are the resistances of the porous layer and the barrier layer, respectively, which are associated with the charge transfer resistance through the porous layer and the involvement of intermediate adsorbed. CPE_1 and CPE_2 are the constant phase elements attributed to the porous layer and the barrier layer, respectively [18,20].

As expected, the values of R_Ω are higher than those obtained on the experience of more dilute solutions of NaCl, [6] due to the higher concentration of Cl^- ions.

R_1 values are markedly higher than the values of R_2, indicating that the corrosion protection is primarily provided by the outer barrier layer [18]. This relationship is consistent with the results observed in the work done in 0.5M NaCl solution and with the values shown in several studies of EIS of aluminum and its alloys [6, 12, 18-20].

Nyquist plots obtained for the three alloys are shown in Figure 5. The equiaxed zone of Al-15wt.%Cu alloy (Figure 5 (c)) has an inductive arc at low frequencies. According to the provisions of the literature the occurrence of these bonds can be attributed to adsorption - desorption of species [14, 20-22] or the dissolution of a uniform layer due to the existence of a process of pitting corrosion [12, 13, 20].

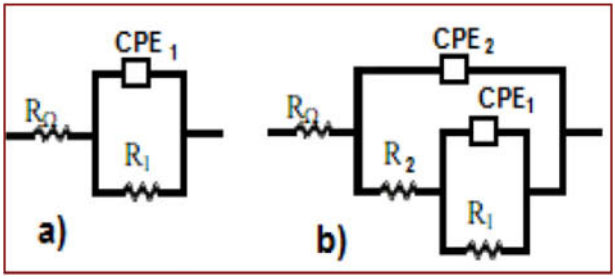

Figure 3. Equivalent circuits for fitting the experimental data.

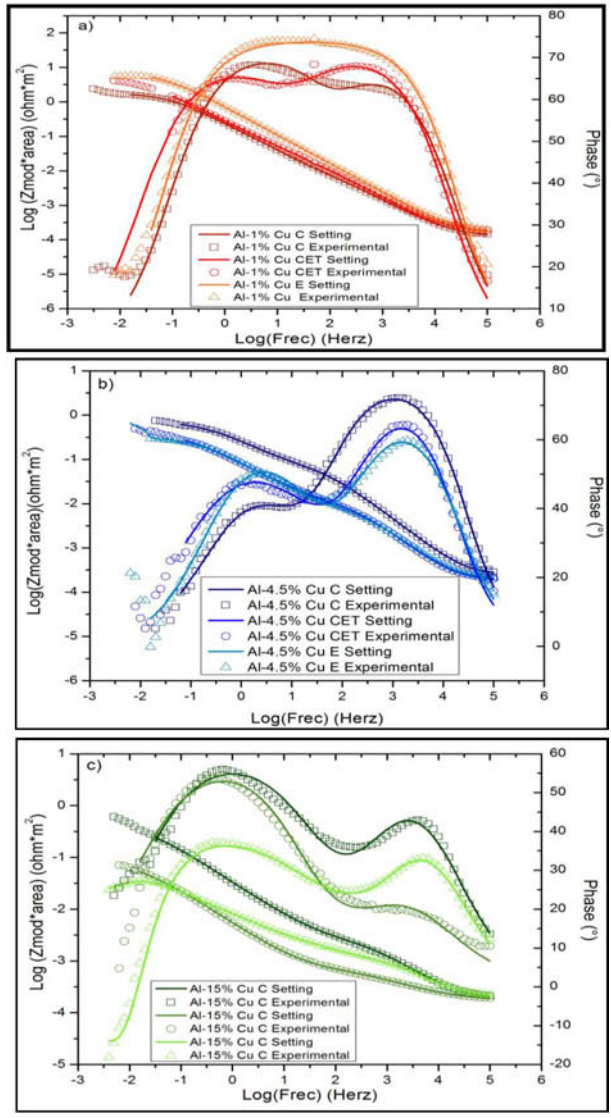

Figure 4. Bode diagrams in 1M NaCl. a) Al-1wt.%Cu; b) Al-4.5wt.%Cu; c) Al-15wt.%Cu.

Table 2. Parameters of impedance adjustment.

	Zone	R_Ω ($\Omega*m^2$)	CPE_1 ($\Omega^{-1}m^{-2}$)	n_1	R_1 ($\Omega*m^2$)	R_2 ($\Omega*m^2$)	CPE_2 ($\Omega^{-1}m^{-2}$)	n_2	Circuit
	C	1.22E-04	0.20	0.84	1.79E00	2.46E-02	0.73	0.78	Figure (b)
Al-1wt.%Cu	CET	1.68 E-04	0.34	0.73	4.90E00	1.01E-01	0.54	0.80	Figure (b)
	E	1.69 E-04	0.30	0.82	6.97E00	-	-	-	Figure (a)
	C	2.49 E-04	1.04	0.66	6.93E-01	7.29E-02	0.11	0.87	Figure (b)
Al-4.5wt.%Cu	CET	1.84 E-04	3.44	0.64	1.13E-02	4.77E-01	0.28	0.85	Figure (b)
	E	1.88 E-04	2.56	0.71	3.08E-01	1.12E-02	0.41	0.81	Figure (b)
	C	1.74 E-04	7.40	0.67	5.37E-01	2.88E00	1.33	0.67	Figure (b)
Al-15wt.%Cu	CET	1.69 E-04	40.00	0.69	9.97E-02	6.16E-04	14.97	0.58	Figure (b)
	E	1.59 E-04	32.62	0.60	2.84E-02	1.83E-03	5.38	0.60	Figure (b)

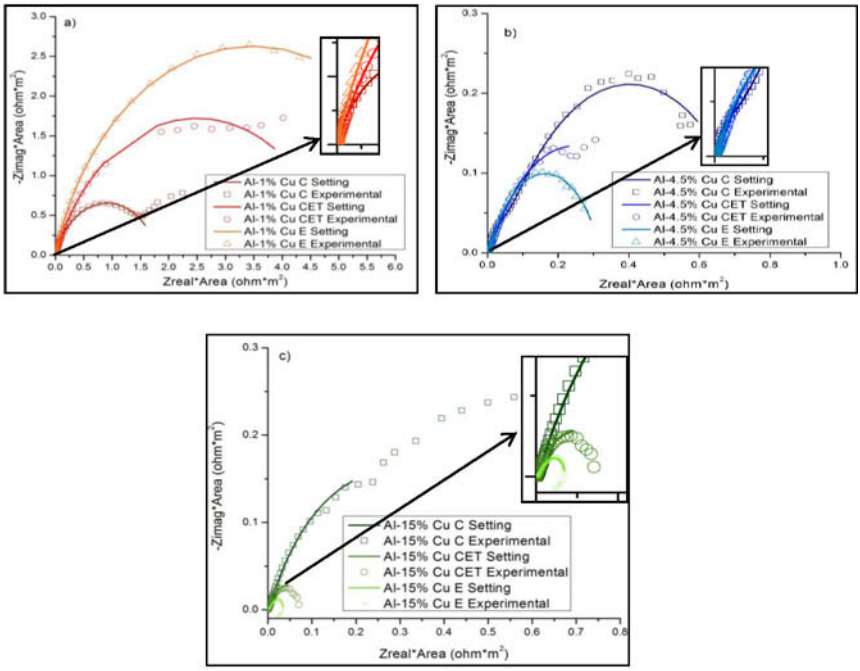

Figure 5. Nyquist diagrams: a) Al-1wt.%Cu; b) Al-4.5wt.%Cu; c) Al-15wt.%Cu.

Conclusions

The evaluation of electrochemical parameters not indicates a relationship between the structure of the alloy and corrosion resistance. However, the microscopic observations demonstrate that, copper-rich interdendritic region acts a as cathode promoting the dissolution of the metal matrix consisting mainly of aluminum.

The values of resistance in the circuit adjustment electrochemical impedance spectra allow concluding that Al-Cu alloys have good corrosion resistance, being the noblest, the alloys with lower copper content. In evaluating the corrosion behavior of the alloys in the two solutions with two different concentrations of NaCl, it was found that while both the materials respond very similarly means a greater susceptibility to corrosion is observed in solution of NaCl.more concentrated

EIS studies indicate that, in general, the behavior of the Al-Cu alloys in 1M NaCl solution can be described from the presence of two capacitive contributions.

Acknowledgements

Thanks are due to the Argentinean Research Council (CONICET) for the financial support.

References

[1] A. E. Ares, L. M. Gassa, C. M. Méndez, Carlos E. Schvezov, 11° Congreso Binacional de Metalrugia y Materiales SAM/CONAMET, Rosario, Argentina, 2011, Anales editados en la página web: http://www.ifirconicet.gov.ar/SAM-CONAMET2011/documentos/topico6/224-927-1-SP.pdf © 2011.

[2] A. S. Román, C. M. Méndez, A. E. Ares, Revista ANALES AFA – PUBLICACION DE LA ASOCIACION FISICA ARGENTINA 25 (2013).

[3] A. E. Ares, L. M. Gassa, C. E. Schvezov, S. F. Gueijman, en Shape Casting: The 4° International Symposium, Murat Tiryakioglu, John Campbell and Paul Crepeau (Eds.), Relationship Between Structure and Properties of Al-Cu Alloys (pp.207-214), (2011).

[4] R. Vera, R. Schrebler, G. Layana, F. Orellana, A. Olguín, Rev. Metalurgica Madrid, 34 (1998).

[5] W. R. Osorio, L. C. Peixoto, L. R. Garcia, A. Garcia, Acta Metallurgica Sinica (English Letters) 22 (2009) 4.

[6] A. S. Román, C. M. Méndez, A. E. Ares SAM/CONAMET, Puerto Iguazú, Argentina, 2013.

[7] W.R. Osorio, J.E. Spinelli, I.L. Ferreira, A. Garcia, ElectrochimicaActa, 52 (2007).

[8] J. Campbell, Complete Casting Handbook, Elsevier Ltd. (2011).

[9] A.E. Ares, S.F. Gueijman, C.E. Schvezov, Journal of Crystal Growth, 312 (2010).

[10] W.R. Osório, J.E. Spinelli, I.L. Ferreira, A. Garcia, Materials Science and Technology 24 (2008).

[11] Z. Szklarska-Smialowska, Corrosion Science 41 (1999).

[12] A. Aballe, M. Bethencourr, RJ. Botana, M. Marcos, J. Pérez-Mariscad, M.A. Rodríguez-Chacón, Rev. Metalurgica Madrid 34 (1998).

[13] L. Chen, N. Myung, P.T.A. Sumodjo, K. Nobe, Electrochimica Acta 44 (1999).

[14] A. Banu, M. Marcu, O. Radovici, C. Pirvu, M. Vasilescu, Revue Roumaine de Chimie 51 (2006) 3.

[15] A. S. Román, C. M. Méndez, A. E. Ares, Materials Science Forum 783-786 (2014) 100-107.

[16] S. Rajendran, J. Jeyasundari,P. Usha, J. A. Selvi, B. Narayanasamy A. P. P. Regis, P. Rengan, PortugaliaeElectrochimicaActa 27 (2009) 2.

[17] B. A. Boukamp, Equivalent Circuit, University of Twente, (1989).

[18] W. R. Osorio, E. S. Freitas, A. Garcia, Eletrochimica Acta 102 (2013).

[19] R. Orozco-Cruz, R. Galván-Martínez, E. A. Martínez, I. Fernandéz-Gómez, XXV Congreso de la Sociedad Mexicana de Electroquímica, Zacatecas, México (2010) CTS215 693-703

[20] J. C. S. Fernández, M.G.S. Ferreyra, C. M. Rangel, Journal of applied electrochemistry 20 (1990).

[21] K. C. Emregül, A. Abbas Aksüt, Corrosion Science 42 (2000).

[22] J. L. Polo, C. L. Torres, E. Cano, J. M. Bastidas, Revista de Metalurgia 35 (1999).

Characterization of Minerals, Metals, and Materials 2015
Edited by: John S. Carpenter, Chenguang Bai, Juan Pablo Escobedo, Jiann-Yang Hwang, Shadia Ikhmayies, Bowen Li, Jian Li, Sergio Neves Monteiro, Zhiwei Peng, and Mingming Zhang
TMS (The Minerals, Metals & Materials Society), 2015

EVALUATION OF ACID TREATMENT ON BROWN BENTONITE

C.G. Bastos Andrade[1*]; V.F. Justo[1]; C.M. Matos[1]; M.G.S. Valenzuela[1]; C. Volzone[2]; F.R. Valenzuela-Diaz[1]

[1]*Department of Metallurgical and Materials Engineering – EPUSP Escola Politécnica Universidade de São Paulo*
Zip Code 05508-900 – São Paulo - SP - Brazil
[2] *CETMIC Centro de Tecnología de Recursos Minerales y Cerámica, Argentina*

**gianesic@usp.br*

Keywords: clays, acid attack, industrial use

ABSTRACT

For industrial use, the smectite clays are usually treated with inorganic acid of high concentration at temperatures under boiling point, which provide the bentonite´s bleaching power. In the present paper, a sample of brown smectite from Paraiba, Brazil, was submitted to treatment under moderate conditions (90°C, reaction times of 1, 6, 12, 18 and 24hours in close reactor, concentration of the aqueous solution of hydrochloric acid 1.5M, clay/acid solution ratio of 1g/10mL), aiming to reduce impurities, responsible for the color of the clay, without causing significant changes in their structure. The samples were characterized by scanning electron microscopy (SEM), energy dispersive X-ray detector (EDS), stereomicroscopy, Cation Exchange Capacity (CEC), Thermal Analysis (TG/DTA), and X-ray diffraction (XRD). It was observed a bleaching in samples with time of 12h to 18h. With the DRX was possible to monitor the peak intensity of the clay structure and the sample with 12 hours of treatment was not significantly altered its crystalline structure, maintaining the peak clay at $d_{(001)}$. The most pronounced changes in the bleaching occurred within the first 12 hours of acid treatment. Thus, clay can be used in products with high added value.

1 INTRODUCTION

Bentonite is a rock formed in most part by smectite clay mineral originated generally from volcanic ashes, mostly acid after a chemical alteration provided by devitrification. Bentonites are clays formed by smectite mineral clays which are responsible for chemical – technological properties and by accessory minerals usually inert (mica, quartz, and cristobalite) [1,2,3].

Brown bentonite from Bela Vista, Paraiba, Brazil is a smectite clay with non-preponderate interlayer cation, presenting white color provided by high iron concentration [4].

There are two types of bentonites, sodium and calcium. Sodium bentonite presents high base exchange capacity, usually between 80 and 130 meq/100g. Otherwise, calcium bentonite presents a range among 40 and 70 meq/100g. The high charge on the lattice provides to sodium bentonite the capacity to exchange the interlayer water and associated cations with more polar organic molecules [5].

The industrial use for clays is also based on cation exchange capacity and clay minerals properties [6].

For some industrial uses the bentonites must be clean of mineral impurities. Acid attack provides an increase at specific area by disorganizing the crystalline structure, the mesopores formation and cleaning the mineral impurities. Other benefit of acid attack is the improving of acid sites with more porosity, excellent properties when applied in catalysis [7,8].

Among the clays to industrial use, several groups have been studied aiming a preparation of bleaching clays, using acid attack with high concentration and temperatures near boiling point. The industrial application of bentonites is vast. In oil industry, mostly used as drilling fluids additives; in pharmaceutics and cosmetics as dissecant; in the food industry as oil bleaching, among others applications [9-15].

The methodology of purifying clays used in this work with mild acid attack is a good alternative for production of clays with more light colors.

2 MATERIAL AND METHODS

2.1 Start Materials

The brown bentonite clay, in its natural form, was from Lages, Paraíba´s State, Brazil. Brown bentonite, passing sieve 200 mesh, was submitted to mild acid attack using a

concentration of the aqueous solution of hydrochloric acid 1.5M, clay/acid solution ratio of 1g/10mL, at 90°C under bellow boiling temperature and at times of reaction of 1, 6, 12, 18 and 24 hours in close reactor.

After filtered and washed with water until pH 5-6 the clay was dried at 60°C and grounded using a manual mortar and vibratory ball mill until completely pass through #200 mesh sieve.

2.2 Materials Characterization

The starting material was characterized by scanning electron microscopy, EDAX INSPECT 50 with energy dispersive x-ray detector (EDS).

To observe the clay was used a stereomicroscope Zeiss, model Stemi 2000C.

The XRD was performed on diffractometer model X'Pert Pro MPD (Panalytical) with Cu anode; scan from 2° to 90° 2Θ; 40kV and 35mA.

CEC was performed using the ammonium acetate method.

Thermal Analysis (TG/DTA) was performed on nitrogen atmosphere at 10°C/min..

3 RESULTS AND DISCUSSION

Figure 1 shows the X-ray diffraction curves of brown bentonite submitted only to H_2O for 24h at 90°C, we observe the $d_{(001)}$ characteristic smectitic peak at 15,00Å with intensity of 170 counts. As impurity the sample presents quartz with a peak at 3,3Å and an intensity of 720 counts.

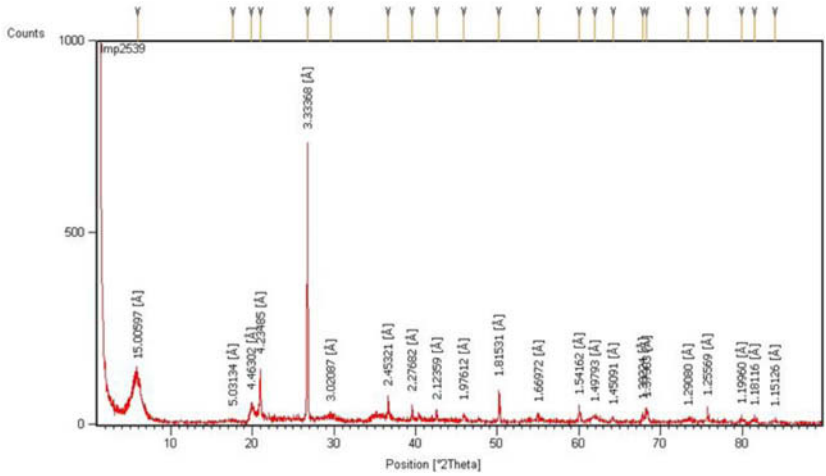

Figure 1 - XRD curve of brown bentonite H_2O 24h at 90°C.

Figure 2 shows the XRD curve of brown bentonite submitted to mild acid attack during 6h at 90°C. The $d_{(001)}$ smectitic peak is present at 14,76Å with an intensity of 140 counts. The quartz, with peak at 3,33Å presents intensity of 750 counts.

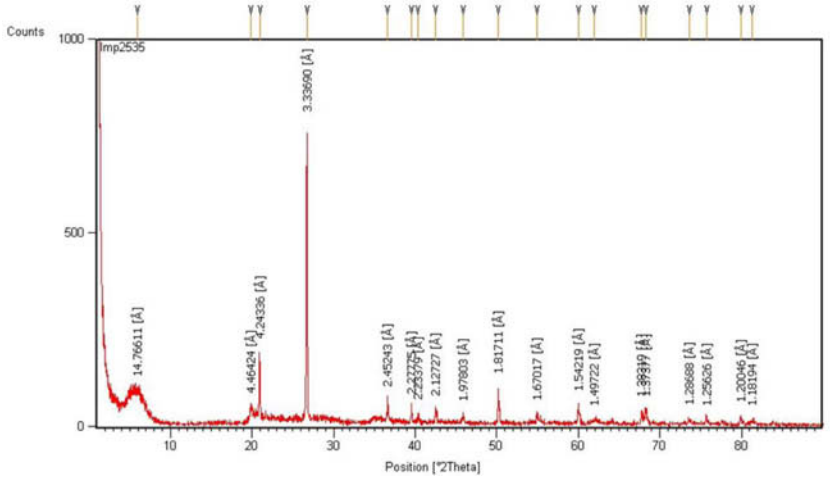

Figure 2 - XRD curve of the Brown bentonite HCl 6h at 90°C.

Table 1 presents the results of $d_{(001)}$ smectitic peaks, smectitic peaks intensities, and intensities of the quartz peaks for the samples of brown bentonite attacked at different times.

Table 1. $d_{(001)}$ smectitic peaks, smectitic peaks intensities, and intensities of the quartz peaks.

Sample	Smectitic peak $d_{(001)}$ (Å)	Smectitic peak intensity (counts)	Quartz peak at 3,33Å intensity (counts)
24h in water	15,00	170	720
1h attack	15,25	140	750
6h attack	14,76	130	750
12h attack	15,28	115	810
18h attack	15,73	95	950
24h attack	16,83	75	915

The sample treated with water only presented a breakdown of the stacking order of layers with the lowest value of peak intensity. The intensity of the smectitic $d_{(001)}$ peak of the acid attack samples tend to diminish its intensity with the time of attack as the acid have more time to destroy the octahedral sheet of the clay mineral. The quartz peak intensity increase with the time of attack, indicating a possible partial dissolution of the clay minerals with the time of acid attack.

The results of energy dispersive X-ray detector (EDS) of brown bentonite are mostly the same, observing in all samples the presence of Si, Al and O.

Figure 3 shows the EDS curves of brown bentonite submitted only to H_2O for 24h at 90°C.

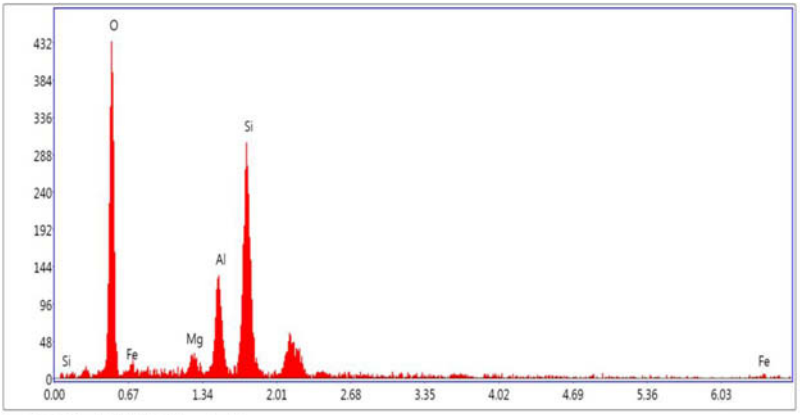

Figure 3 - EDS curve of Brown bentonite H_2O 24h at 90°C.

Figure 4 shows the EDS curves of Brown bentonite submitted to HCl for 6h at 90°C.

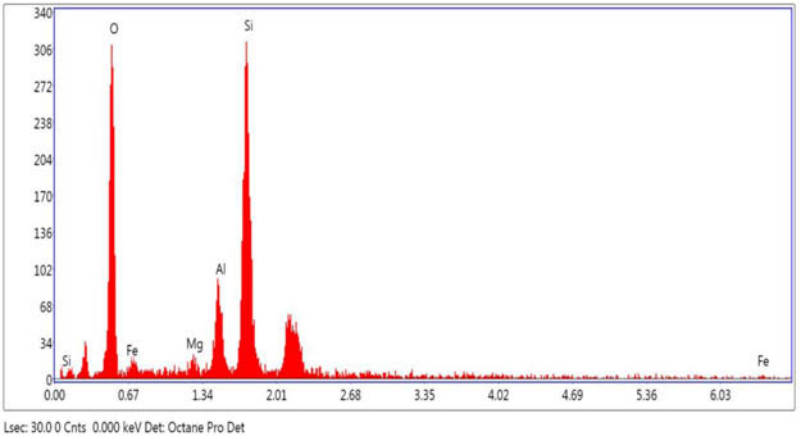

Figure 4 - EDS curve of Brown bentonite HCl 6h at 90°C.

The images generated by scanning electron microscopy produced the figures 6 and 7 were possible to observe in the images of brown bentonite sample submitted to treatment in different times the preservation of the lamellar morphology. The sample

attacked for 18h shows a more open structure with less quantity of small particles, possible dissolved by the acid.

Figures 5 and 6 shows the SEM image of brown bentonite submitted only to H_2O for 24h and submitted to mild acid attack during 18h, both samples at 90°C.

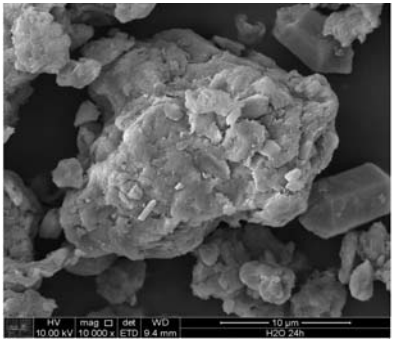

Figure 5 - SEM image of the brown bentonite H_2O 24h at 90°C.

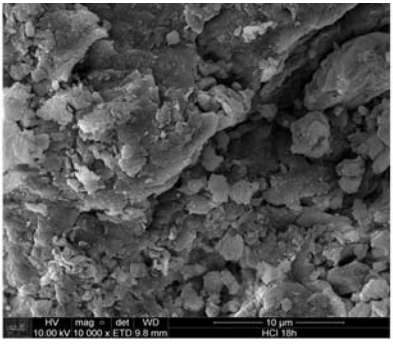

Figure 6 - SEM image of the Brown bentonite HCl 18h at 90°C.

The attacked samples presented an increase in color reduction with time of acid attack. Figure 7 shows a stereomicroscopy image of sample treated with water for 24h. It is possible to observe some impurities in the sample.

Figure 7 - Image of sample - treated with H_2O for 24h. 1cm corresponds to 1.3micron.

Figure 8 - Image of sample - treated HCl 6h at 90°C. 1cm corresponds to 1.3micron.

In Figure 8 is possible to observe a decrease of impurities in the sample submitted to mild attack for 6h. Samples with attack times from 12h to 24h showed a continuous but small decrease of impurities (that is lighter colors) compared with the sample attacked by 6hours.

Figures 9 and 10 shows the TG/DTA curves of samples treated with H_2O and HCl, both treated for 24h at 90°C. Is possible observe a 4% weight loss for the sample treated only with water, that is approximately the hydroxyls' water loss of the bentonites. The sample treated for 24h with HCl does not show that loss indicating an almost destruction of the clay minerals structure.

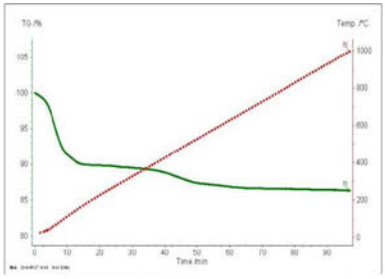

Figure 9 – TG/DTA results of sample treated with H_2O for 24h 90°C.

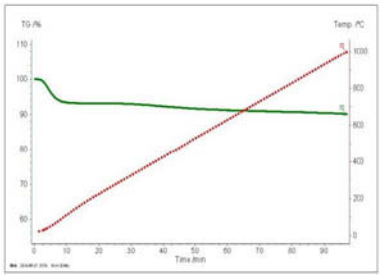

Figure 10 – TG/DTA results of sample treated with HCl for 24h at 90°C.

Table 2 presents the CEC values that, as expected, tend to diminish after treatment, with the time of attack with the 24 hours attacked sample having only 60% of the original value.

Table 2 - CEC results of brown bentonite treated.

Sample	CEC (meq/100g)	% of the no attacked sample
24h in water	62,31	100
1h attack	59,91	96,14
6h attack	57,31	91,97
12h attack	48,63	78,04
18h attack	46,59	75,02
24h attack	38,99	62,57

4 CONCLUSION

The reaction time of treatment is an important factor in purification and decolorizing process.

The crystalline structure of the mineral clay do not presented a significantly destruction otherwise, presented a significant bleaching.

The sample of brown bentonite from Lages submitted to mild acid attack demonstrated a good response to the purification at reaction times of 6 hours.

Thus, the objective to decrease the concentration of impurities that provides color, with no pronounced change in the clay minerals structure, demonstrating an efficient option,

more economical and less aggressive to the environment using the treated clay in products of high value agreed.

REFERENCES

[1]Ross, C.S.; Shannon, E.V. Minerals of bentonite and realted clays and their physical properties. J. American Ceramic Socity, 9 (77) 1926.

[2]Valenzuela-Diaz, F.R. Preparação a nível de laboratório de algumas argilas esmectíticas organofílicas. Tese (Doutorado). Departamento de Engenharia Química da Escola Politécnica da Universidade de São Paulo, SP, 1994.

[3]Abreu, S.F. Recursos minerais do Brasil, Ed. Edgard Blucher, 2ª. Ed., V.1, São Paulo, SP, 324p, 1973.

[4]Valenzuela-Díaz, R.F.; Souza Santos, P.; Souza Santos,H.: A Importância das argilas industriais brasileiras. Química Industrial V.42 p.33-37, 1992.

[5] Murray, H.H. Applied Clay Mineralogy, Elsevier, Develop. in Clay Science 2, p.25 2007.

[6]Grim, R.E. Bentonites, Elsevier Amsterdam, 1978.

[7]Vaccari, A.; Applied Clay Science 14, 1999.

[8]Volzone,C.; López, J.M.; Pereira, E. Activación ácida de un material esmectítico, Revista Latinoamericana de Ingeniería Química y Química Aplicada, v. 16, p. 205-215, 1986.

[9]Souza Santos, P. Ciência e Tecnologia de Argilas, 2a com a colaboração de Soza Santos H., V.3Ed., Edgar Blücher, S. Paulo, SP (1989)vol.1 e 1992 vol.2e3 1ed. Tecnologia das Argilas – vol.2 Edgar Blücher e EDUSP, São Paulo, SP, 1974.

[10]Gomes,C.F.Argilas: o que são e para que servem, 1a Ed., Fundação Calouste Gulbenkian, Lisboa, Portugal Ed., Fundação Calouste Gulbenkian, Lisboa, Portugal (1988) 160.

[11]Ferreira, H.S,; Menezes, R.R; Ferreira, H. S. ; Martins, A. B. ; Neves, G. A. ; Ferreira, H. C.; Cerâmica 54 (2008) 77.

[12]Amorim, L. V. ; Farias, K. V. ; Viana, J. D. ; Barbosa, M. I. R. ; Pereira, E. ; França, K. B.; Lira, H. L.; Ferreira, H. C. Cerâmica 51 (2005) 128.

[13]Dana, J.D.; Manual de Minerologia. Livros Técnicos e Científicos, RJ, 1969.

[14]Pereira, K.R.O.; Hanna, R.A.; Ramos Vianna, M.M.G; Pinto, C.A.; Rodrigues, M.G; Valenzuela-Diaz, F.R. Brasilian organoclays as nanostructure sorbents of petroleum-derived hydrocarbons. Materials Research, v.8, n.1, p.77-80, 2005.

[15]Valenzuela-Diaz, F.R.; Souza Santos, P. Studies on the acid ativation of Brasilian smetetitic clays. Química Nova, v.24, n.3, 2001.

Characterization of Minerals, Metals, and Materials 2015
Edited by: John S. Carpenter, Chenguang Bai, Juan Pablo Escobedo, Jiann-Yang Hwang, Shadia Ikhmayies, Bowen Li, Jian Li, Sergio Neves Monteiro, Zhiwei Peng, and Mingming Zhang
TMS (The Minerals, Metals & Materials Society), 2015

NUMERICAL SIMULATION OF THE COPPER STEEL COMPOSITE STAVE HEAT TRANSFER IN THE BELLY AND LOWER SHAFT REGION OF THE BLAST FURNACE

Qi Liu[1], Shu-sen Cheng[1], Jian-ping Niu[2], Dong-dong Liu[2]

[1]University of Science and Technology Beijing; 30 Xueyuan Road, Haidian District; Beijing, Beijing, 100083, China
[2] Hebei Wanfeng metallurgical spare parts Co., Ltd; Xishan Industrial District; Zhangjiakou, Hebei, 076250, China

Keywords: Blast furnace, thermal test, heat transfer, copper steel composite stave, copper stave

Abstract

A numerical model was developed to simulate the three-dimensional heat transfer in the belly and lower shaft region of the blast furnace wall consisting of copper steel composite stave, packing and shell. The temperature distribution of copper steel composite stave without the slag layer or refractory lining was investigated and then compared with the copper stave. The results showed that copper steel composite stave can satisfy the requirement of overheating-free and had an analogous heat transfer behavior as copper stave but more stable cooling intensity. This model had been validated by the good agreement between the computed and measured temperature in the thermal test.

Introduction

The service life of belly and lower shaft region of blast furnaces is very essential for determining the campaign life of the blast furnaces. A long campaign life avoids blowing out a blast furnace for repairs and refractory relining, thus permitting an extension in production and decrease in capital cost. Actually, refractory linings are not capable of holding molten slag and hot metal for long time under high temperature. Therefore, the campaign life of blast furnace is not determined by the refractory lining but by the cooling apparatus [1, 2, 3, 4].

Now copper stave widely used in the bosh, belly and lower shaft region of the blast furnace due to its high thermal conductivity to prolong the blast furnace campaign life. But copper staves have experienced many problems and early failure, especially the pipe welds failure [5, 6]. On the other hand, damaged pipes were difficult to detect and to repair, and a replacement of a damaged stave from the outside was practically impossible. Due to copper stave failures, the blast furnace campaign life has been cut down to as short as 5 years.

Copper steel composite stave is designed to overcome the pipe welds failure for copper stave, which is made of explosively welded copper/steel composite plate. To gain good heat transfer performance, the copper plate (base plate for explosively welding) is set as the hot-face layer of the stave, and the carbon steel plate is set as the cool-face layer and seamless steel pipe is set as the pipe weld to achieve the high bonding strength. The copper steel composite stave was called a new long-service-life stave used in the belly and lower shaft region of blast furnace.

However, high temperature and its fluctuation inside the staves are one of the important conditions that the stave is destroyed. Understanding the heat transfer in the copper steel composite stave is essential in identifying whether it will be damaged under the blast furnace conditions. In principle, this objective can be achieved by means of the direct measurements of temperature distribution in the copper steel composite stave. Therefore, it is difficult to ascertain the heat transfer process of the copper steel composite stave from the limited

temperature measurements. Consequently, mathematical modeling has played an important role in the quantification of the temperature distribution in copper steel composite stave.

There is a large number of mathematical models describing the heat transfer process of the copper stave. Yeh et al. [7] developed a three-dimensional heat transfer model to predict the temperature field of copper stave with different slag layer thickness. Qian et al. [8] used a 3-dimensional temperature field calculation model to investigate the quantificational indexes for design and evaluation of copper staves. Cheng et al. [9, 11], Wu et al. [10] and Ning et al. [12] carried out extensive research on heat transfer process of the stave by numerical simulation, studied the effect of blast furnace operation parameters and optimized the design parameters of the stave. However, these models only described the steady-state heat transfer process of copper or cast iron stave, but not to satisfactorily describe the complex three-dimensional heat transfer process in the copper steel composite stave. On the other hand, these models were to a large degree concerned with ideal conditions, for example, there was always an accretion layer or refractory lining in front of the stave. Besides, the differences between copper steel composite stave and copper stave on heat transfer behavior was rarely presented.

This paper presents a three-dimensional mathematical model to describe the heat transfer process in blast furnace wall comprised of copper steel composite stave, packing layer and shell. The mathematical model is validated by comparing the measured and calculated temperature distributions of copper steel composite stave in the thermal test stand, and subsequently used to study the differences between copper steel composite stave and copper stave on heat transfer behavior under various operating conditions.

Physical model

The physical model of copper steel composite stave is shown in Figure 1. The physical model (see Figure 1(a)) is usually comprised of copper steel composite stave, packing, shell, whereas their thickness was 80mm, 80mm and 30mm, respectively. The height and width of the physical model is 1420×788mm. The copper steel composite stave is made of copper/steel composite plate which is obtained by explosively welding. Commercial purity copper (T2) and carbon steel (20g) were used to manufacture Cu/Fe composite plate. The thickness of the copper layer and steel layer is 60 and 20mm, respectively. Dovetail grooves (Figure 1(b)) were provided on the hot face of the stave so that they support the refractory lining and slag accretion layer. There are four cooling channel uniform distributed near the copper/steel interface, and the cross-section was comprised of semicircle and rectangle (Figure 1(c)), and the equivalent diameter is 54mm. The pipe welds (inlet/outlet pipes) which connected with cooling channel are made of carbon steel (Q235).

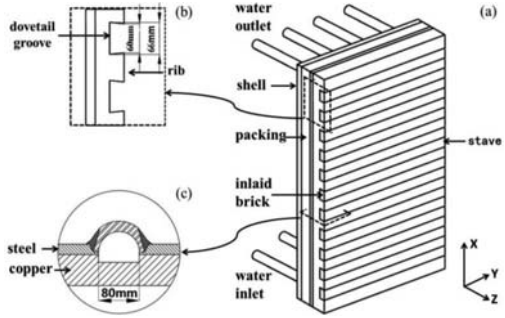

Figure 1. Physical model of copper steel composite stave: (a) physical model; (b) dovetail groove; (c) cross-section of cooling channel

Mathematical model

Governing equation

In this work, The heat transfer in blast furnace wall comprised of copper steel composite stave, packing and shell is modeled under the following assumptions: (1) the heat transfer is unsteady-state conductive heat transfer process without the heat source; (2)there is no refractory lining in the front of this stave; (3) the initial temperature is the temperature distribution of copper steel composite stave with 40mm slag accretion; (4)when the slag accretion disappears, the constant gas flow temperature in periphery direct contacts with the copper steel composite stave. In this case, the heat transfer can be described by the following equation:

$$\rho C_p \frac{\partial T}{\partial t} = \frac{\partial}{\partial x}\left(\lambda(T)\frac{\partial T}{\partial x}\right) + \frac{\partial}{\partial y}\left(\lambda(T)\frac{\partial T}{\partial y}\right) + \frac{\partial}{\partial z}\left(\lambda(T)\frac{\partial T}{\partial z}\right) \tag{1}$$

Where $\lambda(T)$ is the thermal conductivity, W/(m·℃); T is body temperature, ℃; ρ is the density of the materials, kg/m^3; C_p is specific heat at constant pressure, J/(kg·℃); t is the time, s.

Boundary condition

(1) The heat transfer between the copper steel composite stave and gas flow near the blast furnace wall (boundary b1) is the total heat transfer comprised of convection and radiation, which can be described as follow:

$$\lambda(T)\frac{\partial T}{\partial N}\Big|_{b1} = (\alpha_C + \alpha_R)(T_f - T) = \alpha_f (T_f - T) \tag{2}$$

where α_f is the sum of the convective and radiative heat transfer coefficient, $\alpha_f = \alpha_C + \alpha_R$, W/(m^2·℃); α_C is the convective heat transfer coefficient, W/(m^2·℃); α_R is the radiative heat transfer coefficient, W/(m^2·℃); T_f is the gas temperature, ℃; $\partial T / \partial N$ is temperature gradient in normal direction on boundary, ℃/m.

(2) The heat transfer between cooling water and the stave (boundary b2) is convection, namely, the third boundary condition, can be given as following:

$$\lambda(T)\frac{\partial T}{\partial N}\Big|_{b2} = \alpha_w (T - T_w) \tag{3}$$

where T_w is the average temperature of cooling water, ℃; α_w is the convective coefficient between cooling water and stave body, W/(m^2·℃); the convective coefficient α_w is dependent on the flow rate of cooling water velocity v for a given blast furnace, according to Titus-Boelt formula, the convective heat transfer coefficient is:

$$\alpha_w = \frac{\lambda_w}{d_e} Nu_f, \quad Nu_f = 0.023 Re_f^{0.8} Pr^{0.4}, \quad Re_f = \frac{v d_e \mu}{\rho_w} \tag{4}$$

where Re_f is the reynolds number, μ is the viscosity of cooling water, kg/(m·s); Nu_f is the *Nusselt number*; Pr is the *Prandtl number*; λ_w is the thermal conductivity of cooling water, W/(m • ℃); ρ_w is the density of the cooling water, kg/m^3; d_e is the equivalent diameter.

(3) The heat transfer between the shell and environment (boundary b3) is the total heat transfer process comprised of convection and radiation, which can be described as follow:

$$\lambda(T)\frac{\partial T}{\partial N}\Big|_{b3}=\alpha_a(T-T_a) \tag{5}$$

where T_a is the environment temperature, ℃; α_a is the total heat transfer coefficient which is the sum of the convective and radiative heat transfer coefficient, W/(m^2·℃); the total heat transfer coefficient is given as follow [13]:

$$\alpha_a=9.3+0.058T_s \tag{6}$$

where T_s is the surface temperature of the shell, ℃.

(4) The others surface (boundary b4) is adiabatic boundary,

$$\frac{\partial T}{\partial N}\Big|_{b4}=0 \tag{7}$$

Physical property

The physical parameters used in the numerical simulation are listed in Table 1.

Table I. Thermal conductivities of different materials used in the model [14] (W/(m•℃))

Temperature/℃	Pure copper	Carbon steel	Inlaid brick	Packing
17	400	52		
20				0.35
100	380			
300	365			
400			1.45	
700			1.50	
1100			1.65	

Results and discussion

Temperature and heat flux distribution

Figure 2 shows the temperature distribution through the copper steel composite stave thickness. The gas temperature is 1200℃, the cooling water velocity is 2.0m/s, and the time t after the slag accretion loss is 500s. It can be seen that: 1) the temperature increases along the thickness direction (Z direction) from the cool face to hot face and reaches a maximum temperature 127℃ at the working surface of copper steel composite stave; 2) the temperature distribution closed to the cooling channel in the copper steel composite stave is significantly non-uniform; and 3) the temperature of the steel layer near the cool face is very low, especially in the regions of cooling channel, almost equal to the cooling water temperature. It can also be seen that the temperature of the working surface of the copper steel composite stave in front of the cooling channel is almost equal to other positions, suggesting that the uniform temperature distribution along the circumference of the blast furnace wall.

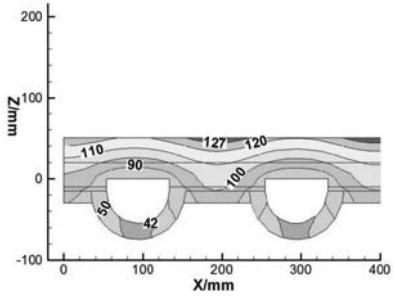

Figure 2. Temperature distribution through the copper steel composite stave thickness

Figure 3 shows the heat flux distribution through the copper steel composite stave thickness. It can be observed that the heat flux decreases along the thickness direction from the hot face to cool face and reachs a zero in the area behind the cooling channle, suggesting that the cross-section area of cooling channel should be reduced in order to save water. Comparison of the heat flux in the copper and steel layer suggesting that exceeding 90% of heat flux through the copper layer and entering the cooling channel, and the heat flux entering into the steel layer is very little, resulting in the temperature of steel layer is lower than the copper layer. Consequently, the design that the cooling channel is machining between the copper and steel layer would achieve a lower temperature near the copper/steel interface.

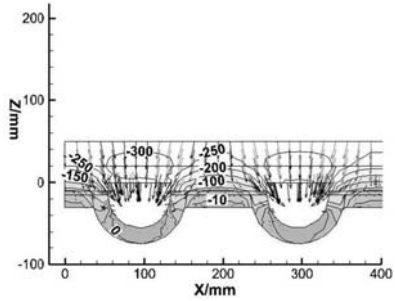

Figure 3. Heat flux distribution through the copper steel composite stave thickness

Figure 4 shows the temperature distribution through the copper stave thickness. The heat transfer boundary condition of copper stave is identical with copper steel composite stave. It can be observed that the isothermal between the cooling channel and hot face is almost straight line, suggesting that temperature distribution through the copper stave width is uniform. It can also be seen that the temperature increases from cool face to hot face and reachs a maximum temperature 120℃ at the working surface of copper stave.

Comparison of Figure 2 and Figure 4 shows that the maximum temperature of copper steel composite stave is about 7℃ higher than that of copper stave and the minimum temperature at the cool face of copper steel composite stave is nearly equal to that of copper stave, suggesting that copper steel composite stave has an approximated heat transfer performance as copper stave.

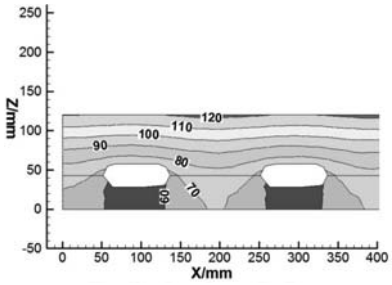

Figure 4. Temperature distribution through the copper stave thickness

Figure 5 shows the heat flux distribution through the copper stave thickness. In copper stave, the maximum heat flux is about -260W/m^2 and 40 W/m^2 lower than that of copper steel composite stave. The heat flux of copper steel composite stave is always higher than copper stave under the same gas temperature and cooling water velocity. It can be seen that the heat flux in the region between cooling channel and cool face is lower than other region, which has the similar heat flux distribution as copper steel composite stave.

Comparison of Figure 3 and Figure 5 reveals a basic difference between copper steel composite stave and copper stave. In the copper steel composite stave, the heat fluxes entering at the edges is deflected at a 45° angle in the direction of the cooling channel. In the copper stave, the heat fluxes are relatively smoothly deflected in the direction of the cooling channels, with larger amount entering the cooling channels from behind. On the other hand, the heat flux distribution in the copper steel composite stave and copper stave, with the lowest in the area behind the cooling channel, caused the lower temperature in the region between cooling channel and cool face. We can conclude that the steel layer has a little influence on the heat transfer performance of copper steel composite stave, suggesting that the design that steel instead of pure copper between cooling channel and cool face in copper stave is reasonable.

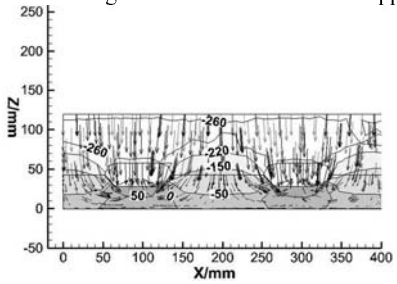

Figure 5. Heat flux distribution through the copper stave thickness

Effect of gas temperature

Figure 6 shows the temperature distribution of the copper steel composite stave in thickness as a function of gas temperature. In blast furnace, thermal load corresponding to gas temperatures between 1200 and 1600℃ and water velocity 2.0m/s were applied. It can be seen that: 1) the temperature increases from the cool face to hot face at the same gas temperature, but the temperature gradient between cool face and copper/steel interface is smaller than that between hot face and copper/steel interface; 2) Increasing the gas temperature by 100℃ would increase the temperature of copper steel composite stave and the temperature differences is almost identical for different distance from cool face; 3) As the gas temperature increases to 1600℃, the temperature near the copper/steel interface is also lower than 150℃. This is because of most of the heat flux entering into the cooling channel as

shows in Figure 3 In common case, if the temperature on the working surface of a copper stave is about 100℃, the molten slag in the blast furnace is easier to be stuck on its working surface [9]. The frozen slag with a low thermal conductivity (about 2W/(m·℃)) will avoid the excessive heat loss. From this point of view, the copper steel composite stave is suitable for using on the wet area of blast furnace.

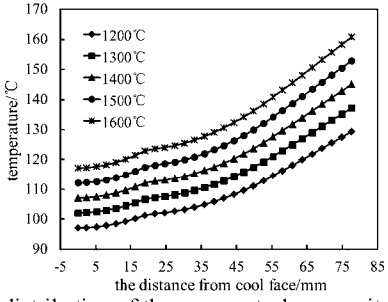

Figure 6. Temperature distribution of the copper steel composite stave in thickness as a function of gas temperature

Figure 7 shows the influence of gas temperature on the maximum hot-face temperature of the bare copper steel composite stave and copper stave. It can be seen that the maximum temperature of copper steel composite stave increases from 169℃ to 229℃ when the gas temperature increases from 1100℃ to 1600℃, corresponding to that of copper stave increases from 159℃ to 202℃. It shows that the maximum temperature of copper steel composite stave is only about 10 to 28℃ higher than that of copper stave, suggesting that copper steel composite stave has the same heat transfer performance as copper stave. As the gas temperature increases to 1600℃, the temperature on the working surface of copper steel composite stave can still keep below 250℃ which is the critical temperature of destruction of pure copper [15], suggesting that copper steel composite stave can satisfy the requirement of overheating-free and can be applied to the belly and lower shaft of the blast furnace.

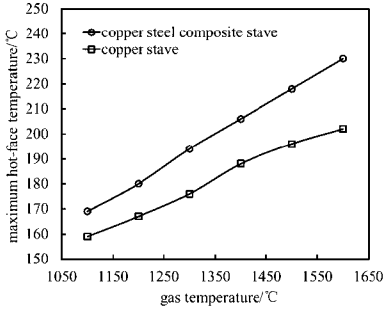

Figure 7. Influence of gas temperature on the maximum hot-face temperature of the bare copper steel composite stave and copper stave

Effect of cooling intensity

The hot-face temperature distribution of copper steel composite stave and copper stave in width wihout cooling water supply is shown in Figure 8. As shown in Figure 8, it can be seen that the hot-face temperature of copper steel composite stave and copper stave without cooling water supply is about 1157～1164℃ and 1147～1154℃, respectively. It shows that

the temperature on the working surface of copper steel composite stave and copper stave without cooling water supply is much higher than 250℃, suggesting that copper steel composite stave and copper stave is easy to be damaged when the cooling intensity is zero. Consequently, it is very important to insure that copper steel composite stave and copper stave have enough cooling intensity. But copper staves have frequently experienced the pipe welds failure as a result of the deformation of the stave. Therefore, it is not necessary to worry about the pipe welds failure of copper steel composite stave because of the satisfactory bonding strength and weld ability between the pipe welds which is made of high-strength steel and the steel layer. Even though the pipe welds will crack under some extreme circumstances, it is easy to be repaired. Thus copper steel composite stave can maintain more stable cooling intensity than copper stave.

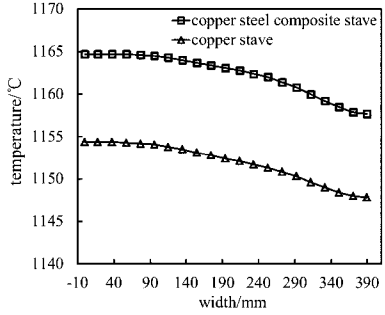

Figure 8. The hot-face temperature distribution of copper steel composite stave and copper stave in width wihout cooling water supply

Transient temperature distribution

Figure 9 shows the temperature history of copper steel composite stave after the accretion loss with an assumed gas temperature 1200℃. Figure 10 is the same for a conventional copper stave. As shown in Figure 9, the temperature on the hot-face and copper/steel interface point increase after the accretion loss, but the temperature of cooling channel and cool face point is almost constant. However, for the copper stave, the temperature on the hot-face, cool-face and cooling channel point increase after the accretion loss. This is probably the result of the higher thermal resistance of the steel layer with respect to the pure copper. Comparison of Figure 9 and Figure 10 suggests that the differences between the two curves of the hot-face point are remarkably small. Both types reach their steady state temperature after approximately 300s (5min). From this point of view, we can conclude that copper steel composite stave and copper stave have an analogous behavior when it comes to the re-formation of accretions.

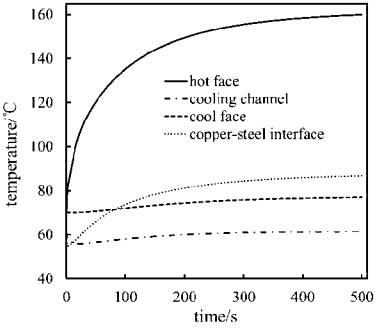

Figure 9. Temperature history of copper steel composite stave after the accretion loss

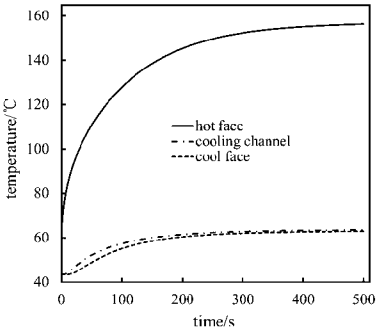

Figure 10. Temperature history of copper stave after the accretion loss

Thermal test

To examine the validity of the mathematical model, the thermal test of copper steel composite stave has been carried out in a thermal test stand. Figure 11 shows a schematic diagram of a thermal test stand of copper steel composite stave. The thermal test stand is comprised of furnace, copper steel composite stave, temperature detecting system, cooling water recirculation system, data collection system.

In the furnace, high temperature gas is produced by combustion of coke with ambient air which is injected into the furnace by air blower, and the gas temperatures between 800℃ and 1200℃ were applied. Copper steel composite stave was installed at the furnace top, whereas its hot surface is set as the inner surface of the furnace. The temperature distribution of copper steel composite stave in experiment was detected by a large number of thermocouples which inserted into the stave for difference planes. Cooling water recirculation system is used to supply the cooling water and keep the cooling intensity of the stave. Data collection system is used to store all the temperature, flow rate information in the whole experimental process.

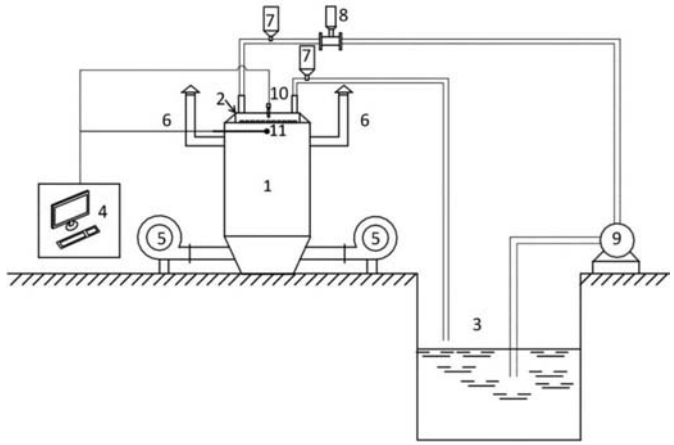

Figure 11. Schematic diagram of a thermal test stand of copper steel composite stave: 1 — furnace; 2 — copper steel composite stave; 3 — pond; 4 — data collection system; 5 — air blower; 6 — chimney; 7 — wireless digital temperature sensor; 8 — wireless digital flowrate sensor; 9 — pump; 10 — K-type thermocouples; 11 — platinum-rhodium platinum thermocouple

Validation of mathematical model

According to the method of data processing which was presented by L. Shi [14], we obtained the boundary conditions which are used to calculate the temperature distribution of copper steel composite stave in the experimental process. Figure 12 shows the results, where the actual temperature were measured by inserting thermocouples and the calculated temperature were simulated by mathematical model in the experimental process. It can be seen that the difference between measured and calculated temperature is about 0℃～2℃, and the relative deviation is approximately 0%～2.47%. The good agreement between the measured and calculated temperature suggests that the model can be used to investigate the heat transfer behavior of the staves in blast furnace.

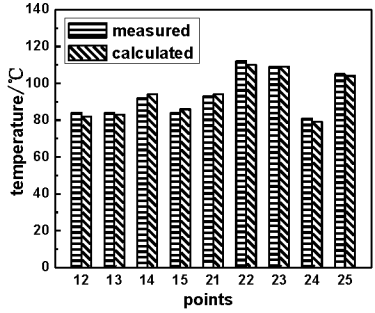

Figure 12. Measured and calculated temperature of copper steel composite stave when the furnace temperature is 1200℃

Conclusions

(1) A three-dimension mathematical model was established to investigate temperature distribution of copper steel composite stave. The model was validated by comparing its results with the measured temperature distribution of copper steel composite stave in a laboratory thermal test.

(2) The maximum temperature of copper steel composite stave is about 7℃ higher than that of copper stave and the minimum temperature at the cool face of copper steel composite stave is nearly equal to that of copper stave, suggesting that copper steel composite stave has the approximated heat transfer performance as copper stave.

(3) The hot-face temperature of copper steel composite stave is almost equal to that of copper stave, and there is a little amount of heat entering into the region between cool face and cooling channel, suggesting that this region has a little influence on the temperature distribution of the stave and the design that steel instead of pure copper between cooling channel and cool face in copper stave is reasonable.

(4) Increasing the gas temperature will increase the temperature of copper steel composite stave. Maximum temperature of copper steel composite stave was lower than the critical temperature of copper, i.e., 250℃ when gas temperature was increased to 1600℃. This is an indication that the copper steel composite stave can satisfy the requirement of overheating-free and can be qualified to be used at the belly and lower shaft region of blast furnaces.

(5) If the cooling water supply is lost, the hot-face temperature of copper steel composite stave and copper stave will exceed the critical temperature of destruction of pure copper. As a result, it is very important to maintain a stable cooling intensity.

(6) The temperature on the hot-face point of copper steel composite stave and copper stave increase after the accretion loss, and the differences between the two curves are

remarkably small. Copper steel composite stave reach their steady state temperature after approximately 300s which is almost equal to copper stave, suggesting that copper steel composite stave and copper stave have an analogous behavior when it comes to the re-formation of accretions.

(7) Copper steel composite stave has the same heat transfer behavior as copper stave, but more stable cooling intensity than copper stave. Consequently, copper steel composite stave is more suitable than copper stave for installing in the belly and lower shaft region of the blast furnace.

References

1. N. Q. Xie et al., "Analysis of Effect of Gas Temperature on Cooling Stave of Blast Furnace", *Journal of Iron and Steel Research*, 17(1) (2010), 1-6.
2. X. J. Ning et al., "Analysis of Temperature, Stress, and Displacement Distributions of Staves for a Blast Furnace", *International Journal of Minerals, Metallurgy and Materials*, 16(5) (2009), 512-516.
3. G. X. Wang et al., "Three-dimensional Modelling of the Wall Heat Transfer in the Lower Stack Region of a Blast Furnace", *ISIJ International*, 37(5) (1997), 441-448.
4. L. J. Wu et al., "Heat Transfer Analysis of Blast Furnace Stave", *International Journal of Heat and Mass Transfer*, 51(11-12) (2008), 2824-2833.
5. L. Shi et al., "Thermal Distortion of Blast Furnace Copper Staves", *The Chinese Journal of Nonferrous Metals*, 15(12) (2005), 2040-2046.
6. Y. W. Huan et al., "Thermo-Mechanical Coupling Finite Element Analysis of Blast Furnace Copper Staves", *Metallurgical Equipment*, 3 (2009), 45-60.
7. C. P. Yeh et al., "Conjugate Heat Transfer Analysis of Copper Staves and Sensor Bars in a Blast Furnace for Various Refractory Lining Thickness", *International Communications in Heat and Mass Transfer*, 39(1) (2011), 1-8.
8. L. Qian et al., "Quantificational Indexes for Design and Evaluation of Copper Staves for Blast Furnaces", *Journal of University of Science and Technology Beijing*, 15(1) (2008), 10-16.
9. S. S. Cheng et al., "Optimum Design and Layout of the Cooling Apparatus for Long Campaign-ship Blast Furnace", *Journal of University of Science and Technology Beijing*, 10(4) (2003), 24-28.
10. T. Wu et al., "Model of Forming-Accretion on Blast Furnace Copper Stave and Industrial Application", *Journal of Iron and Steel Research*, 19(7) (2012), 1-5.
11. S. S. Cheng et al., "Monitoring Method for Blast Furnace Wall With Copper Staves", *Journal of Iron and Steel Research International*, 14(7) (2007), 1-5.
12. X. J. Ning et al., "Thermal State Experiment and Analysis of Thin Copper Cooling Stave", *Journal of University of Science and Technology Beijing*, 9(2) (2007), 126-129.
13. J. C. Zheng et al., "Thermal Test and Numerical Simulation of the Temperature Field of a Blast Furnace Copper Stave", *Journal of University of Science and Technology Beijing*, 30(8) (2008), 938-941.
14. L. SHI et al., "Study on Cast Copper Stave and Cast Iron Stave of Long Campaign Blast Furnace", (Ph.D. thesis, University of Science and Technology Beijing, 2006), 21-156.
15. Zhongyong Xiang, Xiaoliu Wang, *Blast Furnace Design-Design Theory and Practice for Blast Furnace Ironmaking Process* (Bei Jing, BJ: Metallurgical Industry Press, 2007), 373.

Characterization of Minerals, Metals, and Materials 2015
Edited by: John S. Carpenter, Chenguang Bai, Juan Pablo Escobedo, Jiann-Yang Hwang, Shadia Ikhmayies, Bowen Li, Jian Li, Sergio Neves Monteiro, Zhiwei Peng, and Mingming Zhang
TMS (The Minerals, Metals & Materials Society), 2015

EFFECT OF APPLIED PRESSURE ON THE TRIBOLOGICAL BEHAVIOUR OF DUAL PARTICLE SIZE RUTILE REINFORCED LM13 ALLOY COMPOSITE

Rama Arora[1], Suresh Kumar[2], Gurmel Singh[1] and O.P. Pandey[2]

[1]Department of Physics, Punjabi University, Patiala, India
[2]School of Physics and Materials Science, Thapar University, Patiala, India

Keywords: DPS, Aluminium,Rutile

Abstract

The tribological behavior of Dual Particles Size (DPS) rutile reinforced LM13 alloy composite was investigated under varying applied pressure from 125 kPa to 625 kPa at a constant sliding speed of 1.6 m/s. In the present studies, 15 wt.% of rutile particles of different sizes (50-75 μm and 106-125 μm) are reinforced in the Al-12Si alloy (LM13) by liquid metallurgy route. Micro-hardness of the prepared samples was measured in different phases. Microstructure, wear mechanism and surface morphology of the wear surfaces and debris was observed under optical and scanning electron microscope. The change in wear behavior has been explained with reference to the observed EDS analysis of the wear track and debris. However, an interesting change in wear feature, mild to severe wear transition at critical pressure was noticed in wear behavior of the composite. The Al-DPS composite has immense potential to be used as a component material for tribological applications.

Introduction

Materials for many light weight applications can be developed by the incorporation of a ceramic phase in the soft aluminum alloy matrix. The addition of ceramic particles can significantly improve the mechanical and wear properties of the composites [1]. The degree of property enhancement depends upon the choice of the reinforcement which is dictated by several factors like intended application, availability and cost effectiveness. The volume fraction, shape, size, type of the reinforcement and processing technique employed for the fabrication of the composite play significant role in determining the mechanical and tribological properties [2-4]. In recent years, numerous research work have been reported on the composites reinforced with various type of ceramics like SiC, Al_2O_3, B, C, flyash, etc. Minerals like zircon, sillimanite, rutile, garnet etc. [5-9] as reinforcement material has been used because of low cost, availability and their environment friendly nature. Arora et al. [10] found that fine rutile particle size reinforced AMCs offers better wear resistance as compared to the coarse particle reinforced composites. Singh et al. [6] found that the wear rate of the composites and the matrix alloy increased with the increase in applied load and abrasive size of the sillimanite particles. Das et al. [11] used stir casting route for incorporating zircon sand particles of different sizes. The abrasion resistance of the composite increased with increase in the amount of reinforced particles. The increase in particle size of the reinforcement decreases the wear resistance of the aluminium rutile composite [7]. Suresh et al. [9] studied the change in microstructural feature of zircon

reinforced DPS composites containing 75% fine and 25% coarse particles and found that the composite to be better wear resistant material at all temperatures for both low and high loads.
In the present study, 15 wt.% of rutile particles of different sizes (50-75 μm and 106-125 μm) were reinforced in the Al-12Si alloy (LM13) by liquid metallurgy route. The developed samples were subjected to wear tests under the varying applied pressure from 125 kPa to 625 kPa at a constant sliding speed of 1.6 m/s. Microstructure and wear studies of the wear surfaces and debris was observed. It has been found that DPS composites offer great potential of developing materials with better mechanical properties and enhanced wear resistance.

Fabrication of Composites

A well known LM13 alloy was used as base material for the fabrication of the single particle size (SPS) and dual particle size (DPS) composites. Single and dual particle size composites containing 15wt.% rutile particles of different sizes (50-75 μm and 106-125 μm) of fine and coarse size in a defined proportion were prepared by a conventional stir casting process. This process involves the mixing of preheated rutile particles at 350 °C in the vortex created by the melt at 800 °C. The constant stirring of the melt by moving the impellar up and down during mixing ensured the uniform distribution of the rutile particles in the matrix. Further details on the fabrication of these composites are given elsewhere [7].

Experimental Techniques Used for the Characterization

The surface morphology of each sample was studied with the help of optical and scanning electron microscope at different magnifications. Elemental analysis of the composite at different phases was done with SEM-EDS. Micro hardness of the different phases of the composite was measured by using Vickers Hardness Testing Machine. Dry sliding wear test using pin-on-disc method was done to study the wear behaviour of the prepared composite. The samples of the cast composite were machined to 10 mm dia. cylindrical pins and the wear tests were performed on pin on disc tribometer under dry sliding conditions in ambient air at controlled temperature. Wear tests were conducted at different pressure of 125, 250, 375, 500 and 625 kPa. A constant sliding velocity of 1.6 m s^{-1} was maintained throughout the experiment and sliding distance covered during the experiment was about 3000 meters. To study the wear behaviour, wear rate was calculated by using the formula, [W (mm^3/m) = height change (mm) × pin area (mm^2) / sliding distance (m)]. The worn surface regions (wear tracks) and collected debris after the dry sliding wear tests were also examined under scanning electron microscope. The change in wear behavior with the variation in applied pressure has been explained with reference to the observed EDS analysis of the wear track and debris.

Results and Discussion

Morphological Study of the Cast Composites

The SEM micrographs of composites reinforced with rutile fine size particles (50-75μm) and coarse size particles (106-125μm) and dual size particles illustrate the typical microstructure as shown in Figure 1 (a-d) respectively.

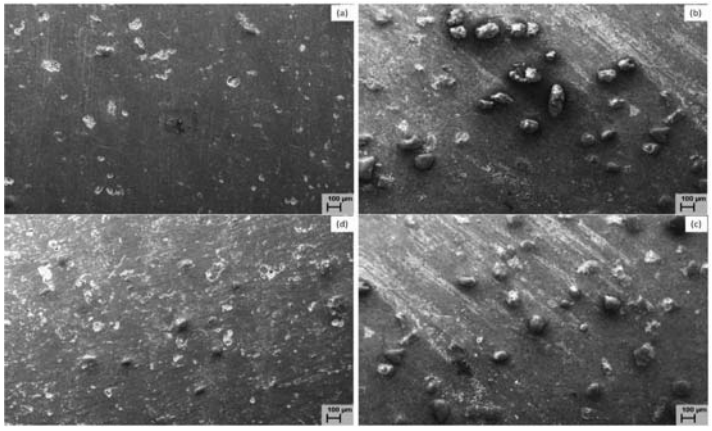

Figure 1 Optical micrograph of composites containing (a) 15wt.% fine (SPS1), (b) 15wt.% coarse (SPS2), (c) 3wt.% fine and 12 wt.% coarse (DPS2) and (d) 12wt.% fine and 3wt.% coarse (DPS1) particles.

The composites have shown the fairly uniform distribution of rutile particles which is achieved by the constant stirring action of the impeller which delays the particle settling tendency [4]. In the composite SPS1 (Fig.1a), the fine rutile particles are well dispersed and embedded in the matrix which confirms the good interfacial bonding between the particle and the matrix. The micrograph of SPS2 (Fig.1b), depicts loose bonding with the matrix owing to the less penetration of coarse particles in the matrix. The addition of 3% coarse size rutile particles as in the DPS1 composite has improved the microstructure as the large protruded rutile particles occupy the space between the fine particles hence lowers the agglomeration tendency of the fine particles during the solidification of the composite (Fig.1d). The inclusion of 3% fine rutile particles in the composite as in DPS2, (Fig.1c), not only enhances the bonding between the particle and the matrix but also hinders the dendritic growth in the particles depleted regions [10], which provides more refinement in the microstructure as compared to the SPS2.

Micro-hardness

Micro-hardness measurement has been carried out on the embedded reinforced particles as well as in the vicinity of particles and matrix shown in Figure 2. Reinforced particles show high hardness which decreases as we move away from particle into the matrix. The high hardness at particle/matrix interface indicates good interfacial bonding between particle and alloy matrix.

Effect of Applied Pressure on the Wear Behaviour

Wear Rate of the Composites: Wear rate of the composites as a function of sliding distance at variable contact pressure from 125kPa to 625 kPa is shown in Figure 3 (a,b). At a particular pressure, two type of wear behaviour are displayed by the composites during the dry sliding. The

initial stages of run have shown very heavy wear loss due to the statistical fluctuations in wear as the abrasive wear between the two surfaces in relative motion is dominant. The continuous grinding of the abrasive particles of the two contacting surfaces while sliding reduces the sharpness of the asperities. These blunt shaped smooth abrasives cause fall in wear loss and the steady state is attained [9].

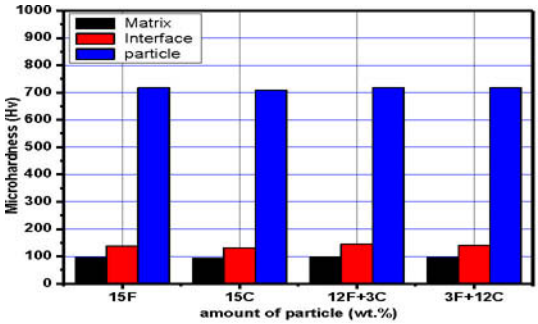

Figure 2. Bar graph of micro-hardness at different amounts ratio of rutile reinforced particle composites.

The difference in wear rates of the initial run in wear and steady state goes on continuously increasing with the applied pressure from 125kPa to 625 kPa. The increased pressure speeds up the crushing and grinding action of the protruded asperities, hence resulting in the increase in the wear loss. Application of high contact pressure of 625kPa causes the abrupt change in the wear rate which is evident from the comparison of the wear rates as shown in Fig 3(a, b). Increase in wear rate with the increase of pressure is on the same pattern as observed by Rao et al. [12]. High pressure during sliding, fractures the oxide film and lead to the exposure of the substrate material thus causing plastic deformation beneath the surfaces. This close contact welds the removed materials which can be transferred to the counterface and some of material may fall out as wear debris.

It may be noted from the Figures 3 (a,b) that the wear rate of the composite SPS1 is lower than that of the SPS2, as the large surface area of fine size rutile particles enhances the hardness of the composite which further lowers the wear rate. Also, the decreased inter-particle distance in the matrix of the composite SPS1 enhances the load bearing capacity of the matrix and hence increases the wear resistance. On comparing the wear rate of the DPS composites as shown in Figure 4 (a, b) it is observed that the DPS1 has shown more improvement in the wear resistance as compared to the DPS2.

The DPS1 has exhibited better wear resistance at all the applied pressures as fine particles provide more hardness to the matrix and subsequent addition of coarse rutile particles safeguard the matrix acting as a load bearing element. At the same time, inclusion of fine particles in the DPS2 has also shown improvement in wear behavior due to modification in the microstructure of the composite but the wear loss is higher as compared to the DPS1. The substitution of a portion of the particles in the SPS composite by fine or coarse particles to produce the DPS composite clearly helps in improving the wear resistance of the DPS composite over that of the SPS composite.

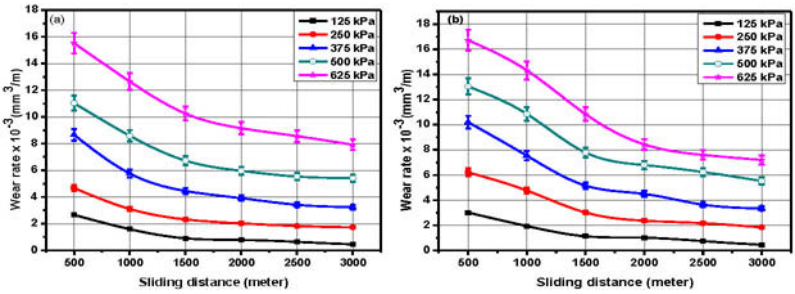

Figure 3.Wear rate of SPS composites against sliding distance at different applied pressure for (a) 15wt.%fine and (b) 15wt.% coarse size reinforced particle

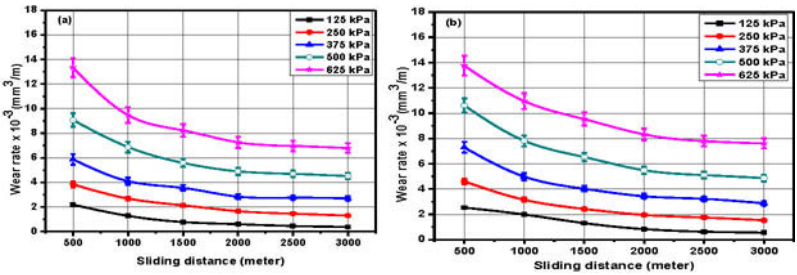

Figure 4.Wear rate of DPS composites against sliding distance at different applied pressure for (a) 4:1 and (b) 1:4 ratio of reinforced particle size.

Morphological Analysis of the Worn Surfaces and Wear Debris: Figure 5(a-d) shows the SEM images of wear tracks of the composites DPS1 and DPS2 tested at 125kPa and 625kPa pressure, respectively. The abrasive grooves on the worn surface of composites at low pressure (125kPa) are due to the abrasive action of the asperities of the steel disc in the matrix. As the hard ceramic particles resisted the deformation of the asperities so the composites wear behaviour lies in the mild wear regime.

At higher contact pressure 625kPa, the material removal is governed by adhesive wear and delamination of matrix material. The material removal is enhanced by adhesive wear mechanism and number of craters is increased showing deep ploughing marks, as shown in Figure 5b. The large craters visible on the surface underneath with the presence of cracks indicate the delamination wear. On increasing the contact pressure to 625kPa, change in wear transition from mild to severe is observed. It is confirmed by heavy damages caused to the specimen surfaces by the delamination wear. At low contact pressure 125kPa, ribbon type morphology in wear debris

is more often visible because of the decreased interspacing between the particles in the composite that reduces the abrasive wear of composite (Figure 6a & 6b).

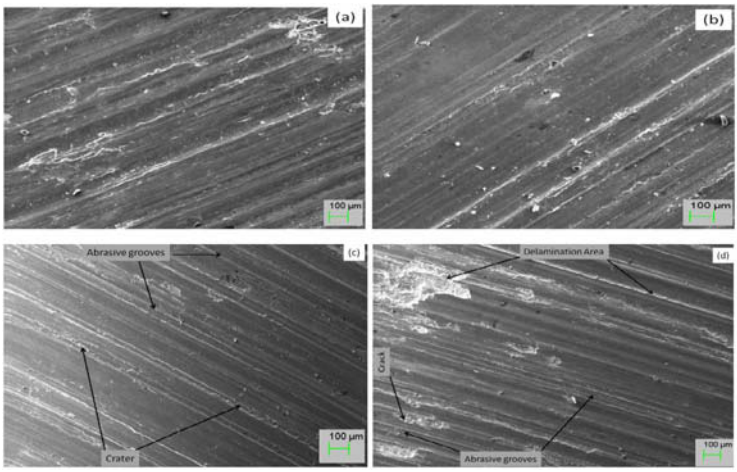

Figure 5. SEM micrographs of wear tracks of composites DPS1 (a) 125 kPa, (b) 625 kPa and DPS2: (c) 125 kPa, and (d) 625 kPa pressure.

Noodles type structure observed on the wear debris is due to the continuous rubbing and crushing of debris between grooves during the wear test of composite SPS1. At higher contact pressure 625kPa, adhesive wear as well as delamination of matrix material resulting from the crack propagation equally contribute towards the loss of material. Rolled delaminated debris depicts that surface has acquired the recrystallization temperature due to the generation of frictional heat during sliding [10]. Molten metal balls are formed by the continuous rubbing of the thread like debris between the two surfaces. Large plate type debris with cracks confirms the dominance of delamination wear which is shown in Fig 6c & d. Shiny and metallic balls as well as corrugated debris are also formed resulting from the adhesive wear. At high contact pressure wear mechanism is governed by the adhesive and delamination wear in the severe wear regime as indicated by the size, shape and the state of the wear debris.

It is observed from EDS spectrum that certain amount of oxide layer has formed and is stably sustained on the contacting asperities. Oxide layer can provide full protection and mild oxidative wear prevailed. EDS analysis (Figure 6c & d) of debris indicate the presence of O, Mg, Al, Si, Ti and Fe elements. This indicates that apart from base metal, rutile is also coming out from the surface. Presence of Fe in the debris may be due to the transfer of steel counterface to the composite surface. The transfer of steel inclusions from counterface surfaces to the composite wear surfaces is another mechanism which contributes to increase in wear resistance of the composites. On comparing the worn surfaces and debris of the composites at high contact pressure, it can be concluded that the DPS1 composite displays the better wear performance at all contact pressures as compared to the other composites as the size of the rutile particles plays dominant role in determining the wear behaviour of the composite.

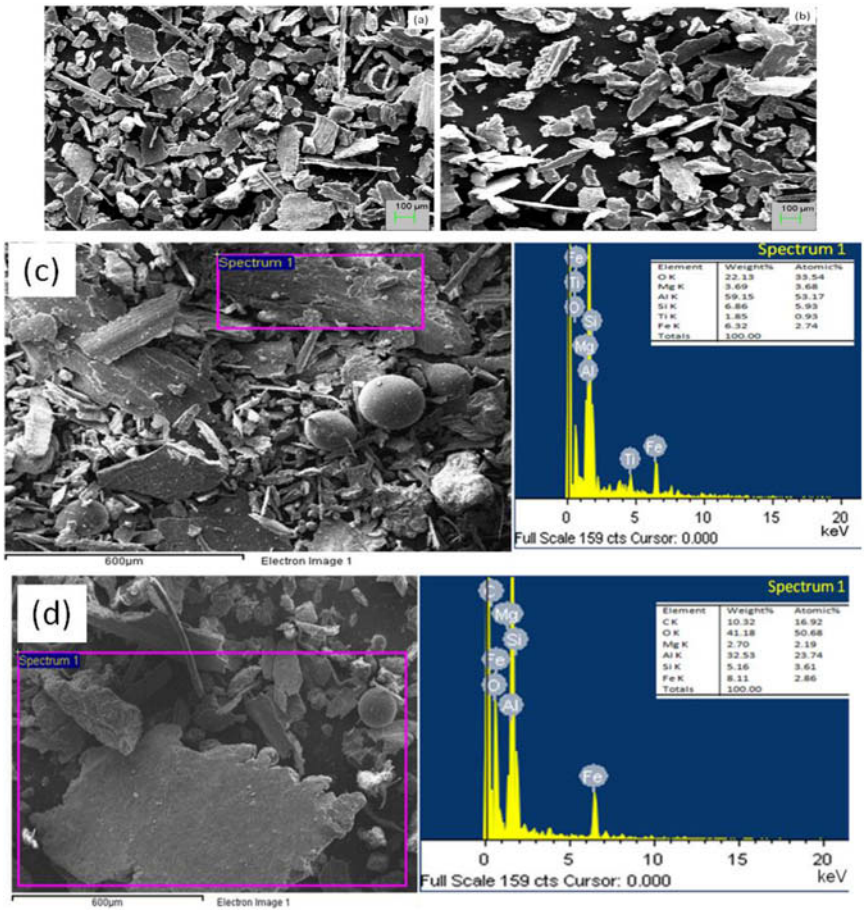

Figure 6. SEM micrographs of composites: wear debris at 125 kPa pressure (a) SPS1 (b) SPS2 wear debris and EDS at 625 kPa pressure of (c) SPS1 (d) SPS2 composites.

Conclusions

The size of the rutile particles greatly influences the tribological behavior of the aluminium alloy. Rutile particles inclusion in the matrix modifies the microstructure which in turn improves the wear behavior of the composite. Dual particle size composites turn out to be better wear resistant material under the high contact pressure as compared to single particle composites. At a critical pressure, change in wear feature, mild to severe wear transition takes place which is confirmed from the morphology of the wear tracks and the wear debris.

References

1. G. B. Veeresh Kumar, C. S. P. Rao and N. Selvaraj, "Studies on Mechanical and Dry Sliding Wear of Al6061-Sic composites a review" *Composites*, 43 (2012), 1185-1191.

2. Kamalpreet Kaur,Ramkishor Anant and O. P. Pandey, "Tribological Behaviour of SiC Particle Reinforced Al–Si Alloy", *Tribol. Lett.*,44(2010), 51-58.

3. S. Kumar, "Effect of Reinforcement Size, and Volume Fraction on the Abrasive Wear of AA7075 Al/SiCp P/M composites-A Statistical Analysis", *Tribol. Inter.*,43 (2010), 414-422

4. J. Hashim, L. Looney and M.S.J. Hashmi, "Metal matrix composites: production by the stir casting method", *J. Mater. Proces. Technol.*92 (1999), 1-7.

5. S. Kumar, R. S. Panwar, and O. P. Pandey, "Tribological characteristics of Aluminium tri-reinforced particles composites developed by liquid metallurgy route", *Advd.Mater.Rearch.*,585(2012), 574-578.

6. M. Singh, D.P. Mondal, A.K. Jha, S. Das and A.H. Yegneswaran, "Preparation and properties of Cast Aluminium Alloy–Sillimanite Particle Composite", *Composites*, 32 (2001), 787-795.

7. Rama Arora, Suresh Kumar, Gurmel Singh and O.P. Pandey, "Influence of Particle Size and Temperature on the Wear Properties of Rutile Reinforced Aluminium Metal Matrix Composite", *Journal of Composite Materials*, DOI: 10.1177/0021998314526079

8. Anju Sharma, Suresh Kumar, Gurmel Singh and O.P. Pandey,"Effect of Particle Size on Wear Behaviour of Al-Garnet Composites,"*Particulate Science and Technology*,(DOI: 10.1080/02726351.2014.954686).

9. S. Kumar, R. S. Panwar, and O. P. Pandey, "Effect of dual reinforced ceramic particles on high temperature tribological properties of aluminum composites", *Ceramics Inter.*,39(2013), 6333-6342.

10. Rama Arora, Suresh Kumar, Gurmel Singh and O.P. Pandey,"Role of Different Range of Particle Size on Wear Characteristics of Al-Rutile Composites", *Particulate Science and Technology*, DOI: 10.1080/02726351.2014.953648

11. Sanjeev Das., V. Udhayabhanu and S. Das "Synthesis and Characterization of Zircon Sand/Al-4.5 wt% Cu Composite produced by Stir Casting route., *J. Mater. Sci.*, 41 (2006), 4668-4677.

12. R.N. Rao and S. Das, "Effect of Applied Pressure on the Tribological Behaviour of SiCp Reinforced AA2024 Alloy", *Tribol. Inter.*,8 (2011), 454-462.

Characterization of Minerals, Metals, and Materials 2015
Edited by: John S. Carpenter, Chenguang Bai, Juan Pablo Escobedo, Jiann-Yang Hwang, Shadia Ikhmayies, Bowen Li, Jian Li, Sergio Neves Monteiro, Zhiwei Peng, and Mingming Zhang
TMS (The Minerals, Metals & Materials Society), 2015

INVESTIGATION ON MECHANICAL AND THERMAL BEHAVIOURS OF COPOLYESTER/PLA BLEND REINFORCED WITH TiO_2 NANOPARTICLE

Roberta A. Lima[1], Rene R. Oliveira [1], Vijaya K. Rangari[2], Shaik Jeelani [2], Esperidiana A. B. Moura[1]

[1]Nuclear and Energy Research Institute, IPEN-CNEN/SP
2242 Prof. L. Prestes Av., São Paulo, SP, 05508-000, Brazil

[2]Department of Materials Science and Engineering,
Tuskegee University, Tuskegee, AL 36088, USA

Keywords: Nanocomposite, biodegradable polymers, TiO_2, mechanical properties, DSC

Abstract

This work present the preparation and characterization of biodegradable nanocomposites based on aliphatic-aromatic copolyester (PBAT)/polylatic acid (PLA) blend reinforced by TiO_2 nanoparticle. The biodegradable polymeric nanocomposites were prepared by melting extrusion process using a twin-screw extruder machine. The influence of the TiO2 nanoparticle addition on mechanical and thermal properties of PBAT/PLA blend was investigated by tensile and impact tests, SEM, DSC and XRD analysis and the correlation between properties was discussed.

1. Introduction

Increasing interest in new materials based on blends of two or more polymers has been observed during the last three decades. Blends of conventional plastics (petroleum-derived polymers) and biopolymer can form a new class of materials with improved mechanical properties compared with those of single components. Polymer blending offers possibility of adjusting the cost-performance balance and tailoring the technology to make products for specific end-use applications; extends engineering resins' performance; improves specific properties or solvent resistance; and provides means for industrial and consumer plastics waste recycling [1].

Biopolymers have advantages over the conventional polymers; biopolymers are biodegradable and renewable materials. Conventional thermoplastic polymers have good mechanical properties and thermal stability, much better than the biodegradable ones. There is also a limitation in the performance and application of biopolymers in comparison to conventional thermoplastics. Therefore the extensive application of these biopolymers is still challenged by one or more of their possible inherent limitations, such as poor processability, brittleness, hydrophilicity, poor moisture and gas barrier, inferior compatibility, poor electrical, thermal and mechanical properties [2,3].

Combination of polymer blends with micro or nanofillers appears quite promising on the basis of balanced performance of biopolymer, to impart better thermal and mechanical properties, improve service temperature, moisture resistance, gas barrier, and in some cases reduce the cost of biodegradable thermoplastic polymers. Incorporation of nanoparticles into polymer materials has attracted a great deal of attention due to its ability to enhance polymer properties such as thermal, mechanical, and gas barrier [2]. Inorganic materials such as metals or metal oxides maintain properties and stability, even in harsh environments leading to a great deal of research activity.

TiO2 among the inorganic materials have particular interesting due to both being a safe material for animals and human and stability under harsh condition processes [4, 5].

The synthesis of inorganic-biopolymer nanocomposites has been intensely studied due to their unique combination of properties and widespread potential applications. These generations of biocomposites have more desirable functional properties like good mechanical strength and low water vapour permeability. Lately, researchers have reported the improvements of biopolymer properties by incorporation of nano particles, such as clay, silica, layered silicate nanoparticles, calcium carbonate, zinc oxide and titanium dioxide. In general, these researchers have reported that the incorporation of nanoparticles improve mechanical properties, as well as barrier and antimicrobial properties of biopolymers [6,7].

This work present the preparation and characterization of biodegradable nanocomposites based on aliphatic-aromatic copolyester (PBAT)/polylatic acid (PLA) blend reinforced by TiO_2 nanoparticle.

2. Material and Methods

2.1. Material

The materials used in this work were biodegradable Aliphatic-aromatic copolyester (PBAT) with biodegradable Poly(lactic acid) (PLA), producing a blend with MFI = 8,59 g/ 10 min at 190°C / 2.16 Kg, and natural Brazilian bentonite light green clay from Boa-Vista, PB, Brazil, and TiO_2 nanoparticle.

2.1.2 Preparation of blend and composite

PLA and PBAT pellets and the TiO_2 nanoparticle were dried at 60 ± 2 °C for 4 h to reduce its moisture content to less than 2 %. The PBAT/PLA blend (40 %/ 60% based on wt%) and PBAT/PLA with 2 % (wt %) of TiO_2 were prepared by melting extrusion process, using a co-rotating twin screw Haake Rheomex P332 extruder. The temperature profile was 135/145/148/150/150/150 °C. Screw speed was 180 rpm. The extrudates coming out of the extruder were cooled down for a better dimensional stability, pelletized by a pelletizer, dried again at 60 ± 2 °C for 4 h and fed into injection molding machine and specimens test samples were obtained.

3. Characterization

3.1. Mechanical tests

Tensile tests (ASTM D 638) and Izod impact (ASTM D 256-97) tests were performed in this work in order to evaluate the mechanical behavior of the materials studied.

3.2. X-rays diffraction (XRD) tests

X-rays diffraction (XRD) were recorded on a Siemens - D5000 diffractometer operated at 40 kV and 40 mA, with CuKα radiation (λ= 15.4 Å).

3.3. Differential scanning calorimetry (DSC)

DSC analyses were carried out using a Mettler Toledo DSC 822e from 25 to 200°C at a heating rate of 10 °C/min under oxygen atmosphere. DSC analyses of the materials were performed on four samples of the irradiated and non-irradiated materials.

3.4. Scanning Electron Microscopy (SEM)

Scanning electron microscopy (SEM) analyses were carried out using a LX 30 (Philips).The samples were cryo-fractured under liquid nitrogen, and then the fractured surface was coated with a fine layer of gold and observed by scanning electron microscopy.

4. Results and Discussion

4.1. Mechanical tests results

Tensile test results - Figure 1 shows the diagram stress (MPa) X strain (mm/mm) for the PBAT/PLA blend and PBAT/PLA/TiO_2 nanocomposite. These results shown the average values calculated from the data obtained in tests, with standard deviations less than 10 % for all tests.

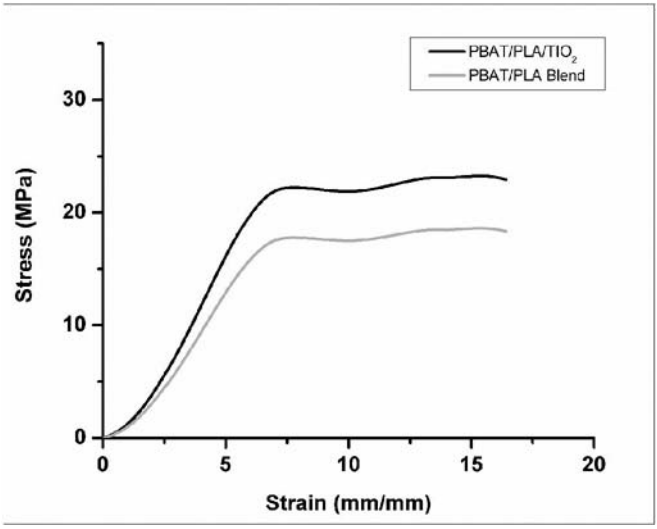

Figure 1. Diagram Stress (MPa) against Strain (mm/mm) the PBAT/PLA blend and PBAT/PLA/TiO_2 nanocomposite.

As can be seen in this Figure the addiction of TiO_2 nanoparticle in PBAT/PLA blend improved the tensile stress (of around 20 %) and modulus properties of blend without cause reduction in the elongation. These changes should be associated with the interfacial interaction between the PBT and TiO_2 nanoparticle.

Impact test results – With regards to impact properties the Izod impact test results showed a gain of about 60 % in impact strength of blend due to TiO_2 addition. The impact strength results of blend was of around 50 J/m and of the nanocomposite was of 80 J/m.

4.2. X-rays diffraction (XRD) analysis results

The XRD patterns of PBAT/PLA blend and PBAT/PLA/TiO_2 nanocomposite are shown in Figure 2. It can be seen, the XRD spectrum of PBAT/PLA blend showed a prominent 2θ peak at around 16.80, which has drastically reduced of intensity due to TiO_2 nanoparticle addition.

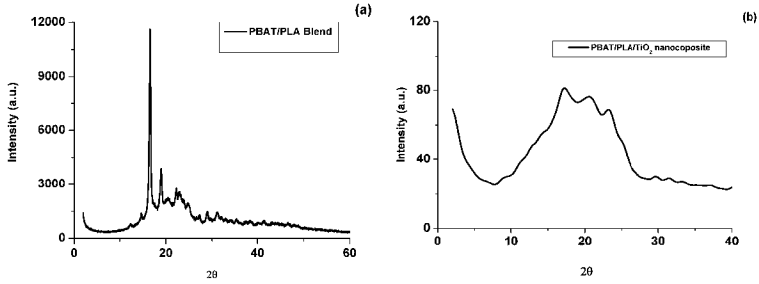

Figure 2. XRD diffraction patterns for the PBAT/PLA blend (a) and PBAT/PLA/TiO_2 nanocomposite (b).

4.3. Differential Scanning Calorimetry (DSC) analysis results

Figure 3 shows the curve of DSC analysis of PBAT/PLA blend (Fig 2 (a)) and PBAT/PLA/TiO_2 nanocomposite (Fig.2 (b))

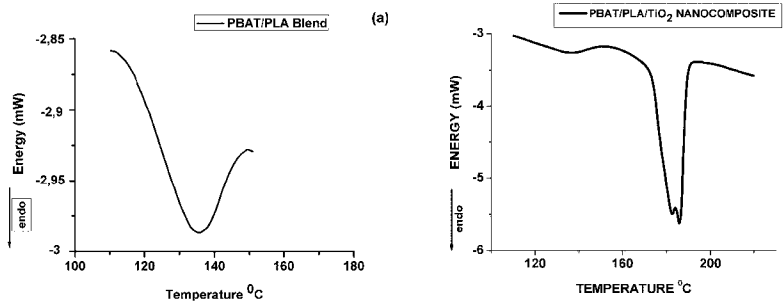

Figure 3. DSC analysis for the PBAT/PLA blend (a) and for the PBAT/PLA/TiO_2 nanocomposite (b).

From Figure 3, it could be inferred that compared with the PBAT/PLA blend (Fig.3(a)) the endothermic melting enthalpy of PBAT/PLA blend increased considerably due to TiO_2 nanoparticle addition. The addition of 3 % in wt of TiO_2 in PBAT/PLA blend leads to obtaining of new material with higher melting enthalpy, and melting temperature than original blend. The increases in the melting enthalpy can be attributed to the increase in crystallinity of material. It indicated that blending PBAT with PLA, followed by TiO_2 nanoparticle addition caused structural

changes in the polymeric chains of blend component. It means that blend processing and TiO_2 nanoparticle addition had a capability to reorient the polymeric molecules presents in crystal form in order to obtain a composite material with high melting enthalpy and, consequently, high crystallinity percentage.

The average values of melting enthalpy (ΔHm) and melting temperature (Tm) of the materials studied are given in Table 3. As it can be seen, the melting temperature and enthalpy of blend and composite were higher than of PLA and lower than of PBAT indicating good miscibility between the components of the blend and also the TiO_2 nanoparticles.

Table 1. DSC analysis results of materials studied

Materials	Melting Temperature (T_m, °C)	Melting Enthalpy (ΔH_m,Jg^{-1})
Neat PBAT	135.7	298.8
Neat PLA	58.9	43.5
PBAT/PLA blend	139.1	135.5
PBAT/PLA/TiO_2 nanocomposite	158.9	185.7

4.4. Scanning Electron Microscopy (SEM) analysis results:

SEM micrographs of cryo-fractured surfaces of PBAT/PLA blend and PBAT/PLA/TiO_2 nanocomposite are showed in Figure 4.

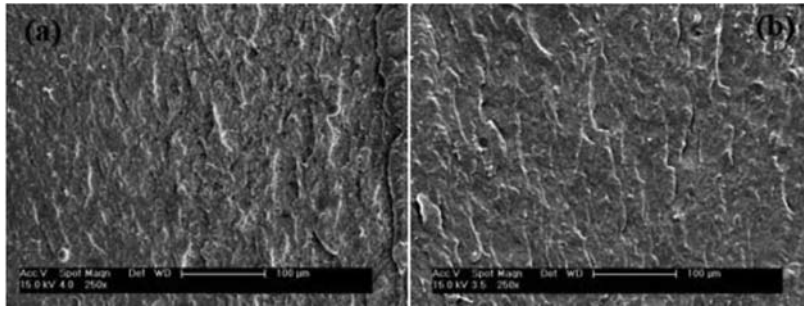

Figure 4. SEM micrographs of cryo-fractured surfaces of PBAT/PLA blend (a) and for the PBAT/PLA/TiO_2 nanocomposite (b).

As it can be seen, both blend Fig. (4a) and nanocomposite Fig. (4b) showed a slightly rough cryo-fractured surface. However, from Figure (4b), it can be see that there are not agglomerates in the surface of the blend due to nanoparticle addition. This result suggests that all TiO_2 nanoparticles were dispersed in the PBAT/PLA blend.

5. Conclusions

The aim of this study was to process and investigate the changes in the mechanical and morphological properties of the biodegradable PBAT/PLA blend due to the incorporation of TiO_2

nanoparticle. Results showed that incorporation of 2 % (wt %) of TiO_2 nanoparticle in the blend matrix of PBAT/PLA, resulted in a gain of mechanical properties of blend. The DSC analysis results indicated that blending PBAT with PLA, followed by of TiO_2 nanoparticle addition caused structural changes in the polymeric chains of blend component, increased the original melting enthalpy and temperature of blend, and consequently, increased the crystallinity percentage. This result indicates that TiO_2 nanoparticle addition in the PBAT/PLA matrix improved the biodegradable blend properties and led to materials with superior properties suitable for several industrial applications.

Acknowledgements

The authors wish to thank BASF and FATEC ZL for the support for this work.

References

1. L.A. Utracki, ed., Polymer 766 Blends Handbook, vol. 1 (Kluwer Academic Publishers, Dordrecht, 2003).

2. R. Nassiri, N.A. and Mohammadi, "Antimicrobial and Barrier Properties of Bovine Gelatin Films Reinforced by Nano TiO_2," *Journal of Chemical Health Risks*, 3 (3) (2013), 12-28.

3. M. Kurian et al., "A Novel Route to Inducing Disorder in Model Polymer-Layered Silicate Nanocomposites," *Macromolecules,* 39 (2006), 1864-1871.

4. P. K. Stoimenov et al., "Metal Oxide Nanoparticles as Bactericidal Agents," *Langmuir,* 18 (2002), 6679-6686.

5. W. Lin et al., "Toxicity of nanoand micro-sized ZnO particles in human lung epithelial cells," *Journal of Nanoparticle Research,* 11 (2009), 25-39.

6. A. Sionkowska, et al., "Molecular interactions in collagen and chitosan blends," *Biomaterials*; 25 (2004), 795–801.

7. C. Chawengkijwanich and Y. Hayata, "Development of TiO_2 powder-coated food packaging film and its ability to inactivate escherichia coli in vitro and in actual tests," *International Journal of Food Microbiology,* 123 (2008), 288-292.

Characterization of Minerals, Metals, and Materials 2015
Edited by: John S. Carpenter, Chenguang Bai, Juan Pablo Escobedo, Jiann-Yang Hwang, Shadia Ikhmayies, Bowen Li, Jian Li, Sergio Neves Monteiro, Zhiwei Peng, and Mingming Zhang
TMS (The Minerals, Metals & Materials Society), 2015

INFLUENCE OF Cu^{2+} AND Zn^{2+} ON THE DISSOLUTION OF Ag IN $S_2O_3^{2-}$ MEDIUM

Julio Cesar Juárez[1], Isauro Rivera[2], Francisco Patiño[2], Juan Hernández[2], Martin Reyes[2], Ma. de los Ángeles Hernández[1]

1) Departamento de Metalurgia y Materiales, ESIQIE-IPN. UPALM, Zacatenco, C.P. 07738, México D.F. E-mail: jutj731101@hotmail.com Tel.: +527717941707

2) Área Académica de Ciencias de la Tierra y Materiales. Universidad Autónoma del estado de Hidalgo. Carretera Pachuca-Tulancingo Km 4.5 Mineral de la Reforma C.P. 42184, Hidalgo México.

Keywords: Silver, Leaching, thiosulfate

Abstract

The dissolution of Ag contained in metallurgical tailings was studied by adding ions Cu^{2+} and Zn^{2+} in $S_2O_3^{2-}$ medium. Chemical analysis of mine tailings by cupellation revealed a Ag concentration of 71 g/ton. The XRF and XRD analysis confirmed the preponderance of SiO_2 in the mineral matrix. The experimental dissolution process was conducted in alkaline solution using six concentrations of NaOH and five of $S_2O_3^{2-}$, at different temperatures, also using five concentrations of Cu^{2+} and Zn^{2+} as a catalyst. The results showed similar values for both systems (96.8% and 97.13%). The ion Cu^{2+} and Zn^{2+} increases the dissolution of Ag, and decrease the reaction time of dissolution. Under the conditions used, pH and stirring rate did not affect the dissolution of Ag.

Introduction

The mining industry is an important activity for many countries throughout the world. Mexico is a good example as it's mines and metallurgical plants exhibit high production of precious metals such as gold and silver. Silver is especially significant to Mexico as the mining industry is the leading supplier of silver across the globe.

Precious metals are usually leached with cyanide as the complexing agent and oxygen as oxidant, because this process has proved very effective for dissolving gold and silver from their ores.

The need to process ores difficult to treat, and care of the environment due to the use of cyanide, has encouraged research and development of new systems leaching of precious metals.

The system thiosulfate-copper-ammonia is considered a promising alternative to cyanide [1] and has been studied by different research groups since 1980 [2, 3].

In this process copper ions oxidize the precious metal while the thiosulfate complexes with them. The ammonia is also added to stabilize the cupric ions in the alkaline solution, preventing their precipitation as copper hydroxide [4].

Recent research has revealed the high efficiency of the leaching solutions-copper-ammonium thiosulfate: precious metals can be recovered from sulfide ores at 48 h. However, the reaction mechanism in this leaching system is reported to be very complicated.

It has been reported that the leaching kinetics of silver can be enhanced by an increase in the concentration of thiosulfate [5]; these investigations suggest that leaching of silver in these solutions would be a promising alternative process; however, the high consumption of the cupric ions and thiosulfate has made this leaching system economically infeasible for industry. Commercially, the cyanide leaching process is much more widely used [6].

Some have sought to use other metal ions to oxidize the silver, for example, [7] ions as an oxidizing agent in the thiosulphate leaching of silver contained in mine waste. Maximum solutions of 97% of precious metals in times of four hours were reached under certain conditions of analysis.

Consequently, research scientists have focused on increasing the oxidation capacity of the leaching system while trying to avoid the oxidative loss of thiosulfate, in order to reduce the time of leaching and increase the percentage of dissolution of silver precious metal.

Experimental

The study area is located in the city of Pachuca, Hidalgo, Mexico, to N20 ° 06' W and an elevation of 2423 meters. The sample was characterized chemical by ICP and also mineralogical using XRD technique. Leaching experiments were carried out in a conventional glass reactor of 500 mL capacity, fitted with a measuring grid agitation speed and temperature controller.

A system of continuous pH measurement based on a pH meter equipped with a pH electrode suitable for operation in extreme conditions of acidity and alkalinity was implemented. PH adjustments of the experiments were performed by adding a 1% H_2SO_4 solution and NaOH concentration of 0.2 mol L^{-1}, depending on the system being studied. Oxygen was injected to give an atm pressure inside the reactor. The system temperature was controlled by a coupled heating grill thermocouple. The start of the reaction was taken as that instant when the sample contacts mineral extraction fluid. Samples at different times t were taken. The experimental conditions used in this study are presented in Tables 1 and 2.

Tabla 1. Experimental Conditions $S_2O_3^{2-}$-O_2-Cu^{2+} System.

Parameters	Experimental Conditions
Partícle Size (microns)	149, 106, 75, 56, 44, 37 y 25
$[Cu^{2+}]$ (gL^{-1})	0, 0.25, 0.50, 0.75, 1 y 1.5
$[S_2O_3^{2-}]$ (gL^{-1})	2.5, 5, 7.5, 10, 20 40, 80
Temperature (K)	288, 298, 308, 318 y 328
Agitation Speed (min^{-1})	250, 350, 450, 550, 650 y 750
Stirring System	Magnético
Partial Pressure of O_2 (atm)	0.2 y 1.0
pH	5, 7, 9, 10, 11 y 12

Tabla 2. Experimental Conditions $S_2O_3^{2-}$-O_2-Zn^{2+} System.

Parameters	Experimental Conditions
$[Zn^{2+}]$ (gL^{-1})	0.55, 1.1, 1.65, 2.2, 3.3,4.4,6.6 , 8.8 y 13.2
$[S_2O_3^{2-}]$ (gL^{-1})	5, 10, 20, 40, 80 y 100.
Temperature (K)	298, 303, 308, 313y 318
Agitation Speed (min^{-1})	450, 550, 650,750 y 850
Partícle Size (microns)	149
Stirring System	Magnético
pH	4, 5, 6, 7, 8 y 10

Results and Discussion

The results of the chemical and mineralogical characterization, obtained by Emission Spectrometry technique of inductively coupled plasma (ICP) and (Cupellation) showed very similar silver content, establishing that the concentration of precious metals in the tailings is in the order of 61 g/ton. and 71 g/ton. respectively as shown in Tables 3 and 4.

Table 3. Shows the chemical composition of the tailings two Carlos Hidalgo State

Element	Percent	Element	Percent
Fe	2.40	Ti	0.0058
S	0.87	V	0.0019
Ca	0.60	Sr	0.0018
Al	0.22	Sb	0.0016
Mg	0.087	As	0.0013
K	0.064	Mo	0.0012
Mn	0.054	Cr	0.0011
Pb	0.047	Se	0.00074
Si	0.044	Ni	0.00052
Na	0.043	Co	0.00031
Zn	0.028	Cd	0.00019
P	0.025	Li	0.00019
Ba	0.011	**Element**	**ppm**
Cu	0.0097	**Ag**	**61**

Table 4. It shows the total content of silver in the tailings two Carlos State of Hidalgo.

Element	Percent
Ag	**71**

As shown silver content obtained by this technique is better than that reported by ICP, because a portion of these precious metals are encapsulated in a siliceous matrix.

The diffractogram obtained identification analysis by XRD, is presented in Figure 1. This diffraction pattern shows that the majority phase is mineral quartz (SiO_2) (JCPDS No. 00-074-3485) which represents the matrix mineralization of these mineral tailings followed by aluminosilicates (JCPDS No. 01-089- 8572), which probably is formed by the combination of silica with metal oxides, especially those having in their molecules the alumina and alkali oxides, while minority mineralogical species corresponding to metal phases as oxides and sulfides.

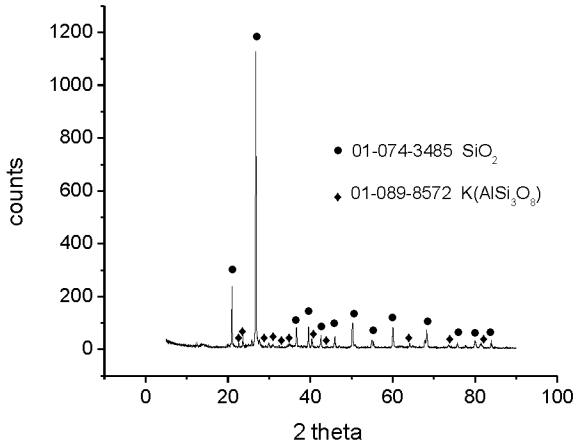

Fig. 1 X ray diffractogram of two Carlos tailings, which are observed mineralogical species present.

To study the effect of metal ions Cu^{2+} and Zn^{2+} on leaching of silver from the tailings and maximum release, a series of experiments at different concentrations were performed.

Figure 2 shows that the addition of Cu^{2+} Ag dissolution into solution is increased, due to a concentration of 0.25 gL^{-1} only 58% leached silver, was obtained.

At the same time as a concentration of Cu^{2+} increases up to 1.5 gL^{-1}. 73% of silver dissolution was obtained at temperature of 273 K.

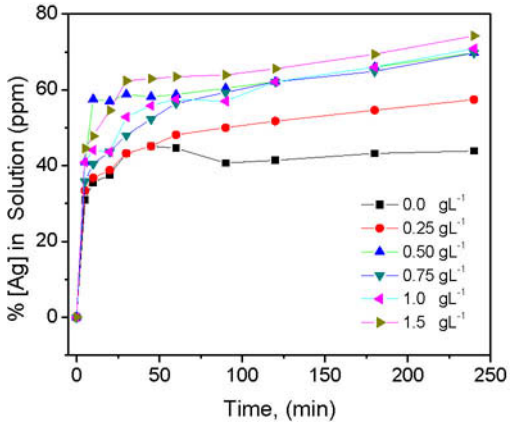

Fig. 2 Plotting silver leaching in function of time for all concentrations of Cu^{2+}.

Figure 3 shows that the behavior of ions of Zn^{2+} is very similar to Cu^{2+} found that dissolution of Ag in solution increases from 52% to 74%, from 0.55 to 2.2 gL^{-1} of Zn^{2+} at 273 K.

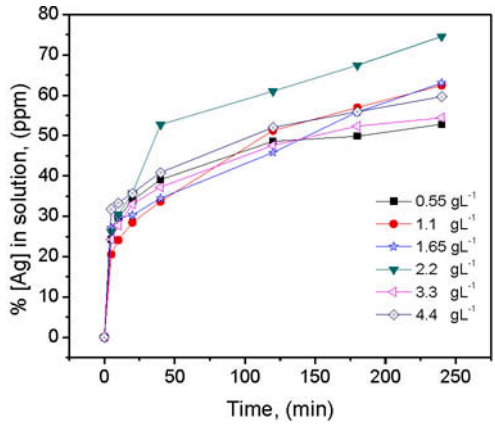

Fig. 3 Graphical silver leaching versus time for all concentrations of Zn^{2+}.

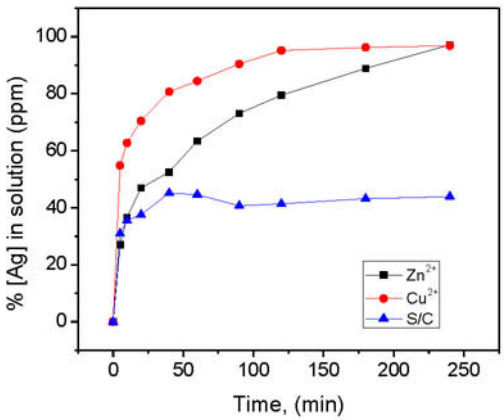

Fig. 4 Plotting silver leaching function of time at 318 K, with the addition of Cu^{2+} and Zn^{2+}.

The results, the addition of Cu^{2+} and Zn^{2+} ions, in the proposed systems are seen in Figure 4. One can appreciate that these ions promote dissolution reaction of the precious metal, the increase in the percentage of leaching in the presence of Cu^{2+} and Zn^{2+}.

Is probably due to a reaction in parallel with the oxidation of silver by oxygen, because it was observed that the leaching reaction of the Ag in the O_2-$S_2O_3^{2-}$ without catalyst system, basically depend on the dissolved oxygen in the system, unlike the reaction in the presence of Cu^{2+} and Zn^{2+}, the reactions of Cu^{2+} to Cu^{+} and Zn^{2+} to Zn^{+} cause oxidations of Ag^0 to Ag^{+}.

Conclusions

The chemical composition of mineral studied, revealed the presence of silver in amounts economically profitable reporting 71 g/ton.

In the concentration range studied, it appears that the presence of Cu^{2+} and Zn^{2+} ions, have a marked influence on the reaction of dissolution of silver increases dramatically as the percentage of dissolution of silver, however, has Cu^{2+} favorably influences the rate of leaching of silver and that for a given reaction time reaches a higher percentage of leached silver.

References

1.- Alonso-Gómez, A.R., Lapidus, G.T., 2009. *Inhibition of lead solubilization during the leaching of gold and silver in ammoniacal thiosulfate solutions (effect of phosphate addition).* Hydrometallurgy 99, 89–96.

2.- Abbruzzese, C., Fornari, P., Massidda, R., Veglió, F., Ubaldini, S., 1995. *Thiosulphate leaching for gold hydrometallurgy.* Hydrometallurgy 39, 265–276.

3. Feng, D., Van Deventer, J.S.J., 2006. *Ammoniacal thiosulphate leaching of gold in the presence of pyrite.* Hydrometallurgy 82 (3–4), 126–132.

4.- Feng, D., Van Deventer, J.S.J., 2007. *Effect of hematite on thiosulphate leaching of gold.* Int. J. Miner. Process. 82, 138–147.

5.- Zipperian, D., Raghavan, S., Wilson, J.P., 1988. *Gold and silver extraction by amoniacal thiosulfate leaching from a rhyolite ore.* Hydrometallurgy 19 (3), 361–375.

6.- Aylmore, M.G., Muir, D.M., 2001. *Thiosulfate leaching of gold.* A review. Miner. Eng. 14,135–174.Eriksson, G., 1979.

7.- Julio C. Juárez, Isauro Rivera, Francisco Patiño, María I. Reyes., *Efecto de la temperatura y concentración de tiosulfatos sobre la velocidad de disolución de la plata en medio $S_2O_3^{2-}$-O_2–Zn^{2+}.* Inf. Tecnol., 23(4), 2012.

Characterization of Minerals, Metals, and Materials 2015
Edited by: John S. Carpenter, Chenguang Bai, Juan Pablo Escobedo, Jiann-Yang Hwang, Shadia Ikhmayies, Bowen Li, Jian Li, Sergio Neves Monteiro, Zhiwei Peng, and Mingming Zhang
TMS (The Minerals, Metals & Materials Society), 2015

PHOTOCATALYTIC H_2 PRODUCTION UNDER VISIBLE LIGHT IRRADIATION ON NOVEL HETEROSTRUCTURE NIS/ZNS NANOSHEET PHOTOCATALYST

Likun Li[a] *, Junfu Chen[b], Jiann-Yang Hwang[a], JiXiong Liu[b] , Yong Zhou[b], Lijun Lu[b]
[a.]Advanced Materials R&D center of WISCO, Beijing 102211, Beijing, China
[b.]Resource and Envionment Section of R&D WISCO, Wuhan, 430080, China

Keywords: Heterostructure; Photocatalytic; NiS/ZnS;H_2 production

Abstract

The sheet-like NiS-ZnS heterostructured composites were prepared by the microwave hydrothermal. The fabrication of the heterojunctions broadened the range of light response of ZnS. The photoexcited electrons of ZnS migrated to the redox potential of NiS/Ni_2S under visible light irradiation, which can facilitate the effective separation of photogenerated electrons and holes in space. The visible photocatalytic activity towards hydrogen production for NiS/ZnS nanosheet heterostructed composites without co-catalyst achieved 0.28 mmol h^{-1}, and the quantum efficiency was up to 18.6% under the wavelength with 420 nm visible light irradiation.

Introduction

As a potential answer to the global energy crises and environmental pollution, the application of hydrogen energy has attracted great attention[1]. At present, hydrogen is mainly produced from fossil fuels or the high-energy consumption process, which are not environmentally friendly and economic[2]. Therefore, photocatalytic water splitting using semiconductors photocatalysts has received more and more attention[3], which is a promising approach for clean, low-cost and environmentally friendly production of hydrogen by using solar energy [4,5]. TiO_2, as one of the first photocatalysts, has been widely used for photocatalytic water splitting [6,7]. However, due to the large band gap (i.e., 3.2 eV for anatase and 3.0 eV for rutile), it could only absorb the UV light, which accounts for only 4% of the total sunlight, and thus restricts its practical applications. So it is highly desirable to develop photocatalysts with high activities under visible light illumination.

Recently, metal sulfides have been intensively studied due to their unique catalytic functions and regarded as good candidates for visible-light-driven photocatalysts [8-10]. Among them, with a narrow band gap (2.4 eV), CdS is the most often applied for photocatalytic H_2-production due to its high activity under visible light and sufficiently negative flat-band potential[11,12]. However, pure CdS is usually not very active in hydrogen production and need of employing noble metal as co-catalysts [13,14]. These noble metals (e.g., Pt, Pd, Rh, Ru, Au) which loaded on semiconductor photocatalysts could efficiently separate photogenerated electrons and holes, and play an important role in the production of H_2 or O_2. Moreover, cocatalysts

offer the low activation potentials for H_2 or O_2 evolution and are often served as the active sites for H_2 or O_2 generation[15-17]. However, in the view of practical application of photocatalytic hydrogen production technique, cost reduction of the photocatalyst is one of the key issues. Thus, efficient photocatalysts without the presence of noble metals have become very attractive. In this regard, numerous efforts have been undertaken to replace noble metals with low-cost additives [18,19]. Taking CdS into account, attempts have also been made to combine a second material (e.g., oxides, sulfide, polymer matrix, transition metal carbides[20-23]) instead of noble metals to improve the photocatalytic H_2-production rate of CdS. In particular, some metal sulfides which have been demonstrated high activity in H_2 involved reactions in heterostructure catalysis[24-26] are suitable candidates for working as a cocatalyst. For example, Li et al. [27,28] found that the activity of CdS can be enormously increased by loading MoS_2 as a cocatalyst though impregnation of molybdenum precursor and subsequent thermal treatment in H_2S. Yan et al.[29] reported that CdS loaded with Pt and PdS achieved the highest reported quantum yield of about 93% in the presence of sacrificial reagents under visible-light irradiation. Some other metal sulfides such as Ag_2S[30,31], SrS[32] are also useful for the enhancement of the photocatalytic H_2-production activity of CdS. However, it is should be noted that these effective sulfides such as MoS_2, Ag_2S and PdS are also very expensive. Thus it is interesting to find out other sulfides which are inexpensive and common used.What's more CdS is a toxic substance and harmful to the environment. In particular ZnS, a II-VI group compound semiconductor, is an important material with a band gap energy (*E*g) of 3.6 eV. Due to its excellent properties of luminescence and photochemistry, its nanostructures have been studied extensively and reported in recent years. Zhang[33] report a remarkble work about CuS/ZnS p orous nanosheets by hydrothermal and cation exchange methods, the as-prepared CuS/ZnS porous nanosheets reach a high H_2 production rate of 4147 μmol $h^{-1}g^{-1}$ at CuS loading content of 2 mol % and an apparent quantum efficiency of 20% at 420 nm, however its prapeard time are quite a severial hours.

In this paper, the Intercrossed heterostrcture NiS/ZnS Nanosheet photocatalyst were first fabricated here by a simple microwave hydrothermal method in short period time, and which shows highly visible light-driven photocatalytic H_2-production activity from aqueous solutions containing Na_2S and Na_2SO_3 without Pt cocatalyst. Since single component semiconductors, such as CdS and TiO_2, usually could not obtain high photoefficiency and high activity for H_2 production. the heterostructure photocatalysts could give rise to an interparticle electron transfer which could enhance the rate of H_2 production when mixed semiconductors contact intimately. This intimate contact can also be called as microheterojunction formed between two semiconductors.Composite CuS/ZnS photocatalyst was prepared and applied to the photocatalytic Water Splitting to produce H_2. The activity for H_2 evolution was better than that of the pure CuS or ZnS, and the same time broaden ZnS's light response range, from UV expand to the visible light, which show excellent visible-driven photocatalytic H_2-production activity.

Experimental Procedure

Synthesis of $ZnS(en)_{0.5}$ precursor. $ZnS(en)_{0.5}$ nanosheets were prepared by a typical hydrothermal synthesis method,1.5 g $Zn(NO_3)_2$ and3.0 g thiourea were dissolved in 40 mL of ethylenediamine under constant stirring and last for30 min. then mixed solution transferred to a 70-mL reaction kettle liningand maintained at 150 °C for 50 min. After that, the as-prepared sample were washed with distilled water and ethanowas collected by centrifuge, at last, centrifuge and dry.

Synthesis of NiS/ZnS nanosheets. $ZnS(en)_{0.5}$ nanosheets (0.15 g) were ultrasonically dispersed in water, and then a certain amount volume of $Ni(NO_3)_2$was added stirring for 30 min at room temperature. 70-mL reaction kettle liningand maintained at 140 °C for 30 min. at last, the as-prepared samples were washed,centrifuged and dry.and the several molar ratio of Ni/Zn is equal to0.6, 1.2,1.8,2.4,3.0.

Characterization Methods

X-ray power diffraction (XRD) patterns were obtained on a D/Max-RBX X-ray diffractometer (Rigaku, Japan) using Cu Kα irradiation at a scan rate of 0.05°/s. sccan electron microscopy (SEM) image were obtained by S4800. UV-Vis diffuse reflectance spectra (DRS) of the samples were obtained on a UV-2550 UV-Vis spectrophotometer (Shimadzu, Japan). $BaSO_4$ was used as a reflectance standard in the UV-Vis diffuse reflectance experiment.

Results and Discussion

Composition and morphology

Figure 1 shows the SEM image of the typical sample of 1.8 mol.%NiS/ZnS. Through Fig1a,it can be seen that the sample of $ZnS(en)_{0.5}$ nanosheets exhibits typical sheet-like structure,The dimension which in the range about 500~700 nm. After second microwave hydrothermal method,which can be shown in Fig 1 b, NiS/ZnS still maintain nanosheet structure and the dimension slightly reduced to 400~700 nm.

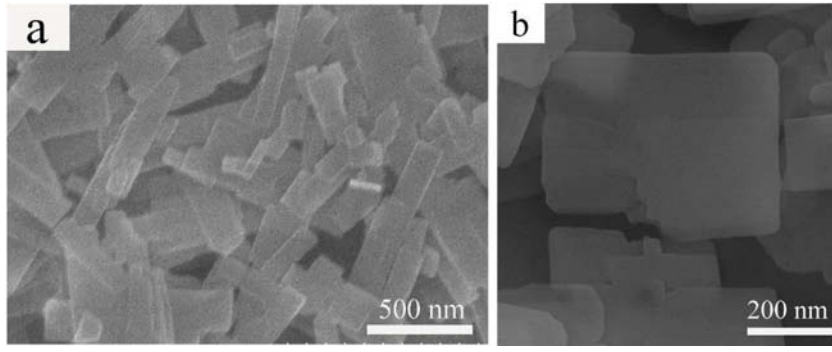

Figure 1 SEM image of the $ZnS(en)_{0.5}$(a), 1.6 mol.% NiS/ZnS (b)

Figure2 shows the XRD patterns of the series as-preapered sanples with different

mol.%NiS/ZnS. In Figure2 the obvious characteristic NiS phase is not detected by XRD here, that mabe NiS show weak crystallization and low content of this heterostructure which difficult for XRD to test, however through XRD result, it can be obtain the rule that with increasing NiS molar content, the diffraction peaks of ZnS become weaker, and at same time becomes to slightly wider. According to Scherrer formula, It implys that the crystallinity of ZnS tend to decreased and its average size of the crystal particle also become smaller. Further more, it is start to appear characteristic peak of NiS which the content of Ni added.

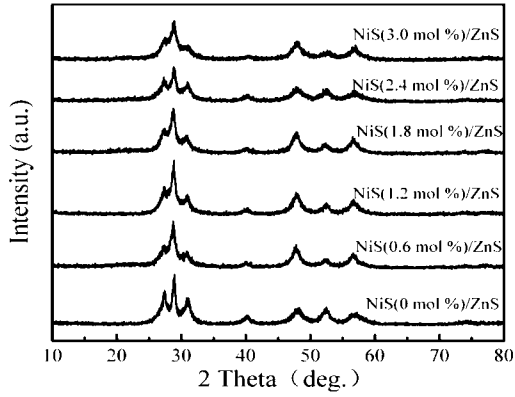

Figure 2. XRD patterns of the as-prepared samples with different Ni content

Optical property

UV–vis DRS of ZnS and the as-prepared NiS/ZnS composites with different Ni contents are shown in Figure 3. It can be clearly observed that ZnS possesses the largest absorption edge at 360 nm. Once NiS partical begin despersed on the surface of ZnS nanosheets, a clear red-shift of the absorption edge occurs for the series as-prepared NiS/ZnS heterostructer. This indicates that the constructed heterogeneous structure, can effectively extend the response optical light wavelength range of the ZnS based photocatalyst, after NiS particals and ZnS crystalline grain conbatin together to form heterostrue, the absorption edge which shown in Figure3. can broaden to 650 nm. The absorption at 600 nm can be assigned to the d–d transition of Ni(II).

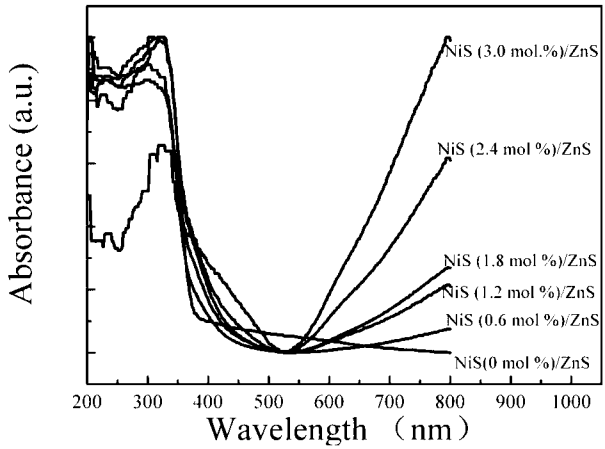

Figure 3 UV-vis absorption spectra of the heterostructure photocatalyst with different Ni content.

Photocatalytic activity for hydrogen production

The photocatalytic activities of the as-prepared NiS/ZnS nano-sheets photocatatysts as well as bare ZnS were evaluated in an aqueous solution containing 0.20 M Na_2SO_3 and 0.30 M Na_2S under visible light irradiation in Figure 3. Pure ZnS shows no H_2 production ability for the absorb wavelength of ZnS cannot visible light response according to UV-vis result. After NiS begin dopping on the surface of the ZnS, the photocatatystic activity of the as-prepared samples improved, when the content of NiS up to 1.8 mol. % the photocatalytic H_2-production activity of composites reaches the highest activity of 0.28 mmol h^{-1} and the corresponding apparent quantum efficiency is 18.6 % at 420 nm. The enhanced H_2 production rates of the as-prepared NiS/ZnS composites regardless of the Ni contents can be attributed to the separation of photogenerated charge between NiS and ZnS by the effect of heterostructure. However the further increasing of the content of NiS the H_2 production moles decreased. The reasonable explanation is that excessive deposition of NiS on ZnS surface caused new recombination of photogenerated charge carriers Moreover, the dopping of excessive NiS particals can decrease the surface active sites of ZnS.

The photoinduced interfacial charge transfer which photogenerated electron on ZnS valence band migrated to the redox potential of NiS/Ni_2S, which can further explains the novel heterostructure could response on the visible light and show excellent photocatalytic hydrogen production quantum efficiency, the follow figure gives more intuitive reveal of photogenerated charge carries separation on heterojunction among NiS and ZnS.

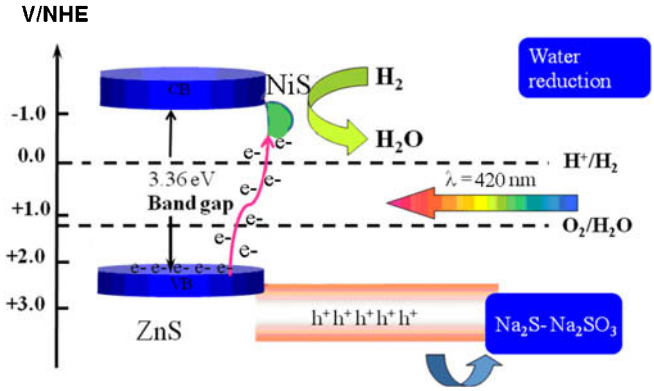

Figure4. Schematic illustration of Ni/ZnS heterostructure as the proposed mechanism for photocatalytic H_2 production.

Conclusions

In summary, In this paper, we have fabricated a novel NiS/ZnS heterostructure pholocatalyst utilized microwave hydrothermal method, under visble light irradiation, this heterostructure performs highly photocatalytic hydrogen prodction activity. The optimal content of NiS was 1.8 mol.% and the rate of hydrogen productin can reached up to 0.28 mmol h^{-1}. The corresponding apparent quantum efficiency is 18.6 % at 420 nm. The construction of the heterojunctions broadened the range of light response of ZnS. The photoexcited electrons of ZnS migrated to the redox potential of NiS/Ni_2S under visible light irradiation, which can facilitate the effective separation of photogenerated electrons and holes in space.

References

1. R.D. Cortright, R.R. Davda, and J.A. Dumesic. "Hydrogen from catalytic reforming of biomass-derived hydrocarbons in liquid water," Nature, 418(6901)(2002), 964-967.
2. Turner and A. John. "Sustainable hydrogen production," Science,305(5686)(2004), 972-974.
3. Kasuga, Tomoko, et al. "Formation of titanium oxide nanotube," Langmuir, 14(12)(1998), 3160-3163.
4. Kudo, Akihiko, and Yugo Miseki. "Heterogeneous photocatalyst materials for water splitting," Chemical Society Reviews, 38(1)(2009), 253-278.
5. Kim, Hyun Gyu, Dong Won Hwang, and Jae Sung Lee. "An undoped, single-phase oxide photocatalyst working under visible light," Journal of the American Chemical Society, 126(29)(2004), 8912-8913.
6. J.G.. Yu, L.F. Qi, and Mietek Jaroniec. "Hydrogen production by photocatalytic water splitting over Pt/TiO2 nanosheets with exposed (001) facets," The Journal of Physical Chemistry, 114(30)(2010), 13118-13125.
7. X.B. Chen, and Samuel S. Mao. "Titanium dioxide nanomaterials: synthesis, properties, modifications, and applications," Chemical reviews,107(7)(2007),

2891-2959.
8. Linsebigler, L. Amy, G..Q. Lu, and T. John Yates Jr. "Photocatalysis on TiO_2 surfaces: principles, mechanisms, and selected results." Chemical reviews 95.3 (1995): 735-758.
9. J.G.. Yu,J. Zhang and S.W. Liu. "Ion-exchange synthesis and enhanced visible-light photoactivity of CuS/ZnS nanocomposite hollow spheres." The Journal of Physical Chemistry , 114(32) (2010), 13642-13649.
10. J.G.. Yu, and J. Zhang. "A simple template-free approach to TiO_2 hollow spheres with enhanced photocatalytic activity," Dalton Transactions ,39(25)(2010), 5860-5867.
11. Matsumura, Michio, et al. "Cadmium sulfide photocatalyzed hydrogen production from aqueous solutions of sulfite: effect of crystal structure and preparation method of the catalyst," The Journal of Physical Chemistry, 89(8) (1985), 1327-1329.
12. Reber, Jean Francois, and Milos Rusek. "Photochemical hydrogen production with platinized suspensions of cadmium sulfide and cadmium zinc sulfide modified by silver sulfide," The Journal of Physical Chemis y C , 90(5) (1986), 824-834.
13. Frank, Arthur J., and Kenji Honda. "Visible-light-induced water cleavage and stabilization of n-type cadmium sulfide to photocorrosion with surface-attached polypyrrole-catalyst coating," The Journal of Physical Chemistry C , 86(11)(1982), 1933-1935.
14. N.Z. Bao, et al. "Facile Cd-thiourea complex thermolysis synthesis of phase-controlled CdS nanocrystals for photocatalytic hydrogen production under visible light," The Journal of Physical Chemistry C, 111(47) (2007), 17527-17534.
15. Maeda, Kazuhiko, and Kazunari Domen. "New non-oxide photocatalysts designed for overall water splitting under visible light," The Journal of Physical Chemistry C, 111(22) (2007), 7851-7861.
16. Ohno, Tomoyuki, et al. "Photocatalytic water splitting using modified GaN: ZnO solid solution under visible light: long-time operation and regeneration of activity," Journal of the American Chemical Society, 134(19) (2012), 8254-8259.
17. Kato, Hideki, Kiyotaka Asakura, and Akihiko Kudo. "Highly efficient water splitting into H_2 and O_2 over lanthanum-doped $NaTaO_3$ photocatalysts with high crystallinity and surface nanostructure," Journal of the American Chemical Society 125(10)(2003), 3082-3089.
18. J. Bandara, C. P. K. Udawatta, and C. S. K. Rajapakse. "Highly stable CuO incorporated TiO_2 catalyst for photocatalytic hydrogen production from H_2O," Photochemical & Photobiological Sciences, 4(11) (2005), 857-861.
19. J.G.. Yu, J. Zhang, and Mietek Jaroniec. "Preparation and enhanced visible-light photocatalytic H 2-production activity of CdS quantum dots-sensitized Zn 1− x Cd x S solid solution," Green Chemistry 12(9) (2010), 1611-1614.
20. Innocenti, M., et al. "Ternary cadmium and zinc sulfides: composition, morphology and photoelectrochemistry," Electrochimica acta, 49(8)(2004), 1327-1337.
21. Yoshimura, Joji, et al. "Visible Light Induced Hydrogen Evolution on CdS/K4Nb6O17 Photocatalyst," Bulletin of the chemical society of Japan, 68(8)

(1995), 2439-2445.
22. H.Zhang , and Y.F. Zhu. "Significant visible photoactivity and antiphotocorrosion performance of CdS photocatalysts after monolayer polyaniline hybridization," The Journal of Physical Chemistry C, 114(13) (2010), 5822-5826.
23. Jang, Jum Suk, et al. "Role of platinum-like tungsten carbide as cocatalyst of CdS photocatalyst for hydrogen production under visible light irradiation,"Applied Catalysis A: General ,346(1)(2008), 149-154.
24. Bataille, Frédéric, et al. "Alkyldibenzothiophenes hydrodesulfurization-promoter effect, reactivity, and reaction mechanism," Journal of catalysis,191(2)(2000), 409-422.
25. Chianelli, Russell R., et al. "Catalytic properties of single layers of transition metal sulfide catalytic materials," Catalysis Reviews , 48(1) (2006), 1-41.
26. Moses, Poul Georg, et al. "Corrigendum to "The hydrogenation and direct desulfurization reaction pathway in thiophene hydrodesulfurization over MoS< sub> 2</sub> catalysts at realistic conditions: A density functional study," Journal of Catalysis , 260(1)(2008), 202-203.
27. Y.P. Bi, et al. "Facile synthesis of rhombic dodecahedral AgX/Ag 3 PO 4 (X= Cl, Br, I) heterocrystals with enhanced photocatalytic properties and stabilities," Physical Chemistry Chemical Physics, 13(21) (2011), 10071-10075.
28. Z. Xu, et al. "Photocatalytic H2 evolution on MoS2/CdS catalysts under visible light irradiation," The Journal of Physical Chemistry C, 114(4) (2010), 1963-1968.
29. H. J. Yan, J. H. Yang, G. J. Ma, G. P. Wu, X. Zong, Z. B. Lei, J. Y. Shi, C. Li, Visible-lightdriven hydrogen production with extremely high quantum efficiency on Pt–PdS/CdS photocatalyst. Journal of catalysis, 266(2009), 165–168.
30. Reber, Jean Francois, and Milos Rusek. "Photochemical hydrogen production with platinized suspensions of cadmium sulfide and cadmium zinc sulfide modified by silver sulfide," The Journal of Physical Chemistry , 90(5) (1986), 824-834.
31. S.H. Shen, et al. "Effect of Ag< sub> 2</sub> S on solar-driven photocatalytic hydrogen evolution of nanostructured CdS," international journal of hydrogen energy ,35(13) (2010), 7110-7115.
32. H.P. Liu, et al. "SrS/CdS composite powder as a novel photocatalyst for hydrogen production under visible light irradiation," International Journal of Hydrogen Energy, 35(13) (2010), 7080-7086.
33. J. Zhang, J. G. Yu, M. Jaroniec. "Noble metal-free reduced graphene oxide-ZnxCd$_{1-x}$S nanocomposite with enhanced solar photocatalytic H_2-production performance,". Nano Letter., 12 (2012),: 4584-4589.

AUTHOR INDEX
Characterization of Minerals, Metals, and Materials 2015

N

O

P

Q

R

S

T

V

SUBJECT INDEX
Characterization of Minerals, Metals, and Materials 2015

E

F

G

H

I

L

M

N

O

P

R

S

T

U

V

W

X

Z

WILEY END USER LICENSE AGREEMENT

Go to www.wiley.com/go/eula to access Wiley’s ebook EULA.